ISSN: 2448-5624

Memorias del Congreso Internacional de Energía de la Academia Mexicana de Energía

No. 1
Enero 2014-Diciembre 2015
Publicación bianual

Energía y desarrollo en el siglo XXI: Un enfoque globalizado

Academia Mexicana de Energía, A.C.

MEMORIAS DEL CONGRESO INTERNACIONAL DE ENERGÍA DE LA ACADEMIA MEXICANA DE ENERGÍA. Núm. 1, enero 2014-diciembre 2015, es una publicación bianual de la Academia Mexicana de Energía, A.C. Calle Tehuantepec No. 39, Col. Roma Sur, Alcaldía Cuauhtémoc, C.P. 06760 Ciudad de México, México. Página electrónica de la revista: _____ y dirección electrónica: jacl@azc.uam.mx Editor responsable: Dr. José Antonio Colín Luna. Certificado de Reserva de Derechos al Uso Exclusivo del Título número en trámite, ISSN: 2448-5624, ambos otorgados por el Instituto Nacional del Derecho de Autor. Responsable de la última actualización de este número: Dr. José Antonio Colín Luna. Calle Tehuantepec No. 39, Col. Roma Sur, Alcaldía Cuauhtémoc, C.P. 06760 Ciudad de México, México. Fecha de última modificación: _____ de ____ de 2023. Tamaño del archivo ___ MB.

CONGRESO INTERNACIONAL DE ENERGÍA 2015 (CIE 2015)/
INTERNATIONAL ENERGY CONFERENCE 2015 (IEC 2015)

CIE 2015

Congreso Internacional de Energía
International Energy Conference 2015

Memoria de la Conferencia

Conference Proceedings

"Energía y desarrollo en el siglo XXI: un enfoque globalizado"

"Energy and development in the XXI century: a global approach"

Ciudad de México, D.F., México
7 - 11 - Sep 2015

ACADEMIA MEXICANA DE ENERGÍA A. C.

Instituciones Organizadoras/ Organizing Institutions

ACADEMIA MEXICANA DE ENERGÍA, A. C.

PRESIDENTA
Margarita Mercedes González Brambila

VICEPRESIDENTE
Carlos Omar Castillo Araiza

SECRETARIO
José Antonio Colín Luna

TESORERA
Ismene Libertad Rosales Plascencia

VOCAL DE COMISIONES DE ESPECIALIDAD
Rocío Sánchez Pérez

VOCAL DE COMUNICACIÓN
José Juan Martínez Nates

VOCAL DE DELEGACIONES Y REPRESENTACIONES REGIONALES
Ma. Del Carmen Monterrubio Badillo

VOCAL DE EVENTOS TÉCNICOS
Isaías Hernández Pérez

VOCAL DE RELACIONES INSTITUCIONALES
Ahmed Zekkour Zekkour

UNIVERSIDAD AUTÓNOMA METROPOLITANA

RECTOR GENERAL
Salvador Vega y León

SECRETARIO GENERAL
Norberto Manjarrez Álvarez

UNIDAD AZCAPOTZALCO

Rector
Romualdo López Zárate

Secretario
Abelardo González Aragón

UNIDAD CUAJIMALPA

Rector
Eduardo Peñalosa Castro

Secretaria
Caridad García Hernández

UNIDAD IZTAPALAPA

Rector
José Octavio Nateras Domínguez

Secretario
Miguel Ángel Gómez Fonseca

UNIDAD LERMA

Rector
Emilio Sordo Zabay

UNIDAD XOCHIMILCO

Rectora
Patricia Emilia Alfaro Moctezuma

Secretario
Guillermo Joaquín Jiménez Mercado

INSTITUTO POLITÉCNICO NACIONAL

DIRECTOR GENERAL
Enrique Fernández Fassnacht

SECRETARIO GENERAL
Julio Gregorio Mendoza Álvarez

SECRETARIO ACADÉMICO
Miguel Ángel Álvarez Gómez

SECRETARIO DE INVESTIGACIÓN Y POSGRADO
José Guadalupe Trujillo Ferrera

CENTRO MEXICANO PARA LA PRODUCCIÓN MÁS LIMPIA

Director
Rogelio Sotelo Boyás

Subdirector de Posgrado
Rubén Vázquez Medina

INSTITUTO TECNOLÓGICO DE QUERÉTARO

DIRECTOR
José López Muñoz

Subdirector Académico
Rodolfo López Vázquez

Subdirectora de Servicios Administrativos
Rosa Aidee Domínguez Ochoa

Subdirectora Planeación y Vinculación
Martha Aracelí López Sauri

UNIVERSIDAD IBEROAMERICANA

RECTOR
David Fernández Dávalos

Director del Departamento de Ingenierías
Maestro Jorge Martínez Alarcón

Palabras de Bienvenida

La Academia Mexicana de Energía A.C., la Universidad Autónoma Metropolitana, el Instituto Politécnico Nacional, la Universidad Iberoamericana y el Instituto Tecnológico de Querétaro se complacen de contar con su participación en el Congreso Internacional de Energía 2015.

Este Congreso es un evento interdisciplinar que tiene por objeto conocer los avances en Fuentes convencionales de energía, Generación y fuentes alternas de energía, Uso eficiente de la energía, Sustentabilidad, Políticas públicas, Educación y cultura, Auditoría de energía y Evaluación del ciclo de vida; para analizar, discutir y proponer proyectos de investigación básica y aplicada, desarrollo tecnológico y políticas en materia de energía.

Por otra parte, reúne a personalidades de los ámbitos industrial, académico, político, e incluso del sector energético público y privado, con el objetivo de crear un espacio en que se logre la difusión del conocimiento, pero esencialmente la cooperación y vinculación de todos estos sectores. Esperamos que esta vinculación genere proyectos de gran trascendencia que impacten en el sector energético.

Entre las actividades del Congreso se contará con la participación de plenaristas a nivel internacional como el Dr. Ignacio Grossmann de la Universidad de Carnegie Mellon, del Dr. Christopher Scott de la Universidad de Arizona, del Dr. Jesús Santamaría de la Universidad de Zaragoza, del Dr. Hugo De Lasa de la Universidad de Western Ontario, del Dr. José Miguel González Santaló del Instituto de Investigaciones Eléctricas, del Dr. Pablo Mulas del Pozo del Capítulo México del Consejo Mundial de Energía, y del Profesor Elio Santacesaria experto en procesos de producción de Biodiesel de la Università degli Studi di Napoli Federico II y fundador también de Eurochem Engineering.

Además de las conferencias magistrales, se ofrecerán talleres previos al Congreso donde se impartirán cursos sobre la utilización de paquetes de software especializados y eficiencia energética, entre otros.

Esperamos que este Congreso sea provechoso para todos ustedes.

¡Sean todos Bienvenidos!

Dra. Margarita M. González Brambila
Universidad Autónoma Metropolitana – Azc
México
Presidente

Dr. Carlos Omar Castillo Araiza
Universidad Autónoma Metropolitana – Izt
México
Vice-Presidente

Chairmans´ Welcome

The Mexican Academy of Energy A.C., the Universidad Autónoma Metropolitana, the Instituto Politécnico Nacional, the Universidad Iberoamericana and the Instituto Tecnológico de Querétaro are pleased to have your participation in the International Energy Conference 2015.

This Conference is an interdisciplinary event aimed to know the progress on different worldwide energy topics: conventional sources of energy, generation and alternative energy sources, efficient energy use, sustainability, public policy, education and culture, energy audit and life cycle assessment. The International Energy Congress 2015, has as main goal to analyze, discuss and propose projects for basic and applied research, technological development and energy policies.

This Conference gathers personalities from the industrial, academic, political, and even areas of public and private energy sector with the aim of creating a space, in which the diffusion of knowledge takes place, but essentially the cooperation and involvement of all these sectors. We hope this conference allows linking those projects of great importance on the energy sector.

Among the activities of the Conference, there will be the participation of international and Plenary Speakers. Namely Dr. Ignacio Grossmann, Carnegie Mellon University, Dr. Christopher Scott, the University of Arizona, Dr. Jesús Santamaría, University of Zaragoza, Dr. Hugo De Lasa, University of Western Ontario, Dr. José Miguel González Santaló, Electric Power Research Institute, Dr. Pablo Pozo Mulas, the Mexico Chapter of the World Energy Council, and Professor Elio Santacesaria of the Università degli Studi di Napoli Federico II.

In addition to the keynote talks the Conference will offer courses on the use of specialized software packages, on energy efficiency, among others.

We do hope that this Conference will be helpful for all of us.

Welcome.

Dra. Margarita M. González Brambila
Universidad Autónoma Metropolitana – Azc
México
Presidente

Dr. Carlos Omar Castillo Araiza
Universidad Autónoma Metropolitana – Iztapalapa
México
Vice-Presidente

Comité Organizador/Organizing Committee

Dra. Margarita M. González Brambila.
Universidad Autónoma Metropolitana – Azc
México
Coordinadora General/Conference Chairman

Dr. Rubén Vázquez Medina
Instituto Politécnico Nacional
México
Coordinador Ejecutivo/Conference Vice-Chairman

Comité Académico/Academic Committee

Dr. Carlos Omar Castillo Araiza
Departamento de Ingeniería de Procesos e Hidráulica
Universidad Autónoma Metropolitana – Iztapalapa
México.

Dr. José Antonio Colín Luna
Departamento de Energía
Universidad Autónoma Metropolitana – Azcapotzalco
México.

Dr. Jesús Isidro González Trejo
Departamento de Sistemas
Universidad Autónoma Metropolitana – Azcapotzalco
México.

Dr. Abhishek Dutta
Faculty of Engineering Technology
KU Leuven, Campus Groep T Leuven
Belgium

C. Dr Ahmed Zekkour Zekkour
Departamento de Energía
Universidad Autónoma Metropolitana Azcapotzalco México.

Dr. Hugo Joaquín Ávila Paredes
Departamento de Ingeniería de Procesos e Hidráulica
Universidad Autónoma Metropolitana – Iztapalapa
México.

M. en D.I. José Juan Martínez Nates
Departamento de Energía
Universidad Autónoma Metropolitana – Azcapotzalco
México.

Dr. Jorge Ramírez Muñoz
Departamento de Energía
Universidad Autónoma Metropolitana – Azcapotzalco
México.

Comité Técnico/Technical Committee

Dra. Ismene Libertad Rosales Plascencia
Departamento de Energía
Universidad Autónoma Metropolitana – Azcapotzalco
México.

Dr. Isaías Hernández Pérez
Departamento de Ciencias Básicas
Universidad Autónoma Metropolitana – Azcapotzalco
México.

Dr. Jesús Isidro González Trejo
Departamento de Sistemas
Universidad Autónoma Metropolitana – Azcapotzalco
México.

Dr. Zeferino Damián Noriega
Departamento de Energía
Universidad Autónoma Metropolitana – Azcapotzalco
México.

Dr. Héctor Fernando Puebla Núñez
Departamento de Energía
Universidad Autónoma Metropolitana – Azcapotzalco
México.

M. en C. Francisco Martín del Campo
Coordinador de Ingeniería Mecánica y Eléctrica
Departamento de Ingenierías
Universidad Iberoamericana. México.

M. en I. Roberto Alcántara Ramírez
Jefe del Departamento de Electrónica
Universidad Autónoma Metropolitana – Azcapotzalco
México

Dra. Rocío Sánchez Pérez
Centro Mexicano para la Producción más Limpia
Instituto Politécnico Nacional
México

Dra. Ma del Carmen Monterrubio Badillo
Centro Mexicano para la Producción más Limpia
Instituto Politécnico Nacional
México

M. en I. Hernando Chagolla Gaona
Instituto Tecnológico de Celaya
México

Dr. José Miguel González Santaló
Director de la División de Sistemas Mecánicos
Instituto de Investigaciones Eléctricas
México

Dra. Ana Friesel
Technical University of Denmark
Denmark.

Dra. Blanca Estela Chávez Sandoval
Departamento de Energía
Universidad Autónoma Metropolitana – Azcapotzalco
México

M. en D. I. Héctor Barreiro Torres
Departamento Evaluación del Diseño en el Tiempo
Universidad Autónoma Metropolitana – Azcapotzalco
México

M. en C. Arturo Zúñiga López
Departamento de Electrónica
Universidad Autónoma Metropolitana - Azcapotzalco
México

Ing. Agustín Francisco Ruiz Amaya
Departamento de Electrónica
Universidad Autónoma Metropolitana - Azcapotzalco
México

Diseño de Imagen/Image design

Dra. Brenda Bravo Díaz
Instituto Politécnico Nacional
México

DCG. Elvia Palacios Barrera
Departamento Evaluación del Diseño en el Tiempo
Universidad Autónoma Metropolitana – Azcapotzalco
México

Gloria Takagui
Departamento Evaluación del Diseño en el Tiempo
Universidad Autónoma Metropolitana – Azcapotzalco
México

Soporte Técnico/Technical Support

Ing. Rogelio David Conde Orrante
Maestría en Ciencias de Ingeniería en Sistemas Energéticos
Sección de Estudios de Posgrado e Investigación
Escuela Superior de Ingeniería Mecánica y Eléctrica Unidad Culhuacan
Instituto Politécnico Nacional
México

Comité Científico/ Scientific Committee

Dr. Ahmed Zekkour Zekkour (UAMA, México)
Dr. Alper Uzun (Universidad Koç, Turkey)
Dra. Ana Friesel (Technical University of Denmark)
Dra. Ana Karina Medina Mendoza (IMP, México)
Dr. Benito Serrano Rosales (Universidad Autónoma de Zacatecas, México)
Dr. Carlos Aníbal Chicojay Coloma (Universidad de San Carlos, Guatemala)
Dr. Carlos Omar Castillo Araiza (UAMI, México)
Dr. Carlos Chávez (UACM, México)
Dr. Christopher Scott (Universidad de Arizona, USA)
Dr. Daniel Romo Rico (IPN, México)
Dr. Eduardo Salvador Pérez Cisneros (UAMI, México)
Dr. Eliel Carvajal Quiroz (IPN, México)
Dr. Felipe Antonio Perdomo Hurtado (Universidad Nacional, Colombia)
Dr. Felipe López Isunza (UAMI, México)
Dr. Fernando Toledo Toledo (UAMA, México)
Dr. Francesco Ciucci (Universidad de Ciencia y Tecnología, Hong Kong)
Dr. Francisco José Torner Morales (UNAM, México)
M. en I. Francisco Martín del Campo (Universidad Iberoamericana, México)
Dra. Gretchen T. Lapidus Lavine (UAMI, México)
M. en D. I. Héctor Barreiro Torres (UAMA, México)
Dr. Hernando Chagolla Gaona (Instituto Tecnológico de Querétaro, México)
Dr. Humberto González Bravo (UAMA, México)
Dr. Hugo Joaquín Ávila Paredes (UAMI, México)
Dr. Ignacio Del Valle Granados (Instituto Tecnológico de Costa Rica)
Dr. Irving López García (UAMA, México)
Dra. Ismene Libertad Rosales Plascencia (UAMA, México)
Dr. Isaías Hernández Pérez (UAMA, México)
Dra. Ivette Montelongo (UAMA, México)
M. en I. Jaime Jasso López (WEG, México)
M Javier Antezana López (Universidad Tecnológica Nacional, Argentina)
Dr. Jorge Ramírez Muñoz (UAMA, México)
Dr. José A. Colín Luna (UAMA, México)
M. en D. José Juan Martínez Nates (UAMA, México)
Dr. José Miguel González Santaló (IIE, México)
Dr. Juan Carlos Fierro González (Instituto Tecnológico de Celaya, México)
M. Kelvin de Jesús Beleño Saenz (Universidad Autónoma del Caribe, Colombia)
Dra. Ma. Claudia Roldán Ahumada (UACM, México)
Dra. Ma del Carmen Monterrubio Badillo (IPN, México)
M. en I. Manuel Gordon Sánchez (UAMA, México)

Dr. Manuel Martínez Fernández (UNAM, México)
Dr. Meng Ni (Universidad Politécnica de Hong Kong)
Dr. Oscar Monroy Hermosillo (UAMI, México)
Dr. Pablo Mulas del Pozo (World Energy Council)
M. en I. Pedro Solares (Universidad Iberoamericana, México)
Dr. Raúl Suárez Parras (UNAM, México)
Dr. Ricardo Morales Rodríguez (UAG, México)
Dr. Ricardo Rafael Ambriz Rojas (IPN, México)
Dra. Rocío Sánchez Pérez (IPN, México)
Dra. Rosa Ma. Espinosa Valdemar (UAMA, México)
Dr. Rubén Dorantes (UAMA, México)
Dr. Umberto Anselmi-Tamburini (Universidad de Pavia, Italia)
Dr. Vicente Ayala Ahumada (UAMA, México)
Dr. Víctor Alcántara Alza (Universidad Nacional de Trujillo, Perú)
Dr. Zeferino Damián Noriega (UAMA, México)

Índice/Contents

		Pag
	Instituciones Organizadoras/Organizing Institutions	***ii***
	Palabras de Bienvenida/ Chairman´s Welcome	***vi***
	Comité Organizador/Organizing Committee	***viii***
	Comité Académico/Academic Committee	***viii***
	Comité Técnico/Technical Committee	***ix***
	Diseño de Imagen/Image design	***xi***
	Soporte Técnico/Technical Support	***xi***
	Comité Científico/Scientific Committee	***xii***
1/P5/EC5	Software SOLEEC optimization methodology for direct steam generation parabolic trough solar collectors designing	**1**
2/P1/EC1	Comparación de la Temperatura Máxima de dos Hidrocarburos con Aire Vs Oxígeno	**7**
3/P46/EC46	Novel Feedback Control to Improve Biohydrogen Production by Desulfovibrio alaskensis	**12**
4/P13/EC13	Estudio de la combustión no estequiométrica de la mezcla Metano-Nitrógeno con Oxígeno	**16**
5/P27/EC27	The mexican oil refining after the 2013 Energy Reform	**22**
6/P47/EC47	Silicon microwires by a combination of chemical etching techniques for application in Li ion batteries- proof of concept	**27**
7/P4/EC4	Flujo asimétrico en cámaras cilíndricas para distintos radios y fluidos	**31**
8/P14/EC14	Evaluation framework for small-dimension solar cookers	**39**
9/P66/EC66	Oxidative dehydrogenation of ethane: Reactor design for ethylene production	**44**
10/P68/EC68	Obtención del coeficiente de difusión en la reacción de fotodegradación del 4-Clorofenol	**49**
11/P8/EC8	Stabilization and control of a delayed recycle thermical process	**54**
12/P51/EC51	Modelling the effects of Si-X (X=F, Cl) bonds on the chemical and electronic	**60**

Índice/Contents

		Pag
	properties of Si-surface terminated porous 3C-SiC	
13/P9/EC9	Experimental Verification of a FPGA synchronization module for a DC energy storage bank of a sustainable electric grid	**66**
14/P49/EC49	Effective medium model for momentum transport in wind turbines	**74**
15/P10/EC10	Evaluation of opportunities for energy efficiency improvement, considering economic and environmental aspects, in a general hospital of Mexico City	**80**
16/P24/EC24	Quality analysis of biodiesel production obtained from crude avocado (Persea americana Mill. Hass, Fuerte and Criollo varieties) oils	**84**
17/P52/EC52	Issues on control of direct-drive wind turbine generators	**90**
18/P15/EC15	Experimental and computational analysis of single phase flow coiled flow inverter focusing on number of transfer units and effectiveness	**96**
19/P25/EC92	Thermal Performance and Sensitivity Analysis of a Parabolic Trough Solar Collector	**103**
20/P7/EC7	Sustainable production of hydrogen from synergy of Solid Oxide Fuel Cells and microreformers	**109**
21/P55/EC55	Analyzing the Stiffness of a Rotor with Triangular Cross Fracture	**115**
22/P56/EC56	Techno-economic analysis of the conceptual design of a biorefinery based on Agave Tequilana Weber	**121**
23/P40/EC40	Cooking time estimation for zucchini, eggplant and apple considering their inside temperature distribution using a solar cooker box-type with internal and external reflectors	**129**
24/P29/EC29	Análisis Térmico de las Celdas Fotovoltaicas en un Sistema Interconectado a la Red	**134**
25/P23/EC23	Pristine perovskite like structured nanowires excised from Sr_2FeMo_6	**139**
26/P2/EC2	Diseño de una Columna de Destilación Reactiva Multitarea para la Purificación de silanos	**143**
27/P26/EC26	Combustión de un Hidrocarburo con Oxígeno en Cámaras de Combustión Abiertas	**148**
28/P35/EC35	Dinámica de flujo sobre un banco de tubos planos	**154**

Índice/Contents

		Pag
29/P63/EC63	Construcción de un equipo medidor de la huella de carbono por consumo eléctrico para edificaciones en tiempo real	**160**
30/P60/EC60	Radiative transfer model of a solar thermochemical multi-tubular reactor: Geometric Optimization	**164**
31/P36/EC36	Simple Model Reduction For High Order Underdamped System	**169**
32/P32/EC32	Estudio y Diseño de una Granja Solar Fotovoltaica de 15 MWp en la Comunidad Indígena de Tzintzuntzan	**174**
33/P59/EC59	Process design for obtaining ethylene trough the oxidative dehydrogenation of ethene (odh-c2) over the multimetal oxide (Mo-Te-V-Nb-O)	**180**
34/P76/EC76	CFD Study of Power Draw of a Disc Plane Impeller in an Unbaffled Stirred Tank	**185**
35/P62/EC62	Descomposición de Óxidos Metálicos para la Producción de Hidrógeno con Energía Solar Concentrada	**191**
36/P38/EC38	Simulación y análisis de falla en tubos por los que circula vapor de agua sobrecalentado	**196**
37/P33/EC33	Proyecto FEL I sobre la factibilidad de una tecnología sustentable para satisfacer el requerimiento energético en la FIQ de la BUAP	**200**
38/P39/EC39	Estudio numérico del comportamiento térmico de superficies extendidas con variaciones en sus secciones transversales y materiales	**208**
39/P43/EC43	Design and Construction of an Inexpensive Alkaline Electrolysis Cell for Transport Applications	**214**
40/P64/EC64	Electrochemical techniques to measure the degree of dispersion of solids inside an aqueous medium	**221**
41/P71/EC78	Ahorro y uso eficiente de energía eléctrica en sistemas de riego de cultivos localizados en el valle del mezquital que emplean aguas residuales no tratadas provenientes de la ciudad de México	**224**
42/P72/EC72	Acetone-Butanol-Ethanol Production from Sugarcane Bagasse: An Experimental & Simulation Analysis	**227**
43/P44/EC44	Nanotubos de Carbono: una Alternativa para Implementar las Celdas Fotovoltaicas	**236**

Índice/Contents

		Pag
44/P6/EC6	Theoretical study of the electronic properties of semiconductor nanowires as anodes for Lithium batteries	**243**
45/P11/EC11	Control de un convertidor CD/CA para aplicaciones en paneles solares	**248**
46/P73/EC73	Análisis exergoeconómico de variables críticas en el control operativo de una torre de enfriamiento	**254**
47/C40/EC85	Experiencias en temas de energía y medio ambiente	**266**
48/c102/Ec88	Energy production by catalytic ethanol steam reforming and combustion of H2	**271**
49/C100/EC82	Obtención de ácido cítrico a partir de papel como residuo sólido urbano por fermentación con Aspergillus niger 10	**275**
50/P12/EC12	Necesidad de redefinir la ingeniería y su método como base y fundamento en la formación de un ingeniero	**280**
51/P45/EC45	Rompiendo las barreras químicas y de ingeniería para la producción de biocombustibles: biorrefinerías de la próxima generación	**285**
52/P30/EC30	Diffusion Path in the Sr-Fe-Mo-O Compounds used for Energy Generation by SOFCs	**292**
53/P20/EC20	Desarrollo de una estufa solar para varios contenedores	**297**
54/P21/EC21	Simulation of an aeroderivative gas turbine via a chemical reactor Gibbs type	**302**
55/P58/EC58	Comparison tools for parametric identification of kinetic model for ethanol production using evolutionary optimization approach	**308**
56/K01/EC79	Fenton's process, a homogeneous or heterogeneous catalytic system?	**315**
57/P78/EC80	Degradación de pesticidas por fotocatálisis heterogénea usando nanopartículas de $Fe2O_3$ preparadas en suspensión acuosa	**319**
58/P16/EC16	Análisis termodinámico de combustibles sólidos quemados en la Central Termoeléctrica "Presidente Plutarco Elías Calles" (C. T. P. P. E. C.) de 2778 M	**322**
59/P42/C88/EC42	Simulación numérica en 2d de la evaporación del agua de una alberca pública	**326**
60/P41/EC41	Visualización del flujo en válvulas	**331**
61/P22/EC22	Determination of the operating Windows of an sweetening sour gas plant employing rigorous process simulators	**336**

Índice/Contents

		Pag
62/P54/EC54	Economic assessment of Velfor 100 Zeolite influence on alcoholic fermentation yields and productivity, performed by three strains of Saccharomyces cerevisiae	**346**
63/P57/EC57	Hydrogen production by a sustainable photocatalytic process using copper metallurgical slag as catalyst	**350**
64/P69/Ec91	Residential consumption of energy electric in Mazatlán: structure, alternatives and impact	**355**
65/P77/EC77	Síntesis y Optimización de un Sistema de Tratamiento Selectivo de Corrientes Efluentes Usando Tres Reactores Electroquímicos Continuos	**357**
66/P3/EC3	Optimización económica y ambiental del proceso para la purificación de biobutanol	**367**
67/P65/EC65	Tendencias actuales y futuras de estado en catálisis para la Refinación	**375**
68/P28/EC89	Expansor rotatorio de desplazamiento positivo para aprovechamiento de energía presente en el peróxido de hidrógeno	**382**
69/P75/EC75	Efecto de la Temperatura y Concentración en el Coeficiente de Partición de un Trazador Orgánico	**386**
70/P31/C48/EC31	Evaluation of the content of hydrolysable sugars in silage supplement processes	**389**
71/P34/EC34	Implementación y control de un ruteador de DC	**393**
72/P37/EC37	Estudio de parámetros de transporte de masa y cinéticos de un trazador químico utilizado en la recuperación de aceites remanentes en yacimientos de petróleo	**398**
73/P53/EC53	Desarrollo de un seguidor solar para un aprovechamiento eficiente de celdas fotovoltaicas para Ecatepec	**404**
74/P74/EC74	Determinación de los parámetros de adsorción de un trazador químico en roca de formación	**410**
75/P70/EC70	Microorganisms isolated from castle manure, involved in the production of methane	**413**
76/P48/EC48	Renewable Energy and Social Development	**419**
77/C72/EC86	Paquete computacional para el cálculo de flujos de potencia por	**424**

Índice/Contents

		Pag
	coordenadas de fase	
78/C50/EC96	Life cycle greenhouse gas emissions of electricity generated from a cogeneration project in Morelos petrochemical complex and CO2 capture options	**430**
79/P84/EC84	Understanding biodiesel spray by study of primary atomization phenomena implementing hybrid numerical schemes	**435**
80/P61/EC61	Olefins and Ethanol from Polyolefins, Chemical Recycling Simulation of Polyethylene and Polypropylene	**440**
81/P19/EC19	Conversion and use of biomass of *agave atrovirens* for the production of fuel bioethanol	**448**
82/C83/EC97	Reducción de la contaminación atmosférica en Lima Metropolitana por el uso de combustibles gaseosos en el parque automotor	**453**
83/C11/EC98	Autoabastecimiento energético en una comunidad rural tipo a partir de la biomasa	**457**
84/C84/EC99	Eliminación de compuestos orgánicos volátiles: Simulación de un reactor catalítico de lecho empacado para la eliminación total de tolueno	**462**
85/C103/EC100	Technology, urban society and nutritional sustainability for everyone	**469**

Software SOLEEC optimization methodology for direct steam generation parabolic trough solar collectors designing

Ernesto Enciso Contreras
Juan Gabriel Barbosa Saldaña
José Alfredo Jiménez Bernal
Claudia del Carmen Gutiérrez Torres
Sección de Estudios de Posgrado e Investigación
ESIME Zacatenco, Instituto Politécnico Nacional
Ciudad de México, México.
eencisoc@hotmail.com
jbarbosas@ipn.mx
jjimenezb@ipn.mx
cgutierrezt@ipn.mx

Abstract— The present work describes the methodology that is been carried out for software SOLEEC optimization (registered to Instituto Nacional del Derecho de Autor with the number 03-2012-070510302900-01). Software SOLEEC is a computational tool for parabolic trough solar collector (PTC) designing and assessment and also solar resource calculation for a specific place where solar technology is pretended to be installed. Software SOLEEC first version has some limitations: heat transfer fluid doesn´t have phase change, it means, liquid state is maintained, parabola rim angle is 90°, only one concentric coating tube is considered and space between the coating and absorber tubes is evacuated.
Main tasks which optimization stage pretends to cover for software SOLEEC are: PTC collector designing for direct steam generation system (DSG), considering the absorber tube in three sections: first for preheating, where water enters to ambient temperature and at the end reaches saturation temperature, at second section evaporation process begins taking the water from saturated liquid state to saturated steam state and at the third section, steam is superheated reaching the temperature condition imposed by the user.

During parabola designing process, optimal rim angle will be calculated for every particular case, depending on latitude where collector is pretended to be installed. Last task for software SOLEEC optimization is centered on PTC collector array assessment for serie, parallel and combinations.

Keywords—parabolic trough solar collectors; SOLEEC, optimization, direct steam generation system, solar energy.

I. INTRODUCTION

For the last 20 years, a considerable effort has been exerted in the design of solar thermal power plants with parabolic trough solar collector fields (PTC). Commercial plants currently working in USA has been using synthetic oil as the heat transfer medium. The outlet of the solar field is connected to a heat exchanger that generates steam to feed a turbine. As the primary energy source, solar radiation is not controllable, the main control parameter is the temperature of the oil at the outlet of the solar field, and the variable controlled is the mass flow at the field inlet.

The direct steam generation (DSG) in PTC collectors is a promising option for the improvement of the reliable parabolic trough technology for solar thermal energy. This technology can be used for electricity generation, process steam for the industry and for heating water or other kind of fluid.

Many works have being developed in this field, a new PTC system to investigate DSG in a solar field using water inside the collectors as the heat transfer medium was erected at Plataforma Solar de Almería, Spain, from 1996 until now, evaluating different operation modes and configurations with promising results for system commercialization [1].

INDITEP Project is another example, promoted by a Spanish-German consortium of engineering companies, power equipment manufacturers, research centers and businesses involved in the energy market. The 5MW plant is composed of a DSG system using PTC collectors connected to a superheated steam Rankine power cycle. The solar field produces superheated steam at 410 ℃ for a working pressure of 70 bar [2].

Some researches about this topic have been carried out in México, at the UNAM a PTC collector was analyzed for evaluating the feasibility of steam generation for electric energy

generation at low power and absorber tube behavior was analyzed as well [3].

Computational tools has become a very important auxiliary devices for processes designing, due to reliable information can be obtained having the advantage of low cost and faster results, offering to the designer the capability of carry out changes at the main variables involved under different conditions.

For PTC collectors analysis, computational tools have been developed for different purposes, such as Dymola/Modelica, used for evaluating a PTC field for DSG system, where water enters the field collector for being partially evaporated, after that is being transported to a separator. Condensed water is recirculated at the inlet of the solar field with constant mass flow while saturated steam is taken to superheating section which consist of another PTC solar field [4].

For optimizing DSG system, a separator tank is installed to a PTC solar field whose analysis was carried out using the tool PTCDES, used for determining the steam quantity produced by the system. Direct solar radiation for a horizontal surface values were used, taking the representative day of each month and air ambient temperature, taking as reference the annual data for Nicosia, Cyprus. Heat losses are taking into consideration, that is, tank separator body, pipes y pump, using the differences of enthalpies between hot water and the water of the separator, after that, steam production of the system is calculated [5].

IPSE-pro, which main objective is the simulation of the components for a conventional power plant has been modified with the purpose of a solar thermal power plant assessment [6].

Following the national strategies in the development of alternative energy technologies, the Instituto Politécnico Nacional has developed a software named SOLEEC, a computational tool for PTC collectors designing and assessment. Software SOLEEC has been finished the first stage, registered to Instituto Nacional de Derechos de Autor and the second stage is been developed which methodology is going to be described in this paper [7].

II. SOFTWARE SOLEEC DESCRIPTION

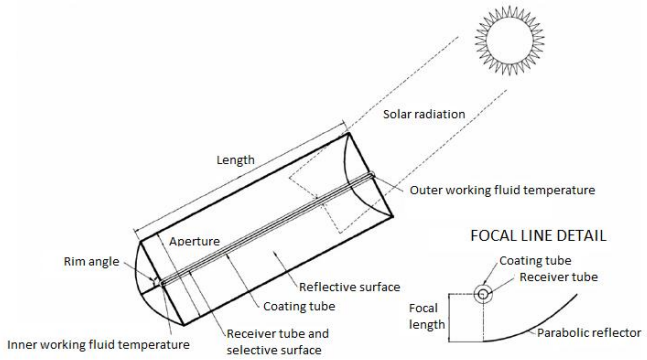

Fig. 1. Parabolic trough solar collector diagram.

A PTC collector consist of a sheet with parabolic cross section with a high reflectance surface, at the focus of the parabola is placed a tube which material must have high thermal conductivity, this tube must be recovered by a selective material for high solar radiation absorptivity and less emissivity. Surrounding the absorber, a coating transparent tube is placed concentric with high solar radiation transmisivity value. Into the absorber tube, the heat transfer fluid will gain energy due to the concentration of the solar radiation giving as a result a temperature increase at the outlet of the solar collector. Figure (1) shows a PTC collector diagram.

Software SOLEEC is a computational tool for PTC designing and assessment as well as solar resource calculation for a specific place on the Earth, figure (2) shows main menu and every option description is explained next.

Software SOLEEC consist of 2 main parts: the first one is for solar resource calculation with three different options:

- Data for a specific day of the year (Datos para un día específico del año).
- Data for a specific month of the year (Datos de un mes).
- Data for every month along the year (Datos mensuales a lo largo de un año).

Input data necessary for these options are: lattitude (°), altitude over sea level (km), choose a kind of climate, day (1-365) and month (1-12). Once data is introduced to the software, the results are showed in tables and charts giving data such as: extraterrestrial solar radiation (W/m^2), solar radiation on the Earth surface (W/m^2) using Hottel's model, the Earth declination along the year, the solar constant along the year, insolation hours for every day and sunrise and sunset hour for every day [8].

Fig. 2. Software SOLEEC main menu.

The second part of the software SOLEEC consists of four options for PTC collectors designing and assessment:

- PTC designing for 12 solar radiation values (Diseño del concentrador solar con 12 valores de irradiación solar).
- PTC designing for 1 solar radiation value (Diseño del concentrador solar con 1 valor de irradiación solar).
- PTC assessment for 12 solar radiation values (Evaluación de un concentrador con 12 valores de irradiación solar).
- PTC assessment for 1 solar radiation value (Evaluación de un concentrador con 1 valor de irradiación solar).

For PTC collector designing (option 1 and 2), the user must introduce some data such as: solar radiation values, choose among many different materials for PTC collector construction for reflective surface, absorber tube, selective surface, coating tube and heat transfer fluid. Also initial conditions, that is air ambient temperature (℃), air velocity (m/s), solar radiation incidence angle (°), inner and outer heat tranfer fluid temperature (℃). Once software SOLEEC is put into operation, results are given in tables for geometric and thermal parameters. For geometric, data is given such as: aperture (m), collector length (m) and focal distance (m). Also thermal data are given such as: heat gain (W), heat losses (W), mass flux (kg/s), volumetric flow (lt/min), optical efficiency (%), thermal efficiency (%), absorber tube temperature (℃) and coating tube temperature (℃).

For PTC collector assessment (option 3 and 4), the user must provide all thermal and optical characteristics for every material used in PTC collector construction, also geometric values and the software provide all thermal parameters mentioned before for PTC designing.

The heat gain is the most important parameter about thermal performance, this parameter is directly involved by all other parameters affecting PTC designing, and therefore, software SOLEEC internally develops an iterative process until equations (1) and (2) are evenly closer.

$$Q_{u1} = \dot{m}C_p\left(T_{fe} - T_{fi}\right) \tag{1}$$

$$Q_{u2} = F_R A_a \left[I - \frac{A_r}{A_a} U_L\left(T_{fi} - T_a\right)\right] \tag{2}$$

In (1) $\dot{m}$ represents mass flux (kg/s), C_p is the specific heat $(J/kg\ K)$, T_{fe} and T_{fi} represents outer and inner temperatures (℃) respectively, all properties for heat transfer fluid.

Equation (2) is exclusively for PTC collectors, where F_R is a flow factor, A_a and A_r (m^2) are the aperture area and absorber area respectively, I is the energy reaching the absorber tube (W/m^2), U_L represents the whole losses factor $(W/m^2\ K)$ and T_a is the ambient temprature (℃).

Equation (1) represents the heat gained internally in the working fluid as a function of its thermal characteristics, while (2) represents the heat gain quantity on solar collector taking into account the solar radiation available, the heat losses and the collector's geometry, thus, both equations involve the same concept of energy gain, the first one as the working fluid and the second one as the collector's performance point of view [9].

Software SOLEEC has some restrictions such as: parabola rim angle is 90° due to using this value, PTC collector reach the maximum concentration ratio, heat transfer fluid remain only in one phase, that is, there is no phase change, only considers one coating tube and space between absorber and coating tubes is evacuated.

Because of the restrictions before mentioned, software SOLEEC optimization in focused on three main tasks: direct steam generation system, parabola optimal rim angle for every case and PTC collector arrays assessment, serie, parallel and combinations. This paper is focused on methodology for DSG system which is explained in the next section.

III. SOFTWARE SOLEEC OPTIMIZATION METHODOLOGY

The first stage of software SOLEEC optimization is direct steam generation system and two phase change theory was consulted and applied, after reviewing some empirical correlation for determining main parameters involved during forced boiling, the next equation were selected.

In the direct steam generating trough collector, the absorber tube will be horizontal and the incident energy input can be considered uniform along the length of the absorber. If the feed water enters the collector at a temperature below the saturation temperature for the working pressure, the bulk temperature increases along the absorber up to the saturation temperature. After this point nucleate boiling in saturated water starts and after a small increase in quality the flow pattern changes to convective boiling or forced convective vaporization as can be seen in figure (3). The heat transfer from the wall to the water improves with increasing quality. For both nucleate boiling in a saturated liquid and convective boiling the heat transfer coefficient is influenced by bubble formation and convection in the liquid film. The heat transfer coefficient in the two phase flow region increases with quality due to increasing vapor shear stress. For high energy input or long collectors, dry out occurs and the low conductivity of dry steam leads to a decrease of internal heat transfer coefficient. The maximum heat transfer coefficient in the two phase flow region has been shown to occur al quality $x = 0.8$ for a wide range of mass flux conditions [10].

A. Heat transfer coefficient calculation

The software SOLEEC optimization for DSG system will consist of a thermal analysis of a direct boiling collector. The absorber tube will be divided into three sections to follows the phase change in the absorber.

The first section will be analyzed for fully developed single phase as can be observed in figure (3), where the heat transfer coefficient can be calculated form Dittus-Boelter correlation as follows:

$$h = 0.023Re^{0.8}Pr^{0.4}\frac{k}{d_{ri}} \tag{3}$$

Where Re is the Reynolds number, Pr is the Prandtl number, k is the fluid conductivity coefficient $(W/m\ K)$ and d_{ri} is the internal absorber diameter (m).

Software SOLEEC will find the necessary mass flux and minimum collector length going from initial water temperature to the saturation temperature at the working pressure.

The second section of the absorber will evaluate the two phase change, this section is characterized because of steam quality, from saturated liquid to saturated steam. This section is the most complex, due to flow patterns formation. As an initial condition, mass flux will be considered as constant. Software SOLEEC will find the minimal length going from saturated liquid to saturated steam.

The heat transfer coefficient is the most complex calculation for two phase change in order to evaluate it, the flow pattern must be determined using the Froude number as follows [11]:

$$Fr = \frac{G^2}{\rho_l^2 g d_{ri}} \tag{4}$$

Where G is the mass flux per unit of area (kg/m^2s), ρ_l is the liquid density (kg/m^3), g represents gravity acceleration (m/s^2).

If $Fr < 0.04$ stratified flow occurs and the heat transfer coefficient is given by Shah correlation [12].

$$\frac{h_{2ph}}{h_l} = 3.9Fr^{0.24}\left(\frac{x}{1-x}\right)^{0.64}\left(\frac{\rho_l}{\rho_g}\right)^{0.4} \tag{5}$$

The heat transfer coefficient for liquid h_l can be calculated modifying Dittus-Boelter equation assuming the liquid fraction fills the tube:

$$h_l = 0.023\left(\frac{G(1-x)d_{ri}}{\mu_l}\right)^{0.8} Pr^{0.4}\frac{k_l}{d_{ri}} \tag{6}$$

Where μ_l is the liquid viscosity (Ns/m^2) and k_l is the liquid conductivity coefficient $(W/m\ K)$.

If $Fr > 0.04$ the absorber tube is completely wet due to anular flow and the heat transfer coefficient can be determined by the Chan correlation. The two phase heat transfer coefficient has two independent components, bubble formation $h'_B = h_B S$ and convection $h'_l = h_l F$.

$$h_{2ph} = h'_B + h'_l \tag{7}$$

Where h_B is the heat transfer coefficient in nucleate boiling, h_l is the heat transfer coefficient for saturated water, and S and F are correction and enhancement factors. For determining h_B the next correlation is used [13].

$$h_B = 3800\left[\frac{q}{20000}\right]^n Fp \tag{8}$$

$$n = 0.9 - 0.3(P_n)^{0.15} \tag{9}$$

$$Fp = 2.55(P_n)^{0.27}\left(9 + \frac{1}{1-P_n^2}\right)P_n^2 \tag{10}$$

$$P_n = \frac{P}{P_{cr}} \tag{11}$$

Where q is the heat flux, in this case, the solar radiation, P is the working pressure (bar) and P_{cr} is the critical pressure for water (221 bar). The correction and enhancement factors S and F are given by next equations.

$$Bo = \frac{q}{\dot{m}\Delta h_{lg}} \tag{12}$$

$$F = 1 + (2.4X10^4)Bo^{1.16} + 1.37X_{tt}^{-0.85} \tag{13}$$

$$S = \frac{1}{1 + (1.15X10^{-6})F^2Re^{1.17}} \tag{14}$$

$$X_{tt} = \left(\frac{\rho_g}{\rho_l}\right)^{0.5}\left(\frac{\mu_l}{\mu_g}\right)^{0.1}\left(\frac{1-x}{x}\right)^{0.9} \tag{15}$$

Where Δh_{lg} is the heat of vaporization (J/kg), Bo is called boiling number and represents a dimensionless relation between the mass of steam generated per area unit of heat transfer and the

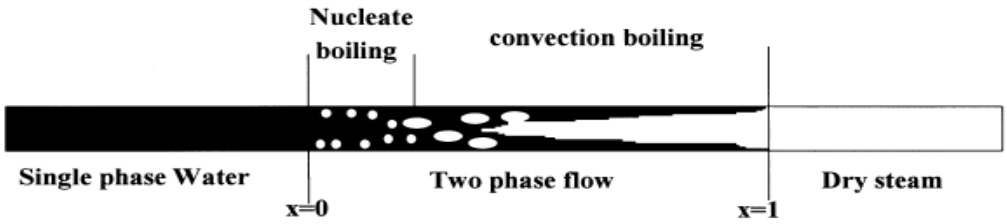

Fig. 3. Flow patterns in the absorber of a DSG system collector.

density of mass flux per cross area unit. X_{tt} is the Martinelli parameter.

Equations before mentioned are going to be used into software SOLEEC codex, in order to calculate the heat transfer coefficient, due to represents the most important and complex variable on heat transfer analysis.

After water become from saturated liquid to saturated steam, the third section of the absorber is superheating. In this section, saturated steam will be superheated to the final condition and temperature prescribed by the user. Software SOLEEC will find the minimal necessary length for reaching the temperature condition, also will calculate the quantity of steam produced. Mass flux is supposed to be constant. To evaluate the heat transfer coefficient for superheated steam, Dittus- Boelter equations is used like was presented in equation (3).

B. *Pressure drop calculation*

The two phase pressure drops for flow inside tubes are the sum of three contributions: the static pressure drop, the momentum pressure drop and the frictional pressure drop. For horizontal tubes, there is no change in static head while the momentum pressure drop reflects the change in kinetic energy of the flow.

The frictional pressure droop in two phase flows is typically predicted using separated flow models. The basic equations for the separated flow model are not dependent on the particular flow configuration adopted. It is assumed that the velocities of each phase are constant, in any given cross section, within the zone occupied by the phase.

There is some common methods for frictional pressure drop intube flow calculation, nevertheless, the most accurate for DSG systems has been identified as the model of Friedel as fitting best

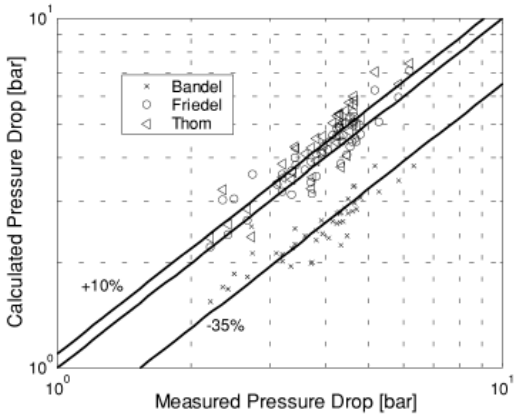

Fig. 4. Comparison of pressure drop measured and calculated for different models.

the results as is showed in the figure (4) [14].

The method for pressure drop calculation using the Friedel model utilizes a two phase multiplier.

$$\Delta P = \Delta P_L \Phi_{fr}^2 \tag{16}$$

$$\Delta P_L = 4 f_l \left(\frac{L}{d_{ri}}\right) G^2 \left(\frac{1}{2\rho_l}\right) \tag{17}$$

ΔP_L is calculated for the liquid phase and f_l is the liquid friction factor, L represents tube length (m).

$$f_l = \frac{0.079}{Re^{0.25}} \tag{18}$$

The Friedel two phase multiplier is calculated using the next equation.

$$\Phi_{fr}^2 = E + \frac{3.24 F_{fr} H}{Fr^{0.045} We^{0.035}} \tag{19}$$

Where Fr is the Froude number before mentioned, We represents Weber number and the dimensionless factors F_{fr}, H and E are calculated as follows.

$$We = \frac{G^2 d_{ri}}{\sigma \rho_h} \tag{20}$$

$$\rho_h = \left(\frac{x}{\rho_g} + \frac{1-x}{\rho_l}\right)^{-1} \tag{21}$$

$$E = (1-x)^2 + x^2 \frac{\rho_l f_g}{\rho_g f_l} \tag{22}$$

$$F_{fr} = x^{0.78}(1-x)^{0.224} \tag{23}$$

$$H = \left(\frac{\rho_l}{\rho_g}\right)^{0.91} \left(\frac{\mu_g}{\mu_l}\right)^{0.19} \left(1 - \frac{\mu_g}{\mu_l}\right)^{0.7} \tag{24}$$

Where σ is the surface tension (N/m), ρ_h is a homogenous density depending on steam quality and the densities for every phase. This method is typically recommended when the ratio μ_l/μ_g is less than 1000, but in the case of water, this ratio always reach below that value, also is applicable to vapor qualities from $0 \leq x \leq 1$ [15].

Once this optimization is done, the user could find the most important parameters for PTC designing and evaluation in a DSG system, including the geometrical characteristics and thermal parameters.

Other tasks for software SOLEEC optimization are: optimal parabola rim angle for every case and array evaluation for serie, parallel and combinations but these tasks are not discussed on this work.

IV. CONCLUSION

On this work, software SOLEEC optimization methodology for parabolic trough solar collector designing and assessment for direct steam generation system was analyzed.

The absorber tube will be divided into three segments, the first one for preheating, reaching the water from initial temperature to saturation temperature for the working pressure, software SOLEEC will find the minimal length for reaching that condition and necessary mass flux will be calculated.

The second stage will maintain constant mass flux, vaporization will start from saturated liquid to saturated steam and software SOLEEC will find the minimal length for reaching the condition. The most important and complex variable for this section is the heat transfer coefficient because of flow patterns formation dominating two main phenomena, nucleate boiling and convective boiling.

Once saturated steam condition is covered, next section will superheat the steam and software SOLEEC will find the minimal length for the final temperature condition dictated by the user also the quantity of vapor produced maintaining constant mass flux condition.

Also the pressure drop phenomena is going to be considered, analyzing some methods for frictional pressure drop in two phase flow, Friedel method is recommended due to the applicability and accuracy.

When this tasks of optimization are covered, software SOLEEC will become a full, versatile and profitable computational tool for parabolic trough solar collector designing and assessment.

REFERENCES

[1] L. Valenzuela, E. Zarza, M. Berenguel and E. F. Camacho, “Control concepts for direct steam generation in parabolic troughs,” Solar Energy, vol. 78, pp. 301-311, 2005.

[2] E. Zarza, M. E. Rojas, L. González, J. M. Caballero, F. Rueda, “INDITEP: The first pre-commercial DSG solar power plant,” Solar Energy, vol. 80, pp. 1270-1276, 2006.

[3] R. Almanza, A. Lentz and G. Jiménez, “Receiver behavior in direct steam generation with parabolic trough,” Solar Energy, vol. 61, pp. 275-278, 1997.

[4] J. Birnbaum, J. Feldhoff, M. Fitchner, T. Hirsch, M. Jöcker, R. Pitz-Paal and G. Zimmermann, “Steam temperature stability in a direct steam generation solar power plant,” Solar Energy, vol. 85, pp. 660-668, 2011.

[5] S. Kalogirou, S. Lloyd and J. Ward, “Modelling, optimization and performance evaluation of a parabolic trough solar collector steam generation system,” Solar Energy, vol. 60, pp. 49-59, 1997.

[6] M. Eck and E. Zarza, “Saturated steam process with direct steam generating parabolic troughs,” Solar Energy, vol. 80, pp. 1424-1433, 2006.

[7] SOLEEC, software, registered number 03-2012-070510302900-01, 2012.

[8] H. C. Hottel, “A simple model for estimating the transmittance of direct solar radiation trough clear atmospheres,” Solar Energy, vol. 129, 1976.

[9] S. Kalogirou, “Solar energy engineering processes and systems,” Elsevier Inc. pp. 200-202, 2009.

[10] S. D. Odeh, G. L. Morrison and M. Behnia, “Modelling of parabolic trough direct steam generation solar collectors,” Solar Energy, vol. 62, pp. 395-406, 1998.

[11] K. E. Gunger and R. H. Winterton, “A general correlation for flow boiling in tubes and annulli,” Heat and Mass Transfer, vol. 29, pp. 351-358, 1989.

[12] M. Shah, “Chart correlation for saturated boiling heat transfer: equations and further study,” ASHRAE, vol. 88, pp. 185-196, 1982.

[13] H. D. Baehr and K. Stephan, “Heat and mass transfer,” Springer, 2nd edition, pp. 465-492, 2006.

[14] M. Eck, E. Zarza, M. Eickhoff, J. Rheinländer and L. Valenzuela, “Applied research concerning the direct steam generation in parabolic troughs,” Solar Energy, vol.74, pp. 341-351, 2003.

[15] J. R. Thome, “Engineering Data Book III,” Wolverine tube Inc., pp. 13-3,13-6, 2004.

Comparación de la Temperatura Maxima de dos Hidrocarburos con Aire Vs Oxigeno

M. De la Cruz Ávila, G. Polupan
Escuela Superior de Ingeniería Mecánica y Eléctrica,
Instituto Politécnico Nacional.
SEPI-ESIME ZACATENCO. Laboratorio de Ingeniería Térmica e Hidráulica Aplicada.
Av. IPN s/n, Edif. 5, Col Lindavista, C.P.07738 México D.F
*mauriciodlca@hotmail.com

M. Serrano Rodríguez, G.Jarquin
Escuela Superior de Ingeniería Mecánica y Eléctrica,
Instituto Politécnico Nacional.
SEPI-ESIME CULHUACAN.
Av. Santa Ana No.1000 Edif.2 Tercer piso C.P.04480
México D.F.

***Resumen*—El estudio presenta la comparación de la temperatura máxima de un proceso de combustión para cuatro casos distintos de mezcla: metano-aire, metano-oxígeno, gas LP-aire, gas LP-oxigeno. Los cálculos matemáticos son realizados para una combustión por difusión no-premezclado en atmosfera abierta para mezclas estequiométricas respectivamente y condiciones de referencia. La temperatura de las especies es de 300 K y una presión de 101.325 kPa.**

El trabajo muestra un análisis comparativo del cálculo de la temperatura adiabática de llama que exhibe una influencia directa en el poder calorífico cuando la combustión se realiza con aire u oxígeno. Mediante el método iterativo para el cálculo de las entalpias, es posible obtener el valor de la temperatura máxima de una mezcla estequiométrica de los hidrocarburos con aire y con oxígeno. Por una parte el análisis muestra que el poder calorífico del gas LP-aire es mayor en un 9.9% que el de metano-aire, sin embargo se libera mayor volumen de productos de combustión. Por otro lado, la combustión de metano-aire libera mayor poder calorífico por mol de CO2 en comparación con la mezcla de gas LP-aire.

Los análisis muestran que cuando la combustión se realiza con aire existe una reacción secundaria con el nitrógeno, esto evita que el oxígeno se mezcle con el hidrocarburo y que el nitrógeno reaccione para producir NOx altamente contaminantes. Mientras esta reacción secundaria sucede, el volumen de oxígeno disminuye por debajo del valor estequiométrico impactando directamente en el poder calorífico representado por una disminución en la temperatura máxima y un aumento en el volumen de los productos de combustión. El volumen de los productos de combustión es menor cuando la combustión se efectúa con oxígeno para ambos hidrocarburos. Por lo tanto la utilización de metano-oxigeno resulta de gran interés por la liberación de mayor cantidad de energía y menor volumen de productos de combustión.

Palabras Clave: Combustión metano, Combustión gas LP, Poder calorífico hidrocarburo, Temperatura adiabática de llama.

I. INTRODUCCIÓN

La combustión es una reacción química exotérmica durante la cual se oxida un combustible y se libera energía en forma de luz y calor. El calor procedente de la combustión es utilizado en diferentes aplicaciones, como en la industria de la generación eléctrica para calentar agua hasta su estado de vapor y producir el movimiento de los alabes de una turbina acoplada a un generador eléctrico.

Dependiendo de los reactivos y productos de la combustión esta puede ser clasificada de dos formas. Cuando el combustible reacciona por completo con el oxígeno se le denomina combustión completa, para este caso se tiene dióxido de carbono (CO_2) y agua (H_2O) como productos para el caso de los hidrocarburos. Si el combustible no reacciona por completo con el oxígeno porqué este último es insuficiente, se conoce como combustión incompleta. En la mayoría de los casos de combustión, el oxígeno necesario para la reacción se obtiene del aire.

Los valores simplificados de la composición del aire son 21% de oxígeno y 79% de nitrógeno. Por consiguiente la relación molar entre nitrógeno y oxigeno es 0.79/0.21 = 3.76. Cada mol de oxígeno es acompañado por 3.76 moles de nitrógeno. Cuando existe una combustión completa de los hidrocarburos metano- aire y gas LP-aire, los productos de la combustión son: dióxido de carbono (CO_2), agua (H_2O) y nitrógeno (N_2). Muchos procesos industriales de calentamiento se pueden mejorar mediante la sustitución de parte o la totalidad del aire con oxígeno de alta pureza [1]. Las aplicaciones típicas incluyen el calentamiento de metal y de fusión, fusión de vidrio, y calcinación, se han identificado algunas aplicaciones:

- A procesos que presentan alta temperaturas en los gases de combustión exhiben típicamente 1400 K[2],
- A procesos que tienen eficiencias térmicas bajas, debido principalmente a las limitaciones de transferencia de calor,
- A procesos que tienen limitaciones de rendimiento que podrían beneficiarse de la transferencia de calor adicional sin impacto significativo a la calidad del producto, y
- A procesos que tienen gases de combustión contaminantes, altas emisiones de NOx, o gas de combustión con limitaciones de volumen [3].

Al utilizar aire como oxidante, sólo es necesario el O_2 en el proceso de combustión. Mediante la eliminación de N_2 desde

el oxidante, se pueden obtener varios beneficios. Por mencionar algunos de estos beneficios de la combustión con oxígeno se incluyen, una eficiencia térmica más alta, menor pérdida de poder calorífico del hidrocarburo, mayor cantidad de calor disponible, relación de cobertura (longitud y diámetro de llama) mayor [4]. Sin embargo, las afectaciones del nitrógeno a las características de combustión no han sido estudiadas a detalle por la complejidad que vuelve el desarrollo de los productos de combustión secundarios y la formación de NOx desviando la atención de los estudios sobre la verdadera influencia del nitrógeno a la estructura física en estos fenómenos de combustión.

K. Loubar et al [5] presentan un método para determinar las propiedades de combustión gas natural-aire, las concentraciones de CO_2 y su conductividad térmica (dejando fuera la influencia del nitrógeno). Este artículo se basa en la medición de estas características y la comparación con datos experimentales. El desarrollo de la llama de combustión ha sido poco analizada desde el punto de vista físico ya que la mayoría de los estudios de los sistemas de combustión realizados con oxígeno puro y/o aire se enfocan en la parte química tal como lo presenta A. Turbiez et al [6] con la comparación de distintas concentraciones de los gases componentes del gas natural. A pesar de esto también existen trabajos los cuales presentan una eficiencia mayor de la combustión con aire enriquecido con oxígeno como el que presenta Kuo-Kuang Wu et al [7].

II. CALCULOS

Los productos de la combustión de un hidrocarburo de formula C_mH_n se escribe:

$$C_mH_n + \left(m + \frac{n}{4}\right) O_2 = mCO_2 + \left(\frac{n}{2}\right) H_2O \quad (1)$$

El metano representa más del 80% de la composición del gas natural. Algunas de sus propiedades más relevantes se enlistan en la siguiente tabla:

TABLA I. PROPIEDADES DEL METANO

Propiedad	Valor
Fórmula química	CH_4
Masa	16 [kmol]
Temperatura de autoignición	595°C
PCI	50,050 [kJ/kg]

Las características más representativas del GLP distribuido por Petróleos Mexicanos (PEMEX) se encuentran enlistadas en la siguiente tabla:

TABLA II. PROPIEDADES DEL GLP.

Propiedad	Valor
Fórmula química	(C_3H_8)+ (C_4H_{10})
Composición másica de propano (C_3H_8)	60%
Composición másica de butano (C_4H_{10})	40%
Composición molar de propano (C_3H_8)	53.20%
Composición molar de butano (C_4H_{10})	46.80%

El propano es la parte dominante de la composición del gas LP con un 60% del volumen y el butano con un 40% aproximadamente despreciando otros gases. Las propiedades más representativas se encuentran enlistadas en la siguiente tabla:

TABLA III. PROPIEDADES DEL PROPANO Y BUTANO

Propiedad	Valor	Valor
Fórmula química	C_3H_8	C_4H_{10}
Masa	44 [kmol]	58 [kmol]
Temperatura de auto ignición	540°C	405°C
PCI	45,370 [kJ/kg]	46,340 [kJ/kg]

Las relaciones aire-combustible utilizadas en el cálculo de las cantidades necesarias de combustible y aire son las que involucra las masas moleculares de aire y combustible, determinados de la siguiente manera:

$$\frac{masa\ de\ aire}{masa\ de\ combustible} = \frac{moles\ de\ aire \times M_{aire}}{moles\ de\ combustible \times M_{comb}} \quad (2)$$

$$\frac{moles\ de\ aire}{moles\ de\ combustible}\left(\frac{M_{aire}}{M_{comb}}\right) \qquad AC = \overline{AC}\left(\frac{M_{aire}}{M_{comb}}\right) \quad (3)$$

III. METODOLOGIA

En química para analizar una reacción en su forma cuantitativa es necesario conocer las masas molares y aplicar el concepto de relación molar. Lo anterior se logra por medio de balances estequiometricos y a través de un estudio cuantitativo de reactivos y productos en una reacción química. La combustión teórica para los dos casos con aire es:

$$CH_4 + 2(O_2 + 3.76N_2) \rightarrow CO_2 + 2H_2O + 7.52N_2 \quad (4)$$

$$(0.6C_3H_8 + 0.4C_4H_{10}) + 5.6(O_2 + 3.76N_2) \rightarrow 3.4CO_2 + 4.4H_2O + 21.056N_2 \quad (5)$$

Un modelo similar es aplicado a la reacción con oxígeno dando como resultado para los siguientes dos caso es:

$$CH_4 + 2O_2 = CO_2 + 2H_2O \quad (6)$$

$$(0.6C_3H_8 + 0.4C_4H_{10}) + 5.6O_2 \rightarrow 3.4CO_2 + 4.4H_2O \quad (7)$$

Cuando los combustibles son quemados, los volúmenes de aire y de los productos de la combustión son determinados de manera similar, basados en las relaciones estequiométricas, bajo condiciones normales, por los que definiremos los siguientes términos:

1) Cantidad de aire teórica para quemar 1 kg de combustible se obtiene mediante:

$$V° = 0.0476[\sum(m + 0.25n)C_mH_n];[m^3/m^3] \quad (8)$$

$$V°_{02}=0.01[\sum(m+0.25n)C_mH_n];[m^3/m^3] \quad (9)$$

donde $V°_{02}$ es la cantidad de oxigeno teórica para quemar 1 kg de combustible m^3/kg, (o m^3/ m^3).

2) El volumen total de los gases de combustión se expresa como:

$$V_{gas} = V_{RO2} + V_{R2} + V_{H20} \ [m^3/m^3] \quad (10)$$

$$V_{RO2} = 0.01[\sum m(C_mH_n)]; [m^3/m^3] \quad (11)$$

donde V_{RO2} = Productos de la combustión de los gases triatómicos. Para el caso de los hidrocarburos metano y gas lp, el cual incluye el volumen teórico de nitrógeno o cálculo del volumen de los gases diatómicos:

$$V_{R2} = V_{N2}\ ; [m^3/m^3] \quad (12)$$

donde V_{R2}= productos de la combustión, m^3/kg, (m^3/ m^3).

$$V_{N2} = 0.79V° \ [m^3/m^3] \quad (13)$$

donde V_{N2} = Volumen teórico de nitrógeno está definido producto de la combustión.

3) El volumen de vapor o cantidad teórica de vapor de agua en los productos de la combustión lo cual se define como:

$$V_{H20} = 0.01[\sum 0.5n(C_mH_n)];[m^3/m^3] \quad (14)$$

La siguiente tabla muestra los volúmenes productos de la combustión para los cuatro casos distintos de combustión:

TABLA IV. VOLÚMENES PRODUCTOS DE LA COMBUSTIÓN.

Productos de la combustión	Metano-aire [m^3/m^3]	Metano-oxigeno [m^3/m^3]	Gas Lp-aire [m^3/m^3]	Gas Lp-oxigeno [m^3/m^3]
$V°$	9.52	-	26.6	-
$V°_{O2}$	-	2	-	5.6
V_{RO2}	1	1	3.4	3.4
V_{R2}	7.52	-	21.056	-
V_{H20}	2	2	4.4	4.4
V_{gas}	10.52	3	28.856	7.8

IV. CALCULO DE LA TEMPERATURA ADIABÁTICA DE LLAMA

La energía liberada en un proceso de combustión se disipa hacia los alrededores; la energía química liberada durante un proceso de combustión es transportada en forma de calor o se utiliza internamente para elevar la temperatura de los productos de la combustión. La temperatura adiabática de llama es una consideración importante en el diseño de cámaras de combustión, de las turbinas de gas y de toberas. Sin embargo, la temperatura máxima de estos dispositivos son menores que la temperatura adiabática de llama, ya que la combustión suele ser incompleta y presenta pérdidas de calor Algunos gases de combustión se disocian a altas temperaturas. La temperatura adiabática de la llama y la composición de equilibrio de mezclas gaseosas formadas por la oxidación de diversos combustibles o por descomposición de reacciones endotérmicas que se calculan por medio del método iterativo de las entalpias. La temperatura adiabática de llama de un proceso de combustión de flujo estacionario, se determina al establecer $Q = 0$ y $W = 0$ con la siguiente ecuación:

$$H_{prod} = H_{react} \quad (15)$$

$$\sum N_p\left(\bar{h}°_f + \bar{h} - \bar{h}°\right)_p = \sum N_r\left(\bar{h}°_f + \bar{h} - \bar{h}°\right)_r \quad (16)$$

Una vez que se especifican los reactivos y sus estados, se determina la entalpía de los reactivos H_{react}. Sin embargo, debido a que la temperatura de los productos no se conoce antes de los cálculos, el cálculo de la entalpia de los productos H_{prod} no es directo. Por consiguiente, la determinación de la temperatura adiabática de llama requiere el uso de una técnica iterativa, a menos que se disponga de ecuaciones para los cambios de entalpía sensible de los productos de la combustión. La relación de la temperatura de flama adiabática $H_{prod} = H_{react}$ en este caso se reduce a:

$$\sum N_p(\bar{h}°_f + \bar{h} - \bar{h}°)_p = \sum N_r\,\bar{h}°_{f,r} = \left(N\,\bar{h}°_f\right)_{CH_4} \quad (17)$$

Puesto que todos los reactivos están en el estado de referencia estándar y $\bar{h}°_f$=0 para O_2 y N_2. Los valores $\bar{h}°_f$ y h de diversos componentes a 298°K son:

TABLA V. ENTALPIAS DE FORMACIÓN.

Sustancia	$\bar{h}°_f$ [kJ/kmol]	$\bar{h}_{298\,K}$ [kJ/kmol]
CH_4	-74850	-
O_2	0	8682
N_2	0	8669
H_2O	-241820	9904
CO_2	-393520	9364
C_3H_8	-103850	-
C_4H_{10}	-126150	-

Se mencionan ciertas suposiciones necesarias antes de resolver el problema, que a continuación se enlistan:

- Es un proceso de combustión de flujo estacionario.
- No existen interacciones de trabajo.
- El aire, oxígeno y los gases de combustión se plantean como gases ideales.
- Son despreciables los cambios en las energías cinética y potencial.

El balance de la ecuación para el proceso de combustión con la cantidad teórica de aire es:

$$CH_4 + 2(O_2 + 3.76N_2) \rightarrow CO_2 + 2H_2O + 7.52N_2$$

Al sustituir (17) se obtiene:

$$(1kmol\ CO_2)\left[(-393520+\bar{h}°_{CO_2}-9364)kJ/kmol\ \ CO_2\right]+$$
$$(2\ kmol\ H_2O)\left[(-241820+\bar{h}°_{H_2O}-9904)kJ/kmol\ \ H_2O\right]$$
$$+(7.52\ kmol\ N_2)\left[(0+\bar{h}°_{N_2}-8869)kJ/kmol\ \ N_2\right]=$$
$$(1\ kmol\ CH_4)(-74850\ kJ/kmol\ \ CH_4)$$

Lo que produce:

$$1\ \bar{h}°_{CO_2}+2\ \bar{h}°_{H_2O}+7.52\ \bar{h}°_{N_2}=896672.88\ kJ$$

Para poder proponer una temperatura adiabática de llama, conviene dividir el producto de la combustión por el número total de moles, al hacer esto obtenemos:

896 672.88 kJ / (1+2+7.52) kmol = 85235.88 J/kmol.

Este es un valor de entalpía que corresponderá aproximadamente a la temperatura máxima de la combustión. En la tabla 7 se muestran valores de entalpias a dos diferentes temperaturas que fueron utilizadas en este análisis.

TABLA VI. ENTALPIA DE CO_2, H_2O, N_2 A DIFERENTES TEMPERATURAS.

Temperatura[K]	CO_2[J/kmol]	H_2O[J/kmol]	N_2[kJ/kmol]
2600	137449	114273	86650
2550	134368	111565	84814
2350	122091	100846	77496
2300	119035	98199	75676

Cabe mencionar que los moles después de la combustión en su mayoría son del N_2, por lo que la temperatura deseada se acercará a 2550K, pero sería inferior a dicho valor. Por lo tanto, se plantea una nueva temperatura de 2350K para los diversos productos de la combustión. Con esta temperatura se reduce a:

$$1\ \bar{h}°_{CO_2}+2\ \bar{h}°_{H_2O}+7.52\ \bar{h}°_{N_2}=$$
$$1\times 122091+2\times 100846+7.52\times 77496=9066552.92\ kJ$$

Este valor es más alto que 896672.88 J. Por consiguiente, la temperatura real está por debajo de 2350°K. A continuación elegimos 2300°K. Esto produce:

$$1\times 119035+2\times 98199+7.52\times 75676=884516.52\ kJ$$

Este valor es inferior que 896672.88 kJ. En consecuencia, la temperatura real de los productos está entre 2300K y 2350K. Por interpolación, se encuentra que su valor será aproximadamente T = 2327 K después de 3 iteraciones.

La siguiente tabla muestra las temperaturas de flama adiabática para los 4 casos distintos de combustión obtenidos mediante este método:

TABLA VII. TEMPERATURA DE FLAMA ADIABÁTICA DESPUÉS DE 3 ITERACIONES.

Mezcla	Temperatura de flama adiabática [K]
Metano-aire	2327
Metano-oxigeno	3748
Gas lp-aire	2396
Gas lp-oxigeno	3867

V. ANALISIS DE RESULTADOS

La tabla 9 muestra la temperatura de los distintos combustibles libres mezclados para la combustión de aire y oxígeno. Se puede apreciar que las temperaturas obtenidas de las mezclas con aire son inferiores con respecto a las temperatura qué se pueden obtener con oxígeno. Esto se debe principalmente a que la reacción endotérmica con el nitrógeno resta poder calorífico. Caso contrario, cuando la mezcla se presenta con oxígeno la combustión librea mayor calor debido a que no existe presencia alguna de reacciones secundarias con nitrógeno.

TABLA VIII. TEMPERATURA ADIABÁTICA DE COMBUSTIBLES LIBRES MEZCLADOS CON AIRE Y OXÍGENO.

Mezcla	Temperatura K (literatura[1])	Temperatura K (software COSILAB[8])	Temperatura K (método iterativo)
CH_4+(O_2+N_2)	2223.2	2207.3	2180.1
C_3H_8+(O_2+N_2)	2279.5	2262.7	2291.2
C_4H_{10}+(O_2+N_2)	2285.5	2311.5	2338.4
CH_4+O_2	3748.36	3751.4	3680.89
C_3H_8+O_2	3819.85	3734.55	3767.86
C_4H_{10}+O_2	3879.56	3780.67	3798.63

También se muestra que el poder calorífico que se obtiene del propano y del butano es mayor ya que posee mayor cantidad de hidrogeno manifestado con un incremento en la temperatura. El butano presenta una temperatura 10.06% con respecto al propano y un 11.9% con respecto al metano. Y el propano muestra un 4.85% con respecto al metano. Este incremento en la temperatura se debe principalmente a que la reacción para producir CO_2 varía en función del combustible y su cantidad de carbonos y la formación de NOx (no contemplado en este análisis).

Cuando la combustión se realiza con oxígeno el acomodamiento entre los carbonos con el oxígeno influye de manera directa en el incremento de la temperatura, también, se da este aumento debido a la ausencia del nitrógeno lo que facilita esta reacción. De manera similar el butano muestra un incremento de un 6.75% con respecto al propano y 10.57% con respecto al metano. Y el incremento producido por el propano es de 4.09% con respecto al metano.

La figura 1 presenta la comparación de las capacidades caloríficas de los 3 distintos combustibles libres. Se puede apreciar que el propano es ligeramente mayor (4.56%) con respecto al butano principalmente debido a que contiene casi la misma cantidad de hidrógenos pero solo un átomos menos de carbono lo que supone este aumento debido a esto. Si bien el metano contiene menor cantidad de átomos de carbono su capacidad calorífica es menor que a la de los dos anteriores,

esto debido a que la cantidad de hidrogeno es menor pero no sustancial.

Fig 1 Capacidad calorífica de los combustibles libres

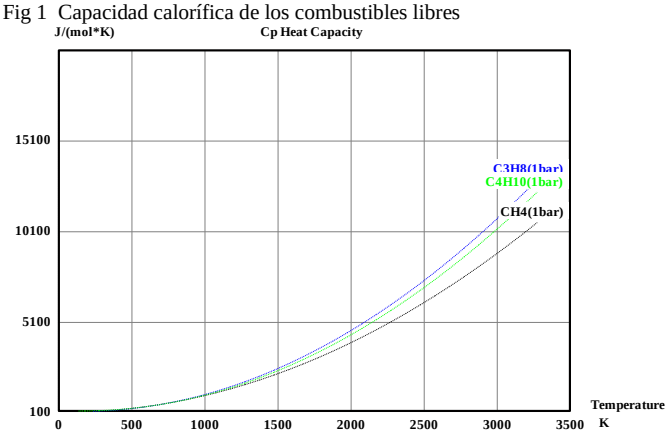

En la figura 2 podemos apreciar que ocurre lo contrario, el butano presenta la mayor cantidad de energía, esto se debe primordialmente a que la cantidad de hidrógenos es la mayor de los 3 combustibles lo que libera mayor cantidad de energía al momento de hacer reacción para descomponer la molécula.

Fig 2 Entalpia de los combustibles libres.

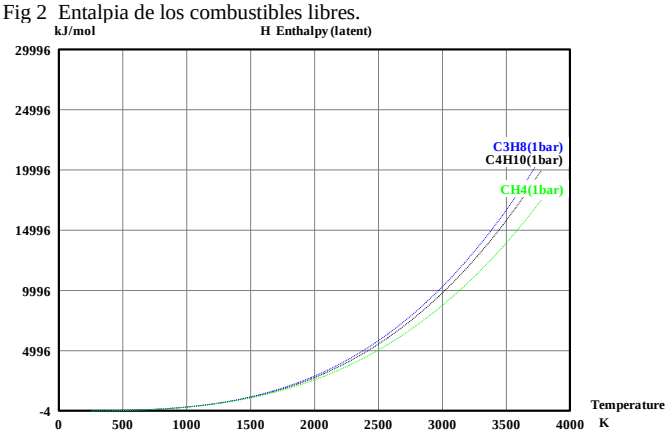

Con estos resultados podemos validar las aproximaciones de temperatura de flama adiabática de la mezcla de Gas LP (60% propano con 40% butano). La tabla 10 presenta las aproximaciones obtenidas mediante el método iterativo de las entalpias.

TABLA IX. TEMPERATURA ADIABÁTICA DE LOS 4 CASOS.

Mezcla	Con Aire	Con Oxigeno
Gas LP	2282.3756 K	3867.057 K
Metano	2227.1302 K	3748.048 K

La mezcla de combustión Gas LP-aire muestra un incremento de la temperatura en un 2.42% con respecto a la mezcla metano-aire y un 3.07%. La mezcla de ambos combustibles tiene una mejora significativa con oxígeno ya que no el nitrógeno no obstaculiza la reacción. Sin embargo la diferencia entre las mezclas de combustión apenas alcanza un 3.07% en el mejor de los caso lo cual indica que la utilización de Gas LP no justifica el poder calorífico en relación del volumen de los productos de combustión.

VI. CONCLUSIONES

En este trabajo se presenta la comparación de la temperatura producto de la combustión para dos hidrocarburos distintos con aire y con oxígeno puro.

La mezcla de gas lp-aire tiene un poder calorífico mayor en un 17% y 2.74 veces mayor en el los volúmenes productos de la combustión que la mezcla con respecto a la de metano-aire. En cuanto a la temperatura de flama adiabática varía en un 2.5% entre la mezclas con aire. La reacción con oxígeno muestra que hay una mejora aunque no sustancial del 3.07 %. De manera similar el volumen de los productos de combustión de Gas LP con oxígeno es de 2.2 veces mayor que la mezcla metano oxígeno. Por lo tanto aunque la mezcla de metano aire o metano oxigeno no entrega la misma cantidad de poder calorífico que las mezclas de Gas LP, son más efectivas por unidad de volumen de los productos de combustión ya que estos productos son menores que los producidos por las mezclas de Gas LP.

Los resultados mostrados de las mezclas de combustión con metano son benéficos y altamente recomendables en la utilización de hidrocarburos para la generación de cualquier tipo de trabajo por su buen poder calorífico, su baja producción de volúmenes productos de combustión y por ser más eficientes por mol de CO_2 producido.

AGRADECIMIENTOS

Los autores agradecen al Instituto Politécnico Nacional, a la Sección de Estudios de Posgrado e Investigación de la Escuela Superior de Ingeniería Mecánica y Eléctrica Unidad Culhuacán y a la Sección de Estudios de Posgrado e Investigación de la Escuela Superior de Ingeniería Mecánica y Eléctrica Unidad Zacatenco.

REFERENCIAS

[1] Williams, S. J., Cuervo, L. A., and Chapman, M. A., High-Temperature Industrial Process Heating: Oxygen-Gas Combustion and Plasma Heating Systems, Gas Research Institute report GRI-89/0256, Chicago, July 1989.
[2] Baukal, C. E., Eleazer, P. B., and Farmer, L. K., Basis for enhancing combustion by oxygen enrichment, Ind. Heating, LIX (2), 22, 1992.
[3] Benedek, K. R. and Wilson, R. P., The Competitive Position of Natural Gas in Oxy Fuel Burner Applications, Gas Research Institute report no. GRI-96-0350, Chicago, September 1996.
[4] Andrés Amell Arrieta - Grupo de Ciencia y Tecnología del Gas y Uso Racional de la Energía, GASURE, Universidad de Antioquia.- Estudio numérico y experimental de las propiedades y fenómenos en una llama de metano y aire enriquecido.
[5] K. Loubar, C. Rahmouni, O. Le Corre, M. Tazerout. A "Combustionless Determination Method For Combustion Properties Of Natural Gases". Fuel 86; 2007: 2535–2544.
[6] A. Turbieza, El Bakali, J.F. Pauwels, Rida, P. Meunier "Experimental Study Of Low Pressure Stoichiometric Premixed Methane, Methane/Ethane, Methane/Ethane/Propane And Synthetic Natural Gas Flames" Fuel 83; 2004: 933–941.
[7] Kuo-Kuang Wu, Yu-Cheng Chang, Chiun-Hsun Chen, Young-Da Chen. "High-Efficiency Combustion Of Natural Gas With 21–30% Oxygen-Enriched Air". Fuel 89; 2010: 2455–2462.
[8] COSILAB, version 3.0.3., Rotexo-Softpredict-Cosilab GmbH & Co KG, Bad Zwischenhahn, 2009

Novel Feedback Control to Improve Biohydrogen Production by *Desulfovibrio alaskensis*

Hugo Iván Velázquez-Sánchez, Ricardo Aguilar-López*
Biotechnology and Bioengineering Department
CINVESTAV-IPN
Mexico City, Mexico
*raguilar@cinvestav.mx

Hector Fernando Puebla-Nuñez
Energy Department
UAM Azcapotzalco
Mexico City, Mexico

Abstract— **In this paper, a novel control algorithm is proposed to increase biohydrogen production in a class of anaerobic continuous bioreactor using the sulphate-reducing bacteria *Desulfovibrio alaskensis* with lactate as carbon source. A kinetic model experimentally corroborated was employed as a benchmark for this proposal and adapted to operate into continuous flow regimen.**

An open-loop analysis with initial inoculum concentration of 110 mg L^{-1} and feeding conditions at a dilution rate of 0.025 h^{-1} and concentrations of sulphate and lactate of 1850 mg L^{-1} and 2500 mg L^{-1} respectively until reaching steady state was made. The proposed controller considers the biomass concentration as measured output and the dilution rate as the control input. The controller was tuned using heuristic criteria and its performance was evaluated through numerical simulations and by comparing the steady state product concentration versus the ones obtained by open-loop operation. Closed-loop regime increased the final hydrogen titter at steady state from 81.5031 mg L^{-1} to 123.5180 mg L^{-1}, an increase of 51.55 percent.

Keywords— Biohydrogen; sulphate-reduction; Desulfovibrio; process intensification; closed-loop.

I. INTRODUCTION

The incoming global energetic crisis, caused by the overexploitation of fossil fuels has motivated the search for viable replacements, both economically and environmentally speaking, for them. One of the most studied alternatives in the last decade is biohydrogen production, which could help to reduce greenhouse effect gaseous emissions coming from the transport sector, as its combustion only yields water vapour instead of carbon dioxide [2].

Among the candidates for H_2 production at industrial scale is the biological system based on bacteria from the genus *Desulfovibrio*. This bacterial genus is being capable of consuming various simple carbohydrates, such as lactate, under anaerobic conditions using sulphate as electron acceptor and reducing it into hydrogen sulphide and H_2, therefore this biological system does not only can be exploited to produce a potentially clean biofuel but also has been proposed to be used in the COD reduction in contaminated effluent from the dairy industry and also to remedy wastewater containing high concentrations of heavy metals such as Pb, Cd or Fe [3].

The main constraint to scale up the biohydrogen production system is that traditional batch operation reactors suffer by low productivity due the relatively slow growth cycle of the culture and the low hydrogen titter obtained at the end of the fermentation. Those shortcomings combined with the growth inhibitory effect of sulphide production within the reactor arise the need to generate operational strategies to reduce the impact of them into the process [4].

As an attempt to remedy this, operational regimes based on continuous mode and closed-loop schemes can be proposed in order to keep the reaction system operating in regions that could maintain a steady conversion rate and prevent sulphide accumulation into the reactor as an attempt to minimize its impact into the fermentation process [1].

Therefore this work proposes to evaluate the behaviour of a CSTR fermentation system for biohydrogen production by *Desulfovibrio alaskensis* via a simulation analysis based on an experimentally validated kinetic model [1] manipulating the dilution rate (D) subject to a novel control law, in order to keep a minimum and steady titter of biomass (X), being a variable that can be easily determined online within the reactor, to indirectly allow the system to increase its biohydrogen productivity.

II. METODOLOGY

A. Numerical simulations

All the numerical simulations were made into a PC equipped with an Intel® Core© i5 560M processor and 4 GB of RAM into the MATLAB® 2013b software, using ODESolver 15s command, to solve the system's set of differential equations at an undefined time-span assuming continuous mode operation until steady state was observed.

B. Kinetic modelling

The kinetic model chosen to carry out the proposed methodology has been validated experimentally and already reported into literature [1]. To describe the kinetics of cell growth a Levenspiel-type expression was considered into the model (1), since it is known that bacteria of the genus *Desulfovibrio* are sensitive to accumulation of sulphur in the culture medium, while equations (2-7) describe the dynamics

of biomass, lactate, sulphate, sulphide, acetate and hydrogen respectively in a reactor operating into a continuous regime. The parametric identification obtained for this model is presented in Table I. The meaning of each symbol and variable is described in the Nomenclature section.

$$\mu = \mu max \left(\frac{SO}{SO+Ks}\right)\left(1-\frac{S^{=}}{Kis}\right)^{n} \quad (1)$$

$$\frac{dX}{dt} = (\mu - Kd)X - (D * X) \quad (2)$$

$$\frac{dLac}{dt} = \left(D(Lac_{in} - Lac)\right) - (\mu X * Y_1) \quad (3)$$

$$\frac{dSO}{dt} = \left(D(SO_{in} - SO)\right) - (\mu X * Y_2) \quad (4)$$

$$\frac{dS^{=}}{dt} = (\mu X * Y_3) - (D * S^{=}) \quad (5)$$

$$\frac{dAc}{dt} = (\mu X * Y_4) - (D * Ac) \quad (6)$$

$$\frac{dH}{dt} = \left(\left(\frac{dLac}{dt}\right)(Y_5)\right) - (D * H) \quad (7)$$

C. *Proposed controller*

The proposed controller (8) considers the biomass concentration as measured output and the dilution rate (D) as the controlled variable. It was tuned using heuristic criteria and its performance was evaluated through numerical simulations by comparing the steady state product titters obtained by the controlled system versus the ones obtained via open-loop operation.

$$D = k_1\left(\|e\|^{-\frac{1}{m}} + k_2\right) \quad where \ e := X - X_{sp} \quad (8)$$

III. Results and Discucssion

Table I shows the reported results of the parametric identification of the chosen model versus experimental data by Aguilar-López and Neria-González [1], while the values of the proposed controller gains after the heuristic tuning stage were $k_1 = 0.01$, $k_2 = 0$ and $m = 7$ respectively.

The simulations to determine the steady state of the system under conditions of continuous cultivation in open loop considered an initial inoculum X_0 = 110 mg L^{-1}, and operational conditions for D, SO_{in} and Lac_{in} of 0.025 h^{-1}, 1850 mg L^{-1} and 2500 mg L^{-1} respectively. The results indicated that the system reaches steady state after 4500 h of fermentation and the concentrations of the compounds of interest at that point were H_2 = 81.5031 mg L^{-1}, SO = 1054 mg L^{-1} and Lac = 1044.6 mg L^{-1}.

Within these simulations there was done a scanning analysis over the dilution rate to set allowable operational values for the controller, finding that the feeding rate that induced reactor washing was D_W = 0.04 h^{-1}, therefore (8) was adjusted to keep the dilution rate bounded into a semi-closed interval [0, Dw).

TABLE I. Parametric identification of the chosen kinetic model.

Parameter	Value	Units	Parameter	Value	Units
µmax	0.163	h^{-1}	Y_1	13.041	mg mg^{-1}
Ks	3.45e-3	mg L^{-1}	Y_2	7.132	mg mg^{-1}
Kis	509.851	mg L^{-1}	Y_3	1.407	mg mg^{-1}
n	0.834	----	Y_4	8.172	mg mg^{-1}
Kd	0.003	h^{-1}	Y_5	0.028	mg mg^{-1}

The closed-loop analysis was made considering the same feeding regime and, as proposed set-point, biomass concentrations into the reactor from a range between 100 and 250 mg L^{-1} in order to assess which of these values could been maintained into the reactor at the highest possible steady state dilution rate to indirectly improve the final hydrogen titter of the fermentation. The initial values for that simulation were 110, 10, 10, 30, 30 and 0 mg L^{-1} for biomass, lactate, sulphate, sulphur, acetate and hydrogen respectively.

Additionally, the control effort was monitored by plotting the punctual dilution rate over time (Fig. 1) to determine the controller's performance at the proposed set-point.

The chosen set-point was X_{Sp} = 135 mg L^{-1}, as it provided the best hydrogen yields and also the maximum titter compared with the ones obtained by the open-loop simulation, having also the added benefit of being able to allow the culture to consume sulphate more efficiently (Table II).

Fig. 2 also demonstrates that the proposed controller stabilises the dilution rate of the fermenter in less than 1500 h, which allows the system not only to increase its hydrogen steady state titter, but also to keep the system productivity close to the one obtained by the traditional open-loop continuous fermentation.

TABLE II. Final titters of the compounds of interest at steady state of both the open-loop system and the closed-loop one under the effect of the proposed control law.

Compound	Open-loop [mg L^{-1}]	Closed-loop [mg L^{-1}]
H_2	81.5031	123.5180
Lactate	1044.6	294.3196
Sulphate	1054	643.6485

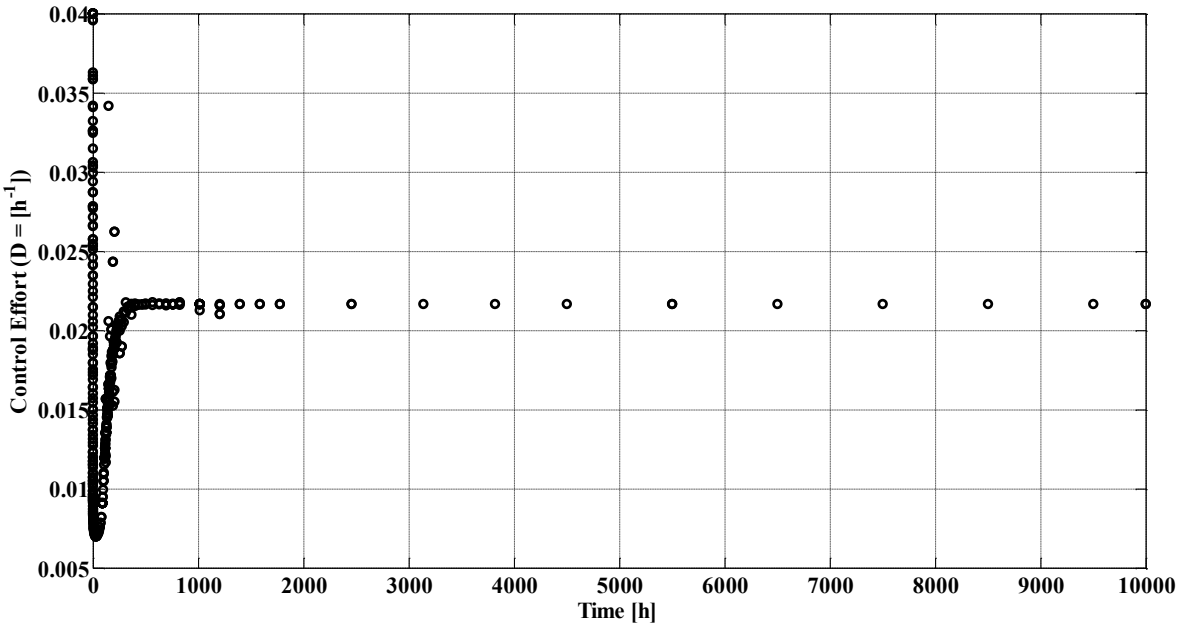

Fig. 1. MONITORING OF THE CONTROL EFFORT INTO THE CLOSED LOOP SYSTEM AS DILUTION RATE OF THE FERMENTOR OVER TIME.

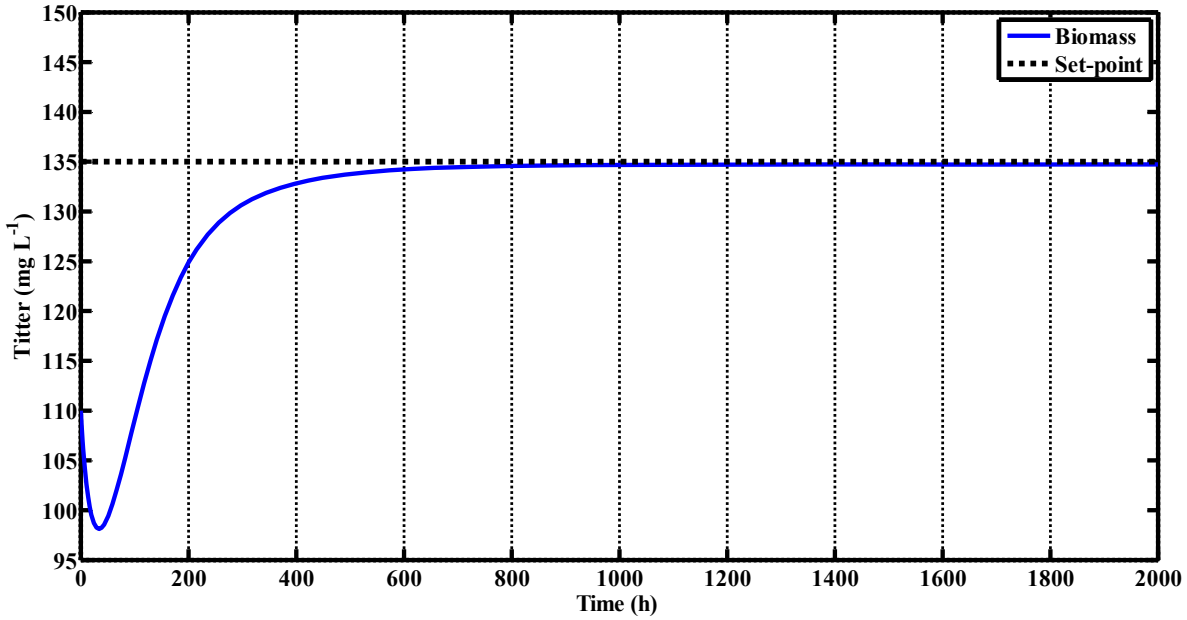

Fig. 2. DYNAMICS OF THE CONTROLLED VARIABLE (BIOMASS) AND SELECTED SET-POINT VALUE.

IV. Conclusions

The proposed control algorithm has the potential to increase the H_2 production of a sulphate-reducing system using *Desulfovibrio alaskensis* up to titters of 123,518 mg L^{-1}. This value is consistent with the one reported by Martins and Pereira [5] for this system. In turn, it was found that the system under closed-loop operation also reduces the residual concentration of sulphate in the reactor outlet at a higher level than the open-loop one, which can benefit its application in wastewater treatment.

Acknowledgment

H.I. Velázquez-Sánchez is very grateful with CONACyT for the financial support via a postgraduate scholarship and with CINVESTAV-IPN for supplying the research facilities to develop this work.

Nomenclature

Symbol	***Meaning***	***Units***
Ac	Acetate concentration within the reactor	mg L^{-1}
D	Reactor's dilution rate	h^{-1}
D_W	Reactor's washing rate	h^{-1}
e	Estimation error	mg L^{-1}
H	Hydrogen concentration into the reactor	mg L^{-1}
Lac	Lactate concentration into the reactor	mg L^{-1}
Lac_{in}	Lactate concentration at the feeding solution	mg L^{-1}
m	Exponential gain of the proposed controller	----
µmax	Bacterial specific growth rate	h^{-1}
k_1	Linear gain 1 of the proposed controller	----
k_2	Linear gain 2 of the proposed controller	----
Kd	Cellular death rate	h^{-1}
Kis	Levenspiel's inhibition growth term	mg L^{-1}
Ks	Substrate affinity constant	mg L^{-1}
n	Levenspiel's inhibition growth exponent	----
S^-	Sulphide concentration into the reactor	mg L^{-1}
SO	Sulphate concentration into the reactor	mg L^{-1}
SO_{in}	Sulphate concentration into the feeding solution	mg L^{-1}
X	Biomass concentration into the reactor	mg L^{-1}
X_0	Biomass concentration into the inoculum	mg L^{-1}
X_{Sp}	Biomass concentration used as set-point into the proposed control law	mg L^{-1}
Y_1	Specific consume of lactate per biomass unit	mg mg^{-1}
Y_2	Specific consume of sulphate per biomass unit	mg mg^{-1}
Y_3	Sulphide production yield per biomass unit	mg mg^{-1}
Y_4	Acetate production yield per biomass unit	mg mg^{-1}
Y_5	Hydrogen production yield per lactate unit	mg mg^{-1}

References

[1] Neria.González, M. I. y Aguilar-López R., "Tracking Trajectories in a Continuous Anaerobic Bioreactor employing a Nonlinear Proportional Controller", *Int. Journal of Chemical Reactor Engineering*, Vol. 5, p. A73, 2007.

[2] Kotay, S. M. y Das, D., "Biohydrogen as a renewable energy resource – prospects and potentials", *Int J Hydrogen Energy*, No. 33, p. 258-263, 2008.

[3] Muyzer, G., Stams, A. J., "The ecology and biotechnology of sulphate-reducing bacteria", *Nat Rev Microbiol*, No. 6, p. 441-454, 2008.

[4] Hallenbeck, P. C., "Fermentative hydrogen production: Principles, progress, and prognosis", *Int J Hydrogen Energy*, No. 34, p. 7379-7389, 2009.

[5] Martins, M. y Pereira, I. "Sulfate-reducing bacteria as new microorganisms for biological hydrogen production", *Int J Hydrogen Energy*, No. 38, p. 12294-12301, 2013.

Estudio de la Combustión No-Estequiometrica de la Mezcla Metano-Nitrógeno con Oxigeno.

G. Reyes Santiago*, G. Jarquin López
Sección de estudios de Posgrado e Investigación Culhuacán
Instituto Politécnico Nacional
México, D.F.
* guillereyeswork@gmail.com

G. Polupan
Sección de estudios de Posgrado e Investigación Zacatenco
Instituto Politécnico Nacional,
México, D.F.

***Resumen*— Se realizó un estudio de combustión no estequiométrica (cantidad de oxigeno menor a 1) de metano con oxígeno bajo condiciones normales Temperatura igual a 273.15 K y presión igual a 101.325 Pa, tomando como variable en el estudio el porcentaje de nitrógeno en el metano.**

Se planteó el modelo matemático de combustión aplicando la ley de conservación de la masa. El comburente es una mezcla de metano con oxígeno, y en cada porcentaje de nitrógeno estudiado 0%, 5%, 10% y 15% se ajusta la composición del combustible. Al resolver el modelo de combustión se obtienen los volúmenes productos de la combustión.

Los resultados obtenidos muestran que a mayor porcentaje de nitrógeno presente en el combustible, se obtuvo una menor cantidad de calor liberado en la combustión. En cuanto a los resultados de poder calorífico del combustible al agregar cinco por ciento de nitrógeno su valor decrece 8 %.

Palabras Clave — Generador de vapor, Combustión no estequiométrica, metano, oxígeno, nitrógeno.

I. INTRODUCIÓN

Por combustión se entiende una reacción de oxidación exotérmica de las sustancias combustibles, exigiendo la obtención máxima de calor posible; que por razones de economía debe ser completa en cuanto al combustible, lo que exige trabajar con cierto exceso de comburente, pero de forma limitada para evitar pérdidas de calor de los productos de la reacción. La combustión de un combustible, aun siendo uno simple, es un proceso complicado; el proceso es aún más complicado para combustibles sólidos. La reacción de combustión puede llevarse a cabo directamente con el oxígeno o bien con una mezcla de sustancias que contengan oxígeno, siendo el aire atmosférico el comburente más habitual ya que se obtiene de manera gratuita. Las fórmulas de cálculo son obtenidas de ecuaciones estequiométricas que dan la proporción de las substancias reaccionando en moles, peso y unidades de volumen de acuerdo a Bezgreshnov A.N., et al, 1991; I. T. Shvets,et al, 1987.

Uno de los principales aspectos en el diseño de un generador de vapor es el tipo de combustible con el cual se va a trabajar ya que de él depende la selección de materiales, la forma en que se va a llevar acabo la combustión entre otras.

Se necesita seleccionar el combustible adecuado a las necesidades de proceso, una de las más importantes es la energía que nos puede proporcionar dicho combustible y la cantidad con la cual podremos llegar a ella, esto se lograra mediante el cálculo de las características termodinámicas obtenidas por la combustión de nuestro combustible, usando la metodología de Prabir Basú, et al (2000).

La combustión incompleta es opuesta a la completa y se caracteriza por la falta de comburente y/o combustible, lo que impide que se dé la oxidación completa del combustible dando como resultado la producción de más gases residuales. Dentro de los posibles productos de esta reacción encontramos los siguientes:

$$CnHm + O_2 \longrightarrow CO_2 + H_2O + CO + H_2 + CnHm + H_2S + C + NOx + SO_2 + H_2O$$

El Nitrógeno (N_2) es un elemento que se encuentra en todo ámbito industrial ya que se encuentra en gran proporción en el comburente más común, que es el aire, y aunado a eso también lo podemos encontrar mezclado en distintos combustibles. En muchos casos se dese eliminar el mayor porcentaje de la concentración N_2 posible, ya que este afecta directamente en la energía producida, absorbiendo el calor desprendido, debido a que este elemento posee una temperatura relativamente baja, Aunado a esto un inconveniente más es que a alcanzando cierta temperatura puede reaccionar con los productos de la combustión, formando NOx que son altamente contaminantes para el medio ambiente.

II. METODOLOGIA

A. *Combustión completa*

Para combustión estequiometrica se utiliza el suficiente oxígeno para poder quemar en su totalidad el combustible. Las fórmulas que nos permiten calcular esa relación nacen a partir de balances estequiométricos, que dan la proporción de las sustancias reaccionando en moles, peso y unidades de volumen.

En general para cualquier hidrocarburo la ecuación que nos permite calcular la relación estequiometrica se describe a continuación:

$$CmHn + \left(m + \frac{n}{4}\right) O_2 = mCO_2 + \left(\frac{n}{2}\right) H_2O \quad (1)$$

$$(m + \frac{n}{4})\, mol = m\, mol + (\frac{n}{2})\, mol \quad (2)$$

$$\left(m + \frac{n}{4}\right) m^3 = m\, m^3 + \left(\frac{n}{2}\right) m^3 \quad (3)$$

donde
m es igual al número de moléculas de carbono
n el número de moléculas de hidrogeno.

Cuando la reacción de combustión es incompleta los balances de materia se ven modificados al presentar nuevos compuestos como productos de la reacción, esto debido a que no se encontraba la cantidad de oxigeno necesaria para oxidar en su totalidad el combustible.

Como se mencionó previamente el nitrógeno no presentara reacción por lo cual el valor que este posea dentro de nuestro comburente será el mismo que estaremos obteniendo como producto.

Continuando con la metodología lo que se hará es calcular el poder Calorífico Inferior (PCI) de nuestro combustible, tomando de tablas el valor del PCI del CH_4, encontramos que tiene 35,880 KJ/m^3, mientras que para poder determinar el PCI de un Kg de CH_4 se realizan las siguientes relaciones:

- 1 kmol de CH_4 es equivalente a 16 kg
- A su vez 1 kmol ocupa 22.41 m^3

Por lo que tendremos que relacionar cuanto volumen ocupa un kilogramo de combustible:

$$\frac{volumen\ que\ ocupa\ un\ kmol\ de\ combustible}{kg\ equivalentes\ a\ un\ kmol\ de\ combustible} \quad (4)$$

Con este valor calculado podemos multiplicar por el PCI determinado en tablas y así saber cuánto se produce al tratar con un kg de combustible o su equivalencia en m^3.

B. Efecto térmico (P.C.I)

El poder calorífico de un combustible es la cantidad de energía desprendida en la reacción de combustión, referida a la unidad de masa de combustible.

Para calcular el poder calorífico inferior, considerando al combustible como un gas que está compuesto por diferentes hidrocarburos, se toma en cuenta el P.C.I de cada uno de los hidrocarburos que lo componen con relación a sus fracciones volumétricas, con ayuda de tablas que nos describan estos valores.

Para este caso se analizan diferentes porcentajes volumétricos de mezcla entre el metano y el nitrógeno (CH_4 95% / N_2 5%; CH_4 90% / N_2 10%; CH_4 85% / N_2 15%; el interés de conocer el comportamiento de variación del PCI en todos estos supuestos es importante para poder determinar la influencia del nitrógeno en la generación de energía.

Los cálculos se abordan a partir de porcentajes volumétricos, sin embargo para una mayor aplicación los convertiremos en porcentajes másicos.

Para realizar esta conversión es necesario dividir el peso en kg de un mol de la sustancia, entre el volumen que ocupa en m^3.

$$\frac{kg\ equivalentes\ a\ un\ kmol\ de\ combustible}{volumen\ que\ ocupa\ un\ kmol\ de\ combustible} \quad (5)$$

El resultado es la densidad de la sustancia y prosigue una relación, esto para ambos componentes de nuestro combustible.

$$\frac{1\ kg}{\%\ volumetrico} \Rightarrow \frac{\rho}{kg} \quad (6)$$

El resultado se suma y se hace una relación nueva para determinar el porcentaje de cada componente por kg de mezcla. Cuando se obtiene el porcentaje másico del metano se multiplica por el PCI que genera un kg de este combustible. El PCI asi como la densidad de los compuestos utilizados a lo largo de este articulo los encontramos en la siguiente tabla:

TABLA I. DATOS DE SUTANCIAS

NOMBRE	FORMULA	DENSIDAD kg/m3	PCI MJ/m3
Metano	CH_4	0.717	35.88
Oxigeno	O_2	1.428	0
Nitrógeno	N_2	1.250	0
Monóxido de carbono	CO	1.250	12.64
Hidrogeno	H_2	0.090	10.79

C. Combustión Incompleta

Para este nuevo balance de combustión incompleta podemos utilizar la ecuación de Kissel.

$$nHm + \left(n + \frac{m}{4} - \frac{x+y}{2} + z\right) O_2 + 3{,}762\left(n + \frac{m}{4} - \frac{x+y}{2} + z\right) N_2 + vN_2 \Rightarrow (n-x)\,CO_2 + xCO + (m/2-y)\,H_2O + yH_2 + zO_2 + (3{,}762\,(n + m/4 - (x+y)/2 + z) + v)\,N_2 \quad (7)$$

Sin embargo no se utiliza esta ecuación tal como está ya que la reacción analizada no tiene aire, por lo cual los valores del nitrógeno en esta serán cancelados; no obstante si aparece en el combustible, de igual manera no participa en la reacción debido a que representa un lastre.

$$CnHm + \left(n + \frac{m}{4} - \frac{x+y}{2}\right) O_2 = (n-x)\,CO_2 + xCO + (m/2-y)\,H_2O + yH_2 \quad (8)$$

donde $\frac{x+y}{2}$ representa el valor del porcentaje del comburente en cuestión, en nuestro caso O_2.

Como se menciona el combustible es una mezcla de CH_4 con N_2 por lo que debe existir una relación volumétrica, la cual afectara la ecuación anterior, al multiplicarla por este valor del combustible.

$$CnHm + \frac{\%}{100} C_mH_n \left[\left(n + \frac{m}{4} - \frac{x+y}{2}\right) O_2 = (n-x)\,CO_2 + xCO + (m/2-y)\,H_2O + yH_2\right] \quad (9)$$

Por esto es que la presencia de los productos resultantes de la combustión e inquemados estará variando derivado de dos factores:

- Cantidad de comburente disponible para la reacción.
- Porcentaje de metano y nitrógeno en la mezcla combustible.

D. Efecto térmico de la combustión incompleta.

En complemento de la sección anterior, un factor que influye de manera relevante tanto en el balance químico como en el efecto térmico, es la composición de los productos de la combustión incompleta; para este análisis presentaremos las variaciones que presentan las relaciones:

$$\frac{CO}{H_2} = 1 \qquad \frac{CO}{H_2} = 0.9 \qquad \frac{CO}{H_2} = 1.1$$

Utilizando la ecuación 8 para el balance de la reacción química, obtenemos la cantidad de moléculas de cada producto, considerando las relaciones antes mencionadas; esto se debe multiplicar por el PCI de su respectiva sustancia, y finalmente restarlo al PCI del metano.

III. RESULTADOS

A. Balance estequiométrico y Poder Calorífico Inferior.

En primera instancia se realiza el balance químico de la reacción con el uso de la ecuación 1 a 3 de nuestra metodología, indicándo tanto el número de moléculas, volúmenes y pesos moleculares de cada compuesto.

$$CH_4 + \left(1+\frac{4}{4}\right)O_2 = 1CO_2 + \left(\frac{4}{2}\right)H_2O$$

$$CH_4 + 2O_2 = 1CO_2 + 2H_2O$$

$$1\,mol + 2\,mol = 1\,mol + 2\,mol$$

$$16\,kg + 32kg = 44\,kg + 36\,kg$$

$$80\,kg = 80\,kg$$

$$1m^3 + 2m^3 = 1\,m^3 + 2m^3$$

Para determinar el PCI del metano comenzamos utilizando la ecuación 4 que se presenta en la metodología, misma que da como resultado el volumen que ocupa 1 kg de combustible.

$$1kg\ CH_4\left(\frac{22.41\ m^3}{16kg}\right) = 1.4\ m^3$$

$$\frac{1m^3}{1.4\ m^3} \Rightarrow \frac{35880\ \frac{KJ}{m^3}}{50254.42\ \frac{KJ}{m^3}}$$

Es decir que por cada kilogramo de metano que se tenga al 100% obtendremos 50254.42 KJ/m^3 .

Sin embargo se mencionó que el combustible no es metano solamente, por lo que hay que calcular las variaciones del PCI en presencia de diferentes concentraciones de metano-nitrógeno.

B. Calculo del PCI con diferentes composiciones de mezcla del combustible.

Como se mencionó estas variaciones están dadas en porcentajes volumétricos por lo que para convertirlo en porcentaje másico se realizaran los siguientes cálculos de acuerdo a la metodología.

Para el caso donde la relación es CH4 95% / N2 5%

Metano 95%

$$\frac{16\ kg}{22.41\ m^3} = 0.714\ \frac{Kg}{m^3}$$

Nitrógeno 5%

$$\frac{28\ kg}{22.41\ m^3} = 1.249\ \frac{Kg}{m^3}$$

Realizar una relación para determinar el peso que representa dicho porcentaje volumétrico

$$\frac{1\ Kg}{95\ \%} = \frac{.714\ \frac{Kg}{m^3}}{0.6783\ Kg} \qquad \frac{1\ Kg}{5\ \%} = \frac{1.249\ \frac{Kg}{m^3}}{0.0625\ Kg}$$

Se suman los pesos para determinar un total de la mezcla

$$0.6783\ Kg + 0.0625\ Kg = 0.7408\ Kg$$

Y se calcula el porcentaje de cada uno de los componentes

$$\frac{0.7408\ Kg}{0.6783\ Kg} = \frac{100\ \%}{91.6\%} \qquad \frac{0.7408\ Kg}{0.0625\ Kg} = \frac{100\ \%}{8.4\%}$$

Finalmente si un solo kilogramos de CH_4 produce 50254.42 $\frac{KJ}{m^3}$ tenemos que

$$91.6\%\left(50254.42\ \frac{KJ}{m^3}\right) = 46{,}016\ \frac{KJ}{m^3}$$

TABLA II. EQUIVALENCIA DE PORCENTAJES Y PODER CALORIFICO INFERIOR GENERADO

% VOLUMÉTRICO	% MÁSICO	PCI
CH_4 95% / N_2 5%	CH_4 92% / N_2 8%	46,016.10
CH_4 90% / N_2 10%	CH_4 95% / N_2 5%	42,073.47
CH_4 85% / N_2 15%	CH_4 95% / N_2 5%	38,396.64

C. Balance no estequiométrico y cálculo de efecto térmico CO/H2 =1.

Para balancear la ecuación correctamente se desarrolla la ecuación de Kissel (ecuación 8), tomando en cuenta la relación entre los productos inquemados de la combustión y el porcentaje de deficiencia de oxígeno en la reacción.

En el primer caso tenemos que se presenta una deficiencia del 5% de Oxigeno en la reacción además de que la relación de los productos inquemados es igual a 1.

Por lo tanto si en la relación estequiometrica se requieren tener dos moléculas de O2 por cada 1 de CH_4, y estamos mencionado una deficiencia del 5% de comburente, esto representa que (x+y)/2 = 0.1 por lo tanto la mezcla de productos inquemados CO y H2 = 0.2

Esto se realiza para los diferentes porcentajes de oxigeno ya mencionados. Obteniendo los siguiente balances químicos.

TABLA III. ECUACIÓN BALANCEADA MEDIANTE ECUACIÓN DE KISSEL

DEFICIENCIA DE OXIGENO	ECUACIÓN BALANCEADA
5%	CH4 + 1.9 O2 ↔ 0.9 CO_2 + 1.9 H_2O + 0.1 CO + 0.1 H_2
10%	CH4 + 1.8 O2 ↔ 0.8 CO_2 + 1.8 H_2O + 0.2 CO + 0.2 H_2
15%	CH4 + 1.7 O2 ↔ 0.7 CO_2 + 1.7 H_2O + 0.3 CO + 0.3 H_2

Partiendo de los balances anteriores se determina el valor de los productos de la combustión en cualquier otro punto mediante el siguiente gráfico.

GRAFICA I. GENERACIÓN DE PRODUCTOS EN RELACIÓN A PORCENTAJE DE OXIGENO RELACION DE CO Y H2 IGUAL A 1

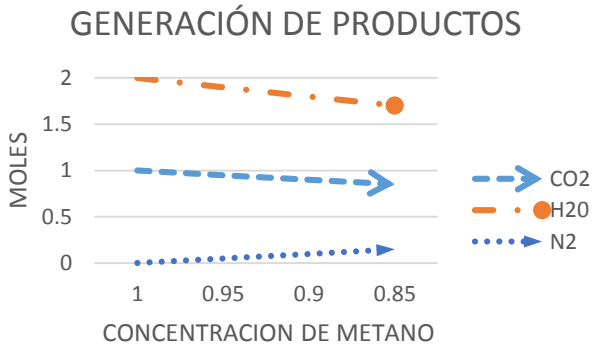

Una vez obtenido la cantidad de moléculas de estos componentes se multiplican por el PCI de su compuesto encontrado en tablas, se suma y se prosigue de acuerdo a la figura 1.

FIGURA I PROCESO DE CÁLCULO DE PCI PARA 100% DE METANO

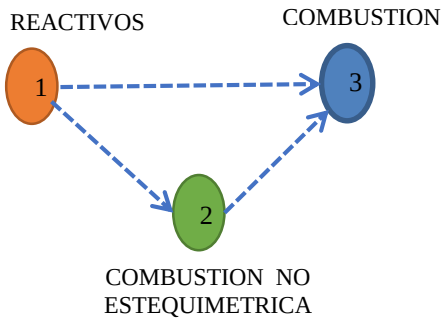

La figura anterior se refiere a que se debe sumar ambos poderes caloríficos y el resultado se resta al PCI del metano. Obteniendo así su valor final, sin embargo esto solo es real cuando se trata de una mezcla estequiometrica entre el combustible y el oxígeno, ya que existen diferentes variaciones se obtiene lo siguiente.

$$0.1CO\left(12640\frac{KJ}{m^3}\right) = 1264\frac{KJ}{m^3} \qquad 0.1H_2\left(10790\frac{KJ}{m^3}\right) = 1079\frac{KJ}{m^3}$$

Por lo tanto $35880\frac{KJ}{m^3} - (1264 + 10790) = \underline{33537\frac{KJ}{m^3}}$

Y de acuerdo a las deficiencias de oxigeno estudiadas esto se ve afectado de la siguiente manera.

$$CH_4 + 0.95[\,(1.9)O_2 = 0.9CO_2 + 0.1CO + 1.9\ H_2O + 0.1H_2]$$

$$CH_4 + 1.8O_2 = 0.855\,CO_2 + 0.095\,CO + 1.8\ H_2O + 0.095\,H_2$$

Una vez obtenido la cantidad de moléculas de estos componentes se multiplican por el PCI de su compuesto encontrado en tablas:

$$0.095CO\left(12640\frac{KJ}{m^3}\right) = 1200.8\frac{KJ}{m^3}$$

$$0.095H_2\left(10790\frac{KJ}{m^3}\right) = 1025.05\frac{KJ}{m^3}$$

Por lo tanto

$$35880(.95)\frac{KJ}{m^3} - \left(1200.8\frac{KJ}{m^3} + 1025.05\frac{KJ}{m^3}\right) = \underline{31860.15\frac{KJ}{m^3}}\}$$

Esta sección se repite para cada relación de productos inquemados y a su vez en cada una de estas habrá que repetir los cálculos para cada deficiencia de oxigeno propuesta; en cada una de ellas se recalcula con el cambio de composición de la mezcla en nuestro combustible.

Como mencionamos para la relación de productos inquemados igual 1 y una vez realizado todos estos cambios podemos agrupar los datos de la siguiente manera:

TABLA IV. RESULTADOS PCI RELACIÓN INQUEMADOS IGUAL 1

PODER CALORIFICO INFERIOR $\frac{CO}{H_2} = 1$				
% CH_4 / % O_2	100	95	90	85
5 %	33,537.00	31,860.15	30,183.30	28,506.45
10 %	31,194.00	29,634.30	28,074.60	26,514.90
15 %	28,851.00	27,408.45	25,965.90	24,523.35

GRAFICA II. PCI A DIFERENTES DEFICIENCIAS DE OXÍGENO EN RELACIÓN DE INQUEMADOS IGUAL A 1

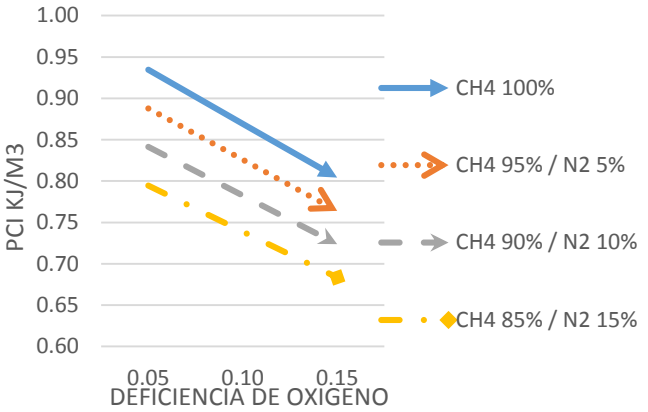

D. Balance no estequiométrico y cálculo de efecto térmico CO/H2 =1.1

En este caso así como en la siguiente relación de inquemados (sección E) se realizaron los mismos pasos que en la sección anterior, obteniendo resultados similares, aunque con la diferencia de que se producirá a mayor cantidad de hidrogeno y/o monoxido de carbono, disminuyendo así la generación de agua y dióxido de carbono respectivamente.

GRAFICO III. GENERACIÓN DE PRODUCTOS EN RELACIÓN A PORCENTAJE DE OXIGENO RELACION DE CO Y H2 IGUAL A 1.1

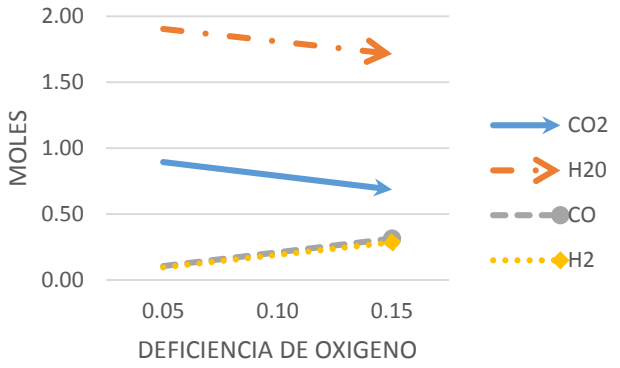

TABLA V. RESULTADOS PCI RELACIÓN INQUEMADOS IGUAL A 1.1

PODER CALORIFICO INFERIOR $\frac{CO}{H_2} = 1.1$				
% CH_4 / % O_2	100	95	90	85
5 %	33,527.75	31,851.36	30,174.98	28,498.59
10 %	31,175.50	29,616.73	28,057.95	26,499.18
15 %	28,823.25	27,382.09	25,940.93	24,499.76

GRAFICA IV. PCI A DIFERENTES DEFICIENCIAS DE OXIGENO EN RELACIÓN DE INQUEMADOS IGUAL A 1.1

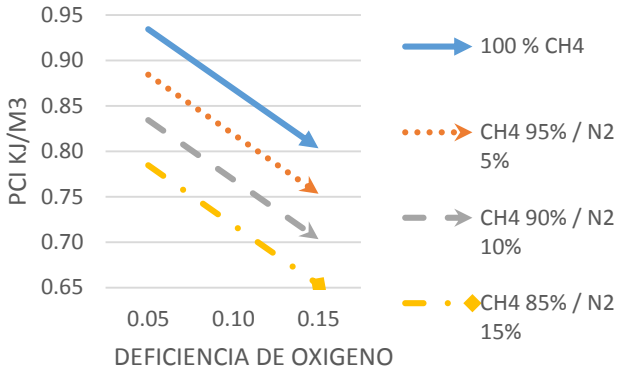

E. Balance no estequiométrico y cálculo de efecto térmico $CO/H_2 = 0.9$

GRAFICO V. GENERACIÓN DE PRODUCTOS EN RELACIÓN A PORCENTAJE DE OXIGENO RELACION DE CO Y H2 IGUAL A 0.9

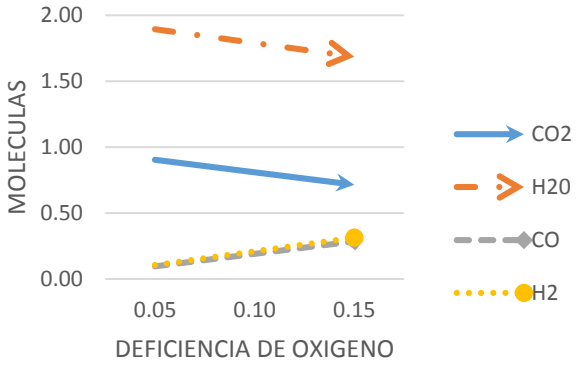

TABLA VI. RESULTADOS PCI RELACION INQUEMADOS IGUAL A 0.9

PODER CALORIFICO INFERIOR $\frac{CO}{H_2} = 0.9$				
% CH_4 / % O_2	100	95	90	85
5 %	33,546.250	31,868.938	30,191.625	28,514.313
10 %	31,212.500	29,651.875	28,091.250	26,530.625
15 %	28,878.750	27,434.813	25,990.875	24,546.938

GRAFICA VI. PCI A DIFERENTES DEFICIENCIAS DE OXIGENO EN RELACION DE INQUEMADOS IGUAL A 0.9

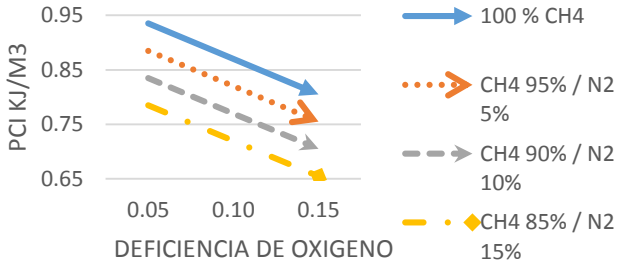

IV. CONCLUSIONES

Como resultado de la incorporación de nitrógeno a la mezcla combustible, el poder calorífico inferior se vio disminuido un 8% con cada 5% de nitrógeno agregado a la mezcla inicial de combustible. Por lo tanto, al disminuir 15% la presencia de metano e incorporar esa misma cantidad de nitrógeno en la mezcla de combustible, el PCI disminuye aproximadamente 24%. No como efecto de la absorción de calor del nitrógeno, sino por la disminución de CH_4 en el reactivo.

Se concluye que en relación de generación de productos incompletos CO/H_2 igual a 1 de, el PCI disminuye al considerar la concentración de oxígeno; en nuestra mezcla inicial de 100% metano con 5% de deficiencia de oxigeno revela que el PCI se reduce un 7% aproximadamente; en un 15% de deficiencia de oxígeno, el PCI a las mismas condiciones se reduce 20% aproximadamente; el comportamiento del PCI con la misma deficiencia de oxígeno en relación a la generación de los productos de la combustión incompleta 0.9 y/o 1.1 es similar, presentando las mismas variaciones.

Por otra parte, la generación de productos de combustión se ve afectada debido a una reacción incompleta, por esto, la producción de CO_2 y H_2O presenta un decremento, mientras que la generación de H_2 y CO se incrementa; no obstante el efecto de la relación con la que se generan estos últimos gases, determina la forma con la que estarán presentes en los productos; ya que al tener una relación entre ellos de 0.9 se produce una mayor cantidad de hidrogeno lo cual repercute en la generación de agua como producto de la combustión; mientras si se presenta una relación de 1.1 la cantidad de dióxido de carbono es inferior a causa de una mayor producción de monoxido de carbono.

El PCI que se obtiene al sustituir cantidades de metano por nitrógeno va disminuyendo no solo en combustión estequiometrica como se menciona previamente, también en combustión no estequiometrica presenta efectos, de manera que en el primer caso el PCI disminuye a razón del 8% con cada incorporación del 5% nitrógeno, mientras en no estequiometrica disminuye entre 4 y 5%, esto sobre la línea de deficiencia de oxígeno en la que se este 5,10 o 15%. Esto representa que PCI puede verse reducido en un 32% tomando en cuenta el valor de combustión completa (100% metano, 100% oxigeno) contra el lado opuesto del estudio, (decremento de aire y de metano del 15%), esto es una mezcla de 85% metano, 15% nitrógeno y 85% aire.

AGRADECIMIENTOS

Los autores agradecen al Instituto Politécnico Nacional, a la Sección de Estudios de Posgrado e Investigación de la Escuela Superior de Ingeniería Mecánica y Eléctrica Unidad Zacatenco Unidad Culhuacán, al Consejo Nacional de Ciencia y Tecnología y al Instituto de Ciencia y Tecnología del Distrito Federal por el apoyo brindado.

AUTOR

Ing. Guillermo Reyes Santiago, nació el 18 de abril de 1989 en México, D.F. estudiante de Maestría en Ciencias de Ingeniería en Sistemas Energéticos en la SEPI ESIME CULHUACAN por parte del IPN de tiempo completo, actualmente se encuentra en el cuarto semestre. Se tituló como Ingeniero químico en el 2011en la Universidad del Valle de México.

Dr. Georgiy Polupan. Profesor investigador de tiempo completo del Posgrado de Ingeniería Mecánica en el Instituto Politécnico Nacional de México. Es profesor de la ESIME-IPN desde 1999 a la fecha. En 1970 se tituló como Ingeniero mecánico en la Universidad Técnica Nacional de Ucrania. Posteriormente se graduó como Maestro en Ciencias de la misma Universidad en el año de 1972. Para el año de 1980 se obtuvo el grado de Doctor en Ciencias en Ingeniería Mecánica por parte de la Universidad Técnica Nacional de Ucrania.

Dr. Guillermo Jarquín López. Ingeniero Mecánico Agrícola de la Universidad Autónoma Chapingo (1994). Maestro en Ciencias en Ingeniería Mecánica en Diseño Mecánico cursado en la Sección de Postgrado e Investigación de la ESIME Zacatenco-IPN (1997) y Doctor en Ciencias en Ingeniería Mecánica Opción Energética en la Sección de Postgrado e Investigación de la ESIME Zacatenco-IPN (2006). Actualmente es profesor Titular "C" de la ESIME Culhuacán en el IPN. Áreas de Investigación: Generadores de vapor, Mecánica de fluidos, Combustión, Contaminación del medio ambiente y transferencia de calor.

REFERENCIAS

[1] Huang Zhao Xiang. Selected Works of combustion: Lecture of combustion course. China, 2006.

[2] Prabir Basú, Cen Kefa y Luis Jestin. Boilers and burners design and theory. Mechanical engineering series. Editorial Springer-Verlag, New York, 2000

[3] Tesis de grado "Estudio numérico del proceso de mezclado de oxígeno-metano para un generador de vapor en fondo de pozo petrolero" Ing. Mauricio de la Cruz Ávila.

[4] Tesis de grado "Estudio Numérico del Proceso de Combustión de Metano con Oxígeno en una Cámara de Combustión a Presiones Mayores a la Atmosférica." Manuel Alejandro Velázquez Priego

[5] Art. Cálculo del intercambio de calor en el hogar de un generador de vapor de 350 MW de potencia que usa combustóleo. SEPI-ESIMEZ, México, 2001

[6] E.M. Pismeny. Ingeniería Termica. Ministerio de Educación superior de Ucrania. 2005.

[7] A.L. Miranda y M Flores. Ingeniería Térmica. Grupo Editorial Ceac, S.A., 1999.

[8] Combustión y quemadores de Manuel Márquez Martínez

The mexican iol refining after the 2013 Energy Reform

Ing. Laura Martínez-Rendón
SEPI from Escuela Superior de Ingeniería y Arquitectura campus Ticomán
Instituto Politécnico Nacional
Mexico's City, Mexico
billerouge@hotmail.com

Dr. Daniel Romo-Rico
SEPI from Escuela Superior de Ingeniería y Arquitectura campus Ticomán
Instituto Politécnico Nacional
Mexico's City, Mexico
dromorico@hotmail.com

***Abstract*— The Mexican oil Refining industry was a monopoly activity, through PEMEX, in the whole value channel, except in retail sales, which was doing by private companies through PEMEX'S franchises. On December 28, 2013, this monopoly was ended and private companies could participate in the industry, just alone or associated with state companies. What will happen with the Mexican oil refining in the becoming years? This paper analyses the set of factors needed to impulse the oil refining industry in Mexico. In the first part is identified the set of structural factors faced by the investors after the monopoly performance. Secondly, it is studied the main conditions to incentive the activity in the country. Finally, it is elaborate a perspective of its performance in the becoming years. It is concluded that new strategies should be created to impulse the refining production, thus private companies will mainly focus in retail sales, storage and transportation activities.**

***Keywords*—** *Mexican, oil, refining, industry, energy, reform*

I. INTRODUCTION (*HEADING 1*)

In recent years, a several number of structural reforms had been approved by Mexican government in order to revitalize the economy and therefore impressive changes in the education system, labour laws, telecommunications, tax system and energy sector are taking place.

The energy reform brings modifications on constitutional articles and secondary laws to finally open the oil, gas and energy market to private investors. When hydrocarbons stays underground are Mexican property but celebrating a contract allows private companies to explore and produce them. In case of downstream activities a permission given by Secretaría de Energía (SENER) it's going to be enough to develop activities as oil refining, transport and storage.

We identify main six effects on refining industry:

1. Oil and gas production. Those two are refining's raw materials and the way they are produce is traduce in prices and costs. Even nature of the oil has a result in processing plants.
2. Distillates and petrochemicals. Every single link in value chain is important and if they achieve to be really integrated it's going to be benefic for both.
3. Transport, storage and distribution of hydrocarbons and their derivatives. The Comisión Reguladora de Energía (CRE) it's going to be in charge to extend permits to private companies, hoping to develop an expansion of pipelines because they are the cheapest way of transport.
4. Producing, transmission, distribution and sale of electricity. Nacional Refining System was designed to cover fuel oil demand to produce electricity, now at days, natural gas is replacing it.
5. Security, sustainability, commitment to the environment, use of technologies and cleaner fuels. International laws are stricter than nationals so there are going to be necessary to follow world's regulations in order to be competitive.

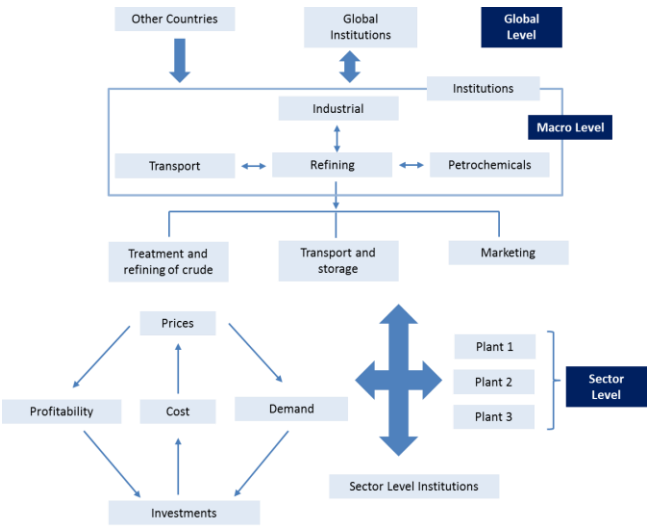

Figure 1 Refining and multidimensional interactions

6. Combat corruption. As corruption decrease there's a probably to clear red numbers on balance sheets.

Now at days, Mexico is facing a transition time and taken desertions from now on are going to be reflected on country's economic performance because of energy is used directly and indirectly in production of goods and services. Figure 1 shows the refining multidimensional interactions to understand how this industry is linked to other markets.

II. WHAT ABOUT OIL REFINING IN MEXICO?

In order to identified the set of structural factors that will be faced by the investors after the monopoly performance we considered necessary to understand the actual situation of Mexico's refining industry by doing a competitive analysis which considers six topics: related institutions, infrastructure and technology, suppliers, dealers and clients, operating and finally finances.

A. Related institutions

Some of them are in different sectors and they are Secretaría de Hacienda y Credito Público (SHCP), Secretaría de Energía (SENER), Comisión Nacional de Hidrocarburos (CNH), national and international chambers of commerce, etc. The real weight of national institutions takes place when efforts need to concentrate on a single direction to make a decision or play an action. The refining macroeconomic environment is a scenario that has been ruled by international institutions and its governments, who determinates the quality and emission standards.

B. Infrastructure and technology

Since 35 years there are 6 refineries with a total capacity of 1.535 mbd (million barrels per day) but only 79.7% of capacity was used in 2013 main. Only half of national refineries have deep conversion technology (Coker) and the rest has FFC, this is important because most of the oil produced in Mexico, Maya crude, is heavy and needs more investment to process it by more sophisticate technologies. In fact, the fuel oil obtained in Mexican refineries it's becoming a huge problem in to the storage and distribution terminals that are more than full so the production level in refineries needs to below the crude processed.

Dispite vacuum residue processing at Tula, clean fuel project, reconfiguration of Salamanca refinery, fleet developments, Tuxpan pipeline and Minatitlán projecst refining industry needs to increase investments talking about infrastructure to be competitive at international level.

Table 1 Mexican refining in 2013

Refinery	Opening	Technology	Total Capacity	Capacity Used in 2013	Real Percentage Used
			(thousand de barreles per day)		
1. Cadereyta	1979	Coker	270	188.8	69.9
2. Madero	1960	Coker	170	129.8	76.4
3. Minatitlán	1967	Coker	200	182.8	91.4
4. Salamanca	1950	FCC Alk Lubs	245	194.5	79.4
5. Salina Cruz	1979	FCC Alk	330	282.4	85.6
6. Tula	1976	FCC Alk H-Oil	320	245.8	76.8

C. Suppliers

Wells and services consumed by Pemex Refining (PR) are divided in two categories a) substantive productive activates like the ones linked to industrial process and b) no alternative activities like the ones not directly related to operation: cleaning and maintenance of offices and administrative buildings, computes equipment, medical nature products and services, etc. Now it's pretty clear that the oil consumed in refineries has being bayed at Pemex Exploration and Production (PEP), who says that each barrel of oil equivalent production cost and exploring and development cost is equal to $22.82 USD in 2013 ($320 MXPs.) and there taking in count PEP's sales data, a barrel of oil equivalent for PR cost 94.4 USD (1321.5 MXPs) in the same year.

In the other hand, the catalysts are very important at the plants because they accelerate the reactions and helps to obtain a better conversion ratio, looking in to Instituto Nacional de Transparencia, Acceso a la Información y Protección de Datos (IFAI) data base, we found out that PR used to have at least four different suppliers but from 2009 practice had finished and now there's only W.R Grace CO CONN some of the best practices in businesses recommends to diversify and expand shareholders not to reduce them.

D. Dealers and clients

Major refined products sales market are celebrated in the country, Comisión Federal de Electricidad (CFE) is the main consumer followed by Aeropuertos y Servicios Auxiliares and the rest through PEMEX'S franchises. The next figure shows the intersegment sales from PR and the main products bayed by each subsidiary.

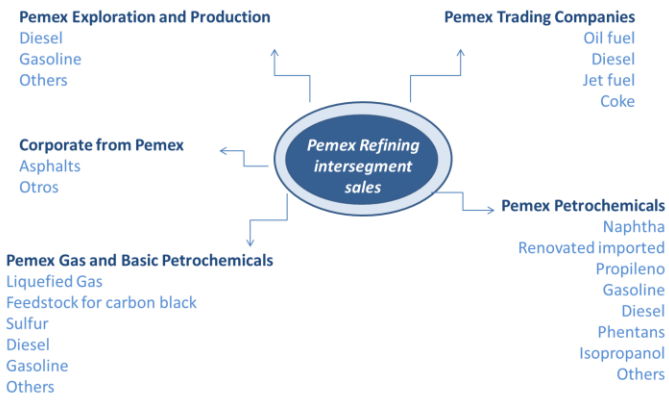

Figure 2 Intersegment sales of distillates

Is important to mention that fuel oil is the more sales product to Pemex Trading Companies, it bays more than any other subsidiary company.

E. Operating

There have been operational problems because of mishaps that could have been avoided by programing a scheduled maintenance instead of have to do non-scheduled maintenance and overhaul work. Production has been stopped or reduced because the startup of reconfigured plants and stabilizing process takes more time. Low efficiently heaters, boilers and turbine generators for obsolescence caused problems as well as fuel oil high inventories (mainly in Salamanca and Tula) are an obstacle factors to obtain a good operating efficiency.

F. Finances

The following table condenses financial ratios calculated with PEMEX balance sheet information.

Table 2 Financial ratios helps to understand refining situation

Pemex Refining's Financial Ratios							
	2007	2008	2009	2010	2011	2012	2013
Liquidity Warnings							
Liquidity	1.5	1.3	1.2	1.1	0.8	0.9	0.8
Working Capital	80,826,947	48,076,060	60,300,353	47,950,117	-81,605,946	-45,684,546	-78,167,818
Acid-Test Ratio	-0.07	1.40	1.20	1.19	1.15	1.69	1.38
Financing of debt							
Property	57.32	-4.12	2.39	-2.30	-25.14	-52.56	-39.83
Indebtedness	90.40	104.12	97.61	102.30	125.14	152.56	139.83
Financial leverage	1.58	-25.28	40.83	-44.52	-4.98	-2.90	-3.51
Profitability							
Rent on equity	-0.19	12.74	-7.80	6.27	0.92	0.37	0.58
Rent on assets	-0.11	-0.52	-0.19	-0.14	-0.23	-0.20	-0.23
Dupont	-0.11	-0.52	-0.19	-0.14	-0.23	-0.20	-0.23
Gross income	-0.16	-0.43	-0.16	-0.17	-0.35	-0.30	-0.18

The segments divide ratios by its study objectives, the firs one includes some liquidity warnings that measure the availability of cash to pay debt. The second segment, financing of debt ratios measure the ability to repay long term debt. The last segment is the profitability ratios measure Pemex Refining use of its assets and control of its expenses to generate rate of return.

With a simple overview we can say that Pemex does not have funds to invest in expanding nor properly maintaining refining capacity to meet the increased demand.

III. WHAT COMES AFTER THE ENERGY REFORM?

After analyzed PR situation, it's time to study the main conditions to incentive the activity in the country under the possibilities of the new energy reform:

- Invest in complex technology that allows processing heavy crude and to obtain mid and light products, reducing oil fuel production and eventually increase total capacity in order to cover the growing national demand of gasoline, diesel, jet fuel and others. In order to achieve higher yields PEMEX need to reduce investment risk by establishing joint ventures or farmouts with big transnational companies who can transfer knowledge to Mexican refining industry.
- Once oil fuel reduce its production some fleet costs will be reduced but the truth is that boost pipeline transportations is going to be necessary when the producing capacity from national refining system growths.
- Within the framework of an open market, the national products have to cover quality standards and environmental laws to stay in contest.
- About human resources, the restructure is in course but impress ethical sense is vital to reduce corruption in and outside the company. The training programs should improve its results and the ones that are not productive are going to disappear.
- Improve logistics and develop a refined product marketing to face different brands.

IV. PERSPECTIVE

SENER's forecast indicates that the growth demand of distillates, particularly low sulfur gasoline and low sulfur diesel, are going to register an annual growth rate of 2.9% and 3.5% respectively mainly for the transport sector. While fuel oil will decrease in 11.8% because of CFE is changing into a natural gas to produce cleaner electricity.

So refining has an opportunity in Mexican national market but, what will happen during the gradual transition to the open market? Next figure shows in blue, the main pillars of the way to prepare the ground for private sector arrival. At the low part of figure 3 there are three possible scenarios 1) PEMEX as a leader in Mexican refining industry, 2) Private industries leading refining in Mexico and 3) Mexico dependents on imports. Each possible line describes the actions that should be made to achieve supply refining products to Mexican people.

V. CONCLUSIONS

The energetic reform is an effect of macroeconomics world's situation, and Mexico needs to wake up and face the powerful wave that comes to catch possibilities of stablish farmouts that really beneficiates the nation improving infrastructure and developing new to boost not only refining growth but also across the entire oil value chain.

In near future big private companies are not going to start producing refining products by it selves, building a new refinery will take more than a couple of years so probably they are going to star in one of PEMEX's refineries and eventually they are going to be able to sell their own brands.

That's way the man activities for private companies are going to be concentrate at retail sales, storage and transportation activities for next five years.

Becoming years are only the first step into a plan to start bilateral energy cooperation between Mexico and USA to continue later with Canada in order to conform the North America's block. Mexico's refining infrastructure would be a

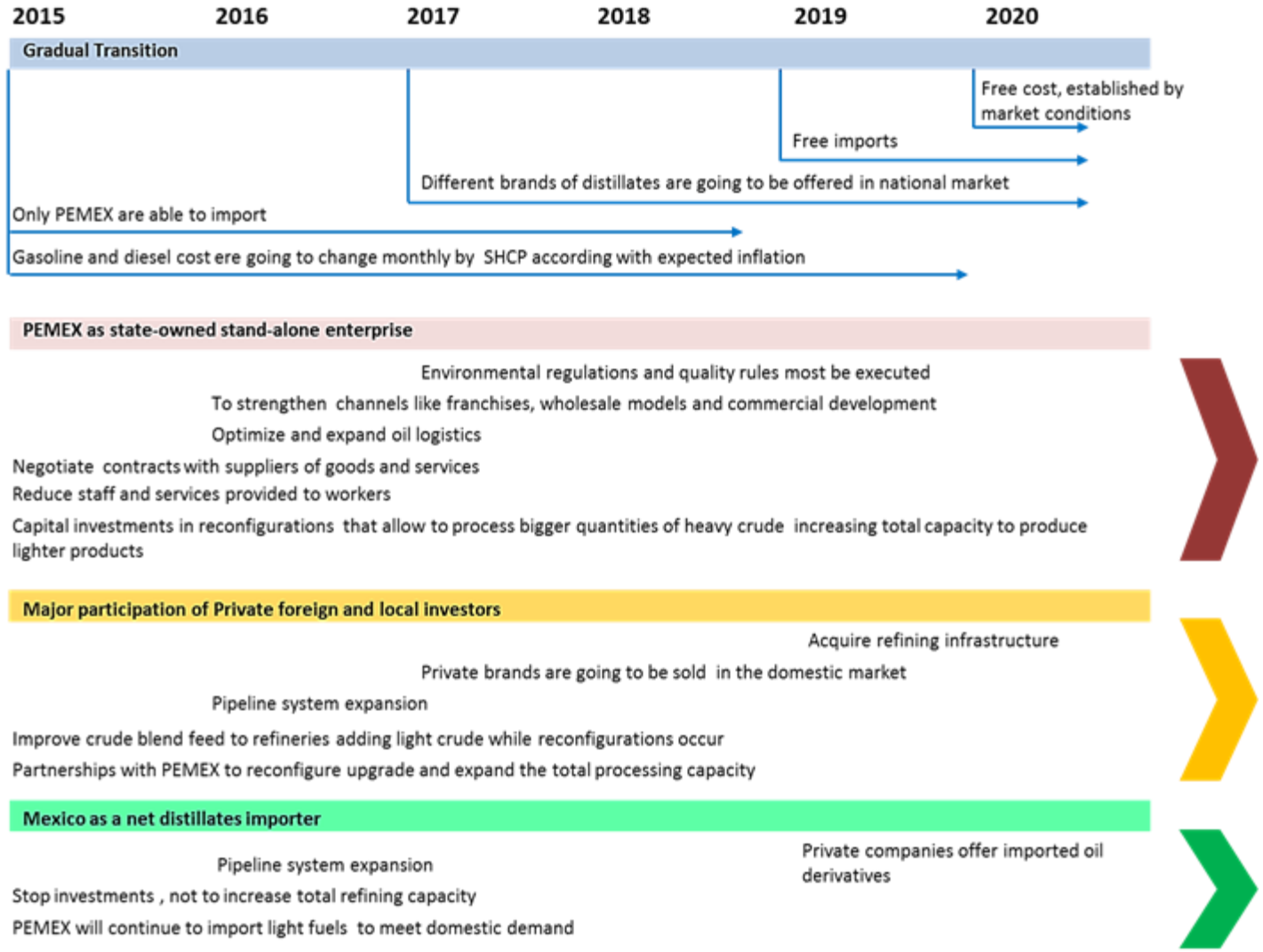

Figure 3 Possible Refining scenarios

good option to process light oil shale from US and heavy Mexican crude will continue to be refined at north.

ACKNOWLEDGMENT *(Heading 5)*

……..

REFERENCES

- Castilla, J., & Prakash, S. (2014). *http://www2.deloitte.com/*. Retrieved 04 2015, from http://www2.deloitte.com/content/dam/Deloitte/us/Documents/strategy/us-cons-mexicoenergyreformpaper2014final-0342014.pdf
- eia. (n.d.). *www.eia.gov*. Retrieved 03 10, 2015, from http://www.eia.gov/todayinenergy/detail.cfm?id=7110
- IFAI. (n.d.). Retrieved Abril 2015, from http://portaltransparencia.gob.mx/pot/contrataciones/showConsulta.do?method=showConsulta&_idDependencia=18576
- OECD. (2014, 03 13). OECD Secretary-General. *Mexico Stands Out: Implementing Reforms for a Historic Transformation*. London, England.
- OECD. (2015, 01). *OECD Economic Surveys Mexico*. Retrieved 02 2015, from http://www.oecd.org/: http://www.oecd.org/eco/surveys/Mexico-Overview-2015.pdf
- PEMEX. (2014). *www.pemex.com*. Retrieved 06 2014, from http://www.pemex.com/en/investors/Paginas/default.aspx#.VWtd8M9_Okp
- Petróleos Mexicanos. (2013). *FORM 20-F*. Ciudad de México.
- Seelke, C. R., Ribando Seelke, C., Villareal, M. A., Ratner, M., & Brown, P. (2015). *Mexico's Oil and*

Gas Sector: Background,Reform Efforts, and Implications for the United States. Congressional Research Service.

- Von Wobeser & Sierra. (n.d.). *www.vonwobeserysierra.com*. Retrieved 2015, from http://www.vonwobeserysierra.com/assets/files/PDF/news/minuta1-esp.pdf
- ZENTENO-LIRA MORA ABOGADOS. (2013). Retrieved 2014, from http://www.pwc.com/es_MX/mx/industrias/archivo/2013-12-14-comunicado-reforma-energetica.pdf

Silicon Microwires by a Combination of Chemical Etching Techniques for Application in Li Ion Batteries- Proof of Concept

O. Pérez-Díaz, E. Quiroga-González*, N. R. Silva-González
Institute of Physics
Benemérita Universidad Autónoma de Puebla
Puebla, Mexico
*equiroga@ieee.org

***Abstract*—This paper presents an alternative method for the fabrication of Si wire anodes for Li ion batteries. The purpose is to make anodes at low-cost.**

Keywords—Silicon, Energy Storage, Microwires, Li Ion Batteries, Chemical Etching

I. INTRODUCTION

In recent years an important factor of breakthrough technology has been developed, like electric cars and smartphones. Nevertheless, these new technologies require more energy while being still portable, so the development of new forms of energy storage is required.

In present days the most commonly used anode material in Li batteries is graphite due to its low production cost, but it can only provide a capacity of 330mAh g^{-1} [1]. On the other hand, Si is an attractive material to replace it, because it has a low discharge potential (about 0.7 V) and high capacity (4200 mAh g^{-1}) [2, 3]. Si is one of the most abundant elements in the earth crust. Additionally, Si has a technologically significant importance because it is the basic material for the manufacture of semiconductor devices for the electronics industry [4], making it relatively cheap.

However, although the capacity of Si is more than ten times that of any existing graphite-based anode, and much larger than the various nitrides and oxides [5, 6], in its bulk state it is useless as anode, since it pulverizes after some charge/discharge cycles due the volume expansion (up to 300 %). The solution is to micro or nano structure it to withstand the volume change. Some of the possible structures are nanowires, nanopillars, microwires or thin films to name a few. The most promising form in which Si can be used as anode for Li ion batteries is in microwires [7]. Many of the others concepts still suffer of short battery lifetime due to pulverization or loss of electrical contact between the active material and the current collector [1]. Si microwires possess an areal capacity (the amount of charge that the electrode can store per nominal area) ten times larger than any other form of Si anodes. Si microwires also exhibit a record charge density rates (charge stored per unit of time, per unit of area of the electrode) just some anodes with conductive additives can be charged faster [8]. For example, Si nanowires present an areal capacity of 0.52 mAh/cm^2 and a charge density rate of 0.17 mAh/cm^2h [9] while Si microwires presents values of 5.67 mAh/cm^2 and 2.84 mAh/cm^2h, respectively. Additionally Si nanowires show considerable fading, while Si microwires maintain the full capacity after 100 cycles.

The objective of this work is the preparation of Si microwires by an alternative method. For manufacturing Si microwires, three main techniques have been used in the past:

- Vapor-liquid-solid technique (VLS). This technique offers the possibility to grow Si wires with controlled diameter, density, length, position and doping [10].
- Metal-assisted catalytic etching of single-crystalline Si [11, 12].
- Electrochemical macropore etching followed by chemical over-etching [7].

The first method can expect problems with respect to mass production. This method generally produces a random array of wires with various sizes and shapes. The second method is more controllable relative to the production of vertical wires, but the lengths of wires that have been obtained until now, are limited to tens of microns. The third method does not suffer the aforementioned disadvantages; however, it is a method which involves processes that can be a bit more expensive due to the equipment required for the preparation of the wires.

Here it is proposed the fabrication of Si microwires by the combination of two methods: Metal assisted chemical etching of mesopores in HF-based solutions, and anisotropic over-etching in KOH-based solutions. It is intended to produce wires at low cost, at different scales of diameter.

II. EXPERIMENTAL DETAILS

The steps for the preparation of the wires can be summarized in the following points where an example recipe is also described:

a) Photolithography and pre-structuring of Si wafers. The first step of the process is standard photolithography to define an array where some parts will be etched. The surface of a Si wafer is covered with a layer of photoresist.

Afterwards, a quadratic pattern is transferred to it through photolithography (exposure to light and further development); in this way, there will be a pattern with regions where there will be no sensitive material (Fig. 1 a).

b) Deposition of catalyst particles and etching of the sample by MACE. The metal catalyst used in this work is Ag. For the deposition of the Ag particles a solution based on HF-H_2O_2 and $AgNO_3$ was used. Si was immersed in the solution and using the ultrasonic bath the deposition took place [13, 14]. Ag particles will cover the entire sample, it means, in the place with photoresist or in the uncovered part (Fig. 1 b).

The next step is dipping the sample in a solution of HF-H_2O_2. Etching takes place in areas where there is Ag particles (MACE). In the present work the used quantities are 2 ml of HF and 3.5 ml of H_2O_2.

c) Chemical over-etching to produce wires. At this point the wires have not formed yet; we only have a pattern with porous regions so an over-etching is required to merge the pores and obtain the wires (zones between porous regions). The over-etching is accomplished with an anisotropic etching solution based on KOH. The etchant was composed of KOH at 0.45 wt % and 2 g polyethyleneglycol (PEG), kept at 50 ºC.

d) Prepare an anode with the Si wires. Anodes can be obtained by depositing a Cu current collector on the top of the array of wires. A second way of making the anodes is to prepare a paste of Si wires, using a binder (CMC, for example) and a conductive additive (carbon black), and subsequently spread it on a current collector (Fig. 1 d).

For the experiments, pieces of 1x1 cm^2 of p-type Si (1 0 0) wafers with resistivity of 15-25 Ω cm were used. Prior the experiments, they were immersed in oxidant solution containing H_2SO_4 and H_2O_2 in a volume ratio 3:1 for 10 min under room temperature to entirely remove organics and to form a thin oxide layer and washed with abundant deionized water (18.1 MΩ cm) and dried with air compressor.

An optical microscope (mini microscope MC108) and a JEOL JSM-7800F scanning electron microscope were used to characterize the prepared samples.

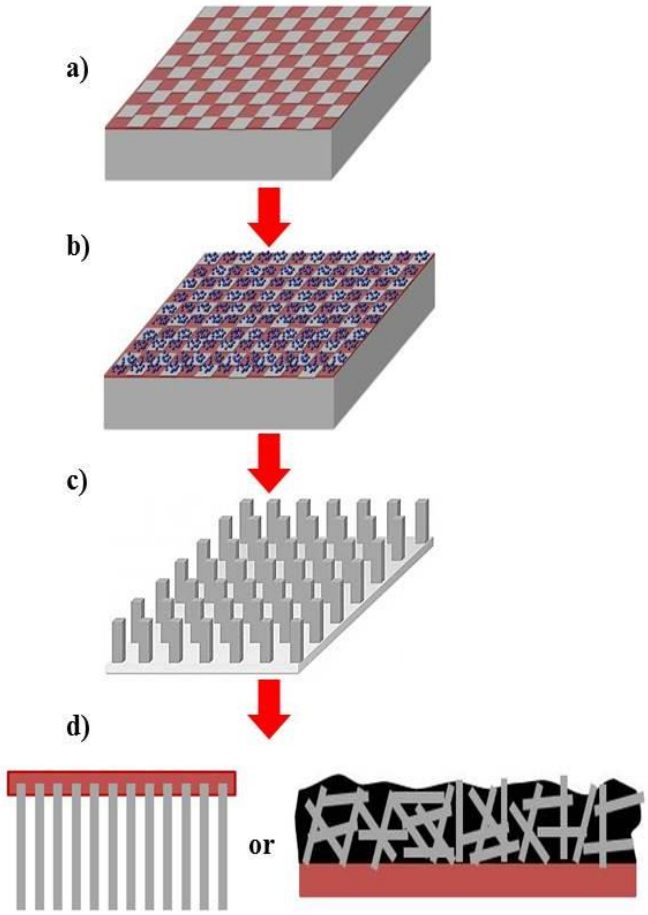

Fig. 1. Process to obtain anodes based on Si microwires.

III. RESULTS AND DISCUSSION

In this section the results obtained to date are presented. Fig. 2 exhibits a sample with a pattern of photoresist. The sample was prepared with a cheap photoresist used for serigraphy; even though, the resulting patterns have good resolution. The pattern used for this work looks like a chess board of square-like holes of about 200 µm per side. The dark sections of the figure are the holes (sections without photoresist).

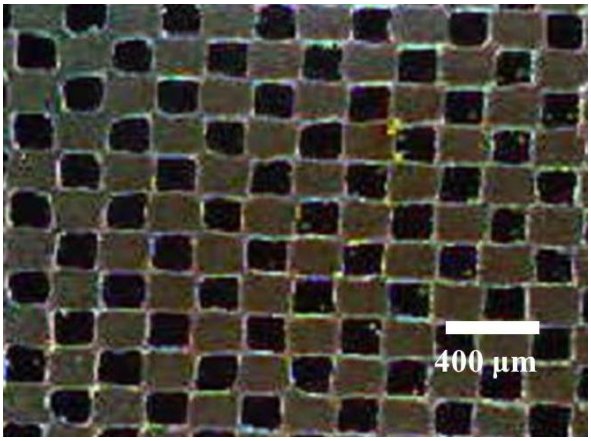

Fig. 2. Si sample with a pattern layer prepared by photolitography.

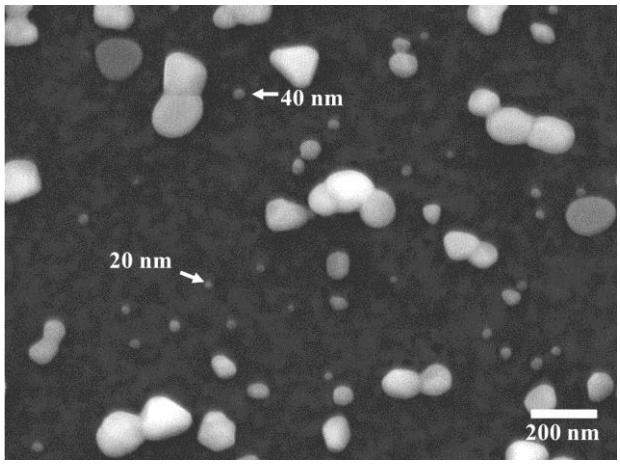

Fig. 3. Ag particles deposited on the uncovered Si sections.

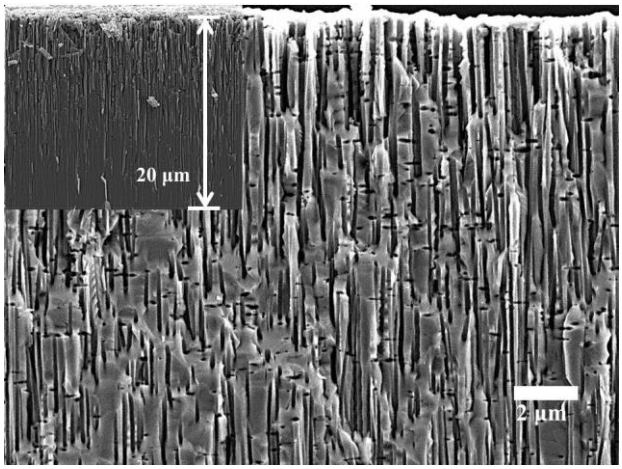

Fig. 4. Cross section of a sample after MACE.

In Fig. 3 it can be seen that the particles are well dispersed on Si. Their smallest sizes are in the rage of 20 to 40 nm indicated with arrows. The formation of clusters can be observed. However the shape of the particles or the formation of clusters is neither important for our work, it only matters that the pores are straight.

Fig. 4 shows a SEM micrograph of a sample after MACE. Based on several tests it was possible to determine an etching rate of approximately 10µm/h in the axial direction with the actual etching concentrations. The formed pores have about the same size, and are straight. In the inset one can see a porous layer obtained after 2 h of etching, with a depth of around 20 µm. The etching rate is relatively constant with time, at least until 8 h of etching (images not shown). In this way, one can vary the length of the pores (wires at the end of the process) without a problem.

Fig. 5 shows the sample resulting after the over-etching step in KOH-based solutions. It can be seen that after the whole process it is possible to obtain wires (mesas in this work). The diameter of the mesas depends mainly on the pattern defined by photolithography. The porous zones are the ones etched away much faster, leaving the mesa-structures standing (zones between porous sections). This proves that the method works. It does not need any expensive material or equipment of difficult access.

For future work, the diameter of the mesas may be reduced significantly by using patterns with smaller holes and reduces distances between them. This would allow the production of real micro-wires. Once having wires, anodes for batteries will be produced.

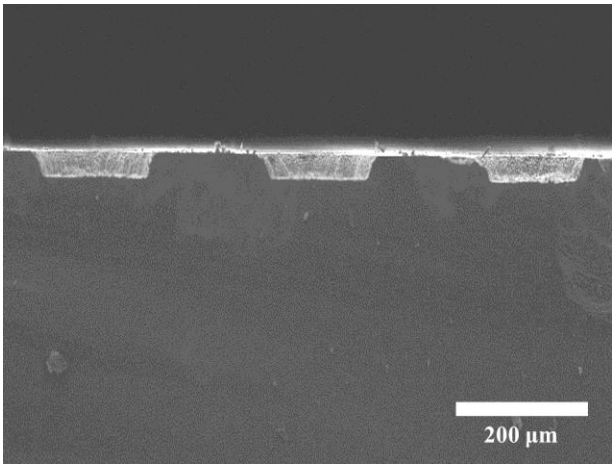

Fig. 5. Si sample at the end of the process.

IV. CONCLUSIONS

A new method for the preparation of Si microwire anodes for Li ion batteries was presented. Wires (mesas, in this work) were obtained at the end of the process, indicating that the fabrication process works quite well. This result is promising.

The diameter of the mesas is well defined by photolithography. The areas of the mesas are protected with photoresist, and the rest is etched away in two steps: metal assisted chemical etching to form a porous layer at a rate of about 10µm/h, and dissolution of this layer in KOH etchant.

ACKNOWLEDGMENT

This work was funded by the projects CONACyT INFR-2011-1-163153, CONACyT CB-2014-01-243407, PROMEP BUAP-NPTC-377, and Plan de Trabajo CA-190.
O.P.-D. acknowledges the economic support from CONACyT through the scholarship with number 378447.

REFERENCES

[1] C. K. Chan, H. Peng, G. Liu, K. McIlwrath, X. F. Zhang, R. A. Huggins, and Y. Cui, "High-performance lithium battery anodes using silicon nanowires" *Nat. Nanotechnol*, vol. 3, pp.31-35, 2008.

[2] C. J. Wen, R.A. Huggins, "Chemical diffusion in intermediate phases in the lithium-Silicon system", *J. Solid State Chem.*, Vol. 37, pp. 271-278, 1981.

[3] B. A. Boukamp, G. C. Lesh, and R. A. Huggins," All-Solid Lithium Electrodes with Mixed-Conductor Matrix" *J. Electrochem. Soc.*, vol. 128, pp. 725-729, 1981.

[4] M. P. Groover, Fundamentals of Modern Manufacturing: Materials, Processes, and Systems, John Wiley & Sons, p. 150, 2010.

[5] T. Shodai, S. Okada, S. Tobishima, J. Yamaki, "Study of $Li_{3-x}M_xN$ (M= Co, Ni or Cu) system for use as anode material in lithium rechargeable cells", *Solid State Ionics*,Vol. 86–88, pp. 785-789, 1996.

[6] P. Poizot, S. Laruelle, S. Grugeon, L. Dupont, J.-M. Tarascon, "Nano-Sized Transition–Metal Oxides as Negative Electrode Material for Lithium-Ion Batteries", *Nature*, Vol. 407, pp. 496-499, 2000.

[7] E. Quiroga-González, E. Ossei-Wusu, J. Carstensen and H. Föll, "How to Make Optimized Arrays of Si Wires Suitable as SuperiorAnode for Li-Ion Batteries"*J. Electrochem. Soc.*, vol.158, pp. 119-123, 201).

[8] E. Quiroga-González, E. Ossei-Wusu, J. Carstensen and H. Föll, "Optimal Conditions for Fast Charging and Long Cycling Stability of Silicon Microwire Anodes for Lithium Ion Batteries, and Comparison with the Performance of Other Si Anode Concepts" Energies, vol. 6, pp. 5145-5156, 2013.

[9] Ruffo, R.; Hong, S.S.; Chan, C.K.; Huggins, R.A.; Cui, Y. "Impedance analysis of siliconnanowire lithium ion battery anodes". J. Phys. Chem. C,Vol. 113, 11390–11398, 2009.

[10] K.-Q. Peng, X. Wang, L. Li, Y. Hu, S.-T Lee," Silicon nanowires for advanced energy conversion and storage", *Nano Today*, vol. 8, pp. 75-97, (2013).

[11] R. Huang, X. Fan, W. Shen, and J. Zhu, "Carbon-coated silicon nanowire array films for high-performance lithium-ion battery anodes" Appl. Phys. Lett.,vol. 95, pp. 133119-1 133119-3-2, (2009).

[12] M.-L. Zhang, K.-Q. Peng, X. Fan, J.-S. Jie, R.-Q. Zhang, S.-T. Lee, and N.-B.Wong, "Preparation of large-area uniform silicon nanowires arrays through metal-assisted chemical etching", *J. Phys. Chem. C*, vol. 112, pp. 4444- 4450, (2008).

[13] K. Tsujino, M. Matsumura," Morphology of nanoholes formed in silicon by wet etching in solutions containing HF and H_2O_2 at different concentrations using silver nanoparticles as catalysts", *Electrochim. Acta*, vol. 53, pp. 28–34, (2007).

[14] M. O. Farooq, "Study of electroless mesoporosification of lightly doped silicon p-type by different methods", M. Sc. thesis, Christian-Albrechts University of Kiel, Germany, (2014).

Flujo asimétrico en cámaras cilíndricas para distintos radios y fluidos

A. Lizardi R.*, H. Terres P., R. López C., M. Vaca M., J. Flores R.,
A. Lara V., S. Chávez S., J. R. Morales G.
Universidad Autónoma Metropolitana-Azcapotzalco
Departamento de Energía, Área de Termofluidos
Av. San Pablo 180, Col. Reynosa Tamaulipas,
Del. Azcapotzalco, C.P. 02200, México D. F.
Email: arlr@correo.azc.uam.mx

Resumen. **En este trabajo se analiza numéricamente la distribución de las líneas de corriente (Ψ) y de las componentes de velocidad radial (u) y axial (w) generadas por el movimiento de un fluido que gira en el interior de una cámara cilíndrica cerrada y que tiene un disco impulsor situado a la mitad de la cámara. Para ello se modelan y resuelven en forma numérica las ecuaciones de Navier Stokes en estado permanente para un fluido incompresible. Los resultados se muestran para once radios del impulsor y dos tipos de fluido: agua y gasolina que, de acuerdo a la situación física del problema, corresponden a un número de Reynolds de $2.74x10^4$ y $0.63x10^4$, respectivamente. Algunos resultados indican que la estructura del flujo se compone de dos zonas: una que gira en sentido horario, ubicada por debajo del disco rotatorio, y otra que gira en sentido anti horario, ubicada por encima del mismo, además de un flujo secundario que se genera para ciertos casos específicos. Al aumentar el radio del impulsor un 75% se encontró que: la componente de velocidad radial positiva (u) aumentó 9.28 veces para $Re=2.74x10^4$ y 7.83 veces para $Re=0.63x10^4$; la componente de velocidad axial negativa (w), por debajo del disco impulsor, aumentó 7.42 y 4.36 veces, para los mismos números de Reynolds; y la componente de velocidad axial negativa (w), por encima del disco impulsor, disminuyó 0.76 y 0.74 veces, para los mismos números de Reynolds.**

Palabras clave: Flujo asimétrico, cámaras cilíndricas, líneas de corriente, velocidad radial y axial.

Abstract. **The streamlines, the velocity components radial (u) and axial (w) generated by the moving of a fluid inside a closed cylindrical vessel with a rotating impeller located in the middle of its longitudinal axis are obtained by a numerical analysis. The Navier-Stokes for an incompressible fluid in steady state flow are modeled and solved numerically together with the adequate boundary conditions. The results for eleven radii of the impeller and two different fluids, water and gasoline, are presented. The corresponding Reynolds number for the physical situation is: $2.74x10^4$ and $0.63x10^4$ respectively. Some results indicate that the flow structure presents two zones, the one located underneath the impeller rotates clockwise, whereas the one located above de impeller moves counter-clockwise; moreover it is noted that there is a secondary flow for certain specific cases. With a 75% increase of the impeller radius it was found that the positive radial velocity component (u) increased 9.28 times for $Re=2.74x10^4$ whereas for $Re=0.63x10^4$ the increment was 7.83 times; the negative axial velocity component (w) underneath of the impeller increased 7.42 and 4.36 times for the same Reynolds numbers. The negative axial velocity component (w) above the impeller decreased 0.76 and 0.74 times for the same Reynolds numbers.**

Keywords: Asymmetric flow, cylindrical vessel, streamlines, velocity radial and axial.

I. NOMENCLATURA

i	punto discreto en la dirección radial
j	punto discreto en la dirección axial
g	aceleración gravitatoria (m/s^2)
Re	número de Reynolds
r	coordenada radial adimensional
z	coordenada axial adimensional
Δr	espacio de la malla en dirección radial
Δz	espacio de la malla en dirección axial
u	componente de velocidad radial adimensional
v	componente de velocidad tangencial adimensional
w	componente de velocidad axial adimensional
P	presión [Pa]
R	coordenada radial dimensional [m]
Z	coordenada axial dimensional [m]
U	componente de velocidad radial dimensional [m/s]
V	componente de velocidad tangencial dimensional [m/s]
W	componente de velocidad axial dimensional [m/s]
γ	función circulación dimensional [m^2/s]
ς	función vorticidad dimensional [1/s]
ψ	función corriente dimensional [m^3/s]
ν	viscosidad cinemática [m^2/s]
ρ	densidad [kg/m^3]
Ω	velocidad angular del impulsor [rad/s]
Γ	función circulación adimensional
ξ	función vorticidad adimensional
Ψ	función corriente adimensional

II. INTRODUCCIÓN

El empleo de métodos numéricos en la solución de problemas de mecánica de fluidos y transferencia de calor se justifica debido a la complejidad de las ecuaciones rectoras que están asociadas a los problemas prácticos del campo de la ingeniería. Las causas que promueven el uso de los métodos numéricos son: una geometría compleja, condiciones de frontera no uniformes o dependientes del tiempo, o bien la solución de sistemas de ecuaciones diferenciales parciales acoplados. Entre los métodos numéricos más comunes están el de: a) diferencias finitas, b) elemento o volumen finito, y c) elemento límite o elemento frontera. De estos tres, el de uso más extendido es el método de diferencias finitas. En este método el campo de flujo se divide en un conjunto de nodos por medio de una malla y las funciones continuas como velocidad, presión, temperatura, etc., se aproximan con valores discretos de estas funciones calculados en los nodos de la malla. Las derivadas de las funciones se aproximan usando las diferencias entre los valores de la función en los nodos de la malla vecinos divididas entre la separación de la malla. Las ecuaciones diferenciales gobernantes del flujo son transformadas a un conjunto de ecuaciones algebraicas que se resuelven mediante técnicas numéricas apropiadas. Mientras mayor sea el número de nodos de la malla usada, mayor será el número de ecuaciones que es necesario resolver [1]. Para el método del elemento finito o volumen finito el campo de flujo se descompone en un conjunto de pequeños elementos de fluido (por lo general áreas triangulares, si el flujo es bidimensional, o pequeños elementos de volumen si el flujo es tridimensional). Las ecuaciones de conservación se escriben de forma apropiada para cada elemento, y el conjunto de ecuaciones algebraicas resultante se resuelve numéricamente para el campo de flujo. El número, tamaño y forma de los elementos está influenciado por la geometría particular del flujo y por las condiciones del mismo para el problema en cuestión. A medida que aumenta el número de elementos en el sistema, el número de ecuaciones algebraicas simultáneas a resolver crece rápidamente [2]. Para el método del elemento límite o elemento frontera, el límite del campo de flujo (no todo el campo de flujo, como en el método del elemento finito) se descompone en segmentos discretos y sobre estos elementos límite se distribuyen singularidades adecuadas como fuentes, pozos, dobletes, y vórtices. La intensidad y el tipo de singularidades se eligen de modo que sobre los elementos límite se obtengan las condiciones de frontera adecuadas del flujo. Para puntos en el campo del flujo que no pertenecen al límite, el flujo se calcula sumando las contribuciones de las diversas singularidades sobre el límite. Aunque los detalles de este método son más bien matemáticamente complejos, éste puede requerir menos tiempo de cómputo y espacio de almacenamiento que el método del elemento finito [3].

El propósito de este trabajo es conocer la estructura del movimiento de un fluido viscoso, incompresible, en el interior de una cámara cilíndrica vertical, movimiento provocado por un impulsor. Las ecuaciones de transporte (Navier-Stokes) a resolver se expresan en función de la vorticidad, la circulación y la función de corriente meridional. Los resultados obtenidos permiten describir el movimiento radial y axial del fluido girando en el interior del depósito, en términos del número de Reynolds, y el factor de forma, dado por la relación alto/radio del recipiente. Se analizan las líneas de corriente (Ψ) y las componentes de velocidad radial (u) y axial (v) para una posición del impulsor respecto al fondo, once radios distintos del disco giratorio y dos tipos de fluido: agua y gasolina, que corresponden a un número de Reynolds de $2.74x10^4$ y $0.63x10^4$, respectivamente.

Algunos trabajos que se han reportado sobre el flujo rotatorio en sistemas cilíndricos, desde el punto de vista numérico, son:

Pao H-P [4] propuso un método numérico para estudiar un fluido viscoso incompresible confinado en una cámara cilíndrica donde la tapa superior está rotando a una velocidad angular constante y las paredes y fondo del recipiente permanecen fijos. Se analiza la función corriente y circulación, la distribución de velocidades y el coeficiente de par para un rango del número de Reynolds de 1 a 400.

Bertelá y Gori [5] presentaron un método numérico que permite resolver el flujo estable y transitorio de un fluido dentro de una cámara cilíndrica con la cubierta rotando. En el estudio se analizan las componentes de velocidad, líneas de corriente y coeficiente de torque para un número de Reynolds de 100 y 1000, y para una relación geométrica de 0.5, 1 y 2.

Lang *et al.* [6] estudiaron numéricamente el flujo laminar estable en un cilindro fijo con un disco rotando en la tapa superior. El trabajo resalta el análisis del coeficiente de torque y de los flujos volumétricos primario y secundario para un rango del número de Reynolds de 1 a 10^5 y para una relación geométrica de 0.02 a 3.

Khalili *et al.* [7] proveyeron una solución numérica para un flujo laminar inducido por un disco rotatorio situado asimétricamente respecto a la altura, dentro de un cilindro. Presentaron el análisis de las líneas de corriente y componentes de velocidad tangencial así como el coeficiente de torque para los distintos posicionamientos del disco para una relación geométrica de 1 a 2 y un rango de números de Reynolds de 1 a 5000.

Yu P., *et al.* [8] estudiaron numéricamente el flujo en una cámara cilíndrica cerrada con un disco giratorio en el fondo y cuyo radio es menor al de la cámara. El comportamiento del flujo se investigó para una amplia gama de parámetros. Se analizaron, en el plano meridional, las líneas de corriente, momento angular y vorticidad, para diferentes Reynolds (1000, 1500 y 2000), relación geométrica H/R (1.5) y relación de radios R/rd (1.5, 1.8, 2.0, 2.2, 2.6, 3.0, 5.0).

Sturzenegger J. C., *et al.* [9] estudiaron el flujo axisimétrico dentro de un recipiente cilíndrico con una varilla a lo largo de su eje de simetría. El flujo se produce por la rotación de uno de los extremos del cilindro, de ambos extremos, o de la pared lateral. Se presentan expresiones analíticas (para números de Reynolds bajos) del campo de

velocidad azimutal, extendiendo la solución para el caso sin varilla.

III. MODELO FÍSICO

El sistema a analizar consiste en una cámara cilíndrico cerrada de 0.045 m de radio y 0.09 m de altura, que tiene un disco impulsor de 0.005 m de espesor, situado a 0.042 m del fondo del depósito, y cuyo radio se variará desde 0.02 hasta 0.035 m. El impulsor se sujeta, desde la parte superior, por medio de un eje de 0.01 m de radio, que gira a una velocidad angular constante de 13.61 rad/s. En el interior del sistema se tiene un fluido viscoso e incompresible de propiedades físicas constantes, Fig.1.

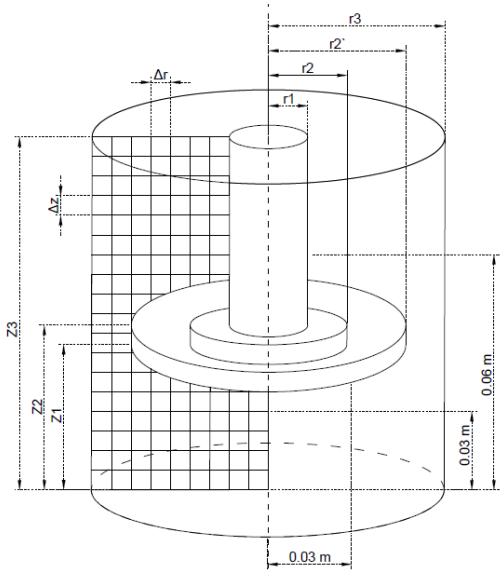

Fig. 1 Representación física del sistema a analizar, malla generada y ejes de referencia para el análisis

IV. PLANTEAMIENTO MATEMÁTICO

El modelo matemático que describe el flujo axisimétrico de un fluido viscoso, incompresible, en estado permanente, que gira en el interior de un depósito cilíndrico, se expresa a través de las ecuaciones de conservación de masa y cantidad de movimiento en coordenadas polares cilíndricas (R, Φ, Z) [10].

$$\frac{\partial U}{\partial R}+\frac{U}{R}+\frac{\partial W}{\partial Z}=0 \tag{1}$$

$$U\frac{\partial U}{\partial R}-\frac{V^2}{R}+W\frac{\partial U}{\partial Z}=-\frac{1}{\rho}\frac{\partial P}{\partial R}+\nu\left[\frac{\partial^2 U}{\partial R^2}+\frac{1}{R}\frac{\partial U}{\partial R}-\frac{U}{R^2}+\frac{\partial^2 U}{\partial Z^2}\right] \tag{2}$$

$$U\frac{\partial V}{\partial R}+\frac{U\,V}{R}+W\frac{\partial V}{\partial Z}=\nu\left[\frac{\partial^2 V}{\partial R^2}+\frac{1}{R}\frac{\partial V}{\partial R}-\frac{V}{R^2}+\frac{\partial^2 V}{\partial Z^2}\right] \tag{3}$$

$$U\frac{\partial W}{\partial R}+W\frac{\partial W}{\partial Z}=-\frac{1}{\rho}\frac{\partial P}{\partial Z}+\nu\left[\frac{\partial^2 W}{\partial R^2}+\frac{1}{R}\frac{\partial W}{\partial R}+\frac{\partial^2 W}{\partial Z^2}\right]-g \tag{4}$$

En este conjunto de ecuaciones dimensionales las incógnitas son las tres componentes de velocidad (U, V, W) y la presión (P). Pero se enfrenta el problema de que la presión en cualquier punto del fluido depende de las componentes de velocidad. Para salvar esta dificultad, reduciendo el término de la presión, se hace una transformación de las ecuaciones de continuidad y cantidad de movimiento en función de la vorticidad (ς), circulación (γ) y función corriente meridional (ψ). Una vez hecha la transformación de las ecuaciones, éstas se adimensionalizan, discretizan y resuelven. La forma adimensional resultante es [4]

$$u\frac{\partial \Gamma}{\partial r}+w\frac{\partial \Gamma}{\partial z}=\frac{1}{Re}\left[\nabla^2\Gamma-\frac{2}{r}\frac{\partial \Gamma}{\partial r}\right] \tag{5}$$

$$u\frac{\partial \xi}{\partial r}+w\frac{\partial \xi}{\partial z}-\frac{u\,\xi}{r}-\frac{1}{r^3}\frac{\partial\left(\Gamma^2\right)}{\partial z}=\frac{1}{Re}\left[\nabla^2\xi-\frac{\xi}{r^2}\right] \tag{6}$$

$$\nabla^2\Psi-\frac{2}{r}\frac{\partial \Psi}{\partial r}=r\,\xi \tag{7}$$

Los parámetros que relacionan las variables adimensionales (r, z, u, v, w, Ψ , Γ , ξ) con las dimensionales (R, Z, U, V, W, ψ, γ , ς) están definidos en las ecuaciones [12]

$$\frac{R}{r_3}=r,\quad \frac{Z}{r_3}=z,\quad \frac{U}{\Omega r_3}=u,\quad \frac{V}{\Omega r_3}=v,$$
$$\frac{W}{\Omega r_3}=w,\quad \frac{\psi}{\Omega r_3^{3}}=\Psi,\quad \frac{\gamma}{\Omega r_3^{2}}=\Gamma,\quad \frac{\varsigma}{\Omega}=\xi, \tag{8}$$
$$Re=\frac{\Omega r_3^{2}}{\nu}$$

$$\gamma=2\pi VR,\quad \varsigma=\frac{\partial U}{\partial Z}-\frac{\partial W}{\partial R}, \tag{9}$$
$$U=\frac{1}{R}\frac{\partial \psi}{\partial Z},\quad W=-\frac{1}{R}\frac{\partial \psi}{\partial R}$$

En donde r_3 es el radio del recipiente, Ω es la velocidad angular del impulsor y Re es el número de Reynolds definido para este sistema. Las ecuaciones de transporte de la circulación (5) y de la vorticidad tangencial (6) son ecuaciones diferenciales parciales de segundo orden no lineales de tipo parabólico. La ecuación de Poisson para la función corriente meridional (7) es una ecuación diferencial parcial de segundo orden de tipo elíptico [11]. Las condiciones de frontera son [13]

$r = 0,$ $0 \le z \le z_1$	$\Psi = 0,$	$\Gamma = 0,$	$\xi = 0$	
$r = r_3,$ $0 \le z \le z_3$	$\Psi = 0,$	$\Gamma = 0,$	$\xi = \frac{1}{r}\frac{\partial^2 \Psi}{\partial r^2}$	
$z = z_1,$ $0 \le r \le r_2$ $z = z_2,$ $r_1 \le r \le r_2$	$\Psi = 0,$	$\Gamma = r^2,$	$\xi = \frac{1}{r}\frac{\partial^2 \Psi}{\partial z^2}$	(10)
$z_1 \le z \le z_2$ $r = r_2$ $z_2 \le z \le z_3,$ $r = r_1,$	$\Psi = 0,$	$\Gamma = r^2,$	$\xi = \frac{1}{r}\frac{\partial^2 \Psi}{\partial r^2}$	
$z = 0,$ $0 \le r \le r_3$ $z = z_3,$ $r_1 \le r \le r_3$	$\Psi = 0,$	$\Gamma = 0,$	$\xi = \frac{1}{r}\frac{\partial^2 \Psi}{\partial z^2}$	

V. SOLUCIÓN NUMÉRICA

Para resolver las ecuaciones de movimiento que rigen en el interior del depósito (5), (6) y (7), junto con las condiciones de frontera (10), es necesario transformarlas a un espacio discreto, el cual es el espacio manejado por las computadoras. En el método numérico se aplica un esquema de diferencias finitas para reemplazar las ecuaciones diferenciales parciales por expresiones algebraicas aproximadas. La aproximación empleada en el método numérico para las ecuaciones que rigen en el recipiente y las fronteras del mismo son de segundo y cuarto orden, respectivamente. En la Fig. 1 se representa la malla en el plano meridional continuo (r, z) para el flujo axisimétrico. Así, las ecuaciones en diferencias finitas que rigen el movimiento del fluido en el interior del sistema son [13].

$$\Psi_{i,j}=\frac{1}{2\left[1+\left(\frac{\Delta r}{\Delta z}\right)^2\right]}\left\{\Psi_{i+1,j}\left[1-\frac{1}{2i}\right]+\right.$$
$$\Psi_{i-1,j}\left[1+\frac{1}{2i}\right]+\left(\frac{\Delta r}{\Delta z}\right)^2\Psi_{i,j+1}+ \tag{11}$$
$$\left.\left(\frac{\Delta r}{\Delta z}\right)^2\Psi_{i,j-1}-i\,(\Delta r)^3\,\xi_{i,j}\right\}$$

$$\Gamma_{i,j}=\frac{1}{2\left[1+\left(\frac{\Delta r}{\Delta z}\right)^2\right]}\left\{\Gamma_{i+1,j}\left[\left(1-\frac{1}{2i}\right)-\right.\right.$$
$$\left.\frac{Re}{4i\,\Delta z}\left(\Psi_{i,j+1}-\Psi_{i,j-1}\right)\right]+$$
$$\Gamma_{i-1,j}\left[\left(1+\frac{1}{2i}\right)+\frac{Re}{4i\,\Delta z}\left(\Psi_{i,j+1}-\Psi_{i,j-1}\right)\right]+ \tag{12}$$
$$\Gamma_{i,j+1}\left[\left(\frac{\Delta r}{\Delta z}\right)^2+\frac{Re}{4i\,\Delta z}\left(\Psi_{i+1,j}-\Psi_{i-1,j}\right)\right]+$$
$$\left.\Gamma_{i,j-1}\left[\left(\frac{\Delta r}{\Delta z}\right)^2-\frac{Re}{4i\,\Delta z}\left(\Psi_{i+1,j}-\Psi_{i-1,j}\right)\right]\right\}$$

$$\xi_{i,j}=i^2\left\{\xi_{i+1,j}\left[\left(1+\frac{1}{2i}\right)-\frac{Re}{4i\,\Delta z}\left(\Psi_{i,j+1}-\Psi_{i,j-1}\right)\right]\right.$$
$$+\xi_{i-1,j}\left[\left(1-\frac{1}{2i}\right)+\frac{Re}{4i\,\Delta z}\left(\Psi_{i,j+1}-\Psi_{i,j-1}\right)\right]+$$
$$\xi_{i,j+1}\left[\left(\frac{\Delta r}{\Delta z}\right)^2+\frac{Re}{4i\,\Delta z}\left(\Psi_{i+1,j}-\Psi_{i-1,j}\right)\right]+$$
$$\xi_{i,j-1}\left[\left(\frac{\Delta r}{\Delta z}\right)^2-\frac{Re}{4i\,\Delta z}\left(\Psi_{i+1,j}-\Psi_{i-1,j}\right)\right]+ \tag{13}$$
$$\left.\left[\frac{Re\,\Gamma_{i,j}}{i^3(\Delta r)(\Delta z)}\left(\Gamma_{i,j+1}-\Gamma_{i,j-1}\right)\right]\right\}\quad\left[2i^2+2i^2\left(\frac{\Delta r}{\Delta z}\right)^2+\right.$$
$$\left.1-\frac{Re}{2\,\Delta z}\left(\Psi_{i,j+1}-\Psi_{i,j-1}\right)\right]^{-1}$$

Para obtener los campos de las funciones corriente meridional (Ψ), circulación (Γ) y vorticidad tangencial (ξ) se generó un programa de cómputo en lenguaje de programación C++. Dicho programa realiza el mallado en el plano (r, z), aplica las ecuaciones (11), (12) y (13) a cada nodo interno del sistema y las ecuaciones (10), previamente discretizadas, a cada nodo ubicado en la frontera del mismo. Posteriormente, por medio de una subrutina, resuelve el sistema de ecuaciones en forma iterativa hasta encontrar la convergencia. El criterio de convergencia utilizado es del tipo de error relativo, de la forma: $\max\left[\frac{\Psi^{\sigma+1}-\Psi^{\sigma}}{\Psi^{\sigma}}\right]<\varepsilon$

El orden de precisión de ε, en este trabajo, fue de 0.0001. Para determinar las componentes de velocidad radial y axial, se adimensionalizan y discretizan las ecuaciones que definen a la función corriente (9), y se emplean los resultados obtenidos en el sistema de ecuaciones anterior. Las expresiones resultantes en diferencias finitas son:

$$u_{i,j} = \frac{\Psi_{i,j-2} - 8\Psi_{i,j-1} + 8\Psi_{i,j+1} - \Psi_{i,j+2}}{12\,\Delta r\,\Delta z\,i}; \qquad w_{i,j} = \frac{\Psi_{i+2,j} - 8\Psi_{i+1,j} + 8\Psi_{i-1,j} - \Psi_{i-2,j}}{12\,\Delta r^2\,i} \tag{14}$$

VI. RESULTADOS Y DISCUSIÓN

Una vez resuelto el sistema de ecuaciones (11), (12), (13) junto con las condiciones de frontera (10), a través del software diseñado, se hicieron corridas para dos tipos de fluido: agua y gasolina que, junto con la geometría del sistema, corresponden a un número de Reynolds de $2.74x10^4$ y $0.63x10^4$, respectivamente. El sistema se acotó con los siguientes valores: $r_1 = 0.01$ m, $0.02 \leq r2 \leq 0.035$ m, $r_3 = 0.045$ m, $z_1 = 0.042$ m, $z_2 = 0.047$ m, $z_3 = 0.09$ m y $\Omega = 13.61$ rad/s. La distribución de las líneas de corriente (Ψ), para los dos casos, se muestran en las Figs. 2 y 3.

En la Fig. 2, sistema con número de Reynolds $2.74x10^4$ y radios del impulsor 0.02, 0.027 y 0.035 m, se observa que las partículas de fluido son impulsadas por el disco hacia la pared de la cámara. Al acercarse a ella el flujo generado se divide en dos: una parte se dirige hacia la zona inferior del depósito, formando una circulación en sentido horario, y otra parte se dirige hacia la zona superior del cilindro, formando una circulación en sentido anti horario. El campo de la función corriente muestra que lejos de los núcleos formados el flujo volumétrico va disminuyendo, haciéndose presente la condición de frontera de gasto cero en las paredes de la cámara, eje de rotación, fondo del depósito y superficie rígida. Los valores máximos que toma la función corriente en los núcleos, para el flujo horario (+) y anti horario (-), y para los radios mencionados previamente, son: +0.027 y -0.035, +0.06 y -0.064, +0.11 y -0.13, respectivamente. Los resultados indican que al aumentar el radio del impulsor el flujo se ve favorecido. Lo anterior es debido a que al incrementar la superficie del disco se genera mayor contacto con el fluido y como consecuencia un mayor número de partículas es impulsado por la fuerza centrífuga hacia la pared del recipiente.

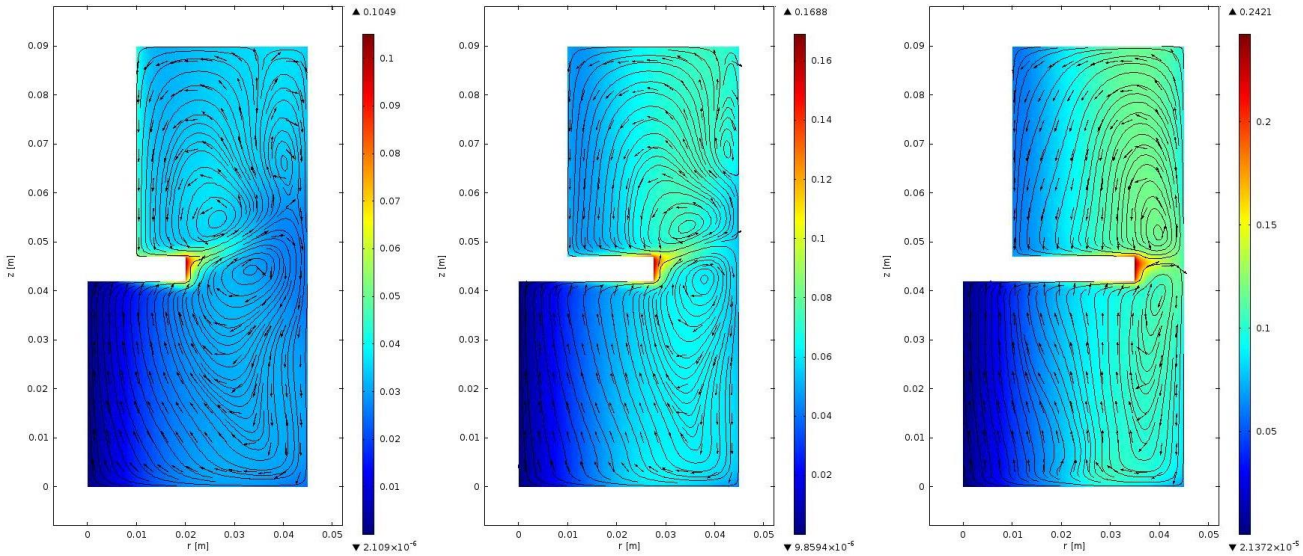

Fig. 2 Líneas de función corriente adimensional (Ψ) para $Re=2.74x10^4$ (agua)y para radios 0.02, 0.027, y 0.035 m

El comportamiento para el sistema con número de Reynolds $0.63x10^4$, Fig. 3, es parecido aunque con magnitudes menores. Para este caso los valores máximos que toma la función corriente, en los núcleos, para el flujo horario (+) y anti horario (-), y para los radios mencionados anteriormente, son: +0.025 y -0.031, +0.058 y -0.062, +0.095 y -0.11, respectivamente. En este caso los resultados también muestran que al aumentar el radio del disco el flujo también se incrementa. La disminución de la magnitud de la función corriente respecto al caso anterior es consecuencia del incremento de la viscosidad cinemática del fluido. Haciendo una comparación entre los valores de la función corriente del número de Reynolds de $0.63x10^4$ respecto al de $2.74x10^4$, y entre los mismos radios, se encontró una disminución de 7.41, 3.33 y 13.63% para el flujo horario, y, 11.42, 3.12 y 15.38% para el flujo anti horario, respectivamente.

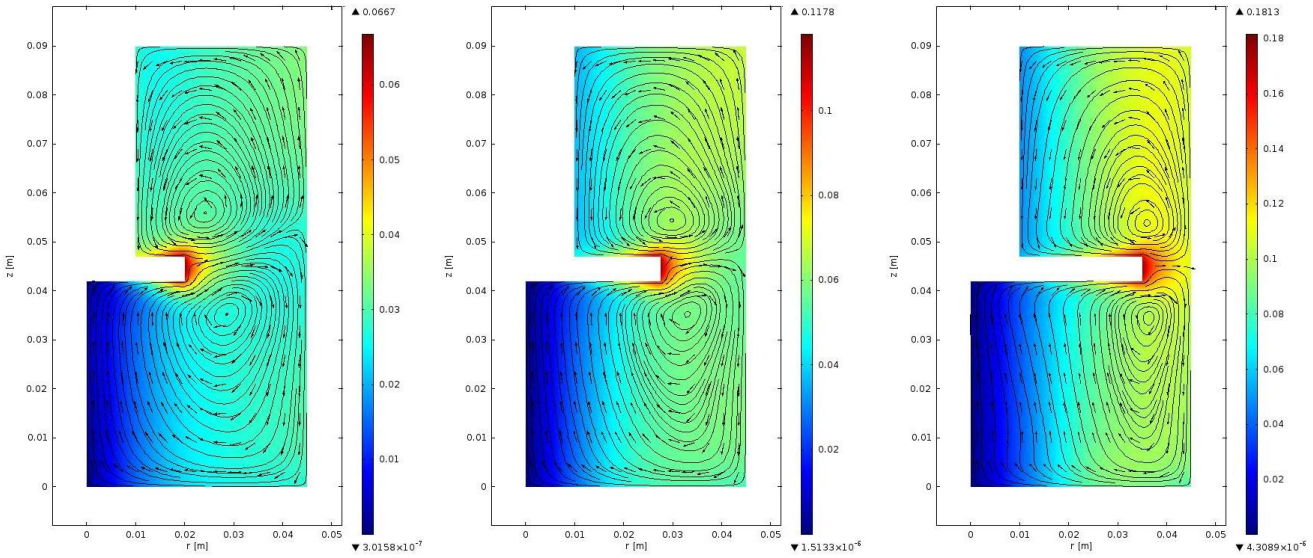

Fig. 3 Líneas de función corriente adimensional (Ψ) para Re=0.63x10^4 (gasolina)y para radios 0.02, 0.027, y 0.035 m

En la Fig. 4, se muestra el comportamiento de la componente de velocidad radial (u), para un Reynolds de 2.74x10^4, en un radio de referencia de 0.03 m, distintas posiciones en el eje "z" y distintos radios del impulsor. Se precia que la componente de velocidad radial comienza en cero debido a la condición de frontera de no deslizamiento que hay sobre el fondo del depósito. Posteriormente se observa la zona de la capa límite hidrodinámica donde el flujo se dirige horizontalmente hacia la pared del recipiente, esto se indica por el signo positivo de la velocidad. Se aprecia que el valor de la velocidad radial va aumentando hasta un máximo positivo y de allí comienza a disminuir hasta cero, al situarse sobre el disco rotatorio. Posteriormente se observa una zona con velocidad cero, que es la parte que ocupa el impulsor. A partir de este punto, se aprecia la zona de la otra capa límite hidrodinámica donde ahora el flujo se dirige hacia el eje del sistema, esto se indica por el signo negativo de la velocidad. En esta parte se observa que la velocidad radial va aumentando hasta un máximo negativo y de allí nuevamente disminuye su magnitud hasta llegar a cero, cuando se ubica sobre la superficie del cilindro. Los valores máximos positivos de la componente de velocidad radial van de 0.78x10^{-3} hasta 8.03x10^{-3} para los radios del disco desde 0.02 hasta 0.035 m, es decir, hay un aumento de 9.28 veces. Para el número de Reynolds de 0.63x10^4, Fig. 5, se aprecia el mismo comportamiento pero con magnitudes distintas, en este caso los valores máximos positivos de la componente de velocidad radial van de 1.51x10^{-3} hasta 7.42x10^{-3} para los radios del impulsor desde 0.02 hasta 0.035 m, es decir, hay un aumento de 7.83 veces. Al tomar como referencia el número de Reynolds de 2.74x10^4 y compararlo con el de 0.634x10^4, se encontró que las magnitudes máximas positivas de la componente de velocidad radial (u) se redujeron en promedio 7.58%.

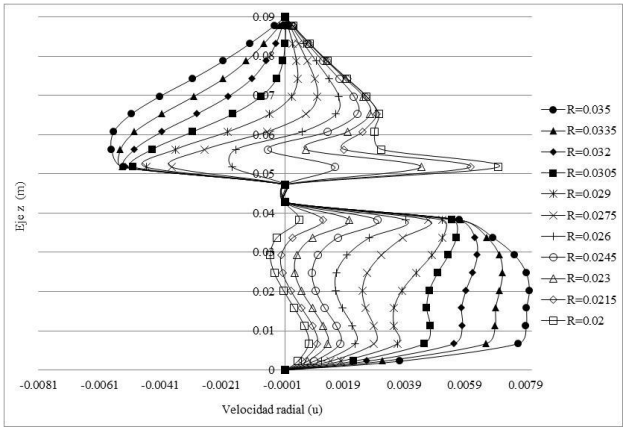

Fig. 4 Componente de velocidad radial (u) en r=0.03m, para Re=2.74X10^4 (agua) y distintos radios del impulsor

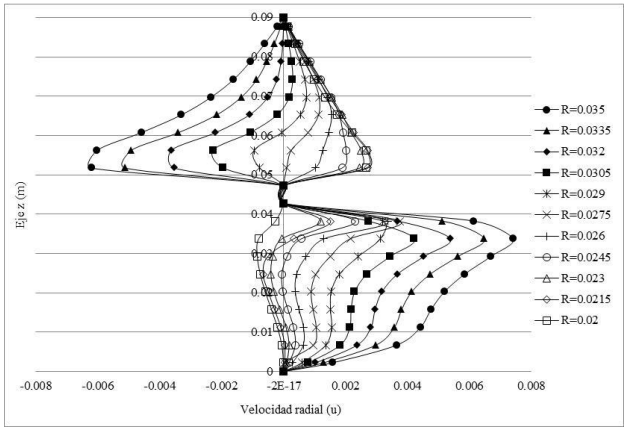

Fig. 5 Componente de velocidad radial (u) en r=0.03 m para Re=0.63X10^4 (gasolina) y distintos radios del impulsor

En la Fig. 6, se muestran los resultados de la componente de velocidad axial (w), para un Reynolds de $2.74x10^4$, una posición constante en la coordenada "z" de 0.03 m, distintas posiciones en el eje "r" y distintos radios del impulsor. Se aprecia que la componente de velocidad vertical comienza en cero sobre el eje de simetría, posteriormente se observa la zona de la capa límite hidrodinámica donde el flujo se dirige verticalmente hacia el disco giratorio, esto se indica por el signo positivo de la velocidad. Se aprecia que el valor de la velocidad axial va aumentando hasta un máximo positivo y de allí comienza a disminuir hasta cero, donde a partir de este punto se presenta un cambio en el sentido del flujo. A partir de allí se observa la zona de la otra capa límite hidrodinámica donde ahora el flujo se dirige hacia el fondo del sistema, esto se indica por el signo negativo de la velocidad. En esta parte se aprecia que la velocidad vertical va aumentando hasta un máximo negativo y de allí nuevamente disminuye su magnitud hasta llegar a cero cuando se ubica sobre la pared del cilindro. Los valores máximos negativos de la componente de velocidad axial van de $-2.13x10^{-3}$ hasta $-17.97x10^{-3}$ para los radios del impulsor desde 0.02 hasta 0.035 m, es decir, hay un aumento de 7.42 veces. Para el número de Reynolds de $0.63x10^4$, Fig. 7, se observa el mismo comportamiento pero con magnitudes distintas, en este caso los valores máximos negativos de la componente de velocidad axial van de $-2.50x10^{-3}$ hasta $-13.40x10^{-3}$ para los radios del disco desde 0.02 hasta 0.035 m, es decir, hay un aumento de 4.36 veces. Al tomar como referencia el número de Reynolds de $2.74x10^4$ y compararlo con el de $0.63x10^4$, se encontró que las magnitudes máximas negativas de la componente de velocidad axial (w) se redujeron en promedio 25.43%.

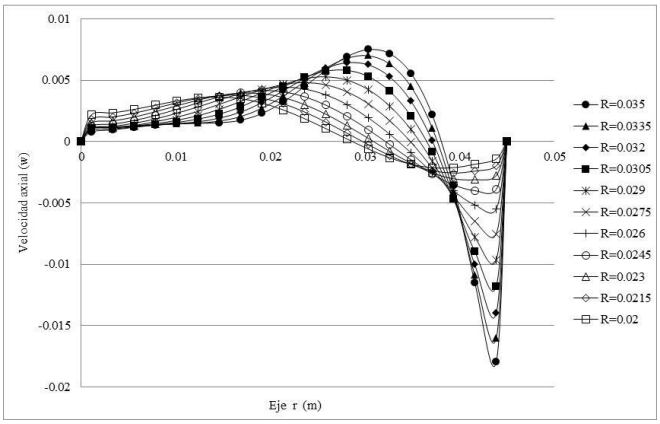

Fig. 6 Componente de velocidad axial (w) en z=0.03 m para Re=$2.74X10^4$ (agua) y distintos radios del impulsor

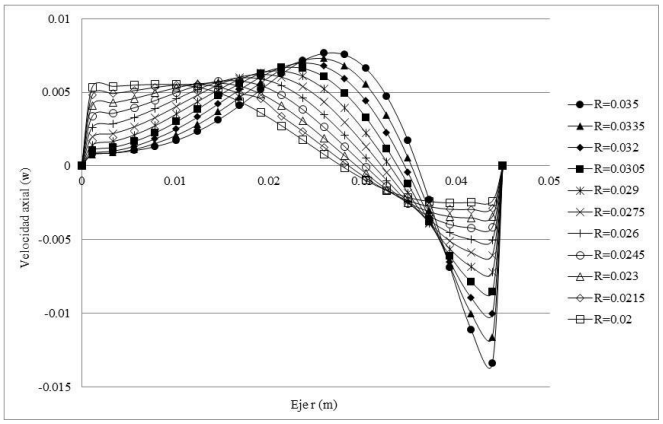

Fig. 7 Componente de velocidad axial (w) en z=0.03 m para Re=$0.63X10^4$ (gasolina) y distintos radios del impulsor

En la Fig. 8, se muestran los resultados de la componente de velocidad axial (w), para un Reynolds de $2.74x10^4$, una posición constante en la coordenada "z" de 0.06 m, distintas posiciones en el eje "r" y distintos radios del impulsor. Se aprecia que la componente de velocidad vertical comienza en cero sobre el eje del impulsor, posteriormente se observa la zona de la capa límite hidrodinámica donde el flujo se dirige verticalmente hacia el disco giratorio, esto se indica por el signo negativo de la velocidad. Se aprecia que el valor de la velocidad axial va aumentando hasta un máximo negativo y de allí comienza a disminuir hasta llegar a cero, donde a partir de este punto se presenta un cambio en el sentido del flujo. A partir de allí se observa la zona de la otra capa límite hidrodinámica donde ahora el flujo se dirige hacia la tapa del sistema, esto se indica por el signo positivo de la velocidad. En esta parte se aprecia que la velocidad vertical va aumentando hasta un máximo positivo y de allí nuevamente disminuye su magnitud hasta llegar a cero, cuando se ubica sobre la pared del cilindro. Los valores máximos negativos de la componente de velocidad axial van de $-7.77x10^{-3}$ hasta $-5.94x10^{-3}$ para los radios del impulsor desde 0.02 hasta 0.035 m, es decir, hay una disminución de 0.76 veces. Para el número de Reynolds de $0.63x10^4$, Fig. 9, se observa el mismo comportamiento pero con magnitudes distintas, en este caso los valores máximos negativos de la componente de velocidad axial van de $-7.79x10^{-3}$ hasta $-5.77x10^{-3}$ para los radios del disco desde 0.02 hasta 0.035 m, es decir, hay una disminución de 0.74 veces. Al tomar como referencia el número de Reynolds de $2.74x10^4$ y compararlo con el de $0.63x10^4$, se encontró que las magnitudes máximas negativas de la componente de velocidad axial (w) se redujeron en promedio 2.89%. Cabe mencionar que el análisis de la componente de velocidad axial (w) se hizo para dos posiciones en el eje vertical con el objeto de observar su comportamiento por encima y por debajo del impulsor.

Los resultados obtenidos en este trabajo han mostrado ser congruentes con los reportados por otros autores. Para esta investigación se ha encontrado que el movimiento del fluido se compone de dos flujos: uno que gira en sentido anti horario, ubicado en la parte superior del impulsor, y otro que gira en sentido horario, ubicado en la parte inferior del mismo. Los valores más altos de la función corriente meridional, Ψ, se encuentran en el centro de los flujos. Este comportamiento es congruente con el trabajo de Khalili *et al.* [7] aunque las magnitudes de la función corriente son diferentes, debido al rango del número de Reynolds que analizan ($100 \leq Re \leq 1000$). Otra característica del flujo, encontrada en este trabajo, fue la formación de vórtices secundarios en la esquina superior

derecha de la cámara, lo cual ocurrió para radios pequeños del impulsor y para el número de Reynolds de $2.74x10^4$. Este comportamiento obedece al rompimiento de las capas límite, provocado por la presencia de las fronteras rígidas del sistema y por la poca influencia que tiene el disco impulsor en estas regiones. La formación de estos vórtices es congruente con los resultados encontrados por Yu *et al.* [8] en donde se muestra la dependencia del Reynolds y de la relación geométrica.

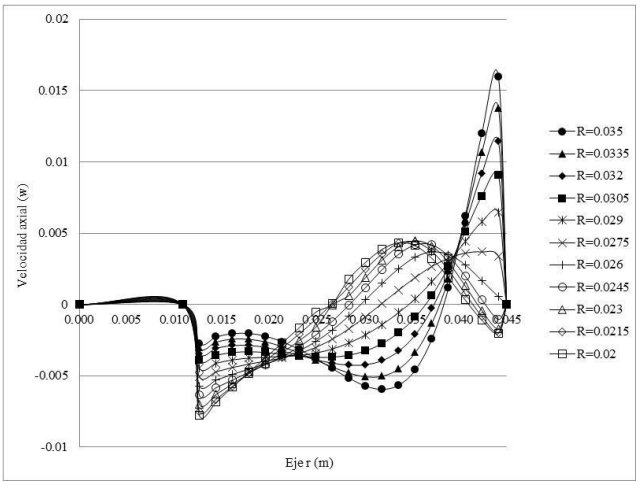

Fig. 8 Componente de velocidad axial (w) en z=0.06 m para Re=$2.74X10^4$ (agua) y distintos radios del impulsor

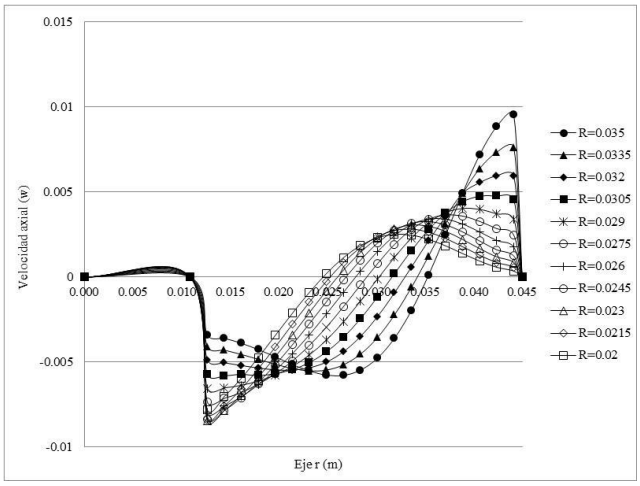

Fig. 9 Componente de velocidad axial (w) en z=0.06 m para Re=$0.63X10^4$ (gasolina) y distintos radios del impulsor

VII. CONCLUSIONES

Los resultados obtenidos indican que el movimiento del fluido en el sistema se compone de dos flujos: uno positivo que se ubica por debajo del disco impulsor y otro negativo ubicado por encima del mismo, además de un flujo secundario que se genera para ciertos casos específicos. Al aumentar el radio del impulsor un 75% se encontró que: la componente de velocidad radial positiva (u) aumentó 9.28 veces para Re=$2.74x10^4$ y 7.83 veces para Re=$0.63x10^4$; la componente de velocidad axial negativa (w), por debajo del disco impulsor, aumentó 7.42 y 4.36 veces, para los mismos números de Reynolds; y la componente de velocidad axial negativa (w), por encima del disco impulsor, disminuyó 0.76 y 0.74 veces, para los mismos números de Reynolds. Al tomar como referencia el número de Reynolds de $2.74x10^4$ y compararlo con el de $0.63x10^4$, se encontró que: los valores máximos positivos de la componente de velocidad radial (u) se redujeron en promedio 7.58%; los valores máximos negativos de la componente de velocidad axial (w), por debajo del disco impulsor, se redujeron en promedio 25.43%; y los valores máximos negativos de la componente de velocidad axial (w), por encima del disco impulsor, se redujeron en promedio 2.89%. Los resultados obtenidos revelan la dependencia que tiene el radio del impulsor y el número de Reynolds en el desarrollo del flujo y muestran que la variación de estos parámetros no es proporcional al cambio en las componentes de velocidad y la función corriente.

REFERENCIAS

[1] Smith, G. D. "Numerical Solution of Partial Differential Equations: Finite Difference Method". 2nd ed., Oxford University Press, London. (1978).
[2] Baker, A. J. "Finite Element Computational Fluid Mechanics". McGraw-Hill, New York. (1985).
[3] Brebbia, C. A. y Domínguez, J. "Boundary Elements: An Introductory Course". McGraw-Hill, New York. (1992).
[4] Pao, H-P. *"Numerical solution of the Navier Stokes equations for flows in the disk-cylinder system"*. Phys. Fluids. 15 (1):4-11. (1972).
[5] Bertelá, M., Gori, F. *"Laminar flow in a cylindrical container with a rotating cover"*. J. Fluids Eng. 104 (1):31-39. doi:10.1115/1.3240849. (1982).
[6] Lang, E., Sridhar, K., Wilson, N. W. "*Computational study of disk driven rotating flow in a cylindrical enclosure"*. Journal of fluids engineering. 116 (4):815-820. (1994).
[7] Khalili, A., Adabala, R. R., Rath H. J. *"Flow induced by a asymmetrically placed disk rotating coaxially inside a cylindrical casing"*. Acta Mechanica. Springer-Verlag. 9-19. Vol 113. (1995).
[8] Yu, P., Lee, T. S., Zeng, Y., Low, H. T. *"Characterization of flow behavior in an enclosed cylinder with a partially rotating end wall"*. Physics of fluids 19, 057104, doi: 10.1063/1.2731420. (2007).
[9] Sturzenegger, J. C., Sarasúa, L. G., Martí, A. C. *"Analytical solutions for the axisymmetric flow inside a cylindrical container with a rod along the axis at low Reynolds numbers"*. Journal of Fluids and Structures, Vol. 28, pp. 473-479. (2012).
[10] Landau y Lisfshitz. Fluids Mechanics. Vol. 6, Pergamon Press. (1982).
[11] Tijonov, A. N., Samarsky, A. A. Ecuaciones de la física matemática. Edit. MIR, Moscú, pp 1-29. (1980).
[12] Gerber N. *"Properties of rigidly rotating liquids in closed partially filled cylinders"*. ASME, Transactions, Series E-Journal of Applied Mechanics. 42:734,735. (1975).
[13] A. Lizardi, H. Terres, R. López, M. Vaca, J. Flores, A. Lara, S. Chávez, J. R. Morales. "Efecto del Reynolds en el flujo rotatorio asimétrico generado en el interior de un cilindro". XX Congreso Internacional Anual de la SOMIM. (2014).

Evaluation framework for small-dimension solar cookers

Luis Bernardo López Sosa
Facultad de Ciencias Físico-Matemáticas
Universidad Michoacana de San Nicolas de Hidalgo
Morelia, México.
sosabernardo@hotmail.com

MauricioGonzález Avilés
Programa Académico de Desarrollo Sustentable
Universidad Intercultural Indígena de Michoacán
Pátzcuaro, México.
gamauricio@gmail.com

***Abstract*—This paper presents an evaluation framework for solar cookers based on three parameters: energy efficiency, facility of use, and economic accessibility. Each parameter evaluates various quantifiable indicators: standardized cooking power, heating time, thermal performance, cost per Wh generated, mass in relation to collector area, orientations per hour, durability of the reflector and/or thermal accumulator. Each indicator was assigned a maximum and minimum evaluation scale, and the data gathered from these indicators were integrated in a radial graph. The sum of the indicators constitutes the aspect to be compared, but the graph also allows us to interpret the strengths and weaknesses described. This framework cannot be used with only one solar cooker, as it is a comparative tool that requires two or more devices. This methodology has been applied to various solar cookers, with different characteristics, and determined solar cooker best features to be implemented in rural communities**

Keywords—solar cooker; evaluation ; framework; radial graph

I. INTRODUCTION

Evaluation frameworks are methodological proposals that allow elaboration of integral, quantifiable analyses of multi-factor systems. Today, there are well-founded frameworks that evaluate the sustainability of agrosystems by incorporating such general attributes as quantifiable indicators. Evaluation frameworks have been a focus of interest since the 1990s for several authors. The FESLM, for example, is one framework for evaluating soils that considers environmental indicators [1]. Likewise, the Evaluation Framework for Natural Resource Management Systems incorporates indicators of sustainability (MESMIS) that span a very broad range [2]. Recently, more comparative evaluation frameworks have been created to offer alternative forms of analysis for agro-ecological systems [3], but they all share one common feature: they evaluate systems on the basis of social, economic and environmental parameters or attributes that generate various quantifiable indicators. The data obtained are integrated into radial- or amoeba-type graphs adequate for both comparative and interpretative analyses [4]. Unfortunately, for energy systems that utilize renewable energy sources, ecotechnical systems and, especially, solar cookers, no such frameworks exist.

Solar cookers are thermo-converters that transform the sun's radiation into calorific power sufficient to cook foods during varying time intervals. Today, a wide variety of solar cookers exist, and the number of models available makes it difficult to conduct comparative evaluations. Although several procedures for evaluating the thermal performance of these devices exist, even the most efficacious ones are limited to assessing cooking power, merit factors, and thermal performance. Work by Funk and Larson [5] led to the creation of American Society of Agricultural Engineering Standard S580 [6], which establishes a rigorous procedure for the thermal testing of solar cookers, based on determinations of standard cooking power.

Other standards, aside from ASAE 8580, exist but tend to be inaccessible. The standard developed in 1992 by the European Committee on Solar Cooking Research, for example, is comprehensive and includes many qualitative factors, such as ease of use and safety [7], while in India, the Bureau of Indian Standards uses a testing method based on research by Mullick et al. [8], which evaluates solar cookers on the basis of derived merit figures.

As a result, the most common evaluation protocols for solar cookers do not offer integral assessments that take into account ergonomic and economic aspects, or environmental benefits. Therefore, efforts have been made to establish more integrated evaluation systems; in some cases by suggesting the incorporation of socio-economic parameters with indicators (*i.e.*, quantifiable criteria) such as safety, ergonomics, and device quality [9]. In their study of the evaluation of solar cookers, Kundapur & Sudhir [10] propose considering not only thermal performance, but also such parameters as stagnation capacity, cost per Watt delivered, weight, ease of handling, and aesthetics. Yahya [11], meanwhile, suggests a new standard global procedure for testing solar cookers based on determining the thermal performance of parabolic concentrating solar cookers. This new standard sets limits for environmental conditions, specifies test procedures, and assesses performance in terms of cooking power. Kimambo [12] carried out a comprehensive, multi-year study in Tanzania that included a theoretical review, developmental work, experimental testing and evaluations of 6 different types of solar cookers. Pohekar & Ramachandran [13], in turn, propose formulating a policy to replace the energy used in cooking with renewable resources based on a multi-criteria approach. They evaluated nine cooking energy alternatives on the basis of 30

criteria that include technical, economic, environmental/social, behavioral and commercial elements. Unfortunately, these two attempts to construct broader, more integral evaluations lack quantitative indicators. Although they strive to improve our evaluation standards, the truth is that they remain at the descriptive level, especially in relation to the socio-economic parameters they suggest.

Solar cookers have been installed in rural areas to improve people's quality of life and mitigate the extraction of forest resources by reducing biomass combustion [14]. However, implementation of these thermal solar technologies often lacks appropriate systems that allow users to employ their solar cookers continuously. In order to determine the viability of inserting a specific model of solar cooker we must understand the elements that may favor its implementation, a process that requires evaluating possible economic, environmental and social benefits; that is, sustainable technology. For this reason, it is of vital importance to elaborate integral evaluation strategies that help us understand the potential advantages of certain solar cooking systems. The following sections present an Evaluation Framework for Small-dimension Solar Cookers that we refer to as EFSC.

II. DESCRIPTION OF THE EVALUATION FRAMEWORK FOR SOLAR COOKERS.

Due to the absence of evaluation frameworks that integrate environmental, social and economic parameters and indicators, we propose a model for small-dimension solar cookers; *i.e.*, those with less than one square meter of capture area. Our proposal centers on three parameters: a) energy efficiency; b) facility of use; and, c) economic accessibility. Then, from these parameters it derives a series of quantifiable indicators. TABLE I shows the indicators that correspond to each parameter.

TABLE I. PARAMETERS AND INDICATORS OF THE EFSC

Parameter	Indicator
Energy efficiency	1- Thermal performance (%)
	2- Standardized cooking power by capture area (Wh/m^2)
	3- Heating time (minutes)
Facility of use	4-Mass by area of the collector (kg per area of the collector)
	5- Load capacity (liters)
	6- Orientations per hour (times per hour)
Economic accessibility	7- Cost per Wh (pesos per Wh of power, in dollars)
	8- Reflector durability (years)

A. *Parameters and indicators.*

In this context, the parameters are variables that can be measurable in relation to certain indicators. In simple terms, sustainable technologies are those with a behavior that falls within the limits of sustainability, or that contributes to achieving those conditions. Their interactions with society, the economy, the environment, and other technologies, must have the smallest possible harmful impact [15]. However, for frameworks of energy sustainability in relation to solar cookers it is difficult to define the most appropriate indicators for measuring –in real terms– just how acceptable this particular technology may be, or how beneficial using a solar cooker may be for the environment. But this is not a determining factor for, as the EFSC proposal suggests, it is possible to overcome the apparent impossibility of developing an evaluation framework for sustainable technologies. Although the EFSC is not an evaluation framework in the strictest sense of the term (sustainable technology), it is clearly one that integrates socioeconomic parameters to help determine the social and economic viability of using solar cookers. Moreover, the indicator "reflector durability" implicitly evaluates the potential need to acquire new food-cooking systems within a certain time interval; a factor that determines the quantity of technological waste generated and, therefore, the dimensions of the impact on the environment. In addition to reducing technological waste, a well-functioning solar cooker entails savings on consumption of LP gas and firewood, thus reducing carbon dioxide emissions [16]. In general, the parameters considered –energy efficiency, facility of use, and economic accessibility– are redefined in social, environmental and economic terms to construct an evaluation framework for solar cookers that operates from the perspective of sustainable technology. The indicators, in turn, are methodological instruments that make it possible to quantify the evaluation on the basis of the three fundamental parameters. The evaluation of each indicator corresponds to well-established methodologies utilized to evaluate solar cookers. Each indicator generates a maximum and minimum quantitative evaluation –see TABLE II– that goes from zero to "the maximum possible value obtained".

TABLE II. VALUES OF THE INDICATORS OF THE EFSC.

INDICATOR	Maximum value	Minimum value
1- Thermal performance	0.5	0
2- Standardized cooking power per capture area	350	0
3- Heating time	300	0
4- Mass per area of the collector	40	0
5- Load capacity	7	0
6- Orientations per hour	5	0
7- Cost per Wh (in dollars)	10	0
8- Reflector durability	20	0

The calculation of these indicators, and their respective maximum and minimum values, involves the following considerations:

- Thermal performance is the average yield of the solar cooking system [10] measured on a scale of 0-to-1; but because in reality it is practically impossible for any such system –especially ones that use solar energy– to achieve 100% of thermal performance, this scale estimates the highest possible thermal performance of solar collecting systems at approximately 50%.
- Standard cooking power is calculated using the norm ASAS580. Measured in Wh and based on mathematical models that predict the thermal behavior of small-dimension solar cookers, the maximum cooking power for these systems is 350 Wh [17]. The final calculation is made by dividing standardized cooking power by the capture area of the solar cooker.
- Heating time is obtained as a function of time and quantified in minutes [18]. In one day, the solar cooker can absorb a maximum of 5 hours of solar resources to cook food. As a result, the maximum heating time is 300 minutes.
- The mass per area of the collector refers to the weight in kilograms of the solar cooker. A device with a mass above 40 kilograms is impractical for users, so that is the maximum value for this indicator.
- The load capacity is the amount of food that can be placed in the cooking container, measured in liters. According to Funk's protocol for solar cookers, the proportion of load used for testing is 7 kilograms of water per square meter of capture area. Therefore, the maximum value for this indicator is 7 liters.
- Orientations per hour, represents the number of times that the device is re-oriented. Intuitively, we consider that is impractical for a user to orient the solar cooker more than 5 times per day, so the maximum value is 5. These are adimensional
- Cost per Wh is calculated by dividing the total cost of the solar cooker by the number of Wh per square meter based on the calculation of standardized cooking power. For commercial cookers like the *Tolokatsin* solar oven, the cost per Wh of cooking power generated was approximately 10 dollars per Wh (in 2014). As this cost is very high, it was taken as the maximum value for a device available for sale in the digital market. This value is measured in dollars.
- Finally, reflector durability is measured in years, in relation to the functionality of optimized reflectors, solar heaters and photovoltaic panels. Their useful lifetime is 20 years, so this is the maximum value for this indicator.

Because the maximum values for these indicators are very disproportionate, a revised scale is suggested; one that takes zero as the minimum and 10 as the maximum. Upon finalizing the quantification of the indicators using this 0-to-10 scale, results were integrated in a radial-type graph to interpret the strengths and weaknesses of each solar cooking system assessed.

III. RESULTS AND DISCUSSION

The EFSC is an instrument proposed for evaluating solar cookers from a comparative perspective; thus it cannot be used to assess individual models of such solar devices. However, the results of comparative analyses of two or more solar cooking systems can serve to demonstrate which device has the best, or most favorable, energy, ergonomic, and economic features.

The following sections present the results of the comparative EFSC analysis for three solar cooking devices with different characteristics.

The first step consists in conducting the evaluation of each indicator for each device. In this study, we analyzed the following three systems: the *Tolokatsin* (Fig. 1) solar oven [19], a multi-component system of parabolic concentrators that operate the device; the *HOT-POT* (Fig. 2) solar cooking system, a commercial apparatus with an extensive chain of industrial production; and, the *Rural Solar Cooker* (Fig. 3), or RSC [20], which is equipped with 3-dimensional parabolic concentrators and has been implemented for use in various communities in the state of Michoacán, Mexico. Figure 1 shows the three models

Fig. 1. The *Tolokatsin* solar oven.

Fig. 2. The HOT-POT solar cooker.

Fig. 3. The Rural Solar Cooker (RSC)

The raw data obtained in relation to the indicators are shown in TABLE III; while TABLE IV presents the values for each indicator after conversion to the EFSC Evaluation Scale (0-to-10).

TABLE III. REAL VALUES OF THE EFSC INDICATORS

Indicator	*Tolokatzin*	*Hot-pot*	CSR
1-Thermal performance (%)	0.252	0.297	0.275
2-Standardized cooking power (Watts per square meter)	113.3	138.0	203.1
3- Heating time (Minutes)	122.5	95.00	120.0
4-Mass per area of the collector (Kg)	20.00	5.000	18.00
5- Load capacity (Liters)	6.000	5.000	6.000
6-Orientations per hour	1.000	1.000	1.000
7-Cost per Wh (pesos per Wh of power)	100.0	52.17	22.72
8-Reflector durability (years)	20.00	20.00	20.00

TABLE IV. VALUES FOR INDICATORS AFTER CONVERSION TO THE EFSC SCALE.

Indicator	*Tolokatsin*	*Hot-Pot*	CSR
1- Thermal performance (%)	5.04	5.94	5.50
2- Standardized cooking power (Wh per square meter)	3.24	3.94	5.80
3- Heating time (Minutes)	5.92	6.83	6.00
4- Mass per area of the collector (Kilograms)	5.00	8.75	5.50
5- Load capacity (Liters)	8.57	7.14	8.57
6- Orientations per hour	8.00	8.00	8.00
7- Cost per Wh (pesos per Wh of power)	0.00	6.00	8.25
8- Reflector durability (years)	10.0	10.0	10.0

Fig. 2 shows the final phase of the EFSC with the radial graph that integrates the results of the comparative analysis of the three solar cookers: CSR, *HOT-POT* and *Tolokatsin*. A spreadsheet can be used to elaborate comparative graphs like this one for any number of solar cookers that one wishes to compare.

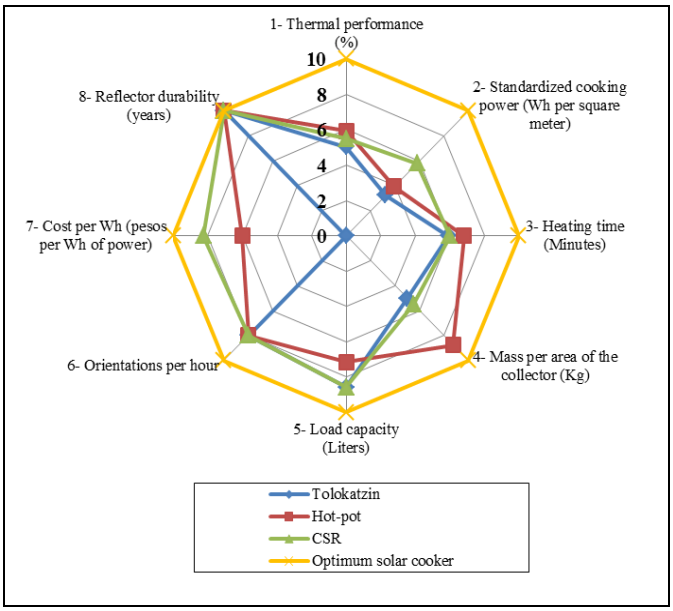

Fig. 4. The EFSC applied to 3 solar cookers

The data from the EFSC scale, together with the results of the evaluation, must present the quantities to two decimal points. The analysis of the EFSC scale for the three solar cookers evaluated is shown in TABLE V, where it is clear that the CSR is the device with the best characteristics

TABLE V. VALUES REFLECTING THE SUM OF ALL INDICATORS.

Tolokatsin	***HOT-POT***	**CSR**
45.77	**56.60**	**57.62**

IV. CONCLUSIONS.

The EFSC is proposed as an evaluation framework for solar cookers that incorporates social, economic and environmental parameters. Based on the assessment of a series of indicators, a data table was elaborated that makes it possible to compare two or more solar cookers. On the basis of this proposal, the following conclusions can be reached:

- The EFSC incorporates evaluations of the thermal performance, cost-benefits, facility of use, and durability, of the solar cookers assessed.
- The EFSC is a simple, integral medium for evaluating solar cookers that is applicable to small-dimension devices (*i.e.*, less than one square meter of capture

area).

- The EFSC provides energy analysis based on the cooking power and thermal performance; a profitable economic analysis for users and; an acceptable analysis in society, based on durability and ease of use. EFSC evaluates the best solar cooking with energy efficient, socially acceptable and economically feasibly.
- EFSC use in small-sized solar cookers has great utility; in three solar cookers: the tolokatsin solar oven, Hot-pot and CSR, the better pondered was the solar cooker that has previously been implemented in indigenous communities and has generated measurable benefits to their users.
- The EFSC has detected improvements that include: reduced consumption of such energy resources as firewood and gas, and reduced carbon dioxide emissions; two key indicators for assessing the parameter of environmental impact.

ACKNOWLEDGMENT

We thank the CONACyT project 166126 and the Universidad Intercultural Indígena de Michoacán (UIIM).

REFERENCES

[1] AJ. Smyth, J. Dumanski. 1995. A framework for evaluating sustainable land management. Canadian Journal Soil Science 75:401-406

[2] O. Masera, M. Astier, & S. López-Ridaura. "Sustentabilidad y manejo de recursos naturales: el marco MESMIS". Mundiprensa, México, 1999, pp. 2-7.

[3] J. Sandón, & C. Flores. "Evaluación de la sustentabilidad en agrosistemas: una propuesta metodológica". Agroecología 4. 2009. PP. 19-28.

[4] T. Brink, B. J. E., S. H. Hosper y F. Colin. "A quantitative method for description and assessment of ecosystems: the AMOEBA- approach". Marine Pollution Bulletin, 1991, 23:265-70.

[5] Funk, P. A. Evaluating the international standard procedure for testing solar cookers and reporting performance. *Solar Energy*, 2000, 68(1), 1-7.

[6] ASAE S580, Testing and Resporting Solar Cooker Performance. American Society of Agricultural Engineers, ASAES580 JAN03, pp.824-826, 2003.

[7] ECSCR, 1992, Solar Cooker Testing Procedure: Proposal.

[8] Mullick, S.C., Kandal, T.C. & Saxena, A.K., Thermal test procedure for box-type solar cookers, Solar Energy Vol. 39, N◦ 4, pags. 353-360, 1987.

[9] S. Fonseca, J. Abdala, Z. Acosta. "Evaluación térmica de una cocina solar tipo caja". Tecnología Química Vol. 23, No. 1. 2003.

[10] Kundapur & C. V. Sudhir. "Proposal for new world standard for testing solar cooker". Journal of Engineering Science and Technology. Vol. 4, pp. 272-281. 2009.

[11] Yahya, D. D. (2013). Thermal Performance Testing of Parabolic Solar Cooker Using New World Standard Procedure. International Journal of Engineering, 6(3), 323-331.

[12] Kimambo, C. Z. M. (2007). Development and performance testing of solar cookers. Journal of Energy in Southern Africa, 18(3), 41-51.

[13] Pohekar, S. D., & Ramachandran, M. (2004). Multi-criteria evaluation of cooking energy alternatives for promoting parabolic solar cooker in India. Renewable Energy, 29(9), 1449-1460.

[14] González-Avilés, M., López L., & Servín H., & González D. (2014) "Cocinas Solares: una alternativa energética para el medio rural". Editorial Académica Española, Alemania, pp. 111-129.

[15] Amemiya M. (2012) "Energía y Sustentabilidad: algunas características de la energía sustentable". Revista Digital Universitaria-UNAM. Vol. 13, No. 10, pp. 6-9.

[16] González-Avilés, M., López Sosa, L.B., Servín Campuzano, H. y Rodríguez Morales, J.A., (2013). Desarrollo, implementación y apropiación de cocinas solares para el medio rural de Michoacán: una alternativa energética para la conservación de recursos forestales maderables. Revista Solar de la ANES No. 17, 2013, pp. 12-15.

[17] González-Avilés, M., González Avilés, J.J., & Servín H. (2014b) "Thermal model of a solar concentration cooker: a parameter variation study to estimate thermal properties". Unpublished article submitted to Journal of Elsevier.

[18] Pejack E. (2003) Technology of Solar Cooking [On line]. The solar cooking archive, Disponible en http//solarcooking.org/Pejack-on-solar cookertechnology.pdf.

[19] Rincón E. & Osorio F. (1999) "El comal Solar Tolokatsin". XXIII Semana Nacional de Energía Solar, Morelia, México.

[20] L. López & M. González. "Desarrollo e Implementación de la Cocinas Solar Rural (CSR)". Primer Congreso Sustentabilidad e Interculturalidad, Pichataro, México, 2013.

Oxidative dehydrogenation of ethane: Reactor design for ethylene production

G. Che-Galicia[a], R.S. Ruiz-Martínez[a], A. Dutta[b,c], F. López-Isunza[a], C.O. Castillo-Araiza[a]*
[a]Grupo de Procesos de Transporte y Reacción en Sistemas Multifásicos, Depto. de Ingeniería de Procesos e Hidráulica, Universidad Autónoma Metropolitana - Iztapalapa, Av. San Rafael Atlixco No. 186, C.P. 09340.
[b]Faculteit Industriële Ingenieurswetenschappen, KU Leuven, Campus Leuven (@ Groep T), Andreas Vesaliusstraat 13, B-3000 Leuven, Belgium
[c]Departement Materiaalkunde, KU Leuven, Kasteelpark Arenberg 44 bus 2450, B-3001 Heverlee-Leuven, Belgium
México D.F., Mexico
*coca@xanum.uam.mx

***Abstract*— In this work we investigate the theoretical performance of an industrial wall-cooled packed-bed reactor for ODH-Et over a highly active/selective MoVTeNbO catalyst. The feasibility of using this complex yet necessary reactor design, as well as the influence of operating conditions on conversion and yield along the reactor are analyzed. The simulations are carried out using a two-dimensional pseudo-heterogeneous model, which makes use of both a reliable kinetic model and reliable transport parameters. Specifically, the kinetic model, obtained from lab-scale experimental data, is coupled to the reactor model accounting for transport phenomena wherein the effect of hydrodynamics on heat transfer is assessed from independent experiments in absence of reaction in an industrial-scale reactor. The developed kinetics successfully accounts for both the inhibiting effect of adsorbed water on oxidative dehydrogenation and total oxidations and the effect of the inlet partial pressure of oxygen and ethane on conversion and selectivity. Besides, the reactor model elucidates the importance of accounting for the role of the hydrodynamics on the heat transport in order to have reliable conversion and yield predictions. From the parametric sensitivity study, the temperature of the coolant fluid is an important variable for tuning the reactor performance.**

Keywords*— *Ethylene, Energy saving process, Reactor design, Oxidative dehydrogenation reaction.

I. Introduction

Olefins are basic building blocks in the petrochemical industry. Ethylene in particular is one of the largest volume petrochemical products in the world with a diverse derivative portfolio. It is widely used for producing various commercially useful products such as plastics, fibers, resins, polymers, packaging materials, etc. [1] Among all derivatives, polyethylene dominates the world market and constitutes roughly 60% of the total use for ethylene consumption. In 2013, global ethylene consumption accounted for ca. 140 million tons, which is expected to reach 150 million tons by 2015. On the whole, ethylene demand is expected to grow by ~3% per annum in the coming years. These numbers clearly demonstrate the industrial importance of its production. Ethylene is currently produced mainly by steam cracking of ethane or naphtha under severe reaction conditions; thus, it is becoming the most energy-consuming process in the chemical industry, devouring a lot of external energy and producing a large amount of coke [1,2]. On the other hand, the oxidative dehydrogenation of ethane (ODH-Et) to ethylene could provide an alternative pathway for ethylene production because of its potential advantages including the exothermic nature of the reaction and less coke formation. Notwithstanding these advantages there are two industrial challenges for producing ethylene via ODH-Et. One of them is related to the design of an active and selective catalyst to produce ethylene, while the other one has to do with the design of the reactor technology. In fact today, to the best of our knowledge, there is not even a pilot plant for ODH-Et worldwide.

The aim of this study is to model the industrial performance of a highly active/selective MoVTeNbO catalyst for the production of ethylene out of ethane via ODH-Et in a wall-cooled packed bed catalytic reactor presenting a d_t/d_p equal to 3.12. This industrial-scale reaction system is simulated using a two-dimensional pseudo-heterogeneous model coupled to a kinetic model developed herein for MoVTeNbO formulation and accounts, in some detail, for the effect of hydrodynamics on heat transfer through the proper estimation of heat transport parameters from pilot plant experiments in absence of reaction.

II. Reaction Kinetics

A. Catalyst

A MoVTeNbO catalyst with a nominal atomic ratio of Mo:V:Te:Nb equal to 1:0.24:0.24:0.18 prepared by slurry method is used. Details concerning the preparation as well as the physicochemical characteristics of this catalyst are given elsewhere [3].

B. Experimental

The data used in the kinetic modeling is obtained from experiments carried out in a laboratory isothermal fixed-bed reactor at atmospheric pressure. The fixed-bed reactor, made of quartz, has an internal diameter of 1.0×10^{-2} m and length of 4.0×10^{-2} m. Experiments were performed using a bed consisting of 0.60 g of catalyst with average particle size of

150 µm. In order to obtain the data required to calibrate the aforementioned kinetic models, three sets of experiments were effectuated. In the first set both temperature and space–time ($W_{cat}/F_{ethane,o}$) were varied within the ranges 400–480 ºC for the former, and 23–70 g_{cat} h/mol_{ethane}, keeping constant the inlet partial pressure of ethane, oxygen, and nitrogen at 7.0, 5.5, and 65.5 kPa, respectively. The second set of experiments was performed at 440 ºC varying the inlet partial pressure of ethane (p_{C2H6}) at constant inlet partial pressure of oxygen (p_{O2}), and vice versa; thus, the inlet partial pressure of each reactant was spanned from 5.1 to 22.3 kPa resulting in a $W_{cat}/F_{ethane,o}$ range from 10 to 140 g_{cat} h/mol_{ethane}. The third set of experiments was carried out feeding into the reactor ethylene instead of ethane at the operating conditions used in the second set of experiments. The reactor effluent was analyzed online periodically by gas chromatography (GC). A detailed description of the equipment has been reported in a previous study [3].

C. Kinetic model

A global reaction network based on the experimental observations is proposed, vide Fig. 1. This reaction network includes the species detected by gases chromatography, namely, ethane, ethylene, carbon monoxide and carbon dioxide. As also indicated in Fig. 1, oxygen is present as a second reagent while water is invariably a reaction product in all reactions. Both parallel and consecutive reactions are accounted for in which ethylene is produced from ethane (r_1), carbon oxides (CO_x) are formed out of the combustion of ethane corresponding to r_2 and r_3, and from the secondary combustion of ethylene, vide r_4 and r_5.

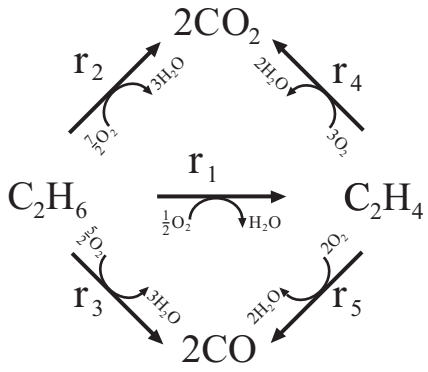

Fig. 1. Reaction network describing the ODH-Et.

The model accounts for the following assumptions: (i) there is a single type of active sites (S) on the catalyst surface, (ii) the only compounds adsorbed on the active sites are oxygen and water, (iii) oxygen adsorption is dissociative while water adsorption is associative, (iv) surface reaction steps are considered to be fast taking place over a finite number of active sites, (v) since the construction of the model is based on the pseudo equilibrium approach, surface reactions are the rate-determining steps and adsorption and desorption steps are quasi-equilibrated.

The equations that describe the rate of reactions for ODH-Et over MoVTeNbO are presented through eqs. (1) to (6) and are written as a function of the partial pressures of the gas phase components according to reaction mechanism. The calculation of r_i involves a rate coefficient denoted by k_i, an adsorption equilibrium coefficient for the n-th component represented by K_n, the partial pressure of the reactant n represented by p_n, and the reaction order related to the partial pressure of the gas phase denoted by m_i:

$$r_1 = \frac{k_1 (K_{O_2} p_{O_2})^{1/2} p_{C_2H_6}}{(1+(K_{O_2} p_{O_2})^{1/2} + K_{H_2O} p_{H_2O})} \quad (1)$$

$$r_2 = \frac{k_2 (K_{O_2} p_{O_2})^{m_2/2} p_{C_2H_6}}{(1+(K_{O_2} p_{O_2})^{1/2} + K_{H_2O} p_{H_2O})^{m_2}} \quad (2)$$

$$r_3 = \frac{k_3 (K_{O_2} p_{O_2})^{m_3/2} p_{C_2H_6}}{(1+(K_{O_2} p_{O_2})^{1/2} + K_{H_2O} p_{H_2O})^{m_3}} \quad (3)$$

$$r_4 = \frac{k_4 (K_{O_2} p_{O_2})^{m_4/2} p_{C_2H_4}}{(1+(K_{O_2} p_{O_2})^{1/2} + K_{H_2O} p_{H_2O})^{m_4}} \quad (4)$$

$$r_5 = \frac{k_5 (K_{O_2} p_{O_2})^{m_5/2} p_{C_2H_4}}{(1+(K_{O_2} p_{O_2})^{1/2} + K_{H_2O} p_{H_2O})^{m_5}} \quad (5)$$

The combination of specific reaction rates gives the net reaction rate of formation for the n-th component, which is expressed by Eq. (6):

$$R_n = \sum_{i=1}^{5} \nu_{n,i} r_i \quad (6)$$

where is the stoichiometric coefficient of the component n in the i-th reaction. In order to reduce correlation between activation energies and pre-exponential factors as well as standard adsorption enthalpies and entropies during the parameters estimation procedure, both Arrhenius and Van't Hoff equations are used in their reparametrized form.

$$k_i = \exp\left[A'_i - \frac{E_{A,i}}{R}\left(\frac{1}{T} - \frac{1}{T^*}\right)\right] \quad (7)$$

$$K_n = \exp\left[\frac{\Delta S^o_n}{R} - \frac{\Delta H^o_n}{R}\left(\frac{1}{T} - \frac{1}{T^*}\right)\right] \quad (8)$$

where A_i is the natural logarithm of the pre-exponential factor for the i-th reaction, $E_{A,i}$ is the activation energy factor for the i-th reaction, T is the reaction temperature, T* is the averaged reaction temperature, ΔS_n is the standard adsorption entropy of component n, ΔH_n is the standard adsorption enthalpy of component n and R is the universal gas constant.

III. Reactor Model

The reliability of the simulations is based on the modeling approach proposed by Castillo-Araiza and López-Isunza [4-6], which allowed to predict adequately observations from a wall-cooled packed bed catalytic reactor presenting a low d_t/d_p. This approach accounted for the role of void fraction and hydrodynamics on heat transport in the reactor through the proper determination in absence of reaction of the effective heat transport parameter (HTP) such as k_{effr}, k_{effz} and h_w. Namely, these HTP parameters are estimated using a heat transport coupled to the Navier-Stokes-Darcy-Forcheimmer equation and the existing void fraction profile.

The wall-cooled packed bed reactor model is based on averaged general conservation relations for mass and energy but considering the system as an effective medium. The two-dimensional pseudo-heterogeneous model is used and given as follows:

Gas phase:

$$\varepsilon\frac{\partial C_n}{\partial t}+u_o\frac{\partial C_n}{\partial z}=\varepsilon D_{effr}\left(\frac{\partial^2 C_n}{\partial r^2}+\frac{1}{r}\frac{\partial C_n}{\partial r}\right)+\varepsilon D_{effz}\frac{\partial^2 C_n}{\partial z^2}+(1-\varepsilon)k_g a_s(C_{ns}-C_n) \quad (9)$$

$$\varepsilon\rho_f C_{pf}\frac{\partial T}{\partial t}+u_o\rho_f C_{pf}\frac{\partial T}{\partial z}=k_{effr}\left(\frac{\partial^2 T}{\partial r^2}+\frac{1}{r}\frac{\partial T}{\partial r}\right)+k_{effz}\frac{\partial^2 T}{\partial z^2}+(1-\varepsilon)h_g a_s(T_s-T) \quad (10)$$

Solid phase:

$$(1-\varepsilon)\frac{\partial C_{ns}}{\partial t}=(1-\varepsilon)k_g a_s(C_n-C_{ns})+\rho_b\sum_{i=1}^{5}\nu_{ni}r_i \quad (11)$$

$$\rho_b C_{ps}\frac{\partial T_s}{\partial t}=(1-\varepsilon)h_g a_s(T-T_s)+\rho_b\sum_{i=1}^{5}(-\Delta H_i)r_i \quad (12)$$

The corresponding initial and boundary conditions are:

$$t=0;\quad C_n=C_{n,ss}\ \text{and}\ C_{ns}=C_{ns,ss} \quad (13)$$

$$T=T_{ss}\quad\text{and}\quad T_s=T_{s,ss} \quad (14)$$

$$z=0;\quad u_o C_{no}=u_o C_n-\varepsilon D_{effz}\frac{\partial C_n}{\partial z} \quad (15)$$

$$u_o\rho_f C_{pf}T_o=u_o\rho_f C_{pf}T-k_{effz}\frac{\partial T}{\partial z} \quad (16)$$

$$z=L;\quad \frac{\partial C_n}{\partial z}=0\ \text{and}\quad \frac{\partial T}{\partial z}=0 \quad (17)$$

$$r=0;\quad \frac{\partial C_n}{\partial r}=0\ \text{and}\quad \frac{\partial T}{\partial r}=0 \quad (18)$$

$$r=R_t;\quad \frac{\partial C_n}{\partial r}=0\ \text{and}\ k_{effr}\frac{\partial T}{\partial r}=h_w(T-T_b) \quad (19)$$

where C_n is the molar concentration of component n in the gas phase, D_{effr} is the radial mass dispersion coefficient, D_{effz} is the axial mass dispersion coefficient, ρ_b is the fixed-bed density (active catalyst density), ρ_f is the fluid density, C_{pf} is the specific heat capacity of the fluid, C_{ps} is the specific heat capacity of the solid, k_{effr} is the radial effective thermal conductivity, k_{effz} is the axial effective thermal conductivity and h_w is the wall heat transfer coefficient. This reactor model accounts for the role of hydrodynamics through the proper estimation of heat transport parameters (i.e., k_{eff} and h_w) in absence of reaction [4]. The performance of the reactor is evaluated by the conversion of reactants as well as by the yield of products. The conversion is defined as:

$$X_n=\frac{\text{number of moles of n reacted}}{\text{number of moles of n fed}} \quad (20)$$

while the yield of the n-th product is defined as:

$$Y_n=\frac{\text{number of moles of product n formed}}{\text{number of moles of ethane fed}} \quad (21)$$

The resulting model is given in terms of a set of parabolic partial differential equations, which is solved numerically by the method of orthogonal collocation using 5 and 50 interior collocation points at the radial and axial coordinates, respectively, employing shifted Legendre polynomials. The resulting set of ordinary differential equations is, then, solved by a Runge-Kutta method.

IV. Results and Discussion

The results are divided in two sections. The first section discusses the kinetics of ODH-Et on MoVTeNbO catalytic system. The model reliability is firstly discussed, in terms of the statistical significance of both the regression and the parameters; thus, the parameter values are analyzed to evaluate whether they are physically meaningful or not. On the other hand, second section presents the industrial-scale catalytic reactor simulations, which are aimed at elucidating the performance of MoVTeNbO catalyst during the ODH-Et in the wall-cooled packed bed reactor. A parametric sensibility analysis is presented with the aim to unfold the influence of coolant temperature on the catalytic performance of MoVTeNbO catalyst.

A. Kinetics

The model adequacy is also evaluated by means of both statistical and phenomenological tests. Fig. 2 shows the parity plot for the molar flow rates of all observed components (C_2H_6, C_2H_4, CO, CO_2, O_2 and H_2O). Model regression presents

statistical significance, yielding adequate agreement with the experimental data over a wide range of experimental conditions, vide Table 1. Namely, deviations from observations are random without presenting any undesired statistical trend. In this result, the random error is constant, without the presence of a systematic association between experimental points at any of the different operating conditions studied.

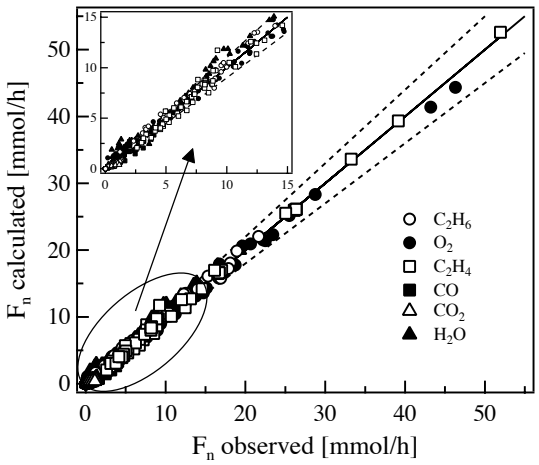

Fig. 2. Parity plot comparing experimental with calculated reactor outlet molar flow rates for the kinetic model. The full lines are the first bisector and the dashed lines represent a deviation of 10 %.

Table 1 presents the F-value of the regression, and the estimated parameters along with the 95% confidence interval and t-value. The calculated F-value amounts to 7642, a value three orders of magnitude larger than the tabulated one (2.79), corroborating the satisfactory global significance of the model regression. Besides, all parameters are statistically significant since their confidence interval is significantly narrow and their t-value (ca. 240-435) is higher than the t-value tabulated (1.97). All parameters are not statistically correlated since their binary correlations coefficients (ρ_{ij}) are always lower than 0.5. The estimated values for the adsorption equilibrium constants for oxygen and water, vide Table 1, indicate that standard adsorption enthalpies are negative with water being the component with the smallest standard adsorption enthalpy (ΔH_n=-128.2 kJ mol^{-1}). This suggests that water binds more strongly to MoVTeNbO catalyst formulation than oxygen (ΔH_n=-45.6 kJ mol^{-1}). Furthermore, Boudart's criteria are totally satisfied since the values of standard adsorption entropies are between 41.8 J (mol K)$^{-1}$ and the corresponding gas phase molecular standard entropy. The magnitude of the estimated standard adsorption enthalpies is similar to those values reported in literature [3,5]. For instance, the standard adsorption enthalpy of oxygen is reported from -19 to -98 kJ mol^{-1} and the adsorption heat of water, measured on various metal oxides surfaces, ranges between -36 and -113 kJ mol^{-1} [3,5]. According to the estimated activation energies, the rate of formation of ethylene from ethane, vide Eq. (1), is the reaction that presents the lowest activation energy i.e., 90.5 kJ mol^{-1}. In contrast, the formation of CO_X from both ethane and ethylene, vide eqs. (2)-(5), require activation energies ranging from 131.8 kJ mol^{-1} to 165.0 kJ mol^{-1}. Specifically, ethylene is the principal contributor to CO_X because total oxidations from ethane (ca. 150 kJ mol^{-1}) require even more energy than the total oxidations from ethylene (ca. 130 kJ mol^{-1}). Our estimated values of activation energies, ranging from 90.5 to 165.0 kJ mol^{-1}, are similar to the values reported in the literature for different catalytic systems for the ODH-Et (from 50 to 150 kJ mol^{-1}) [3,5]. The reaction orders associated to the partial pressure of oxygen are found to be below 1.0, indicating that reaction rates are weakly affected by changes in oxygen partial pressure.

TABLE I. KINETIC PARAMETERS VALUES OF THE KINETIC MODEL.

Parameter	Estimated value	t-value
A'_1, mmol (g_{cat} h)$^{-1}$	5.50E+00	7.59E+02
A'_2, mmol (g_{cat} h)$^{-1}$	6.86E-01	6.79E+02
A'_3, mmol (g_{cat} h)$^{-1}$	1.58E+00	6.61E+02
A'_4, mmol (g_{cat} h)$^{-1}$	2.60E+00	4.80E+02
A'_5, mmol (g_{cat} h)$^{-1}$	7.87E-01	5.14E+02
$E_{A,1}$, kJ mol^{-1}	9.05E+01	7.90E+02
$E_{A,2}$, kJ mol^{-1}	1.65E+02	5.43E+02
$E_{A,3}$, kJ mol^{-1}	1.50E+02	7.91E+02
$E_{A,4}$, kJ mol^{-1}	1.39E+02	5.31E+02
$E_{A,5}$, kJ mol^{-1}	1.32E+02	4.96E+02
$-\Delta S^{o}_{O_2}$, J (mol K)$^{-1}$	2.15E+02	8.33E+02
$-\Delta S^{o}_{H_2O}$, J (mol K)$^{-1}$	4.20E+01	6.75E+02
$-\Delta H^{o}_{O_2}$, kJ mol^{-1}	4.56E+01	8.56E+02
$-\Delta H^{o}_{H_2O}$, kJ mol^{-1}	1.28E+02	7.48E+02
m_2	9.22E-01	7.37E+02
m_3	9.06E-01	7.23E+02
m_4	1.23E+00	5.79E+02
m_5	9.05E-01	6.37E+02

Note: F value = 7642, F_{tab} = 2.79, t_{tab} = 1.97 at 1-α = 0.95 and 396 degrees of freedom.

B. Industrial Reactor

The adequate consideration of heat transport phenomena in the model of a wall-cooled packed bed catalytic reactor with low d_t/d_p is, undoubtedly, one of the most essential aspects to be accounted for during the conceptual design of this type of reaction systems. There are several approximations that have been used to model heat transport in a wall-cooled catalytic reactor with low d_t/d_p. Some studies [4] suggest that the inclusion of velocity profiles improves heat transport

description; however, others studies have neglected the influence of the hydrodynamics in the modeling of this type of reactors. In this regard, a practical but reliable approach, developed by our research group, is herein applied to account for the role of hydrodynamics on heat transport during the modeling of the ODH-Et in a wall-cooled catalytic reactor packed with MoVTeNbO catalyst externally deposited on a nonporous support of TiO_2.

The behavior of a reactor is a function of the initial process conditions, reactor disturbances and the trajectories of the manipulated reactor variables. In order to analyze an open-loop parametric sensitivity study for the performance of MoVTeNbO system during the ODH-Et in an industrial scale wall-cooled packed bed reactor, this section is aimed at simulating the reactor when perturbations of cooling bath temperature are considered. Fig. 3 shows the predicted dynamic response when reactor starts up at T_b of 400ºC with an inlet molar ratio $C_2H_6/O_2/N_2$=9/7/84, once the steady state is reached, it is followed by perturbations of the cooling bath temperature, namely 440ºC and 480ºC.

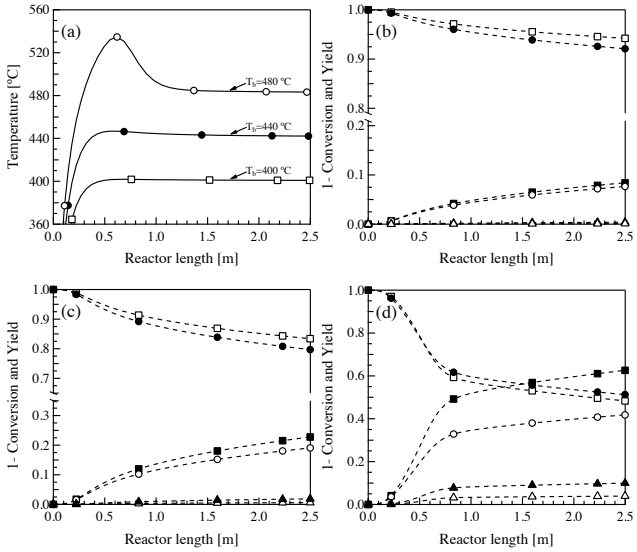

Fig. 3. Reactor model predictions at different T_b with an inlet molar ratio $C_2H_6/O_2/N_2$=9/7/84: (a) Temperature profiles; (b) Conversion and yield profiles at T_b=400 ºC; (c) Conversion and yield profiles at T_b=440 ºC; (d) Conversion and yield profiles at T_b=480 ºC (For (b)-(d): (●) C_2H_6 conversion; (□) O_2 conversion; (○) C_2H_4 yield; (■) H_2O yield; (▲) CO yield and (△) CO_2 yield).

Fig. 3 displays transient and steady state temperature, conversion (ethane and oxygen) and yield (ethylene, CO_X and water) profiles along the reactor length at different coolant temperatures maintaining a fixed inlet molar ratio $C_2H_6/O_2/N_2$=9/7/84. So far, an increment in coolant temperature causes an increase in the magnitude of the hot spot, vide Fig. 3a. Specifically a T_b equal to 400 ºC and 440 ºC leads to mild hot spots of ca. 1 ºC and 7 ºC respectively whereas a T_b equal to 480 ºC provokes a pronounced hot spot with a temperature rise of ca. 56 ºC. In the latter, the rate of heat removal is minor in comparison with the rate of heat generated. Besides Figs. 3b-d displays the effect of coolant temperature on the overall consumption rates of the reactants. The increment of T_b favors both ethane and oxygen conversions. Analyzing the product distribution, an increase in T_b brings out a positive effect on the yield of ethylene out of ethane. However, a higher T_b leads to higher carbon oxides yields, which are the responsible of both the formation of hot spots and the decrease in the selectivity to ethylene. In this regard, a lower T_b is recommended for a satisfactory ethane conversion along with ethylene selectivity avoiding catalyst damage due to high temperatures. The behavior of the industrial scale reactor presented in Fig. 3 shows similar tendencies as those of the typical industrial-scale packed bed reactors used to perform highly exothermic reactions [4-6].

CONCLUSIONS

On the basis of the results obtained herein, the wall-cooled packed-bed reactor represents a promising alternative for petrochemical industry to carry out the ODH-Et over a MoVTeNbO catalyst, which is highly selective to ethylene. Besides, the model developed in this work, in general, and the modeling strategy based on laboratory and pilot plant experiments in absence of reaction, in particular, are potential tools to be used in future studies for the conceptual design and scale-up of industrial reactor system for the ODH-Et on MoVTeNbO material.

ACKNOWLEDGMENT

This study was supported by El Consejo Nacional de Ciencia y Tecnología (CONACyT) under project No. 181104.

REFERENCES

[1] W.R. True, “Global ethylene capacity continues advance in 2011”, Oil Gas J., vol110, pp. 78–84, 2012 .

[2] K. Weissermel, H.-J. Arpe, Industrial Organic Chemistry, WILEY-VCH Verlag GmbH & Co. KGaA, Weinheim, 2003.

[3] G. Che-Galicia, R. Quintana-Solórzano, J.S. Valente, R.S. Ruiz-Martínez, C.O. Castillo-Araiza, “Kinetic modeling of the oxidative dehydrogenation of ethane to ethylene over a MoVTeNbO catalytic system”, Chem. Eng. J. 252 (2014) 75–88.

[4] C.O. Castillo-Araiza, H. Jiménez-Islas, F. López-Isunza, “Heat-transfer studies in packed-bed catalytic reactors of low tube/particle diameter ratio”, Ind. Eng. Chem. Res. 46 (2007) 7426–7435.

[5] G. Che-Galicia, R.S. Ruiz-Martínez, F. López-Isunza, C.O. Castillo-Araiza, “Modeling of oxidative dehydrogenation of ethane to ethylene on a MoVTeNbO/TiO2 catalyst in an industrial-scale packed bed catalytic reactor”, Chemical Engineering Journal (2015), doi: http://dx.doi.org/10.1016/j.cej.2015.05.128

[6] C.O. Castillo-Araiza, F. López-Isunza, “The role of catalyst activity on the steady state and transient behavior of an industrial-scale fixed bed catalytic reactor for the partial oxidation of *o*-xylene on V_2O_5/TiO_2”, Chem. Eng. J. 176-177 (2011) 26–32.

Obtención del coeficiente de difusión en la reacción de fotodegradación del 4-Clorofenol

Julio César Espinoza Tapia*[a], Ernesto Alonso Piña [b], José Antonio Colin Luna [b], Isaías Hernández Pérez [a], Enrique Barrera Calva [c], Teresa de Jesús Sanchez Rosas [a]

[a] Departamento de Ciencias Básicas, UAM-Azcapotzalco, Av. San Pablo 180, Col. Reynosa Tamaulipas, C.P. 02200, Azcapotzalco, México, D.F.
[b] Departamento de Energía, UAM-Azcapotzalco, Av. San Pablo 180, Col. Reynosa Tamaulipas, C.P. 02200, Azcapotzalco, México, D.F.
[c] Departamento de Ingeniería de Procesos e Hidráulica, UAM-Iztapalapa, San Rafael Atlixco 186, Col. Vicentina, C.P. 09340, Iztapalapa, México, D.F.
*julio_espinoza294@hotmail.com

Resumen

En el presente trabajo se realizó el estudio de la influencia de la difusión en la reacción de degradación del 4-Clorofenol mediante el método de dispersión de Taylor de líquidos, debido a que este compuesto es un contaminante ambiental producido por varios sectores de la industria en el país, además debido a su composición química es difícil de degradar por métodos tradicionales de purificación de aguas, por lo cual se recurrió a los procesos de oxidación avanzada para lograr su eliminación; y dentro de este tipo de procesos es importante el conocer el efecto que cause la difusividad. Para realizar la determinación de la difusividad se empleó una solución problema de 100 PPM de 4-Clorofenol (determinado por absorbancia en UV-Vis) que se inyecto a un tubo que contenía agua como disolvente en flujo laminar, después se llevaron a cabo los cálculos necesarios para obtención del coeficiente de difusión. Posterior a la determinación se empleó la solución problema en un proceso de fotodegradación utilizando como fotocalizador el TiO_2 anatasa; la reacción se realizó en un reactor tubular de cristal con un flujo de alimentación controlado por una bomba peristática, se modifica la velocidad de alimentación del reactor para observar el efecto del fenómeno de transferencia de masa dentro del sistema, la fuente luminiscente es una lámpara de luz ultravioleta de 306 nm. Para determinar la constante de difusión se realizó el cálculo atraves de la ley de Fick y la teoría de la catálisis heterogénea.

Palabras Clave: 4-Clorofenol, Difusión, Fotodegradación.

I. INTRODUCCIÓN

El 4-clorofenol es un subproducto en los procesos de transformación en la industria química, petroquímica, papelera, insecticidas y pesticidas, o bien durante los procesos de potabilización de aguas por medio de la cloración. Este compuesto ha ocasionado serios problemas no sólo al medio ambiente, también es causante de serios problemas de salud, los cuales van una simple intoxicación hasta la muerte, ya que se trata de un compuesto altamente toxico y de gran estabilidad química, lo que tiene como consecuencia la dificultad de degradación a través de métodos tradicionales tales como son los métodos físico-químico, coagulación-precipitación y biológicos [1]. En este caso los denominados procesos de oxidación avanzada (POA) han recibido gran atención debido entre otras a que el proceso puede llevarse a cabo a temperatura ambiente y se puede llegar a mineralización completa del contaminante orgánico [2, 3]. En particular, la fotocatálisis es un proceso que consiste de la irradiación de un material semiconductor con luz UV o visible, durante este proceso un electrón de la banda de valencia es promovido a la banda de conducción, generando un par de portadores de carga, denominados electrón-hueco. Estos portadores de carga permiten la degradación de la materia orgánica mediante un mecanismo redox, en el cual los huecos en la banda de valencia, que son especies con deficiencia de electrones (convencionalmente se les ha asignado un signo positivo), pueden reaccionar con los compuestos orgánicos contaminantes adsorbidos sobre la superficie del catalizador para transformarlas a un estados oxidado de acuerdo con la siguientes reacciones [4, 5, 6].

$$Semiconductor \rightarrow e^-_{BC} + h^+_{BV} \quad (1)$$
$$H_2O + h^+_{BV} \rightarrow OH^- + H^+ \quad (2)$$
$$OH^- + h^+_{BV} \rightarrow OH\bullet \quad (3)$$

Mientras que los electrones de la banda de conducción pueden reaccionar con el oxígeno adsorbido o en la interface. A través de la reducción del O2 con el electrón se generan especies reactivas O2•- (radical superóxido), junto con otras especies oxidantes como HO2• (radical hidroperóxido) y H2O2 (peróxido de hidrógeno). Los radicales adicionales •OH son generados por las siguientes reacciones [7, 8].

$$O_2 + e^-_{BC} \rightarrow O_2^-\bullet \quad (4)$$
$$O_2^-\bullet + H^+ \rightarrow HO_2\bullet \quad (5)$$
$$H_2O + 2\,HO_2\bullet \rightarrow H_2O_2 + O_2 \quad (6)$$
$$H_2O_2 + e^-_{BC} \rightarrow OH^- + OH\bullet \quad (7)$$

$$H_2O_2 + O_2^{-}\bullet \rightarrow OH^{-} + OH\bullet \quad (8)$$
$$H_2O_2 + h\nu \rightarrow 2OH\bullet \quad (9)$$
$$OH\bullet + Comp.\ Org. \rightarrow Comp.\ Org._{ox} \quad (10)$$
$$e^{-}_{BC} + Comp.\ Org. \rightarrow Comp.\ Org._{red} \quad (11)$$

Uno de los catalizadores más empleados en este tipo de proceso y que presenta una gran eficiencia es el TiO2 [7, 8], sin embargo, debido a su Eg = 3.2 eV, en este trabajo la prueba de degradación se llevó a cabo en un reactor tipo tubular de cristal con un flujo de alimentación variable mediante una bomba peristática y una lámpara de luz ultravioleta de 306 nm como fuente luminiscente. La reacción se realizó con diferentes velocidades de alimentación para observar el efecto del fenómeno de transferencia de masa dentro del sistema, y se realizó el cálculo para la determinación de la constante de difusión atraves de la teoría de obtención de coeficientes de difusión por el método de dispersión de Taylor.

II. MÉTODO DE DISPERSIÓN DE TAYLOR

Este es un método válido para obtener el valor de la constante de difusión en gases y líquidos, el cual se emplea un tubo largo lleno de disolvente que se mueve lentamente en flujo laminar.Un fuerte pulso de soluto (solución de trazador) se inyecta cerca de un extremo del tubo. A medida que el pulso de soluto se mueve a través del tubo se irá dispersando. Se calcula el perfil de concentración del soluto, cuando el pulso sale por el extremo del tubo, la cantidad de flujo se recoge y se lee su concentración por medio de alguna técnica analítica. Se presume que este sistema tiene el potencial para dar resultados precisos.

El perfil de concentración que se mide a la salida en este dispositivo corresponde al pulso de soluto que se inyectó. Por medio de las siguientes ecuaciones se logra conocer el valor del coeficiente de difusión [9, 10]:

$$C = \frac{M}{\pi R^2} \frac{e^{-(z-vt)^2/4Et}}{\sqrt{4\pi Et}} \quad (12)$$

$$E = \frac{(vR)^2}{48D} \quad (13)$$

En dónde:

M = soluto total inyectado [g mol]
R = radio del tubo [m]
ν = velocidad promedio del disolvente [m/s]
E = coeficiente de dispersión [m^2/s]
z = distancia a lo largo de la tubo [m]
t = tiempo [s]
D = coeficiente de difusión [m^2/s]

Se nota que el sistema está formado por dos ecuaciones y dos incógnitas (el coeficiente de dispersión E y el coeficiente de difusión D), las cuales muestran que un pulso extendido indica que el valor de E es muy grande y el valor de D es pequeño; en caso contrario un impulso fuerte indica una difusión rápida y una pequeña dispersión. La Fig. 1 se muestra el esquema del dispositivo de obtención experimental del método de Taylor [11].

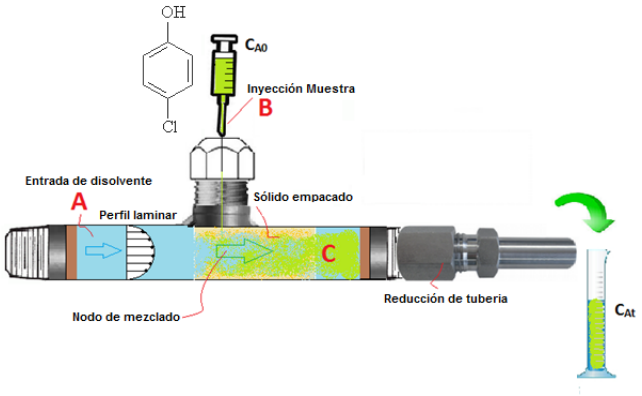

Fig. 1. Sistema de determinación experimental del coeficiente de difusividad de una solución de 4-Clorofenol (Método de Taylor).

Este proceso se describe con un balance de masa, al cual se le considera diluida la solución con un flujo laminar sin cambios de pulso, es decir que la velocidad depende del radio. El transporte de masa se efectúa por difusión radial y convección axial, y para considerar como correcto el cálculo en el sistema se debe cumplir la siguiente condición:

$$7.2\left(\frac{LD}{R^2 v}\right) >> 1 \quad (14)$$

Donde L es la longitud de la tubería, R es el radio interno, ν es la velocidad del fluido en el interior y D es el coeficiente de difusividad obtenido.

III. METODOLOGÍA EXPERIMENTAL

A. *Difusión Experimental*

Se utilizó una solución de problema de 4-Clorofenol con una concentración inicial de 100 PPM (0.00077 gmol/L), en un sistema de obtención del coeficiente de difusión de Taylor, con las siguientes condiciones de experimentación: se emplearon 7.7 X 10-5 gmol de soluto inyectado (M), con un radio interno (R) del sistema de 0.001587 m, efectuándose durante un tiempo (t) de prueba de 150 s, con una velocidad promedio del fluido (ν) 0.003155 m/s y a una distancia de la tubería (z) de 0.4854 m. Con los resultados observados y las ecuaciones antes mencionadas se obtuvo el coeficiente de dispersión (E) en m2/s y el coeficiente de difusión (D) en m-1, todo a temperatura ambiente (298.15 K).

B. *Degradación Fotocatalítica*

La reacción de degradación fotocatalítica se llevó a cabo en un sistema semicontinuo en forma de espiral, con 0.75 g de TiO2 anatasa como fotocatalizador, contando con un sistema de alimentación de flujo variable (desde 9.4 ml/s hasta 27.1 ml/s), con una lámpara de 306 nm, con 0.1 ml de H2O2 como agente oxidante y 1 L de solución problema (4-Clorofenol con una concentración de 100 PPM), durante 300 minutos de reacción. La determinación de la concentración fue monitoreada mediante espectroscopia UV-Vis de líquidos en un equipo Perkin Elmer modelo Lambda 35 y la Ley de Lamber Beer a una λ = 280 nm. Se variaron los flujos de alimentación para observar los efectos de la transferencia de masa durante la reacción de fotodegradación. Adicionalmente los resultados obtenidos de la reacción fotocatalítica se utilizaron para obtener un modelo cinético mediante el modelo propuesto por Langmuir – Hinshelwood para reacciones catalíticas del tipo heterogéneo.

Fig. 2. Sistema de fotodegradacion de la solución de 4-Clorofenol (sistema semicontinuo).

IV. RESULTADOS

A. *Difusión Experimental*

Con los datos obtenidos en la experimentación de difusión experimental y sustituyendo en las ecuaciones 12 y 13 los datos correspondientes se pueden observar los siguientes resultados:

$$C = \frac{7.7\ X\ 10^{-5}}{\pi(0.001587)^2}\ \frac{e^{-((0.4854)-(0.003155)(150))^2/4E(150)}}{\sqrt{4\pi E(150)}}$$

$$E = \frac{(0.003155\ X\ 0.001587)^2}{48\ D}$$

E = 6.6855 X 10^{-5} m^2/s

C = 1.3748 X 10^{-4} gmol / ml

D = 7.8122 X 10^{-9} m^2/s

Conociendo el valor del coeficiente de difusión se realiza la comprobación mediante la ecuación 14, mostrando el siguiente resultado:

$$7.2\left(\frac{(0.4854)(7.8122\ X\ 10^{-9})}{(0.001587)^2(0.003155)}\right) = 3.435994$$

$$3.435994 > 1$$

El resultado observado anteriormente se puede comparar con el reportado por Martins y col. [12] para la solución de este compuesto la cual es la siguiente:

D = 7.8122 X 10^{-9} m^2/s Método Taylor

D = 2.1100 X 10^{-9} m^2/s Referencia 12

Adicionalmente al método de Taylor se manejó un proceso de fotodegradación, en el cual se determinó la constante de difusividad en la reacción la cual se mostrara más adelante.

B. *Degradación Fotocatalitica*

En lo que corresponde a la degradación fotocatalítica del 4-Clorofenol, la variación de concentración fue monitoreada mediante un espectrofotómetro UV-Vis Perkin Elmer Lambda 35 a una λ = 280 nm.

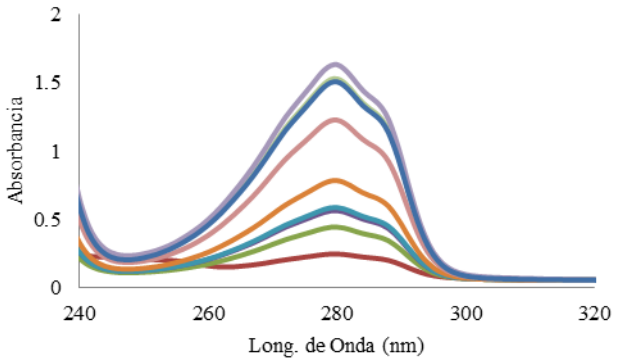

Fig. 3. Maxima absorbancia observada del 4-Clorofenol (λ= 280 nm).

En lo que corresponde a la degradación fotocatalítica del 4-Clorofenol, la variación de concentración fue monitoreada mediante un espectrofotómetro UV-Vis Perkin Elmer Lambda 35 a una λ = 280 nm.

Posteriormente se realizaron pruebas a las condiciones deseadas (mencionadas en la metodología), en un sistema semicontinuo, debido a que su diseño está constituido para tener una variación en el volumen del reactor conforme pasa el tiempo (esto se debe a que se adiciona un pequeño volumen de agente oxidante), que aunque el aumento de volumen es muy pequeño en comparación al volumen total, existe esta diferencia lo cual cambia al sistema de ser por lotes a un semicontinuo.

Para determinar el flujo adecuado de operación se realizaron distintas pruebas a distintos flujos volumétricos de alimentación al reactor, lo que nos proporcionó manejar distintos regímenes de fluido (laminar y turbulento), y considerando que los mejores resultados durante la experimentación se pueden obtener en un flujo laminar debido a que existe una mayor interacción de la solución con la luz, durante el desarrollo se buscó estar lo más cercano a este tipo de flujo para mantener una mayor absorción energética, las pruebas se realizaron durante los primeros 90 minutos a las condiciones deseadas y los resultados se pueden encontrar en la Tabla 1.

Tabla 1. Efecto de la degradación con distinto régimen

Flujo (ml/s)	No Re	C Inic (PPM)	C fin (PPM)	Conversión (%)
11.2275	1607.8568	98.0473	88.1418	10.1027
16.6186	2379.9002	93.5859	86.8984	7.1458
22.4282	3211.8757	93.5859	83.8984	10.3514
27.1296	3884.7196	93.5859	87.5156	6.4863
36.6301	5245.6876	93.5859	87.1556	6.4862

Basados en los resultados de la tabla anterior se puede determinar que los mejores resultados de experimentación se obtendrán cuando se maneje un flujo de alimentación de 11.2275 ml/s, debido a tiene un bajo número de Reynolds además de arrojar unos resultados dentro del régimen laminar, además de que este régimen es el necesario para cumplir el modelo de Taylor para la determinación de la constante de difusividad.

Durante la fotodegradación del 4-Clorofenol, el monitoreo de la reacción se realizó tomando muestras desde iniciada la reacción, y cada 30 minutos hasta obtener 300; el desempeño observado en la reacción fue de un 29.3 % de conversión del compuesto, el comportamiento del desempeño se puede observar en el grafico siguiente:

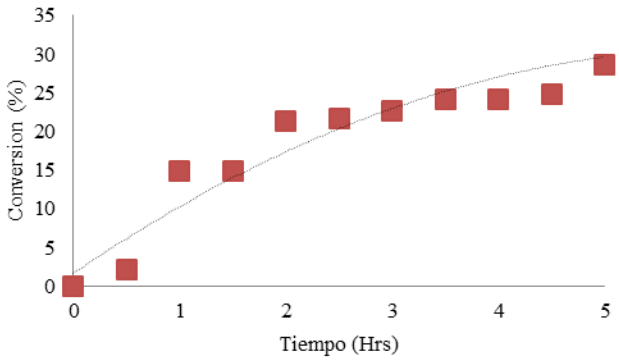

Fig. 4. Comportamiento fotocatalitico del 4-Clorofenol.

Conociendo el desempeño de la experimentación se obtuvo el modelo cinético de la reacción el cual se apegó a un modelo de Langmuir – Hinshelwood, el cual se puede observar en la siguiente ecuación:

$$r = \frac{k_{LH} K_L C_M}{1 + K_L C_M} \qquad (15)$$

Dónde:

k_{LH} = constante cinética observada [m^{-1}]
K_L = constante del modelo de Langmuir–Hinshelwood.
C_M = concentración del 4-Clorofenol.
r = velocidad de la reacción.

Considerando que la velocidad de reacción (r) es la diferencial de la concentración (dC) con respecto al (dt), se puede reescribir la ecuación 15 de la siguiente manera:

$$-\frac{dC}{dt} = \frac{k_{LH} K_L C_M}{1 + K_L C_M} \qquad (16)$$

Con la ecuación anterior y realizando un reacomodo de las variables se puede obtener la siguiente ecuación:

$$\ln\frac{C_0}{C} / t = k_{LH} - \frac{K_L (C_{M0} - C_M)}{t} \qquad (17)$$

Con la ecuación 17 y los resultados de la experimentación se puede obtener el grafico siguiente:

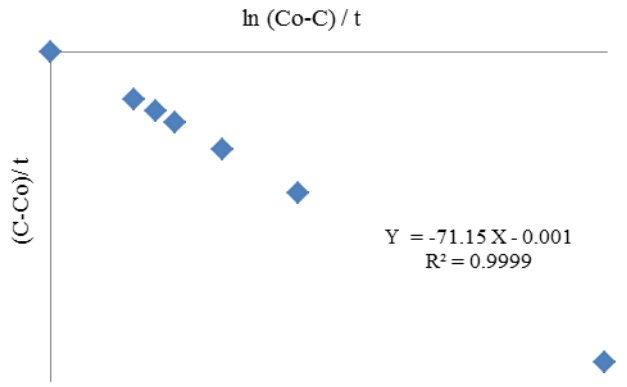

Fig. 5. Comportamienmto cinético del 4-Clorofenol.

El grafico anterior muestra como resultado los siguientes valores a las constantes de la ecuación:

$k_{LH} = 71.15\ m^{-1}$
$K_L = 0.001$

El valor de la constante determinada por el modelo de Langmuir–Hinshelwood es alejado al que se obtuvo por el modelo de Taylor o el reportado en literatura [12].

CONCLUSIONES

En base de los resultados se puede concluir que el modelo de Taylor para la determinación de la constante de difusión otorga un buen resultado, siempre y cuando se mantengan las condiciones óptimas de experimentación, es decir que se mantenga un flujo laminar con una concentración no muy baja; adicionalmente este resultado se asemeja con el que se obtienen por otros métodos por otros autores.

En el caso de la determinación de la constante por el modelo de Langmuir–Hinshelwood, este por sus limitantes otorga un resultado alejado al que se observa por los otros modelos de determinación, esto debido a que el método se basa en algunas suposiciones que no todo el tiempo son ciertos (que la energía de ionización es la misma en todos los puntos de la superficie, o que exclusivamente se forma una monocapa).

AGRADECIMIENTOS

Los autores agradecen a la Dra. Ana Karina Medina Mendoza por el apoyo brindado en desarrollo de este trabajo, así como a la UAM – Azcapotzalco por el respaldo en el desarrollo experimental.

REFERENCIAS

[1] Montiel Palacios E., Medina Mendoza A. K., Sampieri A., Angeles Chavez C., Hernanez Perez I., Suarez Parra R., “Photo-catalysis of phenol derivatives with Fe_2O_3 nanoparticles dispersed on SBA-15,” J. of Ceramic Process. Res. 10(4), 548~552, 2009.J. Clerk Maxwell, A Treatise on Electricity and Magnetism, 3rd ed., vol. 2. Oxford: Clarendon, 1892, pp.68–73.

[2] Sakkas V. A., Islam M. A., Stalikas C., Albanis T.A., “Photocatalytic degradation using design of experiments: A review and example of the Congo red degradation, ” J. of Hazardous Mater., 175, 33–44, 2010..

[3] Zermeño B. B., Moctezuma E., Garcia Alamilla R., “Photocatalytic degradation of phenol and 4-chlorofenol with titania, oxygen an ozone, ” Sustain. Environ. Res., 21(5), 299-305, 2011.

[4] Kaur J., Singhal, “Facile synthesis of ZnO and transition metal doped ZnO nanoparticles for the photocatalytic degradation of Methyl Orange. ” Ceramics International, 2014. 40(5): p. 7417-7424.

[5] Prihod'ko R.V., Soboleva N.M., “Photocatalysis: Oxidative Processes in Water Treatment. ” Journal of Chemistry, 2013. 2013: p. 8.

[6] Zhang L., “Kinetics and mechanisms of charge transfer processes in photocatalytic systems: A review.” Journal of Photochemistry and Photobiology C: Photochemistry Reviews, 2012. 13(4): p. 263-276.

[7] Lam S. M., “Degradation of wastewaters containing organic dyes photocatalysed by zinc oxide: a review.” Desalination and Water Treatment, 2012. 41(1-3): p. 131-169.

[8] Shinde S. S., Bhosale C. H., Rajpure K.Y., “Oxidative degradation of acid orange 7 using Ag-doped zinc oxide thin films.” Journal of Photochemistry and Photobiology B: Biology, 2012. 117(0): p. 262-268.

[9] Cussler E. L., “Diffusion Mass Transfer in Fluid Systems.” Third edition.647 pp. Cambridge 2009.

[10] Ruiz Beviá Francisco, Del Mar Olaya López María, “Mass transfer experiment determination of liquid diffusion coefficients.” ChE laboratory. Chemical Engineering Education. University of Alicante, Spain. 156/159 pp. 2002.

[11] Welty, James R.., “Fundamentos de transferencia de momento, calor y masa.” Universidad Estatal de Oregón. Limusa Wiley. Segunda edición. 2009.

[12] Martins Luís F.G., Parreira M. Cristina B., Prates Ramalho João P., Morgado Pedro, Filipe Eduardo J. M.; “Prediction of diffusion coefficients of chlorophenols in water by computer simulation”; Fluid Phase Equilibria 396 (2015) 9–19.

Stabilization and control of a delayed recycle thermical process

M. A. Hernández-Pérez, B. del Muro-Cuellar
Sección de Estudios de Posgrado e Investigación ESIME-Culhuacán
Instituto Politécnico Nacional
México D.F.
mahp_hernandez@hotmail.com and bdelmuro@yahoo.com

***Abstract*—In this work is addressed the problematic about the stabilization and control of temperature in a heat flow thermic process. This situation is not trivial because the recycle trajectory presents positive feedback to the thermal process, which leads to a unstable system. Due to this phenomena, it is generated an unstable second order system with a zero of minimum phase. Besides, it is considered the existence of a delay in the feedback signal because of the time consumed while the heat measurement is registered in the sensor at the output of the process. In this work is proposed a control strategy based on a PI-modified controller which allows the stabilization and control of this particular type of unstable systems with recycle and time-delay. In this new schema the control improves the stability conditions when compared with previous results stated by the literature about the traditional PI controller for this kind of systems. The results are applied to a laboratory prototype of the QUANSER brand. Finally, it is stated an idea about the possible generalization of the implementation of this control schema to a whole family of systems**

Keywords—Time-delay; recycle-systems; thermic process; PI-control

I. INTRODUCTION

Delayed systems, also termed dead-time systems, occur in most of industrial processes [1]. Time delays are present in systems where some kind of mass or energy is transported, for example in distillation columns, heat exchange processes, etc. Sometimes, delays arise due to the own system design, for example due to computational cost of the control algorithm, remote control and communication networks in distributed systems, etc. However, most of the time, delays are introduced by sensors and/or actuators devices [2]**.** Particularly, unstable processes with time delay are common in chemical and industrial processes, like liquid storage tanks, continuously stirred tank reactor (CSTR) [3], [4], etc.

Delays are perhaps, one of the main causes of instability and poor performance, producing in general unwanted behavior in dynamical systems [5]. Therefore, stability analysis and controller design of delayed systems deserve special attention. As a consequence, there is great motivation for studying the effects that delays cause in dynamic systems behavior. From the control viewpoint, time delays introduce complications that must be overcome by designing control strategies. Such strategies must provide both acceptable performance and stability of closed-loop system.

A particular case of dynamic systems, with or without delay, are the recycle processes in which a certain amount of matter or energy is recovered and this is added to the system input [6]. The most industrial processes contain recycle streams. From the process design point of view, the matter or energy recycle is used for several purposes, for example, increase the conversion reagents, improve process economics and to obtain improved selectivity in the process, among others [7]. Unfortunately, the recycle systems, even without delay have characteristics that make them particularly difficult to control [8]. Therefore, when the recycle is positive, it can be compromise the stability of the process [9]. Luyben in 1994, introduced the term "snowball" to describe an effect of a system with recycle. This effect it implies that a slight change in a process variable can produce extremely large changes in other process variables [10].

In this work it is proposed a strategy control based on a PI-modified controller (which, in this work has been termed as PI_{+f}) in order to stabilized and control the temperature in a heat flow thermical process with recycle and time delay. This situation in not trivial, because the recycle trajectory presents a positive feedback to the thermal process, which leads to the instability system. The sufficient conditions are stated, in this work, to guarantee the stability of the system in closed-loop by using a PI_{+f} controller. Moreover, it is provided a procedure for determining the ranges of the stabilizing controller PI_{+f} parameters (k_p, k_i and k_f) for the considered controller. The results are applied to a laboratory prototype of the QUANSER brand. Finally, it is stated an idea about the possible generalization of the implementation of this schema to a whole family of systems.

The rest of this work is described as follows: Section 2 presents the modeling of the thermic process. Section 3 addresses the proposed control strategy, establishing the sufficient conditions for the existence of a stabilizing control structure. In Section 4, the proposed control strategy is applied to a prototype laboratory in order to control the temperature. Finally, general conclusions of the work are given in Section 5.

II. THE THERMIC PROCESS MODEL

In order to investigate the recycle phenomenon, in this work is used a laboratory prototype QUANSER HFE (Heat Flow Experiment) where the purpose is to control the temperature along a pipeline.

A. *Description of the thermal system QUANSER HFE*

The volume of the prototype HFE is approximately of $60\text{x}15\text{x}10\ cm^3$ and consists of a chamber fiberglass, and it is equipped with a heater and a fan, which they are located in the extreme of the camera. The heater works through a resistor, which is a control variable. Besides, the HFE has three temperature sensors located equidistantly along the chamber. The HFE has an amplifier to supply power to the heater and fan. The power used to the heater and fan is controlled by analog signals. The Fig. 1 illustrates a general scheme of the components of HFE.

Fig. 1. Thermical Process HFE with recicly

TABLE 1: SYSTEM COMPONENTS OF HFE

#ID	Components		
	Component	***#ID***	***Subhead***
1	Recicle tube	10	Tmp Three Connector
2	Fiberglass chamber	11	Temperature sensor 1 offset
3	Blower	12	Tmp Three Connector
4	Heater coil	13	Temperature sensor 2 offset
5	Temperature sensor 1	14	Tmp Three Connector
6	Temperature sensor 1	15	Temperature sensor 3 offset
7	Temperature sensor 1	16	Fan spd Connector
8	Interruptor	17	Fan Cmd Connector
9	Power on/off	18	Heat Cmd Connector

The purpose of this experiment is to control the output temperature in the tube (fiberglass chamber) by the control of the dissipated power in the resistance when it is considered a constant air flow rate. To apply the proposed control strategy in this work and to achieve the control of the temperature in the process, the HFE system is modeled using the "bumptest" model (finding the response under a step type input). Referring to the HFE process, the power dissipated by the resistor (spread through heat) is the measurable variable, which is given by sensor 3. This measurement is manipulated by the control strategy at varying the supply voltage of the electrical resistance and the voltage supplied by the fan. It is worth noting that the fan speed is constant during all the experiment.

Once defined the HFE system variables, the process is addressed to the breakeven points (approximately $20s$ after that the experiment starts), i.e., it is desirable that the temperature obtained by the sensor keeps constant to refer to the initial temperature ($20^{\circ}C$) in order to observe the system behavior when the "bumptest" method is applied. At this point the supply voltage over the resistor and over the fan is from $0V$ to $6V$ respectively, which implies that initially sensor 3 measures the environment temperature (breakeven points). Then, to start with the *bumptest* method, the supply voltage is now set to $2.5V$ and the new values of sensor 3 are recorded. The response for this experiment is illustrated in Fig2.

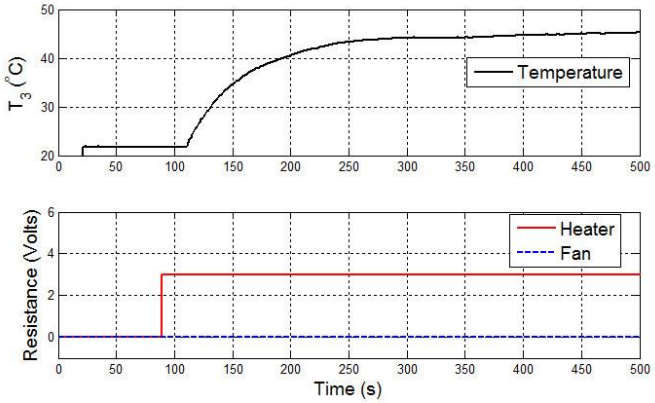

Fig. 2. Signal Input and output to use a bumptest method

Therefore, the transfer function which represents the dynamic of the thermal process HFE is given by

$$G_h(s) = \frac{0.284}{s + 0.024}. \quad (1)$$

To implement the recycle path, similar to the Fiberglass chamber was added to the QUANSER process as illustrated in Fig 2, which generates an extra dynamic in the process since the recycle produces a positive feedback of the thermal flow and is represented by the following transfer function:

$$G_r(s) = \frac{0.353}{s + 0.014}. \quad (2)$$

Besides of the recycle generated during the thermal process, there exist a τ delay that occurs in the measurement given by sensor 3. This delay takes place because the heat flow is transported along the fiberglass chamber of the QUANSER system and it receives feedback through the recycle chamber. This phenomena causes that the sensor records the generated temperature in the next time instant after that a variation in the input voltage of the resistance appears. Therefore, the mathematical model which characterize the system dynamics in the HFE system with recycle and delay are represented by the following transfer function $G(s)$.

$$G(s) = \frac{0.284(s + 0.014)}{(s - 0.296)(s + 0.334)}. \quad (3)$$

III. Proposed Control Strategy

This section presents the sufficient condition to stabilize and control the thermal process (3) by a class of PI-modified (PI_{+f}).

A. Problem Statement

In order to generalize the problem we will take into account the following class of system illustrated in Figure 3. Then, consider the delayed recycle process (3) and its representative scheme given in Fig. 3

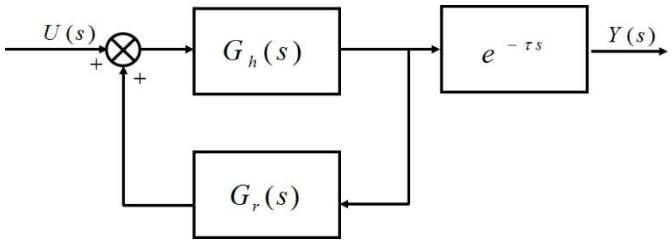

Fig. 3. Thermal process scheme with recycle and time-delay

where G_h is located in the direct path, G_r in the recycle trajectory and the delay τ generated in the measurement of the process. Moreover, $U(s)$ and $Y(s)$ are the input and output of the process respectively. Hence, the transfer function in open-loop is described as follows:

$$G(s) = \frac{G_h}{1 - G_h G_r} e^{-\tau s}. \quad (4)$$

In particular, in this work G_h and G_r are described by two first-order systems, whose transfer function is represented as follows:

$$G(s) = \frac{\alpha(s + \beta)}{(s - \gamma)(s + \delta)} e^{-\tau s}. \quad (5)$$

Therefore, in order to generalize and find the sufficient conditions to stabilize and control the kind of processes (4), in this work, a strategy based on a PI-modified control is used, which is modified using the following control action:

$$PI_{+f}: H(s) = k\left(1 + \frac{k_i}{s} + \frac{k_f}{s + \emptyset}\right). \quad (6)$$

Note that for the previous control (6), the closed-loop system will have the following general form:

$$\frac{Y(s)}{R(s)} = \frac{H(s)G(s)e^{-\tau s}}{1 + H(s)G(s)e^{-\tau s}}, \quad (7)$$

where $R(s)$ is the new input reference. It is clear that the exponential term $e^{-\tau s}$ located in the denominator of the transfer function (7) leads to a system with an infinite number of poles and where the closed-loop stability must be carefully analyzed. Besides, from (7), the control strategy proposed in this work produces a transfer function in open-loop $Q(s)$ represented as follows:

$$Q(s) = H(s)G(s)e^{-\tau s} \quad (8)$$

where $G(s)$ and $H(s)$ are given by (5) and (6) respectively.

B. Control Strategy

In order to design a control strategy for the process HFE (3) and **for** the purpose of generalize to systems with delayed recycle given by (5), the following theorem is stated:

Theorem: Consider the delayed recycle system (5). There exists a control PI_{+f} given by (6) such that the corresponding closed-loop system is stable if the following relation is satisfied:

$$\tau < \frac{1}{\gamma} - \frac{1}{\delta} + \sqrt{\frac{1}{\gamma^2} + \frac{1}{\delta^2}} \quad (9)$$

Demonstration: The proof of this result can be obtained by using a frequency domain analysis. Consider that the condition (9) is satisfied. Taking into account the freedom in selecting the parameter $\emptyset$ of the PI_{+f} controller given by (6), it is possible to obtain a cancellation of the zero of the system (5) in open-loop, equaling$\emptyset = \beta$. Therefore, in the frequency domain, the transfer function in the open-loop Q(s) given by (8) is reduced as follows:

$$Q(j\omega) = \frac{(j\omega)^2 + \left(\frac{1}{k_f}\right)j\omega + \left(\frac{k_i}{k_f}\right)}{j\omega(j\omega - \gamma)(j\omega + \delta)} e^{-\tau j\omega} \quad (10)$$

From the Nyquist stability criteria, the system (10) will be stable iff $N + P = 0$, being P the number of poles in the right

half plane 's' and N the number of rotations to the $(-1, 0j)$ point clockwise in the Nyquist diagram. In this case, since P = 1, the system (10) will be stable if and only if $N = -1$, that is, if and only if there exists a rodeo counterclockwise to the point $(-1, j0)$.

Therefore, if the condition (9) is satisfied, it is possible to select gains k_p, k_i and k_f stabilizers such that the Nyquist stability criterion is fulfilled and ensures the existence of a counterclockwise rotation to point (-1, j0) in the Nyquist diagram. This implies that the magnitude expression $M_Q(j\omega)$ must be a decreasing function of ω, and also, the phase expression $\angle Q(j\omega)$ must be an increasing function about $\omega \approx 0$, i.e., that $\angle Q(j\omega) > -\pi$, for frequencies close to zero.

Therefore, if the magnitude and phase conditions are fulfilled, then there exists gains k_p, k_i and k_f such that the system (5) is stable in the closed-loop. Notice that, in order to facilitate the analysis, let us consider $k_i = 0$, then the phase and magnitude expression to (10) are given by:

$$\angle Q(j\omega) = -\left(\pi - arctan\left(\frac{\omega}{\gamma}\right)\right) - \omega\tau + arctan(k_f\omega) - arctan\left(\frac{\omega}{\delta}\right), \quad (11)$$

$$M_{\ll q(j\omega)} = k_p\alpha\sqrt{\frac{1 + {k_f}^2\omega^2}{(\omega^2 + \gamma^2)(\omega^2 + \delta^2)}}. \quad (12)$$

The decreasing property of $M_Q(j\omega)$, it can be assured by considering the following equivalent condition,

$$\frac{d}{d\omega}\left(\frac{{M_Q}^2}{{k_p}^2\alpha^2}\right) < 0 \quad to \quad \omega = 0 \quad (13)$$

That after some computations, it is possible to conclude that the condition (13) is satisfied if the following relationship (14) is fulfille

$$k_f < \sqrt{\frac{1}{\gamma^2} + \frac{1}{\delta^2}}, \quad (14)$$

The increasing property of the phase expression $\angle Q(j\omega)$, it can be assured by considering the following equivalent condition,

$$\frac{d}{d\omega}\angle Q(j\omega) = -\tau + \frac{1}{\gamma} + k_f - \frac{1}{\delta} > 0. \quad to \quad \omega = 0 \quad (15)$$

Therefore, the phase function is increased if

$$\tau < \frac{1}{\gamma} + k_f - \frac{1}{\delta}, \quad (16)$$

where the parameter k_f is selected from (14) and (16), such that

$$\tau - \frac{1}{\gamma} + \frac{1}{\delta} < k_f < \sqrt{\frac{1}{\gamma^2} + \frac{1}{\delta^2}}, \quad (17)$$

In the follows, in order to take into account the integral partk_i, the magnitude and phase expression are the similar when k_i is near to zero. Taking this fact into account, it is possible to follow the principle of continuity argument for k_i, i.e., it is always possible to choose a gain ki small enough such that the magnitude and phase expression are satisfied. Therefore, if the condition

$$\tau < \frac{1}{\gamma} - \frac{1}{\delta} + \sqrt{\frac{1}{\gamma^2} + \frac{1}{\delta^2}}$$

is satisfied, there exists gains k_p, k_i and k_f that stabilize the thermal process HFE by a PI_{+f} controller. In the same way, there exists always gains k_p, k_i and k_f stabilizers for the class of systems given in general terms in (5) using a PI_{+f} controller.

Finally, assuming that condition of Theorem 1 is satisfied. For a sufficient small k_i, there exists gains k_d and k_p that stabilize system (3), which is describe in the general form by (5) by means a PI_{+f} controller. Moreover, k_d satisfied (17) and the range of k_p values is given by

$$k_p(\omega_{c_1}) < k < k_p(\omega_{c_2}),$$

where $\omega_{c_{1,2}}$ are crossover frequencies and $k_p(\omega_{c_{1,2}})$ are given by

$$k_p(\omega_{c_{1,2}}) = \frac{1}{\alpha}\sqrt{\frac{(\omega_c{}^2 + \gamma^2)(\omega_c{}^2 + \delta^2)}{1 + \left(k_f\omega_c - \frac{k_i}{\omega_c}\right)^2}}.$$

with $\omega_{c_{1,2}}$ being the first two phase crossover frequencies solutions of,

$$arctan\left(\frac{\omega_c}{\gamma}\right) - \omega_c\tau + arctan\left(k_f\omega_c - \frac{k_i}{\omega_c}\right) - arctan\left(\frac{\omega_c}{\delta}\right) = 0. \quad (18)$$

IV. CONTROL OF THERMAL PROCESS: TEMPERARUTRE CONTROL

Taking into account the class of the system (5), the parameters of the transfer function which describe the process HFE are given by an unstable pole$\gamma = 0.296$, a stable pole in $\delta = 0.334$, a zero $\beta = 0.014$ and a time-delay of $\tau = 3s$. According to the control strategy proposed in the previous section, the stability condition given in Theorem 1 is satisfied, since $3 < \frac{1}{0.296} - \frac{1}{0.334} + \sqrt{\frac{1}{0.296^2} + \frac{1}{0.334^2}} = 4.89$.

Consequently, the thermal process HFE can be stabilized using the proposed PI_{+f} controller: $H(s) = k\left(1 + \frac{k_i}{s} + \frac{k_f}{s+\emptyset}\right)$.

Following the methodology proposed in Section III, and as a first step, the free pole that provides the control $H(s)$ is located in the same position as the zero β of the HFE process such that $\emptyset = 0.014$. From this cancellation, it is possible to find the range of values for the stabilizing gains k_p, k_i and k_f.

Therefore, according to (17), a stabilizing gain k_f is taking from the range $1.616 < k_f < 4.50$. For thermal process is choose $k_f = 3$. In order to ensure that the condition of magnitude and phase are satisfied, one is chosen a gain, k_i = 0.008.

Finally, in order to find the range of parameter k_p the equation (18) is solved such that the range of stabilizing gain is given by $0.371 < k_p < 0.719$. Choosing k_p =0.04, the transfer function of the proposed control PI_{+f} is

$$PI_{+f}: H(s) = 0.04\left(1 + \frac{0.008}{s} + \frac{3}{s + 0.014}\right) \qquad (19)$$

In order to illustrate the performance of the HFE process with the proposed control strategy, in Figure 3, is show the temperature control in the HFE process when the reference is around of $60^{\circ}C$.

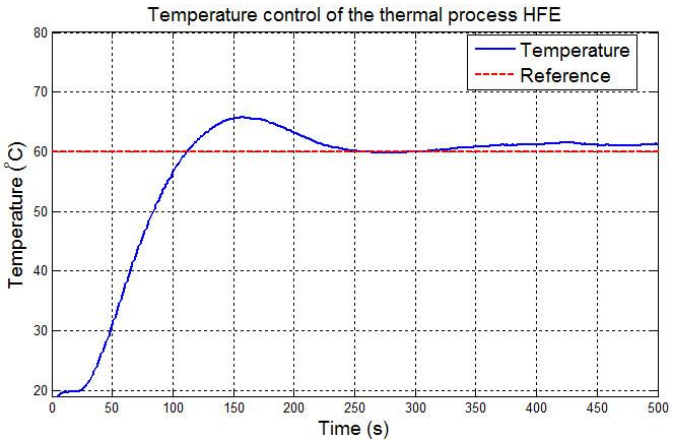

Fig. 4. Temperature control of the thermal process HFE.

In Figure 5 illustrates how the thermic process HFE can achieve the tracking references when it is applied the proposed control PI_{+f}. In this case, the figure show the heat flow path along the fiberglass camera, when the reference is changing from $30^{\circ}C$ to $40^{\circ}C$.

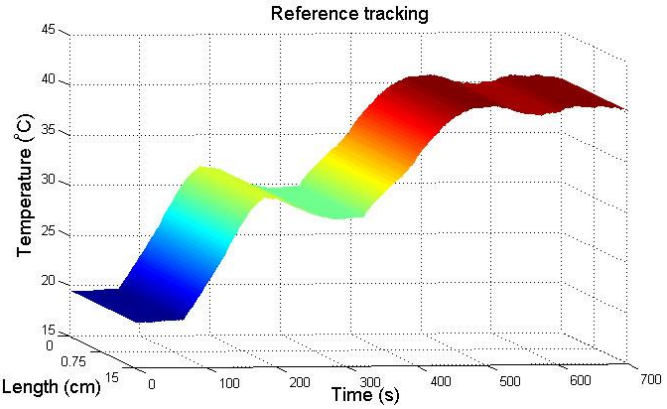

Fig. 5. Temperature control of the thermal process HFE: Reference tracking.

In Fig. 6 is illustrated how the proposed control leads the process to reach a reference of $40^{\circ}C$ at $350s$, in addition we can highlight that the process achieves the disturbance rejection which was introduced at $400s$ approximately. This disturbance was induced when the 60% of the heat flow passage is obstructed in the fiberglass chamber of the QUANSER recycle process. The process returns to the desired reference at $700s$ approximately.

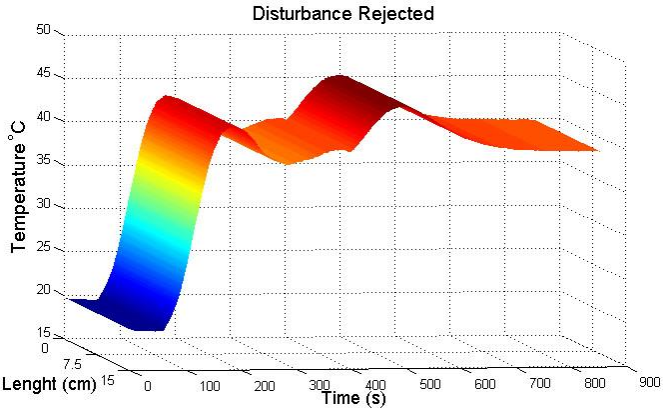

Fig. 6. Temperature control of the thermal process HFE: Disturbance Rejected.

V. CONCLUSION

In this paper, the problem of stabilization and temperature control was addressed in a thermal flow process with recycle and time-delay. The proposed control strategy applied in this work was based on a PI-modified (PI_{+f}). In order to generalize the problem, in this work the proposed solution was addressed to stabilize the unstable second-order system in general form, which are described by one unstable pole, a stable pole, a zero and time-delay. Thus, it was enunciated the

sufficient condition to stabilize this kind of second-order systems. Likewise, it is provided a procedure for determining the ranges of the stabilizing controller parameters k_p, k_i and k_f for the considered controller. Finally this results were applied to a laboratory prototype HFE of the QUANSER brand, obtaining satisfactory experimental results

REFERENCES

[1] Richard J. P. Time-Delay Systems: An Overview of Some Recent Advances and Open Problems. *Automatica*, 2003. *Vol* 39(10), pp. 1667–1694.

[2] Liu T., Zhang W. and Gu D. Analytical design of two-degree-of-freedom control scheme for open-loop unstable processes. *Journal of Process Control, 2005, vol* 15(5), pp. 559-572.

[3] Qing-Chang Z. Robust Control of Time-Delay Systems, Springer, 2006.

[4] Bequette, B.W. Process Control. Modelling, Design and Simulation. Prentice-Hall, 2003.

[5] Murphy G.V., B.J. Evaluation of time delay requirements for a closed-loop stability using classical and modern methods. Twenty first Southeastern Symposium on System Theory, 2002.

[6] Denn M., Lavie R., Dynamics of plants with recycle, Chem. Eng. J, (1982), vol 24, pp.55-59.

[7] Scali, C.; Ferrari, F. "Performance of control systems based on recycle compensators in integrated plants." J. Process Control, 1999, vol 9, pp. 425-437.

[8] B. del Muro, M. Velasco, H. Puebla y J. Álvarez "*Model Approximation for Dead-Time Recycling Systems*" Ind. Eng. Chem. Res, 2005, vol. 44, pp. 4336-4343.

[9] Luyben, W.L., Sonowball effects in reactor / separator processes with recycle, Industrial and Engineering Chemistry, 1994, vol 33, pp. 299-305.

[10] Luyben, W. L., Dynamics and control of recycle systems. Simple open-loop and closed-loop systems, Industrial Engineering Chemical Research, 1993, vol. 32, pp. 466-475.

Modelling the effects of Si-X (X=F, Cl) bonds on the chemical and electronic properties of Si-surface terminated porous 3C-SiC

M. Calvino, A. Trejo, E. Carvajal and M. Cruz-Irisson
Instituto Politécnico Nacional
ESIME Culhuacan
Mexico City, Mexico
irisson@ipn.mx

M. C. Crisóstomo and M. I. Iturríos
Instituto Politécnico Nacional
CECyT No. 8 Narciso Bassols
Mexico City, Mexico

***Abstract*—A study of the effects of different passivation agents on the structure and electronic properties of porous silicon carbide by means of density functional theory and the supercell technique was developed. The porous structures were modeled by removing columns of atoms of an otherwise perfect SiC crystal in the [001] direction, so that the porous structure exhibits a surface exclusively composed of Si atoms (Si-rich) using different surface passivation agents, such as hydrogen (H), fluoride (F) and chloride (Cl). The results demonstrate that all of the passivation schemes exhibit an irregular band gap energy evolution due to a hybridization change of the surface. The structural analysis shows a great dependence of the bond characteristics on the electronegativity of the bonded atoms, all of the structural and electronic changes could be explained due to steric effects. These results could be important in the characterization of pSiC because they provide insight into the most stable surface configurations and their electronic structures.**

Keywords— porous silicon carbide; DFT; surface passivation; electronic band structure; density of states.

I. INTRODUCTION

In recent years the need for the development of alternative energy solutions has issued an increasing interest in the investigation of new materials for devices such as solar and fuel cells. One of the most attractive alternatives to enhance the performance of solar cells are the nanomaterials, specially the nanoporous materials which can be used as a backside reflector, or for an overall better performance [1,2], furthermore, one of the main concerns of the renewable energy sources is the performance of storage devices such as batteries and super capacitors which can be also improved using porous materials electrodes [3,4]. On the other hand Silicon carbide (SiC) is a binary compound which has been identified as an alternative semiconductor material for power electronics, because the SiC exhibits some excellent chemical and physical properties, such as their high strength and hardness, low expansion coefficient, chemical and thermal stability at elevated temperatures, good thermal shock resistance and thermal conductivity, high resistance to corrosion, high Young's modulus, ability to withstand high temperatures and mechanical stresses, and wide band gap [5]. In particular, the β-SiC polytype can be synthesized in a variety of nanostructures, such as nanoporous which is especially interesting since this kind of nanostructure provides a large highly reactive internal surface area, leading to its potential application as a fast response hydrogen sensing material [6] which would be fundamental for applications where the H is used as an alternative to fossil fuels. For these applications, it is essential to understand the effects of surface modifications on the electronic band structure of porous silicon carbide (pSiC). Other interesting applications of pSiC can be found in the biotechnology field, where pSiC could be used as a membrane in implantable biosensors because it exhibits less protein adhesion than porous silicon [7]. Additionally, pSiC exhibits highly efficient blue-to-violet photoluminescence at room temperature [8], which makes it suitable for optoelectronic applications.

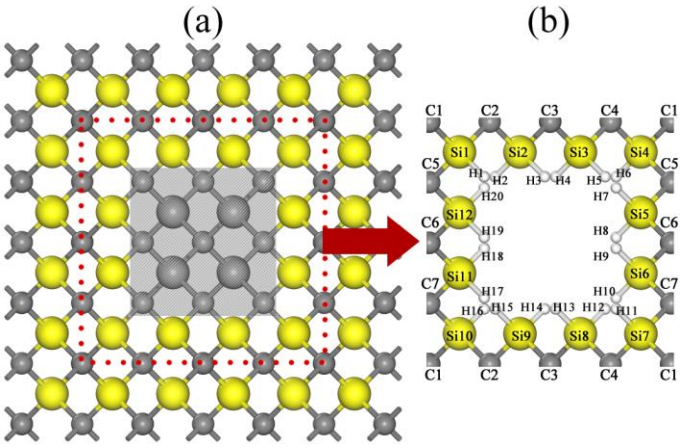

Fig. 1: top view of a) a 32 atom supercell 3C-SiC bulk crystal (dotted line), b) full H passivated Si-rich porous SiC

Motivated by recent theoretical studies and experimental developments on the synthesis and characterization of pSiC [9], we have carried out a study of the effects of different passivation agents on the structure and electronic properties by means of density functional theory (DFT) using the generalized gradient approximation (GGA), based on the pseudopotential plane-wave approach with the supercell technique [10].

The changes of the pSiC electronic states using different surface passivation agents, such as hydrogen (H), fluoride (F), and chloride (Cl) were analyzed.
The results demonstrate that the electronic properties of pSiC are greatly influenced by the surface passivation of the porous structure. The changes of the band gap that arise due to surface pore chemistries leads to the possibility of band gap engineering.

II. Methodology

The nanopores were modeled using the supercell scheme [11], by removing columns of atoms of Si and C in the [001] direction of an otherwise perfect 3C-SiC crystal. To this end, a 32-atom supercell with lattice parameters of A=B=8.6 Å and C=4.3 Å was chosen. Due to the binary nature of SiC, there are multiple surface configurations that the porous structures could give rise. In this work we focus on a pSiC surface composed exclusively composed of Si atoms (Si-phase) at the surface, as shown in Fig. 1. This configuration was chosen to evaluate the viability of this kind of surface since the majority of the experimental evidence suggest that the surface of pSiC is mainly composed of a C-rich phase [12]. This pore morphology was achieved by removing 13 atoms from the supercell as illustrated in Fig. 1.

All surface dangling bonds were passivated with H atoms. To study the effects of different chemical passivation agents on the electronic and structural properties of pSiC, four H atoms were replaced with four F (H+F) and Cl (H+Cl) atoms. In order to evaluate the most probable sites for this atoms to bond to the pSiC surface two positions were chosen for the inclusion of the four F or Cl atoms; one on the center of the pore walls and the second in the corners of the pores, with the main difference being the distance and position of the neighboring H atoms.

The electronic band structure and density of states (DOS) of pSiC were calculated using the first-principles Density Functional Theory scheme based on a generalized gradient approximation with a revised version of the Perdew-Burke-Ernzerhof (RPBE) [13] exchange-correlation functional and norm conserving pseudopotentials [14] as implemented in the CASTEP code [15]. All structures were optimized using the BFGS scheme [16] to obtain their minimum energy configuration, the cutoff energy used was 850 eV, and finally a highly converged set of k points was employed, with grids up to 3×3×5 in size, according to the Monkhorst–Pack scheme [17].

III. Results and Discussion

In Fig. 2 the electronic band structures of pSiC with different chemical passivation schemes; full H, and partially Fluorinated (H+F) and Clorinated (H+Cl) saturations (Fig. 2a-c, respectively) are shown. It can be seen that each of the cases feature a direct band gap, which would enhance the optical activity on this structures. The Full H case has a lower band gap energy compared to that of the H+F and H+Cl passivation. Also it can be observed, that the H+F and H+Cl cases exhibit a similar band gap energy and behavior such as a trap like state near the conduction band minimum. The increased band gap energy of the H+F and H+Cl cases compared to the full H could be attributed to the a charge transfer that occurs on the surfaces of the structures due to the presence of the F and Cl atoms respectively (especially by Si-F and Si-Cl bonds [18, 19]), which in turn enhances the charge transfer between Si and C, thus creating a greater band gap. It is worth noting that especially the H+Cl case has semi-flat states around the maximum valence band energy, which may be due to highly localized orbitals around the Cl and H atoms.

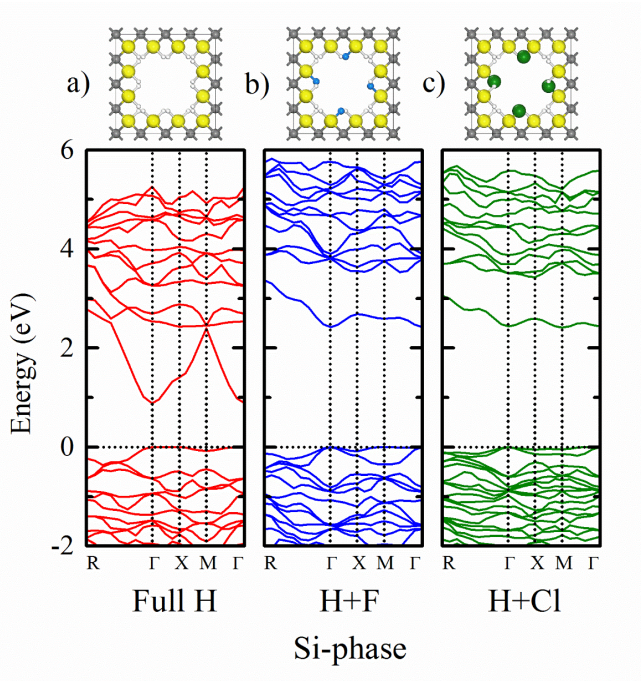

Fig. 2 Electronic band structure of the Si-phase pSiC with a) full H, b) H+F and c) H+Cl passivation at the surface. The respective atomic structure models are shown in the top panel.

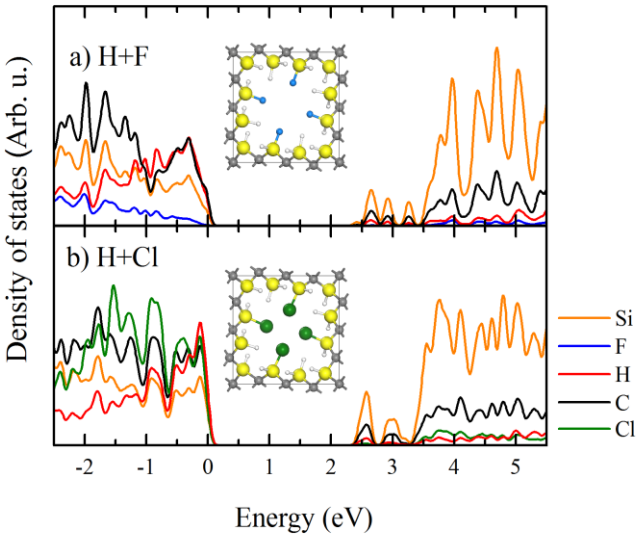

Fig. 3 Atom-resolved densities of states (DOS) for a) H+F and b) H+Cl passivated pSiC. The orange, blue, red, black and green lines represent the DOS of Si, F, H, C and Cl atoms, respectively.

To further the analysis, the electronic structures of the pSiC, we calculated their atom-resolved electronic density of states (DOS). The results for the are shown in Fig. 3. In this figure, the top panel (Fig. 3a) shows the DOS for the H+F case. The low panel (Fig. 3b) represent the DOS for H+Cl case. It is clear that the valence band states in the H+F pSiC are dominated by contributions from the C atoms, while the principal contributor to the conduction band states is Si. This behavior suggests that a donor–acceptor system is operating in the structure, where Si is the electron donor and C is the acceptor of the electrons that fill most of the electronic states of the C atoms in the valence band thus suggesting a highly ionic bond nature. Different behavior is observed for the H+Cl case, in which the main contributors to the valence band are C and Cl atoms and, to a lesser degree, the H atoms. Thus, the donor–acceptor system of the H+F is different from that of the H+Cl pSiC. This difference can be explained since the chloride is more polarizable than fluorine. The bonds of Si-Cl involve considerable covalency - ionicity fluctuations [20]. This may be due to steric effects and the high electronegativity of the Cl atoms, which strongly attract electrons, thus reducing the electronic charge that C can attract from Si.

Fig. 4a,b shows the Highest Occupied Molecular Orbital (HOMO) and Lowest Unoccupied Molecular Orbital (LUMO) orbital isosurfaces of the H+F and H+Cl. For the H+F (Fig. 4a), the HOMO orbital is principally located on a C atom and around of the Si-F and Si-H bonds. The LUMO is located primarily around Si atoms, near to the C atoms and around to the F atoms. For the H+Cl (Fig. 4b) case, a similar behavior is observed, where the HOMO orbital is principally located on a C atoms and around of the Si-Cl and Si-H bonds. The LUMO is located primarily around Si atoms, near to the C atoms and around to the Cl atoms. Both observations are consistent with the information obtained from the DOS analysis in the previous section. It can also be seen that the trap like state observed in the electronic band structure arises from highly localized orbitals around the F and Cl.

Finally, with the previous analysis the general effects of F and Cl have been studied. However due the complexity of the pore surface some interesting effects arise in the pore corners which modify the structure and electronic properties of pSiC. We compared the electronic band structure of the H+F and H+Cl in the corners and wall positions schemes.

In the Fig. 5a for H+F corners case, there is a small crossing of the Fermi level at **k** = **R** = (0.5A, 0.5B, 0.5C) on the last valence band hence creating a metallic state behavior, which might be possibly caused by the formation of H_2 molecules after the geometry optimization, also it can be noted that there was a surface reconstruction at the Si groups in the pore walls creating H-Si-Si-H bonds. Compared to Fig. 5a, the passivation with F in the pore walls presents a large band gap energy which could be attributed to the absence of the surface reconstruction and dangling bonds which are present in the corner passivation, this particular behavior could be caused by steric effects due to the proximity of H and the limited space in the pore corners.

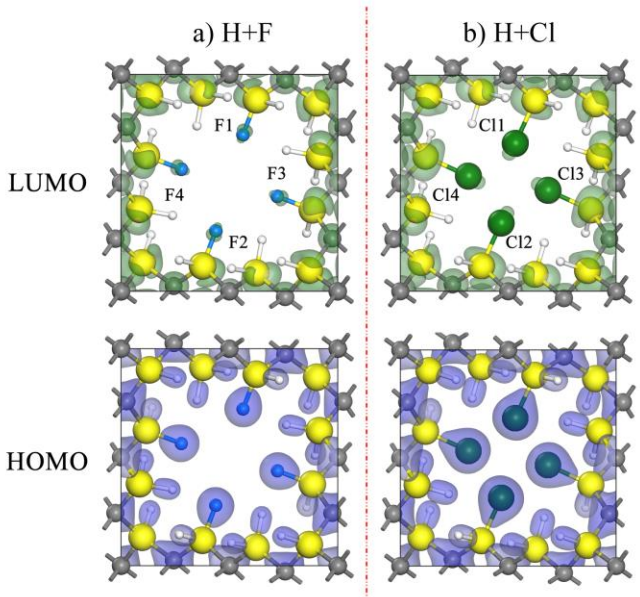

Fig. 4. The HOMO and LUMO orbitals of the a) H+F and b) H+Cl pSiC surfaces with 40.6% porosity are depicted. The blue (lower panels) and green (higher panels) isosurfaces represent the HOMO and LUMO orbitals, respectively with an isovalue of 0.6 for the HOMO surface and 0.18 for the LUMO.

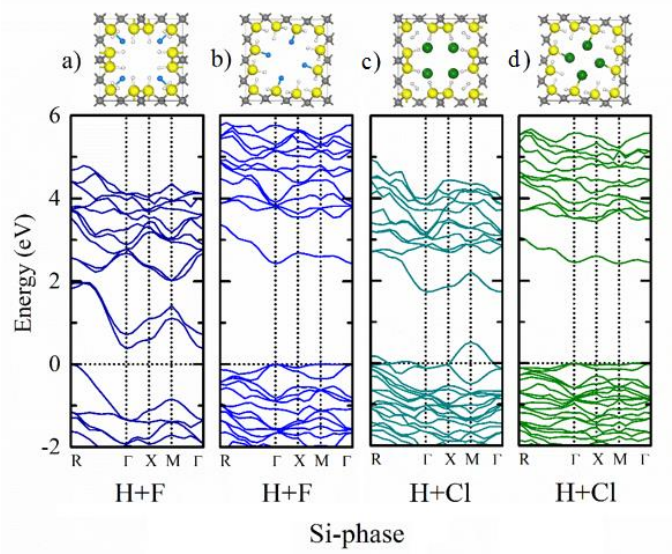

Fig. 5 Electronic band structure of the Si-phase pSiC with a) H+F corners case, b) H+F centers case, c) H+Cl corners case and d) H+Cl wall case passivation at the surface. The respective atomic structure models are shown in the top panel.

Furthermore, in Fig. 5c the band structure of H+Cl corner case shows an accentuated crossing of the Fermi energy compared to Fig. 5a which can be explained by the results of the geometry optimization, where besides the H molecules the Cl atoms are unbounded from the pore surface and concentrate on the pore cavity, this could be explained by the interaction of the Si-Cl generating an inductive effect, distributing a larger positive charge on the Si initially bonded to the Cl, and thus favoring the polarization of the Si-Cl bond and its subsequent departure. This effect produced trap-likes states near the conduction band minimum and the valence band maximum. Cl atoms in the structure are polarized and gain a partial negative charge (as a result of the Si-H bonds), so that in this region a charge repulsion remains, and the steric effects result in the expulsion of all Cl atoms to the pore center positions [21].

Fig. 5d shows the case of H+Cl passivation located in the pore walls, where the chemical environment is the most favorable, since there are no steric repulsions effects involving the Si-Cl bond, the Si atoms gain all the positive charge, the Si bonded to Cl acquire slightly more positive charge since the Si-Cl single bond can be described as having certain ionic character (Si^{+} Cl^{-}) that correspond a the difference in electronegativity between Si and Cl. A Si-Cl bond distance of 2.01 Å has been reported for several molecules, whereas we calculated 2.096 Å. The bond length appears to depend on the difference between the electronegativities of the bonded atoms; the bond is shorter if the difference is large, as is the case for the walled Si–Cl [22] however this distance could be affected by steric effects as seen in Fig. 5c. The highly electronegative Cl generates a high polarity in the Si-Cl bond.

To verify this observations calculations of the Mulliken charges of each atoms were carried out, due to the large quantity of data, the results can be seen on table 1 in appendix A, the guides to the atom labeling are seen in Fig. 1 and Fig 4. In all cases, the Si atoms always maintains a positive charge, in H+F and H+Cl wall cases the Si3, Si6, Si9 and Si12 atoms have the highest positive charge +1.53 and +1.13*e* respectively. The larger positive charge in the H+F case may be due to the nature of the passivating element, because the F is more electronegative than Cl [23].

Analyzing the structures where the surface was passivated at the corners comparing the atoms with either F or Cl bonded, the Si atoms (Si1, Si4, Si7 and Si10) in the H+F passivated pore, the charge increased by + 0.03*e* compared with Si atoms (Si3, Si6 , Si9 and Si12) of the H+F wall case structure. The difference may be that in the corner model each Si atom is surrounded by three C atoms causing a decrease in charge of Si by an inductive effect of these three C attached to Si [24]. The results of the Mulliken charge analysis sustain the observations made at the surface optimization results. The results show that the Si-rich surface could be stable depending the passivation agent in its surface.

IV. Final Remarks

In summary, the electronic properties of porous silicon carbide with a Si-rich surface were studied using the density functional theory scheme. Results show that the electronic properties are highly dependent of the surface passivation of the structure, having the F, and Cl lower energy band gap due to trap like states induced by the high electronegativity of F and Cl which limits the charge transfer between Si, and C. Also it could be observed that the environment around Cl and F could dramatically change the properties of the structure since, when in a proximity of various H atoms, the F and specially Cl become repelled from the structure inducing a surface reconstruction and metallic states within the electronic band structure. These results could be useful to determine the most probable locations for other species other than H in the pore surface, also the orbital analysis suggest that the wall bonds are stable.

Acknowledgments

This work was partially supported by project 252749 from CONACyT and multidisciplinary projects SIP-IPN 2014-1640 y 2014-1641 from Instituto Politécnico Nacional

References

[1] E. Garralaga Rojas, J. Hensen, C. Baur and R. Brendel, “Sintering and reorganization of electrochemically etched mesoporous germanium layers in various atmospheres”, Solar Energy Materials & Solar Cells Vol. 95, pp. 292-295, 2011.

[2] F. Anderson S. Lima, Igor F. Vasconcelos, M. Lira-Cantu, "Electrochemically synthesized mesoporous thin films of ZnO for highly efficient dye sensitized solar cells", Ceram Int, Vol. 41, pp. 9314-9320, 2015.

[3] M. Ge, X. Fang, J. Rong and C Zhou, "Review of porous silicon preparation and its application for lithium-ion battery anodes", Nanotechnology, Vol. 24, pp. 422001, 2013, doi:10.1088/0957-4484/24/42/422001.

[4] Myeongjin Kim, Ilgeun Oh and Jooheon Kim, "Effects of different electrolytes on the electrochemical and dynamic behavior of electric

double layer capacitors based on a porous silicon carbide electrode", In press. Phys. Chem. Chem. Phys.

[5] S.-H. Lee, S.-M. Yun, S. J. Kim, S.-J. Park and Y.-S. Lee, "Characterization of nanoporous β-SiC fiber complex prepared by electrospinning and carbothermal reduction," Research on Chemical Intermediates, vol. 36, no. 6-7, pp. 731-742, 2010.

[6] N. Naderi, M. R. Hashim, K. M. A. Saron and J. Rouhi, "Enhanced optical performance of electrochemically etched porous silicon carbide," Semiconductor Science and Technology, vol. 28, no. 2, pp. 025011, 2013.

[7] K.-S. Kim and G.-S. Chung, "Fast response hydrogen sensors based on palladium and platinum/porous 3C-SiC Schottky diodes," Sensors and Actuators B: Chemical, vol. 160, no. 1, pp. 1232-1236, 2011.

[8] N. Naderi and M. R. Hashim, "Visible-blind ultraviolet photodetectors on porous silicon carbide substrates," Materials Research Bulletin, vol. 48, no. 6, pp. 2406-2408, 2013.

[9] K.-S. Kim and G.-S. Chung, "Characterization of porous cubic silicon carbide deposited with Pd and Pt nanoparticles as a hydrogen sensor," Sensors and Actuators B: Chemical, vol. 157, no. 2, pp. 482-487, 2011.

[10] A. Trejo and M. Cruz-Irisson, "Computational Modeling of the Size Effects on the Optical Vibrational Modes of H-Terminated Ge Nanostructures," Molecules, vol. 18, no. 4, pp. 4776-4785, 2013.

[11] H. Föll, J. Carstensen and S. Frey, "Porous and Nanoporous Semiconductors and Emerging Applications," Journal of Nanomaterials, vol. 2006, pp. 1-10, 2006.

[12] W. Shin, W. Seo, O. Takai and K. Koumoto, "Surface chemistry of porous silicon carbide," Journal of Electronic Materials, vol. 27, no. 4, pp. 304-307, 1998.

[13] B. Hammer, L. B. Hansen and J. K. Nørskov, "Improved adsorption energetics within density-functional theory using revised Perdew-Burke-Ernzerhof functionals," Physical Review B, vol. 59, no. 11, pp. 7413-7421, 1999.

[14] D. R. Hamann, M. Schlüter and C. Chiang, "Norm-Conserving Pseudopotentials," Physical Review Letters, vol. 43, no. 20, pp. 1494-1497, 1979.

[15] S. J. Clark, M. D. Segall, C. J. Pickard, P. J. Hasnip, M. I. J. Probert, K. Refson and M. C. Payne, "First principles methods using CASTEP," Zeitschrift fur Kristallograhie, vol. 220, no. 5-6-2005, pp. 567-570, 2005.

[16] B. G. Pfrommer, M. Côté, S. G. Louie and M. L. Cohen, "Relaxation of Crystals with the Quasi-Newton Method," Journal of Computational Physics, vol. 131, no. 1, pp. 233-240, 1997.

[17] H. J. Monkhorst and J. D. Pack, "Special points for Brillouin-zone integrations," Physical Review B, vol. 13, no. 12, pp. 5188-5192, 1976.

[18] J.A. Tossell, "Quantum Mechanical Studies of Si-O and Si-F Bonds in Molecules and Minerals", Phys Chem Minerals, Vol. 14, pp. 320-326, 1987.

[19] S. Shaik, D. Danovich, B. Silvi, D. L. Lauvergnat and P. C. Hiberty, " Charge-shift bonding—a class of electron-pair bonds that emerges from valence bond theory and is supported by the electron localization function approach", Chem. Eur. J., Vol. 11, pp. 6358–6371, 2005.

[20] J. P. M. Lommerse, A. J. Stone, R. Taylor and F. H. Allen, "The Nature and Geometry of Intermolecular Interactions between Halogens and Oxygen or Nitrogen", J. Am. Chem. Soc. Vol. 118, pp. 3108-3116, 1996.

[21] R. J. Gillespie and E. A. Robinson, "Models of molecular geometry", Chem. Soc. Rev., Vol. 34, pp. 396–407, 2005.

[22] W. Wang, Ning-Bew Wong, W. Zheng and A. Tian, "Theoretical Study on the Blueshifting Halogen Bond", J. Phys. Chem. A., 108, pp. 1799-1805, 2004.

[23] D. Lauvergnat, P. C. Hiberty,D. Danovich and S. Shaik,"Comparison of C-Cl and Si-Cl Bonds. A Valence Bond Study", J. Phys. Chem., Vol. 100, pp. 5715-5720, 1996.

[24] J. B. Lambert and Gen-Tai Wang, “Participation of beta Carbon-Silicon bonds in the development of positive charge in five-membered rings”, J Phys Organic Chem, Vol. 1, pp. 169-178, 1988.

A. Apendix

Table 1. Mulliken charge of each atom of pSiC

H+F passivated (WALL)		***H+F passivated (CORNER)***		***H+Cl passivated (WALL)***		***H+Cl passivated (CORNER)***	
Atom	Charge (*e*)	Atom	Charge (*e*)	Atom	Charge (*e*)	Atom	Charge (*e*)
H1	-0.22	H1	-	H1	-0.2	H1	-
H2	-0.11	H2	-0.05	H2	-0.25	H2	0.03
H3	-0.36	H3	-0.11	H3	-0.32	H3	-0.1
H4	-	H4	-0.11	H4	-	H4	-0.1
H5	-0.29	H5	-0.05	H5	-0.25	H5	0.03
H6	-0.22	H6	-	H6	-0.2	H6	-
H7	-0.11	H7	-0.05	H7	-0.15	H7	0.03
H8	-0.36	H8	-0.11	H8	-0.32	H8	-0.1
H9	-	H9	-0.11	H9	-	H9	-0.1
H10	-0.29	H10	-0.05	H10	-0.25	H10	0.03
H11	-0.22	H11	-	H11	-0.2	H11	-
H12	-0.11	H12	-0.05	H12	-0.15	H12	0.03
H13	-0.36	H13	-0.11	H13	-0.32	H13	-0.1
H14	-	H14	-0.11	H14	-	H14	-0.1
H15	-0.29	H15	-0.05	H15	-0.15	H15	0.03
H16	-0.22	H16	-	H16	-0.2	H16	-
H17	-0.11	H17	-0.05	H17	-0.15	H17	0.03
H18	-0.36	H18	-0.11	H18	-0.32	H18	-0.1
H19	-	H19	-0.11	H19	-	H19	-0.1
H20	-0.29	H20	-0.05	H20	-0.25	H20	0.03
C1	-1.1	C1	-1.09	C1	-1.06	C1	-1.18
C2	-1.14	C2	-1.25	C2	-1.1	C2	-1.13
C3	-1.25	C3	-1.32	C3	-1.17	C3	-1.2
C4	-1.14	C4	-1.25	C4	-1.1	C4	-1.13
C5	-1.14	C5	-1.25	C5	-1.1	C5	-1.13
C6	-1.25	C6	-1.32	C6	-1.17	C6	-1.2
C7	-1.14	C7	-1.25	C7	-1.1	C7	-1.13
F1	-0.63	F1	-0.62	Si1	1.04	Si1	1.07
F2	-0.63	F2	-0.62	Si2	1.07	Si2	0.78
F3	-0.63	F3	-0.62	Si3	1.13	Si3	0.78
F4	-0.63	F4	-0.62	Si4	1.04	Si4	1.07
Si1	1.08	Si1	1.5	Si5	1.07	Si5	0.78
Si2	1.04	Si2	0.82	Si6	1.13	Si6	0.78
Si3	1.53	Si3	0.82	Si7	1.04	Si7	1.07
Si4	1.08	Si4	1.5	Si8	1.07	Si8	0.78
Si5	1.04	Si5	0.82	Si9	1.13	Si9	0.78
Si6	1.53	Si6	0.82	Si10	1.04	Si10	1.07
Si7	1.08	Si7	1.5	Si11	1.07	Si11	0.78
Si8	1.04	Si8	0.82	Si12	1.13	Si12	0.78
Si9	1.53	Si9	0.82	Cl1	-0.36	Cl1	-0.46
Si10	1.08	Si10	1.5	Cl2	-0.36	Cl2	-0.46
Si11	1.04	Si11	0.82	Cl3	-0.36	Cl3	-0.46
Si12	1.53	Si12	0.82	Cl4	-0.36	Cl4	-0.46

Experimental verification of a FPGA sychronization module for a DC energy storage bank of a sustainable electric grid

Francisco E. Rodarte-Gutierrez, Ismael. Araujo-Vargas
Instituto Politécnico Nacional (IPN)
ESIME Culhuacan, Sección de Estudios de Posgrado e Investigación
México D.F., México
e-mail: frodg01@hotmail.com

***Abstract*—The present work describes the FPGA implementation of a PLL synchronization method, based on the rotating frame transformation as a phase detector, together with a Space Vector Modulation (SVM) for a Reduced Matrix Converter (RMC). The use of this implementation technique has two advantages: the reduction of processing time allowing a Master Digital Signal Processor (DSP) execute other tasks, such as internal and external control loops of the power converter, and the parallel operation between control blocks allowing faster calculation and switching action. Simulation and experimental results are shown along the paper to verify the correct operation of the FPGA implementation, showing that the three-phase PLL response is accurate to its ideal design with minimal delay effects.**

Keywords—Matrix Converter; Digital PLL; Space Vector Pulse; Width Modulation; Line Synchronization

I. INTRODUCTION

Energy storage plays an important role in microgrids and Flexible AC Networks (FACTS) when it comes to the efficient distribution and management of energy. Many of these systems contains DC charge storage devices such as batteries, capacitors and more recently supercapacitors (SC) [1]. Such devices requires AC inverters, rectifiers or bidirectional converters to transfer energy from the DC storage device to the AC network, and therefore it is important that the converter must be synchronized with the AC network voltage. Phase Locked Loop (PLL) systems are a typical solution for power converter sincronization, which may be programed in a (DSP), together with the external and internal control loops of the converter. In addition an adequate (DSP) platform capable of containing the program for a Digital Phase Locked Loop (DPLL) together with the external and internal control loops may result very expensive for its commercial application. Space Vector Pulse Width Modulation (SVPWM) is a commonplace technique to obtain a reference rotating frame d-q, where a sine and cosine signals are generated in phase with the line voltage by the aid of the DPLL. A carrier signal is typically used in phase with the line input to generate an equal integer number of pulses which may be aligned for every cycle of the AC line.

In [2] a DPLL was programed on a DSP platform, which share execution time and hardware resources with other processes, as the PWM module is used as the sampling method. The used device should perform all the calculations related to the operation of the power converter each period of time to load values for the next cycle. Several power converters sample their variables at rates in the range of 1 to 100 kHz. The microprocessors capable of perform all the calculations are those with speeds higher than 90 MHz and commonly devices this type are very expensive. The application described in this work is an example, with a sampling frequency of 7.2 kHz, the required response time is in the range at a maximum of a few hundred microsecond

The advantage of the proposed implementation is the use of FPGA, which has already been used in the market, but its applications in control of power converters it is a subject of recent development [3] [4] [5].

The main characteristics of the DPLL presented in this work is an integrated sawtooth or triangular wave carrier generator, which is used by the modulation block to generate the PWM control signals for the switches The advantage of this carrier generator is the precise synchronization between the input line voltages, the carrier together and the switching signal, and generates the reference signals required by the SVPWM technique. In this way the carrier frequency is a multiple of the line frequency, being the cycle divided in a 3 degrees resolution saving calculations and using the same values of the sine-cosine functions instead of calculating new values each time. Also the frequency harmonic components due to switching is also part of the high frequency harmonic content.

This paper presents the implementation of a digital synchronization module in an FPGA based on a typical space vector technique. Together with this module, a space vector pulse width modulator block was constructed, in order to create a single unit that work apart from a digital controller or compensator unit. The principle of operation of the DPLL is described along the paper, which uses SVPWM module as part of the synchronization system. Simulations and experimental results are shown demonstrating its behavior with a practical rig.

II. DPLL AND SVPWM MODULATOR DESCRIPTION

A common scheme for the control of matrix converters is shown in Fig. 1, which is a general scheme where the current control loop (internal loop) and voltage control loop (external loop), are apart from the modulation and the synchronization blocks, The controller receives the angle reference signal from the PLL block, either in the form of a sine- cosine vector or a

ramp function which represents the angle of the three phase power supply. In this fashion the Modulation index signal (M_a) can be used as a control signal for the converter. This method has the advantage of using a signal with a single variable to control the converter.

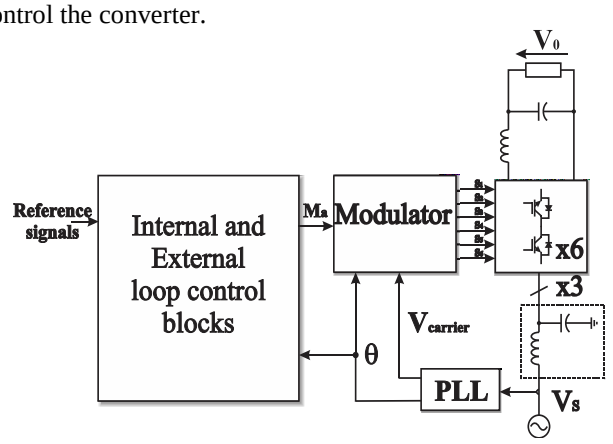

Fig. 1. Schematic of the proposed reduced matrix converter and control its control scheme.

The scheme shown in Fig. 1 is commonly applied to control loops based in space vector, using the Clarke (αβγ) and Park (dq) (rotating frame) transformations. Other control schemes can take advantage from the DPLL presented in this paper [6].

III. Principle of Operation of the DPLL

The principle of operation of the DPLL may be described using the block diagram of Fig. 2, which is based on its analog counterpart and consist of a SV Phase Detector (PD), a loop comparator and a Digital Controlled Quadrature Oscillator (DCQO)

A. SV Phase detector

The SV Phase Detector is a single Clarke-Park transformation, that transform the three-phase supply voltage into a *dq* rotating frame, by using the quadrature unitary vector $[\sin(\theta), \cos(\theta)]$ generated by the DCQO respective to an angular variable θ. This may be expressed with the following equation:

$$\vec{v}_{dq} = \begin{bmatrix} v_d \\ v_q \end{bmatrix} = T_{dq}\, T_{\alpha\beta}\, \vec{v}_s \tag{1}$$

where:

$$T_{\alpha\beta} = \frac{2}{3}\begin{bmatrix} 1 & -\frac{1}{2} & -\frac{1}{2} \\ 0 & \frac{\sqrt{3}}{2} & -\frac{\sqrt{3}}{2} \end{bmatrix}$$

is the Clarke transformation matrix.

$$T_{dq} = \begin{bmatrix} cos(\theta) & sin(\theta) \\ -sin(\theta) & cos(\theta) \end{bmatrix}$$

T_{dq} is the park transformation matrix and $\vec{v}_S = [v_{RN}, v_{SN}, v_{Tn}]^T$ is the supply voltage vector. The PD is shown in the left hand side Fig. 2.

The T_{dq} transform allows to analyze the supply voltage signals either as constant functions, when the DCQO and the supply voltage matches the frequency, or as low frequency function when the DCQO and the supply are slightly different in frequencies. This characteristic may be useful to track the supply frequency and phase by using the DCQO.

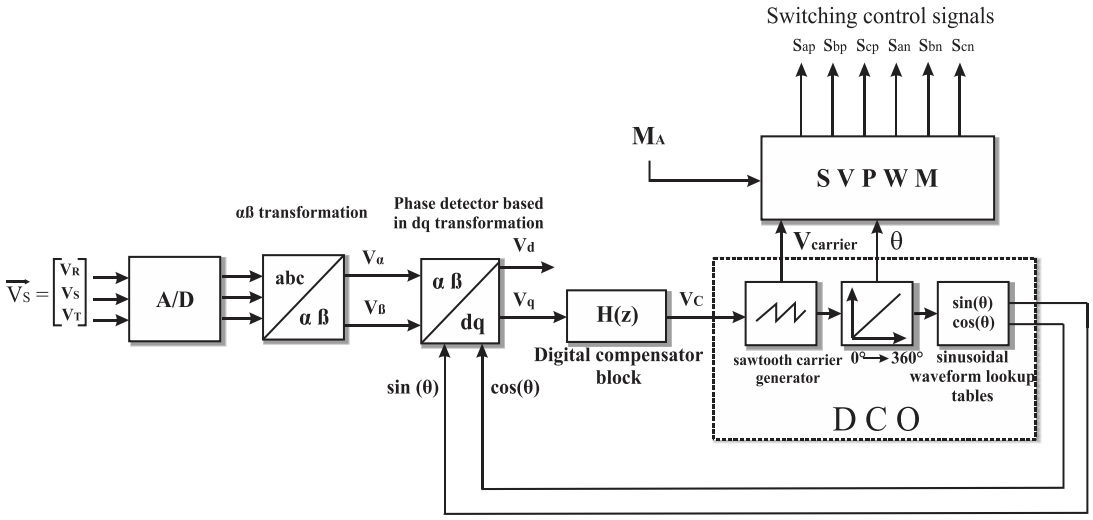

Fig. 2. Block diagram representing the sections of the PLL and modulator implemented on the FPGA.

B. *Digital Controlled Quadrature Oscillator (DCQO)*

The DCO shown in the right hand side of Fig. 2 consist of two incremental counters and a look-up table. The first counter operates as a high frequency sawtooth generator used as the carrier signal for the modulator as shown on the first waveform of Fig. 3(a), which is controlled through the control signal v_c to determine the upper limit of the counter, as shown in the first plot of Fig. 3. The second counter uses the top overflow of the first counter to increment its value and therefore generates, a sawtooth signal, equivalent to θ, shown in the second waveform of Fig. 3(a), which is used to synchronize and calculate the angular position of the supply. The look-up table uses θ to point the required sine and cosine values for the phase detector operation. In this fashion, the DCQO may be adjusted through v_c to produce quadrature sinusoidal, digital signals to be synchronized and phased with the supply, as shown in the third plot of Fig. 3(a)

C. *Phase detector characteristic of the DPLL*

The phase detector characteristic of the DPLL may be derived, by using the Park transformation of the supply voltage $\vec{v}_{\alpha\beta} = [v_\alpha, v_\beta]^T = T_{\alpha\beta}\vec{v}_s = [V_{pk}\cos\theta s, V_{pk}\sin\theta s]^t$, which is plotted on the fourth plot of Fig. 3. In this figure, the above described waveforms are presented in two different conditions: when (a) $f_s = f_o$ and (b) $f_s \neq f_o$. In Fig. 3(a), v_d and v_q become constant signals since the transformation of eq. (1) processes ideal sinusoidal signals of the same frequency and, by using trigonometric identities, v_q may be zero, when the phase between the supply and the DCQO is 0° or ±180°; whereas v_d may be zero when there is a ±90° phase between the supply and the DCQO; otherwise v_d and v_q may have constant values. However, when f_S is slightly different to f_O, the Clarke-Park transformation produces low frequency sinusoidal signals due to the trigonometric identities: $v_d = V_{pk}\, sin(\theta_s - \theta)$ and $v_q = V_{pk}\, cos(\theta_s - \theta)$, where $\theta_e = \theta_s - \theta$ is the phase error between the supply voltage and the DCQO, such that v_d and v_q may be plotted as the waves presented in the last row of Fig. 3(b).

Thereby, the phase detector may be expressed as shown in eq. (2)

$$v_d = V_s\, sin(\theta_e) \tag{2}$$

which may be linearized when θ_e becomes small: $v_d \cong \delta v_d = K_{PD}\theta_e$ where K_{PD} is the phase detector gain.

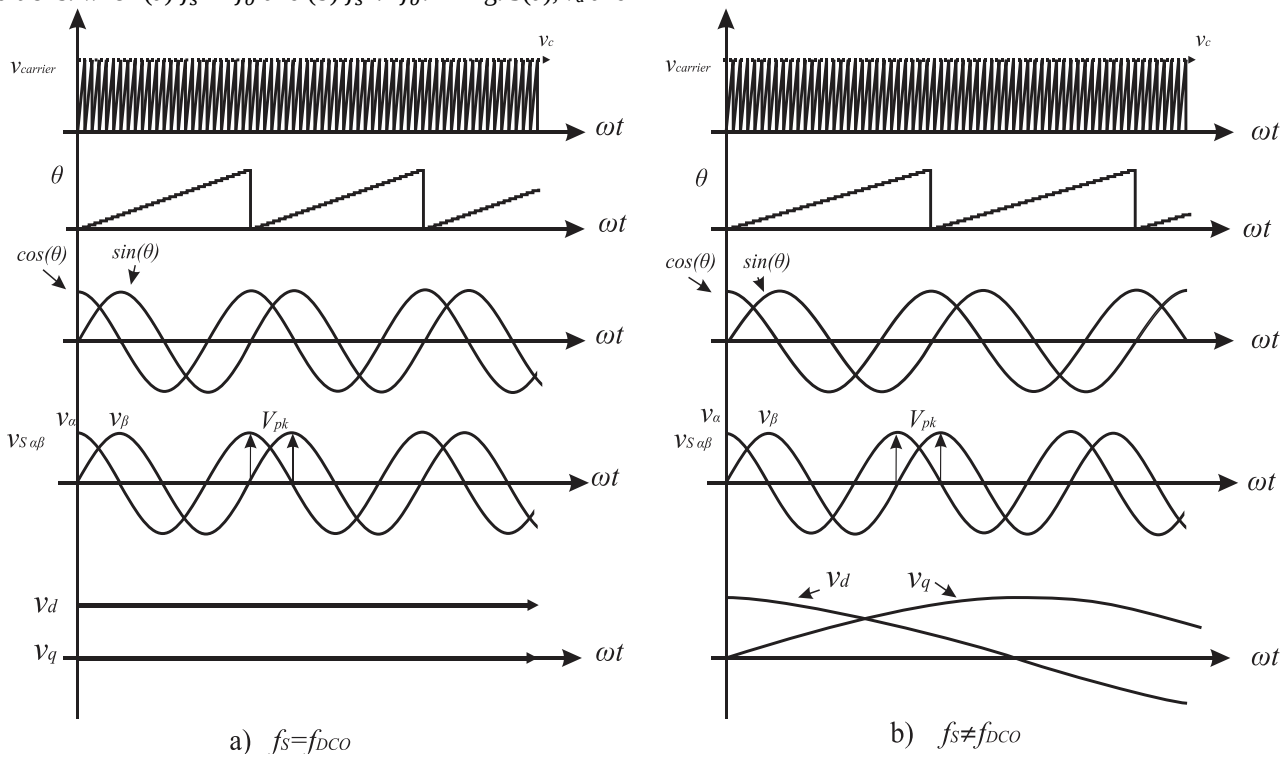

Fig. 3. Ideal waveforms of the digital PLL principle of operation in, (a) supply frequency same as DCO frequency, (b) different frequencies.

D. Loop Compensator

A loop compensator *H(s)* may be used to regulate the tracking of the supply done by the DCQO. This may be calculated by using the linear model of the DPLL shown in Fig. 4. where $H_v(s) = \frac{K_v}{s}$ is the linear model of the DCQO.

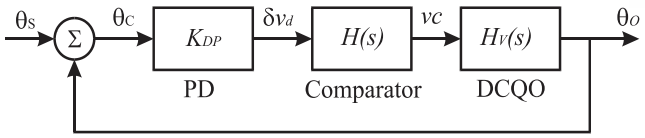

Fig. 4. Linear model of the DPLL

From Fig. 4 the open loop function becomes:

$$H_{Ol}(s) = K_{PD}H_v(s) = \frac{K_{PD}K_v}{s} \quad (3)$$

And the control loop function becomes expressed as:

$$H_{Cl}(s) = \frac{\theta_o(s)}{\theta_e(s)} = \frac{H(s)K_{PD}K_v}{s} \quad (4)$$

where *H(s)* may be designed to produce satisfactory convergence response, such as a critical damped response. The latter may be easily obtained by using the following loop compensator function

$$H(s) = \frac{\left(\frac{s}{\omega_z}+1\right)}{\frac{s}{\omega_i}\left(\frac{s}{\omega_p}+1\right)}$$

with a phase margin near to 62° and a bandwith of $BW = \sqrt{\omega_z\omega_p}$. Since the loop compensator is digitally designed on a FPGA, a bilinear transformation ($s = \frac{2}{T}\frac{z-1}{z+1}$) may be used to obtain a discrete version of *H(s)*, *H(z)*, with a sampling frequency of at least $f_S = \frac{1}{T_S} \geq 40\pi Bw$, such that:

$$H(z) = \frac{V_C(z)}{V_d(z)} = \frac{a_2Z^2+a_1Z+a_0}{b_2Z^2+b_1Z+b_0} \quad (5)$$

which may be discretized as

$$V_c(k) = a_2V_d(k) + a_1V_d(k-1) + a_0V_d(k-2) - \left(b_1V_c(k-1) + b_mV_c(k-2)\right)\frac{1}{b_0} \quad (6)$$

Eq. (6) may be implemented in an FPGA using two short memory queues, as utilized in Infinite Input Response Filters IIR [7], where it is necessary to use memory as a short stack to store the values required by the equation. In [8] a method used to calculate the compensator for this application was described.

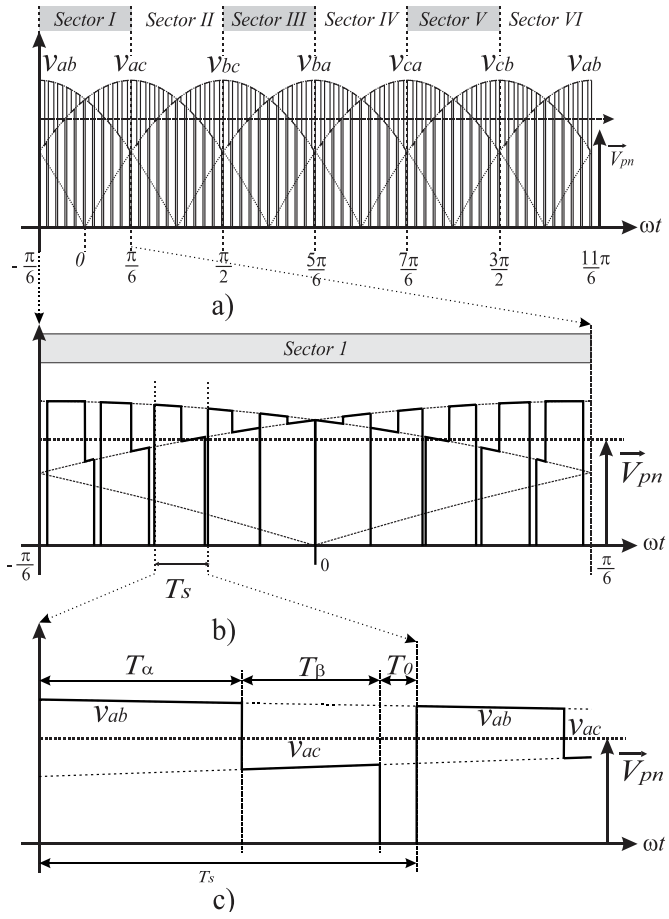

Fig. 5. (a) Source voltages and modulation pattern, with detail of the active times. (b) Time amplification of Sector 1.

IV. Modulation Algorithm

A. Space vector modulation

The operation of the matrix converter of Fig. 1 may be described by using the converter output voltage waveform shown in Fig. 5(a), which may be expressed in terms of the following transformation:

$$v_o = T_R\,\overrightarrow{v_s} \quad (7)$$

where $T_R = [T_{R1}, T_{R2}, T_{R3}]$ and any T_{Ri} may be equal to -1, 0, or 1 such that there are nine combinations for the matrix T_R, being six active vectors and three neutral vectors, These are listed in Table 1

The active vectors uses two active switches of the matrix converter, one top transistor of an inverter leg and one bottom transistor of other inverter leg, such that a line voltage is connected to the converter output; whereas a neutral vector uses again two active switches of the same inverter leg in such a way that a short circuit is produced at the output of the converter. Combinations of more than two active switches causes a short circuit, or even a voltage overshoot, on the AC circuit, which is not allowed for the operation of the circuit. Even more, the switching between the combinations listed in Table 1 may be

done instantaneously, or by using an auxiliary circuit, when the converter is driving an inductive load. These later constraints are important factors for the basic operation of the matrix converter.

TABLE I. ACTIVE AND NEUTRAL VECTORS FOR THE REDUCED MATRIX CONVERTER.

State combination vector						Voltage at output	Current
S_1	S_2	S_3	S_4	S_5	S_6	V_O=T_R V_S	I_O
1	0	0	0	1	0	V_{ab}	I_a=-I_b
1	0	0	0	0	1	-V_{ac}	Ia=-Ic
0	1	0	0	0	1	V_{bc}	Ib=-Ic
0	1	0	1	0	0	-V_{ab}	Ib=-Ia
0	0	1	1	0	0	V_{ca}	Ic=-Ia
0	0	1	0	1	0	-V_{bc}	Ic=-Ib
1	0	0	1	0	0	0	I_a = I_b= I_c = 0
0	1	0	0	1	0	0	I_a = I_b= I_c = 0
0	0	1	0	0	1	0	I_a = I_b= I_c = 0

v_o in Fig. 5 may switch among the adjacent line voltages which are alternating depending on the angular sector as shown in the same figure, either sector I to VI. For example, a time amplification of sector I is shown below Fig. 5(a) in Fig. 5(b), where the line voltages v_{ab} and v_{ac}, are switched together with a neutral combination, that may produce an output voltage average $\overline{V}_o$ depending on the duration of the active and neutral vectors T_α, T_β and T_0 respectively.

When the circuit of Fig. 1 operates as a rectifier, a constant amplitude voltage vector $\vec{v}_{ref}$ may be used as reference which may be generated in the αβ frame with an angle given by θ and a magnitude V_{ref} determined by the control input, This reference may be synchronized with the voltage input $\vec{v}_s$. When the reference is located at a certain sector, the corresponding adjacent vectors may be synthetized to equalize the reference signal $\vec{v}_{ref}$.

In order to achieve a constant DC output the voltage reference $\vec{v}_{ref}$ respective to $\vec{v}_s$ may be expressed for example in sector 1 with the following volt-second balance equation as follows:

$$\overline{v}_o = V_o\angle\theta = \frac{T_\alpha}{T_s}\overline{sv}_{ab} + \frac{T_\beta}{T_s}\overline{sv}_{ac} \tag{8}$$

The maximum amplitude of the output is limited to $Vo = \frac{\sqrt{3}}{2}V_{pk}$ of the source voltage. The active times T_α and T_β may be obtained from the equation representing the active vectors with its complex number representation, for $\overline{sv}_{ab} = V_{pk}\angle\frac{\pi}{6} = V_{pk}\cos\frac{\pi}{6} + j\sin\frac{\pi}{6}$ and $\overline{sv}_{ac} = V_{pk}\angle -\frac{\pi}{6} = V_{pk}\cos\left(-\frac{\pi}{6}\right) + j\sin\left(-\frac{\pi}{6}\right)$ in such a way that the solution is the following:

$$T_\alpha = T_s\ \sin\left(\theta^* + \frac{\pi}{6}\right) \tag{9}$$

$$T_\beta = T_s\ \sin\left(\frac{\pi}{6} - \theta^*\right) \tag{10}$$

where its angular range is $-\frac{\pi}{6} \le \theta^* < \frac{\pi}{6}$. The time for the neutral vector may be obtained from the equation.

$$T_s = T_\alpha + T_\beta + T_0 \tag{11}$$

Equations (9), (10), (11) are indicated to achieve maximum modulation index, if a M_a variable is added to each active time of Eqs (9) and (10), the output amplitude can be controlled, leaving the following expresions:

$$T_\alpha = T_s M_a\ \sin\left(\theta^* + \frac{\pi}{6}\right)$$

$$T_\beta = T_s\ M_a \sin\left(\frac{\pi}{6} - \theta^*\right)$$

with M_a ranging from 0 to 1.

Fig. 6 shows a block diagram of the SVPWM modulator for the reduced matrix converter of Fig. 1. This block diagram depends on the angular signal θ the high frequency carrier v_{saw} which are both supplied from the DPLL, and the modulation index M_a. The SVPWM is divided in the following sections: a sector detection block, which is used by the modulator to indicate the 60° angular range of operation; an active time modulation block used for generating, the periods of time T_α, T_β, T_0 of the active combinations, which use a lock-up table, with the coefficients of duty cycle for each angular location; an interruption generator block that uses T_α, T_β and T_0 for being compared with the carrier and produce interruptions to switch the transistor combination of the converter; and, a control signal generator that selects the transistor state combinations indicated by the interruption generator according to the sector detection block. This last block sends the digital signal to the transistor drivers and thereby, to the power converter.

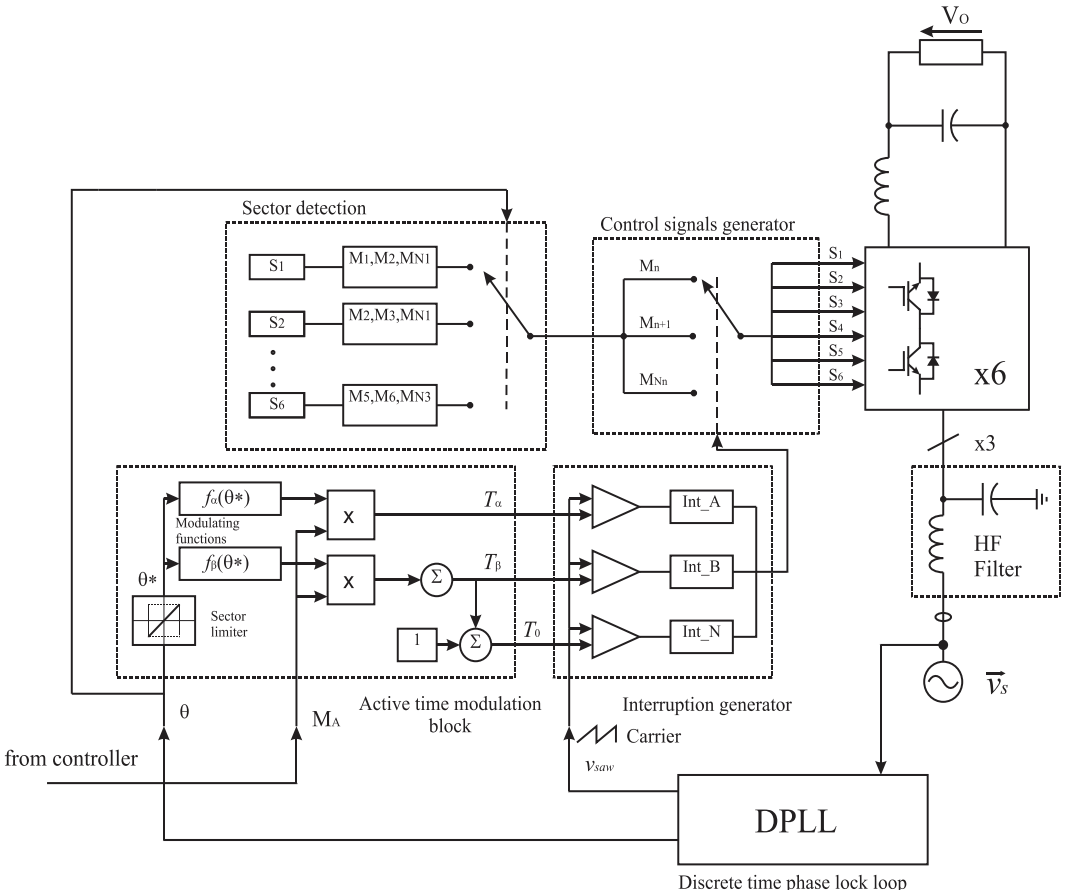

Fig. 6. Space Vector Modulator block diagram for Reduced Matrix Converter.

V. FPGA IMPLEMENTATION

The algorithm described in this article was implemented on the Terasic™ DE0 Nano FPGA development board, the board contains a Cyclone IV EP4CE22F17C6N FPGA device from Altera™, eight 12bit serial A/D converters, a serial EEPROM memory, a SDRAM module, 72 general purpose I/O pins, and an on-board programming circuit. The code was written in VHDL language using the Altera Quartus II analysis and synthesis software [9].

The implementation on the FPGA was made dividing the code in the following modules.

1) An analog digital conversion module (input voltage capture).
2) A Clarke transformation and data word length expansion.
3) A phase detector based on Park transformation.
4) A compensator based on discrete transfer function of Eq (6).
5) A sawtooth waveform generator based on variable limit digital counter.
6) A ramp generator for angle reference.
7) A sine-cosine rotating reference generator based on lookup tables.
8) A Space Vector Pulse Width Modulator.

Since there are not any FPGA that implements embedded analog-digital converters, the external A/D converters were used, in such a way that the analog digital conversion module is mainly the implementation of a communication protocol with the device was used, and set the captured value of each channel on its corresponding register.

The PLL and modulator was constructed in modules represented by the blocks shown in Fig. 2, that exchange signals using registers created inside the device. One important characteristic that made possible the implementation of arithmetic functions in the FPGA were the embedded hardware multiplication blocks, that had been extensively used by the block containing the Clarke and Park transformations, and also by the transfer function equation in the compensator block.

The DCO module was also constructed inside the modulator and control signal generator that was implemented with counters connected in cascade being the sine-cosine values loaded in the FPGA device using a feature to create a ROM memory blocks to permanently store those values that are to be accessed as a vector with two values addressed with the angle register. The SVPWM modulator also used the embedded multiplication block to calculate the required active time of each vector, using arithmetic comparators to switch between vectors.

As depicted Fig. 2, the sawtooth generator, the angle ramp, and the sine cosine reference generator are also part of the overall modulation section. For the Clarke and dq transformation modules, the hardware has to perform only arithmetical operations, such that the multiplication is the most critical function when working with FPGA´s implementations, where special hardware is required for this operation. The FPGA device contains a limited number of embedded multiplier blocks, these are used in diverse digital control blocks and in order to parallelize operation, some of them need to be, leaved for further use.

The digital compensator used embedded multipliers and the addition function were implemented in the regular FPGA logic gates in such a way that a sequential calculation process was performed to optimize hardware usage.

A. Design parameters

The design parameters used for the proper operation of the implementation are listed in Table II:

TABLE II. DESIGN PARAMETERS OF THE DIGITAL IMPLEMENTATION

Parameter	Value	Unit
Line frequency	60	[Hz]
Switching frequency	7.2	[kHz]
PWM cycles resolution per Sector	20	
PWM count resolution at 60 Hz	2500	
Minimum lock frequency	37	[Hz]
Maximum lock frequency	350	[Hz]
Clock frequency	18	[MHz]

VI. EXPERIMENTAL RESULTS.

The experimental setup to verify the code programed in the FPGA development board, used a series of signal conditioning cards matching the ranges with the on board A/D converters. A digital to analog converter was used to observe the different internal variables in order to debug the code and adjust the internal parameters. In addition an extra multiplexer block was created with the purpose of select the desired signals and send it to the D/A converter.

A simulation using the Synopsis™ Saber simulation software was created in order to make a comparison with the experimental results.

The test results of the modulator are shown in Fig. 7, where a comparison is presented between the output signals from the FPGA captured in an oscilloscope, and the signals from the simulation results. In Fig. 7(a) the signals corresponding to the upper switch of each leg are displayed; whereas in the bottom part of the figure the input voltage is shown demonstrating synchrony with the above signals. The pattern of the signals corresponds to a modulation index M_a=1 the group of short duration pulses located at the valley of each signal corresponds to the zero vector sequences of the cycles. The control signals for all the switches in the RMC are presented in fig 7(b) with the same modulation index. In this figure can be observed that the signals of the upper part are not complementary with the signals of the lower part.

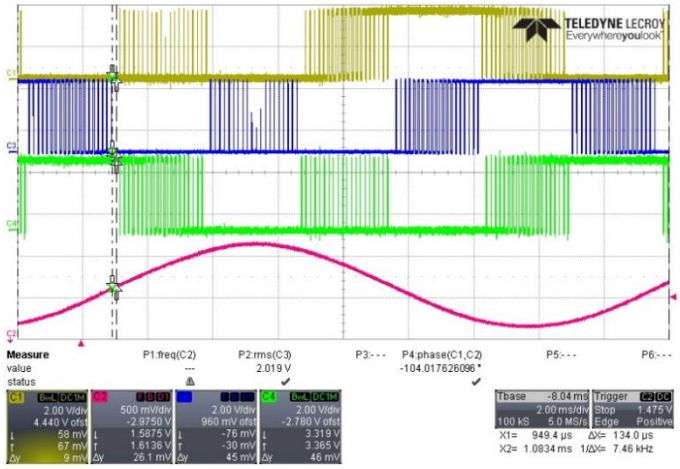

7(a)

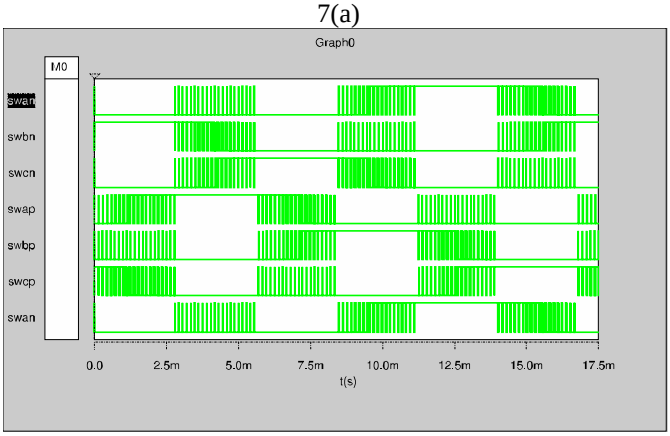

7(b)

Fig. 7. Comparison between the modulation in simulation and waveforms from the FPGA

The test result for the digital PLL of Fig 8(a) and the Simulation results of Fig 8(b) show an accurate correspondence. The test of a 10 Hz step from 60 to 70 Hz is shown in Fig. 8, the compensator was designed to have bandwidth of 10 Hz, giving at the 10Hz frequency step a critically over-damped response.

In other experiments with frequency steps larger than a 30 Hz increment, a no linear response was observed, as a result of the phase detector moving outside the linear approximation range. The output signals from the phase detector and the compensator exhibit strong non-linear characteristics. The experimental range of frequency tracking goes from 38 Hz to 280 Hz, which is far more than the required range of 60±5Hz, as result of the range of the sawtooth counter

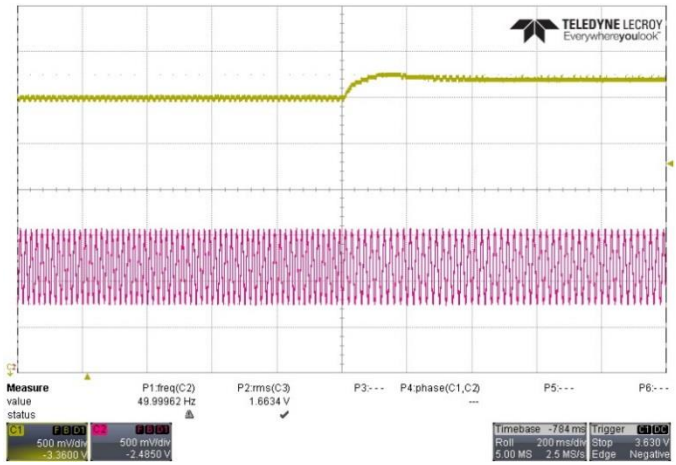

8(a)

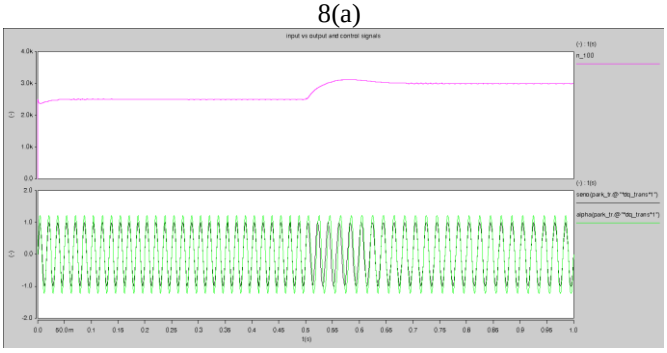

8(b)

Fig. 8. Compensator response to a frequency step from 60 Hz to 50 Hz, experimental vs simulated results.

CONCLUSIONS

This paper presented the application of FPGA technology to perform the functions of a PLL synchronization and SVPWM modulation. The result shown that it was a very effective way to reduce the burden of a microcontroller, and parallelize tasks in the process, by the generation of dedicated hardware. The synchronization method implemented showed an accurate correspondence between simulation and experimental results. Also, a wide range of frequency tracking was observed exceeding the required parameters. The response time was fairly fast stabilizing the system after less than 10 cycles. Some improvements still need to be done in the modulation block as for the code in the compensator, in order to optimize the design.

ACKNOWLEDGMENTS

The authors are grateful to the National Council of Science and Technology (CONACyT) and the National Polytechnic Institute (IPN) of Mexico for their encouragement and the realization of the prototype.

REFERENCES

[1] C. Yonghua, "Super Capacitor Applications for Renewable Energy," in IEEE International Symposium on Industrial Electronics (ISIE), 2011 , Gdansk, 2011.

[2] A. Özdemir and I. Yazici, "Fast and robust software-based digital phase-locked loop for power electronics applications," Generation, Transmission & Distribution, IET, vol. 7, no. 12, pp. 1435 - 1441, 2013.

[3] T. K. Jappe, R. R. Polla and T. B. Soeiro, "An FPGA-based single-phase interleaved boost-type PFC converter employing GaN HEMT devices," in Power Electronics Conference (COBEP), 2013 Brazilian, Gramado, 2013.

[4] M. Curkovic, M. Jezernik and R. Horvat, "FPGA-Based Predictive Sliding Mode Controller of a Three-Phase Inverter," IEEE Transactions on Industrial Electronics, vol. 60, no. 2, pp. 637 - 644, 2012.

[5] C. Yen-Chia, W. Chun-Hsun and . C.-C. Le-Ren, "Implementation of the programmable low power DC-DC voltage converter by FPGA," in Industrial Electronics and Applications, 2008. ICIEA 2008. 3rd IEEE Conference on , Singapore, 2008.

[6] T. A, M. Liserre, R. Teodorescu and F. Blaabjerg, "Synchronization Methods for Three Phase Distributed Power Generation Systems.," in Power Electronics Specialists Conference, 2005. PESC '05. IEEE 36th, Recife, 2005.

[7] L. B. Jackson, J. Kaiser and H. McDonald, "An approach to the implementation of digital filters," IEEE Transactions on Audio and Electroacoustics, vol. 16, no. 3, pp. 413 - 421 , 1968.

[8] K. Cano-Pulido, Técnicas de Modulación de Vector de Espacio y Sincronización para Convertidores Electrónicos De Energía, Mexico City: B.s Thesis, 2013.

[9] Terasic Inc, "DE0-Nano User Manual," 5 December 2012. [Online]. Available: http://www.terasic.com.tw/cgi-bin/page/archive.pl?Language=English&CategoryNo=165&No=593&PartNo=4. [Accessed 27 May 2015].

[10] P. Nielsen, F. Blaabjerg and J. K. Pedersen, "SPACE VECTOR MODULATED MATRIX CONVERTER WITH MINIMIZED NUMBER OF SWITCHINGS," New Delhi, 1996.

[11] C. Klumpner, F. Blaabjerg and I. Boldea, "New Modulation Method for Matrix Converters," IEEE Transaction on Industry Aplications, pp. 797-806, 2006.

[12] M. P. Kazmierkowski, R. Krishnan and F. Blaabjerg, Control in Power Electronics Selected Problems, San Diego, California: Academic Press, 2002.

[13] G. Escobar, S. Pettersson and C. Ho, "Phase-locked loop for grid synchronization under unbalanced operation and harmonic distortion," in IECON 2011 - 37th Annual Conference on IEEE Industrial Electronics Society, Melbourne, 2011.

[14] C. L. Neft and C. D. Schauder, "Theory and design of a 30-hp matrix converter," in Industry Applications Society Annual Meeting, 1992, Pittsburgh, 1992.

[15] R. García-Gil and J. M. Espí, "A bidirectional and isolated three-phase rectifier with soft-switching operation," IEEE Transactions on Industrial Electronics, vol. 52, no. 3, pp. 765-773 , 2005.

[16] A. Garces and M. Molinas, "Reduced matrix converter operated as current source for off-shore wind farms," Ohrid, 2010.

[17] F. Gruson and P. Le Moigne, "A Simple Carrier-Based Modulation for the SVM of the Matrix Converter," IEEE Transactions on Industrial Informatics, vol. 9, no. 2, pp. 947 - 956, 2013.

[18] J. Kolar, "Milestones in Matrix Converter Research," IEEJ Journal of Industry Applications, 2012.

Effective medium model for momentum transport in wind turbines

C.T. Paéz-García and F.J. Valdés-Parada
Depto. de IPH, División de CBI, Universidad Autónoma Metropolitana-Iztapalapa. Av. San Rafael Atlixco 186 col. Vicentina
México D.F., Mexico
iqfv@xanum.uam.mx

Abstract—Currently, there is a need for understanding airflows through large-scale wind turbines. This follows from the need to avoid over-planning of wind farms. Indeed, modern computational capabilities allow simulating momentum transport through wind turbines; however, not all the resulting information is useful. Moreover, high computational costs prevent studying wind farms in their entirety. Motivated from the above, in this work, a macroscopic model that captures the essential microscale momentum transport information is derived using the volume averaging method. In particular, attention is focused on the study of a single high-power wind turbine. The macroscopic model consists of a single equation that predicts the velocity spatial variations (i.e., a one-domain approach) and it is written in terms of position-dependent effective-medium coefficients, which are: the Darcy-Forhheimer coefficient and an inertial coefficient. The results show that with a single effective-medium equation it is possible to describe transport before, through and after the wind turbine. This is verified by comparing the velocity profiles resulting from our model with those arising by conducting direct numerical simulations. The error percent of the model was found to be smaller than 10%. This suggests that the effective medium coefficients are able to capture the essential information of momentum transport through a wind turbine; this motivates the study of more than one wind turbine, which will be performed in a future work.

Keywords — *wind turbines, upscaling, volume averaging, one-domain approach.*

I. Introduction

Demographic growth, along with growing economic expectations have led to an increase of the world energy demand [1], motivating the search for alternative energy sources. Especially, wind energy has had a relevant development both in technological terms but also in electricty production. Nowadays, eolic technological development has been focused on the improvement of airfoils design, as well as to the study of materials that enhance sustentation and resistance [2, 3, 4]. From a theoretical viewpoint, the roots of windfarms planning and design are traced back to the estimates provided by Betz' [5] and Glauert's methodology [6]. Both theories are based upon severly constraining assumptions that seriously limit their reliable applications. This, added to the need to better capture the eolic potential, motivated the derivation of more reliable mathematical models. At the same time, current computational capabilities allow performing direct numerical simulations in order to predict the velocity fields at each point around wind turbines. However, modeling of an entire high-power wind farm is still a computational challenge that can be prohibetly expensive. Furthermore, in general not all the information arising from solving the pointwise mass and momentum governing equations is necessary for onsite decision making and design. Motivated by the above, in this work we derive a predictive macroscale (i.e., at the field scale) model from the governing equations at the microscale (i.e., the continuum scale). The model is derived using the volume averaging method [7] under a one-domain approach formulation [8, 9], with position-dependent effective-medium coefficients. In this way, the macroscopic model should be valid in regions before, through and after a high-power wind turbine.

The paper is organized as follows: in Sections II and III we briefly describe the derivation of the one-domain model. In Section IV we discuss about the computation of the associated effective-medium coefficients and the adequate system size and averaging region dimensions. The validation of the model through direct numerical simulations comparisons is carried out in Section V. Finally, the conclusions are presented in Section VI.

II. Microscopic Model

With the aim of deriving an average model, it is necessary to first consider the total mass and momentum transport at the microscale, these are the continuity and Navier-Stokes equations:

$$\nabla\cdot\mathbf{v}_\beta = 0 \tag{1}$$

$$\underbrace{\rho_\beta \mathbf{v}_\beta\cdot\nabla\mathbf{v}_\beta}_{\text{inertial stress}} = \underbrace{-\nabla p_\beta}_{\text{normal stress}} + \underbrace{\rho_\beta \mathbf{g}}_{\text{volumetric stress}} + \underbrace{\mu_\beta\nabla^2\mathbf{v}_\beta}_{\text{shear stress}} \tag{2}$$

which are subject to the following boundary conditions:

$$\mathbf{v}_\beta = v_{\beta,in}\mathbf{n}_e \qquad \text{at} \quad \mathcal{A}_{\beta e} \tag{3}$$

$$p_\beta \mathbf{n}_s = p_{atm}\mathbf{n}_s \qquad \text{at} \quad \mathcal{A}_{\beta s} \tag{4}$$

$$\mathbf{n}_{AL}\cdot\nabla\mathbf{v}_\beta = 0 \qquad \text{at} \quad \mathcal{A}_{\beta AL} \tag{5}$$

$$\mathbf{n}_{\beta\sigma}\cdot\mathbf{v}_\beta = 0 \qquad \text{at} \quad \mathcal{A}_{\beta\sigma} \tag{6}$$

$$\mathbf{v}_\beta = 0 \qquad \text{at} \quad \mathcal{A}_{\beta p} \tag{7}$$

$$\varsigma_{\beta\sigma}\cdot\mathbf{v}_\beta = v_\omega \qquad \text{at} \quad \mathcal{A}_{\beta\sigma} \tag{8}$$

As shown Fig. 1, equations (3), (4) and (5) represent the boundary conditions at the inlet, outlet and lateral surfaces, respectively. In Eq. (3), $v_{\beta,in}$ denotes the unperturbed system inlet velocity. Equations (6) and (8) refer to the velocity components at the surface of the airfoils in which the normal component is zero and the tangential component is approximated to be the rotation velocity of the blades, v_ω. Since no exogenous losses are considered, it can be assumed that the wind turbine extracts the maximum wind power. According to Betz' theory, the rotation speed of the blades must be 2/3 of the inlet wind velocity. Of course, other wind velocity/rotation speed conditions can be considered. Finally, non-slip boundary conditions are enforced at the ground and at the post of the turbine, as given in Eq. (8). We also show in Fig. 1 the characteristic lengths of the system, with L being associated to the wind tunnel length, l_β is associated to the length of the cross-section of the airfoil and r_0 is associated to the rotation radius of the wind turbine. In the above equations and in the rest of the work, we will use the subscripts β and σ to denote properties associated to the air and solid phases, respectively. Finally, Newtonian, steady and incompressible flow conditions are assumed.

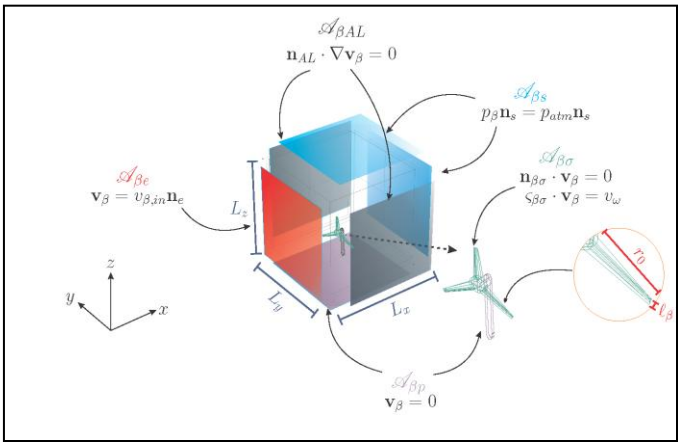

Fig. 1 Sketch of the system including boundary conditions and characteristic lengths.

III. One-Domain Approach

For the sake of brevity in presentation, we list below the main steps of the volume averaging process that leads to the macroscopic model:

1.-An averaging domain that is representative of the system under consideration is defined and applied to the continuity and Navier-Stokes equations. In order to interchange differentiation and integration, the general transport and spatial averaging theorems are used.
2.- Later on, a spatial decomposition of pointwise functions is carried out in order to express the resulting model in terms of average and deviations quantities. At this stage, the model is referred to as the *unclosed model*.
3.- To close the model, an ancillary closure problem is derived and formally solved in terms of the corresponding average sources.
4.- The closure problem solution is substituted into the model derived in Step 2. The resulting closed macroscopic model is written in terms of position-dependent effective-medium coefficients.

The resulting equations from the averaging process described above are:

$$\nabla\cdot\left\langle\mathbf{v}_\beta\right\rangle\Big|_{\mathbf{x}} = 0 \tag{9}$$

$$\underbrace{\rho_\beta\varepsilon_\beta^{-1}\left(\nabla\cdot\left(\varepsilon_\beta\left\langle\mathbf{v}_\beta\right\rangle^\beta\Big|_{\mathbf{x}}\cdot\mathbf{J}\cdot\left\langle\mathbf{v}_\beta\right\rangle^\beta\Big|_{\mathbf{x}}\right)\right)}_{\text{inertial stress}} = \underbrace{-\nabla\left\langle p_\beta\right\rangle^\beta\Big|_{\mathbf{x}}}_{\text{normal stress}} + \underbrace{\rho_\beta\mathbf{g}}_{\text{volumetric stress}}$$
$$+\underbrace{\mu_\beta\nabla^2\left\langle\mathbf{v}_\beta\right\rangle^\beta\Big|_{\mathbf{x}}}_{\text{First Brinkman correction}} + \underbrace{\mu_\beta\varepsilon_\beta^{-1}\nabla\cdot\left(\nabla\varepsilon_\beta\left\langle\mathbf{v}_\beta\right\rangle^\beta\Big|_{\mathbf{x}}\right)}_{\text{Second Brinkman correction}} - \underbrace{\varepsilon_\beta\mu_\beta\mathbf{H}^{-1}\cdot\left\langle\mathbf{v}_\beta\right\rangle^\beta\Big|_{\mathbf{x}}}_{\text{Darcy-Forchheimer term}} \tag{10}$$

Equation (9) is the macroscopic continuity equation and Eq. (10) is the macroscopic version of the Navier-Stokes equation. Both equations resemble their microscale counterparts; however, in the second equation, the last two terms on the right-hand side are a direct consequence of the averaging process. It should be stressed, that the macroscpic model is written in terms of two effective-medium coefficients, namely $\mathbf{H}^{-1}$ and $\mathbf{J}$. Coefficient $\mathbf{J}$ is a fourth-rank tensor that groups microscopic innertial effects and it is defined as:

$$\mathbf{J} = \mathbf{II} + \left\langle\mathbf{M}^T\mathbf{M}\right\rangle^\beta\Big|_{\mathbf{x}} \tag{11}$$

whereas the coefficient $\mathbf{H}^{-1}$, is a second-rank tensor that gathers both inertial and viscous stresses according to:

$$\varepsilon_\beta\mathbf{H}^{-1} = -\frac{1}{V_\beta}\int_{\mathcal{A}_{\beta\sigma}}\mathbf{n}_{\beta\sigma}\cdot\left(-\mathbf{Im}+\nabla\mathbf{M}\right)dA \tag{12}$$

The last two equations are written in terms of the closure variables $\mathbf{m}$ and $\mathbf{M}$, which are resposible of mapping the average velocity onto the spatial deviations of the velocity and pressure. Equations (9) and (10) are the one-domain approach, i.e., they are macroscale equations written in terms of position-dpenedent coefficients that are valid everywhere.

These coefficients are responsible of capturing the essential information of the transport processes that take place at the microscale. It is worth recalling that the macroscopic equation is not exclusive to a particular airfoil design. For this reason, it is safe to state that Eq. (10) is a general momentum transport macroscopic model for wind turbines. It is worth noting that, when the centroid of the averaging domain lies in regions that do not contain the wind turbine, the air volume fraction, ε_β, is equal to the unity and thus the second Brinkman correction vanishes, Furthermore, since no solid phase is involved, the interfacial area is zero, making null the Dary-Forchheimer coefficient, $\mathbf{H}^{-1}$, giving rise to the following expression:

$$\underbrace{\rho_\beta \varepsilon_\beta^{-1}\left(\nabla\cdot\left(\varepsilon_\beta \langle \mathbf{v}_\beta\rangle^\beta\big|_{\mathbf{x}}\cdot\mathbf{J}\cdot\langle \mathbf{v}_\beta\rangle^\beta\big|_{\mathbf{x}}\right)\right)}_{\text{inertial stress}} = \underbrace{-\nabla\left\langle p_\beta\right\rangle^\beta\big|_{\mathbf{x}}}_{\text{normal stress}} + \underbrace{\rho_\beta \mathbf{g}}_{\text{volumetric stress}} + \underbrace{\mu_\beta\nabla^2\left\langle \mathbf{v}_\beta\right\rangle^\beta\big|_{\mathbf{x}}}_{\text{First Brinkman correction}} \tag{13}$$

Furthermore, since there is no solid phase involved, there is no reason for not taking the spatial deviations of the velocity and pressure to be zero. This translates to taking the closure variables **m** and **M** to be null. Under these conditions, the coefficient **J**, reduces to:

$$\mathbf{J} = \mathbf{II} \tag{14}$$

Substitution of this result into Eq. (13), leads to the form of the macroscopic model:

$$\underbrace{\rho_\beta \varepsilon_\beta^{-1}\left(\nabla\cdot\left(\varepsilon_\beta \langle \mathbf{v}_\beta\rangle^\beta\big|_{\mathbf{x}}\langle \mathbf{v}_\beta\rangle^\beta\big|_{\mathbf{x}}\right)\right)}_{\text{inertial stress}} = \underbrace{-\nabla\left\langle p_\beta\right\rangle^\beta\big|_{\mathbf{x}}}_{\text{normal stress}} + \underbrace{\rho_\beta \mathbf{g}}_{\text{volumetric stress}} + \underbrace{\mu_\beta\nabla^2\left\langle \mathbf{v}_\beta\right\rangle^\beta\big|_{\mathbf{x}}}_{\text{First Brinkman correction}} \tag{15}$$

It is worth recalling that the above equation is a simplified version of Eq. (10), that applies to portions of the system where there is no wind turbine present, i.e., in portions of the system that are sufficiently far away (before and after) the wind turbine. In this context, we refer to a *far away* portion of the system in order to localize sections that are unperturbed by the presence of the wind turbine. As a matter of fact, Betz' theory is in agreement with the assumptions adopted in this model. However, the former also neglects the influence of viscous stress, which leads to the Brinkman correction term and to the Darcy-Forchheimer term. If one adopts those assumptions, Eq. (10) takes the form of the well-known Euler equation:

$$\rho_\beta \langle \mathbf{v}_\beta\rangle^\beta\big|_{\mathbf{x}}\cdot\nabla\langle \mathbf{v}_\beta\rangle^\beta\big|_{\mathbf{x}} = -\nabla\langle p_\beta\rangle^\beta + \rho_\beta\mathbf{g} \tag{16}$$

which is quite likely to be the correct model far away from the wind turbine. However, its application is highly questionable around the wind turbine.

The above arguments serve to emphasize the generality that Eq. (10) represents. In addition, in order to use the average model, it is necessary to determine the effective-medium coefficients involved in the model. This is carried out in the following section in an ideal three-dimensional system.

IV. Computation of the Effective-Medium Coefficients

In this section we predict the effective-medium coefficients involved in the macroscopic model. To this end, it is necessary to solve the dimensionless mass and momentum transport equations:

$$\nabla^*\cdot\mathbf{v}_\beta^* = 0 \tag{17}$$

$$\mathrm{Re}\mathbf{v}_\beta^*\cdot\nabla^*\mathbf{v}_\beta^* = -\nabla^* p_\beta^* + \nabla^{*2}\mathbf{v}_\beta^* \tag{18}$$

which are subject to the following dimensionless boundary conditions:

$$\mathbf{v}_\beta^* = \mathbf{n}_\mathbf{e} \quad \text{at} \quad \mathcal{A}_{\beta\mathrm{e}} \tag{19}$$

$$p_\beta^*\mathbf{n}_s = p_{atm}^*\mathbf{n}_s \quad \text{at} \quad \mathcal{A}_{\beta s} \tag{20}$$

$$\mathbf{n}_{AL}\cdot\nabla\mathbf{v}_\beta^* = 0 \quad \text{at} \quad \mathcal{A}_{\beta AL} \tag{21}$$

$$\mathbf{v}_\beta^* = 0 \quad \text{at} \quad \mathcal{A}_{\beta p} \tag{22}$$

$$\varsigma_{\beta\sigma}\cdot\mathbf{v}_\beta^* = v_\omega^* \quad \text{at} \quad \mathcal{A}_{\beta\sigma} \tag{23}$$

here we have taken the inlet velocity and the rotation radius of the turbine as the reference velocity and length, respectively. The dimensionless definitions are:

$$p_\beta^* = \frac{\ell_R p_\beta}{\mu_\beta v_{\beta,in}}; \qquad v_\beta^* = \frac{v_\beta}{v_{\beta,in}};$$
$$\mathrm{Re} = \frac{\rho_\beta \ell_R v_{\beta,in}}{\mu_\beta}; \qquad \nabla^* = \ell_R\nabla \tag{24}$$

In addition, it is necessary to specify the dimensions of other parameters, such as the bridge dimensionless length ℓ_g^*; the dimensionless length of the post h^* and the estimate of the blades width ℓ_a^*. For a typical high-power wind turbine, the rotation radius is l_R = 40 m [11]. In this way, the dimensionless values of the additional parameters of the wind turbine are:

$$h^* = \frac{h}{R} = \frac{100\mathrm{m}}{40\mathrm{m}} = 2.5 \tag{25}$$

$$l_a^* = \frac{\ell_a}{R} = \frac{4\text{m}}{40\text{m}} = 0.1 \quad (26)$$

$$l_g^* = \frac{\ell_g}{R} = \frac{4.5\text{m}}{40\text{m}} = 0.1125 \quad (27)$$

$$R^* = \frac{\ell_R}{R} = 1 \quad (28)$$

To be consistent with the ratio of rotation speed/inlet velocity to be 2/3, we represented the airfoils as a rotating disk as a first approach, since this is consistent with Betz' theory. Under these conditions, the Reynolds number is estimated to be $Re=10^8$.

Before computing the spatial variations of the coefficients $\mathbf{H}^{-1}$ and $\mathbf{J}$, it is necessary to establish the system dimensions L (this is analogous to defining the size of a wind tunnel that does not affect the predictions of momentum transport about the wind turbine) and the dimensions of the averaging region $r_{0,x}$ that captures the effective medium coefficients. After performing an analysis of the influence of the boundary conditions, we found that taking $L_x=60$, $L_y=14$ and $L_z=14$ the results were invariant to the system's dimensions. In Fig. 2, we present an example of the numerical solution of eqs. (17)-(23). Our next step is to define the size and shape of the averaging region. To this end, we evaluate the spatial variations of the effective medium coefficients in different regions that, at least include the boundary layer that is formed around the wind turbine. As a first approach, we propose the averaging region to be a cylinder with either circular or elliptical cross-section as shown in Fig. 3. From the results in Fig. 3 b), it is deduced that the cylinder with elliptical cross-section is more adequate to capture the boundary layer around the turbine. With this choice of the cross-section, it is now necessary to determine the length of the averaging domain. In Fig. 4, we show the predictions of the effective medium coefficients H_{xx}^{*-1} and J_{xxxx}^{*} resulting from taking $r_{0,x}$=4,5,6,10,12,14. In this figure, we observe that, before the wind turbine, the stresses captured by H_{xx}^{*-1} are zero since there is no wind turbine. However, when the averaging region commences to include the wind turbine, the coefficient H_{xx}^{*-1} grows rapidly. As expected, when the averaging region grows, the zone of changes of the effective medium coefficient is also increased.

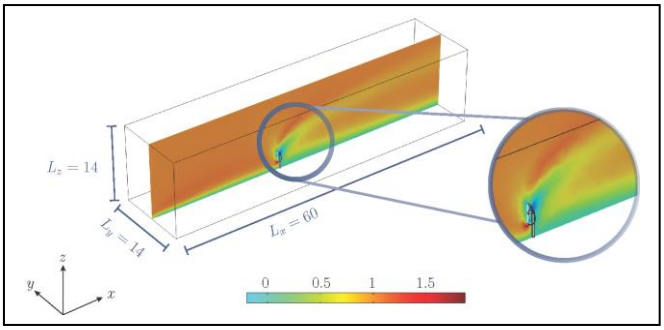

Fig. 2 x-component of the velocity vector $\mathbf{v}_\beta$ for a 3D system with dimensions L_y=14, L_z=14 and L_x=60. The color plume indicates the dimensionless velocity.

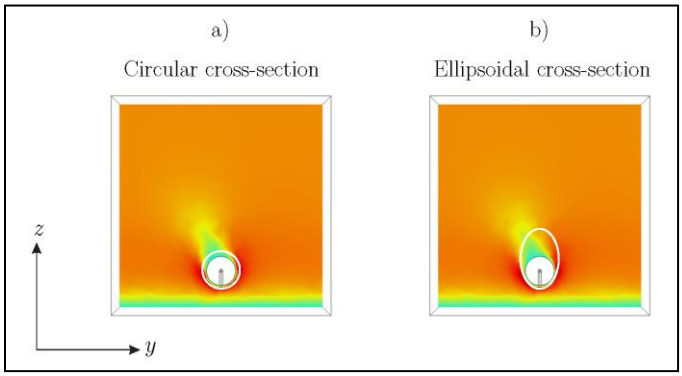

Fig. 3 Proposals for the averaging region cross-section: a) Circular cross-section, b) Ellipsoidal cross-section.

In this way, the changes between curves become insignificant for $r_{0,x}$=12 and $r_{0,x}$=14. To corroborate the above, we perform the following steps:

1. The arithmetic means of each curve H_{xx}^{*-1} are computed, denoting them as $\bar{H}_{xx}^{*-1}$.
2. The means are plotted and statistically fit in order to determine the asymptote.
3. The relative error percent between each value of $\bar{H}_{xx}^{*-1}$ is computed with respect to the asypmtotic value.

In this way, we obtained the results plotted in Fig. 4 b), where we show the relative percent error for the results arising by taking $r_{0,x}$=14, which are below a 10%. Similarly, in Fig. 4 c) we show the spatial variations of the coefficient J_{xxxx}^{*} for each value of $r_{0,x}$ here considered. From this plot, we notice that the minimum value that J_{xxxx}^{*} can acquire is the unity that results for the case in which no wind turbine is included in the averaging region. When this is not the case, the values grow to a value that is 50% larger than its value at the inlet for $r_{0,x}$=4. We observe that, as the length $r_{0,x}$ is increased, the spatial variations of J_{xxxx}^{*} decrease to a value that is only 10% larger than its free-fluid counterpart. In order to determine the adequate value of $r_{0,x}$, we carry out an analysis that is similar to the one performed for H_{xx}^{*-1}, as shown in Fig. 4 d), for values of $r_{0,x}$=12,14 the relative percent error is below the 10% tolerance.

In this way, the functions that describe the spatial variations of the effective-medium coefficients $\mathbf{H}^{-1}$ and $\mathbf{J}$ are presented in tables I and II, respectively. In both cases, the correlation coefficient was found to be larger than 0.99.

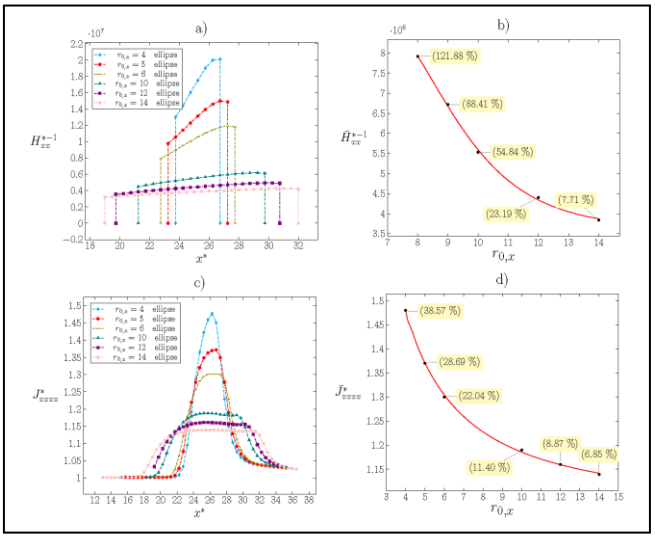

Fig 4. a), b) Spatial variations and error analysis of the coefficient $\mathbf{H}^{-1}$ for lengths of the averaging region $r_{0,x}$= 10.5, 11.5, 12.5, with the wind turbine fixed at x^*=25 c) and d) Spatial variations of the coefficient $\mathbf{J}^*$ and error analysis for $r_{0,x}$=10.5, 11.5, 12.5.

TABLE I Fit function for describing the spatial varitions of the coefficient H_{xx}^{*-1}.

H_{xx}^{*-1}
$f=A+Bx+Cx^2+Dx^3$
A= 1.57361x10^6 B= 474.31198 C= 7380.96835 D= -149.56544

TABLE II Fit function of the coefficient J_{xxxx}^* before, through and after the wind turbine.

J_{xxxx}^*-1		
Before	Through	After
$f_1=A_1e^{\frac{-x}{t_1}}+y_0$	$f_2=A_2+B_2x+C_2x^2+D_2x^3$	$f_3=A_3+B_3x+C_3x^2+D_3x^3$
A_1=6.51464x10^{-13} t_1=-0.7515 y_0=-1.41447x10^{-4}	A_2=-2.61702 B_2=0.30085 C_2=-0.01085 D$_2$=1.29188x10^{-4}	A_3=50.03451 B_3=-4.1037 C_3=0.11227 D$_3$=-0.00102

V. Comparison with Direct Numerical Simulations

Now that we have defined the size of the system, as well as the dimensions of the averaging region and that we have established the function that describes the spatial variations of the effective-medium coefficients $\mathbf{H}^{-1}$ and $\mathbf{J}$, we may proceed to solve the macroscopic model, Eq. (10), which is subject to the following boundary conditions:

$$\langle \mathbf{v}_\beta^* \rangle = \mathbf{n}_e \quad \text{at} \quad \mathcal{A}_{\beta e} \tag{29}$$

$$\langle p_\beta^* \rangle \mathbf{n}_s = p_{atm}^* \mathbf{n}_s \quad \text{at} \quad \mathcal{A}_{\beta s} \tag{30}$$

$$\mathbf{n}_{AL} \cdot \nabla \langle \mathbf{v}_\beta^* \rangle = 0 \quad \text{at} \quad \mathcal{A}_{\beta AL} \tag{31}$$

$$\langle \mathbf{v}_\beta^* \rangle = 0 \quad \text{at} \quad \mathcal{A}_{\beta p} \tag{32}$$

Under this effective-medium formulation, the whole system can be described as a new pseudo-continuum in which it is no longer necessary to draw the wind turbine, since the information it possesses is already captured by the effective-medium coefficients as shown in Figure 5 b). This formulation will be compared with the results from performing direct numerical simulations; an example of this is shown in Fig. 5 a). In this figure, we show the velocity profiles in the *zx* plane. From a qualitative viewpoint, it appears that both approaches are not equivalent. However, the results in Fig. 5 b) correspond to average fields, whereas those in Fig. 5a represent pointwise velocity profiles. In Fig. 6, we compare the average velocity profiles resulting from direct numerical simulations (DNS) and from the average model along with the corresponding relative error percents. As shown in Fig. 6 b), this value is below 10%.

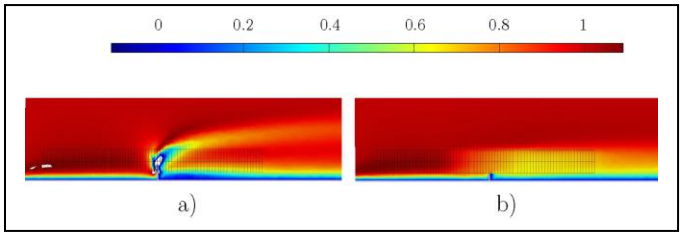

Fig 5 a) Example of the *x*-component of pointwise velocity profile b) *x*-component of the average velocity profile. In both cases, the system dimensions were L_x=60, L_y=14, L_z=14, and the averaging domain was a cylinder of elliptic cross-section with length $r_{0,x}$=14.

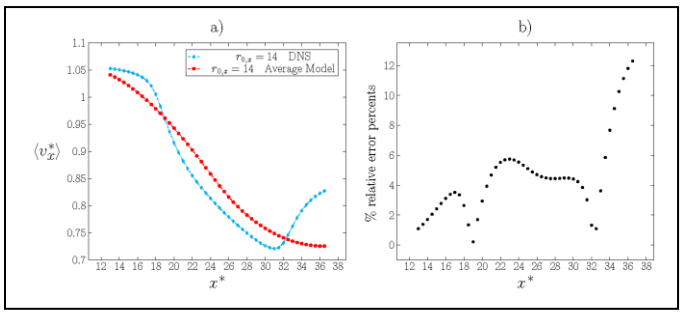

Fig 6 a) Comparison of the velocity profiles obtained using DNS and the average model for the conditions considered in Fig. 5. b) Relative percent error between the results presented in Fig. 6a.

VI. Conclusions

In this work, we derived a macroscopic model for describing momentum transport in a high-power wind turbine. The macroscopic model is written in terms of two effective medium coefficients. One of them encompasses viscous effects produced by the wind turbine and is a direct result of the averaging process. This second-rank tensor, $\mathbf{H}^{-1}$, is known as the Darcy-Forchheimer coefficient. The second effective medium coefficient, **J**, is responsible of capturing the microscopic inertial effects. We carried out a numerical analysis to determine the dimensions of the system that would not influence the computation of these coefficients. In addition, we determined the shape and size of the averaging domain to be a cylinder of elliptic cross-section. Finally, in order to validate the model, we compared the average velocity profiles with those resulting from performing direct numerical simulations, finding that the relative error percent lied below 10%. The results from this work encourage us to carry out more detailed simulations including the real geometry of the wind turbine and to consider several types of flow situations. Nevertheless, the fact that momentum transport can be described by an effective medium model should provide a new way of modeling wind turbines by capturing the essential information from transport at the microscale using effective medium coefficients.

Acknowledgements

CTPG IS GRATEFUL TO THE SCHOLARSHIP PROVIDED BY CONACYT TO CARRY OUT THE MASTER'S DEGREE STUDIES WHERE THIS WORK WAS DEVELOPED.

References

[1] J. Legget, El calentamiento del planeta: Informe de Green peace, FCE, México, 1996.

[2] NASA, Wind Energy, www.nasa.gov; consultada el mes de agosto 2014.

[3] IIE, Energía eólica, www.iie.org.mx; consultada el mes de agosto 2014.

[4] CENER, Análisis y diseño de aeogeneradores, www.cener.com; consultada el mes de agosto 2014.

[5] A. Betz, "Das Maximum der theoretisch möglichen Ausnutzung des Windes durch Windmotoren", Zeitschrift für das gesamte Turbinenwesen, vol. 26, pp. 307-309, 1920.

[6] H. Glauert, "Airplane Propellers", XI Aerodynamic Theory, Springer Verlag, Berlin, 1935.

[7] S. Whitaker, "The Forchheimer equation: A theoretical development", Transport Phenomena in Porous Media, vol. 25, pp. 27-61, 1996.

[8] G. Aguilar-Madera and J. Valdés-Parada and B. Goyeau and A. Ochoa-Tapia, "One-domain approach for heat transfer between a porous medium and a fluid", International Journal of Heat and Mass Transfer, vol. 54, pp. 2089-2099, 2011.

[9] F.J. Valdés-Parada and J. Alvarez-Ramírez and B. Goyeau and J.A. Ochoa-Tapia, "Computation of Jump Coefficients for Momentum Transfer Between a Porous Medium and a Fluid Using a Closed Generalized Transfer Equation", Transport Phenomena in Porous Media, vol. 78, pp. 439-457, 2009.

[10] F.A. Howes and S. Whitaker, "The spatial averaging theorem revisited", Chemical Engineering Science, vol. 40, pp.1387-1392, 1985.

[11] R. Gash and J. Twele, Wind Power Plants: Fundamentals Design and Construction, 2nd ed., Springer, Berlin, 2012.

Evaluation of opportunities for energy efficiency improvement, considering economic and environmental aspects, in a general hospital of Mexico City

Carlos Vázquez Vázquez
Centro Mexicano para la producción más limpia
Instituto Politécnico Nacional
Mexico City, Mexico
carlosvv99@gmail.com

Ignacio García Sánchez
Centro Mexicano para la producción más limpia
Instituto Politécnico Nacional
Mexico City, Mexico
igarcias@ipn.mx

***Abstract*—The General Hospital "Dr. Rubén Leñero" belongs to the public health service network of the government of the Capital City of Mexico. It was founded 1943 and it has 183 beds and several special services. Due to the continuous use and age, the thermal infrastructure of the hospital (boilers and pipelines) does not ensure the right quality of hot water and steam to the final users. That is why, the hospital represented a great opportunity to implement the Energy Efficiency methodology, who was developed by the United Nations Environmental Program (UNEP), and compare new heating technologies, for the Mexican market, as control improvement, heat pumps, fuel cells and Parabolic Trough Solar Collectors; in order to select the best option that have the possibility to reduce greenhouse gases emissions and save public money. Preliminary results indicate that the cost of new technologies can be a limiting factor for its implementation, so it is possible that the thermal efficiency of the hospital is likely to be enhanced by orthodox options, such as changing the pipe´s coating or install smaller boilers near end users.**

Keywords—Hospital, Energy Efficiency, new technologies.

I. INTRODUCTION

The general hospital "Dr. Rubén Leñero" (GHDRL) belongs to the public health service network of the government of the Capital City of Mexico. It was founded in 1943 and it has 183 beds and several special services like: urgencies, general surgery, burned area, among others.

Because of the continuous use, the hospital facilities showed a marked deterioration, especially in the Systems of Generation and Distribution of Steam and Hot Water (SGD-SHW), in some cases the right quality of hot water and steam are not ensure to the final user. The last statement made possible the implementation of the Energy Efficiency methodology (EE) in the in the SGD-SHW.

EE measures are a deliberate effort to minimize the use of energy without sacrificing comfort in homes, industry, or establishments through the application of technology or by behavioral change. Also these measures can reduce costs and release funds for further investment [1]. Similarly, improving EE is the single most effective method of achieving set targets in greenhouse gases emissions and energy cost reductions [2].

For this study, four technologies were selected because they are new among the Mexican market and they have been investigated, in recent years, by other countries with favorable results. These technologies are:

- Control improvement: the use of computer systems and control sensors in boilers and in places where the final users need the steam or the hot water can significantly improve the efficiency of the SGD-SHW.

  The previous mentioned, was demonstrated by Spanish researchers in a hospital, where they implemented a novel control system that obtained 3430 € (3752 USD) per week in savings by decreasing the use of fossil fuels [3].

- Parabolic Trough Solar Collectors (PTSC): parabolic trough solar collectors are a low cost implementation of concentrate solar power technology that focuses incident sunlight onto a tube filled with a heat transfer fluid. The efficiency and cost of the parabolic through collector designs is influenced by structural stiffness, choice materials, assembly tolerances, mirrors cleanliness and wear [4].

  Also, new advances in solar technology have made able to generate heat and electricity with the same equipment. This technology is kwon as Concentrating Photovoltaic Thermal Solar Collectors and in recent years researchers have studied it and model it with satisfactory results in the technic part but not in the economic part [5].

- Fuel cell: this equipment use fuel (liquid or gas) and oxygen to create electricity by an electrochemical process. Furthermore, simulation studies have been proposed the use of fuel cells for generate electricity and heat water in hospitals, one of this studies concluded that the use of fuel cells assure the constant

reduction of greenhouse gases, but the cost of this equipment limits their massive use [6].

- Heat pumps: using the addition of a little amount of energy, a heat pump can transfer heat from outside to inside (during winter) and from inside to outside (during summer). An air conditioner is a heat pump that operates in only one direction [7].

  Also, heat pumps are viewed as a potentially important carbon saving technology and recent surveys made in the United Kingdom show that users of this technology are satisfy with the reliability, heating, hot water, warmth and comfort provided by their systems [8].

Once established the technologies who will be evaluated, it is necessary to say that the main objective of this study is to evaluate and select one of the technologies who excel between the others considering economic, environmental and technical aspects.

II. MATERIALS AND METHODS

This study was based in the EE methodology which is a dynamic and cyclic study formed by 5 main steps:

- Planning and organization: in this step the commitment with the administration must be obtained, involve the employees and organizing the equipment of energy efficiency are other activities that must be realized during this step. Later the researchers have to request or obtain the existent information, identify obstacles and solutions and decide the approach of the EE evaluation.
- Previous evaluation: make a visit to the facilities that are being studied, quantification and characterization of the energy inputs and outputs in order to generate a base line are the actions that have to be done in this step.
- Evaluation: prepare an energy balance which must include energy losses. Eventually, the causes must be diagnosed and options to reduce or eliminate the losses must be proposed.
- Feasibility study: an economic, technical and environmental study must be conducted in order to reduce the options proposed in the previous step and eventually select the best possible option or options.
- Monitoring and implementation: the selected option or options must be implemented with the help of experts (engineers, technicians and managers) and an evaluation program should be started in order to measure the effectivity of the actions. In case to be necessary, adjustments and changes can be applied. This step does not form part of this study, because none of the technologies evaluated has been implemented yet.

A brief description of the E-E methodology is shown below.

Fig. 1. EE methodology.

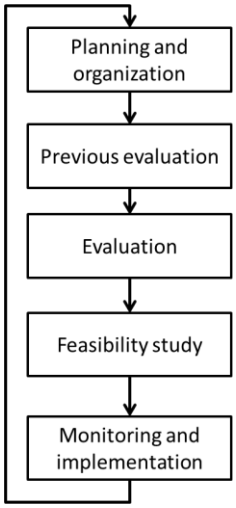

For the feasibility study, the next actions were proposed:

- Technical evaluation: human resources necessary to implement the technology, implementation risk, time required and technological dependence.
- Environmental evaluation: greenhouse gases reduction possibility, toxic wastes generation and noise levels.
- Economic evaluation: economical savings and investment return.

Several tools were used during this study; measuring equipment and software were used to describe the current situation of the SGD-SHW:

- Environmental combustion analyzer ECA-450: this equipment was used to measure the combustion efficiency in the boiler of the hospital; it also measured the concentration of CO and NOx.
- Portable Ultrasonic Measurement System DXN: this equipment was very helpful to measure the input water of the boiler system.
- Software E-3: this software was fed with the length, diameter, schedule and materials of the pipes, which distribute the hot water and steam, in order to predict the heat loses along the hot water and stem path. In case that the measure heat losses were bigger than the predicted by the software, this indicated that something was wrong with the pipelines as damaged coating.

III. RESULTS

This part of the paper is divided in two sections, the first one shows the current situation of the SGD-SHW, the second part involves the results of the feasibility analysis of the new technologies.

A. Current situation

There are two boilers in the engine room of GHDRL, one works daily and the other is off, ready to start when the other one is repaired or when it receive maintenance. The boiler is turned on at 6:00 am and is turned off at 2:30 pm and is

ignited again at 5:00 pm and turned off at 11:00 pm. Three purges are realized during the day.

Part of the generated steam is used in laundry, also is used in autoclaves to disinfect chirurgical material and clothes. Furthermore, the hot water is used in the showers of the workers of the hospital. In both cases, hot water an steam, has to travel a long distance to reach the final users, and is common to have cold water in the showers and bad quality steam (presence of condensate water) in the sterilization room.

Moreover, it was able to obtain the bills of the gas consumption of the hospital of the whole year 2014. The graphics that indicate the consumption and the cost of the gas used by the hospital are shown below.

Graphic. 1. Average boiler gas consumption in the months of the year 2014.

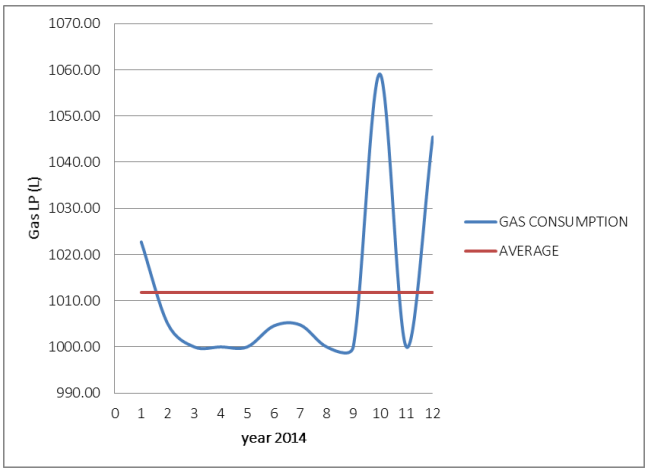

Graphic. 2. Boiler gas bills of the months of year 2014.

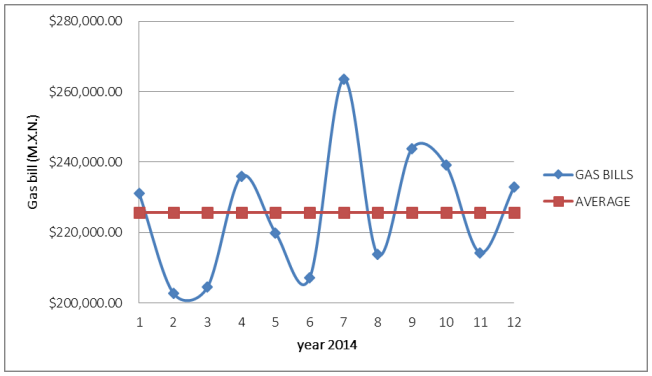

As shown in graphic 1, in year 2014 the gas consumption was very stable. The average consumption of gas in the boiler room reached an amount of 1011.8 liters of gas per day.

The monthly cost of gas is shown in graphic 2 and the same stable situation as graphic 1 is observed. The monthly average cost of gas is $225,732.19 M.X.N. (15,048 USD). The total bill of year 2014 reached $2,708,768.25 (180,584.55 USD).

The measures that have been made to the boilers were the efficiency combustion test. The results are shown in the next table.

TABLE 1. RESULTS OF THE ENERGY EFFICIENCY TEST PERFORMED TO THE BOILERS OF THE HOSPITAL.

Parameter	Value	Unit
O2	2.92	%
CO	46.8	ppm
EFF	84.68	%
CO2	11.86	%
T-CHIM	216.2	%
T-AMB	32.62	°C
EA	14.6	°C
NO	79.8	%
NO2	0.2	ppm
NOX	80	ppm
SO2	0.8	ppm
HC	0.168	%
CO(O)	54.4	ppm
NO(O)	92.2	ppm
NO2(O)	0.4	ppm
NOX(O)	93	ppm
SO2(O)	0.8	ppm
PRESURE	-0.002	mb

The last table shows that the boiler has a good efficiency (that can be improved) and the parameters measured in the exhaust gases of the boiler accomplish the Mexican norms.

B. Feasibility analysis

At this point of the study, the feasibility analysis has not been made, because there are still tests to run, like measure the water flow that goes into the boilers and calculate the amount of steam that the boilers generate. Once the measures, previously mentioned are done, this study can be finished showing which one is the best heating technology for the hospital.

IV. CONCLUSIONS

At this time of the study, final conclusions can´t be written, but some preliminary conclusions are enlisted:

- The quality of the steam and hot water required for the finals users in the hospital is not satisfied by the current heating system.
- Early talks and information provided by suppliers of evaluated technologies show that is possibly that the high cost of this alternatives can be a prohibitive point for their implementation.
- Improve the efficiency of the boilers, change the coat of the pipelines and make minor arrangements, like install

steams traps, can be a feasibility solution to improve the quality of the hot water and steam of the hospital.

- Other alternative can be the use of small boilers near the final users, in order to avoid the long path that the hot water and steam make nowadays.

ACKNOWLEDGMENT

Thanks to all the people involved in this project as well as the directives of the CMP+L.

REFERENCES

[1] Ogenchi G. "Potential economic and social benefits of promoting energy efficiency measures in Nigeria," Energy Efficiency – Springer, 4, pp. 465-472, May 2011

[2] Building Research Energy Conservation Support Unit (BRECSU), "Good Pracice Guide 311: Detecting energy waste-a guide for energy audits and savings in the govermnet state," 2002.

[3] Fraile J. San José J. and González A., "A boiler room in a 600 bed hospital complex: Study, analysis and implementation of energy efficiency improvements," Energies, 7, pp. 3282- 3303, May 2014.

[4] Figueredo S., "Parabolic Trough Solar Collectors: Design for Increasing Efficiency," Massachusetts Institute of Technology, 2011.

[5] Buonomamo A. and Calise F., "Solar heating systems by CPVT and ET solar collector: Anovel transient cimulation model," Applied Energy-Elsevier, 103, pp. 588-606, November 2012.

[6] Bizzarri G. and Luca G., "New technologies for an effective energy retrofits of hospital," Applied Thermal Engineering – Elsevier, 26, pp. 161-169, July 2005.

[7] Harvey H., "Reducing Energy use in the building sector: measures, costs and examples," Energy Efficiency – Springer, 2, pp. 139-163, February 2009.

[8] Caird S., Roy R., and Potter S., "Domestic heat pumps in the UK: user behavior, satisfaction and performance," Energy Efficiency – Springer, 5, pp. 283-301,February 2012.

Quality analysis of biodiesel production from crude avocado (*Persea americana* Mill. Hass, Fuerte and Criollo varieties) oils

Luis Alberto Juárez-Morán
Facultad de Ciencias Fisicomatématicas
Benemérita Universidad Autónoma de Puebla.
Av. San Claudio y 18 Sur. Col. San Manuel, C. U.
Puebla, Puebla. 72570. México.
luisjumo13@hotmail.com

José Alberto Ariza-Ortega
Instituto de Ciencias de la Salud. Área Académica de Nutrición.
Universidad Autónoma del Estado de Hidalgo
Carretera Actopan-Tilcuautla, Ex-Hacienda la Concepción, San Agustín Tlaxiaca. 42086. Hidalgo, México.

Joel Díaz-Reyes
Centro de Investigación en Biotecnología Aplicada
Instituto Politécnico Nacional. Ex–Hacienda de San Juan Molino. Km 1.5 de la Carretera Estatal Santa Inés Tecuexcomac-Tepetitla. Tepetitla, Tlaxcala. 90700. México.

Jorge Indalecio Contreras-Rascón
Universidad de Sonora, División de Ciencias Exactas y Naturales, Col. Centro, Hermosillo, Sonora. 83000. México.

Abstract*—The process of transesterification, also called alcoholysis, is the method most commonly used for the production of biodiesel. Crude oil avocado variety Fuerte was extracted by centrifugation. To the crude avocado oil transesterification was reacted with methanol and two conventional catalyst (KOH and NaOH) for 1 hour at a temperature of 60°C. Room temperature Raman Spectroscopy was used to monitor the process of transesterification. The oil Raman spectrum shows four dominant peaks at 3011, 2930, 2895 and 2851 cm^{-1} attributed to the symmetric stretch =C-H, to the asymmetric bond C-H, to symmetric $-CH_3$ and symmetrical bond $-CH_2$. In particular, two bands were observed in avocado oil located in 1750 and 878 cm^{-1} attributed to C=O bond and C-C, respectively, while in the Raman spectra after transesterification process the first band shift to 1742 cm^{-1} and the second disappears, which confirms the formation of biodiesel.

***Keywords*—Avocado, Oil, Transesterification, Raman**

I. INTRODUCTION

The use of biodiesel from different types of non-food plant resources has increased significantly [1, 2], due to various factors such as instability in the price of oil, is biodegradable, non-toxic, free of sulfur, generating a net reduction of CO_2 emissions up to 79% compared to petrodiesel, among other [3, 4]. The method to produce biodiesel is by transesterification of the oils. In this reaction, the triacylglycerols (as the main components of vegetable oils) react with an alcohol and a catalyst to produce fatty acids methyl esters (FAMEs) and glycerol [5].

An alternative of biodiesel fuel obtaining are avocados, due that these fruits are highly perishable for their nutritional composition and its high moisture content, furthermore, increasing by several factors as physiological deterioration, water loss, mechanical damage, transport, microbiological attack, which as a whole is known as postharvest loss [6]. Due to this, there is a lost around 54% of the crop. This type of avocado [class III (disqualified for eating)] maybe used for biodiesel obtaining.

Mexico is a country with an extensive diversity of avocado fruits, however, Hass variety is the most cultivated, analyzed and marketed in products such as guacamole, pulp and oil, but other varieties such Fuerte and Criollo are also important and its fatty acid content is not well known [7, 8]. Therefore, the aim of this work consists, basically, in the analysis vibrational spectroscopy-Raman of the quality of biodiesel extracted of avocado pulp by centrifugation of the varieties Hass, Fuerte and Criollo.

II. EXPERIMENTAL DETAILS

Samples

Avocado (*Persea americana* Mill *var.* Hass, Fuerte and Criollo) in the stage of commercial ripeness of the State of Puebla, Mexico was used. Three damaged fruits were selected [avocado class III (disqualified for eating)]. After, the fruits were washed and the epicarp and the seed were manually removed.

Commercial ripeness

The commercial ripeness was determined by the maturity index with a brixómetro model Milwaukee MA871. The maturity index calculation was realized by the following equation [9].

$$\text{Madurity index} = \frac{SST}{Acidity} \quad (1)$$

where: TSS: Total soluble solids [10].
Acidity: Is the titratable acidity and was calculated using oleic acid [11].

Oil extraction

For oil extraction was used 100 g of avocado pulp. the pulp was homogenized in a blender (Braun food processor multipractic) during 20 s. the homogenized samples were poured into glass petri plates, until form a thin film, and deposited in an oven memmert (icp-400 model) at 70 ° c for 30 min, until obtain the 10% of the original mass. The dehydrated pulp was deposited in Eppendorf tubes for extracting oil by centrifugation. The centrifugation conditions were realized at 15,557 x gravity (11 000 rpm) at 40°C for 10 min (Eppendorf centrifuge, model 5804 r, Eppendorf ag, Hamburg, Germany).

Physical analysis

Avocado oil is characterized by the following physical analysis: specific weight [12]. The refractive index was obtained by reference oil Brix using a brixometer model Milwaukee MA871 [13]. Each analysis was done in triplicate.

Chemical analysis

Avocado oil was characterized by the following chemical analysis: acidity value [14], peroxide value [15] and saponification [16]. Each analysis was done in triplicate.

Transesterification

The transesterification or alcoholysis of crude avocado oils was realized with methanol (JT Baker 99.90%) at a molar ratio oil: Alcohol 1:6 following the methodology of Meyer [17, 18, 19], mixed with conventional catalysts to 0.90% KOH (Meyer 85.0%) and 0.33% NaOH (Meyer 97.0%) [20], the transesterification reaction was during 1 h at a temperature of 60°C. Each analysis was done in triplicate.

Raman spectroscopy

Raman scattering experiments were performed at room temperature using the 780 nm line at normal incidence for excitation, in a range of 29-3387 cm^{-1}. The light was focused to a diameter of 30.0 μm on the sample. Scattered light was analysed using a micro-Raman System (Thermo Scientific DXR Smart Raman spectrometer), and a grating (400 g/mm). The nominal laser power used in these measurements was 10 mW and scanning 30 times in each sample with an integration time of 5 seconds, the sample was placed in a vial resonance with 500 μL of each sample.

Viscosity of Methyl Esters

The viscosity is the measure of the resistance to the flow of the fuel and can also be used to select the profile of fatty acids in the raw material used for the production of the bio-fuel. The viscosity measured in the laboratory for the biodiesel with the standard ASTM D-445 [21].

Statistical Analysis

Results were expressed as mean value ± SD. Significant differences were evaluated by analysis of variance (ANOVA). A value of α=0.05 was regarded as significant. The software used for these analyses was the MINITAB 17 program.

III. Results and Discussion

Table 1 shows the results of the maturity index of avocado pulps analyzed.

TABLE 1. Maturity index in avocado pulp.

Commercial ripeness	*Variety*		
Maturity index %	*Hass*	*Fuerte*	*Criollo*
	24.3 ± 0.25^a	24.1 ± 0.36^a	24.2 ± 0.40^a

Average of 3 replicates.
Different letters in superscripts in the same row indicate significant differences between treatments ($p<0.05$).

The results shown in Table 1 demonstrate that avocados showed firmness loss, which decreases when moving in the fruit ripening and degradation pulp had color, avocados so these could not be used for food use. An alternative its avocado pulp use is the production of biodiesel

TABLE 2. Physical and chemical parameters of the crude avocado oils

Avocado oil extracted by centrifugation			
Parameters	*Hass**	*Fuerte**	*Creole**
Specific weight ($g\ mL^{-1}$)	0.9165 ± 0.04^a	0.8858 ± 0.005^a	0.9107 ± 0.001^a
Refractive index	1.458 ± 0.25^a	1.469 ± 0.54^a	1.466 ± 0.0002^a
Acidity value (% oleic acid)	0.65 ± 0.145^a	1.03 ± 0.148^a	1.15 ± 0.040^a
Peroxide value ($mEq\ O_2\ kg^{-1}$)	2.4 ± 0.24^a	5.6 ± 0.25^a	6.4 ± 0.23^a
Saponification value ($mg\ KOH\ g^{-1}$)	152.7 ± 0.85^a	163.1 ± 1.58^a	172.5 ± 0.65^a

Average of 3 replicates.
Different letters in superscripts in the same row indicate significant differences between treatments ($p<0.05$).

Table 2 shows the results of the physical and chemical characteristics of the oils obtained from the different types of avocados, which were extracted by centrifugation, properties

are presented no significant difference between them (P> 0.05) Noting that the extracted oils have good quality [22]. Because the results show that any oil can be used to obtain methyl esters, we decided to use avocado oil Fuerte variety. For biodiesel production using avocado seed oil they found an acid index (AI) 5.2 (% oleic acid) and saponification value (SI) of 246 mgKOH/g [17]. For vegetable oil has used an AI = 1.95 mgNaOH/g, SI = 185.13 mg KOH/g [18]. It has been obtained for jatropha oil an AI = 2.23 mgNaOH/g, SI = 193.55 mg KOH/g [23]. The most important parameter for the transesterification is the acid index, a high amount of free fatty acids causes gum formation problems in the transesterification reaction, it is recommended that the percentage of free fatty acids in the oil should be less than 5% [24]. As the purpose of this study was to use avocado oil Class III for biodiesel production, then we can say that the oil extracted by centrifugation avocado Class III presented good chemical properties similar to those reported for the transesterification process.

The Raman spectrum of the avocado oil is shown in Fig. 1, the bands at 3011, 2930, 2895 and 2851 cm^{-1} are attributed to the cis RHC=CHR stretch ν(=C-H), the asymmetric CH_2 stretch, the symmetric CH_3 stretch and the symmetric CH_2, respectively [25,26]. The band at 2723 cm^{-1} is attributed to C-H stretch [26], the band at 1750 cm^{-1} (ester ν(C=O)), 1657 and 1443 cm^{-1} correspond to C=C stretching modes of cis unsaturated fatty acids and to the CH_2 scissoring mode of saturated fatty acids, respectively [27]. The band in the vicinity of 1306 cm^{-1} corresponds to in-phase methylene twisting deformation vibration, whereas the band in 1270 cm^{-1} corresponds to the in-plane =C-H deformation vibration of unconjugated cis double bonds [28].

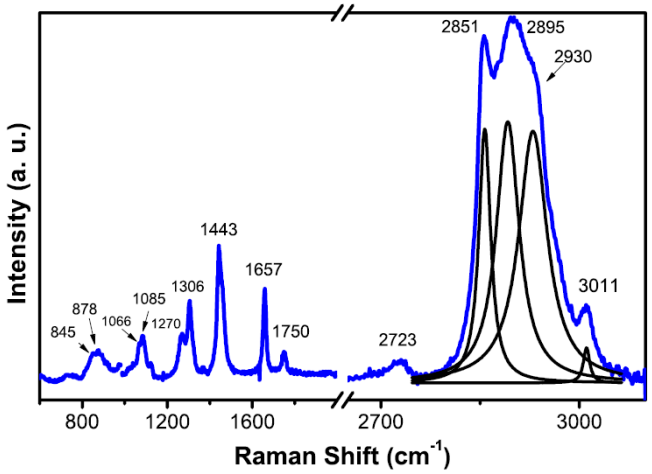

Fig. 1. Raman Spectrum of oil avocado.

Fig. 2 shows Raman spectra of the samples obtained after the transesterification process, comparing them with the Raman spectrum of the oil. There is little significant difference between them, in the region of 1700-1800 cm^{-1} the band at 1750 cm^{-1} is attributed to the ester group carbonyl C=O of triacylglycerol (oil) shifts at 1741 cm^{-1} in the sample that was reacted with KOH and at 1742 cm^{-1} for the sample with NaOH (Fig. 3). This Raman shift should be the change in chain length in the carbonyl group and suggesting the transforming oil to methyl esters [29, 30].

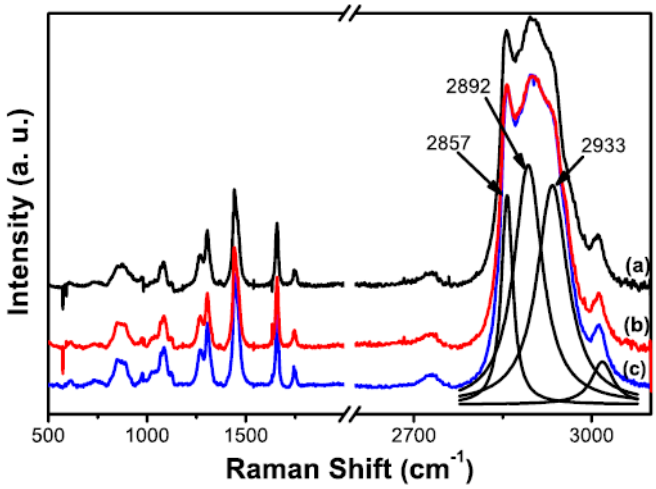

Fig. 2. Raman spectra of the oil (a), the sample with KOH (b) and the sample with NaOH (c).

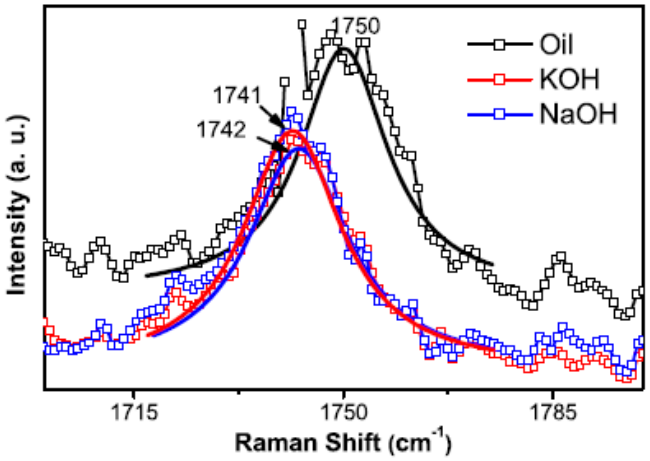

Fig. 3. Raman shift of peak at 1750 cm^{-1} (oil) at 1741 cm^{-1} with KOH and 1742 cm^{-1} NaOH.

The region (700-1200 cm^{-1}), so-called fingerprint, contains bands that are characteristics of C-C skeletal and C-O bond vibrations [28]. In Fig. 4a the bands at 878 and 845 cm^{-1} may be attributed to choline [27, 31] and inositol [27], respectively, Whereas the band at 923 cm^{-1} is attributed to P-OH stretch, ν(C-C) of Pro.ring [32]. In the region 750-960 cm^{-1} bands are observed at 889 cm^{-1} (Fig. 4b) and 890 cm^{-1} (Fig. 4c) attributed to tryptophan [33], the peak at 878 cm^{-1} is no longer observed and another band at 863 cm^{-1} (Fig.s 4b and 4c) (RC = O stretching and CC) is due to ester formation [29].

It has been obtained the glycerine Raman spectrum that resulting after transesterification process, as is shown in Fig. 5 the peak at 1750 cm^{-1} is not appreciated. In Figs 6 and 7 are best appreciated the differences between the three Raman spectra of oil, methyl ester and glycerine. Fig. 6c shows the

vibrational band at 818 cm^{-1} that is assigned to the C-O-C stretching [34] and C-C stretch of peptide backbone [35]. The band at 916 cm^{-1} is attributed to P-OH stretch, ν(C-C) of Pro.ring [32], the vibrational bands at 1085 y 1066 cm^{-1} are attributed to C-O stretching coupled to the C-O group of the carbohydrates and –CH-OH bond, respectively (Figs. 7a and 7b) [36]. The band at 1123 cm^{-1} (Fig. 7a) and 1121 cm^{-1} (Fig. 7b) are attributed to C-OH stretching from C-2 monomers, two bands (1043 and 1116 cm^{-1} (Fig. 7c)) belonged C-OH mode from the C-1 atoms, and C-OH stretching the mode from C-2, respectively [37].

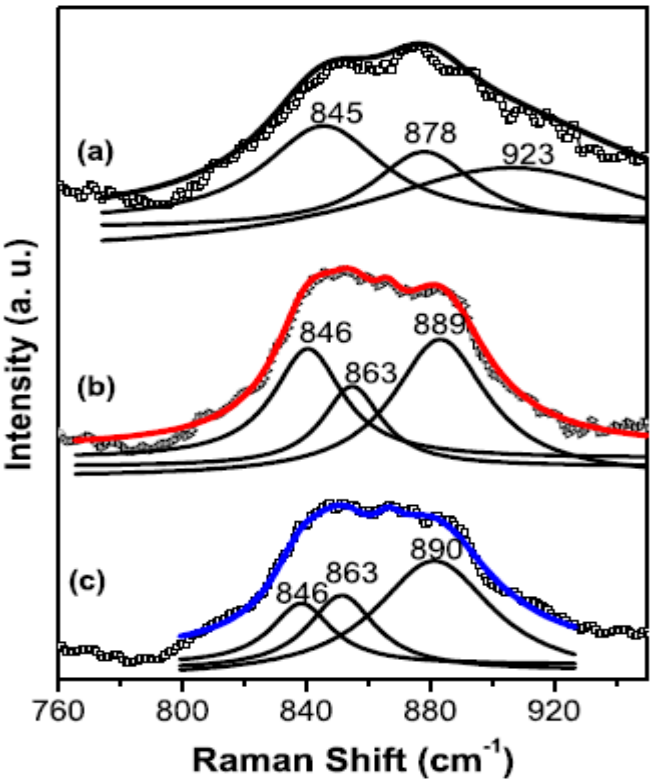

Fig. 4. Raman spectra of oil (a), methyl ester with KOH (b) and methyl ester with NaOH (c).

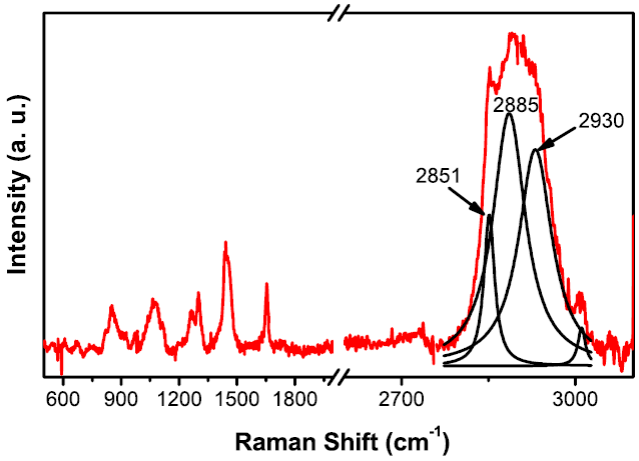

Fig. 5. Raman spectrum of the resulting glycerine after reaction.

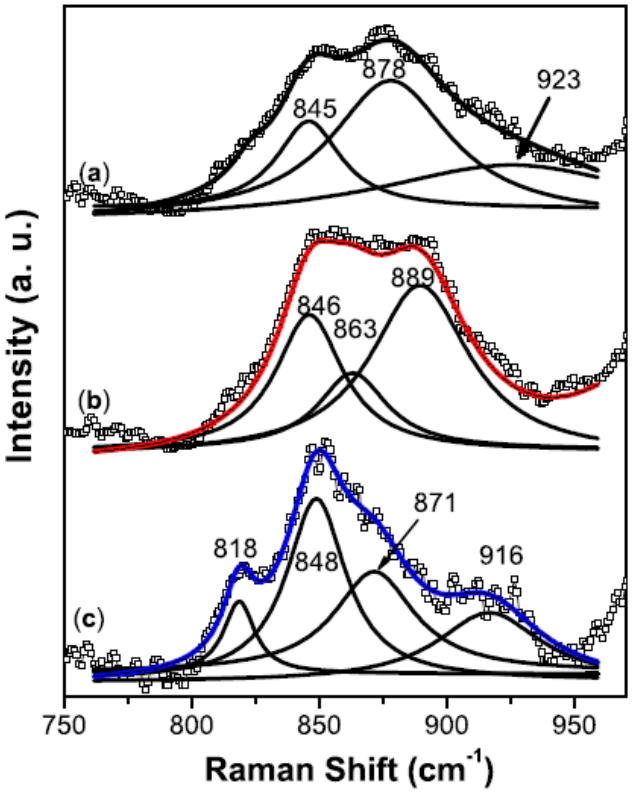

Fig. 6. Raman spectra: (a) Oil, (b) Methyl ester and (c) Glycerine

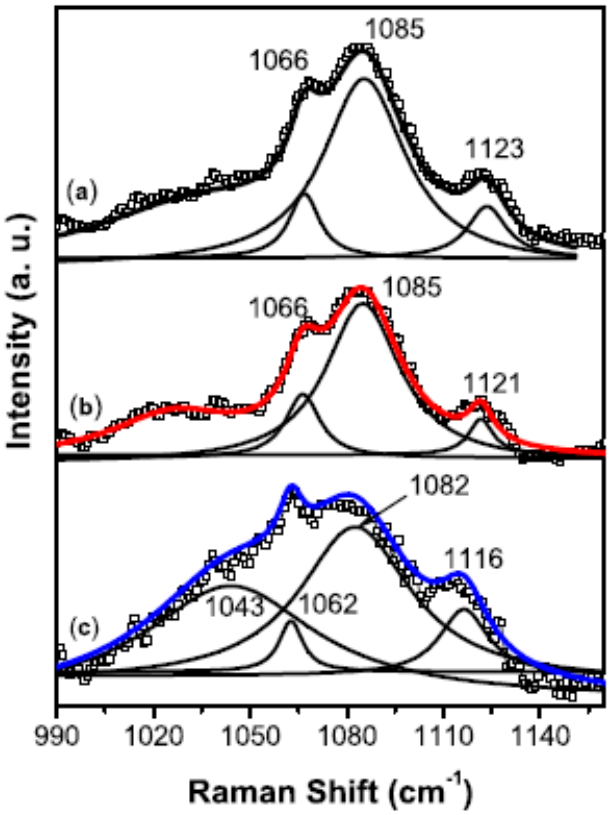

Fig. 7. Raman spectra: Oil (a), Methyl ester (b) and Glycerine (c).

In Table 3 shows the results of the sample viscosities measured in the laboratory at 40°C.

TABLE 3. Sample viscosities

Viscosity sample Methanol-KOH	Viscosity sample Methanol-NaOH	Biodiesel Viscosity ASTM D-445	Petroleum diesel Viscosity
4.88 $mm^2 s^{-1}$	4.69 $mm^2 s^{-1}$	1.9 to 6 $mm^2 s^{-1}$	3 to 12 $mm^2 s^{-1}$

IV. CONCLUSIONS

Transesterification is a viable method for reducing the viscosity of class III avocado oil, which is exploited for use as fuel method. Differences between the oil and the methyl ester by Raman Spectroscopy were identified and obtained viscosity is within the range of the standard. This leads to the conclusion that the transesterification with methanol and KOH and NaOH catalysts produce quality biodiesel avocado oil from class III.

REFERENCES

[1] L. Vega. "Jatropha *curcas l.* Agro-energía," Consultor independiente, México, agro-proyectos y agro-energía, pp. 1-21, 2008.

[2] M. C. Buelvas, "Estado del arte en la producción de biodiesel,". Universidad Nacional de Colombia. Disponible en internet: http://www.unalmed.edu.co, 2007.

[3] J. Hilbert, "Empleo de los biocombustibles en motores diésel," Instituto de Ingeniería Rural, http//www.biodiesel.com.ar, (Verificado en 12/02/2008), 2006.

[4] J. Sheehan, V. Camobreco, J. Duffield, M. Graboski and H. Shapouri, "An Overview of Biodiesel and Petroleum Diesel Life Cycles," http://www.nrel.gov/docs/legosti/fy98/24772.pdf, May 1998.

[5] M. Berrios and R. Skelton, " Comparison of purification methods for biodiesel," Chemical Engineering Journal, vol. 144. pp. 459-65, 2008.

[6] G. Aguilar Gutiérrez, "México desperdicia más de 10 mil toneladas de alimentos al año," http://www.informador.com.mx/mexico/2013/497074/6/mexico-desperdicia-mas-de-10-mil-toneladas-de-alimentos-al-ano.htm, 2013.

[7] M.J. Werman and I. Neeman, "Avocado oil production and chemical characteristics," J. Am. Oil Chem. Soc, vol 64, pp. 229-232, February 1987.

[8] V. Kahn, "Some biochemical properties of polyphenol oxidase from two avocado varieties differing in their browning rates," J. Food Sci., vol 42, pp. 38-43, 1977.

[9] I. M. del Pilar Pinzón, G. Fischer and G. Corredor, "Determinación de los estados de madurez del fruto de la gulupa (Passiflora edulis Sims.)," Agronomía Colombiana, 25(1), pp. 83-95, 2007.

[10] NMX-FF-011, "Productos alimenticios no industrializados, para uso humano. fruta fresca. determinación de acidez titulable. método de titulación," 1982.

[11] NMX-F-103, "Alimentos. frutas y derivados. determinación de grados brix," 1982.

[12] NMX-F-075-SCFI, "Alimentos–aceites y grasas vegetales o animales determinacion de la densidad relativa," 2012.

[13] AOAC, "Refractive Indices of Sucrose Solutions at 20 Degrees C. International Scale," 1936, as presented in the 10th Edition of the Methods of Analysis of the Association of Agricultural. File Code 135-A-50, January 1981.

[14] NMX-F-101, "Alimentos. aceites y grasas vegetales o animales.determinación del índice de acidez," 1987.

[15] NMX-F-154-SCFI, "Alimentos – aceites y grasas vegetales o animales, determinación del valor de peróxido," 2010.

[16] NMX-F-174-SCFI, Alimentos – aceites y grasas vegetales o animales, determinación del índice de saponificación," 2006.

[17] H. M. Rachimoellah, D. Ayu Resti, A. Zibbeni and dan I W. Susila, "Production of Biodiesel trough Transtesterification of Avocado (Persea gratisima) Seed Oil Using Base Catalyst," Journal Teknik Mesin, vol. 11, No. 2, pp. 85-90, 2009.

[18] M. Agarwal, G. Chauhan, S.P. Chaurasia and K. Singh, "Study of catalytic behavior of KOH as homogeneous and heterogeneous catalyst for biodiesel production," Journal of the Taiwan Institute of Chemical Engineers, Department of Chemical Engineering, Malaviya National Institute of Technology Jaipur, 302017, India, vol. 43, pp. 89–94, 2012.

[19] C. Stavarache, M. Vinatoru and R. Nishimura, Conversion of vegetable oil to biodiesel using ultrasonic irradiation. Chem Left 32(8), pp. 716-717, 2003.

[20] J. Tickell, "From the Fryer to the Fuel Tank: The Complete Guide to Using Vegetable Oil as an Alternative Fuel," Published by Biodiesel America, June 2000.

[21] ASTM D-445, "Standard Test Method for Kinematic Viscosity of Transparent and Paque Liquids (and Calculation of Dynamic Viscosity), vol. 5.01

[22] NMX-F-052-SCFI, "Aceites y grasas - aceite de aguacate – especificaciones," 2008.

[23] E. Akbar, Z. Yaakob, S. Kartom Kamarudin, M. Ismail and J. Salimon, "Characteristic and Composition of *Jatropha Curcas* Oil Seed from Malaysia and its Potential as Biodiesel Feedstock," European Journal of Scientific Research ISSN 1450-216X, vol. 29 No.3, pp. 396-403, 2009.

[24] J. Van Gerpen, "Biodiesel processing and production," Fuel Processing Technology, vol. 86, issue 10, pp. 1097–1107, June 25, 2005.

[25] M. Rasha, El-Abassy and P. Donfack, "Rapid Determination of Free Fatty Acid in Extra Virgin Olive Oil by Raman Spectroscopy and Multivariate Analysis," J. Am. Oil Chem Soc, vol. 86, pp. 507-511, 2009.

[26] H. Yang and J. Irudayaraj, "Comparation of Near-Infrared, Fourier Transform-Infrared, and Fourier Transform-Raman Methods for Determining Olive Pomace Oil Adulteration in Extra Virgin Olive Oil," Department of Agricultural and Biological Engineering, The Pennsylvania State University, University Park, Pennsylnania 16802, JAOCS, vol. 78, No. 9, 2001.

[27] S. Gallier, K. C. Gordon, R. Jiménez Flores and D. W. Everett, "Composition of bovine milk fat globules by confocal Raman microscopy," International Dairy Journal, vol 21, pp. 402-412, 2011.

[28] V. Baeten, P. Hourant, Ma. T. Morales and R. Aparicio, "Oil and Fat Classification by FT-Raman Spectroscopy," J. Agric. Food Chem, vol. 46, pp. 2638-2646, 1998.

[29] G. F. Ghesti, J. L. de Macedo, V. S. Braga, A. T. C. P. de Souza, V. C. I. Parente, E. S. Figueredo, I. S. Resck, J. A. Dias and S. C. L. Dias, "Application of Raman Spectroscopy to Monitor and Quantify Ethyl Esters in Soybean Oil Transesterification," JAOCS, vol. 83, No. 7, 2006.

[30] J. Renwick Beattie, S. E. J. Bell and B. W. Moss, " A Critical Evaluation of Raman Spectoscopy for the Analysis of Lipids: Fatty Acid Methyl Esters," Lipids, vol. 39, No. 5, 2004.

[31] S. Kint, P. H. Wermer and J. R. Scherer, "Raman Spectra of Hydrated Phosoholipid Bilayers," The Journal of Physical Chemestry, vol. 96, No. 1, 1992.

[32] G. Penel, C. Delfosse, M. Descamps and G. Leroy, "Composition of bone and apatitic biomaterials as revealed by intravital Raman microspectroscopy," Bone, vol. 36, pp. 893-901, 2005.

[33] E. S. Slezak, K. Malek and M. Baranska, "Complementary analysis of tissue homogenates composition obtaneid by Vis and NIR laser excitations and Raman spectroscopy," Molecular and Biomolecular Spectroscopy, vol. 147, pp. 245-256, 2015.

[34] T.T. Nguyen, C. Gobinet, J. Feru, S. Brassart Pasco, M. Manfait and O. Piot, "Characterization of Type I and IV Collagens by Raman Microspectroscopy: Identification of Spectral Markers of Dermo-Epidermal Junction," Spectroscopy: An International Journal, vol. 27, pp. 421-427, 2012.

[35] B. J. Marquardt and J.P. Wold, "Raman analysis of fish:a potential method for rapid quality screening," Lebensm.-Wiss. u.-Technol; vol. 37, pp. 1–8, 2004.

[36] R. A. Bitar, H. da Silva Martinho, C. J. Tierra Criollo, L. N. Zambelli Ramalho, M. Mourao Netto and A. A. Martin, " Biochemical analysis of human breast tissues using FT- Raman spectroscopy," Laboratory of Biomedical Vibrational Spectroscopy.

[37] A. Mudalige and J. E. Pemberton, " Raman spectroscopy og glycerol/D_2O solutions," Vibrational Spectroscopy, vol. 45, pp. 27-35, 2007.

Issues on control of direct-drive wind turbine generators

L. Y. Villagran Villegas
Instituto Politecnico Nacional (IPN)
DF, México
yvillagran@uv.mx

J. C. Anzelmetti Zaragoza
Facultad de Ingeniería Mecánica y Eléctrica
Universidad Veracruzana (UV)
Poza Rica, Veracruz, México.
janzelmetti@uv.mx

A. Marquina Chávez
Facultad de Ingeniería Mecánica y Eléctrica
Universidad Veracruzana (UV)
Poza Rica, Veracruz, México.
amarquina@uv.mx

Abstract. **This paper provides an overview of control strategies employed in direct drive wind turbine generators. Currently, the technical literature is focused on control of wind turbines with permanent magnet synchronous generators (PMSG) and it is scarce about wind turbines with wound rotor synchronous generators (WRSG). This paper concludes that due to the technical, economic and ecological advantages it is important to develop control strategies for wind turbines with electrically excited synchronous generators.**

Keywords: Wind turbine generator, direct drive, permanent magnet, wound rotor, synchronous generator, control strategy, aerodynamic control, intelligent control.

I. INTRODUCTION

There are three main types of electromechanical conversion system used currently for wind turbines, as it is shown in Figure 1. The first of them used an asynchronous induction generator with squirrel cage; it is used to convert the mechanical energy into electricity. In this case, the rotor speed and the generator speed are different, for this reason it is necessary to have a gearbox to match these speeds. Besides, the generator's slip varies according to the amount of energy generated, which it is not constant, but these speed variations are in the order of 1 %, therefore it is referred to as a constant-speed or fixed-speed turbine. Today, the Danish, or constant-speed, design is nearly always combined with a stall control of the aerodynamic power, although in the past pitch-controlled constant-speed wind turbine types were also built.

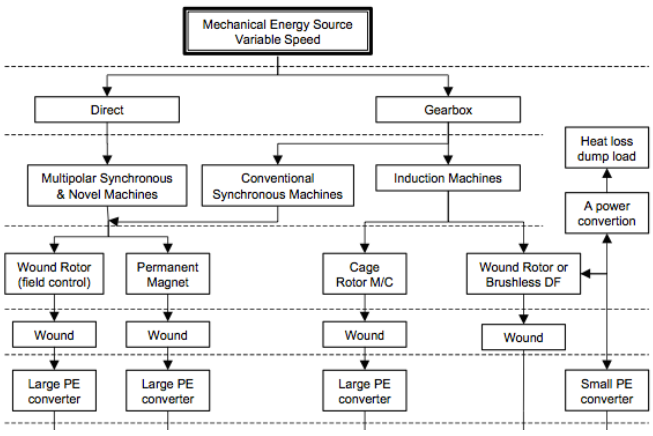

Figure 1.Three main types of electromechanical conversion system [1]

In the second type a doubly fed induction generator is used and a gearbox is also needed. In this case, the stator winding of the generator is coupled to the grid; meanwhile the rotor winding is coupled to a power converter. This power converter is usually a back-to-back voltage source converter (VSC), and it has current control loops. The rotor speed is controlled by changing the generator power in such a way that it equals the value as derived from the goal function. In this type of conversion system, the required control of the aero- dynamic power is normally performed by pitch control.

The third type is known as direct-drive wind turbine ans it works without a gearbox. The gearbox is not needed because in this case is used a low-speed multipole synchronous generator and rotational speed of the generator and wind turbine rotor, is used to convert the mechanical energy into electricity. The generator rotor can be either a wound rotor or a rotor with permanent magnets. The stator is not coupled directly to the grid but to a power electronics converter. This could consist of a back-to-back voltage source converter or a diode rectifier with a single VSC. By using the electronic converter, variable-speed operation becomes possible. Power limitation is again achieved by pitch control, as in the previously mentioned type.

There are two methods for connecting the wind turbine to the generator when the wind turbine is used for energy generation, as it is seen in Figure 2. The most common method is a mechanical speed multiplier or gearbox. In this configuration, the mechanical power is transmitted to the electrical machine with a high speed. This method has a major advantage, the use of the simply designed synchronous or asynchronous generators, which are readily available and cheaper. This method is used for high power wind turbines (above a few tens of kilowatts, to establish an order of magnitude).

A more recent alternative is to link the generator directly to the turbine without the gearbox. This method is known as "direct drive" and has become economically viable in recent years thanks to the progress made on permanent magnets. The cost of permanent magnets has dropped significantly while their performance has continued to improve. They have enabled the design of high performance, high power density, synchronous machines, well suited to the low speed operation imposed by the wind turbine, at reasonable cost. The direct drive method is attractive because it eliminates the weak element of the conversion chain: the speed multiplier gearbox. This indeed is a frequent source of failure, an additional noise source and may

also require regular maintenance, resulting in high operating costs [2].

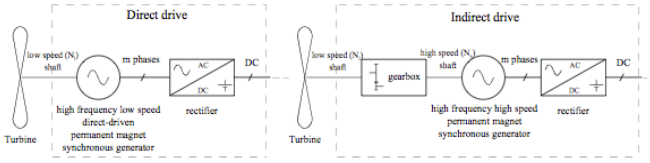

Figure 2. Linking wind turbine to generator [2].

II. GENERAL CLASSIFICATION OF SYNCHRONOUS GENERATORS

A synchronous generator has two elements: the field located on the rotor and the armature located on the stator. The armature has a concentrated three-phase winding as is shown in Figure 3.

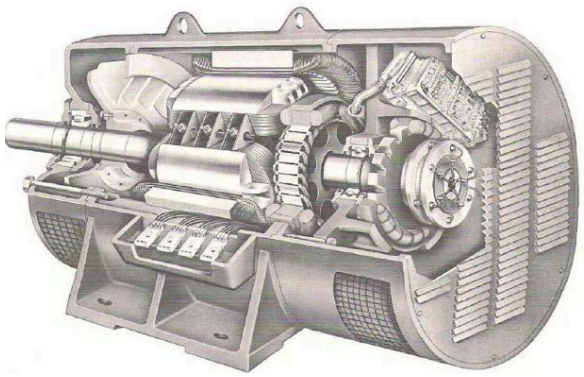

Figure 3. Cutaway of synchronous generator.

There are two classical types of synchronous generators that have been used in the wind turbine industry: the wound rotor synchronous generator (WRSG) and the permanent magnet synchronous generator (PMSG) [3]. Is also important mentioned that the synchronous generator is more expensive and mechanically more complicated than an induction generator of a similar size.

The rotor field in the synchronous generator can be generated by using permanent magnets or with a conventional field winding. The field winding needs direct current to produce a magnetic field which rotates with the rotor.

III. THE WOUND ROTOR SYNCHRONOUS GENERATOR WRSG

The stator windings in a WRSG are connected directly to the grid and therefore the rotational speed is strictly established by the frequency of the supply grid. The rotor winding can be excited either with direct current using slip rings and brushes or with a brushless exciter connected to a rectifier. The rotor winding generates the exciter field using direct current. This exciter field rotates with synchronous speed. The synchronous speed of the generator is determined by the frequency which depends of the poles number of the rotor.

The efficient of the direct-driven generators is minor than the conventional generators and they are also heavier. The direct-driven generators are designed with a large diameter to improve the efficiency and reduce the weight of the active parts. Also, to decrease the weight of the rotor and stator yokes and to keep the end-winding losses small, direct-driven generators are also usually designed with a small pole pitch [4].

The general structure of the models of a variable-speed wind turbine with a direct-drive synchronous generator and a constant-speed turbine are identical. The rotor model as well as the rotor speed and pitch angle controllers are identical to those used in the doubly fed induction generator [3].

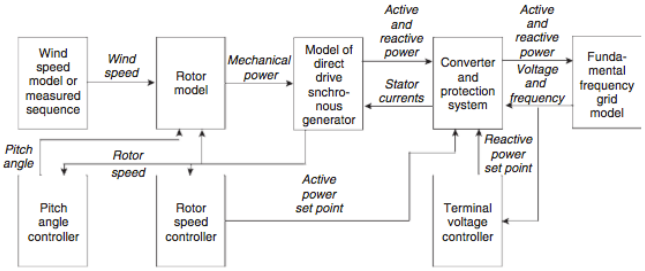

Figure 4.General structure of a model of a variable-speed wind turbine with a direct-drive synchronous generator [3].

IV. THE PERMANENT MAGNET SYNCHRONOUS GENERATOR PMSG

The generator is the centerpiece of a wind turbine. The advent of powerful permanent magnets based on Neodymium has opened the door to compact permanent magnet synchronous generator designs [5] with potentially high efficiencies. Radial flow generators are still the predominant choice, but axial flow designs are becoming increasingly popular because of their modular design and relatively low manufacturing requirements [6].

The modern wind turbines are generally designed with electric generators that use permanent magnets and direct coupling between rotor and generator. The most common topologies that can be found are the following:

- Axial flow air-cored generators
- Axial flow generators with toroidal iron cores.
- Axial flow generators with iron cores and spots.
- Radial flow generators with iron cores and spots.
- Transverse flow generators with slotted iron core.

In the different topologies listed above, the type of flow is refers to the direction of the magnetic flow lines crossing the magnetic gap between the poles with respect to the rotating shaft of the generator. When the flow lines reach the iron core (in practical realizations actually laminated steel), the flow lines change their direction according to the geometry of the core. The axial flow generators with iron cores and slots and the radial flow generators with iron cores and spots are two of the most common topologies.

Table I. COMPARATIVE TABLE OF DIFFERENT GENERATOR TOPOLOGIES COMMONLY USED IN SMALL-SCALE WIND TURBINES [6].

Topology	Advantages	Disadvantages
Axial flow with air core	Simple design and manufacture No cogging torque Quiet operation Low risk of demagnetization of permanent magnets No core losses Stackable and therefore scalable generators Multi-phase operation can be implemented easily	Structural challenges for maintaining a constant air gap for larger diameters Possible thermal instability of the polymer resin encapsulation Large amount of neodymium required Large external diameter Eddy losses in copper windings
Axial flow with toroidal iron core	Simple design and manufacture No cogging torque Quiet operation Low risk of demagnetization of permanent magnets No core losses Stackable and therefore scalable generators Multi-phase operation can be implemented easily Short end-coil connections	Structural challenges for maintaining a constant air gap for larger diameters Large amount of neodymium required Large external diameter Eddy losses in copper windings and in iron core
Axial flow with iron core and slots	Very high torque density Stackable and therefore scalable generators	Structural challenges for maintaining a constant air gap for larger diameters Complex manufacture Presence of cogging torque Relatively noisy Eddy core losses
Radial flow with iron core and slots	Structurally more robust tan axial flow generators; therefore less structural material required More widely used and well-known topology Smaller exterior diameter Diameter can be defined without considering the axial length	Presence of cogging torque Relatively noisy Eddy core losses Large amount of magnetic material due to laminated core.
Transverse flow with slots in iron core	Generally needs the least amount of neodymium Low copper losses Simple coil winding High torque density, if properly designed	Complex design and manufacture Uncommon topology so far Potentially high magnetic dispersion Potentially low power factor Presence of cogging torque Needs a stator for each electric phase Eddy core losses

V. ADVANTAGES AND DISADVANTAGES OF WIND TURBINES WITH DIRECT DRIVE AND ANOTHER WIND TURBINES OF OTHER TECHNOLOGIES

When the permanent-magnet generator is compared to the electrically excited synchronous generator, the number of pole pairs is doubled in the first one in order to reduce the risk of demagnetizing the magnets and also to reduce the dimensions of yokes and end-windings. In the permanent-magnet generator, the number of poles does not increase the excitation losses as it happens in the electrically excited synchronous generator.

The direct-drive permanent-magnet generator (DDPM) is more attractive because the active material weight of the generator for the same air-gap diameter is nearly halved and the energy yield is a little higher. Also, the energy yield of the direct-drive permanent-magnet generator is a few percent higher if it is compared to the others generator systems with gearbox. On the other hand, the DDPM is more expensive compared to the generator systems with gearbox. Further improvements of this generator system may be expected because of the developments in prices of permanent magnets dynamics behaviour, vibration damping, and materials used for PM tend to be brittle and many cases have various metallurgical defects [7].

However the main sources of losses in the WRSG are the copper losses in stator and rotor and the converter losses. The WRSG seems to be the heaviest and most expensive option. The wind turbine manufacturers with: Enercon, Kenersys, Aeronautica and MTorres uses this system but they claim others benefits, for example: the immunity to problems derivate of voltage disturbances due to grid faults as a result of the use of a fully- rated converter [8].

VI. CONTROL IN DIRECT DRIVE WIND TURBINES

The wind turbine control system consists of a number of sensors, a number of actuators, and a system consisting of hardware and software. This hardware and software system processes the input signals from the sensors and generates output signals for the actuators. The actuators might include a hydraulic or an electric pitch actuator, a generator torque controller, generator contactors, switches for activating shaft brakes, yaw motors, etc. [9].

The rotor speed must be controlled for three reasons:

1. To capture more energy, as seen above.
2. To protect the rotor, the generator and the power electronic equipment from overloading at high wind.
3. When the generator is disconnected accidentally or for a scheduled event, losing the electrical load. Under this condition, the rotor speed may run away, destroying it mechanically, if it is not controlled.

The speed control requirement of the rotor has five separate regions [10] as shown in Figure 5:

1) The cut-in speed at which the turbine starts producing power. It is not efficient to turn on the turbine below this speed.

2) The constant maximum Cp region where the rotor speed varies with the wind-speed variation to operate at the constant TSR corresponding to the maximum Cp value.

3) During high winds, the rotor speed is limited to an upper constant limit based on the design limit of the system components. In the constant speed region, the Cp is lower than the maximum Cp, and the power increases at a lower rate than that in the first region.

4) At still higher wind speeds, such as during a gust, the machine is operated at constant power to protect the generator and the power electronics from overloading. This can be achieved by lowering the rotor speed. If the speed is decreased by increasing electrical load, the generator will be overloaded, defeating the purpose. To avoid the generator overloading, some sort of brake, eddy current, or other type, must be installed on the rotor.

5) The cutout speed. Beyond certain wind speed, the rotor is shut off producing power in order to protect the blades, the electrical generator, and other components of the systems.

A control system usually has three subsystems: an aerodynamic control, a variable speed control, and a grid connection control. [11].

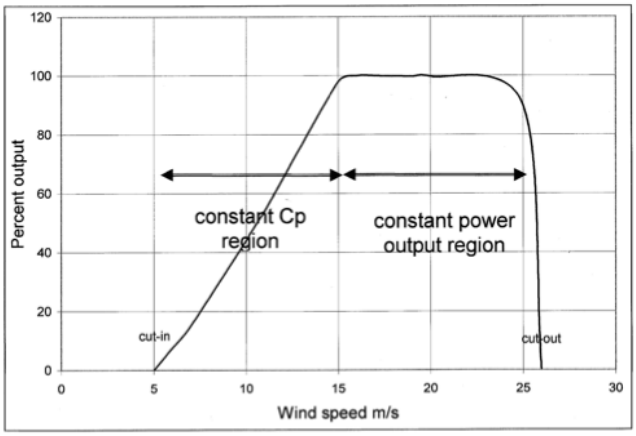

Figure 5. Five regions of the turbine speed control.

5.1 *Aerodynamic Control.*

The aerodynamic of the blades of the wind turbine are similar to the airplane. The blades rotate in the wind and create a lifting force to remove the sheet to rotate. The attack angle of the blade plays a critical role in determining the amount of force and torque generated by the turbine. Therefore, it is an effective means to control the amount of power. There are three methods to aerodynamically control for large wind turbines: passive stall, active stall, and pitch control.

i. Passive Stall Control.

The simplest form of power control is passive stall control, which makes use of the post-stall reduction in lift coefficient and associated increase in drag coefficient to place a ceiling on output power as wind speed increases, without the need for any changes in blade geometry. The fixed-blade pitch is chosen so that the turbine reaches its maximum or rated power at the desired wind speed. Stall-regulated machines suffer from the disadvantage of uncertainties in aerodynamic behaviour post-stall which can result in inaccurate prediction of power levels and blade loadings at rated wind speed and above [18].

For passive-stall-controlled wind turbines permanent magnet direct drive, in which the rotor blades are fixed to the hub at a specific angle, the generator reaction torque regulates rotor speed below rated operation to maximize energy capture. Above a specific wind speed, the geometry of the rotor induces stall. In this manner, the power delivered by the rotor is limited in high wind conditions thanks to a particular design of the blades that provoke loss of efficiency [12].

ii. Active Stall Control.

The stall phenomenon can be induced not only by higher wind speeds, but also by increasing the attack of the blade. Thus, active stall wind turbines have blades with adjustable pitch control mechanism. When the wind speed exceeds the rated value, the blades are controlled towards the wind to reduce the captured power. Consequently, the captured power can remain at the nominal value by adjusting the blade angle of attack [13].

The power coefficient of is maximum at a constant tip speed ratio. Therefore, below rated wind speeds, the rotor speed is made proportional to the wind speed to obtain maximum energy yield. The turbine with pitch control pitches the blades to reduce the power coefficient at wind speeds above rated to keep the rotor speed more or less constant at the rated rotor speed and to produce a constant output power. The turbine with active speed stall control is controlled by reducing the rotor speed at wind speeds above rated. The rotor speed is limited in order to limit the output power. There are a number of possible ways to control the rotor speed of a wind turbine with active speed control [14].

The idea behind the active speed stall control concept is to make a wind turbine that is as simple as possible, and therefore very robust and suitable for offshore wind parks. Therefore, a number of design choices have been made:

- The rotor blades cannot pitch and, therefore, there is no pitch control.
- The blades are designed to maximize aerodynamic performance at wind speeds below rated.
- A direct-drive permanent-magnet generator is used.
- The aerodynamic performance at wind speeds above rated is limited by actively controlling the rotor speed. This means that if the wind speed increases to values above rated, the generator reduces the rotor speed of the wind turbine so that not more than rated power is produced [13].

iii. Pitch control.

Active pitch control achieves power limitation above rated wind speed by rotating all or part of each blade about its axis in the direction which reduces the angle of attack and hence the lift coefficient – a process known as blade feathering. The main benefits of active pitch control are increased energy capture, the aerodynamic braking facility it provides and the reduced extreme loads on the turbine when shut- down [18]. Pitch angle control is mainly used to limit the mechanical power during strong wind speed or to adapt power production according to the grid operator requests.

The aerodynamic behaviour of the wind turbine can be controlled actively by varying the turbine blade angle around their longitudinal axis [15]. In addition, in low and medium wind speed the pitch control is rarely actuated and only set to the optimum value, e.g. 0°. In high wind speeds, the pitch angle control effects to regulate the extracted wind power so that the design limits of the turbine will not be exceeded. Rotor speed, torque or power control can be taken to regulate the pitch angle [16]. The error between the reference power and the measured power at the output of the PMSG is sent to a PI controller to generate the reference value of the pitch angle.

Mechanical power control β ref. and the complete model of the pitch system are shown respectively in Figure 6.

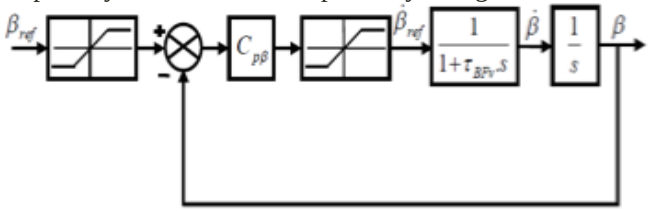

Figure 6. Pitch angle controller block.

In the controller "max" is used for selecting the maximum of the input to ensure that the pitch angle controller actuates only when the actual wind speed is greater than its rated value. This reference value is sent to the pitch actuator, which can be electrical or hydraulic in order to turn the blades of the wind turbine. During normal operation, blade pitch adjustments with a rotational speed of approximately 5-10o/s are expected [17]. Here, the chosen pitch rate is 10o/s which avoids excessive loads during normal operation. Consequently, the complete model of the wind turbine by integrating the aerodynamic control is shown in Figure 7.

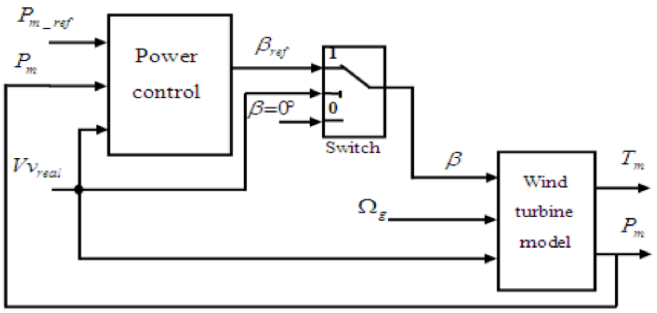

Figure 7. Model of the wind turbine with a pitch angle control technique [18].

5.2. Linear control

The proportional and integral (PI) controller is an algorithm widely used for controlling all kinds of equipment and processes. The control action is the sum of two terms, one that is proportional to the control error (the difference between the desired and actual values of the quantity to be controlled), and another equivalent to the integral of the error. The integral term is used to guarantee that in steady state the control error will tend to zero, if it did not, the integral term would make the control action continue to increase. The proportional term is more responsive to rapid changes in the quantity being controlled. A differential term might be added, and it can give a contribution to the control action proportional to the rate of change of the control error [18].

The main idea is to control the generator speed by varying the resistive load as input. Consider a time invariant system in the form of (1) where x is the state vector, u the vector containing the control signals [19], f (·, ·) is a nonlinear vector function Satisfies the condition of existence of the solution of the differential equation.

$$x = f(x, u) \quad (1)$$

The control target relocation of poles is to find a gain K to feedback the states of the system and behave in the way they are selected closed-loop poles [20, 21].

5.3. Nonlinear control.

Sliding mode control is a robust nonlinear feedback control technique. It can be applied for the wind turbine control. Sliding mode control can be used in the design of state observers, the implementation of advanced ac machine control algorithms such as field oriented control (Field Oriented Control) and direct torque control (Direct Torque Control) require the information of the rotor position and speed.

To be specific, the position angle is used for the coordinate transformation, while the speed information is needed in the closed-loop speed control as the feedback signal. Conventional methods to acquire such information are based on an encoder or a transducer mounted on the rotor shaft. However, the presence of such electrical sensors largely increases the system cost and hardware complexity. There are numerous rotor position self-sensing methods proposed in the literature, and Sliding Mode Observer SMO is one of the most attractive methods, which has been introduced to estimate ac machines' parameters and its robustness to parameter variation and external interference has been verified [22]. With the application of the SMO based rotor position self-sensing control, position sensors can be eliminated from the WECS.

5.4. Intelligent control.

The intelligent control employed in the wind power generation (WPG) system can effectively face the challenges of grid connection requirements. Computational intelligence techniques, such as fuzzy logic (FL), artificial neural network (ANN), evolutionary computation (EC), etc. are recently proposed and utilized for the control of wind turbines direct drive [23].

5.4.1 Artificial Neural Network

Variable speed operation and direct drive generator have been the recent developments in the technology of wind turbine generation system. The use of the variable speed PMSG in wind turbine application can increase the energy capture from wind, and improve efficiency. On the other hand, if a gearbox is used in a wind turbine system, noise, power losses, additional cost, and potential of mechanical failure can cause many problems.

At present, most many wind turbine control systems employ anemometers to measure wind velocity in order to derive the desired shaft speed to vary the generator speed. In most cases, a number of anemometers at some distance away from and surrounding the wind turbine are required to provide adequate information. These mechanical sensors increase the cost and

reduce the reliability of the overall system [24]. ANN is particularly useful to implement nonlinear time-varying input–output mapping. Depending on the learning method (supervised or unsupervised), the neural network tries to correlate the correspondence between the input and target data by adjusting its weights. Following many iterations of incremental training with many different input–output pairs, the ANN weights are optimally adjusted by comparing its output and the designated target. This depends on various factors, like, the learning algorithm, network architecture etc. [25].

5.4.2 Fuzzy logic controller.

The permanent magnet synchronous machine is characterized by a high torque density, very low inertia and low inductances. All these features provide the synchronous generator high performances, high efficiency, and better controllability, which make it a true competitor of the asynchronous generator. The self-control operation of the permanent magnet synchronous machine results in a rotor field oriented control of the torque and flux in the machine. The principle is to maintain the armature flux and the field flux in an orthogonal or decoupled axis [26].

VII. CONCLUSIONS

The target of this paper is present some control strategies of direct drive wind turbines. The majority of strategies from classical control until intelligent control its applied for Permanent Magnet Generator but to know all advantages and disadvantages it´s important to consider technical, economic and ecological elements for to design and in special new control strategies for Wound Rotor Synchronous Generator Wind Turbine [27].

REFERENCES

[1] Hansen, L.H. Helle L., Blaabjerg F. Ritchie E. Munk-Nielsen S. Bindner H. , Sorensen P. Bak-Jensen B. Conceptual Survey of Generators and Power Electronics fot Wind Turbines . RISO National Laboratory, Roskilde, Denmark, 2001.

[2] Carriveau, R. (2012). Advances in wind power, Publishing By Intech Press.

[3] Ackerman, T. (2012). Wind power in power system, John Wiley& Sons, USA/UK.

[4] Anaya, L.O. Jenkins N., Ekanayake A., Cartwrighy P. Hughes M. (2009). Wind energy generation modelling and control, John Wiley& Sons, USA/UK.

[5] Khan, M.A.; Pillay, P.; Visser, K.D. (2005). On Adapting a Small PM Wind Generator for a Multiblade, High Solidity Wind Turbine. IEEE Transactions on Energy Conversion Vol. 20, No. 3, 685-692

[6] Al - Bahadly, T. (2011). Wind turbines, By Intech Press. INDIA.ISBN 978-953-307-221-0

[7] Aleksashkin A. Literature review on permanent magnet generators design and dynamic behaviour. Research report 77 ISBN 978-952-214-708, 2008

[8] Polinder,H. Van der Pijl F. Jan de Vilder G. Tavner P. Comparasion of direct-drive and geared generator concepts for wind turbines IEEE Press, 2005.

[9] Burton, T., Sharpe D., Jenkys N., Bossanyi E. (2009). Wind energy handbook, John Wiley& Sons, USA/UK.

[10] Mukund R. Patel, Ph.D., P.E. U.S. Merchant Marine Academy, Kings Point, New York,W ind and Solar Power Systems,CRC Press,1999, pp 101-104.

[11] Van Baars G.E., “Wind turbine control design and implemen- tation based on experimental models,” in Proceedings of the 31st IEEE Conference on Proceedings of the Decision and Control, vol. 2, pp. 2454–2459, 1992.

[12] Camacho, F. E. Samad, T. Sanz-GArcía M. (2011). The impacy of control Technology, Publishing By IEEECSS

[13] Soriano, L.A.; Wen, Y.; Rubio, J.J. (2013). Modeling and control of Wind Turbine. Mathematical Problems in Engineering Vol. 13, Article ID 982597, 13 pages.

[14] Polinder,H. Van Rooij R. MacDonald A.S. Mueller M. 10MW Wind turbine direct-drive generator design witch pitch or active speed stall control, Electric Machines&Drives Conference 2007 IEMDC´07,IEEE Press, vol. 2, pp. 1390–1395, 2007.

[15] Polinder H., Overview and trends in wind turbine generator systems, IEEE Power and Energy Society General Meeting, 1-8, 2011.

[16] Geng H., Yang, G., Xu D. and Wu B. Unified Power Control for PMSG-Based WECS Operating Under Different Grid Conditions, IEEE Trans. on Energy Conversion, 26(3), pp. 822-830, 2011.

[17] Heier S. Grid integration of wind energy conversion systems, John Wiley & Sons Ltd, 2nd ed.,Chichester, UK, 2006.

[18] Burton, T., Sharpe D., Jenkys N., Bossanyi E. (2009). Wind energy handbook, John Wiley& Sons, USA/UK.

[19] Allagui M.,Othman B.Q. Hasnaoui J.B., Exploitation of pitch control to improve the integration of a direct drive wind turbine to the grid , Journal Electric Systems JES 179-190 2013.

[20] Sanchez,S. Bueno M.,Delgado E. L.A.; Wen, Y.; Rubio, J.J. (2013). Optimal tuning of a controller in a Wind Turbine Equipped with a permanent magnetized synchronous generator. Energetica Num. 41, ISSN 01209833. pp. 4960 , 2009.

[21] Astrom K. J., 2002. Control Systems Design, Lecture notes for ME 155A, Department of Mechanical and Environmental Engineering, University of California Santa Barbara, California.

[22] Li, F., 2007. Robust Control Design, An Optimal Control Approach. John Wiley & Sons, United States.

[23] Young D.K.,Utkin V.I., and Ozguner U. "A control engineer's guide to sliding mode control," IEEE Trans. on Control System Technology, vol. 7, no. 3, pp. 328-342, 1999.

[24] Barath, S.; Snigh, S.; Kyriakides, E. (2010). Intelligent Control of Power Electronic Systems for Wind Turbines. Power Systems. Green Energy and Technology Vol. 0, pp 255-295.

[25] Tan K. and Islam S., “Optimal control strategies in energy conversion of PMSG wind turbine system without mechanical sensors,” IEEE Trans. Energy Convers., vol. 19, no. 2, pp. 392–399, Jun. 2004.

[26] Ren Y. F.,Bao G. Q.; Pillay, P.; Visser, K.D. (2005). Control Strategy of Maximum Wind Energy Capture of Direct-Drive Wind Turbine Generator Based on Neural-Network. IEEE Power energy and engineering conference (APEEC, 2010) Vol. 20, No. 3, 685-692

[27] Ghanig A. A.., Thaour A., Essounbouli., N., Nollet F. and Abid M.. A Fuzzy-PI control to extract an optimal power from wind turbine, Energy Conversion and Management, Elsevier, 65, pp. 688-696, 2013.

Experimental and computational analysis of single phase flow coiled flow inverter focusing on number of transfer units and effectiveness.

Thomas Barthram
Escuela de Ingeniería y Ciencias
Tecnológico de Monterrey
Monterrey, México
A01293907@itesm.mx

Carlos Ivan Rivera Solorio
Escuela de Ingeniería y Ciencias
Tecnológico de Monterrey
Monterrey, México
Rivera.carlos@itesm.mx

***Abstract*— In this work is investigated the number of transfer units (NTU), effectiveness and heat transfer characteristics of a heat exchanger named coiled flow inverter (CFI) experimentally and computationally at laboratory scale. The experiments are carried out with hot fluid in the shell side and cold fluid in the tube side. Experimental and computational fluid dynamics studies are made over a range of Reynolds numbers from 2000 to 10000 in the tube side and 500 to 2000 in the shell side. The fluid used in the tube and shell side of the heat exchanger is water. The temperature range in the shell side is of 20 to 80°C and in tube side was kept constant at 20°C. The coiled flow inverter is made up of coils and 90◦ bends and inserted in a closed shell. The shell side is cylindrical. The average temperatures at input and output of the heat exchanger are reported for different flow rate at tube and shell side. Overall heat-transfer coefficients are calculated as well as the number of transfer units and effectiveness at various tube and shell side process conditions. At the same conditions are reported the computational models results compared to the experimental model. Finally a Nusselt correlation is proposed for the shell side of this configuration. The main results of this study include that the NTU effectiveness curves of the selected heat exchanger has a high resemblance to the parallel flow tube heat exchanger with a maximum of 2.1% error, the coiled flow inverter has a 200% increase in effectiveness compared to a regular parallel flow heat exchanger at same conditions.**

Keywords—Coiled flow inverter (CFI); Coiled tube; Bends; Heat exchanger; CFD; effectiveness; NTU.

I. INTRODUCTION

Enhancement of heat transfer is essential in most of the industrial fields. A method to be able to control the temperature in a certain area or component is via the use of heat exchangers. The consequences of improper heat-transfer include non-reproducible processing conditions and lowered product quality[1], resulting in the need for more elaborate down- stream process system and increased heat-transfer area. As it may be known the miniaturization of heat exchangers and increase in efficiency to reduce costs is of upmost importance, which would become optimization of energy resources. There are two main ways to increase heat transfer, the first one being materials which can be the fluid, for example nanofluids [2], the walls materials. The second one being the geometry, which includes roughness, interferences in flow path to increase turbulence or mixing of the fluid, for example, using rotors [3]. The coiled flow inverter is a patented heat exchanger US 733835 B2, this one focuses on the use of spirals which are considered to have higher heat transfer per unit of surface area compared to straight heat exchangers [4].

A. Coiled flow inverter

When a fluid flows through a curved pipe of any cross-section it is observed that a secondary flow occurs in planes perpendicular to the central axis of the pipe. In particular, the secondary flow arises due to the centrifugally induced pressure gradient, which drives the faster-moving fluid from the core outward to wall. Then, to satisfy the continuity, the low momentum fluid subject to the no-slip condition at the wall moves toward the inner wall of the curved tube[5]. In order to be able to visualize the phenomenon, the secondary flow can be seen as consisting of a pair of counter-rotating helical vortices (called Dean Vortices) placed symmetrically with respect to the plane of symmetry.

It was observed that as the Dean number is increased, the centers of the two vortices move to the outer bend, and that there is a considerable reduction of the flow in the curved pipe compared with a straight pipe. Similarly, for low values of curvature ration, the secondary flow intensity is very high while for higher values of curvature ratio it decreases[6]. Further experiments have also confirmed that the flow in curved pipes is more stable than that in a straight tube due to the secondary flow. This results in the persistence of the laminar flow at higher Reynolds number than the critical Reynolds number for straight tubes, which normally is of 2100 [7].

B. Previous studies

A relative quantity of studies have involved the coiled flow inverter, these mainly conducted by Nigam et al. [1], where the experimental heat transfer characteristics and correlations of the coiled flow inverter (CFI) were defined. The outcome is that the coiled flow inverter increases heat transfer of 25% for flows from 1000 to 16000 Reynolds compared to a coiled tube. It is also noted that at high Reynolds the heat transfer has less effects. Its pressure drop in single and two phase flow was also

This work was funded by the Tecnologico de Monterrey and by the CONACYT governmental entity. (National Council of Science and Technology)

investigated experimentally, the result is that the coiled flow inverter has an increase in pressure drop compared to straight tubes and helix by a factor of 2.5 to 3 [8], the numerical simulation of steady flow fields in coiled flow inverter showed an increase in heat transfer of 20 to 30 percent whereas the pressure drop was only of 5 to 6% compared to a helix [9]. Another numerical study has been performed, this one regarding turbulent forced convection in the coiled flow inverter, the heat transfer increases of 35 to 45% and pressure drop of 29 to 30% compared to a straight tube for the same flow configurations [10]. Numerical studies including nanofluids regarding low Reynolds numbers in the coiled flow inverter are also investigated, with nanoparticles ranging from 0.25 to 4% volume fraction, it is noted that the Nusselt number in the helical coil augments 2.5 times compared to the straight tube, and in the CFI increases of 25 to 30% compared to the helical coil. Correlations were developed to predict the friction factor and Nusselt number in the CFI [11]. Another experimental investigation regarded the experimental comparison of the CFI with known heat exchangers (PHE) plate type heat exchanger and (SHE) shell and tube heat exchanger, results showed that the number of transfer units NTU increased of 3.5 to 7.5 compared to SHE and 2 to 2.5 compared to PHE for the same conditions, more over, Nusselt and pressure drop correlations of the coiled flow inverter were developed [12]

C. Present work

The aim of the present work is to characterize the performance of a coiled flow inverter (CFI) as a heat exchanger for a water–water single phase flow system, experimentally and numerically, this on a laboratory scale and using the Computational Fluid Dynamics (CFD) software Fluent™ for the numerical study. The effect of the fluid flow rate on the heat transfer and the overall heat transfer coefficients were studied in the tube as well as in the shell side of the heat exchanger. In the present work bent coils were considered as tube side which is inserted into a cylindrical shell. From this, it was possible to determine the NTU effectiveness curves for the given setup and provide a study of heat transfer for different relations of mass flow heat capacities. Table 1 represents the nomenclature of the symbols and letters used within this work.

TABLE I. NOMENCLATURE

Nomenclature	
symbol	***Description***
Re	Number of Reynolds
De	Number of Dean
Pr	Prandtl Number
d	Interior tube diameter
D	Coil diameter
A	Area
L	Length of tube
Leh	Hydrodynamic entry length
LeT	Thermal entry length
T	Temperature
Cp	Heat capacity
·	Energy
ṁ	Mass flow rate
C_c or C_h	Mass flow heat capacity
c	Relation of mass flow heat capacities
NTU	Number of transfer units
g	Gravity
Lcoil	projected length of coil
ΔT_{lmtd}	Logarithmic mean temperature difference
U	Overall heat transfer coefficient
V	Velocity
f	Friction factor
P	Pressure
K	Conductivity
Greek letters	
ε	Effectiveness
μ	Coefficient of viscosity
δ_{ij}	Delta function
ϕ	Flux
ρ	Density
Subscripts	
h	Hot
c	Cold
i	In
o	Out
l	Longitudinal

II. EXPERIMENTAL AND NUMERICAL METHODOLOGY

A. *Experimental*

The purpose of the experimental part of the study is to determine the number of transfer units against the effectiveness of a heat exchanger comprised of a coiled flow inverter and cylindrical shell. The studied heat exchanger is shown in fig.1.

Fig. 1. Experimental Coiled flow inverter in shell.

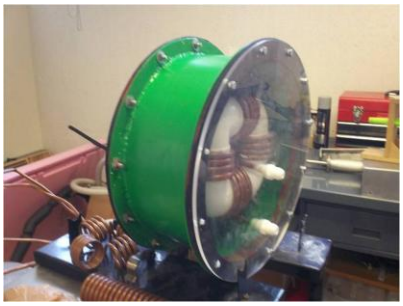

The tube side is made of 4.2 meters of 3/8 inch flexible copper tube, which equals to 7.91mm interior and 9.53 mm exterior diameter. The pitch of the coils is of 15 mm and the coil diameter is of 92.5 mm (these measures can be seen on Fig.2). This inserted in a shell measuring 350 mm diameter and 160 mm deep.

Fig. 2. Dimensions of CFI

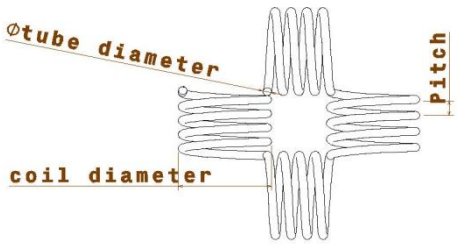

Straight tubes were added at the input of the CFI with sufficient length to permit the hydrodynamic and thermal profiles to develop.

1) *Experimental setup*

_ The Fig. 3, shows the experimental setup of the coiled flow inverter in the test bench and its instrumentations points. This bench uses 2 circuits, a hot fluid one in the shell side of the heat exchanger and a cold circuit in the tube side of the heat exchanger. The temperature acquisition was done at the input and output of the coiled flow inverter, at the points P and T with the corresponding number. The table 2 shows the different components used in the experimental part.

Fig. 3. Experimental setup and components.

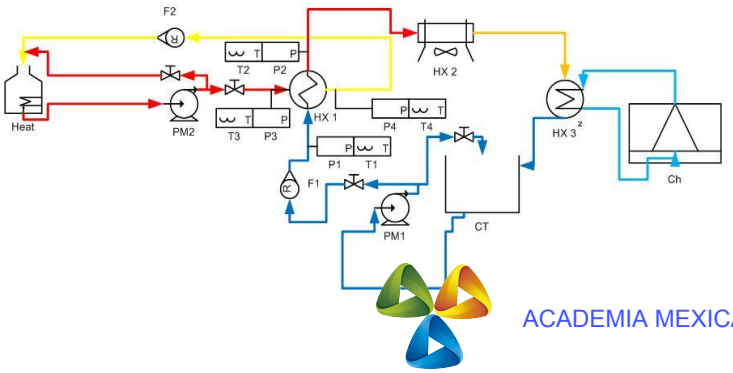

TABLE II. EXPERIMENTAL COMPONENTS DESCRIPTION

Component	*Description*	*Characteristics*
Hot circuit		
Heat	Tank with heating resistance	1800W, 25L tank
PM2	Centrifugal pump	Up to 7lpm
T3,T4	Temperature acquisition	Type K
F2	Flow meter	0 to 10lpm
Heat transfer between circuits		
HX1	Coiled flow inverter	Shell hot circuit tube cold circuit
Cold circuit		
HX2	Forced convection heat exchanger	Car radiator
HX3	Spiral heat exchanger	Heat exchanger between chiller and cold circuit
Ch	Compression chiller	Cooling capacity 1.28kW
Ct	Cold tank	25L tank
PM1	Centrifugal pump	Up to 7LPM
P1,P2	manometer	
T1,T2	Temperature acquisition	Type K

B. *Numerical*

Fig. 4 shows the model developed for this simulation. This one represents the CAD model of the CFI in its shell from Fig. 1. The mesh is shown in Fig. 5, this one composed of tetrahedral elements. This heat exchanger mesh has more than 2.9 million numerical elements that were divided in 3 meshed volumes: the shell, the tube (CFI), and the fluid in the CFI. The support tube was not meshed as a volume, just its outer surface used as a wall.

Fig. 4. CAD modeled CFI and shell.

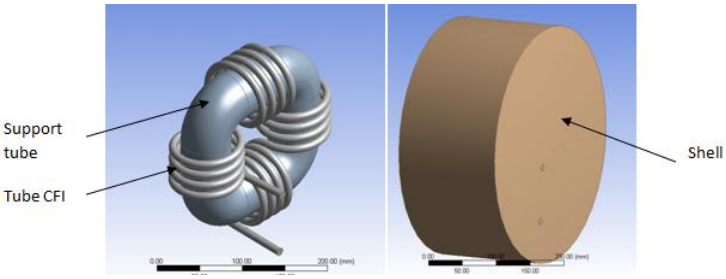

Fig. 5. Mesh of the heat exchanger

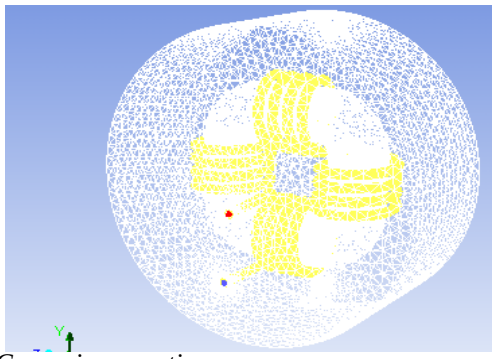

1) *Governing equations*

The flow was considered to be incompressible, steady, and constant thermal properties were assumed. The Navier–Stokes and energy governing equations for incompressible flow in a coiled and shell configuration[13] are given below.

Mass balance equation:

$$\frac{\partial u_i}{\partial x_i} = 0 \tag{1}$$

Momentum Balance Equation:

$$\rho u_j \frac{\partial u_i}{\partial x_j} = -\frac{\partial p}{\partial x_i} + \mu \frac{\partial}{\partial x_j}\left(\frac{\partial u_i}{\partial x_j}\right) \tag{2}$$

Energy equation:

$$\rho C_p u_j \frac{\partial T}{\partial x_j} = k \frac{\partial}{\partial x_j}\left(\frac{\partial T}{\partial x_j}\right) \tag{3}$$

The equations here above were numerically solved in the CFD program.

C. Boundary conditions

The boundary conditions were imposed at the walls of the CFI and shell with a non slip condition, $u_i = 0$.

At the inputs of the shell and tube temperature and velocity boundary conditions were inserted.

At the outputs of the shell and tube a pressure outlet boundary condition was inserted. (0 Pascal)

A conjugate boundary condition was specified at the wall of CFI, therefore, the heat transfer between the hot and cold fluid was made possible.

A wall condition was inserted at the support part of the body, therefore this one did not need to be meshed and processing time was gained.

D. Experimental and numerical methodology

The operating conditions employed in the experiments and simulations of the CFI are shown in Table 3. In the first place both heat capacity flow ratio were fixed. The ratio of these two was of 1, 0.75, 0.5, 0.25.

The entrance temperature at the CFI is always constant, at each experiment the temperature at the shell inlet is increased for a certain flow heat capacity ratio. It was carefully taken into account that the tube part of the heat exchanger does not go beyond the laminar zone. Therefore only low volume flows were chosen.

TABLE III. FLOW SETUPS

Experimental set	*Cold flow CFI (lpm)*	*Hot flow shell (lpm)*	*Cmin/C max*
1st set	3	3	1
2nd set	4	3	0.75
3rd set	2.25	3	0.75
4th set	6	3	0.5
5th set	1.5	3	0.5
6th set	1	4	0.25
7th set	4	1	0.25

Seen that are available the inlet, outlet temperatures and the flow rates, it is possible to calculate the input and output energies. The equations (4) to (14) represent a method used to calculate the effectiveness and NTU of the heat exchanger.

$$\dot{}\text{shell} = \dot{}_{\text{h}} = \dot{m}_{\text{h}} * C_{\text{p,h}} * \left(T_{\text{h,i}} - T_{\text{h,o}}\right) \tag{4}$$

$$\dot{}\text{cfi} = \dot{}_{\text{c}} = \dot{m}_{\text{c}} * C_{\text{p,c}} * \left(T_{\text{c,o}} - T_{\text{c,i}}\right) \tag{5}$$

It is also possible to calculate the minimum mass flow rate heat capacity Cmin using:

$$C_{\text{h}} = (\dot{m}_{\text{h}} * C_{\text{p,h}}) \quad \text{and} \quad \dot{}C_{\text{c}} = \dot{}(\dot{m}_{\text{c}} * C_{\text{p,c}}) \tag{6}$$

And therefore:

$$c_{\min} \begin{cases} c_{\text{c}} \text{ if } c_{\text{c}} < c_{\text{h}} \\ c_{\text{h}} \text{ if } c_{\text{h}} < c_{\text{c}} \end{cases} \tag{7}$$

From there calculate the maximum heat capacity:

$$\dot{}\text{max} = \text{Cmin}(T_{\text{h,i}} - T_{\text{c,i}}) \tag{8}$$

And finally calculate the effectiveness of the heat exchanger.

$$\varepsilon = \frac{\dot{}\text{cfi}}{\dot{}\text{max}} = \frac{\dot{}\text{shell}}{\dot{}\text{max}} \tag{9}$$

Using the logarithmic mean temperature difference, it is possible to extract the global heat transfer coefficient. This step is done by using the mean logarithmic temperature difference (lmtd).

Not being in a configuration of counter flow or parallel flow it was decided to use the counter flow configuration for the logarithmic mean temperature difference as it was used by Nigam et al. [1]. This equation is as:

$$\Delta T2 = T_{h,i} - T_{c,i} \quad (10)$$

$$\Delta T2 = T_{h,o} - T_{c,o} \quad (11)$$

$$\Delta T_{lmtd} = \frac{\Delta T2 - \Delta T1}{Ln\left(\frac{\Delta T2}{\Delta T1}\right)} \quad (12)$$

Finally the overall heat transfer coefficient can be determined as:

$$U = \frac{\dot{Q}cfi}{A_l * \Delta T_{lmtd}} \quad (13)$$

.

From there on it is possible to extract the number of transfer units.

$$NTU = \frac{U * A_l}{Cmin} \quad (14)$$

Using the previous method it is possible to graph the NTU of the CFI against its effectiveness and compare the experimental case to literature and numerical results.

III. Results and Discussion

A. *NTU effectiveness study*

1) *Model validation*

The NTU effectiveness studies were carried out in the CFI experimentally and numerically. In order to be able to validate the numerical simulations, a few repetitive tests were engaged, these ones are shown on table 4.

TABLE IV. Model validation tables

Input values				Experimental		Numerical		Difference (k)
v shell m/s	*v tube m/s*	*T shell in*	*T tube in*	*T shell out*	*T tube out*	*T shell out*	*T tube out*	*T shell out*
0,7	1,02	310,6	303,3	309,1	304,5	309,6	304,1	0,5
0,7	1	314,1	305,3	312,7	307,1	313,4	306,4	0,7
0,7	1	329,4	308,6	324,2	313,5	325,6	312,6	1,4
0,7	1,4	322,1	308,2	318,8	310,6	319,3	310,3	0,5
0,23	1,4	311,4	297,2	306	298,6	307,3	298,3	1,3

As it can be seen here above, the experimental data and numerical results show good agreement. Comparing the temperature at the outputs of the tube part and the shell respectively, between the numerical and experimental studies, the maximum difference encountered is of 1.4 degrees Celsius on the last test, knowing that the K type thermostat has a precision of 0.5 degrees, the results of the simulation and experimental coincide with low temperature difference.

2) *NTU effectiveness*

The NTU effectiveness results as shown on the graph here under recapitulates 18 numerical simulations and 28 validated experimental values. As it can be noted, there is little difference between the numerical and experimental data. Fig. 6 shows the combined experimental and numerical results.

Fig. 6. Effectiveness NTU chart, Coiled Flow Inverter.

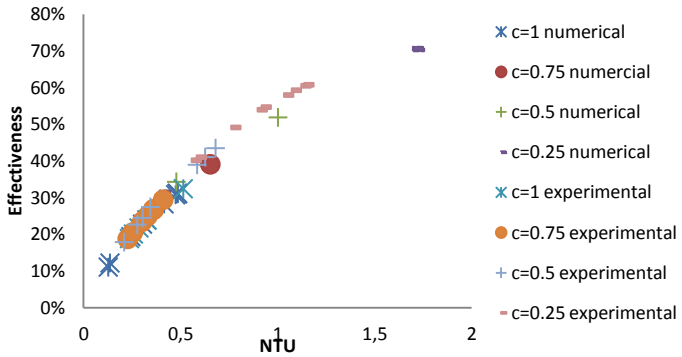

Regarding the Fig. 6 the majority of the points are between 0,2 and 0,5 NTU, this due to the size of the heat exchanger and the heating limitations of the experimental system, therefore it was necessary to add simulations, in the first place to confirm the experimental part and secondly to increase the range of the NTU effectiveness curves. The extrapolation of the curves can be seen on the Fig. 7. It can be noted that the coiled flow inverter seems to have a similar effectiveness NTU curve in this situation as the tube in tube parallel flow heat exchanger.

Fig. 7. Tendencies added to NTU effectiveness

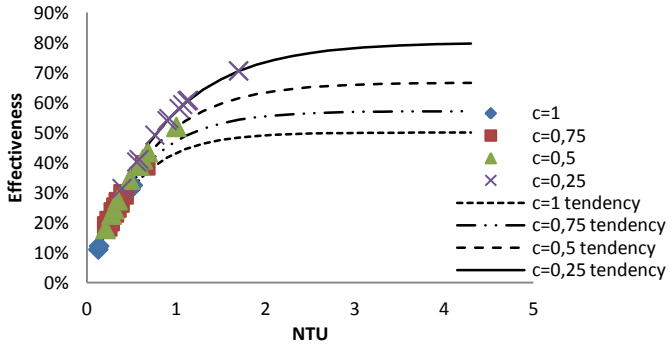

Regarding the tendencies shown in Fig.7 a correlation has been proposed for the NTU Effectiveness curves, the chosen correlation is the one of a parallel flow heat exchanger, which fitted the results with a maximum error of 2.1%. This one being:

$$\varepsilon = \frac{(1 - e^{(-NTU*(1+C))})}{1 + C} \quad (15)$$

Regarding the equation (15) and Fig. 7 shown here above, it can be seen that the Coiled Flow Inverter does not have an excessive effectiveness at heat capacity flow ratios of 0.25, on the other hand previous studies have showed that the inner convection coefficient is high [1]. The equation here under shows the Nusselt equations for the tube side of the heat exchanger referring to Mandals et al. work [12]

$$Nu = 0.08825 * Re^{0.7} * Pr^{0.4} * \lambda^{-0.1} \quad (16)$$

The equation (16) is valid for Re < 10000 and for the tube side Re is defined as:

$$Re = \frac{\rho * v * d}{\mu} \quad (17)$$

A correlation was developed for this specific shell side configuration at low Reynolds numbers (Re<2000), in this neither concurrent nor counter flow scheme (equation 18).

$$Nu = 100 * Re^{0.103} * Pr^{-0.66} \quad (18)$$

The Reynolds in the shell is calculated with the diameter of the coil as the characteristic length.

The velocity was calculated as:

$$v = \frac{\dot{m}}{\rho * D * L_{coil}} \quad (19)$$

And the Reynolds for the shell calculated as:

$$Re = \frac{\rho * v * D}{\mu} \quad (20)$$

3) *Comparison with parallel flow heat exchanger*

The Fig. 8, Fig. 9 and Fig.10 show a sample of the increases in NTU, effectiveness and overall heat transfer coefficient at different temperature differences between input and output of the shell of the CFI compared to the same values calculated for a parallel flow heat exchanger using the same heat exchanger length, volumes, materials, flows and temperatures. The heat capacity ratio was fixed at 0.25 the flow rates are of 4l/min in shell and 1l/min in tube.

Fig. 8. NTU against temperature difference in shell

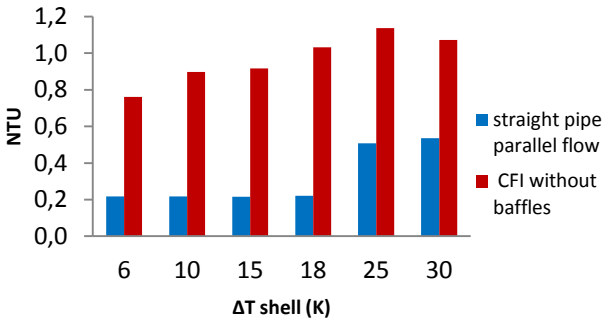

For the same flows, area, temperatures, the Coiled Flow Inverters NTU increases up to 300% compared to the parallel flow heat exchanger.
Fig.9 shows at the same conditions the increase in effectiveness.

Fig. 9. Effectiveness against temperature difference in shell

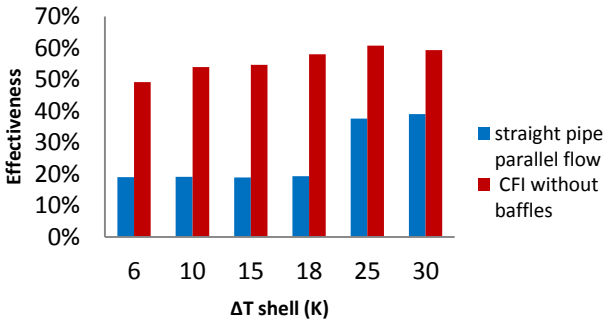

The effectiveness on the other hand increases of 200% compared to the parallel flow heat exchanger for certain temperature differences. The fig.10 shows the increase in overall heat transfer coefficient compared to the temperature difference of the shell side and at the same conditions as the previous

Fig. 10. Overall heat transfer coeffcient temperature difference in shell

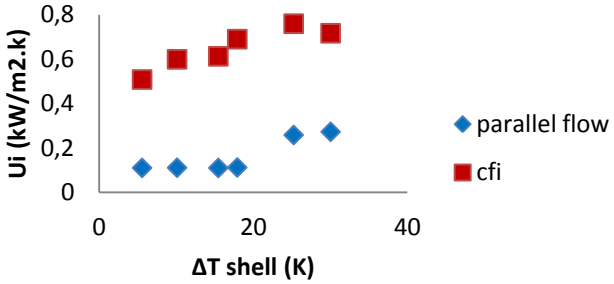

In its case the overall heat transfer coefficient of the Coiled Flow Inverter increases by 500% the overall heat transfer coefficient values of the parallel flow heat exchanger.

IV. Conclusion

In the present study attempts were made to determine under laminar conditions, experimentally complemented with numerical simulations the NTU effectiveness curves of the coiled flow inverter in a shell with neither concurrent nor counter flow paths. Validation of the models showed the highest temperature deviation between numerical and experimental of 1.4 Kelvin, this value was considered acceptable.

It is noted that the coiled flow inverter has a similar NTU effectiveness curve to the parallel flow heat exchanger, this one reaching effectiveness's of 80% at high NTU values of 4. A specific correlation has been proposed for the shell side Nusselt number.

Having the same NTU effectiveness curve tendencies, under the same conditions, the CFI result in higher NTU and effectiveness values than the straight parallel flow heat exchanger at the same heat capacity ratios, for example at c=0.25, the increases in NTU ranges from 100 to 350% the increase in effectiveness range from 50 to 200% and the increases in overall heat transfer coefficients range between 300 and 600%.

Finally it can be seen that the coiled flow inverter is more compact than the regular straight tube parallel flow heat exchanger, therefore this one may be of interest in diverse applications.

Further experimental studies should be performed to validate the proposed shell side Nusselt correlation. Tests could be performed to determine the NTU effectiveness curves of a CFI in a counter flow situation. It would also be interesting to compare this heat exchanger experimentally to other known heat exchangers.

V. ACKNOWLEDGEMENTS

The authors acknowledge the support from the Tecnológico de Monterrey through the Focus Group of Energy and Climate Change.

VI. References

[1] V. Kumar, M. Mridha, A. K. Gupta, and K. D. P. Nigam, "Coiled flow inverter as a heat exchanger," *Chemical Engineering Science*, vol. 62, pp. 2386-2396, 2007.

[2] M. Lomascolo, G. Colangelo, M. Milanese, and A. de Risi, "Review of heat transfer in nanofluids: Conductive, convective and radiative experimental results," *Renewable and Sustainable Energy Reviews*, vol. 43, pp. 1182-1198, 3// 2015.

[3] G. Y. Lin, X. H. Zhang, Z. Liu, and W. M. Yang, "Research on enhanced heat transfer characteristics in heat exchanger inserted with rotors," Wuhan, 2011, pp. 2517-2520.

[4] V. Kumar, S. Saini, M. Sharma, and K. D. P. Nigam, "Pressure drop and heat transfer study in tube-in-tube helical heat exchanger," *Chemical Engineering Science*, vol. 61, pp. 4403-4416, 7// 2006.

[5] J. Eustice, "Experiments on Stream-Line Motion in Curved Pipes," *Proceedings of the Royal Society of London. Series A*, vol. 85, pp. 119-131, 1911.

[6] W. R. Dean, "XVI. Note on the motion of fluid in a curved pipe," *Philosophical Magazine Series 7*, vol. 4, pp. 208-223, 1927/07/01 1927.

[7] G. I. Taylor, "The Criterion for Turbulence in Curved Pipes," *Proceedings of the Royal Society of London. Series A*, vol. 124, pp. 243-249, 1929.

[8] S. Vashisth and K. D. P. Nigam, "Experimental Investigation of Pressure Drop during Two-Phase Flow in a Coiled Flow Inverter," *Industrial & Engineering Chemistry Research*, vol. 46, pp. 5043-5050, 2007/07/01 2007.

[9] V. Kumar and K. D. P. Nigam, "Numerical simulation of steady flow fields in coiled flow inverter," *International Journal of Heat and Mass Transfer*, vol. 48, pp. 4811-4828, 11// 2005.

[10] M. Mridha and K. D. P. Nigam, "Numerical study of turbulent forced convection in coiled flow inverter," *Chemical Engineering and Processing: Process Intensification*, vol. 47, pp. 893-905, 5// 2008.

[11] J. Singh, N. Kockmann, and K. D. P. Nigam, "Novel three-dimensional microfluidic device for process intensification," *Chemical Engineering and Processing: Process Intensification*, vol. 86, pp. 78-89, 12// 2014.

[12] M. M. Mandal, V. Kumar, and K. D. P. Nigam, "Augmentation of heat transfer performance in coiled flow inverter vis-à-vis conventional heat exchanger," *Chemical Engineering Science*, vol. 65, pp. 999-1007, 2010.

[13] A. K. Saxena and K. D. P. Nigam, "COILED CONFIGURATION FOR FLOW INVERSION AND ITS EFFECT ON RESIDENCE TIME DISTRIBUTION," *AIChE Journal*, vol. 30, pp. 363-368, 1984.

Thermal performance and sensitivity analysis of a parabolic trough solar collector

P.D. Tagle-Salazar, C.I. Rivera-Solorio
Escuela de Ciencias e Ingeniería
Tecnológico de Monterrey, Campus Monterrey
Monterrey, N.L., México
pdtagle@gmail.com, rivera.solorio@gmail.com

Abstract— **This work shows the results of an experimental and theoretical analysis of a parabolic trough solar collector. The collector used for experiments was provided by a local enterprise. Experiments were based on the SRCC Standard 600, which evaluates a collector based on the thermal performance and the operational reliability, and it is used to certify the equipment internationally as an efficient and reliable system. Numerical analysis was made by computational simulations to determine thermal performance of the collector based on a steady-state one-dimensional thermal resistance model. The software used was Engineering Equation Solver, which can solve a non-linear equation system, useful to solve the correlations to calculate the heat transfer coefficients.**

A secondary part of the investigation was focused on the sensitivity analysis of the thermal efficiency varying ambient, designing and operational parameters. The results showed that, with the variables and ranges of the analysis, the principal variables that have a strong impact on the efficiency are design and operational parameters.

Finally, the data obtained with computational simulation and experiments were very similar, with a global error less than 10% in the thermal efficiency. This difference could be because of the accuracy of the instruments used on the experiments and the correlations used on the computational model.

Keywords— thermal performance; sensitivity analysis; thermal efficiency; parabolic trough; solar collector

I. INTRODUCTION (*HEADING 1*)

In the previous work, during 2010 and 2012, Agraz [1] and Mejía [2] realized the characterization and technical-economic analysis respectively of a parabolic-trough solar collector made by the enterprise they founded, which is called Inventive Power®. This model of collector was made for water-heating purposes in SMEs and residences; and it was tested on the Solar Energy and Thermo-Sciences Laboratory facilities of Tecnológico de Monterrey, Campus Monterrey. Table I shows the principal characteristics of the collector. Fig. 1 shows the testing system which consists in 4 collectors hydraulically connected in 2 lines (2 collectors each line). The valves in the system make the hydraulic configuration can be switched in serial or parallel. The system also has a pump, a storage tank, a drain pit and a tracking system. The tracking system is controlled by a panel and it can follow the sun automatically. Each line of collector has its own motor, so the tracking system can control both lines independently.

Performance tests were made by the ANSI 93 standard, which evaluates the thermal performance. This standard analyses the collector by three parameters: constant time, thermal efficiency and incident angle modifier. The final report shows these parameters for the collector designed and found some areas for improvement, including for the design itself.

In the later work, during 2013 and 2014, the authors realized the characterization and theoretical analysis of the same collector system. For the experiments, the SRCC Standard 600 was applied. This standard is related with the ISO 9806 standard, which evaluates the reliability and thermal performance of the collector. The reliability tests evaluate the collector resistance under extreme conditions to verify that the collector works on a safe and effective manner. The thermal performance analysis is similar than the ANSI 93 standard with the thermal efficiency model as the main difference. This work only presents the thermal efficiency results obtained during the investigation.

For the theoretical analysis, a one-dimensional thermal resistance model was used to simulate the heat transfer modes involved on the phenomena. This model is explained in detail later. The model was used to determine the sensibility of the collector at different design parameters, work and weather conditions; by comparing the efficiency curves obtained with the model and the constants of the thermal efficiency model used. The results are shown in this paper.

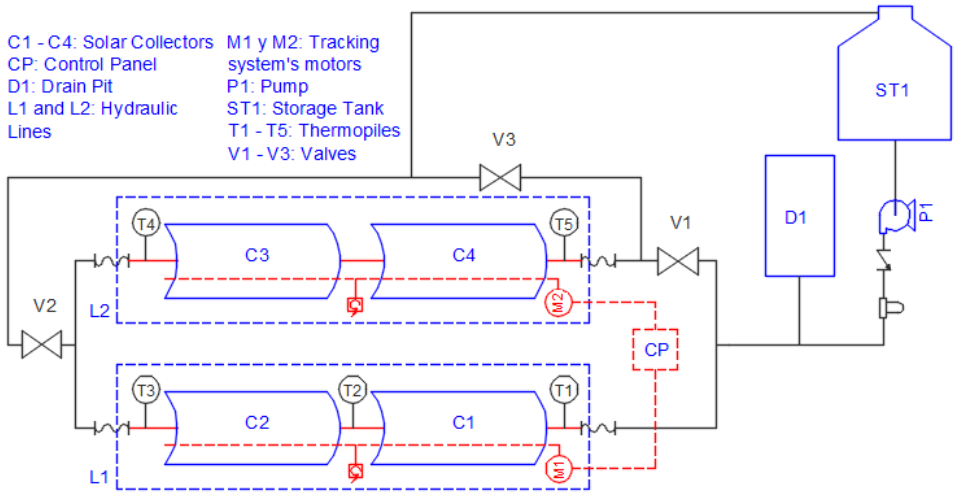

Fig. 1. Diagram of collector system

TABLE I. GENERAL CHACARTERISTICS OF THE COLLECTOR

Design	
Aperture (m)	1.1
Length (m)	2.44
Efective area (m^2)	2.68
Mirror	Anodized aluminum
Structure	Galvanized steel
Receiver	Copper, 3/4" type M, rigid pipe
Cristal cover	Borosilicate
Selective coating	Solkote
Weigth (kg)	26
Estimated lifespan (years)	>20
Thermal Performance	
Thermal efficiency (%)	>60
Mean Power (W)	1685
Temperature (C)	50 – 220

II. METHODOLOGY

The methodology used on the study consists in two parts: an experimental and a theoretical analysis data. Fig. 2 shows a flow diagram of the methodology. First; the parameters of design and operational conditions are established. Then, this data is used as input for both parts. The data obtained by experiments, in combination with the design and operational parameters, are analyzed according the standard ISO 9806 to obtain an experimental efficiency model. As a result of the theoretical analysis is obtained a numerical efficiency model and the sensitivity analysis. Finally, both models are compared. Each block of the flow chart is explained below.

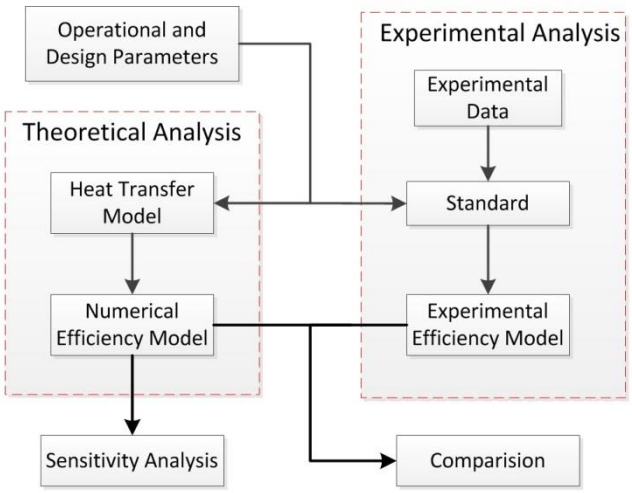

Fig. 2. Flow diagram of the methodology

A. *Operational and Design Parameters*

The operational parameters are defined as all variables that are involved with the work conditions of the collector that can be changed by the operator. The principal operational parameters are: inlet pressure, inlet temperature, fluid flow rate and working fluid. The design parameters are defined as all the data involved with the geometry and material characteristics of the collector. There are many of these parameters: material and diameter of receiver and cover glass, material of mirrors and supports, collector dimensions, optical properties for selective coating, etc. For this study; only the fluid flow rate, nominal diameter of receiver and type of receiver (glazed or unglazed) are taken in consideration in the sensitivity analysis. The working fluid is water only.

B. *Experimental Data*

The experimental data consists on the weather conditions and the experimental temperatures obtained. For the sensitivity analysis are considered the ambient temperature, wind velocity and incidence angle.

C. *Heat Transfer Model*

The heat transfer model is based on a one-dimensional and steady-state thermal resistance model where all the heat transfer mechanics involved on the phenomena are considered. This model is simulated by the Engineering Equation Solver, a software that can solve a non-linear equation system, and the code used on this study was developed by Forristall [3].

The fig. 3 shows the thermal resistance model and the heat transfer modes used. For conduction and radiation heat transfer modes, theoretical equations are used. For convection, the heat transfer is calculated with heat transfer coefficients obtained by correlations. Each heat transfer mechanism is explained below.

1) *Heat transfer to the working fluid*

The heat transfer mode is interior-forced convection. In the literature there are many correlations to calculate the heat transfer coefficient for this mode. The Gnielinsky correlation is considered for turbulent flow, and constant-heat-flux in long cylinder for laminar flow.

2) *Heat transfer trhough the receiver and glass cover*

The heat transfer mode is conduction. In both cases, the heat transfer is modeled as long isothermal cylinders.

3) *Heat transfer in annulus region*

The heat transfer modes presented here are: convection and radiation. For convection, the Raithby-Hollands correlation is used to calculate the heat transfer coefficient. The radiation heat transfer is modeled as long annular cavity with isothermal surfaces.

4) *Heat transfer to the ambient*

Similar to the annular region, the heat transfer modes presented are convection and radiation. Radiation heat transfer mode is modeled as a small gray-body in a long cavity (sky).

In this case, convection heat transfer depends on the external weather conditions, especially wind velocity on the surroundings of the receiver. To obtain the heat transfer coefficient, wind velocity is the "criteria parameter" to define the convection mode. For low wind velocity, convection is modeled as natural convection; and for high wind velocity, convection is modeled as external-forced cross-flow convection for long isothermal cylinder. This criteria is applied for the receiver in case it is unglazed.

5) *Heat transfer through supports*

The heat transfer model include the heat losses by supports. This heat transfer mode is considered as an infinite extended surface with constant cross area. The convection heat transfer coefficient is calculated as a heat transfer to the ambient.

D. *Standard*

As explained before, the standard used on the study is the SRCC Standard 600, which is related with the ISO 9806 standard. In this standard (ISO), the thermal efficiency model for concentrating collectors is a multilinear model. This model includes a transitional component for the efficiency called "effective thermal capacitance" [4]. For purposes of comparing the numerical and experimental data, thermal efficiency is taken as a steady-state model described on the standard. This model is shown in Eq. (1).

$$\eta \quad \eta_0 K \tau\alpha_1 \left(\frac{\theta_{in} - \theta_a}{G}\right) + \alpha_2 \left[G \left(\frac{\theta_{in} - \theta_a}{G}\right)^2\right] \tag{1}$$

$$T_m \quad \frac{\theta_{in} - \theta_a}{G} \tag{2}$$

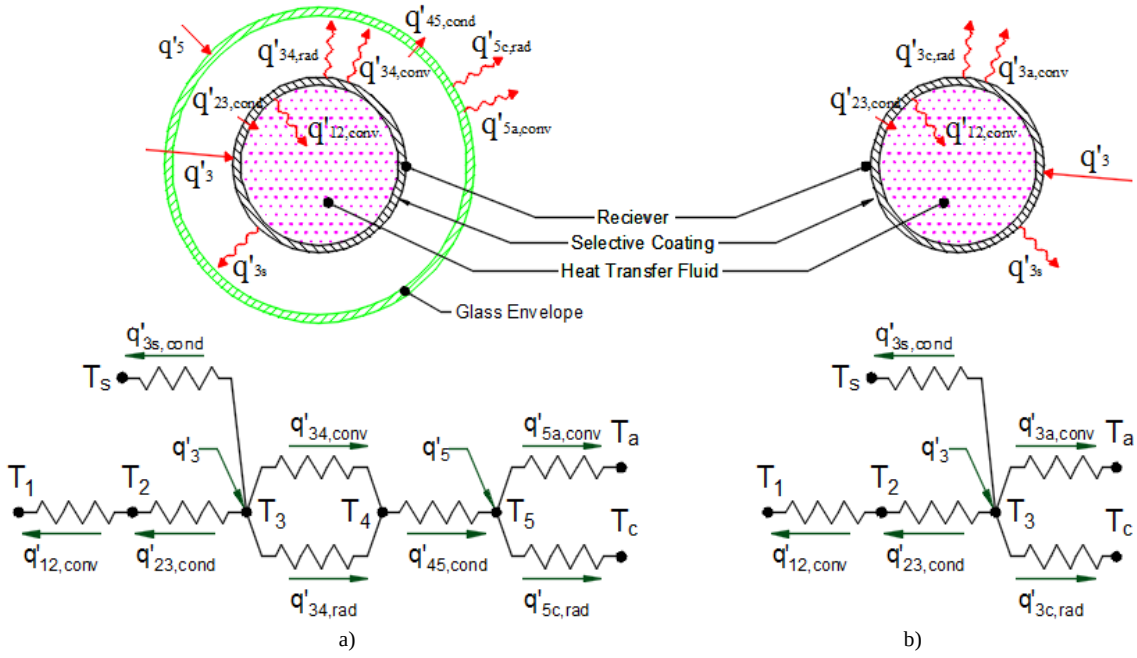

Fig. 3. Thermal resistance model for a) glazed receiver b) unglazed receiver

Where η (in %) is the thermal efficiency, η_0 (in %) is the peak thermal efficiency at 0 heat losses and normal incidence, K is the incident angle modifier, ϑ_a and ϑ_m (in °C) are the ambient and bulk mean temperature respectively, G (in W/m^2) is the global solar radiation at collector plane, T_{rm} (in m^2°C/W) is the reduced mean temperature, a_1 (in W/m^2°C) is the heat losses coefficient, and a_2 (in W/m^2°C^2) is the temperature-dependent heat losses coefficient. The first term ($\eta_0 K$) is the peak efficiency at 0 heat losses and incidence θ where $K=f(\theta)$. All the temperatures (fluid and ambient), global solar radiation and peak efficiency was taken as described in the standard in clear-sky days only and for incidence angles between 40 and 44 degrees. For calculating direct solar radiation on the collector plane, the Hottel model was used. This model is also used on theoretical analysis to determine the constants $\eta_0 K$, a_1 and a_2 for the sensitivity analysis.

E. Sensitivity Analysis

In concept, sensitivity is the uncertainty that input variables produce on an output variable. Mathematically, sensitivity can be expressed as a partial derivate of the output respect the inputs. Eq (3) describe the sensitivity calculated on this work. For this analysis, the constants of the thermal efficiency model are taken.

$$S \quad \left|\frac{\partial C}{\partial x_i}\right|_{max} \tag{1}$$

Where S is the sensitivity, C is the constant under analysis and x_i is the input variable. Table II describe the input variables and values analyzed for sensitivity, only on input "type of receiver" in not calculated. The derivate is obtained by a graphical method.

TABLE II. INPUT VARIABLES FOR SENSITIVITY ANALYSIS

Input	Values
Flow Rate (GPM)	0.75, 1.5, 3, 6.43
Ambient Temperature (°C)	15, 25, 30, 40
Wind Velocity (m/s)	0, 2, 5, 10
Incidence Angle (°)	0, 20, 40, 60
Nominal Pipe Diam. (in)	1/2, 3/4, 1
Type of Receiver	Glazed, Unglazed

Thermal efficiency curves are also used for sensitivity analysis. These curves are basically thermal efficiency vs. reduced mean temperature graphs, which help to visualize the change on the efficiency by changing one parameter at a time. In this graphs, one parameter changes values and the others are fixed according to a "base case". The values of the base case are shown in Table II as underlined values. This case defines the operational conditions of experiments.

III. RESULTS

Thermal efficiency curves obtained in the sensitivity analysis are shown from fig. 4 to fig. 9. They show that the efficiency has a considerable change under the influence of the incidence angle (fig. 7), where efficiency decreases faster than an increment of the incidence angle. This is due to the incident radiation decreases considerably while the incidence angle increases, so the energy transferred to the fluid also decreases. The influence of the type of receiver (fig. 9) shows that without a cover glass, the heat losses increases, making the efficiency decrease faster that a glazed receiver while reduce temperature increases; this is because that for an unglazed receiver, convection heat losses increases. The nominal pipe diameter (fig. 8) has an impact on the heat losses of the receiver. In this case, the flow rate is constant for all pipe diameters, but no the fluid velocity, and as know that for low fluid velocities the heat transferred to fluid decreases making the losses increase at high reduced temperatures. Fig. 6 shows that for wind velocity between 0 and 2 m/s, thermal efficiency curve has a significant change compared to the other curves. This is due to that while wind velocity increases, convection losses also increases but at a lower rate. For flow rate (fig. 4) it is observed that with a decrement of flow efficiency also decreases, because of the same reason explained for pipe diameter. Finally, fig. 5 shows that ambient temperature has a very low impact over the thermal efficiency. This is because heat losses do not depend on the ambient temperature but on the difference temperature respect with fluid temperature.

Table III shows the sensitivity values of each constant for all the parameters analyzed. The underlined values are the maximum sensitivity value for each constant. Peak efficiency at no-normal incidence ($\eta_0 K$) is more sensible to the incidence angle, as shown in fig. 7. Nominal pipe diameter has the biggest sensitivity for heat losses coefficient a_1, as shown in fig. 8; but it was also found that the type of receiver influences over this heat losses. For the temperature-dependent heat losses (a_2), the results show that is more sensible to the incidence angle. It can be observed that ambient temperature has the lowest sensitivity values, which suggest that thermal efficiency model do not depend on this temperature so has no influence over the efficiency, as was explained before.

TABLE III. SENSITIVITY VALUES FOR THERMAL MODEL CONSTANTS

Input	$\eta_0 K$	a_1	a_2
Flow Rate (GPM)	0.6667	5	0.03
Ambient Temperature (°C)	0.0011	0.0348	0.0009
Wind Velocity (m/s)	0.0667	3.3333	0.014
Incidence Angle (°)	1.25	0.258	0.442
Nominal Pipe Diam. (in)	0.14	112.144	0.096

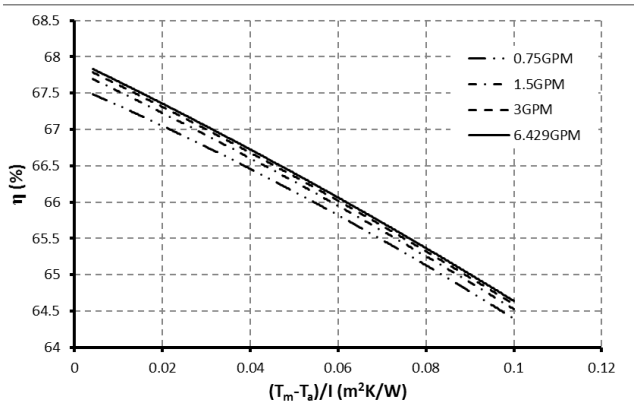

Fig. 4. Efficiency Curves at various Flow Rates

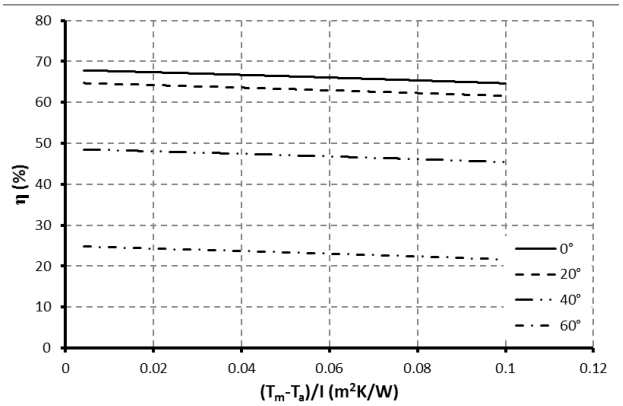

Fig. 7. Efficiency Curves at various Incident Angles

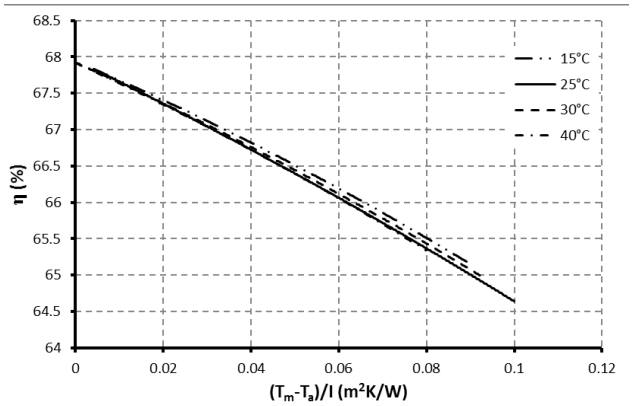

Fig. 5. Efficiency Curves at various Ambient Temperatures

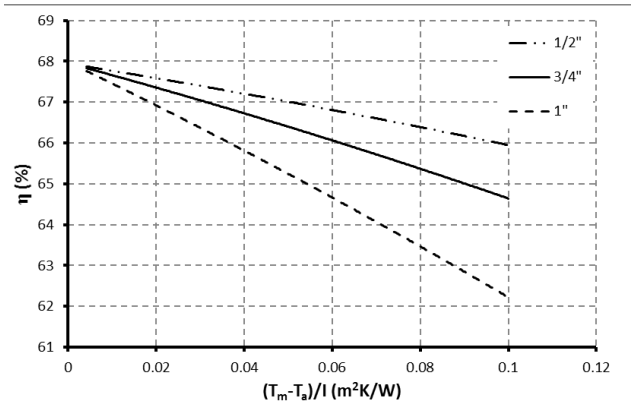

Fig. 8. Efficiency Curves at various Nominal Pipe Diameters

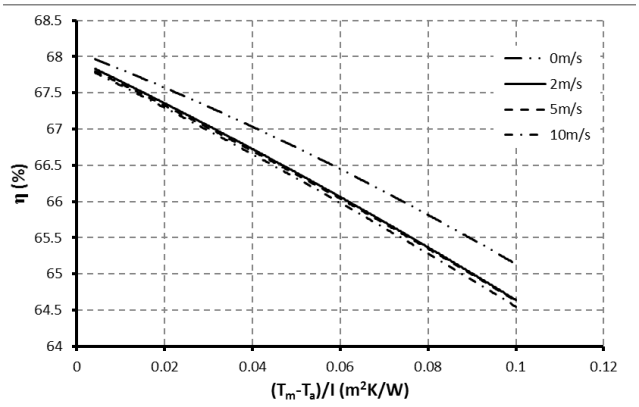

Fig. 6. Efficiency Curves at various Wind Velocities

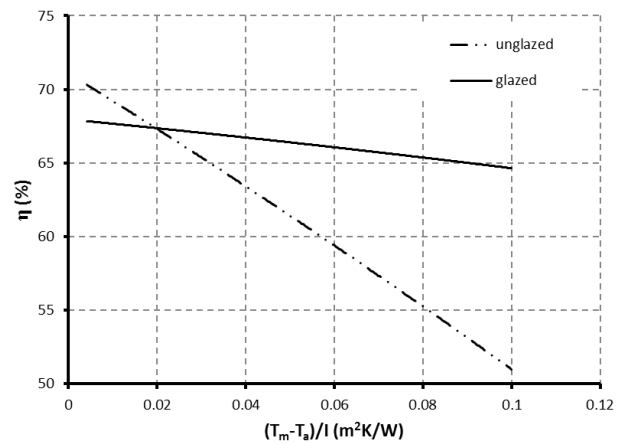

Fig. 9. Efficiency Curves for glazed and unglazed receiver

Fig. 10 shows the comparison of the model with experimental data. Lines are the numerical results of the model at the operational conditions of base case but at 40° and 44° of incidence angle. The experimental data is divided into 4 groups: C1, C2 which are the collectors no. 1 and 2 of the system (fig. 1), L1 and L2 are the lines no. 1 and 2 of the system where each line was taken as a simple collector. It is observed that almost all data is close to the limits predicted by the model, except for L2. The principal problem founded during experiments was that the tracking system did not operate correctly, so it was very difficult to align all the collectors to the sun with the tracking system in manual mode.

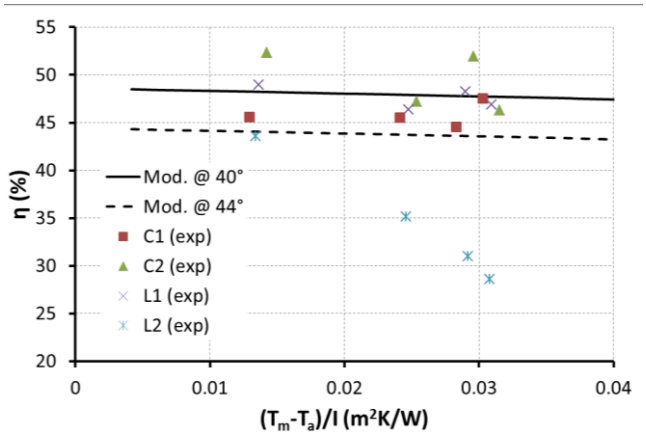

FIG. 10. COMPARISON WITH EXPERIMENTAL DATA

IV. CONCLUSIONS

For the sensitivity analysis it was founded that thermal efficiency is more sensible to the incidence angle, type of receiver and pipe diameter, wind velocity and flow rate has a low impact over the efficiency and that the ambient temperature has no significant influence. The peak efficiency at no-normal incidence is sensible to the incidence angle and thermal losses are sensible to the type of receiver and pipe diameter.

For comparison of experimental data and numerical model it was founded that the model predicts with a good precision what occurs on field. The difference between the data and the model were: the precision of the correlations used on the model, the precision of the thermopiles and other measurement instruments, and the difficulty of maintaining a steady-state work and weather conditions.

ACKNOWLEDGMENT

The authors acknowledge to Inventive Power S.A de C.V., to the Focus Group on Energy and Climate Change, and the Solar Energy Laboratory Staff of Tecnológico de Monterrey for their cooperation during this study.

REFERENCES

[1] A. Agraz, "**Metodología para la caracterización y optimización de un concentrador solar parabólico lineal," M.S. thesis, Eng. Sci. School., Monterrey, México, 2012.**

[2] A. Mejía, "**Análisis técnico-económico de un sistema de colectores solares parabólicos lineales," M.S. thesis, Eng. Sci. School., Monterrey, México, 2012.**

[3] R. Forristall, "Heat transfer analysis and modeling of a parabolic trough solar receiver implemented in Engineering Equation Solver," NREL, Golden, CO, Rep. NREL/TP-550-34169, 2003

[4] *Solar energy – Solar thermal collectors – Test methods*, BS EN ISO 9806, 2013

Sustainable production of hydrogen from synergy of Solid Oxide Fuel Cells and microreformers

Luciano Augusto Gerling*
Alejandro Montesinos-Castellanos**
School of Engineering and Information Technologies
ITESM
Monterrey, México
*aglg23@gmail.com
**alejandro_montesinos@itesm.mx

***Abstract*— The integration of solid oxide fuel cells (SOFCs) microreformers and biogas could offer a sustainable source of energy. The option of reforming biogas, through a combination of dry and steam reforming in a microreactor, using only anodic recirculation from the solid oxide fuel cells (SOFCs) was analyzed through simulations. The ratio of recirculation to avoid coking, the reactor size effect and the delivered energy in a mass of catalysts basis were explored. The results, shown that an increase in the recirculation ratio has a dilution effect, which cause a decrease in the yield of electric energy and an increase in the reactor volume necessary to hold the same conversion. A reflux ratio of 0.22 seems to be the better option, a smaller ratio will be susceptible to cooking and a larger will be inefficient.**

Keywords*— Biogas, Reforming, Fuel Cells, SOFC, Anodic Recirculation

I. INTRODUCTION

Fuel cells (FCs) transform the chemical energy into electricity, without mobile parts and in a compact space [1, 2]. Particularly the solid oxide fuel cells (SOFCs) has advantages over other kinds of FCs like: a relative lower cost of fabrication [3]; flexibility for use several kinds of feeds (H_2, CO, CH_4 and other hydrocarbons) such as biogas, without the drawback of deactivation; also the efficiency higher than 75%-85% in a combinated heat power (CHP) system [2]. Still, they have several issues for example: special materials are needed for the high temperatures; controllability of the load variations and startups; operating stress due to temperature gradients. Even more, SOFCs are exothermic systems operating from 800 to 1000°C. For guarantee a stable operation, it is necessary a heat sink; in this sense, this heat could be use by the reforming reactions in the microreformers, at 800-850°C in an integrated focus. This overlapping of the temperature conditions, makes the integration promising.

Internal and external reforming (InR and ExR respectively) are of great interested for integration, as a result of: the heat sink that they provide and that hydrogen is the most reactive of the several kinds of feeds that SOFCs can use [4]. Nevertheless, complete InR could result in carbon formation in the anode of the SOFC [5] and in temperature gradients, therefore a external reformer could be necessary. Some authors have research configuration of a SOFC-ExR system. For instance, R. Peters et al. [5] built a SOFC with a ExR, fed with natural gas (NG), steam and the recirculated gas from the anode. They found that in a steam-less condition, the anodic recirculation was enough to reformer the NG. Farhad et al. [10, 12] compared partial oxidation, steam reforming and anodic recirculation for a SOFC-ExR by simulation, finding that the gas recirculation has the highest electric efficiency of 42.4%, 45.1% for residential and industrials applications respectively. Kazempoor et al. [8] proposed several configurations considering chemical equilibrium and used recirculation from anode and cathode, they concluded that a pre-heater and recirculations improve the electric and CHP efficiencies. In this sense, anodic recirculation has been explored.

Even several authors have suggested the use of anodic recirculation, most of them considered the fuel as natural gas and use an steam carbon ratio (S/C) bigger than 2 [7, 11], which is the recommended for steam reforming (SR) of methane, but could have drawbacks for the combined stream (made of the NG and anodic recirculation). For obtain this S/C ratio, CO_2 is recirculated together with the steam, then the molar fraction of CO_2 is raised, which dilute the methane fraction and may block the active sites [5]. The net effect could be a decrease in the production rate of hydrogen, needing a larger reformer (for portable applications the size is an issue). Yaofan Yi et al. [13] determinate by simulation the optimum reflux ratios of a Siemens Westinghouse 25 kW tubular SOFC fed with several fuels at 750 °C, for biogas the better reflux ratio was of 30%, for coal syngas was 15% and for NG was of 40% instead of the 55% recommend by the manufacturer. Ming Liu et al. [14] found that a similar Siemens Westinghouse system has a higher electrical efficiency without recirculation, when gasification syngas is use. Therefore, there is evidence that type of feed affects the optimum recirculation ratio.

As Yaofan Yi et al. [13] and Ming Liu et al. [14] have shown that optimum recirculation rate changes with the feed. In particular the biogas composition of CH_4/CO_2 could varied from day to day [15]. This is variation is for a series of reasons, such as: changes in temperature, pH and the type of feed to the digester [15]. In places with a semi desert weather

conditions like the northern part of Mexico and southern of U.S., temperature may change hugely even in the same day, which could affect the digester conditions, if is not isolated. By analysis the effects of the anodic recirculation over the ratio of reformer agents to methane, the variations in biogas composition can be compensated. Therefore, an analysis of the recirculation is needed. This work focus on the effects of the reflux ratio, microreformer dimensions, number up (number of channels) and efficiencies. For doing so a deeper analysis of the thermodynamic of SR, DR (dry reforming) and combined are made, to check if a S/C > 2 condition is necessary; a kinetic model for the reformer considered, for taking in account the catalysis and space needed; and an analysis in the performance is done.

II. METHOLOGY

A. *Variables definition*

For compare the performance of the system, the following variables are defined:

- Water methane relationship (WMR)

$$WMR = \frac{F_{in\_H_2O}}{F_{in\_CH_4}} \tag{1}$$

where F_{in_H2O} and F_{in_CH4} are respectively the inlet molar flow of water and methane to the system.

- Carbon dioxide methane relationship (DMR)

$$DMR = \frac{F_{in\_CO_2}}{F_{in\_CH_4}} \tag{2}$$

this is similar to WMR but with CO_2 instead of water.

- Conversion (X) of the specie "i"

$$X_i = \frac{F_{in\_i} - F_{out\_i}}{F_{in\_i}} \tag{3}$$

where and are the inlet and outlet molar flows of the specie "i".

- Hydrogen production per methane mol fed (ϕ)

$$\phi = \frac{F_{out\_H_2} - F_{in\_H_2}}{F_{in\_CH_4}} \tag{4}$$

- Fraction of hydrogen output (ψ)

$$\psi = \frac{F_{out\_H_2}}{2F_{in\_CH_4} + F_{in\_H_2O} + F_{in\_H_2}} \tag{5}$$

where ψ is the fraction of the molecular hydrogen at the outlet versus one half of the inlet of atomic hydrogen in any form. A low ψ at high temperatures (>800°C) could indicate either an excess or a lack of reforming agents.

If the ratio of reforming agents/methane is too high, there will be a high ϕ, but a low ψ and y_{H2} (mole fraction) could be small, because the produced hydrogen is diluted by the excess of reforming agents.

- Finally the fraction of carbon deposition (Cfrac)

$$C_{frac} = \frac{F_{out\_Cs}}{F_{in\_CH_4}} \tag{6}$$

this represent the solid carbon versus the inlet of methane.

B. *Thermodynamic Analysis*

The minimization of the reaction Gibbs energy is used to solve problems of the equilibrium state (phase and chemical equilibrium). This method determinates the molar composition of each component in each phase, in function of the temperature and pressure, without given information of the reactions [16]. The minimization of Gibbs free energy is done using the lagrange multiplier method [17]:

$$\sum n_i (\Delta G_{f_i^0} + RT \ln(\frac{\hat{f}_i}{f_i^0}) + \sum \lambda_i a_{ik}) + n_c \Delta G_{fc(s)} = 0 \tag{7}$$

The software Aspen Plus 11.0 was used to solve this equation, with an Gibbs Reactor and the properties method was set to Redlich-Kwong-Soave. In order to break down the performance of the system, the thermodynamic analysis was divided in three parts: SR, DR and a combination of the last ones.

C. *Kinetics Analysis*

In the real world, many reactions take place simultaneously and would be impractical to make an analysis. So, in order to simplificate the system, only reforming reactions are considered:

$$CH_4 + CO_2 \leftrightarrow 2CO + 2H_2 \tag{8}$$

$$CH_4 + H_2O \leftrightarrow CO + 3H_2 \tag{9}$$

$$CH_4 + 2H_2O \leftrightarrow CO_2 + 4H_2 \tag{10}$$

$$CO + H_2O \leftrightarrow CO_2 + H_2 \tag{11}$$

The authors supposed, that no oxygen will enter the reactor and no coking will take place because of the conditions (the kinetics of the reaction 8 was taken from [18] and for the reactions 9-11 from [19]).

Even with these simplifications, a complex network of reactions is formed; the fig. 1 (where the dot lines represent consumption and the solid ones production) shows that the CO_2 is the only reactive that has two effects. In one hand, it reforms methane and in other, it consumes the hydrogen by the reverse the water gas shift (RWGS) reaction. So the concentration of CO_2 must be fixed appropriately.

The software used for the reactor simulation, was Comsol 4.2 and for the rest of the process was Aspen Plus 11.0. It was

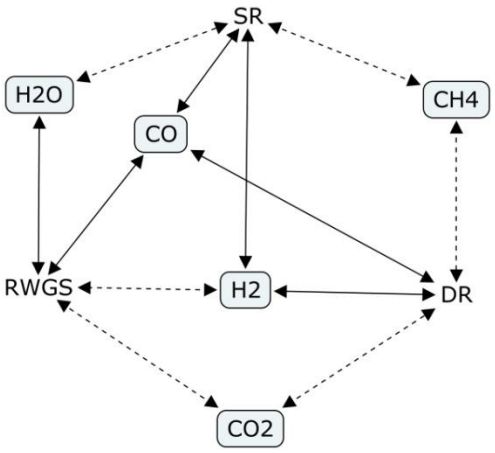

Fig. 1. Reforming reactions interactions

supposed that the biogas has a composition of 60% methane and 40% carbon dioxide; and that the pressure loss will be negligible. The fuel utilization of the SOFC is supposed to be 80% with an efficiency of 60%.

III. Results

A. Steam Reforming Thermodynamic Analysis

For this analysis, is assumed that only water and methane would enter the system. The parameters analyzed are: methane conversion (X_{CH4}), water conversion (X_{H2O}), ϕ, ψ and C_{frac}. These variables are in function of the temperature and the water methane relationship (WMR). The methane conversion is plotted in the fig.3-a. It shows a ticked effect, first the conversion decrease with the increase in the WMR, this is because water prevents the decomposition of methane and carbon monoxide. They following reactions clarify this point:

$$CH_4 + CO_2 \leftrightarrow 2C + 2H_2O \quad (12)$$

$$CO + H_2 \leftrightarrow C + H_2O \quad (13)$$

$$CH_4 + 2CO \leftrightarrow 3C + 2H_2O \quad (14)$$

Since these reactions are exothermic, at higher temperatures the curve starts shifting with less moisture

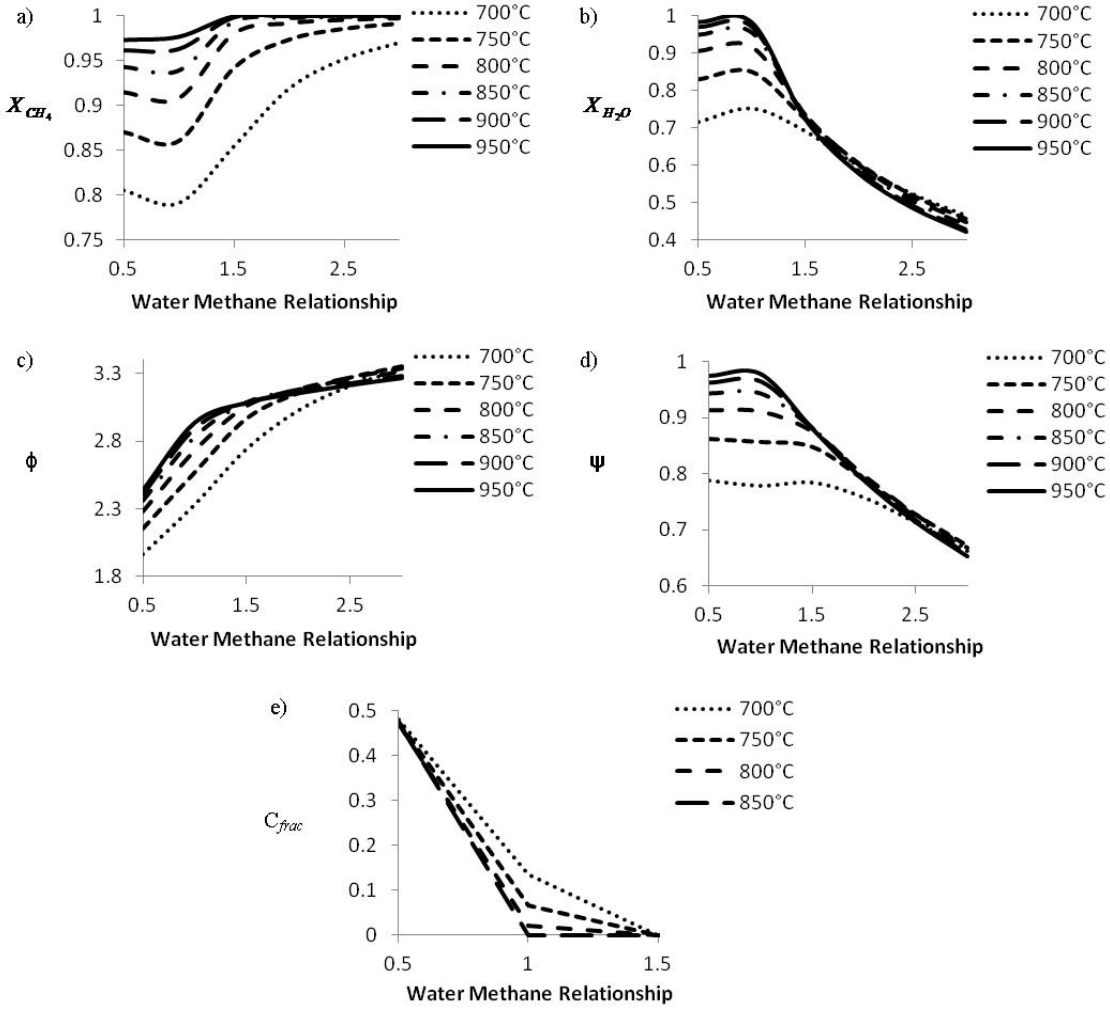

Fig. 2. Steam Reforming diagrams.

needed. The initial behavior of water conversion (fig.3-b), is opposite to X_{CH4}, and at higher WMR the X_{H2O} decrease because of it excess. It is use ϕ and ψ to measure the performance of the system. In the fig.3-c and 3-d, they show that increasing the WMR, rise ϕ; but not ψ, this because of the excess of water, this decrease y_{H2} and could affect the SOFC efficiency, because of the Nerst potential. Finally comes the carbon coking, in fig. 3-e it is seen that an increase of the WMR or the temperature will decreased it, and when the WMR gets bigger than 1.5, almost no coke is formed for the temperature range. The typical reported value used is WMR > 2 [6-9, 11].

B. *Dry Reforming Thermodynamic Analysis*

For this analysis, is assumed that only carbon dioxide and methane are present at the inlet of the system. The parameters that will be analyzed are: X_{CH4}, X_{CO2}, ψ (in this case ϕ is 2 times ψ) and the C_{frac}. All this parameters will be plotted against DMR for several temperatures.

The fig 4-a shows an increase in the X_{CH4} with the DMR and the temperature. As the DR reaction is endothermic and use CO_2 to reform methane, these conditions favors the equilibrium displacement to the products. Then in the fig. 4-b, it is seen an increase in the X_{CO2} with the temperature but a decrease with the DMR, since more CO_2 is present in the system. However, the optimal conditions for the conversion of CO_2 are a DMR near one and a temperature of 1000°C. The hydrogen production is plotted in the figure 4-c, where it is seen that for DMR ≈ 1 the higher production is reached. This is because different reactions are taking place and are in opposite sides. An increase in the temperature and CO_2 levels promotes DR reaction rate but also the RWGS, so the optimum relationship of DMR is $CO_2/CH_4 \approx 1$ at 1000°C. Finally the carbon deposition (fig. 4-d), similar to the SR it is reduce with the increase of the temperature and the reforming reagents, in this case CO_2. Nevertheless, it is required a bigger relationship of DMR than WMR to prevent the coking at the same temperature, when reforming only with CO_2, the system needs to operate at high temperature (T > 1000°C) and a DMR > 1. This is in agreement, with several theoretical calculations, for example, J. Bradford et al. [20] concluded that in order to avoid coking, a high operation temperature is need (T>1000 K) and DMR bigger that the unit.

C. *Combinated Reforming Thermodynamic Analysis*

In the last section, it is show that DMR further than one will have several drawbacks in the production of hydrogen, and lower to one would produce coking. For these reason, it was used a DMR near and slightly up to one and two cases where analyzed. The first case has a WMR of 0.44 and DMR of 1.03; the second case has WMR of 0.5 and DMR of 1.08 (these molar relationships are achieved by adjusting the recirculation ratio). The two cases where very similar, the bigger difference is the preheat temperature necessary to avoid coking. The case 2 has a bigger ratio of recirculation than case 1, therefore, has bigger WMR and DMR, so it need less preheat. However, the difference is just of 10°C so either condition could work. The other difference is the optimum temperature for the hydrogen production, because the case 2 has more CO_2, and this reacts in the RWGS reaction, a decrease of 25°C is observe in the optimum temperature. Results are shown in the table 1.

TABLE I. COMBINATED STEAM AND DRY REFORMING. CASE 1 WMR = 0.44 AND DMR = 1.03. CASE 2 WMR = 0.5 AND DMR = 1.08.

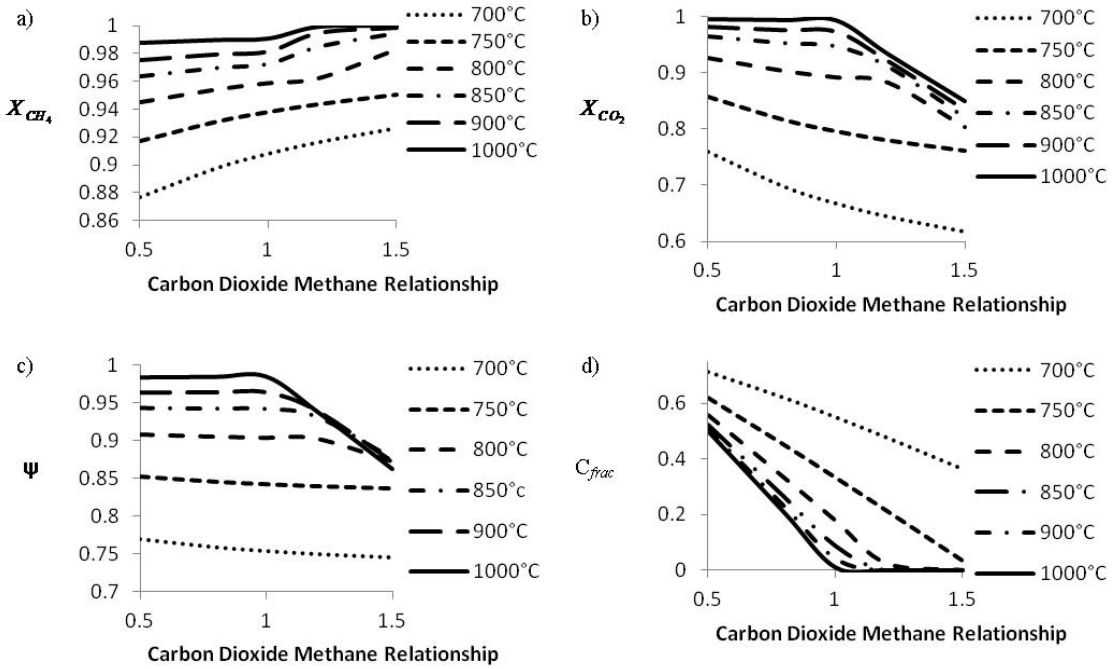

Fig. 3. Dry reforming diagrams.

	Case	
	1	*2*
Preheat Temperature [°C]	750	740
Optimum Temperature [°C]	850	825
Max ψ at Optimum Temperature	0.88	0.86
Max φ at Optimum Temperature	2.15	2.15

D. Initial Rate Kinetics Analysis

Fig. 5 shown that the recirculation has a dilution effect and makes the rates go slower, so it will be unwise to recirculated more than necessary. This is because, the recirculation will raises the WMR and DMR, but the y_{CH4} will decrease and the net effect is shrinking the hydrogen production. In the other hand, the temperature has an exponential effect in the reaction rate.

E. Reflux Overall Effect Kinetics Analysis

This analysis considering a system with reflux, similar to the one in the fig. 5 at a temperature of 850°C. As is expected the WMR and DMR will grow with the reflux ratio (fig. 6). However, at a reflux ratio of 0.22, ψ presents its maximum value of 0.87, close to the thermodynamic maximum is of 0.88. It also was found, that the number of the microreformers necessary to process the same amount of biogas grows with the reflux and a decrease of the power generation in a mass of catalysts basis. This is because; the recirculation has a dilution effect.

In the other hand, the electric per mol of CH_4 is 10% higher at a reflux ratio of 0.65 than at 0.22, however, this study does not take in account the effect lowering y_{H2} and y_{CO} over the Nerst potential, from reported models [6-9, 11] it can be expected a decrease in the power output with the decrease in y_{H2}. Therefore, a reflux ratio of 0.22 seems to be the better option for getting the highest ψ, a smaller ratio will be

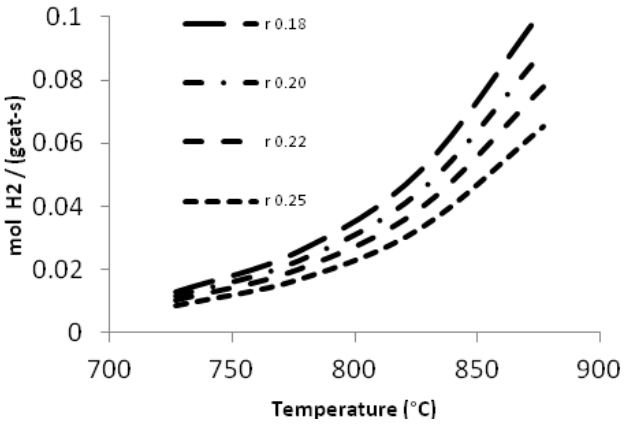

Fig. 4. Initial rate of hydrogen production.

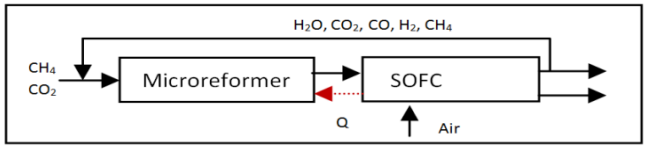

Fig. 5. Simplified process diagram.

susceptible to cooking and a larger will be inefficient.

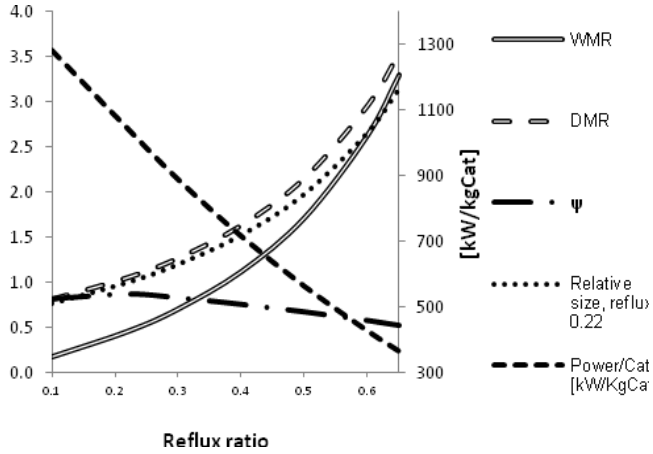

Fig. 6. Performance of the system vs recirculation.

CONCLUTIONS

From this study, it is concluded the following:

- Observing the reactions diagram, even considering only three reactions a complex network of interactions is formed. From this, it is concluded that it is important to fix carefully the WMR and DMR of the system, for avoid coking without dropping the hydrogen production.
- From the thermodynamic study, it was found that the DMR equal to one, will minimize the coking, previous works had noted these condition [17, 21]. Also is reported that CO_2 can block the active sites [5]. Besides it was seen that a DMR bigger than one, promotes the RWGS reaction, and so the consumption of hydrogen. For these reasons, it is concluded that the DMR must be near one.
- From the initial rate analysis, it was found that an excess in the recirculation for raises the DMR and the WMR, these makes an dilution effect, which have a global drawback in the hydrogen production. For this reason, the recirculation must be fixed to get only the needed of DMR (1.03) and WMR (0.44).
- The reflux analysis, confirmed that the dilution effect, so the reactor size that will go up and the power generation in a mass of catalysts basis will go down with the excess of recirculation. Therefore, it will have

a direct impact in the cost of the system, which can make the distributed power generation unviable.

- Reflux ratio of 0.22 seems the better option. However, the preheat temperature must be carefully fixed. If the stream enters below 750 °C to the microreformer, coking could happen.

REFERENCES

[1] Junxiang Shi, X.X., *CFD analysis of a novel symmetrical planar SOFC design with micro-flow channels.* Chemical Engineering Journal, 2010. **163**: p. 119-125.

[2] Xiongwen Zhang, S.H.C., Guojun Li, H.K. Ho, Jun Li, Zhenping Feng, *A review of integration strategies for solid oxide fuel cells.* Journal of Power Sources, 2010. **165**: p. 685-702.

[3] Brian D. James, A.B.S., Whitney G. Colella (2012) *Manufacturing Cost Analysis of Stationary Fuel Cell Systems*.

[4] M. Lo Faro, V.A., P.L. Antonucci, A.S. Aricò, *Fuel flexibility: A key challenge for SOFC technology.* Fuel 2012. **102**: p. 554-559.

[5] R. Peters, E.R., P. Cremer, *Pre-reforming of natural gas in solid oxide fuel-cell systems.* Journal of Power Sources, 2000. **86**: p. 432-441.

[6] Vincenzo Liso, A.C.O., Mads Pagh Nielsen, Søren Knudsen Kær, *Performance comparison between partial oxidation and methane steam reforming processes for solid oxide fuel cell (SOFC) micro combined heat and power (CHP) system.* Energy, 2011. **36**: p. 4216-4226.

[7] L. Barelli, G.B., F. Gallorini, A. Ottaviano, *An energetic and exergetic comparison between PEMFC and SOFC-based micro-CHP systems.* International Journal of Hydrogen Energy, 2011. **36**: p. 3206-3214.

[8] P. Kazempoor, V.D., F. Ommi, *Evaluation of hydrogen and methane-fuelled solid oxide fuel cell systems for residential applications: System design alternative and parameter study.* International Journal of Hydrogen Energy, 2009. **34**: p. 8630-8644.

[9] Dimitrios Georgis, S.S.J., Ali S. Almansoori, Prodromos Daoutidis, *Design and control of energy integrated SOFC systems for in situ hydrogen production and power generation.* Computers and Chemical Engineering 2011. **35**: p. 1691-1704.

[10] Siamak Farhad, F.H., Yeong Yoo *Performance evaluation of different configurations of biogas-fuelled SOFC micro-CHP systems for residential applications.* international Journal of hydrogen energy, 2010. **35**: p. 3758-3768.

[11] Vincenzo Liso, Y.Z., Nigel Brandon, Mads Pagh Nielsen, Søren Knudsen Kær, *Analysis of the impact of heat-to-power ratio for a SOFC-based mCHP system for residential application under different climate regions in Europe.* International Journal of Hydrogen Energy, 2011. **36**: p. 13715-13726.

[12] Siamak Farhad, Y.Y., Feridun Hamdullahpur, *Effects of fuel processing methods on industrial scale biogas-fuelled solid oxide fuel cell system for operating in wastewater treatment plants.* Journal of Power Sources, 2010. **195**: p. 1446-1453.

[13] Yaofan Yi, A.D.R., Jacob Brouwer, G. Scott Samuelsen, *Fuel flexibility study of an integrated 25kW SOFC reformer system.* Journal of Power Sources, 2005. **144**: p. 67-76.

[14] Ming Liu, A.L., W. Halliop, V.R.M. Cobas, A.H.M. Verkooijen, P.V. Aravind, *Anode recirculation behavior of a solid oxide fuel cell system: A safety analysis and a performance optimization.* International Journal of hydrogen energy, 2013. **38**: p. 2868-2883.

[15] E.P. Sánchez-Hernández, P.W., R. Borja, *The effect of biogas sparging on cow manure characteristics and its subsequent anaerobic biodegradation.* International Biodeterioration & Biodegradation, 2013: p. 10-16.

[16] Jianjun Xie, D.S., Xiuli Yin, Chuangzhi Wu, Jingxu Zhu, *Thermodynamic analysis of aqueous phase reforming of three model compounds in bio-oil for hydrogen production.* International Journal of Hydrogen Energy, 2011. **36**: p. 15561-15572.

[17] Yunhua Li, Y.W., Xiangwen Zhang, Zhentao Mi, *Thermodynamic analysis of autothermal steam and CO2 reforming of methane.* International Journal of Hydrogen Energy, 2008. **33**: p. 2507-2514.

[18] Unni Olsbye, T.W., Leslaw Mleczko, *Kinetic and Reaction Engineering Studies of Dry Reforming of Methane over a Ni/La/Al_2O_3 Catalyst.* Ind. Eng.Chem. Res., 1997. **36**: p. 5480-5188.

[19] Kaihu Hou, R.H., *The kinetics of methene steam reforming over a Ni/α-Al_2O.* Chemical Engineering Journal, 2001. **82**: p. 311-328.

[20] Vannice, M.C.J.B.M.A., *CO2 Reforming of CH4.* Catalysis Reviews Science and Engineering, 1999. **41**: p. 1-42.

[21] A. Effendi, Z.-G.Z., K. Hellgardt, K. Honda, T. Yoshida, *Steam reforming of a clean model biogas over Ni/Al_2O_3 in fluidized and fixed bed reactors.* Catalysis Today, 2002. **77**: p. 181-189.

Analyzing the stiffness of a rotor with triangular cross fracture

H. Jiménez, G. Alvarez
Department of Energy
UAM Azcapotzalco
México D. F., MÉXICO
hjr@correo.azc.uam.mx, gdam@correo.azc.uam.mx

***Abstract*—In this work, the stiffness of a rotor with triangular cross fracture in the middle part, within its elastic range, in static condition, simply supported at its ends and middle concentrated load is determined. The functional relationship for the variation of second area moment of their different cross sections is deduced. It was calculated the slope and deflection by numerical integration double obtaining its elastic curve and the frequency range in which the fractured rotor resonates. Additionally the numerical solution to the critical orientation of the fracture was obtained. The calculated values for the rotor fractured are compared with corresponding values to the rotor without fracture, including the comparison the result of the numerical solution. The above parameters were calculated based on the angle of orientation of the fracture with respect to the normal line. From the values obtained it is concluded that, given the geometry of the rotor and of the fracture, the load applied, the support conditions and physical properties of the material and considering the birth and growth of the fracture; there are some frequencies of resonance for the rotor with fracture, in relation with the rotor without fracture, where the last one just have one resonance frequency. The variation between the first resonance frequency of the rotor with fracture and the value of the frequency of the rotor without fracture is of the order of a quarter for the same conditions.**

Keywords—fracture; numerical integration; numerical simulation; resonance; stiffness

I. INTRODUCTION

The birth and growth of a fracture in a rotor can cause rupture with catastrophic effects [1]. In recent years there have been investigations to timely detection of a rotor fracture, monitoring the mechanical, thermal and acoustic fields. On the other hand, it also has been studied the influence of the opening and closing mechanism in the performance of the rotor. Additional to this, the variation of second area moment of their different cross sections, as a function of the orientation of the fracture in the life of the rotor were also investigated.

Numerous fracture modelling techniques were reported by G. Sabnavis, R. G. Kirk, M. Kasarda and D. Quinn [2] and by V. Kumar and C. Rastogi [3].

II. NOTATION

a = Fracture width = 1 mm.

b = Fracture depth (mm).

$\frac{dY}{dX}$ = Slope, dimensionless.

E = Young's modulus [2] = $1.94 * 10^6 \frac{Kg}{cm^2} = 190314 \frac{N}{mm^2}$, stainless steel 18-8.

F = Vertical force applied in the middle of the rotor = 100 N.

I_{sf} = Second area moment, no fracture, with respect to X (mm^4).

I_{cf} = Second area moment, fractured, with respect to X (mm^4).

I_c = Second area moment, a circle, with respect to X (mm^4).

I_{sc} = Second area moment, the circular sector, with respect to X (mm^4).

I_{st} = Second area moment, the triangular sector, with respect to X (mm^4).

k = Stiffness N/mm.

L = Rotor length = 160 mm.

M = Bending moment (N.mm).

p = Maximum depth of fracture = 1.25 mm.

r = Rotor radius = 5 mm.

(X, Y, Z) = Inertial coordinate system.

X = Longitudinal coordinates of the rotor.

Y = Vertical transverse coordinates the rotor.

Z = Horizontal transverse coordinates the rotor.

(x, y, z) = Coordinates system fixed to the rotor.

x = Longitudinal coordinates of the rotor.

y = Transverse coordinates of the rotor, in first position, vertical.

z = Transverse coordinates of the rotor, in first position, horizontal.

α = Orientation angle of the fracture = angle between the z axis and Z axis, in first position $\alpha = 0^0$.

β = Fracture angle in the xz plane, invariant without opening and closing = 21.80140949^0.

δ = Fracture angle parallel to yz plane, variable based on x

Δ = Maximum deflection of the rotor (mm).

γ = Maximum angle of fracture on plane parallel to yz = 41.40962211^0.

$\varphi_i = \alpha - \delta$ = Angle, with respect to Z axis, in which initiates the fracture on plane parallel to yz plane.

$\varphi_f = \alpha + \delta$ = Angle, with respect to Z axis, in which ends the fracture on plane parallel to yz plane.

ρ = Density of the rotor = 0.000007817 Kg/(mm^3), stainless steel 18-8.

ω = Resonance frequency in radian per second.

III. Coordinates Sistems

The origin of inertial coordinate system (X, Y, Z), is located on the middle of the left side of the rotor cross section as shown in Fig. 1. The X axis coincides with the longitudinal axis of the rotor. The Y axis is transverse to the rotor and vertical. The Z axis is transverse to the rotor and horizontal.

The origin of the coordinates system fixed to the rotor, (x, y, z), coincides with the origin of the inertial coordinates system (X, Y, Z). The x axis coincides at all times with the X axis. The z and y axes are moved together with the rotor. In Figure 1 is shown the condition of the rotor for α = 0°, that is, consider that the fracture is represented by its external surface, then it is possible to assign a normal unit vector to this surface, then α = 0° if the normal unit vector of the surface is parallel and with the same sense to the Z axis. In Fig. 2 it is shown the condition for α = 90°. From Fig. 1 and Fig. 2 it follows that the rotation is positive in the counterclockwise observed from the left side of the rotor.

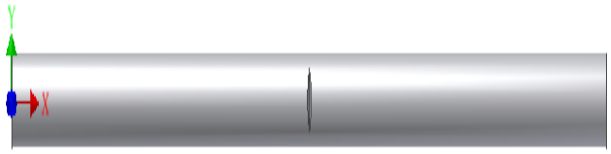

Fig. 1. Inertial coordinates system, with the rotor in starting position, α = 0°.

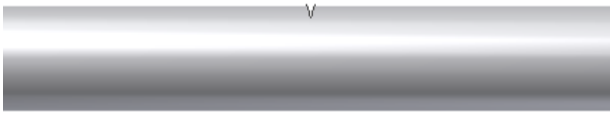

Fig. 2. Fracture in the rotor oriented in the direction and sense of Y axis, α = 90°.

IV. Second Area Moment

For the second area moment, in Fig. 3 the dimensions of the rotor are shown along with its longitudinal axis, in Fig. 4, a detail of the longitudinal section in the x-z plane is shown; from these figures, (1), (2) and (3) are obtained.

$$\beta = arc\ tg\left(\frac{a}{2p}\right) \quad (1)$$

$$\frac{a}{2p} = \frac{x-0.5(L-a)}{b} \quad (2)$$

$$b = \frac{2px-p(L-a)}{a} \quad (3)$$

Where $a = 2\overline{AE}$ $p = \overline{AB}$ and $b = \overline{CD}$.

A representation of the cross section rotor along with its fracture is represented by a combination of several sections, complete circular section of radius *r*, a circular sector and a triangular sector [4] as shown in Fig. 5; from which.(4) is obtained. In the limit, when the parameter *b* tends to parameter *p*, (4) becomes in (5).

$$\delta = arc\cos\left(\frac{r-b}{r}\right) \quad (4)$$

$$\gamma = arc\cos\left(\frac{r-p}{r}\right) \quad (5)$$

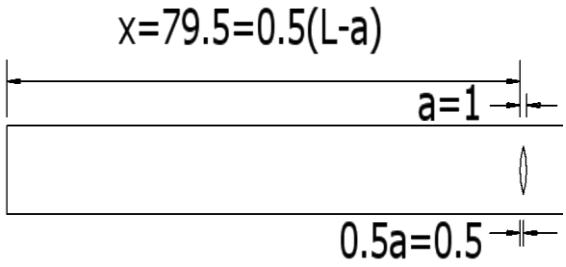

Fig. 3. Rotor dimensions along the X axis.

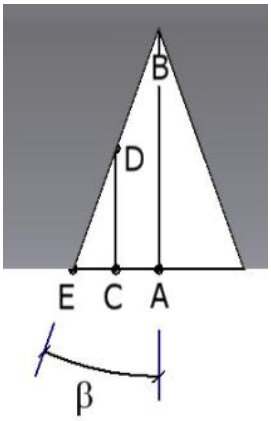

Fig. 4. Fracture detail, α = -90°.

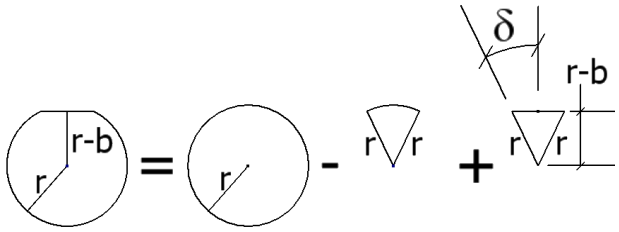

Fig. 5. Cross Section CD, in plane parallel to the yz plane.

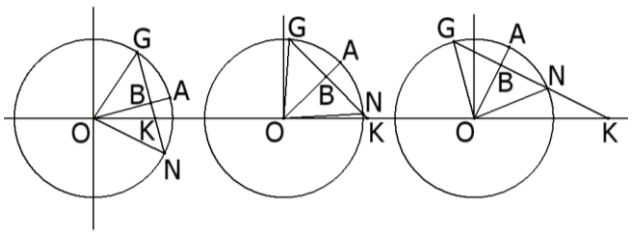

Fig. 6. Cross section of the rotor, in the area of the fracture. $\alpha = BOK$.

In Fig. 5, the second area moment can be obtained with (6) in which the moment Ic and the moment Isc, parameters are given by (7) and (8).

$$I_{cf} = I_c - I_{sc} + I_{st} \quad (6)$$

$$I_c = \pi \frac{r^4}{4} \quad (7)$$

$$I_{sc} = \frac{(\varphi_f - sen\varphi_f cos\varphi_f) - (\varphi_i - sen\varphi_i cos\varphi_i)}{2}\left(\frac{r^4}{4}\right) \quad (8)$$

A cross section of the rotor in the area of the fracture when growing α is shown in Fig. 6. The fissure is represented by the AGNA area. For subparagraph a of Fig. 6 the triangular OGNO area, is equal to the OGKO area plus OKNO area; for b and c of Figure 6 is equal to the OGKO area minus OKNO area.

Equation (9) is obtained from Fig. 6, along with Fig. 5. This equation is transformed in (10), using trigonometric identities and simplifying.

$$\frac{1}{12}\left(\frac{r-b}{cos\alpha}\right)[rsen(\alpha+\delta)]^3 - \frac{1}{12}\left(\frac{r-b}{cos\alpha}\right)[rsen(\alpha-\delta)]^3 \quad (9)$$

$$I_{st} = \frac{r^4[3sen\delta\,(sen\alpha)^2(cos\delta)^3 + cos\delta\,(cos\alpha)^2(sen\delta)^3]}{6} \quad (10)$$

Substituting (7), (8) and (10) into (6) we obtain the expression of the second area moment I_{cf}, in the zone of the fracture, this expression is parameterized in terms of α and X. In Fig. 7 is shown the variations of the I_{cf} for four values of α and X.

Note that in the fracture region (79.5 - 80 mm.) I_{cf} decreases while X increases, on the other hand, the influence of α on I_{cf} affects significantly, when α increases, I_{cf} not only decreases, the ratio of decreasing is greater.

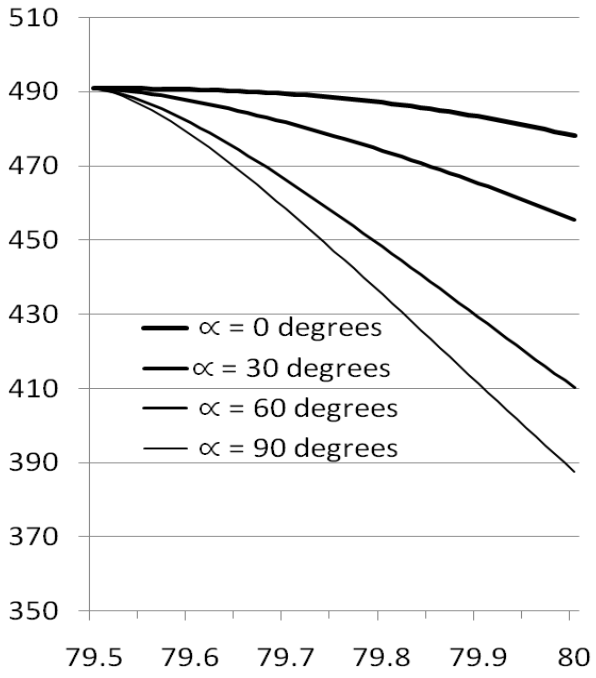

Fig. 7. Second area moment in the fracture for α = 0°, 30°, 60° and 90°

V. Slopes and Deflections

The slopes and the deflections denote mechanical characteristics on the dynamics rotors, the structural behaviour of rotors is affected by the presences of fractures, and then in this section we analyze the presence of a fracture, evaluating the slopes and deflection of the rotor near to its fracture.

Applying the Timoshenko beam theory and by numerical integration procedure to (11), the slopes and deflections of the rotor are obtained. In Fig. 8 and Fig. 10, the slops and deflections of the rotor are shown respectively, and corresponds to half of the rotor (X=0, X=80).

$$\frac{d^2Y}{dX^2} = \frac{0.5F}{E}\frac{X}{I_{cf}} \quad (11)$$

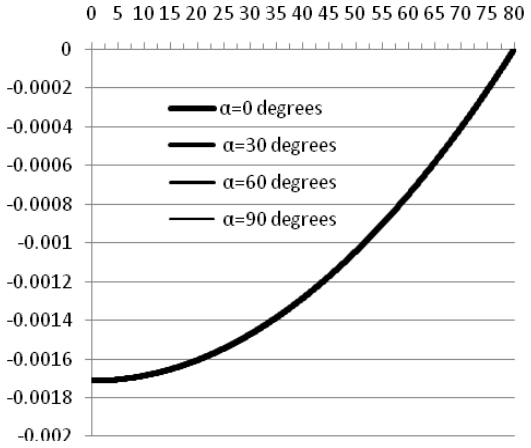

Fig. 8 Slopes for α = 0°, 30°, 60° and 90 °, for (X=0, X=80).

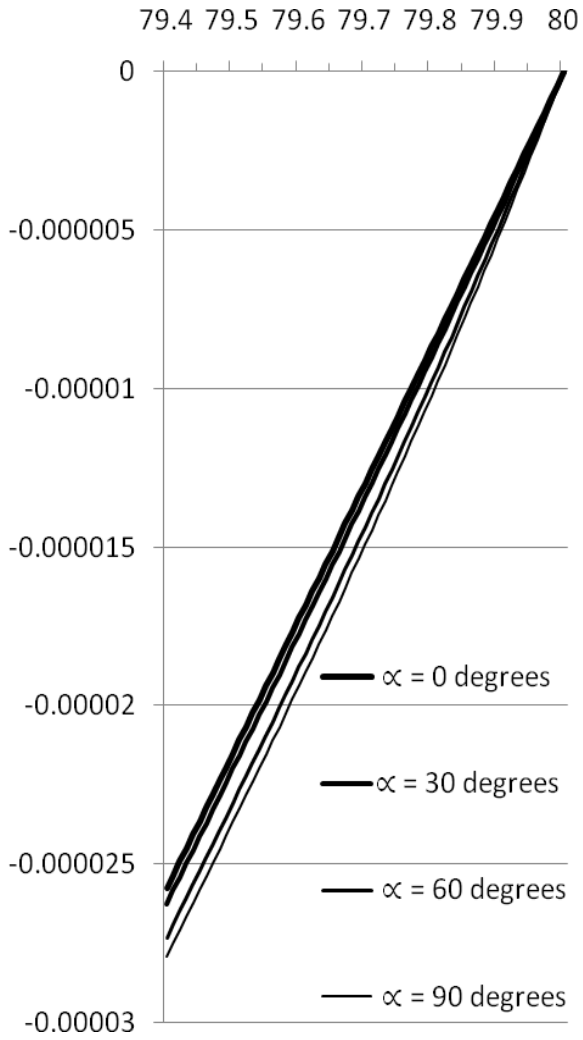

Fig. 9. Slopes in the zone of the fracture for α = 0°, 30°, 60° and 90°, for range near to the fracture (X=79.4, X=80)

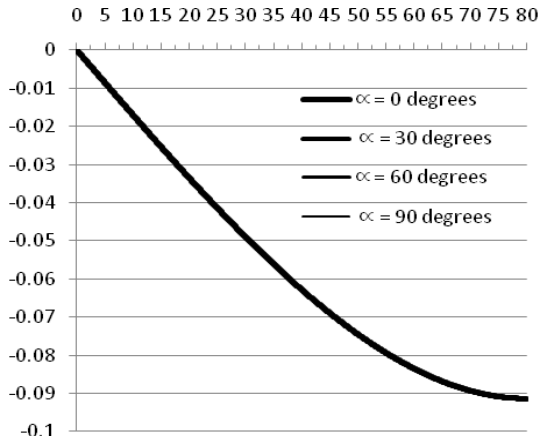

Fig. 10. Deflections for α = 0°, 30°, 60° and 90°, for (X=0, X=80).

In Fig. 9 and Fig. 11, the slopes and deflections are shown for the case near of half of the fracture (X=79.5-ε, X=80), where $|\varepsilon| = 0.1$. In each case, the slopes and deflections are shown for α = 0^0, 30^0, 60^0 and 90°, Fig. 8 and Fig. 10 are displayed as a single curve due to the scale. In Fig. 9 and Fig. 11 are clearly differentiated the four curves.

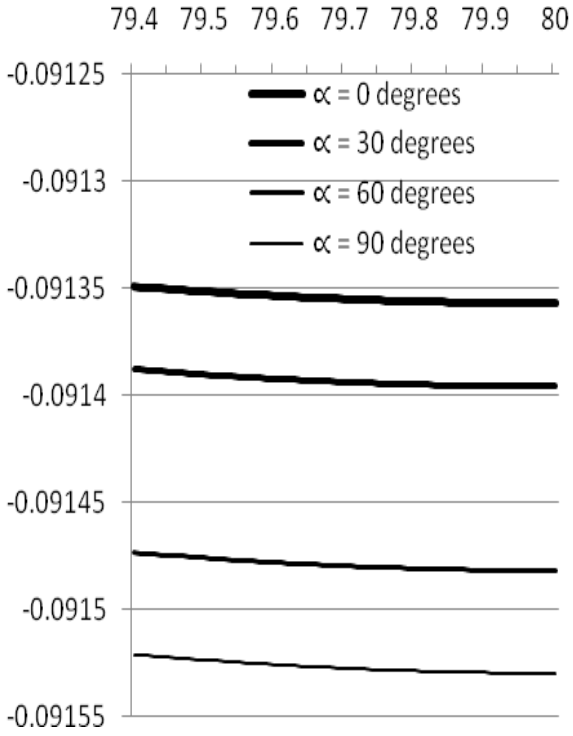

Fig. 11. Deflections in the zone of the fracture to α = 0°, 30°, 60° and 90°, for range near to the fracture (X=79.4, X=80)

VI. Stiffness and Resonance Frequency

From the numeric results of the deflections of the rotor with a fracture, we have determined a correlation between the stiffness of the rotor and its natural frequency.

In Fig. 11 is shown a graphic of the deflections for α = 0°, 30°, 60° and 90°, then considering the expression for the natural frequency of a rotor on static conditions, which depends on the deflections, then we can determine a spectrum of natural frequencies, that for each α, there exists one deformation and one natural frequency. We must mention that in this case the fracture was modelled without damping, for this reason the resonance frequency, approaches to the natural frequency.

In Fig. 12 shown the range of stiffness calculated from the deflections. For this range the spectrum of resonance frequencies is shown in Fig. 13.

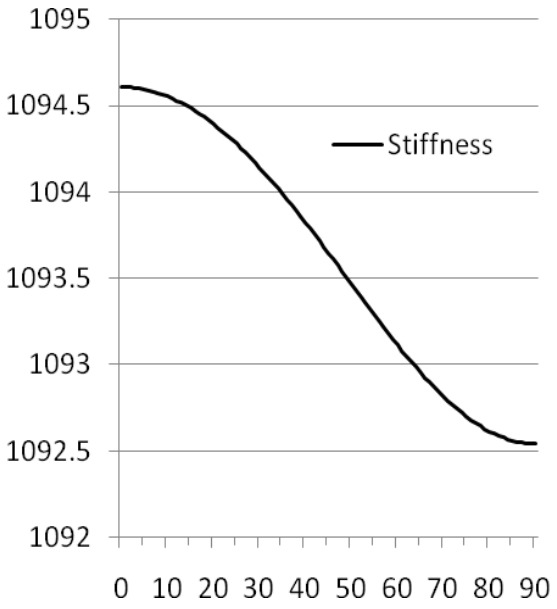

Fig. 12. Stiffness based on α.

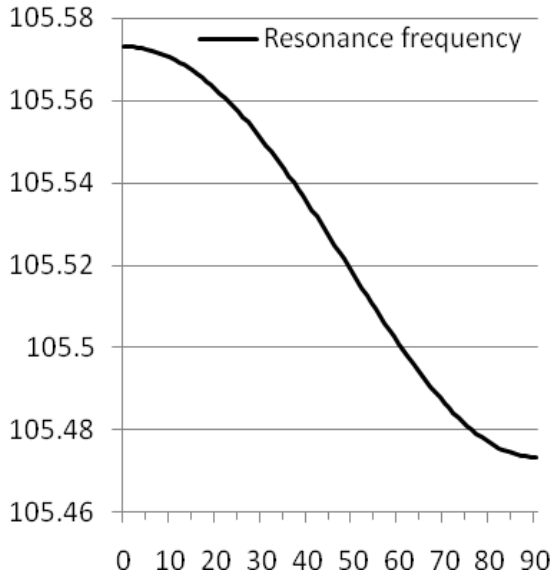

Fig. 13. Resonance frequency based on α.

VII. Numerical Simulation

Numerical simulations was performed using the finite element method, in Fig. 14 is shown the rotor with the fracture in the most critical orientation, that is, the simulation includes a fracture for α = -90°, in this situation the deflection determined was of 0.1646 mm.

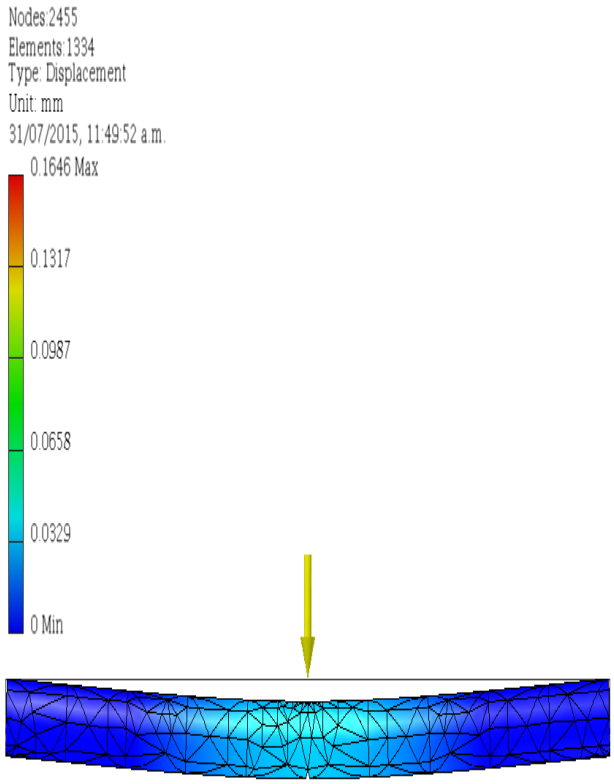

Fig. 14. Deflection for α = -90°.

VIII. Comparative Analysis

The effects of the fractures in the dynamical behaviour of rotors, leads us to evaluate the natural frequencies and then the resonance frequencies, in this work we have obtained resonance frequencies for three different methods, analytical without fracture, analytical with fracture and numerical with fracture. From the results we can compare in the following sense.

Comparing the results of the frequencies from Table 1 and Table 2 (α=90°), then the resonance in the rotor fracture present in a range of 0.1% below the resonance in the rotor without fracture, comparing the results of the frequencies from Table 2 (α=90°) and Table 3, it follows that resonance, obtained analytically, is approximately 34% higher than the corresponding obtained numerically.

Finally, comparing results of the frequencies from Table 1 and Table 3, it follows that the rotor fractured enter into resonance at a frequency range of approximately 25.5% below the resonant frequency of the rotor without fracture.

We considered that the case α=90° corresponds to the case α=–90° for the analytical procedure, in both of the cases the deflections are equivalent, if is not considered stress concentrations and other dynamics conditions.

TABLE 1. PARAMETERS OPTAINED ANALYTICALLY FOR THE ROTOR WITHOUT FRACTURE

$\Delta\,(mm)$	k $\frac{N}{mm}$	$\omega\,\frac{rad}{s}$
0.09134359	1094.76757	105.568895

TABLE 2. PARAMETERS OPTAINED ANALYTICALLY FOR THE ROTOR WITH FRACTURE

α°	$\Delta\,(mm)$	k	$\omega\,\frac{rad}{s}$
0	0.09135695	1094.60749	105.573078
30	0.0913958	1094.14219	105.550637
60	0.09148179	1093.11367	105.501015
90	0.09152965	1092.54218	105.473433

TABLE 3. PARAMETERS OPTAINED ANALYTICALLY FOR THE ROTOR WITH FRACTURE

α°	$\Delta\,(mm)$	k	$\omega\,\frac{rad}{s}$
-90	0.1646	607.533414	78.6518713

IX. CONCLUSIONS

In this paper we have analyzed the case of a rotor with a fracture since the point of view of the second area moment. The analysis was performed using basically the finite element method and an analytical procedure, in both of the cases we determined, stiffness and deflections of a fractured rotor. In the analytical procedure, we considered a fracture in different orientations and their effect in the deflections. Then for each orientations of the fracture there is a particular deflection and in consequence a corresponding natural frequency and the associated resonance frequency. In the case of the comparing between the rotor without fracture and with fracture, from the results, we can conclude while the rotor without fracture just it has associated one deflections, in the case of the rotor with fracture, the fracture induces a range of deflections because the second area moment varies continuously. Any way we have analyzed just for cases, or four orientations.

X. ACKNOWLEDGMENT

The authors thank the institutional support of the Autonomous Metropolitan University and the Azcapotzalco Unit in general and of the Division of Basic Sciences and Engineering and the Department of Energy in particular.

REFERENCES

[1] T. Morais, "Control of the breathing mechanism of a cracked rotor by using electro-magnetic actuator numerical study," Latin American Journal of Solids and Structures. vol. 3, 2013.

[2] G.Sabnavis, R. G. Kirk, M. Kasarda, D. Quinn, "Cracked shaft detection and diagnostics: a literature review," Shock Vibration Digest. 2004.

[3] V. Kumar, C. Rastogi, "A brief review on dynamics of a cracked rotor," International Journal of Rotating Machinery. 2009.

[4] Ferdinand P. Beer, E. Russell Johnston, Vector Mechanics for Engineers: Statics and Dynamics, McGraw-Hill, 2010.

Techno-economic analysis of the conceptual design of a biorefinery based on Agave Tequilana Weber

Blanca A. García García; Agustín J. Castro Montoya; Jaime Saucedo Luna
Facultad de Ingeniería Química
Universidad Michoacana de San Nicolás de Hidalgo
Morelia, Michoacán

Carlos A. Cardona Alzate
Departamento de Ingeniería Química
Universidad Nacional de Colombia
Manizales, Colombia

***Abstract*—An alternative to petroleum-based economy is the use of renewable energy from agro resources whose development is based on the biorefinery concept. However, in recent years, the existing biochemical processes of biomass conversion into fuels have shown that the economic goal is not reached under this scheme. Therefore, taking into account the above, the lack of conversion technology, and the overabundance of objectives, we developed a conceptual design of a biorefinery to analyze different production scenes of ethanol, xylitol and sorbitol. This was carried out with the purpose of building a flexible and systematic model to analyze the production process of biofuels from an economic and technical point of view to determine the feasibility of the production process, using agave Tequilana Weber as a raw material. The production process was modelled in Aspen Plus v8.4, based on data collected from the literature. The analysis of the proposed cases allowed determining a minimum selling price for ethanol, which was possible to decrease due to the incorporation of value-added chemicals and electricity generation in the process of ethanol production.**

Keywords—biorefinery; bioethanol; conceptual design;

I. Introduction

The growing need to expand in a sustainable way the use of renewable energy sources to provide a higher security in the energy supply, and reduce environmental impacts associated with fossil fuels, finds in the biorefineries an alternative with significant potential, especially to satisfy the energy requirements of the transport sector.

The production and use of first generation ethanol as fuel has been practiced regularly in the United States and Brazil, with an annual volume of 52.6 and 22.7 billion liters respectively. The successful development of this industry in both cases corresponds to the following points: the establishment of consistent national policy on direct government investment, establishing legal requirements for the use of ethanol as fuel, and the implementation of subsidies and other incentives. Currently, in Mexico, with the enactment of the energy reform, strategies have started to be developed for the incorporation of bioethanol as a gasoline component; therefore, one of the great challenges to overcome is to develop biorefineries under a scheme that allows make the production process economically viable. The main obstacles are facing this development the lack of incentives to this sector, the type of raw material used, and the limits on the bioethanol selling price. Therefore, an alternative to make the process economically viable is to develop alternative value-added products, or complementary to existing petrochemicals, which are facing two major challenges: the lack of conversion technology and the overabundance of targets. Therefore, it is necessary to identify a group of primary products analogous to those used in the petrochemical industry.

Taking into account these adverse features, with this work we develop a conceptual design for the combined production of bioethanol, xylitol and sorbitol, basing the selection of the product portfolio from the results developed by previous studies [1-2] with the purpose of building a systematic model to analyze the production process from an economic and technical point of view and its viability.

II. Materials and Methods

A. Raw Material

The agave Tequilana Weber is an endemic plant of the country, whose main use is the production of alcoholic beverages because of its high sugar content.

Annually, an average of 495594 MT of bagasse is produced in the tequila industry [3], as waste of the process. Therefore, the use of agave bagasse as raw material in the production of ethanol is attractive because of its low cost and availability. Besides that, recent studies have shown that ethanol from agave is a fuel with low environmental impact, since it is demonstrated from a complete energy cycle that the production of ethanol from agave emits 35 g MJ^{-1} of CO_2 whereas the production of ethanol from corn has an index of 85 g MJ^{-1} [4].

B. Product Portfolio

The definition of the product portfolio was carried out in two stages; the first one as a preliminary screening of the five products with the highest score of the Petersen study [1], which correspond to ethanol, glycerol, sorbitol, levulinic acid, and xylitol. Fig 1 shows the score of such compounds as well as Table I shows the criteria employed in the assessment [1]. From the resulting five compounds ethanol and sorbitol were selected because of their high scores, while glycerol was removed, due to one of the most common methods used for

purification of ethanol corresponds to the extractive distillation using glycerol as separating agent. Finally, the last component selected was xylitol this selection was based on the scores awarded in the field of conversion technology. Also considering products that have a similar production process with a wide market demand, and emphasizing in the products whose existing technology is applicable for industrial scale production.

C. *Scenarios Description*

In this work, two-biorefinery schemes and three scenarios for each one of them, were techno-economic assessed. For that, in the cases that were analyzed, it is assumed that the raw material has gone through a preconditioning process that allows uniform supply of raw material to the pretreatment stage, with approximately 20% humidity, according to the National Renewable Energy Laboratory of United States, NREL [2]. The first biorefinery scheme considers that the raw material is submitted to pretreatment and hydrolysis, where the xylose and glucose rich fractions were extracted, for processing according to the following case studies:

Case 1: The xylose rich fraction and the glucose rich fraction were destined to produce ethanol.

Case 2: The xylose rich fraction was destined to produce xylitol. On the other hand, the glucose rich fraction was used to produce ethanol and the rest to produce sorbitol.

Case 3: The xylose rich fraction was destined to produce xylitol, and half the glucose fraction was used to produce ethanol and the rest to produce sorbitol.

For the second biorefinery scheme, we considered the same case studies and the current use for this raw material for power production through a direct combustion process. For that, the lignin present in the bagasse is submitted to a combustion process at 870°C and 1 atm. The resulting stream goes through a heat exchanger to heat a water stream, and the resulting steam at 650°C and 40 atm goes through a steam turbine where the pressure decreases up to 1 atm to produce electricity.

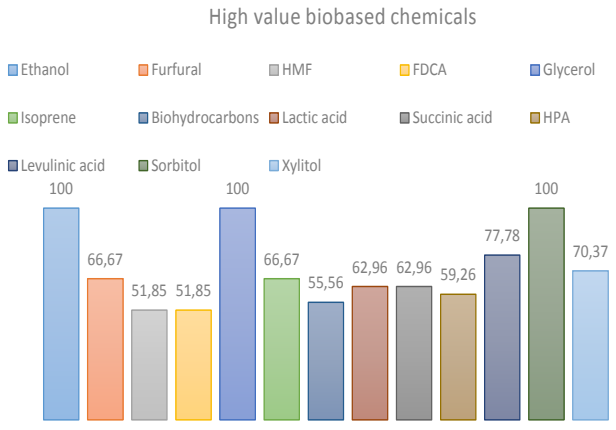

Fig. 1. Score of the high value chemicals for the portfolio production

TABLE I. CRITERIA USED IN EVALUATIING BIOBASED PRODUCT OPPORTUNITIES FROM CARBOHYDRATES

1	The compound or technology has received significant attention in the literature.
2	The compound illustrates a broad technology.
3	The technology provides direct substitutes for existing petrochemicals.
4	The technology is applicable to high volume products.
5	A compound exhibits strong potential as a platform.
6	Scale up of the product or a technology to pilot, demo, or full scales is underway.
7	The bio-based compound is an existing commercial product, prepared at intermediate or commodity levels.
8	The compound may serve as a primary building block of the biorefinery.
9	Commercial production of the compound from renewable carbon is well established.

D. *Simulation Process*

For both biorefinery schemes analyzed, flowsheet synthesis was carried out using process simulation tools, with the purpose of generating the mass and energy balances for calculating the raw materials, consumables, utilities and energy requirements.

Before performing simulations, extensive information was reviewed and analyzed to define the operation parameters for each one of the processing steps. Paying particular attention to the appropriate selection of the thermodynamic models that describe the liquid and vapor phases. The non-random two-liquid (NTRL) thermodynamic model was applied to calculate the activity coefficients of the liquid phase and the Soave Redlich Kwong model for liquid and vapor phases were needed when the NTRL model does not predict the properties. These methods are used to calculate successfully phase equilibria in the type of mixtures with non-conventional compounds [5-6].

The simulations were modelled using the commercial package Aspen Plus v8.4 (Aspen Technology, Inc., USA). The physicochemical properties of the most polymeric compounds such as cellulose and hemicellulose were obtained from studies reported by NREL [2], while the most common compounds were taken from Aspen Plus Library.

Fig. 2 shows the simplified flowsheet that includes all the scenarios proposed where the different stages of the process are observed, which are: pretreatment, enzymatic hydrolysis, fermentation, purification, and for the second scheme, the cogeneration system. In order to achieve the sugar extraction the process initially consists in two hydrolysis steps. In this case, for the pretreatment step, we use an acid hydrolysis. Currently, this is a very effective and well known process to obtain suitable xylose extraction for conversion in fermentation [7]. In the flowsheet, acid and enzymatic hydrolysis have been included together. In the first stage, the hemicellulose fraction is hydrolyzed with sulfuric acid (1.1% w) at a temperature of 158°C. During this process, the acid medium attacks the polysaccharides, especially hemicelluloses that are easier to be hydrolyzed than cellulose, resulting in an almost unaltered non-converted solid fraction and the rich pentose liquor.

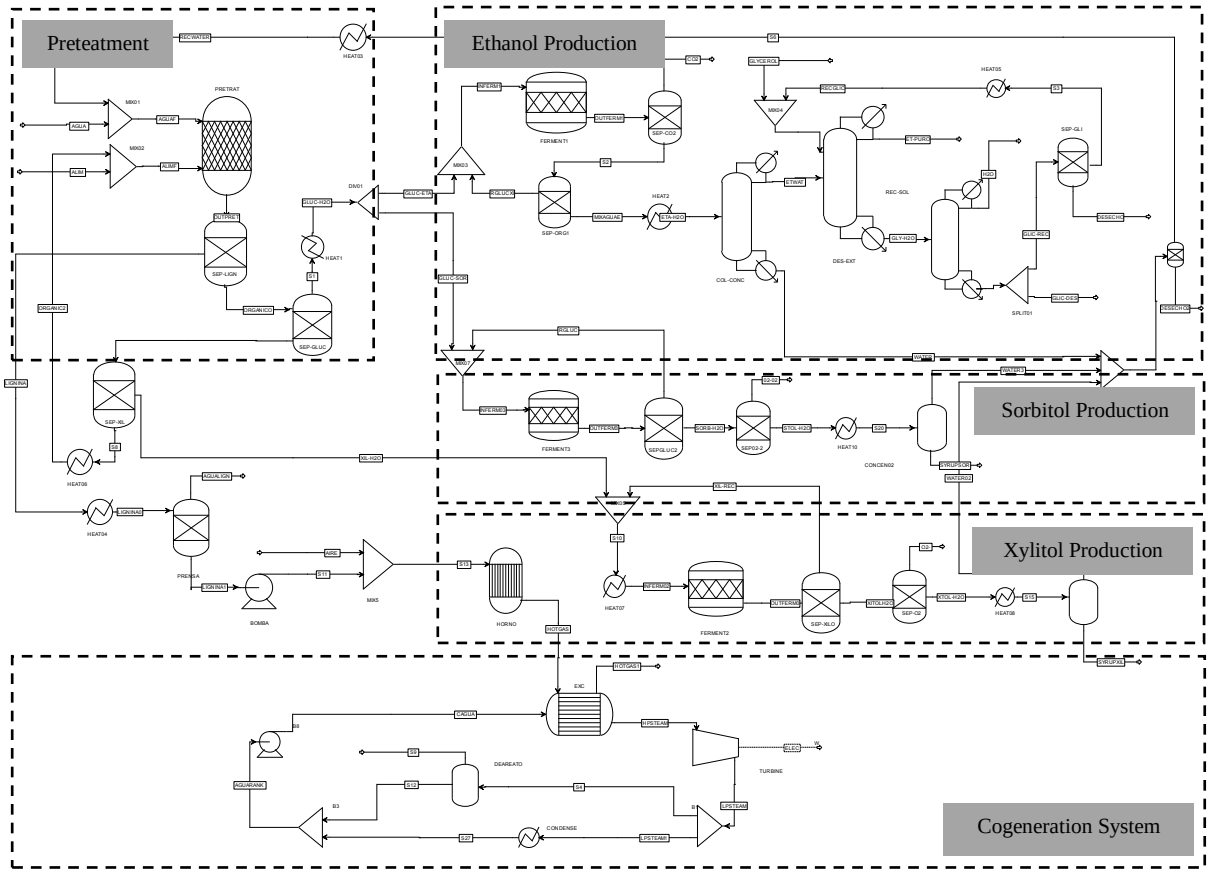

Fig. 2. Flowsheet of the process

This stream is separated by filtration. Table II shows the pretreatment conditions reactor.

Then the solid fraction, rich in cellulose and lignin, is submitted to the next step. A disadvantage of using acids as precursor for hydrolysis is that it can facilitate decomposition reactions of sugars to undesired compounds such as furfural and hydroxymethyl furfural. To avoid the above, we consider working at low temperature and acid concentration, taking as the main reactions the following:

$$(Glucan)_n + n\ H_2O \rightarrow n\ Glucose \quad 9.9\% \quad (1)$$

$$(Xylan)_n + n\ H_2O \rightarrow n\ Xylose \quad 90.0\% \quad (2)$$

$$(Lignin)_n \rightarrow n\ Soluble\ Lignin \quad 5.0\% \quad (3)$$

Higher temperatures are favorable towards cellulose hydrolysis [8]. This pretreatment can be carried out either at short retention time and high temperature, or at long retention time and lower temperature. However, if the reaction time is longer than 1 h, xylose concentration decreases due to degradation [9].

TABLE II. PRETREATMENT REACTOR CONDITIONS

Sulphuric acid loading	18 mg/g biomass
Temperature	158 ºC
Total solids loading	30 wt%

In the study, we apply an enzymatic hydrolysis because it has advantages over chemical hydrolysis. Among the advantages applying enzymatic hydrolysis are: enzymatic hydrolysis does not generate large corrosion, low consumption and low toxicity enzyme hydrolysate [10], as well as lower equipment cost because it is performed at atmospheric pressure and near environmental temperature and higher yields.

The process assumed in this design is known as sequential hydrolysis and fermentation SHF because enzymatic hydrolysis is initiated while the slurry is still at an elevated temperature after pretreatment and conditioning. At this temperature, the enzyme activity is higher, so conversion is faster and a smaller amount of enzyme is required. Once the conversion of cellulose to glucose is complete, the slurry is cooled to fermentation temperature and inoculated with the ethanologen. Based on recent experience with Zymomonas Mobilis, a 5-day SHF process with batch fermentation was

selected as a more realistic case for the present design [2]. The reactions and conversions taking place during enzymatic hydrolysis are shown below:

$(Glucan)_n + ½\ n\ H_2O \rightarrow ½\ n\ Cellobiose$ 1.2% (4)

$(Glucan)_n + n\ H_2O \rightarrow n\ Glucose$ 90.0 % (5)

$Cellobiose + H_2O \rightarrow 2Glucose$ 100.0 % (6)

For this study, the amount of enzyme used is 20 mg enzyme/g cellulose to achieve a 90% conversion to glucose. After that, the saccharified slurry is cooled by a heat exchanger specific to this task and send to a fermenter at 32°C. For fermentation, recombinant Zymomonas Mobilis bacterium was used as the ethanologen. This strain of Z. Mobilis, has the ability to uptake hexose as carbon source or a combination of a hexose-pentose mixture [11].

The process consists of five reactors operating in batch mode with a 24-h batch time and an additional 12-hour turnaround time. The seed fermenters are cooled with chilled water to maintain the temperature at 32°C. One of the most important advantages of using Z. Mobilis as fermentation microorganism is the reduction of the organic charge present in stillage because the amount of biomass produced during fermentation is not as high, compared with the conventional process using yeast e.g. Saccharomyces Cerevisiae [12]. Another advantage is that this microorganism and much of its genome are in the public domain [13]. The above, represents an interesting technological possibility compared with the conventional processes where yeast is used as microorganism. Nevertheless, the S. Cerevisiae strain could have a higher productivity than Z. Mobilis when only hexoses are considered as carbon source. For that reason, we consider Z. Mobilis to produce ethanol for case one and S. Cerevisiae for cases 2 and 3, while xylitol is synthesized from xylose by the yeast Candida Moggi, and sorbitol by Z. Mobilis [14].

The reactions and conversions considered during the fermentation are shown below:

Case 1:

$Glucose \rightarrow 2\ Ethanol + 2\ CO_2$ 95 % (7)

$3\ Xylose \rightarrow 5\ Ethanol + 5\ CO_2$ 80 % (8)

Case 2:

$Xylose + H_2O \rightarrow Xylitol + 0.5\ CO_2$ 85 % (9)

Case 3:

$Glucose + H_2O \rightarrow Sorbitol + 0.5\ CO_2$ 97 % (10)

Finally, in the purification stage, ethanol is concentrated by an extractive distillation using glycerol as solvent because this method of separation is the most used in the industry and also represents a lower energy cost. The culture broth containing approximately 15% (w/w) of ethanol enters into the first column, and leaves the column at 52% of ethanol by weight. The next column uses glycerol as separation agent in a ratio 4.9:1. From this column, we obtain ethanol at 99% (w/w), and the last column is used to recover the solvent.

In the case of xylitol and sorbitol purification, the conventional method requires high energy, so we just concentrated them at 70% (w/w) to sale it as syrup.

The cogeneration can be defined as a thermodynamically efficient way of energy use, that is able to cover complete of partially both heat and electricity requirements of a factory [15]. For this study, the technology used for cogeneration is based on the Rankine cycle, which is the traditional model employed in the Brazilian biorefineries [16].

In the system, lignin with 10% of moisture content is used as fuel to supply energy to the cogeneration system. Fig 3 shows the basic configuration of the thermodynamic Rankine cycle.

This configuration displays a burner that was described through a Gibbs reactor considering the incomplete combustion of lignin, and taking into account the formation not only of CO2 but also of CO. the boiler was simulated as a heat exchanger where the feed water enters and the steam generated exist at 650°C and 40 atm. A pump elevates the pressure of the feed water up to 42 atm; also, the system is composed by a steam turbine simulated as an isentropic compressor and a deaerator.

For the simulation, this scheme did not take into account that the combustion gases leaving the boiler were used in another part of the process, this procedure was considered in order to evaluate the influence of the cogeneration system on the overall performance of the biorefinery process with the purpose to know the impact in the minimum ethanol-selling price (MESP).

E. Economic assessment

The economic analysis was performed using the design information provided by Aspen Plus v 8.4, and the capital and operating costs were calculated using the software Aspen Economic Analyzer. For that, specific parameters such as the raw material and products costs were defined in order to calculate the production cost per unit for the different obtained products. Table III shows prices for utilities and main raw materials and products used in the analysis.

The economic analysis was estimated in US dollars under the following conditions, an Internal Rate of Return (IRR) was set to 10%, the income tax of 35%, and the plant lifetime set to 30 years. For this analysis, it was assumed that the plant would be 40% equity financed, so the terms of the loan were taken to be 8% interest for 10 years, the principal being taken out in stages over the three-year construction period, and the interest in the loan is paid during this period, but principal is not paid back.

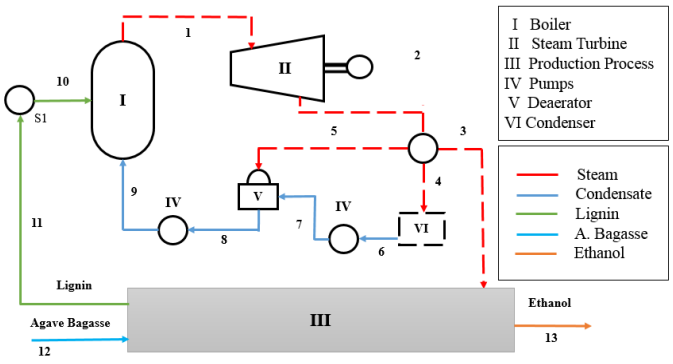

Fig. 3. Configuration of the cogeneration system based on Rankine Cycle: Non condensing steam turbine.

To determine the capital depreciation amount for the calculation of federal taxes to be paid we used the Modified Accelerated Cost Recovery System (MACRS). This offers the shortest recovery period and the largest tax deductions, using a 7-year recovery period according to the Internal Revenue Service IRS. [17].

With the total capital investment (TCI), the fixed and operating costs determinated, a discounted cash flow analysis was used to determine the MESP required to obtain a zero net present values (NPV) with a fixed IRR.

The above was done for the first and fourth scenarios, and the resulting MESP in both scenarios was evaluated in the other cases. Table IV shows the assumptions made in completing the discounted cash flow analysis.

TABLE III. PRICES USED IN THE ECONOMIC ANALYSIS VALUES FOR 2014

Item	Unit	Price
Agave bagasse	USD/U.S. Ton	24.9[a]
Water	USD/m3	1.250[b]
Glycerol	USD/Ton	200[c]
Enzyme	USD/Kg	3[d]
Sulphuric acid	USD/Kg	0.094[c]
Ethanol	USD/l	0.900[c]
Xylitol	USD/Kg	1.500[c]
Sorbitol	USD/Kg	0.838[c]
Electricity	USD/Kw	1.150[b]
L.P.Steam (7 bar)	USD/Kg	2.535[b]
Labor Operator	USD/h	2.500[b]
Labor Supervisor	USD/h	5.000[b]

a. Taken from Mexican producers of Agave, 2014.

b. Taken from Aspen Plus, 2014.

c. Taken from ICIS Prices (ICIS, 2014).

d. Taken from Alibaba International Prices (Alibaba, 2014)

TABLE IV. DISCOUNTED CASH FLOW ANALYSIS PARAMETERS

Plant Life	30 years
Discount rate	10%
General plant depreciation	200% declining balance
General plant recovery period	7 years
Federal tax rate	35%
Financing	40% equity
Loan terms	10-year loan at 8%APR
Construction period	3 years
First 12 months' expenditures	8%
Next 12 months' expenditures	60%
Last 12 months' expenditures	32%
Working capital	5% of fixed capital investment
Start-up time	3 months
Revenues during start-up	50%
Variable costs incurred during strat-up	75%
Fixed costs incurred during start-up	100%

III. RESULTS AND DISCUSSION

Simulations of the six scenarios were used to generate their respective mass and energy balance, which are the basic input for the techno-economic analysis. Table V shows the bagasse composition used for this study.

For simulation purposes, a raw material flow of 56 Ton/h, (approximately at 490896 Ton/year) is considered due to recent bidding processes by Petroleos Mexicanos (PEMEX), where the ethanol demand to be used as additive in gasoline to cover partial national demand corresponds to 60 Mgal/year [18].

According to the Consejo Regulador del Tequila (CRT), approximately 901080 MT of agave Tequilana Weber from the denomination zone, which includes the states of Jalisco, Colima, Michoacan, Guanajuato, and Tamaulipas, are used in the tequila industry to be processed [3]. This agave production is able to deliver the requirements of raw material for ethanol production demanded in the country. However, the agave production exists in all the country; the above can be a good opportunity to use the agave as an integral raw material for a biorefinery.

TABLE V. BAGASSE AGAVE COMPOSITION USED FOR SIMULATION PRODECURE

Compound	Percent
Cellulose	38.79%
Hemicellulose	21.62%
Lignin	19.59%
Moisture	20.00%

a. Taken from, (Jaime Saucedo Luna et al., 2011)

For this study, the capacity of the scenarios simulated is shown in Table VI. The first scheme was simulated without cogeneration system, and the first case of this scheme was destined to produce 61.4 Mgal/year of 99% ethanol. This amount was decreasing for the other scenarios due to the diversification of the product portfolio.

The main target of the economic assessment was to determine the minimum ethanol sales price, the variations that this presents respect to the raw material cost, opportunities to improve this price by the production of value added products and the use of cogeneration system. The above was done with the purpose to establish a rank of the ethanol-selling price, which oscillates between the export ethanol-selling price that imposes PEMEX ($2.15/gal) and the minimum ethanol-selling price calculated, as well as the total production costs and revenue from product sales.

The operating cost includes various aspects inherent to the production process such as raw materials, utilities, labor and maintenance, and general and administrative costs. Besides, annualized capital costs are included using the discounted cash flow analysis. The evaluation was based on the results obtained from simulation as well as the calculations of energy consumption that were carried out, based on the data related to the thermal energy required by the heat exchangers, reboiler, and related units. This approach allowed us to determine the minimum ethanol-selling price keeping fixed sale prices of sorbitol, xylitol and electricity for scenarios 2 and 3.

Figure 4 shows the results of the discounted cash flow analysis of the 1a and 1b scenarios, according to the financial parameters in Table IV. From the analysis, it was determined that the minimum ethanol selling price for a plant with a capacity of 61.34 Mgal/year without cogeneration corresponds to $1.3068/gal, while using a cogeneration system the minimum ethanol selling price decreased by 5.4% resulting in $1.2357/gal. The decrease in the selling price of ethanol occurs because the electricity cogeneration system generates enough electricity to cover the needs of the plant, and excess energy is considered that it is sold to the grid.

TABLE VI. PRODUCTION OF THE SCENARIOS ASSESSED

Scenario	Production			
	Ethanol [Mgal/year]	Xylitol al 70% [Mlb/year]	Sorbitol al 70% [Mlb/year]	Electricity Cogeneration [Kw/h]
Case 1a[a]	61.34	-----	-----	-----
Case 2[a]	39.1	348.5	-----	-----
Case 3[a]	19.5	348.5	294.4	-----
Case 1[b]	61.34	-----	-----	6153
Case 2[b]	39.1	348.5	-----	6153
Case 3[b]	19.5	348.5	294.4	6153

a. First scheme production without cogeneration system from lignin

b. Second scheme production with cogeneration system from lignin

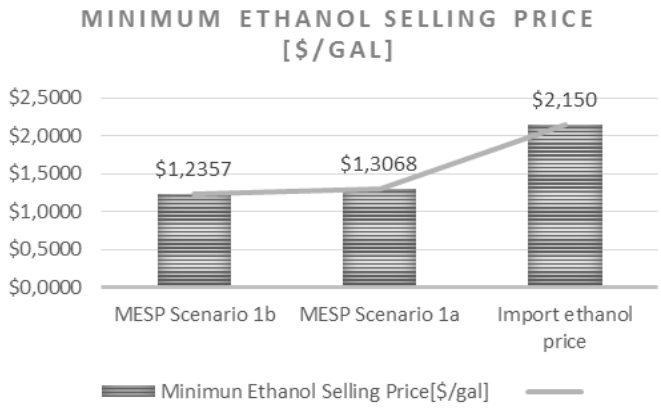

Fig. 4. Minimum ethanol selling price for the biorefinery schemes analyzed.

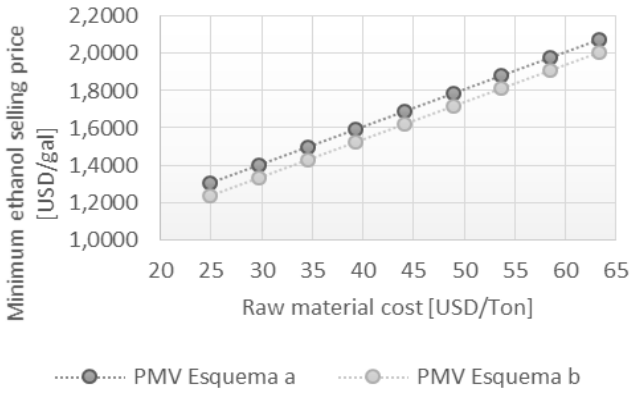

Fig. 5. Behavior of the minimum ethanol selling price compared with the increase cost of raw material.

These results allow establishing an ethanol-selling price between $1.2357/gal - $2.15/gal and $1.3068/gal-$2.15/gal, for the scenarios analyzed respectively, wherein a positive profit margin is obtained. The above is attributed to the very low price of the raw material price used in the analysis because currently this material has no commercial value.

However, increasing the demand for this raw material, its will increase value. The above will be reflected directly in the minimum ethanol-selling price. Figure 5 shows the behavior of the minimum ethanol-selling price relative to the increased cost of raw material. The results show that if the raw material cost increase at the price of corn the MESP, $58.5/U.S. Ton, for the scenario 1a and 1b will increase in a 51.5% ($1.9794/gal)) and 54.4% ($1.9083/gal) respectively.

It is important to keep in mind this effect to predict the best ethanol-selling price to avoid losses. Fig 6 and 7 show the behavior of the economic profit in respect to the percentage of increase in the raw material cost, keeping the MESP obtained in both schemes.

In figure 6 we can see that the economic profit is affected directly by the increase of the raw material, having losses even if the increase in the raw material cost is very small.

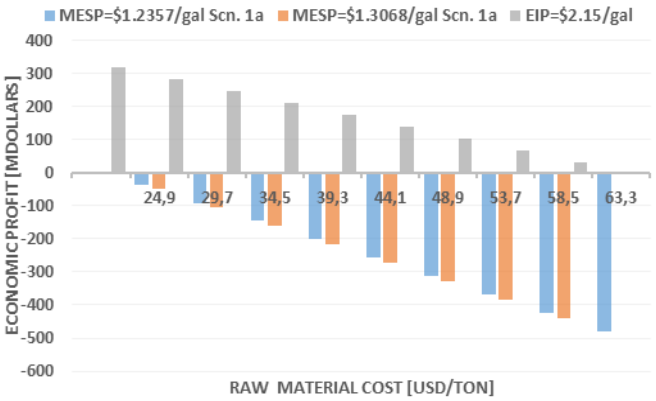

Fig. 6. Behavior of the benefit profif compared with the increase cost of raw material for scheme a.

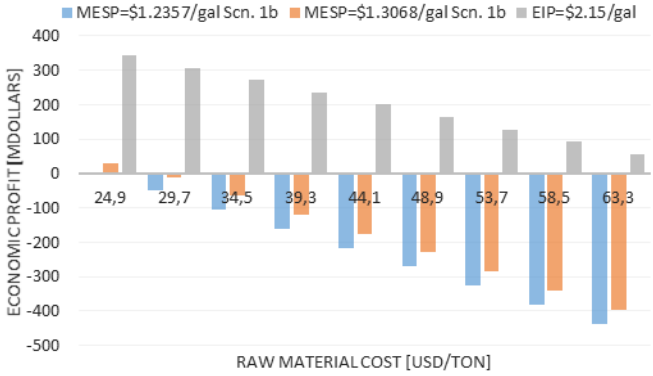

Fig. 7. Behavior of the benefit profit compared with the increase cost of raw material for scheme b.

On the other hand, although the scheme b of the biorefinery also presents losses with the rising cost of raw material. We can see that these are lower than those observed in the scheme a, thanks to the incorporation of the electricity cogeneration system, which allows to reduce utility costs.

A way to avoid losses in the economic profit of the process associated with the uncertainty in the raw material cost and other factors corresponds to the diversification of the portfolio. This allows to produce value added products which represent the highest percentage of contribution to the economic benefit of the process.

Taking into account the results of the discounted cash flow analysis, the profitable index for each scenario proposed was calculated. These results were obtained varying only the selling ethanol price and keeping the xylitol and sorbitol price fixed. In the case of the scheme b, the electricity price considered was the value specificity by Aspen Plus.

The results are shown in Table VII. It can be seen that the incorporation of value added products, as well as the electricity cogeneration system, allow having more attractive economic benefits, and even offering the possibility of reducing the selling price of ethanol below those obtained in the equilibrium point.

TABLE VII. PRODUCTION COSTS OF THE PROPOSED SCENARIOS FOR THE BIOREFINERY BASED ON AGAVE

Scheme	**Without Cogeneration**			**With Cogeneration**		
Scenarios	**Case 1a**	**Case 2a**	**Case 3a**	**Case 1b**	**Case 2b**	**Case 3b**
Categories	**Cost [$/year]**	**Cost [$/year]**	**Cost [$/year]**	**Cost [$/year]**	**Cost [$/year]**	**Cost [$/year]**
Raw Material	26459735.99	25941715.99	25354535.99	26459735.99	25941715.99	25354535.99
Operating labour and maintenance cost	1996460,00	1648010,00	2144380,00	2075350,00	2224370,00	2199170,00
Utilities	25285700,00	26055400,00	20463600,00	24490000,00	16292800,00	8696470,00
Plant Overhead	998228,00	824004,00	1072190,00	1037680,00	1112190,00	1099590,00
General and Administrative cost	2859970,00	2831270,00	2407050,00	2805780,00	2129950,00	1472250,00
Operating charges	427343,00	339683,00	471173,00	427343,00	471173,00	471173,00
Total cost	58027436.99	58250881.56	52523727.56	57906687.56	48782997.56	39903987.56
[a]Profitable index MESP Case 1a	0.00	42.00	59.00	1.00	52.20	59.08
[b]Profitable index MESP Case 1b	-1.32	41.00	58.00	0.00	51.54	58.02
[c]Profitable index import ethanol selling price	11.65	48.00	62.00	11.00	59.96	62.14

c. MESP without cogeneration system of $1.0186/gal

d. MESP with cogeneration system of $0.9474/gal

e. Export ethanol selling price of $2.15/gal, (Iowa, 2014)

IV. Conclusion

In this study we could see that the economic behavior is mainly affected by the cost of the raw material, this effect could be modified with the incorporation of value added co-products in the portfolio as xylitol and sorbitol. The above allows to have the possibility to reduce the ethanol selling price keeping a margin of the price under the ethanol import cost.

Also the incorporation of the cogeneration system allowed to reduce the production costs, showing that the distribution of raw material technologies and integration affects the economic behavior of a biorefinery system.

Acknowledgment

The authors express their gratitude to the Universidad Michoacana de San Nicolás de Hidalgo, to the Investigation Direction of the Chemical Engineering Faculty, financial support from Consejo Nacional de Ciencia y Tecnología (CONACyT) is acknowledged.

References

[1] Petersen, and Werpy, "Technology development for the production of biobased products from biorefinery carbohydrates," The US department of rnergy's "top ten", green chemistry, vol. 12, No. IV, pp.525-728, 2010.

[2] NREL, "Process design and economics for biochemical conversion of lignocellulosic biomass to ethanol", Technical Report, NREL, 2011

[3] Consejo Regulador del Tequila, (CTR), www.crt.org.mx

[4] Xiaoyu Yan, Oliver R. Inderwildi, Daniel K. Y. Tan, J. A. C. Smith and David A. King, "Life cycle energy and greenhouse gas analysis for agave-derived bioethanol" Energy & Environmental Science, 4, pp.3110-3121,2011.

[5] Cardona, C.A., Sànchez, O.J.,"Energy consumption analysis of integrated flowsheets for production of fuel ethanol from lignocellulosic biomass", Energy 31 (13), pp. 2447-2459.

[6] Quintero J.A., Montoya M.I, Sànchez O.J., Giraldo O.H, and Cardona C.A., "Fuel ethanol production from sugarcane and corn: compartive analysis for a colombian case". Energy 33(3), pp.385-399.

[7] Cruz J.M., Dominguez H., Parajo J.C., "Preparation of fermentation media from agricultural wastes and their bioconversion into xylitol", Taylor and Francis, Food Biotechnol, pp. 79-97, 2002.

[8] Taherzadeh M.J., KArimi K., "Pretreatment of lignocellulosic wastes to improve ethanol and biogas production", A review Int J Mol Sci, Sept 9(9), pp.1621-1651, 2008.

[9] Mussatto S., Roberto I.C., "Alternatives for detoxification of diluted-acid lignocellulosic hydrolyzates for use in fermentative processes, a review", Bioresour Technol, 93(1), pp. 1-10, 2004.

[10] Taherzadeh M. J., and Karimi K., "Acid-based hydrolysis processes for ethanol lignocellulosic material a review", Bioresources, 2, pp.472-479, 207.

[11] Leksawasdi N., Joachimsthal E., Rogers P., "Mathematical modelling of ethanol production from glucose/xylose mixtures by recombinant Zymomonas mobilis", Biotechnol Lett, 23, pp. 1087-93, 2001.

[12] Moncada J., El-Halwagi M.M., Cardona C.A., "Techno-economic analysis for a sugarcane biorefinery: Colombian case", Bioresource Technology, 135, pp. 533-543, 2013.

[13] Zhang M., Eddy C., Deanda K., Finkelstein M., Picataggio S., "Metabolic engineerinf of a pentose metabolism pathway in zymomonas mobilis", Science, Vol. 267, pp. 240-243, 1995.

[14] Hernández V.,Romero-García J.M., Dávila J. A., Castro E., Cardona C. A, "Techno-economic and environmental assessment of an olive stone based biorefinery", Resources, conservation and recycling, 92, pp.145-150, 2014.

[15] Nagel, J., "Determination of an economic energy supply structure based on biomass using a mixed-integer linear optimization model", Ecol. Eng. 16 (Suppl.1), pp. 91-102, 2000.

[16] Macedo I, Nogueira LFH., "Assess of expansion ethanol production on Brazil in: biofuels- strategic issue of Brazilian government".

[17] Internal Revenue Service. "How to depreciate property", Publication #946, Washington, DC, Department of the Treasury Internal Revenue Service, 2009. http://www.irs.gov/pub/irs-pdf/p946.pdf

[18] Petróleos Mexicanos, PEMEX, "Suscribe PEMEX contratos para la producción de etanol anhidro", http://www.pemex.com/saladeprensa/boletines_nacionales/Paginas/2015-036-nacional.aspx

[19] Saucedo-Luna J., Castro-Montoya A. J., Martínez-Pacheco M. M., Sosa-Aguirre C. R., Campos-García J., "Efficient chemical and enzymatic saccharification of the lignocellulosic residue from agave tequilana bagasse to produce ethanol by Pichia Caribbica", Ind. Microbiol Biotechnol, Vol. 38, pp. 725-732, 2011.

Cooking time estimation for zucchini, eggplant and apple considering their inside temperature distribution using a solar cooker box-type with internal and external reflectors

A. Salazar, S. Maldonado, H. Terres, R. López, A. Lizardi, M. Gordon, A. Lara, S. Sánchez*
Departamento de Energía, Área de Termofluidos
Universidad Autónoma Metropolitana
México, D. F.

al2112002330@alumnos.azc.uam.mx

***Abstract*—The Cooking time of food products in solar cooker box-type can be an important element to the energy savings, besides, it participates in the quality of food or the consumer's health.**

The solar cookers box-type need too time's exhibition under to solar radiation for a long time for their nature, for this reason, is considered important to determine the products' Cooking time when the solar cookers are used.

In this work the Cooking time for Zucchini, Eggplant and Apple using a solar cooker box-type with internal and external reflectors as energy source is determined.

The temperature distribution inside of each product is considered for different times, therefore is managed to determine the thermic behavior of products in their process cooking. With this aim, thermocouples K-type on pots different (surface and center) of products are put, also in heating fluid (water). The equations of conduction in transient state are applied subsequently considering cylindrical models (Zucchini and Eggplant) and spherical (Apple), make it possible to get two else temperatures inside of products.

With findings are determined the required times to cooking of products when them are compared with literature's information. The results indicate that the cooking time to Eggplant is 1 hour 15 minutes with schedule of 10:30 to 11:45, to Zucchini is 1 hour 50 minutes with schedule of 10:30 to 12:20 and to Apple is 1 hour 15 minutes with schedule of 10:30 to 11:45.

These results can be useful to estimating the cooking time to products and to give the better use for solar cookers box-type with the characteristics mentioned.

Keywords*—*Cooking time, Temperature distribution, Cooking temperature, solar cooker box-type.

I. INTRODUCTION

For many years, the need for improved thermal processes have promoted its study. There are many studies, where characteristics of thermal process or cooking process were studied.

A paper was realized about temperature distribution inside the sample of agar gel cylinders were heated using pulsed and continuous microwave energy was measured, these results were compared with numerical predictions based on the Lambert's law and Maxwell's equations. The results measured temperature distributions and the corresponding predictions using both models indicate better temperature uniformity in the agar gel cylinders under pulsed microwave heating, though the total process time is longer, than under continuous microwave heating [1].

The other temperature distribution application was studied, where was studied the microwave heating but however, uneven heating often occurs. This work studied 'cold spot' problem of chilled instant rice during microwave reheating, online monitor was used to determine the temperature distribution during reheating. The Lambert's law was utilized and was showed that the predicted results were accurate [2].

An application was studied in a Solid oxide fuel cell (SOFC), the temperature distribution can also be used for control and monitoring purposes, the selection of both materials and the operating point of a stack is heavily affected by temperature gradient. The experimental work which consisted in measure the temperature distribution in different current densities and in two oven temperatures. Five thermocouples were inserted inside the middle cell to measure temperatures in four corners and in the middle of the cell. The Voltage was also measured for different cells. Higher oven temperature caused more uniform temperature distribution, while increasing the current density resulted in higher temperature gradient over the cell surface [3].

Also are considered other variables to calculate temperature distribution, between them, the external heat transfer coefficient, this was obtained in steam processing was determined experimentally in a pilot scale retort for this, the heat transfer equations were solved applying finite elements and using the actual retort temperature profile as boundary condition. The instantaneous values of the heat transfer coefficient were determined, to analyze its time-variability along a retort cycle [4].

It is common knowledge that an object with a higher thermal diffusivity will always heat faster in comparison to that with a lower thermal diffusivity. In a work was undertaken to demonstrate numerically and experimentally that this is not always true. To accomplish this, a finite difference model was developed, and temperature changes at the surface and geometric center of cubic particles of different thermophysical properties were obtained for different convective heat transfer coefficient values (50 and 1000 W/m2 K) [5].

Thermal processing is the most important and utilized method for food preservation, being those carried out with the food inside the package the most appropriated for safety consumption guarantee. During processing, the packaged food was surrounded by a heat transfer medium, in general a fluid as water, steam, air or its mixtures. To pointed out this, in a work is described an appropriated method to determining the convective heat transfer coefficient (h) in thermal process of foods [6].

In this work experimental results for the temperature distribution inside of Zucchini, Apple and Eggplant are presented. The temperature distribution was calculated with transitory state heat transfer equation and three measurements temperature in different positions.

With these results and cooking temperature, the time cooking was obtained for each product.

II. Nomenclature

T_c Center temperature of product [°C]

T_s Surface temperature of product [°C]

T_f Fluid temperature [°C]

Θ Temperatures difference ratio [dimensionless]

T_o Center temperature of product for each sampling instant [°C]

T_∞ Fluid temperature of product for each sampling instant [° C]

Ti Initial temperature from the center of product [°C]

τ Fourier number [dimensionless]

α Diffusivity [m2/s]

t Time [seconds]

r_0 Radio [m]

A_1 Constant [dimensionless]

λ_1 Constant [dimensionless]

III. Experimentation

For the experimental work, a solar cooker with eggplant, zucchini and apple was used. Each product was evaluated in individual tests, and they were done outdoor, on the "Solarium" at the Universidad Autonoma Metropolitana.

The solar cooker is integrated by the following elements: 1. a cover with two flat glasses with a clearance between them. 2. Internal reflectors made in reflective silver paper placed to three different tilt angles 65°, 75° y 85°, 3. Thermal insulator placed in the lateral part of the same one, and 4. Recipient contains the product to cook. The solar cooker is locked air tightly; this allows reaching considerable temperatures in the test fluid, Fig. 1.

Fig. 1 Solar cocker box-type

Thermocouples k-type at surface, central points of the vegetables and water were placed. The temperature measuring was realized each 5 minutes.

In the test was sought that the masses of the vegetables were as similar as possible. The average value was 220 g. The average value for the water was 250 ml.

The geometrical characteristics and the thermocouples colocation at eggplant, zucchini and potato are shown, Fig. 2-4.

In the temperature measures multi-meters were used.

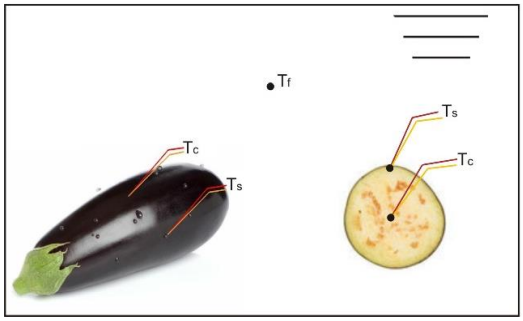

Fig. 2 Thermocouples position for eggplant

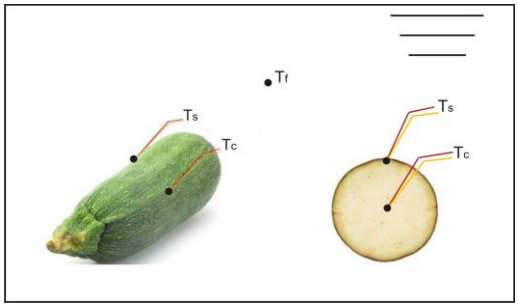

Fig. 3 Thermocouples position for zucchini

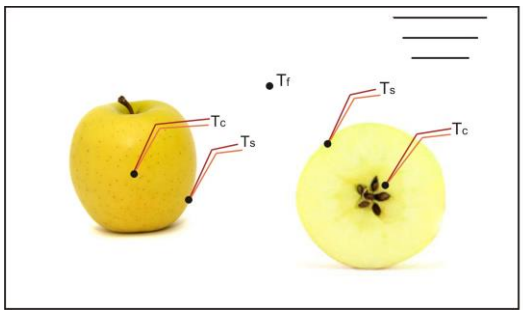

Fig. 4 Thermocouples position for apple

In the global radiation measures a pyrometer Eppley model 8-48 was used, Fig. 5.

Fig. 5 Pyrometer Eppley mod. 8-48

IV. Results

The measures obtained for eggplant, zucchini and apple in the experimental procedure are graphed, Fig. 6 to 8.

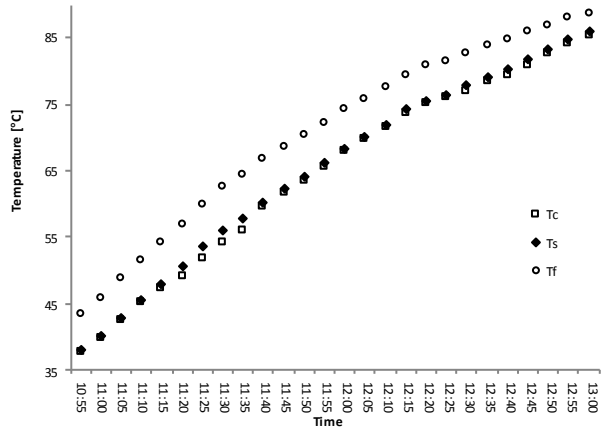

Fig. 6 Experimental temperatures: Eggplant

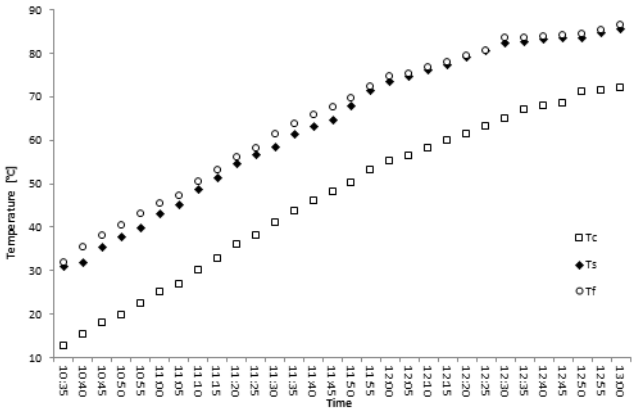

Fig. 7 Experimental temperatures: Zucchini

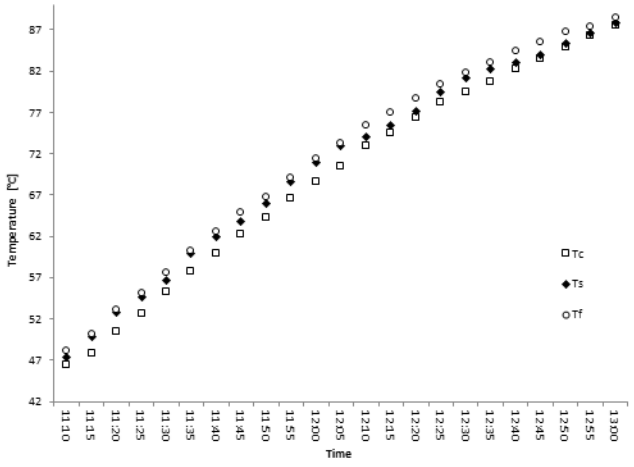

Fig. 8 Experimental temperatures: Apple

Once temperature data is obtained, heat transfer equations are used to determine the heat transfer convection coefficient. Some considerations were done for this purpose: 1. Thermal conductivity constant. 2. One-dimensional flow. 3. Without heat generation. 4. Cylindrical and spherical coordinates.

Agree to data measured, is possible to determine for each instant the temperatures difference ratio in function of water, surface and center (1) [8]

$$\theta_{0,cylinders} = \frac{T_0 - T_\infty}{T_i - T_\infty} \quad (1)$$

$$\theta_{0,sphere} = \frac{T_0 - T_\infty}{T_i - T_\infty} \quad (2)$$

The Fourier number was calculated using the thermal properties of products (3)

$$\tau = \frac{\alpha t}{r_0^2} \quad (3)$$

Subsequently, The Biot's number was calculated. The procedure was iterative, the coefficients A_1 and λ_1 were proposed to cylinders (4) and sphere (5).

$$\theta_{0,cylinders} = \frac{T_0 - T_\infty}{T_i - T_\infty} = A_1 e^{-\lambda_1^2 \tau} \quad (4)$$

$$\theta_{0,esphere} = \frac{T_0 - T_\infty}{T_i - T_\infty} = A_1 e^{-\lambda_1^2 \tau} \quad (5)$$

When coefficients A_1 and λ_1 were encountered, the positions were established to calculate the temperature distribution of products.

The table I shows the position of those points.

Table I Evaluated distance in the products

Product	Position [m]
Apple	r=0
	r=0.0084
	r=0.017
	r=0.025
Eggplant	r=0
	r=0.0084
	r=0.017
	r=0.025
Zucchini	r=0
	r=0.015
	r=0.030
	r=0.045

The temperature for the several distances were calculated whit (6) and (7).

$$\theta_{cylinder} = \frac{T_{(r,t)} - T_\infty}{T_i - T_\infty} = A_1 e^{-\lambda_1^2 \tau} \left(J_0 \left(\frac{\lambda_1 r}{r_0} \right) \right) \quad (6)$$

$$\theta_{esphere} = \frac{T_{(r,t)} - T_\infty}{T_i - T_\infty} = A_1 e^{-\lambda_1^2 \tau} \left(\frac{\sin\left(\frac{\lambda_1 r}{r_0}\right)}{\frac{\lambda_1 r}{r_0}} \right) \quad (7)$$

Where A_1 and λ_1 are constant functions of the Bi number, J_0 is the zeroth-order Bessel function of first kind [8].

The temperature results for each point are graphed to eggplant, zucchini and apple, Fig. 9 to 11.

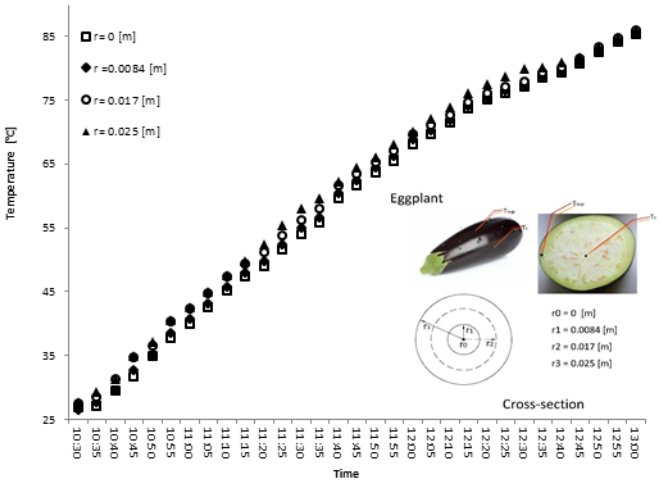

Fig. 9 Temperature distribution for Eggplant

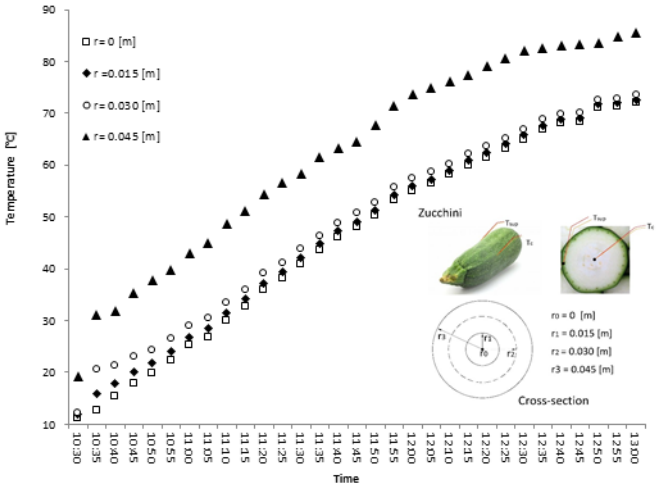

Fig. 10 Temperature distribution for Zucchini

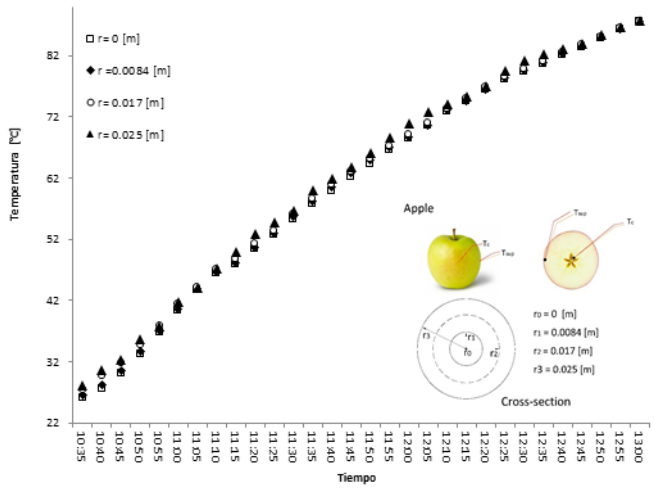

Fig. 11 Temperature distribution for Apple

V. Discussion

In figures 6 to 8 the temperature behavior for each product are shown.

Using experimental temperature data and calculated data for different positions (r), one can find out the temperature distribution for each product.

As one can see, the temperature values are $T_f > T_s > T_c$, therefore the heat transfer mechanism goes from fluid to product center. It is consistent with the heating process for the cooking.

The experimental values allow to determine when the temperature inside of the product is near to the fluid temperature, which is a reference to establish the cooking time agree to [7].

The temperature differences between fluid and the center for Eggplant, Zucchini and Apple were 3.2 °C, 14.4 °C and 1 °C respectively, figures 6 to 8.

However, the fluid temperature could be different of the real temperature to reach the complete cooking of the products.

The criteria to define the cooking time was the inspection and the value reported in the specialized literature [7].

The cooking times for the products were 1 hour 15 minutes, 1 hour 50 minutes and 1 hour 15 minutes that correspond to Eggplant, Zucchini and Apple respectively.

According to figures 9 and 11, the temperature distribution inside of the Eggplant and Apple is uniform. For the Zucchini, the distribution does not present the same behavior.

This behavior is explained by the product properties, particularly the heat specific in the same ones.

VI. Conclusions

The knowledge of the temperature distribution is useful, because it allows to know how the heating inside of the products occur.

A description of the temperature distribution inside of the products considered were presented.

The values obtained in this work indicates the potential of the solar cookers when those are applied to the heat of products.

When the cooking time is estimated, results can be very important to give the better use for solar cookers box-type with internal and external reflectors.

VII. References

[1] H.W. Yang, S. Gunasekara, "Comparison of temperature distribution in model food cylinders based on Maxwell's equations and Lambert's law during pulsed microwave heating" Journal of Food Engineering, vol 64, pp. 445-453, October 2004

[2] Daming Fan, Chunxiang Li, Wenrui Ma, Jianxin Zhao, Hao Zhang2 & Wei Chen, "A study of the power absorption and temperature distribution during microwave reheating of instant rice" International Journal of Food Engineering, vol 47, pp. 640-647, March 2012

[3] Omid Razbani, Ivar Wærnhus, Mohsen Assadi, "Experimental investigation of temperature distribution over a planar solid oxide fuel cell" Applied Energy, vol 105, pp. 155-160, May 2013

[4] Varga S. and Oliveira J. C., Determination of the heat transfer coefficient between bulk medium and packed containers in a batch retort, Journal of Food Engineering, Vol. 44, 2000, pp. 191-198.

[5] Palazoglu K., Influence of convective heat transfer coefficient on the heating rate of materials with different thermal diffusivities, Journal of Food Engineering, Vol. 73, 2006, pp. 290-296.

[6] Esteves P., Augusto D., Cristianini M., Determining the Convective Heat Transfer Coefficient (h) in Thermal Process of FoodsDetermining the Convective Heat Transfer Coefficient (h) in Thermal Process of Foods, International Journal of Food Engineering, Volume 7, Issue 4, 2011, pp. 1-22.

[7] Y. H. Hui, L. Bernard Bruinsma, J. Richard Gorham, Wai-Kit Nip, Phillip S. Tong, Phil Ventresca, Food Plant Sanation,1a ed. CRC press, United States of America, 2002.

[8] Çengel, Yunus A., Transferencia de calor, 4a ed. McGraw-Hill, Mexico, 2011.

Análisis térmico de las celdas fotovoltaicas en un sistema interconectado a la red

Raúl Alberto López Meraz/Jorge Arturo Del Ángel Ramos
Facultad de Ingeniería Mecánica Eléctrica
Universidad Veracruzana
Xalapa, México
meraz_raul@hotmail.com

***Abstract*— The power loss of a photovoltaic system occurs for various reasons such as ambient temperature, shading areas in the generator, erroneous angular placement, dirt, etc., many of these are directly related to the overheating of the modules being the temperature of the most important variables in the performance of these systems. This paper will aim to determine the thermal effect on the electrical parameters and, therefore, in the production of energy at temperatures above 25 ° C in the solar cells connected to a network of CFE, located in the city of Xalapa residential facility, Veracruz, with a capacity of 1.08 kWp. The behavior of the interaction with the network generator is measured with the network analyzer PowerPad 8335. The energy study is obtained through monitoring of weather variables (irradiance, wind speed and temperature) obtained with Vantage Pro 2 weather station from 22 March to 6 May 2012. The PV array temperature is measured with 4 sensor LM35 and irradiance in the plane of the modules is achieved with a calibrated cell. The acquisition of these data is performed using the software LabView 2010 and NI USB-6008 card. The model that compares the experimental part was proposed by Alonso and Chenlo (2006). Finally, thermography is used by TI25 Thermal Imager to observe the temperature distribution in said system.**

Keywords*— *Temperature; irradiance; power; voltage; data acquisition.

I. INTRODUCCIÓN

La cantidad de energía solar que recibimos anualmente es de 5.4 x 10 24 J, lo que corresponde a 4,500 veces la energía que se consume mundialmente [3]. En 2012, la capacidad total instalada con energías renovables alcanzó 1,471 GW representando, aproximadamente, el 26% de la potencia eléctrica global. La energía fotovoltaica (FV) aportó 100 GW del total [10]. Por su parte, México contaba ese mismo año, con una capacidad de energía solar instalada en operación de 37 MW y en construcción estaban 156 MW. Se prevé que para el año 2026 la generación FV se incrementará a 6MW, 752 MW y 1,170 MW que corresponden a servicio público, autoabastecimiento y generación distribuida respectivamente [7]. Sin duda, la normativa actual como el Contrato de interconexión para Fuentes de Energías Renovables (2006), el Contrato de Interconexión para Fuentes de Energía Solar en Pequeña Escala (2007) y la Ley para el Aprovechamiento de las Energías Renovables y el Financiamiento de la Transición Energética (2008) han promovido y promoverán el interés, participación y el desarrollo de estas energías, en particular la solar FV.

Sin embargo, los medios de transformación de la tecnología FV no permiten que el recurso solar se pueda aprovechar en su totalidad, así, estos generadores tienen una eficiencia de 10 % aproximadamente [5]. Los factores que influyen en la máxima potencia disponible en un sistema FV son: irradiancia, temperatura, patrón de sombreado y la configuración del arreglo (AFV) [6]. Posiblemente el factor determinante en el funcionamiento de las celdas solares es la temperatura a la que están sometidas durante su operación. En este sentido en [9] se expone que el voltaje en circuito abierto (V_{OC}) disminuye, de forma significativa, aproximadamente 2.3 mV/ºC y la potencia máxima (P_p) lo hace en el orden de 0.4%/ºC-0.5%/ºC. Por otro lado, [4] menciona que la corriente de corto circuito (I_{SC}) se incrementa 0.1%/ºC, mientras que V_{OC} y P_p se ven disminuidos 2 mV/ºC y 0.35%/ºC, respectivamente.

II. DESCRIPCIÓN DEL SISTEMA

El sistema interconectado se encuentra en la Ciudad de Xalapa, Ver., que está localizada a una latitud de 19º32´24” y una longitud de 96º55´39”. Se compone de 12 módulos, de silicio monocristalino de 36 celdas, conectados en serie cada uno con una potencia de 90 W. En condiciones estándar de medida (STC)[1] entrega un V_{OC} 262.68 V y una I_{SC} de 5.37 A, produciendo una P_p de 1.08 kW. El AFV está orientado 20º al sur y está libre de sombras. Además, el inversor tiene una capacidad de 2kW a 120 V y 60 Hz.

III. METODOLOGÍA

A. *Comportamiento del generador FV*

Con el fin de verificar el comportamiento del sistema FV se colocó el analizador de redes Powerpad 8335 en el punto de inyección a la red eléctrica (centro de cargas del usuario). La frecuencia de muestreo fue de 5 minutos.

B. *Modelo*

El modelo que se emplea para simular el comportamiento del sistema fotovoltaico interconectado es el propuesto en [1] donde se consideran las principales variables ambientales que

[1] Irradiancia 1000 W/m^2, temperatura de celda de 25ºC, velocidad del viento de 1 m/s y masa de aire de 1.5.

afectan sus características eléctricas. Las ecuaciones (1) a (4) determinan estos parámetros.

$$I_{SC}(G, T_C) = I^*_{SC}(G^*, T^*_C) \quad [1+ Z(T_C - T^*_C)] \qquad (1)$$

$$V_{OC}(G, T_C) = V^*_{OC}(G^*, T^*_C) + mv_tLn \quad + B(T_C - T^*_C) \qquad (2)$$

$$P_p(G, T_C) = P^*_p(G^*, T^*_C) \quad [1 + D(T_C - T^*_C)] \qquad (3)$$

$$T_C = \quad (T_1 e^{bv} v + T_2) + T_a + \quad AT \qquad (4)$$

Donde G es la irradiancia global incidente en la superficie del sistema FV; T_C es la temperatura de la celda; Ta corresponde a la temperatura ambiente; Z es el coeficiente de variación de la corriente respecto a la temperatura; B representa el coeficiente de variación del voltaje respecto a la temperatura; D es el coeficiente de variación de la potencia respecto a la temperatura; G, T_C son condiciones determinadas de irradiancia y temperatura; G*, T^*_C se relacionan con las condiciones STC de irradiancia y temperatura, respectivamente; vv indica la velocidad del viento; m es el factor de idealidad del diodo; vt corresponde a voltaje térmico; AT, T_1, T_2 y b son parámetros empíricos para el tipo de módulo de la instalación

C. Base y adquisición de datos

Los datos obtenidos con la estación meteorológica Vantage Pro 2 se registraron cada 5 minutos, realizándose su descarga cada día desde el software WeatherLink 5.9.3, el periodo comprendió del 22 de marzo al 6 de mayo de 2012. En la Fig. 1 se aprecia la irradiancia en el plano horizontal.

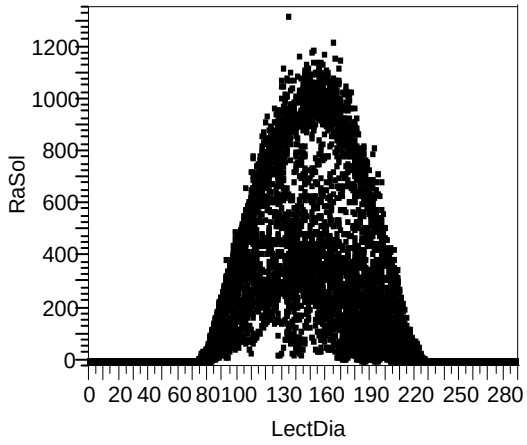

Fig. 1. Irradiancia del 22 de marzo al 6 de mayo 2012

En la Fig. 2 la temperatura ambiente y en la Fig. 3 la velocidad del viento durante este periodo.

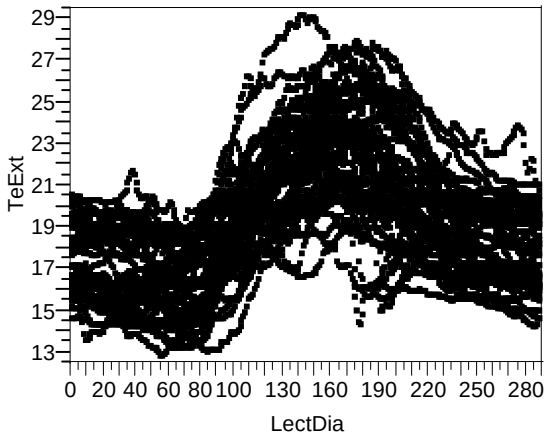

Fig. 2.Temperatura del 22 de marzo al 6 de mayo 2012

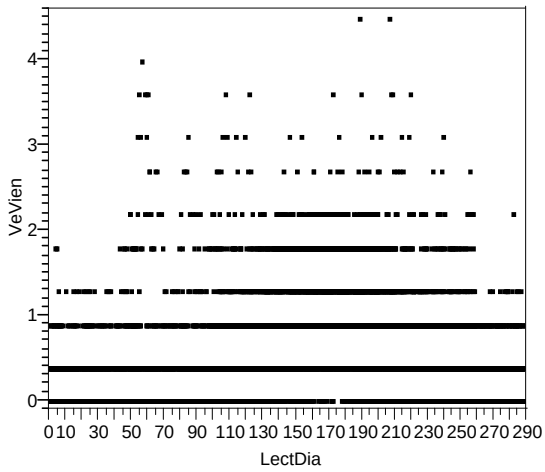

Fig. 3.Velocidades de viento del 22 de marzo al 6 de mayo 2012

Por otro lado, la irradiancia en el plano del AFV y la temperatura de 4 de sus puntos se obtuvieron con la ayuda de una celda calibrada[2] y 4 sensores LM35, su adquisición se logró con la tarjeta NI USB-6008 realizándose su programación en Labview 2010, la frecuencia de muestreo fue de 1 segundo para después obtener un promedio a 5 minutos para que coincidieran con los registros de las variables ambientales. En la Fig. 4 se muestra el programa en Labview 2010.

[2] Con la ayuda de un piranómetro LICOR (12 mV = 1000 W/m^2)

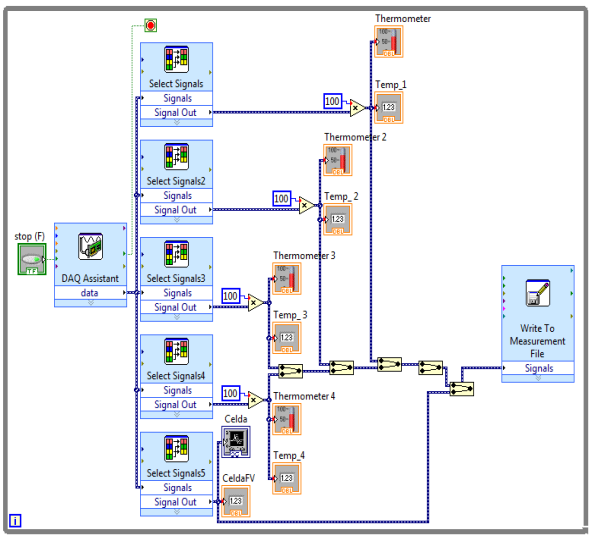

Fig. 4. Programa para adquirir temperaturas e irradiancia en el AFV

D. Termografía

La cámara termográfica es el modelo TI25, con ella se tomaron termogramas cada 30 minutos desde la parte posterior del AFV. La emisividad [3] de este material (Tedlar) que se introdujo en las mediciones fue de 0.86 siendo un poco menor que el propuesto en [8]. La información obtenida se trató en el software SmartView 3.1

IV. RESULTADOS Y DISCUSIÓN

En la Fig. 5 se presenta la potencia consumida del sistema eléctrico y la suministrada por el AFV.

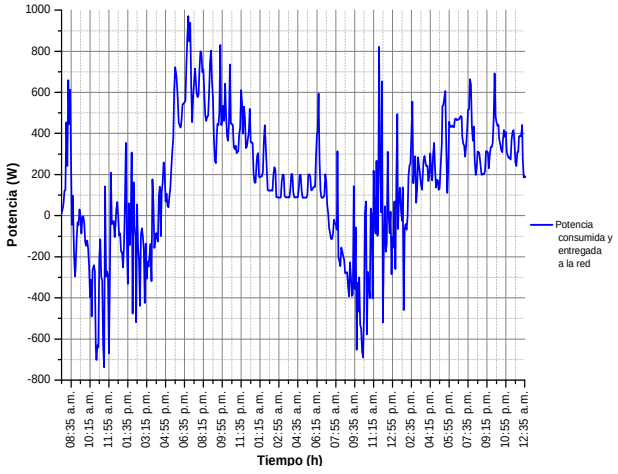

Fig. 5. Potencia entregada y recibida por el sistema FV del 22 al 24 de marzo de 2012.

Se destaca que en este periodo el generador solar entregó valores cercanos al 70% de su capacidad consiguiéndolo entre las 9:45 – 11:55 am que es cuando se cuenta con un recurso solar considerable. Sin embargo, este porcentaje se ve afectado por las condiciones climatológicas afectando su producción.

[3] Emisómetro AE1

En la Fig. 6 está el comportamiento de los 4 puntos seleccionados respecto a la temperatura ambiente y la irradiancia en el plano del AFV.

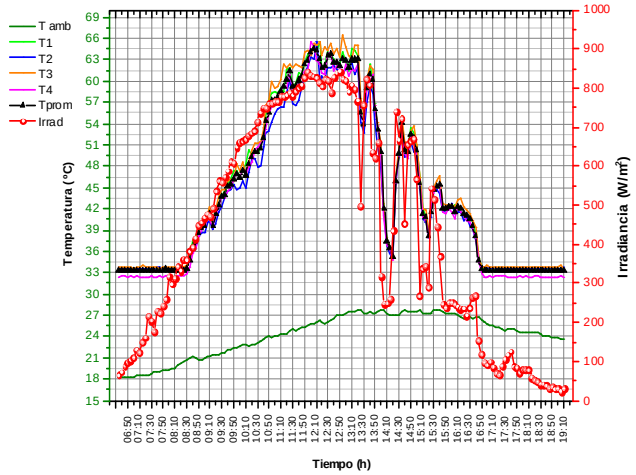

Fig. 5. Distribución de temperaturas del generador FV el 6 de mayo de 2012

Es observable que las 4 temperaturas varían de forma lineal respecto a la irradiancia, la diferencia es de acuerdo a la hora del día presentándose el mayor contraste entre ellas cercano a los 6 ºC, en este sentido la temperatura promedio máxima que se presentó en los módulos fue de 64 ºC. De igual forma se identifica que existen 2 picos de irradiancia, el primero superando los 800 W/m^2 y el segundo alcanza 750 W/m^2. Por su parte la temperatura ambiente máxima es de 28 ºC.

Las características eléctricas de la planta FV se aprecian en la Fig. 7, en ella aparecen, además la temperatura ambiente, la temperatura promedio de las celdas y la irradiancia correspondiente.

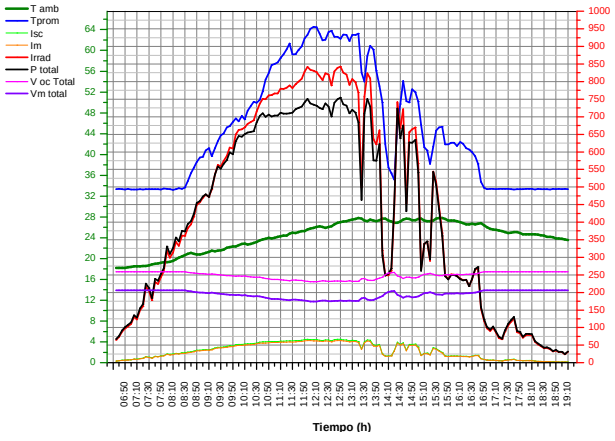

Fig. 7. Variables eléctricas del AFV el 6 de mayo de 2012

La temperatura ambiente no muestra un patrón respecto a la potencia generada. La potencia máxima del AFV es de 756 W ésta se genera cuando la irradiancia y la temperatura de los módulos alcanzan sus valores más altos. La relación de potencia es del 70% de la P_P de las especificaciones del fabricante, esta diferencia corresponde a que la irradiancia no

alcanza, en ningún momento del día, 1 kW/m^2 y a que el calentamiento promedio de las celdas supera los 64 ºC, es decir, 39 ºC por arriba de la condición STC. Por otra parte, las corrientes se ven afectadas mínimamente con la temperatura.

Una característica fundamental para el acoplamiento del AFV con el inversor es el voltaje generado ya que si éste no se encuentra en su ventana de operación no se podrá lograr la interconexión. En la Fig. 8 se advierte la conducta de esta variable.

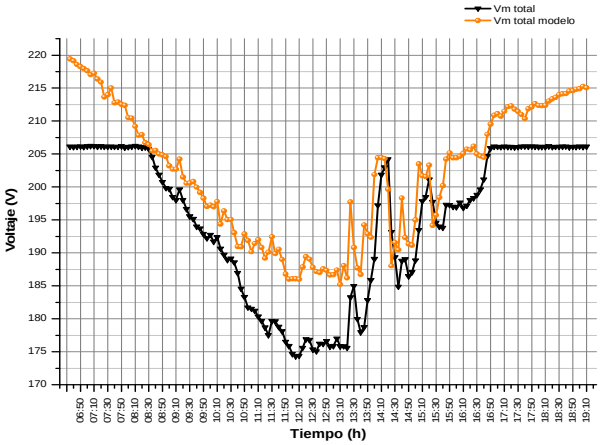

Fig. 8. Comportamiento del voltaje generado por el AFV el 6 de mayo de 2012.

La curva negra representa el voltaje producido en función de la temperatura obtenida con los sensores y se nota que en los momentos de mayor recurso solar la tensión cae drásticamente a valores inferiores de 180 V provocando que el inversor se desconecte y no pueda aportar la energía producida por el AFV. Por el contrario, la curva naranja se obtuvo determinando la temperatura de las celdas considerando las variables ambientales de irradiancia en el plano del sistema solar, temperatura ambiente y velocidad del viento, de esta manera se aprecia que en ningún momento el inversor se desconectaría, sin embargo sí hay registros que están por debajo de los 190 V que es el valor mínimo que supone la operación correcta de este convertidor de energía.

El análisis termográfico se realizó en la sección donde aparecen los sensores, se eligió el 1º de mayo de 2012. En las Fig. 9, 10 y 11 se presentan los termogramas en tres horas distintas

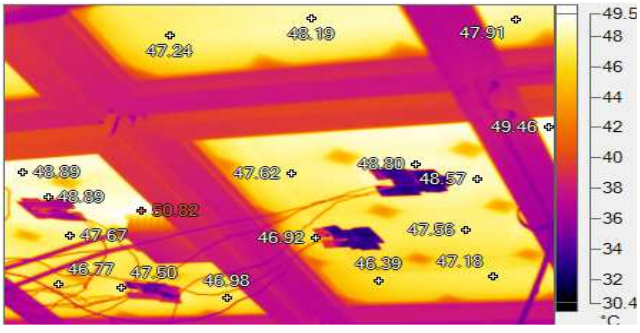

Fig. 9. Termograma tomado a las 9:30 hrs

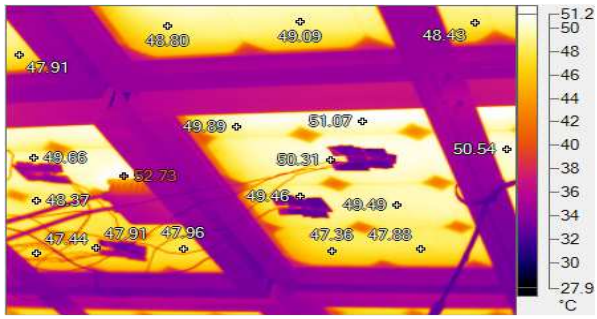

Fig. 10. Termograma tomado a las 11:30 hrs

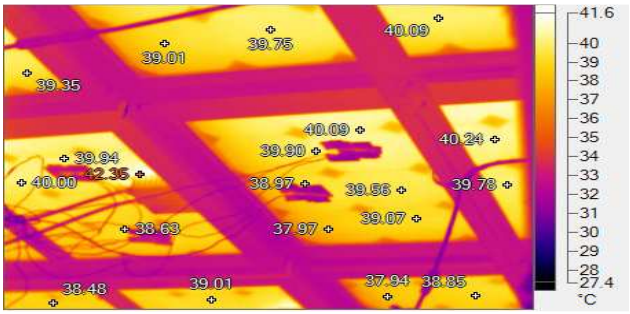

Fig. 11. Termograma tomado a las 13:25 hrs

El valor más alto que proporciona la termografía no es igual al promedio obtenido con las mediciones, sin embargo, si se toman las medias de los puntos considerados en cada imagen la diferencia entre ambas lecturas tiene un límite superior de 5.09 ºC y el mínimo de 0.2 º C. Asimismo, la disparidad existente entre los lugares seleccionados son menores a 7.5 ºC lo que es inferior a la diferencia máxima expuesta en [2] donde ésta no debe exceder en ± 10ºC

V. CONCLUSIONES

A partir de este análisis, se puede decir que cerca del 10% de las mediciones de temperatura promedio en el AFV podrían provocar que no se produjera el voltaje mínimo requerido por el inversor. Se comprueba que el modelo empleado proporciona aproximaciones aceptables usando variables ambientales. Además, la termografía permitió observar que la temperatura en los módulos no es uniforme y que no existen puntos calientes. Por último, a pesar de que el sistema presenta pérdidas energéticas el usuario ha reducido considerablemente su consuno de energía y por ende el costo de su factura.

REFERENCES

[1] Alonso, M., Chenlo, F. (2006). Estimación de la energía generada por un sistema fotovoltaico conectado a la red. Laboratorio de sistemas fotovoltaicos. CIEMAT. Madrid.

[2] Asociación Española de Normalización y Certificación (2006). UNE-EN61215. Módulos fotovoltaicos (FV) de silicio cristalino para uso terrestre. Cualificación del diseño y homologación.

[3] Dirección General de Industria, Energía y Minas. 2002. Energía Solar, el recorrido de la energía. E.i.S.E Domenech, S.A.

[4] Lasnier, F., Gan, T. (1990). Photovoltaic Engineering Handbook. Gran Bretaña. Adam Hilger

[5] Mousazadeh H, Keyhani A, Javadi A, Mobli H, Abrinia K, Sharifi A. A review of principle and sun-tracking methods for maximizing solar

systems output. Renewable and Sustainable Energy Reviews 13(2009) 1800-1818.

[6] Patel, H.; Agarwal, V, 2008. "MATLAB-Based Modeling to Study the Effects of Partial Shading on PV Array Characteristics," Energy Conversion, IEEE Transactions on , vol.23, no.1, pp.302-310.

[7] PER 2012-2026/Secretaría de Energía (SENER)

[8] Pérez, M. (2010). Estudio termográfico de la influencia de la temperatura en los módulos fotovoltaicos. Universidad Carlos III de Madrid.

[9] Prudhvi, P. y Chaitanya, P. Efficiency Improvement of Solar PV Panels Using Active Cooling. 978-1-4577-1829-8/12. IEEE

[10] Renewables Global Status Report, REN 21 2013.

Pristine perovskite like structured nanowires excised from Sr_2FeMo_6

J. Pilo, E. Carvajal, R. Vázquez-Medina and M. Cruz-Irisson
ESIME-Culhuacán
Instituto Politécnico Nacional
Av. Santa Ana 1000, México, D.F., C.P. 04430, MÉXICO
ecarvajalq@ipn.mx

M. I. Iturrios, M. C. Crisóstomo
CECyT No. 8 Narciso Bassols
Instituto Politécnico Nacional
Av. de las Granjas 618, México, D.F., C.P. 02530, MÉXICO

***Abstract*—The polycrystalline double perovskite Sr_2FeMoO_6 (SFMO) is a notorious compound because it is half-metallic, colossally magnetoresistive and has a high Curie temperature. That set of properties makes it a promising material for spintronic applications besides it has been used in solid oxide fuel cells for a long time. Moreover, by changing the transition metals or even their relative ratio, it is possible to modify the electric and magnetic behavior. Having that background, the proposal in this work is to study an unidimensional system excised from the monocrystalline SFMO, keeping the axis parallel to the [001] direction in the SFMO conventional cell. The motivation is to modify the energy gap magnitude and also the gap kind, associated with the majority spin channel, by changing the transition metals sequence along the nanowire model axis. Calculations for the pristine nanowires were made within the framework of the Density Functional Theory, using the generalized gradient approximation and the functional proposed by Perdew-Burke-Ernzerhof (PBE). The electronic density of states and band structure were calculated for the optimized wires; also, coordination is discussed.**

Keywords— double perovskita; nanowires; Density Functional Theory; half-metallicity

I. Introduction

The perovskite structures ABX_3 exhibit a diversity of properties among which the catalytic, magnetic, electronic and optical are noteworthy [1–3]. Every physical or chemical property is linked to the chemical composition, the simple or double character of the perovskite, the crystalline degree, the impurities content, the antisite occupation, etc.; however, it is possible to get a specific set of properties by controlling the mentioned parameters. Because of that, double perovskites have been widely studied for their potential application in various technological fields: spintronics, fuel cells and, in recent years, photovoltaic devices [4]. Among those double perovskites, the Sr_2FeMoO_6 (SFMO) case is interesting; since, being widely used as an electrode material in the solid oxide fuel cells (SOFCs) for many years, has attracted attention because of their half-metallic and colossally magnetoresistive behaviors as well as their high Curie temperature [5]. That properties set makes the SFMO a strong candidate to be incorporated in the development of spintronic devices, in which the energy consumption could be diminished drastically, at the same time that the high spin polarization can be used as the central property for the device operation. Furthermore, nanostructuring the material should generate modifications on their physical properties own to the quantum confinement, allowing exploit the enormous exposed surface which passivated or pristine character would define the catalytic properties of the nanostructured material.

II. Model and Computational Method

Employing the reported experimental information about the Sr_2FeMoO_6 bulk double perovskite (*e. g.* space group I4/mmm and lattice parameters a = 5.5704 Å and c = 7.8983 Å in [6]) it was constructed a crystalline model from where a nanowire (NW) was excised, keeping the axis of the latter parallel to the [001] direction in the former. The geometry of the pristine NWs was optimized in the Density Functional Theory scheme [7], using the Generalized Gradient Approximation (GGA) and the Perdew-Burke-Ernzerhof (PBE) [8] functional, as implemented in the DMol^3 code. Three wires were considered for this work, keeping the edge length of the transversal section equal to the first lattice parameter of the SFMO crystal; even being structurally identical (Fig. 1), the associated charges for the wires were different: zero, 2e and 3e. The parameter criteria considered for convergence were: 2.72×10^{-4} eV for the energy change, 5×10^{-3} Å for the maximum displacement and 5.42×10^{-2} eV/Å for the maximum force.

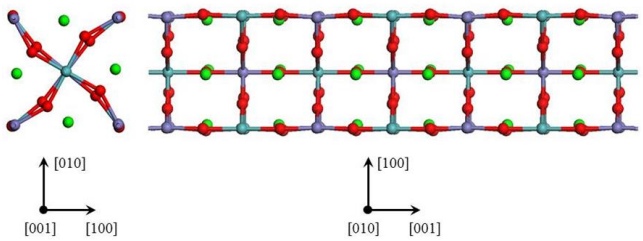

Fig. 1. Modeled pristine nanowire, excised from the crystalline compound Sr_2FeMoO_6. The wire axis is parallel to the [001] crystal direction and the shown views are the transversal cut (left) and the longitudinal (right); blue, green, purple and red spheres represent Mo, Sr, Fe and O atoms, respectively.

III. Results and Discussion

After the uncharged wire geometry optimization, their axis becomes a C_4 one. While the longitudinal wire supercell parameter diminishes (7.726 Å), respect to the c bulk material, the lengths of the edges at the perpendicular planes change their values, depending which atomic species are at the vertices on the plane of interest: the measure is 5.623 Å for those with Mo atoms, it contracts to 5.515 Å for the planes with Fe atoms, but increases to 5.716 Å for the planes with O (Fig. 2). Excepting the Sr atoms all the additional have a different coordination, it means that coordination depends on where each atom is placed: at the central chain or at one of the lateral chains. The axial Fe and Mo are hexavalent and have the higher charge values (Table I) because they are fully surrounded by oxygen atoms, contrasting with the similar lateral placed atoms, which are responsible for the bonding polarization. For both charged nanowire cases the c cell parameter increases, being greater the change for the negative wire (Table II). Respect to the a parameter, which measures the same as the separation between O atoms at the correspondent transversal plane, it reduces their value for both charged wires; being almost identical, the parameter for the negative charged wire is slightly greater than the other, as occurs for c. Separation between atoms at the vertices, of planes perpendicular to the axis wires, are 5.554 Å and 5.545 Å for Mo and 5.542 Å and 5.566 Å for Fe, when charges are –2 or 2, respectively.

One remarkable result is that the modeled nanowire is half metallic (Fig. 3), as it is the bulk material; the energy band gap is direct for the majority spin channel, with a magnitude of 0.604 eV. The four Fe (T) atomic magnetic moments are parallel one to each other, but are antiparallel to the Mo (O) which is placed at the wire axis and they surround, leading to the smallest cross section area along the nanowire.

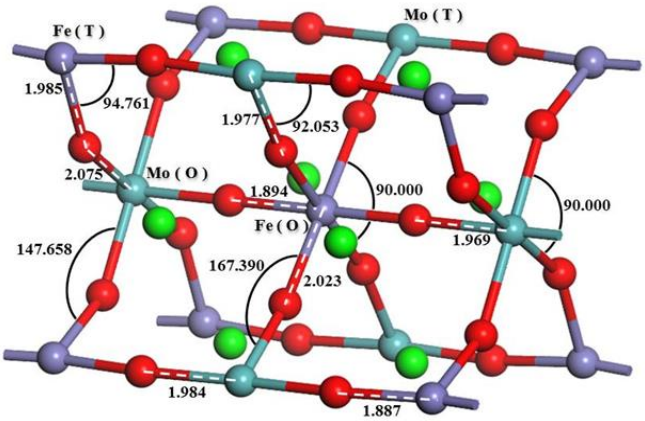

Fig. 2. Bond distances and dihedral angles are shown for the pristine uncharged wire. Equivalent information was omitted for clarity. Length values are in angstroms and angles in degrees. Transition metals (Fe, Mo) coordination is indicated in parenthesis by capital letters: O for octahedral and T for trigonal. The symmetry group is P4/m and blue, green, purple and red spheres represent Mo, Sr, Fe and O atoms, respectively.

On the other hand, at the intermediate sized transverse plane where there is a central Fe atom, all magnetic moments are parallel. Even more, all atomic magnetic moments along the wire axis are parallel. For the transverse plane with the bigger area, conformed by oxygen and strontium atoms, the magnetic moments of the latter are antiparallel to the corresponding magnetic moments associated to the lateral oxygen atoms. The magnetic moment for each unit cell is 3.682 ħ. When the pristine nanowire is charged (2e), the magnitude of the energy gap associated to the majority spin channel changes from 0.604 eV to 0.474 eV, but remains being direct (Fig. 4).

TABLE I. Atomic charge and magnetic moment values, for each atomic species in the pristine nanowire; capital letters O and T labels octahedral and trigonal coordination, respectively.

Sr–Fe–Mo–O NW, Ch 0		
atom	*charge (e)*	*spin (ħ)*
Sr	1.211	–0.032
Fe (T)	0.541	3.144
Fe (O)	0.815	–0.117
Mo (T)	0.619	–1.851
Mo (O)	1.385	–1.431
O (Mo (O))[a]	–0.960	0.089
O (Fe (O))[a]	–0.950	–0.070
O (lateral)[a]	–0.872	0.077
O (axial)[a]	–0.957	–0.035

[a.] The O atoms labels axial/lateral/Fe(O)/Mo(O) indicate their locations: along the central or lateral chains (first and second) or as tagged metal first neighbor at transverse section (third and fourth).

This fact is very important because it is possible to use the nanowire for optical applications, which is the aim to study these NWs. On the contrary, if the nanowire is negatively charged (–2e) then the half metallic character is lost; the NW turns to be a conductor with identical behavior for both spin channels. It seems like taking apart Fe atoms by a distance greater than the separation between Mo atoms permit that the electronic states occupation turns spin symmetrical. However, to keep charge condition of the pristine nanowires seems very difficult, at least without some passivating species which nature will depends on the synthesis process.

TABLE II. Nanowire charge, cell parameters and separation between atoms at the vertices of transversal planes.

Sr–Fe–Mo–O NWs					
charge (e)	*a (Å)*	*c (Å)*	d_{O-O} *(Å)*	d_{Mo-Mo} *(Å)*	d_{Fe-Fe} *(Å)*
–2	5.598	7.899	5.598	5.554	5.542
0	5.716	7.726	5.716	5.623	5.515
2	5.595	7.751	5.595	5.545	5.566

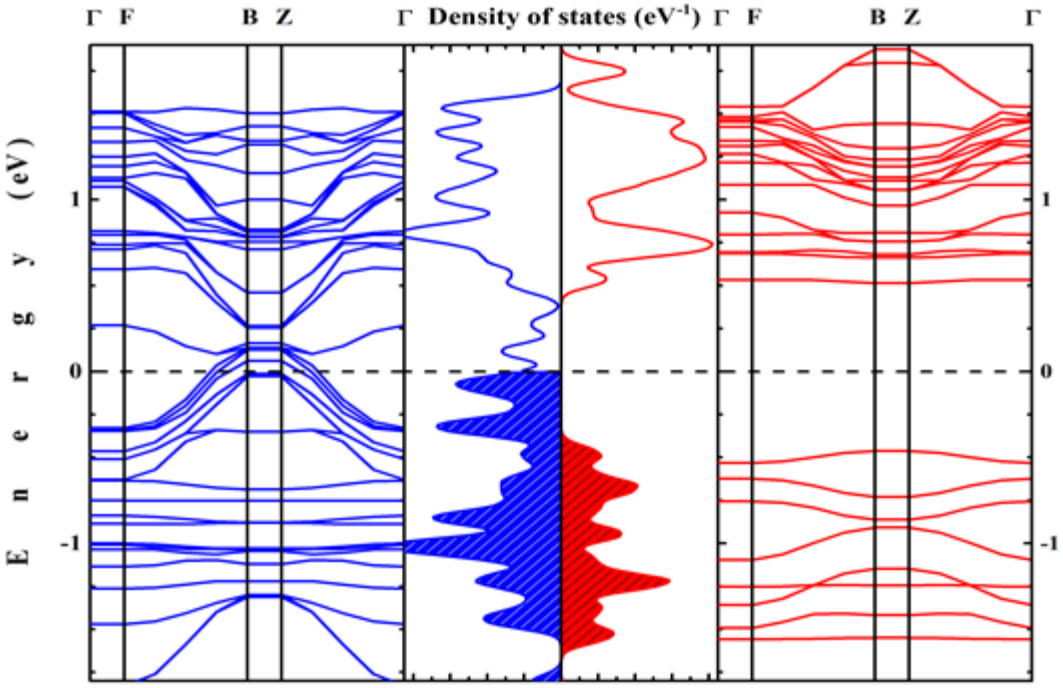

Fig. 3. Band structures and electronic density of states for the uncharged pristine nanowire. Graphs in blue correspond to the down-spin channel, while graphs in red correspond to the up-spin channel. The black horizontal discontinuous line indicates the Fermi level and the central filled graphs indicate the occupied states.

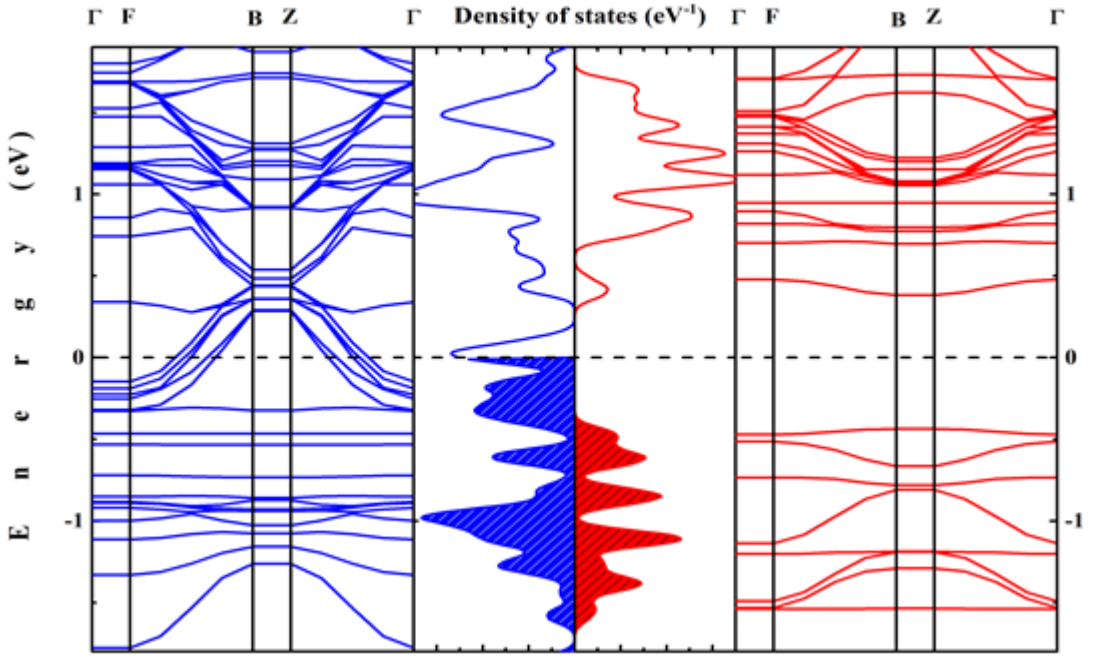

Fig. 4. Band structures and electronic density of states for the pristine nanowire with charge 2e. Graphs in blue correspond to the down-spin channel, while graphs in red correspond to the up-spin channel. The black horizontal discontinuous line indicates the Fermi level and the central filled graphs indicate the occupied states.

IV. Conclusions

We found that it is possible to keep the characteristic half-metallic behavior of the bulk Sr_2FeMoO_6, associated to a nanostructured system excised from it. At least if the NW is uncharged or positively charged. For these cases, the energy band gap result smaller than the corresponding to the crystalline material but is direct, giving the possibility to use this kind of NWs for optical applications. On the other hand, the negatively charged NW differs from the bulk, being a conductor without any spin polarization. At the lateral chains metals are trivalent and bond to oxygen mostly in an ionic way, contrasting to the metals on the central chain, where are hexavalent. It must be done further investigations on the way to synthesis those NWs with the desired charge but without a reactive surface.

Acknowledgment

This work was partially supported by the multidisciplinary projects SIP2014-1640 and SIP2014-1641 from Instituto Politécnico Nacional, also by the project 252749 from Consejo Nacional de Ciencia y Tecnología (CONACyT). J. Pilo wants to acknowledge the scholarship from CONACyT.

References

[1] L. Bi, *et al.*, "Structural, magnetic, and optical properties of $BiFeO_3$ and Bi_2FeMnO_6 epitaxial thin films: An experimental and first-principles study," Phys. Rev. B, vol. 78, pp. 104-106, 2008.

[2] R. J. Gorte, J. M. Vohs, "Catalysis in Solid Oxide Fuel Cells," Annu. Rev. Chem. Biomol. Eng., vol. 2, pp. 9–30, 2011.

[3] C. Li, *et al.*, "Double perovskite oxides $Sr_2Mg_{1-x}Fe_xMoO_{6-\delta}$ for catalytic oxidation of methane," J. Natural Gas Chem., vol. 20, pp. 345–349, July 2011.

[4] E. Barrera–Calva, *et al.*, "Caracterización superficial de películas de óxidos de Co y Co–Fe," Rev. Mex. Ing. Quim., vol. 4, pp. 147–156, 2005.

[5] K. I. Kobayashi, T. Kimura, H. Sawada, K. Terakura, Y. Tokura, "Room-temperature magnetoresistance in an oxide material with an ordered double-perovskite structure," Nature, vol. 395, pp. 677–680, October 1998.

[6] Q. Zhang, *et al.*, "Crystal structure, magnetic and electrical-transport properties of rare-earth-doped Sr_2FeMoO_6," Physica B, vol. 381, pp. 233–238, May 2006.

[7] E. Chigo–Anota and J. F. Rivas-Silva, "Efectos de la correlación electrónica en sólidos. Metodologías para su tratamiento," Rev. Mex. Ing. Quim., vol. 5, pp. 105–117, June 2006.

[8] J. P. Perdew, K. Burke and M. Ernzerhof, "Generalized Gradient Approximation Made Simple," Phys. Rev. Lett. Vol. 77, pp. 3865–3868, May 1996.

Diseño de una columna de destilación reactiva multitarea para la purificación de silanos

C. Ramírez–Márquez, J. G. Segovia-Hernández*, J. A. Cervantes Jáuregui
Universidad de Guanajuato, Campus Guanajuato
Guanajuato, Gto. México
*gsegovia@ugto.mx

***Resumen*—La energía solar fotovoltaica al igual que otras energías renovables, constituye frente a los combustibles fósiles, una fuente inagotable de energía, contribuyendo al autoabastecimiento energético nacional y por lo tanto social, con un impacto comparativamente mucho menor que las fuentes convencionales de energía. Por lo anterior, es importante centrar la atención en la obtención de productos para elaboración de celdas solares. La obtención de los silanos es sin duda, un proceso que presenta muchos inconvenientes, principalmente, en el costo para su obtención debido a que se requieren purezas bastante elevadas. En este trabajo se presenta la propuesta de un diseño conceptual de una columna de destilación reactiva (DR) multitarea para la producción de silano de alta pureza, así como de monoclorosilano y diclorosilano, éstos últimos también siendo productos de gran interés comercial e industrial en el sector energético. Se utilizaron estrategias de intensificación de procesos, asumiendo como objetivos la recuperación de los tres productos de interés, así como el impacto ambiental. Se ha demostrado que es factible obtener un diseño único multitarea, en el cual se obtienen los tres productos de interés en el domo de la columna, esto variando condiciones de operación como los son la presión y la temperatura, se han obtenido purezas de 99.5% para los tres productos y una conversión completa de triclorosilano a silano por medio de una columna de destilación reactiva. Por los resultados obtenidos en este trabajo, se confirmó que ésta tecnología DR es rentable y competitiva para la producción de silano y sus precursores destinados a usos en el sector energético.**

Palabras Clave — Destilación Reactiva, Columna Multitarea, Silanos

I. INTROCUCCIÓN

La energía solar fotovoltaica al igual que otras energías renovables, constituye frente a los combustibles fósiles, una fuente inagotable de energía, contribuyendo al autoabastecimiento energético nacional y por lo tanto social, con un impacto comparativamente mucho menor que las fuentes convencionales de energía.

A nivel mundial con la reducción de las reservas de los combustibles fósiles (petróleo particularmente), la necesidad urgente de contar con fuentes alternas de energía que sean preferentemente renovables, limpias y económicamente viables tales como la eólica, la hidroeléctrica y la solar, ha tomado gran relevancia. La búsqueda de estas fuentes alternas es uno de los más importantes retos que enfrenta actualmente la humanidad. En particular, la energía solar está siendo explotada de varias formas, pero el método más conocido usa celdas solares basadas en silicio donde la transformación directa de la luz del sol en electricidad se realiza a través del efecto fotovoltaico (efecto PV por sus siglas en inglés).

El crecimiento en el interés en la obtención de silicio como materia prima para celdas solares ha evolucionado de manera importante en las últimas décadas (Ver TABLA I), y se espera un incremento en la demanda de alrededor del 30% [1]. Un análisis un poco más detallado señala que el mercado fotovoltaico ha crecido a una velocidad promedio de 45% por año en la última década, pero con un crecimiento entre 2007 a 2011 de aproximadamente el 70% por año; con una disminución del 15% en el 2012 debido a que algunos países europeos redujeron los incentivos. Mientras que los números hablan de gran crecimiento, la capacidad instalada de 27 GW en 2011 es solamente una fracción que representa el 1% del total de la cantidad de energía que fue generada por todas las fuentes, indicando con ello que hay muchísimo campo para que continúe el desarrollo en el futuro inmediato [2].

TABLA I. DEMANDA Y DISPONIBILIDAD DE SILICIO POLICRISTALINO EN LA DÉCADA PASADA [1].

Año	Capacidad [t]	Demanda (Semiconductor) [t]	Demanda (Fotovoltaico) [t]	Disponibilidad (Fotovoltaico) [t]
2003	26,700	17,000	9,000	9,700
2004	28,800	19,350	14,032	9.450
2005	30,200	20,085	18,181	10,115
2006	34,500	21,166	16,705	13,334
2007	38,050	23,071	17,435	14,979
2008	48,550	26,301	24,089	22,249
2009	53,800	26,837	28,233	26,973
2010	5,800	27,632	32,108	31,168

Aun cuando las celdas de silicio se encuentran compitiendo en la actualidad con otro tipo de celdas de materiales avanzados, se ha predicho que las celdas solares de silicio continuarán con una contribución importante al mercado en función de la madurez de la tecnología, de su disponibilidad y principalmente si se presentan desarrollos tecnológicos que reduzcan su costo [3].

En la actualidad hay celdas de silicio policristalino, monocristalino y amorfo, siendo las primeras las que más se emplean dado su costo. Sin embargo, es importante saber que el alto costo del silicio policristalino se debe tanto al proceso

de obtención del mismo como al proceso de producción de su materia prima, el silano (SiH_4) [4].

Uno de los procesos desarrollados hace ya tiempo pero vigente en la actualidad para la producción de silano involucra la desproporción del triclorosilano (que se obtiene a partir de la reacción entre silicio grado metalúrgico y cloruro de hidrógeno. El silicio metalúrgico es el resultado a su vez de la reducción carbotérmica del cuarzo natural) hacia silano y tetracloruro de silicio [5]. Se ha analizado que para un panel solar basado en silicio, cerca del 40% de la energía requerida para su fabricación es consumida en la producción del precursor. Por ello, la reducción del consumo de energía en esta etapa en crucial para minimizar el módulo de retorno y con ello el costo de la tecnología [6].

Las reacciones del sistema Si-H-Cl son muy complejas y pocos son los estudios que han abordado el llamado proceso Siemens (que es el proceso mediante el cual se deposita el silicio a partir del silano) por medio de cálculos basados en la selección de datos termodinámicos [7]. La obtención de los silanos es, sin duda, un proceso que presenta muchos inconvenientes, principalmente, en el costo para su obtención debido a que se requieren purezas bastante elevadas. Una alternativa al proceso convencional de producción de silanos involucra el uso de destilación reactiva (DR), la cual abate la gran desventaja del proceso convencional, el cual requiere un gran número de columnas de destilación para obtener el producto final.

Dicho esto, se presenta la propuesta de un diseño conceptual de una columna única de DR para la producción de silano, diclorosilano y monoclorosilano de alta pureza, productos con interés comercial e industrial, utilizando estrategias de intensificación de procesos, asumiendo como objetivos la recuperación de los productos de interés y el minimizar el impacto ambiental.

II. Desarrollo del Modelo

A. *Reacción Química*

La reacción consiste en tres etapas. En la primera etapa, el triclorosilano ($SiHCl_3$) se convierte en diclorosilano (SiH_2Cl_2) y tetracloruro de silicio ($SiCl_4$). Posteriormente, el diclorosilano reacciona para obtener monoclorosilano (SiH_3Cl) y triclorosilano. Finalmente, el monoclorosilano es transformado en silano (SiH_4) y diclorosilano. Las tres etapas de reacción se muestran en las ecuaciones 1.1 a 1.3.

$$2SiHCl_3 \rightarrow SiH_2Cl_2 + SiCl_4 \quad (1.1)$$

$$2SiH_2Cl_2 \rightarrow SiH_3Cl + SiHCl_3 \quad (1.2)$$

$$2SiH_3Cl \rightarrow SiH_4 + SiH_2Cl_2 \quad (1.3)$$

En donde, las ecuaciones de velocidad de reacción se presentan según las ecuaciones 1.4 a 1.6.

$$r_1 = k_1\left(x_1^2 - {}^{x_0x_2}/_{K_1}\right) \quad (1.4)$$

$$r_2 = k_2\left(x_2^2 - {}^{x_1x_3}/_{K_2}\right) \quad (1.5)$$

$$r_3 = k_3\left(x_3^2 - {}^{x_2x_4}/_{K_3}\right) \quad (1.6)$$

Donde x_0, x_1, x_2, x_3 y x_4 son la fracción molar del tetracloruro de silicio, del triclorosilano, del diclorosilano, del monoclorosilano, y del silano en líquido, respectivamente; r_1, r_2, y r_3 son las velocidades de reacción del triclorosilano, del diclorosilano y del monoclorosilano desproporcionado, respectivamente; k y K son la constantes de reacción y las constantes de equilibrio químico, respectivamente (Ver Tabla II).

Tabla II. Parámetros cinéticos para la desproporción del triclorosilano en fase líquida [8].

	k_0 [s^{-1}]	E [J/mol]	K_0	ΔH [J/mol]
r_1	73.5	30045	0.1856	6402
r_2	949466.4	51083	0.7669	2226
r_3	1176.9	26320	0.6890	-2548

Ya que la mezcla es no polar, se seleccionó la ecuación de estado Peng-Robinson para realizar el cálculo termodinámico.

B. *Modelo de la Columna DR*

Para una reacción catalítica heterogénea, la columna de destilación reactiva típica es una columna de destilación que incluye algunas zonas de catalizador sólido, llevándose a cabo un fenómeno de transferencia de masa interna, y así, la reacción de acoplamiento y la separación por destilación se llevan a cabo en el mismo equipo. La columna de destilación reactiva típica se muestra en la Fig. 1. Primeramente se observa que consta de tres secciones: la rectificación, zona de reacción y la sección de agotamiento, situados en la parte superior, media e inferior, respectivamente, con el catalizador sólido empacado en el medio de la columna. Habitualmente, se utilizan perlas de resina de intercambio iónico, con tamaños de partícula de 0,3-1,2 mm, éstas están soportadas por una malla de alambre de acero inoxidable para una buena fijación y ayudando a tener una baja caída de presión. Las zonas de rectificación y de agotamiento se pueden rellenar con cualquier tipo de embalaje utilizado habitualmente en las aplicaciones de destilación convencionales, tales como los tipos de relleno estructurado y al azar [8].

Se alimenta triclorosilano a la columna en la parte inferior de la sección de reacción (parte superior de la sección de agotamiento). Luego de que la desproporción se lleva a cabo en la sección de reacción y la mezcla de producto de vapor que contiene componentes ligeros tales como silano, diclorosilano y monoclorosilano ascienden a la sección de rectificación, el componente pesado tetracloruro de silicio descienden a la sección de agotamiento.

Este modo de operación resulta muy efectivo, ya que hace que la reacción se complete totalmente, y el producto más deseado (silano, diclorosilano o monoclorosilano) es capaz de ser retirado en la parte superior de la columna, mientras que el subproducto (tetracloruro de silicio) puede ser retirado de la parte inferior [8]. En la práctica, el Tetracloruro de silicio es generalmente reciclado a un reactor de hidrocloración aguas arriba para regenerar triclorosilano de nuevo.

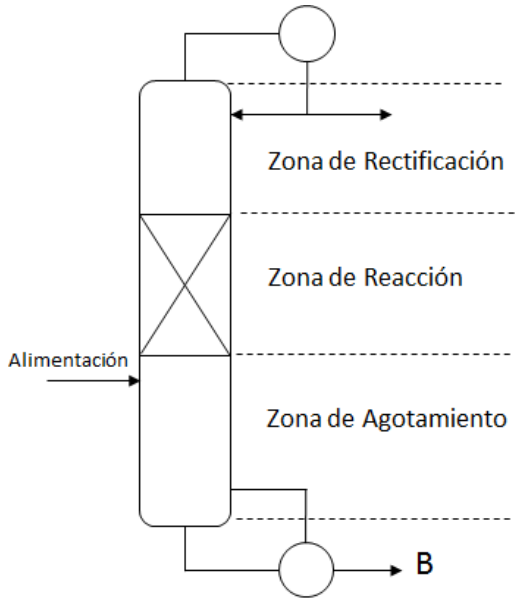

Fig. 1. Columna de destilación reactiva.

III. METODOLOGÍA

La metodología de diseño de una columna de destilación reactiva para la producción de silano se presentó en un trabajo realizado por Xun Huang et al. [8]. Con base en dicho trabajo se realizó el diseño de una columna de destilación reactiva multitarea (producción de silano, monoclorosilano y diclorosilano) se presenta a continuación (Ver Fig. 2).

Se comenzó realizando el diseño de una columna individual para cada componente, esto ayudaría a ver las condiciones de diseño en las cuales debe basarse la columna única multitarea.

El diseño de cada columna individual se realiza con el uso del software Aspen Plus para poder reproducir el modelo. Inicialmente se elige un modelo de columna riguroso "RadFrac", el cual es un modelo aplicable en un amplio número de situaciones y, además, ofrece suficiente rigor en el cálculo, compatibles ambos con la sencillez en la construcción del modelo de columna en Aspen plus. La simulación se realiza empleando un método termodinámico adecuado para los componentes. Se introducen los componentes a emplearse.

En la ventana del "Setup" de la columna "RadFrac", se introduce el número de etapas, la relación de reflujo, la carga térmica del sistema, o alguna de las variables a seleccionar; para posteriormente elegir la etapa de alimentación, las etapas por las cuales se obtienen los productos y la presión con la que el sistema trabajara. Se introduce la reacción que se lleva a cabo dentro de la columna y se eligen las etapas reactivas; al elegir las etapas reactivas se tiene que definir el tiempo de residencia o el holdup adecuado, , como se muestra en la Fig. 2. El sistema cuenta con muchas variables a manipular para obtener el producto deseado a la pureza requerida, sabiendo esto se buscan dichos parámetros para la obtención del silano, diclorosilano y monoclorosilano, a una pureza molar de 0.995.

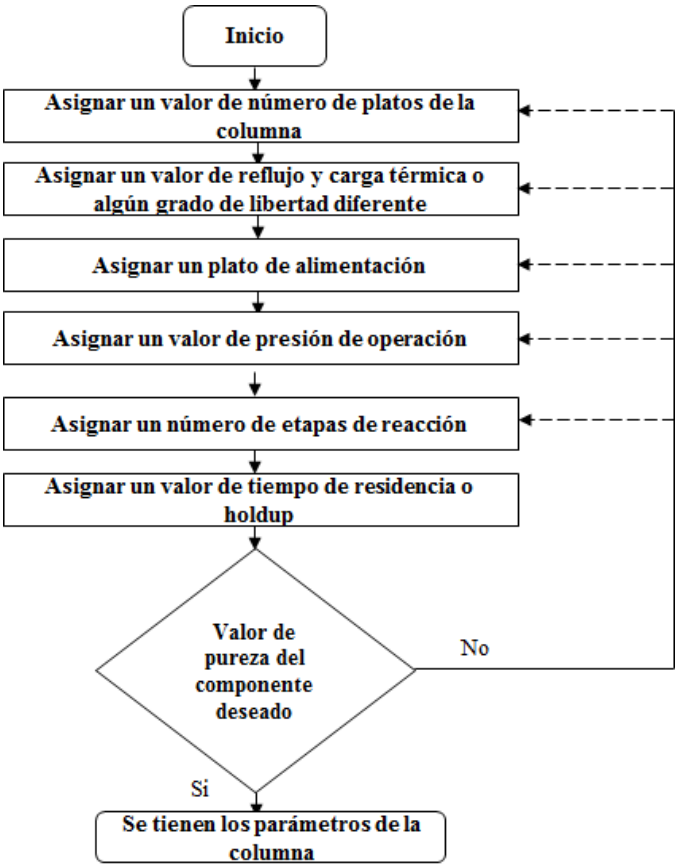

Fig. 2. Metodología de diseño de la columna DR.

IV. RESULTADOS

Para la separación del silano, el diseño consta de una columna DR de 62 platos, 29 etapas de reacción que se encuentran en el intervalo del plato 21 al 50, con una relación de reflujo de 63 moles. La alimentación se lleva a cabo en el plato 51 a una presión de 5.5 atm, a una temperatura de 323.15 K y a un flujo de 10 kmol/h, con una presión de 2.5 atm en el condensador y una caída de presión en la columna de 0.5 kPa, y con un holdup de 0.15 en volumen metro cúbico.

En el caso de la separación del monoclorosilano, el diseño consta de una columna DR de 62 platos, 29 etapas de reacción que se encuentran en el intervalo del plato 21 al 50, con una relación de reflujo de 47 moles. La alimentación se lleva a cabo en el plato 51 a una presión de 5.5 atm, a una temperatura de 323.15 K y a un flujo de 10 kmol/h, con una presión de 2 atm en el condensador y una caída de presión en la columna de 0.5 kPa, y con un holdup de 0.15 en volumen metro cúbico.

Y finalmente para la separación del diclorosilano, el diseño consta de una columna DR de 65 platos, 29 etapas de reacción que se encuentran en el intervalo del plato 21 al 50, con una relación de reflujo de 33 moles. La alimentación se lleva a cabo en el plato 51 a una presión de 5.5 atm, a una temperatura de 323.15 K y a un flujo de 10 kmol/h, con una presión que puede ir desde los 1.5 atm en el condensador y una caída de presión en la columna de 0.5 kPa, y con un holdup de 0.15 en volumen metro cúbico.

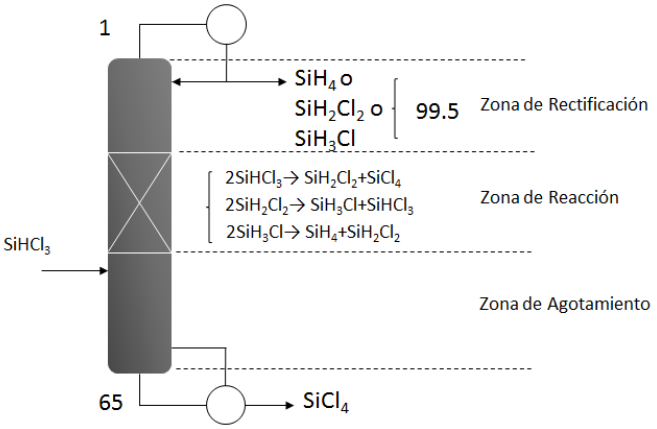

Fig. 3. Columna DR multitarea para la producción de silanos.

Una vez obtenidos los tres diseños se observa cual es el que requiere el mayor número de etapas para usar ese como base y obtener los otros dos productos en ese diseño, como se observa el diseño en el cual se basó la columna multitarea es el que purifica el diclorosilano.

La columna de DR multitarea consta de 65 etapas, 29 etapas de reacción que se encuentran en el intervalo del plato 21 al 50. La alimentación se lleva a cabo en el plato 51 a una presión de 5.5 atm, a una temperatura de 323.15 K y a un flujo de 10 kmol/h, una caída de presión en la columna de 0.5 kPa, y con un holdup de 0.15 en volumen metro cúbico (Ver Fig. 3). Las condiciones de operación como los es la presión, carga térmica y relación de reflujo para cada uno de los componentes a una pureza molar de 0.995 se muestra en la TABLA III, los valores señalados con un guión [-] son puntos de operación no factibles.

TABLA III. CONDICIONES DE OPERACIÓN DE LA COLUMNA DR PARA PURIFICAR SILANO, DICLOROSILANO Y MONOCLOROSILANO

	Silano		Monoclorosilano		Diclorosilano	
Presión [atm]	Reflujo	Carga Térmica [kW]	Reflujo	Carga Térmica [kW]	Reflujo	Carga Térmica [kW]
0.50	-	-	-	-	17.89	633.3
0.60	-	-	-	-	19.14	671.3
0.70	-	-	-	-	20.62	716.5
0.80	-	-	-	-	22.14	762.9
0.90	-	-	-	-	23.68	809.7
1.00	-	-	-	-	25.24	856.8
1.10	-	-	-	-	26.82	904.2
1.20	-	-	53.19	1016.4	28.41	951.9
1.30	-	-	46.60	892.4	30.03	999.9
1.40	-	-	43.42	831.9	31.66	1048.3
1.50	-	-	42.69	816.3	33.32	1097.2
1.60	-	-	42.66	813.4	35.01	1146.6
1.70	106.81	987.2	42.89	815.5	36.72	1196.6
1.80	93.53	866.5	43.26	820.0	38.46	1247.3
1.90	83.68	777.1	43.72	826.3	40.23	1298.7
2.00	76.58	712.5	44.26	834.0	42.04	1350.8
2.10	71.40	665.3	44.86	842.7	43.88	1403.7
2.20	67.52	629.9	45.52	852.5	45.76	1457.5
2.30	64.56	602.7	46.23	863.2	47.67	1512.2
2.40	62.24	581.2	46.98	874.5	49.63	1568.0
2.50	60.39	564.0	47.78	886.6	51.64	1624.8
2.60	58.89	549.9	48.61	899.4	53.69	1682.9
2.70	57.65	538.1	49.48	912.7	-	-
2.80	56.62	528.4	50.39	926.6	-	-
2.90	55.78	520.2	51.32	940.9	-	-
3.00	55.08	513.3	52.27	955.6	-	-
3.10	54.50	507.4	53.25	970.6	-	-
3.20	54.01	502.3	54.25	986.0	-	-
3.30	53.60	498.0	-	-	-	-
3.40	53.25	494.3	-	-	-	-
3.50	52.97	491.1	-	-	-	-
3.60	52.74	488.4	-	-	-	-
3.70	52.55	486.0	-	-	-	-
3.80	52.41	484.0	-	-	-	-
3.90	52.30	482.4	-	-	-	-
4.00	52.22	481.0	-	-	-	-
4.10	52.18	479.9	-	-	-	-
4.20	52.15	479.0	-	-	-	-
4.30	52.16	478.3	-	-	-	-
4.40	52.19	477.8	-	-	-	-
4.50	52.23	477.5	-	-	-	-

CONCLUSIONES

Se ha demostrado que es factible obtener una columna DR multitarea capaz de obtener los tres productos de interés (silano, diclorosilano y monoclorosilano) a partir de la desproporción del triclorosilano. Los tres productos de interés se destilan a purezas de grado electrónico, teniendo una conversión completa de triclorosilano a silano, monoclorosilano o diclorosilano por medio de una columna de destilación reactiva.

AGRADECIMIENTOS

Al Consejo Nacional de Ciencia y Tecnología (CONACYT) y a la Universidad de Guanajuato, por su apoyo y patrocinio para la realización de este proyecto.

REFERENCIAS

[1] A.F.B. Braga, S. P. Moreira, P.R. Zampieri, J.M.G. Bacchin and P.R. Mei, "New Processes for the Production of Solar-Grade Polycrystalline Silicon: A Review", Sol. Energy Mater. Sol. Cells, 92, 418, 2008.

[2] K. Zweibel, J. Mason and V. Fthenakis, "Solar Grand Plan: Solar as a Solution", Sun&Wind Energy, 4 pp. 112-117, 2008.

[3] A. Morales-Acevedo, G. Casados-Cruz, "Forecasting the development of different solar cell technologies", Int. J. Photoenergy., pp. 1-5, 2013.

[4] S. Pizzini, M. Acciarri, S. Binetti, "From electronic grade to solar grade silicon: chances and challenges in photovoltaics", Phys. Status Solidi A, 202, pp. 2928-2942, 2005.

[5] C. J Bakay, "Process for Making Silane". U.S. Patent 3,968,199, 1976.

[6] O. F Werner., M. Trygve, H. Arve, M. Morten, K. Hallgeir, "Production of Silicon from SiH4 in a Fluidized Bed, Operation and Results". Report Institute for Energy Technology, Solar Institute 18, Kjeller, Norway, and Telemark University College, Porsgrunn, Norway, 2013.

[7] M. Jun Jian, C. Shao-Chun, Q. Ke-Qiang, "Thermodynamic study on production of multicrystalline silicon by Siemens process". Chinesse Journal of Inorganic Chemistry, V. 23, 5, pp. 795-801, 2007.

[8] X. Huang, W.J. Ding, J.M. Yan, W.D. Xiao, "Reactive Distillation Column for Disproportionation of Trichlorosilane to Silane: Reducing Refrigeration Load with Intermediate Condensers", Ind. Eng. Chem. Res., 52, 6211, 2013.

Combustión de un hidrocarburo con oxigeno en cámaras de combustión abiertas

M. De la Cruz Ávila, M.A. Montejo Ehuán,
G. Polupan, R. Navarro Soto
Escuela Superior de Ingeniería Mecánica y Eléctrica,
Instituto Politécnico Nacional.
SEPI-ESIME ZACATENCO. Laboratorio de Ingeniería Térmica e Hidráulica Aplicada.
Av. IPN s/n, Edif. 5, Col Lindavista, C.P.07738 México D.F. *mauriciodlca@hotmail.com

M. Serrano Rodríguez
Escuela Superior de Ingeniería Mecánica y Eléctrica,
Instituto Politécnico Nacional.
SEPI-ESIME CULHUACAN.
Av. Santa Ana No.1000 Edif.2 Tercer piso C.P.04480
México D.F.
*imoy529@gmail.com

***Resumen*— El presente trabajo exhibe la influencia de las características geométricas en 3 tipos de arreglos de boquillas de inyección de gas licuado de petróleo sobre las llamas por difusión turbulentas de oxígeno con gas licuado de petróleo. Las investigaciones fueron realizadas utilizando velocidades de inyección de 5, 10 y 15 m/s para el gas LP. El estudio muestra la comparación de longitud las boquillas de inyección de ambas especies y ajustando velocidad de inyección de oxígeno. Se diseñaron y fabricaron tres tipos de arreglos de boquillas variando la relación de la longitud tanto de las boquillas de gas como de oxigeno L/d. Las boquillas fueron montadas en un banco de pruebas construido para quemadores de gas LP. Para medir la presión fueron utilizados y ajustados manómetros del mismo tipo. Para medir el caudal de los fluidos, rotámetros para aire ajustados para medir el oxígeno y el gas LP. Montada en la estructura del banco de pruebas se colocó una escala graduada permitiendo obtener la relación de las comparaciones y tener una medición de las longitudes características de las llamas. Una cámara termo-gráfica del tipo o modelo fue usada para apreciar el contorno de la llama en comparación a una cámara fotográfica.**

La altura alcanzada por la llama y la posición máxima de temperatura registrada por la cámara termográfica en el análisis de los datos experimentales, muestran que existe una dependencia directa en relación al tipo de quemador y no de la longitud de la cámara de combustión.

***Palabras Clave*: Combustión metano, Combustión gas LP, *Combustión con oxígeno*.**

I. INTRODUCCIÓN

En la actualidad se cuenta de una gran demanda de energéticos, por lo que en la industria es muy importante su uso eficiente. La mayoría de los combustibles utilizados en el mundo son aquellos basados en hidrocarburos provenientes de la destilación del petróleo crudo. Los tipos más comunes de combustibles son aquellos provenientes de los hidrocarburos, que son sustancias formadas de hidrogeno y carbono, provenientes de la descomposición de residuos orgánicos durante millones de años. El oxígeno (O2) es el comburente por excelencia [1], en la mayor parte de los procesos industriales de combustión, el oxígeno necesario para la reacción se obtiene del aire.

Se conoce como combustión a una reacción química de oxidación donde un material denominado combustible arde mientras que otro llamado comburente facilita la oxidación del primero. El aire utilizado para la mayor cantidad de cálculos, tiene una composición ideal postulada técnicamente con un 79% de nitrógeno y 21% de oxígeno exclusivamente despreciando las trazas de los demás elementos [2]. Por lo tanto, la relación molar entre nitrógeno y oxigeno es 0.79/0.21 = 3.76.

Dependiendo de los reactivos y productos de la combustión esta puede ser clasificada de dos formas. Cuando el combustible reacciona por completo con el oxígeno se le denomina combustión completa, para este caso se tiene dióxido de carbono y agua como productos para el caso de los hidrocarburos. Si el combustible no reacciona por completo con el oxígeno porqué este último es insuficiente, se conoce como combustión incompleta [3].

II. DETALLES OPERACIONALES

El gas licuado de petróleo (GLP) es un combustible de tipo secundario, derivado de la extracción primaria de hidrocarburos tales como el gas natural y el petróleo. El propano y el butano los cuales conforman el GLP se encuentran dentro de la composición general del petróleo crudo, que son necesarios extraer por medio de diferentes etapas de refinación para obtener un producto más estable. Las características más representativas del GLP distribuido por PEMEX [4] se encuentran enlistadas en la tabla:

Tabla 1.- Propiedades del GLP.

Propiedad	**Valor**
Fórmula química	$(C_3H_8)_+(C_4H_{10})$
Composición másica de propano (C_3H_8)	60%

Composición másica de butano (C_4H_{10})	40%
Composición molar de propano (C_3H_8)	53.20%
Composición molar de butano (C_4H_{10})	46.80%

Las llamas se dividen en dos tipos dependiendo de su interacción con el oxidante:

1.- Llamas premezcladas donde los reactivos se mezclan antes de la zona activa de combustión sólo se producen si el combustible y el oxidante alcanzan ciertas niveles de mezcla llamados limites flamabilidad [5].

2.- Llamas por difusión se producen cuando tanto la mezcla de combustible y el oxidante producen la combustión al momento de la mezcla sobre el borde de los chorros de las especies y después de ser inyectados dentro de un reactor o cámara de combustión [5].

Los productos de la combustión de un hidrocarburo de formula C_mH_n se escribe:

$$C_mH_n + \left(m + \frac{n}{4}\right)O_2 = mCO_2 + \left(\frac{n}{2}\right)H_2O \qquad (1)$$

Existe un proceso de combustión ideal durante el cual todo el combustible suministrado al sistema es quemado con el aire teórico conocido como combustión estequiométrica, en donde los productos de la combustión serán dióxido de carbono (CO_2), agua (H_2O) y nitrógeno (N_2). La combustión teórica del gas lp con aire es:

$$(0.6C_3H_8 + 0.4C_4H_{10}) + 5.6(O_2 + 3.76N_2) \rightarrow 3.4CO_2 + 4.4H_2O + 21.056N_2 \qquad (2)$$

Un modelo similar es aplicado a la reacción de gas lp con oxígeno puro, dando como resultado:

$$(0.6C_3H_8 + 0.4C_4H_{10}) + 5.6O_2 \rightarrow 3.4CO_2 + 4.4H_2O \qquad (3)$$

Por otra parte, cuando existe defecto o exceso del agente oxidante los productos serán distintos. Si existe defecto de oxígeno durante el proceso, como productos de combustión se obtiene agua (H_2O) y monóxido de carbono (CO), debido a que no hay suficiente cantidad de oxidante que reaccione con el combustible para formar la molécula de dióxido de carbono por lo que se trata de una combustión incompleta. La ecuación para el GLP con defecto de oxígeno es:

$$aO_2 + bC_3H_8 + cC_4H_{10} \rightarrow dCO + eH_2O \qquad (4)$$

En el proceso de combustión cuando la cantidad de oxidante es mayor que la estequiométrica, y como resultado de esta entre los productos de combustión existe una cantidad de oxígeno que no reacciona durante el proceso y no aporta ninguna reacción. Para GLP con exceso de oxígeno la ecuación es:

$$iO_2 + jC_3H_8 + kC_4H_{10} \rightarrow lCO_2 + mH_2O + nN_2 \qquad (5)$$

El quemador tiene una geometría cilíndrica de 25.4 mm de diámetro y consta de un arreglo de boquillas 4-Lug Bolt de 4 x 16.9 mm con una boquilla central de oxígeno con 4 mm y cuatro boquillas periféricas de metano de 0.8 mm de diámetro como se muestra en la figura 1.

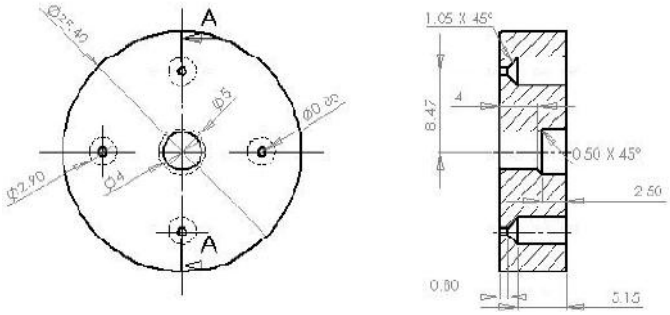

Figura 1, boquilla #1. La relación L/d=1.

Para la fabricación de las boquillas se eligió como material latón con 70% de cobre. Este material es una aleación de 70% cobre y 30% zinc, convirtiéndolo en un material fácil de maquinar, debido a los pequeños diámetro utilizados para el GLP.

Se fabricaron 3 tipos de quemadores con boquillas diferentes y una relación de longitud/diámetro (L/d) con valores asignados de 1, 3 y 6 para conocer el efecto de la cámara (reactor) sobre las características de la llama, dichas longitudes se encuentran en la siguiente tabla:

Tabla 2.- Medidas de la geometría para las boquillas de GLP

#	DQ [mm]	LGLP [mm]	DGLP [mm]	LO2 [mm]	DO2 [mm]	L/D
1	25.4	0.8	0.8	4	4	1
2	25.4	2.4	0.8	12	4	3
3	25.4	4.8	0.8	24	4	6

Donde # es el tipo de quemador, D_Q es el diámetro del quemador, L_{GLP} es la longitud del ducto de GLP, D_{GLP} es el diámetro de la boquilla de GLP, L_{O2} es la longitud del ducto del oxígeno y D_{O2} es el diámetro de la boquilla de O_2,

La velocidad de inyección se determina a partir de flujo volumétrico [7], tanto para el chorro de oxigeno como los de gas Lp. El diámetro de las boquillas se diseñó en función de la velocidad de inyección planteada en 5 m/s, 10 m/s y 15 m/s.

III. EQUIPO EXPERIMENTAL

Un banco de pruebas para los quemadores fue diseñado y construido para dar soporte al equipo durante las pruebas [7]. El concepto de dicho equipo se presenta en la figura 2:

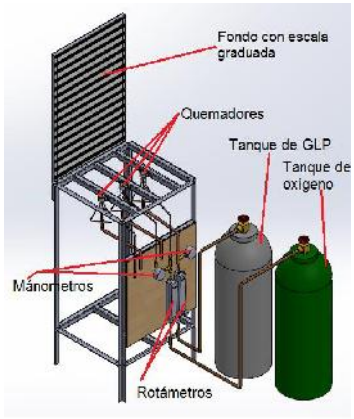

Figura2: Diseño conceptual del banco de pruebas para quemadores

Los tres quemadores son alimentados con 3 distintas con líneas para el GLP y el oxígeno respectivamente, un tanque de GLP, un tanque de oxígeno, rotámetros para medir el flujo volumétrico de cada gas, manómetros para medir la presión en cada gas, una escala cuya graduación fue de 20 mm cada una para tener el punto de comparación con la llama y poder medir sus características geométricas.

Los quemadores fueron maquinados para ser montados y sujetados al banco de pruebas. Después de ser diseñado, se construyó el banco de pruebas, obteniendo la configuración final mostrada en la figura 3.

Debido a la alta intensidad lumínica de la llama presente en las fotografías, se optó por usar termografías que presentan mejor los perfiles temperatura y cuya escala de colores permite apreciar de una mejor manera las diferentes escalas de temperatura durante la experimentación [8].

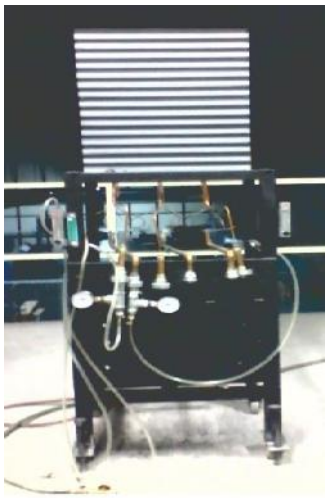

Figura 3.-Banco de quemadores terminado

La figura 4 fue tomada para un proceso de combustión con U_{GLP}= 15 m/s y α = 1.09 sin cámara de combustión (*Le* = 0). Esta figura ilustra y demuestra el anterior planteamiento. La imagen de la llama es más definida con la lectura de termografía infrarroja de la figura 4.1b que en la fotografía de la figura 4.1a

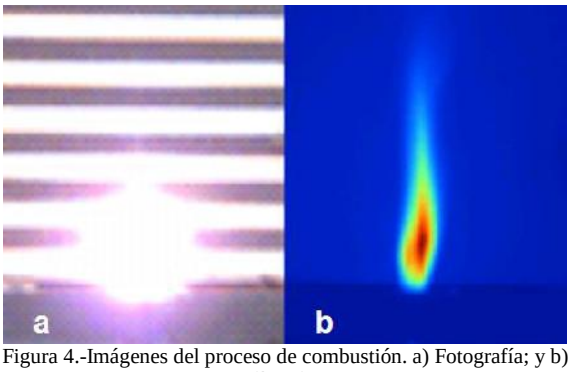

Figura 4.-Imágenes del proceso de combustión. a) Fotografía; y b) Termografía infrarroja.

IV. ANÁLISIS DE RESULTADOS

Cada una de las pruebas se realizaron con las siguientes variables: una mezcla de GLP con oxígeno en donde el coeficiente de oxígeno α variaba desde un valor 0.98 a 1.09, siendo 1.00 el valor estequiométrico, a una velocidad de inyección U_{GLP} = 5 m/s; y otra variación fueron los tipos de cámaras de combustión, con longitud equivalente *Le* = 0 in, 1 in, 4 in, 6 in y 10 in. Una muestra representativa de las pruebas realizadas en la boquilla #1 quedo representada en la fig. 5 para las diferentes longitudes de la cámara de combustión.

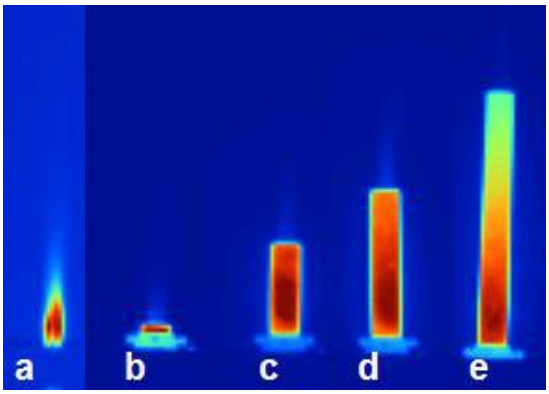

Figura 5.-Pruebas realizadas para la boquilla #1 con velocidad U_{GLP} = 5 m/s: a) Le = 0 in; b) Le = 1 in; c) Le =4 in; d) Le = 6 in; y e) Le = 10 in.

Cada prueba fue repetida 3 veces bajo las mismas condiciones de mezcla y respetando las correcciones de medición de flujo para la temperatura y presión ambiental. Un total de 81 pruebas fueron realizadas con las variables mencionadas y para fines prácticos se prefirió mostrar una media geométrica de cada una de las mediciones realizadas por cada mezcla de oxidante – combustible.

Las medias geométricas calculadas de las mediciones obtenidas en el experimento fueron registradas en la tabla 3. Cada una de las dimensiones medidas de la llama fue dividida entre el diámetro de la boquilla (0.0254 m) para obtener relaciones adimensionales que fueron denotadas como *L** en

el caso de longitudes o D^* para los diámetros. En las 5 series de pruebas, se realzaron en los tres tipos de quemadores.

En la primera serie de pruebas se realizaron sin usar una cámara de combustión, como se muestra en la fig. 5(a).

En la segunda serie de pruebas con longitud equivalente Le = 1 in, fig. 5(b). En este caso no se obtuvo $L_{mín}$ y L_{ZCA} debido a la presencia de la cámara de combustión.

En la fig. 6 el número 1 denota al gas oxígeno, mientras que los flujos numerados con 2 se refieren a GLP, también se muestra que L_{max} es la longitud máxima desde la superficie del quemador, donde los flujos de combustible y oxidante fueron inyectados al medio, hasta el final de la llama. $L_{mín}$ se refiere a la zona de despegue de la llama, donde el GLP y oxígeno tienen una interacción únicamente física sin llegar al proceso de oxidación. L_{ZCA} es la longitud que abarca desde el inicio del proceso de combustión hasta el final de la llama. L_{nuc} es la dimensión desde la parte superior del quemador hasta el punto donde la cámara termográfica registro la mayor temperatura obtenida en el proceso.

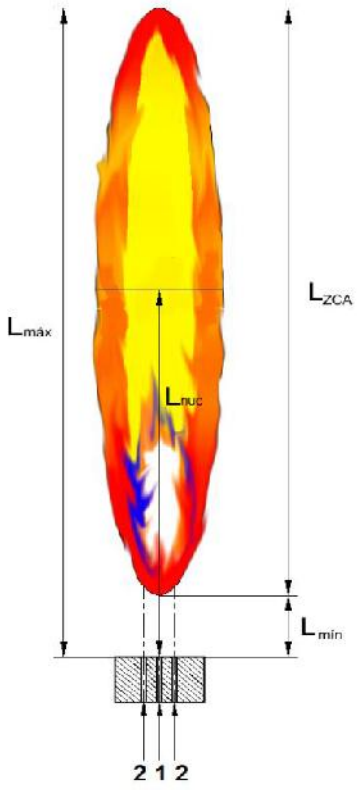

Fig. 6 .-Dimensiones medidas en las termografías tomadas a las llamas del proceso de combustión.

En la tercera serie de pruebas con longitud equivalente Le = 4 in, fig. 5(c), así como en la cuarta serie de pruebas con longitud equivalente Le = 6, fig. 5(d) y en la quinta serie de pruebas con longitud equivalente Le = 10, fig. 5(e), se obtuvieron solamente L_{nuc} debido a la presencia de la cámara de combustión.

#	L*mín	L*max	L*ZCA	L*nuc	α	Le
1	0.24	2.98	2.7	1.02	0.98	0
2	0.26	3.80	3.5	1.1	0.98	0
3	0.18	4.19	4.0	1.49	0.98	0
1	0.19	2.76	2.6	0.86	1	0
2	0.18	3.65	3.5	1.29	1	0
3	0.18	3.84	3.7	1.46	1	0
1	0.18	3.11	2.9	0.94	1.09	0
2	0.19	3.29	3.1	1.12	1.09	0
3	0.18	3.62	3.4	1.46	1.09	0
#	L*mín	L*max	L*ZCA	L*nuc	α	Le
1	~	1.99	~	0.79	0.98	1
2	~	2.73	~	0.83	0.98	1
3	~	2.77	~	0.97	0.98	1
1	~	1.89	~	0.76	1	1
2	~	2.72	~	0.81	1	1
3	~	2.99	~	1.05	1	1
1	~	1.92	~	0.81	1.09	1
2	~	3.08	~	0.81	1.09	1
3	~	2.99	~	1.02	1.09	1
1	~	~	~	2.02	0.98	4
2	~	~	~	1.88	0.98	4
3	~	~	~	2.17	0.98	4
1	~	~	~	2.02	1	4
2	~	~	~	2	1	4
3	~	~	~	2.14	1	4
1	~	~	~	2.07	1.09	4
2	~	~	~	2	1.09	4
3	~	~	~	2.17	1.09	4
1	~	~	~	1.93	0.98	6
2	~	~	~	1.75	0.98	6
3	~	~	~	2.43	0.98	6
1	~	~	~	1.95	1	6
2	~	~	~	1.81	1	6
3	~	~	~	2.45	1	6
1	~	~	~	1.93	1.09	6
2	~	~	~	1.73	1.09	6
3	~	~	~	2.09	1.09	6
1	~	~	~	1.76	0.98	10
2	~	~	~	1.16	0.98	10
3	~	~	~	2.07	0.98	10
1	~	~	~	1.76	1	10
2	~	~	~	1.1	1	10
3	~	~	~	2	1	10
1	~	~	~	1.73	1.09	10
2	~	~	~	1.12	1.09	10
3	~	~	~	2.12	1.09	10

Tabla 3.- Medias geométricas de las mediciones realizadas para los quemadores #1, #2 y #3 a U_{GLP} = 5 m/s y α = 0.98, 1.00 y 1.09 con longitudes equivalentes de la cámara de combustión Le =0 in, 1 in, 4 in, 6 in y 10 in.

En la fig. 7 se ilustran las curvas de tendencia de L*máx para U_{GLP} = 5 m/s y Le =0 y 1 construidas con datos de la tabla 3.

En la fig. 7 la máxima longitud de llama para la prueba con U_{GLP} = 5 m/s y Le = 0 fue registrado con α = 0.98 (−■−) en

#3, mientras que la mínima correspondió para α = 1.00 (-■ -) en el quemador #1.

En la fig. 7 se ilustran las curvas de tendencia de L*máx para U_{GLP} = 5 m/s y Le =1. La máxima longitud de llama para este caso fue registrado en α = 0.98 (−●−) y 1.00 (- ● -) en #3, mientras que la mínima correspondió para α = 1.00 (- ● -) en el # 1, esto es debido a que el comburente y el combustible no están en la proporción adecuada, a menor cantidad de oxígeno en el proceso de combustión, tomó más tiempo en realizarse, por lo que el oxígeno presente en la parte externa de la cámara de combustión logro quemarse lo que se tradujo en una mayor longitud de llama.

La comparación entre L*máx en la fig. 7 obtenidas en Le = 0 y Le = 1 demostró que al añadir la cámara de combustión se reduce el tamaño de la llama, debido a que todo el oxígeno reacciono con todo el combustible, lo que se traduce en una menor influencia del oxígeno presente en el medio ambiente, con lo cual el proceso de combustión fue más estable en Le = 1 y la propia cámara permitió un mejor mezclado entre combustible y oxidante.

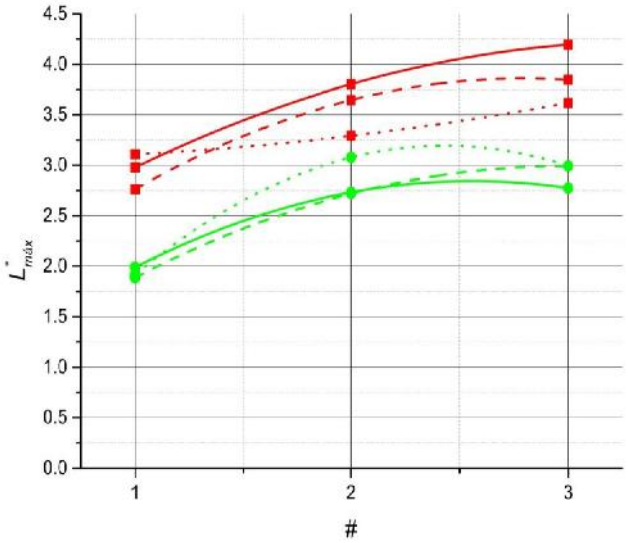

Figura 7.- Curvas de tendencia de L*$máx$ para U_{GLP} = 5 m/s y Le = 0 y 1. ■ fue usado para Le = 0, mientras que ● fue utilizado para Le = 1. Para α = 0.98 se utilizó una línea continua (—), con α = 1.00 se usó un estilo de línea discontinua (- - -) y α = 1.09 fue simbolizada con una serie de puntos (·····).

La posición de la máxima temperatura registrada en el núcleo por la cámara termográfica en la figura 8 en Le = 0 para este caso fue en α = 0.98 (—■—) en #3, mientras que la mínima correspondió para α = 1.00 (- ■ -) en el quemador # 1.

Para las curvas de tendencia en la fig. 8 con Le = 1 la posición de la máxima temperatura registrada en el núcleo por la cámara termográfica para este fue en α = 1.00 (- ● -) en #3, mientras que la mínima correspondió para α = 1.00 (- ● -) en el quemador # 1. Cuando el flujo del GLP y el oxígeno están con una mayor velocidad en el #3 a la salida del quemador nos da como resultado un proceso de mezclado más lento y una posición más alta de la temperatura máxima.

En la fig. 8 la posición de la máxima temperatura registrada en el núcleo por la cámara termográfica para Le = 4 en este caso ocurrió en α = 1.09 (· ▲ ·) y 0.98 (—▲—) en #3, mientras que la mínima correspondió para α = 0.98 (—▲—) en el quemador # 2. La longitud más pequeña en el quemador #2 se debió a un mejor mezclado, lo que permitió un proceso de combustión completo, debido a que todo el oxígeno reacciono con todo el combustible. Por otro lado, la posición más alta de la máxima temperatura registrada se debió a productos sin quemar y un mezclado en un punto superior en comparación con la posición de la temperatura máxima en #2.

Para la fig. 8 la posición de la máxima temperatura registrada en el núcleo por la cámara termográfica con Le = 6 fue en α = 1.09 (· ▼ ·) y 0.98 (—▼—) en #3, mientras que la mínima correspondió para α = 1.00 (-▼-) en el quemador # 2. La longitud más pequeña en el quemador #2 se debió a un mejor mezclado Sin embargo, la posición más alta de la máxima temperatura registrada en #1 se debió a productos sin quemar y a un mezclado más lento de los chorros de combustible y oxidante, lo que propició que la zona de combustión activa se comenzará en un punto más arriba que para otros quemadores.

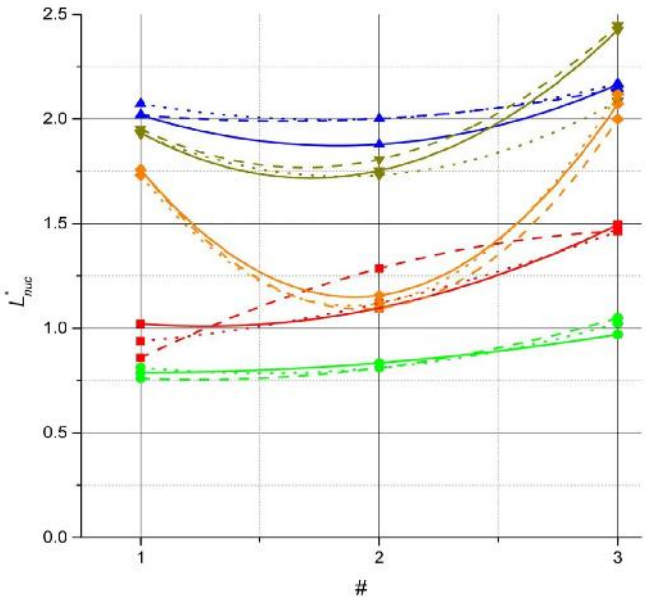

Figura 8.- Curvas de tendencia de L*nuc para U_{GLP} = 5 m/s y Le = 0, 1, 4, 6 y 10. ■ fue usado para Le =0, mientras que ● fue utilizado para Le = 1, para Le = 4 se usó ▲, el símbolo ▼ fue usado para Le = 6 y en Le = 10 se utilizó ♦. Para α = 0.98 se utilizó una línea continua (—), con α = 1.00 se usó un estilo de línea discontinua (- - -) y α = 1.09 fue simbolizada con una serie de puntos (·····).

En la fig. 8 se ilustran las curvas de tendencia con L^*_{nuc} con U_{GLP} = 5 m/s y Le = 10 la posición de la máxima temperatura registrada en el núcleo por la cámara termográfica para este caso fue en α = 1.09 (· ♦ ·) en #3, mientras que la mínima correspondió para α = 1.00 (- ♦ -) en el quemador # 2.

Las curvas de tendencia en este caso se observan con una mayor similitud que en la gráfica previa, lo que corresponde a un proceso de combustión completamente controlado por la presencia de la cámara de combustión que contienen la llama.

Se pudo observar el mismo patrón de que las posiciones más bajas se registraron en #1, mientras que las más altas fueron en #3.

Una revisión de la fig. 8 mostró que la posición relativa de la máxima temperatura registrada por la cámara termográfica *L* nuc* varia con el cambio de la longitud equivalente de la cámara de combustión, *Le*. *L*nuc* disminuyó entre los valores de *Le* = 0 a 1, demostrando que cuando se incluye una cámara de combustión la cual no cubre por completo la longitud máxima de la llama el punto de mayor temperatura en la misma baja de posición con respecto a una llama sin cámara de combustión.

Cuando la llama fue cubierta por completo en *Le* = 4 se obtuvo la mayor altura en *L*nuc*, y a partir de este valor de la cámara de combustión al aumentar la longitud de la misma la posición de *L* nuc* comenzó a decrecer. En esta serie de pruebas se encontró que en función de la longitud equivalente de cámara, la posición de la máxima temperatura quedo de la forma *L*nuc*(*Le* = 10)<*L*nuc*(*Le* = 6)< *L*nuc*(*Le* = 4), con lo que se estableció que al aumentar *Le* una vez que se ha cubierto la llama por completo la geometría de llama variaba obteniéndose alturas más pequeñas.

CONCLUSIONES

Tanto los valores *L*max* y *L*nuc* se vieron modificadas en función a las variables tipo de quemador (#), *α*, *Le* y U_{GLP}

Se observó que la mayor variación de la posición relativa de la máxima temperatura registrada por la cámara termográfica (*L*nuc*) fue debido a la longitud de la cámara de combustión, a mayor longitud de Le se presentó una mayor altura en la posición de la máxima temperatura. La siguiente variable que influyo en *L*nuc* fue para los cambios en la velocidad del combustible U_{GLP} .El tercer parámetro que modifico *L*nuc* consistió en el tipo de quemador, siendo la mayor altura obtenida para #3 y el de menor #1. El último parámetro que modifico *L*nuc* fue para el coeficiente de oxígeno *α*.

A partir de los resultados obtenidos se concluye que los parámetros más importantes para controlar la altura de la llama se trataron de la longitud equivalente de la cámara de combustión *Le* y el tipo de quemador. Con combinaciones entre ambos, se puede lograr una posición de núcleo baja, por ejemplo con el quemador #1 y *Le* = 4, longitud de cámara para la cual se cubre toda la zona activa de combustión, hasta la máxima posición con el quemador #3 y *Le* = 10.

AGRADECIMIENTOS

Los autores agradecen al Instituto Politécnico Nacional, a la Sección de Estudios de Posgrado e Investigación de la Escuela Superior de Ingeniería Mecánica y Eléctrica Unidad Culhuacán, a la Sección de Estudios de Posgrado e Investigación de la Escuela Superior de Ingeniería Mecánica y Eléctrica Unidad Zacatenco y el apoyo proporcionado por el Consejo Nacional de Ciencia y Tecnología CONACYT.

REFERENCIAS

[1] Yunus A. Cengel, Michael A. Boles “Termodinámica”, Septima edición, 2012,J. Clerk Maxwell, A Treatise on Electricity and Magnetism, 3rd ed., vol. 2. Oxford: Clarendon, 1892, pp.68–73.

[2] Manuel Marquez Martinez “Combustión y quemadores” Segunda edición, 2005, “Aire húmedo”11-18.

[3] Moran M, Fundamentos de termodinámica técnica, España: Reverté, 2008.

[4] PEMEX, «Gas licuado de petróleo,» México.

[5] El-Mahallawy F, Fundamentals and technology of combustion, Reino Unido: Elsevier, 2002.

[6] C. W. Chang R, Química, 7a edición, México: McGraw-Hill, 2002.

[7] M. Montejo Ehuán, U. Hernández Guerrero, G. Polupan, G. Jarquin Lopéz, “Diseño Energético para Prototipo de Quemador en un Generador de Vapor en Fondo de Pozo” Noviembre 2013.

[8] M. Montejo Ehuán, R. Navarro Soto, G. Polupan “Estudio Comparativo de Longitudes de Llama para Generador de Vapor en Fondo de Pozo” Noviembre 2013.

Dinámica de flujo sobre un banco de tubos planos.

R. Teodoro Cristóbal, I. Carvajal Mariscal, F Sánchez Silva.
Laboratorio de ingeniería térmica e hidráulica aplicada – ESIME.
Instituto politécnico nacional.
D.F., México.
sigmarobt@hotmail.com.

Resumen **– En este artículo se presenta una breve revisión de la literatura referente al estudió de la dinámica de flujo y la transferencia de calor sobre los tubos planos usados en la construcción de intercambiadores de calor. Se incluyen las investigaciones, tanto de tipo numérico como experimental. En la mayoría de las investigaciones realizadas se analizó la caída de presión y la transferencia de calor a través de un banco de tubos, en configuración escalonada y lineal. El análisis de los resultados ha mostrado que la geometría del tubo, así como la distribución de los tubos en los intercambiadores de calor influye de una manera positiva en la capacidad de recuperación de calor.**

Con el fin de llegar a desarrollar una alta eficiencia en los intercambiadores de calor, es esencial conocer a detalle la transferencia de calor local y la dinámica de flujo local. Se han aplicado diferentes estrategias para lograr aumentar la eficiencia de la transferencia de calor. Las técnicas pasivas para el ahorro de energía no requieren de un subministro de energía adicional, o la intervención de algún otro equipo, como por ejemplo: los perturbadores de flujo y las superficies no convencionales, por lo tanto, para el uso eficiente de la energía se debe buscar tener las condiciones para obtener la mayor transferencia de calor, con la más mínima caída de presión.

Se ha observado que con el uso de los tubos planos se obtienen características más apropiadas en lo que se refiere a la caída de presión comparados con tubos circulares, debido a la pequeña área de desarrollo de las estelas. Por esta misma razón se espera que el ruido y la vibraciones producidas sean menores en intercambiadores de calor de perfiles planos comparados con intercambiadores de calor de tubos redondos. Por lo tanto, existe la oportunidad de investigar experimentalmente diferentes configuraciones y geometrías de tubos planos que permitan validar con certeza los resultados numéricos.

Palabras Clave – Tubos planos, Caída de presión, recuperación de calor.

I. INTRODUCCIÓN

En la actualidad existe una gran demanda de energía, por lo que en las industrias es de gran importancia el uso eficiente de la energía. Muchos de los procesos de transmisión de calor son efectuados mediante el uso de diferentes intercambiadores de calor. Actualmente un factor importante es la relación de los aspectos económicos y ambientales, para poder ser competitivos en el ahorro y en el uso eficiente de los recursos no renovables.

Entre estos se encuentran la energía térmica y el aire, estos tienen una relación en los criterios ambientales como consumo de combustible y emisión de contaminantes [1]. Una opción de impacto inmediato que no requiere cambios estructurales importantes en el sector industrial es el planteamiento de proyectos de recuperación de energía térmica.

Para incrementar la eficiencia de los intercambiadores de calor compactos se necesita conocer a detalle la distribución de la transferencia de calor, por lo que se han realizado investigaciones respecto a la forma de los tubos utilizados en los bancos de tubos, así como el como la configuración, que son parámetros que conlleva al diseño de los intercambiadores de calor. Para tener un diseño cada vez más óptimo es necesario una evaluación profunda de los mecanismos de transferencia de calor; como el de las estructuras secundarias del flujo, que frecuentemente se encuentran en pequeñas escalas.

El flujo de fluido y la transferencia de calor en un banco de tubos simboliza una idealización de muchos procesos industriales significativos. Los haz de tubos son ampliamente usados en intercambiadores de calor en contraflujo, el diseño de estos se basa en correlaciones empíricas de transferencia de calor y caída de presión. Los intercambiadores de calor con un banco de tubos en contraflujo son de gran interés en muchos procesos de ingeniería química y térmica, por lo que se ha introducido en el diseño de modernos intercambiadores de calor el uso de tubos planos, en aplicaciones como el de los radiadores automotrices. Se han observado características apropiadas con el uso de los tubos planos, en lo que se refiere a la caída de presión cuando son comparados con los tubos circulares.

T. Ahmad [2] realizó el estudio de la transferencia de calor y la caída de presión en un banco de tubos planos con configuración en línea y flujo cruzada, mediante el uso de una red neuronal artificial. Las consideraciones en el estudio numérico fueron: análisis bidimensional, estado estacionario y flujo laminar e incompresible. El rango del número de Reynolds se encontró entre 10-320. Los resultados del coeficiente de transferencia de calor y caída de presión fueron presentados para diversas configuraciones de tubos; con tres pasos transversales de 2.5, 3.0 y 4.5, y con dos pasos longitudinales de 3.0 y 6.0. La precisión en el enfoque del modelo de red neuronal artificial para el número de Nusselt promedio fue menor de 4.1% de error relativo absoluto, 4.8% para la caída de presión adimensional y 3.8% para el factor de fricción.

M. Ishak [3] presentó una investigación experimental sobre las características de la transferencia de calor y la caída de presión en un banco de tubos planos con las siguientes condiciones: aire como fluido de trabajo, configuración escalonada, flujo cruzado, flujo laminar y transferencia de calor mediante convección forzada. Las mediciones fueron

realizadas para un banco con un total de dieciséis tubos en dirección al flujo, distribuidos mediante cuatro filas. El intervalo de velocidad se ubicó entre 0.6 – 1.0 m/s., y el número de Reynolds en el intervalo de 373-623. El flux total de calor suministrado en todos los tubos varió de 967.23 – 3629.70 W/m^2. Los resultados mostraron que el número de Nusselt promedio de todos los tubos planos incremento de 11.46% a 46.42%, con un número de Reynolds que tuvo una variación de 373 a 623, con un flux de calor fijo. El número de Nusselt promedio tuvo un incremento del 21.39% al 84%, y la variación del flux de calor total fue del 967.23-3629.70 W/m^2 con la condición de un número constante de Reynolds de Re=498. Adicionalmente la caída de presión disminuye cuando se produce un aumento en el número de Reynolds.

H.M.S. Bahaidarah [4] realizó un estudió numérico en estado estacionario y bidimensional, en el que se desarrolla el flujo de fluido y la transferencia de calor a través de cinco tubos colocados en línea, confinados en un canal, con un fluido con un número de Prandtl de 0.7. Se estudiaron las superficies de la sección transversal de los tubos, con diferentes formas que fueron circular, plano, oval y diamante.

Además de la investigación de diversos perfiles de tubos se ha consideró el estudio sobre bancos de tubos planos usados en aplicaciones de intercambio de calor con las condiciones de flujo en forma bidimensional, laminar, en estado estacionario e incompresible, con configuración en línea y escalonada, en el que se identificaron los efectos que producen varios parámetros independientes, como el número de Reynolds (Re), el número de Prandtl (Pr), la relación de longitud (L/Da), y la relación de altura (H/Da), al actuar sobre la caída de presión y la transferencia de calor.

II. DESARROLLO

A. Perfiles de tubos

Se han realizado investigaciones sobre las características de la transferencia de calor y la caída de presión, principalmente sobre cilindros, ya que son los elementos principales en los intercambiadores de calor. H.M.S. Bahaidarah [5] realizó un estudio sobre diversos perfiles de tubos, como se muestran en la Figura 1.

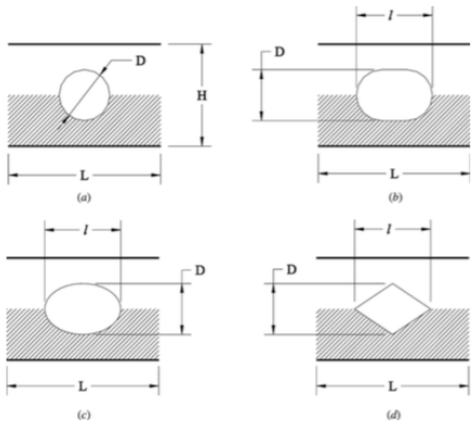

Fig. 1. Módulos geométricos de varios perfiles de tubos (a) circular, (b) plano, (c) ovalo, (d) diamante.

Los resultados obtenidos para el tubo plano, ovalado y diamante fueron comparados entre si, y con tubos circulares. Los conclusiones obtenidas mostraron que los tubos de forma plano y ovalada ofrecen una gran resistencia al flujo y a la tasa de transferencia de calor cuando son comparados con tubos circulares, para la totalidad del intervalo del número de Reynolds (Re) considerados en él estudió.

Los tubos de forma de diamante ofrecen una baja resistencia al flujo cuando son comparados con los tubos circulares para un número de Reynolds Re<250. Para todos los valores de Re, los tubos de forma de diamante exhiben las más baja tasa de transferencia de calor.

Cuando ambos parámetros; la resistencia al flujo y la tasa de transferencia de calor son considerados, los tubos de forma de diamante ofrecen características más óptimas que los tubos en forma ovalada y los planos para Re<40. Para Re>50, los tubos de forma ovalada y planos ofrecen una mejor eficiencia. El campo de flujo tiene un mayor efecto sobre el rendimiento de la transferencia de calor para Re<50, mientras que el factor geométrico del tubo tiene efectos mas significativos en el rendimiento para Re>50.

B. Perfiles de tubos planos.

El estudio de los tubos planos ha abarcado diversas aplicaciones, una de ellas es su uso en nano fluidos, un método para incrementar o intensificar la transferencia de calor en tubos es mediante el uso de tubos planos en lugar de los tubos circulares. Comparado a los tubos circulares, los tubos planos tienen una mayor área de superficie en relación a su sección transversal, que puede ser usada para incrementar la compactibilidad y la transferencia de calor de los intercambiadores de calor [6].

La Figura 2 ilustra las características de la transición del tubo circular hasta la forma plana. El punto A y E exhiben la menor caída de presión y el mayor coeficiente de transferencia de calor, respectivamente.

Los puntos B y D, conocidos como los puntos de quiebre son puntos interesantes en el diseño, se observa que a medida que se avanza del punto A al punto B, el ΔP aumenta muy poco, mientras el coeficiente de transferencia de calor ($\bar{h}$) aumenta considerablemente.

Similarmente a medida que se avanza del punto E hacia el punto D, $\bar{h}$ aumenta ligeramente, mientras el ΔP se mejora para un nivel superior. El punto C es el punto con el enfoque que satisface las condiciones de la transferencia de calor y la caída de presión.

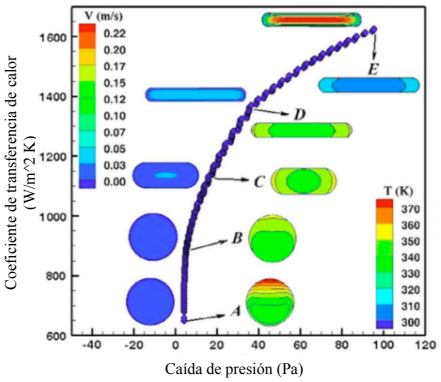

Fig. 2. Diagrama de Pareto con los puntos óptimos para el coeficiente de transferencia de calor y la caída de presión.

G. Singh [7] realizó un estudió hidráulico y térmico en CFD de un tubo plano aletado de un intercambiador de calor, con un arreglo escalonado, simulando las características del flujo de fluido y la transferencia de calor para modelos de flujo laminar y turbulento. El problema se simulo para diferentes tasas de flujos másicos con un intervalo del número de Reynolds de 330 – 7200, en el cual se determina la caída de presión y el número de Nusselt, y de esta se obtuvo el cálculo de los principales parámetros de interés como el factor de fricción y el número de Colburn, respectivamente.

Los resultados obtenidos mostraron que el factor de fricción para la configuración de los tubos redondos es siempre mayor a lo largo del intervalo del número de Reynolds en comparación con la configuración de tubos planos, lo que muestra claramente que las pérdidas de presión debido a la fricción son comparativamente altas en el tubo redondo como se observa en la Figura 3.

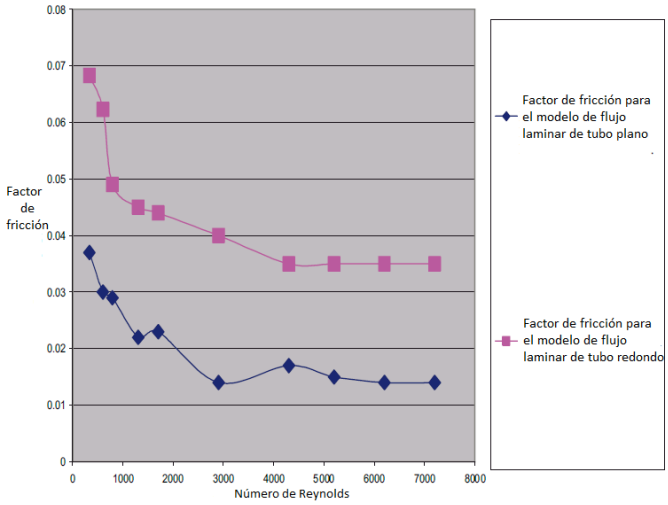

Fig. 3. Gráfica comparativa del factor de fricción para el modelo de flujo laminar, para la configuración de tubo redondo y plano.

Además se ha estudiado el comportamiento del flujo a través de los tubos planos y redondos, como se muestra en la Figura 4 y la figura 5.

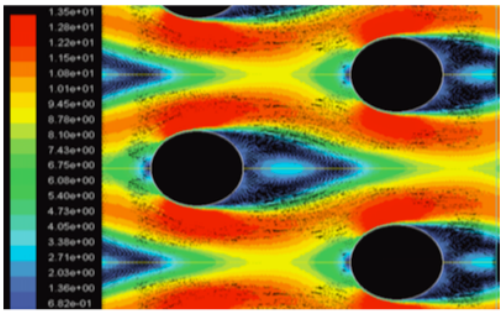

Fig. 4. Módulo de tubos redondos inmersos en flujo turbulento a una v=6.2 m/s

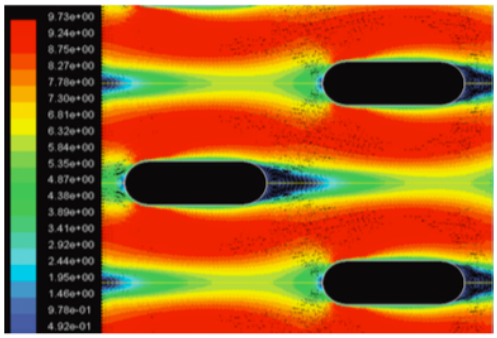

Fig. 5. Módulo de tubos planos inmersos en flujo turbulento a una v=6.2 m/s

En la figura se observa como el flujo entra a la región del intercambiador de calor casi a una velocidad igual a la de entrada. El flujo se bifurca en magnitud mientras pasa sobre la fila de tubos y gradualmente gana velocidad cuando pasa a través del área entre los tubos.

A baja velocidad cuando el flujo pasa sobre la fila de tubos, la separación toma lugar. Así el flujo en la región aguas abajo, después de cada tubos consigue convertirse en estelas que generan una zona de recirculación, mientras que en el lado aguas arriba de la fila de tubos se da la generación de vórtices de herradura. Posteriormente el flujo hace una ligera transición a través de la mínima área de flujo a altas velocidades.

La comparación del flujo para dos velocidades muestra que no hay regiones de estancamiento o bloqueo de flujo que sean observadas en el frente de la primera y segunda fila a bajas velocidades, mientras en el caso del flujo a altas velocidades la región de estancamiento es observada solo en el frente del segundo tubo. En una comparación relativa de velocidades para el tubo aletado de configuración plana, se observa claramente que para el modelo de flujo laminar las zonas de estancamiento comienzan a ser observadas en el frente de cada fila de tubos a bajas velocidades, mientras estas zonas se desvanecen totalmente a altas velocidades.

La parte posterior de cada fila de tubos experimenta una zona de estelas, las cuales tienen muy poca resistencia , por lo tanto, las pérdidas de fricción son pequeñas en el lado superior para bajas velocidades, mientras son comparativamente despreciables a bajas velocidades.

El flujo en transición a través de la región de circulación del flujo entre los tubos es totalmente lisa, ya que el tubo plano no ofrece mucha resistencia al flujo, aunque la velocidad del flujo aumenta ligeramente en la región entre dos tubos.

III. RELACIONES DE PASO

Además del comportamiento del flujo de fluido y la transferencia de calor sobre el perfil del tubo plano, se ha investigado la disposición en que deben estar distribuidos los tubos en el arreglo del banco de tubos, con el fin de tener el mayor coeficiente de transferencia de calor.

H.M.S. Bahaidarah [5] realizó una simulación numérica. En él estudió se observó un aumento en el número de Nusselt promedio calculado por módulo para un número de Prandtl de Pr=0.7, cuando es comparado con un número de Prandtl de Pr=7.0.

El rendimiento total para la configuración en línea, para bajas relaciones de altura (H/Da=2) y a altas relaciones de longitud (L/Da=6) son preferibles ya que proporcionan una mayor tasa de transferencia de calor para el intervalo de número de Reynolds considerados en él estudió, excepto para los valores de Re menores a 25. Como se espera, la configuración escalonada se desempeña mejor que la configuración en línea desde el punto de vista de la transferencia de calor.

También desde el punto de vista de la transferencia de calor, el banco de tubos circules equivalentes tiene un mejor desempeño que el banco de tubos planos, sin embargo la relación de desempeño de la transferencia de calor es siempre mayor a 1, lo que significa que desde el punto de vista de la caída de presión el desempeño del banco de tubos planos es mejor que el de un banco de tubos circulares equivalentes.

Z. Sayed Abdel Rehim [8] estudió el efecto de la relación de aspecto ((H/D)/(L/D)) sobre la caída de presión, la temperatura y el contorno de velocidad para flujo laminar y turbulento sobre un banco de tubos planos con configuración escalonada, además realizó la comparación del estudió con otros métodos analíticos para números de Reynolds contra números de Nusselt, los resultados mostraron que el número de Reynolds aumenta cuando la velocidad es máxima en el corredor entre los dos tubos superior e inferior.

La Figura 6 muestra el mallado del módulo de un tubo plano inmerso en flujo laminar para Re=400, para diferentes relaciones de aspecto seleccionados ((H/D)/(L/D)). En la Figura 7 se muestra la caída de presión para flujo laminar con un número de Reynolds para diferentes relaciones de aspecto ((H/D)/(L/D)). Como la relación de aspecto ((H/D)/(L/D)) aumenta la caída de presión normalizada disminuye.

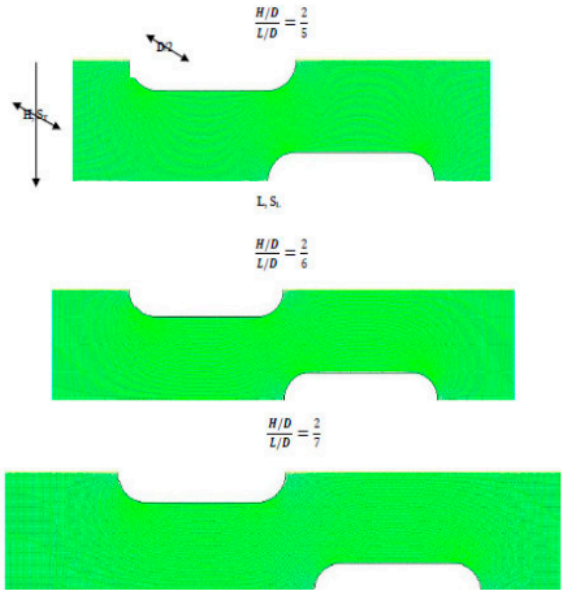

Fig. 6. Mallado de flujo laminar para Re=400.

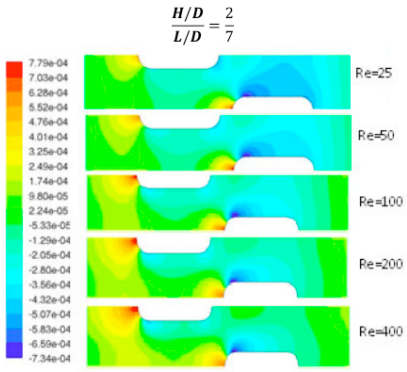

Fig. 7. Contorno de caída de presión para flujo laminar con una relación de aspecto de 2/7.

Se observó que como la relación de aspecto ((H/D)/(L/D)) aumenta la caída de presión normalizada disminuye. Los altos valores de la distribución de la caída de presión usualmente son reportados inicialmente cerca de la superficie externa de los tubos en todos los casos.

Se determinó que el comportamiento es una función de la relación de la caída de presión a los términos de la velocidad al cuadrado en el cálculo de la distribución de la temperatura. Los contornos se expusieron a la temperatura aumentando en el fluido la transferencia de calor de los tubos, además se observó que el número de Reynolds Re aumenta cuando la velocidad es máxima entre el espacio de los tubos superior e inferior.

N. Benarji [9] realizó simulaciones numéricas en estado transitorio de flujo de fluido y transferencia de calor sobre un banco de tubos planos, para las configuraciones en línea y en escalón, tal como se muestra en la Figura 8 y la Figura 9.

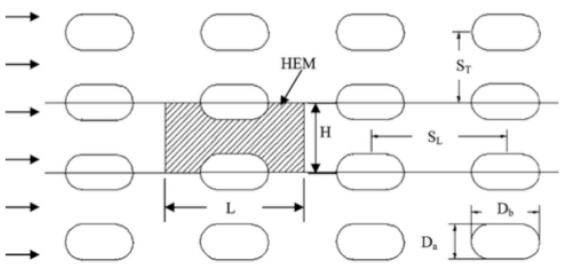

Fig. 8. Configuración en línea del banco de tubos planos.

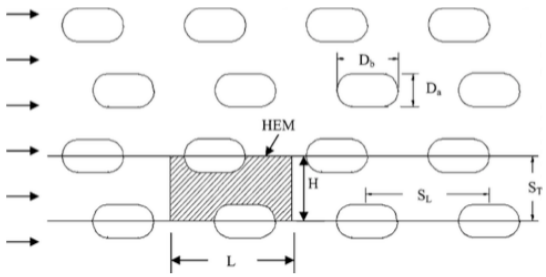

Fig. 9. Configuración en escalón del banco de tubos planos.

Para muchos de los casos existe la condición de flujo completamente desarrollado desde el punto de vista de la caída de presión y la transferencia de calor. Con agua como fluido, para algunos casos la condición térmica de flujo completamente desarrollado no es alcanzada con la condición de frontera de isoflux.

La configuración en línea ofrece mejores características que la configuración escalonada para muchos de los casos, desde el punto de vista de la transferencia de calor. Al mismo tiempo los valores de la caída de presión adimensional son más altos para la configuración en línea que para la configuración escalonada.

Las configuraciones óptimas han sido seleccionadas para ambas condiciones, para la caída de presión y la transferencia de calor mediante el uso del diagrama de Pareto y estas son: (a) En la configuración en línea cuando se tienen una relación de altura de (H/Da=4.) y una relación de longitud de (L/Da=4, 5, 6.). (b) En la configuración en escalón cuando se tiene una relación de altura de (H/Da=5) y una relación de longitud de (L/Da=5, 6, 7).

IV. APLICACIONES

Para las condiciones mostradas se infiere que el uso de los tubos planos en intercambiadores de calor ofrece un amplio panorama de aplicaciones.

T. Matsuda et al. [10] desarrollaron un intercambiador de calor de tubos planos de aluminio, para unidad de bomba de calor al aire libre, con el fin de obtener una mejora en el sistema de la bomba de calor. Cuando se aplica un intercambiador de calor de tubos planos a unidades de bomba de calor al ambiente, se dificulta lograr una buena condensación en el drenaje del serpentín, una alta eficiencia durante la acumulación de escarcha y la distribución del refrigerante.

Con el fin de lograr la misma condensación en el drenado del serpentín y una alta eficiencia en la acumulación de escarcha como con un intercambiador de calor convencional de tubos redondos, los tubos planos fueron insertados en un nuevo diseño de aletas de placa con recortes elípticos. Con el fin de lograr siempre la distribución del refrigerante, un distribuidor de aluminio y 3 formas de tubos fueron instaladas hacia el evaporador.

U. Ahrend [11] realizó una metodología para él estudió de un novedoso intercambiador de tubos planos inclinados, que es un adecuado candidato para mejorar el rendimiento inferior de los intercambiadores de calor comparados con los intercambiadores de calor de tubos redondos bajos condiciones de humedad. La inclinación de los tubos causa una distribución compleja de los coeficientes de transferencia de calor.

El incremento es continuo en la dirección aguas abajo a través de la geometría completa. No se encuentran condiciones totalmente desarrolladas para las cuatro filas en el análisis con un número de Re=3000.

V. CONCLUSIONES

Se han realizada diversas investigaciones en el estudio de los intercambiadores de calor, debido a la continua necesidad de aumentar la eficiencia de estos equipos, a fin de tener un consumo menor de energía. En la actualidad el creciente proteccionismo ambiental y dificultad en el aumento de la eficiencia de los equipos de recuperación de energía han permitido retomar él estudió de estos dispositivos. Muchos estudios sobre perfiles de tubos se han realizado mediante simulación, en modelos matemáticos y experimentación, con lo que se muestra la amplia gama de investigación y aplicaciones en torno a este tipo de perfil de tubos y su arreglo en los intercambiadores de calor

REFERENCIAS

[1] S. Boggia and K. Rud, “Intercooled Recuperated Aero Engine,” MTU Aero Engines, 2002. Munchen, Germany

[2] T. Ahmad, M.M. Rahman and M. Ishak, “Heat transfer and pressure drop prediction in an flat tube bundle by radial basis function network,” IJAME, Malaysia, vol. 10, pp. 2003-2015, December 2014.

[3] M. Ishak, T. Ahmad Tahsenn and Md. Mustafizar Rahman, “Experimental investigation on heat rtansfer and pressure drop characterics of airflow over a staggered flat tube bank in crossflow,” IJAME, Malaysia, vol. 7, pp. 900-911, June 2013.

[4] H. M. S. Bahaidarah, M. Ijaz and N. K. Anand, “Numerical study of fluid and heat transfer over a series on in-line noncircular tubes confined in a parallel-plate channel,” Taylor and Francis Grup, Numerical heat transfer, pp. 97-119, 2006.

[5] H. M. S. Bahaidarah and N. K. Anand, “A numerical study of fluid and heat transfer over a bank of flat tubes,” Taylor and Francis Grup, Numerical heat transfer, pp. 359-385, 2005.

[6] H. Safikhani, A. Abbassi, A. Khalkahli and M Kalteh, “Multi-objective optimization of nanofluid flow in flat tubes using CFD, Artificial neural Networks and genetic algorithms,” Advanced powder technology, pp. 1608-1617, 2014.

[7] G. Singh and G. Sachdeva, “CFD simulation of around and flat tube fin heat exchangers for laminar and turbulent flow,” 4 th. International conference of fluids mechanics and fluid power, December 2010.

[8] Z. Sayed Abdel Rehim, "Heat transfer and fluid flow past staggeered flat-tube bank using CFD," International Journal of Mechanical Engineering, vol. 7, no. 10, 2013.

[9] N. Benarji, C. Balaji and S.P. Venkatashan, "Unsteady fluid flow and heat transfer over a bank of flat tubes," Springer – Heat mass transfer, pp. 445-461, 2007.

[10] T. Matsuda et al., "Development of flat tube heat exchanger for heat pump air conditioning ," 15th International refrigeration and air-conditioning, July 2014.

[11] U. Ahrend, A. Hartmann and J. Koehler, "Measurements of local heat transfer coefficients in heat exchangers wth inclined flat tubes by means of the ammonia absortion method," IHTC–ASME, 2010.

Construcción de un equipo medidor de la huella de carbono por consumo eléctrico para edificaciones en tiempo real

William Fernando Álvarez Castañeda, Laura Alejandra Martínez Tejada, Sergio A. Hernández, Yadir Fernando Medina
Facultad de Ingeniería Electrónica
Universidad Santo Tomás
Tunja, Colombia
william.alvarez01@usantoto.edu.co, laura.martinez@usantoto.edu.co, sergio.hernandez@usantoto.edu.co,
yadir.medina@usantoto.edu.co

***Abstract*—this paper presents the design and the implementation of a carbon footprint measuring device noninvasive to determinate the gas carbonic production due to electricity consumption, to which we define two phases: design and test of the implemented equipment. The first phase focuses in the characterization of the elements, the obtainment of the carbon footprint measure by the current, voltage and power value. The design and construction of the equipment allow determined, not only the real time consumption of an electric charge in kilowatts, also the emission level of CO2 generated in that moment, making visible the electric consumption and the generated pollution. Also, the result is presented as an analog comparison with the pollution generated by a specific automobile that travel a determined distance.**

Keywords—Carbon footprint; measuring device; power consumption.

I. INTRODUCCIÓN

La demanda de energía eléctrica en Colombia en 2012 alcanzó los 59 370 GWh registrando un crecimiento del 3,8% con relación al año 2011, convirtiéndose así, en el mayor crecimiento de demanda en los últimos cinco años. Por el tipo de día, la demanda de los domingos y festivos fue la que presento un mayor crecimiento (4,3%), seguido por los días sábados (3,9%) y los días ordinarios (3,6%). El crecimiento de 3,8% en la demanda 2011-2012 fue, entre otras razones, producto del incremento en un 6,8% de la demanda no regulada (industria y comercio) y de un 2,3% de la demanda regulada (consumo residencial y pequeños negocios). [1]

Según las proyecciones el consumo de energía en los países en desarrollo crecerá a un ritmo promedio anual del 3 por ciento entre 2004 y 2020. En los países industrializados con economías maduras y un crecimiento demográfico previsible relativamente escaso, la demanda proyectada de energía crecerá al ritmo más bajo del 0,9 por ciento anual, pero partiendo de un nivel mucho más alto. La generación de energía eléctrica representará alrededor de la mitad del incremento de la demanda mundial de energía. [2]

En estos tiempos la energía eléctrica es un elemento importante en nuestro diario vivir del cual es imposible dejar de prescindir de ella, pero lamentablemente en la actualidad, la generación de energía eléctrica no se hace de la manera más respetable con el medio ambiente. Cómo toda actividad, la generación de electricidad conlleva una serie de contaminantes. Los contaminantes dependen de la fuente de energía primaria utilizada, de la tecnología elegida y del entorno del emplazamiento de la instalación.

Las centrales térmicas generan contaminantes debido a dos causas esencialmente. Por un lado, la quema de combustibles fósiles como el carbón o el fuel generan cenizas y humos entre los cuales encontramos emisiones de CO2 (dióxido de carbono), SO (óxidos de azufre) y NO (óxidos de nitrógeno). Por otro, generan un cambio térmico en el agua que utilizan para refrigeración. El CO2 es uno de los gases que favorecen el efecto invernadero. Este efecto es el responsable de que la tierra tenga su temperatura, pero un exceso de CO2 en la atmosfera puede provocar un exceso de temperatura. Hay diferentes maneras de reducir el CO2 la más extendida es con el uso de filtros que lo retienen. El SO y el NO son los causantes de la lluvia ácida. La asociación de los óxidos con el oxígeno y el agua forman ácidos nítricos HNO3 y ácidos sulfúricos H2SO4. Estos ácidos cambian el PH de la lluvia, esta lluvia acidifica ríos y aguas, matando a los seres vivos que viven en ellos , otro efecto de la lluvia ácida es la deposición de protones H+, que arrastran ciertos iones del suelo empobreciendo los nutrientes de los ecosistemas. Para eliminar estos contaminantes se realizan diferentes tratamientos, como por ejemplo la introducción de convertidores catalíticos en las centrales o la adición de compuestos alcalinos en los ríos.

En lo que respecta a contaminación térmica, se produce al devolver agua a los ríos o al mar Las centrales térmicas tienen un rendimiento entre el 40 y el 60% en función del tipo de central. La energía que no transforman en electricidad se convierte en energía térmica. Para disminuir esta energía se utilizan los sistemas de refrigeración que utilizan agua de ríos o mares. Hay que controlar la temperatura a la que se devuelve el agua ya que puede afectar negativamente a las especies que habiten en ella. Las centrales nucleares pese a no emitir humos y estar apartadas de núcleos urbanos tienen el problema de los residuos del combustible nuclear y el salto térmico del agua [3].

De esta manera es evidente que independiente del método de generación siempre existe una afectación al medio ambiente, y en algún momento durante el proceso se realiza una emisión de gases de efecto invernadero (GEI), los cuales son producidos de manera directa durante el proceso o de manera indirecta, cuando hacemos uso de la energía eléctrica en cualquiera de nuestras actividades cotidianas. Existen metodologías para el cálculo de la huella de carbono, especialmente para las producidas por una organización, las más relevantes son:

a) NORMA ISO 14064: tiene como objetivo dar credibilidad y aseguramiento a los informes de emisión de GEI y a las declaraciones de reducción o eliminación de GEI. Esta norma puede ser usada por cualquier organización. En la parte 1 de la norma iso 14064 se detallan los principios y requerimiento para el diseño, desarrollo, gestión y elaboración de un informe de huella de carbono.

b) EL GHG PROTOCOL: es una iniciativa puesta en marcha por el World Resources Institue (WRI) y el World Business Council for Sustainable Development (WBCSD), apoyada además por numerosas empresas, organizaciones no gubernamentales y administraciones públicas. El GHG PROTOCOL provee una guía minuciosa para empresas interesadas en cuantificar e informar de sus emisiones de GEI. [4]

c) METODOLOGÍA MC3: ha venido desarrollándose durante los últimos 9 años, se basa en la huella ecológica, presenta un "enfoque a la organización" que incluye un enfoque "bottom-up" para los productos de entrada y "top-down" para los productos de salida permitiendo el cálculo simultáneo de la huella de organizaciones y de productos. La totalidad de los datos se obtiene a partir de las cuentas contables de la organización lo cual permite una relación total entre el aspecto económico y el aspecto ambiental de la organización. [5]

II. MATERIALES Y MÉTODOS

El desarrollo del presente proyecto se divide en varias etapas. En la primera etapa se pretende obtener un equipo que pueda realizar la medición de una carga de AC (corriente eléctrica alterna) determinada y conocida, con el objetivo de poder hacer una evaluación del correcto funcionamiento del equipo, considerando para esto que el circuito de prueba debe manejar una configuración similar a la encontrada en una edificación típica en Colombia y debe manejar unas cargas en AC de potencia conocida, con la capacidad de variar la cantidad de carga aplicada al circuito, estas cargas tienen en primer lugar una característica adicional que es la de ser monofásica.

La primera prueba se realizó con un circuito de potencia, el cual fue utilizado para ajustar y calibrar el primer prototipo del equipo medidor, este contiene 8 cargas, cada una de 60 W a 120 V, las cargas corresponden a bombillas incandescentes, el circuito de prueba se implementó teniendo en cuenta las condiciones de seguridad necesarias. Entre los elementos de seguridad utilizados en el circuito se encuentra los fusibles, los cuales tiene la función que en caso de presentarse un flujo elevado de corriente, el filamento ubicado dentro de este se funda y de esta manera interrumpa el flujo de corriente a través del circuito. El circuito fue acondicionado con un interruptor termo magnético conocido popularmente como Breaker, con el objetivo de proteger el circuito contra sobre saltos de corriente, haciendo un salto en un interruptor el cual abre el circuito protegido. Finalmente se dispuso como dispositivos de seguridad las cuchillas, las cuales son una protección que consta de una lámina metálica que cuando excede su máxima capacidad de amperaje se abre la línea de conexión donde ocurrió el sobresalto de corriente, estas trabajan como un interruptor cortando totalmente el paso de la electricidad. La configuración con la cual se conectan las cargas es en paralelo, de esta manera en todos los puntos del circuito se presenta el mismo nivel de voltaje y el circuito exige una variación de corriente, que es similar a como ocurre en una edificación real. El circuito desarrollado en su primera etapa se presenta en la figura 1.

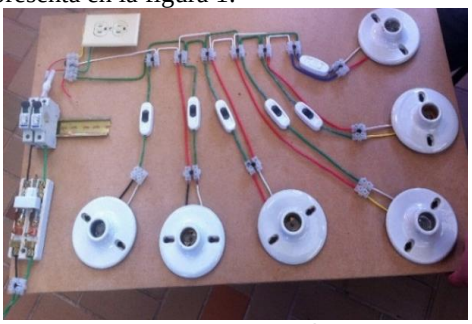

Fig. 1. Circuito desarrollado para la calibración del equipo medidor de la huella de carbono.

La relación existente entre el voltaje, corriente y potencia es una relación lineal determinada por la ley de ohm que se presenta en la ecuación (1).

$$P=V*I \quad (1)$$

Con esta ecuacion se pretende determinar y caracterizar el comportamiento del circuito de prueba para evaluar el desempeno del equipo medidor implementado. Posteriormente fue necesario establecer la relación existente entre el consumo de los KW/h y su equivalente en la producción de Kg CO_2 con la distancia recorrida por un automóvil para emitir la misma cantidad de Kg CO_2 y de esta forma generar la misma huella de CO_2. Para poder determinar está relación, en primer lugar se determinó la huella de carbono generada por consumo eléctrico, para esto se utilizó la calculadora de huella de carbono ofrecida por Berkeley Institute en su página web. La selección de esta calculadora se hizo considerando el resultado del análisis de algunas calculadoras de huella de carbono disponibles en la web que se presentan en la Tabla I. [6] Los valores en la columna R de Resultados están en toneladas métricas de CO_2 por año, GR en la penúltima columna es Guarda Resultados. Posteriormente se selecciono un automovil que sea fácilmente identificable en Colombia, el automóvil seleccionado es el Chevrolet Spark, y el valor de emisión de CO_2 seleccionado es el presentado en el trabajo de

de proyecto de grado realizado por Mauricio Duplat y Johan Silva en la Universidad ICESI denominado.Huella de carbono de producto de consumo masivo en empresa delvalle del cauca.

TABLA I. COMPARACIÓN DE ALGUNAS CALCULADORAS DE LA HUELLA DE CARBONO DISPONIBLES EN LA WEB.

Organización	Alcance	Dificultad y Transparencia	Destacable	GR	R
Berkeley Institute of the Environment (educacional)	Amplio: Casa, transporte, alimentos, servicios y emisiones indirectas.	Muy completa, requiere muchas variables incluyendo información indirecta. Muchos cálculos.	Buen resumen de resultados en forma gráfica.	Si	11,1
British Petroleum, BP (comercial)	Modesto: casa y transporte, incluyendo viajes de negocios.	Baja dificultad, muchos valores promedios. No dice como se hacen los cálculos.	Destacable que una gran empresa de petróleo se preocupe del tema.	No	19
EPA (gubernamental / educacional)	Modesto: casa y transporte, y algo sobre el estilo de vida.	Dificultad media, con una planilla Excel manejable y con los resultados a la vista.	Muchos enlaces a otros calculadores más especializados.	No	9,69
Global Footprint Network (ONG / educacional)	Amplio: casa, transporte, alimentos, consumos y reciclaje.	Alta dificultad, y va más allá de la huella de carbono determinando otros impactos ambientales en el estilo de vida.	Animación molesta pero otorga mayor información sobre el impacto de la huella.	Si	19,6
An Inconvenient Truth / Native Energy (comercial / vende servicios)	Limitado: casa y transporte solamente	Baja dificultad estima gastos energéticos por la cuenta que se paga. Las instrucciones no son muy claras.	Usa diferentes factores de emisión en particular para transporte.	No	8,85
Low impact Living (comercial / vende artefactos)	Muy amplio: casa, transporte, artefactos, basura y agua.	Alta dificultad. Indica estar basada en literatura de alto nivel pero no se dan detalles.	Entrega información del dinero perdido y los ahorros por acciones favorables.	Si	11,6
Nature Conservancy (ONG / educacional / vende servicios)	Amplio: casa, transporte, alimento y reciclaje.	Bja dificultad con muchos valores medios e incluye emisiones indirectas. Las instrucciones no son claras.	Buenos graficos que comparan resultados con promedios en USA y mundiales.	No	25,4
Redefining Progress (ONG, educacional / vende servicios)	Muy amplio: Casa, transporte, alimentos, agua, reciclaje y consumos.	Alta dificultad con cálculos en rangos y va más allá de las emisiones de carbono.	Cuantifica el consumo de energía en forma detallada.	No	63,1
Terrapass (comercial/ vende servicios)	Limitado: casa y transporte.	Dificultad media y enfocada a transporte en avión. Es confusa sin explicaciones.	Calcula consumos y permite comparar su consumo con otras casas del área.	No	9,8

Fuente: Huella de carbono, un concepto que no puede estar ausente en cursos de ingeniería y ciencias. José Valderrama & otros.

Utilizando los datos y la herramienta mencionada anteriormente, se realizaron varios cálculos para determinar una ecuación que caracterice el funcionamiento de las variables involucradas en el cálculo de la huella de carbono. De esta manera se tiene que la relación existente entre los Wh y los gramos de CO_2 están dados por la ecuación 2, y la relación entre los Wh y los kilómetros recorridos en automóvil está dado por la ecuación 3.

$$Y = 0{,}3503X + 0{,}0068 \quad (2)$$

$$Y = 7{,}015X - 0{,}8579 \quad (3)$$

Estas serán las ecuaciones que serán programadas en el equipo para que se realicen las equivalencias en los resultados esperados. Posteriormente para poder aplicar el dispositivo al circuito fue necesario conseguir un sensor de corriente que pueda ser aplicado inicialmente al circuito de pruebas, ajuste y calibración diseñado anteriormente. Se utilizó el circuito ACS 714, el cual es un sensor de corriente capaz de medir de forma lineal corrientes de hasta 30 Amperios en ambos sentidos (+30A y -30A). Produce en su salida una tensión lineal proporcional a la corriente que atraviesa sus pines de medición, lo cual es extremadamente útil para medir consumos o excesos de consumo en diversos proyectos.

La salida produce 66 mV por cada Amperio, centrado en 2,5 V, con un margen de error de 1,5%. La resistencia interna del sensor es de 1.2 mΩ por lo que el consumo generado por la medición es muy bajo. Puede funcionar desde -40 °C a 150 °C. La implementación de este circuito se muestra en la figura 2.

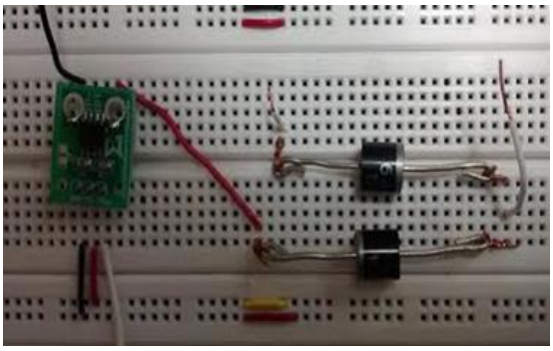

Fig. 2. Implementación del sensor ACS 714

Al realizar las primeras mediciones con el sensor fue necesario realizar algunos ajustes eléctricos para mejorar el comportamiento de todo el circuito. Cuando se obtienen los resultados esperados se procedió a diseñar e implementar un circuito de prueba, ajuste y calibración del equipo que tenga una presentación y pueda tener un uso más fácil para cualquier usuario. De esta manera se tiene la versión dos del equipo que se presenta en la figura 3, donde tiene implementada una pantalla de cristal líquido y el programa era ejecutado por un DSPIC 4013 que lee los datos sensados el cual permite enviarlos vía Bluetooth a un computador para poder registrarlos, almacenarlos y posteriormente analizarlos. La versión dos tiene dos botones, uno llamado incremento (donde al accionarlo encienden cada vez más cargas) y el otro llamado decremento (donde se apagan progresivamente las cargas), el tercer botón es para cambiar en la LCD los datos visualizados.

Fig. 3. Versión dos del equipo medidor de la huella de carbono.

Finalmente, y considerando los buenos resultados obtenidos con la versión dos, y buscando la posibilidad de obtener un circuito más versátil y dinámico que pueda ser aplicado a situaciones reales, se trabaja la versión tres en la cual el equipo no está integrado al circuito de pruebas, ajuste y calibración como en las versiones anteriores. En esta nueva versión únicamente se busca hacer un equipo que pueda ser instalado en la edificación a la cual se desea determinar la huella de carbono, permitiendo que este procedimiento sea de una manera no invasiva al circuito eléctrico. La nueva versión maneja una pantalla táctil que permiten una mejor interacción y mayor facilidad a la hora de su uso, así como comunicación a un computador vía inalámbrica y mayor capacidad de sensado de corriente. Para lograr una mejor lectura en el rango de corriente se utiliza el sensor marca XiDi Technology modelo SCT-013-000 mostrado en la figura 4.

Fig. 4. Sensor utilizado en la última versión.

III. Resultados

En la primera versión del dispositivo (versión 1.0), se obtuvieron los valores correspondientes a los niveles de tensión y corrientes consumidos por la red a la cual se encontrase dispuesto el medidor de huella de carbono, al igual que la cantidad de CO2 emitida al medio, se visualizaba en una pantalla de cristal líquido, en donde a través de unos interruptores se escogía la variable a visualizar en la pantalla. En la versión 2.0, en la cual aún se está trabajando, se ha reemplazado la pantalla de cristal líquido, por una pantalla táctil de 3.1" en la cual se han realizado importantes avances, pues a través de su programación en una tarjeta de desarrollo ARDUINO, se ha creado una interfaz de inicialización en la cual se muestran los nombres de los diferentes desarrolladores del programa, al igual que los logos correspondientes al semillero de investigación al cual se encuentra inscrito el proyecto y la institución educativa a la cual pertenece el grupo de investigación. En lo concerniente a la aplicación del dispositivo (medidor de huella de carbono), en la parte visual y de interfaz de usuario se ha creado un menú que cuenta con cuatro botones dispuestos en la pantalla táctil con los cuales se selecciona la variable que se desea conocer, remplazando así los interruptores existentes en la versión 1.0 el dispositivo. Tras ingresar a cada una de las opciones del menú, se puede retornar nuevamente a este último a través de un botón denominado atrás. El sensor posee una resolución de 20 mV/A, con lo cual se obtienen unos resultados parciales iniciales para el consumo de una lámpara incandescente común de tungsteno (Ver Tabla II).

TABLA II. COMPARACIÓN DE ALGUNAS CALCULADORAS DE LA HUELLA DE CARBONO DISPONIBLES EN LA WEB.

Datos Ideales de carga resistiva	Datos Adquiridos (Multimetro)	Datos Adquiridos (Sensor)
100 W	117,9 W	19,256 mV
120 V	122,5 V	
833 mA	962,8 mA	
15 W	15,17 W	2,48 mV
110 V	122,5 V	
122 mA	123,9 mA	

Basándonos inicialmente en el factor ofrecido por el instituto nacional de tecnología industrial de argentina en donde: 0,39 Kg CO_2/KWh. Por lo anterior se consumirán aproximadamente 133,07 W/h, y su equivalente de contaminación es de aproximadamente 0,051897 Kg de CO_2, o 51,9 g de CO_2 por cada hora de consumo de dichas lámparas incandescentes.

AGRADECIMIENTOS

Los autores del presente trabajo queremos manifestar nuestro especial .agradecimiento a todos los estudiantes que han estado y están vinculados en la realización de este proyecto. De igual manera a las directivas de la Universidad Santo Tomás y a la facultad de ingeniería electrónica de la seccional Tunja.

REFERENCIAS

[1]. Energía Eléctrica. Memorias al congreso de la república 2012-2013. Ministerio de minas y energía. Http://www.minminas.gov.co/minminas/downloads/userfiles/File/Memorias/Memorias_2013/4-Energia.pdf
[2]. Oferta y demanda de energía: tendencias y perspectivas. Fao. Ftp://ftp.fao.org/docrep/fao/010/i0139s/i0139s03.pdf.
[3]. http://www.endesaeduca.com/Endesa_educa/recursos-interactivos/el-uso-de-la-electricidad/xxv.-la-energia-electrica-y-el-medio-ambiente
[4]. OBSERVATORIO DE SOSTENIBILIDAD EN ESPAÑA, Manual de cálculo y reducción de la huella de carbono en el sector del comercio, España.
[5]. CEPAL (Comisión Económica para América Latina y el Caribe), Metodologías de cálculo de la huella de carbono, Documento de trabajo, ONF 2010.
[6]. VALDERRAMA, José O; ESPINDOLA, César y QUEZADA, Rafael. Huella de Carbono, un Concepto que no puede estar Ausente en Cursos de Ingeniería y Ciencias. 2011, vol.4, n.3, pp. 3-12. Disponible en: <http://www.scielo.cl/scielo.php?Script=sci_arttext&pid=S0718-50062011000300002&lng=es&nrm=iso>. ISSN 0718-5006.

Radiative transfer model of a solar thermochemical multi-tubular reactor: Geometric Optimization.

Patricio J. Valades-Pelayo, Camilo A. Arancibia-Bulnes*, Heidi I. Villafan-Vidales
Instituto de Energias Renovables
Universidad Nacional Autonoma de Mexico
Temixco, Morelos, Mexico
caab@ier.unam.mx*

Hernando Romero-Paredes
Área de Ingeniería en Recursos Energéticos
Universidad Autónoma Metropolitana
Iztapalapa, México, D.F.

***Abstract*— The present study explores optimal tube distributions in a cubic cavity thermochemical reactor. The reactor prototype consists of a cubic receptacle made of woven graphite; housing nine tungsten tubes. With this end, a simulation is developed by implementing a radiative Monte Carlo-Finite Volume Method (MC-FV) to solve the radiative transfer equation (RTE) considering high-temperature surface emission within the cavity. More specifically, the simulation model considers: 1) specular and diffuse reflection, 2) temperature-averaged emissivity for each material and 3) a gaussian radiative energy inlet, fitted to irradiance data obtained from the solar furnace at Instituto de Energias Renovables, UNAM (HoSIER-UNAM). Afterwards, the simulation is enclosed within a custom-made, global, multi-parameter Monte Carlo optimization algorithm, aiming towards finding patterns among the multiple expected optimum tube arrangements. The optimization subroutine, consists of two subroutines that: 1) generates random symmetric tube distributions and 2) stores them in a list-like matrix, reordering them based on the system performance for every distribution. Finally, multiple optimal tube distributions are grouped to plot 2D contours, where higher values at every given location depend on likelihood (frequency of tube appearance), weighted by their respective cavity performance (higher average tube temperature). The patterns obtained suggest the following: 1) one to two tubes should be positioned at each side of the focal point and 2) all other tubes should be positioned behind the focal point.**

Keywords: Cavity receiver; Thermochemical Reactor; Radiative Heat Transfer; Multi-Parameter Optimization.

I. INTRODUCTION

Concentrated solar energy can be converted into hydrogen or syngas through several processes that involve highly endothermic reactions, e.g. thermochemical cycles, gasification of carbonaceous materials, cracking of hydrocarbons, reforming of methane and water-splitting [1]. In these processes endothermic reactions are performed in solar reactors, whose design is different of conventional reactors. Although some concepts of traditional reactors are combined in its design, e.g particles distribution or reactants feeding [2]. Usually solar reactors consists of cavity-type receivers in which concentrated solar energy enters and is directly absorbed by the reactants (directly irradiated reactors) or absorbed by a material that transfers heat to the reaction site (indirectly irradiated reactors). Nevertheless, both must deal with a non-uniform solar distribution that produces non-uniform temperatures. In this sense, the modeling of solar reactors is an useful tool still under development, seeking to improve and optimize reactor configurations, such as maximizing absorbed energy while homogenizing temperature distributions, thereby reducing thermal stress and increasing energy efficiency. In this regard, Villafán-Vidales et al. [3] developed a model that predicts the thermal behaviour of a thermochemical reactor based on porous media under different operational conditions, i.e. incident solar flux, inert gas flow rate, porosity of the media, length of the foam and the influence of chemical reactions. In the field of indirectly irradiated reactors, specially tubular reactors, only a few works have been done.

Yao and Epstein [4] modeled a solar-driven tubular reactor, that consisted in a directly irradiated tube. In their study they find the optimal operating temperature for an isothermal rector and the effect of solar flux distribution in the conversion of reactants. Moreover, they observed that solar irradiance distribution affects the conversion of reactants and that inlet temperature has a significant effect on reactor performance. Melchior et al. [5], developed a heat transfer model for a cylindrical cavity receiver containing a tubular absorber. The model comprises radiation, convection and conduction coupled with the chemical reaction in order to predict temperatures and reaction rates. Their computed values were in reasonable agreement with experimentally obtained data and they find that the major heat losses are due to re-radiation through the aperture and conduction through the walls. The authors also used this model to study the thermal performance of a 100 kW and 1 MW scaled-up solar reactor containing multiple tubular absorbers [6]. They concluded that when scaling-up, conduction losses are reduced due to an increase of volume-to-surface ratio.

Other models are related with the modeling of solar reactor with multiple tubular absorbers [7-13]. However, the optimization of the tube array have been scarcely analyzed[13]. Previous studies present unoptimized tube arrays with highly non-uniform temperature distributions and low average temperatures [10-12]. In this sense, the present study explores different optimal tube distributions in a indirectly irradiated reactor that consists of a cubic cavity housing nine tungsten tubes. The developed model solves the radiative transfer

equation by Monte Carlo and Finite volume methods considering the optical properties of the materials involved, the directional characteristics of the radiation entering the cavity and the high-temperature emission within the cavity.

Moreover, tube distributions are analyzed through a custom-made global optimization algorithm that allows investigating this issue from a general perspective. The main results indicate that at least one of the tubes should be positioned at each side of the focal point and all other tubes should be positioned behind the focal point.

II. Mathematical Modelling

A model describing the thermal behaviour of a solar thermochemical cubic-cavity reactor is proposed assuming radiative transfer equilibrium. The model integrates the radiative transfer equation (RTE) coupled to the heat transfer equation on steady state. The RTE is solved using a ray tracing technique, considering Monte Carlo methods to determine the probability density function (PDF) of photon absorption on the tubes and cavity walls, for every given point of emission. Within this subroutine, Lambertian emission is considered along specular and diffuse reflection. Additionally, a Gaussian distribution is used to represent the solar flux from the aperture window.

On this basis, the PDFs of photon absorption are used as form factors into a Finite Element method (FEM) that considers the Stephan-Boltzman law of emission, to determine the temperature distribution inside the woven graphite cavity and the tungsten tubes. The system of equations was linearized by considering energy rather than temperature as the unknown variables and solved using LU factorization to yield the tube and cavity walls temperature distributions.

Afterwards, the simulation is enclosed within a custom-made, global, multi-parameter Monte Carlo optimization algorithm, aiming towards finding patterns among different global optimum tube arrangements. This algorithm generates random symmetric tube distributions and classifies them in a list-like matrix, according to the system performance. Multiple optimal tube distributions are grouped to plot 2D contours, where higher values at every given location depend both on likelihood (frequency of tube appearance in the list) and their respective cavity performance (higher average tube temperature of the tube arrangement).

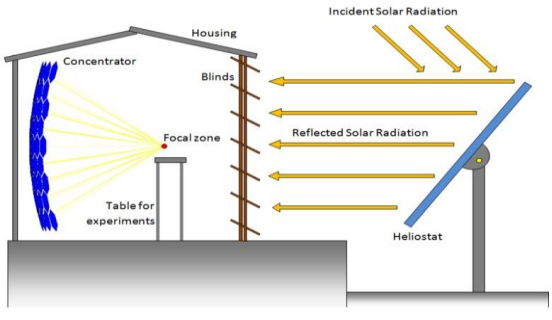

Fig. 1. Concentrating system layout at IER-UNAM solar furnace; the reactor is to be placed in focal zone.

A. Solar Flux Profile

The solar flux considered on the aperture window, is obtained from measurements carried out in the HoSIER Solar Furnace, at Instituto de Energias Renovables of Universidad Nacional Autonoma de Mexico (IER-UNAM) [14]. The HoSIER consists of a double concentrating system: 1) a single flat heliostat and 2) a parabolic arrangement of hexagonal mirrors. In Figure 1, a general layout of the concentrating system is presented.

Performance of this solar furnace has been previously reported by Riveros-Rosas et al. [14], where a concentrating factor of about 18,000 suns was reported. Inside the HoSIER temperatures above 3,100 K can be attained, given its high optical quality.

More specifically, to account for the inlet information, obtained at HoSIER, a gaussian distribution, with a standard deviation of 2.5 cm was used [15], where the focal point is varied in the plane parallel to the cubic-cavity radiative inlet.

B. Monte Carlo Model for the RTE

The cubic cavity and tube walls surface are discretized. On this basis, the strategy adopted within the present study, utilizes the MC method as a tool for determining form factors among the different discretized elements, while considering intermediate reflections. i.e. photon bundles are emitted from one element and tracked down, to determine the probability of a photon from being emitted from an element and absorbed on another one.

Direction of emission from a discretized element is considered to be Lambertian, whereas subsequent reflections are considered to be, either specular or diffuse. In this regard, optical properties are selected for woven-graphite and tungsten as presented in table 1, where optical properties are assumed not to vary greatly with changing element temperature.

TABLE I. TUNGSTEN AND GRAPHITE AVERAGED OPTICAL PROPERTIES.

Materials	Averaged optical properties		
	Emissivity	*Reflectance*	*% of Diffuse Reflectance*
Tungsten	0.25	0.75	0.5
Graphite	0.76	0.50	0.8

[a] Sample of a Table footnote. (*Table footnote*)

Radiation entering the cubic-cavity, is assumed to be emitted from the entrance element, where location and direction of emission are considered to be described by an uniform distribution and a Gaussian distribution. This Gaussian distribution, assumes a standard deviation , representing the statistical variation of the entering rays from the average focal point, located 5.5 cm from the opening and right at the reactor centerline (center of the opening). This deviation is assumed to affect the focal point location on the horizontal and vertical axis, as it is assumed to be caused, mainly due to wind loads on the heliostat.

C. *Finite Element Method for Energy Equation*

The energy balance for the present study assumes the discretized cavity, tubes and opening elements to be in thermal equilibrium. Additionally, emissivity is assumed to be non-dependent on surface temperature; rather a temperature - averaged emissivity is selected for each material, as presented in TABLE 1.

On the basis of the above mentioned, the energy balance equation, can be written, for element "i" in the following way:

$$\Delta S(i)\, \sigma\varepsilon\, T(i)^4 = \Sigma\, P(j,i)\, \Delta S(j)\, \sigma\varepsilon\, T(j)^4 \qquad (1)$$

where ΔS is the emitting surface of a discretized element, ϵ is its emissivity, T its temperature. P(j,i) represents the fraction of radiation absorbed by element "i", coming after surface emission from element "j". These factors are obtained by Monte Carlo ray tracing techniques.

D. *Optimization Algorithm*

The optimization scheme considers random generation of vertically oriented, symmetrical tube locations on a 2D space, as presented by the red rectangle in Figure 2. As the multi tubular distributions are generated, four main aspects are considered: 1) tubes location probability is uniformly distributed throughout all the 2D space, 2) tubes center locations cannot be closer to each other by less than one inch and a half, 3) or to a wall by less than half an inch and 4) any given combination of tube locations must be different to all past generated combinations.

In this sense, the first aspect was considered to avoid higher preference to any region within the 2D space. The second and third aspects were implemented based on a practical consideration: tubes are one inch diameter and are to be grabbed by half-inch flanges. Finally, the last consideration was accounted to avoid unnecessary evaluation of the same tube permutations, given that ultimately the tube combinations are relevant for the physics of the problem.

Based on different scenarios, the fit function was chosen to maximize the average tube temperature of: a) a single tube, b) three tubes and c) all tubes. After a new symmetric random tube distribution is implemented, the optimization algorithm evaluates the fitness function based on the information obtained by the cavity-tubes simulation. Finally, the tube distributions are stored on a list, ordered by decreasing fitness value, where the best 10,000 combinations are kept along their respective fitness value. Process is repeated until about 10,000 different combinations are evaluated and compared.

E. *Multiple Optimum Tube Distributions: Pattern Generation*

The recorded multiple optimal tube distributions are grouped according to their location. The quantity and quality are accounted for at every location. This information is then used to generate a probability density distribution, that helps us to identify the tube locations that tend to favor an increase in the average tube temperature.

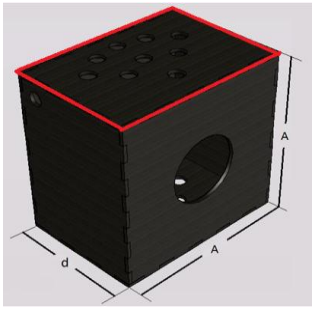

Fig. 2. Cubic-cavity with opening. Highlighted in red, 2D space where the nine tube distribution is to be optimized.

More specifically, 2D contours where generated, where higher values at every given location depend on likelihood (frequency of tube appearance), weighted by their respective cavity performance (higher average tube temperature).

III. RESULTS

In this section the main results are summarized and presented. First a subsection presents the temperature distributions on the tubes and cavity, as calculated by the MC-FV model previously presented. After that, a list of several optimum points is presented along their respective average tube temperature.

Finally, by weighting frequency and fitness of all optimum combinations, a pattern is presented and discussed along general guidelines for tube positioning. In this regard, selection of a specific tube arrangement from the proposed pattern, can be done based mostly on practical considerations and according to specified reaction criteria.

A. *Simulation: temperature distributions*

Figure 2, presents the temperature distributions of all surfaces within the reactor: six planes representing the woven-graphite cubic cavity and nine cylinders representing the nine Tungsten tubes. Temperature is presented in K while dimensions are presented in centimeters.

This arbitrarily chosen tube distribution, with one tube located right on the focal point (Gaussian distribution mean value) and all other tubes behind it, tends to generate a very high hotspot (on the surface right on the focal point). Additionally, this hotspot, being so close from the cavity opening, generates a relatively low average tube temperature due to reflection and emission.

Moreover, this tube arrange causes some tubes overshadow each other while leaving some gaps which allow radiation go through. More specifically four gaps are observed, with the two centermost gaps leaving more radiation going through, given their proximity to the radiative focal point.

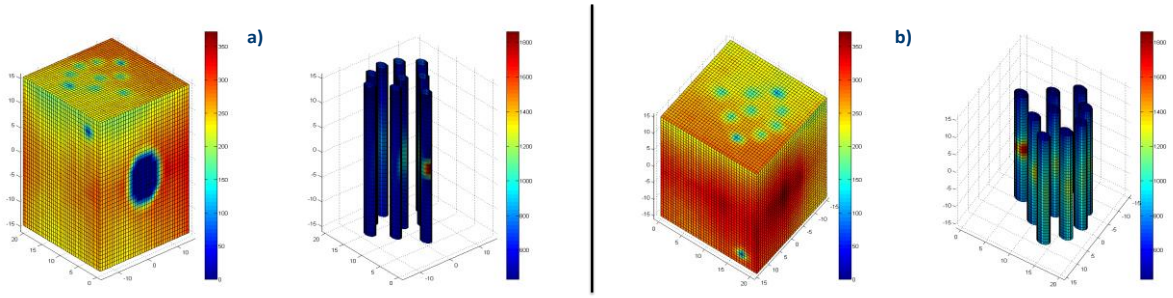

These gaps allow radiation to reach the back cavity wall, where most of the radiation is absorbed due to the high absorption coefficient of graphite. This heats up the back cavity wall, which emits radiation due to its high emissivity. This radiation being emitted by the back cavity wall, in turn heats the backside of the Tungsten tubes located further back, which tends to generate this characteristic pattern on the back tube surface.

B. Optimization: pattern for best tube distributions

Making use of the model presented, an average temperature was calculated considering all surface elements on the nine tubes. About 10,000 random symmetric tube combinations where filtered to obtain the best 1,000 set ups. From these combinations and their respective fit-values (how well did the cavity behaved), the following distribution is presented in Figure 3, where the highest values represents best place to position the tube center (red means higher, blue means lower).

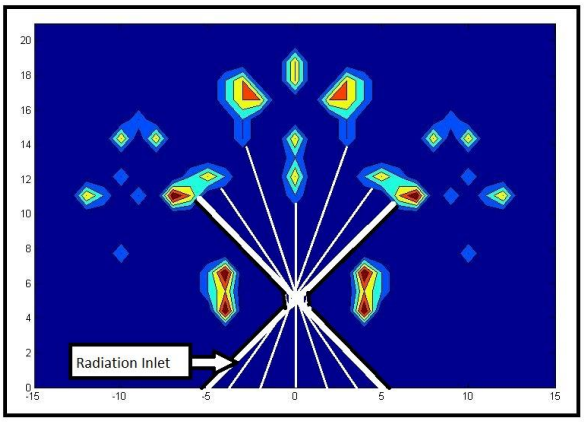

Fig. 3. Pattern obtained from filtering random tube distributions based on maximum average tube temperature. Focal point and radiation cone entering the cavity are presented. Diagram in centimeters, contours in arbitrary units.

IV. Conclusion

From Figure 3, the following guidelines can be stated: 1) one to two tubes should be positioned at each side of the focal point and 2) all other tubes should be positioned behind the focal point, and 3) be arranged in a way that they form a "wall" from when looked from the perspective of the opening. In general a cavity-like tube arrangement within the cavity is suggested.

Acknowledgment

The authors acknowledge the financial support received through the Mexican Center for Innovation in Solar Energy (CeMIE-Sol), as part of the Call 2013-02, the SECTOR FUND CONACYT -SENER-ENERGY SUSTAINABILITY within strategic Project No. 10, entitled: "SOLAR FUELS AND INDUSTRIAL PROCESSES", and IER-UNAM for their support of Dr. Patricio Valades Pelayo.

References

[1] Steinfled. Solar thermochemical production of hydrogen–a review. Solar Energy 78 (2005), 603–615.

[2] C. Agrafiotis, H. Von Storch, M. Roeb, C. Sattler. Solar thermal reforming of methane feedstocks for hydrogen and syngas production- A review. Renewable and Sustainable Energy Reviews 29 (2014), 656–682.

[3] H.I. Villafán-Vidales, Stéphane Abanades, Cyril Caliot, H. Romero-Paredes. Heat transfer simulation in a thermochemical solar reactor based on a volumetric porous receiver. Applied Thermal Engineering 31 (2011) 3377-3386.

[4] C. Yao, M. Epstein. Maximizing the output of a solar-driven tubular reactor. Solar Energy 57 (1996) 283-190.

[5] T. Melchor, C. Perkins, A. W. Weimer, A. Steinfeld. A cavity-receiver containing a tubular absorber for high-temperature thermochemical processing using concentrated solar energy. International Journal of Thermal Sciences 47 (2008) 1409-1503.

[6] T. Melchior, C. Perkins, P. Lichty, A.W. Weimer, A. Steinfeld. Solar-driven biochar gasification in a particle-flow reactor. Chemical Engineering and Processing 48 (2009) 1279-1287.

[7] S. Rodat, S. Abanades, J-L. Sans. G. Flamant. A pilot-scale solar reactor for the production of hydrogen and carbon Black from methane splitting. International Journal of Hydrogen Energy 35 (2010) 7748-7758.

[8] T. Melchior, A. Steinfeld. Radiative transfer within a cylindrical cavity with diffusely/specularly reflecting inner walls containing an array of tubular absorbers. Journal of Solar Energy Engineering 130 (2008) 021013.

[9] F.J. Valdés-Parada, H. Romero-Paredes, G. Espinosa-Paredes. Numerical simulation of a tubular solar reactor for methane cracking. International Journal of Hydrogen Energy 36 (2011) 3354-3363.

[10] J. Martinek, C. Bingham, A. W. Weimer. Computational modeling of multiple solar reactor with specularly reflective cavity walls. Part 2: Steam gasification of carbon. Chemical Enginnering Science 81 (2012) 285-297.

[11] J. Martinek, C. Bingham, A. W. Weimer. Computational modeling and on-sun model validation for a multiple tube solar reactor with specularly

reflective cavity walls. Part 1: Heat transfer model. Chemical Engineering Science 81 (2012) 298-310.

[12] G. Maag, S. Rodat, G. Flamant, A. Steinfeld. Heat transfer model and scale-up o fan entrained-flow solar reactor for the thermal decomposition of methane. International Journal of Hydrogen Energy 35 (2010) 13232-13241.

[13] J. Martinek, A. W. Weimer. Design considerations for a multiple tube solar reactor. Solar Energy 90 (2013) 68-9.

[14] Riveros-Rosas D, Herrera-Vázquez J, Pérez-Rábago CA, Arancibia-Bulnes CA, Vázquez-Montiel S, Sánchez-González M, Granados-Agustín F, Jaramillo OA, Estrada CA. Optical design of a high radiative flux solar furnace for México. Solar Energy, 84 (2010) 792-800.

[15] Pérez Enciso R. PhD Thesis (in Spanish), Universidad Nacional Autónoma de México.

Simple model reduction for high order underdamped system

G. Hernández, D.F Novella, B. Del Muro
Sección de Estudios de Posgrado e Investigación Unidad Culhuacán
Instituto Politécnico Nacional
Ciudad de México, D.F, México.
german.h.team@gmail.com, dnovellar@gmail.com, bdelmuro@ipn.mx

***Abstract*—This work presents a procedure to reduce high order linear oscillating systems into a second order underdamped system with time delay. Previous works have been developed on this topic but on the particular case of overdamped systems, i.e. only real roots in the characteristic equation (see Skogestad, 2002). High order systems appear in the modeling of mechanical and civil structures, such as mass-spring-damper interconnected systems. The design of proper controllers for this class of systems represents a challenge. The proposed methodology is based on a frequency domain approach of the high order plant. The procedure for model reduction is simple and can be computed considering the Bode plot of the original plant. Then, the characteristic parameters of the process are introduced in a reduced system which includes a time delay in the direct path. Both models are compared taking into account the response behavior to different inputs. The main advantage of the model reduction is to simplify the controller design. There are in the literature rules to obtain PID controller parameters for second order delayed systems, such as the model obtained with the proposed reduction. The use of PID controllers designed for the reduced model yield an acceptable performance on the original plant.**

Keywords— High order system; Time delay; Reduced model; PI/ PID controller; RLC circuit

I. INTRODUCTION

In many areas such as electronic, mechanical and energetic engineering there are applications which result in high order systems models, particularly if the elements of these systems are interconnected between them, like in spring-mass-damper systems or RLC circuits in cascade, therefore, the high order system reduction can be an alternative to treat with such models without much difficulty.

Dealing with high order systems could yield different problems and bring some complications, for instance, one of them appear in analyzing and designing control systems, this means that should be considered several parameters, as well as, a significant number of dynamics and calculations, which would involve a poor performance in these systems. In addition, the time response and frequency response analysis [1,2,3]. result more complicated than a first or second order system. There are some works that present techniques to reduce high order systems, one of them is the work presented by Skogestad [4] which gives a methodology to reduce these kind of systems and obtain a first or second order model with time delay, in order to design PI or PID controllers using specific tuning rules. However, this work only considers stable high orders systems with real poles, unstable and oscillating processes have not been studied.

In this paper a useful and simple methodology is presented to reduce linear high order systems with complex conjugates poles, to obtain an underdamped second order system with time delay, allowing designing control systems considering less number of parameters, simplifying the PI/PID tuning, for instance. In the first part of this work a general approach for model reduction and a frequency response analysis was carried out to estimate specific parameters, which allows keeping the general behavior of the high order system and also use them to calculate the parameters for the reduced model. In order to prove the methodology an illustrative example was presented. In the second part a fourth-order system which represents two RLC circuits in cascade is used to obtain a reduced model using the proposed methodology. In the last part PI/PID controllers are designed for the reduced model and then used in the fourth-order system, obtaining good results in both systems. In addition one of the proposed PI/PID is implemented in the RLC circuits systems to obtain the desired output voltage..

II. MODEL REDUCTION GENERAL APPROACH

Considering a high order system as follows,

$$(s) = \frac{b_0 s^m + b_1 s^{m-1} + \ldots b_{m-1} s + b_m}{a_0 s^n + a_1 s^{n-1} + \ldots a_{n-1} s + a_n} \quad (1)$$

Rewritten (1) and considering oscillating systems we have,

$$(s) = \frac{K \prod_{j=1}^{m/2} (s^2 + 2\xi_j \omega_{nj} s + \omega_{nj}^2)}{\prod_{i=1}^{n/2} (s^2 + 2\xi_i \omega_{ni} s + \omega_{ni}^2)} \quad (2)$$

where *n* and *m* are even.

The main goal is to obtain an underdamped second order system with time delay, for the system given in (2),

$$_r(s) = \frac{\bar{K} e^{-\tau s}}{(s^2 + 2\zeta \omega_n s + \omega_n^2)} \quad (3)$$

where $\boldsymbol{\tau}$ is the delay system, $\boldsymbol{\zeta}$ is the damping ratio and $\boldsymbol{\omega_n}$ is the undamped natural frequency. The reduced model given in (3) must describe the dynamic behavior of the high-order system.

A. *High Order Underdamped System Reduction Using Frequency Response*

To obtain a reduced model the proposed methodology focuses on the high order system frequency response. In addition, using the Bode diagram of the high order system, it is possible to find three important parameters as shown in Fig. 1, which allow calculating a reduced model.

- Resonance frequency, ω_r
- Resonant peak value, M_r
- Phase angle of the resonance frequency, θ_r

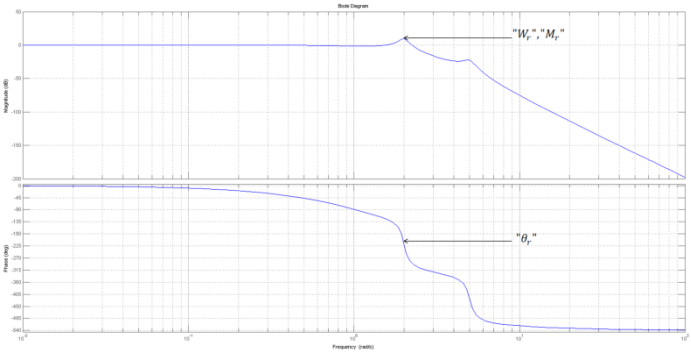

Fig. 1. Frequency response for a high order system.

Based on the above characteristics, it is possible to obtain the reduced model parameters, it means, that we can estimate the undamped natural frequency $\boldsymbol{\omega_n}$, the damping ratio $\boldsymbol{\zeta}$, and the time delay $\boldsymbol{\tau}$ as follows.

Due to the underdamped behavior of both systems, we can establish that the resonance frequency of the high order system can be related with the undamped natural frequency, i.e. $\omega_n \rightarrow \omega_r$. In addition it can be proved using the damping ratio and the resonance frequency [3]. as shown in (4),

$$\omega_n = \frac{\omega_r}{\sqrt{1-2\zeta^2}} \tag{4}$$

In the same way there exist, a relationship between the resonant peak value $\boldsymbol{M_r}$ and the damping ratio $\boldsymbol{\zeta}$ [3]. as shown in Fig.2, given by,

$$M_r = \frac{1}{2\zeta\sqrt{1-\zeta^2}} \tag{5}$$

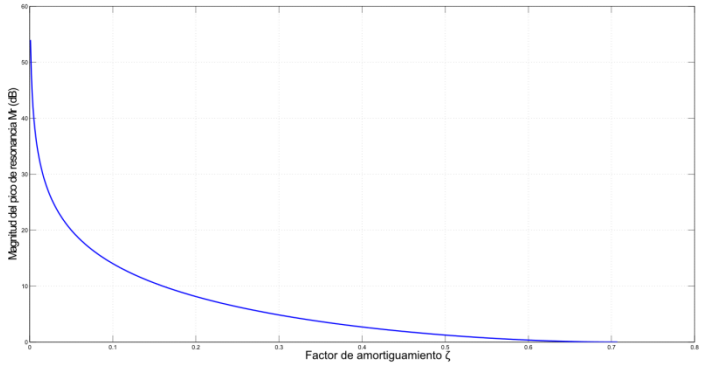

Fig. 2. Relationship between $\boldsymbol{M_r}$ and $\boldsymbol{\zeta}$.

To conclude the delay term is related with the phase shift between the high order system and the reduced model, considering the following aspects,

- The corner frequency ω_n, for the underdamped second order system is associated with the phase angle $\Phi = -90°$
- The phase angle of the delay term is $\theta = -57.3\omega_r\tau$

Such that,

$$\theta_r = -90° + (-57.3\omega_r\tau) \tag{6}$$

From (6) we have,

$$\tau = \frac{\theta_r + 90°}{-57.3\omega_r} \tag{7}$$

Finally once the parameters of the reduced model have been calculated, the value corresponding to the proportional gain should be determined, as follows,

$$\overline{K} = K\frac{\lim_{n\to 0} G(s)}{\lim_{n\to 0} G_r(s)} \tag{8}$$

B. *Evaluating the Methodology*

Example 1

The following example is given to validate the proposed methodology, so it is possible to compute the parameters mentioned before and obtain reduced model.

Considering the high order system,

$$(s) = \frac{125.7636}{(s^2+2s+1.25)(s^2+0.25s+4.01)(s^2+0.6s+25.09)} \tag{9}$$

Based on the frequency response analysis and using the Bode diagram of the system given in (9) we can find the following parameters,

- Resonance frequency, $\omega_r = 1.991\ rad/s$
- Resonant peak value, $M_r = 9.75\ db$
- Phase angle of the resonance frequency, $\theta_r = -210.936°$

According to the previous information, it is possible to obtain the parameters of the reduced model, such that,

- The resonance frequency is associated with the undamped natural frequency, i.e., $\omega_n \rightarrow \omega_r = 1.991\ rad/s$
- Considering $M_r = 9.75\ db$ and the relationship with the damping ratio we obtain $\zeta = 0.165$
- Finally the delay term is computed according to (7) such that, $\tau = 1.0601\ s$

With the parameters $\boldsymbol{\omega_n}$, $\boldsymbol{\zeta}$ and $\boldsymbol{\tau}$ we can calculated the reduced model describing by the following transfer function,

$$_r(s) = \frac{3.96414e^{-1.0601s}}{(s^2 + 0.657s + 3.964)} \tag{10}$$

The comparisons between the high order system and the reduced model are shown in Fig. 3, and Fig. 4.

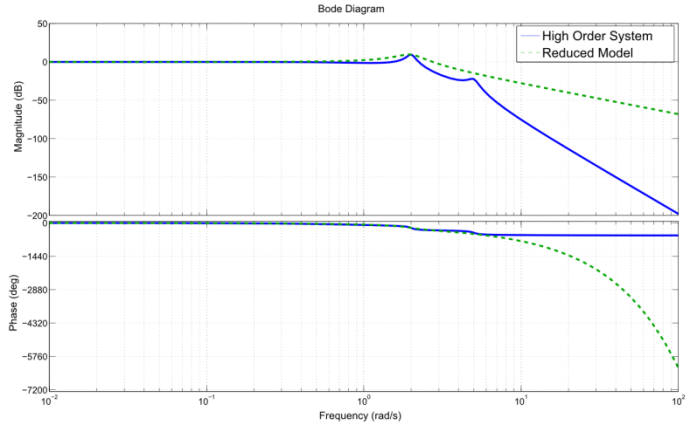

Fig. 3. Frequency response for the high order system and the reduced model.

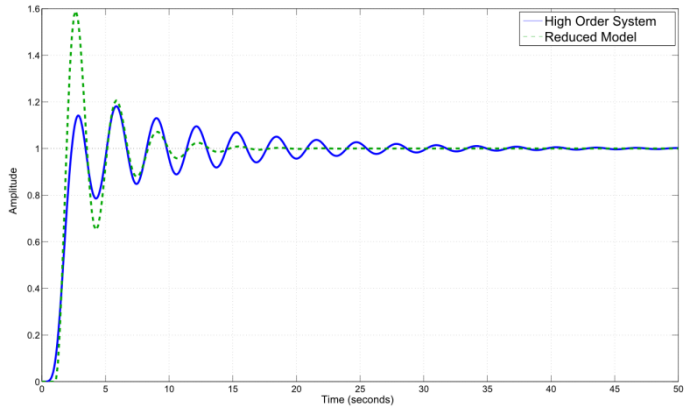

Fig. 4. Step response for the high order system and the reduced model.

III. Application of the Methodology: Obtaining a Reduced Model for a RLC Circuit's System

In this part of the work, an electrical system is used to validate the methodology. Considering two RLC circuits in cascade as shown in Fig. 5, and assuming the transfer function for this system given in (11), where V_i is the input voltage and V_o is the output voltage.

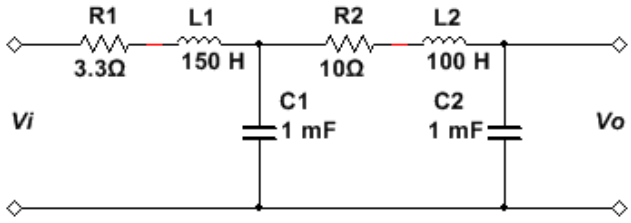

Fig. 5. RLC circuits system.

$$num = 1$$

$$den = L_1L_2C_1C_2s^4 + (R_1C_1L_2C_2 + R_2C_2L_1C_1)s^3 + (L_1C_2 + L_2C_2 + R_1C_1 + R_2C_2 + L_1C_1)s^2 + (R_1C_2 + R_2C_2 + R_1C_1)s + 1$$

$$\frac{V_o(s)}{V_i(s)} = \frac{num}{den} \tag{11}$$

Using the proposed methodology, we can obtain an uderdamped second order system with time delay. The current system represents a stable fourth-order system with complex-conjugate poles given by,

$$(s) = \frac{1}{0.015s^4 + 0.0083s^3 + 0.4s^2 + 0.0166s + 1} \tag{12}$$

The transfer function in (12) yields the relation between the output voltage and input voltage for the circuit shown in Fig. 5.

Based on the frequency response analysis and using the Bode diagram of the system given in (12), we can find the following parameters,

- Resonance frequency, $\omega_r = 1.671\ rad/s$
- Resonant peak value, $M_r = 34.3\ db$
- Phase angle of the resonance frequency, $\theta_r = -90.117°$

According to the previous information, it is possible to obtain the parameters of the reduced model, such that,

- The resonance frequency is associated with the undamped natural frequency, i.e., $\omega_n \rightarrow \omega_r = 1.671\ rad/s$
- Considering $M_r = 34.3\ db$ and the relationship with the damping ratio we obtain $\zeta = 0.0090$
- Finally the delay term is computed according to (7) such that, $\tau = 0.0012\ s$

With the parameters $\boldsymbol{\omega_n}$, $\boldsymbol{\zeta}$ and $\boldsymbol{\tau}$ we can calculated the reduced model describing by the following transfer function,

$$_r(s) = \frac{2.7922e^{-0.0012s}}{(s^2 + 0.03008s + 2.792)} \quad (13)$$

The comparisons between the fourth-order system and the reduced model are shown in Fig. 6, and Fig. 7.

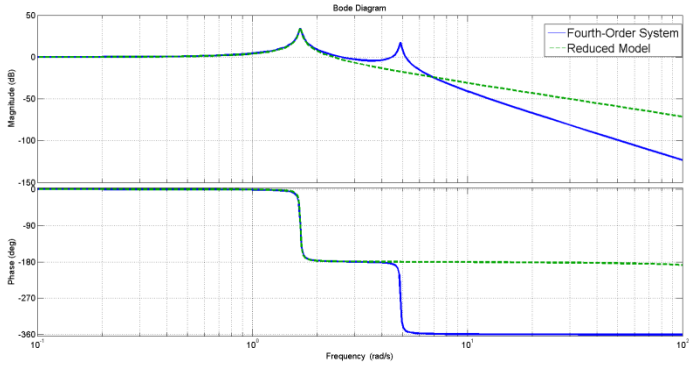

Fig. 6. Frequency response for the fourth-order system and the reduced model.

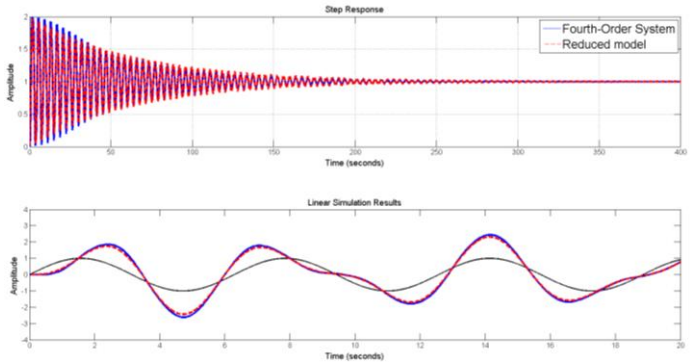

Fig. 7. Response between the fourth-order system and the reduced model using a step and sinusoidal input.

IV. Control Strategy

In order to design a controller and obtain the desired output voltage in the RLC circuits system, we focus on the reduced model given in (13), which allow designing an adequate control strategy, considering less number of dynamics.

A. *Design of a PI/PID Controller for the Reduced Model*

There exist several tuning rules for PID controllers that deal with underdamped second order systems and time delay [5]. However, the proposed PID must achieve favorable and similar results for the reduced model and the fourth-order system; therefore numerical simulations were carried out considering different tuning rules. As a result the PI/PID controllers [6-9]. which provide the best results in both systems have particular characteristics, which are illustrated in Tables 1-3. The comparisons between both systems using different PI/PIDs are shown in Fig. 8.

TABLE I. Tuning Rules for the PI

Rule	K_c	T_i
Panda et al [9]	$K_c = \frac{8\zeta_m^2 T_{m1} + 2\zeta_m \tau_m + T_{m1}}{2\lambda K_m}$ Kc=.0855;λ=3.5	$T_i = \frac{4\zeta_m^2 T_{m1} + \zeta_m \tau_m + .5T_{m1}}{2\zeta_m}$ $T_i = 16.6337$

TABLE II. Tuning Rules for the PID 1

Rule	K_c	T_i	T_d
Wang and Shao [6]	$K_c = \frac{2\zeta_m T_{m1}}{K_m \tau_m}\left(1.451 - \frac{1.508}{M_{max}}\right)$ $K_c = 2.098e-4$ $M_{max} = 1.0393$	$T_i = 2\zeta_m T_{m1}$ $= 0.0108$	$\frac{2\zeta_m}{T_{m1}}$ T_d =Td=33.244

TABLE III. Tuning Rules for the PID 2

Rule	K_c	T_i	T_d
Huang et al [7], Rivera and Jun [8]	$K_c = \frac{2\zeta_m T_{m1}}{K_m(\tau_m + \lambda)}$ K_c =7.179e-4 λ=15	$T_i = 2\zeta_m T_{m1} = 0.0108$	$\frac{2\zeta_m}{T_{m1}}$ $T_d = 33.244$

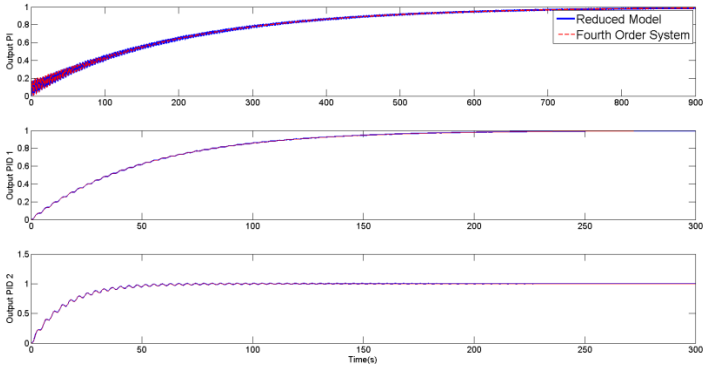

Fig. 8. Comparison between the fourth-order system and the reduced model using PI/PID controllers.

V. PI/PID Controller Application in the RLC Circuits System

The principal goal is to obtain the desired output voltage in the RLC circuits system, considering the similar behavior between both models; it is possible to implement the PI/PID controller in the fourth-order system, yielding an acceptable closed loop performance.

Fig. 9, shows the comparison between uncontrolled and controlled fourth-order system considering 5v as input voltage and using the tuning rules for the PID given in Table 2. In Fig. 10, the same input voltage is used but considering the tuning rules of the PI controller.

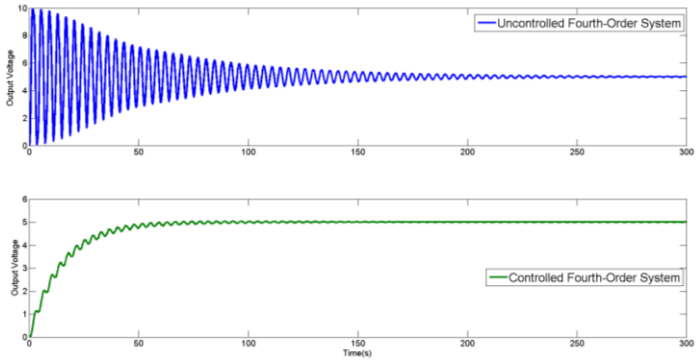

Fig. 9. Uncontrolled and Controlled fourth-order system using PID 2 controller

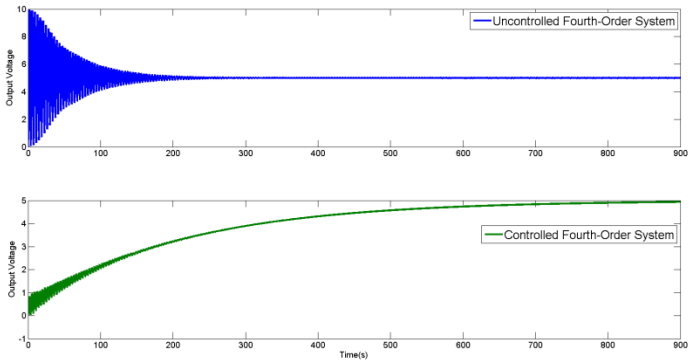

Fig. 10. Uncontrolled and Controlled fourth-order system using PI controller

VI. CONCLUSIONS

This paper presents a methodology for the reduction of high order systems that have oscillating dynamics. The methodology is based on a frequency domain analysis and yields a second order underdamped system with a time delay. The reduced model is obtained following some simple guidelines and allows designing controllers in a straightforward way. Numerical simulations were developed in order to compare the open loop response of the high-order (original) system and the obtained low-order delayed system. PI/PID controllers are computed, based on the model reduction and methodologies given in the literature, yielding an acceptable closed loop performance of the high-order oscillating system. The methodology is implemented on the model of a RLC circuits network, obtaining satisfactory response of the closed loop system.

REFERENCES

[1] Norman S Nise. Control Systems Engineering. John Wiley & Sons, 2007.

[2] Eronini Umez-Eronini, Juan Carlos Jolly, and Enrique Palos. Dinámica de sistemas y control. Thomson, 2001.

[3] Ogata Katsuhiko. Modern control engineering, 1990.

[4] Sigurd Skogestad. Simple analytic rules for model reduction and PID controller tuning. Journal of process control, 13(4):291-309, 2003.

[5] Aidan O'Dwyer. Handbook of PI and PID controller tuning rules, volume 57. World Scientic, 2009.

[6] Ya-Gang Wang and Hui-He Shao. PID auto-tuner based on sensitivity specification. Chemical Engineering Research and Design, 78(2):312-316, 2000.

[7] Hsiao-Ping Huang, I-Lung Chien, Yueh-Chung Lee, and Gow-Bin Wang. A simple method for tuning cascade control systems. Chemical Engineering Communications, 165(1):89-121, 1998.

[8] Daniel E Rivera and Kyoung S Jun. An integrated identification and control design methodology for multivariable process system applications. Control Systems, IEEE, 20(3):25-37, 2000.

[9] Panda, R.C., Yu, C.-C. and Huang, H.-P. (2004). PID tuning rules for SOPDT systems: review and some new results, ISA Transactions, 43, pp. 283-295.

Estudio y diseño de una granja solar fotovoltaica de 15 MWp en la comunidad indígena de Tzintzuntzan

D. Torres, M. Madrigal, M. Hernández, V. J. Gutiérrez, J. N. Ponciano, R. C. Reyes
Tecnológico Nacional de México, Instituto Tecnológico de Morelia

Morelia Michoacán, México
domingotorres@hotmail.com

***Resumen*— El presente trabajo consiste en el estudio y diseño de una Granja Solar Fotovoltaica de 15 MWp con una producción anual de 21,435 MWh, en la comunidad indígena de Tzintzuntzan Michoacán, con la finalidad de satisfacer las necesidades de consumo de energía del propio municipio (4.2%) y venta a municipios vecinos (95.8%). La energía será destinada a Alumbrado Público, Bombeo de Agua Potable y Edificios Públicos. El proyecto cuenta con una fase Piloto de 500 kWp con una producción anual de 714.5 MWh que satisface el 72% del consumo de energía eléctrica del municipio de Tzintzuntzan. En el artículo se abordan no solamente la parte técnica del proyecto, sino la parte social e integración de la comunidad en el proyecto.**

Palabras Claves*—Sistemas solares fotovoltaicos, sistemas interconectados a la red, energías renovables, comunidades indígenas, reforma energética.

I. Introducción

Las energías renovables han tenido un gran desarrollo a nivel mundial en los últimos años, debido a la necesidad dejar de consumir energías provenientes de combustibles fósiles, las cuales son un factor muy importante en el cambio climático y el efecto invernadero. Las tecnologías en la energía eólica y solar fotovoltaica son las que van a la vanguardia en capacidad instalada y maduración. Debido a la alta irradiación que prevalece en el territorio mexicano y a los grandes terrenos ociosos con los que cuenta el país, la energía solar fotovoltaica se ve como la energía renovable más versátil y viable para desarrollarse en México.

La reforma energética del 2013 en México libera el mercado del sector energético, permitiendo al sector privado poder competir con las empresas de Estado, como son la Comisión Federal de Electricidad (CFE) y Petróleos Mexicanos (Pemex) en los sectores de electricidad e hidrocarburos, respectivamente. Debido a la apertura de este mercado, las grandes empresas extranjeras y nacionales han volteado hacia la inversión en este nuevo sector en México, en plantas del orden de las decenas y centenas de MW. Para ello la necesidad de grandes dimensiones de terreno es inminente. La mayoría de los parques eólicos y granjas fotovoltaicas en México adquieren terrenos bajo un arrendamiento, de por lo menos 20 años, con los propietarios, las comunidades ejidales o indígenas; el precio de la renta de la tierra en México está muy por debajo de precios internacionales [1] por lo que no llega a reflejarse en el beneficio de las comunidades involucradas. Sin embargo se pueden aprovechar estas mismas fuentes renovables de energía en beneficio de la propia comunidad, no con la renta de las tierras, sino como dueños o inversionistas de las plantas de generación [2,3].

En este artículo se muestran los avances que se tienen en el estudio y desarrollo de una granja solar fotovoltaica de 15 MWp en la comunidad indígena de Tzintzuntzan Michoacán, en donde la comunidad es la principal interesada y promotora del proyecto para beneficio propio.

II. La Comunidad de Tzintzuntzan

La comunidad de Tzintzuntzan se localiza en la rivera del Lago de Pátzcuaro a 50 km de la ciudad de Morelia. Es una comunidad indígena con mucha historia, tradición y cultura.

A. Historia de Tzintzuntzan

Es importante conocer la historia de Tzintzuntzan para entender la importancia de este municipio dentro de la cultura de Michoacán y de México. Esta población fue fundada por el Señor de Michhuacan o Mechoacan llamado Tariácuri, alrededor del año 1325 en la rivera del lago de Pátzcuaro. Tzintzuntzan fue sede del poderoso Señorío P'urhépecha (como le llaman actualmente) desde la mitad del siglo XV hasta su caída ante los conquistadores españoles., y resistió diversos intentos de conquista por parte de los Aztecas. Se calcula que en su época de mayor apogeo, Tzintzuntzan albergó una población de 40 mil habitantes. Después de la conquista, Tzintzuntzan fue el lugar de residencia del alcalde mayor, el obispo, el cabildo español y el gobernador indígena. Los franciscanos establecieron aquí su primer convento. En 1534 Tzintzuntzan recibió el título de "ciudad de Michoacán", con lo que se reconocía su carácter de capital de la provincia. Sin embargo, en 1538, se trasladó la sede episcopal a Pátzcuaro así como el título de ciudad, quedando reducido Tzintzuntzan a la condición de pueblo. A raíz de peticiones de nobles indígenas, la Corona española otorgó a Tzintzuntzan el título de ciudad en 1593, con su propio gobernador y cabildo indígena, dependiente del alcalde mayor de Michoacán. Tzintzuntzan

perdió poco a poco su antiguo esplendor, su importancia política, económica y demográfica. En 1786, Tzintzuntzan pasó a ser parte de la intendencia de Michoacán, con capital en Valladolid (hoy Morelia). En reconocimiento a su antigua historia, se le otorgó en 1861 el título de Ciudad Primitiva, pero no fue sino en 1931 cuando se constituyó en municipio. A partir de una serie de restauraciones de sus monumentos históricos, en el año de 2012 Tzintzuntzan recibe el título de Pueblo Mágico, exhibiendo actualmente su legado histórico con las Yácatas, zona arqueológica ceremonial de adoración de los dioses del pueblo P'urhépecha, así como el Convento Franciscano de Santa Ana, que data del siglo XVI; la Iglesia de San Francisco de Asís, de estilo plateresco, concluida en 1601, Iglesia de la Soledad, construcción barroca del siglo XVII, vestigios del Hospital de Indios, entre otros monumentos históricos. Como se puede comprender, Tzintzuntzan tiene una riqueza histórica de casi 700 años, por lo que promover y preservar la cultura de esta comunidad tiene un valor incalculable.

B. Condición actual de Tzintzuntzan

Actualmente el municipio de Tzintzuntzan cuenta con una población aproximada de 13,600 habitantes con un promedio de edad de 24 años, cuyas actividades económicas principales comprenden [4]:

a) Sector primario: Agricultura, ganadería, silvicultura y pesca.
b) Sector secundario: Manufacturas. Principalmente en la elaboración de artesanías utilizando materiales como la cantera, madera, chúspata, cobre y barro.
c) Sector terciario: Comercio.

Del total de la población se ha reportado que tan sólo 2621 personas realizan las actividades económicas mencionadas, resultando en un elevado índice de desempleo o involucradas dentro del sector informal o migración hacia los Estados Unidos. El municipio de Tzintzuntzan se comprende de 22 poblaciones que son principalmente la cabecera municipal de Tzintzuntzan y las tres poblaciones más pobladas: Ihuatzio cuya principal actividad económica es la pesca y la venta de artesanías, se localiza a 7 km de la cabecera municipal, cuenta con aproximadamente 4000 habitantes. Cucuchuchu con principal actividad económica la agricultura, la pesca y la venta de artesanías, se localiza a 8 km de la cabecera municipal, cuenta con aproximadamente 2100 habitantes. Y Los Corrales con principal actividad económica la agricultura, se localiza a 6 km de la cabecera municipal, cuenta con aproximadamente 600 habitantes.

III. Recursos para el Proyecto Solar Fotovoltaico

Las partes principales o recursos requeridos en el proyecto de una granja solar fotovoltaica son cuatro: Producción energética solar de la zona, los terrenos, los clientes y los recursos financieros.

A. Producción energética solar de la zona

Los datos de localización y producción energética solar del lugar son los siguientes:

Lugar geográfico: Tzintzuntzan Mich., México.
Temperatura: max 24ºC, min 8ºC.
Localización: Latitud 19.605855º, Longitud -101.58682º, Altitud 2,192 m.
Paneles: Fijos, sin seguidores solares.
Producción: Producción especifica 1,429 kWh/kWp/año.

Se puede considerar muy aceptable la producción de energía si se considera que el máximo que se podría obtener en una de las mejores zonas del país sería del orden de 1,800 kWh/kWp/año.

B. Los Terrenos

El municipio de Tzintzuntzan tiene una superficie de 167 km^2 de los cuales aproximadamente 50 km^2 son de uso no agrícola y de tipo comunal [4]. El Comisariado de los Bienes Comunales del Municipio de Tzintzuntzan Michoacán año tras año define la forma de utilización o explotación de sus bienes comunales. En este sentido el Comisariado tiene designadas algunas áreas para la explotación de material de construcción, rellenos sanitarios, cultivo de nopal (en proyecto), y 50 Ha para uso exclusivo de fuentes renovables de energía (en proyecto). Por lo anterior, el terreno en esta comunidad no sería un problema.

C. Los Clientes

Los principales municipios de la región son Pátzcuaro, Quiroga y Tzintzuntzan con un consumo total de 70,000 MWh/año, de los cuales aproximadamente el 16% (11,200 MWh/año) corresponde a los servicios propios de los municipios como alumbrado público, bombeo de agua potable y edificios públicos. La comunidad de Tzintzuntzan consume 6,100 MWh/año de los cuales 990 MWh/año corresponden al consumo de los servicios propios del municipio. Estos tres municipios son los principales clientes potenciales los cuales requerirían el 52% de la producción anual de energía de la granja de 15 MWp. Por otro lado, el proyecto Piloto de 500 kWp cubriría el 72% del consumo anual del municipio de Tzintzuntzan. De ahí que se pretende iniciar con 500 kWp a ser escalado a los 15 MWp.

D. Los recursos financieros

Los costos de los proyectos se indican a continuación.

Proyecto de 15 MWp: Producción anual de 21,435 MWh, se requieren 37.5 Ha de terreno, y el costo del proyecto es de $22.5 millones de dólares. La inversión del proyecto a 10 años y una tasa de interés del 10% da como resultado un Valor Actual Neto (NPV) de $1.03 millones de dólares y una Tasa Interna de Retorno (IRR) del 11.18%, considerando la venta de energía (10% más barata que con la CFE) a $2,700/MWh (pesos mexicanos por MWh).

Proyecto piloto de 500 kWp: Producción anual de 714.5 MWh, requiere 1.25 Ha requeridas de terreno, y el costo del proyecto es de $12 millones de pesos. Los recursos para este proyecto Piloto los espera conseguir el Comisariado de los Bienes Comunales del Municipio de Tzintzuntzan Michoacán, de fondos del gobierno federal. Considerando la venta de energía (10% más barata que la CFE) a $2,700/MWh, se tendrían ventas anuales de $1,929,150 pesos a ser administrados por el Comisariado de los Bienes Comunales del Municipio y destinados a obras y proyectos en beneficio de la comunidad con el objetivo de preservar su cultura, y mejorar las condiciones de salud y educación de su población. Es importante mencionar que la presidencia municipal de Tzintzuntzan tendría ahorros anuales de $214,350 pesos por comprar electricidad a su propia comunidad 10% más barata.

De estas dos opciones el presidente del Comisariado de Bienes Comunales ve más viable el proyecto Piloto por la razón de ser dueños únicos del mismo, que de tener éxito podrían conseguir en corto plazo recursos para llegar al MWp el cual cubriría el 100% de las necesidades del municipio de Tzintzuntzan.

IV. Características de la Granja Piloto de 500 kWp

Para el sistema piloto de 500 kWp se tienen las siguientes características generales del sistema:

Módulo FV:
- Si-poly, Modelo S60PC-250
- Fabricante SOLARTEDI.

N° de módulos FV:
- En serie 13 módulos
- En paralelo 154 cadenas

No. total de módulos FV:
- No. módulos 2002
- Pnom unitaria 250 Wp

Potencia global generador:
- Nominal (STC) 501 kWp
- En cond. funciona. 444 kWp (50°C)

Caract. funcionamiento del generador (50°C):
- Vmpp 368 V
- Impp 1206 A

Inversor:
- Modelo PVI-Central-100-US-480
- Fabricante Power-One

Características:
- Tensión Funciona. 330-600 V,
- Pnom unitaria 100 kW AC

Banco de inversores:
- No. de inversores 5 unidades
- Potencia total 500 kW AC

Energía total producida:
- 714,988 kWh/año
- Producción específica de 1,429 kWh/kWp/año
- Factor de rendimiento (PR) 74.2%

Costo del SPV:	$11,106,610 pesos
Sistema de Potencia:	
Línea de transmisión:	
1.5 km, 13.8 kV,	$241,500 pesos
Subestación tipo pedestal:	
500 kVA,	$362,000 pesos
Adecuación del terreno:	$100,000 pesos
Malla ciclónica:	$150,000 pesos
Gran total:	$11,960,110 pesos

Los trabajos de adecuación del terreno los realizará la misma comunidad así como la puesta de malla ciclónica, todo ello con trabajo voluntario Se daría prioridad a las empresas michoacanas para construir la granja fotovoltaica.

Las figuras 1 a 3 muestran la localización del terreno destinado a la granja solar fotovoltaica.

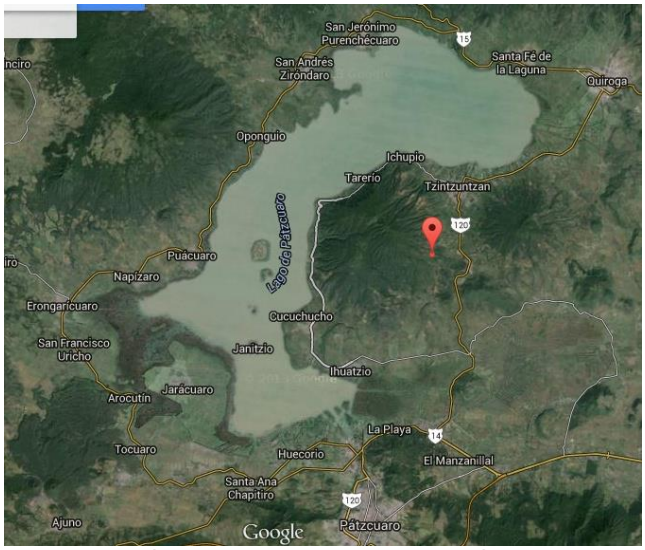

Fig. 1. Localización del terreno en la rivera del lago de Pátzcuaro.

Fig. 2. Localización del terreno

Fig. 3. Vista del terreno seleccionado

V. Análisis de Riesgos y Beneficio Social

El terreno seleccionado no es de uso agrícola, ni presenta algún riesgo ambiental visible. El Comisariado de bienes comunales, conocedor del lugar, considera que dichos terrenos no presentan ningún riesgo ambiental por las características de la fauna, flora y características del terreno.

A. Riesgos ambientales

La vegetación del terreno seleccionado se compone de pasto, pequeños arbustos y algunos encinos jóvenes. El lugar no tiene endemismos ni especies protegidas, ni es apto para la agricultura.

La fauna del lugar se compone principalmente de aves, conejos y reptiles. Los cuales no serán afectados debido a la pequeña área de terreno a ser ocupada. El lugar no tiene especies de interés natural.

B. Riesgos arqueológicos

La región de la rivera de Pátzcuaro cuenta con dos zonas arqueológicas importantes, una en Tzintzuntzan y la otra en Ihuatzio, la zona arqueológica más cercana al terreno, Las Yácatas de Tzintzuntzan, se encuentra a 3 km al noreste.

Fig. 4. Vista de Las Yácatas de Tzintzuntzan

C. Beneficio social

El nivel educativo del municipio es bajo, ya que la cantidad de egresados de bachillerato representa tan sólo el 4.9% respecto a la cantidad de alumnos egresados de primaria. Con el proyecto a desarrollar se podrán financiar programas de becas, regularización y promoción que permitan al municipio elevar el número de estudiantes egresados. Además, se podrán implementar fideicomisos para que los egresados de bachillerato estudien carreras profesionales en áreas que beneficien a la comunidad, tales como la forestal, apicultura y el área de la salud.

En la localidad en últimas fechas se ha reportado un aumento de plagas que han dañado la flora y reducido drásticamente la producción de miel. Por otra parte existe aproximadamente tan sólo un médico por cada mil habitantes, cuatro unidades médicas que no cuentan con quirófano, por lo que resulta obvio que la salud representa una importante área de oportunidad donde se pueden emplear los recursos económicos provenientes de la venta de la energía eléctrica de la granja solar a desarrollar. La comunidad podrá invertir en la construcción de unidades médicas adecuadas, dispensarios médicos y contratación de personal médico originario de la comunidad misma. Además, se contarán con recursos para la implementación de programas de salud preventiva y hábitos saludables.

D. Evaluación del impacto ambiental

Como se muestra en la Figura 5, los sectores con mayor contribución de emisiones de CO2 en el 2010, en el país, son: transporte, representando un 31.1%; generación eléctrica, con un 23.3%; manufactura y construcción, con 11.4%; consumo propio de la industria energética, con 9.6%; conversión de bosques y pastizales, con 9.2%, y otros (residencial, comercial y agropecuario), con 6.7% [5].

Lo anterior muestra que la generación de energía eléctrica ocupa el segundo lugar en emisiones de gases contaminantes, y la reducción de los mismos juega un papel crucial para el desarrollo de la industria eléctrica.

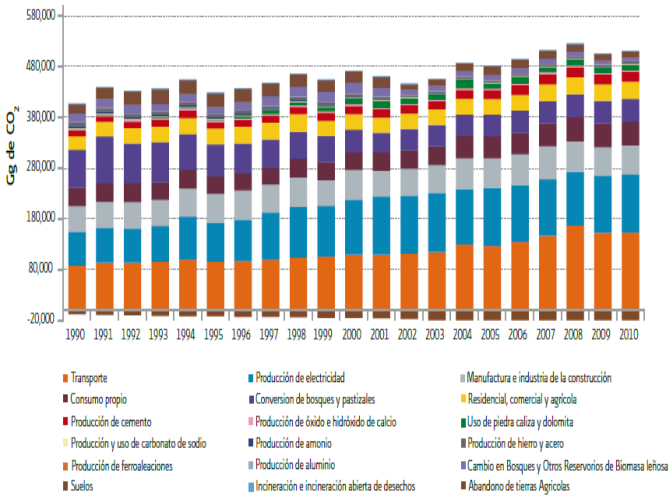

Fig. 5. Emisiones por sector en Giga-grámos (Gg) de CO2, 1990-2010.

Para realizar una estimación simplificada de la reducción en la emisión de gases contaminantes provenientes de la generación de energía eléctrica resultante del desarrollo del proyecto, se considera la emisión de gases contaminantes de las 82 principales plantas del país, mostrada en la Tabla I [6].

TABLA I. Emisión de gases contaminantes de las 82 plantas principales del país.

Contaminantes	**Total de emisiones anuales (millones de tons.)**	**Producción total de electricidad (millones de GWh)**	**Tasa de emisión colectiva (Kg/MWh)**
SO2	1.6	0.137	11.35
NOx	0.25	0.137	1.83
CO2	94	0.137	688

Como resultado de interpolar los datos anteriormente mostrados, se puede observar en la Tabla II que se presentará una reducción muy importante en la emisión de dióxido de carbono a la atmósfera con la instalación de la granja solar. Para el caso de la planta de 15 MW se alcanzará una reducción de más de 10 toneladas de CO2 emitidas a la atmósfera. Lo anterior permitirá la comercialización de los certificados de energías limpias que otorgue la Comisión Reguladora de Energía, representando un beneficio económico adicional del desarrollo del proyecto.

TABLA II. Reducción en la emisión de gases contaminantes.

Granja solar	**SO_2 (Kg)**	**NO_x (Kg)**	**CO_2 (Kg)**
Piloto	5.675	0.915	344
15 MW	170.25	27.45	10320

VI. Conclusiones

En el presente trabajo podemos apreciar que el proyecto cumple con cuatro puntos principales para su desarrollo; buena producción energética solar de la zona, disponibilidad de terrenos, clientes potenciales y la habilidad de la comunidad para conseguir recursos financieros para proyectos comunitarios, lo cual presenta un panorama muy favorable para, de inicio, desarrollar la planta piloto. En lo referente al impacto ambiental se muestra que las tierras son adecuadas para este proyecto ya que no son aptas para la agricultura y no se tienen especies endémicas o protegidas en el área considerada. Por otro lado, las dos zonas arqueológicas importantes de la región se encuentran a varios kilómetros de distancia, no existiendo vestigios arqueológicos en el terreno considerado.

Uno de los problemas grandes para entrar a las comunidades indígenas es la falta de conocimiento de su historia, cultura, tradiciones, conflictos, intereses y arraigo a su tierra, cuando todo ello se respeta, se pueden realizar grandes proyectos en conjunto en beneficio de sus comunidades. En la fecha de la escritura del presente documento, el proyecto está en la fase de solicitud de permisos ante la CFE y la CRE, y la de gestión de recursos por parte del Comisariado de los Bienes Comunales de Tzintzuntzan.

Agradecimientos

Al presidente del Comisariado de Bienes Comunales de Tzintzuntzan, al Presidente municipal de Tzintzuntzan y al Director del Instituto Tecnológico de Morelia por todo el apoyo e interés recibido en el proyecto. Así como a Intrust Global Investments y Harvard School of Public Health, a través del Diplomado en Liderazgo Aplicado a Energías Renovables y Eficiencia Energética, por la motivación a desarrollar proyectos de energía renovables en beneficio de las comunidades indígenas.

Referencias

[1] Comsión para el Diálogo con los Pueblos Indígenas de México, *La Energía Eólico en México: Una perspectiva social sobre el valor de la tierra*, Secretaia de Gobernación, 2012.

[2] Monique Barbut, *La Inversión en Proyectos de Energía Renovable: La Experiencia del FMAM*, fmam Fondo para el Medio Ambiente Mundial, 2009.

[3] S.V. Brown, D.G. Nderitu, P.V. Preckel, D.J. Gotham, B.W. Allen, *Renewable Power Opportunities for Rural Communities*, United States Department of Agriculture USDA, 2011.

[4] Instituto Nacional de Estadística y Geografía INEGI, http:www.inegi.org.mx.

[5] *México. Quinta comunicación nacional ante la convención marco de las Naciones Unidas sobre el cambio climático, Secretaría de Medio Ambiente y Recursos Naturales (SEMARNAT)*, Instituto Nacional de Ecología y Cambio Climático (INECC), 2012.

[6] P. J. Miller, C. V. Atten, *Emisiones atmosféricas de las centrales eléctricas en América del Norte*, Comisión para la cooperación ambiental de América del Norte, 2004, ISBN: 2-923358-12-0.

Process design for obtainig ethylene trough the oxidative dehydrogenation of ethene (ODH-C_2) over the multimetal oxide (Mo-Te-V-Nb-O)

J.C.Castillo Rodríguez, C. Tzompantzi Flores, R.S. Ruiz Martínez, C.O. Castillo Araiza
Grupo de Procesos de Transporte y Reacción en Sistemas Multifásicos, Depto. de IPH
Universidad Autónoma Metropolitana – Iztapalapa
Av. San Rafael Atlixco No. 186, México D.F. C.P. 09340.
coca@xanum.uam.mx

Abstract

Ethylene is one of the most valuable products in the chemical industry. It is used as raw material for the generation of various products with higher market value such as: polymers, resins, fibers, among others. This work was aimed to propose a process to produce ethylene out of ethane through oxidative dehydrogenation, an alternative that has significant advantages over the conventional methods of pyrolysis and catalytic cracking. The main advantages of the oxidative dehydrogenation process are: (i) promising conversion and selectivity are obtained, 60% and 90%, respectively; (ii) the reaction is carried out below 500 ° C; (iii) the reaction is highly exothermic; (iv) coke formation is avoided. All these advantages lead to large energy savings compared to the conventional pyrolysis of ethane. The design of the process accounteds for the following points: (i) determination of the limits of flammability; (ii) the development of the kinetic model following the Eley Rideal formalism; (iii) the development of the industrial reactor model and; (iv) the design of the reactor and the peripheral equipment. Thus an industrial process able to produce 60000 tons /year was proposed.

Keywords— ethylene obtaining, fluidized bed reactor, oxidative dehydrogenation of ethane.

I. INTRODUCTION

In last years the importance of ethylene has increased because this olefin is required for carry out several industrial processes, the statistics shows that 30% of commercial products worldwide are ethylene derivatives. Therefore has been estimated that the global demand will grow by 4.7% per year during this decade, going from a production of 130 million tons in 2010 until 160 million tons in 2020. In the national case, Mexico produced 1062 to 1128 thousands for the period 2008-2012, therein 60 thousand tons were destined to the international market.

Iindustrially, the principal technologies used to get ethylene are thermal pyrolysis and catalytic cracking. However, these conventional processes present some limitations, such as: (i) low selectivities and conversions, (ii) they are highly endothermic processes and (iii) there is a formation of byproducts including coke, causing the shut- down for cleaning the process equipment and catalyst regeneration. An alternative to these technologies is the oxidative dehydrogenation of ethane (ODH-C2) over the Mo-V-Te-Nb-O catalyst. Compared to the conventional processes, advantages in the ODH-C2 are : (i) conversions and selectivities industrially acceptable (80% and 90%, respectively); (ii) the number of byproducts due to the reaction is limited; (iii) the reaction is carried out below 500 ° C; (iv) the reaction is exothermic; (v) coke formation is avoided; (vi) a substantial energy saving is achieved.

This work was aimed to design a process for the ODH-C2 over the Mo-V-Te-Nb-O catalys. To acchieve this goal, several steps were followed: (1) the inflammability limits were determined using reported correlations; (2) the inflammability limits results were used to design experiments at laboratory scale with the aim of developing a kinetic model based on Eley Rideal formalism; (3) the kinetic was used to design the industrial fluidized catalytic bed reactor model; (4) finally the peripheral equipment design was developed.

II. METHODOLOGY

A. Development of thermodynamic study

In this stage it was verified that there was no limitations in the reactions of the ODH-C2. Therefore some thermodynamic calculations were carried out to calculate the reaction enthalpy, free energy and entropy reaction. The reactions involved in the ODH-C2 are shown in Table 1. Thermodynamic parameters were obtained at temperatures ranging from 300-500 ° C.

Table 1. DHO-C_2 reactions

	Reaction
R1	$C_2H_{6(g)} + {}^1/_2\, O_{2(g)} \rightarrow C_2H_{4(g)} + H_2O_{(g)}$
R2	$C_2H_{6(g)} + {}^7/_2\, O_{2(g)} \rightarrow 2CO_{2\,(g)} + 3H_2O_{\,(g)}$
R3	$C_2H_{6(g)} + {}^5/_2\, O_{2(g)} \rightarrow 2CO_{(g)} + 3H_2O_{\,(g)}$
R4	$C_2H_{4(g)} + 3O_{2(g)} \rightarrow 2CO_{2(g)} + 2H_2O_{(g)}$
R5	$C_2H_{4(g)} + 2O_{2(g)} \rightarrow 2CO_{(g)} + 2H_2O_{(g)}$

B. *Analysys of the explosion limits*

The main objective was minimizing the risk of fire or explosion during the production of ethylene by the ODH-C2. The analysis of the mixtures was made by using correlations that capture the effects of temperature, pressure and concentration of inert gas on explosion limits. Finally ternary diagrams destined to evaluate the explosive mixtures were built. The ternary diagrams presented an error margin of 10%.

C. *Construction of kinetic model*

Eley-Rideal formalism was followed. The parameters related to the reaction rate equations were estimated. The obtained parameters are: enthalpies and entropies of adsorption, reaction orders, activation energy and pre-exponential factors. These kinetic values were estimated by minimizing a weighted objective function and using the form of the reparametrized Van't Hoff and Arrhenius equations.

D. *Design of fluidized bed reactor*

The proposed reactor model assumed that: the reactor operate in steady-state; the system is operated as non-isothermal and non-adiabatic; the phenomena related to the catalyst deactivation are not significant; inter and intra-particle mass transfer resistances are neglected due to the small particle diameter of the catalyst, approximately 150 microns; due to the small bubble diameter, the inter and intra-bubble mass transport resistances are neglected as well; the catalytic behavior of multi-metallic catalyst is described by the kinetic model, developed at laboratory level; and mass and heat transport parameters are considered as effective ones. Finally, the reactor design was selected from modeling trough a study that evaluated the reactor performance)conversion and selectivity) when some operational parameters were varied, i.e., the particle diameter, minimum fluidization velocity, reaction temperature and inlet concentration.

E. *Process flow diagram.*

In this stage it wasproposed the process design. Once it was designed the heart of the process (the reactor), were made the mass and energy balances for every peripheric equipment. The balances leaded to determine the kind and the number of equipment required for the purification of ethylene. The needed equipments were absorption and desorption towers, heat exchangers and pumps, vide Fig. 5.

III. DISCUSSION AND RESULTS

A. *Thermodynamic study*

Table 2 shows the Keq values that were obtained from thermodynamic basis. Thermodynamic limitations in the studied reactions were not observed. Keq values varied from 109 to 10306 and increased when the temperature increased, impliying that reactions are favored.

TABLE 2. K_{EQ} VALUES TO 300, 400 AND 500 °C

	R1	R2	R3	R4	R5
K_{eq} a 300°C	1.44E+217	9.66E+181	6.04E+240	6.47E+133	3.86E+17
K_{eq} a 400°C	1.16E+252	1.27E+226	1.51E+270	2.14E+166	9.57E+12
K_{eq} a 500°C	4.40E+300	1.34E+281	4.32E+306	7.69E+207	5.75E+09

B. *Analysis of explosive limits.*

Figures 1 and 2 show the results obtained. The shaded area represents the danger zone. From this end, any mixture within this region leads to an explosion. The segment parallel to the inert gas axis is formed by several low limits, while the diagonal segment located from the oxygen axis to the inert gas axis represents the upper limits. Input and output mixtures are represented by symbols (▲ □) and (•) respectively. The segment from the top of the triangle to the fraction (0.20, 0.80) oxygen-inert is named "air line" and indicates the upper explosive limit when air is used as oxidant rather than oxygen.

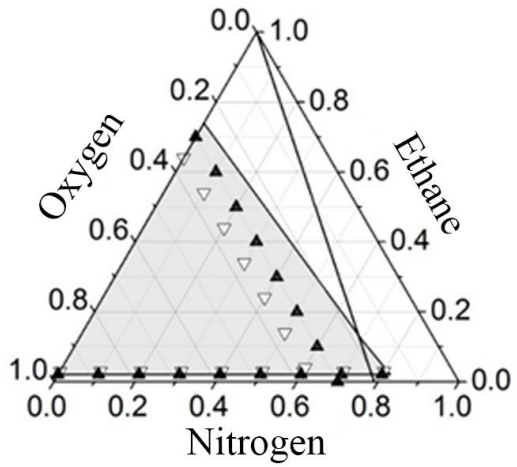

Figure 1. Ternary diagram at 440 ° C and 0.77 atm. Includes flammability limits for mixtures at 25 ° C (▽) and 300 ° C (▲).

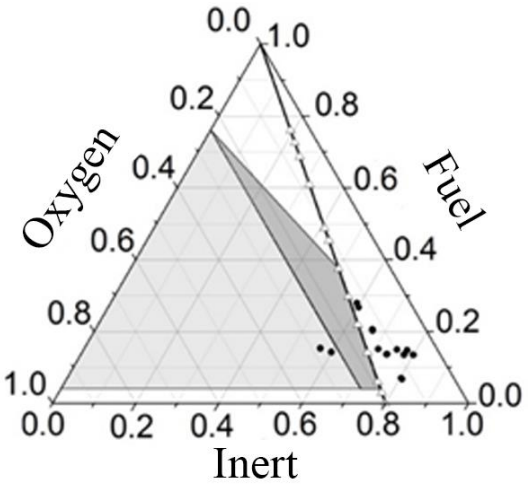

Figure 2. Ternary diagram of the reactor effluent at 440 ° C and 0.77 atm.

C. Eley Rideal kinetic Model

Table 3 shows the reaction mechanism that was proposed for the Eley Rideal formalism. It was assumed that: (i) only one reactive (molecular oxygen) and product (water and carbon dioxide) was adsorbed in the same kind of catalytic site; (ii) the ethane without being adsorbed approaches to the surface and reacts with the adsorbed molecular oxygen; and (3) the oxygen was not adsorbed dissociatively, it means the molecular oxygen was adsorbed only in a catalytic site.

TABLA 3. STEPS REACTION AND CATALYTIC CYCLES CONSIDERED TO THE ELEY-RIDEAL MODEL FOR TO THE ODH-C_2.

Paso	Etapa de reacción
A	$O_2 + 2S \longrightarrow 2O\text{-}S$
1	$C_2H_6 + O\text{-}S \longrightarrow C_2H_4 + H_2O\text{-}S$
2	$C_2H_6 + 7O\text{-}S \longrightarrow 2CO_2 + 3H_2O\text{-}S + 4S$
3	$C_2H_6 + 5O\text{-}S \longrightarrow 2CO + 3H_2O\text{-}S + 2S$
4	$C_2H_4 + 6O\text{-}S \longrightarrow 2CO_2 + 2H_2O\text{-}S + 4S$
5	$C_2H_4 + 4O\text{-}S \longrightarrow 2CO + 2H_2O\text{-}S + 2S$
B	$H_2O\text{-}S \longrightarrow H_2O + S$

D. Simulation-design of the fluidized bed reactor.

Figures 3 and 4 show the reactor performance in terms of the temperature and concentration profiles. The reactor was designed to operate at 11 times the minimum fluidization (9.44m / s) and a reaction temperature of 434.25. In Figure 4 the consumption of reagents (Ethane and oxygen) and the product formation are observed. Fig. 3 displays the temperature profile expected for a fluidized bed reactor. The Table 4 represents the necessary quantities of each reagent to achieve the production target.

Table 4. industral fluidized bed reactor results

Reactors number:			**4**	
Reactor feed	**Flow**		**Flow by carbon atom**	**Mol fraction**
Component	**kgmol/h**	**ton/h**	**ton/h**	
Oxygen	300.00	9.60	0.00	0.20
Ethane	134.00	4.02	3.22	0.09
Nitrogen	1054.89	29.54		0.71
Total	1488.89	43.16		1.00

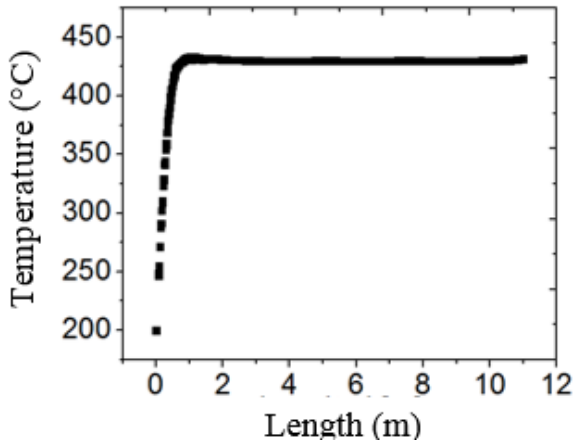

Fig.3. Temperature profile to a particle diameter of 150 µm and 11 times the minimum fluidization velocity

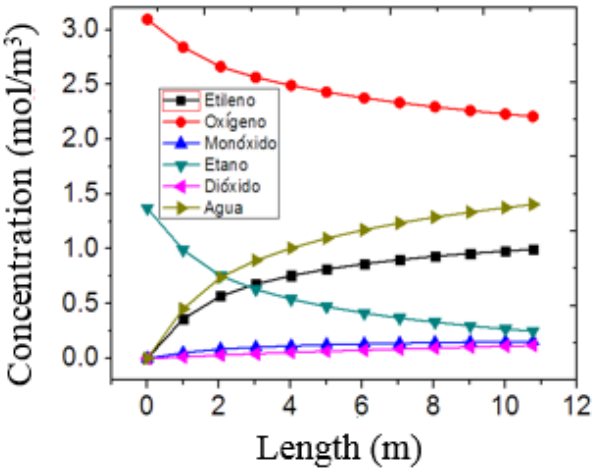

Fig.4. Concentration profiles to a particle diameter of 150 µm and 11 times the minimum fluidization velocity

In general, modeling yielded the following information: four reactors are need in the process, and 25.81 tons of catalyst are necessary to achieve a total production of ethylene 384.84 kgmol / h (production target is 384.7 kgmol / h); for conversions and selectivity of industrial interest (82 and 87% respectively) reactors should be operated at a maximum reaction temperature of 434 ° C.

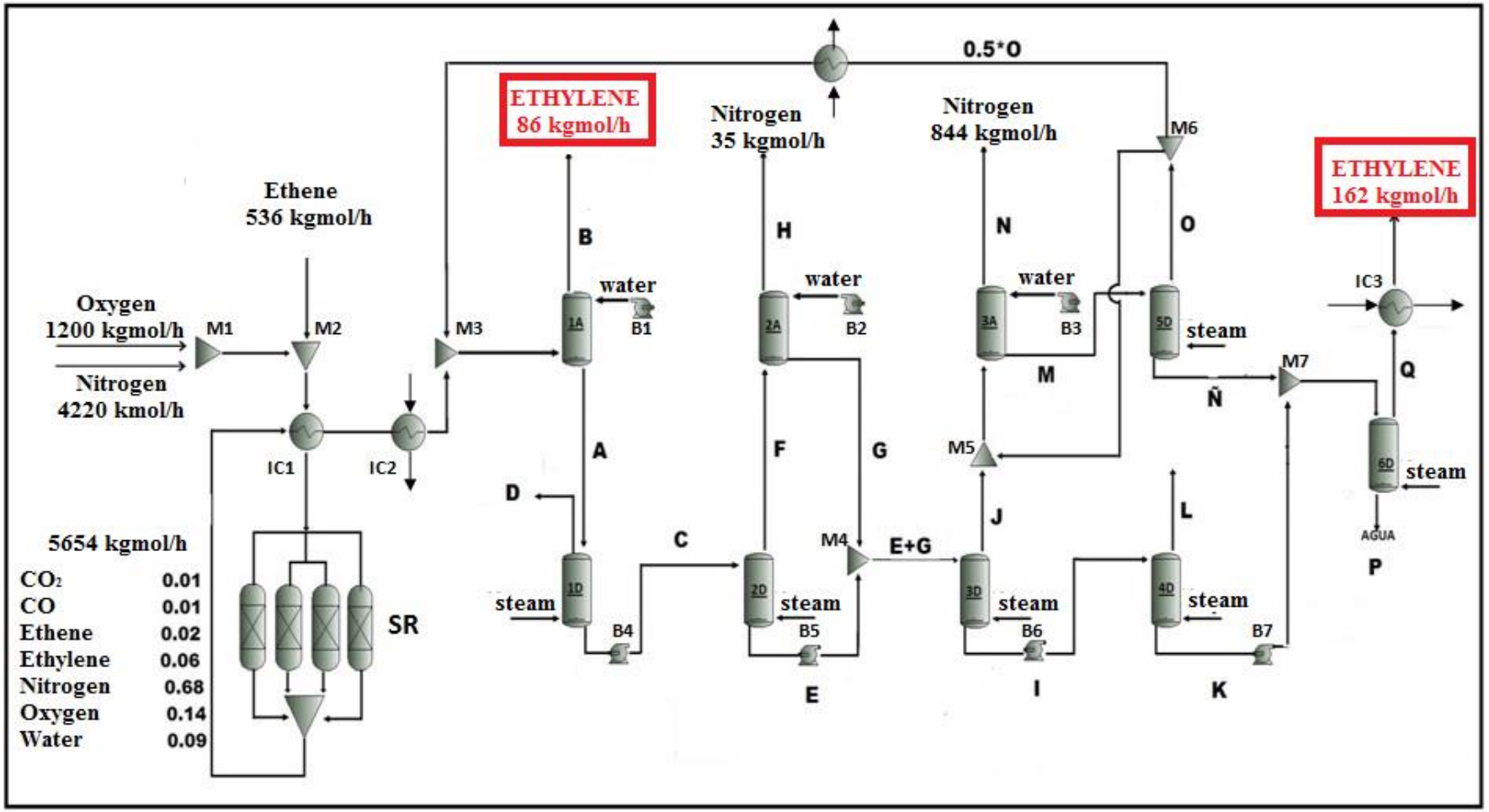

Figure 5. Process flow diagram to ethylene; Reaction system (SR); Mixers towers (1A, 2A, 3A); Strippers (1D,2D,3D,4D,5D,6D); Pump (M1,M2,M3,M4,M5,M6,M7); Heat exchangers (IC1,IC2,IC3); Absorption (B1,B2,B3,B4,B5,B6,B7)

IV. CONCLUSIONS

It is possible to design a process for the DHO-C2. The results obtained in this study indicate that the use and implementation of a fluidized bed reactor for the process of DHO-C2 is promising considering that this new technology reduce separation and energy costs.

ACKNOWLEDGMENTS

Thanks to the Consejo Nacional de Ciencia y Tecnologia (CONACyT) for the accorded financial support (Project No. 181 104).

REFERENCES

[1] Ardissone, D.E., Borio, D.O., Heracleous, E., Lemonidou, A.A., López, E., Pedernera, M.N., y Rodríguez, E. (2010). Oxidative dehydrogenation of ethane to ethylene in a membrane reactor; Atheorical study. Catalysis Today, 157, 303-309.

[2] Levenspiel O. (1986). Ingeniería de las reacciones químicas. New York: Reverté.

[3] Zhao, F. (2008). Experimental measurements and modeling prediction of flammability limits of binary hydrocarbon mixture. Tesis de maestría no publicada, Universidad de Texas A&M, Texas, Estados Unidos de América.

[4] Crowl, D., y Louvar, J. (2002). Chemical Process Safety. Massachusetts: Prentice Hall.

[5] Galicia, G., Quintana-Solórzano, R., Ruiz-Martínez, R.S., Valente, J.S. y Castillo Araiza, C.O. (2014). Kinetic Modeling of the Oxidative Dehydrogenation of Ethane to Ethylene over the MoVTeNbO catalytic system. Chemical Engineering Journal, 252, 75-88.

[6] Armendáriz, H., Barragán, G., López, G., Quintana, R., y Valente, J.S. (2014). Kinetic Study of Oxidative Dehydrogenation of Ethane over MoVTeNb Mixed-Oxide Catalyst. Industrial and Engineering Chemistry Research, 53, 1775-1786.

[7] Ardissone, D.E., Borio, D.O., Lopez, E., Pedernera, M.N., y Rodríguez, M.L. (2011). Reactor Designs for Ethylene Production via Ethane Oxidative Dehydrogenation: Comparison of Performance. Industrial Engineering Chemistry Research, 50, 2690 – 2697.

CFD Study of power draw of a disc plane impeller in an unbaffled stirred tank

G. Martínez de Jesús, J.A. Colín Luna, A. Alonso, M. González Brambila and J. Ramírez Muñoz
Departamento de Energía
Universidad Autónoma Metropolitana-Azcapotzalco
Ciudad de México, México
jrm@correo.azc.uam.mx

D. García Cortés
Departamento de Medio Ambiente
Instituto Superior de Tecnologías y Ciencias Aplicadas
La Habana, Cuba

***Abstract*—The energy delivered during the mechanical agitation produces pumping (macro-mixing) and shear rate (micro-mixing). The relative importance of these simultaneous actions is appreciated according to the application to be accomplished by the agitation device. A Disc Plane (DP) is the simplest impeller in terms of design and manufacture. It can be operated at high peripheral speeds with low power consumption and can be classified as a high shear impeller (HIS). In this work, a numerical and experimental study of the hydrodynamic of a DP was carried out in the transitional flow regime ($25 \leqslant Re \leqslant 75$). The obtained results were compared with the hydrodynamic performance of a Rushton Turbine (RT). The dependency of power (N_P) and pumping (N_Q) numbers with regard to the Reynolds number (Re) was calculated. Experimental measurements of power consumption were used to validate the numerical results. It was found that the values of the ratio N_P/N_Q varied from 28 to 76 for DP at $25 \leq Re \leq 75$. The velocity field showed a flow pattern characterized by two circulation loops. The energy dissipation field illustrates that the maximum energy dissipation is confined on the blade edge of the impellers. The obtained results suggest that DP has a poor pumping capacity, but is able to generate high values of shear rate and energy viscous dissipation near impeller edge which could useful for dispersing processes.**

Keywords—High Shear Impeller, Disc Plane, power consumption

I. INTRODUCTION

Power draw is a very important variable in chemical process carried out in stirred tanks. It is defined as the amount of energy necessary in a period of time in order to induce the fluid motion. It is well know that the cost associated with power draw contribute significantly to the overall operation costs of industrial plants [1].

The power applied by any impeller produce pumping effect and shear rate (for every shear rate there is a corresponding shear stress due to viscosity of fluid), which can be stressed such that a large flow-small shear rate, or large shear rate-small flow, may be produce for the same power draw [2].

In practice, any impeller used as a mixing device can be classified according their pumping (Q) and shear capabilities [2, 3]. The importance of pumping or shear rate depends on the process; approximately 80% of mixing applications primarily involve impeller pumping capacity and mass flow. However, the other 20% that involve shear rate are extremely important [2].

The global performance of different impellers can be evaluated by comparing their N_Q and N_P values, which are a function of impeller type, geometry and Re [2, 3]. When the ratio N_P/N_Q is large the impeller is inferior in pumping efficiency (and superior in shear) and if it is small the impeller is superior in pumping efficiency. The impellers having large N_P/N_Q are called shear type and those having small N_P/N_Q are called circulation type [4]. This criterion can be useful to evaluate the effectiveness of an impeller for a given injected power (P) to maximise Q or shear or vice versa.

The power draw and pumping are very important factors to estimate mixing performance and to design and operate mixing vessels. In addition these are fundamental to select or design the impeller and for the optimization and scale-up of mixing processes.

The devices that can generate higher values of shear stress in the volume around the impeller are commonly called high shear impellers (HSI's). However, the volume of this region is relatively small and, therefore, a very small amount of the material experiences these shear at every instant of time, so that a certain amount of pumping is required to ensure that all material flow through this region. Consequently, a particular dispersing process has an optimum requirement of high shear and pumping action which should be investigated in laboratory scale before implementing the industrial process [5].

The most frequent application of HSI's is to incorporate and disperse fine solid in viscous liquids during dispersion process [6, 7]. In dispersion processes, the zone of high shear stress provides the energy necessary to break up particles, lumps and conglomerates. For example, in the paint industry, an optimal dispersion maximizes the hiding power of pigment and minimizes the amount of pigment in a specific formulation [5].

Recently, HSI's have been used for preparing nanoparticles dispersions which due to their unique properties have shown huge potential to be formulated into numerous products with important applications (transparent coatings resistant abrasion, sunscreen lotions providing UV protection, polishing slurries providing pristine surfaces for optics, and environmental catalysts to reduce pollution) [8].

With the increasing use of high-shear mixing devices, there is a corresponding need for performance and design data. Nevertheless, practically, the process development, scale-up, and operation of high-shear mixing devices are mostly relied on engineering judgments and trial-and-errors instead of through sound engineering principles, which lead to higher development costs, start-up problems, lost time to market and considerable materials wastes [9].

In comparison with conventional impellers (radial, axial and mixed flow impellers), the hydrodynamics induced by high shear impellers have been little studied, in spite of being widely used industrially [5]. Although there are some studies about high shear devices, these have been focused in devices like sawtooth and rotor stator in the turbulent flow regime [8, 10], however this condition occurs only in processes in which the concentration of particles and liquid viscosity are low. In contrast, there are many processes carried out in highly viscous fluid operating in the laminar to transitional flow regime.

During the last two decades Computational Fluid Dynamics (CFD) has become an important tool for understanding flow phenomena to develop new processes and optimizing existing processes. The capability of CFD tools to forecast the flow behavior in several fields is considered a successful of these methods and acceptable experimental results have been found [11]. With CFD is possible to examine various hydrodynamic parameters of stirred tanks in a shorter time and with less expense that with experimental techniques.

The Norstone® type impeller is a commercial HSI which is built subtracting one half of seven horizontal cylinders from the upper and lower surfaces of disc plane. This impeller was studied by mean of CFD simulation by G. Martínez de Jesús et al. [12] who reported its performance in the transitional regime ($50< Re <75$). In this Re interval N_P value varied between 2 and 3 and its N_Q from 0.031 to 0.037. They also reported the contour of the viscous energy dissipation and stated that the maximum values are very located on the upper and lower surfaces at the impeller tip. These results suggest that in order to maximize the energy dissipation is advisable to increase the surface at the impeller tip. In this way a DP would be the impeller that maximizes the viscous energy dissipation.

Baldyga et al. [8] and Xie et al. [10] justified the use of energy dissipation as a key parameter in dispersion processes arguing that this parameter is responsible of the break up of lump or agglomerates in turbulent regime. Similarly, J, Y Oldshue [2] has mentioned that the shear rate and the corresponding shear stress tend to break up particles, lumps, conglomerates or bubbles.

Taking into account all mentioned above, the aim of this work was to gain insight about the viscous energy dissipation in the volume surrounding a DP and get its hydrodynamic performance and compare it with those generated by RT at the laminar to transitional flow, ($25 \leqslant Re \leqslant 75$) in a unbaffled stirred tank.

II. MATERIALS AND METHODS

A. *Experimental set-up*

Experiments were performed in a cylindrical stainless-steel vessel with dished bottom, unbaffled and jacketed to control temperature. The diameter T of tank was equal to 0.132 m (Fig. 1a). The dimensionless geometric ratios corresponding to the impeller off-bottom clearance (C), liquid height (Z) and impeller diameter were: C/T=0.3848, Z/T=1 and D/T=0.3848, respectively. Agitation was provided by a 0.75 HP variable-speed motor Dispermat® type AE01 (Fig. 1b). In this equipment, the power under no load conditions, which includes all frictional losses such as ball bearing friction, motor ventilation, mechanical seals, etc., can be measured previously and later, during measurements, this value is subtracted and thus, the net power transferred to the liquid (power draw or P) is obtained. The experimental values of P can be visualized directly in the equipment display as well as recorded for further processing of the data. In this work, the measurements obtained from the Dispermat® AE01 equipment were used to validate the results obtained by simulations.

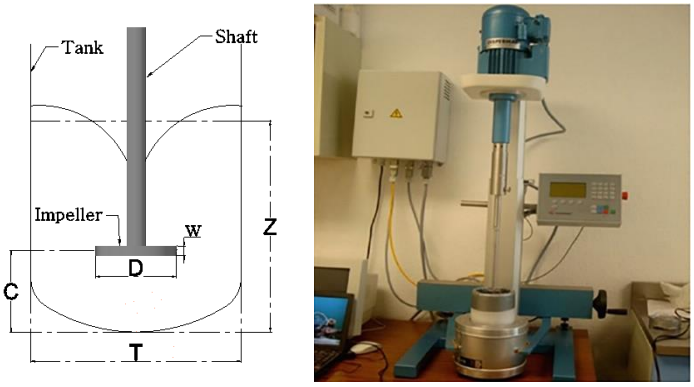

a) b)

Fig. 1. Experimental set-up.

The studied impellers in this work are shown in Fig. 2. The used fluid was a mixture of food grade glucose (45° Bx) and distilled water. Two solutions of 80 and 84 % by weight of glucose were prepared. Thus fluid properties were: viscosity (μ) =0.95, 1.7 Pa s and density (ρ) = 1376.46, 1386.26 kg m^{-3}, respectively. A cooling bath was used to hold temperature process fluid at 25 ± 0.2 °C during experiments. Simulations in $50 \leqslant Re \leqslant 75$ were run with the lower viscosity solution, while in $25 \leqslant Re \leqslant 55$ simulations and experiments were carried out with the other solution.

Experimental measurements of the power draw in the system with each impeller were performed capturing power draw measurements each 5 s and averaging the data captured during 5 min.

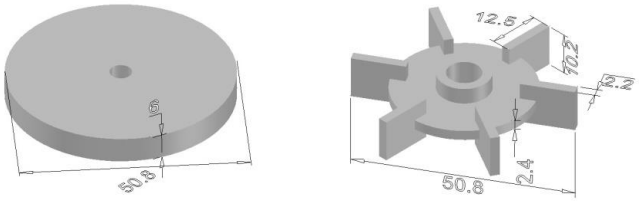

a) b)

Fig. 2. a) Disc Plane (DP) and b) Rushton Turbine (RT) (dimensions in mm).

B. *Numerical simulation*

The CFD model of the stirred tank was developed to analyze the performance of the impellers in the transitional flow regime. The system geometry was carefully constructed and precise details of the impellers were incorporated in order to simulate velocity field, the local shear rate and viscous energy dissipation.

Two-dimensional cross sections of the computational grids used in the simulations are shown in Fig. 3

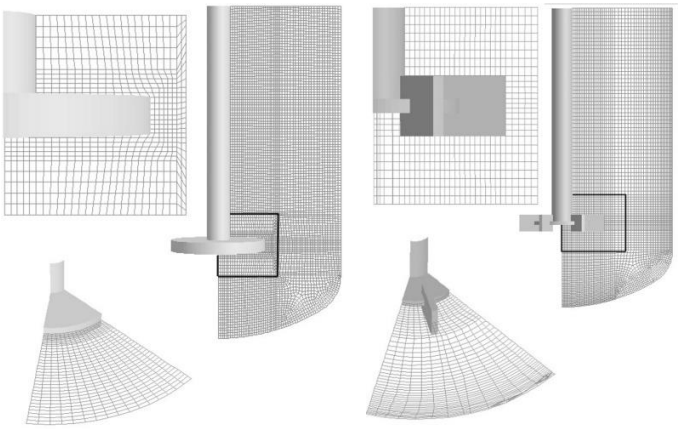

a) DP b) RT

Fig. 3. CDF computational grid.

Due to their symmetric nature, only a fraction of the domains were modelled, one-seventh of DP and one-sixth of RT. This allowed decreasing the number of cells for each model by 83%, which leads to a significant reduction in computational time.

The shaft and surfaces of impeller were assigned as moving wall boundary condition with a defined absolute motion and no slip condition. The cylindrical tank wall and the tank bottom were treated as stationary walls with no slip condition.

The unsteady-state numerical solution of the system was obtained by using the commercial CFD solver ANSYS 14.5 FLUENT®. The multiphase volume of fluid (VoF) model was used to simulate the evolution of the gas-liquid interface and the multiple reference frame (MRF) approach was adopted to model the flow in the region enclosing agitated impeller [13]. Standard pressure–velocity coupling scheme was used along with QUICK discretization scheme. A single mesh was built and a continuum surface force model incorporated in Fluent was employed. The VoF model required the definition of a primary fluid (air) and a secondary fluid (solution of glucose). A force balance model was applied through the gas-liquid boundary.

The simulations were performed on a HP Z1 workstation with intel (R) core (TM) i5-4200U CPU @ 1.6 GHz and 6 Gb of RAM installed. At 1200 rpm, a time step corresponding to 12 degrees of rotational angle of each impeller have been simulated. All simulations were stopped at 10 s because it was observed an increase in the volume of the liquid phase with long simulation times (i.e. air drawdown). At this computation time, the solutions could be considered to be fully converged because the residuals of the equations stayed constant with a value of approximately 10^{-5}.

Several meshes by increasing cell density were created to evaluate the independence of the numerical predictions with respect to mesh size. Fig. 4 shows the dependency of N_P and CPU time estimated for DP with a grid resolution of 52344, 103264 and 207301 cells, at 1200 rpm. As can be seen, the N_P is practically the same for the three used grid, whilst the CPU time increases significantly. Analogous analysis was made for RT obtaining similar results. Therefore, in this work it was decided to use mesh with aproximately 100000 cells. The maximum cell skewness value of each mesh was below 0.9.

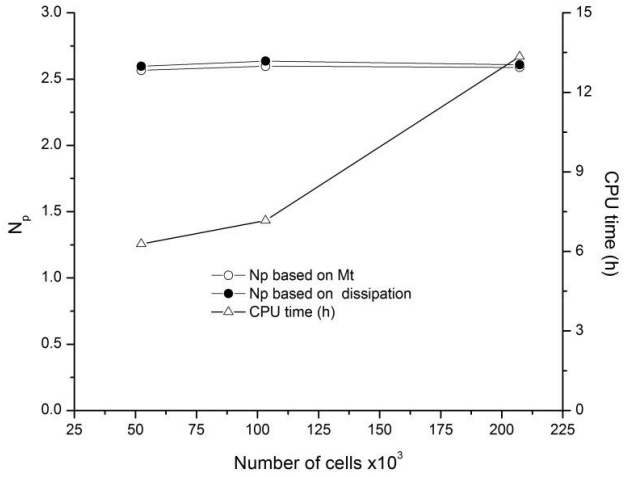

Fig. 4. Mesh independence analysis and CPU time for DP at 1200 rpm.

III. RESULTS AND DISCUSSION

A. *Power and pumping number*

To characterize an impeller and compare its performance with others is useful to define the dimensionless numbers of pumping (N_Q) and power (N_P).

The N_Q is defined as:

$$N_Q = \frac{Q_P}{ND^3} \tag{1}$$

$$Q_P = \pi(D_i + 2d)\int_W v_r(z)dz \tag{2}$$

where, Q_P (m^3 s^{-1}) is the volumetric flow rate of the fluid passing through an area surrounding the impeller with a width equal to impeller blade a diameter equal to (Di +$2d$). D_i is the impeller diameter and "d" is an arbitrary radial distance from the blade tip to the point where Q_P is determined. In this work d=8.58x10^{-3} m for DP, i.e. Q_P was calculated at the position 1.3% of T away from the impeller tip, such as was recommended by [14], while for RT, d=0 m. N (s^{-1}) is the velocity of agitation, D (m) is the diameter of impeller and v_r (m s^{-1}) is the radial velocities that can be obtained from CFD results.

The N_P is defined as:

$$N_P = \frac{P}{\rho N^3 D^5} \tag{3}$$

where P is the delivered power to the fluid by the impeller.

Two approaches can be used for the estimation of P. In the first case, P can be calculated by using (4), where M_t is the torque on the impeller, which can be obtained from CFD results.

$$P = 2\pi N M_t \tag{4}$$

The other approach to calculate P is by using (5). Here, ε_t, is the turbulent energy dissipation that can be obtained directly from the simulation results, and ε is the viscous energy dissipation rate which can be expressed in term of the rate of energy dissipated by viscosity per unit volume, Φ_v (6) [15].

$$P = \int \left(\rho\varepsilon_t + \varepsilon\right) dV \tag{5}$$

$$\varepsilon = \mu\Phi_v\left(x, y, z\right) \tag{6}$$

For a Newtonian and compressible fluid in Cartesian coordinates (x,y,z), Φ_v is defined by (7).

$$\Phi(x,y,z) = \left\{ \begin{array}{l} 2\left[\left(\frac{\partial v_x}{\partial x}\right)^2 + \left(\frac{\partial v_y}{\partial y}\right)^2 + \left(\frac{\partial v_z}{\partial z}\right)^2\right] \\ + \left[\frac{\partial v_y}{\partial x} + \frac{\partial v_x}{\partial y}\right]^2 + \left[\frac{\partial v_z}{\partial y} + \frac{\partial v_y}{\partial z}\right]^2 + \\ \left[\frac{\partial v_x}{\partial z} + \frac{\partial v_z}{\partial x}\right]^2 - \frac{2}{3}\left(\frac{\partial v_x}{\partial x} + \frac{\partial v_y}{\partial y} + \frac{\partial v_z}{\partial z}\right)^2 \end{array} \right\} \tag{7}$$

By substituting (7) in (6) and introducing the resulting expression as a custom field function in Fluent®, it is possible to calculate ε throughout the volume of fluid and finally, obtain the P dissipated by the fluid by using (5).

The values of ε_t obtained in the volume enclosing the impeller and in the fluid bulk for the two impellers studied in this work were at least five orders of magnitude lower than ε. Thus, for $Re\leqslant 75$ one may consider a laminar flow regime in the entire volume of the fluid. For that reason, in this work it was considered only the viscous energy dissipation, ε, for the calculation of P.

These results are in agreement with B. Gibbardo et al. [16] whom studied numerically the flow field and the N_P induced by a RT in an unbaffled stirred tank. They found that for $Re\leqslant 70$ using a turbulence model in simulations yields substantially the same N_P values that a laminar model because no turbulence is present at this Re.

Then, one way to validate the simulation results is the calculation of global or macro-mixing parameters N_Q y N_P and to compare them with experimental or literature data. In Fig. 5, 6 and 7 are shown the N_P, N_Q and the ratio N_P/N_Q respectively for $25\leqslant Re\leqslant 75$ for the DP and RT.

In Fig 5 it can be seen that for RT there is good agreement of the N_Q values obtained by simulation in this work and those report by Lamberto et al. [17]. The N_Q curve of the RT is higher than that of the DP. In general, the values of the N_Q are of an order of magnitude smaller than the ones for RT. This indicates that the DP has a relatively poor pumping capacity. Similar results have been reported by Nagata for axial impellers [4].

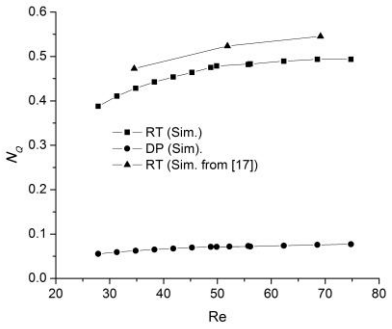

Fig. 5. Pumping numbers, N_Q, for DP and RT.

The N_P values for DP and RT are shown in Fig. 6. The obtained values by simulation for DP based on (4) and those using (5) are very similar, and are in good agreement with the experimental results of this work. The error barrs in experimental results for N_P were obtained considering the accuracy of Dispermat® equipment (± 1 W), therefore the errors decrese when Re increase. Notwithstanding, the experimental values are within error range of equipment.

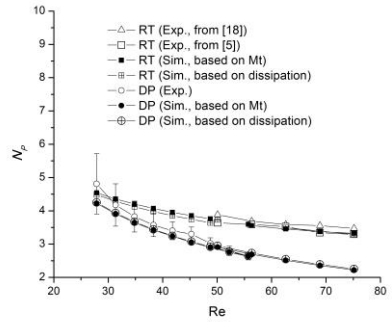

Fig. 6. Power numbers, N_P, for DP and RT.

For the RT, N_P values based on (4) and (5) are practically the same. In adition, when these values are compared with literature data [5] and [18] it can be observed that these values are also very close. As can be seen, the *Np* curve of the RT is higher.

On the other hand, when the N_P/N_Q values of the two impellers were calculated and plotted in Fig. 7, it results that the curve of the DP is higher ($28<N_P/N_Q<76$) that RT ($6<N_P/N_Q<12$). The values of N_P/N_Q for DP are similar those reported by Ramírez-Gómez et al. [5] whom obtained values $20<N_P/N_Q<45$ for Re between 50 and 75 studing two commertial HSI`s Hockmeyer® type. These result suggests that DP would be appropriate for solid dispersion processes.

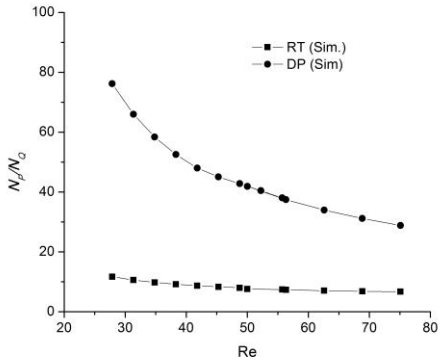

Fig. 7. Ratio N_P/N_Q for DP and RT.

B. *Velocity Fields*

In Fig. 8, the flow patterns at the same *P*=23.45 W are presented for the two studied impellers. The vertical plane for the RT is the plane through the middle of the blade. Note that for both impellers two strong circulation loops are generated above and below the center of the impellers. These loops produce segregated mixing regions in the form of toroidal vortices, which has been reported by D.J. Lamberto et al. [17] for RT and by L. Mununga et al. [14] by a DP. They observed that these regions not to easily exchange material with surrounding zones where active mixing takes place.

Race et al. [19] reported that for *Re*<500, the flow induced by many flat blade turbines divides the tank in two secondary circulation regions of two ring vortices. Thus, the flow structure induced by the impellers evaluated in this work is similar to that reported by these radial flow impellers.

C. *Viscous energy dissipation*

In order to gain insight on the viscous energy dissipation around the impellers, in Figs. 9 and 10 are shown the contours of shear rate and viscous energy dissipation respectively, these were genered at *P*=23.45 W. In Figs. 9 and 10 the vertical planes are equivalents to that ilustraded in Fig. 8. It can be observed in Fig. 9 for the two impellers there is an intense shear rate (i.e. viscous energy dissipation) confined on the blade edge of impellers. In addition, there is symmetry in the vertical planes with respect to the center of the impellers. In Fig. 10, the vertical plane again shows that the highest viscous dissipation values are confined on the upper and lower edges of impellers (only is shown the upper edge in the horizontal plane at height *y/C*=1.06, 1.10 for DP and RT respectively). It should be noted that the areas of high energy dissipation for DP are broader than RT. Although the latter generates areas of the highest energy dissipation these are very small.

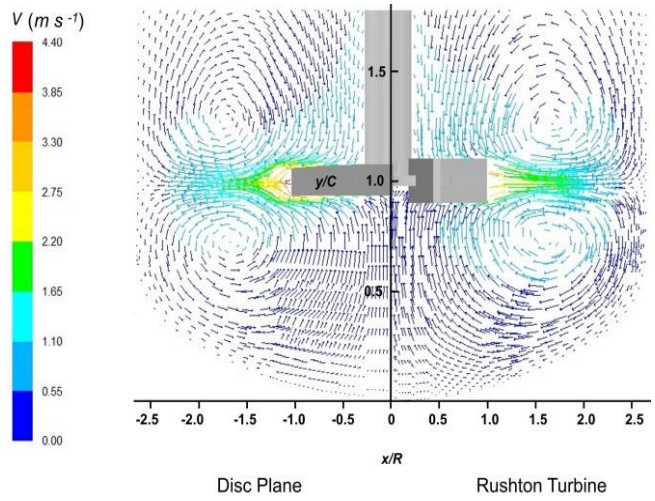

Fig. 8. Velocity vector magnitudes at the same *P*= 23.45 *W* for DP (1610 rpm) and RT (1425 rpm) with fluid viscosity = 1.7 Pa s . *R*=D/2.

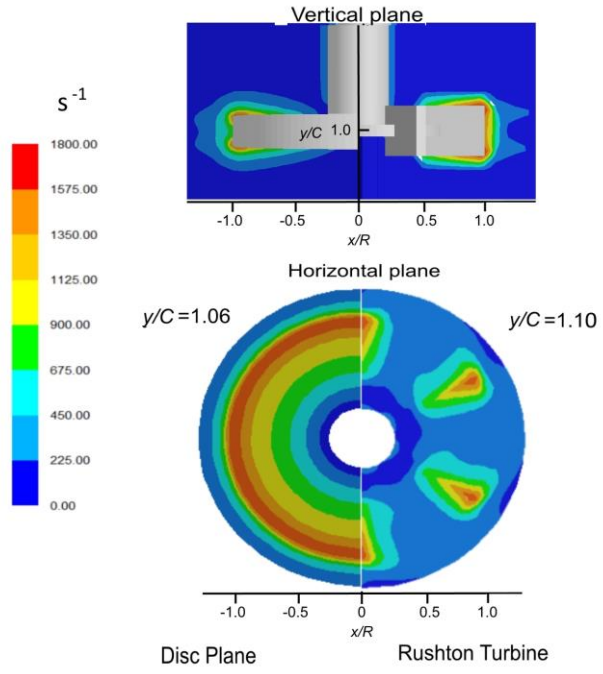

Fig. 9. Shear rate at the same power draw *P*= 23.45 *W* for DP (1610 rpm) and RT (1425 rpm) with fluid viscosity = 1.7 Pa s . *R*=D/2.

Two aspects should be mentioned, first, as it was mentioned early, RT present the highest values of viscous energy dissipation, but are located in a region very small. In fact, H. Hockmeyer [7], has stated than a conventional impeller like RT, typically cannot generate sufficient shear to disperse

powders in dispersion processes, regardless of how long it is mixed, i.e. the probability that the material passes through of region high viscous dissipation is very small. On the other hand, despite there are large areas of viscous dissipation on DP, this it is not guaranty that particles circulate through this region due to this present the lower values of N_Q. Therefore it would be advisable modify the geometry of DP to increase its pumping capacity.

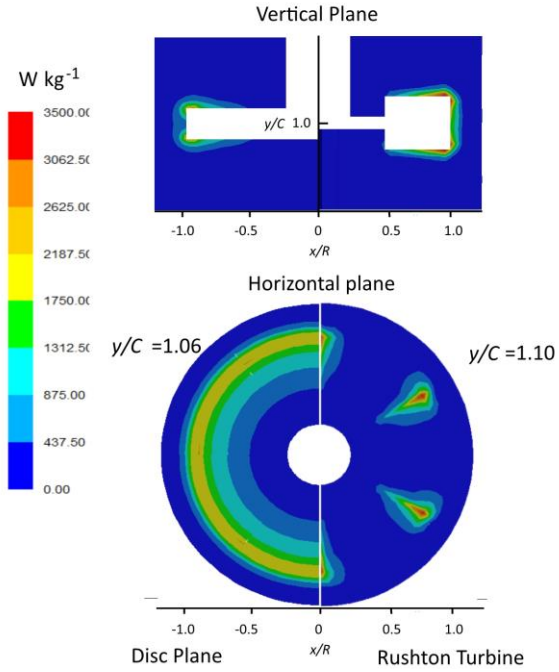

Fig. 10. Viscous energy dissipation in W kg^{-1} at the same power draw P= 23.45 W for DP (1610 rpm) and RT (1425 rpm) with fluid viscosity = 1.7 Pa s . R=D/2.

IV. Conclusions

In this work a CFD analysis was carried out to evaluate the hydrodynamic of a Disc Plane in the transitional flow regime ($25 \leqslant Re \leqslant 75$) and its performance was compared with Rushton Turbine. The numerical results were validated with experimental measurements of consumption power. Pumping and power numbers and contours of viscous energy dissipation were obtained from numerical results. The Disc Plane has a large ratio N_P/N_Q, this means that it is inefficient for pumping. The contours of shear rate and viscous energy dissipation have suggested that Disc Plane has a high capacity to concentrate energy near of impeller, which could be useful for dispersion processes, e.g. pigment dispersion in liquids. However, Disc Plane should be evaluated experimentally to study its experimental efficiency of dispersion and to determine if it has sufficient pumping capacity or if it is necessary modify its geometry to increase it.

References

[1] G. Ascanio, B. Castro and E. Galindo, Measurement of power consumption in stirred vessels – A review, Chemical Engineering Research and Design. Vol. 82, pp. 1282–1290, 2004.

[2] J. Y. Oldshue, Fluid mixing technology and practice, McGraw-Hill Publications Co., New York, 1983, pp. 44-45.

[3] E. L. Paul, V. A. Atiemo-Obeng, S. M. Kresta, Handbook of Industrial Mixing, Science and Practice, John Wiley & Sons, Inc. New Jersey, 2004.

[4] S. Nagata, Mixing Principles and applications, John Wiley & Sons. Tokyo, 1975.

[5] R. Ramírez-Gómez, D. García-Cortés, G. Martínez-de Jesús, M. González-Brambila, A. Alonso and J. Ramírez-Muñoz. Performance evaluation of two high shear impellers in an unbaffled stirred tank. Chem. Eng. Technol. 10.1002/ceat.201400792.

[6] T. C. Patton, Paint flow and pigment dispersion. John Wiley and Sons, Inc. New Jersey, 1979.

[7] H, Hockmeyer, Practical guide to high-speed dispersion. Paint & Coatings Ind. (US), vol. 26, No 2, pp. 32-6, 2010.

[8] J. Baldyga, W. Orciuch, L, Makowski, K. Malik, G. Özcan-Taskin, W, Eagles and G. Padron, Dispersion of Nanoparticle Clusters in a Rotor-Stator Mixer, Ind. Eng. Chem. Res., vol. 47, pp. 3652-3663, 2008.

[9] V.A. Atiemo-Obeng and R.V. Calebrase, Rotor-stator mixing devices, in: E.L. Paul, V.A. Atiemo-Obeng, S.M. Kresta Handbook of Industrial Mixing: Science and Practice, John Wiley & Sons, Inc, New Jersey, 2004, pp. 145–250.

[10] L. Xie, C.D. Rielly, W. Eagles and G. Özcan-Taskin, Chem. Eng. Res. Des., vol. 85, pp. 676–684, 2007.

[11] H. Ameur and M. Bouzit, Power consumption for stirring shear thinning fluids by two-blade impeller, Energy, vol. 50, pp. 326-332, 2013.

[12] G. Martínez de Jesús, R. Ramírez Gómez, J. Ramírez Muñoz, D. García Cortés. Simulación CFD de la hidrodinámica inducida por un dispersor tipo Norstone. 17 Convención Científica de Ingeniería y Arquitectura. La habana, Cuba, Noviembre 2014.

[13] G.M. Cartland Glover, J.J. Fitzpatrick, Modelling vortex formation in an unbaffled stirred tank reactors, Chem. Eng. J., vol. 127, pp. 11–22, 2007.

[14] L. Mununga, K. Hourigan, M. Thompson and S. Johnson "Numerical investigations of discharge flow and circulation flow in an unbaffled mixing vessel agitated by a plain disk". 2nd International Conference on Heat Transfer, Fluid Mechanics and Thermodynamics. Victoria Falls, Zambia. Jun. 2003. Paper number: ML1.

[15] R. B. Bird, W. E. Stewart, E. N. Lightfoot, Transport Phenomena, 2a ed., John Wiley & Sons, Inc., New Jersey, 2002, pp. 82, 849.

[16] B. Gibbardo, G. Micalea, F. Grisafia, A. Brucato, M. Ciofalo, Numerical simulation of low-Reynolds flow fields in unbaffled stirred vessels, 12th European Conference on Mixing, Bologna, Italy, June 2006.

[17] D.J. Lamberto, M.M. Alvarez and G.J Muzzio, Experimental and computational investigation of the laminar flow structure in a stirred tank. Chem. Eng. Sci., vol. 54, pp. 919-942, 1999.

[18] S. Ibrahim, A. W. Nienow, Power curves and flow patterns for a range of impeller in Newtonian fluids: $40<Re<5x10^5$, Trans. IChemE., vol. 73, pp. 485-495, 1995.

[19] M. Rice, J. Hall, G. Papadakis, M. Yianneskis, Investigation of laminar flow in a stirred vessel at low Reynolds number, Chem. Eng. Sci., vol. 61, pp. 2762-2770, 2006.

Descomposición de óxidos métalicos para la producción de hidrógenos con energía solar concentrada

J. Valle-Hernández, M. López-Arroyo, V. Castillo-Jimenez
Programa Educativo de Ingeniería en Energía
Universidad Politécnica Metropolitana de Hidalgo
Tolcayuca, Hidalgo, 43860, México
jvalle@upmh.edu.mx, moni_la_ie@hotmail.com

H. Romero-Paredes
Área de Ingeniería en Recursos Energéticos
Universidad Autónoma Metropolitana- Iztapalapa
Iztapalapa, Ciudad de México, D.F, 09340
hrp@xanum.uam.mx

Resumen*— En el presente trabajo se describe la primera etapa del modelado de un proceso de producción de hidrogeno mediante la descomposición de óxidos metálicos utilizando energía solar concentrada. El ciclo termoquímico permite la obtención de hidrógeno y oxígeno mediante reacciones de reducción térmica e hidrólisis indirecta de la molécula de agua. Los compuestos utilizados para llevar a cabo la reacción pueden ser recirculados, requiriendo únicamente suministrar agua en la etapa de hidrólisis. Para modelar el proceso termoquímico se diseñó un prototipo de reactor solar de cavidad; que consiste en un ensamble cúbico de fibra de grafito aislado térmicamente, en cuyo interior contiene nueve tubos de tungsteno arreglados de manera piramidal con respecto al punto focal. La simulación del proceso de reducción térmica dentro del reactor solar, en CFD (Dinámica de Fluidos Computacional), permite obtener una distribución de temperatura en los tubos dentro del reactor, así como la dinámica del fluido y la transferencia de calor en ellos. A partir de los resultados se llevará a cabo un proceso de optimización del diseño que permita tener las condiciones apropiadas para la producción de hidrógeno. Este trabajo forma parte del proyecto de Combustibles Solares y Procesos Industriales perteneciente al Centro Mexicano de Innovación en Energía Solar (CEMIE-sol) financiado por Conacyt-SENER. Una de las metas del proyecto es contar con un modelo completo del ciclo termoquímico solar, además de la cinética de diferentes tipos de óxidos metálicos para la producción de hidrógeno. Una vez simulado cada una de las etapas del sistema se realizarán pruebas experimentales y de escalamiento.

Keywords*— *Ciclo termoquímico, Energía Solar Concentrada, Reactor Solar, Reducción térmica; Producción de Hidrógeno.

I. INTRODUCIÓN

El uso de combustibles alternos a los hidrocarburos jugará un papel trascendental en la reducción de contaminantes de efecto invernadero y en la desaceleración del calentamiento global. La producción de hidrógeno, para su uso como vector energético limpio que supla gradualmente a algunos combustibles fósiles, jugará un papel determinante para esta reducción, siempre y cuando sea producido por fuentes de energías limpias como la energía solar concentrada. No obstante la importancia, el poder contar con combustibles limpios plantea retos tecnológicos que hay que resolver. Este trabajo presenta parte de un proyecto, a desarrollar en varias etapas, que pretende demostrar la viabilidad técnica, energética y económica de la producción de hidrógeno y/o gas de síntesis utilizando energía solar [1].

En la actualidad existen tres tipos de procesos para la producción de hidrogeno mediante el uso de energía solar: electroquímicos, fotoquímicos y termoquímicos. Los procesos termoquímicos que emplean energía solar concentrada como fuente de energía para llevar a cabo reacciones a muy alta temperatura que producen hidrogeno son los más eficientes [2]. Una característica importante en el uso de estos ciclos radica en que sólo necesitan agua como materia prima, ya que el resto de los reactivos se regeneran, y no se generan emisiones de CO_2 durante la disociación indirecta de la molécula de agua en hidrogeno y oxígeno. A primera vista esta disociación de la molécula de agua parece sencilla:

$$H_20 \overset{\Delta}{\rightarrow} H_2 + 0.5O_2$$

No obstante, para llevar a cabo esta reacción es necesario temperaturas muy altas (>2200ºC) si deseamos tener un grado de disociación significante; además es necesario contar con materiales y membranas extremadamente caras. [2]

Los procesos termoquímicos más prometedores actualmente son lo que utilizan óxidos metálicos en ciclos redox de dos pasos, que se basan en materiales redox que actúan como separadores de la molécula del agua a temperaturas menores que en otros procesos. El primer paso del ciclo es la reducción del óxido metálico quitando oxígeno. En el segundo paso el óxido reducido es oxidado mediante la hidrólisis del agua para ser usado de nuevo (regeneración). La reacción se muestra a continuación.

Reducción: (endotérmica):

$$M_xO_y \rightarrow M_xO_{y-1} + \frac{1}{2}O_2$$

Hidrolisis (exotérmica):

$$M_xO_{y-1} + H_20(g) \rightarrow M_xO_y + H_2(g)$$

Una de las ventajas de este tipo de reacción es que el hidrógeno producido es puro y la remoción de oxígeno se realiza en pasos separados, evitando la necesidad de una disociación a muy alta temperatura y la posibilidad de formar de mezclas explosivas. Algunos de los ciclos con óxidos metálicos más probados son el ZnO/Zn y Fe_3O_4/FeO, ambos ciclos han sido estudiados y reproducidos experimentalmente.

II. Energía Solar Concentrada en la Producción de Hidrógeno

La tecnología para la producción de hidrógeno en reactores solares, a partir de óxidos metálicos, que utiliza energía concentrada como fuente de calor es innovadora y cada vez más estudiada [3]. Los reactores solares son dispositivos donde la energía solar recibida, mediante un receptor, se emplea para llevar a cabo una transformación química. El receptor es un dispositivo que transfiere la radiación solar concentrada a un absorbedor para ser utilizada en forma de energía térmica. La energía transferida es aprovechada dentro del reactor por un fluido, un sólido o una combinación de ambos para realizar una reacción endotérmica. El diseño del receptor debe favorecer el intercambio de calor entre la radiación solar y el elemento absorbente. En el presente trabajo se describen tanto el reactor solar diseñado para la aplicación, como el ciclo termoquímico empleado para la producción de hidrógeno.

A. Diseño del Reactor Solar

El reactor solar es el dispositivo en el que se lleva a cabo la parte endotérmica del proceso termoquímico. Actualmente se han diseñado diversas variedades de reactores que se emplean en un gran número de procesos termoquímicos [3]. Para el proceso que se presenta en este trabajo se diseñó un reactor de cavidad, este prototipo consiste de una caja de fibra de grafito aislada térmicamente, en cuyo interior se alojan nueve tubos de tungsteno arreglados de manera piramidal con respecto al punto focal. En el punto focal se concentra la energía suministrada por el horno solar de Alto Flujo de Radiación. La Figura 1, muestra la estructura del reactor con sus respectivas cubiertas aislantes. En los tubos de tungsteno es en donde se realiza la reacción para la producción de hidrogeno, La Figura 2 muestra el tubo frontal del arreglo donde se lleva a cabo la reacción de reducción.

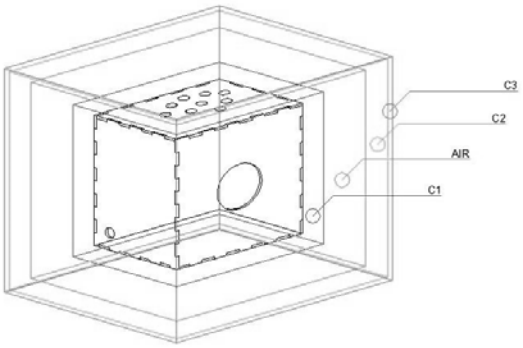

Fig. 1. Perspectiva del acoplamiento de las diferentes capas que integran el reactor.

Los materiales aislantes que envuelven el cubo de grafito, que contiene los tubos donde se lleva a cabo la reacción para la producción de hidrogeno, son de fibra de alúmina (óxido de aluminio, Al_2O_3), elemento con una resistencia a altas temperaturas cuyo punto de fusión es de 2072° C.

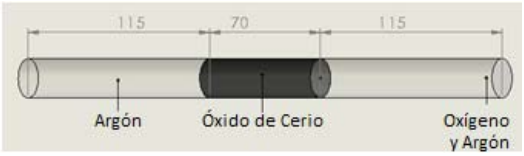

Fig. 2. Tubo de reacción para la reducción del óxido de cerio.

La radiación solar incide dentro del reactor por medio de una apertura angular como se muestra en la Fig. 3, esta apertura está sellada por medio de una ventana de vidrio de cuarzo, el material alrededor de este debe resistir altas temperaturas.

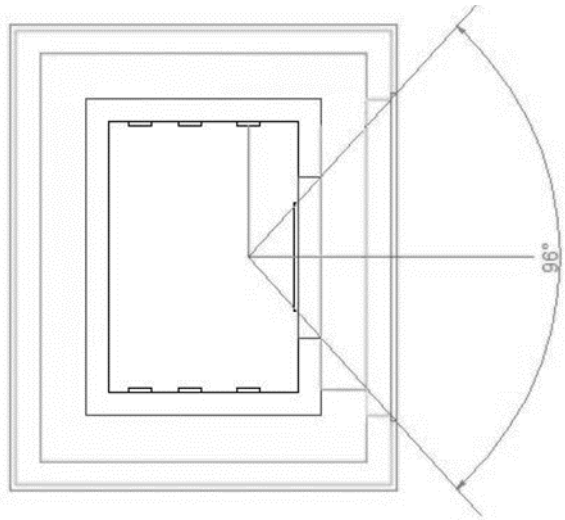

Fig 3. Corte de vista lateral; Angulo de apertura angular para la incidencia de radiación solar.

III. Ciclo Termoquímico

El ciclo termoquímico basado en óxidos metálicos que se eligió para este proyecto fue el del óxido de cerio, el cual se compone de dos pasos:

$$CeO_2 \rightarrow CeO_{2-\delta} + \frac{\delta}{2} O_2 \quad (1)$$

$$CeO_{2-\delta} + \delta CeO_2 \rightarrow CeO_2 + \delta H_2 \quad (2)$$

La dinámica del ciclo se observan en la Figura 4, y algunas propiedades del óxido de cerio se enlistan en la Tabla 1.

El primer paso consiste en la liberación del O_2, que es una reacción altamente endotérmica (ΔH = 198 KJ/mol de CeO_2 a 2300 K) y el calor lo proporciona el Horno Solar de Alto Flujo Radiactivo. El segundo paso es la reacción de hidrólisis de vapor, que es exotérmica (ΔH = -125 KJ/mol a 700 K). La síntesis de hidrogeno se hace en un lecho fijo.

Debido a que la producción de hidrogeno y oxigeno se realiza en dos pasos diferentes, se evita tener reacciones adicionales con producción de gases no deseados. [3]

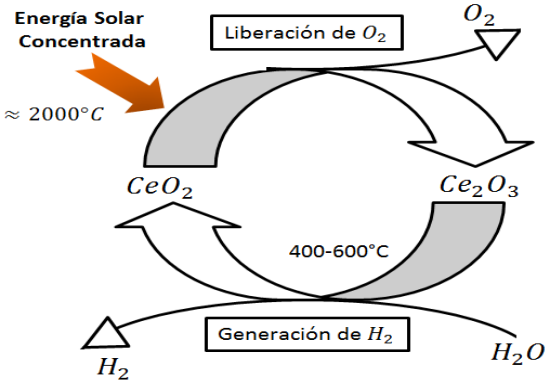

Fig 4. Esquema del ciclo termoquímico de dos etapas.

TABLA I. PROPIEDADES DEL ÓXIDO DE CERIO [3]

Masa molar (g/mol)	Punto de fusión (°C)	Densidad (kg/m3)	Color
Ce_2O_3	1687-2230	62	Gris-Ammarillo-Verde
CeO_2	1950-2400	76.5	Blanco-Verde

IV. MODELADO MATEMÁTICO

Para el desarrollo del modelo matemático se considero la matriz de óxido de cerio, la cual se fija de manera que esté expuesta a un flujo de calor considerable a través del contacto con la cara interna del tubo de tungsteno que la aloja, como un medio poroso. Bajo estas condiciones el óxido de cerio se reduce endotérmicamente, produciendo oxígeno molecular que es arrastrado por un flujo de gas argón que fluye dentro del tubo.

El modelado del proceso de reducción endotérmica se basa en balances de energía, momentum y masa, los cuales son simulados a partir de software de Dinámica de Fluidos Computacionales (CFD). El modelo resultante describe la mecánica del fluido a través del tubo de tungsteno y los procesos de transferencia de masa y energía que se presentan dentro del mismo.

La mecánica de fluidos se modela a partir de la transferencia de momentum del fluido, oxígeno y gas de arrastre, dentro del tubo de tungsteno. Por consiguiente, para el modelado se consideraron tres regiones; la de entrada del gas de arrastre (Argón), la de la matriz de óxido de cerio (modelada como un medio poroso), y la de salida de oxígeno y gas de arrastre.

El modelo matemático está representado por las ecuaciones de Brinkman, las cuales se presentan a continuación:

$$\left(\frac{n}{k-Q}\right)u = \nabla\cdot\left[-pI+\left(\frac{1}{\varepsilon_p}\right)\left\{\eta(\nabla u+(\nabla u)^T)-\left(\frac{2\eta}{3}-k_{dv}\right)(\nabla\cdot u)I\right\}\right]+F \quad (3)$$

$$\nabla\cdot u = \frac{Q}{p} \quad (4)$$

Dónde: ρ es la densidad del fluido, η la viscosidad dinámica, κ_{dv} la viscosidad dilatacional, ε_p la porosidad, κ la permeabilidad y F la fuerza aplicada al volumen que contiene al fluido. [4][5]

En el modelo de la transferencia de calor se considera la conducción de calor a través del tubo de tungsteno y hacia el fluido, donde la fuente de energía Q se determinará a partir del modelo externo del reactor y considerando las propiedades ópticas y térmicas del tubo. [6][7]

El proceso de transferencia de calor se modelo a partir de la ecuación de conducción de calor:

$$\nabla\cdot(-k\nabla T) = Q-\rho C_p u\cdot\nabla T \quad (5)$$

Dónde: Q es la fuente de calor, k la conductividad térmica, C_p la capacidad térmica, u el campo de velocidades y ρ la densidad.

En el transporte de masa se consideran los fenómenos de convección y difusión del oxígeno, la ecuación que modela este proceso es la siguiente:

$$\nabla\cdot\left(-D\nabla C_{Oxígeno}\right) = R-u\cdot\nabla C_{Oxígeno} \quad (6)$$

Dónde: $C_{oxígeno}$ es la concentración de oxígeno a lo alto del tubo, D es el coeficiente de difusión del oxígeno en el gas de arrastre, u la velocidad de flujo y R la tasa de reacción. [6] [8]

La tasa de reacción se puede determinar a partir del modelo basado en la ecuación de Arrhenius y descrito por Bulfin B., et al. [9]

La reacción de reducción depende de la concentración de oxígeno que puede ser removido del óxido de cerio [O_{Ce}], y la reacción de oxidación depende de la concentración de vacantes de oxígeno [O_{vac}] y de oxígeno disponible [O_{gas}].

La velocidad de cambio en las vacantes de oxigeno será la razón en que el oxígeno deje al CeO_2 (reducción) menos la velocidad de recombinación (oxidación):

$$\frac{d[O_{vac}]}{dt} = [O_{Ce}]k_{red}-[O_{vac}][O_{gas}]^n k_{ox} \quad (7)$$

k_{red} y k_{ox} son las constantes de velocidad de reducción y oxidación, respectivamente. Estas constantes de velocidad se toman de la ecuación de Arrhenius.

$$k_a = A_a exp\left(\frac{-E_a}{RT}\right) \quad (8)$$

La división de las concentraciones de oxígeno [O_{Ce}] y [O_{vac}] entre la concentración de cerio [Ce], que es constante, define los parámetros estequiométricos:

$$\frac{[O_{Ce}]}{[Ce]} = x-\delta \quad (9)$$

$$\frac{[O_{vac}]}{[Ce]} = \delta \quad (10)$$

Dado que la concentración de oxígeno es directamente proporcional a la presión parcial del mismo P_{O_2}, además de que en equilibrio la velocidad de oxidación es igual a la tasa de reducción, podemos expresar la concentración de vacantes de oxígeno de equilibrio en función de la presión parcial de oxígeno y la temperatura.

$$\left(\frac{\delta}{x-\delta}\right) = \frac{A_{red}}{A_{ox}} P_{O_2}^{-n}\, exp\left(\frac{-(E_{red}-E_{ox})}{RT}\right) \quad (11)$$

Para finalmente expresar la dinámica de la disociación de oxígeno en la reacción con la siguiente ecuación:

$$\frac{d\delta}{dt} = (x-\delta)A_{red} exp\left(\frac{-E_{red}}{RT}\right) - \delta P_{O_2}^{n} A_{ox} exp\left(\frac{-E_{ox}}{RT}\right) \quad (12)$$

Con rango de valores para la energía de oxidación de $E_{ox} = 36 \pm 4\ kJ\ mol^{-1}$ y para el factor de frecuencia de $A_{ox} = 82 \pm 41 s^{-1} bar^{-n}$. [9]

V. Resultados

La simulación del modelo de la etapa de reducción del óxido de cerio dentro del tubo frontal del arreglo piramidal en el interior del reactor, se realizó en software CFD. Los resultados obtenidos se muestran en las siguientes figuras; para el perfil de velocidades del fluido en el tubo (Figura 5), la distribución de temperaturas (Figuras 6 y 7), y el transporte de masa (Figura 8).

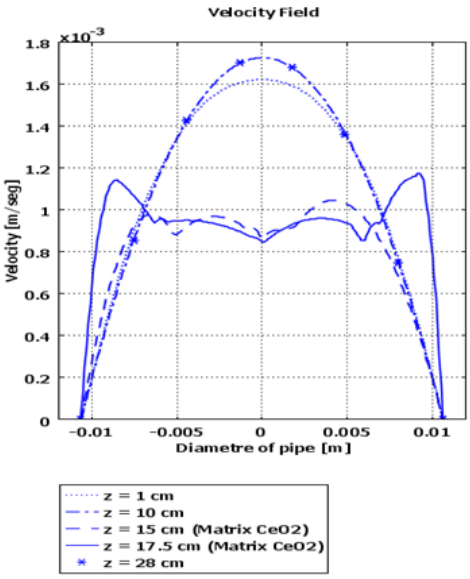

Fig 5. Perfil radial de velocidades a lo alto del tubo de tungsteno.

En la gráfica de la figura 5, se muestra el perfil radial de velocidades del flujo de gas de arrastre a lo alto del tubo de tungsteno. El flujo presenta un comportamiento laminar en el centro del tubo fuera de la matriz del óxido de cerio, con una menor velocidad en las paredes. En tanto que el campo de velocidades se vuelve oscilante dentro del medio poroso.

Para la transferencia de calor se muestra la distribución de temperatura dentro del tubo (Figura 6), donde se aprecia que la mayor temperatura se alcanza en la región de concentración donde se lleva a cabo la reacción de reducción del óxido de cerio. La distribución de temperaturas muestra un perfil adecuado a lo que requerimos, no obstante este modelo aún debe acoplarse al de la estructura del reactor. [10] [11]

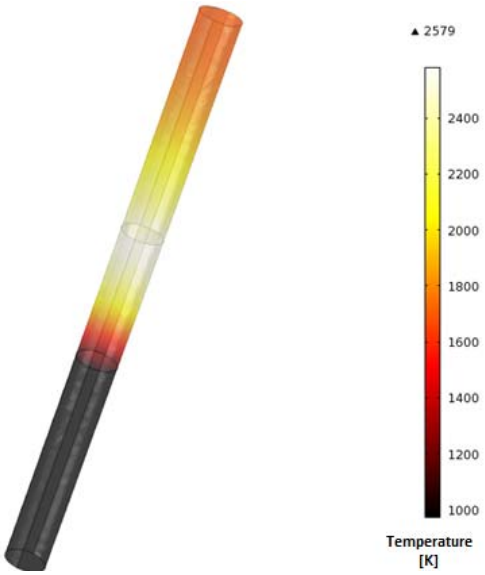

Fig 6. Distribución de Temperaturas dentro del tubo de tungsteno.

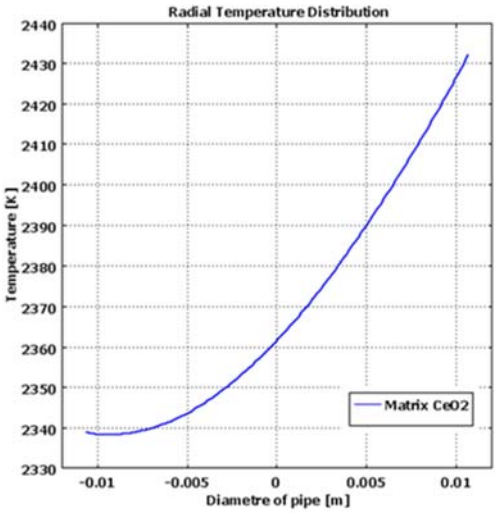

Fig 7. Distribución radial de temperatura radial.

La figura 7 muestra la distribución radial de temperatura en el centro de la matriz de óxido de cerio. Como era de esperarse la mayor temperatura se presenta en el frente del tubo donde recibe la radiación directa (2430 K), aunque puede apreciarse por el gradiente de temperatura que la contribución de la energía reemitida por las paredes del reactor es significativa, algo que se requiere para poder alcanzar la temperatura necesaria para la reducción del óxido de cerio. [12]

En tanto el modelo de la transferencia de masa, aunque debe ajustarse de manera más detallada a la cinética de la reacción, presenta un comportamiento cualitativamente adecuado, ya que la concentración de oxígeno se origina a partir de la región porosa (CeO_2) que es donde se lleva a cabo la reacción y después se mantiene constante, como se muestra en la figura 8.

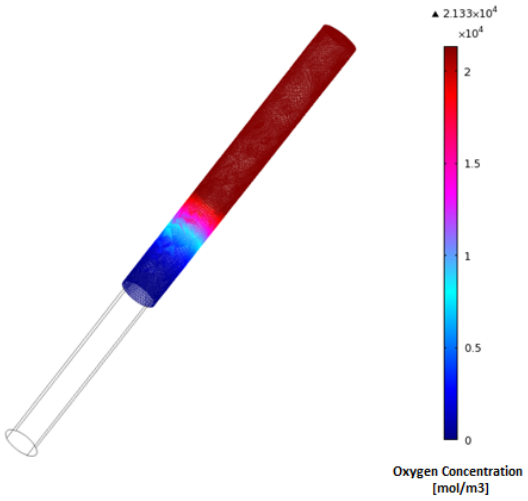

Fig 8. Concentración de oxígeno dentro del tubo de reducción endotérmica.

VI. Conclusiones

Los resultados obtenidos del modelado de la etapa de reducción endotérmica del óxido de cerio en base a Dinámica de Fluidos Computacionales (CFD) fueron satisfactorios. Sin embargo, estos datos deben considerarse preliminares puesto que el modelado del tubo donde se lleva a cabo la reacción de reducción se realizó de manera independiente a la estructura externa del reactor solar. Los resultados del modelo cualitativamente se comportan de forma acertada y en particular algunos parámetros de los mismos son determinados cuantitativamente. El acoplamiento de las dos etapas del ciclo termoquímico permitirá tener una idea más precisa del comportamiento global del proceso, pero para ello hace falta ajustar algunos parámetros de los modelos a datos experimentales. En la siguiente etapa del proyecto se realizará el ajuste, acoplamiento de etapas de reacción e integración del ciclo termoquímico al modelo del reactor solar de cavidad, así como un análisis de resultados que permita tener un estudio detallado de los fenómenos de transporte de masa y transferencia de calor dentro del reactor.

Agradecimientos

Los autores agradecen el apoyo económico recibido a través del Centro Mexicano de Innovación en Energía Solar (CeMIE-Sol), en el marco de la Convocatoria 2013-02, del Fondo SECTORIAL CONACYT-SENER-SUSTENTABILIDAD ENERGÉTICA, dentro del Proyecto Estratégico No. 10, con título: “COMBUSTIBLES SOLARES Y PROCESOS INDUSTRIALES”, por medio del cual fue posible desarrollar la investigación y apoyar la formación de recursos humanos a nivel posgrado.

Referencias

[1] Funk, J. (2001). Thermochemical hydrogen production: past and present. Int J Hydrogen Energy 26, 185-190.

[2] Kodama, T. (2003). High-temperature solar chemistry for converting solar heat to chemical fuels. Progress in Energy and Combustion Science, 29: 567-597.

[3] M. I. Roldán, E. Zarza y J.I.Casas. (2015). "Modelling and testing of a solar-receiver system applied to high-temperature processes,". http://elservier.com/locate/renene.

[4] Whitaker, S., (1999). The Method of Volume Averaging. Kluwer Academic Publishers.

[5] Whitaker, S., (1992). Improved constraints for the principle of local thermal equilibrium. Ind. Eng. Chem. Res. 30 (5), 978–983.

[6] Romero-Paredes H, Torres A, Ambriz JJ. (1997) Characterization of a thermochemical reactor for thermal solar energy. Renew Energy, 10(2):231–4.

[7] Yang, W.-J., Taniguchi, H. & Kudo, K., (1995). Advances in Heat Transfer, Volume 27: Radiative Heat Transfer by the Monte Carlo. London: Academic Press, Inc.

[8] Roeb, M., M. Neises, J-P. Säck, P. Rietbrock, N. Monnerie, J. Dersch, M. Schmitz, C. Satler (2009). Operational strategy of a two-step thermochemical process for solar hydrogen production. International Journal of Hydrogen Energy 34, 4537-4545.

[9] Bulfin. B., Lowe A. J., Keogh., Murphy B. E., Lübben O., Krasnikov S. A. and Shvets I. V. (2013). Analytical Model of CeO_2 Oxidation and Reduction. J Phys Chem. C, 117, 24129 – 24137.

[10] Valdés- Parada, F. J., Romero-Paredes, H., Espinosa-Paredes, G., (2011), “Numerical Simulation of a Tubular Solar Reactor for Methane Cracking,” Int. J. Hydrogen Energy, 36, pp. 3354–3363.

[11] Villafan V. H., Arancibia B. C., Dehesa C. U., Romero P. H. Int. J. Hydrogen Energy 34, 115-124.

[12] Laboratorio Nacional de Sistemas de Concentración Solar y Química Solar Informe. (2010). Informe Técnico Final. http://lacyqs.cie.unam.mx/es/index.php/instalaciones/horno-solar-de-alto-flujo-radiativo.

Simulación y análisis de falla en tubos por los que circula vapor de agua sobrecalentado

S. Maldonado, A. Salazar, H. Terres, M. Gordon, A. Lara*
Departamento de Energía
Universidad Autónoma Metropolitana
México, D.F.
al2112002330@alumnos.azc.uam.mx

***Resumen*—En este trabajo se muestra tanto el estudio como el análisis Termográfico de una falla en dos tubos, para poder asociar el efecto de la falla con la distribución de temperatura y así poder establecer el estado en que se encuentra el tubo. Se realizó el análisis para dos tipos de materiales (acero inoxidable y cobre), por los cuales circula vapor de agua sobrecalentado. Para cada tubo se muestran variaciones en la geometría de la falla con el fin de analizar su comportamiento Termográfico. Para estudiar y analizar cada caso, fue empleando el software ANSYS el cual se basa en el método del elemento finito. Se estudió cada tubo por separado y se analizó la variación de la distribución de temperatura respecto a la profundidad y longitud de la falla, teniéndose como condiciones iniciales la temperatura de la superficie interior y exterior de los tubos. Finalmente, la técnica desarrollada en este trabajo usando el software ANSYS resulta de gran utilidad y generándose así una herramienta computacional para el caso específico de fallas en tuberías.**

Palabras Clave —análisis termográfico; falla en tubos; ANSYS

I. INTRODUCCIÓN

La detección de defectos en tubos sometidos a presión interna es un aspecto poco estudiado. Uno de los problemas a resolver es el modelado de los defectos, en particular los del tipo grieta cerrada. La dinámica de un tubo con un fluido interno a presión implica dificultades adicionales al problema.

Existe un trabajo donde se presentan los principios y las ecuaciones necesarias para poder modelar por el método de los elementos finitos la presencia de una grieta transversal parcial en un tubo de paredes delgadas en varios escenarios: vacío, con un fluido interno y con un fluido a presión [1]. El análisis modal es empleado para determinar los cambios en los parámetros del modelo y valorar la influencia de la grieta en los mismos. El trabajo parte del experimento de S.M. Murigendrappa y S.K. Maiti [2, 3], donde el efecto de la grieta está representado por una reducción de la rigidez a la flexión del tubo en la zona de extensión d, cuya extensión es determinada a partir del concepto de energía potencial de la deformación, planteado por A P. Bovsunovsky y V. V. Matveev [4].

En otro trabajo se presenta un nuevo método para identificar la ubicación y el tamaño de la falla en tuberías, que se basó en el factor de intensidad de tensiones adecuado para la estructura de tubo y en el método de elementos finitos de ondas de segunda generación (SGW-FEM). El trabajo consiste en dispersar una serie de tubos de pared delgada anidados en la estructura de tubería. Al hacer uso del factor de intensidad de tensiones de la tubería de pared delgada, se propone un nuevo método de cálculo de grieta rigidez equivalente a resolver el factor de intensidad de tensiones de la estructura de tubos. Sobre esta base, el método de elementos finitos de ondas de segunda generación se utiliza para establecer el modelo dinámico de la tubería agrietada. Luego se combina el problema directo con problema inverso a fin de establecer el método de identificación cuantitativa de la grieta basado en el cambio de frecuencia, que ofrece una tecnología de ensayos no destructivos con la vibración de la estructura de la tubería. La eficiencia del método propuesto fue verificada por experimentos.

Se ha desarrollado también un estudio basado en la técnica (dc-pd), corriente directa y caída potencial para desarrollar un procedimiento teórico de detección y así identificar la existencia de grietas simuladas en una tubería. Por este procedimiento, tiene que ser calculado de antemano el potencial eléctrico en el tubo pseudo-perfecto por el método de elementos finitos. El factor defecto de influencia propuesto, que se define como la relación entre el potencial eléctrico de la tubería defectuosa dividido por el del pseudo-perfecto, se emplea para revelar el efecto de grietas en el potencial eléctrico. Por lo que se representa los contornos del factor defecto de influencia con la resolución suficiente, no sólo la posición, sino también el tamaño de la forma y la longitud de las grietas en el tubo se pueden identificar con precisión por el criterio de detección ideado en el trabajo. Los tipos de grietas detectables a través de la pared incluyen grieta circunferencial, fisura inclinada, y múltiples grietas.

En este trabajo se realizó un estudio de falla en tuberías para los materiales de acero inoxidable y cobre, se simularon en ANSYS diferentes casos de fallas (longitud y profundidad de la falla) para analizar la distribución de temperatura respecto a éstas.

II. MODELADO

En la parte del modelado, la primera fase se denominada *Pre-Proceso*, donde se realizó la geometría del tubo considerando los datos mostrados en la tabla I para cada caso, cuyas característica de la falla están mostradas en las tabla II para el acero inoxidable y el cobre, respectivamente. Para esto se consideró el modelo SOLID70 definido en el software. En la Fig. 1 se muestra la geometría del tubo de acero inoxidable Caso 1.

TABLA I. CARACTERÍSTICAS DE LOS TUBOS DE ACERO INOXIDABLE Y COBRE

Material	Acero inoxidable Cedula 5	Cobre Tipo L
Bajo norma	ASME B36.19M	ASTM B88
Longitud (m)	1	1
Diámetro nominal (mm)	50	50
Diámetro exterior (mm)	60.3	60.3
Diámetro interior (mm)	57	57

TABLA II. CARACTERÍSTICAS DE LA FALLA

Material	**Acero Inoxidable**		**Cobre**	
	Longitud de la falla (m)	***Profundidad de la falla (m)***	***Longitud de la falla (m)***	***Profundidad de la falla (m)***
Caso 1	0.025	8.25x10-4	0.025	9x10-4
Caso2	0.05	8.25x10-4	0.05	9x10-4
Caso3	0.075	8.25x10-4	0.075	9x10-4
Caso4	0.1	8.25x10-4	0.1	9x10-4

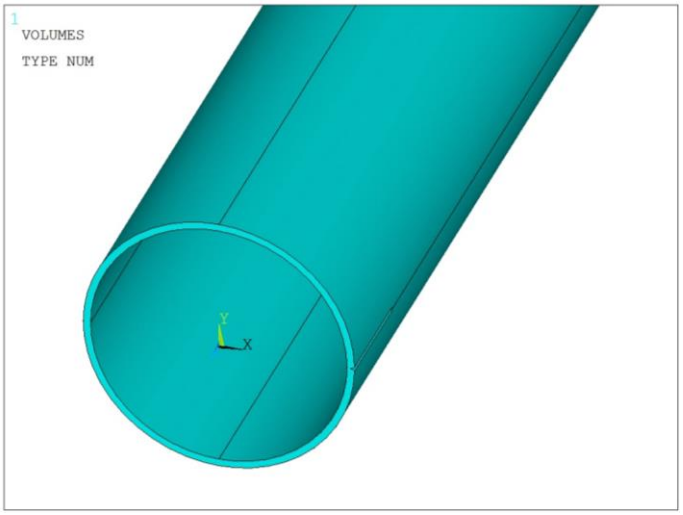

Fig. 1. Geometría del tubo de acero inoxidable, Caso 1

De acuerdo a los requerimientos de ANSYS, se definió la conductividad térmica; 15 (W/mºC) para el acero inoxidable y 380 (W/mºC) para el cobre, de ésta manera se pudo llevar a cabo la discretización del modelo mostrado en la Fig. 2.

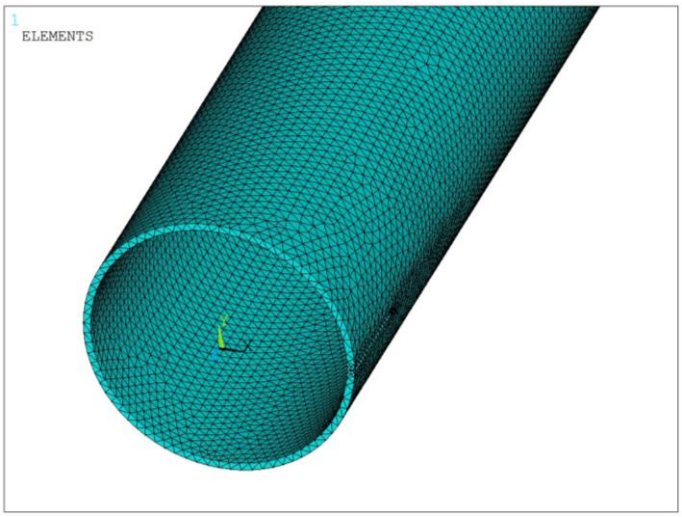

Fig. 2. Discretización del tubo de acero inoxidable, Caso 1

La segunda fase del modelado llamada Proceso, se definieron las condiciones de frontera (aplicación de cargas), para la temperatura ambiente alrededor del área superficial de transferencia de calor y la temperatura interna (temperatura del fluido) para cada geometría, en la Fig. 3 se muestra la aplicación de cargas para la geometría, Fig. 2.

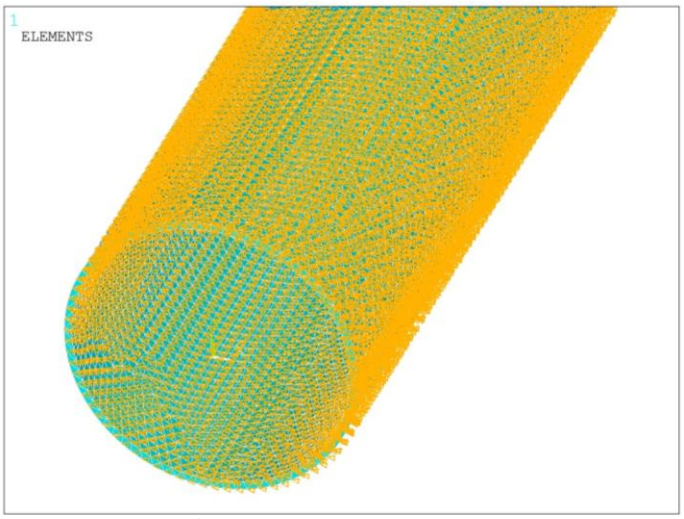

Fig. 3. Condiciones de frontera del tubo de acero inoxidable, Caso 1

En la fase final del modelado conocida como Post-Proceso se generaron los resultados, donde se muestra la distribución de la temperatura en la vista frontal del tubo (espesor) con las condiciones de frontera mencionadas. Las Fig. 4 a 7 muestran la distribución de temperatura del tubo de acero inoxidable y en las Fig. 8 a 11 muestran la distribución de temperatura para el tubo de cobre.

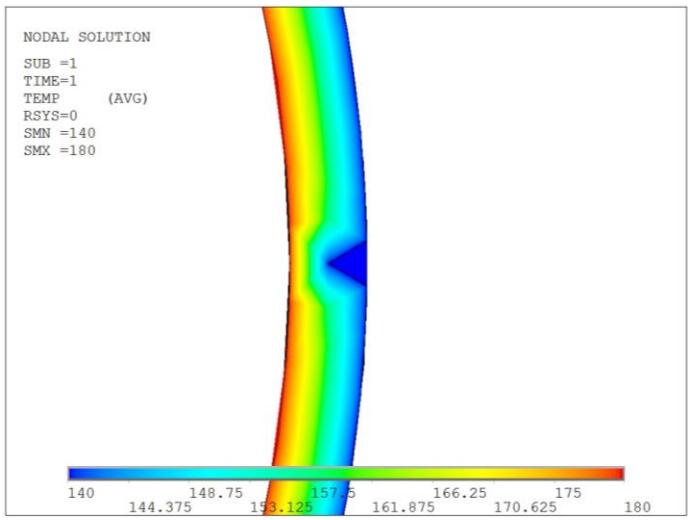

Fig. 4. Caso 1, Distribución de temperatura: tubo acero inoxidable, (°C)

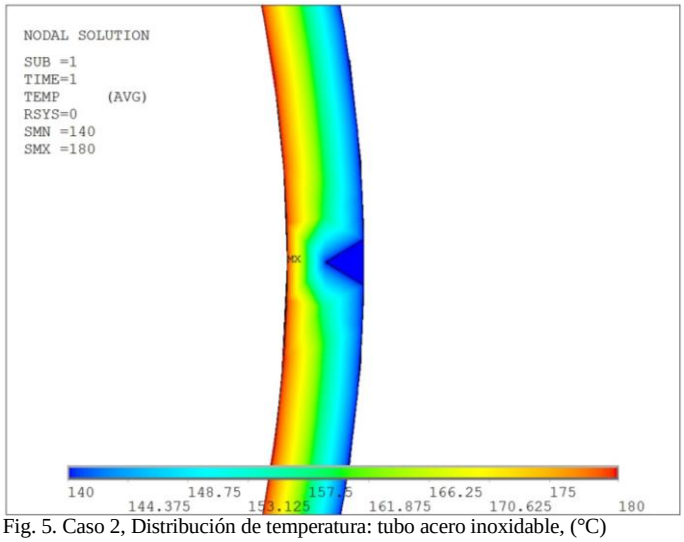

Fig. 5. Caso 2, Distribución de temperatura: tubo acero inoxidable, (°C)

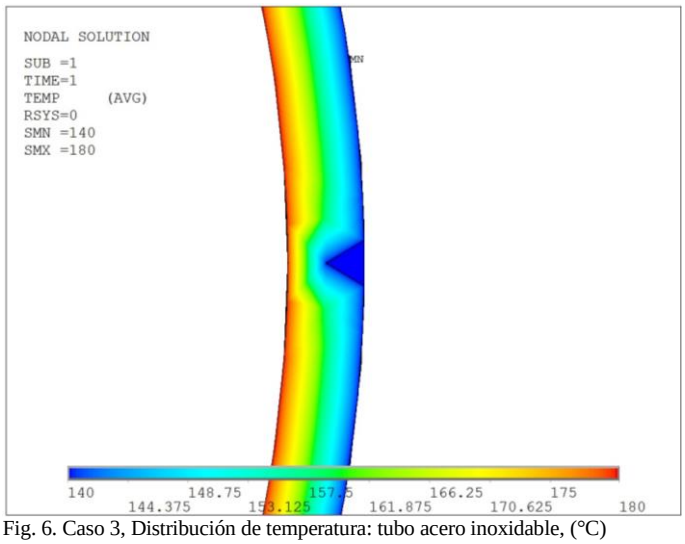

Fig. 6. Caso 3, Distribución de temperatura: tubo acero inoxidable, (°C)

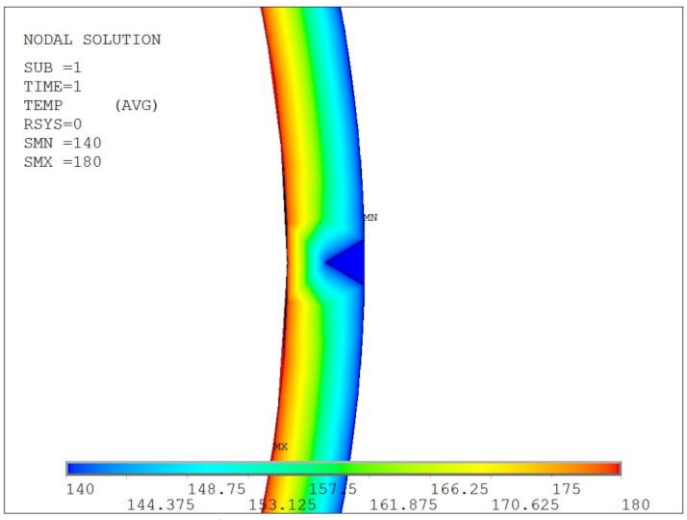

Fig. 7. Caso 4, Distribución de temperatura: tubo acero inoxidable, (°C)

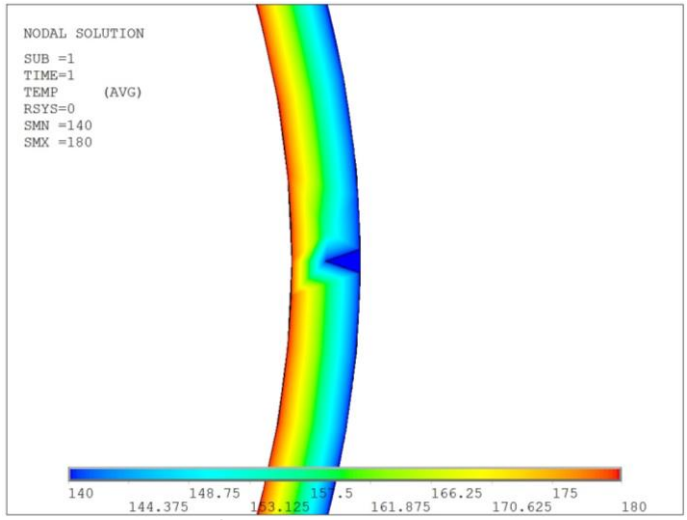

Fig. 8. Caso 1, Distribución de temperatura: tubo de cobre, (°C)

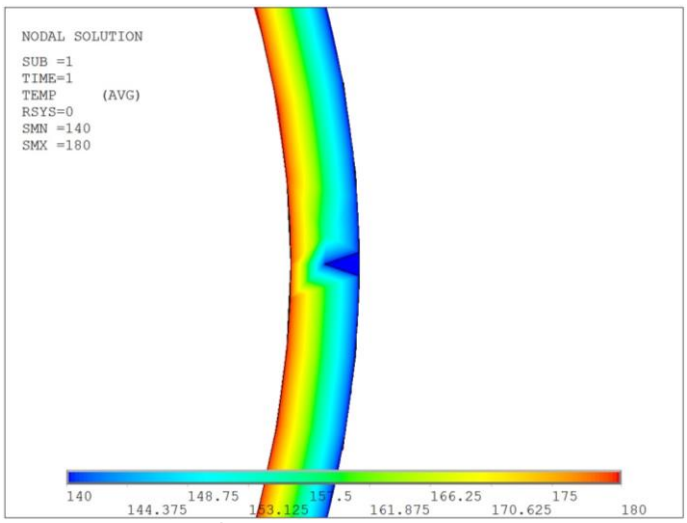

Fig. 9. Caso 2, Distribución de temperatura: tubo de cobre, (°C)

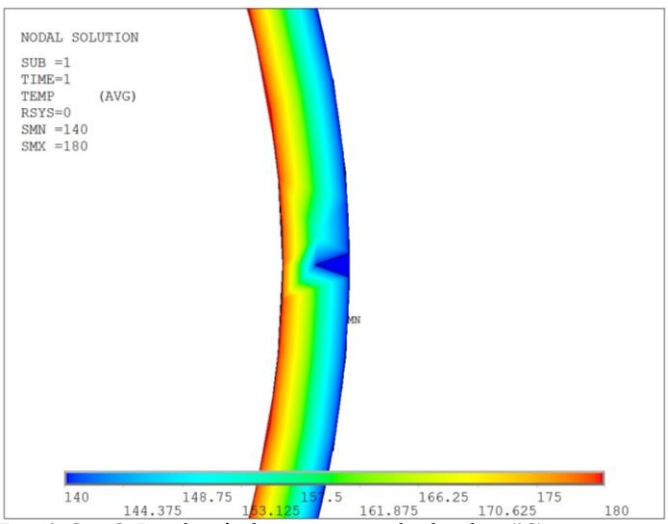

Fig. 10. Caso 3, Distribución de temperatura: tubo de cobre, (°C)

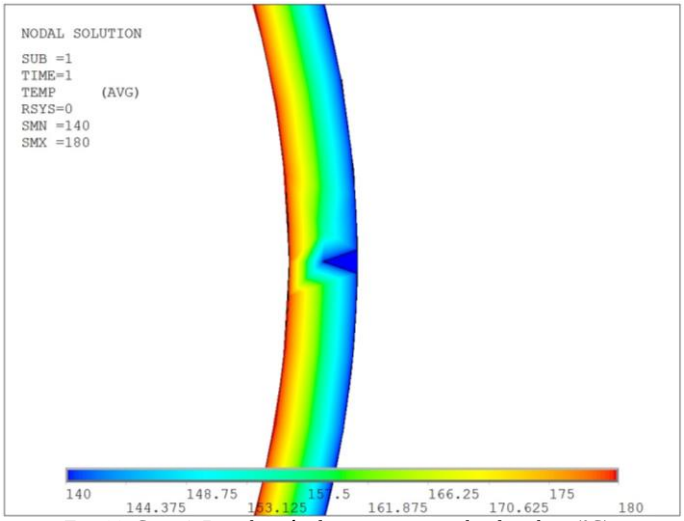

Fig. 11. Caso 4, Distribución de temperatura: tubo de cobre, (°C)

III. Análisis de resultados

Como puede verse en las Fig. 4 a 7 para el caso de falla en el tubo de acero inoxidable, es imperceptible la influencia del daño en el material del tubo. Mucho de esta situación está asociada a las propiedades del material.

La forma de la distribución de temperatura para la falla en el tubo de cobre es diferente que en el caso del tubo fabricado en acero inoxidable, tal y como puede verse en las Fig. 8 a 11. Sin embargo, también no logran apreciarse cambios notorios en la falla en estas figuras.

Se puede establecer que la variación en el comportamiento de la distribución de temperatura, se asocia a las características de los materiales en que se fabrican los tubos.

De acuerdo con las distribuciones generadas se puede apreciar que existe una distinción entre materiales en cuanto a la forma en que se distribuye la temperatura en torno a la falla, ya que en el tubo de acero inoxidable la forma tiene una forma de arco, en el tubo de cobre la forma no tiene este comportamiento.

Es posible notar que la distancia entre el interior del tubo y la punta de la falla, es más cercana en el caso del tubo de cobre, situación distinta que en el tubo de acero inoxidable.

De interés particular es identificar la cercanía de la temperatura en el interior del tubo a la falla, ya que este es el que propicia la inminente fisura y riesgo de fuga a través del material.

IV. Conclusiones

Se presentó un estudio basado en la consideración de la posible falla en tubos elaborados en acero inoxidable y cobre, por los circula vapor.

Los resultados permiten identificar la cercanía de la temperatura interior del tubo hacia la falla simulada, lo que representa un resultado de interés, ya que su aplicación puede orientarse a la interpretación termográfica de fallas, tal y como se logra mediante cámaras termográficas. Sin embrago, la interpretación que puede lograrse mediante cámaras solo refiere a la superficie externa de interés, por lo cual, este trabajo dado un paso adicional, ya que permite la visualización de la falla al interior del material.

Se contemplan trabajos futuros que asocien los resultados termográficos logrados mediante cámaras con los que pueden lograrse mediante software tal y como se hizo en ente empleando ANSYS.

Referencias

[1] F. E. Rodríguez y J. Rodríguez, “Model por elementos finitos de un tubo a presión interna con una grieta transversal parcial”, Ingeniería Mecánica. Vol. 13. No. 3, septiembre-diciembre, 2010, pp. 46-55.

[2] S. M. Murigendrappa, S. K. Maiti and H. R. Srirangarajan, "Experimental and theoretical studyon crack detection in pipes filled with fluid". Journal of Sound and Vibration. 2004. vol. 270, pp. 1013-1032.

[3] S. M. Murigendrappa, S. K. Maiti and H. R. Srirangarajan, "Frequency-based experimental and theoretical identification of multiple cracks in straight pipes filled with fluid". NDT&E International. 2004. vol. 37, nº 6, pp. 431-438.

[4] A. P. Bovsunovsky and V. V. Matveev, "Analytical approach to the determination of dynamic characteristics of a beam with a closing crack". Journal of Sound and Vibration. 2000. vol. 235, nº 3, pp. 415-434.

[5] J. Ye, Y. He, X. Chen, Z. Zhai, Y. Wang and Z. He, “Pipe crack identification based on finite element method of second generation wavelets”, Mechanical Systems and Signal Processing 24 (2010) pp. 379–393.

[6] W. H. Chen, J. S. Chen and H. L. Fag, “A theoretical procedure for detection of simulated cracks in a pipe by the direct current–potential drop technique”, Nuclear Engineering and Design 216 (2002) pp. 203–-211.

Proyecto FEL I sobre la factibilidad de una tecnología sustentable para satisfacer el requerimiento energético en la FIQ de la BUAP

Edgar Carmona Cuevas, Daniel Cruz Gonález, Nancy Tepale Ochoa
Facultad de ingeniería química
Benemérita Universidad Autónoma de Puebla, BUAP
Heroica Puebla de Zaragoza, México
iqcarmona@gmail.com, daniel.cruz@correo.buap, ntepale@hotmail.com.

Celso Moises Bautista Rodríguez
CEO Dirección
Alter Energies Consulting and Research. S.C.
Heroica Puebla de Zaragoza, México
moiseb38@yahoo.fr

***Resumen* – El presente trabajo está dirigido a la evaluación de una tecnología sustentable para satisfacer el requerimiento energético en la Facultad de Ingeniería Química (FIQ) de la Benemérita Universidad Autónoma de Puebla (BUAP). Bajo este contexto la sustentabilidad aparece como un elemento que se define para los objetivos de este trabajo y las tecnologías sustentables como elementos a ser evaluados. La metodología aplicada en este trabajo es el *Front End Loading* (FEL), la cual es una mejor práctica usada para el desarrollo de proyectos. Esta metodología establece la caracterización de la planeación en tres etapas FEL (I, II y III); este proyecto se limita a la etapa FEL I cuyo alcance se basa en una visualización del proyecto a través de un estimado previo del consumo eléctrico de la FIQ en los equipos y aparatos eléctricos de aulas, cubículos, laboratorios, talleres, baños y edificios en general actualmente y a 20 años, seguido de la evaluación de recursos renovables en el municipio de Puebla y en la FIQ, posteriormente se pasa a la selección de la tecnología óptima basada en capacidad, viabilidad previa, costo y sustentabilidad, concepto que incluye lo social, ambiental y económico, finalizando con un estudio de factibilidad de la tecnología seleccionada. La Universidad está trabajando en la conformación de una agenda sustentable que considera los retos actuales y futuros que enfrenta la Institución, se espera que a partir de este proyecto la FIQ contribuya firmemente en este objetivo. En los próximos años la Universidad seguirá creciendo tanto en población como en infraestructura, este trabajo encamina a la BUAP hacía la tendencia mundial en términos de la aplicación de la sustentabilidad y energías renovables.**

***Palabras clave: Sustentabilidad, Energía, Front End Loading,* Tecnología, Proyecto.**

I. INTRODUCCIÓN

El sector energético es una de las varias condiciones para el crecimiento económico de los países debido a la estrecha relación que existe entre el crecimiento del producto interno bruto (PIB) y la demanda de energía de cada país.

Los recursos energéticos se encuentran natural y aleatoriamente distribuidos, debido a lo anterior gran parte de las reservas de petróleo y gas natural (los principales combustibles actualmente) a nivel mundial se ubican en unos pocos países, esto genera problemas que se ven reflejados en las constantes fluctuaciones en el precio de los combustibles fósiles (carbón, gas y petróleo); que no solo es por su extracción, distribución, refinación y comercialización; sino también por complicaciones de tipo geopolítico [1].

La producción de electricidad a partir de combustibles fósiles constituyó aproximadamente el 65% de la generación de energía mundial al cierre de 2011. En el año 2010, esta cifra aún era reportada como el 80%.

A nivel global el carbón sigue siendo preponderante en la producción de electricidad, sin embargo, la creciente demanda de electricidad "limpia" ha puesto a las energías alternativas como una seria competidora, ya que el acceso a la electricidad tiene un enorme impacto social, económico y ambiental. La fig. 1 muestra el consumo de energía eléctrica mundial per cápita, es decir, por persona.

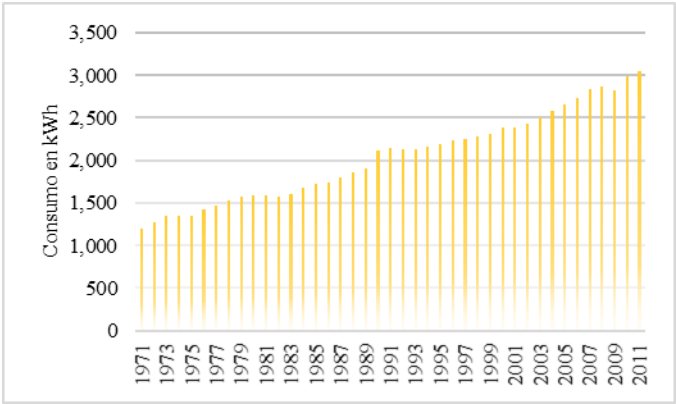

Fig. 1. Consumo de energía eléctrica mundial (kWh per cápita).

Mundialmente se espera que la participación global de generación de electricidad a partir de energías alternativas (todas aquellas diferentes a los combustibles fósiles) aumente alrededor del 34% en el año 2030. Oliveira y Campos [2] con el uso de dos de las herramientas de previsión tecnológica, es decir, la curva logística (técnica cuantitativa) y la técnica *Delphi* (técnica cualitativa), estimaron la participación de las

principales energías para la generación de electricidad en un determinado periodo, como se muestra en la fig. 2.

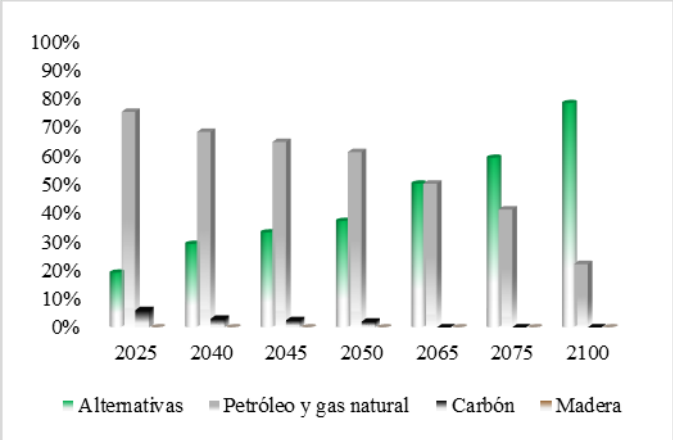

Fig. 2. Participación de las principales energías para la generación de electricidad.

Actualmente Norte América es la principal zona consumidora de electricidad, como es posible apreciar en la fig. 3, pero una gran proporción de la demanda de energía resulta del rápido crecimiento de las economías asiáticas.

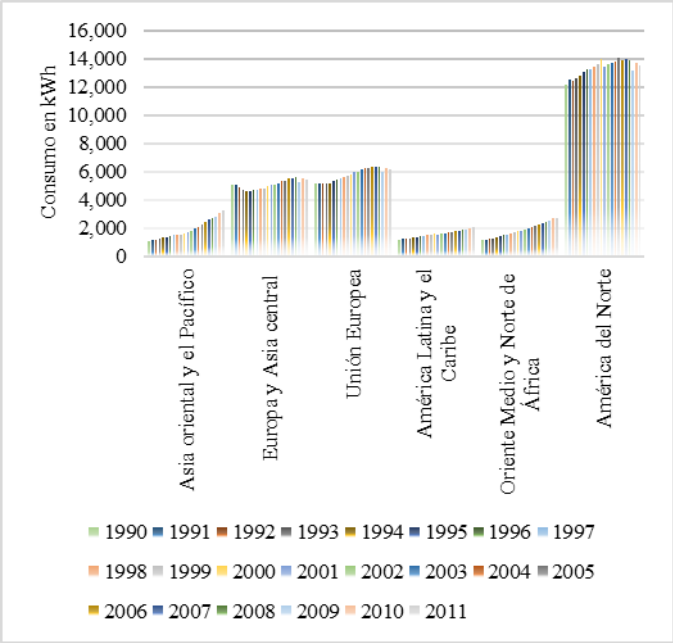

Fig. 3. Consumo de energía eléctrica por zonas (kWh per cápita).

Por su parte América Latina y el Caribe funge como una zona de poco consumo eléctrico pero de con alto potencial de generación. En esta zona se encuentra México, país que ocupa el noveno lugar en el mundo de reservas de petróleo, cuarto en reservas de gas natural en América y tiene un enorme potencial en fuentes de energía renovables como: solar, eólica, biomasa, energía hidroeléctrica y geotérmica [3].

El Centro de Investigación para el Desarrollo, A. C. (CIDAC) define a la seguridad energética como la capacidad que tienen los países para acceder a la energía a precios competitivos con el fin de que esto sea un motor y no un freno del crecimiento y desarrollo económico. Según la Secretaría de Energía (SENER), de 2000 a 2011, la sociedad mexicana incrementó su consumo de energía a una tasa promedio anual de 2.08%. Por el contrario, la producción de energía primaria disminuyó a una tasa anual de 0.3% como se muestra en la fig. 4. De acuerdo a este escenario, para 2020 México se convertirá de un país exportador a uno importador de energía.

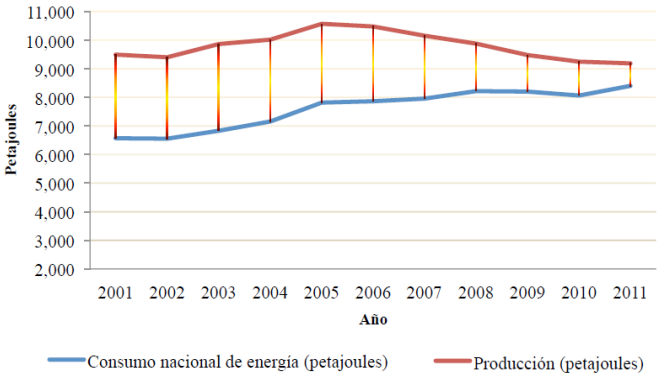

Fig. 4. Cierre de brecha entre el consumo y la producción nacional de energía.

A lo largo de las últimas dos décadas se han planteado interrogantes acerca de la creciente escasez de los recursos de combustibles fósiles y el inminente cenit del petróleo. Debido a esto México siendo un país petrolero no puede garantizar su abasto de energía si las principales empresas de producción y generación de energéticos, es decir, Petróleos Mexicanos (PEMEX) y Comisión Federal de Electricidad (CFE), mantienen una simbiosis con el Estado y su operación queda en función de objetivos políticos a corto plazo.

De ahí que la reforma energética impulsada por el presidente Enrique Peña Nieto y aprobada en lo general y en lo particular por la cámara de diputados y senadores en agosto de 2014, tenga como finalidad atraer inversiones y modernizar el sector energético mexicano. La propuesta de ley de la industria eléctrica, presentada por el Ejecutivo al Senado es un nuevo paradigma del sector eléctrico en México. Los desarrolladores de energías renovables y de electricidad en general se han topado con un gran problema: la falta de capacidad de transmisión, la calidad de transmisión y, sobre todo, la manera de acceder a ella por parte de los nuevos proyectos [4].

A través del Sistema de Información Energética (SIE), la SENER da a conocer la producción de energía en México presentada en la fig. 5, en función de sus principales fuentes primarias cuya información es en una base de datos alimentada por las empresas, comisiones e institutos que forman el sector energético en México, así como por la propia SENER.

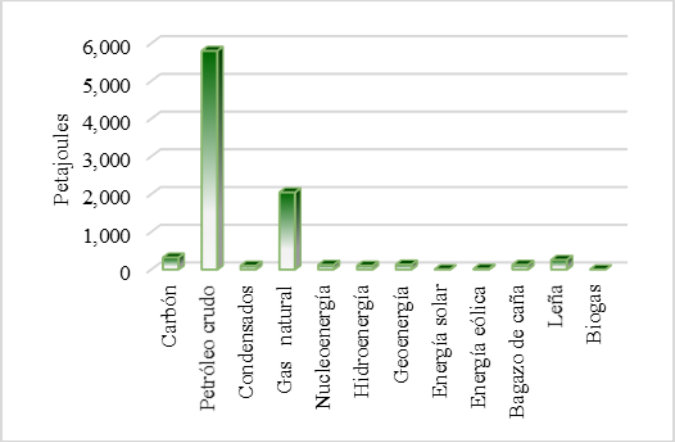

Fig. 5. Producción de energía primaria en México durante 2013.

Como se puede observar gran parte de la producción de energía se basa en combustibles fósiles los cuales abarcan más del 91% de la producción de energía en México, siendo preponderantes el petróleo y el gas natural. La producción de energía es una de las actividades económicas más importantes de México la cual contribuye al 3% del PIB. La comercialización de petróleo representa el 8% de las exportaciones totales, y los impuestos relacionados con el petróleo representan el 37% del presupuesto federal, donde alrededor del 56.5% de toda la inversión pública se dirige a proyectos de energía. Las empresas públicas en los sectores del petróleo y de la energía tienen una plantilla aproximada de 250,000 trabajadores [3] sin incluir contratistas externos.

México es un país en desarrollo en donde el aumento de la población es un foco de atención por su estrecha relación con el consumo eléctrico el cual prácticamente ha sido cuadruplicado en cuarenta años, y conforme la población urbana aumente la tendencia permanecerá a la alta, es posible apreciar lo anterior a través de la fig. 6.

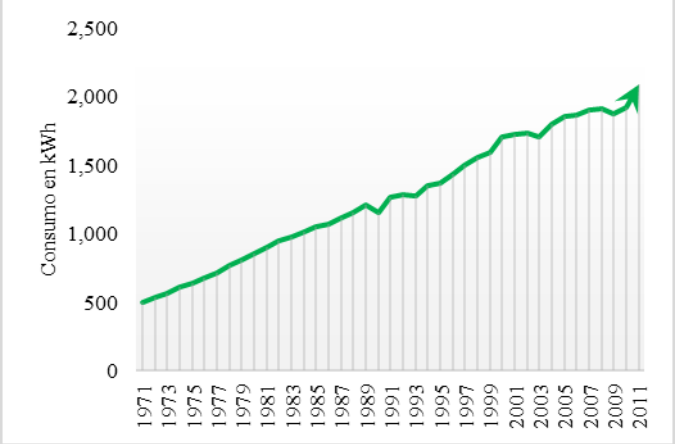

Fig. 6. Consumo de energía eléctrica per cápita en México.

Al igual que otros países del mundo, México experimentó importantes reformas en el sector de la energía en los segmentos de gas y petróleo durante la década de 1990. Estas reformas fueron impulsadas por la creencia ideológica, las presiones presupuestarias y el deseo de aumentar la eficiencia y atraer capital privado.

En términos de generación de electricidad, México ocupa el décimo sexto en todo el mundo, y la CFE es la sexta compañía de electricidad más grande en el mundo. La cobertura de electricidad alcanza el 95% de la población nacional, una de las tasas de cobertura más altas de América Latina [3].

La generación de electricidad en México está dominada por las termoeléctricas (a través de combustibles fósiles) y es seguido por las fuentes de energía renovables, la fig. 7 muestra la generación bruta de energía por el tipo de tecnología, con datos del SIE, CFE y la ahora extinta Luz y Fuerza del Centro (LyFC).

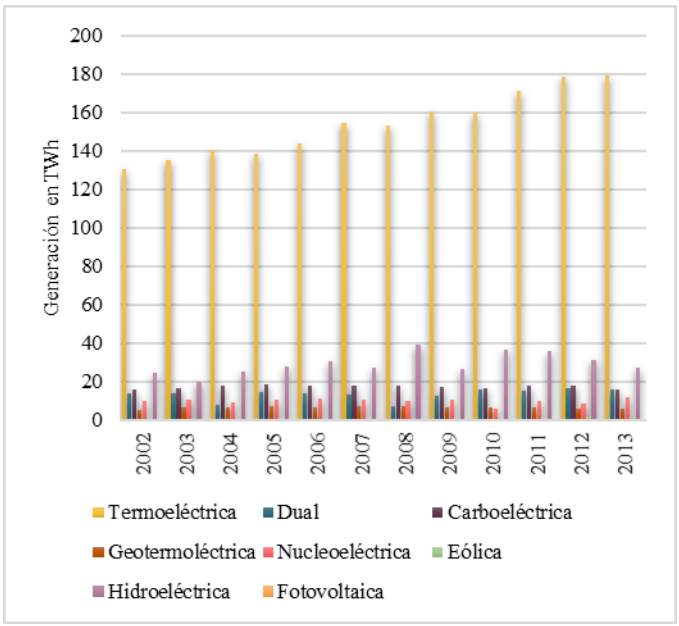

Fig. 7. Generación bruta de energía eléctrica por tecnología.

La generación de energía a partir de Fuentes de Energía Renovables (FER) se incrementó de 26 TW en 2003 a 46 TW en 2008 y disminuyó a 34 TW en 2013 como se observa en la fig. 8.

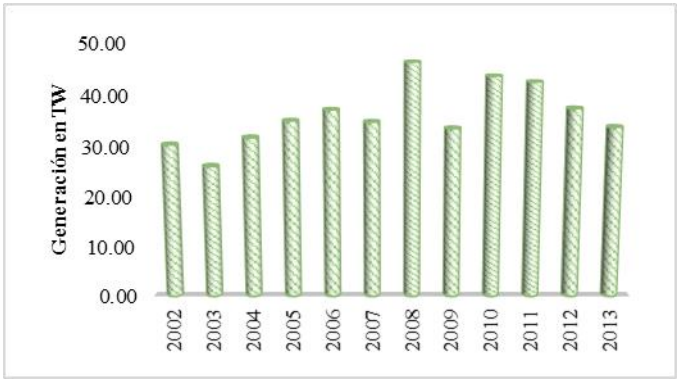

Fig. 8. Generación bruta energías renovables.

La contribución a la generación de energía en general de las FER se ha mantenido estancada, con un promedio de 22% frente al 78% de las energías convencionales. A continuación, en la fig. 9, se muestra la contribución de las diversas FER con respecto al 22% de la generación total en México que la CFE y la Comisión Reguladora de Energía (CRE) reportan.

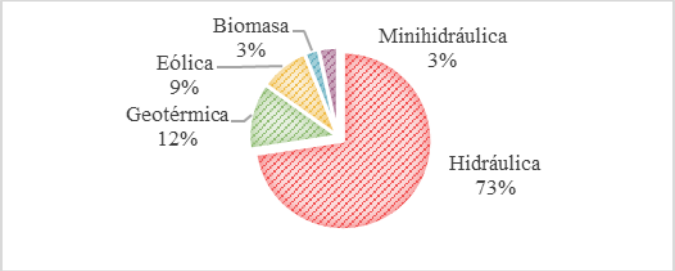

Fig. 9. Generación de energía eléctrica renovable.

En cuanto a la capacidad instalada de energía, el Inventario Nacional de Energía Renovables (INER) informa que las energías convencionales mantienen la evidente supremacía con un 74% frente al 26% de las FER, de ese porcentaje de energías renovables en la fig. 10 se presenta su capacidad instalada:

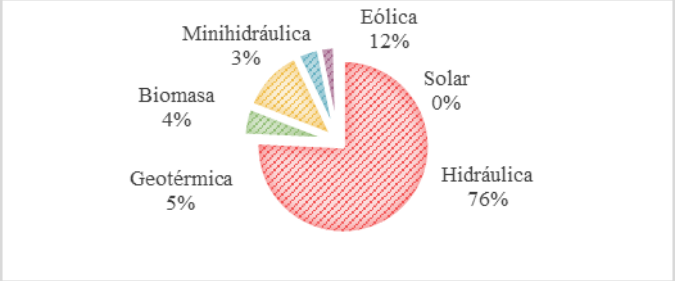

Fig. 10. Capacidad instalada de energía eléctrica renovable.

México se encuentra en un punto de inflexión con respecto a sus recursos energéticos, hasta hace poco no se tenía problemas porque el costo de extraer combustibles fósiles era mucho menor que el gasto de energía, pero esto está cambiando, se debe viajar más lejos a mares profundos, arriesgarse a conflictos internacionales, desastres ecológicos y las fluctuaciones económicas.

El país tiene que estar preparado para afrontar estos cambios a nivel mundial, por ello es fundamental abordar el desarrollo tecnológico de las energías renovables en el marco de la discusión de la reforma energética con una visión de largo plazo que procure, desde hoy y para el mañana, mejores oportunidades para lograr el desarrollo sustentable del país en beneficio de los mexicanos.

II. PLANTEAMIENTO DEL PROBLEMA

En cuanto a los recursos de energía renovable identificados con anterioridad para México, es menester tener en cuenta que no todos ellos estarán disponibles y serán económicamente viables en toda la república mexicana. El Inventario Nacional de Energías Renovables (INER) de la SENER contiene una aplicación de navegación que brinda información sobre los recursos energéticos renovables en el país.

Con el apoyo de esta plataforma se puede tener un dato certero del tipo de centrales de generación eléctrica a partir de energías renovables existen por ejemplo en el estado de Puebla, y que se muestra en la fig. 11:

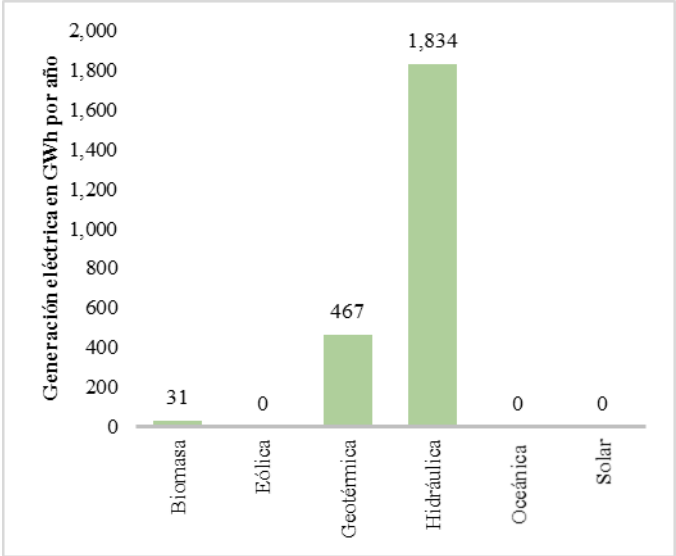

Fig. 11. Generación de electricidad a partir de energías renovables en el estado de Puebla.

A nivel local el municipio de la Heroica Puebla de Zaragoza (capital del estado) o simplemente municipio de puebla, es un beneficiario de este tipo de centrales pero no genera a gran escala algún tipo de energía renovable, más sin embargo, la misma plataforma del INER contiene una herramienta que muestra el potencial de aprovechamiento de este tipo de energías.

La tabla 1 muestra las alternativas energéticas renovables en México, estado de Puebla y municipio de Puebla.

TABLA 1. ALTERNATIVAS ENERGÉTICAS RENOVABLES EN MÉXICO, ESTADO DE PUEBLA Y MUNICIPIO DE PUEBLA.

	Alternativas renovables usadas en México	**Alternativas renovables usadas en el estado de Puebla**	**Alternativas potenciales renovables en el municipio de Puebla**
Eólica	✓		✓
Solar	✓		✓
Hidráulica	✓	✓	
Biomasa	✓	✓	✓
Geotermia	✓	✓	✓
Oceánica			

Tanto gobierno municipal como la ciudadanía, empresas, oficinas y escuelas en el municipio de Puebla han adoptado tecnologías a pequeña escala a base de energías renovables para autoabastecimiento eléctrico. A una escala aproximada de la Facultad de Ingeniería Química (FIQ) de la Benemérita

Universidad Autónoma de Puebla (BUAP) es necesario analizar a más detalle los recursos renovables disponibles en el municipio de puebla, considerando criterios como la sustentabilidad la cual, como se mencionó en el capítulo anterior, es un aspecto basado en tres pilares: económico, ambiental y social.

Cada día la investigación, el desarrollo y aplicación de tecnologías a base de energías renovables para satisfacer la demanda energética se ha intensificado. La responsabilidad de desarrollar e implementar este tipo de tecnologías no es solo de los gobiernos o de las grandes empresas e industrias, la participación de la sociedad civil es indispensable. Ante este contexto la necesidad de estudiar la factibilidad y aplicación de tecnologías sustentables que puedan satisfacer los requerimientos energéticos de un determinado sector de la sociedad es imprescindible. Los centros de estudios como las universidades forman parte fundamental de la sociedad y como tal, son una comunidad que tiene un conjunto de necesidades, entre ellas, las energéticas. La BUAP está en constante crecimiento al igual que sus facultades, como la FIQ donde su matrícula de alumnos, personal de apoyos y en particular, su personal académico han ido en aumento como se observa en la Fig. 12.

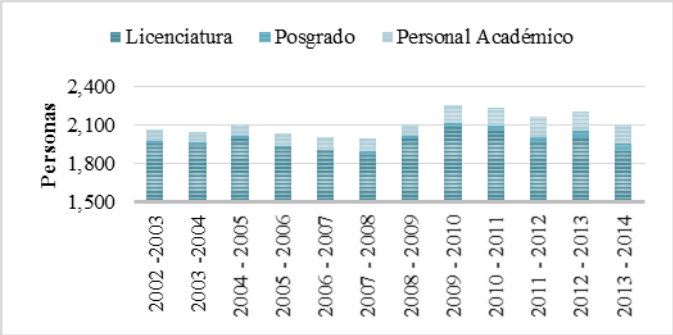

Fig. 12. Población FIQ-BUAP 2002 – 2014.

El aumento de personal académico (83% con respecto a 2002-2003) y alumnos ha generado un incremento en aulas, laboratorios, cubículos para profesores y la adquisición de equipos para la investigación.

En los últimos años se han adaptado o construido laboratorios y edificios como se muestra en la tabla 2.

TABLA 2. INSTALACIONES DE LABORATORIOS Y EDIFICIOS MÁS RECIENTES.

Año	Instalación
2001	Laboratorio de alimentos 106 C /104
2007	Laboratorio de procesamiento de residuos sólidos
2010	Laboratorio de biocombustibles
2012	Edificio 106 H de aulas y cubículos

Todos ellos demandan una cantidad de recursos energéticos debido a iluminación y servicios pero, en mayor medida, a los equipos que los laboratorios manejan. Ante la construcción del edificio 106 H la pasada administración de la FIQ actualizó su estación de transmisión de energía eléctrica (con una capacidad de 225 kVA) y la actual administración modernizó su instalación perimetral.

De acuerdo con Arzate (2011), los edificios son los responsables de 72% del consumo de electricidad; 39% de las emisiones de bióxido de carbono y 13.6% del consumo de agua potable; 25% de la madera cosechada, 30% de los desperdicios sólidos y 20% del agua contaminada. Actualmente los edificios e instalaciones de la FIQ cuentan con un sistema de suministro de energía eléctrica tradicional, con la problemática principal de no tener una dato certero y mucho menos un histórico de su consumo eléctrico, en la zona perimetral de la facultad no hay medidores de consumo y la BUAP, de la misma forma, no cuenta algún dato particular de la FIQ con respecto a su consumo. Este trabajo de tesis presenta además de la propuesta de la tecnología sustentable, una importante y primera base de datos para futuros estudios energéticos, de infraestructura o de conocimiento general.

III. MARCO TEÓRICO

Los proyectos en las organizaciones se originan de un proceso de planificación. La planificación consiste en definir las metas de la organización, establecer una estrategia general para alcanzarlas y trazar planes exhaustivos para integrar y coordinar el trabajo de la organización [5]. Debido a lo anterior, se puede decir que un proyecto es una planificación, un conjunto de actividades coordinadas e interrelacionadas con la finalidad de alcanzar objetivos específicos en tiempo y forma, o como lo define el *Project Management Institute* (PMI):

"Un esfuerzo temporal que se lleva a cabo para crear un producto, servicio o resultado único" [6].

Temporal significa que cada proyecto tiene un comienzo y un final definidos en el tiempo. El final se alcanza cuando se han logrado los objetivos principales del proyecto o cuando queda claro que los objetivos del proyecto no serán o no podrán ser alcanzados.

Dentro de un proyecto, puede distinguirse distintas etapas. En principio surge una idea, que establece la necesidad u oportunidad a partir de la cual se diseña el proyecto, luego en la etapa del diseño propiamente dicha, se realiza una valoración de las opciones y estrategias a seguir, con el objetivo a cumplir como guía; finalmente llega el momento de la ejecución y, una vez finalizada, se realiza la evaluación. Esto puede resumirse en cuatro etapas distintas: conceptualización, planificación, ejecución y culminación.

Otro concepto importante en la administración, dirección y ejecución de proyectos son las buenas prácticas. En proyectos, una buena práctica es toda aquella actividad que minimice los errores o desviaciones en toda la cadena de valor. Cuando una buena práctica funciona para varias actividades se convierte en una mejor práctica.

Por su parte el *Front End Loading* o FEL, término acuñado por la compañía DuPont hace más de 20 años, es una metodología para el desarrollo de proyectos que se basa en el concepto de aprobación por compuertas a través de las cuales se desarrollan suficiente información estratégica para identificar riesgos y comprometer recursos con el fin de maximizar el éxito del proyecto. El FEL es una mejor práctica, es decir, una metodología probada y que ha dado resultados satisfactorios.

Todas las definiciones FEL tienen una sola esencia: planear para reducir riegos, es decir, ir progresivamente y no realizar todo de una vez. Dicha metodología establece la división de la planeación en tres etapas FEL: visualización (FEL I), conceptualización (FEL II) y definición (FEL III) al final de las cuales se encuentran las compuertas de aprobación.

Los países se distinguen no solo por su historia, sino por sus proyectos y en los últimos años, los profesionales de proyectos, los dueños de negocios y los de la construcción, han comenzado a apreciar el impacto positivo que el FEL puede lograr en los resultados de los proyectos, incorporando esta metodología a todo tipo de proyectos posibles.

IV. RESULTADOS Y DISCUSIÓN

La FIQ de la BUAP no cuenta con medidores de energía eléctrica y por tanto no hay un historial de consumo. Ante tal situación un estimado de requerimiento energético a base de la contabilización de los equipos eléctricos con los que cuenta la FIQ fue necesario. Algunos datos presentados a continuación fueron obtenidos a través de la Unidad de Transparencia y Acceso a la Información de la BUAP y el DGO, los cuales proporcionaron el número de equipos de cómputo oficiales registrados y la cantidad de luminarias internas de los edificios y una fracción de las luminarias externas de la FIQ. Sin embargo gran parte del trabajo fue a través de la contabilización *in situ* de los equipos eléctricos en las oficinas, cubículos, laboratorios y edificios en general. La fig. 13 muestra el número de equipos y luminarias contabilizadas en la FIQ.

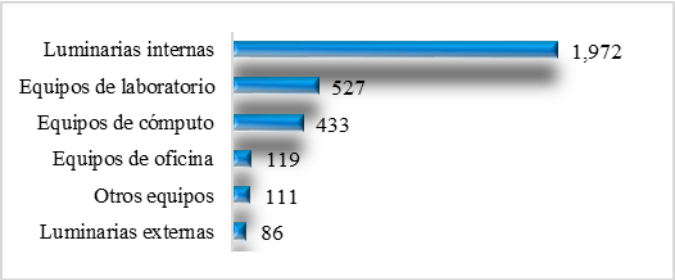

Fig. 13. Número de equipos eléctricos y luminarias en la FIQ.

Sin otro dato certero, en esta etapa FEL I del proyecto se toma como dato de referencia la potencia nominal de los equipos eléctricos para obtener una cifra estimada de la potencia requerida en la facultad. En la fig. 14 se muestra la potencia (nominal) estimada en seis categorías: equipos de laboratorio, de oficina, luminarias, equipos de cómputo y otros equipos; este último contempla electrodomésticos en su mayoría.

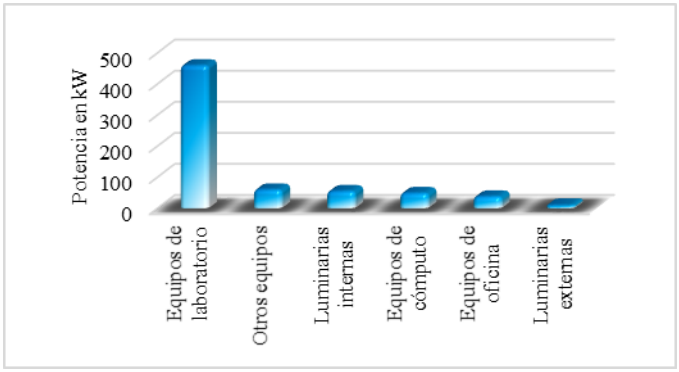

Fig. 14. Potencias estimadas de los equipos eléctricos en la FIQ.

En la fig. 15 se presenta la suma total de la potencia de los 3,248 equipos eléctricos y luminarias de la FIQ (cuantificados) bajo el rubro de "requerimiento nominal" el cual representa 679.762 kW (redondeados en 680 en la gráfica). Este dato no incluye a los posibles equipos eléctricos almacenados, luminarias no oficiales, laptops, celulares y pequeños equipos eléctricos que tanto los alumnos, personal académico y de apoyo, que puedan traer consigo, de la misma forma los equipos hidroeléctricos de la facultad. Debido a esto se agrega un 20% como factor de seguridad al requerimiento nominal dando consigo 815.714 kW (816 redondeado) y que en figura se muestra como el "requerimiento estimado".

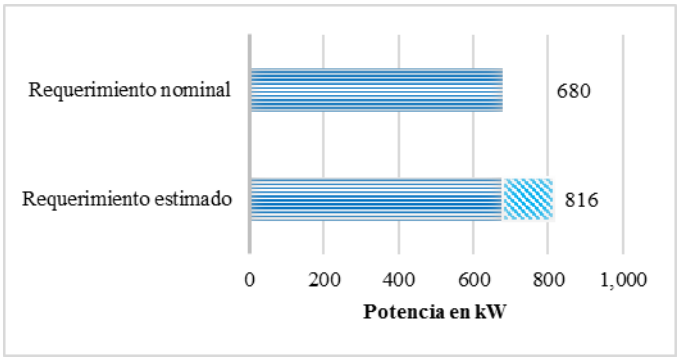

Fig. 15. Potencia requerida nominal y estimada en la FIQ.

Los proyectos a base de energías renovables se estiman con un ciclo de vida de alrededor de 20 años, es decir, el tipo de energía y su tecnología implicada debe cubrir ese periodo como mínimo. De tal forma que se debe proveer posibles expansiones, construcciones de nuevos edificios e incluso aumento de población en la FIQ. Este último será el dato de referencia para el estimado a 20 años, siendo la población el consumidor de energía y la pauta para posibles expansiones estructurales. Dado lo anterior, la fig. 16 muestra una gráfica de dispersión sobre la tendencia en el aumento de población de la FIQ.

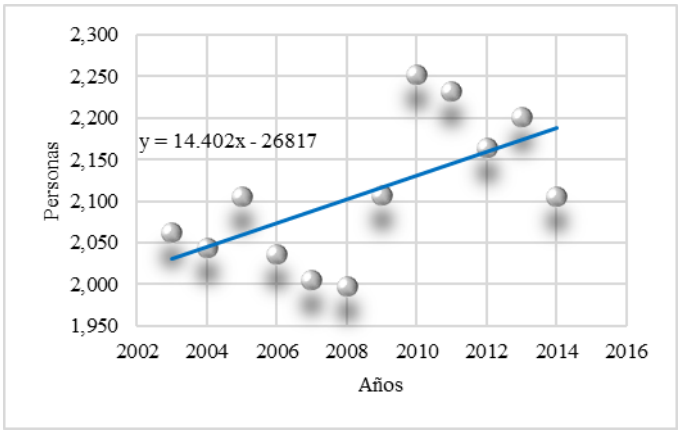

Fig. 16. Ecuación de la recta y línea de la tendencia de población la FIQ.

Con la propia función y los datos de población de la FIQ es posible reportar un estimado de la población a 20 años (véase tabla 3):

TABLA 3. POBLACIÓN DE LA FIQ EN 20 AÑOS.

Año	Población
2003	2,063
2004	2,044
2005	2,105
2006	2,036
2007	2,005
2008	1,997
2009	2,107
2010	2,252
2011	2,232
2012	2,164
2013	2,201
2014	2,105
:	:
2034	**2,477**

Finalmente se puede estimar el consumo energético con los siguientes resultados de la tabla 4:

TABLA 4. REQUERIMIENTO ENERGÉTICO ESTIMADO A 2034 EN LA FIQ.

Población en 2034	Requerimiento energético	Requerimiento energético estimado a 20 años
2,477	961.076 kW	**1 MW**

En la actualidad existen dos grupos de tecnologías diferentes para la generación eléctrica a partir de la radiación solar. El primer grupo es el de las tecnologías fotovoltaicas (FV), el cual consiste en transformar directamente la radiación solar en electricidad y que la fig. 17 muestra en clasificación.

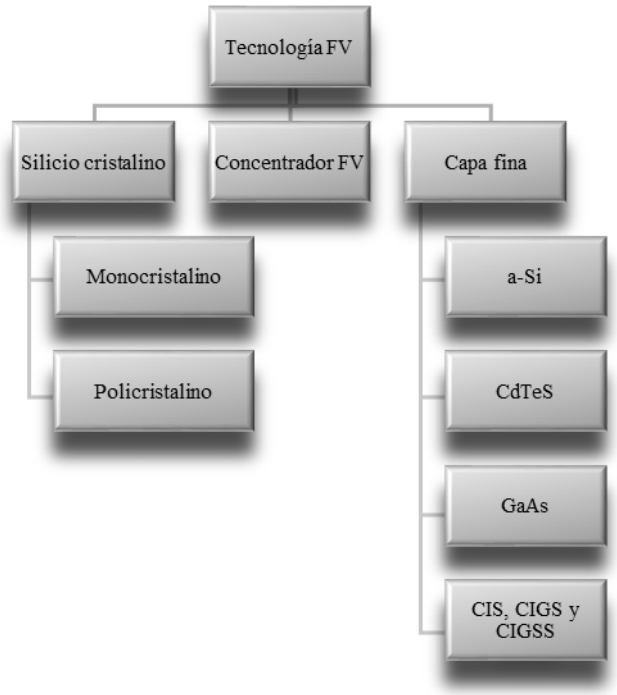

Fig. 17. Clasificación de las tecnologías FV.

El segundo grupo es el de las tecnologías solar termoeléctricas (STE), las cuales se basan en emplear la radiación solar en energía térmica para después convertirla en electricidad se resumen en la fig. 18.

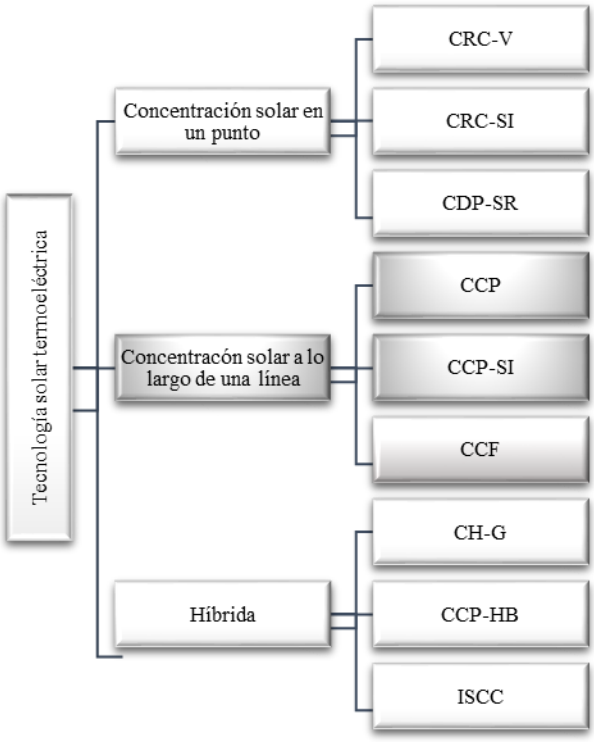

Fig. 18. Clasificación de las STE.

En donde:

- Centrales de concentrador cilíndrico-parabólico (CCP)
- Centrales de concentrador cilíndrico-parabólico con almacenamiento térmico utilizando sales inorgánicas (CCP-SI)
- Centrales de concentrador lineal Fresnel (CCF)
- Centrales de receptor central con generación directa de vapor (CRC-V)
- Centrales de receptor central con sales inorgánicas fundidas (CRC-SI)
- Centrales de disco parabólico equipados con motor Stirling (CDP-SR)
- Centrales híbridas (CCP, CCF, CRC) con caldera de gas (CH-G)
- Centrales de concentrador cilíndrico-parabólico hibridadas con biomasa (CCP-HB)
- Centrales de concentrador cilíndrico-parabólico hibridadas con centrales de ciclo combinado o Integrated Solar Combined Cycle (ISCC).

Con un área aproximada de 20,243 m^2 netos ocupado por la FIQ y un requerimiento estimado de 1 MW, es posible empezar a comparar las tecnologías. A continuación en la tabla 5 se presentan las especificaciones y ponderación de los factores que se consideran claves para una tecnología solar adecuada en la FIQ.

TABLA 5. FACTORES CLAVES DE SELECCIÓN.

Número de referencia	Especificación	Ponderación
1	Espacio requerido	20%
2	Costo aproximado	15%
3	Eficiencia	15%
4	Madurez de la tecnología	20%
5	Impacto ambiental	10%
6	Capacidad de almacenamiento energético	10%
7	Complejidad de la tecnología	10%
	Total	**100%**

Finalmente la fig. 19 muestra el resultado de la evaluación de las tecnologías:

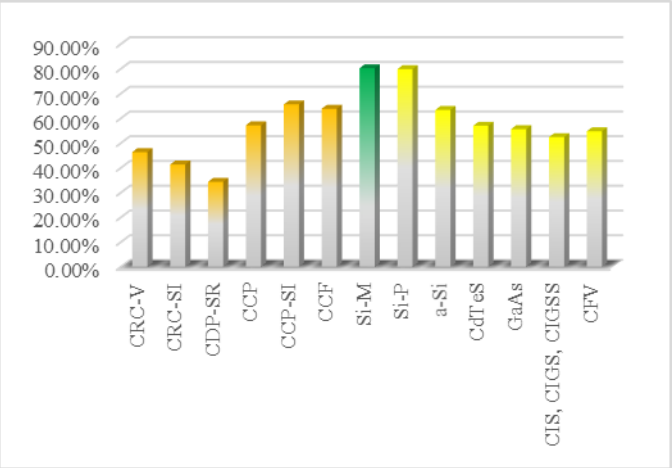

Fig. 19. Acumulado porcentual de la evaluación de las tecnologías.

Con un 80.26% la tecnología solar FV a base de paneles solares de silicio monocristalino supera ligeramente a la FV de silicio policristalino (79.90%), seguido de las CCP-SI (65.65%) y CCF (63.88%). Las tecnologías de silicio cristalino FV lograron imponerse muy ligeramente frente a las STE las cuales en su mayoría se encuentran aún en plantas piloto que en ocasiones se apoyan de combustible fósil para mantener las temperaturas de depósito para sales fundidas.

La tecnología seleccionada será sometida a un estudio de factibilidad que entregará los aspectos económicos y financieros necesarios para la etapa FEL I.

REFERENCIAS

[1] World Energy Council (2013, octubre). Recursos energéticos mundiales. Recuperado de: http://www.worldenergy.org/publications/

[2] Oliveira, J. y Campos, T. (2003). Construção de Cenários Futuros para as Fontes de Energia Primária. Disertación doctoral no publicada, University of Beira Interior, Covilhã, Portugal.

[3] Alemán, G., Casiano, V., Cárdenas, D., Díaz, R., Scarlat, N., Mahlknecht, J., Dallemand, J., Parra, R. (2014). Renewable energy research progress in Mexico: A review. Renewable and Sustainable Energy Reviews, 32, 140 – 153.

[4] Renée, C. (2014, Julio). ¿Estamos listos para la Ley de la Industria Eléctrica? energíahoy, p. 26.

[5] Oliveros, M., Rincón, H. (2010). Gestión de costos en los proyectos: un abordaje teórico desde las mejores prácticas del Project Management Institute. Visión gerencial, Año 10, N° 1, Enero - Junio 2011, p. 85-94.

Estudio numérico del comportamiento térmico de superficies extendidas con variaciones en sus secciones transversales y materiales

S. Maldonado, A. Salazar, H. Terres, M. Gordon, A. Lara*
Departamento de Energía
Universidad Autónoma Metropolitana
México, D.F.
al2112002330@alumnos.azc.uam.mx

***Resumen*—Las superficies extendidas, también conocidas como aletas, son de uso común en la práctica para mejorar la transferencia de calor. Estas incrementan la velocidad de la transferencia de calor desde una superficie al exponer un área más grande a la convección y la radiación. Se realizó el análisis térmico de diferentes tipos de aletas (cuadrada, circular y triangular), cada uno de estos análisis se llevó a cabo con tres materiales diferentes (cobre, aluminio y acero). Se determinó la distribución de temperatura de cada uno de los casos, considerando los materiales propuestos. Se propusieron las dimensiones de las aletas buscando que el área superficial en estas fuera prácticamente la misma y manteniendo las demás variables constantes (longitud y temperaturas aplicadas). De esta manera, la única diferencia la constituye el tipo de sección transversal, teniéndose así, un parámetro distintivo en la determinación de la mejor superficie extendida para disipar calor. Este trabajo se resolvió con la ayuda del software "ANSYS". Se obtuvo la distribución de temperatura a lo largo de las aletas, lo que permitió identificar a la aleta más funcional que es la que tiene una sección transversal circular y material de cobre respecto a la menor que es la que tiene una sección transversal triangular con material de acero. Este tipo de trabajo resulta importante para estudiar casos de la transferencia de calor y su flujo en aletas.**

Palabras Clave— Aletas; Convección; Sección transversal; Distribución de temperatura

I. INTRODUCCIÓN

Cuando a las superficies ordinarias de transferencia de calor se le añaden piezas adicionales de mental, estas últimas extienden la superficie disponibles para propiciar aumento o disminución de la transferencia de calor. Mientras que las superficies extendidas aumentan la transmisión total de calor, su influencia como superficie se trata de una manera diferente de la simple conducción y convección.

En las tiras de metal o piezas que se emplean para extender las superficies de transferencia de calor fundamentalmente están involucrados en las correlaciones de las aletas: (1) determinar la geometría y conductividad de la aleta, la naturaleza de la variación de la temperatura, y (2) determinar el coeficiente de transferencia de calor para la combinación de la aleta y superficie estándar o no extendida.

Se han realizado trabajos diversos sobre aletas tratando todos ellos de dar explicaciones de sus comportamientos operacionales, teniéndose con esto aportaciones relevantes que mejoran los diseños en equipos de transferencia de calor. En uno de ellos se estudió el flujo de calor tridimensional en un arreglo en línea de aletas circulares montadas den un intercambiador de calor, para varios números de Reynolds y diversas configuraciones geométricas. Se presentaron los resultados generados mediante la utilización de las ecuaciones de Navier-Stokes y de energía, aplicadas a discretizaciones espaciales de las configuraciones consideradas. Los resultados reportados consisten en simulaciones que reflejan el comportamiento funcional del arreglo para condiciones de flujo estable y permiten realizar la elección del aspecto del radio de las circunferencias [1].

En otro trabajo realizado se utilizó el método de simulación de Monte Carlo para evaluar tres formulaciones clásicas de la eficiencia de una aleta. Se mostró la utilidad del modelo de Gardner para realizar estimaciones de puntos de interés en aletas. Además se resalta en el trabajo la importancia de las consideraciones y condiciones de frontera que se deben de utilizar en aplicaciones concretas de estudio y finalmente se propuso una formulación para la evaluar la eficiencia de aletas [2].

También se ha estudiado el flujo turbulento en la entrada de un intercambiador de calor que contenía un sistema aletado. Este estudio se caracterizó mediante simulación en CFD y por experimentación haciendo uso de un PIV, ambas bajo condiciones de operación equivalentes. Para la configuración estudiada, se lograron obtener las gráficas de vectores y líneas de corriente. Los resultados obtenidos de la experimentación, fueron validados convenientemente con la información experimental, teniéndose grandes concordancias entre ambos, lo que permite flujos complicados para los sistemas de intercambiador de calor, como el estudiado [3].

Se han realizado trabajos de simulación en 3-D para condiciones de flujo laminar y la correspondiente transferencia de calor en tubos aletados, los cuales fueron considerados para casos diversos en la inclinación de sus aletas. La variación se realizó para ángulos de 0° a 50° y rangos de hileras de 1 a 4. Los resultados obtenidos teóricamente fueron comparados con los experimentales que resultan del trabajo asociado a modelos elaborados idóneamente para tales fines. Lograron establecer los efectos que implican hacer uso de diversas hileras,

determinando así, la relación de los comportamiento térmicos asociados [4].

El mayor campo de aplicación de superficies extendidas se refiere a los disipadores de calor utilizados comúnmente en la industria. Por lo que con su estudio se pueden proporcionar mejoras en cuanto a la eficiencia basados en los arreglos de aletas, tamaño de la superficie del disipador de calor, así como en la geometría del área transversal de ésta. Existen estudios que abordan el tema de la mejora de eficiencia a través de los modelos de disipadores como es el caso de F. Zhou e I. Catton [5] quienes realizaron una investigación numérica del comportamiento térmico e hidráulico de 20 diferentes disipadores de calor de aletas con diferente sección transversal y diferentes proporciones de ancho en la separación de aletas en la. Se utilizó el Software CFD basado en el método de volúmenes finitos, ANSYS CFX, utilizando un promedio de Reynolds-3-D para resolver las ecuaciones de Navier-Stokes. Se utilizó un modelo de esfuerzo cortante y transporte con sede κ-ω para predecir el flujo turbulento y la transferencia de calor a través de los canales del disipador de calor. Así, se comprobó que mediante la colocación de aletas en el canal de flujo de la placa del disipador de calor, las capas límite dinámico térmicas y de fluidos se interrumpen periódicamente y las partes de fluidos con diferentes temperaturas se mezclan mejor.

En este trabajo se considera el estudio de superficies extendidas por simulación numérica en ANSYS. Después de considerar materiales como cobre, aluminio y acero, los resultados logrados, sirven para establecer de ser necesario, la economía de material si estos fueran recortados, además de describir como ocurre su distribución de temperatura.

II. MODELADO

Se definieron las características geométricas de las aletas mostradas en la tabla procurando que el área superficial de transferencia de calor fuera similar.

Se realizó la investigación de las propiedades [6] de los materiales a utilizar en la simulación, estas son mostradas en la tabla II. Los datos son necesarios para definir dichas propiedades en el software.

TABLA I. CONFIGURACIÓN DE LAS SUPERFICIES ESTUDIADAS

Sección Transversal	**Cuadrada**	**Circular**	**Triangular**	**Unidades**
	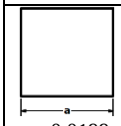 a =0.0199	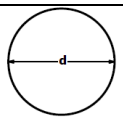 d =0.00254	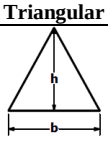 b=0.0266 h=0.0231	m
Longitud (L)	0.76	0.76	0.76	m
Área de la sección transversal (A_C)	$3.99x10^{-4}$	$5.06 x10^{-4}$	$3.07x10^{-4}$	m^2
Área superficial de transferencia de calor (A_S)	0.06	0.06	0.06	m^2

TABLA II. PROPIEDADES DE LOS MATERIALES ESTUDIADOS

Material	**Cobre**	**Aluminio**	**Acero**
Conductividad (W/m°C)	399	237	43
Densidad (kg/m^3)	8666	2787	7801
Calor específico (J/kg K)	410	833	473

El coeficiente de convección natural utilizado fue de 200 W/m2°C para una temperatura ambiente de 20°C. Además se propuso una temperatura para la base de la cual sobresale la aleta, cuyo valor se mantuvo constante para todos los modelos, este valor es TS=500°C.

En la parte del modelado, la primera fase se denominada Pre-Proceso, donde se realizó la geometría de la aleta en ANSYS, para esto se consideró el modelo SOLID87 definido en el software y fue aplicado para cada caso mostrado en las Fig. 1 a 3.

De acuerdo a los requerimientos de ANSYS, se definieron las propiedades de los materiales (conductividad, densidad y calor específico) para así poder llevar a cabo la discretización del modelo mostrado en las Fig.4 a 6.

La segunda fase del modelado se llama Proceso, en esta se definieron las condiciones de frontera (aplicación de cargas), para la temperatura ambiente alrededor del área superficial de transferencia de calor, el coeficiente de convención y la temperatura de la base de la aleta (área de la sección transversal) para cada geometría mostradas en las Fig. 7 a 9.

En la fase final del modelado conocida como Post-Proceso se generaron los resultados, donde se muestra la distribución de la temperatura a lo largo de su longitud con respecto al origen y las condiciones de frontera mencionadas. Las Fig.10 a 12 muestran la distribución de temperatura de la aleta cuadrada para los 3 materiales considerados. Las Fig.13 a 15 muestran la distribución de temperatura para la aleta circular. Y en las figuras Fig.16 a 18 se muestra la distribución de temperatura para la aleta cuadrada.

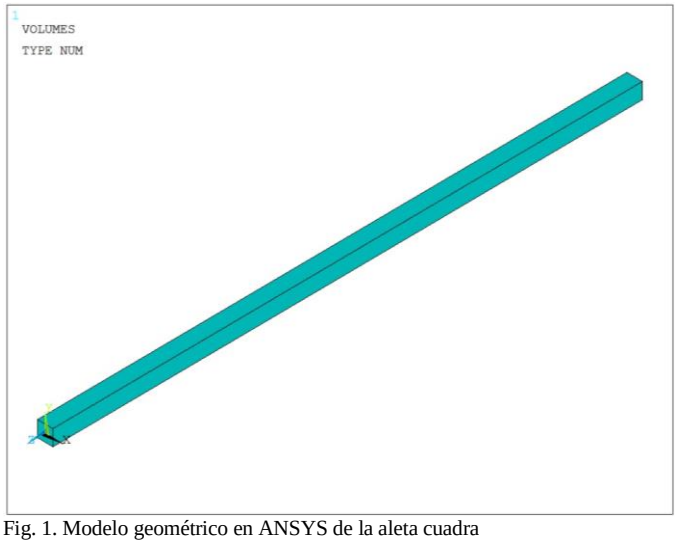

Fig. 1. Modelo geométrico en ANSYS de la aleta cuadra

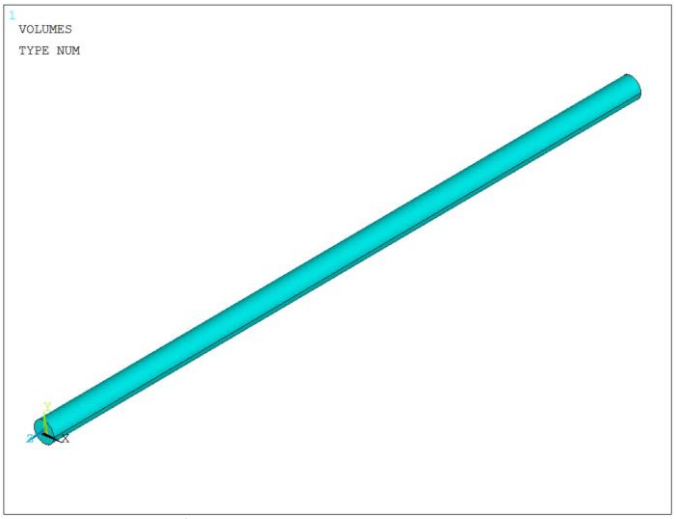

Fig. 2. Modelo geométrico en ANSYS de la aleta circular

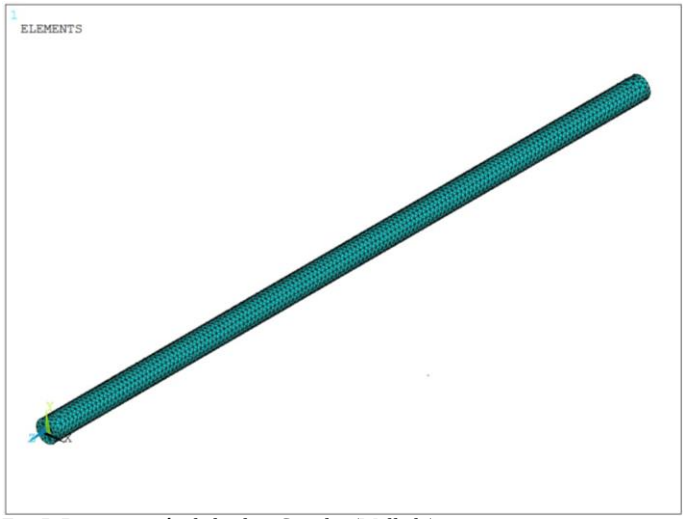

Fig. 5. Discretización de la aleta Circular (Mallado)

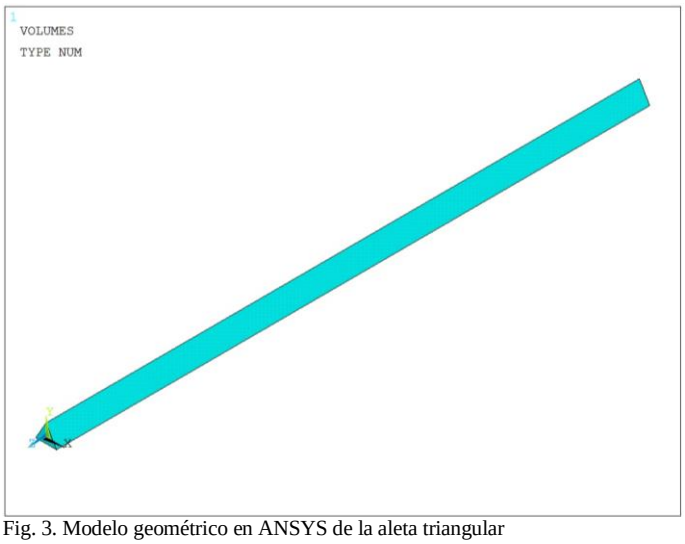

Fig. 3. Modelo geométrico en ANSYS de la aleta triangular

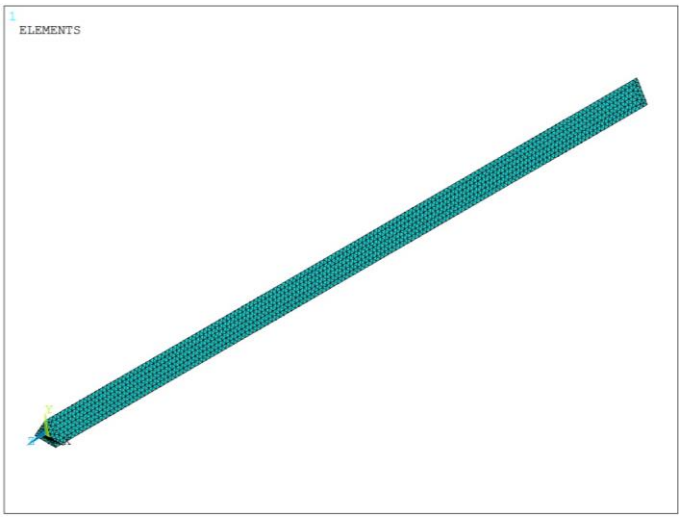

Fig. 6. Discretización de la aleta Triangular (Mallado)

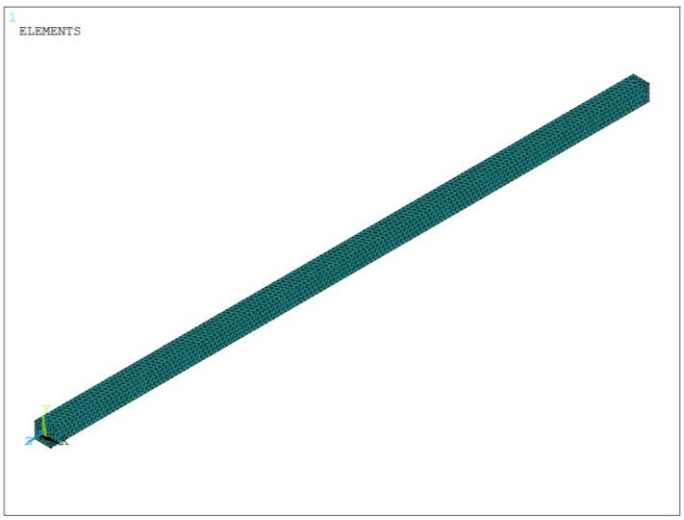

Fig. 4. Discretización de la aleta Cuadrada (Mallado)

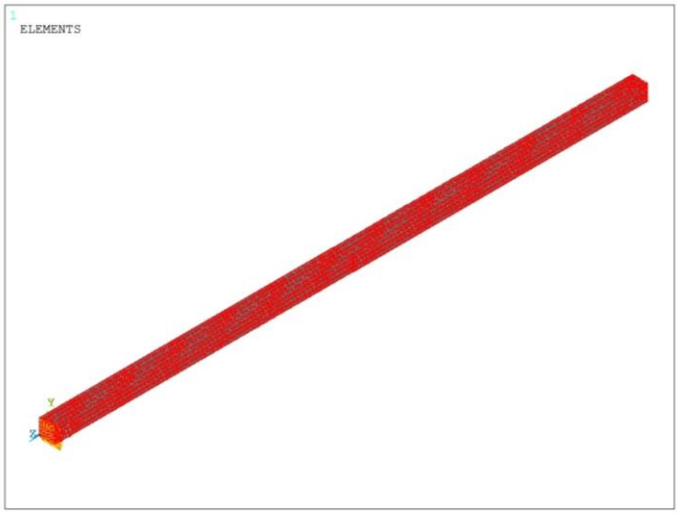

Fig. 7. Condiciones de frontera de la aleta Cuadrada

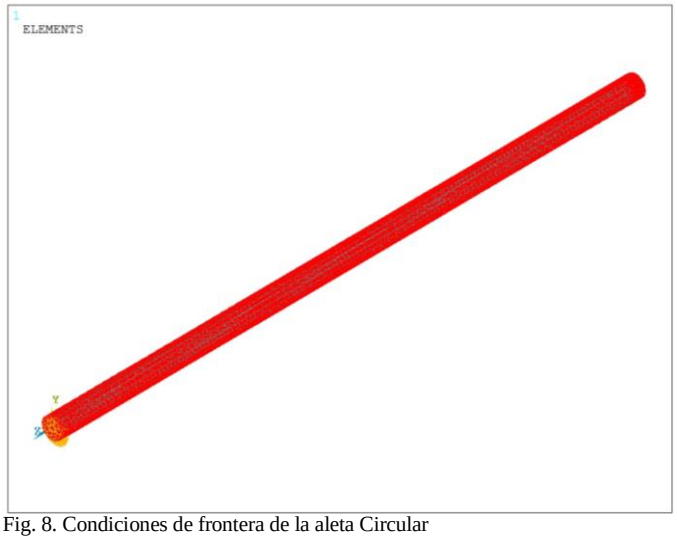

Fig. 8. Condiciones de frontera de la aleta Circular

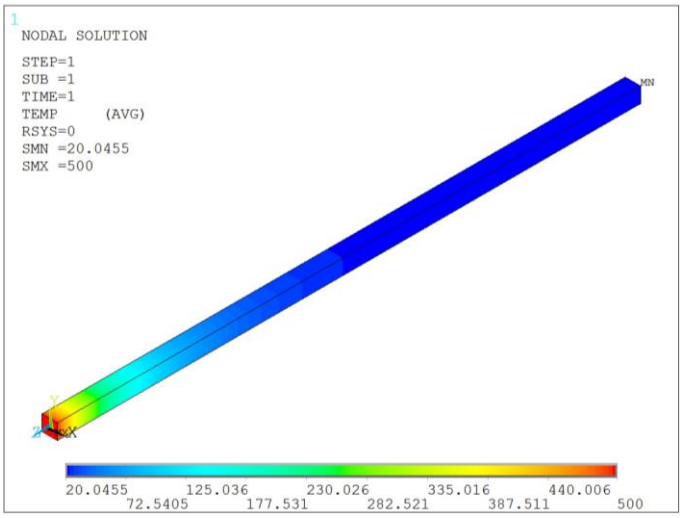

Fig. 11. Distribución de temperatura de la aleta Cuadrada, Aluminio [°C]

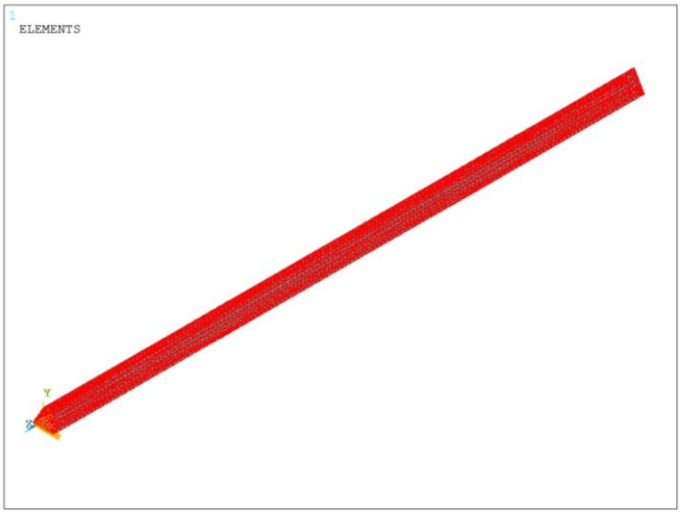

Fig. 9. Condiciones de frontera de la aleta Triangular

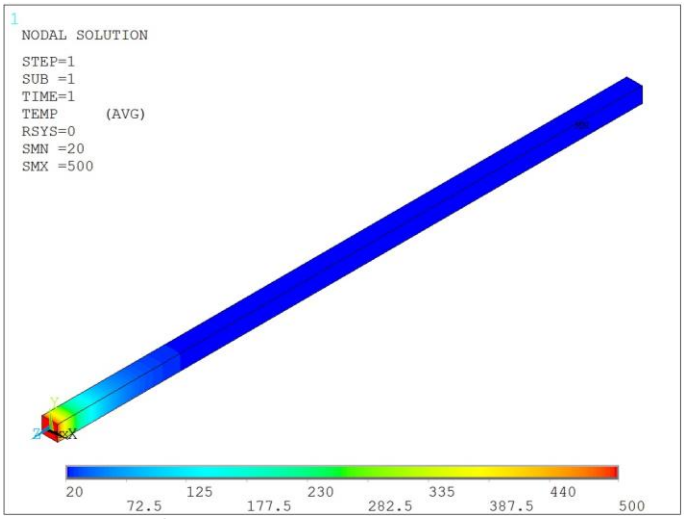

Fig. 12. Distribución de temperatura de la aleta Cuadrada, Acero [°C]

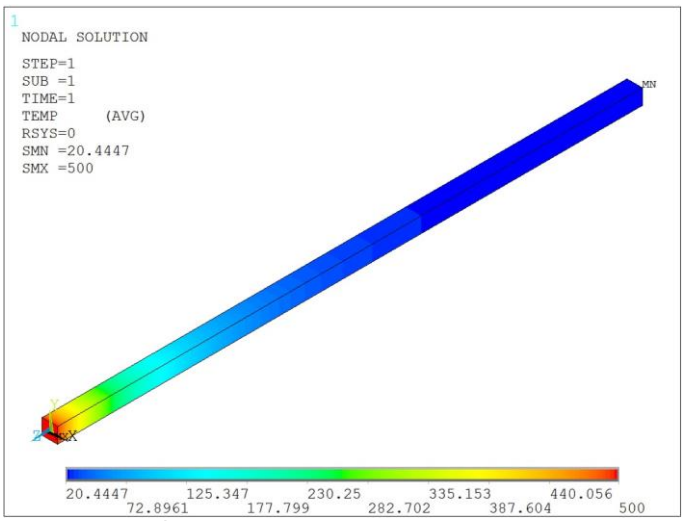

Fig. 10. Distribución de temperatura de la aleta Cuadrada, Cobre [°C]

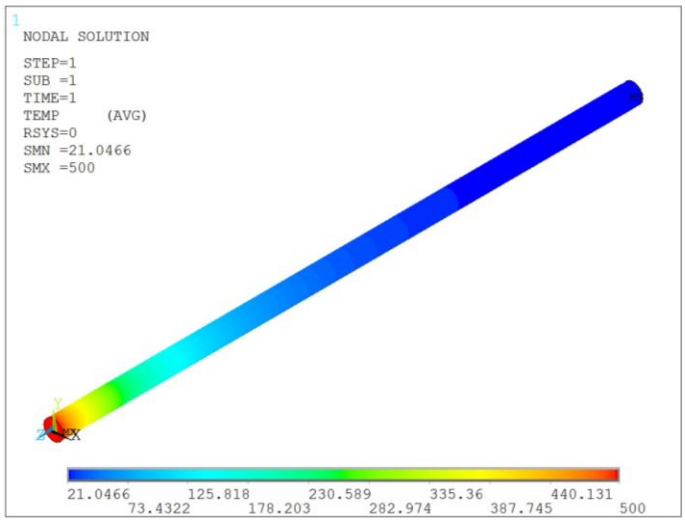

Fig. 13. Distribución de temperatura de la aleta Circular, Cobre [°C]

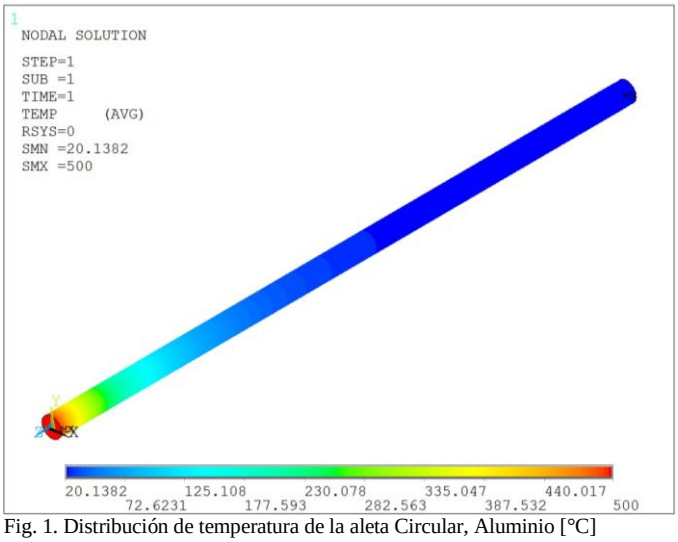

Fig. 1. Distribución de temperatura de la aleta Circular, Aluminio [°C]

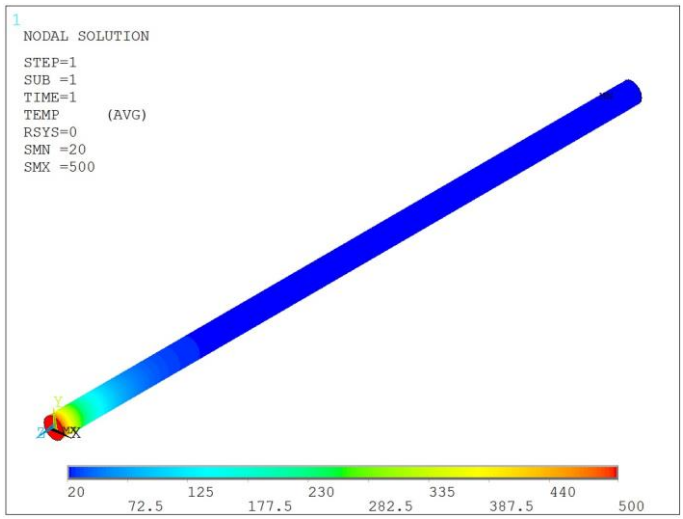

Fig. 2. Distribución de temperatura de la aleta Circular, Acero [°C]

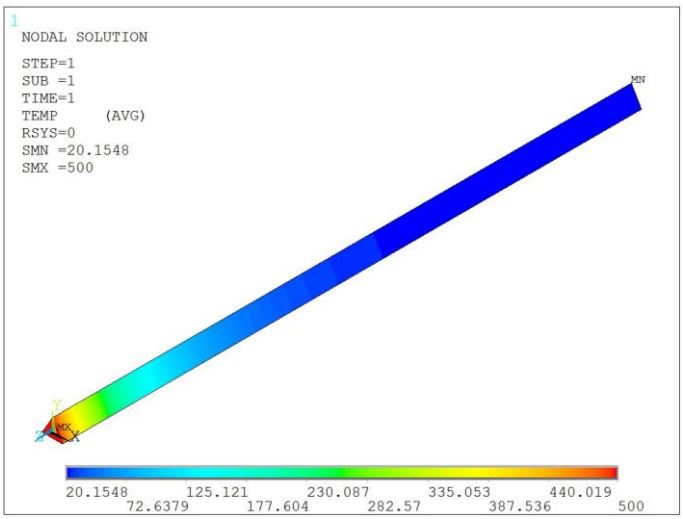

Fig. 3. Distribución de temperatura de la aleta Triangular, Cobre [°C]

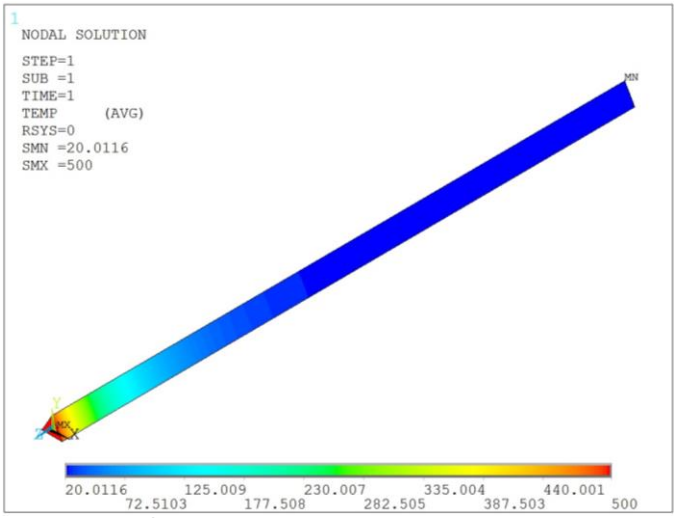

Fig. 4. Distribución de temperatura de la aleta Triangular, Aluminio [°C]

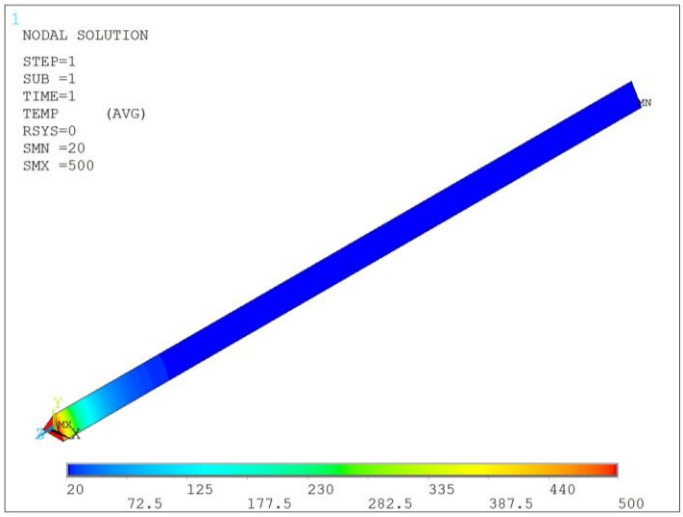

Fig. 5. Distribución de temperatura de la aleta Triangular, Acero [°C]

III. Análisis De Resultados

Los resultados gráficos muestran que el material que mejor conduce el calor es el cobre, ya que su coeficiente de conducción (k) es mayor que el de los otros materiales. Con lo que respecta a la forma, para que el parámetro de comparación fuera adecuado, la superficie de cada aleta fue de aproximadamente 0.06 m^2, esto fue para que las pérdidas de calor por convección (entre la aleta y el medio) no se vieran afectas por el área de transferencia de calor superficial sino por la forma de la aleta.

Como se observa en las figuras 10 a 18 hay una gran longitud que tiene una temperatura constante, esto indica que hay desperdicio de material. Para analizar este fenómeno se realizó un corte en longitud de la aleta Cuadrada en cobre, Fig.1, estableciéndose así una longitud recortada de 0.47 m. Por medio del software, se identificó en la aleta original que la temperatura en esa longitud fue de 24.2 °C. En la Fig.19 se muestra la aleta cuadrada en Cobre con dicha longitud donde

se observa que la temperatura es de 28.0 °C, por lo que para encontrar la longitud correcta de la aleta se debe tomar en cuenta cuanto calor se busca eliminar en la misma.

Este recorte ahorraría 0.29 m de material lo cual puede ser de gran importancia para los costos que pudieran representar la elaboración de sistemas con este tipo de aleta.

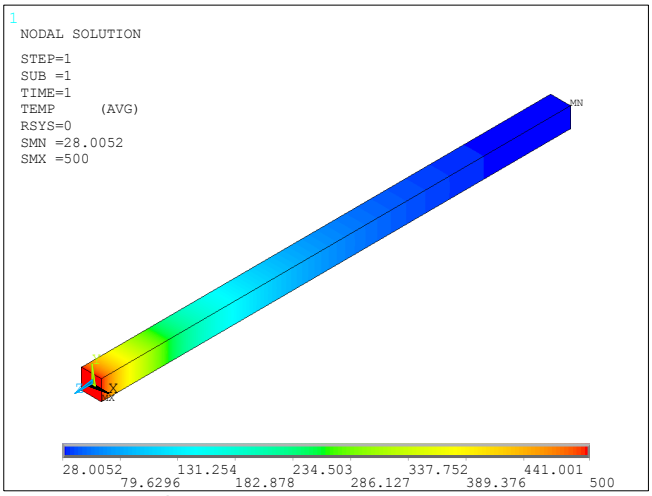

Fig. 19. Distribución de temperatura de la aleta Cuadrada Recortada, Cobre [°C]

Cuando se revisan los datos de temperatura a lo largo de la longitud de la aleta para el mismo material y diferente geometría en la sección transversal, se puede apreciar que el tipo de geometría también repercute en la longitud que puede eliminarse.

Cuando se aplica este mismo procedimiento a las otras configuraciones de aletas, se puede entender la importancia de la naturaleza del objetivo de este trabajo.

IV. Conclusiones

En este trabajo se evaluó y comparó el comportamiento térmico de nueve aletas con diferntes configuraciones de formas (cuadrada, circular y triangular) y materiales (cobre, aluminio y acero).

La aleta que presenta la distribución de temperatura más más amplia a lo largo de la aleta es la de sección transversal circular y material en cobre y la de menor longitud en su temperatura es la aleta con sección transversal triangular y material en acero.

Estas conclusiones están respaldadas en la literatura especializada, sin embargo, el interés de este trabajo está en que se ha podido resolver un caso tridimensional para ciertas formas de aletas y su comportamiento visual propicia resultados que en su conjunto no son posibles de percibir de manera analítica; y los cuales ayudan a mejorar el diseño de conjuntos aletados para ciertos sistemas como los intercambiadores de calor.

Referencias

[1] A.K. Saha y S. Acharya, “Parametric study of unsteady flow and heat transfer in a pin-fin heat exchanger”, International Journal of Heat and Mass Transfer 46 (2003) pp. 3815–3830.

[2] U. Maheswaran y S.C Sekhar, “Evaluation of concepts of fin efficiency using Monte Carlo Simulation method”, International Journal of Heat and Mass Transfer 49 (2006) pp. 1643–1646.

[3] J. Wen, Y. Li, A.Zhou y K. Zhang, “An experimental and numerical investigation of flow patterns in the entrance of plate-fin heat exchanger”, International Journal of Heat and Mass Transfer 49 (2006) pp. 1667–1678.

[4] Y. B. Tao, Y. L. He, J. Huang, Z. G. Wu y W. Q. Tao, ”Three-dimensional numerical study of wavy fin-and-tube heat exchangers and fields synergy principle analysis”, International Journal of Heat and Mass Transfer 50 (2007) pp. 1163–1175.

[5] F. Zhou e I. Catton, “Numerical evaluation of flow and heat transfer in plate-pin fin heat skins whit various pin cross-sectios”, Numerical Het Transfer, Part A, 60:107-128, 2011.

[6] Y. A. Cengel y A. J. Ghajar, Trasferencia de calor y masa, 4ta Ed. p. 868.

Design and construction of an inexpensive alkaline electrolysis cell for transport applications

Jimena Molina Gómez*
Luciano Augusto Gerling Garza
Alejandro Montesinos Castellanos
Department Chemical Engineering
ITESM
Monterrey, México
*jimenin@gmail.com

***Abstract*— The current energy system relies heavily on fossil fuels. This fact, combined with an ever growing population, has derived on damages on the environment and on health provoked by fossil fuel combustion emissions. An important contributor to these emissions is the land transport sector, and many alternative energy technologies have been developed. A short term response can ease the apparently difficult transition between traditional vehicles and alternative energy vehicles. This research consists on the design, construction and testing of an inexpensive alkaline electrolysis cell, envisioned to be a part of a solar electrolysis system to be used for vehicle hydrogen on-board production. The prototype, called Pseudo Zero-Gap cell, achieved an adequate size, 62 cm, and efficiencies around 60%. A comparative cost analysis against other water electrolysis projects revealed the cost of the prototype is the second lowest value. Further cost analysis was made for the future solar electrolysis system, and the results showed the system cost is reasonable comparing it to another emissions reduction project.**

Keywords*— *alternative fuel, transport, hydrogen, alkaline electrolysis

I. INTRODUCTION

Despite being convenient in many ways, fossil fuels are beginning to lose their appeal as a long term source of energy, due to the many problems caused by their combustion and their unreliable availability [1]. All fossil fuel deposits are limited and non-renewable, for it takes millions of years to form a fossil fuel deposit, while its extraction is immediate in comparison. Some of the issues with fossil fuel combustion are also health related, either referring to sickness caused by exposure to its emissions [2,3] or damages to the natural environment [2]. This makes it even more urgent to move from the current energy structure to one that takes more into account the concern for human health and welfare.

Of all anthropogenic combustion gas sources, light duty cars and trucks are the third largest contributor, emitting 14\% of the global CO_2 emissions [4]. An emission reduction on this sector would significantly help diminish greenhouse gases (GHGs) emission, especially on large cities where vehicle use is the highest. But alternative technologies for vehicles have not been widely adopted due to use of food crops, the need of deep infrastructure changes and/or too high costs [5, 6]. A short term solution to ease the transition between fossil fuel vehicles and alternative technology vehicles would help not only to reduce GHG emissions but also to overcome the barriers in the market entry for alternative vehicle technologies [7].

Small on board hydrogen production for conventional combustion engine vehicles, is a good option. Hydrogen has many features that make it attractive as an energy carrier, such as its high energy content, widely available raw material, versatility, and environment compatible emission [8]. The use of hydrogen in conventional internal combustion engines uses existing infrastructure and can be a first step to achieve widespread use of hydrogen on the transport sector [9]. The role of hydrogen would be of an energy carrier for alternative energies, so the electrical energy most of them supply can be used on combustion engines. To achieve on board production both mobile energy source and hydrogen production process are needed. Solar power is a viable option, as solar cells can be arranged to conveniently fit varied surfaces.

One of the ways to produce hydrogen using electricity is water electrolysis, which is the use of an electrical current to transform water into gaseous hydrogen and oxygen. There are many water electrolysis technologies, like alkaline, proton exchange membrane, solid oxide, and other less conventional ones [10]. Of these, alkaline electrolysis is one of the most developed electrolysis technologies, widely used on the hydrogen production industry due to its low manufacture complexity and cost. This makes it an ideal candidate for its widespread use, even when its efficiency is less than those of other more recent technologies [10].

It is because of its simplicity and low manufacture cost that the use of alkaline electrolysis on present motor vehicles is feasible and practical. An alkaline electrolysis powered with an alternative source of electric energy could allow a significant fuel saving, considering the great size of the vehicular fleet of a city, and also make hydrogen available to be used by conventional motor vehicles, helping developing countries reduce fossil fuel use without purchasing costly alternative

vehicle technologies. This research work main objective is the design, construction and testing of an inexpensive and robust water alkaline electrolysis cell, suitable for installation in a common motor vehicle and to be powered by an alternative energy source.

II. Alkaline Electrolysers

A. Basics

An alkaline water electrolysis cell decomposes water by passing an electric current between two electrodes in contact with an alkaline medium. An alkaline electrolyser is formed by one or more of these cells. Electrodes go from the cathode to hydrogen ions to form hydrogen gas, and hydroxide ions yield their electrons on the anode, forming water and oxygen gas. A membrane is normally placed between the electrodes to separate the generated gases. Figure 1 shows an electrolysis cell with all its basic components. There are more steps involved on the reactions of each electrode, but the gas production reactions can be summarized as follows:

Cathode:

$$2H^+ + 2e \rightarrow H_2 \quad (1)$$

Anode:

$$2OH^- \rightarrow 1/2\, O_2 + H_2O + 2e \quad (2)$$

B. Thermodynamic aspects

Water splitting is not a spontaneous process, so it needs an energy input to be carried out. In an electrolyser, this energy is supplied as an electric current, and the theoretical minimum amount to carry out the reaction is called open circuit cell voltage, E_o. This voltage is also called electromotive force, and it is the value of its potential when no current is going through and the electrical and chemical reactions are in equilibrium. On these conditions, there is a potential on both the electrodes, E^- and E^+, called galvani potential, and the cell open voltage is defined as

$$E_o = E^- - E \quad (3)$$

On electrolysis this value is less than zero, so it is necessary to overcome it to get the reaction going, in this case to obtain chemical energy by producing the gaseous hydrogen and oxygen. For the electrolysis of water, the open circuit voltage value at 25°C and ambient pressure is -1.23 V. These are standard conditions, on which open circuit voltage is called standard reversible potential. This value is related to the standard Gibbs free energy of formation of water by

$$\Delta G° = -nFE° \quad (4)$$

where n are the number of electrodes transferred in the reaction, F is the Faraday constant (96,487 C/mol), and $E°$ is the standard reversible potential [12]. Using the standard Gibbs energy of formation for liquid water we obtain the equilibrium potential value at 25°C, but the products of the reaction are gases and the energy needed for that phase change must be supplied, either by providing heat or additional electrical energy. If electrical energy is used, the total voltage applied is called thermoneutral voltage, with which the reaction can be

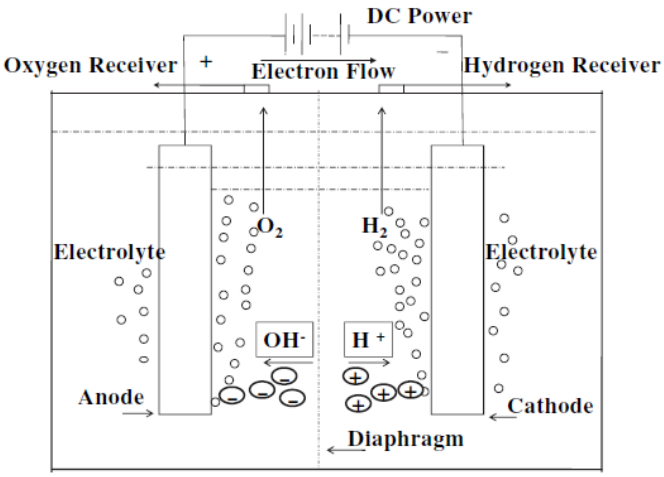

Fig. 1. Basic alkaline electrolyser diagram. [11]

maintained without any heat input. The value is -1.48 V [11]. If heat is applied, the open circuit voltage will decrease [12].

In a real process, the reactions do not occur at the equilibrium voltage. There is an electrode overpotential, which is a property that depends on temperature, pressure, electrode material, electrolyte nature and composition, and current density at their surface. The thermoneutral voltage includes the electrode overpotentials. Adding to the overpotentials of the electrodes, there is an ohmic potential loss due to the electrolyte, the separating membrane and the electrical connections, which increases with increasing current density [11]. The voltage of the cell, considering all of the previous aspects, can be expressed as:

$$E = E° + \eta_c - \eta_a - IR_\Omega \quad (5)$$

where η_c and η_a are the overpotentials for the cathode and anode respectively. The term IR_Ω refers to the ohmic potential loss [12]. The overpotentials of the electrodes are the additional energy that has to be applied to the cell besides the equilibrium voltage, due to the nature of the relation between the electrode material and the adjoining electrolyte. They increase with the current density [11], so the applied energy is used less efficiently as the current rises.

The ohmic potential loss depends, among other parameters, on the geometry and arrangement of the electrolyser components, since they determine the form of the medium between electrodes that the species involved on the reaction need to cross. It also includes the circuit and gas bubble resistances, the later increasing with current density, as it increases gas production. Of all the components of the total overpotential, the ohmic potential loss is the one that could be reduced the most by an adequate electrolysis cell geometric design.

C. Practical considerations and operating condition

An electrolyser stack, be it alkaline or other type, can have many electrolysis cells connected either in series or in parallel, which is called bipolar or monopolar configuration respectively. Monopolar configuration is called thus because each electrode has only one polarity, and produces hydrogen or oxygen exclusively; the total voltage applied to this module is

equal to the individual voltage of each cell. On the other hand, an electrode in a bipolar cell has two polarities, and produces hydrogen on the cathode side and oxygen on the anode side; in this case, the current flowing through each cell is the total current applied to the stack. The way in which the individual cells are arranged on the stack varies between designs, but most of the industrial electrolysers are configured on a filter press style, for its advantages on space saving and simple maintenance [11, 13, 10]. Concerning the electrodes, not only their material affects the behavior of the process, but also their size, position and shape [14].

As described before, the current density of an electrolyser determines the rate of production of the process, but also affects the overpotentials directly. This means that at a higher current density, a larger portion of the applied energy must be used to overcome the electrode overpotentials, yielding lesser energy efficiencies. Also, a higher production rate increases the gas fraction on the electrolyte, which is one of the contributions of the omhic voltage. There must be a balance between production rate and energetic efficiency, depending on the intended purpose of the electrolyser and the produced gas.

Finally, temperature, pressure and electrolyte nature are considered. As stated before, the equilibrium voltage decreases with increasing temperature, and many industrial electrolysers work at 80-90°C [11]. But high temperatures require more resistant materials and the risk of water loss due to evaporation is higher. On the other hand, operating pressure depends mostly on the end use of the produced gas and its pressure requirements, as it does not affect the process importantly [11]. The most widely used electrolyte on industrial alkaline water electrolysis is 30% potassium hydroxide, as it is a concentration with good conductivity at the operating temperatures [15].

On recent years advanced alkaline electrolysers have been developed modifying certain component materials and configurations: first, the space between electrodes has been reduced to minimize ohmic losses of the electrolyte, in a configuration called zero-gap [16,17,18]; second, new membrane materials with better conduction properties were developed; third, high temperature alkaline electrolysis has been explored, as high temperatures improve efficiencies; fourth and last, catalytic materials are being developed to reduce electrode overpotentials, especially for the oxidation reaction [10,16,11]. Modifications on the spatial configuration of the cell components are the cheapest way to improve their efficiency, and also allow the space reduction necessary for small scale applications.

III. METHODOLOGY

The behavior of the alkaline electrolysis process varies depending on its components arrangement and material. In order to design the cheapest possible functional alkaline electrolysis cell, single cell tests and observations are needed. Electrolytic cell prototypes are designed considering their intended final application and the theoretical basic arrangement of its components. Figure 1 contains all the basic elements of an electrolysis cell and was considered as a good starting point. The style of the design is based on the filter press type electrolyser mentioned before, aiming for its advantages on space saving and simple maintenance.

The component and cell dimensions are mostly defined by practical considerations, as the size of the cell needs to fit the limited space inside the hood of a conventional vehicle, near the air feed of the engine. This space was empirically determined to be approximately a 15x15x50 cm box. On the filter press electrolyser type, electrode area determines the size of the ends of the electrolyser stack, and the space between electrodes determines the electrolyser length. The prototype was designed to test an approach of space saving and management, as well as electrode shape and connection configuration.

Although nickel is known to be the best choice for electrodes considering effectiveness and cost [19], stainless steel is a cheaper material, and was chosen as the process can be carried out acceptably without purchasing nickel electrodes. For the electrolyte, potassium hydroxide with a 6M concentration was chosen, as it is cited to be the best and most common choice [15]. Acrylic was chosen for the structure of the prototypes as it can be bought as sheets in any custom design and with any desired perforation; it also can withstand the alkaline medium indefinitely.

A very important characteristic of the developed prototype is that it produces an oxygen and hydrogen gas mix. Traditional electrolysers separate the produced gases, as gas purity is one of the electrolytic hydrogen production assets, but this is also a security measure: the hydrogen and oxygen stoichiometrical gas mix produced by electrolysis is explosive. However, hydrogen-oxygen mixes have been tested on conventional gasoline engines [20] trying to imitate on board electrolytic hydrogen production, so the gases do not need to be separated. This allows us to avoid the ohmic loss and cost associated to the membrane.

A. Prototype

The conventional zero-gap configuration consists on an electrode-membrane-electrode array, very similar to the PEM electrolysis membrane electrode assembly (MEA). The electrodes are adjacent to the separating membrane, which functions as conductor for the chemical species that need to travel between electrodes and as a gas separator. The electrodes are made from materials that allow contact between the electrolyte and the membrane.

The design of the prototype was based on the zero-gap configuration, but cannot be considered as such. As the produced gases do not need to be separated, the membrane between the electrodes only needs to contain the electrolyte between the electrodes for the water to be separated. This configuration is called Pseudo-Zero-Gap. The electrodes are made of stainless steel mesh (4 cm diameter circles) and the membrane of qualitative filter paper, a much cheaper material than the membrane material used for electrolyser stacks that separate produced gases. The electrolyte is distributed on a canal adjacent to each electrode and wets the paper through the electrodes. The produced gas leaves the cell through the same distribution canals. The electrical connections were made with stainless steel screws that go through the plates to make contact with the center of the electrodes. A viton o-ring encases the electrodes and the paper between the two engraved plates. Figure 2 shows a diagram of the PZG prototype.

The original zero-gap configuration decreases ohmic loss by reducing the space between electrodes and by eliminating the void fraction between them. The reduced interelectrode space and the absence of bubbles between the electrodes are meant to lower the omhic overpotentials in order to have a good enough performance and a small enough size.

B. *Experiment design*

Water electrolysis does not occur at the equilibrium voltage, since the electrode overpotentials and the electrical resistance of the components of the cell add energy requirements. The experiments were performed at voltages close to this theoretical value to maintain the highest possible efficiencies, but without compromising the production speed considerably. For alkaline electrolysers, the typical voltage on industrial processes is 2.2 V on each electrolytic cell [11], which was used on preliminary experiments to define a voltage range to work with. The voltage range was fixed on 1.9 to 2.3 V, with five values to test within it. The energy input can be obtained measuring the voltage and current applied to the cell. The prototype is connected to a DC power supply and its gas outlet to a bubble flow meter; the DC power supply must allow voltage or current control to obtain results useful for comparison between different energy inputs.

The performance of the prototype is assessed considering two important parameters: efficiency, and electrolyser size. Taking the envisioned application into account, enough hydrogen must be produced in a fixed time and space to supply a small fraction of the energy used by a land vehicle, traditionally obtained from gasoline. Making the construction materials as cheap as possible, the goal is to assess if the energy saving due to the gas produced is worth the investment on the system. Finally, a cost analysis will be made.

C. *Efficiency*

The efficiency usually reported for electrolysis cells describes the cells effectiveness to produce hydrogen with the used energy, as hydrogen is not generally used as an energetic. Reports that assess hydrogen production to be used as an energetic consider the energy than can be obtained from the produced hydrogen. The later is calculated using the lower heating value of hydrogen, and is more useful on energy application analysis.

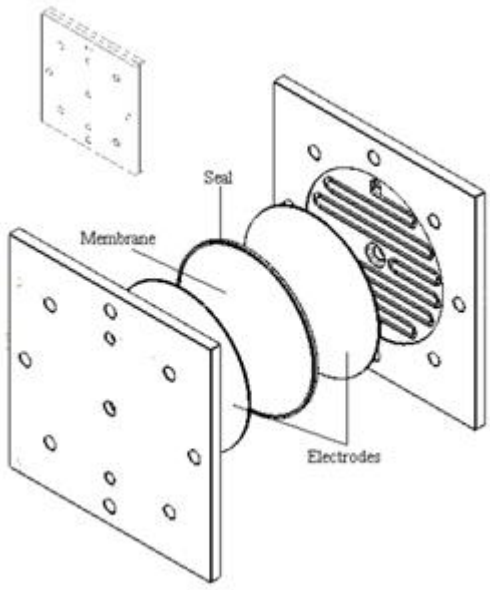

Fig. 2. Pseudo Zero Gap Diagram

D. *Electrolyser size*

Once the production rate and the volume of a single electrolysis cell is calculated, including only the space occupied by the electrodes and the electrolyte, an approximation of the volume of the whole electrolyser can be obtained. Given a gasoline consumption and energy replacement scenario, the hydrogen production needed can be calculated, and with the individual production rate of the prototype cell, the number of cells needed. The scenario consists on a one hour trip at a low speed, 20 km/hr, which usually happens when moving by car on a city with heavy traffic. The energy fraction intended to be replaced is 5% of the gasoline consumed on that trip, considering an average compact car. The gasoline consumption per kilometer was calculated as an average of the values reported on the Energy Efficiency and Vehicular Emission Indicators portal of the Mexican federal government [21].

E. *Cost analysis*

The low cost of the components of the electrolyser will reflect on the electrolyser stack cost. The stack cost parameter used is cost per hydrogen kilogram produced. This is the parameter used on the 2013 Progress Report for the DOE Hydrogen and Fuel Cells Program [22] for electrolyser stack cost and the electrolyser prototypes reported were chosen for cost comparison. To obtain the cost of production the total cost of the electrolyser is divided by the electrolyser hydrogen production rate, expressed on kg/h, and multiplied by the stack lifetime. This way, the parameter shows the cost of all the hydrogen produced on the total lifetime of the stack. To evaluate if the cost of saved fuel justifies the use of the system, a hypothetical array of solar panels, battery and electrolyser is considered to calculate a system total cost. The gasoline price is set on 13.78$/L, the most recent value, and the time of investment recovery is calculated. All costs are calculated on US dollars.

IV. Results and Discussion

Figure 2 shows the energetic efficiencies of the prototype for all tested voltages, which are around the value reported for alkaline electrolysis (~60%) [18]. As expected, the general efficiency behavior is of decreasing values with increasing applied voltage, as a higher current density is needed to maintain a higher voltage, which in turn increases the electrode and ohmic overpotentials of the cell.

The size of a hypothetical electrolyser stack was calculated for the cell prototype. The size varies with the applied voltage because it determines the production rate. The cell is small enough to fit four times on the 15x15cm space, and this was considered when calculating the electrolyser length. As stated before, the measures of the extremes of the electrolyser stack are 15x15 cm. The results are shown on Table 1.

TABLE 1. Hypothetical Electrolyser Length

Voltages (V)	Electrolyser Length (cm)
1.9	588
2	240
2.1	130
2.2	87
2.3	62

The electrolyser length achieved for the largest voltage tested is close to the 50 cm value and could fit on the space available of inside the hood of a conventional vehicle. The only setback is that the electrolyte needs its own space for this prototype, but the design of a functional electrolyser stack is out of the scope of this work.

The hypothetical electrolyser length of the PZG prototype shows it could be used on a conventional land vehicle. The first cost analysis parameter is the stack cost, which is calculated for a hypothetical stack formed by the calculated number of cells needed for the energy consumption scenario previously described. Some components of the stack are individual for each cell, like the electrodes and the membrane, and others are used for the whole stack, like aligning rods and tubing. Table 2 shows the components of the cell, its prices and the total cell cost, all expressed on US dollars.

Table 2 shows the total prices of each electrolyser stack components. The engraved sheet is listed as PVC in an effort to lower its price; both acrylic and PVC endure on alkaline mediums. The membrane material is the mayor contributor to the stack total cost, almost half of the total cost, which was not expected since the membrane material was chosen without the separating feature in hope of reducing the cell price. Further research is needed to find other cellulose materials that could contain the electrolyte as or more effectively than filter paper, but with a smaller cost. The other considerable component costs are the electrodes, the seals, and the engraved sheet as they are repeated for each cell. The total number of needed cells on the stack almost reaches one thousand units, hence the elevated price of its components. The rest of the components have comparatively insignificant costs.

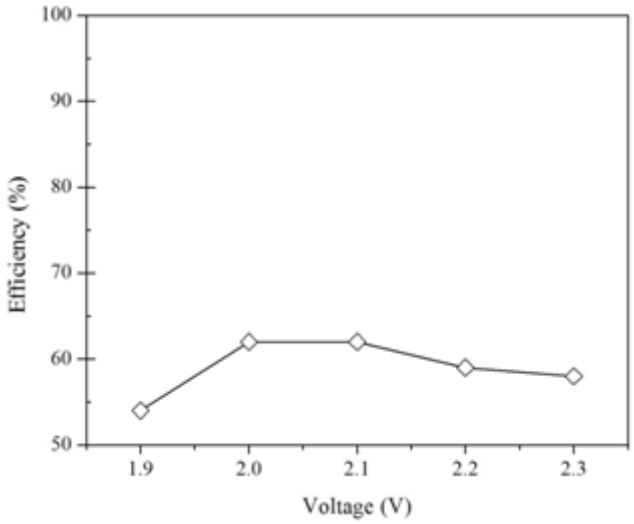

Fig. 3. Cell efficiency values calculated for all tested potential values

TABLE 2. Hypothetical Electrolyser Stack Costs

Component		Cost ($)
Each cell (Total for 1000 cells)	Stainless steel mesh	29.54
	PVC sheet	34.10
	Viton o-ring	73.33
	Electric cable	33
Electrolyser stack	Electric accessories	0.24
	Threaded rod	16
	Nuts	1.66
	Washers	0.44
	Acrylic adapters	3.56
	Tubbing	1.57
	Electric cable	0.53
Total		345.71

In order to assess the cost of the electrolyser stack in comparison to other electrolyser technologies, other research work was consulted. The 2013 Progress Report for the US DOE Hydrogen and Fuel Cells Program [22] has eight research works on the electrolysis section, and five were chosen to have a fair comparison, as they reported stack price reduction due to cheaper materials or stack efficiency improvement. The description of each of these research works can be consulted on the mentioned report [22]. As mentioned before, to calculate the stack electrolyser cost, the total stack cost is divided by production rate and multiplied by its total lifetime. The lifetime of the electrolysis cell was set on five years, considering the durability on the materials chosen. The prices are shown on Figure 4. As seen on Figure 4, the PZG cell cost is the second cheapest of all the presented costs, being bested only by the PEM with Low-cost membrane. Usually the prices increase as the production scale decreases, as described by the source report. This highlights one of the assets of the PZG cell, because despite being a small scale production electrolyser, its price is around the prices reported

for the big scale production electrolysers. If the lifetime of the PZG cell could be increased without increasing price significantly, the stack cost could be even smaller than the PEM with Low-cost membrane. Furthermore, the calculated cost for the PZG prototype could be lowered even more with mass production.

Due to the high cost of the solar panels ($444), considering an array of multiple solar panels is unpractical, so a system configuration of one solar panel was considered. The energy provided by one solar panel is approximately 17.5% of the total electrolyser energy requirement and the rest should be provided by the battery. The battery is ideally charged when the car is parked under the sunlight, with an estimated parking time of 5 hours, which is considered the time a car spends parked during minimum office hours. The battery can be charged to supply the resting 82.5% of the energy requirement. This system of one solar panel, one absorbent glass mat battery ($196) and electrolyser stack has a cost of $986. Considering a gasoline cost of $1.02 per liter (September 2014), the gasoline saving per trip is calculated to be $0.08. With four trips per day, there is a daily saving of $0.34. The investment on the system can be recovered on approximately eight years. The investment recovering time is still quite high, but it could be lowered with cheaper solar panel and electrolyser costs.

On the frame of emission reduction per dollar invested, the project provides accessible emission reduction costs. The transport emission problems on the Monterrey Metropolitan Zone (MMZ), has been addressed by many projects, one of which is the Ecovia: Corredor Ruiz Cortines-Lincoln. This project consists on the construction of a 30 km corridor to be used by 80 public transport buses working with natural gas [23]. The investment cost is $121.3 million with a CO_2 reduction of 16,750 CO_2 tons. To be able to compare this project cost with the cost of the solar electrolysis system, the grams of CO_2 reduced are divided by the investment cost, obtaining 138.1 gCO_2/$. According to the Transport and Roads Sector Plan for the Monterrey Metropolitan Zone [24] as much as 8.2 million trips per day were made on the MMZ on 2005 and 41.18% were made by 1.3 million cars. Considering a 15 km trip and a 2.35 $kgCO_2$ emitted per gasoline liter consumed [25], the reduced CO_2 per $ invested on the solar electrolyser system is calculated to be 686.2 gCO_2/$, which is five times larger than the Ecovia project. This way, the investment cost is seen as a feasible investment on emission reduction, not only on fuel saving. With an appropriate design, the system could even be applied to the public transport mentioned on this project to further increase the emissions reduction.

VI. CONCLUSIONS

An alkaline electrolysis cell prototype was designed, constructed and tested to assess its performance on production and efficiency. Then, the feasibility of the construction of an electrolyser stack composed of this cell that fits on the reduced space available on the hood of an average car was evaluated. Next, the cost of a hypothetical electrolyser stack was compared to other water electrolysis projects to determine if the low cost materials managed a stack cost reduction. Finally, the cost of a hypothetical solar electrolysis system was calculated and compared with the gasoline saving achieved by the technology, to conclude if the system is economically viable.

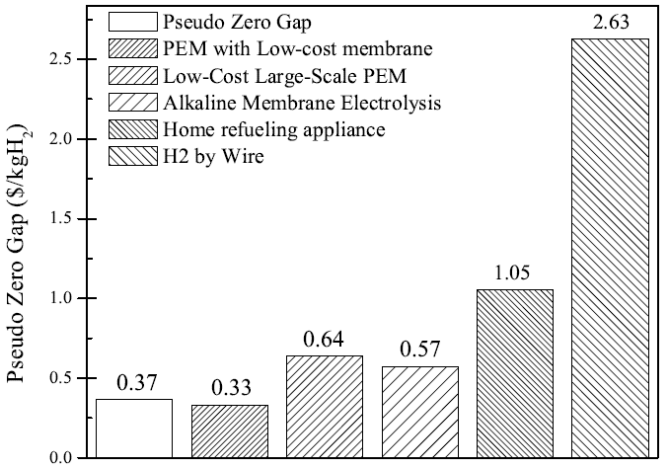

Fig. 4. Electrolyser stack costs comparison

The efficiency of the prototype decreased with raising voltages, as the energy applied is used more to overcome electrode and ohmic resistances than to production. The efficiencies vary around the 60% value reported for alkaline electrolysis technology. When the length of a hypothetical electrolyser stack was calculated, the prototype achieved lengths of 62-87cm for some of the highest voltages. Its hypothetical stack cost was compared to the cost of other developing electrolytic hydrogen production technologies. The cost of the stack was the second cheapest of them. Further search for resistant and cheap membrane and structure materials could lower this price even more.

A hypothetical solar electrolysis system was considered to make an economic feasibility evaluation. The total cost of the system, consisting of one 240 watt solar panel, a storage battery and an electrolysis stack, is $986. The gasoline saved considering four trips as the one described on the Electrolyser size section of the methodology allows for a $0.34 cost save per day. At this rate, the cost of the whole system would be recovered in approximately eight years, which is still relatively high. The system was also assessed on the frame of emission reduction, establishing a scenario where the vehicles making trips inside the Monterrey Metropolitan Zone (Nuevo León, México) all use the system. The emission reduction per \$ invested is 686.2 gCO_2/$. The cost for the Ecovia: Corredor Ruiz Cortines-Lincoln project was calculated to compare the emission reduction of the investment, getting a value of 138.105 gCO_2/$. The solar electrolysis system is five times more effective than this project, which makes it attractive as an emission reduction investment, not only considering cost savings due to gasoline consume reduction.

This research project fulfilled the objectives of designing and constructing an electrolysis cell with the adequate performance and size requirements to be the basic element of a future alkaline electrolyser stack, as a part of a solar electrolysis energy system with car applications. While the investment cost is still relatively high, further material research will surely reduce the stack price. The hypothetical system is

proved to be also attractive as an emission reduction investment, compared to another project with similar goals.

ACKNOWLEDGMENT

We would like to express our gratitude to the ITESM for providing the needed resources and installations during the development of the prototype. Thanks also, to the Chemical Engineering Laboratory personnel for their assistance on the construction of the prototype.

REFERENCES

[1] C. Withagen, "Pollution and exhaustibility of fossil fuels" Resource and Energy Economics, 1994.

[2] F. Barbir, T. Veziroglu, and H. Plass Jr, "Environmental damage due to fossil fuels use," International Journal of Hydrogen Energy, vol. 15, no. 10, pp. 739 – 749, 1990.

[3] B. Machol and S. Rizk, "Economic value of u.s. fossil fuel electricity health impacts," Environment International, vol. 52, no. 0, pp. 75 – 80, 2013

[4] J. S. Gaffney and N. A. Marley, "The impacts of combustion emissions on air quality and climate from coal to biofuels and beyond," Atmospheric Environment, vol. 43, no. 1, pp. 23 – 36, 2009.

[5] L. Chapman, "Transport and climate change: a review," Journal of Transport Geography, vol. 15, no. 5, pp. 354 – 367, 2007.

[6] P. Moriarty and D. Honnery, "Greening passenger transport: a review," Journal of Cleaner Production, vol. 54, no. 0, pp. 14 – 22, 2013.

[7] G. Cipriani, V. D. Dio, F. Genduso, D. L. Cascia, R. Liga, R. Miceli, and G. R. Galluzzo, "Perspective on hydrogen energy carrier and itsautomotive applications," International Journal of Hydrogen Energy, vol. 39, no. 16, pp. 8482 – 8494, 2014.

[8] M. Momirlan and T. Veziroglu, "The properties of hydrogen as fuel tomorrow in sustainable energy system for a cleaner planet," International Journal of Hydrogen Energy, vol. 30, no. 7, pp. 795 – 802, 2005.

[9] S. Verhelst, "Recent progress in the use of hydrogen as a fuel for internalcombustion engines," International Journal of Hydrogen Energy, vol. 39, no. 2, pp. 1071 – 1085, 2014.

[10] A. Urs´ua, L. M. Gand´ıa, and P. Sanchis, "Hydrogen production from water electrolysis: Current status and future trends," Proceedings of the IEEE, vol. 100, no. 2, pp. 410 – 426, 2012.

[11] K. Zeng and D. Zhang, "Recent progress in alkaline water electrolyelectrolysis for hydrogen production and applications," Progress in Energy and Combustion Science, vol. 36, no. 3, pp. 307 – 326, 2010.

[12] K. Scott, Electrochemical Reaction Engineering. Academic Press, 1991.

[13] M. I. Ismail, ed., Electrochemical Reactors, Their Science and Technology, vol. A. Elsevier, 1989.

[14] N. Nagai, M. Takeuchi, T. Kimura, and T. Oka, "Existence of optimum space between electrodes on hydrogen production by water electrolysis," International Journal of Hydrogen Energy, vol. 28, no. 1, pp. 35 – 41, 2003.

[15] R. Gilliam, J. Graydon, D. Kirk, and S. Thorpe, "A review of specific conductivities of potassium hydroxide solutions for various concentrations and temperatures," International Journal of Hydrogen Energy, vol. 32, no. 3, pp. 359 – 364, 2007. Fuel Cells.

[16] S. Marini, P. Salvi, P. Nelli, R. Pesenti, M. Villa, M. Berrettoni, G. Zangari, and Y. Kiros, "Advanced alkaline water electrolysis," Electrochimica Acta, 2012.

[17] D. Pletcher, X. Li, and S. Wang, "A comparison of cathodes for zerogap alkaline water electrolysers for hydrogen production," InternationalJournal of Hydrogen Energy, vol. 37, no. 9, pp. 7429 – 7435, 2012. 7thPetite Workshop on the Defect Chemical Nature of Energy Materials, 14-17 March 2011, Storaas, Kongsberg, Norway.

[18] D. L. Stojic´, M. P. Marˆceta, S. P. Sovilj, and S´cepan S. Miljani´c, "Hydrogen generation from water electrolysis: possibilities of energy saving," Journal of Power Sources, vol. 118, no. 12, pp. 315 – 319, 2003. Scientific Advances in Fuel Cell Systems.

[19] M. P. M. Kaninski, A. D. Maksi´c, D. L. Stoji´c, and ˆ S´cepan S. Miljani´c, "Ionic activators in the electrolytic production of hydrogen: cost reduction-analysis of the cathode," Journal of Power Sources, vol. 131, no. 12, pp. 107 – 111, 2004.

[20] S.Wang, C. Ji, J. Zhang, and B. Zhang, "Improving the performance of a gasoline engine with the addition of hydrogen/oxygen mixtures," Inter national Journal of Hydrogen Energy, vol. 36, no. 17, pp. 11164 – 11173, 2011. International Conference on Hydrogen Production (ICH2P)-2010.

[21] P. INECC, CONUEE, "Portal de indicadores de eficiencia energtica y emisiones vehiculares." Web page, 11/19/14, 2014.

[22] S. Satyapal, "Progress report for the doe hydrogen and fuel cells program,"tech. rep., US Department of Energy, 2013.

[23] Instituto de Calidad del Aire,"Programa de transporte y calidad del aire, Monterrey."Web page, 11/19/14, 2013.

[24] "Plan sectorial de transporte y vialidad del área metropolitana de Monterrey," Consejo Estatal de Transporte y Vialidad, tech. rep., Gobierno de Nuevo Leon, Consejo Estatal de Transporte y Vialidad, 2008.

[25] U.S. Energy Information Administration, "Frequently Asked Questions", Web page, 11/19/14, May 2014.

Electrochemical techniques to measure the degree of dispersion of solids inside an aqueous medium.

A.D. De La Concha Gómez, A. Alonso Gómez, J. Ramírez M.
Dept. De Energía
Universidad Autónoma Metropolitana, Azcapotzalco.
Mexico City, Mexico.
adelaconcha@gmail.com, aralonsogo@conacyt.mx

Catalina Haro Pérez
Dept. Física de Procesos Irreversibles.
Universidad Autónoma Metropolitana, Azcapotzalco.
Mexico City, Mexico.

***Abstract*—The dispersion of solid particles inside liquids is an important step in several industrial processes such as cosmetics, food processing, pharmaceutics, paintings and coatings. Dispersing is an act of separating pigment agglomerate into smaller particles. Thus, in pigment dispersing processes, the design objective is to achieve maximum dispersion efficiency, which ideally is attained when agglomerate particles are reduced to its primary particle size. Nowadays, most methods used to measure the degree of pigment dispersion are based on optical measurements, however those might become inefficient when they are used in high reflectivity pigments (e.g. titanium dioxide, silicon dioxide). In this work we present the results obtained through the use of two electrochemical techniques known as cyclic Voltammetry and Chronoamperometry. It was found a strong relationship between the degree of dispersion and the electrical current passing through the system under analysis. This behavior might lead to a model where predictions of the dispersion degree could be obtained when values of the electrical current are known**

Keywords— Chronoamperometry, cyclic voltammetry, degree of dispersion, powder dispersion.

I. Introduction

Silicon dioxide (SiO_2) is commonly used in the formulation of latex water paints and therefore is an important ingredient in the production of coatings and paintings. By adding SiO_2 in the coating formulation, the performance of suspension stability, the rheology, the strength of combination between substrate and coating and the finish degree can be improved significantly. However, such properties depend drastically on the wet SiO_2 efficiency dispersion. Therefore, an industrial relevant problem on these systems is to measure the degree of dispersion of SiO_2 in the solution.

When measuring dispersion, the vast majority of methods use light as their main source. Those using DLS (Direct Light Scattering, also known as PCS, Photon Correlation Spectroscopy), measure Brownian motion and relate it to the actual size of the particle. The problem here is that the sample under analysis must have such motion in order to perform measuring, or in other words, samples under analysis should be nearly ideal. Turbidimetry might be another option to measure dispersion, in fact it uses the same DLS principle, but it has another problem that has to be taken into account. Turbidimetry uses index of refraction, which is the degree of how light propagates inside a medium when it passes through, but Turbidimetry needs a clear difference between the index of refraction of the particle and that of the medium that contains it, otherwise is useless.

II. Problem Solving

To avoid aforementioned problems, in the present work two well-known electrochemical techniques are proposed and they rely exclusively on electrical properties such as voltage (v) and current flux (I). These techniques measure the current flux over a thin layer called interface, which is located inside the control medium that contains either the solid SiO_2 or some other compound under analysis. Cyclic Voltammetry uses a potential sweep as the input signal and records the electrical current passing over two electrodes, whereas Chronoamperometry uses a constant potential pulse and records also the electrical current as response. The leading hypothesis here is: the more dispersed the SiO_2 is, the harder will be for the electrical current to pass through the electrode-solution interface, or in other words, the degree of dispersion can be measured by recording variations in the electrochemical behavior of the interface.

III. Experiments

In order to test the previous hypothesis, two experiments were carried out on which we used SiO_2 in the first one, and high purity Sulfate latex on the second one. Discussion starts with a brief description of the first experiment followed by the description of experiment two.

Experiment one consisted of five 80 mL samples of a solution of KCl at 0.01 M within deionized water (18 MΩ cm^{-1}), first sample consisted with no SiO_2 diluted within, while the remaining four consisted each one of 1 gr of SiO_2 diluted within the solution. To achieve different degrees of dispersion for the samples containing SiO_2, a stirrer and ultrasonic waves (usw) were used. For the first sample with SiO_2, a stirrer was used for 3 minutes, and for the remaining three of them, it was used full amplitude ultrasonic waves at various time intervals:

3 minutes, 12 minutes and 15 minutes. Voltammetry was used at scan rate sr=50mV/sec, which was verified to be the optimum value to obtain a clean signal and meaningful information about the current flux passing over the interface. Voltammetry showed that in addition to sr=50 mV/sec, in general, the first inversion potential V1 can be set to V1=-1.0V, while for the second inversion potential V2, that can be set to V2=0.8V for this case in particular.

Experiment two consisted of three samples of 200 µL of high purity Sulfate latex diluted within 15 mL of deionized water. To get different degrees of dispersion, it was used ultrasonic waves only on the last two samples; at 60% wave amplitude in the first one, and full 100% wave amplitude over the last one for a time period of 2.5 minutes each. Voltammetry analysis was applied all over these three samples, fixing sr=50mV/sec with V1=-1.0 V and V2=0.5 V for this case in particular. Finally, Chronoamperometry was used over the same samples applying a fixed potential E1=-1.0 V for a time period T1=30 sec., and final potential of E2=0.5 V for a time period of T2=45 sec. For both analysis, Voltammetry and Chronoamperometry, results were recorded and are shown in the next section.

IV. Results

Results coming from experiment one (Figure 1) show an interesting behavior. At first, we can see a signal coming out from sample one with no SiO_2 and no agitation used, that the maximum peak for the current-flux in this case is -243.1 µA when potential reached -1.0 V, whereas for the second signal ("stirrer 3 min") that represents SiO_2 inside the solution KCl-H_2O with 3 minutes of agitation using only a stirrer, the maximum peak is found to be at -196.7 µA in the same potential value, which is a significant difference between these two systems if we considered that only one of them is containing SiO_2. In this case we believe that the presence of SiO_2 inside the medium with a simple mean of agitation ("stirrer") steers up the phenomenon of dispersion as we think it is.

As our analysis goes on, we can see that when using usw to disperse SiO_2, a clear distinction rises when using this dispersion method. Signal 3 coming out from sample 3 on which it was used usw for 3 minutes, shows a maximum peak of -187.5 µA, which is not that far from sample 2 but clearly marks the beginning of a region where the current flux passing through the interface decreases as more usw is used over larger periods of time. As can be seen on the remaining signals, signal 4 and 5 coming out from sample 4 and 5 respectively on which usw was used at times 12 minutes and 15 minutes respectively, there exists an obvious difference over the previous methods, for these two signals recorded maximum peaks of -143.5 µA and -135 µA respectively, not that different between them but clearly a lot different from the previous ones. Somehow this was something it was expected.

Data suggested that when using more intensive agitation methods over increasing periods of time, the system under analysis is somehow set to show more resistance to current-flux over the two electrodes at the same potential, therefore through the interface. This decreasing-like behavior (Table 1) we think is due to the degree of dispersion of solid SiO_2 within the solution KCl-H_2O.

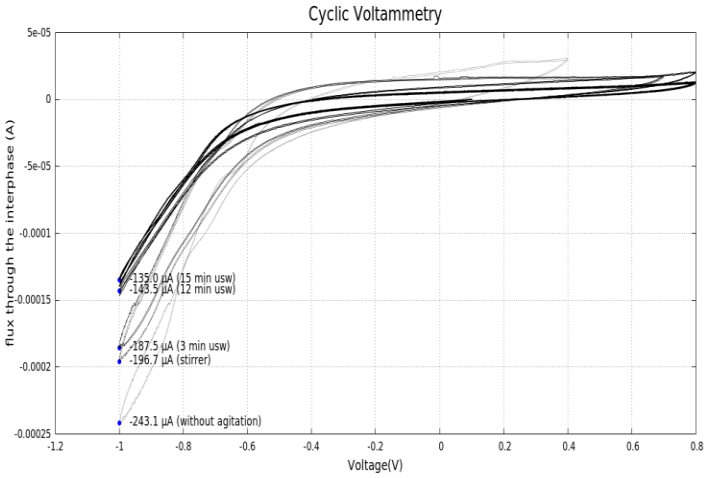

Table 1. Current values for the process observed at -1.0 V for experiment one.

Agitation Method	*Sample #*	*Agitation time (minutes)*	*Flux (µA)*
Without Agitation	1	--	-243.1
Stirrer	2	3	-196.7
usw	3	3	-187.5
	4	12	-143.5
	5	15	-135

In light of the results obtained in experiment 1, a second experiment very similar to the previous one was carried out but with the exception that it was decided to use high purity Sulfate latex instead of SiO_2. It was decided to use this compound since all its characteristics were known beforehand such as particle size.

This second experiment consisted of three 15 mL samples of deionized water, on which it was diluted 200 µL of Sulfate latex over each one. A process of agitation took place over them by means of usw, applying no usw on the first sample, but 60% wave amplitude over the second sample, and full 100% amplitude for the third sample; time period was for 2.5 minutes. Voltammetry analysis came next on each sample, the results obtained from it show a similar behavior to those obtained from experiment 1, that is, it seems that the more intensive the agitation procedure is used, the less flux is passing through the interface (figure 2).

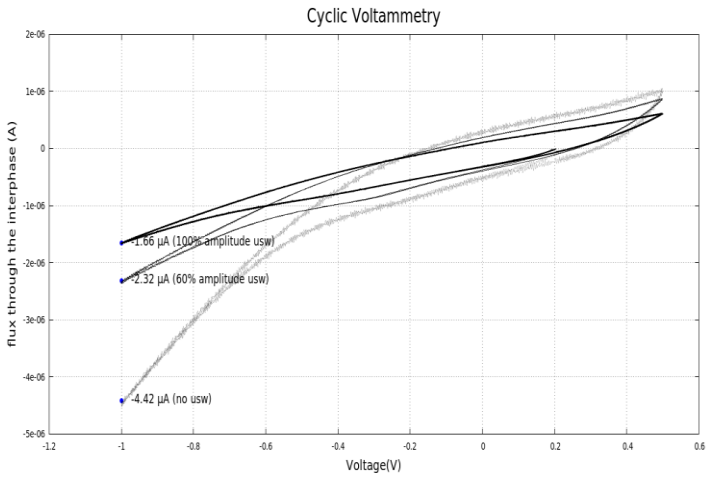

Figure 2. Typical voltammograms obtained on a vitreous carbon electrode (0.19 cm^2 geometrical area) with solutions containing 200 µL of Sulfate latex/15 mL deionized water for different deagglomeration conditions

According with Voltammetry, a maximum peak of -4.42 µA is reached when no agitation method is used, significantly different from peaks at -2.32 µA and -1.66 µA when agitation at 60% and 100% usw amplitude is used. We wanted to verify this results with Chronoamperometry for which it was used the same settings as in experiment one (figure 3).

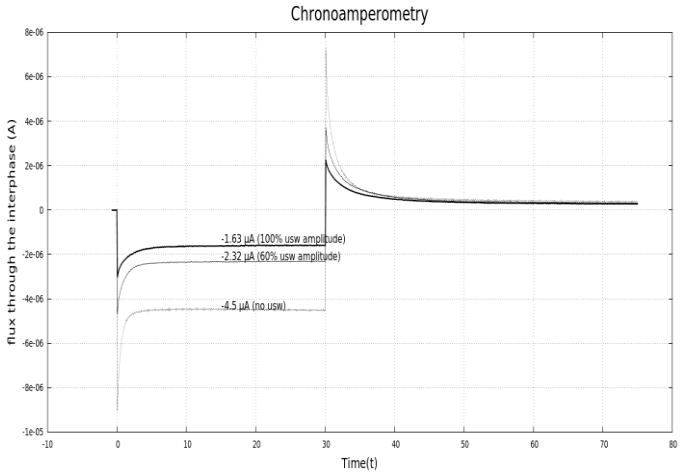

Figure 3. Typical Chronoamperometry obtained on a vitreous carbon electrode (0.19 cm^2 geometrical area) with solutions containing 200 µL of Sulfate latex/15 mL deionized water, applying -1.0 V constant potential for different deagglomeration conditions.

Chronoamperometry shows that when steady-state behavior is reached (flat region) we can compute a mean value for the current-flux passing through the electrodes, in which case is -4.5 µA for the signal that represents sample 1, -2.32 µA for the signal in sample 2, and -1.63 µA for signal representing sample 3. If we compare all those values obtained from Voltammetry and Chronoamperometry, we can see that they almost match, they differ only by small quantities, but a clear decreasing-like pattern can be seen here (Table 2).

Table 2. Current values for the processes obtained at -1.0 V for experiment two.

Agitation Method	***Sample #***	***Agitation time (minutes)***	***Voltammetry (µA)***	***Chronoamperometry (µA)***
Without Agitation	1	--	-4.42	-4.5
60% usw amplitude	2	2.5	-2.32	-2.32
100% usw amplitude	3	2.5	-1.66	-1.63

CONCLUSIONS

So far we have found statistical data that suggest a strong relationship between the agitation method used to disperse a compound within a medium and the current passing over the electrodes inside the medium. Also, we have found that in addition to the method used, other variables have a strong influence over the degree of dispersion. In this work we studied two of them, which are time of application and percentage of amplitude of the ultrasonic wave.

Based on this data, we strongly believe that Voltammetry and Chronoamperometry can be used as an effective tool to measure the degree of dispersion of a compound since the starting hypothesis appears to hold true, but still more experiments are needed to confirm such statement.

REFERENCES

[1] Michael J. Sadar, Turbiditry Science, Technical Information Series, Booklet No. 11, p. 4.

[2] Zetasizer Nano Series User Manual. England. July 2004.

[3] Allen J. Bard, Larry R. Faulkner, Electrochemical methods: fundamentals and applications, Wiley, 1980.

Ahorro y uso eficiente de energía eléctrica en sistemas de riego de cultivos localizados en el Valle del Mezquital que emplean aguas residuales no tratadas provenientes de la Ciudad de México

V. Ayala Ahumada
Departamento de Energía
UAM-A
México, México
ava@correo.azc.uam.mx

J. D. Juárez Cervantes
Departamento de Energía
UAM-A
México, México
jjc@correo.azc.uam.mx

F. Toledo Toledo
Departamento de Energía
UAM-A
México, México
Ftoledo2@correo.azc.uam.mx

J. M. Rodríguez Guerrero
Sector de Servicios
México, México
joma_485@hotmail.com

V. M. Flores Altamirano
Sector de Servicios
México, México
Altamirano100@hotmail.com

P. Puerta Huerta
Departamento de Energía
UAM-A
México, México
jpaph@correo.ler.uam.mx

***Resumen*—Este trabajo presenta varias estrategias derivadas de trabajos de campo y de gabinete para atender problemas específicos de carácter eléctrico hidráulico y mecánico, que propician el ahorro y uso eficiente de energía eléctrica en la operación de sistemas de riego de cultivos localizados en el Valle del Mezquital del Estado de Hidalgo que usan aguas residuales no tratadas provenientes de la Ciudad de México.**

Palabras clave—energía; ahorro; eficiente; aguas residuales; no tratadas.

I. INTRODUCIÓN

El problema del agua es cada vez más agudo por la escasez que se padece y que dificulta el proceso de suministro para atender necesidades básicas en zonas urbanas, situación que se agrava por la dependencia que de ella se tiene en algunos sistemas de riego de cultivos agrícolas. Existen diversos estudios que señalan con toda claridad la evolución de los estándares microbiológicos para el uso del agua residual [1]. Hasta principios de los ochenta los criterios sobre la calidad y el uso de agua para riego agrícola exigían niveles de pureza equivalentes a los del agua potable, con esta idea se formularon los estándares de California [2] que después fueron retomados como guía internacional por algunos países en desarrollo; sin embargo, para los que se empeñaron en alcanzarlos el desafío significó inversiones difíciles de sostener, además de serios problemas técnicos aún para los altamente industrializados.

En un trabajo de investigación realizado por expertos en el Valle del Mezquital del Estado de Hidalgo [3] [4], en donde se encuentran los distritos de riego más importantes del México, tanto por su superficie como por el valor económico de su producción agrícola, se le identificó como el esquema de reuso de agua de mayor tamaño en el mundo; situado a 60 km de la Ciudad de México, la mayoría de sus habitantes se dedican principalmente a la agricultura con un estándar de vida mayor al resto de la población que no tiene acceso al uso del agua residual para el riego. En esta zona existen sistemas de irrigación agrícola con aguas negras, siendo la producción de granos y forrajes los cultivos más importantes, además de otros que usan aguas limpias o grises en la producción de hortalizas y verduras; en ambos sistemas de riego la producción de frutales es muy rica y variada [5]. Para el cultivo de productos se usan extensiones territoriales del orden de 300 hectáreas o más, y un gran número de las parcelas de la zona se irrigan mediante técnicas de inundación que emplean láminas y surcos con agua residual "cruda" que llega directamente de la Ciudad de México; aunque la legislación vigente prohíbe el uso de este tipo de agua en el cultivo de vegetales que se consumen crudos, en la práctica en algunos casos esto no siempre se cumple.

II. CARACTERÍSTICAS DE LOS SISTEMAS HIDRÁULICOS

Se alimentan a través de derivaciones del canal de aguas residuales no tratadas provenientes de la Ciudad de México. Usan canales internos (fig. 1 a) para conducir el agua hacia los cárcamos que tienen sistemas de rejillas para retener sólidos en suspension (fig. 1 b). Las redes de tuberías son de acero de 12 pulgadas de diámetro (15 y 10 en algunos tramos) con trayectorias y longitudes totales diversas; tienen válvulas de paso y boquillas terminales en los puntos de inundación de canaletas de concreto, desde donde inicia el riego de parcelas por gravedad. Las bombas son eléctricas de montaje en superficie y flecha vertical hueca (fig. 2 b) con características técnicas desconocidas por falta de documentación original de fabricante; sólo se llaga a tener la potencia en hp, y en algunos casos la altura manométrica (h_b); no hay programas de mantenimiento preventivo y varias bombas han sido reparadas en talleres sin un buen control de calidad en los trabajos, por lo que han perdido sus especificaciones técnicas originales de fábrica y operan en forma ineficiente [6].

III. CARACTERÍSTICAS DE LAS REDES ELÉCTRICAS

Tienen una subestación eléctrica tipo rural alimentada desde una red de distribución aérea de 23 kV, equipada con un transformador tipo estación conexión delta-estrella aterrizada con relación 23 kV:440/254 V, protegido contra sobretensiones de origen atmosférico con apartarrayos y un esquema fusible-interruptor termomagnético para protegerlo contra cortocircuito y condiciones de sobrecarga; dicho transformador alimenta los circuitos de las bombas que operan en 440 V, además de un tablero para el servicio de alumbrado de la estación de bombeo.

IV. ESTRATEGIAS PARA EL AHORRO Y USO EFICIENTE DE ENERGÍA EN LA OPERACIÓN DE LAS REDES ELÉCTRICAS.

A. Evaluación de la calidad de energía eléctrica.

Se debe analizar detenidamente las opciones de operación de la red para decidir el número de puntos para monitorear los parámetros indicados en la tabla 1, aunque se sugiere considerar al menos un punto en las terminales de carga del interruptor del secundario del transformador y otro más en las terminales del motor de la bomba de mayor capacidad.

TABLA 1. LISTADO DE PARÁMETROS A MONITOREAR

PARÁMETRO	PUNTOS		
	1	2	…n
Secuencia de fases			
$V_{L\ PROMEDIO}$ (V)			
% Desbalance V_L			
$I_{L\ PROMEDIO}$ (A)			
F (Hz)			
$\%THD_V$			
$\%THD_I$			
$FP_{PROMEDIO}$			
$P_{MÁXIMA}$ (MW)			
$P_{PROMEDIO}$ (MW)			
W_P (MWh)			

Donde: V_L– Voltaje de línea; I_L– Corriente de línea; F– Frecuencia
THD_V– Total de distorsión por armónicas en voltaje.
THD_I– Total de distorsión por armónicas en corriente.
FP– Factor de potencia; P– Consumo de energía activa.
W– Consumo de energía activa.

Para validar los resultados se recomienda que el monitoreo se haga por lo menos durante una semana [7]. Dado que por lo general las estaciones de bombeo se encuentran localizadas en zonas alejadas y aisladas de las poblaciones, por razones de seguridad del equipo y de quien haga las mediciones, es aceptable que sólo se realice durante el periodo de tiempo que dura un ciclo de riego por inundación de láminas y surcos, el cual se repite por lo general cada día de la semana.

B. Optimización de la operación de la red eléctrica.

Las bombas son ineficientes ya que llevan muchos años operando y son de tecnología vieja, además de que han sido reparadas sin un buen control de calidad en los trabajos, por lo que se presentan grandes pérdidas de energía en su operación. De ello se infiere que las redes eléctricas operan con $FP_{PROMEDIO}$ por debajo del mínimo establecido por la normatividad (0.9) por lo que se recomienda evaluar el uso de sistemas centralizados de compensación de potencia reactiva empleando capacitores conectados en paralelo para incrementarlo y bajar el monto y el costo de la energía consumida, evitando también la penalización por bajo factor de potencia que impone CFE. Los beneficios y el ahorro de energía obtenidos por esta acción se deben a lo siguiente:

- Reducción en la componente atrasada de la $I_{CIRCUITO}$.
- Elevación del voltaje en la carga.
- Reducción de pérdidas de potencia activa (I^2R) por reducción de la I_{CARGA}
- Reducción de pérdidas de energía reactiva (I^2X*T) por reducción de la I_{CARGA} (T = tiempo en horas).
- Reducción de la demanda de potencia aparente S (kVA).

Además de que se generarán ahorros económicos para los agriculturos debido que CFE otorga una bonificación en la factura de consumo de energía por operar la red eléctrica del sistema de bombeo con un FP superior a 0.9

V. ESTRATEGIAS PARA EL AHORRO Y USO EFICIENTE DE ENERGÍA EN LA OPERACIÓN DE LOS SISTEMAS HIDRÁULICOS

A. Identificación de puntos crticos del riego.

Se deben identificar y analizar los puntos críticos en los que la demanda de agua sea mayor, registrándose la capacidad en hp de la bomba involucrada, la altura en metros del punto donde desemboca el agua para riego, además del diámetro en pulgadas y longitud en m de la tubería acoplada a partir del eje de dicha bomba con el objeto de verificar su idoneidad.

B. Verificación de la idoneidad de las bombas.

A fin de verificar la idoneidad de las bombas y del circuito del sistema de riego de cultivos, con base a las normas mexicanas NOM-002-ECOL-1996 [8] y NMX-AA-51-81 [9] se debe realizar un análisis fisicoquímico del agua residual empleada, esto para cuantificar los parámetros señalados en la tabla 2, de los que resulta de especial interés el contenido de *sólidos disueltos totales* (ρ) debido a que interviene en el cálculo del rendimiento de la bomba empleando un método analítico para determinar la potencia hidráulica actual PH_a (1) en hp de la bomba bajo revisión; el gasto actual de la bomba (Q_a) se puede determinar mediante una prueba de campo ya que en la mayoría de los casos no se conoce ni siquiera el valor del gasto original de fábrica.

$$PH_a = Q_a * P_{ba} \quad (1)$$

Donde: P_{ba} = presión de salida actual en la bomba en N/m^2 siendo:

$$P_{ba} = \rho * g * h_b \quad (2)$$

Donde:

ρ = sólidos disueltos en el agua residual en kg/m^3 obtenidos a partir de la prueba fisicoquímica.

g = valor de la gravedad terrestre en m/s^2 de la zona geográfica donde se localiza la estación de bombeo [10].

h_b = altura total manométrica de la bomba en m según especificación de fabricante.

TABLA 2. ANÁLISIS FISICOQUÍMICO DEL AGUA RESIDUAL [10]

Parámetros	Unidades	Resultados
Ph	unidades	
Acidez	mg $CaCO_3$/L	
Alcalinidad	mg/L	
Sólidos suspendidos totales	mg/L	
Sólidos disueltos totales (ρ)	mg/L	
Coliformes totales	UPC/100mL	
Calcio	mg/L	
Magnesio	mg/L	
Dureza	mg/L	
Sodio	mg/L	

Laboratorio de Calidad de Agua y Residuos *(UAM-A)*.

La velocidad actual del agua V_a (3) en m/s a la salida de la bomba, se puede determinar a partir del gasto actual y del área en m^2 del tubo acoplado ya que se conoce su diámetro:

$$V_a = Q_a/A_T \quad (3)$$

Además, considerando 3 m de pérdida por cada 100 m de la longitud del tubo (L_T) se puede obtener la altura de pérdida h_P en metros del gasto que proporciona la bomba bajo revisión.

C. Optimización del Sistema Hidráulico.

1) Evaluación del rendimiento de las bombas y su impacto sobre el uso eficiente de energía eléctrica: con el método descrito en el inciso *B*, se comprueba que la potencia hidráulica actual (PH_a) de las bombas sea del orden del 90% [11] de la potencia eléctrica del motor acoplado; entre menor sea su valor con respecto a este referente, más bajo será su rendimiento e impactará en su eficiencia energética.

2) Inspección visual del diseño de la obra civil: el nivel del agua en el cárcamo después de que éste se llena para iniciar cada uno de los ciclos de bombeo, no debe estar por debajo del nivel mínimo establecido por la altura manométrica de las bombas, ya que de lo contrario se presentará el fenómeno de cavitación con desgaste severo en los sellos de la flecha por falta de lubricación en los tazones (fig. 2 a).

3) Confirmación de la posición vertical de la fecha de las bombas: hundimientos en la cimentación de las bombas por vibración y el tiempo que han estado operando, producen inclinación de la flecha que también provoca desgaste en sus rodamientos y sellos provocando graves problemas mecánicos y disminución de la potencia hidraúlica, por lo que a la brevedad deben tomarse acciones correctivas (fig. 2 b).

Fig. 1. Canal de alimentación (a) y rejillas del cárcamo (b) [6].

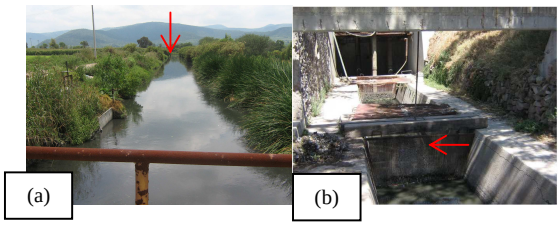

Fig. 2. Tazones fuera del nivel del agua del cárcamo (a) y pérdida de la verticalidad de la flecha de una bomba (b) [6].

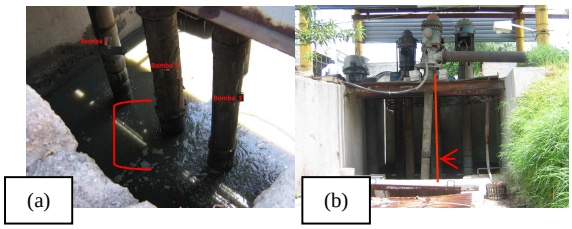

CONCLUSIONES

Los resultados obtenidos mediante el estudio de calidad de energía resultan indispensables para formular estrategias que permiten la optimización de la operación de la red eléctrica. Asimismo, la verificación de la idoneidad de las bombas es esencial para identificar si éstas operan en forma eficiente, o en su caso implementar un plan para sustituirlas por otras más eficientes. Se debe revisar la congruencia entre el diseño civil y la infraestructura que integra el sistema hidráulico a fin de identificar anomalías que impacten en un mal funcionamiento del sistema de riego en su conjunto y, en su caso, planear acciones correctivas. Sin lugar a dudas, las acciones señaladas y descritas en el presente trabajo coadyuvarán en el ahorro y uso eficiente de energía eléctrica.

REFERENCIAS

[1] G. Bartone RC, Arlosoroff S, Shuval HI. Implementing water reuse. En: Proceedings Water Reuse Symposium IV AWWA. Denver: Research Foundation, 1988.

[2] State wide standards for the safe direct use of reclaimed wastewater for irrigation and recreational impoundments. Berkeley, Ca. California State Department of Public Health, 1968.

[3] Strauss M. Examples of wastewater and excreta use 5. Practices in agriculture and aquaculture. IRCWD News 1988; 13:24-25.

[4] Cifuentes, Enrique *et all*. Escenario epidemiológico del uso agrícola del agua residual: El Valle del Mezquital, México. Salud Pública de México: Enero-Febrero de 1994, Vol. 36, No.

[5] Enciclopedia de los Municipios de México-Medio Físico del Estado de Hidalgo. Instituto Nacional para el Federalismo y el Desarrollo Municipal.

[6] *V. Ayala Ahumada. J. D. Juárez Cervantes. F. Toledo. J. M. Rodríguez Guerrero. V. M. Flores Altamirano. P. Puerta Huerta.* Estrategias de ahorro y uso eficiente de energía eléctrica en sistemas de riego de cultivos con aguas de reuso. El caso de Teltipan de Juárez, Estado de Hidalgo, México. IEEE XXIII RVPA-I, Acapulco Gro. México. GIN-05 P114.

[7] CFE (2005). Especificación CFE L0000-45. Desviaciones permisibles en las formas de onda de tensión y corriente en el suministro y consumo de energía eléctrica. México: CFE. B.3.2, p. 12.

[8] NOM-002-ECOL-1996. Límites máximos permisibles de contaminantes en las descargas de aguas residuales a los sistemas de alcantarillado urbano o municipal. México: SEMARNAT.

[9] NMX-AA-51-81. Determinación de Metales. Método Espectrofotométrico de Absorción Atómica. México.

[10] Laboratorio de Calidad de Agua y Residuos de la Universidad Autónoma Metropolitana Unidad Azcapotzalco

[11] Referencia documental del rango (S/F).

Acetone-Butanol-Ethanol production from ugarcane Bagasse: An Experimental & Simulation Analysis

Ricardo Morales-Rodriguez, Zeferino Gamiño-Arroyo, Fernando I. Gómez-Castro
Departamento de Ingeniería Química
Universidad de Guanajuato
Guanajuato, México
ricardo.morales@ugto.mx

Lisette Samarti-Rios, Maribel Sanchez-Morales, Sandra Avalos-Farfán, Eduardo S. Perez-Cisneros, Divanery Rodriguez-Gomez
Departamento de Ingeniería de Procesos e Hidráulica; Departamento de Biotecnología
Universidad Autónoma Metropolitana-Iztapalapa
Ciudad de México, México

Merlín Alvarado-Morales
Department of Environmental Engineering
Technical University of Denmark
Kongens Lyngby, Denmark

Manuel Enríquez-Poy
Dirección General
Ingenio Central Motzorongo S.A. de C.V.
Ciudad de México, México

***Abstract*—This study presents an integral analysis for acetone, butanol and ethanol (ABE) process production including experimental activities and a simulation-based approach. A detailed experiments were performed for the pretreatment of sugarcane bagasse and fermentation of the liberated sugar molecules, involving a detailed statistical analysis in the results. The experiments allowed to obtain the most reliable process conditions for the sections of the process analyzed in the lab activities. The collected information was used to perform a rigorous simulation of the complete ABE production process and propose an alternative configuration for downstream processes, since, it is one of the most analyzed section of this process from the simulation and modelling point of view. An integration of energy streams was also performed in order to analyze the feasibility of the reduction in energy consumption, which also included the *in situ* combustion of remaining solids process in order to produce the necessary vapor in the process. The results illustrates the feasibility of the ABE process from the economic and environmental perspective because of the significant reduction of carbon dioxide emissions from fossil fuel source.**

Keywords*— *Acetone-Butanol-Ethanol; sugarcane bagasse; process design; modeling; simulation

I. INTRODUCTION

The production of biofuels and high value-added products from lignocellulosic biomass has gained special interest due to the possible reduction of crude oil production, the greenhouse effects in the environment, etc. Among the different products from lignocellulosic material, butanol has been identified as a potential biofuel since it shows diverse advantages compared to other biofuel such as bioethanol. For example, the energy content of butanol is closer to gasoline than the energy content of ethanol and its low vapor pressure facilitates its use in existing gasoline supply and distribution channels; moreover, butanol can be blended in a better manner and it is less hydrophilic compared to bioethanol [1].

The acetone, butanol and ethanol (ABE) production process employing lignocellulosic biomass included four main sections, the pretreatment of lignocellulosic, the enzymatic hydrolysis, the fermentations and the downstream processes.

The authors kindly acknowledge the Council for Science and Technology of Guanajuato State (CONCyTEG, project number 123-2015UG) and the Universidad de Guanajuato for the financial support.

The production of butanol by a biotechnological pathway has been performed employing bacteria from the genus *Clostridium*, such as *Clostridium acetobutylicum*, *Clostridium beijerinckii*, among others. In this process, the simultaneous production of acetone, butanol and ethanol (ABE) could be seen as an advantage due to the diverse products from the fermentation process. However, the simultaneous acetone and ethanol production could also be a disadvantage because it would increase the complexity in the purification and separation of butanol after the fermentation unit; in addition with the diluted concentrations of the solvents produced in the process. Those have been identified as one of the main drawbacks for applying this process at industrial scale.

The research activities regarding to ABE process have been mostly performed studying the different sections of the process separately, which can provide relevant information; but the successive and integral analysis for these process must be performed.

This work presents the process design for acetone, butanol and ethanol (ABE) production from sugarcane bagasse, which included experimental and simulation tasks. The experimental part involved the pretreatment of the biomass and fermentation of the released sugars from the sugarcane bagasse. The optimal information from the laboratory (such as, compositions from the pretreatement reactor and fermenter) was employed to scale-up and simulate the processing plant for ABE production. The sections of the processing plant included in the simulation are: pretreatment, enzymatic hydrolysis, fermentation, microorganisms growing and a novel downstream process configuration for products purification and recovery of reactants [2].

The simulation was carried out including all the compounds found in the experimental activities, which allowed to perform a more realistic analysis rather than considering a hypothetical mixture, as it is commonly found especially for downstream processes analysis. The simulation employed a rigorous thermodynamic model (NRTL and Hayden-O'Connell equation of state) for the phase equilibria calculations in order to predict the behavior of the compounds at the separation

units. The recovered butanol was obtained with purity of 98.8 wt % and one recovery ratio (downstream/fermenter) of 0.98. The results illustrated a reliable scenario for ABE production from sugarcane bagasse in Mexico.

II. Acetone, Butanol and Ethanol Process

The ABE production process consists of four principal sections: 1) pretreatment (PT): the main objective is breaking down the lignocellulosic matrix to leave the cellulose available for the hydrolysis by the enzymes; 2) enzymatic hydrolysis (EH): this section employs some cellulases that liberate the remaining glucose from the polysaccharide chain; 3) ABE fermentation: the glucose previously produced is processed by the microorganisms to produce acetone, butanol and ethanol; 4) downstream process: the main purpose of this section is the purification of butanol and high valued-added products, as well as the recovery of some reactants.

III. Methodology

The development of this study relied on two principal parts, the experimental and the simulation activities. The experimental approach consisted on the data collection such as, biomass selection and characterization, selection of the amount and type of acid employed in the pretreatment, determination of the degree of conversion in the fermentation process and the selection of the proper operating conditions for the pretreatment and fermentation unit. Regarding to the simulation approach, the process structure for ABE production was mainly based on previous works [3,4]; while the experimental data and operating conditions collected from the experimental part [5] were employed to perform the simulation.

A. Experimental approach

The experimental activities were performed in a lab scale following a rigorous statistical analysis and methods.

1) Lignocellulosic raw material

The high production of lignocellulosic residues in Mexico as a result of agroindustry activities illustrates the potential production of biofuels and high valued-added products. The sugarcane bagasse is one of the residues from sugar production that could be efficiently used for bioproducts production, especially in the State of Veracruz where the sugar industry is located. The sugar cane production company "Central Motzorongo" provided the raw material employed in this work. The study included two types of bagasse: the bagasse obtained after the harvesting (dry bagasse, BS) and the bagasse after the sugar extraction (humid bagasse, BH).

2) Pretreatment section

The first step in this activities was the drying of the raw material (both sugarcane bagasses) during 24 hours at 68°C, followed by the grinding of the solid until getting a particle size of 0.64 mm.

The pretreatment of the sugarcane bagasse was performed at different process conditions, aiming to perform a grid screening and select the best operating points. The variables employed were temperature (100°C, 110°C and 120°c) and sulfuric acid concentration (0, 2, 4, 6, 8, 10 %wt/wt). Three repetitions per each grid point. The reaction time was 5 minutes. After the pretreatment, a neutralization and toxicity analysis were performed in order to verify whether the employed microorganisms could grow in the pretreated product. The concentration of released sugars was determinated through reduced sugars using the method proposed by Miller that uses 3,5-dinitrosalicylic acid (DNS) as a reactant [6]. More details about the experimental steps could be find at [5,7].

3) Enzymatic hydrolysis section

An enzymatic hydrolysis was accomplished employing the product from pretreatment section. The enzymatic hydrolysis was performed using Celluclast from Novozymes ®, in a reactor operating at 50°C for 36 hours.

4) ABE fermentation

The product from the enzymatic hydrolysis was employed to perform an ABE fermentation using *C. acetobutylicum*. The cultivation was done in four different substrates: a) BG (pretreated product plus 50 g/L of glucose); b) B (pretreated product); c) G (50 g/L glucose) and d) AB (50 g/L of glucose plus 0.3 g/L of butyric acid). For cultivation system a), the concentration of reducing sugars after the pretreatment was adjusted with glucose addition to reach a more realistic initial concentration. The fermentation was carried out at 37°C with initial pH of 5.0 and an initial glucose concentration between 60-80 g/L. The fermentation was carried out at anaerobic conditions for 233 hours. A sampling schedule was proposed in order to accomplish a subsequent determination of products concentration. More details about the experimental steps could be find at [5].

5) Analytical method.

a) Pretreatment

The reduced sugars concentration determination employing the DNS method, was performed employing a temperature cycler (Robocycler 96) and the ELx808™ Absorbance Microplate Reader. The reduced sugars concentration was quantified employing a standard curve with absorbance as a function of glucose concentration.

b) Toxicity

The toxicity analysis was done determining the cell growth. Thus, a spectrophotometer at 560 nm was employed in order to analyze the cell growth of *C. acetobutilycum* on released sugars from the pretreatment and compare it with a control sample of grown cells without pretreated extract.

c) Fermentation analysis

The samples obtained from fermentation were analyzed to determine the cell biomass density and products concentration. The cell biomass density was quantified employing a spectrophotometer Genesys 10 S UV-VIS (thermos scientific brand). The acetone, butanol and ethanol concentration were determined employing a chromatograph Agilent model 7820 employing an Innowax column and flame ionization detector. The temperature ramp was from 80 °C to 300°C for 15 minutes. Commercial acetone, butanol and ethanol were

employed in order to identify the retention time. The identification of other byproducts, such as acetic acid and butyric acid was performed qualitatively in the chromatogram.

The pH was obtained employing a potentiometer pH120 – Conductronic. This was employed in all the sections of the process where it was necessary.

B. *Simulation approach*

The methodology followed in this study (see Fig. 1) consists of three main stages: data collection, simulation and data analysis; and finally the determination of process configuration for ABE production.

1) Data collection

The first stage starts with the collection of the necessary information to know the composition of the raw material and the possible compound that could be produced in a chemical or biochemical reaction, as well as the possible technologies and operating conditions from publications or lab results. The next step is to determine the appropriate thermodynamic models to be employed for each unit operation in the process.

2) Simulation and data analysis

The second stage continues with the generation of process configuration relying on the previous studies to be improved or for proposing new process configurations including the design of a conventional unit operation, intensification or hybrid process. The unit design could be firstly done employing some shortcut method followed by rigorous simulation of unit operations. Here, a previous results could be employed as process conditions or the some results obtained at lab scale.

3) Determination of process configuration

The last stage to determine the process configuration involves the setup of the benchmarking criteria to compare the different process configuration and specification of the variables, in order to select the most promising process configuration in terms of the benchmarking criteria. The criteria could involve economic, environmental and also social aspects.

The simulation of the process was performed using PRO/II software version 9.0.

IV. Results

A. *Experimental approach*

1) Pretreatment

The results obtained for the pretreatment are illustrated in Fig. 2. The highest yield was found at the temperature of 120°C and acid concentration of 6 % wt/wt, for the dry bagasse; regarding to humid bagasse, the best results were found at the temperature of 100°C a 10 %wt/wt of acid concentration.

The best process conditions for dry bagasse were selected to be used in subsequent experiments of the process. The percentage of conversion from cellulose to glucose was 66.1%, which a valuable data to be used in the simulation part.

The toxicity analysis was performed for all the samples. The results showed that there was not the presence of inhibitory compounds at the different process conditions since there was no significant difference at the absorbance measurements between pretreated product and control (see Fig. 3)

2) Fermentation

The best culture medium for microorganism growth and glucose consumption was the medium identified as G, which in fact was a model substrate. The media including pretreated bagasse with better specific growth rate was for BG. Table I shows the kinetic parameters obtained for culture medium.

The conversion selected to be used in the simulation approach was the obtained for the SG media. The percentage of glucose conversion to products was 89.7 %.

B. *Simulation approach*

1) Data collection

The first step is the collection of data that was mostly obtained from experimental approach, such as, temperatures and pressure conditions in the unit operation, percentage of reactants conversion, compositions entering and leaving to the unit operation, among others.

The process conditions in the pretreatment extracted from experiments were: percentage of cellulose conversion to ethanol (66.13%), operating temperature (120°C) and sulfuric acid concentration (6 %wt/wt).

Fig. 1. Methodology for simulation approach for ABE production process

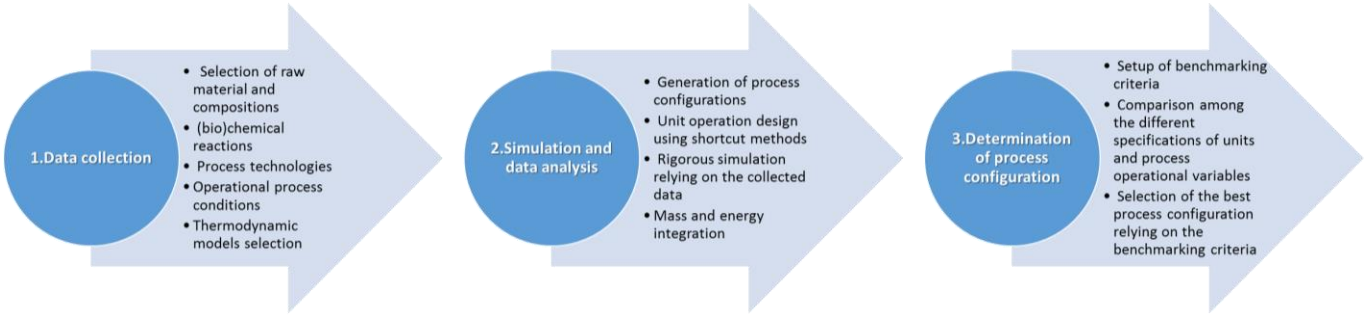

Fig. 2. Experimental results of sugarcane bagasse pretreatment at different temperatures and acid concentration. BH: Humid bagasse: BS: dry bagasse at 100°C, 110°C and 120°C.

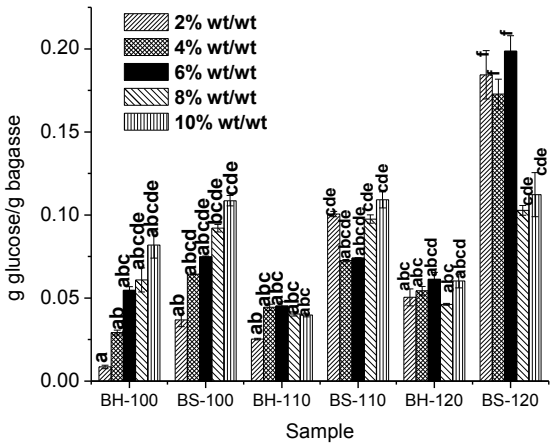

TABLE I. KINETIC PARAMETERS FOR ABE FERMENTATION EMPLOYING *C. ACETOBUTYLICUM*

Culture medium	Biomass (g/L)	Residual substrate (g/L)	μ (h^{-1})	Consumed substrate (CS), %	$Y_{X/S}$ ($g_{biomass}$/g de CS)
G	1.88±0.098	3.11±0.083	0.290	94	0.040
AB	1.57±0.163	42.97±5.410	0.0021	14	0.220
BG	2.67±0.103	91.26±0.083	0.0048	8.7	0.611
SG	3.83±0.234	12.33±5.410	0.0142	89.7	0.728

BG: pretreated product plus 50 g/L of glucose. B: pretreated product. G: 50 g/L glucose. AB: 50 g/L of glucose plus 0.3 g/L of butyric acid.

Fig. 3. Toxicity analysis for pretreatment sugarcane bagasse at different temperatures and acid concentration. BH: Humid bagasse: BS: dry bagasse at 100°C, 110°C and 120°C.

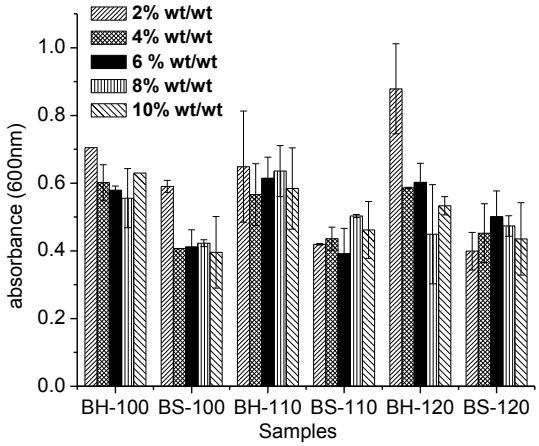

The operating conditions for the enzymatic hydrolysis were obtained from a previous publication [8]. The temperature proposed in the publication was 50°C, pressure of 1 atm and a cellulose to glucose conversion percentage of 66%. The selection of the conditions were according to the similar data set consulted in [8].

The collected information from the fermentation was the operating temperature (37°C), fermenter pressure (1 atm) and percentage of glucose conversion into ABE products (89.7%).

The simultaneous production of acetone, butanol and ethanol in the fermentation unit could also be seen as a disadvantage, because it would increase the complexity in the purification and separation of butanol after the fermentation unit. Thus, as far as purification and separation processes for ABE process is concerned, several studies have tried to employ and combine diverse separation technologies to overcome those issues. Heitmann et al. performed a simulation to compare three separation process configurations for a hypothetic binary water-butanol mixture, where the authors proposed the use of heteroazeotropic distillation, integrated extraction-distillation using an ionic liquid and an integrated pervaporation-distillation process [9]. Using a similar representative mixture, Luyben also proposed and simulated a heteroazeotropic distillation process but at vacuum conditions for one of the distillations columns [10]. Kraemer et al. simulated the separation of acetone, butanol, ethanol and water leaving the fermenter, using a hybrid extraction-distillation that consisted of an extraction process using an organic solvent (1,3,5-trimethylbenzene) for ABE and a train of three distillation columns [11]. Anbarasan et al. relying on an experimental approach, proposed an in situ process for ABE removal with liquid-liquid extraction using glyceryl tributyrate as an extractant, followed by a hypothetical distillation process [12]. On the other hand, Qureshi et al. presented a collection of experimental studies for butanol recovery mostly from a water-butanol mixture, employing adsorption to separate butanol [13]. Other studies has proposed the use of gas stripping for in situ removal of ABE from fermentation broth, for instance, employing nitrogen [14] or recirculating the hydrogen and carbon dioxide that was produced in the same fermentation unit [15]. There are several technology options for the purification and separation of the products of ABE process, but most of the previous works have considered a hypothetical mixture using the main compounds of the fermentation broth, such as, a butanol-water binary mixture or a blend containing acetone, butanol, ethanol and water, which could be a close approximation to the real mixture, but the presence of other compounds leaving from the fermenter (e.g. not converted sugars, carbon dioxide and hydrogen) can really introduce a difference in the thermodynamic behavior of the downstream processes.

The performed literature survey allowed to identify the possible process candidates for improving or proposing a new process configuration for ABE separation and purification; according to Douglas [16], the use of a distillation column should be considered as the first option among the possible candidates, thus, the first trial was employing the necessary distillation columns at the downstream section. Based on previous publication proposed by Heitmann et al. and Luyben, the downstream section proposed in this work consists of three distillation columns and three flash units; the operating

conditions for the distillation columns were considered and modified from the same publications [9,10].

The analysis of process conditions and involved compounds allowed to select the thermodynamic models: NRTL and Hayden-O'Connell method [17]. As far as NRTL model parameters for this system is concerned, previous studies have published and employed this model for bioethanol purification from lignocelluloses and this production process also includes most of the involved compounds for ABE process [18,19].

In order to carry out a realistic simulation, the capacity of the plant was calculated considering a certain demand of biobutanol in Mexico, to blend with gasoline and cover part of the daily consumed fuel. The biobutanol demand calculated was 3,561.62 kg/day. Thus, knowing the amount of required biobutanol and using the data collected from the experiments, it was possible to calculate the required amount of sugarcane bagasse to be processed to produce the biofuel demand. The amount of sugarcane bagasse to be treated was 27,243 kg/day. The sugarcane bagasse composition fed to the process is illustrated in Table II.

TABLE II. SUGARCANE BAGASSE COMPOSITION

Compound	Composition, %
Cellulose	72.33
Hemicellulose	2.75
Lignin	15.75
Ash	9.17

2) Simulation and data analysis

Using the collected data and relying in previous studies [2,19-20], a process configuration for ABE production was proposed. The Fig. 4 illustrates the process configuration proposed for the ABE production.

The process starts mixing the sugarcane bagasse with a sulfuric acid solution (6 % wt/wt) in a mixer (M2). This mixture is fed to the pretreatment reactor (R1:PT) were high pressure vapor (268°C and 13 atm) is also fed in order to reach the operation conditions of 120°C.

The stream leaving the pretreatment reactor (R1:PT) is a vapor, solid and liquid mixture that is sent to a solid separator (SEP1) to subsequently separate the vapor and liquid phase in two streams. A portion of the liquid phase (2% of the total flowrate) is splitted (SP1) and fed to a reactor (R2:NS) together with an ammonia stream in order to produce ammonium sulfate, which is employed as a nitrogen source for microorganism growth and reproduction. The reaction at R2:NS is carried out at 1 atm and 50°C with a conversion percentage of 89% for sulfuric acid. The stream leaving the reactor is mixed (M4) again with the liquid and vapor flowstreams coming from a mixer (M3). This mixture pass through a heat exchanger (H1) to reach 25°C and then is fed to a neutralization tank (R3:NE) where it is mixed with a sodium hydroxide.

The neutralized liquid flowstream is mixed (M5) with the solid stream that was previously separated (after pretreatment reactor). The solid-liquid stream is divided in a splitter (SP2) in two streams, 10 % of the flowrate is sent to the inoculation section and the 90% is sent to the enzymatic hydrolysis section.

The flowstream sent to the inoculation section must reach 37°C of temperature passing through a heat exchanger (H2) and subsequently the stream is mixed (in M5 unit) with one diluted enzyme stream and sent to the inoculation reactor (R4:IN) to liberate the glucose molecules from solids. The fed ratio for enzyme must be 20 mg of enzyme for 1 g of cellulose; and the dilution must be 30% of enzyme the rest of water. The liberated glucose is used to grow the microorganism, which is used at the fermentation reactors.

The flowrate from SP2 previous to enter to the enzymatic hydrolysis reactor must increase its temperature up to 50°C in a heat exchanger (H3). A diluted enzyme stream is also fed to the enzymatic hydrolysis reactor (R5:EH) with the same enzyme/cellulose ratio and dilution percentage (as at the inoculation section). The conversion percentage from cellulose to glucose was 66%. The leaving stream from the enzymatic hydrolysis must decrease the temperature until 37°C in a heat exchanger (H4) to reach the appropriate conditions for the fermentation section.

The stream from the inoculation reactor (R4:IN) and the stream leaving the H4 are sent to solid-liquid separators (SEP2 and SEP3, respectively). The liquid phase streams are sent to the fermentation reactor, while the solid phase streams are disposed to be combusted and use the energy for power generation.

The microorganism stream (from inoculation section) together with the stream from enzymatic hydrolysis section are fed to fermenter (R6:FM) where the glucose is transformed into acetone, butanol, ethanol, water, carbon dioxide and hydrogen by the microorganism action. The percentage of glucose converted into products was 89.7% relying on the following stoichiometry:

$$18C_6H_{12}O_6 \rightarrow 6C_3H_6O + 12C_4H_{10}O + 3C_2H_6O + 15H_2O + 6H_2 + 36C\,O_2$$

The ABE fermenter is followed by a flash unit (F1), which separates the leaving stream from the fermenter (R6:FM) that contains liquid and vapor phases, the vapor phase is sent to the second flash unit (F2) to recover the acetone and butanol from the mixture in liquid phase and take out most of the hydrogen and carbon dioxide leaving the fermenter as vapor. The liquid phase from F1 is fed to the first distillation column (DC1) that separates most of the water and glucose at the bottom of the column. The top stream from the DC1 is mixed (in M8 unit) with the recovered butanol and acetone from F2 and sent to the second distillation column (DC2) where the butanol is obtained at the bottom with a purity of 98.8 wt % and a recovery ratio (DC2 bottom stream/R6:FM stream) of 0.98. The following distillation column (DC3) was employed to separate the ethanol at diluted concentration with water; the bottom stream is sent to the last flash unit (F3) to obtain the acetone at the liquid stream with a purity of 91 wt%; the vapor stream contains part of acetone and carbon dioxide that was still absorbed in the liquid phase due to the interaction with water.

Fig. 4. Process flowsheet for ABE production.

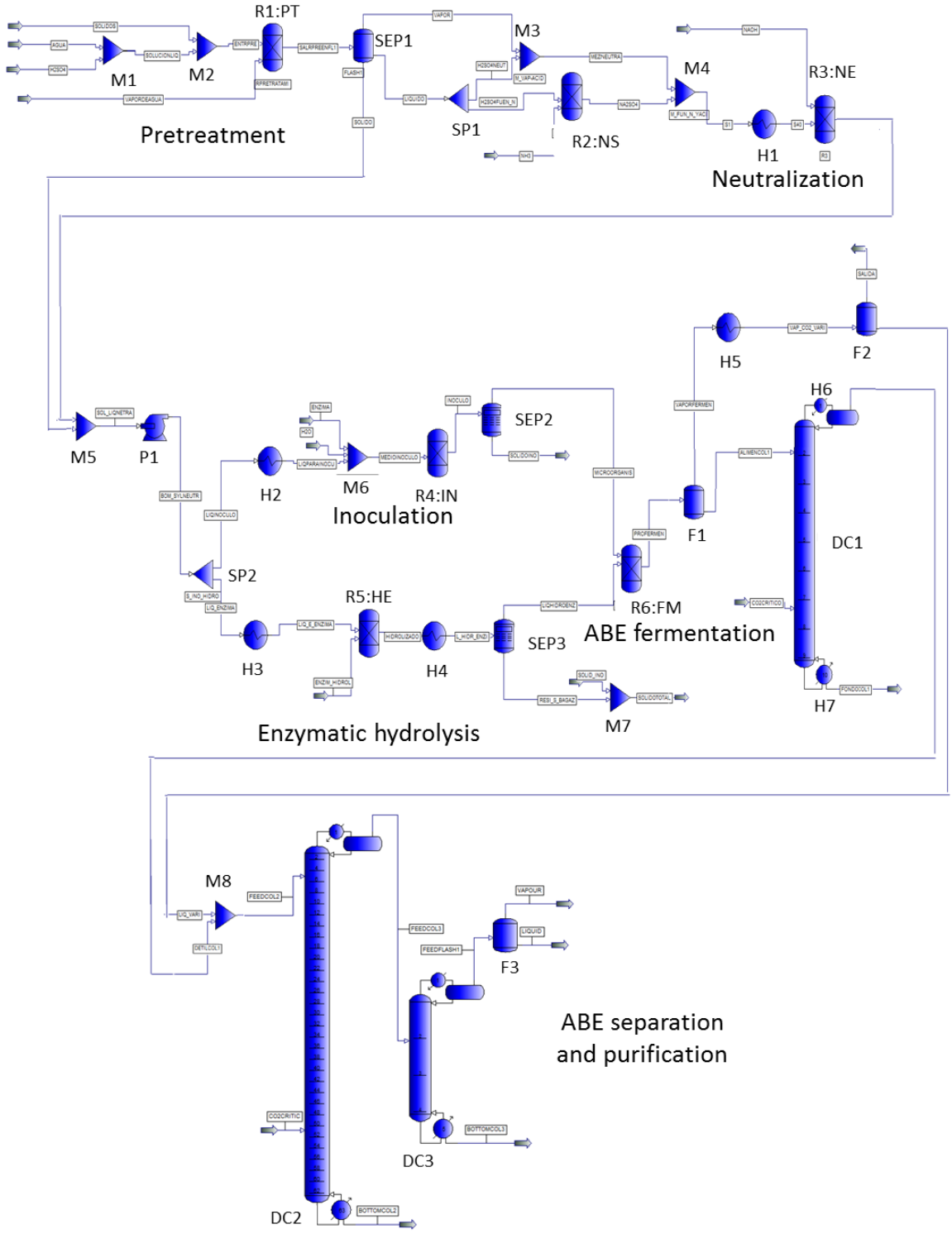

The energy integration was performed in order to analyze the possible reduction in the energy consumption together with the cost analysis. The energy integration was performed employing the seven heat exchangers (H1-H7, see Fig. 4). Table III illustrates the simulation results employed for the integration of stream for the efficient energy use and Table IV shows the data used in the cost of the network. The Results of the energy and streams integration are illustrated in Fig. 5.

TABLE III. STREAM DATA FOR ENERGY INTEGRATION IN THE ABE PROCESS

Stream	T_{in}, °C	T_{out}, °C	F, kW/K	q_{dis}/q_{req}	m, kg/hr	Cp, kJ/kg/K
H1	102	25	62.93	4846.01	77,721.51	2.91
H2	48.6	37.5	8.23	91.44	9,498.96	3.12
H4	50	37	73.77	959.09	85,611.66	3.10
H5	37	15	3.30	72.78	6,511.78	1.83
H6	93	86	5.27	36.93	11,811.80	1.61
H3	48.6	50	74.13	103.79	85,490.64	3.12
H7	86	100	68.85	963.99	60,030.14	4.13
AS	20	268	68.85	17076.05	59,301	4.18
HU	300	300				
CU	5	25				

TABLE IV. STREAM DATA FOR ENERGY INTEGRATION IN THE ABE PROCESS

Cooling cost	20 $\$kW^{-1}$ año^{-1}
Heating cost	80 $\$kW^{-1}$ año^{-1}
Cost function for heat transfer equipment, $ año^{-1}	1,300 A $^{0.6}$ [A en m^2]
Global heat transfer coefficient, U, $kW/m^2/K$	0.8

Fig. 5. Integrated heat exchangers network for ABE process

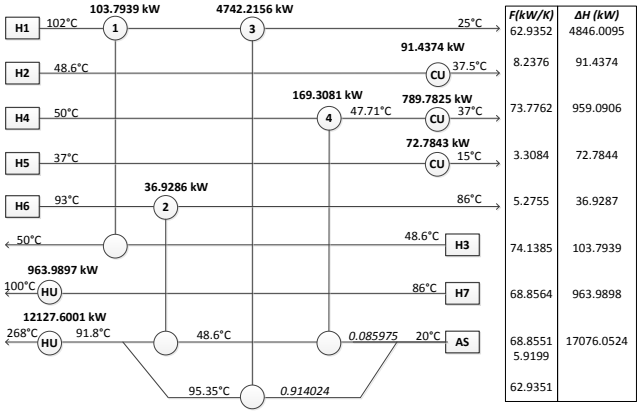

The energy integration also includes the combustion of the remaining solid from the process, since The solid fraction obtained after a drying process, could be transformed into pellets in order to be combusted in a power plant for electricity production or for the vapor production required in the process [21] due to the high heating value that is around 17.88 MJ/kg-solid [22].

Table V shows the results for heat integration in terms of energy consumption, energy recovery and process cost. Comparing the process configuration using only vapor and water from the services plant and the configuration with stream energy integration, it is possible to get a reduction up to 28% in the consumed heat services and 84% in the cooling services, which means a 32% of reduction in the operating annual cost. The comparison between the integrated configuration and the use of the remaining solids from the process to be combusted for producing vapor, indicates that the necessary energy produced from crudeoil-based fuel could be 100% replaced by combusting the remaining solids, thus, the operating annual cost could be reduced 98% with respect to the integrated configuration and 99% compared with the configuration without energy integration. Further economic analysis allowed to determine the feasibility of the process and it was found that the period for recovering the investment would be seven years.

TABLE V. STREAM DATA FOR ENERGY INTEGRATION IN THE ABE PROCESS

	No heat integration	Heat integration	Heat integration with solid combustion
Recovered heat for integration, kW	0.0	4974.38	4974.38
Total heat services employing crudeoil fuel, kW	18,143.84	13,091.59	0.0
Total cooling services, kW	6,006.25	954.00	954.00
Total capital annual cost, USD$/year	81,075.80	150,389.75	150,389.75
Total operating annual cost, USD$/year	1,571,631.89	1,066,407.28	19,080.08
Total annual cost of the network, USD$/year	1,652,707.69	1,216,797.02	169,469.83

There is also a positive impact regarding to the carbon dioxide depletion with the energy integration and the use of solids as fuel for vapor production. Table VI shows the carbon dioxide depleted by the energy integration and the total carbon dioxide produced due to the heating services production. The analysis was performed considering the use of diesel as a fuel for the production of heating services, considering the emission of 0.6938 kg of carbon dioxide per MJ produced [23]. The results illustrates a depletion of 1,242.45 kg/h of CO_2 when the energy integration is performed, while a 100% of carbon dioxide production is reduced when using the remaining solid to generate the necessary heating services.

TABLE VI. CARBON DIOXIDE DEPLETION BECAUSE ENERGY INTEGRATION AND REMAINING SOLIDS COMBUSTIONS

	No heat integration	Heat integration	Heat integration with solid combustion
Carbon dioxide depleted for integration, kg/h	0.00	1,242.45	1,242.45
Total carbon dioxide produced for heating services, kg/h	4,531.79	3,269.89	0.00

3) Determination of process configuration

Based on the previous results, the selected benchmarking criteria rely on economic and environmental aspects accounted by the CO_2 production in the process employing crude oil-based fuel.

The results showed three potential process configurations: 1) Process configuration employing the heating and cooling needs from the service plant; 2) process configuration employing an energy integration and 3) process topology including the energy integration and combustion of remaining solid in the ABE process. According to the economic and environmental aspects and analyzing Table V and Table VI, the most appropriate configuration to select was the one with energy integration and combustion of the residual solids from the process to produce vapor; the energy integration allows to take advantage of energy content of the streams. The combustion of the solids also permits the generation of vapor and extra energy that could be employed to produce electricity.

V. CONCLUSION

The implementation of an integral investigation including the experimental activities and simulation-based examination, allowed to perform a detailed analysis for the ABE process production. The experimental approach for the different analyzed sections such as the acid pretreatment of lignocellulosic biomass and the ABE fermentation provided the best process conditions for the step. The collected information was employed to carry out a rigorous simulation for the complete ABE production process. Three different process configurations were analyzed where the main difference was related with the energy use and integration. The configuration with the integration of energy and combustion of the remaining solids allowed to reduce the use of crudeoil-based fuel in a 100%, thereby, reducing significantly the carbon dioxide emissions from fossil source. This is a significant finding since most of the time the feasibility of biofuel and high value-added products have been highly criticized because of the energy use and economical drawbacks, such as the investment recovery. Therefore, this study have illustrated that it is possible to produce ABE from sugarcane bagasse with lower environmental impact and economic feasibility.

REFERENCES

[1] Anon, "Biobutanol of the Horizon", Chemical Engineering Progress, March 2007.

[2] R. Morales-Rodriguez, L. Samarti-Rios, M. Sanchez-Morales, D. Rodriguez-Gomez, M. Salez-Cruz, E.S. Perez-Cisneros, Downstream Process Design for an Efficient Acetone, Butanol and Ethanol Separation from ABE Fermentation Broth. PSE-2015/ESCAPE-25 conference, poster presentation, 31 May-4 June, Copenhagen, Denmark, 2015

[3] R. Morales-Rodriguez, D. Rodriguez-Gomez, M. Sales-Cruz, J.A. de los Reyes-Heredia, E.S. Pérez-Cisneros, "Model-Based Analysis for Acetone-Butanol-Ethanol Production Process through a Dynamic Simulation", Computer Aided Chem Eng, vol. 33, pp. 133-138, 2014

[4] M. Alvarado-Morales, J. Terra, K.V. Gernaey, J.M Woodley, R. Gani, "Biorefining: Computer aided tools for sustainable design and analysis of bioethanol production", Chem Eng Res and Design, vol. 87, pp. 1171–1183, 2009.

[5] A. Avalos-Farfán, M. Sánchez-Morales, L. Samarti-Rios, "A Process Design for Acetone, Butanol and Ethanol Production through a biological Route [Diseño de una planta para la producción de Acetona, Butanol y Etanol a través de una ruta biológica]", *BSc thesis*, Universidad Autónoma Metropolitana-Iztapalapa, 2014.

[6] G. Miller, "Use of Dinitrosalisyc Acid Reagent for determination of reducing sugar", Analytical Chemistry, 31, 426-428, 1959.

[7] L. Samarti Rios, M. Sánchez Morales, S. Avalos Farfán, D. Rodriguez-Gomez, O. Loera-Corral, E. Favela-Torres, R. Morales-Rodriguez, "Experimental Analysis for Acetone, Butanol and Ethanol Production using sugar industry residues [Análisis Experimental para la Producción de Acetona, Butanol y Etanol a partir de Residuos de la Industria Azucarera]", Proceeding of National meeting of AMIDIQ, 6-9 May, Puerto Vallarta, Mexico, 2014.

[8] C.-T. Tsai, R. Morales-Rodriguez, G. Sin, A.S. Meyer, "A dynamic model for cellulosic biomass hydrolysis: a comprehensive analysis and validation of hydrolysis and product inhibition mechanisms", Applied Biochemistry and Biotechnology, vol. 172, pp. 2815-2837, 2014.

[9] S. Heitmann, M. Stoffers, P. Lutze, "Integrated Processing for Separation of Biobutanol. Part B: Model-based Process Analysis", Green Processing and Synthesis, Vol. 2, p. 121-14, 2013.

[10] W.L. Luyben, "Control of the Heterogeneous Azeotropic n-Butanol/Water Distillation System", Energy & Fuels, Vol. 22, p. 4249-4258, 2008.

[11] K. Kraemer, A. Hardwardt, R. Bronneberg, W. Marquardt, "Separation of butanol from acetone-butanol-ethanol fermentation by a hybrid extraction-distillations process", Computer Aided Chemical Engineering, Vol. 28, p. 7-12, 2010.

[12] P. Anbarasan, Z.C. Baer, S. Sreekumar, E. Gross, J.B. Binder, H.W. Blanch, D.S. Clark, F.D. Toste, "Integration of chemical catalysis with extractive fermentation to produce biofuels" Nature, Vol. 491, p. 235-239, 2012.

[13] N. Qureshi, S. Hughes, I.S. Maddox, M.A. Cotta, "Energy recovery of butanol from model solutions and fermentation broth by adsorption", Bioprocess Biosynthesis Engineering, Vol. 27, p. 215-222, 2005

[14] T.C. Ezeji, N. Qureshi, H.P. Blanchek, "Production of acetone, butanol and ethanol by Clostridium beijerinckii BA101 and in situ recovery by gas stripping", World Journal of Microbiology and Biotechnology, Vol. 19, p. 595-603, 2003

[15] C. Lu, J. Dong, S.-T. Yang, "Butanol production from wood pulping hydrolisate in an integrated fermentation-gas stripping process. Bioresource Technology. Vol. 143, p. 467-75, 2013.

[16] J.M. Douglas, "Conceptual Design of Chemical Processes", McGraw Hill, 601 p., 1988.

[17] J.G. Hayden, J.P. O'Connell, "A Generalized Method for Predicting Second Virial Coefficients", Ind. Eng. Chem., Process Des. Dev, vol 14, pp. 209-216, 1975.

[18] R.J. Wooley, V. Putsche, "Development of an ASPEN PLUS Physical Propety Database for Biofuels Components", National Renewable Energy Laboratory, NREL/TP-425-20685, 1996.

[19] M. Alvarado-Morales, J. Terra, K.V. Gernaey, J.M Woodley, R. Gani, "Biorefining: Computer aided tools for sustainable design and analysis of bioethanol production", Chemical Engineering Research and Design, Vol. 87, p.1171–1183, 2009.

[20] R. Morales-Rodriguez, A.S. Meyer, K.V. Gernaey, G. Sin, "Dynamic model-based evaluation of process configurations for integrated

operation of hydrolysis and co-fermentation for bioethanol production from lignocelluloses", Bioresour Technol, vol 102, pp. 1174–1184, 2011.

[21] J. Larsen, M.Ø. Petersen, L. Thirup, H.W. Li, F.K. Iversen, "The IBUS Process – Lignocellulosic Bioethanol Close to a Commercial Reality", Chem Eng Technol, vol. 31, pp. 765-772, 2008.

[22] W. Alonso-Pippo, P. Garzone, G. Cornacchia, "Agro-industry residues disposal: The trend of their conversion into energy carries in cuba", Waste Manag, vol. 27, pp. 869-885, 2007.

[23] Environment: Carbon dioxide emission coefficients. U.S. Energy Information Administration. http://www.eia.gov/environment/emissions/co2_vol_mass.cfm, May 10, 2015.

Nanotubos de carbono: una alternativa para implementar las celdas fotovoltaicas

Rita Aguilaro Osorio y Uriel A. Martínez Huitle
Instituto Politécnico Nacional. SEPI-ESIME Zacatenco.
Unidad Profesional Adolfo López Mateos. Edificio 5, 3er.
Piso Col. Lindavista, C.P. 07738, México, D.F.
raguilaro@ipn.mx

Stephen Muhl
Instituto de Investigaciones en Materiales, Universidad
Nacional Autónoma de México.
Coyoacán, México, D.F. C.P. 04510 México.

***Abstract*— El descubrimiento de los nanotubos de carbono, NTC, revolucionó la tecnología de los materiales, entre otras áreas, buscando aprovechar con mayor eficiencia sus propiedades eléctricas, mecánicas, electromecánicas y químicas. Debido a los desarrollos tecnológicos generados en los últimos años, las aplicaciones potenciales de estos materiales han ido en aumento. En el sector de energías alternativas, usando nanotubos de carbono como base, se han fabricado dispositivos fotovoltaicos, es decir, dispositivos capaces de transformar la luz en energía eléctrica. Los prototipos diseñados en el laboratorio con nanotubos, en uno o varios de sus componentes presentan buenas eficiencias, por lo cual estos materiales podrían ser la base para la próxima generación de dispositivos solares denominados como dispositivos fotovoltaicos orgánicos. La tendencia actual es la elaboración de conductores eléctricos transparentes, CETs, de bajo costo y capaces de ser depositados en superficies flexibles. El principal material utilizado para la fabricación de los CETs en las celdas solares es el Oxido de Estaño Indio (ITO). El costo de la fabricación de este material es muy elevado. Además, las reservas de indio en el planeta son muy limitadas, por lo cual es necesario buscar un material que remplace al ITO. Algunos investigadores han demostrado que los NTC son una alternativa potencial para desarrollar los CETs. Una de sus principales aplicaciones es como componente de las celdas solares. El propósito de este trabajo es presentar la aplicación de nanotubos de carbono de paredes múltiples en el desarrollo de conductores eléctricos transparentes, CETs, considerando que el método de fabricación es determinante en las propiedades de los NTC tales como la pureza, las dimensiones, la cristalinidad, entre otros. Los CETEs fabricados con los NTC de paredes múltiples, en esta investigación, tuvieron una transparencia de aproximadamente 60% y una resistividad superficial de 5.86 kΩ/□.**

Palabras claves— Conductores eléctricos transparentes, dispositivos fotovoltaicos, nanotutos de carbon.

I. Introduction

El carbono es un elemento [1] con características extraordinarias debido a la gran variedad de materiales que con él se pueden obtener. Con el descubrimiento de los fulerenos C60 y C70 se observó que se podían formar una gran variedad de estructuras de carbono.

En el año 1990 el Dr. Sumio Iijima [2-4] analizó una muestra de hollín de carbono, la cual se la envió Yoshinori Ando de la Universidad de Meijo, utilizando un microscopio de transmisión. Las imágenes analizadas con el microscopio revelaron estructuras cilíndricas anidadas concéntricamente, también fue posible visualizar el número de tubos que formaban esta estructura, conocidas actualmente como nanotubos de carbono de paredes múltiples. Además, se comprobó que los nanotubos estaban constituidos de hojas de grafeno enrolladas sobre sí mismas. El interés en la investigación de los nanotubos de carbono de paredes múltiples fue motivado por la publicación de Iijima en 1991 de las imágenes presentadas un año antes.

Este descubrimiento cobró un mayor interés cuando algunos estudios teóricos revelaron que los nanotubos podrían ser metálicos o semiconductores dependiendo del diámetro y del arreglo helicoidal. Debido a esto las expectativas de los nanotubos de carbono fueron altas. El problema, en ese tiempo, fue que los nanotubos solamente se podían obtener en pequeñas cantidades, por lo cual no había suficiente material para caracterizar sus propiedades. En ese tiempo, investigadores de ciencia molecular de la compañía Japonesa Nippon Electric (NEC) estaban estudiando los fulerenos. Tratando de combinar el C_{60} con boro se dieron cuenta de que al modificar las condiciones de fabricación se podían producir mayores cantidades de nanotubos de carbono [1].

Un nanotubo de carbono es una estructura de carbono unidos entre sí por enlaces tipo π. La cual se considera como el enrollamiento de una o más láminas de grafeno [2, 5, 6]. Éstos se clasifican en dos tipos, el primero denominado nanotubo de carbono de paredes múltiples (NTCPM) y el segundo, llamados nanotubos de carbono de pared simple (SWNT), descubiertos por el Dr. Bethune de IBM y el Dr. Iijima de NEC en 1993 [7].

El descubrimiento de los nanotubos de carbono revolucionó la tecnología de los materiales, buscando aprovechar más eficientemente sus propiedades eléctricas, mecánicas, electromecánicas y químicas. La determinación de las propiedades de los nanotubos de carbono fue responsable del gran impacto que han tenido en los últimos años.

Dentro de los temas de estudio más sobresalientes en la actualidad se encuentran los nanotubos de carbono. J. Roberson [8] en su publicación muestra que los nanotubos de carbono tienen una amplia capacidad de conductividad eléctrica inclusive con la posibilidad de exhibir superconductividad haciendo que la temperatura crítica para este fenómeno sea más alta. La superconductividad es la resistencia nula a la corriente eléctrica, es decir, permita el libre flujo de electrones sin oponerse a ello. Finalmente, se ha reportado que posee una alta conductividad térmica.

Los dispositivos de mayor eficiencia que existen en la actualidad son celdas solares inorgánicas a base de silicio, aluminio, plata e ITO. Estos dispositivos fotovoltaicos, son catalogados como celdas de alta tecnología, lo que significa que su proceso de fabricación es complejo y requiere altos costos de producción. Las celdas solares de reciente desarrollo, han buscado reemplazar uno o varios de sus componentes por materiales de menor costo, cuyo rendimiento se aproxime a los originales y uno de estos componentes son los conductores eléctricos transparentes. Como ejemplo de esto, en la literatura se ha reportado el uso de NTCs para la generación de conductores eléctricos transparentes, CETs, debido a su alta conductividad eléctrica.

La fabricación, caracterización y aplicación de los NTCs ayudaría en primer lugar a la inserción de la investigación nacional al ámbito internacional y la solución de problemas, como por ejemplo, el desarrollo de fuentes energéticas complementarias, de ahorro o fuente principal en lugares remotos donde no hay servicio de energía eléctrica.

El propósito de este trabajo es presentar la importancia de los nanotubos como una alternativa para implementar las celdas solares fotovoltaicas, como caso de estudio se presentó la fabricación y la caracterización de los conductores eléctricos transparentes con nanotubos de carbono.

II. Aplicación de los Nanotubos de Carbono en la Elaboración de Celdas Solares

La Fig. 1 muestra una gráfica de los diferentes tipos de celdas solares fabricados de 1975 al 2010, así como las mejores eficiencias obtenidas. Esta gráfica es una recopilación realizada por el Laboratorio Nacional de Energías Renovables (NREL por sus siglas en ingles) del Departamento de Energía de los Estados Unidos de Norteamérica [9].

De la gráfica se observa que los diferentes tipos de celdas en un principio exhibieron eficiencias muy bajas, sin embargo, el avance tecnológico en los procesos de fabricación y tipos de materiales usados propiciaron el aumento de las eficiencias. En la parte inferior derecha se muestran los nuevos dispositivos fotovoltaicos, incluyendo las celdas orgánicas y las celdas orgánicas-inorgánicas. Una celda fotovoltaica orgánica es un dispositivo que utiliza polímeros conductores orgánicos o pequeñas moléculas orgánicas para la absorción y conversión de la luz solar, así como el transporte de la carga. Una celda fotovoltaica orgánica-inorgánica es aquella en la cual al menos una parte o componente es orgánico y el resto utiliza tecnología inorgánica.

El uso de los NTCs en la fabricación de celdas solares ha generado un gran número de publicaciones, esto se debe a su alta conductividad eléctrica. En las publicaciones se muestra que tanto los NTCPMs [10-16] como los NTCPSs [17-20] o ambos [21].se utilizan para aumentar la eficiencia de la celda. También los nanotubos son utilizados para fabricar el contacto posterior de las celdas [22-23)] con la finalidad de transportar con menor resistencia las cargas hacia un dispositivo de almacenamiento. En cualquiera de estas dos aplicaciones no es necesario que el compuesto producido de nanotubos de carbono sea transparente, debido a que entre mayor sea la cantidad de nanotubos mayor será su eficiencia y menor la transparencia.

Otra aplicación no menos importante pero si menos explorada es la fabricación de CETs utilizando nanotubos de carbono. Comúnmente se han utilizado NTCPSs [19-20, 24-29] para la elaboración de esta parte de la celda, puesto que son los nanotubos de carbono con mejor conductividad eléctrica. Existen también algunas publicaciones enfocadas al uso de los NTCPMs [30-31] para la fabricación de éstos conductores debido que su costo de fabricación es inferior comparado con los NTCPSs.

La principal motivación del uso de NTCs en la elaboración de CETs es la disminución en el costo de fabricación de los CETs que se elaboran en la actualidad. El principal material usado para la fabricación de CETs en las celdas solares es el Oxido de Estaño Indio (ITO). El costo en la fabricación de este material es muy elevado, de aproximadamente $\$300/cm^2$ [34], costo que depende directamente de su proceso de fabricación. Además, las reservas de indio en el planeta son muy limitadas, por lo que es indispensable obtener un material que remplace al ITO.

La tendencia actual es la elaboración de CETs de bajo costo y capaces de ser depositados en superficies flexibles, como por ejemplo PET. El ITO no es un material viable para este tipo de aplicación, porque bajo deformación por flexión o torsión se fractura fácilmente. Debido a esto, la utilización de NTCs para remplazar al ITO representa una excelente aternativa. La generación de CETs en superficies o materiales flexibles pueden reducir el espacio de los paneles solares y aumentar el tiempo de exposición de los mismos a la luz solar.

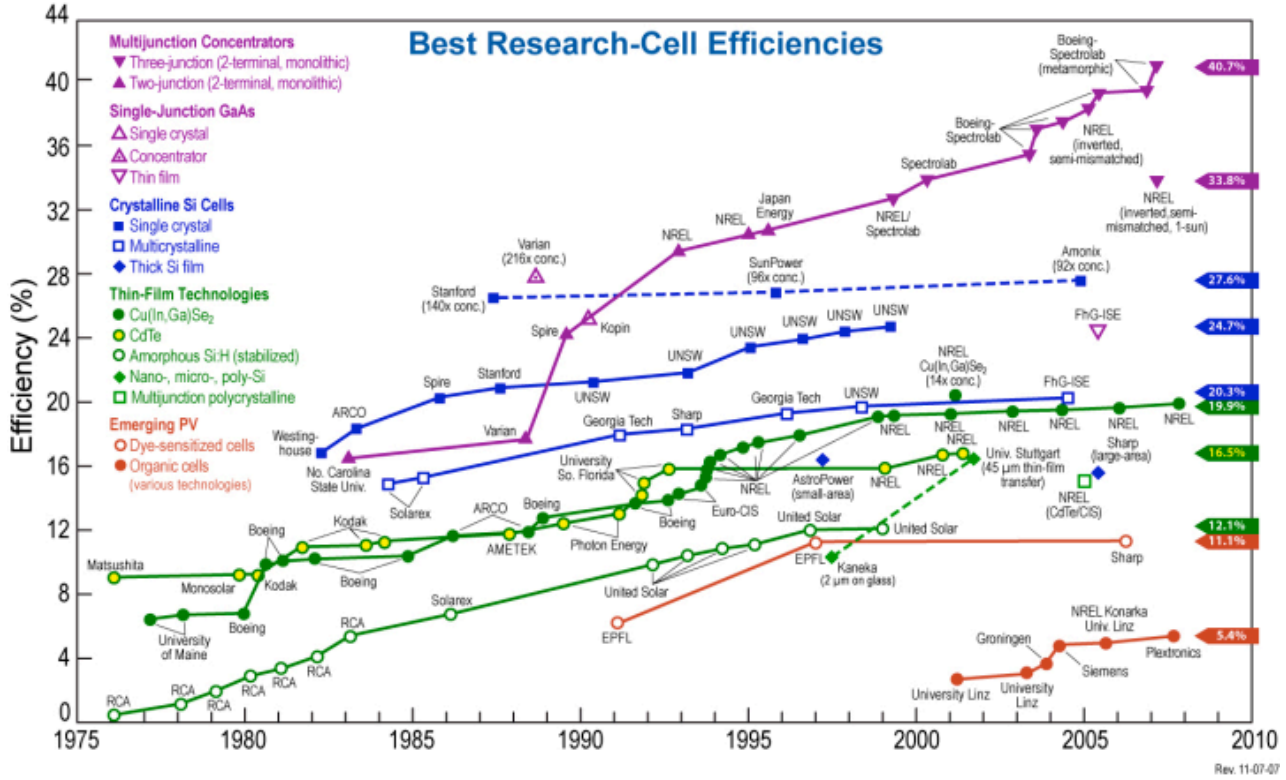

Fig. 1. Celdas solares fabricadas de 1975 al 2010.

La disminución de los costos de fabricación de los CETs repercutirá en la disminución paulatina de todos aquellos dispositivos que utilizan estos conductores. Es importante señalar que la aplicación de los NTCs para el desarrollo de CETs es de ascendente desarrollo, por lo que la experimentación constante en el desarrollo de esta tecnología implicará un avance en el mejoramiento de la eficiencia de éstos.

III. IMPORTANCIA DE LA FABRICACIÓN Y LA APLICACIÓN DE LOS NANOTUBOS DE CARBONO

Los países desarrollados dirigen su educación a la investigación y ésta a su vez, a la resolución de problemas concretos en la industria, es decir, que la investigación científica cumple el objetivo de satisfacer las necesidades que la industria de estas naciones requiere.

El principio para solucionar esta problemática es realizar investigación enfocada a la solución de problemas industriales nacionales, por ejemplo, la dependencia energética nacional de los hidrocarburos. La esta dependencia radica en que los hidrocarburos no son renovables, así que se debe pensar en un ahorro energético con miras al futuro nacional. Al mismo tiempo, se debe contribuir a la disminución del impacto ambiental preocupándose por el bienestar colectivo de las presentes y futuras generaciones. Por esta razón, se tiene la necesidad, pero sobre todo la responsabilidad, de comenzar a desarrollar tecnología enfocada a la aplicación de fuentes alternas de energía. Como principal fuente alternativa se encuentra la luz solar, la cual está disponible en cualquier punto de la superficie terrestre y las condiciones geográficas del país son idóneas para su aprovechamiento.

Por otro lado la nanotecnología a pesar de haberse concebido como una gran idea hace más de 50 años por Feynman, sus primeras aplicaciones para la generación de nuevas tecnologías fueron llevadas a cabo en los últimos años. Debido a esto, el estudio de los nanomateriales en nuestro país es totalmente innovador, aunque su trascendencia no se enfoca en el estudio mismo sino en las aplicaciones que estos pueden tener para beneficio general. De manera más específica, la fabricación, caracterización y aplicación de los NTCs ayudaría en primer lugar a la inserción de la investigación nacional al ámbito internacional y la solución de problemas, como por ejemplo, el desarrollo de fuentes energéticas complementarias, de ahorro o fuente principal en lugares remotos donde no hay servicio de energía eléctrica.

IV. CASO DE ESTUDIO

V. FABRICACIÓN Y CARACTERIZACIÓN DE CONDUCTORES ELÉCTRICOS TRANSPARENTES

Los CETs se fabricaron sobre soportes (sustratos) transparentes no conductores. Estos sustratos sirvieron principalmente como superficie de depósitos, y también como protección para el depósito, en la fabricación de celdas solares. Las dimensiones de los depósitos dependen directamente del dispositivo para el cual serán usados.

Para esta investigación se seleccionó vidrio como el material para los sustratos para el depósito de los CETs. La Fig. 2 muestra el diagrama esquemático de las capas que forman los depósitos fabricados. Las dimensiones de los sustratos rectangulares fueron de 2.5 cm de ancho por 3.5 de largo. Sobre los CETs se colocaron dos electrodos (pintados con pintura de plata) de 0.5 cm de largo y 2.5 cm de ancho, con la finalidad de realizar la caracterización eléctrica.

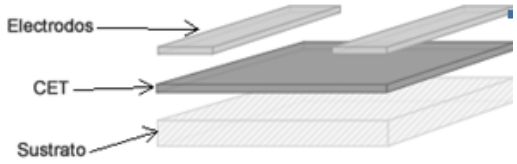

Fig. 2. Diagrama esquemático de las capas que forman un CETs sobre un determinado sustrato.

El método utilizado para el depósito de los CETs fue el de recubrimiento por giro, el cual consiste en depositar la tinta de nanotubo de carbono, por goteo, sobre una superficie giratoria denominada sustrato, para distribuir de manera uniforme la sustancia en la totalidad del sustrato. La mezcla de SDS (dodecil sulfato de sodio) es la técnica más utilizada para la dispersión de los nanotubos, por esta razón las proporciones de SDS, agua desionizada y NTCPMs son conocidas.

En los primeros experimentos se utilizaron los valores reportados en la literatura. Sin embargo, no se logró una dispersión completa de los nanotubos. Por esta razón, se seleccionó acetona y agua desionizada como solvente. Después de dispersar los tubos se pesó una porción de los nanotubos y se diluyó en acetona de 99.6% de pureza (Fermont ACS 06015). La muestra se dispersó con un baño sónico durante 50 min y se depósito sobre el sustratos de vidrio para su análisis con microscopía óptica. Este proceso se repitió varias veces variando la concentración de NTCPMs, con la finalidad de lograr una buena adherencia al sustrato y al mismo tiempo evitar un exceso de polímero. Con la finalidad de lograr una mejor dispersión, se realizaron un total de 37 experimentos, en los que variaron factores como la temperatura, proporción de los nanotubos contra el surfactante y la cantidad de agua desionizada.

El equipo utilizado para el depósito de los CETs consta de un aerógrafo (1) o pistola de aire, con un recipiente de 25 ml (2) para colocar la tinta. El aerógrafo es alimentado de una toma de aire presurizado (3) del laboratorio. Un soporte universal (4) para fijar el eje de disparo (5) y la distancia de disparo (6) del aerógrafo. La superficie donde se depositó la tinta, llamado sustrato (7), se sujetó a una base giratoria (8) que se sujetó al eje del motor eléctrico (9). La velocidad de giro del motor eléctrico se controló por medio de una fuente de alimentación conmutable (10). El sustrato y la base giratoria se colocaron dentro de un contenedor (11) para evitar contaminar el entorno y la muestra. Todo el equipo se está inmerso en una campana de extracción (12) para prevenir la inhalación de los solventes con nanotubos. La Fig. 3 muestra el diagrama esquemático del equipo.

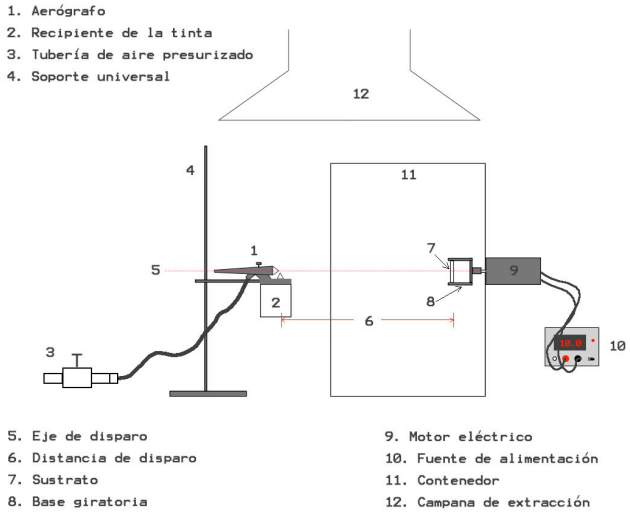

Fig. 2. Diagrama esquemático de las capas que forman un CETs sobre un determinado sustrato.

Los principales parámetros a evaluar en los CETs, fueron la resistividad superficial, para obtener este valor se utilizó la norma ASTM D257 [35] y la publicación [36], y su transparencia. Con la finalidad de analizar el efecto de las impurezas de los nanotubos de carbono se compararon los resultados de la resistividad superficial en función de la transparencia con nanotubos sin purificación y purificados.

VI. RESULTADOS

De la figura 4 Se observa que los nanotubos tienden a expandirse con facilidad en la totalidad del volumen del líquido utilizando como solvente acetona sin agregar SDS a la solución.

Fig. 4. Dispersión de los NTCPMs en acetona.

El mejor resultado de la dispersión fue obtenido con una proporción de NTCPMs y acetona fue de 225 ml por cada mg de nanotubos, con la cual se generó una tinta grisácea y transparente, ésta se muestra en la figura 5.

Fig. 5. Tinta obtenida.

La Fig. 6 muestra el tipo de separación que se logró entre los NTCPMs, utilizando esta concentración. Como se observa en la imagen la separación entre nanotubos es bastante uniforme, y el material obtenido fue suficiente para fabricar los CETs. Tampoco se observan grandes cantidades de residuo de acetona.

El siguiente paso fue determinar la cantidad de polímero necesario para lograr una buena adherencia de los NTCPMs al sustrato, es decir buscar la concentración mínima de nitrocelulosa para la cual el material se mantenga fijo en el sustrato. Las mejores muestras se obtuvieron con una proporción entre los NTCPMs y el barniz (de uñas) de aproximadamente 1:100, lo que significa que la proporción entre los nanotubos y la nitrocelulosa fue de aproximadamente 1:15.

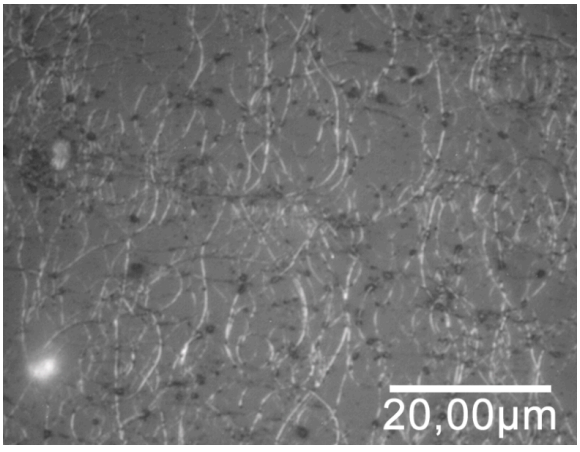

Figura 6. Concentración de NTCPMs en la tinta de acetona y barniz.

Para evaluar la adherencia se utilizó una cinta adhesiva, pegando un trozo y despegándolo suavemente, verificando que el material no se haya despegado y transferido a la cinta. En el análisis de las publicaciones se observó que este es un método común de evaluación de la adherencia del depósito.

Los CETs se fabricaron a partir de la tinta obtenida. Además, se realizaron algunos depósitos con material no purificado para valorar si la pureza afecta las características de los CETs. Para analizar la resistencia de los CETs se varió la cantidad de tinta utilizada para el proceso. Después de haber realizado los depósitos, se extrajo cuidadosamente el sustrato de la base giratoria y se calentó en una atmosfera de gas de argón para eliminar la mayor parte de los residuos de los solventes y los excedentes del barniz.

Las Tablas 1 y 2 muestran los valores de resistividad superficial y el porcentaje de la transparencia de los CETs fabricados con NTCPMs sin purificación y purificados. De la tabla se puede observar que existe una gran diferencia de la resistividad superficial entre los CETs fabricados con NTCPMs purificados y sin purificar. Los resultados confirman que las impurezas afectan en gran medida la resistividad y la transparencia de los CETs.

TABLA 1. RESULTADOS DE LA TRANSPARENCIA Y LA RESISTIVIDAD SUPERFICIAL (SIN PURIFICAR)

CET	**Transparencia % a 550nm**	**Resistividad Superficial KOhm/sq Barniz con MWCNTs S/P**
A	28.83	2.34
B	53.96	12.48
C	68.02	72.02
D	82.94	240.68

TABLA 2. RESULTADOS DE LA TRANSPARENCIA Y LA RESISTIVIDAD SUPERFICIAL (PURIFICADOS)

CET	**Transparencia** % a 550nm	**Resistividad Superficial KOhm/sq Barniz con MWCNTs Purificados**
A	29.90	1.41
B	48.4	3.59
C	60.00	5.82
D	64.70	13.57
E	69.58	19.05

En la Fig. 6 se muestra la gráfica de la resistividad térmica, ρs, en función de la transparencia de los CETs fabricados con la mezcla de los nanotubos de carbono, acetona y barniz. En cada uno de los casos se observa que al utilizar los NTCPMs purificados los valores de resistividad superficial disminuye y el % de transparencia aumenta en los CETs.

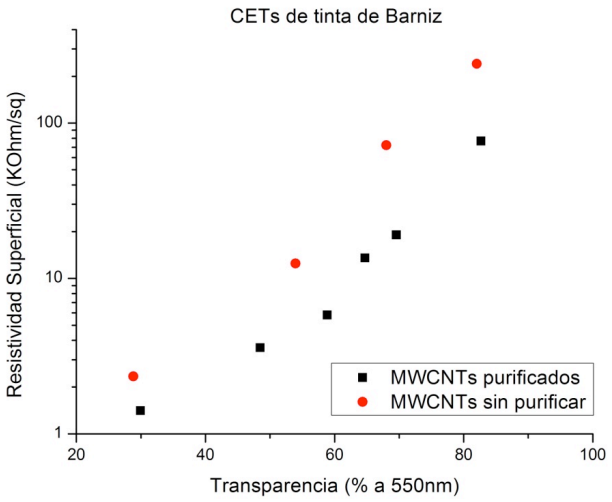

Fig. 6. Resistividad superficial contra transparencia de los CETs fabricados con tinta de barniz.

VII. CONCLUSION

En este trabajo se presentó la importancia de los nanotubos como una alternativa para implementar las celdas solares fotovoltaicas, como caso de estudio se presentó la fabricación y la caracterización de los conductores eléctricos transparentes con nanotubos de carbono.

Para la fabricación de los CETs, los nanotubos se dispersaron con 225 ml por cada miligramo de nanotubos. Utilizando estas proporciones se obtuvieron tintas de nanotubos visiblemente estables durante un par de horas. En el caso de la dispersión en acetona de nanotubos mezclados con materiales a base de polímeros no conductores, a pesar de las dudas, el barniz (de uñas) resultó una excelente matriz para adherir los nanotubos a los depósitos, sin disminuir en gran medida la transparencia. Otra de las ventajas que ofreció el barniz de uñas fue su bajo costo y accesibilidad.

Para la fabricación de los CETs se utilizó el método de recubrimiento por rocío, la cual fue una excelente alternativa para el depósito, dado que promovió eficientemente la uniformidad del depósito de las tintas sobre el sustrato.

De la caracterización de CETs, se consideró que el mejor resultado fue de una resistividad superficial de de 5.86 kΩ/□ con una transparencia de 60% .

Como toda tecnología, la posibilidad de aumentar la eficiencia de este tipo de conductores es muy amplia. Por el momento estos CETs podrían ser utilizados en la fabricación de dispositivos fotovoltaicos que no demanden tanta eficiencia, como en el caso de las celdas solares que proporcionan energía a una casa habitación promedio.

ACKNOWLEDGMENT

Los autores agradecen el apoyo para realizar esta investigación a la DGAPA-UNAM IN112608, al INSTITUTO POLITÉCNICO NACIONAL y al CONACyT.

VIII. REFERENCES

[1] T. W. Ebbesen. “Carbon nanotubes”, American Institute of Physics. Physics Today, pp. 26-32, 1996.

[2] S. Ijima. “Helical microtubules of graphitic carbon.” Nature, Vol. 354, Pag. 56-58, 1991.

[3] D. Hongjie. “Carbon nanotubes: opportunities and challenges”, Surface Science, num. 500, 2002.

[4] S. Iijima. “Carbon nanotubes: past, present and future”, Physics B, num. 323, 2002.

[5] U. A. Martinez Huitle, R. Aguilar 0sorio, S-Muhl. “Breve historia de los nanotubos de carbono.” México D.F.: XI Congreso Nacional de Ingeniería Electromecánica y de Sistemas, 2009.

[6] U. A. Martínez Huitle. “Fabricación y Purificación de nanotubos de carbono para el desarrollo y caracterización de conductores eléctricos transparentes”. Tesis de Maestría. SEPI-ESIME Zac. IPN. México. 2011.

[7] http://www.balzan.org/en/prizewinners/sumio-iijima/the-discovery-of-carbon-nanotubes-iijima. 2006.

[8] J. Robertson. “Realistic applications of CNTs.” Materials today,. Pag. 46-52. 2004.

[9] http://www.green-blog.org/2010/03/09/solar-power-will-take-over-soon/. 2010.

[10] S. Somani, P. Somani, M. Umero. “Carbon nanotube incorporation: A new route to improve the performance of organic–inorganic heterojunction solar cells.” Diamond & Related Materials, Vol. 17. Pag. 585–588, 2008.

[11] G. Kalita. “Cutting carbon nanotubes for solar cell application.” Applied Physics Letters. Vol. 92, 123508. 2008.

[12] J. Wei. “Double-Walled Carbon Nanotube Solar Cells.” Nano Lett., Vol. 7, No. 8, Pag. 2317-2321.2007.

[13] P. Somani, R. Somani, M. Umeno, “Improving photovoltaic response of poly(3-hexylthiophene)/n-Si heterojunction by incorporating double walled carbon nanotubes.” Applied Physics Letters. Vol 89, 223505. 2006.

[14] J. A. Miller, R.A. Hatton, P. Silva. Interpenetrating multiwall carbon nanotube electrodes for organic solar cells. Applied Physics Letters. Vol. 89, 133117, 2006.

[15] R. Somani, P. Somani, M. Umero. “Improving the photovoltaic response of a poly(3-octylthiophene)/n-Si heterojunction by incorporating double-walled carbon nanotubes.” Nanotechnology, Vol. 18, 185708. 2007.

[16] R. Somani. “Double-Walled Carbon Nanotubes-Incorporated Donor–Acceptor-Type Organic Photovoltaic Devices Using Poly(3-octylthiophene) and C60.” Japanese Journal of Applied Physics. Vol. 47, No. 2, Pag. 1219–1222. 2008.

[17] J. A. Rud, “Water soluble polymer/carbon nanotube bulk heterojunction solar cells.” Journal Of Materials Science. Vol. 40, Pag. 1455 – 1458. 2005.

[18] E. Kymakis, G. A. J. Amaratunga. “Single-wall carbon nanotube/conjugated polymer photovoltaic devices.” Applied Physics Letters. Vol. 80, No. 1. 2002.

[19] J. Lagemaat, “Organic solar cells with carbon nanotubes replacing In2O3:Sn as the transparent electrode.” Applied Physics Letters. Vol. 88, No. 233503. 2006.

[20] J. Li. “Organic Light-Emitting Diodes Having Carbon Nanotube Anodes.” Nano Lett., Vol. 6, No. 11. 2006.

[21] I. Khatri, “Improving photovoltaic properties by incorporating both single walled carbon nanotubes and functionalized multiwalled carbon nanotubes.” Applied Physics Letters. Vol. 94, No. 093509. 2009.

[22] H. Ago, K. Petritsch, M.S.P. Shaffer, A. H. Windle. “Composites of Carbon Nanotubes and Conjugated Polymers for Photovoltaic Devices. “Adv. Mater. Vol. 11, No. 15. 2009.

[23] T. M. Barnes, X. Wu, J. Zhou, A. Duda, J. Lagemaat, and T. J. Coutts. “Single-wall carbon nanotube networks as a transparent back contact in CdTe solar cells.” Applied Physics Letters. Vol. 90, No. 243503. 2007.

[24] A. D. Pasquier, H.E. Unalan, A. Kanwal, “Conducting and transparent single-wall carbon nanotube electrodes for polymer-fullerene solar cells.” Applied Physics Letters. Vol. 87, No. 203511. 2005.

[25] G Fanchini, S Miller, BB Parekh, M Chhowalla. Optical Anisotropy in Single-Walled Carbon Nanotube Thin Films: Implications for Transparent and Conducting Electrodes in Organic Photovoltaics. Nano Lett., Vol. 8, No. 8. 2008.

[26] Z Wu, Z. Chen, X. Du, J.M. Logan, J. Sippel, M. Nikolou, Transparent, Conductive Carbon Nanotube Films. Science. Vol. 305. 2004.

[27] M.W. Rowell, M.A.Topinka, M.D. McGehee,. Organic solar cells with carbon nanotube network electrodes. Applied Physics Letters. Vol. 88, No. 233506. 2006.

[28] C. Weeks, J.Peltola, I. Levitsky, P. Glatkowski, "Single-wall carbon nanotubes as transparent electrodes for photovoltaics." Photovoltaic Energy Conversion, Conference Record of the 2006 IEEE 4th World Conference on. Vol. 1. 2006.

[29] J. D. Pei, Y Zeng, C Liu, HM Cheng, "The fabrication of a carbon nanotube transparent conductive film by electrophoretic deposition and hot-pressing transfer." Nanotechnology. Vol. 20 No. 235707. 2009.

[30] H.R. Astorga, D. Mendoza, "Electrical conductivity of multiwall carbon nanotubes thin films." Optical Materials. Vol. 27, Pag. 1228–1230. 2005.

[31] B Safadi, R Andrews, EA Grulke. "Multiwalled Carbon Nanotube Polymer Composites: Synthesis and Characterization of Thin Films." Journal of Applied Polymer Science. Vol. 84, Pag. 2660–2669. 2002.

[32] A. A. Green y M. C. Hersam. "Processing and properties of highly enriched double-wall carbon nanotubes." Nature Nanotechnology. Vol. 4. 2009.

[33] G.H. Xu, J.Q. Huang, Q. Zhang, M.Q. Zhao, F. Wei, "Fabrication of double- and multi-walled carbon nanotube transparent conductive films by filtration-transfer process and their property improvement by acid treatment." Appl Phys A, Vol. 103. Pag. 403–411, 2011.

[34] http://www.sigmaaldrich.com/materials-science/material-science-products.html?TablePage=9548901. 2011.

[35] ASTM International. Standards. ASTM D257-07.[En línea] http://www.astm.org/Standards/D257.htm.

[36] W. A. Maryniak, T. Uehara, M. A. Noras. "Surface Resistivity and Surface Resistance Measurements." Trek Application Note, 1005. Pag. 1-4, 2003.

Theoretical study of the electronic properties of semiconductor nanowires as anodes for lithium batteries

A F. Salazar-Posadas, E. Carvajal-Quiroz
ESIME-Culhuacán
Instituto Politécnico Nacional
México D. F., México
fsalazarp@ipn.mx

M. Cruz-Irisson§, L. A. Pérez-López
Instituto de Física
Universidad Nacional Autónoma de México
México D. F., México

***Abstract*— The high energy storage electrode materials for rechargeable batteries are currently one of the most important challenges for the search of alternative energies. The silicon (Si) and (Ge) germanium crystals have high theoretical energy storage capacity, however when lithium (Li) is stored, their volumetric expansion is larger than 300%, resulting in pulverization and capacity fading after few cycles. The nanowire arrays offer an alternative since their morphology could reduce the structural stress and their high surface allows more Li storage. In this work, we present a first-principles study of the electronic band structure and the electronic density of states of Si and Ge nanowires, grown along the [001] crystallographic direction and passivated with hydrogen (H) and substitutional Li atoms. The results show that the energy band gap (ΔE) decreases as function of the diameter of the nanowire due to the quantum confinement effect and as a function of the concentration of Li atoms. The later effect is stronger than the quantum confinement. On the other hand, the ΔE is direct for all the analyzed nanowire morphologies with the maximum studied concentration of Li atoms. These results show that the magnitude of ΔE of the Si and Ge nanowires can be tuned by changing their Li surface concentration and diameter conserving a direct band gap.**

Keywords*— *silicon nanowires; germanium nanowires; lithium batteries; electronic band structure; electronic density of states

I. INTRODUCTION

Lithium batteries are potential candidates for alternative energy sources, their graphite anode currently offers an specific energy density enough to be used in mobile electronic devices (~372 $mAhg^{-1}$) but they cannot sustain a current enough to move a vehicle neither they can be used as large scale energy storage devices. The improvement of the new generation of Li batteries requires specific features in the materials used as electrodes such as sustainable high currents with large discharge capacity, high specific energy ($mAhg^{-1}$), a great number of charge/discharge cycles without loss of capacity in the electrodes (coulomb efficiency) and a low working potential respect Li/Li^+ for the electrodes. The bulk Si and Ge have high theoretical energy storage densities of 4200 and 1600 $mAhg^{-1}$ respectively [1], and have a low potential respect the Li/Li^+ (~0.4 V and 0.5 V for Si and Ge, respectively) [2]. Moreover, the diffusion of Li ions is higher in Ge that in Si [3]. However, there are some difficulties that must be overcome when Li is stored. In particular, the volumetric expansion is larger than 300% for Si and Ge [1], [2], [4] resulting in pulverization and loss of capacity after few cycles of charge/discharge. Theoretical works have shown that the volumetric expansion is anisotropic and indicate that, during the insertion process, the Li atoms occupy interstitial sites on the superficial planes of the Si bulk structure breaking the bonds between Si atoms resulting in an amorphous structure with much less electron conduction capacity [5], [6], [7]. The mechanical stress in bulk Si and Ge can be solved by using nanostructures such as nanowires (NWs) coated with nanotubes [8], porous Si NWs [9], coated nanoparticles [10], [11] and pristine NWs [12], [13] since their structures could avoid the fractures between planes that occur in crystalline structures, then reducing the structural stress and possibly solving the volumetric expansion problem. The high aspect ratio of NWs offers a major surface where Li atoms can be stored increasing their specific energy capacity. Experimental reports indicate that during the Li insertion in [112] Si NWs there are important plastic deformations [14]. However, after the Li insertion the nanowire can sustain large inelastic deformations before breaking [15]. Another experimental work shows that after 100 cycles of Li insertion/desinsertion in pristine Ge nanowire arrays, the structure becomes a continuous porous network with specific capacities of 900 $mAhg^{-1}$ and capacity to sustain discharge rates of 20-100 C over 1000 cycles [16]. In this context, understanding the effects of surface Li atoms on the electronic properties of semiconductor NWs is fundamental to incorporate new materials in the new generation of Li batteries.

In this work we present a density functional study of the effects of the surface Li atoms on the electronic properties of Si and Ge NWs, grown along the [001] crystallographic direction and passivated with hydrogen (H).

II. THE MODEL AND COMPUTATIONAL DETAILS

The calculations were performed using the Density Functional Theory (DFT) within the Local Density Approximation (LDA) and using standard norm-conserving pseudopotentials [17] in their fully nonlocal form [18] incorporated in the SIESTA code [19]. In order to define the real space grid for numerical integrations, we use 150 Ry as the energy cutoff and double-ζ s, p-basis. All NWs were let free to relax until the Hellmann-Feynman forces were less than 2 meVÅ-1. The distance between neighboring NWs is at least 10 Å to avoid the interactions between them. The pseudopotentials for Si and Ge were generated with atomic valence-electron configuration s2p2. The pseudopotential core radii (in atomic units) are as follows: s(1.89), p(1.89), d(1.89) for Si and s(2.06), p(2.85), d(2.58) for Ge. The reliability of the pseudopotentials was verified by calculating the lattice constants for bulk Si and Ge diamond structures and the bulk Si-Si and Ge-Ge bond lengths. The predicted lattice constants for Si and Ge are 5.39 Å and 5.64 Å respectively, and the corresponding experimental values are 5.43 Å and 5.658 Å [20], the predicted bulk bond lengths for Si-Si and Ge-Ge were 2.17 Å and 2.33 Å in comparison to the experimental values 2.35 Å and 2.45 Å, respectively [20]. All calculated physical quantities have a relative error less than 8%. The studied NWs were grown along the [001] crystallographic direction and the initial morphologies are depicted in Fig. 1, where the violet spheres correspond to Si or Ge atoms, and the pink and green ones correspond to H and Li atoms, respectively. The numbers indicate the sequence in which the Li atoms replace the H ones. The right side of Fig. 1 shows the side view of the unit cell of the NWs and the left side shows the corresponding cross section views. It is convenient to label the studied morphologies as (a) NW1, (b) NW2, (c) NW3, and (d) NW4 as shown in Fig. 1. It is worth to mention that all initial morphologies were taken from the optimized morphologies of Si or Ge NWs, passivated with H, and then some of the H atoms were substituted by Li ones.

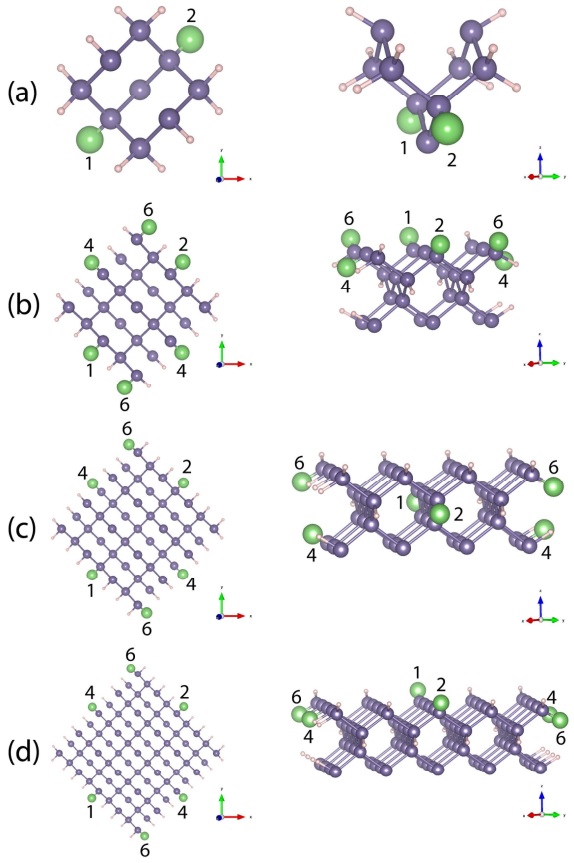

Fig. 1. The studied morphologies as function of the diameter and labeled as (a) NW1, (b) NW2, (c) NW3, and (d) NW4. The violet spheres represent Si or Ge atoms, whereas the pink and green spheres correspond to H and Li atoms, respectively. The numbers on the Li atoms indicate the sequence in which the Li atoms replaced the H ones.

III. RESULTS AND DISCUSION

The electronic band structure, the electronic density of states and the energy band gap are very sensitive to the presence of impurities or defects in structures with crystalline symmetries, in this sense, the effects of Li atoms on the surface of the Si and Ge NWs will be reflected in their electronic properties. Fig. 2 shows the electronic band structures and the densities of states of Ge and Si NWs with different concentrations of Li atoms. The left side of Fig. 2 corresponds to Ge NWs whose morphologies are (a) NW1, (b) NW2, (c) NW3 and (d) NW4 with 2, 4, 6 and 4 Li atoms per unit cell respectively. Likewise, the right side corresponds to Si NWs whose morphologies are (e) NW1, (f) NW2, (g) NW3, and (h) NW4 with 2, 6, 6, and 6 Li atoms, respectively. The violet line indicates the energy band gap (ΔE), and the dashed line corresponds to the Fermi energy that is placed at zero energy. Fig. 2 also shows the corresponding total electronic density of states (black line), and the density of states per atomic species, Ge (orange line), Si (red line), H (blue line) and Li (green line). The known quantum confinement effect is clearly observed as the energy band gap diminishes when the NW diameter increases for both passivated Si and Ge NWs [21].Other effects can be observed in Fig. 2. In particular, notice that in Figs. 2(a) and 2(e) the upper valence bands correspond to trap states originated from the dangling bonds and impurities [22], [23]. For higher concentrations of Li, there are more states originated from these atoms (green lines) in the conduction band for both Si and Ge NWs in the NW2, NW3, and NW4 morphologies as shown in Figs. 2(b)-(d) for Ge NWs and Figs. 2(f)-(h) for Si NWs.

The effects of the surface Li atoms on the electronic properties of NWs is also evident in Fig. 3, which shows the energy band gap (ΔE) as function of the concentration of Li atoms per unit cell for (a) Ge and (b) Si NWs, with different morphologies. The electron quantum confinement leads to an increase in the band gap when the NW diameter decreases. Notice how this effect diminishes when the NWs have one or more Li atoms per unit cell, in particular the band gap also diminishes when the concentration of Li atoms augments. As expected, if more Li atoms are placed on the nanowire, a metallic behavior should be observed. The gray dashed line in Fig. 3 indicates the value of the energy band gap of bulk Si (or Ge) calculated with SIESTA, and it serves as reference to observe how the nanowires lose their semiconductor behavior.

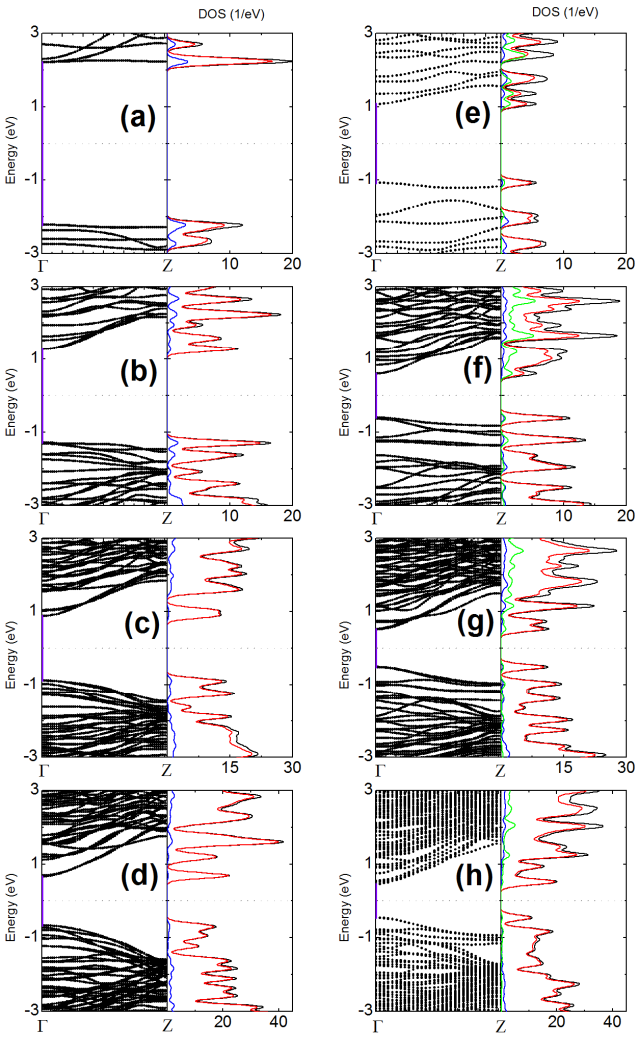

Fig. 2. Electronic band structures and electronic densities of states of Ge (left side) and Si (right side) NWs with morphology NW1 and 2 Li atoms [(a), (e)], NW2 with 4 (b) and 6 (f) Li atoms, NW3 [(c), (g)] with 6 Li atoms, and NW4 with 4 (d) and 6 (h) Li atoms per unit cell. The density of states for each atomic species Ge (orange), Si (red), H(blue) and Li (green) as well as the total density of states (black line) are depicted at the rigth side of each electronic band structure

For the maximum studied concentration in Si NWs (6 Li atoms per unit cell) it is possible to appreciate that the size of the band gap is similar for the morphologies NW2, NW3 and NW4, and it seems that there is a critical concentration at which all the band gaps converge to the same value, however a more extensive study is necessary. For morphologies NW1 and NW2 of Ge NWs, the energy band gap changes from indirect to direct at the maximum studied concentration, whereas for the rest of the morphologies and for all studied concentrations, the energy band gap conserves its direct nature as occurs for hydrogen-passivated NWs. In the case of Si NWs, all morphologies have a direct band gap except for morphology NW1 which possesses an indirect band gap when there is one Li atom per unit cell.

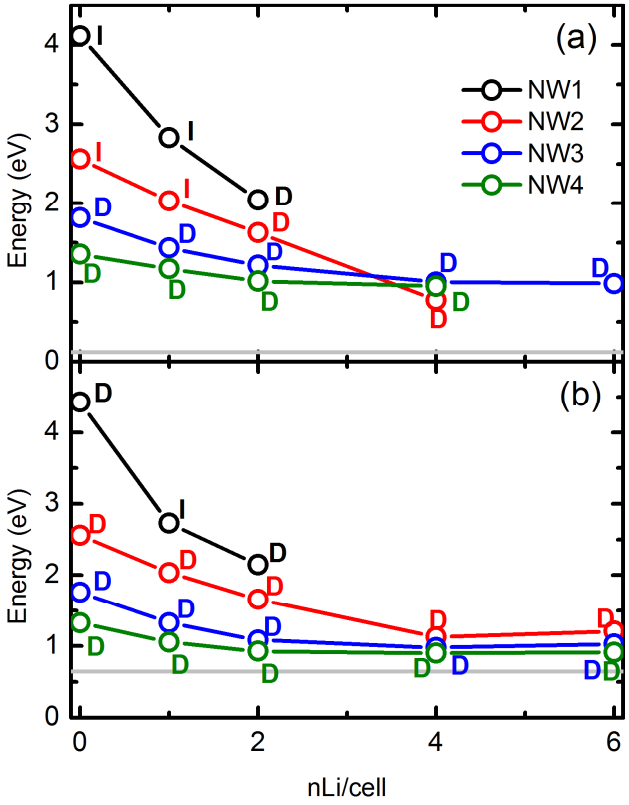

Fig. 3. Energy band gap for the different studied morphologies of (a) Ge and (b) Si NWs as a function of the concentration of Li atoms per unit cell. The letters indicate the type of band gap, I for indirect and D for direct. The gray line indicates the calculated value of the energy band gap for bulk Ge (or Si).

The Fig. 4 shows the optimized morphologies for Ge (right side) and Si (left side) NWs with the same concentration of Li atoms as in Fig. 2. Notice that all Si bonds are preserved in contrast to the Ge NW2 morphology (f) with 4 Li atoms per unit cell, where there are broken bonds, illustrating the change from a crystalline NW surface to an amorphous one in accordance with experimental reports [16] and the mechanism by which Li atoms reduce the mechanical resistance of the nanowire. It is worth mentioning that the maximum Li concentration for the morphology NW1 of Si and Ge NWs, shown in Figs. 4(a) and 4(e), is 2. For higher concentrations, the structure is unstable. On the other hand, the NW3 morphology, shown in Figs. 4(c) and 4(g), is still stable with 6 Li atoms. Likewise, the structures corresponding to the Si NW4 with 6 Li atoms, Fig. 4(d) and Ge NW4 with 4 Li atoms, Fig. 4 (h), are also stable. Finally, notice that the bonds around the substitutional Li atoms are strongly affected, however a more detailed study is needed in order to find a relation between the stability and the concentration of Li atoms that can be supported by the NWs.

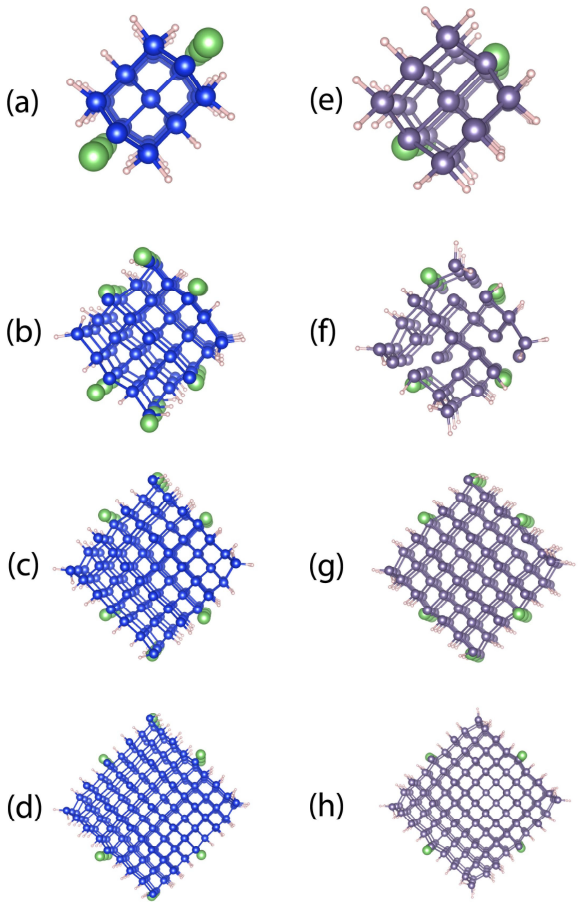

Fig. 4. Optimized structures of Si (left) and Ge (rigth) NWs for NW1 with 2 Li atoms [(a), (e)], NW2 with 6 (b) and 4 (f) Li atoms, NW3 with 6 Li atoms [(c), (g)] and NW4 with 6 (d) and 4 (h) Li atoms per unit cell. The blue, violet, pink and green spheres correspond to Si, Ge, H and Li atoms respectively

IV. SUMMARY

In this work, we presented a theoretical study of the electronic properties of hydrogen-passivated Si and Ge NWs, grown along the [001] crystallographic direction and with several diameters, as function of the concentration of substitutional Li surface atoms. The presence of Li atoms on the surface diminishes the energy band gap and this effect is stronger than the electronic quantum confinement. For the NW1 morphologies, the maximum number of Li atoms per unit cell is 2 for both Si and Ge NWs, whereas for the NW2 morphology, this number is 4 for Ge NWs. The NW2, NW3, and NW4 morphologies are stable for concentrations up to 6 Li atoms per unit cell for Si NWs. For the Ge NWs, this concentration is less or equal than that corresponding to the Si NWs. The deformation and elongation of the Si and Ge surface bonds, due to the presence of Li atoms, help to understand the mechanical process that the semiconductor NWs suffer during the Li insertion, and a further study of their mechanical properties is necessary. These results show that the electronic properties of the Si and Ge NWs can be controlled with the concentration of surface Li atoms, maintaining a direct band gap which is adequate for anodic electrodes in Li batteries.

ACKNOWLEDGMENT

This work was supported by the IPN multidisciplinary projects 2014-1640 and 2014-1641, PAPIIT-DGAPA-UNAM project IN106714, and CONACyT project 252749. Computing resources from the Supercomputing Department of DGTIC-UNAM were given through project SC15-1-IR-27.

REFERENCES

[1] B. A. Boukamp, G. C. Lesh, and R. A. Huggins, “All-solid lithium electrodes with mixed-conductor matrix,” J. Electrochem. Soc., vol. 128, pp. 725-729, 1981.

[2] N. Liu, W. Li, M. Pasta and Y. Cui, “Nanomaterials for electrochemical storage,” Front. Phys., vol. 9, pp. 323-350, 2014.

[3] J. Graetz, C. C. Ahn, R. Yazami, and B. Fultz, “Nanocrystalline and thin film germanium electrodes with high lithium capacity and high rate capabilies,” J. Electrochem. Soc., vol. 151, pp. A698-A702, 2004.

[4] C. K. Chan, X. F. Zhang, and Y. Cui, “High capacity Li ion battery anodes using Ge nanowires,” Nano Lett., vol. 8, pp. 307-309, 2008.

[5] Q. Zhang, Y. Cui, and E. Wang, “First-principles approaches to simulate lithiation in silicon electrodes,”, Modelling Simul. Mater. Sci. Eng., vol. 21, pp. 074001 (29 pp), 2013.

[6] W. Wan, Q. Zhang, Y. Cui, and E. Wang, “First principles study of lithium insertion of bulk silicon,” J. Phys.: Condens. Matter, vol. 22, pp. 415501 (9pp), 2010.

[7] P. Kaghazchi, “Theoretical studies of Li incorporation into Si(111),” J. Phys.: Condens. Matter, vol. 25, pp. 095008 (6pp), 2013.

[8] C. K. Chan, R. N. Patel, M. L. O’Connell, B. A. Korgel, and Y. Cui, “Solution-grown silicon nanowires for lithium-ion battery anodes,” ACS nano, vol. 4, pp. 1443-1450, 2010.

[9] M. Ge, J. Rong, X. Fang, and C. Zhou, “Porous doped silicon nanowires for lithium ion battery anode with long cycle life,” Nano Lett., vol. 12, pp. 2318-2323, 2012.

[10] T. H. Hwang, Y. M. Lee, B. S. Kong, J. S. Seo, and J. W. Choi, “Electrospun core-sell fibers for robust silicon nanoparticles-based lithium ion battery anodes,” Nano Lett., vol. 12, pp. 802-807, 2012.

[11] D. Chen, X. Mei., G. Ji, M. Lu, J. Xie, J. Lu, and J. Y. Lee, “Reversible lithium-ion storage in silver treated nanoscale hollow porous silicon particles,” Angew. Chem. Int. Ed., vol. 51, pp. 2409-2413, 2012.

[12] C. K. Hhan, H. H. Peng, G. Liu, K. McIlwrath, X. F. Zhang, and Y. Cui, “High-performance lithium battery anodes using silicon nanowires,” Nature Nanotech., vol. 3, pp. 31-35, 2008.

[13] H. Föll, H. Hartz, E. Ossei-Wusu, J. Carstensen, and O. Riemenschneider, “Si nanowire arrays as anodes in Li ion batteries,” Phys. Status Solidi RRL., vol. 4, pp.4-6, 2010.

[14] X. H. Liu, H. Zhen, L. Zhong, S. Huang, K. Karki, L. Q. Zhang, *et al.*, “Anisotropic swelling and fracture of silicon nanowires during lithiation,” Nano Lett. vol. 11, pp. 3312-3318, 2011.

[15] D. M. Tang, C. L. Ren, M. S. Wang, X. Wei, N. Kawamoto, C. Liu, Y. Bando, M. Mitome, N. Fukata and D. Golberg, “Mechanical properties of Si nanowires as revealed by in situ transmission electron microscopy and molecular dynamics,” Nano Lett., vol. 12, pp. 1898-1904, 2012.

[16] T. Kennedy, E. Mullance, H. Geaney, M. Osiak, C. O’Dwyer, and K. M. Ryan, “High-performance germanium nanowire-based lithium battery anodes extending over 1000 cycles through in situ formation of a continuous porous network,” Nano Lett., vol. 14, pp. 716-723, 2014.

[17] N. Troullier, J. L. Martins, “Efficient pseudopotentials for plane-wave calculations,” Phys. Rev. B, vol. 43, pp. 1993-2006, 1991.

[18] L. Kleinnman, D. Bylander, "Efficacious form for model pseudopotentials," Physc. Rev. Lett., vol. 48, pp. 1425-1428, 1982.

[19] J. Soler, E. Artacho, J. Gale, A. García, J. Junquera, P. Ordejón, D. Sánchez-Portal, "The SIESTA method for ab initio order-n materials simulation," J. Physc.: Condens. Matter, vol. 14, pp. 2745-2779, 2002.

[20] C. Kittel, Introduction to Solid State Physics, 7th ed., John Wiley & Sons, 1996, pp. 23.

[21] F. Salazar, and L. A. Pérez, "Theoretical study of electronic and mechanical properties of GeC nanowires," Com. Mater. Sci., vol. 63, pp. 47-51, 2012.

[22] A. Miranda, J. L. Cuevas, A. E. Ramos, and M. Cruz-Irisson, "Effects of morphology on electronic properties of hydrogenated silicon carbide nanowires," Journal of Nano Research, vol. 5, pp. 161-167, 2009.

[23] H. Raza, "Theoretical study of isolated dangling bonds, dangling bond wires, and dangling bond clusters on a H:Si(001)-(2x1) surface," Phys. Rev. B, vol. 76, pp. 045308 (8 pp), 2007.

§ Permanent address: ESIME-Culhuacán, Instituto Politécnico Nacional, Av. Santa Ana 1000, 04430 México, D.F., México.

Control de un convertidor CD/CA para aplicaciones en paneles solares

[1]Navarro, David [2]Cortes, Domingo
Sección de Estudios de Posgrado e Investigación
Instituto Politécnico Nacional ESIME Culhuacán
México D. F.
[1]david.navarro.d@gmailcom, domingo.cortes@gmail.com

Vazquez, Nimrod
Departamento de ingeniería electrónica
Instituto Tecnológico de Celaya
Celaya Guanajuato
n.vazquez@ieee.org

***Resumen*— Las energías renovables son las fuentes de generadoras de energía del futuro. En particular la energía solar es una de las que actualmente se encuentra en auge, pero requieren de inversores monofásicos para regular el voltaje a la salida. Existen distintas topologías de inversores, pero casi todas presentan una salida de voltaje en modo diferencial. Debido a la construcción del panel solar los inversores presentan corrientes de fuga hacia tierra, lo cual se ve reflejado en bajas eficiencias y reducción de la vida útil del panel. Para minimizar las corrientes de fuga se propone el uso de un inversor sin salida diferencial, pero esto complica el diseño de un controlador.**

En este trabajo se propone una estrategia de control, en donde las referencias de los estados se obtienen a partir del modelo del convertidor. El análisis se realiza considerando la salida deseada y posteriormente encontrando los valores de cómo deben ser los estados. La metodología es sencilla de implementar y puede implementarse dentro de un microcontrolador. Resultados en simulación son obtenidos para validar que el desarrollo para obtener las referencias junto con un control se pueden aplicar al inversor.

***Palabras clave*— Inversor monofásico, control no lineal, paneles fotovoltaicos**

I. INTRODUCCIÓN

En el año 2050 se estima que la población se incremente de 7 a 9 millones de habitantes a nivel mundial. Al mismo tiempo la economía crecerá casi cuatro veces, causando un incremento en la demanda de recursos naturales y energía [11]. Según un estudio realizado por la compañía petrolera BP en Junio de 2012 [1], el consumo de energía en el mundo es en su mayoría proveniente de combustibles fósiles, aproximadamente un 87%, la energía nuclear corresponde al 5%, la hidroeléctrica el 6% y un 2% a otras fuentes renovables (incluyendo eólica, solar, biodiesel entre otros).

Actualmente la energía generada por combustibles fósiles presenta desventajas, puesto que los recursos en algún momento se agotarán y además su quema produce contaminantes que a su vez provocan el cambio climático. Para evitar estos inconvenientes se ha tomado medidas para aprovechar recursos renovables, tales como aerogeneradores, micro turbinas hidráulicas, sistemas híbridos, paneles fotovoltaicos entre otras.

Actualmente se encuentra en auge el uso de la energía fotovoltaica, pero para poder aprovechar la energía proveniente del sol los inversores fotovoltaicos son de vital importancia, la utilidad de esta clase de inversores es la de convertir la energía en corriente directa (CD) proporcionada por un panel solar fotovoltaico en energía en corriente alterna (CA). De acuerdo con datos de la Asociación Europea de la Industria Fotovoltaica (EPIA) al final del año 2007 la energía proporcionada por sistemas fotovoltaicos era de poco más de 7 GW, para finales de 2012 dicha cifra superó los 100 GW, dejando claro que hay un fuerte mercado para el desarrollo y uso de esta tecnología [4].

Una de las desventajas más discutidas en varios artículos es el hecho que debido a su conexión la mayoría presentan una corriente de fuga hacía tierra por medio de capacitancias parásitas (C_p) generadas en el panel solar fotovoltaico debido a la naturaleza del mismo [13]. Esta corriente no deseada resulta en: bajas eficiencias de todo el sistema, distorsión en la corriente de salida, interferencia electromagnética, problemas de seguridad y reduce eventualmente la vida del panel solar. Varios investigadores se han dado a la tarea de reducir estas corrientes de fuga, aun y cuando en [5], [6], [13] se han logrado algunas mejoras todavía hay mucho trabajo para mejorar la eficiencia de los paneles.

Un inversor sin salida de voltaje diferencial es presentado en [12], de esta manera las corrientes parasitas en sistemas fotovoltaicos se reducen significativamente. En esta topología el número de transistores se reduce a dos, mientras que los componentes pasivos (inductores y capacitores) se incrementan a cuatro. Para demostrar que la topología funciona como inversor en [12] se planteó un control por modos deslizantes, con el que se puede apreciar que la salida de voltaje es de forma senoidal. Si bien se presentan resultados favorables, la superficie deslizante se puede mejorar, ya que muchos de los estados no fueron considerados, ya que resulta complicado obtener las referencias. En este trabajo se presenta una estrategia de control, la cual generan las referencias de todos los estados a partir de conocer el voltaje de salida deseado, como se ha planteado para convertidores DC-DC en [2]. Una vez que se conoce la corriente de referencia se implementa un control por modos deslizantes, el cual permite llevar al sistema a un voltaje de salida deseado.

En la sección II se presenta una breve reseña sobre los inversores monofásicos desarrollados para reducir las corrientes de fuga en aplicaciones fotovoltaicas. En la sección III se presenta la topología y el desarrollo para modelar el inversor, se presenta un análisis de puntos de equilibrio para

conocer el rango de voltajes de salida que le es posible proporcionar. En la sección IV se presentan las complicaciones para el diseño de un control para el inversor, debido a que resulta complicado obtener algunas de las referencias, se propone un desarrollo para obtener las referencias y a partir de las mismas controlar el inversor. En IV.A se presentan los resultados en simulación de la forma de onda de las corrientes y voltajes considerando que a la salida se obtiene el valor deseado. En la sección V se propone un control por modos deslizantes (CMD), considerando las referencias obtenidas en la sección anterior. En la sección V.A se presentan los resultados de implementar el CMD con las referencias obtenidas. Por último en la sección VI se presentan las conclusiones obtenidas de este trabajo.

II. INVERSORES MONOFÁSICOS

Un inversor monofásico es un convertidor electrónico que permite realizar conversión de corriente directa a corriente alterna. Dependiendo de la aplicación se deben de seleccionar los transistores apropiados (BJTs, MOSFETs, IGBTs, MCTs, SITs y GTOs), los cuales determinan la técnica de modulación a implementar [9]. Otro factor que determina la aplicación es la topología, pero casi en todos los casos son una variante del inversor tradicional presentado en la Fig. 1. En el caso de paneles solares un inversor con salida de voltaje diferencial presenta corrientes de fuga. Este problema ha llamado la atención de los investigadores y por lo tanto se han propuesto diferentes topologías.

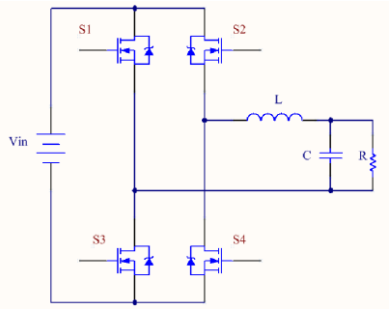

Fig. 1 Inversor monofásico tradicional

Uno de los primeros intentos es usar MOSFET en un puente H tradicional. Derivado del uso de diferentes componentes se deriva el inversor hibrido que consta de un puente H con MOSFET en la parte inferior e IGBT en la superior de cada rama. Estas dos modificaciones presentan obtienen buenos resultados solamente cuando cuentan con aislamiento galvánico, ya que si no está presente las corrientes de fuga se incrementan. La topología 5 es un puente H, pero cuenta con un interruptor en el lado de CD el cual opera en alta frecuencia en ambos semiciclos de la red eléctrica, nuevamente se obtienen buenos resultados cuando existe aislamiento galvánico. La topología HERIC consta de un puente H al que se le agregan un par de interruptores en direcciones opuestas colocados en paralelo del filtro y la carga, se obtienen menores corrientes de fuga en comparación a las topologías anteriores, pero aun así considerable para las aplicaciones. En [13] se presenta un inversor H6, el cual se construye con 6 transistores, esta topología tiene como ventaja que no necesita de un tiempo muerto entre los interruptores porque los tres interruptores de una rama nunca están encendidos. Su corriente parásita es menor que la del puente H tradicional, pero para aplicaciones prácticas son perdidas altas cuando no existe aislamiento.

La topología propuesta en [12] elimina los problemas de fugas de corrientes parásitas, ya que la salida del inversor no se da de manera diferencial, sino que tiene tierra común con respecto a la fuente de alimentación. Esta topología se revisará con mayor detalle en las siguientes secciones.

III. MODELADO DE LA TOPOLOGÍA DEL INVERSOR

El inversor monofásico desarrollado en [12] presenta una muy valiosa ventaja para aplicaciones fotovoltaicas, considerando que la tierra de la fuente y la tierra de la salida son comunes. Otra ventaja que presenta es que solamente requiere de dos interruptores, a diferencia de otros inversores que por lo menos requieren de cuatro transistores. Pero a su vez se requiere de dos capacitores y dos inductores, provocando que el sistema se un orden mayor, lo cual podría llegar a complicar el diseño de un buen controlador.

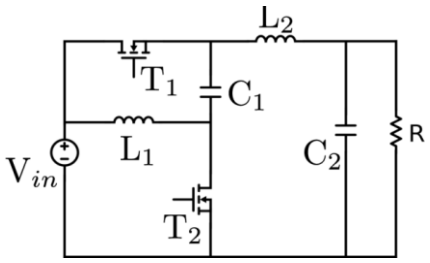

Fig. 2 Topología de inversor monofásico

En la Fig. 2 se presenta la nueva topología de inversor propuesta en [12], de dicho diagrama se puede apreciar que la salida del inversor está referida a la misma tierra de la fuente.

Considere de la Fig. 2 el transistor T_1 está activado y el transistor T_2 está desactivado, el circuito resultante se presenta en la Fig. 3, a partir del cual se obtienen las ecuaciones

$$\dot{x}_1 = \frac{x_2}{L_1} \quad (1a)$$

$$\dot{x}_2 = \frac{x_1}{C_1} \quad (1b)$$

$$\dot{x}_3 = \frac{V_{in} - x_4}{L_2} \quad (1c)$$

$$\dot{x}_4 = \frac{x_3}{C_2} - \frac{x_4}{RC_2} \quad (1d)$$

donde x_1, x_2, x_3 y x_4 son la corriente en el inductor L_1, el voltaje en el capacitor C_1, la corriente en el inductor L_2 y el voltaje en el capacitor C_2 respectivamente. Las inductancias L_1 y L_2, capacitancias C_1 y C_2, y el voltaje de entrada V_{in}, son constantes conocidas. Mientras que la resistencia R permanece como constante desconocida para propósitos de análisis.

Por otra parte si de la Fig. 2 el transistor T_1 está desactivado y el transistor T_2 está activado, se obtiene el circuito equivalente presentado en la **Fig.** 4, de donde se obtienen las ecuaciones

$$\dot{x}_1 = \frac{V_{in}}{L_1} \quad (2a)$$

$$\dot{x}_2 = \frac{x_3}{C_1} \quad (2b)$$

$$\dot{x}_3 = \frac{x_2 - x_4}{L_2} \quad (2c)$$

$$\dot{x}_4 = \frac{x_3}{C_2} - \frac{x_4}{RC_2} \quad (2d)$$

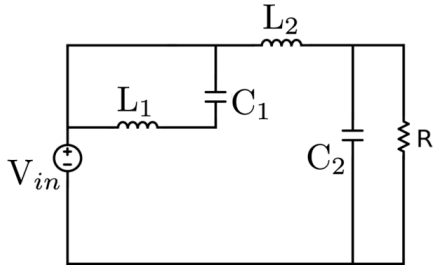

Fig. 3Topología considerada como $u = 1$

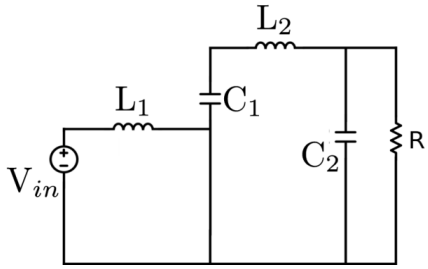

Fig. 4 Topología considerada como $u = 0$

Combinando los modelos (1) y (2) se obtiene

$$\dot{x}_1 = \frac{V_{in}(1-u) - ux_2}{L_1} \quad (3a)$$

$$\dot{x}_2 = \frac{ux_1 + (1-u)x_3}{C_1} \quad (3b)$$

$$\dot{x}_3 = \frac{V_{in}u - (1-u)x_2 - x_4}{L_2} \quad (3c)$$

$$\dot{x}_4 = \frac{x_3}{C_2} - \frac{x_4}{RC_2} \quad (3d)$$

tomando en cuenta que $u \in \{0,1\}$.

Uno de los puntos importantes es conocer las capacidades del inversor a partir del modelo (3), sobre todo conocer los límites dentro de los cuales se puede encontrar la salida del sistema. Para poder comprobar que esta topología tiene capacidad de generar una señal sinusoidal dentro de ciertos parámetros deseados se realiza un análisis de puntos de equilibrio, los cuales se encuentran igualando las derivadas de (3) a cero obteniendo

$$0 = V_{in}(1-u) - ux_2 \quad (4a)$$

$$0 = ux_1 + (1-u)x_3 \quad (4b)$$

$$0 = V_{in}u - (1-u)x_2 - x_4 \quad (4c)$$

$$0 = x_3 - \frac{x_4}{R} \quad (4d)$$

despejando cada uno de los estados y dejándolos en función de la variable u se obtiene

$$x_1 = \frac{V_{in}}{R}\left(\frac{-1 + 3u - 2u^2}{u^2}\right) \quad (5a)$$

$$x_2 = \frac{(1-u)V_{in}}{u} \quad (5b)$$

$$x_3 = \frac{V_{in}}{R}\left(\frac{2u-1}{u^2}\right) \quad (5c)$$

$$x_4 = V_{in}\left(\frac{2u-1}{u}\right) \quad (5d)$$

el estado que representa la salida del sistema es x_4, por lo tanto de (5) se puede obtener el intervalo de los voltajes que el inversor puede proporcionar. Si en (5a) se sustituye $u = 1$ el voltaje de salida es V_{in}, mientras que si se sustituye $u = 0$ el valor de voltaje es $-\infty V_{in}$, por lo tanto se puede concluir que esta topología puede generar un voltaje a la salida de $V_{in}\sin(\omega t)$ sin ningún problema. Sin embargo, aun y cuando se ha determinado que el convertidor puede generar la señal deseada, el diseño del control para lograr dicho objetivo es un trabajo complicado debido a las no linealidades y dinámicas de fase no mínima que tiene el inversor.

A partir de conocer que el convertidor es capaz de proporcionar una salida sinusoidal, el paso siguiente es realizar un control que permita regular de manera automática el voltaje de salida. Por lo general los inversores presentan solamente dos estados, lo que hace relativamente sencillo el diseño de un controlador. En el caso de esta nueva topología se cuenta con 4 estados lo cual dificulta un poco la realización del control, debido a que hay que cuidar que ninguno de los estados se dispare como consecuencia de la dinámica de fase no mínima de la mayoría de los convertidores. En la siguiente sección se revisarán los problemas que se presentan para el diseño del controlador, así como un tipo de controlador que sea posible aplicarlo a este convertidor.

IV. Problemática de control

El desempeño esperado de un inversor monofásico es lograr conmutar los transistores para que se obtenga una salida sinusoidal de frecuencia y amplitud deseada. En [12] se diseñó un CMD para verificar de manera experimental que la topología podía funcionar como inversor, pero solamente se tomaron en cuenta dos de los cuatro estados. Aun y cuando el convertidor logró proporcionar el voltaje deseado a la salida, es importante tomar en cuenta a todos los estados y verificar que se mantengan dentro de sus límites de operación, de esta manera se puede realizar un uso más eficiente de la fuente de energía renovable. Para el caso de este convertidor es sencillo encontrar la referencia solo para dos de estos estados (x_3 y x_4), pero para los otros dos (x_1 y x_2) resulta ser una tarea un poco más complicada, motivo por el que el control del inversor en [12] solamente considera un estado (x_3).

A partir del modelo (3) se puede apreciar que el obtener las referencias de los estados x_3 y x_4 son relativamente fáciles de encontrar, pero la referencia de los estados x_1 y x_2. Para el caso de x_4 es sencillo obtener la referencia, debido a que es la salida del sistema la cual se espera que sea $k\sin\omega t$, en donde k es la amplitud deseada y ω es la frecuencia deseada. Ahora

el problema es encontrar como debería ser las referencias de los estados x_1, x_2, y x_3 cuando $x_4 = x_{4d}$.

Conocer el valor que debe tener x_3 cuando $x_4 = x_{4d}$ se puede obtener de la ecuación (3d), de donde

$$x_4 = x_{4d} = k\sin(\omega t) \tag{6}$$

mientras que se obtiene derivando (6) obteniendo

$$\dot{x}_4 = \dot{x}_{4d} = k\omega\cos(\omega t) \tag{7}$$

sustituyendo (6) y (7) en (3d) y despejando x_3 se obtiene

$$x_3 = \dot{x}_{4d}C_2 + \frac{x_{4d}}{R} \tag{8}$$

que es la corriente de deberá circular en el inductor L_2 cuando $x_4 \to x_{4d}$. Para poder encontrar las referencias de los estados x_1 y x_2 es un poco más complicado, ya que se debe de conocer por lo menos la variable u. Encontrar la forma que debe de ser u se puede realizar a partir de (3c), notese que uno de los términos que se desconocen es $\dot{x}_3$, pero este puede ser encontrado al derivar (8) obteniendo

$$\dot{x}_3 = \ddot{x}_{4d}C_2 + \frac{\dot{x}_4}{R} \tag{9}$$

ahora de (9) el término desconocido es $\ddot{x}_{4d}$, pero este se puede obtener fácilmente derivando (7) una vez, resultando

$$\ddot{x}_4 = \ddot{x}_{4d} = -k\omega^2\sin(\omega t) \tag{10}$$

Si se sustituye (6) y (9) en (3c) y se despeja u se obtiene

$$u = \frac{\dot{x}_3 L_2 + x_2 + x_4}{V_{in} + x_2} \tag{11}$$

en donde todos los términos son conocidos menos x_2.

Una vez que se conoce la manera en que se debe comportar u para generar a la salida (6), el problema restante es encontrar de que manera se comportan x_1 y x_2. Del sistema (3) se han ocupado las ecuaciones (3c) y (3d) para obtener (8) y (11), pero quedan disponibles

$$\dot{x}_1 = \frac{V_{in}(1-u) - ux_2}{L_1} \tag{12a}$$

$$\dot{x}_2 = \frac{ux_1 + (1-u)}{C_2} \tag{12b}$$

Si se trata de seguir el procedimiento anterior es algo complicado, puesto que se tiene de incógnita x_1, x_2, $\dot{x}_1$ y $\dot{x}_2$, que analizando desde un punto de vista matemático, se debe resolver un problema de 4 incógnitas con dos ecuaciones lo cual no es posible realizar.

Una manera en que se podrían encontrar las referencias para x_1 y x_2 es simular el sistema (12) considerando que u se obtiene como se indica en (11). La manera más sencilla de realizar la simulación del modelo (12) es mediante la solución numérica de la ecuación diferencial, por lo tanto para una implementación física se podría programar un método numérico para resolver ecuaciones diferenciales en un dispositivo programable. Está metodología ha sido usada para encontrar la referencia de algunos convertidores de corriente directa en [2].

Aun cuando ya se cuenta con el sistema a simular, hace falta conocer las condiciones iniciales para que el sistema llegue mucho más rápido al voltaje deseado de salida. Para en controlar las condiciones iniciales del sistema se pueden obtener de los puntos de equilibrio (5). De este modo si se selecciona el valor de voltaje con el que debe de iniciar x_4 se puede despejar u de (5d) y al sustituir el valor encontrado de u en (5a) y (5b) se obtienen los valores de las condiciones iniciales de los estados x_1 y x_2.

Para simular el sistema cabe hacer notar que la mayoría de los convertidores electrónicos son sistemas de fase no mínima por lo tanto suelen ser sistemas que tienden a ser inestables de no controlarse apropiadamente. Note que el sistema (12) es inestable si se simula considerando t, pero si el sistema se trabaja considerando el tiempo $\tau = -t$ es posible obtener un resultado en simulación en donde los estados convergen a una solución particular.

A. Simulación

TABLE I. PARAMETROS DE DISEÑO

V_{in}	350V
L_1	$2mH$
C_1	110µF
L_2	$1mH$
C_2	2.2µF
R	7 Ω
x_{4d}	$\mathbf{127\sin(2\pi 60t)}$

Con la finalidad de verificar los resultados obtenidos para generar las referencias en esta sección se realiza una simulación del sistema (12) considerando los parámetros de la Tabla I. Un punto importante es colocar las condiciones iniciales apropiadas para que el sistema llegue más rápidamente a la solución esperada. De esta manera se sustituyen los valores de la Tabla I en (5) obteniendo

$$x_1(0) = 0 \tag{13a}$$

$$x_2(0) = 350 \tag{13b}$$

como las condiciones iniciales del sistema. La simulación se realiza considerando el tiempo como τ para que no se dispare alguno de los estados y converjan a un valor acotado. En la **Fig. 5** se presentan las formas de onda que deberán tener los estados x_1 y x_2 considerando que la salida del sistema se mantiene en $x_4 = 127\sin(2\pi 60t)$. Note que pese a que las señales de la **Fig. 5** no presentan una forma sinusoidal, pero si mantienen una frecuencia de oscilación constante de la misma frecuencia de la referencia.

Ahora tomando en cuenta que la simulación del sistema (12) con el tiempo τ, permite conocer la forma de onda que tendrían los estados x_1 y x_2 cuando el sistema es forzado a $x_4 = k\sin(2\pi f t)$, se puede considerar que se ha desarrollado un generador de referencias para el inversor presentado en

[12]. Por lo tanto si se cuenta con una manera de encontrar las referencias ahora el trabajo del diseño del controlador se puede decir que es una tarea mucho más sencilla y se pueden aplicar distintas técnicas de control. En la siguiente sección se muestra ejemplificando que el generador de referencias se puede aplicar en conjunto con un CMD.

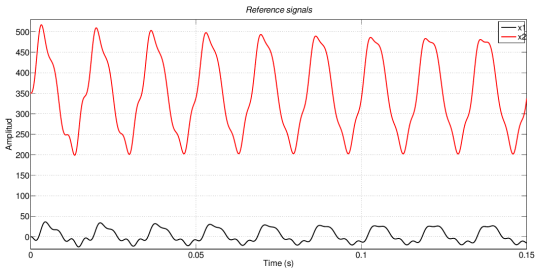

Fig. 5 Señales de referencia

V. CONTROL POR MODOS DESLIZANTES

El CMD es una técnica de control que puede ser aplicada tanto a sistemas lineales como no lineales, ya que la estabilidad se estudia en base a la superficie deslizante. En el caso de convertidores ha probado ser una técnica bastante robusta ante variaciones de parámetros [1], [3], [10]. Su implementación y modificación es bastante sencilla, puesto que con solo modificar la superficie deslizante el control puede ser actualizado y mejorado. Además de que la naturaleza discontinua de los convertidores se adapta mejor a la naturaleza del CMD

Desde hace ya varias décadas se conoce que el control en modo corriente proporciona resultados más rápidos [7], [8]. Por tal motivo para poder permitir obtener una mejor respuesta del inversor monofásico se propone la ley de control

$$u = \begin{cases} 1 & if\ \sigma > 0 \\ 0 & if\ \sigma < 0 \end{cases} \qquad (14)$$

tomando en cuenta la superficie deslizante

$$\sigma(x) = x_1 - x_{1ref} \qquad (15)$$

En general el uso del CMD no se puede ajustar a frecuencia constante, si no que la frecuencia de conmutación será determinada por la dinámica de los componentes del sistema. El ajuste del CMD a una frecuencia constante en convertidores DC/DC se ha realizado por medio de introducir el resultado de la superficie deslizante a un PWM. En [3] y [10] se ha demostrado que el control equivalente de CMD es en si el ciclo de trabajo de los controladores basados en modelos linealizados. Para el caso de la topología de inversor presentada en este trabajo, es posible aprovechar este resultado, ya que como el inversor cuenta solo con dos transistores es posible implementarlo con un PWM.

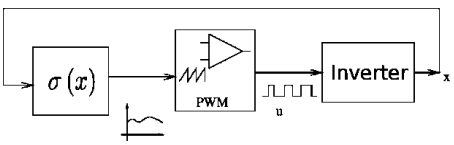

Fig. 6 Implementación de control por modos deslizantes a frecuencia constante

La Fig. 6 presenta la implementación de como ajustar un CMD con un PWM, pero para realizar el control del inversor propuesto se requiere modificar ligeramente la implementación. En la Fig. 7 se presenta la implementación final del generador de referencias en conjunto con el CMD. Este esquema de implementación será simulado y los resultados se presentarán en la siguiente subsección.

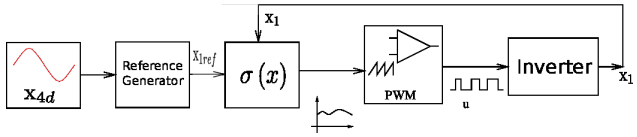

Fig. 7 Implementación de control con generador de referencias

A. Simulación

En esta sección se simula el CMD para el inversor monofásico, se debe considerar que para la aplicación del control se siguió el esquema de generación de referencias como se muestra en la Fig. 7, considerando los parámetros de Tabla II.

Aplicando el generador de referencias (11) y (12) y el CMD (14) y (15) se presenta en la Fig. 8 el voltaje y corriente a la salida del inversor, junto con la referencia del voltaje deseado. Note que el voltaje de salida presenta un ligero desfase con respecto a la referencia, pero se mantiene una amplitud casi idéntica, el control es bueno puesto que la diferencia de los voltajes no supera los $5V$. Los resultados obtenidos en la Fig. 8 muestran que el generador de referencias en conjunto con el CMD permite que el inversor proporcione un voltaje a la salida deseado.

TABLE II. PARAMETROS DE SIMULACIÓN

V_{in}	350V
L_1	$1mH$
C_1	110µF
L_2	$1mH$
C_2	2.2µF
R	7 Ω
x_{4d}	$127\sin(2\pi 60t)$
f_{sw}	$40kHz$

Con respecto a los estados estimados, la simulación también compara la corriente deseada, con respecto a la corriente que circula en el inductor. En la Fig. 9 se presenta la corriente de referencia y la corriente en el inductor L_1, se puede apreciar que el control sigue perfectamente la referencia. El problema que se presenta de la pequeña variación del voltaje no se debe a un mal funcionamiento del control, este puede ser ocasionado por la misma dinámica de los componentes y del convertidor, inclusive realizando un mejor CMD se puede mejorar el desempeño de la simulación.

A manera de ejemplificar el desempeño del convertidor con distintos componentes en la Fig. 10 se repitió la simulación, pero ahora en esta ocasión el inductor $L_1 = 2mH$. En esta nueva simulación, el control del inversor es mucho más precisa, debido a que se obtiene una mejor regulación de voltaje y con un menor error con respecto a la amplitud del

voltaje deseada. El desfasamiento de la señal es nuevamente el problema, ya que en este resultado la señal de referencia fue desplazada para poder compararse con el voltaje deseado del sistema.

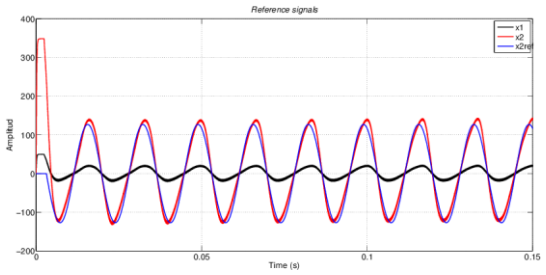

Fig. 8 Salida del inversor monofásico

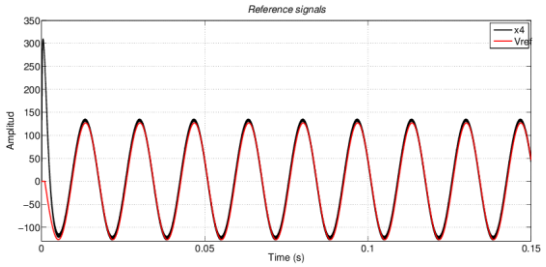

Fig. 9 Corriente de referencia y corriente real

Esta propuesta es un buen inicio para realizar el control del inversor monofásico, claro que es necesario enfocarse en el estudio de un algoritmo de control más completo. Para poder mejorar el desempeño del convertidor se requiere estudiar mejor el generador de referencias, con la finalidad de reducir el error de la señal deseada. Inclusive colocar otro tipo de controlador en conjunto con el generador de referencias podría mejorar significativamente el desempeño del inversor.

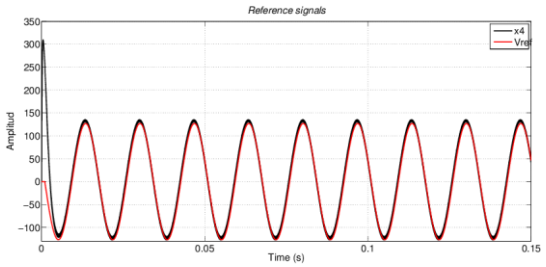

Fig. 10 Voltaje de salida contra voltaje de referencia

VI. Conclusiones

En este trabajo se presenta diseñó un control por modos deslizantes a una nueva topología de inversor para paneles fotovoltaicos. Debido a su complicación para obtener las referencias para algunas de sus variables fue usada una técnica para invertir el tiempo y crear un generador de referencias. Este generador de referencias permite que a partir de un voltaje deseado sea posible conocer el comportamiento deseado del resto de las variables.

Una vez que se conocen las referencias es posible implementar un control para que el inversor proporcione el voltaje deseado a la salida. Se selecciona el control por modos deslizantes ya que se acopla a las discontinuidades naturales de los convertidores electrónicos. Presentando al final una manera de conjuntar el control por modos deslizantes y la manera de generar las referencias como una buena opción a aplicar al inversor monofásico.

Agradecimientos

Este artículo fue apoyado parcialmente por el Instituto de Ciencia y Tecnología del Distrito Federal bajo el proyecto ICYTDF-198-2012

Referencias

[1] Alvarez, J., D. Cortes, and J. Alvarez. 2000. “Indirect Control of High Frequency Power Converters for AC Generation.” In *Decision and Control, 2000. Proceedings of the 39th IEEE Conference on*, 4:4072–4077 vol.4. doi:10.1109/CDC.2000.912352.

[2] “BP Statistical Review of World Energy.” 2010 (June).

[3] Cortes, Domingo, Jaime Alvarez, and Joaquin Alvarez. 2011. “Output Feedback and Dynamical Sliding-Mode Control of Power Converters.” *International Journal of Electronics* 98 (4): 505–519. doi:10.1080/00207217.2010.547805. http://dx.doi.org/10.1080/00207217.2010.547805

[4] European Photovoltaic Industry Association EPIA. “Global Market Outlook: For Photovoltaics 2013-2017.” *Http://www.Epia.Org/Home/*.

[5] Gu, Bin, J. Dominic, Jih-Sheng Lai, Chien-Liang Chen, T. LaBella, and Baifeng Chen. 2013. “High Reliability and Efficiency Single-Phase Transformerless Inverter for Grid-Connected Photovoltaic Systems.” *Power Electronics, IEEE Transactions on* 28 (5) (May): 2235–2245. doi:10.1109/TPEL.2012.2214237.

[6] Kerekes, T., R. Teodorescu, P. Rodriguez, G. Vazquez, and E. Aldabas. 2011. “A New High-Efficiency Single-Phase Transformerless PV Inverter Topology.” *Industrial Electronics, IEEE Transactions on* 58 (1) (Jan): 184–191. doi:10.1109/TIE.2009.2024092.

[7] Liu, Yan-Fei, and P.C. Sen. 1994. “A General Unified Large Signal Model for Current Programmed DC-to-DC Converters.” *Power Electronics, IEEE Transactions on* 9 (4) (Jul): 414–424. doi:10.1109/63.318900.

[8] Middlebrook, R.D. 1989. “Modeling Current-Programmed Buck and Boost Regulators.” *Power Electronics, IEEE Transactions on* 4 (1) (Jan): 36–52. doi:10.1109/63.21871.

[9] Muhammad H. Rashid. *Power Electronics: Circuits, Devices, and Aplications*. Ed. Pearson Prentice Hall, Tercera edición.

[10] Navarro-López, Eva M., Domingo Cortés, and Christian Castro. 2009. “Design of Practical Sliding-Mode Controllers with Constant Switching Frequency for Power Converters.” *Electric Power Systems Research* 79 (5): 796–802. doi:http://dx.doi.org/10.1016/j.epsr.2008.10.018. http://www.sciencedirect.com/science/article/pii/S0378779608002903.

[11] OECD. “OECD Environmental Outlook to 2050: The Consequences of Inaction.” *OECD Publishing, Doi:10.1787/9789264122246-En., 2012.*

[12] Rosas Compeán, Marco Luis. 2014. “Convertidor CD/CA Sin Aislamiento Con Conexión a La Red Eléctrica Para Aplicaciones En Paneles Solares.” PhD thesis, IPICYT.

[13] Yu, Wensong, Jih-Sheng Lai, Hao Qian, C. Hutchens, Jianhui Zhang, G. Lisi, A. Djabbari, G. Smith, and T. Hegarty. 2010. “High-Efficiency Inverter with H6-Type Configuration for Photovoltaic Non-Isolated Ac Module Applications.” In *Applied Power Electronics Conference and Exposition (APEC), 2010 Twenty-Fifth Annual IEEE*, 1056–1061. doi:10.1109/APEC.2010.5433372.

[14] Zhang, Li, Kai Sun, Yan Xing, and Mu Xing. 2014. “H6 Transformerless Full-Bridge PV Grid-Tied Inverters.” *Power Electronics, IEEE Transactions on* 29 (3) (March): 1229–1238. doi:10.1109/TPEL.2013.2260178.

Análisis exergoeconómico de variables críticas en el control operativo de una torre de enfriamiento

S. Núñez C.,* E. Aquino Ch., H. Pérez P.

Facultad de Ciencias Químicas
Universidad Veracruzana
Coatzacoalcos, Veracruz, México
sarnunez@uv.mx

D. Colorado G., J.V. Herrera R.
Centro de Investigación de Recursos Energéticos y Sustentable
Universidad Veracruzana
Coatzacoalcos, Veracruz, México

***Abstract*—For a water-air direct contact cooling system are important as environmental variations as such operating changes. In the work the exergy analysis of a wet cooling tower is developed. This cooling system furnishes services to dissipate heat for some petrochemical plants around the Pacific Coasts from México. This exergy analysis doesn't replace a thermodynamic one, just add on it because accounts dead state importance between the cooling yield and the system. Through mass, energy and exergy balances it developed a mathematical model to achieve predict the exergy cooling tower behavior. Also, Carrier and Liley equations are available in a truthful manner to determine the thermodynamics properties. It calculated exergy of the main system cooling´s streams. It was compared the energy and exergy cooling tower behavior in its current operational and design conditions and also was found important relationships between variables and streams than have impact in the cooling and exergy tower yield. operational variables costs are developed in order to be analyzed. During the cooling process, the total irreversibility rate (119.000 kW) generates due to: 8 percent for waste streams than leave the tower, 6 percent due to evaporation losses water and the 86 percent rest for the heat transfer during the whole process. For operating conditions of 2013, the total annual variable cost is 1,85 MMUSD. The 65 percent is for the power consumption of pumps, the 34 percent for fan power consumption and just one percent due to chemical treatment and make up water. exergy analysis considers environmental changes, therefore through the seasons there is a potential economical saving for the fan power consumption due to the natural dead state changes. There are available saving for 7.81 percent of the total annual cost and 23 percent for the total fan consumption.**

Keywords*— *Exergy analysis, cooling tower, analysis Availability.

I. INTRODUCCIÓN

Debido a la importancia que tiene la demanda de energía en los procesos industriales en México, se ha derivado un interés profundo en medir, analizar y mejorar las variables críticas en el control operativo en los equipos de proceso y en especial de los sistemas de transferencia de calor. En el caso de los sistemas de enfriamiento de contacto directo como lo es una torre de enfriamiento (TE) húmeda, la transferencia de calor del istema a los alrededores se lleva a cabo principalmente por la evaporación del agua caliente al ambiente. La tasa de evaporación es una función de la istema ure de agua que retorna caliente del proceso y de las condiciones del ambiente. Es por ello que la aplicación de un análisis exergético es adecuado para un istema en donde las variaciones del ambiente (que en el equilibrio termodinámico es representa el estado muerto) tienen impacto considerable en el proceso de enfriamiento.

En una TE la evaporación se logra cuando a una gota que se pone en contacto con el aire, se le evapora la película exterior, requiriendo para este proceso de absorber calor, el cual se toma de la propia gota, enfriándola consecuentemente, es decir, el enfriamiento se realiza tanto por calor sensible (diferencia de temperatura entre el aire y el agua) como por calor latente (cambio de estado físico del agua a vapor).

Así, el objetivo que se persigue en la TE es que la gota este el mayor tiempo posible en contacto con el aire, lo cual se logra con la altura de la misma y además interponiendo obstáculos (relleno), que le van deteniendo y al mismo tiempo la van fragmentando facilitando el proceso evaporativo. Siendo estos sistemas esenciales para el funcionamiento confiable y eficiente de los equipos y plantas a los cuales da servicio, los medios de control basados en un apropiado *análisis exergético*, tienen gran importancia en el desarrollo de sistemas térmico con uso efectivo de los recursos energéticos y económicos empleados, además de evitar un impacto ambiental desfavorable.

El análisis exergético es un método que emplea los principios de conservación de masa y energía junto con el segundo principio de la termodinámica para el diseño y análisis de sistemas térmicos, a veces también llamado análisis de la disponibilidad [1,2].

El objetivo general de este trabajo, es generar una metodología de evaluación de variables críticas en el control de una torre de enfriamiento con base a su análisis exergético y económico.

II. GENERALIDADES

A. *Agua de enfriamiento*

La disponibilidad de agua en la mayoría de las áreas industriales y su gran capacidad para absorber y desprender calor han hecho del agua el medio de transferencia de calor preferido en las aplicaciones industriales y de servicios [1]. Debido a su elevado calor específico, el agua de enfriamiento es un refrigerante industrial muy valioso. Sin embargo, debido a la tendencia de agua a disolver muchas sustancias, muchas veces contiene un porcentaje elevado de sólidos disueltos, los cuáles, si se utiliza el agua sin tratar, perjudica gravemente a cualquier sistema de enfriamiento y causa desperdicio excesivo de energía.

El uso de agua de enfriamiento raramente es abundante o se dispone sin costo, además de que esta bajo estricto control tanto desde el punto de vista ambiental como del energético. Es por ello que en muchos sistemas el agua de enfriamiento se pasa a través de la planta sólo una vez y se retorna a la corriente de suministro. Esto crea una tasa elevada de retiro de agua y además añade calor a la corriente de suministro. Por otra parte, en una torre de enfriamiento se permite la reutilización de agua hasta tal punto que en la mayor parte de estos sistemas de enfriamiento se reducen las tasas de toma de la corriente de suministro hasta en un 90% [2].

B. *Intercambiador de calor*

La transferencia de calor es el tránsito del calor de un cuerpo caliente a otro más frío. En general, el agua de enfriamiento no entra en contacto directo con el proceso o producto; los dos materiales se suelen separar por una barrera que sea buena conductora de calor para que brinde poca resistencia a la transmisión de calor, por lo común un metal. La barrera que permite el paso del calor del proceso o producto hacia el agua, se llama área de transferencia de calor. En muchos intercambiadores de calor, el producto a enfriar es un líquido y si el producto del proceso es un vapor, al intercambiador se le conoce como condensador. Para ambos casos, el agua es el fluido de enfriamiento más común en la industria química. Sin embargo, la capacidad del intercambiador de transferir calor disminuye cuando el área de transferencia (por lo regular tubos) se recubren de materiales aislantes, tales como incrustaciones inorgánicas o colonias de microorganismos. Si no se transfiere la cantidad de calor necesaria el rendimiento del proceso disminuye.

Para facilitar la evaluación del rendimiento de un intercambiador de calor, la mayoría de las variables que afectan al sistema (espesor de tubos, incrustaciones, lodos, basuras, coeficientes convectivos, microorganismos, flujo) se agrupan en una sola constante del sistema, conocida como "coeficiente global de transferencia de calor", U. Así, el flujo de calor que se transmite en un intercambiador es:

$$Q = U_D \cdot A \cdot \Delta T_{MLDT} \qquad (1)$$

U_D = Coeficiente global de transferencia de calor de diseño

A = Área de transferencia de calor

Q = Flujo de calor

ΔT_{MLDT} = Diferencia media logarítmica de temperaturas.

Como el tratamiento del agua de enfriamiento, afecta en gran medida al U en los intercambiadores en los que el agua es el refrigerante, es muy importante evaluar constantemente el coeficiente U para predecir el momento adecuado en que el intercambiador de calor ha dejado de cumplir con las condiciones de proceso requeridas y es necesario sacarlo de operación para su limpieza y mantenimiento.

C. *Calor sensible y calor latente*

En una TE se utiliza la evaporación para extraer calor del agua de enfriamiento que ha absorbido de los fluidos del proceso. La descripción general de éste proceso se basa en el hecho que las moléculas del agua se mueven a mayor velocidad cuando se calientan y tratan constantemente de separarse de la masa de agua. Cuando una molécula absorbe suficiente calor y se separa, se dice que se ha evaporado.

El relleno de la torre divide el agua en pequeñas gotitas, creando más vías de escape para que las moléculas puedan separarse; adicionalmente, el flujo rápido de aire a través de la torre, se lleva moléculas de agua que se han separado, permitiendo que otras moléculas hagan lo mismo. El agua que se evapora disipa alrededor de 570 kcal por cada kg de agua convertida en vapor. Como el calor específico del agua es en promedio 1 kcal kg^{-1} $°C^{-1}$, la vaporización de 1 kg de agua enfría 57 kg de agua líquida 10 °C.

$$m_{vap} \cdot \lambda = m_{agua} \cdot Cp \cdot \Delta T \qquad (2)$$

Cuando una molécula de agua pasa de una fase líquida a una fase vapor absorbe una gran cantidad de calor de moléculas adyacentes de agua en la fase líquida, ocasionando un efecto de enfriamiento. A ese calor que se relaciona con el cambio de fase de una fase líquida a una gaseosa, o viceversa, se conoce como *calor latente* de vaporización, o de condensación, respectivamente.

El calor latente del agua es tan grande, que una cantidad pequeña de evaporación, produce grandes efectos de enfriamiento [4]. Este es el principio de transferencia de calor de una torre de enfriamiento. No obstante, en una torre de enfriamiento, cerca del 20% del calor transferido del agua al aire se da por *calor sensible* debido a la diferencia de temperatura entre el agua caliente y el aire fresco; mientras que el otro 80% se da por transferencia de calor latente.

D. *Sistemas de agua de enfriamiento*

Los sistemas de agua de enfriamiento se componen de dos partes fundamentales: el sistema de enfriamiento y el sistema del proceso. El sistema de enfriamiento consiste normalmente

por una torre de enfriamiento y sus componentes asociados (ventiladores, bombas). Por su parte, el sistema del proceso consiste en intercambiadores de calor, condensadores, camisas de reactor, entre otros.

Existen tres tipos de sistemas de agua de enfriamiento: de un paso, de recirculación cerrada y de recirculación abierta (evaporativos). Este proyecto se realizó en un sistema recirculación abierta. En estos sistemas se incorpora una torre de enfriamiento o un estanque de evaporación para disipar el calor retirado de proceso o del producto a través de la transferencia de calor y de masa. Estos sistemas toman agua fresca del estanque o del pozo de una torre de enfriamiento, esta agua pasa a través del equipo de proceso que requiera enfriamiento y luego retorna a la unidad de evaporación [1]. En la Fig. 1 se presenta un esquema general de un sistema de enfriamiento de agua a través de una torre.

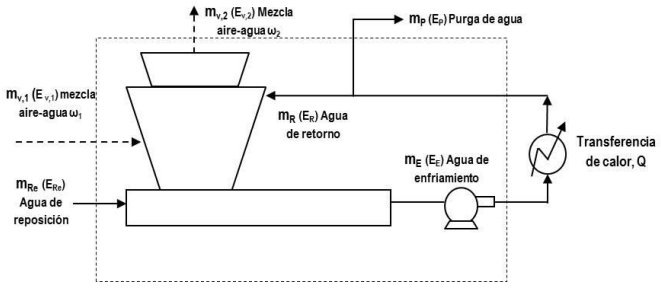

Fig. 1. Sistema de enfriamiento de recirculación abierta.

A las torres que transfieren calor a la atmósfera en forma de vapor de agua, se les conoce como torres húmedas. Allí el agua de enfriamiento hace contacto directo con el aire que circula a través de la torre. Para compensar las pérdidas de agua por evaporación, estos sistemas cuentan con agua de reposición. El agua que viene del intercambio de calor pasa por un sistema de distribución sobre la torre de enfriamiento, el agua al caer divide en gotitas diminutas debido a la construcción de las placas de salpicadura con tablillas que constituyen el relleno de la torre [2].

El relleno en la torre, y la correcta distribución de agua en la torre permiten que el agua llegue lo suficientemente fría al fondo de la torre, y finalmente se canaliza a un pozo y la bomba la envía al proceso de transferencia de calor.

E. Psicrometría y humidificación

Para abordar balances de materia y energía a un sistema de enfriamiento con aire, es necesario definir ciertos conceptos de psicometría y humidificación, así como modelos matemáticos. A fin de indicar el grado de saturación de una mezcla vapor/gas, se utiliza el término de *humedad o saturación relativa* (Θ), definido como la razón entre la presión parcial del vapor y la presión de saturación del vapor correspondiente a la temperatura de bulbo seco.

$$\Theta = \frac{P_{vap}}{P^*_{vap}} \tag{3}$$

Asumiendo que la mezcla se comporta como un gas ideal, y para la mezcla vapor de agua-aire se tiene que:

$$\Theta = \frac{m_{vap} \cdot R \cdot T_{vap}}{M_{agua} \cdot V_{vap}} \cdot \frac{M_{agua} \cdot V^*_{vap}}{m^*_{vap} \cdot R \cdot T^*_{vap}} = \frac{m_{vap}}{m^*_{vap}} \tag{4}$$

Por lo tanto, la humedad relativa porcentual de una mezcla de aire-vapor de agua, representa la cantidad de humedad que al aire contiene (m_{vap}) respecto a la cantidad máxima de humedad que el aire puede contener en equilibrio (m^*_{vap}) a la misma temperatura.

La *humedad específica* es la razón entre la masa de vapor y la masa de gas seco contenido en el mismo volumen, para la mezcla vapor de agua-aire:

$$\omega = \frac{m_{vap}}{m_{as}} \tag{5}$$

Asumiendo que tanto el vapor de agua como el aire se comportan como gases ideales a condiciones de presión y temperatura cercanas a las condiciones normales:

$$m_{vap} = \frac{M_{vap} P_{vap} V}{R \cdot T} \tag{6}$$

$$m_{as} = \frac{M_{as} P_{as} V}{R \cdot T} \tag{7}$$

Sustituyendo:

$$\omega = \frac{M_{vap} P_{vap}}{M_{as} P_{as}} = \frac{18.02 \cdot P_{vap}}{28.96 \cdot P_{as}} = 0.622 \frac{P_{vap}}{P_{as}} \tag{8}$$

De la ley de Dalton, la suma de las presiones parciales será la presión total P de la mezcla; la presión atmosférica en condiciones de operación de una torre de enfriamiento.

$$P = P_{vap} + P_{as} \tag{9}$$

Por lo tanto,

$$\omega = 0.622 \cdot \frac{P_{vap}}{P - P_{vap}} \tag{10}$$

En términos de la humedad relativa (del grado de saturación de la mezcla).

$$P_{vap} = \Theta \cdot P^*_{vap} \tag{11}$$

$$\omega = 0.622 \cdot \frac{\Theta \cdot P^{*}_{vap}}{P - \Theta \cdot P^{*}_{vap}} \qquad (12)$$

La humedad específica o humedad absoluta ω es una razón o fracción peso de la masa de agua en términos del gas seco (aire). La importancia de esta relación en las torres de enfriamiento (y en casi todos los procesos de humidificación y secado) se debe a que la masa de gas seco permanece constante a través del proceso de enfriamiento, es decir, los kg o lb_m de aire seco permanecen constantes través de una torre de enfriamiento o cualquier proceso de transferencia de masa que involucre humidificación o deshumidificación (la masa de aire sin agua que entra es igual a la masa de aire sin agua que sale del sistema) y la diferencia entre la humedad específica del aire húmedo que entra y el que sale, es la masa de agua agregada al aire por masa de aire seco debido a los efectos de evaporación.

Mediante un diagrama psicrométrico parcial y usando la Ec. (8) a diferentes temperaturas de bulbo seco y humedades relativas para una presión total de 760 mmHg, se grafica la humedad relativa respecto a la temperatura de bulbo seco para la mezcla vapor de agua-aire.

Otro término importante es el calor húmedo, y se define como la capacidad calorífica de una mezcla aire-vapor de agua asumiendo que esta es la suma de los calores específicos de ambos componentes, suponiendo que estos calores son constantes dentro del intervalo de condiciones que prevalecen los cálculos de humidificación y torre de enfriamiento.

$$\hat{C}_P = C_{P,aire} + C_{P,vap} \cdot \qquad (13)$$

F. Balance de masa para el aire

El aire que entra a la torre con una humedad ω_1, es distinto en condiciones y en masa del aire que sale de la torre impulsado por el ventilador con una humedad ω_2; sin embargo, el aire en términos de gas seco que entra a la torre, es exactamente igual al aire seco que sale impulsado por el ventilador por el domo de la torre.

$$\begin{pmatrix}\text{flujo másico de aire}\\ \text{seco de entrada}\end{pmatrix} = \begin{pmatrix}\text{flujo másico de aire}\\ \text{seco de salida}\end{pmatrix}$$

$$m_{as,1} = m_{as,2} = m_{as} \qquad (14)$$

G. Balance de masa para el agua

El vapor de agua que sale de la torre lleva consigo gotas de agua líquida hacia el exterior de la torre, debido al tiro de los ventiladores y la velocidad del vapor; es decir, agua en estado líquido se pierde por arrastre mecánico, m_A. Ésta pérdida por arrastre no puede ser determinada teóricamente.

$$\begin{pmatrix}\text{flujo másico}\\ \text{de agua de retorno}\end{pmatrix} + \begin{pmatrix}\text{flujo másico}\\ \text{de agua contenida}\\ \text{en el aire de entrada}\end{pmatrix} + \begin{pmatrix}\text{flujo másico}\\ \text{de agua de}\\ \text{reposición}\end{pmatrix} =$$

$$\begin{pmatrix}\text{flujo másico}\\ \text{de agua contenida}\\ \text{en el aire de salida}\end{pmatrix} + \begin{pmatrix}\text{flujo másico}\\ \text{de agua de}\\ \text{enfriamiento}\end{pmatrix} + \begin{pmatrix}\text{flujo másico}\\ \text{de purga}\\ \text{de agua}\end{pmatrix}$$

$$m_R + m_{v,1} + m_{Re} = m_{v,2} + m_E + m_P \qquad (15)$$

El flujo de agua que se pierde por evaporación es una función directa de la ganancia de humedad que tiene el aire entre la entrada y salida de la TE. Mientras mayor sea la diferencia de humedades entre el aire húmedo que enfría y el aire húmedo que sale de la torre, mayor será el agua perdida por evaporación, aunque mayor será la transferencia de calor.

H. Balances generales de transferencia de calor

Puesto que una torre de enfriamiento, la remoción de calor implica un fenómeno de humidificación y que a su vez involucra difusión de masa y transferencia de calor, el aire se humidifica, pero producto principal no es el aire húmedo si no el agua fría. En la TE, el agua caliente es enfriada por aire frío. Cuando el agua pasa a través de la torre, la temperatura de aquella puede descender debajo de la temperatura de bulbo seco del aire de entrada, pero no más bajo que la temperatura de bulbo húmedo de este aire, es entonces la temperatura de bulbo húmedo, la temperatura límite al que el agua de salida puede llegar [3]. Dado que la transferencia de calor total en la TE es el paso de calor por evaporación y convección del agua aire, el calor total transferido será:

$$Q_T = Q_{convectivo} + Q_{latente} = 0 \qquad (16)$$

El calor Q, en función del agua de enfriamiento, que debe remover la torre es el calor necesario para enfriar el agua de enfriamiento y el calor necesario para que el flujo de reposición salga a la misma temperatura de enfriamiento:

$$Q = m_R C_P (T_R - T_E) + m_{Re} C_P (T_E - T_{Re}) \qquad (17)$$

Sustituyendo el calor Q, en el balance de la torre:

$$m_R C_P (T_R - T_E) + m_{Re} C_P (T_E) = m_{as} (H_{V,2} - H_{V,1}) \qquad (18)$$

III. METODOLOGÍA

A. Estudio termodinámico

Para el estudio termodinámico se consideró un volumen de control en la TE y determinaron las condiciones del aire atmosférico a la entrada y salida, así como el caudal másico y la temperatura del proceso. Utilizando la ecuación de Antoine se determinó la humedad absoluta y con ella la entalpía y entropía del aire húmedo.

Planteando un balance de masa, se determinó el caudal de aire y del agua de reposición para el proceso. Utilizando el balance de entropía, considerando a la torre como adiabática, es posible calcular la entropía generada por intermedio de las entropías de flujo.

B. *Cálculo de la exergía*

Existe entonces una propiedad termodinámica y extensiva de un sistema, conocida como entropía. La entropía de un sistema cerrado y adiabático nunca puede decrecer, debido a que la entropía sólo se transfiere por calor y masa.

La Segunda Ley establece que el cambio de la entropía total asociado con cualquier proceso debe ser positivo, con un valor límite de 0 para un proceso reversible Ec. (19). Este requisito se considera al escribir el balance de entropía, tanto para el sistema como para los alrededores considerados en conjunto, así como al incluir un término de *generación de entropía* de importancia para las irreversibilidades del proceso.

$$\Delta S \geq 0 \qquad (19)$$

Este término de generación de entropía, es la suma de otros tres; uno para las diferencias de entropía que entran y salen, uno para los cambios de entropía dentro del volumen de control y uno más para los cambios de entropía en los alrededores.

Muchos de los problemas encontrados en termodinámica que requieren la aplicación del segundo principio, pueden resolverse usando sólo la entropía o con el concepto de exergía. Los procesos donde interviene el aire húmedo presentan un inconveniente adicional pues, no solo existe un desequilibrio térmico y mecánico sino también un desequilibrio difusional de un componente (el agua). Para el cálculo de la exergía es necesario definir un estado muerto cuyos parámetros serán: P_{v0} = presión de vapor de saturación a 20°C (0,0234 bar), T_o=20°C, y 100% de humedad. Calculados los valores de referencia, para el aire húmedo, w_o (humedad absoluta kg agua/kg aire seco), h_o (entalpía del vapor saturado para la temperatura de referencia).y S_o (entropía específica en kJ/kg K del vapor saturado a las condiciones de referencia, se determina las exergías puntuales y la eficiencia (η).

Para aplicar las ecuaciones de los balances de masa, energía, entropía, exergía y eficiencia de la TE, se desarrolló una hoja de cálculo en Excel, en donde se aplicaron las condiciones de diseño y de operación de la TE [1,2].

IV. Caso de estudio

Se estudió un sistema de enfriamiento situado en la ciudad de Salina Cruz, Oaxaca, cerca de las costas mexicanas del litoral del Pacífico; dicho sistema de enfriamiento de agua es de recirculación abierta y da servicio a diversas plantas de un complejo petroquímico.

La TE es de doble flujo transversal, puesto que tiene entradas de aire atmosférico a sus lados; de tiro inducido, el aire es orientado a fluir a través de la torre desde las laterales al domo por ventiladores; los deflectores son fijos y elaborados en concreto; y con sistema de distribución de agua por gravedad con charolas perforadas en su plataforma.

A. *Condiciones de diseño*

Las condiciones de diseño, Tablas 1 a 3, son el punto de referencia para comparar la operación de la torre. Estas condiciones suelen ser mayores en dimensiones y eficiencia que lo requerido por la operación con el objetivo de absorber posibles incrementos en la capacidad de la planta y la torre.

Tabla 1. Condiciones de diseño para la torre de enfriamiento.

Capacidad, m^3/h	13.63
Temperatura del agua de retorno, °C	46
Temperatura agua de suministro, °C	32
Temperatura de bulbo húmedo, °C	26
Temperatura de bulbo seco, °C	29
Pérdidas por arrastre (máx.), m^3/día	65
Pérdidas por evaporación, m^3/día	5.2
Purga, m^3/día	1.235
Agua de repuesto, m^3/día	6.5
Celdas	6
Ciclos de concentración (CC)	5
Carga térmica, MMBTU/h	757
Capacidad el pozo, m^3	3.9

Tabla 2. Equipo mecánico rotativo auxiliar de la TE.

Bombas	
Bombas	3
Flujo, GPM	20,000
Tipo	Centrífuga
Orientación	Vertical
Amperaje nominal, A	183
Voltaje nominal, kV	4.16
RPM	1175
Potencia nominal, HP	1610
Ventiladores	
Ventiladores	6
Orientación	Horizontal
Potencia nominal, HP	140
Amperaje nominal, A	154
Voltaje nominal, kV	0.48

Tabla 3. Condiciones climatológicas (Salina Cruz, Oaxaca).

Condiciones climatológicas	
Temperatura máxima extrema, °C	40
Temperatura mínima extrema, °C	14.5
Temperatura máxima promedio, °C	38
Temperatura mínima promedio, °C	17
Precipitación pluvial, mm.	82.2
Dirección de los vientos dominantes	NW a SE

Velocidad máxima del viento, km/H	100
Velocidad máxima del viento regional de diseño, km/h	185
Presión barométrica, mmHg	760
NSNM, m.	3-11

B. *Condiciones de operación*

La operación de la TE se considera estacionaria a pesar de las variaciones de temperatura y humedad a lo largo de día, debido a que los flujos de masa de aire y agua que proporcionan los ventiladores y bombas son estables. Las condiciones de operación de la Tabla 4 pertenecen a un estado específico en la operación de la torre.

En la operación de la torre el nivel del pozo se mantiene constante debido al flujo de agua de reposición. Para medir el caudal de flujo de agua de reposición, una forma simple y económica, es colocar un medidor de flujo de turbina que registre el caudal volumétrico de agua.

Las tasas de agua de reposición, se encuentran restando la lectura que marque el medidor a una hora determinada menos la lectura del día anterior medida a la misma hora.

TABLA 4. CONDICIONES DE OPERACIÓN DE LA TE.

CONDICIONES DE OPERACIÓN	
Capacidad, GPM	57.8
Temperatura del agua de retorno, °C	38
Temperatura del agua de suministro, °C	29
Temperatura de bulbo húmedo, °C	27
Temperatura de bulbo seco, °C	31

C. *Condiciones climatologicas*

En una TE en donde se transfiere el calor del agua al aire por efectos convectivos y evaporativos hacia el ambiente, las condiciones atmosféricas predominantes de ese aire son de impacto considerable. En la ciudad de Salina Cruz, Oaxaca, la temperatura media anual varía entre 26 y 27 ºC (registros estadísticos de la temperatura promedio del día entre 1999-2013). Se observa que el registro de temperatura alta se presenta durante el mes de mayo, con una máxima promedio de 32 ºC. La temperatura promedio baja en invierno es de 22 ºC. La información anterior es importante para determinar cuan eficiente es la torre durante las diferentes épocas del año; el análisis energético y exergético que se desarrolla considera el perfil anual de temperatura para medir la eficiencia del sistema de enfriamiento. Se observa que la humedad relativa predominante en la ciudad fluctúa entre el 60 y 70% para todas las temporadas del año, siendo de otoño a inicios de verano la época más "seca" del año y el verano e invierno las temporadas más húmedas.

V. ANÁLISIS EXERGÉTICO A LA TORRE DE ENFRIAMIENTO EN CONDICIONES DE OPERACIÓN Y DISEÑO

A. *Balance de materia*

Se desarrollaron los balances de materia en la TE a partir de la Fig. 1. La torre, en su operación normal, enfría 3643.7 kg/s ($m_E = m_R$). Esta corriente de agua debe ser enfriada al menos 9 ºC en cualquier temporada del año. A las condiciones de entrada de aire (temperatura de bulbo seco, 31 ºC y bulbo húmedo, 27 ºC, constantes), se determina la masa de vapor disuelto en aire seco a través de tablas de vapor y carta psicrométrica. Mediante la Ec. 12, se determinó la humedad específica (ω_1) del aire a la entrada de la torre y a la salida (ω_2). La humedad relativa, Θ_1, se calculó del 73,4 % para el aire de entrada a la TE. Esta humedad coincide con las humedades promedio anuales registradas.

El aire que sale de la torre se supone saturado en un 95%. La diferencia entre las humedades ω_2 y ω_1 representan los kg de agua de enfriamiento que se evaporan por kg de aire seco que circula por la torre.

El agua pérdida por evaporación es la ganancia de humedad entre el aire que entra y el aire que sale de la torre.

$$\text{agua evaporada} = m_{as}(\omega_2 - \omega_1) \tag{19}$$

Y el agua pérdida por arrastre mecánico puede estimarse por:

$$m_A = m_{Re} - (m_{evap} + m_P) \tag{20}$$

El flujo de agua reposición (m_{Re}) se determinó a través de la Ec. (16) y los 5 CC, sin tomar en cuenta las pérdidas por arrastre mecánico.

$$m_{Re} = m_{evap}\left(\frac{CC}{CC-1}\right) = m_P + m_{evap} \tag{21}$$

Los balances de materia desarrollados sólo aportan un 2,2% de error contra la tasa de reposición real en planta. En la Tabla 5 se presentan los resultados del balance de materia de la TE en su operación normal y en sus condiciones de diseño.

TABLA 5. BALANCE DE MATERIA DE LA TORRE.

CORRIENTES DE LA TE, kg/s		
m_{Re}	69.32	102.84
m_R	3643.69	3785
m_P	13.86	20.57
m_E	3643.69	3785
$m_{vap,1}$	2444.64	1751.97
$m_{vap,2}$	2493.97	1831.36
m_{as}	2394.41	1713.53

CONCEPTO	OPERACIÓN	DISEÑO
Capacidad, GPM	57.76	60.00
Arrastre, m_A, m^3/día	531.4	654
Agua evaporada, m^3/día	4.263	6.859
Tiempo medio de recirculación, min	18	17
Reposición, m_{Re}, m^3/día	5.989	8.885
Aire requerido, MMACFM	4.771	3.641
Humedad absoluta entrada, ω_1	0.0210	0.0201
Humedad absoluta salida, ω_2	0.0416	0,0663
Humedad relativa, Θ_1, %	73.4	78.9
Ciclos de concentración, CC	5	5

B. Balance de energía

El calor removido por la TE en operación normal es:

$$Q_{Total} = m_R C_P (T_R - T_E) \qquad (22)$$

Industrialmente, al calor total que remueve la torre se le conoce como *capacidad de la torre***.** Y La entalpía de la corriente de aire atmosférico húmedo que entra a la torre es determinada por la Ec. (23), Tabla 6.

$$H_v = H_{as} + \omega \cdot H_{vap} \qquad (23)$$

TABLA 6. PROPIEDADES DE LAS CORRIENTES DE MATERIA.

Corriente	T, °C	M, kg/s	H, kcal/kg
m_{Re}	25	69.32	25
m_R	38	3643.70	38
m_P	38	13.86	38
m_E	29	3643.70	29
$m_{vap,1}$	27	2444.23	20.26
$m_{vap,2}$	38	2493.54	36.66

La razón entre el calor removido por efectos del calor sensible y los del calor latente es:

$$\frac{Q_{Sensible}}{Q_{Latente}} = \frac{1}{\lambda} \cdot \frac{(H_{V,2} - H_{V,1})}{(\omega_2 - \omega_1)} - 1 \qquad (24)$$

$$\frac{Q_{Sensible}}{Q_{Latente}} = 17.05\%$$

Esta relación nos indica que por cada 100 BTU/h que se remueven del agua caliente del retorno a la torre, 17.05 se remueven por efectos del calor sensible del aire al agua, y la otra gran mayoría, 82.95 BTU/h por efectos del enfriamiento evaporativo del agua.

Del balance de energía se calcula el flujo de aire seco necesario para el enfriamiento deseado. La masa de aire seco establece la pendiente de la línea de operación de la torre.

$$m_{as} = \frac{m_P \cdot (h_P - h_{Re}) + m_E (h_E - h_R)}{H_{V,1} - H_{V,2} + h_{Re}(\omega_2 - \omega_1)} \qquad (25)$$

Así, la relación (m_R/m_{as} =1.52) o relación L/G, nos indica que la torre necesita un kilogramo de aire seco por cada 1,52 kg de agua caliente para lograr un enfriamiento de 9 ºC.

El volumen húmedo, Ec. (26), del aire saturado y tibio que abandona la torre por la descarga de los ventiladores es:

$$\hat{V} = \frac{V}{m_{as}} = \frac{RT}{P}\left(\frac{1}{M_g} + \frac{1}{M_{vap}} \cdot \frac{m_{vap}}{m_{as}}\right) = \frac{RT}{P}\left(\frac{1}{M_g} + \frac{\omega}{M_{vap}}\right) \qquad (26)$$

A pesar de que es un valor de operación conocido, a través del balance de energía se puede estimar el flujo de agua de reposición necesario, Ec. (27), para compensar las pérdidas por evaporación del agua.

$$m_{Re} = \frac{Q}{\frac{(H_{V,2} - H_{V,1})}{(\omega_2 - \omega_1)} - C_P(T_{Re})} \qquad (27)$$

En la Tabla 7 se presentan los resultados del balance energético de la torre en su operación normal y en sus condiciones de diseño.

TABLA 7. BALANCE DE ENERGÍA DE LA TE.

CONCEPTO	OPERACIÓN	DISEÑO
Capacidad térmica (MMBTU/H)	468	757
Entalpía del aire húmedo a la entrada, $H_{vap,1}$, kcal/kg as	20.26	19.20
Entalpía del aire húmedo a la salida $H_{vap,2}$, kcal/kg as	34.66	51.99
$Q_{sensible}/Q_{latente}$ %	17.05	18.80
m_{Re} a través de balance de energía, m^3/día	4207	6689
Aire seco requerido, m_{as}, kg/seg	2394	1718
Relación m_R/m_{as}	1.52	2.20

C. Garantía de la torre de enfriamiento

La TE debe tener la capacidad de remover el calor que demandan los procesos a los que da servicio. El aseguramiento de que la torre es capaz de cumplir con las demandas de remoción de calor es la garantía de la torre. Ya que la torre usa la atmósfera como medio de enfriamiento, está también sujeta a las variaciones de ésta.

La gráfica entalpía – temperatura, en las condiciones de operación se muestra en la Fig. 2. La línea de operación tiene une pendiente de 1.52 como se demostró en el balance energético. El área entre la línea de saturación, H* y la de operación representa el potencial para la transferencia de calor.

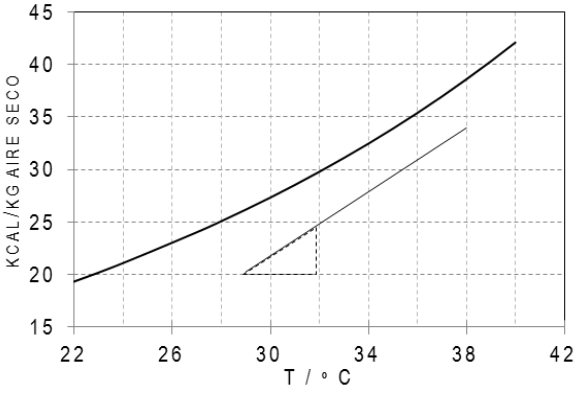

FIG. 2. Diagrama H vs T para la línea de saturación (curva) y la línea de operación (recta) para la TE.

A través de la integración de la Ec. (15) se pueden determinar el número de unidades de difusión, NUD, para la torre en sus condiciones de operación.

$$\int \frac{dH}{dT} = \frac{m_R}{m_{as}} \qquad (28)$$

Utilizando el método numérico de cuadratura de cinco puntos**,** se determina que para las condiciones de operación y durante el período de condiciones atmosféricas estables, la torre rinde 1,843 unidades de difusión.

D. Balance de entropía

El balance de entropía de la torre demuestran que la irreversibilidad del proceso de enfriamiento se dan a través de las corrientes de materia que entran y salen de la torre y la masa de agua evaporada desde el seno de la torre hacia la atmósfera.

En la Tabla 8, se presentan las entropías de las corrientes de proceso. La entropía generada ($\sigma_{Generada}$), Ec. (29), durante el proceso de enfriamiento es:

$$\underbrace{m_{as}\left(s_{as,2}+\omega_2\cdot s_{agua,2}-s_{as,1}-\omega_1\cdot s_{agua,1}\right)}_{\text{Entropía generada por efectos de la evaporación}}+$$

$$\underbrace{m_P\cdot s_P+m_E\cdot(s_E-s_R)-m_{Re}\cdot s_{Re}}_{\text{Entropía generada por las corrientes de materia de entrada y salida de la torre}}=\sigma_{GENERADA}$$

TABLA 8. ENTROPÍA DE LAS CORRIENTES DE LA TE.

CORRIENTE	FASE	ENTROPÍA
m_E	Líquida	$s_E = C_{P,E}\ln\frac{T_E}{T_{Ref}}$
m_R	Líquida	$s_R = C_{P,R}\ln\frac{T_R}{T_{Ref}}$
m_{Re}	Líquida	$s_{Re} = C_{P,Re}\ln\frac{T_{Re}}{T_{Ref}}$
m_P	Líquida	$s_P = C_{P,P}\ln\frac{T_P}{T_{Ref}}$
$m_{vap,1}$	Vapor	$S_{vap,1} = s_{as,1} + \omega_1 s_{vap.agua.1}$
$m_{vap,2}$	Vapor	$S_{vap,2} = s_{as,2} + \omega_2 s_{vap.agua.2}$
$m_{as,i}$	Vapor	$s_{as,i} = s^*_{as,i}\Big\vert_{T_i} - \frac{R}{M_{as}}\ln\frac{P_{as,i}}{P_{Ref}}$
N/A	Vapor	$s_{vap.agua,\,i} = s^*_{vap.agua,\,i}\Big\vert_{T_i} - \frac{R}{M_{vap}}\ln\Theta$

Las entropías específicas del vapor de agua saturado y del aire seco, $s^*_{as,i}$ y $s^*_{vap.agua,i}$ se grafican e interpolan para la temperatura de bulbo seco y de salida de vapores de la torre. Los resultados de la entropía específica de las corrientes complementan la Tabla 9 del balance energético.

TABLA 9 ENTROPÍA ESPECÍFICA EN LAS CORRIENTES DE LA TORRE**.**

CORRIENTE	T, °C	m, kg/s	H, kcal/kg
m_{Re}	25	69.32	25.00
m_R	38	3643.70	38.00
m_P	38	13.86	38.00
m_E	29	3643.70	29.00
$m_{vap,1}$	27	2444.23	20.26
$m_{vap,2}$	38	2493.54	36.66
CORRIENTE	**s, kcal/kg °C**	**S, kcal/ s °C**	
m_{Re}	0.0875	6.070	
m_R	0.1302	474.606	
m_P	0.1302	1.805	
m_E	0.1009	367.658	
$m_{vap,1}$	0.6550	1601.256	
$m_{vap,2}$	0.7098	1770.437	

La $\sigma_{Generada}$ en la TE está relacionada con las siguientes formas de generación de entropía:

$$\underbrace{m_{as}\left(S_{vap,2}-S_{vap,1}\right)}_{\text{Entropía generada por efectos de la evaporación, transferencia de calor latente}} + \underbrace{m_E\cdot\left(s_E-s_R\right)}_{\text{Entropía generada por la transferencia de calor sensible}} + \underbrace{m_P\cdot s_P-m_{Re}\cdot s_{Re}}_{\text{Entropía generada por las corrientes de materia de entrada y salida de la torre}} = \sigma_{GENERADA}$$

Durante el proceso de enfriamiento de agua a través de la TE se genera entropía, puesto que es un proceso real e irreversible, resaltando que la mayor irreversibilidad en el proceso de enfriamiento de agua se da en la evaporación que se lleva a cabo desde la fase líquida a la fase vapor. Del balance de energía se obtuvo que cerca del 83% del calor total que se remueve en la torre es por efectos evaporativos. Sin embargo, a la evaporación se le atribuye el 100% de la generación de entropía, es decir, de irreversibilidad durante el proceso de enfriamiento. En la Tabla 10 se presentan los resultados del balance entrópico de la torre en su operación normal y en sus condiciones de diseño.

TABLA 10. BALANCE DE ENTROPÍA DE LA TORRE.

CONCEPTO	OPERACIÓN	DISEÑO
Entropía generada, kW/K	84.35	171.96
Entropía generada por efectos de evaporación, kW/K	549.22	899.41

E. Eficiencia de enfriamiento

Para las condiciones de operación, después del intercambio de calor con el proceso el agua retorna a la torre a una temperatura de 38 °C; a través de la transferencia de calor latente y sensible, llega al pozo a una temperatura promedio de 29 °C, por lo que el *rango* de enfriamiento es de 9 °C.

La aproximación al bulbo húmedo es de 11°C (para un bulbo húmedo de 27°C), así la eficiencia de enfriamiento es:

$$\eta_E=\frac{\langle t_R\rangle-\langle t_E\rangle}{\langle t_R\rangle-t_{bh}} \qquad (30)$$

La eficiencia de enfriamiento nos indica que, en sus condiciones de operación la torre es capaz de remover 81.8 BTU/h de los 100 BTU/h que enfriaría si la temperatura de salida del agua de enfriamiento alcanzara el bulbo húmedo.

VI. ANÁLISIS EXERGÉTICO

A. Balance de exergía

El análisis exergético (ε) se desarrolló tomando las condiciones de operación.

$$m_R\cdot\varepsilon_R+m_{Re}\cdot\varepsilon_{Re}-m_E\cdot\varepsilon_E-m_P\cdot\varepsilon_P-m_{as}\cdot[\varepsilon_{as,2}+\omega_2\cdot(\varepsilon_{vap.agua,2}+\varepsilon_{quimica,2})]=I$$

Las exergías de las corrientes de materia que entran y salen de la TE representan el balance exergético, en la Tabla 11 se presenta los resultados de la exergía calculada. Cuando se denota el sub índice "vap. agua *i*" se refiere a la exergía del agua pura en fase vapor que corresponde a la mezcla aire-vapor de agua de las corrientes de entrada y salida de la TE.

Tabla 11. Exergías de las corrientes de materia de la torre de enfriamiento.

CORRIENTE	FASE	TIPO	EXERGÍA
m_E	Líquida	$\varepsilon_{Física}$	$\varepsilon_E=(h_E-h_0)-T_0(s_E-s_0)$
m_R	Líquida	$\varepsilon_{Física}$	$\varepsilon_R=(h_R-h_0)-T_0(s_R-s_0)$
m_{Re}	Líquida	$\varepsilon_{Física}$	$\varepsilon_{Re}=(h_{Re}-h_0)-T_0(s_{Re}-s_0)$
m_P	Líquida	$\varepsilon_{Física}$	$\varepsilon_P=(h_P-h_0)-T_0(s_P-s_0)$
$m_{vap,1}$	Vapor	$\varepsilon_{Física}$, $\varepsilon_{Química}$	$\varepsilon_{vap,1}=\varepsilon_{as,1}+\omega_1\cdot\left(\varepsilon_{vap,agua,1}+\sum_{vap,1}RT_0y_i\ln\frac{y_i}{y_{i,0}}\right)=0$
$m_{vap,2}$	Vapor	$\varepsilon_{Física}$, $\varepsilon_{Química}$	$\varepsilon_{vap,2}=\varepsilon_{as,2}+\omega_2\cdot\left(\varepsilon_{vap,agua,2}\right)+\sum_{vap,2}RT_0y_i\ln\frac{y_i}{y_{i,0}}$
$m_{as,i}$	Vapor	$\varepsilon_{Física}$	$\varepsilon_{as,i}=C_{P,as}(T_i-T_0)-T_0\left(C_{P,as}\ln\left(\frac{T_i}{T_0}\right)-R\ln\left(\frac{P_i}{P_0}\right)\right)$
N/A	Vapor	$\varepsilon_{Física}$	$\varepsilon_{vap,agua.i}=C_{P,vap.agua}(T_i-T_0)-T_0\left(C_{P,vap.agua}\ln\left(\frac{T_i}{T_0}\right)-R\ln\left(\frac{P_i}{P_0}\right)\right)$

El estado muerto representa el equilibrio termodinámico del sistema con el ambiente por lo que las propiedades del ambiente representan al mismo tiempo las del estado muerto. En la Tabla 11 se presentan las propiedades y composición del estado muerto.

TABLA 11. **PROPIEDADES Y COMPOSICIÓN DEL ESTADO MUERTO**

Temperatura, °C	T_0	27
Presión, mmHg	P_0	760
Humedad relativa, %	Θ	76
Composición, % mol	O_2	20.40
	N_2	76.05
	H_2O	2.675
	Ar	0.945

Es importante aclarar que sí y sólo sí una corriente proveniente de la atmósfera interactúa con el sistema, tendrá la misma entalpía y entropía en el estado muerto que la inherente a la corriente, y por lo tanto la exergía de esta corriente será 0.

El aire húmedo que abandona la torre, $m_{vap,2}$, que se encuentra muy cercano a la saturación tiene exergía física porque su temperatura y presión son diferentes de las del estado muerto, y una exergía química asociada porque su composición también lo es.

En Tabla 12 se presentan las exergías específicas de las corrientes calculadas a partir de los datos presentados en las Tablas 10 y 11.

TABLA 12. EXERGÍAS ESPECÍFICAS

CORRIENTE	**T, °C**	**M, kg/s**	**H, kcal/kg**
m_{Re}	25	69.32	25
m_R	38	3643.70	38
m_P	38	13.86	38
m_E	29	3643.70	29
$m_{vap,1}$	27	2444.23	20.261
$m_{vap,2}$	38	2493.54	36.661
CORRIENTE	**s, kcal/kg °C**	**ε, kcal/kg**	**E, kcal/s**
m_{Re}	0.0875	20.06	1390.46
m_R	0.1302	31.91	116260.05
m_P	0.1302	31.91	442.34
m_E	0.1009	23.70	86354.35
$m_{vap,1}$	0.6550	-	-
$m_{vap,2}$	0.7098	0.91	2258.12

De los datos obtenidos en la Tabla 12, se puede inferir que el máximo trabajo por unidad de masa que se pudiera obtener de las corrientes de agua en fase líquida m_{Re}, m_R, m_P, y m_E son todas del mismo orden de magnitud debido a que las temperaturas de estas son relativamente cercanas a la del estado muerto, lo que indica que de forma aproximada cada corriente líquida tiene el mismo potencial de trabajo si se llevara de su estado inicial al estado muerto involucrando únicamente interacciones de calor con el ambiente.

Por otra parte, la exergía por unidad de masa que aporta la corriente de mezcla vapor de agua – aire que abandona la torre no tiene una influencia destacable puesto que su composición, temperatura y presión no difieren demasiado de las del estado muerto, por lo tanto el máximo trabajo que pudiera entregar esta corriente es poco. Esta, lejos de ser una situación negativa para el sistema de enfriamiento, reduce la exergía perdida durante el proceso.

La irreversibilidad generada en la torre de enfriamiento está relacionada con las siguientes formas del balance exergético. El proceso de enfriamiento de agua por la transferencia de calor es la mayor aportación de irreversibilidad, no así para la corriente de aire y agua que abandona la torre en forma de vapor.

$$\begin{pmatrix}\text{Exergía}\\ \text{total de}\\ \text{entrada}\\ \text{por calor}\end{pmatrix} - \begin{pmatrix}\text{Exergía}\\ \text{total de}\\ \text{entrada}\\ \text{por trabajo}\end{pmatrix} + \begin{pmatrix}\text{Exergía}\\ \text{total de}\\ \text{entrada}\\ \text{por masa}\end{pmatrix} -$$

$$\begin{pmatrix}\text{Exergía}\\ \text{total de}\\ \text{salida}\\ \text{por masa}\end{pmatrix} - \begin{pmatrix}\text{Exergía}\\ \text{destruida}\\ \text{(Irreversibilidad)}\end{pmatrix} = \begin{pmatrix}\text{Cambio en}\\ \text{la exergía total}\\ \text{del sistema}\end{pmatrix}$$

En la Tabla 13 se presentan los resultados del balance exergético del sistema de enfriamiento en su operación normal y en sus condiciones de diseñoo. Se observa que el proceso de enfriamiento evaporativo de agua es más irreversible en las condiciones de diseño. En esta irreversibilidad influye que el bulbo húmedo y bulbo seco son más altas que en la operación.

TABLA 13 BALANCE EXERGÉTICO DE LA TORRE.

FLUJO DE EXERGÍA, KW	**OPERACIÓN**	**DISEÑO**
E_{Re}	5812	6867
E_R	485967	597373
E_P	1849	2273
E_E	360960	402590
$E_{vap,1}$	0	0
$E_{vap,2}$	9439	15835
$\hat{I}$	119531	184526

VII ANÁLISIS ECONÓMICO

Con base al costo operativo de la torre, es posible evaluar el impacto económico de las variables en el rendimiento energético y exergético de la torre.

Los costos unitarios variables (C_V) principales de la torre son: costo eléctrico de bombeo (C_{Bom}), costo eléctrico de ventiladores (C_{Ven}), y costo de tratamiento de agua de puesto (C_{Rep}). Para el análisis se consideran los siguientes costos unitarios, basados en [10]: 1,51 pesos/kWh y 0.13 pesos/m^3 por tratamiento de agua.

$$C_V = C_{HP,Vent} + C_{HP,Bomb} + C_{Re} \qquad (33)$$

Por otro lado, los costos fijos de la torre pueden considerarse de menor magnitud debido a que son costos operacionales y de mantenimiento periódico, por lo que su evaluación está fuera de alcance.

Tomando como base de cálculo un día, el costo variable de operación de la torre es de $68.527,00 por día de operación de la torre. En la Fig. 3 se presenta la distribución del costo.

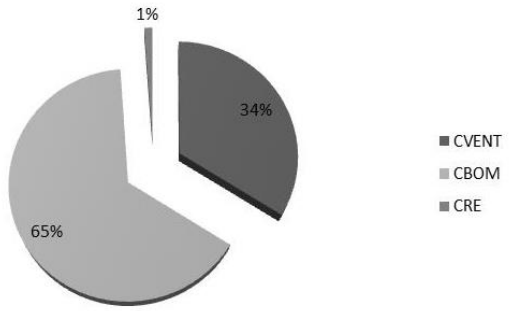

Fig. 3. Distribución de costo variable por día de operación de la torre.

El costo anual de operación normal de la torre es 24.913 MDP. El costo de tratamiento por m^3 de agua de repuesto es pequeño en comparación del costo por la potencia de los motores eléctricos que proporcionan aire y desplazan el agua por todo el sistema de enfriamiento. Esto arroja una idea que las oportunidades de ahorro se encuentran principalmente en los equipos mecánicos rotativos.

Puesto que la potencia nominal de los seis ventiladores que componen la torre es constante a lo largo de la operación cualesquiera sean las condiciones del ambiente (estado muerto), existen ahorros potenciales durante las épocas secas y frías del año, donde la torre tiene como producto un agua más fría que la garantizada y necesitada por el proceso. Desde luego esta situación no impacta negativamente al proceso, pero se tiene un desperdicio energético en los ventiladores.

CONCLUSIONES

A través del análisis de exergía desarrollado se realizó la metodología para la evaluación energética y de exergía de una TE a través de balances de materia, energía y exergía en las condiciones de operación y de diseño. El análisis exergético no sustituye al energético, al contrario lo complementa y enriquece puesto que la Primera Ley sólo distingue entre transformaciones de energía y el análisis exergético permite detectar los procesos intrínsecos del sistema donde se generan las degradaciones y pérdidas de energía.

El flujo másico que requiere la torre en condiciones de operación es 31% mayor al especificado por el diseño.

La variable con mayor impacto energético en la operación es la tasa con que el agua se evapora en la torre, porque impacta en la tasa de agua de reposición, en el calor removido, en la temperatura de salida del agua de enfriamiento, en la cantidad de aire seco requerido y en el arrastre mecánico de la torre. Así, la evaporación en el sistema de enfriamiento en estudio es el mecanismo más importante de transferencia de calor, pues aporta cerca del 80% del calor total removido.

La generación de entropía en la torre es atribuible al proceso de evaporación del agua, y por lo tanto es 200% mayor en las condiciones de diseño que de operación.

Para cuando el bulbo húmedo está por debajo del bulbo húmedo de diseño, es posible entregar al proceso agua enfriada por debajo de la temperatura garantizada, entonces existe un potencial energético de ahorro por las variaciones del estado muerto en su humedad y bulbo seco cuando se tienen estas condiciones.

De todo el calor removido de la torre (468 MMBTU/h, 137 MW) que es desechado a la atmósfera, sólo 11 kW se pierden como exergía por las corrientes de purga.

En el proceso de enfriamiento en la torre se pierde exergía por irreversibilidad a una tasa de 86 kW por cada 100 kW de calor removido.

El potencial nominal de los 6 ventiladores de cada celda de la torre es constante, y de los 25 MDP de costo anualizado al 2013 en las condiciones de operación de la torre, el 65% es por consumo eléctrico de las bombas de recirculación, el 34% por el consumo eléctrico de los abanicos de la torre y el 1% es debido al costo de tratamiento y de reemplazo por agua de repuesto a la torre. Se consideraron las variaciones del ambiente a lo largo del año, y se revela que existe un potencial ahorro económico disponible para el consumo eléctrico por los ventiladores de la torre debido a los cambios naturales del estado muerto, siendo estos del 7.81% del costo total de operación y del 23.05 % del costo eléctrico total por ventiladores.

REFERENCIAS

[1] N. Frank N. Kemmer, *"Manual del agua. Su naturaleza, tratamiento y aplicaciones"*. Vol. III. Mc Graw Hill. México 1999. Capítulo 38.

[2] Nalco Chemical Company, "Manual técnico de agua de enfriamiento". Sección 3, 1999.

[3] D. Kern. "Procesos de transferencia de calor". Compañía editorial Continental. México 1997. Cap. 7.

[4] R. E. Treybal. "Operaciones de transferencia de masa". 2da edición. Mc Graw Hill. México 1998. Cap. 7.

[5] W.L.Mc Cabe, "Operaciones unitarias en ingeniería química". Mc Graw Hill. Cuarta Edición. España. 1998. Capítulo 28.

[6] H.F. Rase & M.H Barrow, "Ingeniería de proyecto para plantas de proceso. Compañía Editorial Continental. México 1988. Capítulo 21.

[7] G.F. Hewitt, "Process Heat Transfer. Editorial CRC. EUA 1994. Chapter 23 Water Cooling Towers.

[8] F.F. Huang, "Engineering Thermodynamics - Fundamentals and applications". Compañía Editorial Continental. Segunda edición. México 2004. Capítulo 14.

[9] P.E Liley. "Approximations for the Thermodynamic Properties of Air and Steam Useful in Psychometric Calculations", Mechanical Engineering News, 1980, Vol. 17, No 4.

[10]http://app.cfe.gob.mx/Aplicaciones/CCFE/Tarifas/Tarifas/tarifas_negocio.asp?Tarifa=CMAS&Anio=2012.

Experiencias en temas de energia y medio ambiente

Federico González G.
Área de Ingeniería en Energía, Departamento de Ingeniería de Procesos e Hidráulica, CBI.
Universidad Autónoma Metropolitana-Iztapalapa.
México D.F.
Enrique Barrera C.
Área de Ingeniería en Energía, Departamento de Ingeniería de Procesos e Hidráulica, CBI.
Universidad Autónoma Metropolitana-Iztapalapa.
México D.F. ebc@xanum.uam.mx
Elisa Sanchez C.
Área de Ingeniería en Energía, Departamento de Ingeniería de Procesos e Hidráulica, CBI.
Universidad Autónoma Metropolitana-Iztapalapa.
México D.F.
C. Álvarez-Macías.
Área de Ingeniería en Energía, Departamento de Ingeniería de Procesos e Hidráulica, CBI.
Universidad Autónoma Metropolitana-Iztapalapa.
México D.F.
Ricardo Rosas C. C.
Área de Ingeniería en Energía, Departamento de Ingeniería de Procesos e Hidráulica, CBI.
Universidad Autónoma Metropolitana-Iztapalapa.
México D.F.
Carlos Hernandez P.
Área de Ingeniería en Energía, Departamento de Ingeniería de Procesos e Hidráulica, CBI.
Universidad Autónoma Metropolitana-Iztapalapa.
México D.F.

***Abstract*—Todas las actividades o procesos energéticos generan impactos al medio ambiente, consumen recursos, emiten sustancias al medio ambiente y provocan otras modificaciones ambientales durante su periodo de vida. En este trabajo, el grupo de investigación de materiales solares y dispositivos solares de IRE, IPH, UAM-I, muestra algunos ejemplos de investigación enfrentados en nuestra área de investigación, en esta temática, por lo que se muestran ejemplos desde temáticas ambientales hasta puramente energéticas, mostrando que la faceta mixta es hoy en día la más relevante para tomar en cuenta en el México actual, que enfrenta grandes retos.**

Los recubrimientos solares selectivos, representan los materiales idóneos en la manufactura de los llamados colectores solares planos, para aprovisionar fluidos a temperaturas importantes para el sector doméstico. Tales superficies que realizan una conversión foto térmica eficiente debido a que tienen alta absortancia solar (α_s) y baja emitancia térmica (ε_t) a la temperatura de operación del dispositivo que haga uso de ellas; están compuestos por partículas uniformemente distribuidas, que son depositadas sobre un sustrato metálico, a este sistema se lo denomina tándem reflector absorbedor.

Se esquematizan algunos ejemplos clásicos y sus vínculos con variables ambientales, en el ánimo de mostrar que tales procesos, buscan ser benévolos con el medio ambiente al situar este nicho como parte importante de los conceptos desarrollados.

Otros ejemplos de aprovisionamiento energético que se desarrollan en nuestro cuerpo académico, se muestran y describen, mostrando los avances logrados y sus principales cuellos de botella energético y ambiental.

Keywords*— *Energía Solar, medio ambiente, sustentabilidad energética

I. Experiencias en energia y medio ambiente

a) Materiales con propiedades ópticas apropiadas para el aprovechamiento y uso limpios de la energía. Una forma importante que adopta la energía es como radiación electromagnética, que por cierto es limpia. Si se reflexiona un poco, es posible caer en cuenta que es justo en esta forma como la energía se usa a una escala significativa en el mundo actual, posiblemente más por su uso tan extendido que por la fracción que representa respecto al conjunto de la energía que consume la humanidad. En el mismo sentido se puede decir que muchas de las tecnologías que han revolucionado a las sociedades a partir del siglo pasado, están ligadas al control de ondas electromagnéticas para fines específicos. Pero, sin duda alguna, el hecho de que el Sol sea la fuente de energía para la Tierra y que además sea en forma de radiación electromagnética (fundamentalmente como luz visible debido a la temperatura de la superficie solar), resulta de una trascendencia capital para la especie humana –y para la vida misma- que surgió y evolucionó en presencia suya. Así, en nuestra opinión hay dos grandes áreas de investigación en relación a las propiedades ópticas de materiales y la energía en forma de radiación electromagnética. La primera es simplemente aprovechar toda la energía asociada al espectro solar, sea por su transformación

en trabajo eléctrico o en calor útil. La segunda área tiene que ver con la iluminación artificial, que en cierta manera es un problema inverso al que representa la primera área. La explicación a este planteamiento está en relación a que el ojo humano, que es nuestro sensor de luz, evolucionó, como se dijo ya, en presencia del Sol. Así, una fuente de iluminación de calidad para los humanos debería emular en algún sentido a la parte visible del espectro solar; es decir, se requiere de tecnologías que transformen algún tipo de energía, por ejemplo el trabajo eléctrico, en radiación electromagnética como la que emite el Sol. En términos de los materiales, el propósito es conferirles propiedades que den lugar a su interacción con luz en forma controlada en regiones espectrales específicas. Estas propiedades pueden consistir simplemente en su capacidad de absorción de luz en un intervalo de longitudes de onda y en su no absorción en otro intervalo de longitudes de onda como ocurre en los recubrimientos selectivos de las tecnologías de aprovechamiento fototérmico de la energía solar. El caso del aprovechamiento fotovoltaico es más complejo, pues en este caso no basta con la absorción de la luz, ya que es además necesaria su transformación en trabajo eléctrico. Desafortunadamente por ahora no hay un dispositivo que sea capaz de absorber la luz de todo el espectro solar que incide en la superficie terrestre para su posterior transformación en trabajo eléctrico. Una razón que impide que ello ocurra, es que los semiconductores de los que están hechas las celdas fotovoltaicas tienen absorciones en regiones espectrales específicas. Una propuesta que ha ganado interés a nivel de investigación es adaptar el espectro del Sol, de modo que fotones que no son absorbidos por las celdas fotovoltaicas se transfieran a regiones en donde dicha absorción ocurre. En la Fig. 1, se ilustra cómo en sistemas hechos a base de óxidos metálicos dopados con algunos lantánidos trivalentes es posible transferir fotones en la forma señalada anteriormente, para su óptimo aprovechamiento en este caso por una celda de silicio. Este proceso de denomina conversión descendente, cuando un fotón de alta energía se parte en al menos dos fotones de menor energía; o corrimiento descendente cuando un fotón de alta energía se traslada de una región de alta energía –en cuyo caso no es absorbido por el semiconductor- a una de menor energía en donde éste si se absorbe, (1,2)

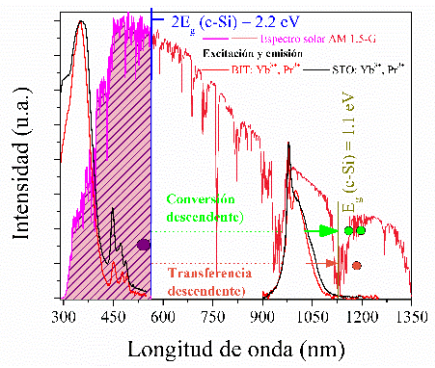

Fig 1. Se ilustra a través de datos medidos en nuestro laboratorio, la posibilidad de que el $Bi_4Ti_3O_{12}$ y el $SrTiO_3$ dopados con Yb_{3+} puedan transferir o convertir descendentemente fotones con la intención de adaptar el espectro solar (también ilustrado en la figura) para su mejor aprovechamiento en una celda fotovoltaica de silicio.

En el caso de la iluminación artificial, se trata, generalmente, de convertir trabajo eléctrico en luz. Por ahora la forma más eficiente de este proceso es a través de diodos emisores de luz (LED). Sin embargo por sí solo un LED no produce luz en el conjunto de longitudes de onda que da lugar a una iluminación de calidad. Esto se debe a que un LED por su naturaleza, emite luz en regiones muy acotadas del espectro visible, lo cual contraviene las características de un dispositivo de alta calidad que es emitir luz en todos los colores, o al menos en las regiones del azul, verde y rojo. Para superar este inconveniente, los LED se acoplan con materiales, denominados fósforos, que tienen la cualidad de absorber parte o toda la luz emitida por un LED y transferirla a regiones de longitud de onda específicas. Este tipo de tecnologías que involucran la asociación LED + fósforo se les denomina de iluminación de estado sólido. En la Fig. 2, se muestran las características luminiscentes de óxido de itrio-circonio dopado con Dy^{3+}. Es posible observar que este material es capaz de ser excitado (absorber luz) en un amplio rango de longitudes de onda, como por ejemplo en donde varios LED´s emiten, para su ulterior transformación a través del Dy^{3+} en luz con un índice de reproducción cromática de 92 que es de muy buena calidad. Esto se debe a que el Dy^{3+} tiene emisiones en el azul, amarillo y rojo.

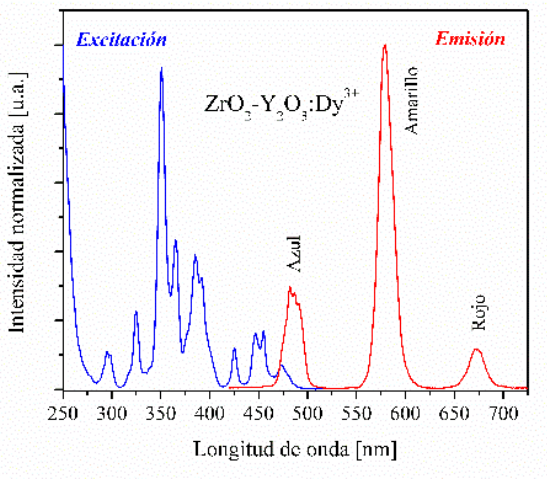

Fig. 2. Espectros de excitación y emisión de un fósforo con alta índice de reproducción cromática a base de ZrO_2-Y_2O_3: Dy^{3+}.

b) Películas delgadas para la conversión fototermica de la energía solar.

Los compuestos químicos, Fe_3O_4 y Fe_2O_3 son algunos de los óxidos que son ampliamente estudiados en los campos de la nano ciencia y nanotecnología debido a sus propiedades físicas y químicas inusuales, las cuales los hacen especialmente útiles para diversas aplicaciones por ejemplo la creación de terapias para enfermedades como cáncer, en remediación ambiental, en dispositivos de almacenamiento de información, en el área de ciencia de materiales para la creación de materiales con propiedades específicas.

Existen métodos no agresivos que han sido reportados en la literatura para sintetizar partículas de Fe_3O_4 y Fe_2O_3 como la coprecipitación de iones ferroso (Fe2 +) y férrico (Fe3 +) y mediante una reducción con glucosa. Los cuales no utilizan reactivos peligrosos, de difícil degradación y no conllevan a daños al medio ambiente.

Una línea de investigación en el laboratorio es superficies selectivas para absorbedores solares basadas en pinturas. Los absorbedores son la parte más importante de un calentador solar de agua, la eficiencia de un colector depende de la absortancia solar y emitancia térmica, estas últimas son las características de una superficie selectiva: alta absortancia solar y baja emitancia térmica. Las superficies selectivas basadas en pinturas se componen de un aglutinante en el que se incorporaran diversos pigmentos de tal manera que se forman dispersiones estables, las cuales se depositan mediante una técnica sencilla como serigrafía sobre sustratos metálicos. Una baja emitancia térmica se logra mediante el uso de pigmentos de óxido de hierro (Fe_2O_3) y con diferentes concentraciones de Fe:Mn en bixbita, $((FeMn)_2O_3)$. Los pigmentos se caracterizan estructuralmente mediante difracción de rayos X. La caracterización óptica se realiza por espectrofotometria UV-Vis-Infrarrojo. Usando el Perfilometro Dektak-XT motorizado se obtienen la rugosidad y espesor de los recubrimientos, (3, 4 y 5)

La caracterización estructural del sistema FeMnO para uso en pigmentos se presenta en la figura 3. Los espectros de difracción refieren a que hemos sintetizado la fase hematita (Fe_2O_3), con la variación en la concentración de Fe:Mn se ha producido una solución sólida y con otra composición de Fe:Mn se segregaron las fases, según el difractograma contiene: Fe_2O_3-Mn_2O_3. Un resumen de algunas concentraciones con las que se ha trabajado se presenta en tabla 1.

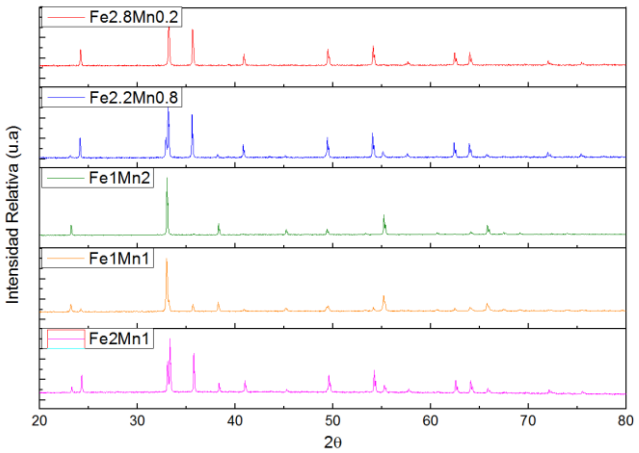

Fig.3. Espectro de DRX, de los pigmentos selectivos preparados

TABLE 1. RESULTADOS DE DRX DE LOS PIGMENTOS.

	Composición de fase XRD	**Parámetros de celda**		
	α-Fe₂O₃: ***α-Mn₂O₃***	***α-Fe₂O₃***		***α-Mn₂O₃***
		a=b	***c***	***a=b=c***
Fe2Mn1	87.75: 12.25	5.03	13.74	9.41
Mn1Fe1	41.06: 58.94	5.03	13.73	9.41
Mn2Fe1	0:100	-	-	9.41
Hematita	100:0	5.03	13.74	-
Fe2.2Mn0.8	93.62:6.38	5.03	13.73	9.41
Fe2.8Mn0.2	100:0	5.03	13.73	-

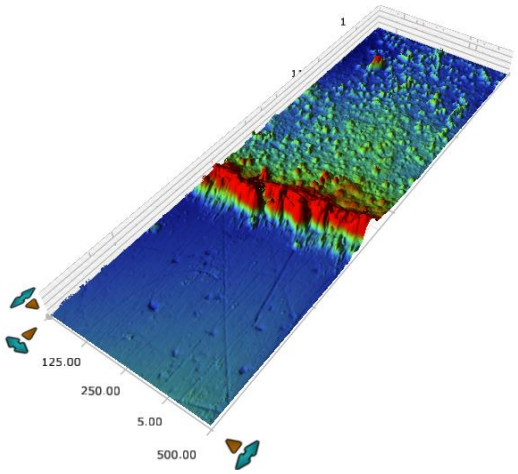

Fig. 4. Morfología superficial de un sustrato y de la interfase sustrato película selectiva, Oxido de hierro sobre aluminio en una gran área de barrido 0.5x2mm.

c) Estudio de carga y descarga de baterías con paneles fotovoltaicos

Parte de las necesidades básicas de electricidad de una casa humilde son para iluminación (con unas 4 lámparas fluorescentes de 30 W cada una), donde el consumo resultante es típicamente 5 kWh/mes. Estas necesidades se pueden satisfacer con un "Sistema Fotovoltaico Domiciliario" consistente en un módulo fotovoltaico de 50 W_p, en una batería y en un controlador de carga/descarga de la batería. El sistema trabaja normalmente a 12 V de corriente continua (CC), y si se consideran otros dispositivos, con inversores para corriente alterna (CA), 12 V CC / 220 V CA. Mientras que los módulos FV de las principales marcas comerciales ofrecen hoy una alta confiabilidad con certificaciones de laboratorios de renombre y vidas útiles encima de los 20 años, no se puede decir lo mismo de las baterías ni tampoco de los componentes electrónicos del

sistema, es decir del controlador de carga y de los inversores. Por otro lado, en el costo inicial de un pequeño sistema FV la batería puede representar de 10 - 30 %, y en el costo por kWh de electricidad usado, el porcentaje correspondiente a la batería muchas veces es mayor que el 50 % del costo total. Por estos motivos de confiabilidad y costos, la selección de la batería para una aplicación FV específica debe realizarse cuidadosamente.

Un módulo FV de 50 W_p puede entregar diariamente a una batería de 170 a 250 Wh de energía eléctrica, es decir de 5 a 7,5 kWh / mes, en condiciones de radiaciones solares típicas de 4 - 6 kWh/m^2 día. En el caso usual de baterías de 12 V, esto corresponde a una carga diaria de 12 - 18 Ah. Esta carga debe ser almacenada cada día en la batería para poder ser usada también diariamente. Por otro lado es deseable tener una autonomía energética de algunos días frente a una secuencia de varios días sin sol. En sistemas domésticos es recomendable una autonomía energética de 3-5 días. En otras palabras, para un módulo FV de 50 W_p se requiere una batería que tenga una capacidad de almacenar y entregar diariamente una carga de 12 - 18 Ah y que eventualmente pueda entregar una carga de 50 Ah.

Es importante saber que la capacidad de una batería depende de la temperatura y del régimen de descarga, es decir que descargando con una corriente menor, la batería puede proporcionar más carga. En aplicaciones FV la capacidad de la batería se define por su capacidad de entregar una determinada carga en 20 o 100 horas a 25 ºC, denominada C_{20} y C_{100}, respectivamente. Esto debe tenerse en consideración si se compara diferentes baterías, porque la información comercial no es siempre completa al respecto. Los principales parámetros de la carga de una batería vienen definidos por el equipo de carga utilizado y son principalmente:

- Corriente de carga
- Voltaje de carga
- Tiempo de carga

La carga en la batería debe realizarse de forma continua. El método de carga debe adaptarse a la aplicación y su importancia es decisiva en la vida útil de la batería, el objetivo del sistema de carga ha de ser el de conseguir un método rápido de carga eficiente y que no produzca daños en la batería. Los métodos de carga pueden clasificarse en función de la variación en tiempo del voltaje y la corriente. La duración de la carga es un factor a tener en cuenta a la hora de elegir el sistema óptimo de carga para cada aplicación. Los métodos de carga más comunes son:

- Carga a voltaje constante
- Carga a corriente constante
- Carga a corriente y voltaje constante
- Carga con voltaje creciente

La situación de sobrecarga y descarga profunda corresponde a un voltaje excesivamente elevado o nulo, respectivamente. Para evitarlos se introduce un dispositivo electrónico denominado regulador que de acuerdo a donde se ubique puede ser:

- Regulador paralelo: Se encarga de disipar el exceso de potencia generada por los módulos solares.
- Regulador serie: Desconecta la batería del cargador solar.

En este trabajo se determinan las curvas de carga y descarga de una batería típica, con el fin de estudiarlas para poder aportar a estos esquemas de almacenamiento de energía, que son atractivos aun para grupos electrógenos autónomos.

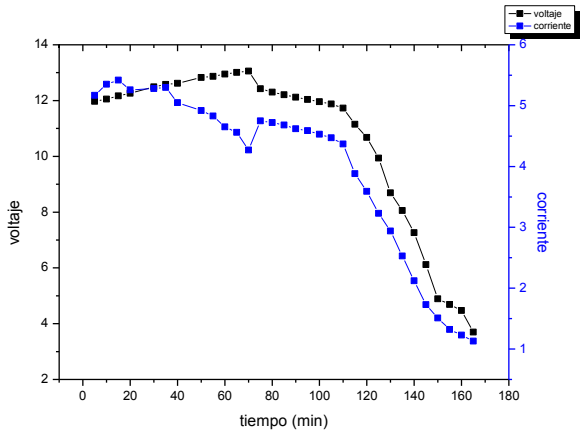

Fig. 5. Curva típica de descarga de una batería, como un medio de almacenamiento de energía solar fotovoltaica.

d) Elaboración de espejos de alta reflectancia a partir del electropulido de aluminio para uso en concentradores solares.

El objetivo del presente proyecto es elaborar espejos usando láminas de aluminio, material más resistente que los espejos de alta reflectancia convencionales, este objetivo se lograra usando electro-pulimiento en una de las caras de la lámina de aluminio, lo que nos permitirá obtener un acabado más suave que el que se puede obtener con el pulido mecánico. Poder elaborar espejos a partir de materiales que permitan un manejo práctico y su mantenimiento sea mínimo ara más funcional el uso general de los colectores solares. Además al elaborar un espejo puliendo la cara de un metal se elimina la posibilidad de una fractura y los costos de un transporte cauteloso, también el uso de estructuras de montaje se ven reducidos

Para la realización de las mejores muestras experimentales se ocupó como electrolito la siguiente mezcla:

- 6% (Ácido Nítrico)
- 20%(Ácido Sulfúrico)
- 3mMol de
- (Ácido fosfórico)
- Agua

Este electrolito nos permitió una excelente relación entre el aluminio y el acero inoxidable. Los mejores resultados que se obtuvieron fueron con muestras de 4 cm por 4 cm, bajo las siguientes condiciones:

- Temperatura: 80 °C.
- Voltaje: 5 °C.
- Tiempo: 5 minutos.
- Revoluciones: 1200.
- Baño posterior al electro-pulido de sosa (NaOH) al 40%.

Los resultados que se presentan a continuación en la gráfica representan, en el eje x, la longitud de onda del UV hasta el IR, de 200 a 2500 nm, y el porciento reflejado, en el eje y.

Fig. 6 reflectancia de un espejo de Al electropulido, que muestra un alto valor de la propiedad en el espectro uV-Vis-NIR.

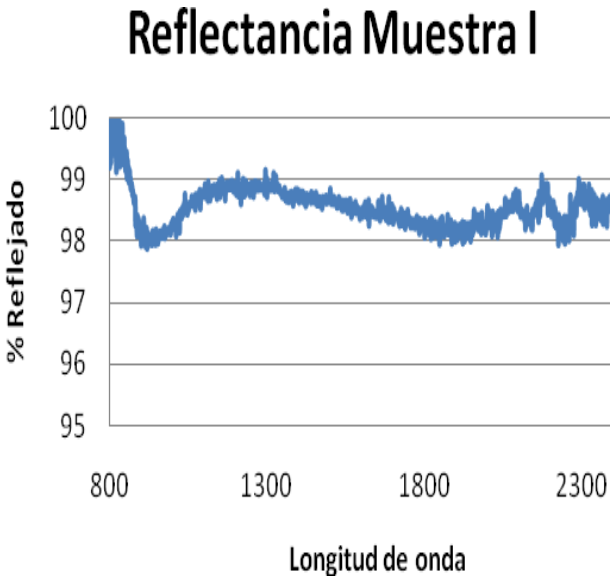

Se define reflectancia como el porcentaje del espectro electro magnético incidente reflejado por una superficie, mientras más alto sea este, indica que la superficie refleja más del espectro que incide sobre ella, materiales útiles en temas de energía solar concentrada.

CONCLUSION.

Las líneas de trabajo mostradas por nuestro grupo de investigación cubren diversos tópicos en el área de síntesis y caracterización de materiales para aprovechamiento de la energía solar y por tanto impacta algunos sectores de la ingeniería ambiental y en general de problemas de la energía y el medio ambiente. La breve descripción mostrada, es solo ilustrativa, donde parte del trabajo de dos profesores de tiempo completo, estudiantes posdoctorales y de Doctorado y licenciatura, reflejan una parte de los logros de nuestro cuerpo académico.

AGRADECIMIENTOS

Se agradece el apoyo financiero a CONACYT, proyectos: 166032 y 154962. También se agradece al programa de becas para alumnos de posgrado de nueva creación UAM, otorgado a Elisa Sánchez C.

REFERENCES

[1] .R. López, R. Castañeda, F. Rubio, M.E. Villafuerte, E. Barrera, F. González, Insights into the dielectric and luminescent properties of Na0.5Pr0.003Bi0.497-xLaxTiO3 synthesized by Pechini method. Dalton Transactions, vol. 42, pp. 6879-6885, 2013.

[2] .E. Barrera, J.C. Martinez, F. Gonzalez, M. Ortega, R. Rosas, Spectroscopic Ellipsometry Study of Co3O4 Thin Films Deposited on Several Metal Substrates, The Open Surface Science Journal, Sharjah, 2013/07/31, 2013/10/10. Vol. 5. pp 9-16.

[3].V. Rentería, C. Velásquez, M. Ojeda, E. Barrera, F. González. Silver nanoparticles dispersed on silica glass for applications as photothermalselective material. Energy Procedia, Vol 57, pp 22241-2248.

[4].E. Sánchez-Cruces, E. Barrera-Calva, K. Lavanderos, F. González. Life cycle analysis (LCA) of solar selective thin films by electrodeposition and by sol-gel techniques. Energy Procedia 57, pp 2812-2818.

[5].Ma. Luisa Lozano, Laura Galicia, E. Barrera, Electrochemical Formation and Optical Characterization of Poly Fe(III)-APHEN on ITO, Journal on Photonics and Spintronics, Vol. 3, pp 7-14.

Energy production by catalytic ethanol steam reforming and combustion of H_2

M.A.Ortiz [1], J.L. Contreras [1*], B.Quintana[1], C. Tapia[1],G.A. Fuentes[2], L. Nuño[1] ,B.Zeifert[3], J. Salmones[3] y R.Luna[1].
[1] Depto. de Energía, CBI, Universidad Autónoma Metropolitana-Azcapotzalco,
Av. Sn. Pablo 180, Col. Reynosa, México, D.F, 02200, México
[2] Depto. de IPH, CBI, Universidad Autónoma Metropolitana-Iztapalapa, Av. San Rafael Atlixco No. 186, Col. Vicentina, Iztapalapa, México, D.F. 09340, México,
[3] Posgrado de Ing.Química y Metalúrgica,ESIQIE-Instituto Politécnico Nacional, Edif. 8, Unidad Profesional Adolfo López Mateos, Zacatenco, Delegación Gustavo A. Madero, C.P. 07738, México, D.F., México
*jlcl@correo.azc.uam.mx

***Abstract*—Ethanol steam reforming (ESR) to produce H_2 was studied using Ni-Co/Hydrotalcite-WOx catalysts, the presence of CH_4, CO_2, and CO in some catalysts were observed. The presence of Ni and Co in the bimetallic catalysts changed the products selectivity observed respect to the selectivity of the monometallic catalysts. The bimetallic catalysts of Ni-Co showed higher selectivity to H_2 than the selectivity of the monometallic Ni catalyst. The surface area in the Ni and Co catalysts was inversely proportional to the metal concentration. Metal oxides of Ni and Co in the bimetallic catalysts interacted with the hydrotalcite structure, causing a partial blockage of pores, resulting in a decrease of pore volume. By scanning electron microscopy (SEM), the particles on the bimetallic catalysts showed a semi-cubic shape observed instead of laminar shape typical of hydrotalcites. By X-ray diffraction (XRD), hydrotalcite, $MgNiO_2$, Periclase (MgO), κ-Al_2O_3 and bunsenite (NiO) were identified. The bimetallic catalysts of Ni-Co-hydrotalcite-WO_X showed high selectivity to H_2 and total conversion of ethanol. The bimetallic catalysts did not produce CO. The reaction of ESR is capable of producing H_2 at a rate sufficient to produce energy beyond that required for heating the currents of ethanol, water and the heating of reactor.**

***Keywords*—Hydrogen, ethanol, steam-reforming, Ni-Co-hydrotalcite -WOx, catalysts.**

I. Introduction (*Heading 1*)

Ethanol has several advantages as a fuel and can be stored more easily and without significant risk of handling and can be obtained in large quantities from biomass [1-2]. Then in order to produce H_2 by ESR, the catalysts must show high thermal stability, because the relative high operation temperatures at which reforming reactions take place, as well as high selectivity to H_2 production. Several studies have shown that supported noble metals such as: Ir, Pt, Pd, Ru or Rh [3, 4], or inexpensive metals such as Co [5-7], Ni [8], or bimetallic materials [9,10] are good options to catalyze the ESR reaction. Thereby, supports such as: MgO, ZnO, SiO_2, Al_2O_3, La_2O_3 or CeO_2, among others, are the most commonly used to support the active metals [11].

We have chosen the so-called hydrotalcite-like compounds as supports, also known as layered double hydroxides (LDHs) [12]. LDHs are a family of lamellar materials derived from brucite layers, which are currently of academic and industrial interest [12-14]. These compounds contain Mg^{2+} and Al^{3+} metal cations. In this study, bimetallic Ni-Co and hydrotalcite catalysts were prepared by the coprecipitation method and then evaluated in the ESR reaction.

II. Experimental

The hydrotalcite was made by coprecipitation using two salt solutions as precursors. First, in a stirred reactor a salt solution of $Mg(NO_3)_2$ and $Al_2(NO_2)_3$ (J.T. Baker) with a molar ratio of 2:1 was made and a second solution of Na_2CO_3 (5%) and NaOH (pH = 10) (Carlo Erba) were prepared. These two solutions were added simultaneously drop by drop to a third stirred reactor using water as solvent (60 drops/min) at 60°C maintaining an atomic ratio of Mg^{2+}/Al^{3+} of 1.55. In this step a solution of $(NH_4)_{12}W_{12}O_{41}•5H_2O$, (Aldrich) was added in order to get 0.5%wtW of the final solid and also an aqueous solution containing $Ni(NO_3)_2$ and $Co(NO_3)_2$ (Aldrich) was added. This final suspension was maintained at 70°C in the reactor with stirring for 18 h. This precipitated solid was washed, dried and calcined at 450°C for 5h. A sample of hydrotalcite without Ni or Co was prepared in a similar manner (sample HTA). The solids obtained were characterized by X-ray diffraction (XRD) in a Phillips X´ Pert instrument. N_2 physisorption at 77 K was made in a Micromeritics 2000 instrument. Each sample was pretreated at 200°C under vacuum (1 x 10^{-4} torr). The samples were analyzed by scanning electron microscope (SEM) using a microscope with high-resolution Jeol model JFM 6701 F, using secondary electrons. The qualitative chemical analysis and their corresponding spectra were obtained by coupling a probe SEM, and EDS (energy dispersive spectroscopy of X-rays). The catalytic reaction was made in a U-shaped stainless steel fixed bed reactor. The catalyst (1 g) was charged and the feed of the reactants consisted of ethanol, water as steam and N_2. The gas mixture of H_2O and CH_3CH_2OH (molar ratio of 4/1) in N_2 stream was fed using two glass saturators. The temperature of the catalyst was controlled to 450°C in flow of N_2 for 30 min to clean the catalyst surface and then the flow of reactants started at the same temperature. The catalyst was held at that temperature for 30 min in order to make three analyses. The analysis of the reactants and all the reaction products was carried out online by gas chromatography. Inside an automated injection valve, the sample was divided into two portions which were then analyzed in order to obtain a complete

quantification of the reaction products. H_2, CO, CO_2 and CH_4 were identified using a column of silica gel 12 grade 60/80 (18´x 1/8") with a thermal conductivity detector (Gow-Mac apparatus).

III. Results and Discussion

The samples showed the IV type hysteresis (Figure 1) which corresponded with the structure of parallel plates typical of the hydrotalcites, these catalysts were mesoporous and macroporous (see Table 1).

The surface area of the hydrotalcite, decreased when Ni and Co compounds were impregnated by coprecipitation and the pore diameter distributions were mesopores and macropores (Table 1).

By XRD the presence of hydrotalcite(HTA), $MgNiO_2$, Periclase (MgO), κ-Al_2O_3 and Bunsenite (NiO) were observed (Figure 2)

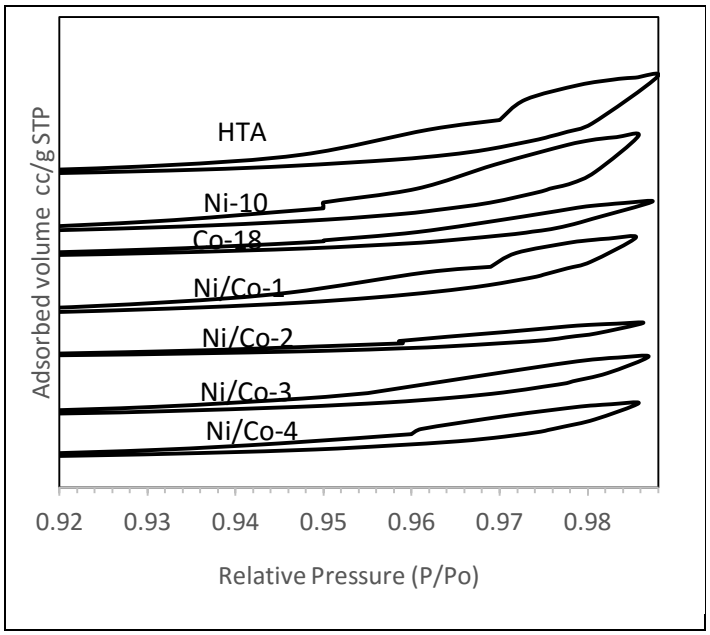

Fig, 1. N_2 Isotherms for the hydrotalcite and Ni-Co catalysts.

Table 1. Characterization of Ni-Co-hydrotalcite-WOx catalysts prepared by coprecipitation

Catalyst	Ni wt%	Co wt%	A_{BET} [m^2/g]	Dp [Å]	XRD Compounds	SEM Particles	EDS Elements
HTA	0	0	226	578	Hydrotalcite,Periclase(MgO), κ-Al_2O_3	20-55nm	Mg,Al
Ni-10	10	0	152	108	Hydrotal.,$MgNiO_2$,MgO,Bunsenite(NiO)	20-70	Mg,Al,Ni
Co-18	0	18	220	64	Hydrotalcite,Periclase(MgO), κ-Al_2O_3	30-66	Mg,Al,Co
Ni/Co-1	10	4.5	200	84	Hydrotal.,MgNiO2,MgO,Bunsenite(NiO)	20-45	Mg,Al,Co,Ni
Ni/Co-2	7.5	9	160	88	Hydrotal.,MgNiO2,MgO,Bunsenite(NiO)	20-65	Mg,Al,Co,Ni
Ni/Co-3	5	13.5	117	107	Hydrotal.,MgNiO2,MgO,Bunsenite(NiO)	-----	----
Ni/Co-4	2.5	18	142	84	Hydrotal.,MgNiO2,MgO,Bunsenite(NiO)	-----	----

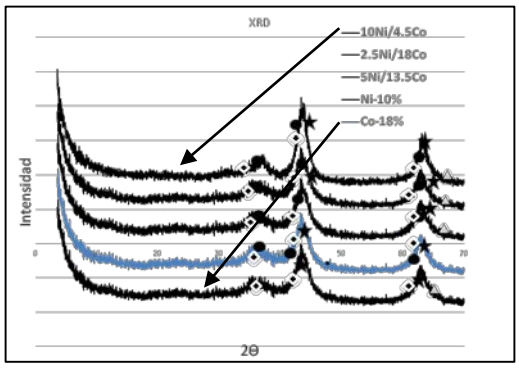

Fig. 2. XRD of calcined hydrotalcite and Ni-Co-hydrotalcite catalysts.

In the hydrotalcite sample, particles with diameters between 20-55nm were observed by SEM having a lamellar shape (Figure 3) while in the catalysts with Co and Ni, particles between 20 to 70 nm having a semi-cubic form were observed (Figure 4).

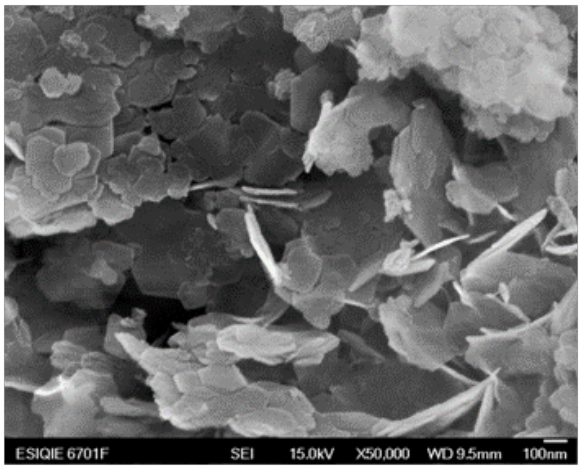

Fig. 3. SEM of calcined hydrotalcite

High H_2 selectivity and conversion were obtained at 450°C (Table 2) and no CO was observed in the bimetallic catalysts: Ni/Co-1 to Ni/Co-3. These catalysts produced CH_4, CO_2 and H_2 and all the ethanol was converted (Figure 5). We did not find CH3CHO and CH_2=CH_2.

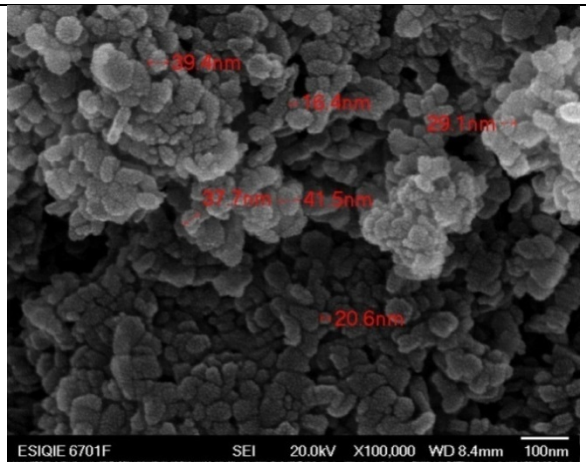

Fig. 4. SEM of calcined Ni/Co-1 catalyst.

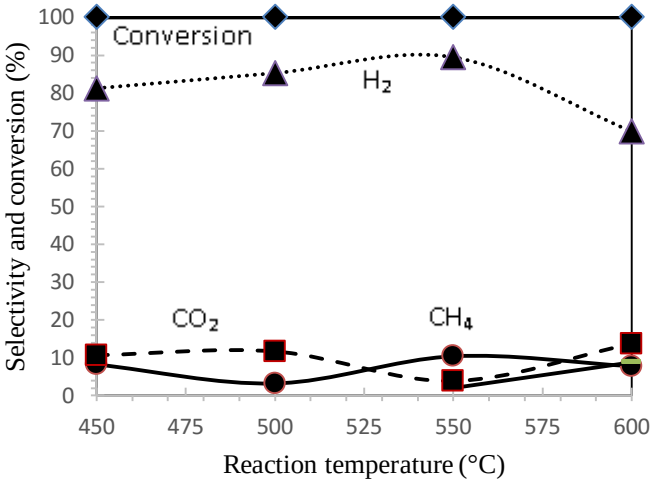

Fig. 5 Selectivity and conversion for the ESR reaction of the Ni/Co-3 catalyst.

Table 2. Selectivity and conversion for the Ni-Co-Hydrotalcite-WOx catalysts at 450°C

Catalyst	H_2	CO_2	CH_4	CO	Conv,%
HTA	21	57	4	18	100
Ni-10	67	20	3	10	100
Co-18	89	10	1	0	100
Ni/Co-1	91	8	1	0	100
Ni/Co-2	84	10	6	0	100
Ni/Co-3	81	10	8	0	100
Ni/Co-4	89	9	1	1	100

In this study, an energy balance of the reaction of ethanol steam reforming has been made. This study shows that ESR is an energy generator process, the calculations included: (1) the energy to heat ethanol , (2) the energy to heat water and (3) the energy to heat N_2 from 25°C to 450°C and the calculation of heat of reaction at 450°C (Fig. 6) in accordance with the reaction (1).

$$CH_3CH_2OH + 3H_2O \rightarrow 2CO_2 + 6H_2 \quad (1)$$

The energy required to heat the three gases of the feed (ethanol, water and N_2) was calculated using the following equation:

$$\Delta H_f = \Sigma(\Delta H_E + \Delta H_w + \Delta H_{N2}) \quad (2)$$

Where:

ΔH_f = Energy to heat the mixture of gases from 25 to 450°C.

ΔH_E = Energy to heat ethanol in the feed.

ΔH_w = Energy to heat water in the feed.

ΔH_{N2} = Energy to heat N_2 in the feed.

The energy required at 450°C for the endothermic reaction is:

$$\Delta Hr = \Delta Hr^o + \int_{298}^{723} \Delta Cp\, dT \quad (3)$$

ΔHr = Energy required to the endothermic reaction (at 723K)

ΔHr^o = Energy required to the reaction at 298 K

$$\Delta Cp = \Delta\alpha + \Delta\beta T + \Delta\gamma T^2 \quad (4)$$

In the case of total combustion of H_2, the reaction:

$$H_2 + 1/2\ O_2 \rightarrow H_2O \quad (6)$$

will produce: ΔHc = 241818 J/mol H_2

Using 6 mol of H_2, the reaction will produce:

ΔHct = 1450908 J/mol

The energy obtained from the system will be:

$$\Delta H_{tot} = \Delta Hct - (\Delta H_f + \Delta Hr) \quad (5)$$

$$= (1450908 - (333244.07 + 173\,536))$$

$$= 944\,127.93 \text{ J/mol}$$

Where

ΔH_{tot} = Net energy obtained from the ESR process.

Conclusions

The bimetallic catalysts of Ni-Co-hydrotalcite-WO_X showed high selectivity to H_2 and total conversion of ethanol between 450 to 600°C. The hydrotalcite and the monometallic

Ni catalyst produced CO, but in the bimetallic Ni-Co catalysts this product was absent. The best catalyst to produce H_2 was Ni/Co-1 having 10wt% Ni and 4.5wtCo. The monometallic Co catalyst did not produce CO and this fact could suggests that Co inhibits the production of CO on the Ni-Co bimetallic systems. In accordance with the total conversion of ethanol a 450°C the reaction of ethanol steam reforming is capable of producing H_2 at a rate sufficient to produce energy beyond that required for heating the currents of ethanol, water and the heating of the reactor.

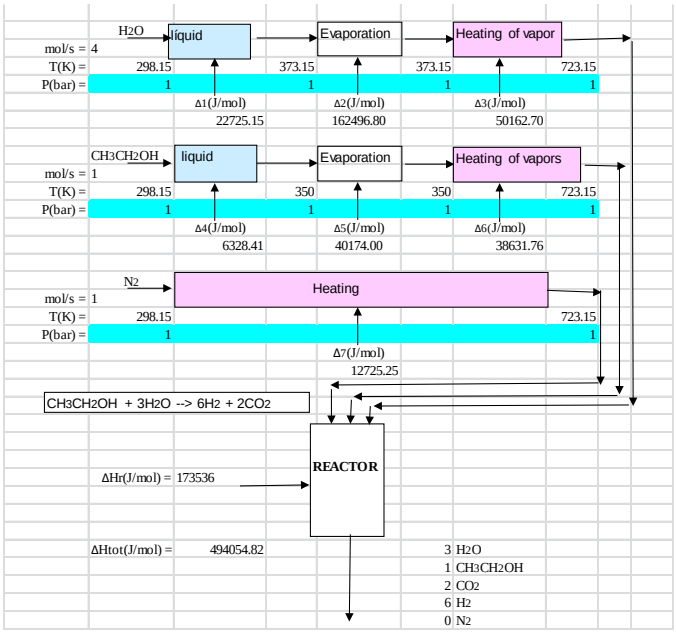

Fig. 6. Total energy balance from the ethanol steam reforming to obtain hydrogen.

5. References

[1] R.D. Cortright, R.R. Davda, J.A. Dumesic, Nature 418, 964(2002).
[2] J. Llorca,N.,Homs,J.Sales,J. L. G. Fierro and P. Ramírez de la Piscina, J. Catal. 222, 470-480(2004).
[3] J. L.Contreras, J. Salmones, L. A. García, A. Ponce, B. Zeifert and G.A. Fuentes, J. of New Materials for Electrochemical Systems 11, 109-117(2008).
[4] M. N.Barroso, M. F.Gómez, L.A.Arrúa,M. C.Abello, Appl. Catal. A:General 304, 116-123(2006).
[5] J. Llorca, N. Homs, J. Sales, and P. Ramírez de la Piscina, J. Catal. 209, 306-317(2002).
[6] K. Sing, D. Everett, R. Haul, L. Moscou, R. Pierotti, J. Rouquerol, and T. Siemieniewska, Pure Appl. Chem. 57, 603 (1985).
[7] L. D. Gelb, K. E. Gubbins, R. Radhakrishnan, and M. Sliwinska-Bartkowiak, Reports on Progress in Physics 62, 1573 (1999).
[8] Lowell,S.J. E. Shields, M. A. Thomas, and M. Thommes, Characterization of Porous Solid and Powders: Surface Area, Pore Size and Density, Kluwer Academic Publishers, (2004).
[9] M. del Arco, D. Carriazo, S. Gutiérrez, C. Martín and V. Rives, Inorg. Chem. 43, 375-384(2004).
[10] F. Basile, G. Fornasari, M. Gazzano, A. Vaccari, Appl. Clay. Sci. 16,185(2000).
[11] T.Shishido, M.Sukenobu, H.Morioka, R.Furukawa, H.lShirahase, K.Takehira, Catal. Lett.73, 21 (2001).
[12] C. Resini, T. Montenari, L. Barattini, G. Ramis, G. Busca, S. Presto, P. Riani, R. Marazza, M. Sisani, F. Marmottini, U. Costantino, Appl. Catal.A: General, 355, 83-93(2009).
[13] A. Bartecki and Dembicka, D. J. of Inorg. and Nuclear Chem.V. 29, I. 12 , 2907-2916(1967).
[14] A. Iannibello, L. Villa, and S. Marengo, Gazzetta Chimica Italiana,109, 521(1979).

Obtención de ácido cítrico a partir de papel como residuo sólido urbano por fermentación con *Aspergillus niger 10*

R. Guzmán Gil, M. M. González Brambila, H. E. Solís Correa* [a]

[a] División de Ciencias Básicas e Ingeniería, Universidad Autónoma Metropolitana-Azcapotzalco, Av. San Pablo #180, Col. Reynosa Tamaulipas, Cd. de México, D.F., C.P. 02200, México.
zafes_oldnick@hotmail.com

***Resumen*— En el presente trabajo se tiene como objetivo el desarrollo de un proceso biotecnológico para la obtención de ácido cítrico a partir de celulosa de papel como Residuo Sólido Urbano (RSU), por fermentación con *Aspergillus niger 10*, en un biorreactor agitado. Las condiciones de operación en general son: pH de 2 y 3, temperatura de 30 °C y 40 °C, y concentración alta y baja de: Cobre (Cu), Manganeso (Mn) y Zinc (Zn). El papel de desecho se analizó para obtener la concentración de azúcares reductores totales por el método del ácido 3,5-Dinitrosalicilico (DNS), encontrándose que en 1.0056 g de celulosa de papel, la concentración de glucosa fue de 0.56 g. El producto obtenido de la fermentación se cuantificó por el método espectrofotométrico de la piridina-anhídrido acético, además se determinó su punto de fusión e identificaron sus grupos funcionales mediante la espectroscopía de IR; la biomasa se determinó con el reactivo Bradford. La Metodología de Superficie de Respuesta (MSR) se empleó para la optimización de las condiciones de fermentación: pH, temperatura y concentración de metales. Fue utilizado un diseño de experimentación factorial 2^k, con tres factores y dos niveles por factor. La experimentación consistió en 16 corridas, las cuales se utilizaron para desarrollar un modelo estadístico para la optimización de las condiciones de fermentación. Las condiciones de fermentación óptimas dieron como resultado la concentración máxima de ácido cítrico. Estas condiciones fueron: pH de 3; temperatura de 30 °C y concentración de metales alta. En estas condiciones, la concentración de ácido cítrico producido fue de 5727.79 ppm.**

Palabras Clave: Aspergillus niger, fermentación, ácido cítrico, papel.

I. INTRODUCION

El ácido cítrico cumple un gran número de funciones como: amortiguador de pH, conservador, saborizante, promotor de reacciones de curado en los cárnicos, secuestrador de metales, modifica la viscosidad, inhibidor de las reacciones de oscurecimiento, hidrolizante de la sacarosa y de almidón, promotor de la gelificación de las pectinas e inhibidor de la cristalización de la sacarosa. En el sector farmacéutico este ácido orgánico y sus sales se usan para la fabricación de pastillas o polvos efervescentes, también se aprovecha su efecto antioxidante, antimicrobiano y anticoagulante. Otros sectores que usan ácido cítrico son la: industria cosmética, industria textil, industria agrícola e industria de detergentes [1]. Según Mostafa la producción mundial de ácido cítrico para 2008 era más de 1,6 millones de toneladas, además se espera que esta tendencia aumente en el futuro [2].

Durante el proceso de la fermentación con *Aspergillus niger* para obtener ácido cítrico intervienen varios factores como: el tipo de sustrato, ***temperatura***, ***pH***, ***concentración de metales traza***, concentración de inóculo, aireación, agitación, macronutrientes y micronutrientes. Los tipos de sustratos utilizados para el proceso esencialmente contienen un alto contenido de carbohidratos, en general estos son variados, por ejemplo, melazas de caña y de remolacha, suero de leche, residuos agroindustriales: yuca, bagazo de caña, cáscara de café, cáscara de nuez de karité, salvado de trigo, pulpa de manzana, piña, cáscara de kiwi, pulpa de uva, etc. [3-6]. Con la finalidad de obtener el mejor rendimiento durante la fermentación, es necesario optimizar algunos de los factores anteriormente mencionados [7-10].

La metodología de superficie de respuesta, o MSR, es un conjunto de técnicas matemáticas y estadísticas que son herramientas de modelado y análisis, útiles en aplicaciones donde una respuesta de interés recibe la influencia de varias variables, y el objetivo es optimizar esta respuesta. El propósito inicial de estas técnicas es diseñar un experimento que proporcione valores razonables de la variable respuesta y, a continuación, determinar el modelo matemático que mejor se ajusta a los datos obtenidos. La MSR se ha aplicado con éxito a la optimización de muchos bioprocesos [7-10].

El presente estudio se enfoca en la adaptación de *A. niger* para producir enzimas celulolíticas, el desarrollo de un proceso biotecnológico y el análisis de datos estadísticos, para la obtención de ácido cítrico a partir de la fermentación de la celulosa de papel proveniente de Residuos Sólidos Urbanos (RSU). Fue utilizado un diseño de experimentación factorial 2^k, con tres factores y dos niveles por factor. La Metodología de Superficie de Respuesta (MSR) tridimensional se empleó para la optimización de las condiciones de fermentación: pH, temperatura y concentración de metales.

II. MATERIALES Y MÉTODOS

A. *Pretratamiento del papel*

En este proceso fue necesario eliminar tintas y grasas principalmente. Para ello, se utilizó NaOH 0.1 M, HCl 0.1 M y extran neutro 2% v/v. En un recipiente de plástico con tapa se acopló un motor que proporciona agitación mecánica por medio de una paleta de teflón, para someter a lavados y enjuagues al papel. El primer lavado del papel se llevó a cabo con NaOH 0.1 M, seguido de HCl 0.1 M y extran neutro 2% v/v respectivamente. Cabe resaltar que antes de usar otra solución para lavado se hicieron enjuagues con agua destilada (los enjuagues se realizaron hasta alcanzar el pH del agua destilada, pH=5.42). Para separar la pulpa de papel de las soluciones de lavado y del agua de enjuague, se usó filtración al vacío con papel filtro en un embudo Buchner acoplado a un Kitasato de 2 L. Una vez lavado el papel se secó a 90 °C, se trituró y almacenó [11].

B. *Implementación de técnica analítica*

Se realizó una curva de calibración de ácido cítrico en un espectrómetro de UV-vis, marca: Perkin Elmer, modelo: Lambda 35 [12]. Para la cuantificación del ácido cítrico se utilizó el método de la piridina-anhídrido acético [5].

C. *Preparación de soluciones buffer*

La elaboración de buffer se llevó acabó como describe G. Speight para tener pH 2 y 3 usando HCl 0.1 M y glicina 0.1 M [13].

D. *Diseño de experimentación factorial 2k*

Se eligieron 3 factores (variables independientes) con 2 niveles por cada factor, la región de los factores que producen la respuesta óptima en la producción de ácido cítrico fueron pH, temperatura y concentración de metales [12], véase tabla I. Las variables independientes también son conocidas como factores controlables (véase figura 1).

En la figura 1 se puede apreciar un diagrama para el proceso de fermentación dentro de un biorreactor, usando a *A. niger*, donde se tiene una entrada (celulosa de papel) y una salida (ácido cítrico), además de las variables controlables (x_1, $x_2 \ldots x_p$) y las variables no controlables (z_1, $z_2 \ldots z_p$).

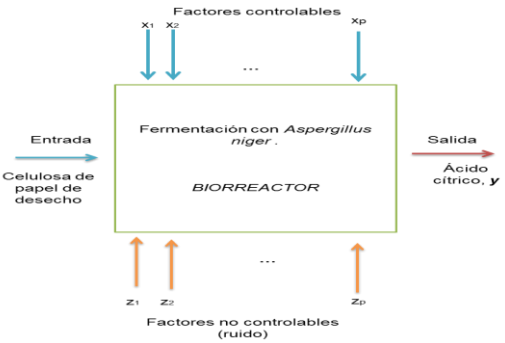

Fig. 1. Diagrama de experimento para fermentación con *A. niger* (Biorreactor) [12].

En la tabla I, se observan los factores, niveles reales y codificados (-1, 1) para el diseño de experimentación factorial 2^k.

TABLA I. Niveles reales y codificados para el diseño de experimentación factorial 2^k

Variables independientes	*Símbolo*	*Código y niveles reales*	
		-1	*1*
A: pH (UpH)	X_A	2	3
B: Temperatura (°C)	X_B	30	40
C: Concentración de metales (ppb)	X_C	1 Cu, 75 Zn, 56 Mn Alta	0.5 Cu, 72 Zn, 51 Mn Baja

Para generar el diseño experimental factorial 2^k de este estudio se utilizó el software STATGRAPHICS Centurion XVI®, resultando 16 corridas aleatorizadas para los 8 experimentos (con una réplica por cada uno), véase tabla II. La metodología de superficie de respuesta fue utilizada para estudiar los efectos principales y combinados (interacciones) entre el *pH, temperatura y concentración de metales* durante la operación de los biorreactores. Se usó la representación gráfica de superficie de respuesta tridimensional para visualizar los efectos en la concentración de ácido cítrico esperado como una función de los factores elegidos (variables controlables o independientes). La forma gráfica de la relación entre la respuesta y las variables independientes proporciona información relevante para elegir el grado del polinomio que modela dicha relación, véase figura 3 de la cual se deduce que un *modelo de primer orden* es adecuado para modelar los datos estadísticos.

Para estimar la respuesta de la variable dependiente (***Y***) y predecir el punto óptimo se ejecuta una regresión lineal múltiple en STATGRAPHICS Centurion XVI® y se tiene la siguiente expresión:

$$Y = \beta_0 + \beta_A x_A + \beta_B x_B + \beta_C x_C \quad (1)$$

Donde ***Y*** (concentración de ácido cítrico, ppm) es la respuesta calculada (el predicho), β_0 es el efecto promedio global, x_A, x_B y x_C son variables independientes (efectos principales) y β_A, β_B y β_C son constantes de los efectos principales en la regresión lineal múltiple.

Sin embargo, en la ecuación (1) no se contemplan los efectos provocados por las *interacciones*, por lo que se ejecutó otra regresión lineal múltiple, de tal forma que el modelo se expresa como sigue:

$$Y = \beta_0 + \beta_A x_A + \beta_B x_B + \beta_C x_C + \beta_{AB} x_A x_B + \beta_{AC} x_A x_C + \beta_{BC} x_B x_C + \beta_{ABC} x_A x_B x_C \quad (2)$$

Donde ***Y*** (concentración de ácido cítrico, ppm) es la respuesta calculada (el predicho), β_0 es el efecto promedio global, x_A, x_B y x_C son variables independientes (efectos principales), β_A, β_B, β_C, β_{AB}, β_{AC}, β_{BC} y β_{ABC} son constantes de los efectos principales y sus interacciones de la regresión lineal múltiple.

III. Inóculo: espora sexual (conidios) de *Aspergillus niger 10* inmovilizada.

En esta etapa se operaron biorreactores a 30 °C y 40 C° para inmovilizar la espora sexual de *Aspergillus niger 10* adaptada a producir enzimas celulolíticas para desdoblar la celulosa de papel, se usó como sustrato celulosa de papel y como cosustrato glucosa. En esta etapa se observó que la biomasa tiene un crecimiento diáuxico y la actividad de las enzimas celulolíticas se observó mediante el incremento en la concentración de glucosa en el medio de cultivo. Al día 7 se separó la celulosa de papel del licor post-fermentativo por filtración al vacío con papel filtro en un embudo Buchner acoplado a un Kitasato de 2 L. Posteriormente se resuspendió la celulosa de papel en 250 mL de agua ultrapura estéril por separado, es decir, la celulosa de papel de los biorreactores que operaron a 30 °C, se resuspendió y almacenó. Lo mismo ocurrió con la celulosa de papel de los biorreactores que operaron a 40 °C, se resuspendió y almacenó. Estas resuspensiones fueron usadas como inóculo para los biorreactores en el diseño experimental factorial 2^k. Cabe resaltar que la resuspensión de celulosa de papel obtenida de los biorreactores que operaron a 30 °C fue utilizada como inóculo para los experimentos que operaron a esa temperatura en el diseño de experimentación. Lo mismo ocurre con la resuspensión de celulosa de papel obtenida de los biorreactores que operaron a 40 °C [11].

IV. Germinación, operación de los biorreactores.

Fueron usados para esta etapa matraces Erlenmeyer de 2 L (biorreactores), en cada matraz se colocaron 20 g de papel (pre-tratado), un agitador magnético, 2 difusores y 1 L de medio de cultivo con la siguiente composición: NaCl 0.32 g/L, KH_2PO_4 2.47 g/L, NH_4NO_3 6.6 g/L, $CaCl_2$ 0.48 g/L, $MgSO_4 \cdot 7H_2O$ 0.38 g/L, $FeSO_4$ 0.124 g/L, aceite vegetal de canola 1 mL, oligoelementos 1 mL. Oligoelementos: $ZnSO_4 \cdot 7H_2O$ 2.2 g/L, H_3BO_3 2.2 g/L, $MnCl_2 \cdot 4H_2O$ 0.5 g/L, $CoCl_2 \cdot 6H_2O$ 0.16 g/L, $CuSO_4 \cdot 5H_2O$ 0.16 g/L. Los medios de cultivo se esterilizaron a 121 °C y 15 psi, durante 15 minutos. Se inoculó cada biorreactor con 20 mL de suspensión (obtenida en la etapa anterior). Cada biorreactor cuenta con una parrilla para proporcionar calor y mantener la temperatura deseada, además de agitación magnética para mantener homogeneidad en el medio de cultivo. Durante la germinación se operó a temperatura ambiente (25 °C), agitación de 100 rpm, flujo de aire estéril de 0.3 lpm, después de 5 horas el flujo de aire se aumentó a 1 lpm, la agitación a 200 rpm y la temperatura se incrementa a (30 o 40) °C, esto depende del experimento que se esté ejecutando del diseño experimental [12].

Durante 7 días, se tomaron muestras de 10 mL a intervalos de tiempo de 24 horas; cada muestra se filtró en papel filtro con tamaño de poro de 11 µm para lo cual se utilizó un equipo de filtración Millipore. La reacción de las enzimas celulolíticas se detuvo agregando 0.5 mL de HCl puro a cada muestra, las muestras se congelaron para analizar ácido cítrico posteriormente. Al primer día de operación se agregaron a cada biorreactor 10 mL de etanol absoluto (facilita a la célula la excreción del ácido cítrico). El agua con la que se trabajó en los experimentos es Ultrapura (conductividad: 0.055 µS/cm). Para las concentraciones de metales (Cu, Zn y Mn) se utilizaron estándares Titrisol [12].

V. Resultados y Discusión

A. *Análisis estadístico*

Los resultados obtenidos a partir de las 16 corridas experimentales llevadas a cabo de acuerdo con el diseño de experimentación factorial 2^k, se resumen en la tabla II. La regresión lineal múltiple se utilizó para calcular el predicho y determinar las condiciones de fermentación óptimas que dieron como resultado la concentración máxima de ácido cítrico. Mediante la aplicación del análisis de regresión lineal múltiple sobre los datos estadísticos, se obtiene la expresión de la ecuación (3) con R^2=0.7243, para representar la relación entre la concentración de ácido cítrico y las variables independientes (los efectos de pH, temperatura y concentración de metales):

$$Y = 3397.84 + 1098.67x_A - 722.734x_B - 28.9587x_C \quad (3)$$

En la ec. (3) no se contemplan los efectos provocados por las *interacciones*, por lo que se ejecutó nuevamente la regresión lineal múltiple contemplando estos efectos, obteniendo la expresión de la ecuación (4) con R^2=0.9978, el modelo así ajustado explica el 99.78% de la variabilidad en la concentración de ácido cítrico (el predicho, véase tabla II):

$$Y = 3397.84 + 1098.67x_A - 722.734x_B - 28.9587x_C - 442.91x_Ax_B - 101.38x_Ax_C + 363.987x_Bx_C - 559.961x_Ax_Bx_C \quad (4)$$

TABLA II. Diseño de experimentación factorial 2^k, así como la respuesta observada y el predicho de la variable dependiente (concentración de ácido cítrico, ppm)

Corrida	Factores						Respuesta	
	Valores codificados			Valores reales			Concentración de ácido cítrico (ppm)	
	X_A	X_B	X_C	X_A	X_B	X_C	Observado	Predicho
1	-1	-1	-1	2	30	Baja[a]	3353.02	3430.52
2	1	1	1	3	40	Alta[b]	3023.13	3004.55
3	1	-1	1	3	30	Alta	*5847.01*	*5727.79*
4	1	-1	-1	3	30	Baja	5508.45	5596.52
5	-1	-1	1	2	30	Alta	1671.01	1727.47
6	-1	1	-1	2	40	Baja	1002.85	1022.98
7	1	1	-1	3	40	Baja	3628.89	3657.18
8	-1	1	1	2	40	Alta	2887.64	3015.72
9	-1	-1	-1	2	30	Baja	3508.01	3430.52
10	-1	1	-1	2	40	Baja	1043.09	1022.98
11	-1	1	1	2	40	Alta	3143.78	3015.72
12	1	-1	1	3	30	Alta	*5608.57*	*5727.79*
13	1	1	1	3	40	Alta	2985.98	3004.55
14	-1	-1	1	2	30	Alta	1783.91	1727.47
15	1	1	-1	3	40	Baja	3685.47	3657.18
16	1	-1	-1	3	30	Baja	5684.59	5596.52

[b]Alta (1 Cu, 75 Zn, 56 Mn) ppb, [a]Baja (0.5 Cu, 72 Zn, 51 Mn) ppb

En la tabla III se presenta el ANOVA que particiona la variabilidad de la concentración de ácido cítrico en piezas separadas para cada uno de los efectos, con la finalidad de evaluar la significancia de cada efecto comparando su cuadrado medio contra un estimado del error experimental. En este caso, 6 efectos tienen un valor-P menor que α=0.05, indicando que son significantes con un nivel de confianza del 95%.

TABLA III. Análisis de Varianza (ANOVA) para la regresión lineal múltiple de los datos estadísticos (concentración de ácido cítrico)

Fuente	Suma de Cuadrados	Gl	Cuadrado Medio	Razón-F	Valor-P
A:pH	1.93E+07	1	1.93E+07	1664.19	***0.0000***
B:Temperatura	8.36E+06	1	8.36E+06	720.15	***0.0000***
C:Concentración de metales	13417.7	1	13417.7	1.16	0.3179
AB	3.14E+06	1	3.14E+06	270.46	***0.0000***
AC	164446	1	164446	14.17	***0.007***
BC	2.12E+06	1	2.12E+06	182.66	***0.0000***
ABC	5.02E+06	1	5.02E+06	432.3	***0.0000***
bloques	16991.1	1	16991.1	1.46	0.2656
Error total	81236.7	7	11605.2		
Total (corr.)	3.82E+07	15			

B. *Optimización de la fermentación para obtener ácido cítrico*

Con la finalidad de optimizar las variables que influyen en la producción se ácido cítrico a partir de papel de desecho, se generó un diagrama de Pareto estandarizado para la concentración de ácido cítrico, véase figura 2, donde se pueden apreciar los efectos estandarizados para los factores y sus combinaciones (en sus niveles codificados), A: pH, seguido de B: Temperatura son los efectos estandarizados principales para este proceso. Se aprecia para C: Concentración de metales un efecto estandarizado bajo, sin embargo, la concentración de metales tiene un efecto importante al combinarse con A y B. Esta identificación de los efectos principales facilitó la elección del factor que se mantendrá constante para generar el gráfico tridimensional, en este caso será C: Concentración de metales. La superficie de respuesta resultante mostró el efecto en la concentración de ácido cítrico esperado como una función del pH y la temperatura, véase figura 3.

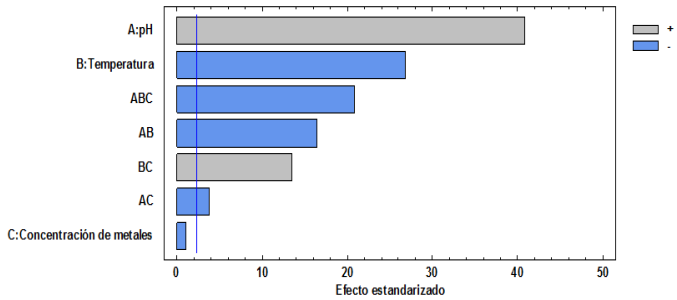

Fig. 2. Diagrama de Pareto estandarizado para la concentración de ácido cítrico.

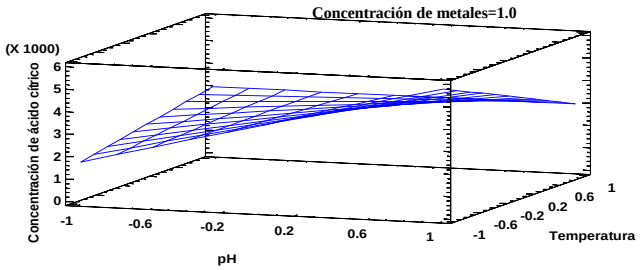

Fig. 3. Superficie de respuesta tridimensional que indica la concentración de ácido cítrico esperada como una función del pH y temperatura.

En la figura 3 se aprecia la superficie de respuesta tridimensional donde la obtención de ácido cítrico esperado es una función del pH y temperatura. Las condiciones de fermentación óptimas obtenidas con MSR fueron pH 3, temperatura de 30 °C y concentración de metales alta.

La validez de los resultados predichos por el modelo de regresión lineal múltiple, se confirmó mediante la realización de un experimento con una réplica en condiciones de fermentación óptimas (es decir, pH de 3, temperatura de 30 °C y concentración de metales alta). Los resultados obtenidos demostraron que la media de la concentración máxima de ácido cítrico (5727.7890 ppm) obtenida fue un valor cercano

al calculado con la ecuación 4 (5727.7893 ppm). La excelente correlación entre los valores predichos y obtenidos experimentalmente, véase tabla II, indica la validez del modelo de respuesta.

VI. Conclusiones

En el presente trabajo se desarrolló un proceso biotecnológico, en el cual se modelaron y optimizaron variables elegidas para la producción de ácido cítrico a partir de papel de desecho, usando a *Aspergillus niger 10* para sacarificar la celulosa y posteriormente producir ácido cítrico. Esas variables fueron pH, temperatura y concentración de metales. La obtención de este ácido orgánico ocurre durante el metabolismo del microorganismo, a nivel de mitocondria, donde surten efecto los metales traza usados para este proceso: éstos inhiben parcialmente la *aconitasa* en el ciclo de los ácido tricarboxílicos, de tal forma que el anión citrato se acumula en la mitocondria, luego el ácido cítrico es expulsado al citoplasma para posteriormente ser excretado al medio de cultivo. Las siguientes conclusiones se pueden extraer de este estudio.

- La metodología de superficie de respuesta demostró las condiciones óptimas para la producción de ácido cítrico a partir de papel de desecho, pH de 3, temperatura de 30 °C y concentración de metales alta. En estas condiciones, se obtuvo la concentración máxima 5727.79 ppm de ácido cítrico.

- La fermentación para obtener ácido cítrico está influenciada principalmente por los efectos provocados por el pH y la temperatura, seguido de la concentración de metales que tiene un efecto bajo, sin embargo, el efecto de ésta variable es importante al interactuar con el pH y la temperatura.

- El análisis de regresión lineal sobre los datos estadísticos representó la relación entre la concentración de ácido cítrico y las variables independientes (pH, temperatura y concentración de metales), explicando un 99.78 % de la variabilidad en la concentración de ácido cítrico (predicho), durante la fermentación con *Aspergillus niger 10.*

Agradecimientos

Los autores agradecen a la UAM-A y al CONACYT, por el apoyo otorgado para la conclusión de este trabajo.

REFERENCIAS

[1] Soccol, C. R.; Vandenberghe, L. P.; Rodrigues, C.; Pandey, A. (2006). New perspectives for citric acid production and application. *Food Technology Biotechnology. 44(2):141-149.*

[2] Mostafa, Y. S.; Alamri, S. A. (2012). Optimization of date syrup for enhancement of the production of citric acid using immobilized cells of *Aspergillus niger*. *Saudi Journal of Biological Sciences.* 19:241-246.

[3] Femi-Ola, T. O.; Atere, V. A. (2013). Citric acid production from brewers spent grain by *Aspergillus niger* and *Saccharomyces cerevisiae. International Journal of Research in BioSciences.* 2(1): 30-36.

[4] Kareem, S. O.; Akpan, I.; Alebiowu, O. O. (2010). Production of citric acid by *Aspergillus niger* using pineapple waste. *Malaysian Journal of Microbiology*. 6(2):161-165.

[5] Kobomoje, O. S.; Mohammed, A. O.; Omojasola, P. F. (2013). The production of citric from shea nut shell (*Vitellaria paradoxa*) using *Aspergillus niger. Pelagia Research Library. Advances in Applied Science Research.* 4(2):25-28.

[6] Sukesh, K.; Jayasuni, J. S.; Gokul, C. N.; Anu, V. (2013). Citric acid production from agronomic waste using *Aspergillus niger* isolated from decayed fruit. *Journal of Chemical, Biological and Physical Sciences.* 3(2):1572-1576.

[7] Amenaghawon, N. A.; Nwaru, K. I.; Aisien, F. A.; Ogbeide, S. E.; Okieimen, C. O. (2013). Application of Box-Behnken desing for the optimization of citric acid production from corn starch using *Aspergillus niger. British Biotechnology Journal.* 3(3):236-245.

[8] Areguamen, S. O.; Amenaghawon, N. A.; Agbroko, N. T.; Ogbeide, S. E.; Okieimen, C. O. (2013). Modelling and statistical optimization of citric acid production from solid state fermentation of sugar cane bagasse using *Aspergillus niger. International Journal of Sciences.*2:56-62.

[9] *Barrington, S.; Kim, J. S.; Wang, L.; Kim, J-W. (2009).* Optimization of citric acid production by *Aspergillus niger* NRRL 567 grown in a column bioreactor. *Korean Journal of Chemical Engineering.* 26(2):422-427.

[10] Gurpreet, S. D.; Satinder, K. B.; Surinder, K.; Mausam, V. (2013). Bioproduction and extraction optimization of citric acid from *Aspergillus niger* by rotating drum type solid-state biorreactor. *Industrial Crops and Products. 41: 78-84.*

[11] Guzmán, G. R.; González, B. M. M.; Solís, C. H. E. (2013). *Inmovilización-Adaptación de Aspergillus niger 10 para la biotransformación de celulosa de papel a ácido cítrico.* Memorias del IV Congreso Internacional de Docencia e Investigación en Química. UAM-A. D.F., México.

[12] Guzmán, G. R. (2013). *Obtención de ácido cítrico a partir de papel como Residuo Sólido Urbano poor fermentación con Aspergillus niger 10.* Tesis de Maestría en Ciencias e Ingeniería Ambientales. UAM-A. D.F. México.

[13] G. Speight, J. (2005). Lange's Handbook of Chemistry. USA. Mc Graw-Hill. pp 80-81 Sección 5.

Necesidad de redefinir la ingeniería y su método como base y fundamento en la formación de un ingeniero

Víctor Alcántara Alza
Escuela de Post Grado, Sección: Doctorado en Ingeniería
Universidad Nacional de Trujillo, UNT
Trujillo, Perú
Victoralc_unt@hotmail.com

***Resúmen*--- Aunque la ingeniería es considerada, hoy en día, como claramente distinta de la ciencia, los componentes científicos en la educación de los ingenieros transmiten la idea de que la ingeniería es, poco más que la mera aplicación de las ciencias exactas y naturales a la realidad práctica. Para esclarecer esta visión, se propone hacer un análisis acerca de las bases en que se fundamenta el conocimiento en ingeniería, estableciendo su método, con la finalidad de iluminar algunos de los atributos típicos y distintivos de este nuevo tipo de conocimiento basado en la moderna tecnología**.

Resulta imposible definir al ingeniero por lo *que* hace, ya que en la actualidad sus especialidades son muy variadas. Es el *como* lo hace lo que marca la identidad de un ingeniero; es decir, es el método el que lo define. Por otro lado, el uso que el ingeniero hace del conocimiento científico es puramente instrumental, pues su interés se centra en predecir comportamientos y no explicar leyes empíricas.

En la actualidad, las tres dimensiones del conocimiento en la formación de todo profesional son: el aprendizaje cognitivo, el aprendizaje práctico y el aprendizaje moral, y en esto está incluida la formación del ingeniero. Por lo tanto, su formación ya no puede seguir siendo orientada únicamente por la asimilación de puras tecnologías fundadas en las ciencias básicas. Se hace necesario adquirir otras competencias que están fuera del conocimiento puramente cognitivo.

Definido el estatus epistemológico de la ingeniería, estableciendo el criterio de demarcación entre el científico y el ingeniero y analizando la función del ingeniero en el contexto global actual, podemos redefinir la ingeniería, para luego sentar las bases que permitan establecer los perfiles de su formación profesional independientemente del lugar donde se forme.

Palabras clave--- Epistemología, Ciencia e Ingeniería, Tecnología, Tecnociencia, heurística.

I. INTRODUCTION

La distinción tradicional entre ciencias puras y aplicadas fue recogida de Mario Bunge por los años 60 del siglo pasado [1] y las versiones revisadas en Mitcham y Mackey, 1972, y Rapp, en 1974 [2,3]. En su artículo Bunge hizo la propuesta de entender la ingeniería como una clase específica de ciencia aplicada.

Bunge explica que no es la orientación hacia la satisfacción de las necesidades lo que marca la diferencia entre ciencia pura y aplicada, "pero el límite debe trazarse entre el investigador que busca una nueva ley de la naturaleza y el investigador que aplica las leyes conocidas por el diseño de una cosa útil". Mientras el primero quiere entender mejor las cosas, este último desea mejorar nuestro dominio de ellas. Esto deja en claro que el ingeniero está apuntando a fines prácticos, mientras que el científico pretende conocimiento cognitivo. Esta definición de Bunge sobre la Ingeniería ha sido y sigue siendo un paradigma hasta la fecha.

La tesis que se sostiene en el presente artículo es que la Ingeniería es algo más que ciencia aplicada.

Las propuesta de Bunge no excluye que las ciencias de ingeniería hagan uso de idealizaciones o de conceptos teóricos, de lo contrario no serían capaces de predecir objetivos que resultan de la aplicación de las tecnologías. Pero estas predicciones no funcionan como pruebas de las teorías en cuestión, la idea detrás de ellas es "encontrar lo que se debe hacer con el fin de llevar a cabo, prevenir o simplemente cambiar el ritmo de los acontecimientos en el curso de un modo pre asignado. Por lo tanto, la ingeniería como una ciencia aplicada no puede consistir en la mera aplicación de la ciencia pura. Las ciencias aplicadas tienen sus propias metas y en consecuencia, sus propios métodos.

Si bien el Ingeniero puede aplicar conceptos derivados de la ciencia también aplica otros que son propios de su disciplina y que no existen en la ciencia o que son utilizados de manera diferente. Para el Ingeniero el conocimiento no es un fin en sí mismo sino solo un medio para lograr sus objetivos siempre vinculados con el diseño, construcción y operación de objetos y artefactos.

Muchos investigadores [4, 5, 6] afirman que el conocimiento de ingeniería es más que ciencia aplicada: tiene diferentes propósitos, utiliza diferentes métodos para producir conocimientos muy diferentes con diferentes resultados. Sin embargo, el trabajo realizado en esta área tiende a permanecer

en el nivel de conjeturas acerca de las diferencias bastante superficiales en el contenido de las disciplinas.

La mayoría de epistemólogos concuerdan en que un Ingeniero es un tecnólogo, pero no siempre un tecnólogo es un Ingeniero. Por lo tanto, *buscar las bases epistemológicas del conocimiento en Ingeniería implica buscar la posibilidad de una epistemología en la misma Tecnología.*

Por otro lado, se hace necesario definir con precisión lo que es la ingeniería moderna y como debe centrar el ingeniero su labor dentro del contexto global actual, lo que nos permitirá sentar las bases sobre las cuales se debe construir todo currículo o programa que pretenda formar un ingeniero que responda a las exigencias de la actual modernidad.

II. POSIBILIDAD DE UNA EPISTEMOLOGIA EN LA TECNOLOGIA.

La posibilidad de plantear una epistemología en la tecnología se sustenta sobre la prueba empírica que mostraría que la tecnología es un conocimiento. Si la tecnología es un conocimiento, entonces sus actividades entran en la epistemología. La prueba la provee Hugo Padilla quien sostiene la existencia de un conocimiento obtenido a raíz de generalizaciones, nacidas a su vez, de la resolución práctica de problemas tecnológicos llegando a la conclusión: ***"Es posible adquirir conocimientos desde una generación de las funciones y creación de la tecnología"*** [7]. Luego entonces, si la tecnología es un conocimiento, está implicada dentro de los problemas de la epistemología, por lo que se hace necesario estudiar de qué modo la tecnología aporta información a la ciencia. Podemos adelantar que sus relaciones con la ciencia son, por lo menos, las siguientes: verificación de paradigmas científicos, aporte de soluciones prácticas a problemas teóricos, generalizaciones reformulables en términos científicos, ampliación de la ciencia básica o corroboración de la ciencia básica. No es posible separar ciencia y tecnología pues son partes de un mismo proceso [8]

En cuanto a la tecnología se observan algunas limitaciones: (1) No se tiene claridad en cuanto a qué es tecnología e innovación tecnológica; lo cual permite que se establezcan filtros mentales y sociales que detienen el proceso de conocer en su especificidad y en su generalidad, depositando el asunto en una especie de futuro venidero, (2) La definición de tecnología, como la aplicación del conocimiento científico parece no llenar las exigencias epistemológicas que un proceso de creación de tecnología requiere. ¿Por qué decimos que no satisface? Porque basta estudiar cualquiera de los paradigmas clásicos de la teoría de la ciencia, para ver su inconsistencia y su sentido empirista.

No se trata de aplicar sin más, el conocimiento científico para crear tecnología. Para poder crear algo hay que saber, no sólo cuáles son sus fundamentos científicos, sino hay que saber cómo hacerlo. Este *cómo hacerlo* es lo que diferencia y permite hacer tecnología (teoría tecnológica), que es un conocimiento nuevo de un determinado objeto o fenómeno. Entonces, no es a partir del pensamiento puro que se debe determinar o definir la tecnología, son más bien las condiciones sociales las que determinan cierto grado de desarrollo tecnológico, sobre la cual debe definirse.

La tecnología debe ser discutida en el plano de un conocimiento nuevo, que se adquiere a partir de una apropiación de una necesidad sentida por el hombre en sociedad. Puesto que sólo mediante el aporte de diferentes disciplinas y criterios acerca del desenvolvimiento del hombre y sus necesidades, es que se logra un pensamiento lo suficientemente explicativo, de lo que son esas necesidades, del porqué de las mismas, y de cómo vencerlas y superarlas.

III. ESTATUS EPISTEMOLOGICO DE LA INGENIERIA.

Al generar la tecnología un nuevo tipo de conocimiento y siendo la Ingeniería una de las más altas expresiones de la tecnología, nos queda discutir en que estatus epistemológico se encuentra la ingeniería moderna.

Según H. Poser, la ingeniería es un modo de conocimiento distinto de la ciencia por sus métodos y sus objetivos. Por sus métodos, porque existe un método ingenieril que es heurístico y, por sus objetivos, porque la ingeniería no se propone alcanzar leyes explicativas y predictivas sino la solución de problemas acotados dentro de tiempos muy breves [9]. Poser establece que el estatus epistemológico de la ingeniería correspondería a una ciencia tecnológica, diferenciándola de la tecnología, debido a que, en su opinión, ésta se refiere a procesos reales y artefactos.

Para alcanzar su propósito, Poser establece la distinción tradicional entre ciencia pura y ciencia aplicada con la creatividad como criterio discriminador. Esto le permitió establecer la diferencia entre reglas y leyes, el saber cómo y el saber por qué. Por otro lado, nuestro autor discute el criterio que pretende identificar la distinción entre ciencia e ingeniería en base al diseño de artefactos, ya que hoy, debido a los adelantos tecnológicos, no es posible tratar los artefactos de la manera tradicional. Poser se pregunta ¿es una oveja clonada un artefacto? ¿El trasplante de corazón o la implantación de un marcapasos me convierte en un artefacto? Al tratar de responder estas interrogantes, nos vemos enfrentados al hecho de que el contenido semántico de muchos términos propios del conocimiento de los ingenieros ha cambiado a tal punto que se hace necesaria una revisión profunda. Por lo tanto se debe marcar la diferencia entre ciencia e ingeniería a partir de aspectos metodológicos y no ontológicos.

Por otro lado ¿Podemos avanzar en la diferenciación entre ciencia e ingeniería considerando la creatividad como un elemento distintivo? Consideramos que no. Primero, que si bien el método heurístico implica creatividad por parte del ingeniero, ésta no es una facultad primordial. Segundo, que es posible enseñar y aprender ingeniería sin ser creativo. Entonces, ¿cuáles serían los elementos diferenciadores entre ciencia e ingeniería? Es sin duda el método empleado en ambas disciplinas.

Considerando que la ciencia busca una verdad universal, la ingeniería no se fija ni en la verdad ni en la universalidad. El telos del ingeniero es utilitario, mientras que la teleología del científico es cognitiva.

Respecto a los métodos, la ingeniería se caracteriza por el uso de una metodología heurística centrada en procesos o diseño tecnológico que permitan la transformación de una situación A en otra B para lograr un fin utilitario. La ciencia en cambio, utiliza el método explicativo que se caracteriza por su estructura nomológico-deductiva.

También podemos considerar que la creatividad tampoco es un elemento distintivo entre ciencia e ingeniería pues ambos dominios del conocimiento requieren de ella. Un científico puro busca leyes, pero también crea teorías o hipótesis que sirven para explicar la realidad que estudia. Las teorías científicas son creaciones de la mente humana, y toda teoría científica es siempre provisional [10].

Se observa pues que tanto la ciencia como la ingeniería se proponen ser racionales; ambas pretenden ser dominios naturalistas, ambas son falibalistas, pues aceptan que sus resultados son provisionales.

La diferencia metodológica que lo distingue es la siguiente: El método científico comienza con la observación de un fenómeno para luego ser explicado por medio de una conjetura o hipótesis que no es otra cosa que la respuesta a una 'pregunta de investigación científica'. De manera distinta, el método heurístico, se configura a partir de una anomalía detectada en la praxis cotidiana. Esta anomalía no exige preguntas de investigación, sino que demanda soluciones. Las soluciones se pueden o no expresar en lenguaje matemático, sin embargo, no son hipótesis que se sometan a contrastación como lo hace la ciencia. Por el contrario, la solución a un problema de ingeniería, o anomalía detectada en el campo de la ingeniería, es el resultado de la aplicación de una norma práctica, que a su vez, ha sido desarrollada en el ámbito de la misma ingeniería. Una solución favorable no representa una ley de carácter universal sino que se restringe a una regla de utilidad práctica de carácter local y dentro de una especialidad y temporalidad determinadas. Por lo tanto, la ingeniería no genera leyes ni teorías sino que, en el mejor de los casos, guías de buenas prácticas acotadas a la solución de problemas específicos.

Walter Vicente [11], afirma que para poder resolver los problemas de ingeniería, los ingenieros aplican distintos conocimientos que ayudan al diseño y que están basados en orígenes de diversa extracción, algunos provenientes de la ciencia y otros desarrollados internamente por la propia Ingeniería, algunos claramente distinguibles y otros no. Independientemente de su origen todos estos conocimientos comparten el hecho de que son de utilidad para la solución de problemas prácticos.

Eugene Ferguson [12], plantea la tesis de que gran parte del progreso tecnológico se debe a una gran cantidad de decisiones que son y deben ser tomadas por el tecnólogo de un modo no científico, de un modo creativo e intuitivo y por ende altamente subjetivo y no atado a las reglas de la ciencia. Ferguson expresa que el uso que el ingeniero hace del conocimiento científico es puramente instrumental, en el sentido que solo le interesa su capacidad para predecir comportamientos y no su potencialidad para explicar leyes de la naturaleza. Es por ello que la ingeniería sigue haciendo uso de teorías y modelos que ya han sido descartados por la ciencia por su pérdida de verosimilitud, pero que siguen siendo útiles con fines instrumentales para la actividad del ingeniero.

IV. SOBRE EL METODO HEURISTICO

La heurística se define como la estrategia, método o criterio usado para hacer más sencilla la solución de problemas difíciles. El conocimiento heurístico es un tipo especial de conocimiento usado por los humanos para resolver problemas complejos. Según George Pólya [13], la base de la heurística está en la experiencia de resolver problemas y en ver cómo otros lo hacen. Consecuentemente se dice que hay búsquedas ciegas, búsquedas heurísticas (basadas en la experiencia) y búsquedas racionales.

En ingeniería, la heurística es un método basado en la experiencia que puede utilizarse como ayuda para resolver múltiples problemas, como en el diseño, lo usamos desde cuando calculamos los recursos necesarios, hasta cuando planeamos las condiciones de operación de los sistemas.

Decimos que la heurística crea conocimiento, pues nos da las hojas de ruta, o procedimientos de cómo resolver problemas nuevos, en base a un saber instrumental o *Know how*, que puede encontrarse en la experiencia acumulada de un Ingeniero experimentado, o en la base de datos de cualquier ordenador. Otro ejemplo de utilización de la heurística, la tenemos en el ámbito de la optimización, como cuando tratamos de describir el algoritmo adecuado para optimizar procesos o sistemas; pues se sabe, que en todo *problema de optimización* existen diferentes soluciones, donde el objetivo es encontrar la mejor. De forma más precisa, estos problemas se pueden expresar de la manera, como encontrar el valor de unas *variables de decisión* para los que una determinada *función objetivo* alcanza su valor máximo o mínimo. El valor de las variables en ocasiones está sujeto a unas *restricciones*.

Podemos encontrar una gran cantidad de problemas de optimización, tanto en la industria como en la ciencia. Desde los clásicos problemas de diseño de redes de telecomunicación u organización de la producción hasta los más actuales en ingeniería y reingeniería de software. En este sentido podemos decir, "Un método heurístico es un procedimiento para resolver un problema de optimización bien definido mediante una aproximación intuitiva, en la que la estructura del problema se utiliza de forma inteligente para obtener una buena solución.". En los últimos años ha habido un crecimiento espectacular en el desarrollo de procedimientos heurísticos para resolver problemas de optimización en ingeniería. Este hecho queda claramente reflejado en el gran número de artículos en publicados en revistas especializadas. En 1995 se editó el primer número de la revista *Journal of Heuristics* dedicada íntegramente a la difusión de procedimientos heurísticos [14].

V. INGENIERO Ó CIENTIFICO? : CRITERIO DE DEMARCACIÓN.

Resulta imposible definir al ingeniero por lo *que* hace, ya que las actividades que cubre en sus distintas especialidades son muy variadas: telecomunicaciones, obras públicas, industria, agricultura, montes, minas, aeronáutica, por citar

algunas de las más conocidas. Es *como* lo hace lo que marca la identidad de un ingeniero; es decir, es el método lo que lo define. Sin embargo, este método es difícil de precisar por ser el resultado de la conjunción de capacidades creativas, conocimientos y habilidades, todos ellos difíciles de concretar. En todo caso, es algo que se aprende con el ejercicio de la profesión, pero que requiere que se asienten adecuadamente las bases en las Escuelas en las que se forman los ingenieros.

El científico se forma para alcanzar la exactitud, la precisión y la generalidad en un dominio muy limitado de conocimiento, con el que se aísla en su gabinete o en su laboratorio, y produce resultados en forma de proposiciones que se expresan mediante enunciados o expresiones matemáticas; mientras que el otro adopta una postura mucho más pragmática en la búsqueda de soluciones efectivas y satisfactorias a problemas concretos, sin poder sustraerse a toda su complejidad, lo que hace normalmente en forma de máquinas, artefactos o sistemas. El primero es, por lo tanto, un conocimiento que gira sobre sı mismo; mientras que el segundo se "sale" del dominio del conocimiento para nutrir el mundo concreto de los objetos artificiales.

Tanto en ingeniería como en ciencia se emplean representaciones matemáticas que por su propia naturaleza son buenas aproximaciones. Pero, estas aproximaciones tienen un carácter distinto para la ciencia y para la ingeniería. Para la primera son meramente transitorias en una búsqueda persistente e interminable de la verdad, mientras que para la ingeniería el carácter aproximado es inherente a su propio método, ya que es el producto en correcto funcionamiento es lo que sanciona la labor del ingeniero.

El ingeniero debe combinar hábilmente los procedimientos disponibles para alcanzar la solución deseada, mediante una peculiar mezcla de métodos analíticos e intuición, para llegar a un objeto que presente el comportamiento artificial que él persigue. El diseño de un coche, de un avión o de un teléfono móvil no se desprende de ningún cuerpo teórico preestablecido, ya que no hay ningún método ni ninguna teoría o conjunto de ellas que los "cubra". Puede que existan conocimientos previos que permitan el cálculo de alguna de sus partes, o que sugieran soluciones a algunos de los sub problemas que presenta el diseño, pero la concepción del conjunto no se desprende de ninguna disciplina teórica. Los métodos analíticos, que tanta importancia tienen en la moderna ingeniería, nunca aportan una solución completa al problema. Tienen que ser complementados con procesos creativos, por una parte, y con exhaustivos experimentos relacionados directamente con el sistema en cuestión, por otra. Todo ello hace que el diseño en ingeniería sea un proceso complejo en el que se despliegan múltiples habilidades por parte de los que lo llevan a cabo.

En algunos casos, puede ser el propio ingeniero el que elabore una teoría, desprendida del caso concreto en que está trabajando, alimentando así lo que se han venido en denominarse*: ciencias de la ingeniería*. Sin embargo, esto no es lo general, y ese modo de actuar sólo sería usado normalmente por ingenieros que trabajen en centros de investigación. El ingeniero, carente de un conocimiento completo respecto a aquello que está diseñando, tiene que recurrir por lo general a reglas heurísticas [15].

Como dijo H. Simón: el científico se ocupa de las cosas como *son*, mientras que el ingeniero lo hace de cómo *deben ser* para lograr un determinado objetivo [16]. Algo análogo expresó el ingeniero aeronáutico Theodore von Karman: el científico describe lo que *es*; el ingeniero crea lo que *nunca ha existido*. Estas dos citas ilustran de forma patente las diferencias entre un científico y un ingeniero. Lo que no excluye que exista una frontera permeable entre unos y otros, y que una misma persona pueda ser las dos cosas: pero siempre lo será en momentos diferentes. Cuando actúe como científico su meta será conocer las propiedades de las cosas, en último extremo las leyes que gobiernan los procesos que son de su interés; mientras que cuando actúa como ingeniero lo que hará es contribuir a producir el mundo artificial en el que vivimos. En consecuencia, en cada uno de los casos el canon al que se sometería sería distinto. Por otra parte, el ingeniero atiende un problema concreto, un caso particular – ha sido formado para resolver problemas específicos–. Si alcanza soluciones generalizables, tanto mejor, pero ese no es su objetivo final [17].

En resumen el ingeniero científico; es aquel ingeniero que hace ciencia sobre los objetos artificiales, para contribuir a concebirlos, calcularlos y explotarlos y que asume como labor la reflexión metódica y sistemática sobre los propios conocimientos para el progreso del mundo artificial.

VI. EL INGENIERO EN EL CONTEXTO GLOBAL ACTUAL

El mundo actual está regido por una sociedad de economía globalizada. Esas fuerzas económicas justifican las demandas de reformas, transformaciones, alteraciones, adecuaciones y cambios de paradigmas coherentes con el modelo empresarial modernizante. En este contexto la educación superior debe cumplir su nuevo papel dentro de las exigencias de la globalización económica y de la llamada "sociedad del conocimiento y de la información".

Para que las actuales instituciones que forman Ingenieros estén en sintonía con la dinámica del cambio global, es necesario que ellas busquen nuevas opciones de enseñanza. La experiencia reciente muestra que estas instituciones están respondiendo sólo a las necesidades inmediatas que demanda la disponibilidad de nuevas tecnologías convergentes en el sector industrial. Por lo tanto, es urgente realizar esfuerzos permanentes de planeación en el área de educación en ingeniería, teniendo en cuenta que la educación superior debe adaptarse de la mejor manera posible *a los cambios económicos y sociales.*

El objetivo central es ofrecer una visión para la formación de las futuras generaciones de estudiantes y aportar elementos que puedan servir como ideas previas para el desarrollo de procesos de planeación de la educación en ingeniería.

Las tres dimensiones del conocimiento que debemos reconocer para la formación de profesionales son: el aprendizaje cognitivo, el aprendizaje práctico y el aprendizaje moral y en esto está incluida la formación del ingeniero. Por lo

tanto, debemos tener en cuenta la importancia de una planeación estratégica en las carreras de profesionales en investigación, desarrollo e ingeniería (RD&E), pues es fundamental para el desarrollo de la economía de un país.

En el mundo moderno, toda empresa que no es innovadora está condena al fracaso. Las empresas *requieren cada vez perfiles profesionales más altos*, lo que obliga a sus integrantes a una permanente capacitación, que no debe ser una mera acumulación de información inútil y estéril, mientras no la transforme en conocimiento nuevo y aplicativo como producto de su creatividad. La creatividad es solo una de las tantas competencias que debe tener todo Ingeniero.

Por lo expuesto, la formación del ingeniero ya no puede sólo seguir siendo orientada hacia la asimilación de tecnologías para resolver problemas relativos a la instalación, operación y mantenimiento de los sistemas productivos. Este conocimiento especializado debe ir acompañado de nuevas competencias que la Industria moderna exige, a partir del cual se podrá establecer los perfiles de formación de todo ingeniero, independientemente del lugar donde se forme. Estas capacidades son:

1. Desarrollo de habilidades de comportamiento humano.
2. Comunicación.
3. Trabajo en equipo
4. Habilidades interpersonales
5. Inteligencia emocional
6. Ética y autonomía moral
7. Desarrollo continuo de capacidades y competencias: Aprendizaje de por vida en ingeniería
8. Creatividad.
9. Liderazgo
10. Habilidades gerenciales.

VII CONCLUSIONES.

1. La ingeniería se distingue de la ciencia, por su método, que fundamentalmente es heurístico; método que aspira a establecer normas estables, que indiquen como proceder para conseguir un fin predeterminado.
2. La aplicación de la ciencia es solo parte del saber Ingenieril; lo que no significa que la ciencia no represente ningún rol, sino que este no es el único, ni necesariamente el más importante. El uso que el ingeniero hace del conocimiento científico es puramente instrumental.
3. El Ingeniero debe estar capacitado para actuar como científico; pero debe hacerlo, buscando leyes y/o teorías que den mayor sustento a la tecnología. Cuando actúe como ingeniero lo que debe buscar es cambiar o innovar el mundo artificial en que vivimos. El tipo de investigación: científica y/o tecnológica que reciban en su formación definirá su modo de actuar.
5. El conocimiento especializado debe ir acompañado de las competencias arriba señaladas; las que se deben adquirir dentro de su propia formación, empleando estrategias especializadas y planificadas; pues estas competencias, mayormente se adquieren fuera del campo puramente cognitivo.
6. Se concluye que formar un Ingeniero, significa formar un profesional, con amplias capacidades de desarrollo humano, capaz de crear conocimiento científico y/o tecnológico, que permita transformar o innovar la realidad, según las exigencias que demande el progreso del mundo moderno en que vivimos.

REFERENCIAS

[1] M. Bunge:, Technology as applied science. technology and culture, 7:329-347, 1966; revised version reprinted in Mitcham and Mackey (below), pp. 62-76, and in Rapp (below), pp. 19-39.

[2] C. Mitcham, and R. Mackey: “Philosophy and technology”, readings in the philosophical problems of technology. New York: free press. eds.1972.

[3] F. Rapp, “Contributions to a philosophy of technology: studies in the structure of thinking in the technological sciences” . Dordrecht: Reidel. ed. 1974.G. Eason, B. Noble, and I. N. Sneddon, “On certain integrals of Lipschitz-Hankel type involving products of Bessel functions,” Phil. Trans. Roy. Soc. London, vol. A247, pp. 529–551, April 1955. *(references)*

[4] A. D. De Figueiredo, Toward an epistemology of engineering. Retrieved from http://ssrn.com/paper=1314224, 2013

[5] S. Johnston, P. Gostelow, E. Jones: “Engineering and society: an Australian perspective”. (2nd Ed.). Melbourne: Longman, 1999.

[6] E. Layton: Technology as knowledge. Tech nology and culture, 15(1), 31-41., 1986.

[7] H. Padilla: “Los objetos tecnológicos y su base gnoseológica”. en: varios autores. La filosofía y la ciencia en nuestros días (México: editorial Grijalbo, 1976), pp. 157-170.

[8] D. Jiménez y Q. Gil,: Aportes para una epis temología de la tecnología (bases para una epistemología de la tecnología), 2012.

[9] H. Poser: “On structural differences between science and engineering”. phil & tech 4:2, 1998.

[10] S. Hawking, ”Historia del tiempo” edit. Orbis, Barcelona 2005, pp. 27-28

[11] W.G. Vincenti: “What engineers know and how they know it”: analytical studies from aeronautical history: johns hopkins university press. 1990.

[12] E. Ferguson: “Engineering and the mind’s eye”, mit pres, massachusetts. USA. 1999.

[13] G. Polya., “How to solve it”, Princenton University press, second edition, 1945.

[14] R.. Martí Cunquero, Algoritmos heurísticos en optimización combinatoria, Departamento de Estadística e Investigación Operativa, Universidad de Valencia, España.2006.

[15]] K. Billy Vaughn:. “Discussion of the Method” OxfordmUniversity Press. 2003.

[16]] H. Simon: “The Sciences of the Artificial”. The MIT Press. 1996. Versión española: Las ciencias de lo artificial, Comares 2006

[17] P. Forman:. The primacy of science in modernity, of technology in postmodernity, and of ideology in the history, 2007.

Rompiendo las barreras químicas y de ingeniería para la producción de biocombustibles: biorefinerías de la próxima generación*

Felipe de Jesus Ortega García
Gerencia de Servicios Químicos
Instituto Mexicano del Petróleo
México, D.F.
fjortega@imp.mx

Elizabeth Mar_Juárez
Gerencia de Transformación de Biomasa
Instituto Mexicano del Petróleo
México, D.F.
emar@imp.mx

***Abstract*— Impulsada principalmente por el evidente cambio climático, la producción de combustibles derivados de biomasa se ha acelerado significativamente. La producción de hidrocarburos "verdes" es una visión que paulatinamente se hace realidad para sustituir al menos parcialmente a los combustibles derivados del petróleo. Sin embargo, muchas de las rutas hasta ahora estudiadas, si bien resuelven el problema técnico, no son competitivas frente a los métodos de producción convencionales; el reto es que sin modificar la infraestructura actual (por ejemplo ductos, motores) el proceso de bio-refinación pueda incorporarse a las refinerías tradicionales y que la producción de estos combustibles verdes sean equivalentes energéticamente a los derivados del petróleo. Teniendo presente esto, se propone como ejemplo un par de esquemas de procesamiento de lignocelulosa para coadyuvar a la producción de combustibles en las refinerías.**

Keywords*— *biodiesel, biorrefinerías, catálisis, economía

I. INTRODUCCIÓN

Antes del descubrimiento de los combustibles fósiles de bajo costo, nuestra sociedad dependía de la biomasa vegetal para satisfacer su demanda de energía. El descubrimiento de petróleo crudo, y su uso masivo en el siglo XX, creo una fuente de combustibles líquidos de bajo costo que ayudó a industrializar el mundo y a mejorar los niveles de vida.

Ahora, con la disminución de los recursos petroleros de fácil acceso, combinado con el aumento de la demanda de petróleo por parte de las economías emergentes, y las preocupaciones políticas y ambientales sobre los combustibles fósiles, es imperativo desarrollar un proceso de producción de combustibles y productos químicos que sean sostenibles, eficientes y viables económicamente [1].

A este respecto, la biomasa vegetal es la única fuente sostenible de carbono orgánico que tiene la característica particular de producir combustibles similares a los derivados del petróleo, pero con la enorme ventaja de que generan significativamente menos emisiones de gases de efecto invernadero en comparación con los combustibles fósiles e incluso pueden ser neutrales en emisiones dependiendo de los métodos de producción de los biocombustibles [1,5]

El costo actual de la biomasa es significativamente menor que el del petróleo crudo y varía según el tipo y la región. Conforme a datos de la Unión Europea, el costo de la biomasa por barril equivalente de petróleo (bep)[1] varía de entre US$ 11 para los residuos industriales sólidos a US$ 39 para los cultivos energéticos [5,12]. En los Estados Unidos se estima que el costo de la biomasa lignocelulósica tiene un costo de US$ 5 a 15 / bep, [1,8], que es significativamente inferior al costo actual de petróleo crudo que registra un costo de US $ 56 / barril (costo promedio en 2005) [7]. En el caso de México, el precio promedio en lo que va del presente año (2015) es de US$ 44.8 /barril para la mezcla mexicana [10]. A pesar de la caída de los precios del petróleo, la diferencia de precio entre la biomasa y el petróleo es significativa y si a esto le adicionamos consideraciones geoestratégicas el precio de la biomasa como bien estratégico lo sitúa en una posición hegemónica.

Para concluir con esta visión sobre como los bioenergéticos serán parte del panorama mundial, es importante mencionar que la historia tiene ciclos y estos se repiten. A mediados de la década de 1890, la biomasa suministraba más del 90% de la demanda energética, sin embargo para iniciar el siglo XX, los combustibles fósiles se convirtieron en el recurso energético preferido [11]. Si bien el petróleo se convirtió en la base energética del mundo al contribuir con el 47% del total energético, la biomasa continua siendo parte de la canasta de combustibles de diversos países como son Suecia, 17.5%; Finlandia, 20.4%; y Brasil, 23.4% [3]. De acuerdo a estimaciones internacionales se tiene que para el 2030 el 20% del combustible para el transporte y el 25% de los productos químicos serán producidos a partir de biomasa [3,4,8].

[1] Para realizar equivalente energético, se empleó la información reportada por Klass [2], el cual considera que el contenido de energía de 1.0 tonelada métrica de biomasa lignocelulósica seca equivale a 3.15 barriles de petróleo, y 1 barril de petróleo tiene 5.904 GJ.

Esta transición a una economía base biomasa ya está ocurriendo en muchos países y se están creando los marcos legales y económicos para que suceda de forma más rápida, por ejemplo Alemania, Austria, Italia, Polonia, España, Alemania y Suecia, dan una exención fiscal al transporte que emplee biocombustibles, mientras que el Reino Unido otorga una exención fiscal parcial [12]. La Unión Europea incluso proporciona un crédito de carbono de $ 54 / ha para los agricultores que siembran cultivos energéticos utilizados para la producción de biodiesel y bioetanol [12].

Para continuar en la transición a la economía base biomasa, es vital reducir los costos de las tecnologías de procesamiento para la conversión de la biomasa en combustibles y productos químicos. El propósito de este trabajo es presentar algunos métodos que pueden aplicarse actualmente al sistema de refinación e integrar los bioenergéticos a las refinerías tradicionales con la meta de producir combustibles para el transporte a partir de la biomasa. Se presentan una serie de opciones con una evaluación económica para sustentar su viabilidad.

II. LIGNOCELULOSA COMO COMBUSTIBLE

Los biocombustibles líquidos producidos a partir de biomasa lignocelulósica puede ser una respuesta para ampliar el espectro de opciones energéticas que requiere el país, además permite crear nuevos puestos de trabajo, mejorar la economía del campo nacional, reducir las emisiones de gases de efecto invernadero, y mejorar los índices de seguridad energética.

Es importante mencionar que México viene trabajando una serie de medidas para incorporar a los bioenergéticos dentro de la matriz de combustibles desde el 2006 [13]. Es decir se cuenta con un marco legal y acciones políticas que buscan promover el uso extendido de la biomasa para producir energéticos, asimismo existe una serie de avances tecnológicos tanto en agricultura como biotecnología que han hecho posible que la materia prima base lignocelulosa sea económicamente viable al ubicarse en alrededor de los $ 15 por barril equivalente de petróleo.

La ventaja de trabajar con biomasa lignocelulósica es que se puede producir de manera sostenible sin afectar las actividades propias del sector alimentario, forrajero y forestal. El cuello de botella en esta opción energética se ubica en tres puntos clave: el transporte de la biomasa al centro de procesamiento, el costo del pretratamiento y la falta de tecnología para la conversión eficiente de la biomasa en combustibles líquidos.

Idealmente, sería deseable usar cultivos energéticos que requieren de pocos nutrientes, fertilizantes y energía de entrada. También sería deseable tener un proceso de conversión de biomasa total a un combustible de transporte que pueda fácilmente encajar en la infraestructura existente. En la práctica, es imposible convertir toda la energía de la biomasa en un combustible, igual que es imposible convertir toda la energía del petróleo en gasolina y diesel. Las tecnologías de conversión tienen una amplia gama de eficiencias energéticas como se discutirá en esta revisión.

En este análisis nos centramos en la conversión de biomasa en un combustible con las tecnologías tradicionales que se encuentran en una refinería de petróleo. Algunas tecnologías actuales de biomasa han sido criticadas porque tienen una baja eficiencia de conversión térmica global, en los que sólo una pequeña parte de la energía de la planta se convierte en el producto final de combustible. Los biocombustibles se encuentran en una etapa temprana, y es probable que los avances en la tecnología de conversión y la integración de procesos evolucionen para mejorar su eficiencia técnica y económica. Nuevas tecnologías de conversión de biomasa se están desarrollando con una eficiencia térmica más alta que las tecnologías tradicionales [14,15], y es necesario que continuemos desarrollando nuevas rutas tecnológicas.

Además, el fitomejoramiento está produciendo plantas que tienen mayores rendimientos, que requieren menos agua, que pueden crecer en tierras áridas, y cuyo consumo de fertilizantes es menor.

Producir biocombustibles para el transporte también está requiriendo que pensemos en nuevas formas de tecnologías para los vehículos, como son las membranas de electrolito, las celdas de combustible, vehículos eléctricos híbridos y la mejora en los sistemas de compresión para el encendido de los motores.

La elección de la materia prima particular dependerá en última instancia de los rendimientos de los cultivos, de las condiciones regionales, de la coproducción de alimentos, la economía, de la eficiencia térmica y el ciclo de vida. El proceso de la biomasa inicia separando la parte comestible y la no comestible; la fracción no comestible puede entonces ser convertida en un combustible. Los nutrientes de la biomasa también pueden ser reutilizados para emplearse nuevamente en el crecimiento de la biomasa (Figura 1).

Mientras que en diferentes países se han realizado diversas investigaciones orientadas a desarrollar tecnologías centradas en romper las barreras biológicas de los biocombustibles, principalmente para producir etanol[19,29], nuestra visión se centra en producir combustibles líquidos como la gasolina y el diesel a partir de la biomasa.

La producción de combustibles de hidrocarburos a partir de biomasa tiene muchas ventajas. En primer lugar, los combustibles de hidrocarburos "verdes" son esencialmente los mismos que los actualmente derivados del petróleo, excepto que se producen a partir de biomasa, por ello no es necesario modificar la infraestructura existente (por ejemplo, tuberías y motores) y los procesos de biorrefinación se pueden conjuntar con los sistemas de producción de combustible de las refinerías de petróleo existentes. En segundo lugar, los combustibles de hidrocarburos basados en biomasa son energéticamente equivalentes a los combustibles derivados del petróleo. Tercero los combustibles verdes a partir de biomasa lignocelulósica son inmiscibles en agua; se elimina la necesidad de una etapa de destilación que resulta cara por su consumo de energía.

En cuarto lugar los procesos químicos de producción de combustibles son mucho más rápidos en comparación con los

procesos biológicos y tan flexibles que las unidades de producción se pueden instalar cerca de la fuente de biomasa.

Fig. 1. Producción de combustibles verdes a partir de biomasa en un proceso de conversión integrado

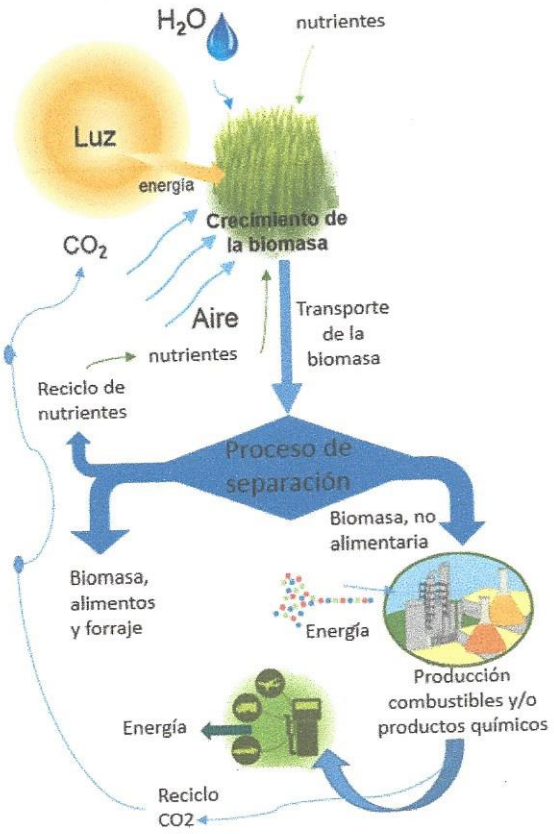

Fuente: *Realización propia con esquema de EM Rubin Nature **454**, 841-845 (2008) doi:10.1038/nature07190 & Huber et al [13]*

En quinto lugar, la cantidad de agua necesaria para el procesamiento de hidrocarburos combustibles a partir de biomasa puede ser reducido en gran medida, en comparación con la producción basada en azúcares diluidas a las que se someten enzimas. Esto es porque los catalizadores orgánicos o heterogéneos funcionan bien en soluciones concentradas de agua.

Finalmente, los catalizadores heterogéneos son inherentemente reciclables. Para que puedan ser utilizados a lo largo de meses e incluso años, lo que reduce significativamente los costos en comparación con los procesos biológicos [14].

La eliminación de una etapa de destilación intensiva en energía, tener velocidades de reacción más altas, y una huella de carbón reducida por cambio de procesos, pueden resultar en menores costos en la producción de biocombustibles en comparación con las rutas biológicas como sucede actualmente para la producción de etanol celulósico [15].

III. VIABILIDAD DE PRODUCIR BIOCOMBUSTIBLES A PARTIR DE BIOMASA LIGNOCELULÓSICA

El objetivo de la presente investigación es describir aquellas tecnologías y procesos que resulten competitivas en una economía regida por los precios del petróleo, teniendo presente la tesis del Premio Nobel de Medicina, François Jacob, titulada "Le jeu des possibles, essai sur la diversité du vivant" (1981), la cual señala básicamente que al combinar dos sistemas diferentes surgirá un tercero evolucionado. Aquí proponemos que la unión de un sistema de biomasa más un sistema de refinación de petróleo, al parecer conjuntos excluyentes, al unirlos surgirá un tercer conjunto con innovaciones, es decir se iniciara la evolución de las biorrefinerías. Este concepto abrirá opciones para realizar una transición rápida hacia una economía verde, donde se tenga como base el petróleo mientras surge como energético emergente la biomasa en tanto evolucionan/innovan los equipos y diseños tradicionales. Para llegar a esta meta, es importante continuar con el estudio y diseño de catalizadores y de todos aquellos desafíos involucrados en la producción de biocombustibles.

Emplear biomasa lignocelulósica ofrece un espectro amplio de materias que pueden emplearse sin afectar el mercado alimentario y forestal de un país. La incorporación de los bioenergéticos a una economía tradicional es posible.

Técnicamente es factible convertir materiales lignocelulósicos y desechos orgánicos en biocombustibles. Desde mediados de 1990, se han desarrollado diversas técnicas que han permitido probar catalizadores y comprender la interfaz catalizador – reacción, estas técnicas incluyen microscopios de alta resolución, espectroscopia láser y la espectroscopia de resonancia magnética nuclear. Las cuales han permitido mejorar el conocimiento de las propiedades de la estructura en relación con las reacciones de conversión catalítica de la biomasa. En conjunto, estas y otras herramientas relacionadas están ayudando a desentrañar los secretos de las reacciones químicas a escala molecular.

El dióxido de carbono, agua, luz, aire y nutrientes son los insumos para la producción de biocombustibles. La obtención de biocombustibles y alimentos son las salidas. Las tres principales áreas donde es necesario concentrar esfuerzos deben orientarse a: (1) el crecimiento acelerado, de bajo costo, competitivo y sustentable de biomasa; (2) el desarrollo de procesos eficientes y rentables para la conversión de biomasa en combustibles; y (3) la optimización de los mecanismos apropiados para su integración a los sistemas de producción de combustibles actuales. (Figura 1) [12].

A. Tratamiento de biomasa vía catalítica

La biomasa puede convertirse en diferentes tipos de combustibles de hidrocarburos "verdes", como gasolina, diesel y combustible para aviones. A través de las tecnologías de conversión que se describen más adelante, los combustibles de hidrocarburos derivados de biomasa son virtualmente indistinguibles de hidrocarburos a base petróleo, particularmente con respecto a su densidad energética. Las ventajas adicionales de hidrocarburos derivados de biomasa

incluyen eliminar los costos de separación e infraestructura pues su compatibilidad con la infraestructura actual, no hay necesidad de realizar modificaciones en el motor o a los sistemas de distribución.

El procesamiento catalítico es la principal técnica empleada para producir combustibles líquidos a base de petróleo. Este mismo concepto puede aplicarse a la producción de combustibles de hidrocarburos líquidos derivados de biomasa lignocelulósica.

Existen diferentes tecnologías de conversión las cuales presentan una gama amplia de eficiencias. Existen avances en las tecnologías de conversión y su integración a procesos actuales permitirá mejorar la eficiencia energética general del proceso y su viabilidad económica de los biocombustibles. Los biocombustibles líquidos pueden ser producidos a través de una amplia gama de procesos (Figura 2).

Fig. 2. Esquemas de producción de combustibles verdes a partir de biomasa empleando rutas biológicas y químicas

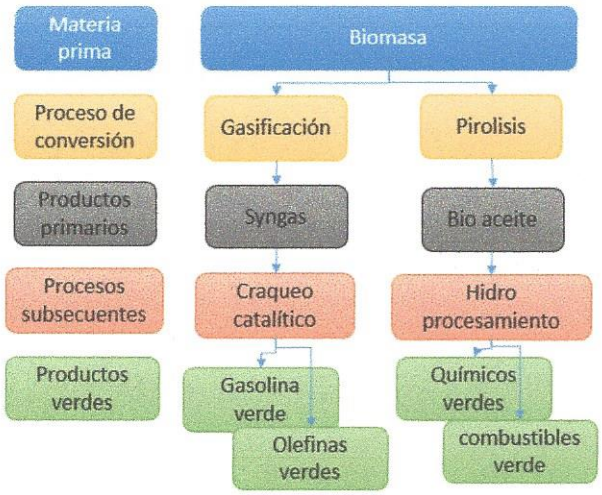

Fuente: *Realización propia con esquemas IMP*

B. Catalizadores

Para la catálisis de la biomasa se emplean dos tipos de catalizadores: los biológicos o los químicos (Tabla 1). Los catalizadores biológicos, tales como la levadura que se usa para producir etanol, son catalizadores homogéneos, lo que significa que están en la misma fase líquida como la alimentación de biomasa. Aunque la humanidad ha estado utilizando catalizadores biológicos en la fermentación (es decir, la producción de etanol) por miles de años, sólo recientemente los catalizadores heterogéneos se han aplicado para la producción de biocombustibles [16]. Los catalizadores químicos difieren de los catalizadores biológicos en diferentes aspectos (Tabla 1).

Los catalizadores químicos van desde de ácidos homogéneos hasta catalizadores heterogéneos sólidos. Si bien los catalizadores químicos funcionan a temperaturas significativamente más altas que los biológicos, también tienen velocidades de reacción mucho mayores y pueden operar en un conjunto más amplio de condiciones.

Un punto de interés sobre el tipo de catalizador a emplear es el tiempo de producción que se desea, por ejemplo el tiempo de residencia para una reacción utilizando catalizadores biológicos se mide en días en comparación con segundos o minutos para los catalizadores químicos.

Los catalizadores biológicos son muy selectivos para ciertas clases de reacciones tales como la hidrólisis y la fermentación. Los catalizadores químicos también pueden ser selectivos para ciertas clases de reacciones y se pueden producir nuevas clases de catalizadores químicos para usos específicos que trabajen con materias biológicas específicas.

TABLA 1. DIFERENCIAS ENTRE PROCESOS CATALÍTICOS

Aspectos	Catálisis biológica	Catálisis química
Productos	Alcoholes	Diferentes combustibles
Condiciones de reacción	Menores a 70°C, 1 atm	100 – 1200 °C, 1 – 250 atm
Tiempo de residencia	2 – 5 días	0.01 segundos a 1 hora
Selectividad	Puede ser muy selectivo (más del 95%)	Depende de la reacción. Necesitan desarrollarse nuevos catalizadores con una selectividad mayor al 95%
Costos del catalizador	US $ 0.50/galón de etanol (se estima el costos de las enzimas celulasa y los requerimientos de azúcar) US $ 0.04/ galón de etanol base maíz	US $ 0.01/ galón de gasolina (costo para una industria madura)
Esterilización	Esterilización de la materia prima (se están desarrollando enzimas que no requieran la esterilización de la materia prima)	No necesaria
Reciclo	No es posible por el momento	Con catalizadores sólidos
Tamaño de la planta_biomasa celulósica	2,000 – 5,000 ton/día	100-2,000 ton/día

Fuente: *Realización propia con esquemas IMP*

Los catalizadores biológicos también son más caros que la mayoría de los catalizadores químicos. Por ejemplo el Departamento de Energía de los Estados Unidos estima que el costo de las enzimas celulasa para la producción de etanol se ubica entre $ 0.30 a 0.50 dólares por galón de etanol [17, 24]. En contraste, el costo de los catalizadores químicos en la industria del petróleo oscila alrededor de 0.01 dólares por galón de gasolina.

La mayoría de los procesos basados en catalizadores biológicos requieren que las materias primas sean esterilizadas antes de la conversión enzimática. En contraste, no se requiere ninguna etapa de esterilización para la conversión química. Los catalizadores químicos sólidos pueden ser reciclados, prolongando su vida útil por semanas e incluso años. En contraste, es difícil de reciclar catalizadores biológicos

porque no pueden ser separados fácilmente de medios acuosos, una vez que se produce el combustible.

Mientras que la mayor investigación en biocombustibles hasta la fecha se ha centrado en el desarrollo de catalizadores biológicos se debe enfatizar que las biorrefinerías futuras probablemente utilizarán una combinación de catalizadores biológicos y químicos para producir biocombustibles [19].

C. Integración de biomasa a los sistemas de refinación

El bajo costo de la biomasa y su alto potencial para producir combustibles es un gran incentivo para integrarla ya sea como combustible para calderas únicamente o para procesarla y producir combustibles líquidos. En la figura 3 se presenta un balance económico en el que se asume que tan sólo el 20 % de la biomasa se convierte en diésel y gasolina. La producción de combustibles líquidos sería de 1.67 B/ton de biomasa, lo que reportaría un beneficio bruto de 121 USD/ton de biomasa procesada, lo cual parece suficiente para cubrir los costos de procesamiento, hidrógeno, energía, infraestructura, etc.

Partiendo del hecho que se tiene un gran avance en la comprensión de la química fundamental, de la ciencia y de la ingeniería que sustenta la producción química de biocombustibles lignocelulósicos, en conjunto con los muchos avances que ya se han hecho en el desarrollo de procesos de producción de biocombustibles, la incorporación de la biomasa a los sistemas de refinación es solo cuestión de tiempo [18].

Fig. 3. Esquema económico empleando biomasa para la producción de combustibles

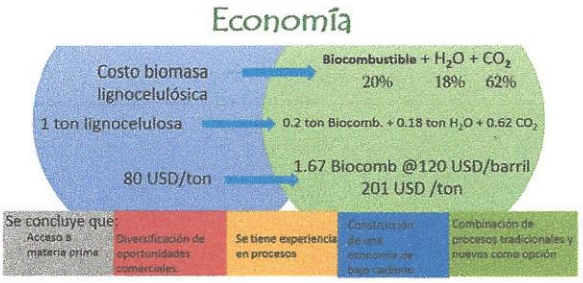

Fuente: Realización propia

La optimización de procesos es fundamental para lograr con éxito escalar las operaciones de producción de biocombustible. De acuerdo con datos de la Universidad de Massachusetts Amherst [19] es posible que el 80% de las instalaciones de producción de biomasa sean escalables a producción de combustibles verdes variando la fase final del diseño del proceso.

De igual forma, al desarrollar toda la ingeniería es importante tener presente el análisis técnico-económico para que la producción de biocombustibles a gran escala sea rentable. Se tiene detectado que los procesos que los factores de mayor peso desde el punto de vista económico incluyen las necesidades de: reducir los consumos de hidrógeno; aumentar la eficiencia y la estabilidad del catalizador; y aumentar el valor del producto final.

Teniendo presente lo anterior se realizó un ejercicio, ilustrado en la Figura 4, para la conversión de biomasa en combustibles verdes. El esquema combina los procesos de gasificación, craqueo catalítico e hidroprocesamiento conocidos y empleados ampliamente en la industria petrolera. El sistema pretende ser autónomo utilizando una parte de la biomasa para producir la energía requerida y otra para la producción de combustibles. En el proceso de desintegración catalítica las grandes moléculas constitutivas de biomasa se fragmentan produciendo gases, hidrocarburos oxigenados y coque, los hidrocarburos oxigenados se envían a la unidad de hidrotratamiento donde se saturan las olefinas generadas en el proceso y se elimina el oxígeno de la biomasa fragmentada. La energía requerida para esta transformación se suministra a través de la combustión del coque producido en el proceso. Los hidrocarburos libres de oxigeno se alimentan a una unidad hidrodesintegradora donde se fragmentan en diésel y gasolina. En la unidad gasificadora la biomasa se transforma en monóxido de carbono e hidrógeno, el primero se envía al combustor de coque para oxidarlo completamente y extraerle toda su energía, el hidrógeno se envía a las unidades hidrogenadora e hidrodesintegardora. El calor de los gases de combustión se aprovecha para secar la biomasa.

Fig. 4. Esquema de producción de combustibles verdes en un proceso de refinación tradicional (FCC-hidrotratamiento-hidrodesitegración).

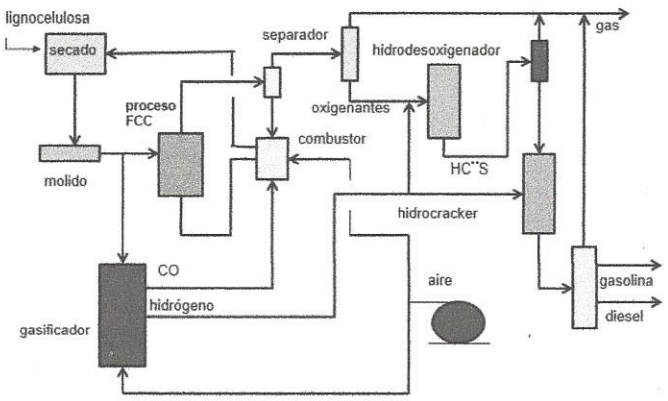

Fuente: Realización propia

En la Figura 5 se presenta otra opción viable para convertir la biomasa en diésel y gasolina a través del ampliamente conocido proceso Fisher-Tropsch que convierte el gas de síntesis en hidrocarburos líquidos (gasolina y diésel), en combinación con un proceso de gasificación. Este sistema también es autónomo y convirtiendo parte de la biomasa en la

energía requerida por el mismo. Para satisfacer los requerimientos de hidrógeno por el proceso Fisher Tropsch, se incluye una unidad productora de hidrógeno que se alimenta con parte del CO producido en la gasificación.

En la Figura 5 se presenta otra opción viable para convertir la biomasa en diésel y gasolina a través del ampliamente conocido proceso Fisher-Tropsch que convierte el gas de síntesis en hidrocarburos líquidos (gasolina y diésel), en combinación con un proceso de gasificación. Este sistema también es autónomo y convirtiendo parte de la biomasa en la energía requerida por el mismo. Para satisfacer los requerimientos de hidrógeno por el proceso Fisher Tropsch, se incluye una unidad productora de hidrógeno que se alimenta con parte del CO producido en la gasificación.

En este caso el beneficio económico bruto es alrededor de 600 USD/ton de biomasa procesada, lo cual deja un amplio margen para cubrir los costos de producción, mantenimiento, infraestructura, etc.

Fig. 5. Esquema de producción energéticamente autónomo empleando un proceso Fisher Tropsh.

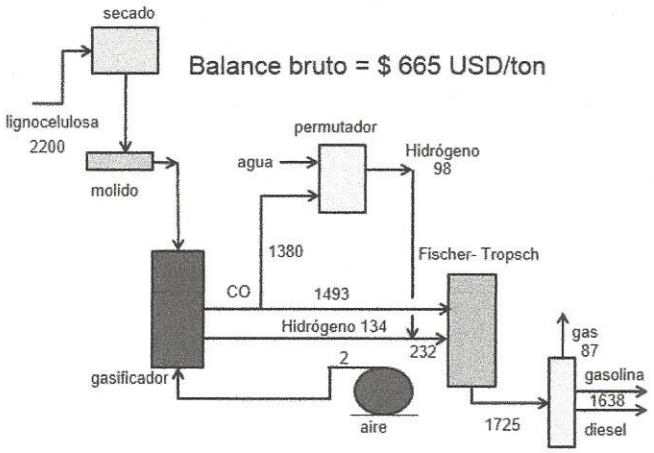

IV. BIORREFINERÍAS_PRÓXIMA GENERACIÓN PARA PRODUCCIÓN DE COMBUSTIBLES LÍQUIDOS

Una biorrefinería es un centro que integra procesos y equipos para producir combustibles, energía y productos químicos de alto valor teniendo como base la biomasa: El concepto de biorrefinería es análogo al que se emplea para una refinería de petróleo, que producen múltiples combustibles y productos de petróleo.

Un sector industrial basado en biorrefinerías se plantea como un camino prometedor a la creación de una nueva industria de base biológica. Al producir múltiples productos, una biorrefinería puede tomar ventaja de los diferentes componentes de la biomasa e intermedios y maximizar el valor derivado de la materia prima [22].

Una biorrefinería podría, por ejemplo, producir grandes volúmenes de productos químicos de alto valor o grandes volúmenes de combustibles líquidos para el sector transporte, mientras que de forma simultanea autogenera electricidad y calor de proceso para su propio uso. La producción de grandes volúmenes de combustible es importante tanto para aumentar la seguridad energética del país como para reducir las emisiones de gases de efecto invernadero [20].

Existen diferentes tipos de biocombustibles, incluyendo los combustibles que se utilizan actualmente y los que todavía están en la mesa de diseño. En términos de "elegir un ganador", es importante determinar la mejor solución posible. Si el combustible de origen biológico se ajusta al encendido por chispa motores (similar uso al de la gasolina), si no afecta la compresión en el encendido del motor (uso similar al diesel) o no afecta el funcionamiento de las turbinas (jet fuel), entonces es un ganador.

En el diseño de una ruta tecnológica "viable" es importante tener presente la siguiente pregunta: "¿Qué combustible o propiedades del combustibles tienen que cumplirse para no afectar el funcionamiento actual?" Si bien esta es una pregunta clave que se responderá en el mediano y largo plazo, los problemas inmediatos que merecen atención son: la reducción del contenido de oxígeno (un menor contenido de oxígeno aumenta la densidad energética en el contexto de procesamiento catalítico en la fase líquida de corrientes derivados de la biomasa), asegurándose de que el peso molecular está dentro del rango de los combustibles compatibles para los motores de combustión interna, y que el producto final este diseñado para optimizar la compatibilidad con los combustibles de hidrocarburos convencionales [23-25].

Por otra parte, el uso de las instalaciones de procesamiento de hidrocarburos convencionales es una opción para explotar la disponibilidad de procesamiento de combustible y la infraestructura de distribución existente para la producción de biocombustibles

La biorrefinería del futuro será análoga a la refinería de petróleo actual: un sistema altamente integrado de procesos mecánicos y químicos.

Conclusiones

La tendencia mundial es que la demanda de energía continuará aumentando, por ello es probable que los biocombustibles desempeñarán un papel cada vez más importante en nuestro futuro energético. El procesamiento de materias primas derivadas de biomasa (incluyendo celulosa, almidón, azúcar y grasas vegetales) por craqueo catalítico e hidrotratamiento es una alternativa prometedora para el futuro de la producción de biocombustibles.

La integración de la biomasa en los esquemas de refinación es una opción tecnológicamente factible que se puede implementar en el corto plazo al utilizar los propios procesos de refinación conocidos. El beneficio económico bruto es muy

atractivo y es un fuerte incentivo para realizar estudios más robustos para lograr la integración.

La biomasa es el único recurso disponible en cantidad y poder energético equiparable al petróleo, que ofrece una serie de ventajas como producir combustibles y productos químicos similares a los que demanda el mercado, sin afectar mayormente el medio ambiente. Pero también la biomasa lignocelulosa enfrenta tres obstáculos: (1) los altos costos de procesamiento ($ / galón de etanol), (2) la inversión de capital inicial ($ ~4-10 / galón de capacidad de producción de etanol anuales), y (3) logística de transporte a las centros procesadores. Tanto la tecnología de fraccionamiento de lignocelulosa y la co-utilización eficaz de los subproductos (como el ácido acético, la lignina y hemicelulosa) será vital para la puesta en marcha masiva de las biorrefinerías basadas en lignocelulosa, ya que los ingresos de co-productos aumentaría el margen de hasta 6.2 veces, dado que todos los co-productos lignocelulósicos purificados tienen precios de venta más altos (> aproximadamente 1,0 / kg) que el etanol (~ 0,5 / kg de etanol). Existe la tecnología y la materia prima para aumentar la participación de los combustibles verdes, primero en el sector transporte (por ejemplo, 30%) en el corto plazo, y aumentar la proporción en el largo plazo.

REFERENCIAS

[1] Holmgren, J."Opportunities for Biorenewables in Oil Refineries" presented at the First International Biorefinery Workshop,Washington, DC, July 2005

[2] Klass, D. L. In Encyclopedia of Energy; Cleveland, C. J., Ed.; Elsevier: London, 2004; Vol. 1.

[3] Energy Information Administration. 2015. Annual Energy Outlook 2015 with Projections to 2050. Consulta 30 Abril del 2015: http://www.eia.doe.gov/oiaf/aeo/index.html

[4] Huber, G.W.; Corma,A."Synergies between Bioand Oil Refineries for the Production of Fuels from Biomass." Angew. Chem. Int. Ed. 46, 2007

[5] Lichtenthaler, F.W. and S. Peters (2004). "Carbohydrates as green raw materials for the chemical industry." Comptes Rendus Chimie 7: 65- 90.

[6] Lange, J.-P. Lignocellulose conversion: an introduction to chemistry, process and economics. Biofuels, Bioprod. Bioref. 1:39–48, 2007.

[7] Energy Information Administration Official Energy Statistics; U. S. Department of Energy, Washington, DC, 2006; http://tonto.eia.doe-.gov/dnav/pet/pet_sum_top.asp

[8] Marinangeli, R.; Marker,T.; Petri, J.; Kalnes,T.; McCall, M.; Mackowiak, D.; Jerosky, B.; Reagan, B.; Nemeth, L.; Krawczyk, M.; Czernik, S.; Elliott, D.; Shonnard, D; "Opportunities for Biorenewables in Oil Refineries," Report No. DE-FG36-05GO15085, UOP, 2006

[9] Ugarte, D. G. D. L. T.; Walsh, M. E.; Shapouri, H.; Slinsky, S. P. The Economic Impacts of Bioenergy Crop Production on U. S. Agriculture; Agricultural Economic Report No. 816; U. S. Department of Agriculture: Washington, DC, 2003.

[10] Secretaria de economía. "Seguimiento precio del Petróleo Mezcla Mexicana (MME)". Consulta 1 Mayo 2015. http://portalweb.sgm.gob.mx/economia/es/energeticos/mezcla-mexicana.html

[11] Zhang, P. Y_H. "Reviving the carbohydrate economy via multi-product lignocellulose biorefineries" Journal of Industrial Microbiology & Biotechnolog, May 2008, Volume 35, Issue 5, pp 367-37

[12] Bendz, K. EU-25 Oilseeds and Products Biofuels Situation in the European Union 2005; GAIN Report No. E35058; USDA Foreign Agricultural Service: Washington, DC, 2005.

[13] Secretaria de Energía. " Potenciales y Viabilidad del Uso de Bioetanol y Biodiesel para el Transporte en México", Secretaría de Energía/Banco Interamericano de Desarrollo/ Deutsche Gesellschaft für Technische Zusammenarbeit. México, 2006.

[14] Huber, G. W.; Dumesic, J. A. Catal. Today 2006, 111, 119.

[15] Huber, G.W.; Iborra, S.; Corma,A. "Synthesis of Transportation Fuels from Biomass: Chemistry, Catalysts, and Engineering." Chem. Rev. 106:4044- 4098, 2006.

[16] Furimsky, E. Catalytic Hydrodeoxygenation,Applied Catalysis A: General, 199:147-190, 2000.

[17] Song, C.S. Global Challenges and Strategies for Control, Conversion and Utilization of CO2 for Sustainable Development Involving Energy, Catalysis,Adsorption and Chemical Processing. Catalysis Today, 115: 2–32, 2006.

[18] Reed,T.B.; and Guur, S.; "A survey of Biomass Gasification 200 – Gasifier Projects and Manufactures around the World", DOE Contract No. DE-AC36-83CH10093, Subcontract No. ECG- 6-16604-01(BEGF).

[19] Natural Resources Defense Council. "How Biofuels Can Help End America's Oil Dependence". The Natural Resources Defense Council. US, 2004.

[20] U.S. Department of Energy, Office of Energy Efficiency and Renewable Energy (US-DOE-EERE). 2007. Mission. Consulta noviembre 2014. Internet site: http://www.eere.energy.gov/office_eere/mission.html

[21] Lynd, L. R.; Wyman, C. E.; Gerngross, T. U. Biotechnol. Prog. 1999, 15, 777.

[22] Perlack, R. D.,Wright, L. L.,Turhollow,A. F., Graham, R. L., Stokes, B. J. & Erbach, D. C. (2005) Biomass as Feedstock for a Bioenergy and Bioproducts Industry:The Technical Feasibility of a Billion-Ton Annual Supply.

[23] Elliott, D.C. "Historical Developments in Hydroprocessing Bio-oils." Energy & Fuels, 21:1792-1815, 2007.

[24] Gayubo,A. G.,Aguayo,A.T. et al. (2005), Undesired components in the transformation of biomass pyrolysis oil into hydrocarbons on an HZSM-5 zeolite catalyst. J Chem Technol Biotechnol 80, 1244.

[25] Lange, J.-P. Lignocellulose conversion: an introduction to chemistry, process and economics. Biofuels, Bioprod. Bioref. 1:39–48, 2007. Marinangeli, R.; Marker,T.; Petri, J.; Kalnes,T.; McCall, M.; Mackowiak, D.; Jerosky, B.; Reagan, B.; Nemeth, L.; Krawczyk, M.; Czernik, S.; Elliott, D.; Shonnard, D; "Opportunities for Biorenewables in Oil Refineries," Report No. DE-FG36-05GO15085, UOP, 2006.

Diffusion path in the Sr-Fe-Mo-O compounds used for energy generation by SOFCs

J.L. Rosas, E. Carvajal and M. Cruz-Irisson
ESIME-Culhuacan, Instituto Politécnico Nacional
Av. Santa Ana 1000, México, D.F., C.P. 04430, MÉXICO
ecarvajalq@ipn.mx

M.I. Iturrios and M.C. Crisóstomo
CECyT No. 8 Narciso Bassols, Instituto Politécnico Nacional
Av. de las Granjas 618, México, D. F., C. P. 02530, MÉXICO

***Abstract*—Research and development on renewable energy sources and devices are pertinent due to the energy needs and because of the related global pollution problem. Although not all current developed alternative ways to generate energy are entirely sustainable, renewable or profitable, solid oxide fuel cells (SOFCs) are the kind of devices to obtain electricity efficiently (with efficiencies greater than 60 %) by converting the chemical energy of hydrogen rich fuels, generating a very low environmental contamination, compared to other processes. However, the high operating temperature that is needed to work optimally and the high production cost keep active the research around these promising devices. Particularly, the polycrystalline double perovskite Sr_2FeMoO_6, has been used as an electrode for SOFCs because it has good electronic and ionic conductivities. In this work, the $Sr_2Fe_{1+x}Mo_{1-x}O_6$ compounds were studied, placing hydrogen at interstitial sites. Calculating the energy associated to every occupied position by atomic H in the compounds, it is proposed a diffusive path in each compound, searching for improvements in the SOFCs' electrodes; also, the charge density modifications induced by the interstitial ion coordination is discussed in our dynamics from an energetics model. This work was carried out within the framework of the Density Functional Theory, using the Generalized Gradient Approximation and the functional proposed by Perdew-Burke-Ernzerhof.**

Keywords*—*double perovskite; solid oxide fuel cell; density functional theory; interstitial sites

I. Introduction

Renewable energy sources development and pollution beat down concerns support the research on fuel cells [1]; also, regulations are setting limits for desulfurizing the fuel sources because the sulfur content of commercial fuels troubles the equipment and the environment. Being the latter problems associated with conventional fuels, there are implemented diverse solutions, as the hydrotreating method employed at refineries, the oxidation-extraction [2] or the use of catalysts [3, 4] among others, which permitted both to achieve the standards and reduce the cost process. At the same time but in the fuel cells area, the low sulfur resistivity and carbon deposition shown by some anodic materials (as Ni) have permitted that the polycrystalline double perovskite Sr_2FeMoO_6 (SFMO) has been extensively used as a solid oxide fuel cell electrode material by many commercial manufacturers [5, 6]. Although the research on SFMO is focused around their magnetic properties because of the high spin polarization, improvements on the electronic and ionic diffusion [6] are very important, being both relevant for the fuel cell applications of this material; however, characterization on SFMO diffusivities are made on the bulk polycrystalline material without a clearly differentiation among grain boundaries diffusion and through crystalline SFMO diffusion. Because the SFMO electronic behavior is very sensitive to antisite occupation, oxygen vacancies and also to the Fe-Mo ratio content, we studied the electronic properties associated with a SFMO supercell model where it is possible to emulate both antisite occupation and different Fe-Mo content, where it is possible to locate the diffusive species at interstitial sites. The associated energies and densities of states were calculated in the Density Functional Theory (DFT) scheme, to propose a diffusion path in those Sr-Fe-Mo-O compounds.

II. Model and Computational Method

From well-known experimental information about the bulk Sr_2FeMoO_6 (*e. g.* space group I4/mmm and lattice parameters a = 5.5704 Å and c = 7.8983 Å in [7] a monocrystalline model was constructed, for which the geometry was optimized (Fig. 1). To model different composition, as well as antisite occupation, atoms at the central chain ([001] direction) were substituted, generating the out stoichiometric compounds $SrFe_{1+x}M_{1-x}oO_6$, with x = –0.50, 0.00, 0.25 and 0.50; which correspond to MMMMM, MFMFM, MFFFM and FFFFF atomic sequences (M = Mo, F = Fe) along the mentioned central chains. Once the minimum energy configuration was identified for each case, a set of high symmetry interstitial points in that cell was tagged (Table I), to put at them different atomic species and/or their ions to calculate the formation energy (E_f) of the new system. E_f can be obtained as the difference between the energies associated to: the compound with an H atom, the compound without that H and the H molecule, respectively ($E_f = E_d - (E + (1/2)\ E_{H2})$), calculated at the same theory level. From experimental results it is known that H moves away from the compound, even if it was synthesized under H atmosphere or after the operation cycle being a SOFC electrode. Then, H could be modeled as a harmonic oscillator in the sense that the smallest the perturbation on the system (the nearest to zero) it will be less difficult to return to its original state. Calculations were made within the DFT framework, with the Generalized Gradient Approximation (GGA) and the Perdew-Burke-Ernzerhof

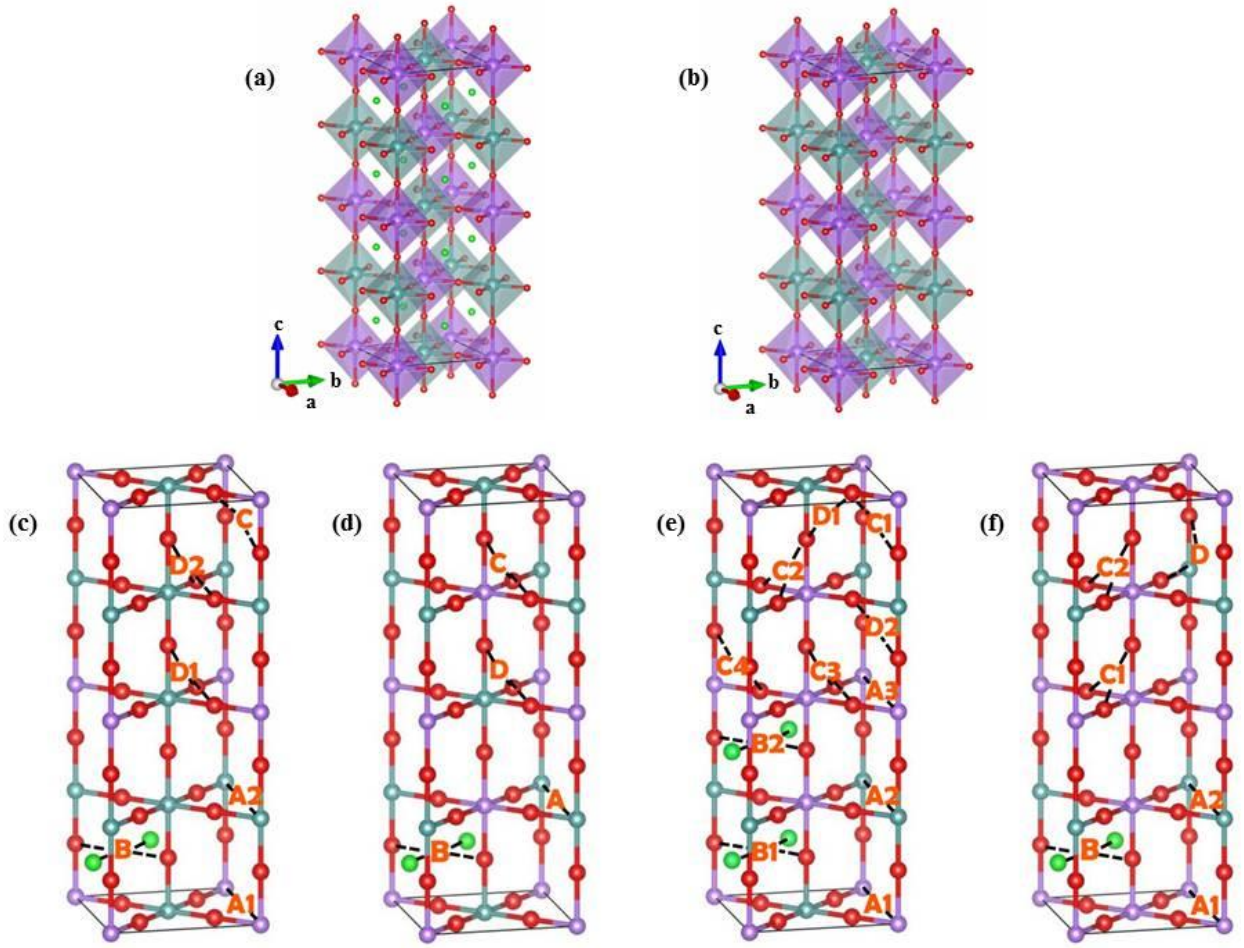

Fig. 1. Modeled monocrystalline compound Sr_2FeMoO_6. The supercell is built up using two conventional cells (a), along the [001] crystallographic direction, from which Sr atoms were erased for clarity (b). Even the octahedra were erased ((c)−(f)) to show the high symmetry points in each compound $Sr_2Fe_{1+x}Mo_{1-x}O_6$, where *x* values are −0.50, 0.00, 0.25 and 0.50 from left to right. Capital letters are used to tag sites, according to the code: A for points between transition metals; B for points at the intersection of lines from Sr−Sr and O−O; C for points at the surface of Fe centered octahedra and D for points at the surface of Mo centered octahedra. Blue, green, purple and red spheres represent Mo, Sr, Fe and O atoms, respectively.

(PBE) functional [8], as implemented in the DMol[3] code.

III. Results and Discussion

As background, we have the acknowledge that the distinctive SFMO physical behavior resides on the Fe and Mo combination, because it differs from the corresponding to the simple perovskites $SrFeO_3$ and $SrMo0_3$: the latter, even having high electric conductivity for a ceramic material, needs to be doped with trivalent elements to induce the necessary oxygen vacancies to adequate the ionic-electronic conduction [9] while the former is an ionic conductor with an O^{2-} migration barrier of 0.95 eV higher than the corresponding to the SFMO [10].

Four different high symmetry points were identified in the SFMO cell (A–D), where an H atom was fixed. Placing this atom at each A, C and D points leads to the occupation of electronic states and semiconductor behavior of the compound, contrasting with the case where H is at the B place and the compound remains half metallic (Fig. 2). It seems like the ionic conduction will be more probable when H is placed at the A or B points, because the other couple of points have associated higher energies (Fig. 3). Whereas, being H more localized at B, the compound still as a down spin electron conductor with a smaller energy gap for the up spin channel. The H should diffuse following a zigzag path nearly parallel to the [001] direction.

It is well known that the growing of the Fe/Mo ratio in the $SrFe_{1+x}M_{1-x}oO_6$ compounds (x > 0) modify the electric behavior; the material miss their half metallicity and the dilution of the electronic spin differentiation makes it a conductor (Figs. 4–5). However, placing H at sites C and D (x = 0.5) diminish drastically the number of accessible states and consequently the electronic conduction, while the C2 case must transform the material to a semiconductor. Even for small amounts of Fe atoms over the number of Mo atoms (x = 0.25), the up-spin valence band broads their energy domain leaving the superior edge at the Fermi level. That behavior is preserved when the H atom is placed at the A1, A3 or D1 sites (Fig. 5), but setting the H at the other points generates an energy gap

TABLE I. LOCATION OF THE INTERSTITIAL SITES IN THE DIFFERENT COMPOUNDS

$Sr_2Fe_{0.5}Mo_{1.5}O_6$ (x = – 0.5)			
site [a]	lattice parameter fraction		
	a = 5.5700 [Å]	**b** = 5.5700 [Å]	**c** = 15.7600 [Å]
A1	1/2	1	0
A2	1/2	1	1/4
B	1/4	1/4	1/8
C	1	7/8	15/16
D1	1/2	5/8	9/16
D2	1/2	5/8	13/16
Sr_2FeMoO_6 (x = 0)			
site	lattice parameter fraction		
	a = 5.6079 [Å]	**b** = 5.6079 [Å]	**c** = 16.0019 [Å]
A	1/2	1	1/4
B	1/4	1/4	1/8
C	1/2	5/8	13/16
D	1/2	5/8	9/16
$Sr_2Fe_{1.25}Mo_{0.75}O_6$ (x = 0.25)			
site	lattice parameter fraction		
	a=5.5885 [Å]	**b**=5.5885 [Å]	**c**=15.8565 [Å]
A1	A1	1/2	1
A2	A2	1/2	1
A3	A3	1/2	1
B1	B1	1/4	1/4
B2	B2	1/4	1/4
C1	C1	1	7/8
C2	C2	1/2	3/8
D1	C3	1/2	5/8
D2	C4	0	1/8
D3	D1	1/2	5/8
D4	D2	1	7/8
$Sr_2Fe_{1.5}Mo_{0.5}O_6$ (x = 0.5)			
site	lattice parameter fraction		
	a = 5.4924 [Å]	**b** = 5.4924 [Å]	**c** = 15.5360 [Å]
A1	1/2	1	0
A2	1/2	1	1/4
B	1/4	1/4	1/8
C1	1/2	3/8	9/16
C2	1/2	3/8	13/16
D	1/8	1	13/16

[a] Points tagged as A correspond to sites between transition metals, B is used to tag the crossing points of lines from O to O and from Sr to Sr. C and D are used to identify the points at the faces of octahedra around Fe and Mo atoms, respectively. Numerals signal environment differences for equivalent sites.

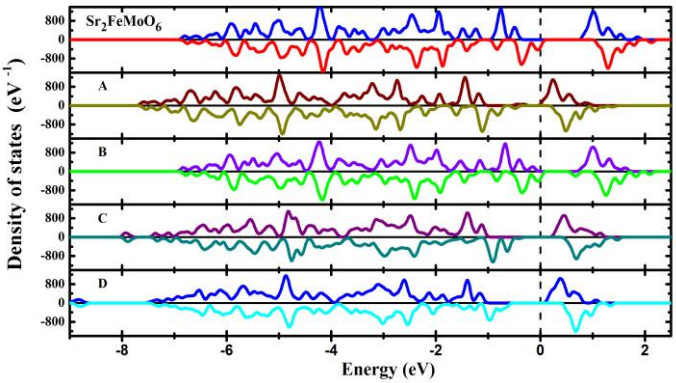

Fig. 2. Electronic density of states (DOS) for the Sr_2FeMoO_6 compound, around the Fermi level. The top graph is for the pure stoichiometric compound, the other four correspond to the same compound with an H atom located at the point tagged with the capital letter at the left. The Fermi level is marked with the discontinuous vertical line and positive and negative DOS values correspond to the up− and down−spin channels, respectively.

grow or the displacement of states toward lower energies, nevertheless above the Fermi level (*e.g.* A2, B1, B2). For the down-spin channel, just the placement of H at A2 or B2 disappear the conduction possibility for these electrons.

From the information about the energy for each system, it is possible to see that placing the H at sites A2 or C4 will not favor electronic but ionic conduction. Having the lower energies associated to locate H atoms at the set of sites these also have the Fermi level at the band borders (x = 0.25). If H is at an A2 site the Fermi level will be at the lower border of the conduction band, for the up spin channel, but occupied states are at lower energies for both spin channels. On the contrary, energy values indicate that H must prefer to move along a broken trajectory which could pass by the sites A1, A3, C2 and C3; jumping from one to another of these points, the effective displacement will be in a plane parallel to the (001) plane.

The most likely path to diffuse H in the $SrFe_{1.5}Mo_{0.5}O_6$ compound seems to be such that H jumps choosing A type points, in the middle of which there are Sr atoms, making necessary to consider the D and C two points as part of the path. Then, the route followed by the H atoms will be parallel to the (001) crystalline plane, irrespective of the necessary mentioned deviations.

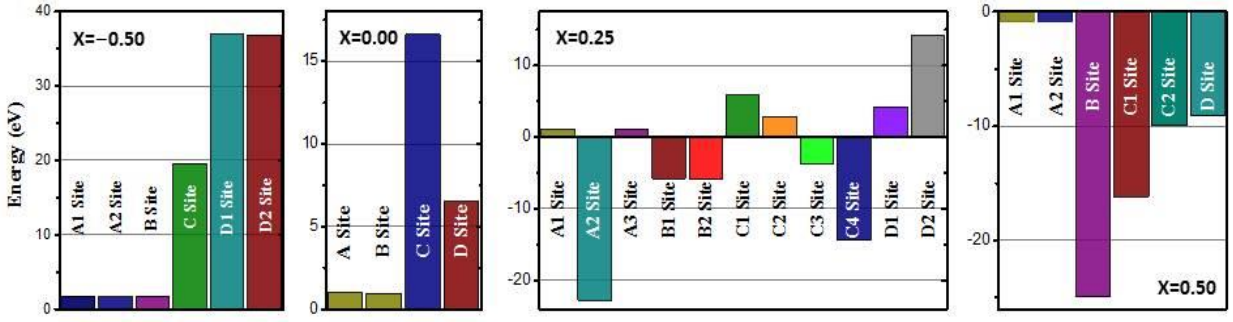

Fig. 3. Formation energies for the $Sr_2Fe_{1+x}Mo_{1-x}O_6$ compounds, with an H atom placed at the indicated site. All energies were calculated as indicated in the text.

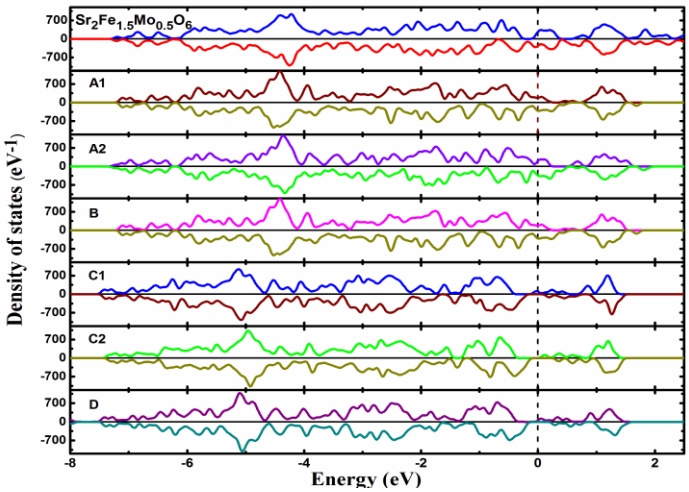

Fig. 4. Electronic density of states (DOS) for the $Sr_2Fe_{1.5}Mo_{0.5}O_6$ compound, around the Fermi level. The top graph is for the compound without H, the other six correspond to the same compound with an H atom located at the point tagged with the capital letter at the left. The Fermi level is marked with the discontinuous vertical line and positive and negative DOS values correspond to the up− and down−spin channels, respectively.

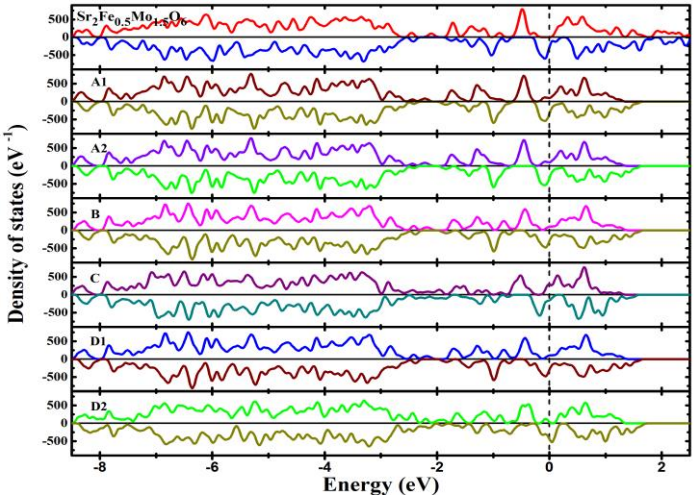

Fig. 6. Electronic density of states (DOS) for the $Sr_2Fe_{0.5}Mo_{1.5}O_6$ compound, around the Fermi level. The top graph is for the compound without H, the other six correspond to the same compound with an H atom located at the point tagged with the capital letter at the left. The Fermi level is marked with the discontinuous vertical line and positive and negative DOS values correspond to the up− and down−spin channels, respectively.

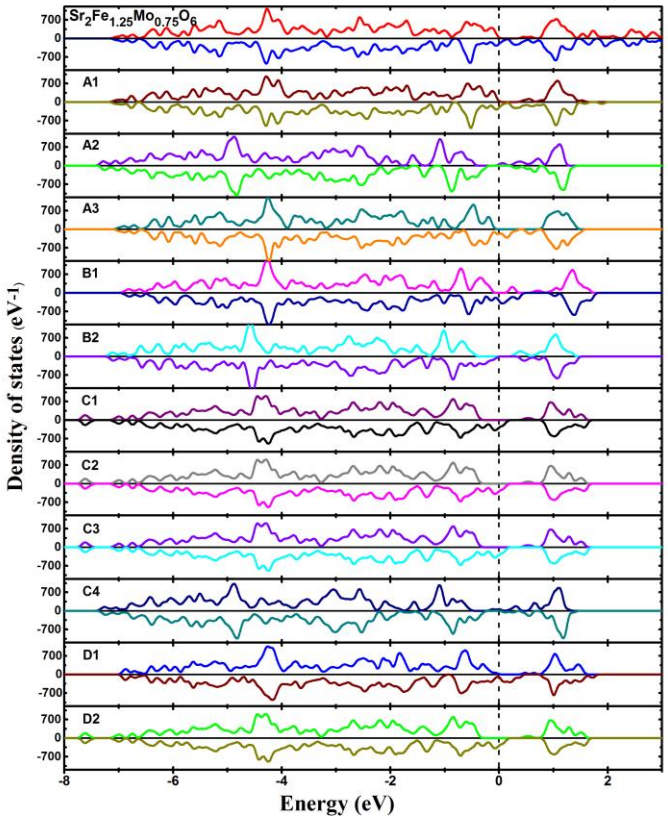

Fig. 5. Electronic density of states (DOS) for the $Sr_2Fe_{1.25}Mo_{0.75}O_6$ compound, around the Fermi level. The top graph is for the compound without H, the other eleven correspond to the same compound with an H atom located at the point tagged with the capital letter at the left. The Fermi level is marked with the discontinuous vertical line and positive and negative DOS values correspond to the up− and down−spin channels, respectively.

Otherwise ($x < 0$), to increase the Mo content traduces in a tendency to a conducting behavior of the compound (Fig. 6) [11], also eliminating the half metallicity. The insertion of H reduces the magnitude of the energy gap for the up-spin channel or, by moving states toward lower energies, changes the compound into an up spin conductor. The $Sr_2Fe_{0.5}Mo_{1.5}O_6$+H compound becomes an electronic conductor, except when the H is placed at the D2 site, because a small band moves in such a way that their upper edge matches the Fermi level and is separated from the next band.

From the calculated energies it is possible to consider that the H atom could diffuse in the SFMO compound by occupying alternatively the A and B sites (Fig. 3); both cases generate an electronic insulator behavior and passing H by the B site will permit the electronic conduction in addition to the ionic one, but with a slightly lower energy. When the Mo content increases ($x = -0.5$) the H atoms will occupy favorable the A and B sites; the H should diffuse in an almost parallel [001] direction.

IV. Conclusions

When an H atom is placed at a high symmetry point, in the stoichiometric ($x = 0.0$) and Mo rich ($x = -0.5$) compounds, it would move along a zigzag path almost parallel to the [001] direction, avoiding the positions on the faces of the metal centered octahedrons. The associated energy values were found closest to zero. On the other hand, for the Fe rich compositions (*i.e.* $x = 0.25$ and 0.50) the H should move on a plane which contains the (001) plane, becoming relevant the sites on the surface of the O metal centered octahedra and the B edging out sites, turning to be the most feasible to constitute the diffusion path. While the Mo rich compound make possible to have ionic and electronic conduction, slightly spin polarized, the Fe rich compound ($x = 0.5$) loses the spin channel behavior differentiation. Finally, the smallest increment of Fe over Mo in the compound promotes a variety of high symmetry points which at first sight are equivalent, but differs because of their

neighbors environment; this diversity could resembles the situation found in a polycrystalline sample where the aggregation of crystals makes hard to identify the diffusion routes of interest.

ACKNOWLEDGMENT

This work was partially supported by the multidisciplinary projects SIP2014-1640 and SIP2014-1641 from Instituto Politécnico Nacional, also by the project 252749 from Consejo Nacional de Ciencia y Tecnología (CONACyT). J.L. Rosas wants to acknowledge the scholarship from CONACyT.

REFERENCES

[1] A. B. Muñoz-García, *et al.*, "Unveiling structure-property relationships in $Sr_2Fe_{1.5}Mo_{0.5}O_{6-\delta}$, an electrode material for symmetric solid oxide fuel cells," J. Am. Chem. Soc., vol. 134, pp. 6826-6833, March 2012.

[2] H. Gómez-Bernal, and L. Cedeño-Caero, "Efecto de la temperatura en el proceso de oxidación y extracción de compuestos dibenzotiofenicos del dielsel," Rev. Mex. Ing. Quim., vol. 5, pp. 269-277, April 2006.

[3] J. S. Becerra-Hernández, H. Gómez-Bernal, J. F. Navarro-Amador, and L Cedeño-Caero, "Efecto del proceso de extacción sobre la desulfuración oxidativa de compuestos benzotiofenicos con catalizadores soportados de V_2O_5," Rev. Mex. Ing. Quim., vol. 5, pp. 301-310, May 2006.

[4] M. A. Alvarez-Amparán, and L. Cedeño Caero, "Efecto del hidroperóxido de cumeno sobre la desulfuración oxidativa," Rev. Mex. Ing. Quim., vol. 13, pp. 787-797, August 2014.

[5] L. Zhang, Q. Zhou, Q. He, and T. He, "Double-perovskites $A_2FeMoO_{6-\delta}$ (A=Ca, Sr, Ba) as anodes for solid oxide fuell cell," J. Power Sources, vol. 195, pp. 6356-6366, April 2010.

[6] R. Mishra, O. D. Restrepo, P. M. Woodward, and W. Windl, "First-principles study of defective and nonstoichiometric Sr_2FeMoO_6," Chem. Mater., vol. 22, pp. 6092-6102, September 2010.

[7] Q. Zhang, *et al*., "Crystal structure, magnetic and electrical−transport properties of rare−earth−doped Sr_2FeMoO_6," Physica B, vol. 381, pp. 233-238, 2006.

[8] J. P. Perdew, K. Burke, and M. Ernzerhof, "Generalized gradient approximation made simple," Phys. Rev. Lett., vol. 77, pp. 3865-3868, May 1996.

[9] R. Martinez-Coronado, J. A. Alonso, A. Aguadero, and M. T. Fernández-Díaz, "Optimized energy conversion efficiency in solid-oxide fuel cells implementing $SrMo_{1-x}Fe_xO_{6-\delta}$ perovskites as anodes," J. Power Sources, vol. 208, pp. 153-158, February 2012.

[10] A. B. Muñoz-García, M. Pavone, A. M. Ritzmann, and E. A. Carter, "Oxide ion transport in $Sr_2Fe_{1.5}Mo_{0.5}O_{6-\delta}$, a mixed ion-electron conductor: new insights first principles modeling," Phys. Chem. Chem. Phys., vol. 15, pp. 6250-6259, March 2013.

[11] J. Pilo, E. Carvajal, R. Oviedo-Roa, M. Cruz-Irisson, O. Navarro, "Interactions among magnetic moments in the double perovskites $Sr_2Fe_{1+x}Mo_{1-x}O_6$," Physica B, vol. 445, pp. 103-105, 2013.

Desarrollo de una estufa solar para varios contenedores

Hemerlinda Servín Campuzano[1], Mauricio González-Avilés[1], Mario Morales Máximo[1]
Programa académico, Desarrollo Sustentable
[1]Universidad Intercultural Indígena de Michoacán
Pátzcuaro Michoacán, México. C. P. 61614
merlysc@gmail.com gamauricio@gmail.com mmoralesmaximo@gmail.com

***Abstract*—Monitoring the research project "Implementation and adaptation of solar stoves in Michoacan communities" which is currently in development by researchers at the Intercultural Indigenous University of Michoacán (UIIM). One of the stages of the project involved the implementation of solar stoves concentration and non-imaging optics (solar stove Jorhejpatarnskua) in an indigenous community of Michoacan - Mexico, and at the stage of monitoring is shown the need for the users , to contemplate a solar heater with the ability to cook more than one food at the same time, since the heater Jorhejpatarnskua contemplates a single container , so that only the cooking of food. The solar cooker was redesigned, resulting Xate solar stove, basically is a solar cooking device includes more than a container for cooking food. The solar stove was subjected to basic international standards for their thermal parameters and the analysis shows similar results to the original solar stove.**

***Keywords:* concentration, solar stoves, non-imaging optics.**

***Resumen*—Monitoreando el proyecto de investigación "Implementación y adaptación de estufas solares en comunidades del estado de Michoacán" que actualmente se encuentra en desarrollo, por investigadores de la Universidad Intercultural Indígena de Michoacán (UIIM). Una de las etapas del proyecto consistió en la implementación de estufas solares de concentración y óptica anidólica (estufa solar Jorhejpatarnskua) en una comunidad indígena de Michoacán-México, y en la etapa de monitoreo se manifiesto la necesidad por parte de los usuarios, de contemplar una estufa solar con la capacidad de cocinar más de un alimento a la vez, ya que la estufa Jorhejpatarnskua contempla un solo recipiente, por lo cual solamente la cocción de un alimento. La estufa solar fue rediseñada, obteniendo como resultado la estufa solar Xate, básicamente es un dispositivo de cocción solar que contempla más de un recipiente para la cocción de alimentos. La estufa solar se sometió a estándares internacionales básicos para conocer sus parámetros térmicos y el análisis muestra resultados similares a la estufa solar original.**

***Palabras Clave*: Concentración, Estufa solar, óptica anidólica.**

I. Introducción

La energía solar, proporciona energía limpia y barata, que puede ser aprovechada para la cocción de alimentos mediante la implementación de cocinas solares y al mismo tiempo alberga un potencial para reducir problemas económicos y de salud.

En muchos hogares de México los combustibles maderables (leña) son utilizados para cocinar alimento y la inhalación de humo por causa de la combustión provoca enfermedades del pulmón y por esta causa, el número de muertes cada año es más grande. Aunque este problema es poco estudiado, se estima que aproximadamente 3 millones de personas en el planeta dependen de combustibles maderables, por lo tanto, el uso de cocinas solares también tiene el potencial de aumentar la productividad de las personas mediante la reducción del tiempo dedicado a la búsqueda de la madera.

Además el uso de las estufas solares puede contribuir a disminuir: el conflicto por los recursos energéticos, la contaminación al medio ambiente y a la deforestación.

El análisis térmico de la estufa solar Xate muestra resultados similares a la estufa solar original, la cual, contaba con un solo recipiente, ahora esta nueva estufa tiene tres recipientes absorbedores y los parámetros térmicos encontrados para cada recipiente se asemejan a la original.

II. Fundamentación

Las cocinas solares son dispositivos que funcionan con la energía solar tales como estufas, hornos, comales, etc. estos dispositivos se pueden clasificar en dos tipos: de concentración y de acumulación; cocinas tipo caja, parabólicas, de tubo, de revolución o híbridos. El uso de hornos y estufas es más común, comparados con los comales. Para implementar el uso de cocinas solares, es recomendable considerar las condiciones climáticas del lugar para tener un mejor funcionamiento y rendimiento térmico del dispositivo.

Por las características térmicas y la construcción que tiene la estufa solar Jorhejpatarnskua y las condiciones climáticas de la comunidad de Sta. Fe de la laguna municipio de Quiroga, Michoacán-México, se implementó la estufa, minimizando las necesidades de los usuarios, respecto a sus usos y costumbres, y en consecuencia en el monitoreo se registró el requerimiento de cocinar más de un guiso por vez [1].

De acuerdo con los datos obtenidos del monitoreo del uso de las estufas solares en la comunidad de Sta. Fe de La Laguna, las costumbres de alimentación de las familias de esta comunidad, son: cocinar de 2 a 3 platillos por vez, por lo cual, el diseño de la estufa solar implementada se modificó, con la innovación es posible cocinar más de un alimento a la vez en el mismo dispositivo.

Figura 1. estufa solar Jorhejpatarnskua

La estufa solar Jorhejpatarnskua [2] se diseñó para cocinar un alimento por vez y puede cocinar más de uno guiso utilizando recipientes fraccionados. Generalmente las estufas solares contienen un solo recipiente para la cocción de alimentos, pero con la problemática manifestada se consideró la opción de fraccionar el recipiente absorbedor en dos o tres partes [3], para poder cocinar más de un alimento a la vez, los resultados del análisis térmico mostraron: primero la cantidad de alimento para cocinar debe ser menor y segundo y más importante para el desarrollo científico los parámetros térmicos también fueron menores, y como las familias de esta región, generalmente son grandes debido a que son familias extendidas, la estufa Jorhejpatarnskua no cumple dicha necesidad.

Una alternativa para solucionar la problemática encontrada fue el diseño de una nueva estufa solar de concentración a la que se le dio el nombre de "estufa solar Xate".

III. Definiciones

La estufa solar Xate es una estufa en base a la aplicación de concentradores parabólicos compuestos de revolución, la cual permite la cocción de hasta tres alimentos, simultáneamente, los componentes que la conforman son: un colector, tres recipientes absorbedores y una base para orientar el concentrador hacia el sol

Figura 2. Estufa solar Xate

IV. Revisión de literatura

La estufa solar Xate es una innovación de la estufa solar Jorhejpatarnsku y a la vez esta fue modificada de la estufa solar de concentración parabólica compuesta de revolución, la cual se sustenta baja la premisa de Narasimha Rao y Subramanyam [4], ellos consideran una modificación al contenedor, proporcionando un par de aletas para aumentar la superficie de captación, mejorando el rendimiento y los tiempos para llegar a la temperatura de saturación y el tiempo de cocción se redujo notablemente, comparada con una convencional.

El desarrollo científico de las cocinas solares, viene acompañado con el desarrollo de las investigaciones sobre implementación de tecnologías solares, debido a la necesidad de conocer parámetros térmicos para hacer comparación entre dispositivos de un mismo tipo y/o entre dispositivos similares.

Existen varios estudios térmicos de cocinas de concentración, como el que realizó Esteves [5] este estudio hace una comparación entre tres cocinas de concentración, obteniendo los mejores resultados para un modelo en base a un paraboloide como colector. Otro estudio sobre comparación entre estufas solares muestra las experiencias en campo de una cocina solar tipo caja “solar cookit”, de costo mínimo para determinar las condiciones con que la cocina pueda ser competitiva comparada con otra estufa tipo caja [6].

Existen alternativas de construcción de cocinas solares tipo caja, utilizando materiales de bajo costo para la evaluación térmica [7], para este mismo tipo de cocinas [8] se compararon resultados experimentales de distintos tipos de ollas. Los resultados obtenidos muestran que las ollas de altura reducida y con tapa transparente mejoran el rendimiento de la cocción, para estufas tipo caja.

V. Formulación de objetivos

La innovación que hace posible la construcción de la estufa solar Xate consiste en aumentar el área de captación considerando el diseño de la estufa solar Jorhejpatarnskua, proporcionando un par de aletas para aumentar la superficie de captación y el re-diseño para tres recipientes.

VI. Metodología de prueba

Para el estudio de las propiedades térmicas de la estufa solar Xate, se han aplicado la prueba estadarizada [9] para obtener la potencia de cocción en campo, el rendimiento térmico de la estufa se obtuvo de acuerdo con Ashok y, Sudhir [10], los tiempos de calentamiento y de cocción tomando la prueba de Pejack [11]. Para obtener los parámetros térmicos de la estufa solar Xate fue necesario colocar una cubierta de plástico semitransparente para disminuir las pérdidas de energía por convección.

A. *Instrumentación*

Para lograr el análisis térmico, fue necesario el uso de la siguiente instrumentación:

- Un piranómetro marca hukseflux
- Un termómetro tipo K,
- 4 termopares tipo K.
- Una estación meteorológica inalámbrica “Vantage Pro2”.
- Un cronómetro digital.

B. *Lugar de la prueba*

Pátzcuaro, Michoacán, México.

Altura: 2,035,.0 MSNM

- Latitud: 19º 38’ 00’’ N
- Longitud: 101º 36’ 00’’ W
- Inicio de la prueba: 11:52 hrs de tiempo oficial = 10 hrs, 9 min, 21 seg tiempo solar
- Temperatura ambiente al inicio: 21.9
- Volumen de agua en cada una de las tres ollas de presión: 3 litros.

VII. Resultados

Una vez que se obtuvieron los parámetros térmicos con sus protocolos respectivos, se compararon y se realizaron sus gráficas respectivas para presentarse según cada uno de los protocolos.

- Potencia de cocción estandarizada
- Aumentos de temperatura del contenido de los recipientes absorbedores.
- Tiempos de calentamiento y de cocción

Para realizar la gráfica de la potencia de cocción estandarizada se grafican: En el eje y, los datos que se obtuvieron utilizando el protocolo ASAE, en el eje x, la diferencia de las temperaturas del ambiente con la del líquido que se encuentra en el interior del recipiente, en el gráfico se refleja la potencia de cocción estandarizada cuando la diferencia de las temperaturas alcanza los 50 °C.

En las figuras 1, 2 y 3, se muestran las gráficas de la potencia de cocción para cada una de las tres ollas contenedoras absorbentes.

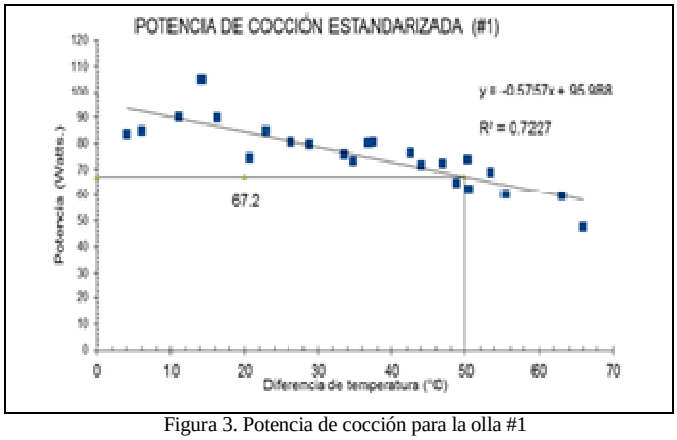

Figura 3. Potencia de cocción para la olla #1

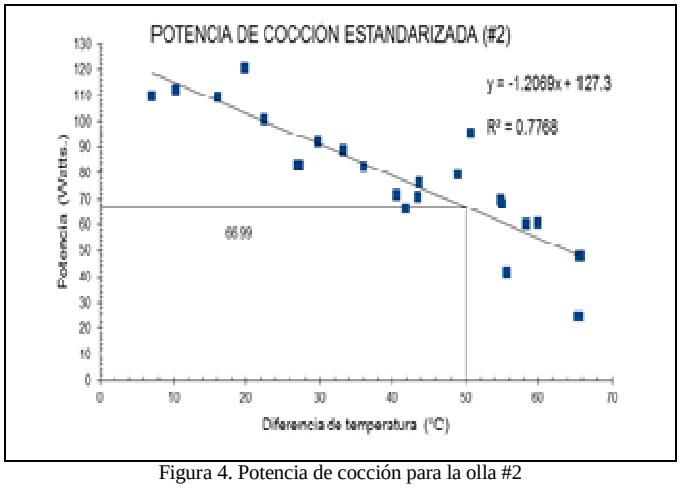

Figura 4. Potencia de cocción para la olla #2

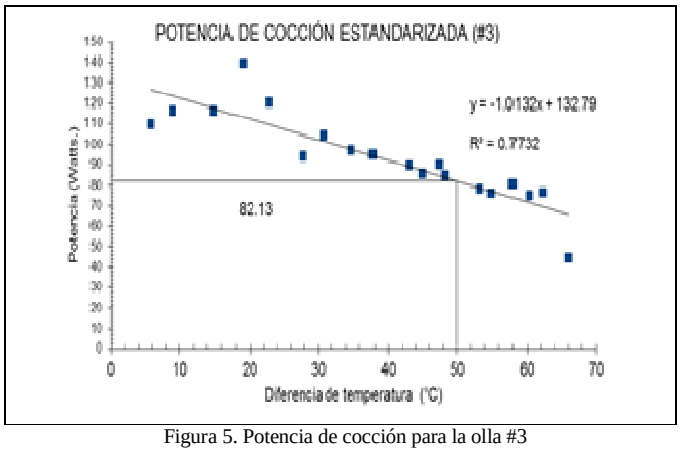

Figura 5. Potencia de cocción para la olla #3

La potencia de cocción para cada una de las ollas contenedoras fue un tanto diferente: #1 67.2, #2 67 y #3 82,1

Watts, el área de captación de la estufa solar Xate es de aproximada de 1.25 metros cuadrados y el volumen de las ollas de 5 litros.

En las figuras 4, 5 y 6, se muestran las gráficas del aumento y diferencia de temperatura entre el fluido del interior de las ollas y de la temperatura ambiente en función del tiempo, donde se aprecia que para cada fluido del interior de las ollas es muy similar, lo cual quiere decir que la cocción de los alimentos tardara tiempos similares. En las gráficas 8, 9 y 10 se observan los tiempos de calentamiento y de cocción para cada uno de los recipientes.

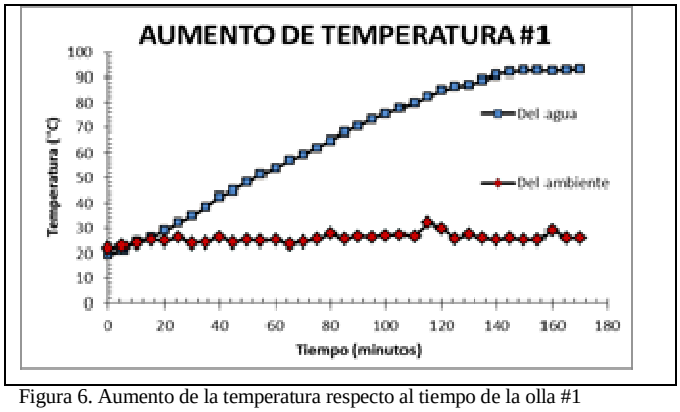

Figura 6. Aumento de la temperatura respecto al tiempo de la olla #1

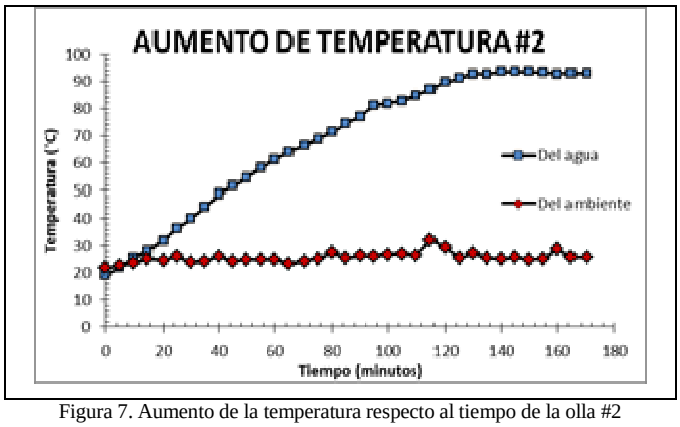

Figura 7. Aumento de la temperatura respecto al tiempo de la olla #2

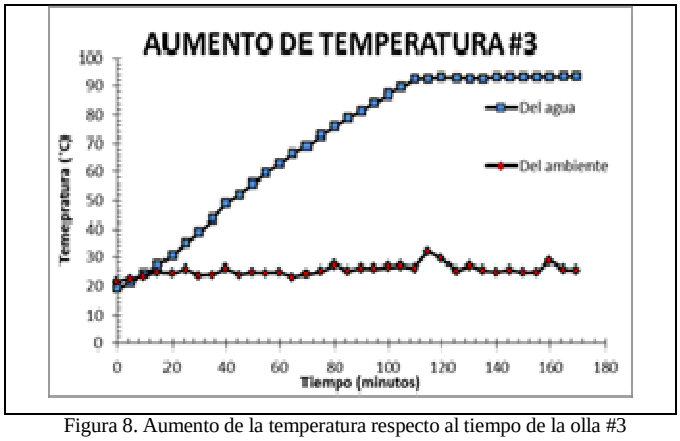

Figura 8. Aumento de la temperatura respecto al tiempo de la olla #3

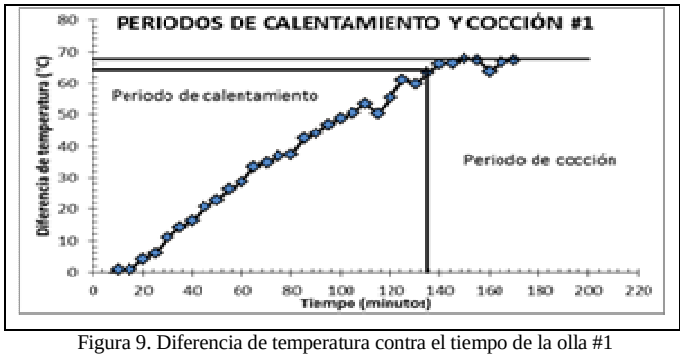

Figura 9. Diferencia de temperatura contra el tiempo de la olla #1

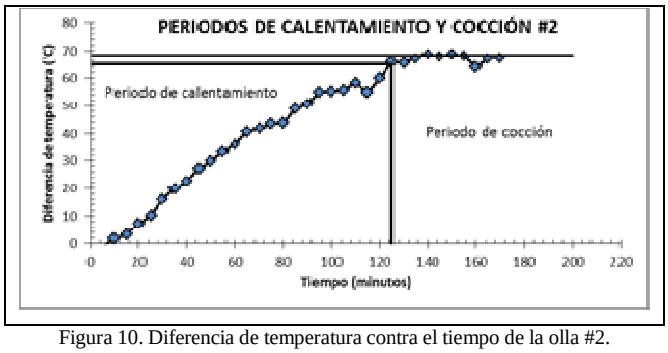

Figura 10. Diferencia de temperatura contra el tiempo de la olla #2.

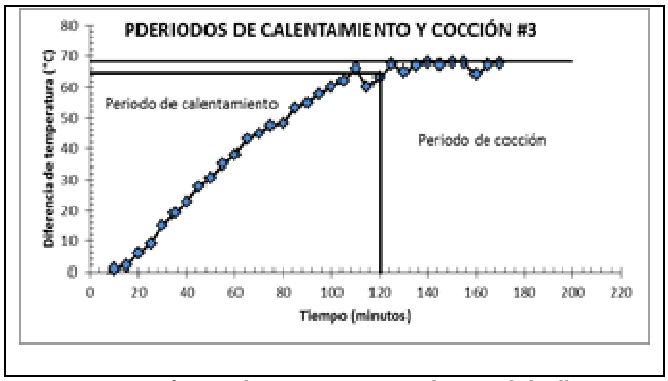

Figura 11. Diferencia de temperatura contra el tiempo de la olla #3.

En cuanto al rendimiento térmico, para c/u de los recipientes es: #1 7.8, #2 8.7 y #3 9.9%, en total un 26.4% al sistema de tres ollas.

En la tabla I se muestra el resumen con los resultados más relevantes.

TABLE I. PARÁMETROS TÉRMICOS DE LA ESTUFA SOLAR XATE

Parámetro	olla #1	olla #2	olla #3	Total.
potencia de cocción (Watts)	67.2	67.0	82.1	216.3
Rendimiento térmico (porcentaje %)	7.8	8.7	9.9	26.4
Tiempo de calentamiento (minutos)	138	126	120	
Tiempo de cocción (horas)	3.5	3	3	

VIII. CONCLUSIONES

De acuerdo al análisis térmico de la cocina solar Xate, presenta una aceptable potencia de cocción estandarizada para las tres ollas contenedoras. Por cuestiones de asimetrías, dos resultan con menor potencia de cocción, lo cual implicaría que el alimento con mayor tiempo de cocción se pondría en la olla de mayor potencia de cocción.

La menor potencia de cocción estandarizada obtenida es casi lo doble que la obtenida en condiciones similares que la cocina solar "hot pot" que es del orden de 35 Watts y con una capacidad máxima de 3 kg de alimento, mientras que cada olla de la Xate es para 5 kg.

Tanto la potencia de cocción estandarizada total como el rendimiento térmico del sistema de las tres ollas es bastante aceptable del orden del 26%, muy por encima de los hornos tipo caja.

La potencia estandarizada total casi es el doble de la potencia de cocción de la estufa solar Jorhejparanskua, con un incremento proporcional del área de captación.

Los tiempos de cocción de alimentos están en el orden de 3 a 4 horas, que resultan razonables de acuerdo a las condiciones en la región de su implementación potencial.

The preferred spelling of the word "acknowledgment" in America is without an "e" after the "g". Avoid the stilted expression "one of us (R. B. G.) thanks ...". Instead, try "R. B. G. thanks...". Put sponsor acknowledgments in the unnumbered footnote on the first page.

REFERENCIAS

[1] M. González-Avilés, H. Servín Campuzano, L. B. López Sosa y J. A. Rodríguez Morales. Desarrollo, implementación y apropiación de cocinas solares para el medio rural de Michoacán: una alternativa energética para la conservación de recursos forestales maderables. Revista Solar de la ANES No. 17, pp. 12-15. 2013

[2] M. González-Avilés, L. B. López Sosa, & H. Servín. Cocinas Solares: una alternativa energética para el medio rural. Saarbrücken, Germany: Editorial Académica Española. 2014. W. Rafferty, "Ground antennas in NASA's deep space telecommunications," Proc. IEEE vol. 82, pp. 636-640, 1994

[3] H. Servín & M. González-Avilés. Development of the solar cooking Jorhejpatarnskua: thermal standard analysis of solar cooking with several absorber pots. Presentada en el ISES Solar World Congress 2013

[4] A. V. Narasimha Rao, S. Subramanyam. Solar cookers—part I: cooking vessel on lugs. Solar Energy, vol. 75, no 3, p. 181-185. 2003

[5] A. Esteves, V. N. Quiroga, F. Buenanueva. & D. Orduna. Estudio de la potencia de cocción en concentradores solares de distinto tipo. Avances en Energías Renovables y Medio Ambiente, ASADES Vol. 14, 2010

[6] V. Passamai & M. Passamai. Experiencias con cocinas solares tipo cookit de costo mínimo. Avances en Energías Renovables y Medio Ambiente, vol. 6, no 2, p. 10.33-10.36. 2002

[7] L. E. Sánchez Mealla, P. D. Arangoan Bonaveri. Alternativas de construcción utilizando materiales de bajo costo para la evaluación térmica de cocinas solares tipo caja. Revista ION, vol. 25, no 1. 2012

[8] F. Filippin, A. Iriarte, L. Saravia. Estudio comparativo de ollas en una cocina solar tipo caja. AVERMA, vol. 10, p. 3.15-3.20. 2006

[9] ASAE S580, Testing and Resporting Solar Cooker Performance. American Society of Agricultural Engineers, ASAES580 JAN03, pp.824-826. 2003

[10] A. Kundapur & C. V. Sudhir. Proposal for new world standard for testing solar cookers. Journal of Engineering Science and Technology, Vol. 4, pp. 272-281. 2009

[11] E. Pejack, Technology of Solar Cooking. The solar cooking archive, 2003. Disponible en http//solarcooking.org/Pejack-on-solar cookertechnology.pdf

Simulation of an aeroderivative gas turbine via a chemical reactor Gibbs type

Rodríguez Hernández I.N
Facultad de Ciencias Químicas
Universidad Veracruzana
Orizaba, Veracruz, 94340, MÉXICO
ingridnayelir@gmail.com

A. Osorio Mirón
Facultad de Ciencias Químicas
Universidad Veracruzana
Orizaba, Veracruz, 94340, MÉXICO
anosorio@uv.mx

L. M, Reyes Grajales
Facultad de Ciencias Químicas
Universidad Veracruzana
Orizaba, Veracruz, 94340, MÉXICO
luireyes@uv.mx

H. Pérez Pastenes
Facultad de Ciencias Químicas
Universidad Veracruzana
Coatzacoalcos, Veracruz, 96535, MÉXICO.
huperez@uv.mx

R. Melo-González
Facultad de Ciencias Químicas
Universidad Veracruzana
Orizaba, Veracruz, 94340, MÉXICO
lmelog@uv.mx

***Abstract*— In recent years the use of software for rigorous process simulation in dynamic and steady state has been of great importance in industries as they are tools that can represent virtually stages of a process or the entire process for analysis and decision making in the design, simulation and process control. The aim of this work is the simulation of flow diagrams on integration processes, include combined heat and power. A model aeroderivative gas turbine, Brayton cycle, is built and evaluated, based on changes in profiles pressure and temperature, as well as mass and energy balances to verify operating conditions in open cycle. Here the combustion chamber of a gas turbine is represented by a chemical reactor Gibbs type model available in the databases of commercial simulators, for example PROII 9.2. To find the convergence of the solution of the proposed model was necessary to include three numerical controllers to maintain conditions and principles of operation of the gas turbine associated with the excess air, thermal efficiency and expansion efficiency. Based on the numerical results it shows that the flue gases leaving the reactor stand for the chemical energy available in the gas turbine and the efficiency of conversion to mechanical energy, residual thermal energy and energy loss, corresponds to the level of efficiency that is reported in the technical and scientific literature.**

Keywords*— *Aeroderivative gas turbine; Chemical reactor Gibbs type; Conversion efficiency; Numerical simulation.

***Resumen*— En los últimos años el uso de software para simulación rigurosa de procesos en estado estable y dinámico ha sido de gran relevancia en las industrias, ya que son herramientas que permiten representar de forma virtual las etapas de un proceso o el proceso completo para su análisis y toma de decisiones en el diseño, simulación y control de procesos. El presente trabajo tiene como objeto realizar la simulación rigurosa de esquemas sobre integración, incluyendo la combinación de calor y potencia. Se construye y se evalúa un modelo de turbina de gas aeroderivada, ciclo Brayton, tomando como base los perfiles de cambios de presión y de temperatura, así como los balances de materia y energía para verificar sus condiciones de operación en ciclo abierto. Se representa la cámara de combustión de una turbina de gas por medio de un modelo de reactor químico tipo Gibbs disponible en las bases de datos de simuladores comerciales, por ejemplo PROII 9.2. Para obtener la convergencia de la solución del modelo propuesto se incluyeron tres controladores numéricos para mantener las condiciones y principios de operación de la turbina de gas relacionados con el exceso de aire, rendimiento térmico y eficiencia de expansión. Con base en los resultados numéricos se observa que los gases de combustión a la salida del reactor representan la energía química disponible en la turbina de gas y la eficiencia de conversión a energía mecánica, energía térmica residual y energía pérdida, que corresponde al rango de eficiencia que reportan en la literatura técnica y científica.**

***Palabras clave*—Turbina de gas aeroderivada; Reactor químico tipo Gibbs; Eficiencia de conversión; Simulación numérica.**

I. INTRODUCTION

Gas turbines are machines which generally work based on an open cycle. A feature of this cycle is that it takes the air (active substance) environmental and returns again as combustion gases at high temperature to the environment, in order to produce energy. In recent years there has been tremendous growth in the performance of these turbomachinery, thanks to advances in materials technology, combined cycle plants, new coatings, etc. This has driven out the use of lead aeroderivative turbines, which are used in aviation, because they have a compact, lightweight system with a high ratio of potency. For these reasons and others it has also decided to implement from several years ago. For

these reasons and others it has also decided to implement from several years ago speaking of industry.
This work was carried out simulating a chemical reactor type Gibbs performing thermodynamic analysis and mass and energy balances for the representation of the combustion chamber of a gas turbine; the same way the complete model of the gas turbine is built. Towler (2013) mention "The art and practice of design cannot be learned from books. The intuition and judgment necessary to apply theory to practice will come only from practical experience." and motivates engineering students to use professional software of process simulation.
Because the simulation is a very powerful tool that has been used in recent years in different areas of research and application in industry, to conduct rigorous steady-state simulation, the process simulation package PRO II 9.2 was used.

II. The Brayton Cycle

Some background that mention the Brayton cycle gas turbines for chemical engineering students were mentioned in the late 50's in a classic book that was written by Hougen *et al* (1959). Currently there are different books that specifically address the behavior of the cycle as shown Boyce (2012) y Razak (2007), in their representative diagrams of temperature-entropy change.

The Brayton cycle is a ideal thermodynamic cycle which consists of two isobaric processes and two isentropic processes. [1].

1. Air passes through an axial compressor where the pressure and temperature change (isentropic process).
2. The flow reaches the combustion chamber where the reaction takes place at constant pressure (isobaric process).
3. Expansion process where temperature and pressure change (isentropic process).
4. Cooling, the combustion gases are sent to the atmosphere (isobaric process).

This cycle is performed in a gas turbine of open cycle, in some applications a regenerator is arranged so that the energy carried by combustion gases is exploited, the Brayton cycle is renamed regenerative cycle, the same way you can make combined cycle [2].

III. Methodology

A. *Gibbs Reactor*

Gibbs reactor was used in the model of the proposed reactor that represent the combustion chamber, because in this system it is involved the reaction coordinate which in turn is related to the reaction constant K, this latter determined by the stoichiometry.

The Gibbs reactor works with the minimization of Gibbs free energy of the components that are specifically involved in the reaction, so it is not necessary to include the stoichiometry of the reaction, since the equilibrium is reached when the free energy of Gibbs reaches a minimum or is zero, this criterion is defined as shown in the following equation:

$$(dG^t)_{T,P} = 0 \qquad (1)$$

Fig. 1 Gibbs free energy.

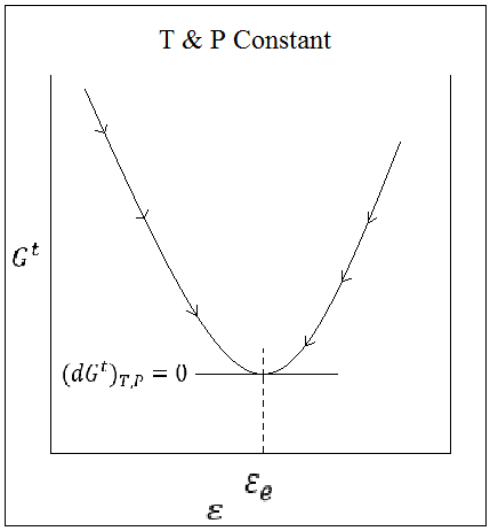

where the temperature (T) and pressure (P) are constant and epsilon represents the coordinate of the reaction, according to the graph showing the Figure 1 [3].

B. *Construction of the process flow diagram of a gas turbine.*

For model building was analyzed the gas turbines taxonomy presented in ISO 14224 [4], which has the general taxonomy gas turbines, including therein the disclosures of industrial gas turbines and aero-derivative type. Also it was considered the features that includes NRF-100-PEMEX [5].
It was built a flow diagram wherein was located the main components that constituting an aeroderivative gas turbine, shown in Figure 2

Fig. 2 Flow diagram of a gas turbine.

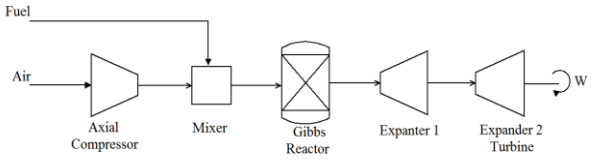

Based on the diagram of Figure 2 it is proceeded to build the model representing the gas turbine in simulation. Table 1 shows the selected units and nomenclature for each are shown

TABLE I. UNITS FOR THE CONSTRUCTION OF MODEL GAS TURBINE

Units for the construction of model gas turbine	
Unit	***Name***
C-101	Axial compressor
M-101	Mixer
R.101	Gibbs Reactor
EX-101	Expander 1
EX-102	Expander 2 (Turbine)
CN1	Controller 1
CN2	Controller 2
CN3	Controla 3

In the environment of process simulator PRO II 9.2, the model gas turbine via Gibbs reactor was built, being as shown in Figure 3

Fig. 3 Model gas turbine in PRO II.

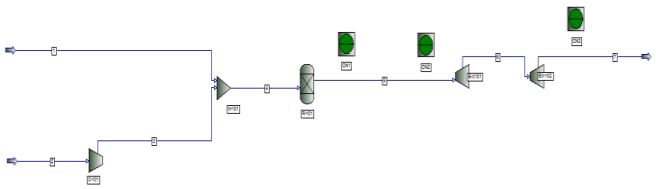

C. *Simulation model of a gas turbine: Base Case*

To conduct rigorous simulation is selected the equation of state Soave-Redlich-Kwong (SRK), as the thermodynamic system; once selected this equation will be used by default for all units entered. Subsequently, the streams entering the field of simulation are defined, which the air and the fuel were being methane gas (CH4), the fuel used.

The input values of the air flow and gas are shown in Table 2.

TABLE II. VALUES OF THE INLET STREAMS

Values considered for the base case simulation				
Streams		***Input Flows (Lb/hr)***	***Temperature (°F)***	***Pressure (psia)***
1	CH4	922.169	60	200
2	Air	110033.284	60	14.696

For the definition of the parameters used in each unit of flow diagram it was considered the heuristic rule of compressors.

In the case of reactor Gibbs, as this by default operates with the inlet temperature should be set the desired temperature of 1200 ° F, based on those reported in the literature [6].

D. *numerical controllers*

To adjust and maintain constant values in thermodynamic properties and flows mainly in the steady state simulation were used numerical controllers, located in the tool palette of the process simulator PRO II 9.2. In these numerical controllers must determine restrictions such as upper and lower limits, which are specified taking into account the stream is adjusted.

Controller 1. Adjusting the airflow required respect to the reaction temperatura: This controller will adjust the airflow to the defined value (or default) is the stream 5 (flue gas leaving the reactor Gibbs), and the value of the reaction temperature is maintained.

Controller 2. Adjust the compressor pressure ratio to the power of expander 1: The compressor pressure ratio is adjusted so that the defined value is the power of the expander 1, with the aim of maintain the required power, in the base case is 4989.4 hp, and thus comply with the efficiency of the first expansion.

Controller 3. Adjust the fuel flow required to maintain the power of the gas turbine: As the turbine power is related to the amount of incoming fuel, methane gas flow is adjusted to maintain the power of the gas turbine; in this way it can satisfy the turbomachine efficiency

E. *Setting values for Case 1 and Case 2*

Two additional runs were performed, causing changes in the amount of fuel input, air and the temperature of the latter; this data is based on the behavior of a gas turbine to almost ideal conditions considering different location areas in the operation such as the marine region [7] and the southern region [8].

TABLE III. SPECIFICATIONS FOR SIMULATING CASE 1 AND CASE 2

Values for simulations			
Case	***Fuel Flow (Lb/hr)***	***Air Flow (Lb/hr)***	***Temperature (°F)***
1	703.26	92665	86
2	703.26	92665	60

By having a change in input flows in both quantity and the air temperature, the reaction in the reactor is affected, so they will have to set the temperatures in the reactor, which are: 1178.5 °F y 1135 °F, respectively, in each case; the corresponding amounts were adjusted in the same way on controller 1.

IV. RESULTS AND DISCUSSION

was performed Steady-state simulation, according to the figure 4, when this converge the color of the equipment it turns to blue, it is indicative that there was no problem and that is

managed to solve the balance of matter and energy of the process flow diagram.

Fig. 4. Resolved model of the gas turbine (Convergence).

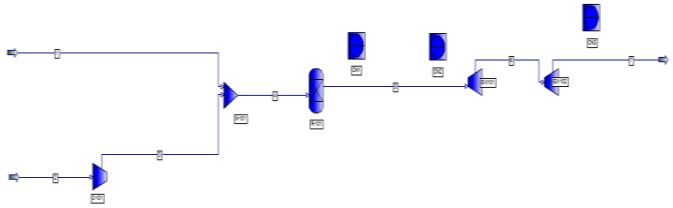

A. Checking the Brayton cycle

The changes that occur in a gas turbine are those of the Brayton cycle. It was performed checking that cycle according to the changes that were obtained in each simulation unit.

C-101: Axial compressor (isentropic). The first stage of the Brayton cycle is performed at the compressor, when the air is compressed so that its temperature is raised to 532 263 ° °F and reaches a pressure of 98,463 psia.

M-101: Mixer. This equipment was placed with the aim of make the air-fuel mixture in the proportions required; since air exits the compressor with a temperature of 532 263 ° °F and the fuel has a temperature of 60 ° F, in the mixer it has a heat exchange and the resulting mixture is 522 362 ° F, while the pressure was maintained at 98,463 psia.

R-101: Gibbs reactor (isobaric). Under isobaric conditions carried out the second stage of Brayton cycle, the pressure is 98,463 psia and the temperature of the reaction is conducted at about 1200 ° F. The results obtained in the balance of the reaction show that the fraction of methane conversion is 1, it is indicating that all reactant is being consumed in the reaction and therefore the Gibbs reactor can properly represent the combustion chamber of the gas turbine.

EX-101: Expander 1 y EX-102: Expander 2 (isentropic). In the EX-101 unit the flue gas leaving the reactor is spread, which it translates as the chemical energy released in the reaction, by expanding gas temperature decreases and with it the pressure, solving the mass and energy balances in this unit indicates a shift to 773.436 ° F in the gas temperature and a pressure of 24.366 psia

The EX-102 unit is the expander of discharge where the latest expansion of gases occurs and conversion to mechanical energy, seen as shaft work, the balance of matter and energy shows a shift to 654.348 ° F in the temperature of the combustion gases and a pressure of 15.5 psia.

The last change of the Brayton cycle is isobaric, this occurs in the output of combustion gases to the atmosphere, Being an open cycle.

B. controller results

Controller 1. It was confirmed that the values (parameters) included in the controller allow modulate the inlet air flow to maintain the temperature required in the reactor, and likewise satisfy the balances of mass and energy , table 4.

TABLE IV. CN1 UNIT RESULTS

Controller CN1	
Controller	***CN1***
Vary value	
CYCLE 1	1200
CYCLE 2	1200
CYCLE 3	1200
Vary value	
CYCLE 1	3798.398
CYCLE 2	3798.398
CYCLE 3	3798.398

Where the first value is the reaction temperature, the second is the amount of air to the compressor inlet in lbmol / hr (or 110033.284 lb / hr). At each cycle the quantity of values remained, which shows that not there were mismatches in the convergence and the balance of matter and energy.

Controller 2. The results obtained by this second numerical controller shown in Table 5, Which it indicates that the power obtained in the expander is 4989.3 hp, maintaining a pressure ratio of 6.7 in the compressor this unit helped to keep the thermal efficiency, because if the pressure ratio in the compressor decreases, the temperature of the airflow will also decrease, flow therefore enter the reaction with a lower temperature and hence reduce the reaction temperature in the combustion chamber.

TABLE V. CN2 UNIT RESULTS

Controller CN2	
Controller	***CN2***
Vary value	
CYCLE 1	4989.374
CYCLE 2	4989.345
CYCLE 3	4989.350
Vary value	
CYCLE 1	6.7
CYCLE 2	6.7
CYCLE 3	6.7

Controller 3. With this controller proved that you can keep the balance of mass and obtain the necessary power in the last expansion, because the power is related to the amount of fuel

entering the reaction, also this power must be maintained for turbine efficiency.

The power is 1345.264 hp in the base case turbine (expander 2) and fuel flow is in 57.482 lbmol / hr, equivalent to 922.169 lb / hr table 6.|

TABLE VI. CN3 UNIT RESULTS

Controller CN3	
Controller	***CN3***
Vary value	
CYCLE 1	1345.264
CYCLE 2	1345.264
CYCLE 3	1345.264
Vary value	
CYCLE 1	57.482
CYCLE 2	57.482
CYCLE 3	57.482

Likewise this controller having the fuel and power setting, it can help determine the amount of methane gas to be used for a power required, only needs to define the power and the controller will perform the calculations for estimating the amount of fuel that must enter into the reaction.

C. Comparison of data in the base case, case 1 and case 2.

To perform the comparison was necessary to go to a manufacturer in the market, data from a company dedicated to the manufacture of these turbomachinery were taken, from variety of gas turbine having the manufacturer selecting a gas turbine was made, that being the design presents similar values to which they were used in the simulation. Likewise, the comparison with real data of this turbine in operation coast outside a oil industry was made.

The Table 7 presents comparisons of air temperature, amount of methane gas, the power output of the turbine, exhaust temperature and the efficiency of each case and the reaction temperature.

As compared case 2 above is the values which is close to the operation data and temperature data in the reaction, followed by the case 1 and the base case.

TABLE VII. COMPARISON OF DATA

		Data manufacturer of gas turbines for the model analyzed	**Data operation of a gas turbine for the model discussed in facilities coast outside oil industry** Hernández Arroyo, A. (2015)	**Data obtained by the process simulator PRO II.- base Case**	**Data obtained by the process simulator PRO II.- Case 1**	**Data obtained by the process simulator PRO II.- Case 2**
Airflow temperatura.	(°F)	-40 --- 122	86	60	86	60
Quantity of fuel (CH4)	(Lb/hr)	Maximun: 880 Standard: 703	703.26	922.169	712	707
Output power W	(Hp)	400 --- 1590	1150	1345	1189	1156
Exhaust temperatura	(°F)	572 --- 970	**ND**	654.5	639	609
LHV (Lower Heating Value)	(Btu/hr)	800 --- 1100	913	**ND**	**ND**	**ND**
Eficiencia		24.5 %	**ND**	18%	20%	20%

Reaction temperature				
	Registered data Sierra *et al.* (2005)	**Data set to perform the simulation using the process simulator PRO II.- case base**	**Data set to perform the simulation using the process simulator PRO II.- case 1**	**Data set to perform the simulation using the process simulator PRO II.- case 2**
Temperature °F	1112	1200	1178.50	1135.00

V. CONCLUSIONS

The modeling and simulation in steady state of aeroderivative gas turbine, via a chemical reactor type Gibbs showed effective results that justify changes that occur theoretically in a open cycle turbine, Known as Brayton cycle.

The use of numerical simulation controller in steady state helps the gas turbine keep the balance of matter and energy in each stream, adjust streams for the work and efficiency are satisfied according to the values reported in the literature

with turbomachinery equipment manufacturers and with real data from outside coast operations.

The obtained results of numerical simulation run steady state of base case, Case 1 and Case 2, compared with information from manufacturers and operating data of oil installations allow the evaluation of the combustion chamber of a gas turbine aeroderivative using one of the different chemical reactors that are in the process simulator package PRO II 9.2 fulfilling with efficiency parameters reported.

VI. Recommendations

It proposes a steady state simulation for energy integration of the flue gases through a heat recovery system, with the gases that are sent into the atmosphere, further placing a thermal oil closed circuit to transfer heat to a heat exchanger network.

Perform a steady-state simulation of closed cycle.

Using a dynamic process simulator which can evaluate the gas turbine, using process controllers, to regulate the temperature of the combustion gases.

Perform the analysis of combined cycles in industrial plants.

References

[1] Boyce, M. P. (2012). *Gas turbine engineering, 4th ed.* USA. Butterworth-Heinemann.

[2] Garcia Garrido, S. (2012). *Fundamentos tecnicos de los ciclos combinados.* Madrid, España: Diaz de Santos.

[3] Smith, J.M., Van Ness, H.C., Abbott, M.M. (2007). *Introduction to chemical engineering thermodynamics*, 7 ed. México: McGraw-Hill.

[4] ISO-14224. (2006). Petroleum, petrochemical and natural gas industries- Collection and exchange of reliability and maintenance data for equipment. Switzerland, Suiza.

[5] NRF-100-PEMEX. (2009). Comite de normalizacion de pretróleos mexicanos y organismos subsidiarios. Turbinas de gas para accionamiento de equipi mecánico en instalaciones costa fuera.

[6] Sierra, F., Kubiak, J., Gonzalez. G. (2005). *Prediction of temperature front in a gas turbine combustion chamber*. Elsevier

[7] Hernández Arroyo, A (2015): Comunicación personal. Instituto Mexicano del Petróleo. Región Marina. Ciudad de Carmen, Campeche. México.

[8] Teopa Calva, H. E. (2015). Comunicación personal. Instituto Mexicano del Petróleo. Región Sur. Villahermosa, Tabasco. México.

[9] Boyce, M. P. (2006). *Gas turbine engineering handbook, 3ed edition.* United States of America: Gulf Professional Publishin.

[10] Martínez Sifuentes, V. H., Alonso Dávila, P. A., López Toledo , J., Salado Carbajal, M., & Rocha Uribe, J. A. (2000). *Simulacion de procesos en ingeniería química.* Mexico, D.F: Plaza y Valés Editores.

[11] Turton, R., Bailie, R., Whiting, W., Shaeiwitz, J., Bhattacharyya, D. (2012). *Analysis, synthesis, and design of chemical processes, 4th ed.* USA: Pearson.

[12] Towler, G., Sinnott, R. (2013). *Chemical engineering design, principles, practice economics of plant and process design.* Oxford: Butterworth-Heinemman

[13] Seider, W., Seader, J., Lewin, D., Widagdo, S. (2009). *Product and process design principles, 3rd ed.* USA.: John Wiley & Sons.

[14] Hougen, O.A., Watson, K.M., Ragatz, R.A. (1959). Chemical process principle, part II, thermodynamics. New York: Reverte.

[15] Razak, A.M.Y. (2007). *Industrial gas turbines, performance and operability.* North America: Woodhead Publishing Limited.

[16] Serth, R. W., Lestina, T. (2014). *Process heat transfer, principles and applications 2nd ed.* Academic Press

[17] Puigjianer, L., Ollero, P., de Prada. C., Jiménez, L. (2006). *Estrategias de modelado, Simulacion y optimizacion de procesos quimicos.* España: Sintesis.

[18] Kemp, I. C. (2007). *Pinch analysis and process integration, Second Edition.* Oxford: Butterworth-Heinemann.

[19] El-Halwagi, M., M. (2012). *Sustainable design through process integration.* USA: Butterworth-Heinemann

Comparison tools for parametric identification of kinetic model for ethanol production using evolutionary optimization approach

Nonlinear techniques for parametric identification of a kinetic model ethanol

P. A. López-Pérez
Escuela Superior de Apan,
Universidad Autónoma del Estado de Hidalgo
Hidalgo, México
save1991@yahoo.com.mx

H. I. Velázquez Sánchez, R. Aguilar-López
Departamento de Biotecnología y Bioingeniería
CINVESTAV-IPN
D.F., México
raguilar@cinvestav.mx

H. F. Puebla Núñez
Departamento de Energía
Universidad Autónoma Metropolitana-Azcapotzalco
D.F., México
hpuebla@correo.azc.uam.mx

***Abstract*—Living cells, type of substrate, enzymatic hydrolysis play an important role in the efficiency of ethanol production; however, the kinetic parameters of biochemical reactions necessary for modelling these processes are often not accessible directly through experiments. In this context, for the implementation of suitable operational strategies, it is necessary to have kinetic models able to describe the process as realistically as possible. This paper proposes a comparative study of two nonlinear techniques for parametric identification of a kinetic model for ethanol production from recycled paper sludge in order to improve process performance. The parameters of the model are optimized by two methods: using the Levenberg–Marquardt optimization approach and Genetic Algorithms. The performances of both techniques are evaluated using a numerical simulation. Finally, the effect of parametric adjustment and dilution rate on productivity was demonstrated by changing the batch operation to the continuous operating model. The maximum ethanol concentration was about 13.9 g/l (model), in batch process and about 13.75 g/l at Dilution rate = 0.005 h^{-1} in continuous process. The optimization parameters via genetic algorithms showed the best results.**

Keywords— genetic algorithm; simultaneous saccharification-fermentation; parametric identification; recycled paper sludge component

I. INTRODUCTION

The biomass has emerged as one of the dependable nontraditional feed stocks for the ethanol, diesel and methane production which are major areas of interest in the energy scenario. Biofuels such as ethanol are one alternative to replace non- renewable petroleum-based energy sources [1]. Current bio- ethanol production relies on the hydrolysis (pretreatment) of agricultural crop material into soluble sugars, and yeast (*Saccharomyces cerevisiae*) is used to convert sugars into ethanol [2]. However, ethanol produced from grain crops like corn or wheat increases food prices due to its competition with food supplies [3]. Cellulose is the most abundant, sustainable bio-polymer that can be degraded into soluble sugars for ethanol production. Due to its recalcitrant nature, most cellulose on earth is not utilized.

Techniques to convert lignocellulose biomass into ethanol have been developed. Conventional cellulosic ethanol processes involve substrate pretreatment (to provide accessible cellulose), cellulase production (enzyme that degrade cellulose), cellulose hydrolysis, ethanol fermentation and product recovery. Nonetheless, low ethanol yield and inefficient cellulose hydrolysis remain challenges to commercial cellulosic ethanol production[4-6]. The ethanol industry needs to be more competitive, and therefore, all stages of its production process must be simple, inexpensive, efficient, and "easy" to control. However, a lot of research effort is still required in optimization and control, where the first step is the development of suitable models of the process, which can be used as a simulated plant, as a soft sensor or as part of the control algorithm [7,8].

The goal of the recently emerging interest in modelling of biological processes is to understand and describe quantitatively the dynamics of living cells. In order to attain this purpose, new experimental procedures and modelling techniques are needed to generate and analyse relevant biological data. The kinetic modeling is an important aim in the bio-chemical reaction engineering in order to design, optimize, operate and control bio-chemical reactors. However the

develop of accurate kinetic models is still a challenging issue, due to the lack of knowledge to identify the main phenomena related to proceed and identify the corresponding parameters of the kinetic models actually employed [9].

Parameter estimation has also been accomplished using a variety of nonlinear procedures. Most of these techniques are calculus-based search algorithms that use the gradient of the response surface to search for a minimum in the residual sum of squares [10]. In general, a genetic algorithm (GA) can be described as a calculus-free, heuristic optimization tool [11]. Its principal strength is that it obtains parameters that satisfy the optimization problem even for poorly behaved functions. GAs have been widely used for optimization problems in biotechnology and bioengineering [12-15]. Chen et al. [16] introduced the use of GA for identifying the unknown parameters of seventh-order nonlinear model of fed-batch culture of hybridoma cells on-line and to optimize feed rate control profiles for glucose and glutamine. In [17] a systematic method to support the building of bioprocess models through the use of different optimization techniques is presented. The method was applied to a tower bioreactor for bioethanol production. As the first step, the potential of global searching of real-coded genetic algorithm (RGA) was applied for simultaneous estimation of the parameters. Subsequently, the most significant parameters were identified using the Placket-Burman (PB) design. Nowadays, some improvements associated with this type of operation strategy, are required in industrial plants, when optimized operation is a target.

Therefore, there is a models and procedures development demand that describe the process in such way optimization, control and improved operation techniques may be used [18, 19] This paper proposes a comparative study of two nonlinear techniques for parametric identification of a kinetic model for ethanol production from recycled paper sludge in order to improve process performance. The investigated kinetics model can be used to describe simultaneous saccharification and fermentation (SSF), for the production of ethanol, this model was modified considering the following changes: a variable associated with enzyme deactivation, and a biomass parameter. The parameters of the model are optimized by two methods: estimation using the method of Levenberg–Marquardt (L-M) optimization approach and Genetic Algorithms. The performances of both techniques are evaluated using a numerical simulation. After parameter estimation, the effect of using the parametric methods and dilution rate on productivity was demonstrated when changing of the batch operation to the continuous operating model.

II. METHODOLOGY

A. *Kinetic model*

Model describing SSF can be very simple or very complex and the degree of complexity needed is decided by the purpose of the model. Some mathematical models of SSF have also been proposed to predict the performance of SSF, a common shortcoming of these studies is that the models have not been completely verified because the variation in microorganism concentration over time was not simulate, continuous SSF model is incorrect because the model does not include enzyme addition [20, 21].

To the present date several models describing enzymatic hydrolysis of cellulose [22, 23], but only a few describing SSF have been developed [24]. Therefore, for industrial application, it is necessary to develop models with the following characteristics: few parameters, easy determination of the values of these parameters, they are easily mastered by process engineers, strong potential in on-line estimation and control of bioprocess and these parameters must have physical-biological meaning rather than empirical[25].

For these reasons, in this paper we analyze the proposed model by Shen et al. [26] [27], this model has demonstrated flexibility for different operational conditions of SSF. The fermentation process occurs in a bioreactor and was modeled as a batch reactor. The continuity equation of mass was applied to the batch reactor to develop mathematical equations that were used to monitor the concentrations of: the rate of substrate (cellulose) utilization, the rate of biomass formation (bacteria), the rate of cellobiose, the rate of glucose and the rate of product formation (ethanol) all in g/l, the equations are:

Batch Operating Mode

Cellobiose (B) mass balance:

$$\frac{dB}{dt} = \left(\frac{\alpha_1 C}{0.947(1+G/\alpha_2)}\right)\left[\frac{e_0}{\alpha_{10}+e_0\alpha_3 t}\right]^n - \frac{\alpha_4 B}{1+G/\alpha_5} \tag{1}$$

Glucose (G) mass balance:

$$\frac{dG}{dt} = \left(\frac{\alpha_4 B}{0.95(1+G/\alpha_2)}\right) - \left[\frac{\alpha_6 XG}{(\alpha_7+G)Y_{X/G}}\right] - \alpha_8 X \tag{2}$$

Biomass (X) mass balance:

$$\frac{dX}{dt} = \frac{\alpha_6 XG}{(\alpha_7+G)Y_{X/G}}\left(1-\frac{X_0}{X}\right)exp^{(-\alpha_{11}t)} \tag{3}$$

Ethanol (E) mass balance:

$$\frac{dE}{dt} = \frac{\alpha_9\alpha_6 XG}{(\alpha_7+G)Y_{X/G}} \tag{4}$$

The equations (1-4) can be used in principle to simulate the concentration changes of cellobiose, glucose, biomass mass, and ethanol with respect to time. However, the mass balance on cellulose can be expressed in terms of cellobiose, glucose, ethanol, and biomass in the culture as follows:

$$C = C_0 - 0.9G - 0.947B - 0.9E/0.511 - 1.137(X - X_0) \tag{5}$$

Where C_0 is the initial cellulose concentration (g/l), X_0 is the initial cell concentration (g/l), the constant 0.9 is the conversion factor of a glucan unit in cellulose to glucose, 0.511 is the inverse conversion factor of glucose to ethanol, and the constant 1.137 is the conversion factor of cellulose consumed to produce yeast (g cellulose/g dry biomass) assuming the molecular formula of the yeast, *Saccharomyces cerevisiae*, to be $CH_{1.74}\ N_{0.2}\ O_{0.45}$ during anaerobic fermentation of glucose [28].

Assumptions of the model are that:

1) Cellulose is converted into glucose through cellobiose. Direct conversion of cellulose to glucose is negligible.
2) The effects of external and internal mass transfers on the enzyme reaction and microorganism metabolic processes can be neglected based on the assumptions that mixing was perfect
3) The product (ethanol) formation associated with the biomass growth can be represented as

$$Glucose \xrightarrow{X,G,E} Ethanol + Cell + CO_2$$

4) The enzyme deactivation is caused by the ineffective adsorption of endo-β-1,4- glucanase and exo-β-1,4-cellobiohydrolase on the solid substrate. The ineffective complex formation rate can be expressed as [24]

$$e = \left[\frac{e_0}{\alpha_{10} + e_0 k_3 t}\right]^n$$

5) The new term is added to balance of biomass based on reference [24, 29, 30]

$$\left(1 - \frac{X_0}{X}\right) exp(-\alpha_2 t)$$

6) This theoretical ethanol yield is similar to other experimental and industrial data [28].

$$Y_{X/G} = 0.515$$

Here

α_1 specific rate constant of cellulose hydrolysis to cellobiose (l/g h), α_2 inhibitory constant of glucose to the endo-β-1,4-glucanase and exo-β-1,4-cellobiohydrolase (g/l), α_3 specific rate constant of enzyme deactivation (l/(g h)), α_4 specific rate constant of cellobiose hydrolysis to glucose (h^{-1}), α_5 inhibitory constant of glucose to the glycosidase (g/l), α_6 maximum specific biomass growth rate constant (h^{-1}), α_7 glucose saturation constant for the microbial growth (g/l), α_8 maintenance coefficient for endogenous metabolism of the microorganisms (h^{-1}) or total number of initial enzyme concentration, α_9 product formation coefficient associated with biomass growth (dimensionless), α_{10} Enzyme deactivation constant (h^{-1}), α_{11} is the constant of declining substrate-enzyme reactivity (dimensionless, *n* is the constant (dimensionless).

B. *Parameter identification methods*

a) Levenberg–Marquardt optimization approach

Biological systems have been traditionally fit using graphical-based techniques, in which parameter estimation is converted to a linear regression problem [30]. However, the applicability of this approach is related to the functionality of the model. Furthermore, graphical methods have been shown to produce inferior parameter estimates than those generated using nonlinear regression techniques. Nonlinear regression was used based on the Levenberg-Marquardt least squares minimization algorithm, which is a hybrid of the Gauss-Newton and the steepest descent methods [30].

Equations (1)-(5), were used for the parameter fitting with the following initial conditions: B_0 = 3.5 g/l; G_0 = 0.29 g/l, X_0: = 0.10 g/l, E_0 = 0.2 g/l. The Model-Maker® software (based on Levenberg–Marquardt optimization approach) was used for the non-linear fitting data as shown in Figure 1. The performance of the proposed mathematical model was statistically evaluated using the dimensionless coefficient of efficiency (Π), as suggested by Köhne et al. [31]

$$\Pi = 1 - \frac{\sum_{i=1}^{N}\left[\left|Y - Y^*\right|\right]}{\sum_{i=1}^{N}\left|Y^* - \overline{Y}\right|} \qquad (6)$$

Where Y is the simulated value of the variable at time t_i, Y^* is the observed value of the same variable at time, and $\overline{Y}$ is the mean value of the observed variable. Π varies between ($-\infty$, 1]. A positive value of Π represents an acceptable simulation whereas Π > 0.5 represents a good simulation

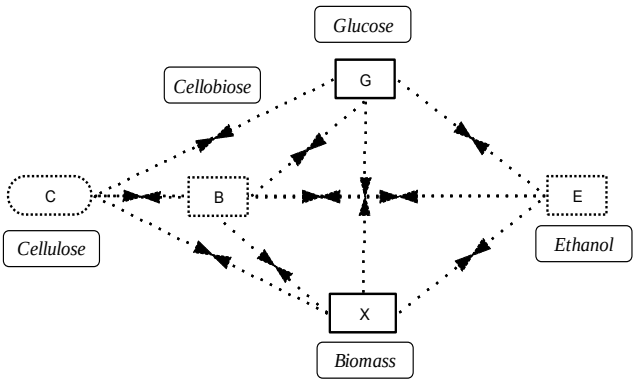

Fig. 1. Graphic algorithm generated in model maker®

b) Based on a genetic algorithm (GA)

For this work, a GA was used to estimate the model parameters from sets of experimental data. This was accomplished using the genetic algorithm package developed by Matlab™ R2009 library "gatool". As with most GAs, were incorporated three basic genetic operators: selection, crossover, and mutation. By combining these three operators, the algorithm converges on the optimal solution while maintaining sufficient diversity (see figure 2). Data used for the system (1)-(5).

To implement the genetic algorithms, the model's parameters have to be presented in terms of chromosomes. Decimal numbers for the parameter values have been used to represent this principle instead of a binary profile. Each chromosome corresponds to one different objective function value. In the literature the most often used optimization criterion is defined as a modelling error, i.e. the mean square deviation between the model output and the corresponding data obtained during the fermentation. The optimization criteria are presented as follows:

$$\lambda_Y = \sum \left(Y - Y^*\right)^2 \rightarrow min \qquad (7)$$

where Y is the simulated value of the variable at time t_i and Y* is simulated values (experimental), respectively for C, B, X, G, and E

The initial values of other algorithm's parameters and functions are:

- Population:
- Population type: Double vector
- Population size: 250
- Fitness scaling
- Scaling function: Proportional
- Selection: Stochastic uniform
- Reproduction
- Elite count: 150
- Crossover fraction: 0.8
- Crossover : Single point
- Mutation
- Mutation function: Adaptive feasible

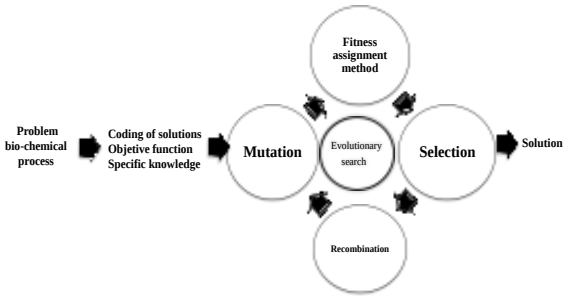

Fig. 2. Evolutionary algorithms

III. Results and Discussion

Batch simulation were performed for estimation of kinetic parameters. The experimental data served to obtain the 12 parameter values of the model developed. With all parameters determined (Table I), the model was solved and compared to this experimental data. The model accurately predicted cellulose, cellobiose, glucose and ethanol concentrations (solid lines, Fig. 3).The initial values of the state variables (B_0 = *3.5 g/l;* G_0 = *0.29 g/l,* X_0*: = 0.10 g/l,* E_0 = *0.2 g/l*), where the parameter vector to be estimated is:

$$\theta = \alpha_1, \alpha_2, \alpha_3, \alpha_4, \alpha_5, \alpha_6, \alpha_7, \alpha_8, \alpha_9, \alpha_{10}, \alpha_{11}, n \qquad (8)$$

The parameter values obtained in the present study are similar to those reported in the literature, this may be due to the different operating conditions used in each case, i.e., microorganims, different carbon source, continuous or batch operation, temperature, pH, among others (see Table 1). The rest of parameters in Table I were maintained constants according to literature values.

The performance of the model in describing the experimental observations for batch fermentation is shown in Figure 3 and quantified through the Π. From this criterion, it was concluded that the model described the experimental data accurately, as evaluated by Π with better performance for the method of genetic algorithms above 0.9923. Also, in all cases Π was close to unity, indicating a good fit of the model, in comparison with the method of L-M (0.9606), as can be seen in Table II. Results showed that it is possible to accurately infer concentration in batch fermentation.

Moreover, the ethanol concentration increased rapidly within the first 25 hours, and then leveled off until 40 hours. After 50 hours, the ethanol concentration slightly decreased probably because of the microbial conversion of ethanol into organic acids. .

It was concluded that the ethanol production in the initial period was controlled by biomass growth concentrations (solid lines, Fig. 3). Furthermore, the experiment showed that the maximum ethanol concentration was about 13.9 g/l (model), which was equal to a theoretical ethanol yield of 61.2% in batch processes.

The maximum specific growth rate obtained was

0.312 h^{-1}(α_6) which is quite similar to reported in table 1.

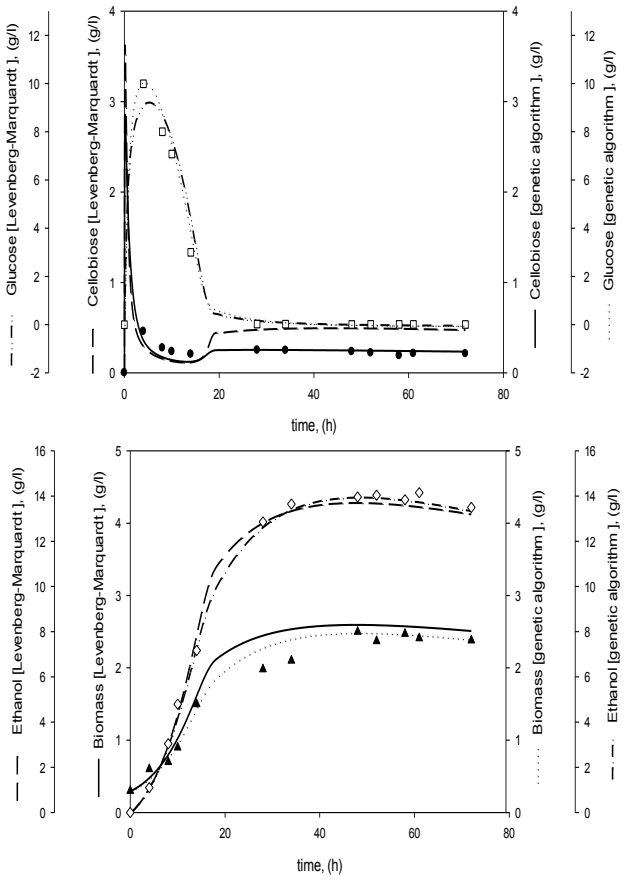

Fig. 3. Comparison of experimental data (symbol) and predictions of the model (line)

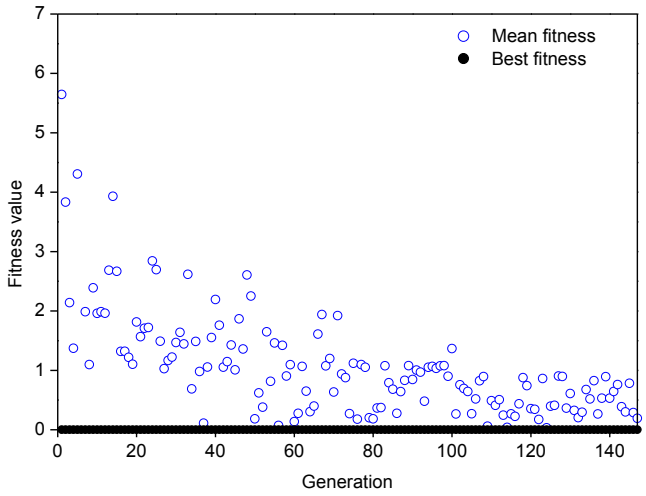

Fig. 4. Genetic algorithm

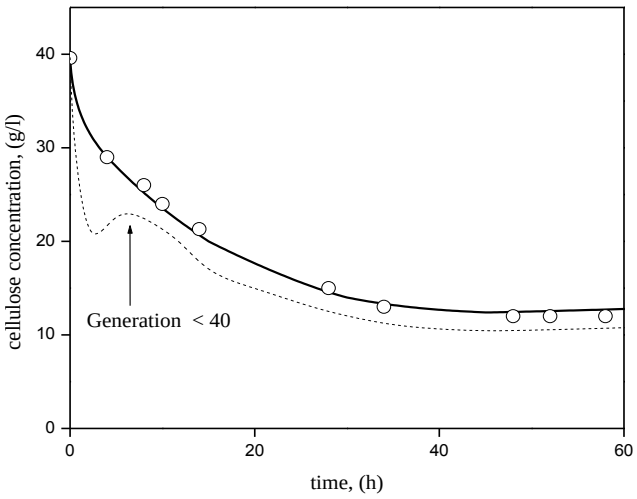

Fig. 5. Cellulose concentrations validated by GA

The best combination of parameter values was found at greater than generation >40 function evaluations which is according to Hansen and Kern [32] have reported that increasing the population, in many cases considerably increases the performance of the algorithm. In our applications, this kind of behaviour could be observed in significant magnitude. It is though possible that the population size should have been increased even more than we did to obtain an increase in algorithm performance (see Figure 4, 5).

TABLE I. The model parameters

Parameter	Values				
	L-M	***GA***	***[25]***	***[33]***	***[34]***
α_1	0.612	0.661	0.601	—	0.038
α_2	0.229	0.230	0.174	386.2	0.418
α_3	0.070	0.080	0.099	—	0.12
α_4	3.000	3.133	3.200	0.321	2.38
α_5	14.3	16.904	16.28	5.389	—
α_6	0.164	0.312	0.176	0.053	0.596
α_7	3.85	3.258	3.396	5722	0.722
α_8	0.647	0.348	0.643	5.5x10-6	—
α_9	3.589	3.052	3.075	50.3	14.66
α_{10}	1.3	0.9	—	—	0.12
α_{11}	1.2	0.95	—	—	—
n	0.9	0.95	—	—	4.49

— Not reported

TABLE II Model efficiency coefficients for the mathematical model.

Mass balance	Π	
	L-M	***GA***
Cellobiose	0.923	0.9939
Glucose	0.979	0.9956
Biomass	0.973	0.9796
Ethanol	0.978	0.9984
Cellulose	0.95	0.9940
Global	**0.9606**	**0.9923**

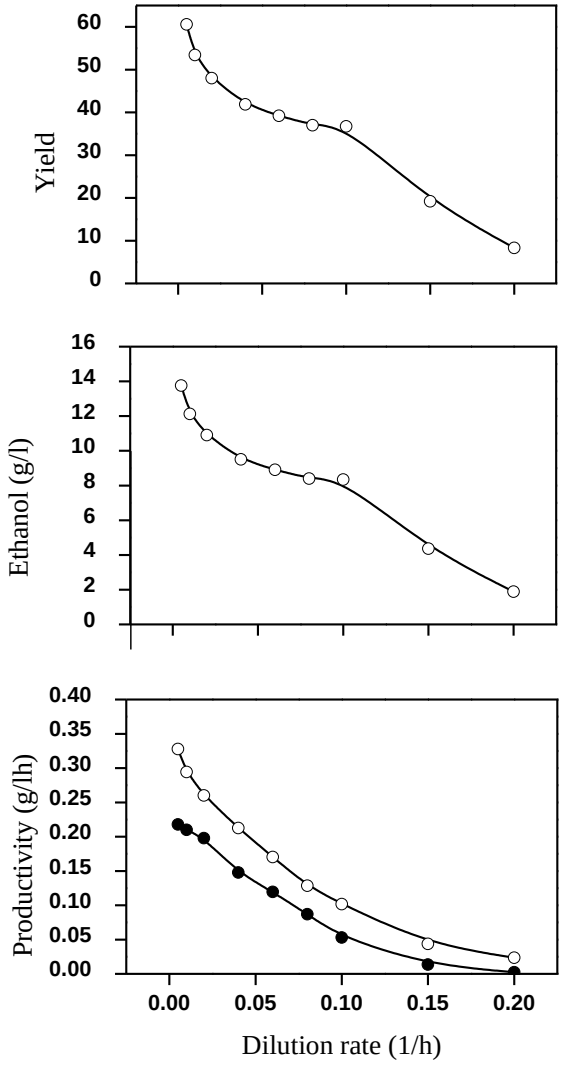

Fig. 6. Ethanol concentration, productivity and yield in continuous processes, ● L-M and ○GA.

After parameter estimation, the kinetic model was tested considering a continuous operating process with different dilution rate D = [0.005, 0.01, 0.02, 0.04, 0.06, 0.08, 0.1, 0.15, 0.2] in h^{-1}. The maximum ethanol concentration was about 13.75 g/l at D = 0.005 h^{-1}, this value was slightly lower than that in the batch experiment (13.9 g/l) because, the highest ethanol concentration was dependent on the dilution rate (see Fig. 6). and rapidly decreased to zero at a washout point. Moreover, it can be seen that productivity using the method GA is greater than the overall productivity of the method L-M it should be noted that these results are due only by the type of parametric adjustment, taking a difference between the productivities of 0.11 (g/lh) corresponding to one concentration of ethanol 2.44 between the stationary states of both methods (see Figure 6). However, when the dilution rate approached the washout point (D = 0.2 h^{-1}), the steady state of the system immediately reached the point at which both the biomass and ethanol concentrations were very low.

IV. Conclusion

Genetic algorithm gives the better results, which are in good agreement with the experimental data, when compared to simulations conducted with optimized parameters obtained by method of Levenberg–Marquardt. Also the changes in the kinetic parameters and the dilution rate have an effect on ethanol productivity in a continuous system. The promising results obtained indicate the feasibility of the technique for future application in the design and control of bioreactors.

References

[1] D. Karonis, C. Chapsias, F. Zannikos, E. Lois, "Impact of Ethanol Addition on Motor Gasoline Properties," 5th. International Fuels Congress, Esslingen, Germany, pp.301, October 2005.

[2] R. Razmovski and V. Vučurović, "Bioethanol production from sugar beet molasses and thick juice using *Saccharomyces cerevisiae* immobilized on maize stem ground tissue," Fuel, vol. 92, pp. 1–8, February 2012.

[3] E. Waltz, "Cellulosic ethanol booms despite unproven business models," Nat. Biotechnol., vol. 26, pp. 8-9, February 2008.

[4] L. T. Fan and Y. H. Lee, "Kinetic studies of enzymatic hydrolysis of insoluble cellulose: derivation of a mechanistic kinetic model," Biotechnol. Bioeng., vol. 25(11), pp. 2707–33, November 1983

[5] C. Piccolo and F. Bezzo, "A techno-economic comparison between two technologies for bioethanol production from lignocelluloses," Biomass Bioenerg., vol. 33, pp. 478–491, March 2009

[6] Y. Sun, J. Cheng, "Hydrolysis of lignocellulosic materials for ethanol production: A review," Bioresource Technol., vol. 83, pp. 1–11, May 2002

[7] Y. Wang, J. Chu, Y. Zhuang, Y. H. Wang, J. Xia and S. Zhang, "Industrial bioprocess control and optimization in the context of systems biotechnology," Biotechnol Adv., vol. 27, pp. 989–95, Nov-Dec 2009.

[8] P. A. López-Pérez, R. Maya-Yescas, V. Peña-Caballero, R. Valentín Gomez-Acata and R. Aguilar-López, "Software sensors design for a model of a simultaneous saccharification and fermentation of starch to ethanol," FUEL, vol.110, pp.219-226, August 2013

[9] H. Resat, L. Petzold and M. F. Pettigrew, "Kinetic Modeling of Biological Systems Methods," Mol. Biol., vol. 541, pp. 311–335, Mar 2009.

[10] J. Roubos, G. van Straten and A. van Boxtel, "An evolutionary strategy for fedbatch bioreactor optimization: Concepts and performance," J. Biotechnol, vol. 67, pp. 173–187, January 1999.

[11] L. Chen, S. Nguang, X. Chen and X. Li, "Modelling and optimization of fedbatch fermentation processes using dynamic neural networks and genetic algorithms," Biochem. Eng. J., vol. 22, pp. 51–61, December 2004.

[12] K. Patil, I. Rocha, J. Forster and J. Nielsen, "Evolutionary programming as a platform for in silico metabolic engineering. BMC Bioinformatics," vol. 6(308), pp. 1–12, December 2005.

[13] D. Sarkar and J. Modak, "Optimisation of fed-batch bioreactors using genetic algorithms," Chem. Eng. Sci., vol. 58, pp. 2283–2296, June 2003.

[14] S. Moonchai, W. Madlhoo, K. Jariyachavalit and H. Shimizu, "Application of a mathematical model and differential evolution algorithm approach to optimization of bacteriocin production by Lactococcus lactis c7," Bioprocess Biosyst. Eng., vol. 28, pp. 15–26, October 2005.

[15] J. F. Cuadros, D. C. Melo Maciel, R. Filho and M. R., Wolf Maciel. "Fluid catalytic cracking environmental impact: Factorial design coupled with genetic algorithms to minimize carbon monoxide pollution," Chem. Eng. Transactions, pp. 243-248, June 2012.

[16] L. Z. Chen, S. K. Nguang, X. D. Chen, "On-line identification and optimization of feed rate profiles for high productivity fed-batch culture of hybridoma cells using genetic algorithms," ISA Trans., vol.41, pp. 409-419, October 2002.

[17] E. Ccopa Rivera, A. Carvalho da Costa, B. Hoss Lunelli, M. Regina Wolf Maciel and R. Maciel Filho, "Kinetic Modeling and Parameter Estimation in a Tower Bioreactor for Bioethanol Production" Appl Biochem. Biotechnol., vol. 148(1-3), pp. 163-73, Mar 2008.

[18] R. R. Andrade, E. C. Rivera, D. I. P. Atala, R. Maciel Filho, F. Maugeri Filho and A. C. Costa, "Study of kinetic parameters in a mechanistic model for bioethanol production through a screening technique and optimization," Bioprocess Biosyst. Eng., vol. 32, pp. 673-680, 2009.

[19] J. Almquista, M. Cvijovicc, V. Hatzimanikatise, J. Nielsen, M. Jirstrand, "Kinetic models in industrial biotechnology – Improving cell factory performance," Metab. Eng., vol. 24, pp. 38–60, July 2014.

[20] G. P. Philippidis, D. D. Spindler and C. E. Wyman, "Mathematical modeling of cellulose conversion to ethanol by the simultaneous saccharification and fermentation process," Appl. Biochem. Biotechn., vol. 34 (1), pp. 543-556, September 1992.

[21] M. T. Holtzapple, H. S. Caram and A. E Humphrey, "The HCH-1 Model of Enzymatic Hydrolysis," Biotech. Bioeng. vol. 26, pp.775-780, February 1984.

[22] C. Brandam, X. M. Meyer, J. Proth, P. Strehaiano and H. Pingaud, "An original kinetic model for the enzymatic hydrolysis of starch during mashing," Biochem. Eng. J., vol. 13, pp. 43–52, January 2003.

[23] R. E. T. Drissen, R. H. W. Maas, J. Tramper and H. H. Beeftink, "Modelling ethanol production from cellulose: separate hydrolysis and fermentation versus simultaneous saccharification and fermentation," Biocatal. Biotransformation, vol. 27 (1), pp. 27-35, 2008.

[24] L. K. Kadam, E. C. Rydholm and J. D. McMillan, "Developement and Validation of a Kinetic Model for Enzymatic Saccharification of Lignocellulosic" Biomass. Biotechnol. Prog., vol. 20, pp. 698-705, May-Jun 2004.

[25] J. Shen and F. A. Agblevor, "The operable modeling of simultaneous saccharification and fermentation of ethanol production from cellulose," Appl. Biochem. Biotechn., vol. 160(3), pp. 665-681, March 2010.

[26] J. Shen and F. A. Agblevor, "Kinetics of enzymatic hydrolysis of steam exploded cotton gin waste". Chemi. Eng. Commun., vol. 195(9), pp.1107-1121, May 2008.

[27] M. L. Shuler and F. Kargi, Bioprocess Engineering. 2Ed, Prentice Hall PTR, 2002, pp. 217.

[28] C. R. South, D. A. L. Hogsett and L. R. Lynd, "Modeling simultaneous saccharification and fermentation of lignocellulose to ethanol in batch and continuous reactors," Enzyme Microb. Technol., vol. 17, pp. 797-803, September 1995.

[29] K. Belkacemi, "Enzymatic hydrolysis of dissolved corn stalk hemicelluloses: reaction kinetics and modeling," J. Chem. Technol. Biotechnol., vol. 78, pp. 802-808, June 2003.

[30] K. Vasanth Kumar, "Linear and non-linear regression analysis for the sorption kinetics of methylene blue onto activated carbon," J. Hazard. Mater., vol. B137, pp. 1538–1544, October 2006.

[31] J. M. Köhne, S. Köhne and J. Šimůnek, "Multiprocess herbicide transport in structured soil columns: experiments and model analysis," J. Contam. Hydrol., vol. 85, pp.1–32, May 2006.

[32] N. Hansen, S. Kern, Evaluating the CMA evolution strategy on multimodal test functions, in: Xin Yao, Edmund K. Burke, José A. Lozano, Jim Smith, Juan Julián Merelo-Guervós, John A. Bullinaria, Jonathan E. Rowe, Peter Tino, Ata Kabán, HansPaul Schwefel, Parallel Problem Solving from Nature - PPSN VIII, Springer–Verlag, Berlin, 2004, pp. 282–291

[33] D. López, T. Barz, H. Arellano-Garcia, G. Wozny, A. Villegas, S. Ochoa, "Subset selection for improved parameter identification in a bio-ethanol production process" Czasopismo Techniczne, Mechanika, vol. R. 109, pp. 137—147, June 2012.

[34] K. K. Podkaminer, X. Shao, D. A. Hogsett and L. R. Lynd, "Enzyme Inactivation by Ethanol and Development of a Kinetic Model for Thermophilic Simultaneous Saccharification and Fermentation at 50 -C with Thermoanaerobacterium saccharolyticum ALK2" Biotechnol. Bioeng., vol. 108, pp. 1268-78, June 2011.

Fenton's process, a homogeneous or heterogeneous catalytic system?

M. Ocampo-Gaspar[1], L. F. Payan-Martínez[1], R. Suárez-Parra[*1]

[1]Instituto de Energías Renovables IER-UNAM.

Priv. Xochicalco S/N, Temixco, Morelos 62580 México.

*rsp@ier.unam.mx

L. González-Reyes[2], I. Hernández-Pérez[2], J. A. Colin-Luna[2]

[2]Universidad Autónoma Metropolitana-A

Av. Sn. Pablo No. 180, México, D.F. 02200, México.

V. Garibay-Febles[3]

[3]Instituto Mexicano del Petróleo

Eje Central Lázaro Cárdenas Norte 152 Colonia San Bartolo Atepehuacan, 07730, México D. F.

Abstract **— Fenton and photoFenton reactions are well known as advanced oxidation processes. The stablished reaction mechanism, redox reactions of iron(II/III) ions considers a homogeneous catalytic process. Besides, the best results of Fenton's reactions are reached using iron(II) sulfate salt. In the present work, we show the degradation process of Basagran 480 pesticide with iron oxide (Fe_2O_3) nanoparticles (NPs). The Fe_2O_3 NPs were prepared using three iron salts ($FeCl_2$, $FeCl_3$, $FeSO_4$) and hydrogen peroxide (H_2O_2) in similar conditions as Fenton's processes at pH 2.5 and pH 3. In accordance with the obtained results, we suggest a different explanation to the Fenton's process (homogeneous catalytic reaction), instead the degradation process considers the presence of Fe_2O_3 NPs prepared with all the mentioned iron salts. At the same time, the Fe_2O_3 NPs characterization, by HRTEM and Nanoflex, supports that the Fenton's and photoFenton's processes should be considered as heterogeneous catalytic systems.**

Keywords — homogeneous catalysis, heterogeneous catalysis, nanoparticles, iron oxide

I. INTRODUCTION

The Fenton's reaction is known since 1894 [1] and in the first half of XX century Haber and Weiss proposed the interaction way between iron(II) and iron(III) ions with hydrogen peroxide molecules to form hydroxyl radicals [2]. Recently, the increase in the new environmental regulations and water quality concerns, extensive research has focused on upgrading current water treatment technologies and developing more economical processes that can effectively reduce the high levels of toxic organic and biologically refractory pollutants in wastewater. Among Advanced Oxidation Process, the Fenton's reagent is an interesting solution since it allows high depuration levels at room temperature and pressure conditions using innocuous and easy to handle reactants. The inorganic reactions involved in Fenton process are well established and the process has been used for the treatment of a variety of wastewaters. The high efficiency of this technique can be explained by the formation of strong hydroxyl radical (.OH) and oxidation of Fe^{2+} to Fe^{3+}. Most studies focused on applying the Fenton or Photo-Fenton processes to wastewater treatment, have considered as homogeneous.

By Haber and Weiss and subsequent studies it was stablished that using iron(III) ions the degradation rate of organic compounds is slower than using iron(II) ions with hydrogen peroxide [3, 4]. Further investigations stablished that the presences of different anions also affect the degradation process of organic compounds, as a result of a lower rate generation of hydroxyl radicals or complexation reactions with iron (II) ions, or scavenging process of hydroxyl radicals [5]. The explanation of Basagran 480 pesticide degradation in the systems of $FeSO_4$-H_2O_2, $Fe_2(SO_4)_3$-H_2O_2, $FeCl_2$-H_2O_2 and $FeCl_3$-H_2O_2 considers, in a first place, the formation of Fe_2O_3 or iron oxohydroxide (FeOOH) NPs when iron(II/III) ions interact with H_2O_2 [6, 7].

II. EXPERIMENTAL METODOLOGY

In order to prepare the Fe_2O_3 NPs, initially 12 aqueous mixtures of iron(II/III) salts were prepared using $FeSO_4$, $Fe_2(SO_4)_3$, $FeCl_3$ y $FeCl_2$). Four of these mixtures were prepared at pH 4, the next four mixtures were prepared at pH 2.8 and the last four mixtures were prepared at pH 2.3. In all these mixtures the iron (II/III) ions concentration $C=1x10^{-3}$ M. Then, in a Batch reactor of 600 mL the degradation reaction of Basagran 480 was developed in darkness or illuminated conditions with Fe_2O_3 NPs and H_2O_2. When the reaction system was illuminated, a domestic lamp of 15 W, with visible emission spectrum, was used [6]. The colloidal system was vigorously stirred on a magnetic plate. The degradation and photodegradation of Basagran 480 was developed in the next conditions: in a beaker batch reactor of 600 mL, 50 ml of an iron salt dilution, at pH 4, were diluted in 200 ml of deionized water. This system was stirred ten minutes in order to restore the equilibrium conditions of aqueous iron complexes, meanwhile in a second beaker 2 mL of H_2O_2 were diluted with

223 mL of deionized water. This second system also was strongly stirred. After ten minutes of stirring, the mixture of H_2O_2 was added to the mixture of aqueous iron salt. The interaction of iron (II/III) ions with H_2O_2 forms the Fe_2O_3 or FeOOH NPs. At this point the pH 4 was adjusted to pH 3 or pH 2.5 with hydrochloric or sulfuric acid, depending of the anion of the precursor salt. Finally, 25 mL of the pesticide, Basagran 480, were added to the mixture and the lamp was turned on. The initial concentration of the pesticide was 100 mg/L and the iron ions concentration in the system was $1*10^{-4}$ M. A similar procedure was done for the systems, when acidic conditions were adjusted from pH 2.8 to pH 3, and from pH 2.3 to pH 2.5. The only change was related with the addition of H_2O_2 as the last and not diluted component to the system. It is important to denote that the initial strong conditions of pH 2.8 or pH 2.3 to get, respectively, pH 3 or pH 2.5 were stablished to simulate the Fenton's initial conditions. In order to measure the size's distribution and to verify the presence of Fe_2O_3 NPs, instead to add the pesticide to the catalytic system, it was added deionized water. In order to determine the presence an size of Fe_2O_3 nanoparticles in the different systems investigated, it was conducted by using a Nanoflex particle size-meter and by high resolution transmission electron microscopy JEOL JEM-2200FS at 200 kV.

III. RESULTS AND DISCUSSION

In Figures 1a and 1b, using a Nanoflex device it could be seen the detection of different particles with different sizes in each system at pH 2.5 and pH 3. The systems got pH 2.5 and pH 3 from iron(II/III) aqueous mixtures with initial pH 4. In the Fig. 1a, at pH 2.5, the particles, which were prepared with $FeSO_4$, show a size around 1 nm and the size of particles which were prepared with $FeCl_3$, show different sizes between 1-100 nm. In the Fig. 1b, at pH 3, the particles' sizes, for those which were prepared with $FeSO_4$ and $FeCl_3$, are around 1 nm. In both pH, the size of the particles prepared with $Fe_2(SO_4)_3$ or $FeCl_2$, is larger than 100 nm, Figs. 1a and 1b. Fig. The great importance of these results lay revealing the formation of a suspension of different iron oxide compounds when mixing iron salts with H_2O_2. Indeed, these results also would indicate the formation of heterogeneous systems for the interaction of $FeSO_4$-H_2O_2 at pH⩽3, refusing the Fenton's interpretation of ionic homogeneous system.

Figure 1a. Size distribution of particles prepared at pH 2.5, with different iron(II/III) aqueous solutions at pH 4 and hydrogen peroxide

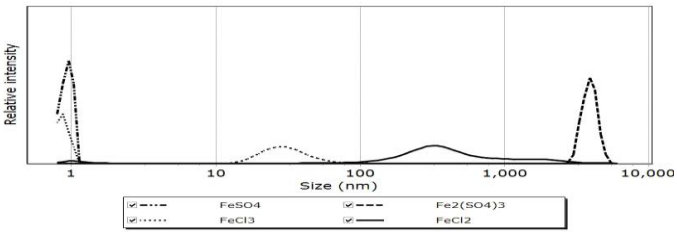

Figure 1b. Size distribution of particles prepared at pH 3, with different iron(II/III) aqueous solutions at pH 4 and hydrogen peroxide.

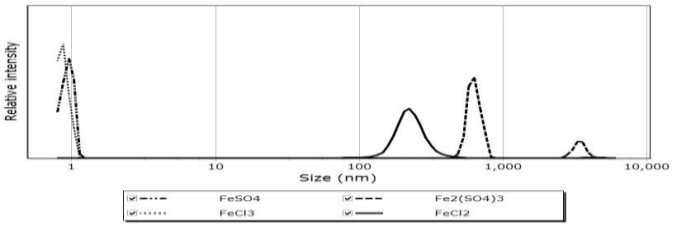

Another consideration from these results suggests that those systems with particles' size of 1 nm should show a higher surface area than other systems. Moreover, this assumption suggests the presence of a higher number of active catalytic centers improving the catalytic activity of those systems to degrade different organic compounds.

In Figure 2, the HRTEM analysis, on the suspension prepared with iron(II) sulfate and hydrogen peroxide, confirms the presence of a mixture of iron oxide compounds in a same nanoparticle: two iron(III) oxides phases - α-Fe_2O_3 (Hematite) and ε-Fe_2O_3, and one iron oxohydroxide phase FeOOH (Goethite). These iron oxide compounds were identified measuring the interplanar distances.

Figure 2. Two iron oxide α-Fe_2O_3 (Hematite) and ε-Fe_2O_3, and one iron oxohydroxide FeOOH (Goethite) phases are identified in a nanoparticle prepared with iron(II) sulfate and hydrogen peroxide at pH 3.

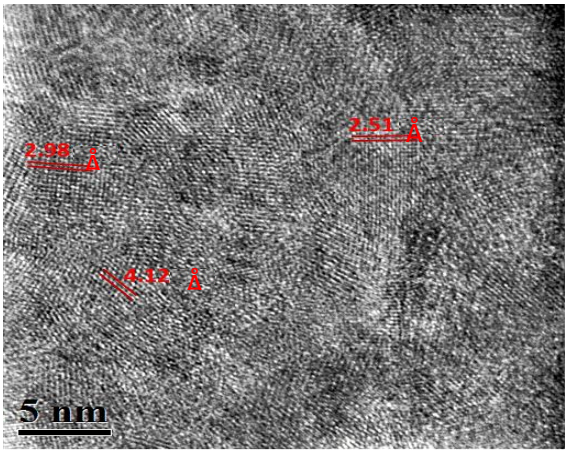

As can be seen in figure 3, under darkness or illuminated conditions, there is a better degradation process of pesticide using Fe_2O_3 NPs prepared with $FeSO_4$ and H_2O_2 at both pHs. For the $FeSO_4$ and H_2O_2 at pH 2.5 the degradation process of Basagran 480 is faster under Vis illumination than under darkness conditions, figures 3a y 3c. Under Vis illumination the Fe_2O_3 NPs prepared with $FeSO_4$ cannot change the absorbance of the system for near to one hour, meanwhile under darkness conditions they do not influence changes in the absorbance for more than three hours, and then the absorbance decreases unexpectedly indicating a diminution of the pesticide concentration respectively.

Figure 3. Depicts the degradation process of Basagran 480 with Fe_2O_3 NPs prepared with three different iron salt precursors, at pH 2.5 (λ=311 nm) and pH 3 (λ=334 nm) with illumination and under darkness conditions.

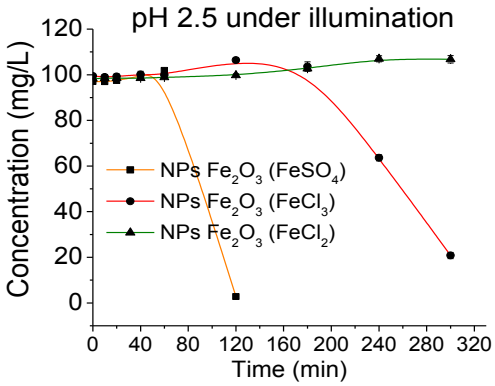

3a

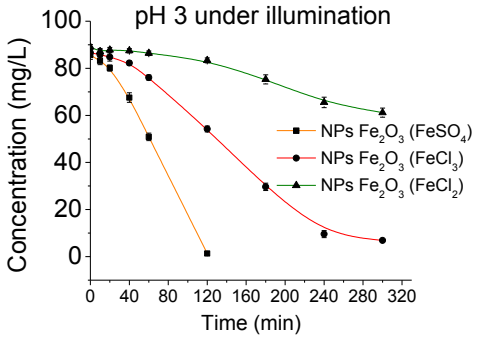

3b

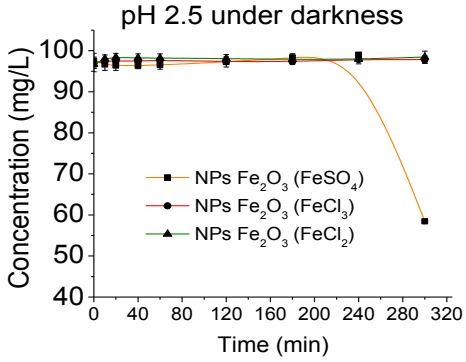

3c

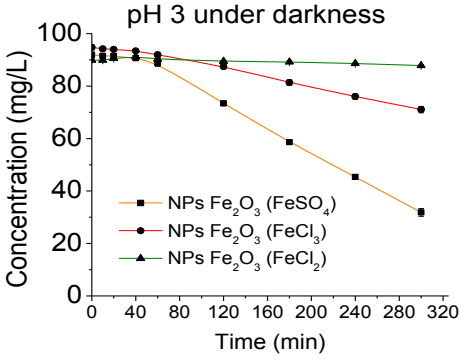

3d

In the systems Fe_2O_3 NPs prepared with $FeCl_n$, the photodegradation processes generate byproducts with a higher molar absorptivity constant, figure 3a, wich absorb more Vis radiation than the pesticide. For this reason, the pesticide's concentration seems to increase. In the other hand, these Fe_2O_3 NPs cannot degrade the pesticide under darkness conditions.

The degradation process of Basagran 480 by Fe_2O_3 NPs prepared with $FeSO_4$ and H_2O_2, at pH 3, under visible illumination conditions, suggests the almost simultaneous degradation of the Basagran 480 molecules and byproducts, figure 3b. The degradation process of Basagran 480 by Fe_2O_3 NPs prepared with $FeCl_n$ and H_2O_2, at pH 3, under visible illumination conditions suggests an improvement in the degradation of this pesticide and the partial elimination of the byproducts comparing with the photodegradation processes at pH 2.5. However, these results are not better than those reached by Fe_2O_3 NPs prepared with $FeSO_4$.

The Fe_2O_3 NPs prepared with $FeSO_4$ or $FeCl_n$ and H_2O_2, at pH 3, under darkness conditions does not reach a full degradation of Basagran 480, figure 3d.

Indeed, the comparison of the degradation processes of Basagran 480, at pH 2.5 and pH 3, under darkness and visible illuminated conditions suggests that there is a kind of Fe_2O_3 NPs, in each system, which is differently stimulated by the visible radiation improving the catalytic activity. In addition, the Fe_2O_3 NPs prepared with $FeSO_4$ and H_2O_2, at pH 3, remain as the best catalytic system to remove Basagran 480 pesticide (see Table 1).

TABLE I. REMOVAL EFFICIENCIES OF COD OF 480 BASAGRAN WITH Fe_2O_3 NPs PREPARED WITH THREE DIFFERENT IRON SALT PRECURSORS, AT pH 2.5 AND pH 3, WITH ILLUMINATION.

COD		NPs Fe_2O_3 ($FeSO_4$)	NPs Fe_2O_3 ($FeCl_3$)	NPs Fe_2O_3 ($FeCl_2$)
pH 2.5	Inicial	801	794	817
	Final	453	610	808
% Remoción		43	23	1
pH 3	Inicial	821	805	813
	Final	421	587	765
% Remoción		49	27	6

The COD analyses for the photodegradation processes at pH 2.5 and pH 3 indicate that the best remotion of the pesticide and byproducts is reached with Fe_2O_3 NPs prepared with $FeSO_4$, Table 1. The COD analysis for the degradation processes under darkness conditions at pH 2.5 and pH 3 show that the best remotion of the pesticide and byproducts is reached with Fe_2O_3 NPs prepared with $FeSO_4$, Table 2.

TABLE II. REMOVAL EFFICIENCIES OF COD OF 480 BASAGRAN WITH Fe_2O_3 NPs PREPARED WITH THREE DIFFERENT IRON SALT PRECURSORS, AT pH 2.5 AND pH 3, UNDER DARKNESS CONDITIONS.

COD		NPs Fe_2O_3 ($FeSO_4$)	NPs Fe_2O_3 ($FeCl_3$)	NPs Fe_2O_3 ($FeCl_2$)
pH 2.5	Inicial	825	822	824
	Final	739	808	815
% Remoción		10	2	1
pH 3	Inicial	827	827	839
	Final	715	772	823
% Remoción		14	7	2

CONCLUSIONS

1 - Nanoparticles and microparticles of iron compounds were detected by Nanoflex device in systems, which usually are considered homogeneous dilutions at pH⩽3.

2 - Two iron oxide and one oxohydroxide phases (α-Fe_2O_3 and ε-Fe_2O_3, and FeOOH) were identified by HRTEM in the $FeSO_4$-H_2O_2 mixture.

3 - Iron oxide nanoparticles prepared with iron(II) sulfate and hydrogen peroxide are the best catalyst to degrade Basagran 480 pesticide.

ACKNOWLEDGEMENTS

Authors thank the financial support of CONACYT-LIFYCS123122 and CONACYT-CEMIE-SOL 35 projects. We also thank To. R. Morán for the technical assistance.

REFERENCES

[1] Fenton H.J.H. Oxidation of Tartaric Acid in Presence of Iron. J. Chem. Soc., 65, 1894, pp 899-910

[2] Haber F., Weiss J., The Catalytic Decomposition of Hydrogen Peroxide by Iron Salts. Proceedings of The Royal Society of London, Series A, Mathematical and Physical Sciences, 147, 861, 1934, pp 332-351

[3] Neyens E., Baeyens J., A review of classic Fenton's peroxidation as an advanced oxidation technique. J. of Hazardous Materials, B98, 2003, pp. 33-50

[4] Walling Ch., Fenton's reagent revisited. Accounts of Chemical Research. 1975, 8 (4), 125-131

[5] De Laat J., Truong Le G. y Legube B., 2004. A comparative study of the effects of chloride, sulfate and nitrate ions on the rates of decomposition of H_2O_2 and organic compounds by Fe(II)/H_2O_2 and Fe(III)/H_2O_2. Chemosphere 55, 715–723.

[6] Suárez-Parra R., Hernández-Pérez I., Montiel-Palacios E., Pérez-Orozco J. P., Sampieri A., Vázquez-Avella D., Jiménez-González A. E. y Guardián-Tapia R., 2011. Photodegradation of Phenol, 2-Chlorophenol and o-Cresol by Iron Oxide Nanoparticles. Nanoscience & Nanotechnology-Asia, 1, 31-40.

[7] Montiel-Palacios E., Medina-Mendoza A. K., Sampieri A., Angeles-Chávez C., Hernández-Pérez I. y Suárez-Parra R., 2009. Photo-catalysis of phenol derivatives with Fe_2O_3 nanoparticles dispersed on SBA-15. Journal of Ceramic Processing Research. Vol. 10, No. 4, pp. 548-552.

Degradación de pesticidas por fotocatálisis heterogénea usando nanopartículas de Fe_2O_3 preparadas en suspención acuosa

M. Ocampo-Gaspar[*1], L. F. Payan-Martínez[1], R. Suárez-Parra[1]

[1]Instituto de Energías Renovables IER-UNAM.

Priv. Xochicalco S/N, Temixco, Morelos 62580 México.

*mog@ier.unam.mx

L. González-Reyes[2], I. Hernández-Pérez[2], J. A. Colin-Luna[2]

[2]Universidad Autónoma Metropolitana-A

Av. Sn. Pablo No. 180, México, D.F. 02200, México.

V. Garibay-Febles[3]

[3]Instituto Mexicano del Petróleo

Eje Central Lázaro Cárdenas Norte 152 Colonia San Bartolo Atepehuacan, 07730, México D. F.

***Resumen*— Las propiedades físico-químicas de las nanopartículas (NPs) de diferentes fases de óxido de hierro (Fe_2O_3), están siendo estudiadas en varios campos de la ciencia; como es el caso de administración de fármacos, en imágenes de resonancia magnética, en terapias de cáncer y remediación ambiental. En este trabajo se prepararon NPs de Fe_2O_3 en suspensión acuosa con cuatro sales de hierro. Estas NPs de Fe_2O_3 fueron utilizadas para la degradación del Carbarilo a pH 3 y pH 2.5 con peróxido de hidrógeno (H_2O_2) y radiación visible. El seguimiento y monitoreo de los sistemas de degradación se determinó por espectrofotometría UV-Vis y Demanda Química de Oxígeno (DQO). La distribución del tamaño de las NPs de Fe_2O_3 se midió con el instrumento Nanoflex y la presencia de las NPs en el sistema se corroboró con microscopía de transmisión de electrones de alta resolución (HRTEM). La degradación del Carbarilo fue más eficiente con las NPs de Fe_2O_3 preparadas con la sal sulfato ferroso ($FeSO_4$). Por otro lado, en la distribución de tamaños, la proporción de NPs de Fe_2O_3 más pequeñas se obtuvieron con las sales $FeSO_4$ y $FeCl_3$; consecuentemente, en este sistema se tendría una mayor área superficial en el catalizador y por ende un mayor número de centros activos. La DQO muestra una mayor remoción del Carbarilo con las NPs de Fe_2O_3 preparadas con la sal $FeSO_4$, obteniendo una eficiencia de remoción del 69%.**

Palabras clave — Fotodegradación, NPs de óxido de hierro, Pesticidas.

I. INTRODUCTION

Existen diversas tecnologías para la remoción de contaminantes recalcitrantes, sin embargo, algunos procesos no son suficientemente eficaces para disminuir el contenido de éstos en aguas de desecho como por ejemplo los pesticidas o fenoles y en otros casos estos procesos no son económicamente viables [1]. Por esta razón, con mayor frecuencia se está recurriendo al uso de los Procesos Avanzados de Oxidación (PAO) que involucran la generación y uso de especies transitorias poderosas, principalmente el radical hidroxilo (HO•) que posee alta efectividad para la oxidación de la materia orgánica [2, 3].

Dentro de estos PAO se encuentran procesos fotoquímicos como la fotocatálisis heterogénea que se basa en la absorción directa o indirecta de energía radiante (visible o UV) por un material semiconductor [4]. Estos materiales sólidos pueden ser NPs de Fe_2O_3. En general las propiedades físico-químicas de los Fe_2O_3 han sido bien estudiadas y en particular la magnetita (Fe_3O_4) y hematita (α-Fe_2O_3) se han usado como catalizadores o soportes en diversas transformaciones orgánicas importantes [5-10]. Las propiedades de las NPs de Fe_2O_3 no sólo son catalíticas aplicadas en procesos de remediación ambiental, también tienen aplicación para obtener imágenes por resonancia magnética, aplicaciones biomédicas, separación de células, identificación de cáncer y terapia [11-15].

II. METODOLOGÍA EXPERIMENTAL

El proceso de degradación del pesticida se llevó a cabo en un reactor tipo *Batch* de 0.6 L con una lámpara doméstica de 15 W en su interior. El espectro de emisión de la lámpara está en el intervalo de radiación visible (Vis). La mezcla dentro del sistema se agitó de manera constante con un agitador magnético sobre una parrilla. Se prepararon mezclas acuosas de hierro (II) y hierro (III) ($FeSO_4$, $Fe_2(SO_4)_3$, $FeCl_2$ y $FeCl_3$) con una concentración de iones de hierro $1x10^{-3}$ M. El pH de estas mezclas se estableció como 4.2 ± 0.1, 2.8 ± 0.1, 2.7 ± 0.1 y 2.9 ± 0.1 respectivamente; estas mezclas se almacenaron en un frasco color ámbar para ser usadas posteriormente. Las suspensiones de Fe_2O_3 se prepararon con las diluciones de

hierro anteriores y peróxido de hidrógeno en un vaso de precipitado de 600 mL. En un vaso de precipitado se añadieron 50 mL de una de las diluciones acuosas de hierro y se agregó 200 mL de agua desionizada (vaso 1), esta mezcla se agitó 10 minutos para alcanzar el equilibrio químico. En otro vaso de precipitado se diluyó 2 mL de H_2O_2 con 233 mL de agua destilada (vaso 2) y habiendo trascurrido los 10 minutos en el vaso 1 se añadió lentamente el contenido del vaso 2 para formar las NPs de Fe_2O_3. Inmediatamente se ajustó las condiciones de pH (pH 2.5 o pH 3), se activó la lámpara y se adicionó 15 mL del pesticida que corresponden a una concentración inicial de 60 mg/L del Carbarilo. La mezcla total tiene un volumen de 500 mL donde la concentración de iones de hierro es $1x10^{-4}$ M. El comportamiento y la efectividad del proceso de degradación del contaminante se evaluó con base en el cambio de la absorbancia del sistema reaccionante. Las muestras se tomaron del reactor y se midió el cambio de concentración del pesticida y la DQO correspondiente.

Para determinar la distribución de tamaño de las NPs de Fe_2O_3 con el dispositivo Nanoflex y confirmar el tamaño de la nanopartícula (únicamente para el sistema $FeSO_4$-H_2O_2) por HRTEM se prepararó un sistema similar con cada sal de hierro y H_2O_2, pero sin agregar el pesticida en condiciones de pH 3.

III. RESULTADOS Y DISCUSIÓN

Como se puede ver en la Figura I en los sistemas $FeSO_4$-H_2O_2 y $FeCl_3$-H_2O_2 se detecta la presencia de NPs de compuestos de hierro de menor tamaño, mientras que en los sistemas $Fe_2(SO_4)_3$-H_2O_2 y $FeCl_2$-H_2O_2 se detecta la presencia de partículas con un tamaño mayor a 100 nm. Estas NPs pueden ser óxidos u oxihidróxidos de hierro. Si consideramos que el número de centros activos catalizadores está en función del área superficial de las nanopartículas, entonces encontramos una explicación parcial de porque los sistemas catalíticos de NPs de Fe_2O_3 preparados con $FeSO_4$-H_2O_2 y $FeCl_3$-H_2O_2 son más activos que los sistemas que se prepararon con $Fe_2(SO_4)_3$-H_2O_2 y $FeCl_2$-H_2O_2.

Figura I. Distribución del tamaño de NPs Fe_2O_3 a pH 3.

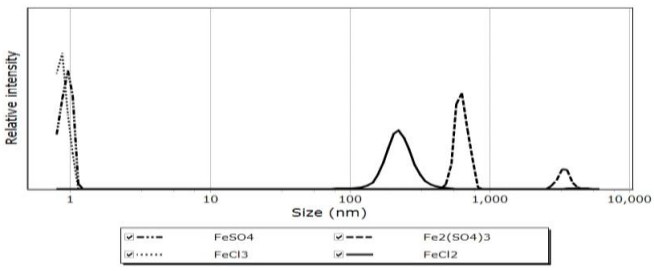

En la Figura II se presenta una micrografía de HRTEM que confirma la presencia NPs de Fe_2O_3. En una de estas NPs se identificó la fase de óxido de hierro que corresponde a la hematita (α-Fe_2O_3) con una distancia interplanar de 2.51 Å. En este trabajo presentamos únicamente una micrografía de HRTEM, sin embargo en otros análisis se ha identificado las fases de otro óxido (ε-Fe_2O_3) y un oxohidróxido de hierro como la goetita (FeOOH).

Figura II. Micrografía de la Hematita (α-Fe_2O_3)

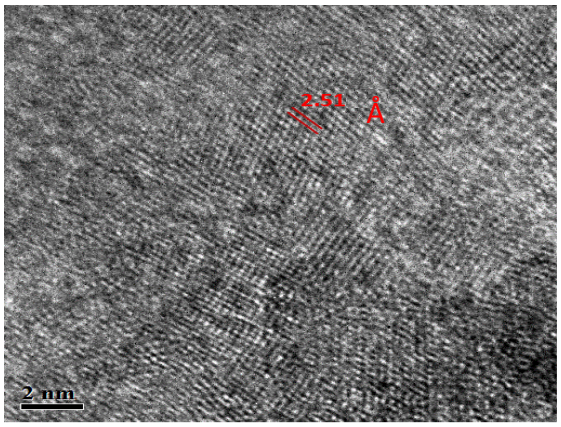

En las Figuras IIIa (pH 2.5) y IIIb (pH 3), los perfiles de la degradación muestran una tendencia similar. Las NPs de Fe_2O_3 preparadas con la sal sulfato ferroso degradan más rápidamente al pesticida que las NPs de Fe_2O_3 preparadas, en condiciones similares, con las otras sales de hierro. Sin embargo, la comparación de los dos procesos de degradación del Carbarilo a pH 2.5 y pH 3 con las NPs de Fe_2O_3, preparadas con el precursor sulfato ferroso, indica una mayor degradación de la molécula del pesticida cuando el sistema trabaja a un pH 2.5 en un intervalo de tiempo de 60 minutos. Considerando que el catalizador es una mezcla de NPs de óxidos y oxohidróxidos de hierro [8] y la única diferencia radica en las condiciones de pH al momento del inicio de la reacción, entonces este resultado sugiere que una mayor concentración de iones hidronio favorece el proceso de degradación porque éstos (con carga positiva) interactúan con la molécula del pesticida (con exceso de electrones). De esta manera, las moléculas del pesticida se encuentran desestabilizadas y la interacción con la superficie de las NPs de Fe_2O_3 y los radicales HO• es más intensa.

Figura III. Fotodegradación del Carbarilo con NP Fe_2O_3 pH de 2.5 (a) y pH 3 (b).

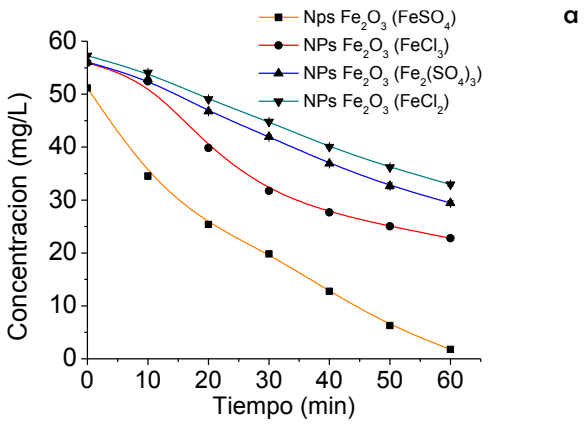

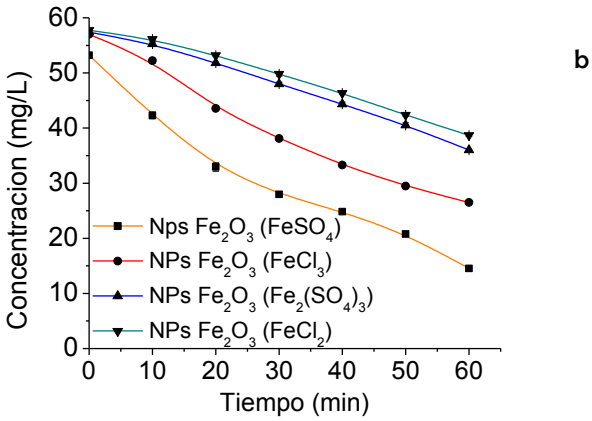

Por otro lado, en la Tabla I, se muestran los niveles de remoción del Carbarilo en los diferentes sistemas de NPs de Fe_2O_3. Como se puede observar, la remoción de la materia orgánica medida como DQO indica que las NPs de Fe_2O_3 en condiciones de pH 2.5 no alcanzan a remover los compuestos secundarios que absorben menos radiación visible. Es decir, que en condiciones de pH 3 el proceso de degradación del pesticida, si bien presenta una menor remoción del compuesto principal, también muestra una mejor degradación de los compuestos secundarios.

TABLA I. REMOCIÓN DE LA MATERIA ORGÁNICA DEL CARBARILO MEDIDA COMO DQO.

DQO		NPs Fe_2O_3 ($FeSO_4$)	NPs Fe_2O_3 ($FeCl_3$)	NPs Fe_2O_3 ($Fe_2(SO_4)_3$)	NPs Fe_2O_3 ($FeCl_2$)
pH 2.5	Inicial	827	831	850	837
	Final	304	443	504	685
% Remoción		63	47	41	18
pH 3	Inicial	856	838	866	848
	Final	267	439	496	643
% Remoción		69	48	43	24

CONCLUSIONES

El sistema de NPs de Fe_2O_3 preparado con $FeSO_4$-H_2O_2 fue el que alcanzó una mayor degradación de la materia orgánica en ambos sistemas (pH 2.5 y pH 3), respecto a las NPs Fe_2O_3 preparadas con el resto de las sales,.

La remoción del Carbarilo con NPs Fe_2O_3 preparadas con la sal $FeSO_4$ fue más eficiente, alcanzando el 69 % de DQO cuando el sistema se preparó a pH 3.

Se encontró que las NPs de Fe_2O_3 preparadas con las sales $FeSO_4$ y $FeCl_3$ presentan el menor tamaño por lo que pueden presentar un mayor número de centros activos en el área superficial del catalizador.

AGRADECIMIENTOS

Los autores agradecen el apoyo financiado de los proyectos CONACYT-LIFYCS123122 y CONACYT-CEMIE-SOL 35. También agradecemos a M. Guevara y R. Morán por la asistencia técnica.

REFERENCIAS

[1] Blake D. M., 1999. National Renewable Energy Laboratory. Technical Report NREL/TP-570-26797.
[2] De Laat J., Truong Le G. y Legube B., 2004. A comparative study of the effects of chloride, sulfate and nitrate ions on the rates of decomposition of H_2O_2 and organic compounds by Fe(II)/H_2O_2 and Fe(III)/H_2O_2. Chemosphere 55, 715–723.
[3] Ghaly M. Y., Hartel G., Mayer R. y Haseneder R., 2001. Photochemical oxidation of p-chlorophenol by UV/H_2O_2 and photo-Fenton process. A comparative study. Waste Management 21, 41-47.
[4] Domènech X., Wilson F. J. y Marta I., 1987. Procesos avanzados de oxidación para la eliminación de contaminantes. Litte Rev. Metal., 23, 341.
[21] Kale S. R., Kahandal S. S., Gawande M. B. y Jayaram R. V., 2013. Magnetically recyclable [gamma]-Fe_2O_3-HAP nanoparticles for the cycloaddition reaction of alkynes, halides and azides in aqueous media. Rsc. Adv., 3 (22), 8184−8192.
[5] Gawande M. B., Branco P. S. y Varma R. S., 2013. Nano-magnetite (Fe_3O_4) as a support for recyclable catalysts in the development of sustainable methodologies. Chem. Soc. Rev., 42 (8), 3371−3393.
[6] Li P. H., Li B. L.; An Z. M., Mo L. P., Cui Z. S. y Zhang Z. H., 2013. Magnetic Nanoparticles ($CoFe_2O_4$)-Supported Phosphomolybdate as an Efficient, Green, Recyclable Catalyst for Synthesis of β-Hydroxy Hydroperoxides. Adv. Synth. Catal., 355 (14−15), 2952−2959.
[7] Montiel-Palacios E., Medina-Mendoza A. K., Sampieri A., Angeles-Chávez C., Hernández-Pérez I. y Suárez-Parra R., 2009. Photo-catalysis of phenol derivatives with Fe_2O_3 nanoparticles dispersed on SBA-15. Journal of Ceramic Processing Research. Vol. 10, No. 4, pp. 548~552.
[8] Suárez-Parra R., Hernández-Pérez I., Montiel-Palacios E., Pérez-Orozco J. P., Sampieri A., Vázquez-Avella D., Jiménez-González A. E. y Guardián-Tapia R., 2011. Photodegradation of Phenol, 2-Chlorophenol and o-Cresol by Iron Oxide Nanoparticles. Nanoscience & Nanotechnology-Asia, 1, 31-40.
[9] Karunakaran C., Vinayagamoorthy P. y Jayabharathi J., 2014. Nonquenching of Charge Carriers by Fe3O4 Core in Fe_3O_4/ZnO Nanosheet Photocatalyst. Langmuir, 30, 15031−15039.
[10] Bing J., Hu C., Nie Y., Yang M. y Qu J., 2015. Mechanism of Catalytic Ozonation in Fe_2O_3/Al_2O_3@SBA-15 Aqueous Suspension for Destruction of Ibuprofen. Environ. Sci. Technol., 49, 1690−1697.
[11] Mero O., Sougrati M. T., Jumas J. C. y Margel S., 2014. Engineered Magnetic Core−Shell SiO_2/Fe Microspheres and "Medusa-like" Microspheres of SiO_2/Iron Oxide/Carbon Nanofibers or Nanotubes. Langmuir, 30, 9850−9858.
[12] Kathleen D., Bin Q., Witmer M., Kitchens C. L., Brian A. Powell B. A. y Mefford T., 2014. Quantitative Measurement of Ligand Exchange on Iron Oxides via Radiolabeled Oleic Acid. Langmuir, 31, 9950−9958.
[13] Jolivet J. P., Chanéac C. y Tronc E., 2004. Iron oxide chemistry. From molecular clusters to extended solid networks. Chem. Commun., 481–487.
[14] Jones C. J., Chattopadhyay S., Gonzalez-Pech N. I., Avendano C., Hwang N., Soo Lee S., Chom M., Ozarowski A., Prakash A., Mayo J. T., Yavuz C. y Colvin V. L., 2015. A Novel, Reactive Green Iron Sulfide (Sulfide Green Rust) Formed on Iron Oxide Nanocrystals. Chem. Mater., 27, 700−707.
[15] Campo G., Pineider F., Bonanni V., Albino M., Caneschi A., Fernández C. J., Innocenti C. y Sangregorio C., 2015. Magneto-Optical Probe for Investigation of Multiphase Fe Oxide Nanosystems. Chem. Mater., 27, 466−473.

Análisis termodinámico de combustibles sólidos quemados en la Central Termoeléctrica Presidente Plutarco Elías Calles (C.T.P.P.E.C) de 2778 MW

L.C. Lara Guzmán, G. Polupan, G. Jarquin López
SEPI ESIME Culhuacan, SEPI ESIME Zacatenco
Instituto Politécnico Nacional
Ciudad de México, México

***Resumen*—Con el objetivo de realizar un análisis termodinámico de los tres tipos de carbón importado que utiliza la C.T.P.P.E.C para llevar a cabo sus operaciones, se consideraron tres características importantes como Poder Calorífico Inferior (PCI), Poder Calorífico Superior (PCS) y Exergía química ($Ex_{quím}$) en condiciones de cambio en su composición másica. Para el estudio se determinó la composición elemental de los carbones minerales que incluye: carbono, hidrógeno, azufre, oxígeno, cenizas y humedad, la cual es importante para el cálculo del PCI, el PCS y la Exergía química. Finalmente, se obtuvieron las dependencias de PCI, PCS y Exergía respecto a la composición másica de los tres tipos de carbones minerales y sus combinaciones, que influyen en la eficiencia térmica de la Planta.**

***Palabras clave*—carbón bituminoso; composición másica; poder calorífico inferior; poder calorífico superior; exergía química**

I. Introducción

La C.T.P.P.E.C, se ubica en el estado de Guerrero, en la localidad de Petacalco. Tiene una capacidad total de 2778 MW, está integrada por seis unidades con una capacidad de 350 MW, y una séptima unidad con capacidad de 678 MW.

Esta Planta inició operaciones en 1993 y fue diseñada como central dual para operar con carbón mineral como combustible principal y combustóleo (como combustible alterno solo en las unidades 1 a 6) [1].

La clasificación general del carbón que utiliza es carbón bituminoso [2]. La Planta necesita quemar 130.21 toneladas de éste combustible por hora, con las cuales se producen alrededor de 1078 toneladas de vapor por hora en cada unidad de 350 MW, para generar su máxima potencia [3].

Debido a que la Central Termoeléctrica no tiene combustible sólido de diseño, utiliza combustibles sólidos alternativos con diferentes composiciones másicas, de las cuales se posee información incompleta como puede observarse en la Tabla I publicada por la Comisión Federal de Electricidad en 2009 en [2].

A causa de que el contenido de los elementos presentes en la composición másica tiene influencia directa en el cálculo del Poder Calorífico y la Exergía química, fue necesario investigar una metodología para determinar la composición elemental del combustible a partir de los datos proporcionados por la Tabla I.

El carbón es una mezcla de impurezas inorgánicas conocidas como cenizas, humedad y otros elementos tales como carbono, hidrógeno, oxígeno, azufre y nitrógeno [4]. El contenido de nitrógeno es pequeño y no todos los carbones lo contienen, por lo tanto en este estudio no es tomado en cuenta.

TABLA I. Especificaciones de la Calidad del Carbón Mineral Térmico

Características	Especificaciones (Límites)		
	Carbón Tipo 1	***Carbón Tipo 2***	***Carbón Tipo 3***
Poder Calorífico Superior, kcal/kg (bcsr)	6300 Mínimo	6200 Mínimo	5900 Mínimo
Contenido de Cenizas, % Peso (bcsr)	12.2 Máximo	13.0 Máximo	15.0 Máximo
Contenido de Materia Volátil, % Peso (bcsr)	25.0 Mínimo 38.0 Máximo	22.0 Mínimo 40.0 Máximo	22.0 Mínimo 40.0 Máximo
Contenido de Humedad, % Peso (bcsr)	9.5 Máximo	12.0 Máximo	14.0 Máximo
Contenido de Azufre, % Peso (bcsr)	1.0 Máximo	1.0 Máximo	1.5 Máximo

bscr = base como se recibe

II. Metodología de Cálculo

Las especificaciones de la licitación para la adquisición del carbón bituminoso (Tabla I) no incluyen el contenido de carbono total, hidrógeno y oxígeno, información que es importante para determinar su Poder Calorífico y Exergía química, por esta razón se desarrolló una metodología para recalcular los parámetros del carbón mineral utilizado.

A. Cálculo de cenizas, humedad, materia volátil y carbono fijo.

Como datos iniciales se hizo una aproximación de los valores promedio del contenido de ceniza, materia volátil y humedad.

Por diferencia a 100 de los contenidos, en tanto por ciento, de humedad (W), materia volátil (MV) y cenizas (A) del carbón se puede obtener el contenido de carbono fijo (CF) [5]:

$$CF = 100 - W - A - MV \quad (1)$$

B. Cálculo de carbono, hidrógeno y oxígeno

Para conocer la composición másica de los parámetros restantes se recurrió al método de Gebhardt [6].

Porcentaje de carbono (C):

$$C = CF + 0.9(MV - 14) \quad (2)$$

Porcentaje de hidrógeno (H):

$$H = MV(7.35/(MV+10)) - 0.013 \quad (3)$$

Porcentaje de oxígeno (O):

$$O = 100 - C - H - A - W - S \quad (4)$$

En (4) el término (S) corresponde al porcentaje de azufre.

C. Cálculo de Poder Calorífico Inferior (PCI) y Poder Calorífico Superior (PCS)

Una vez conocida la composición másica del carbón se determinaron los poderes caloríficos empleando las fórmulas de Mendeleiev [7]. Considerando que el carbón se quema estequiométricamente.

$$PCI = 338(C) + 1256(H) - 109(O - S) - 25(9H+W) \quad (5)$$

$$PCS = 338(C) + 1256(H) - 109(O - S) \quad (6)$$

Las unidades de (5) y (6) son [kJ/kg]

D. Cálculo de Exergía química

La exergía química ($Ex_{quím}$) del carbón se calcula con el método descrito en [8] de la siguiente manera:

Se determina el número de moles por kilogramo de la sustancia (N_m) [kmol] con la siguiente expresión:

$$N_m = m/M \quad (7)$$

Donde (m) representa la masa de cada uno de los componentes del combustible y (M) corresponde a su masa molar.

Los valores obtenidos con (7) se sustituyen en la ecuación de combustión:

$$[N_{mC}C+N_{mH}H+N_{mO}O+N_{mS}S+N_{mN}N]_{combustión} + n_1O \rightarrow$$

$$n_2CO_2+n_3H_2O+n_4SO_2+n_5N_2 \quad (8)$$

Para determinar la cantidad molar de los productos de la combustión (n_1, n_2, n_3, n_4, n_5) se aplica un balance de masa:

$$n_2 = N_{mC}\ ;\quad n_3 = N_{mH}\ ;\quad n_4 = N_{mS}\ ;\quad N_5 = N_{mN}$$

$$n_1 = (2n_2 + n_3 + 2n_4 - N_O) / 2$$

La entalpía de formación ($\Delta h°_f$) se obtiene de la ecuación:

$$\Delta h°_f = n_2{\cdot}\Delta h°_{fCO2} + n_3{\cdot}\Delta h°_{fH2O} + n_4{\cdot}\Delta h°_{fSO2} + n_5{\cdot}\Delta h_{fNO2} - n_1{\cdot}\Delta h°_{O2} + h°_R \quad (9)$$

Los valores de la entalpía de formación de los productos de la combustión CO_2, H_2O y SO_2 se obtienen de tablas de propiedades termoquímicas [8] en condiciones estándar a 25°C y 1atm.

El incremento de entalpía de la reacción ($\Delta h°_R$) es igual a:

$$\Delta h°_R = - PCS \quad (10)$$

Es necesario también calcular la entropía estándar del combustible (s°):

$$s° = 8.883 - 7.523\exp(-0.565{\cdot}(h/(1+n))) + 4.807{\cdot}(o/(1+n)) + 12.981{\cdot}(n/(1+n)) + 10.67{\cdot}(s/(1+n)) \quad (11)$$

Donde (h, o, s, n) representan el número de moles de hidrógeno, oxígeno, azufre y nitrógeno respectivamente, por mol de carbono y se calculan con:

$$h = H/C;\quad o = O/C\ ;\quad s = S/C\ ;\quad n = N/C$$

Las unidades de (11) son [cal/kmol], por tanto hay que efectuar la conversión a [kJ/kg] y seguir con el cálculo.

La entropía de combustión ($s°_{f\_comb}$) se calcula:

$$s°_{f\_comb} = s° - (N_{mC}{\cdot}s°_C) - (N_{mH}{\cdot}s°_H) - (N_{mS}{\cdot}s°_S) - (N_{mN}{\cdot}s°_N) - (N_{mO}{\cdot}s°_O) \quad (12)$$

Los valores de entropía estándar para los elementos ($s°_C$, $s°_H$, $s°_S$, $s°_N$, $s°_O$) se obtienen de tablas propiedades termoquímicas [8] en condiciones estándar a 25°C y 1atm.

Entonces se puede obtener el valor de la energía libre de Gibbs:

$$\Delta G°_{f\ combustible} = \Delta h°_f - (\Delta s°_{f\ comb} \cdot K) \quad (13)$$

Finalmente, se calcula la exergía química del combustible:

$$Ex_{quím} = \Delta G°_{f\ combustible} + N_{mC}{\cdot}ex_{qC} + N_{mH}{\cdot}ex_{qH} + N_{mS}{\cdot}ex_{qS} + N_{mN}{\cdot}ex_{qN} + N_{mO}{\cdot}ex_{qO}\ ,\quad [kJ/kg] \quad (14)$$

III. Resultados y Análisis

En la Tabla I se puede notar que aparecen valores máximos y mínimos de la composición del carbón bituminoso por lo que fue necesario calcular sus valores promedio y sustituirlos en (1), (2), (3) y (4) de la metodología.

De esta forma se obtiene una composición másica promedio de los tres tipos de carbón (Tabla II) para posteriormente calcular PCI, PCS y $Ex_{quím}$.

TABLA II. Composición Másica de los Combustibles

Porcentaje (%)	*Carbón Tipo 1*	*Carbón Tipo 2*	*Carbón Tipo 3*
Carbono	66.17	63.47	60.13
Hidrógeno	5.17	5.15	5.15
Azufre	1.0	1.0	1.5
Cenizas	7.92	10.00	11.67
Humedad	10.17	10.83	12.5
Oxígeno	9.58	9.55	9.05
TOTAL	100.0	100.0	100.0

Los valores promedio fueron tomados como base de comparación al hacer algunas variaciones en los elementos del combustible. Con estas variaciones fue posible determinar aquellos parámetros que influyen en mayor medida a incrementar o disminuir el PCI, PCS y $Ex_{quím}$.

La Tabla III muestra las variaciones hechas al carbón tipo 1 y los valores de Poder Calorífico Superior, Poder Calorífico Inferior y Exergía química calculados.

El Carbón Tipo 1A se obtuvo calculando la composición másica con los porcentajes máximos de humedad, cenizas y materia volátil que aparecen en la tabla I, lo cual disminuyó el contenido de carbono.

El Carbón Tipo 1B es aquel cuyo contenido de humedad, cenizas y materia volátil es mínimo, y aumenta el contenido de carbono.

TABLA III. VARIACIÓNES DE LA COMPOSICIÓN MÁSICA DEL CARBÓN TIPO 1

Composición másica y parámetros termodinámicos	***Carbón Tipo 1A***	***Carbón Tipo 1***	***Carbón Tipo 1B***
Carbono	61.90	66.17	70.43
Hidrógeno	5.32	5.17	4.93
Azufre	1.0	1.0	1.0
Cenizas	12.2	10.17	8.13
Humedad	9.50	7.92	6.33
Oxígeno	10.08	9.58	9.18
Poder Calorífico Inferior	**25,185**	**26,560**	**27,834**
Poder Calorifico Superior	**26,620**	**27,921**	**29,101**
Exergía química	**27,294**	**28,636**	**29,907**

En la Fig.1 se presenta una gráfica comparativa de los valores de los parámetros termodinámicos del Carbón Tipo 1 y sus variantes 1A y 1B que aparecen en la Tabla III. De acuerdo a la gráfica el Carbón Tipo 1B es el que tiene los valores más altos de PCI, PCS y Exergía química.

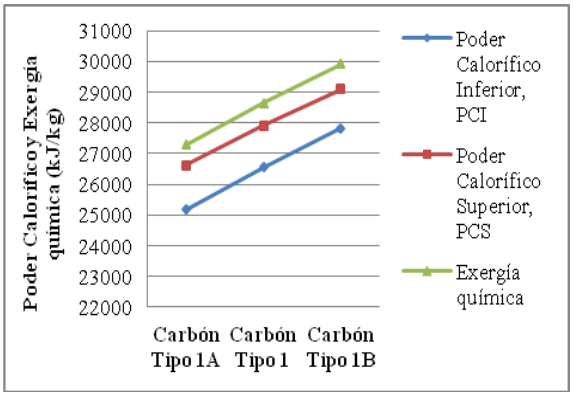

Fig. 1 Parámetros termodinámicos de los tipos de carbón 1, 1A y 1B.

La Tabla IV muestra la composición másica y los parámetros termodinámicos calculados para el Carbón Tipo 2 y dos tipos de carbón derivados de éste.

El Carbón Tipo 2A es una variante del carbón tipo 2, el cuál contiene los porcentajes máximos de cenizas, humedad y materia volátil dados en la Tabla I para éste tipo de carbón, con esta composición se obtiene el contenido mínimo de carbono.

El Carbón Tipo 2B, está constituido por los porcentajes mínimos de humedad, cenizas calculados a partir de la composición del Carbón Tipo 2, y el porcentaje mínimo de materia volátil de la Tabla I para este tipo de carbón.

TABLA IV. VARIACIONES DE LA COMPOSICIÓN MÁSICA DEL CARBÓN TIPO 2

Composición másica y parámetros termodinámicos	***Carbón Tipo 2 A***	***Carbón tipo 2***	***Carbón Tipo 2B***
Carbono	58.40	63.47	68.53
Hidrógeno	5.36	5.15	4.77
Azufre	1.0	1.0	1.0
Cenizas	13.0	10.83	8.67
Humedad	12.0	10.0	8.0
Oxígeno	10.24	9.55	9.03
Poder Calorífico Inferior	**23,958**	**25,584**	**27,003**
Poder Calorifico Superior	**25,464**	**26,994**	**28,276**
Exergía química	**26,069**	**27,672**	**29,047**

En la Fig. 2 se presenta una gráfica comparativa de los valores de los parámetros termodinámicos del Carbón Tipo 2 y sus variantes 2A y 2B que aparecen en la tabla IV.

Como se puede apreciar en la gráfica el Carbón Tipo 2B posee mejores características termodinámicas.

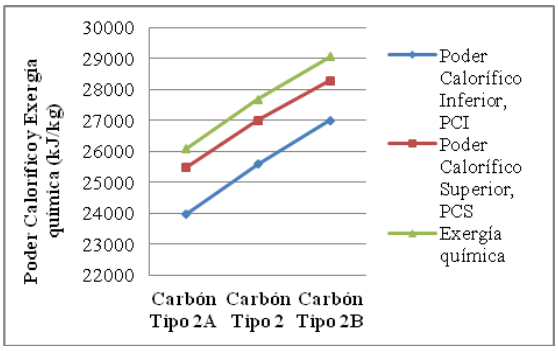

Fig. 2 Parámetros termodinámicos de los tipos de carbón tipo 2, 2A y 2B

La Tabla V presenta la composición másica y parámetros termodinámicos que fueron calculados para los tipos de carbón 3, 3A y 3B.

El Carbón Tipo 3A resulta de la combinación de porcentajes máximos de humedad, cenizas y materia volátil obtenidos de la Tabla I para el carbón tipo 3, de ésta combinación resulta un bajo contenido en carbono.

El Carbón Tipo 3B se obtuvo al combinar los porcentajes mínimos de humedad y cenizas calculados de la composición del carbón tipo 3 y el porcentaje mínimo de materia volátil que aparece en la Tabla I para el carbón tipo 3, lo que da como resultado un alto contenido en carbono.

TABLA V. VARIACIONES DE LA COMPOSICIÓN MÁSICA DEL CARBÓN TIPO 3

Composición másica y parámetros termodinámicos	*Carbón Tipo 3A*	*Carbón Tipo 3*	*Carbón Tipo 3B*
Carbono	54.40	60.13	65.87
Hidrógeno	5.36	5.15	4.77
Azufre	1.5	1.5	1.5
Cenizas	15.0	12.5	10.0
Humedad	14.0	11.67	9.33
Oxígeno	9.74	9.05	8.53
Poder Calorífico Inferior	**22,665**	**24,525**	**26,177**
Poder Calorifico Superior	**24,221**	**25,976**	**27,483**
Exergía química	**24,814**	**26,650**	**28,259**

La Fig. 3 muestra la gráfica correspondiente al PCI, PCS y Exergía química de los tipos de carbón 3, 3A y 3B. De acuerdo a ella el Carbón Tipo 3B tiene los valores termodinámicos más altos, mientras el carbón tipo 3A tiene los valores más bajos.

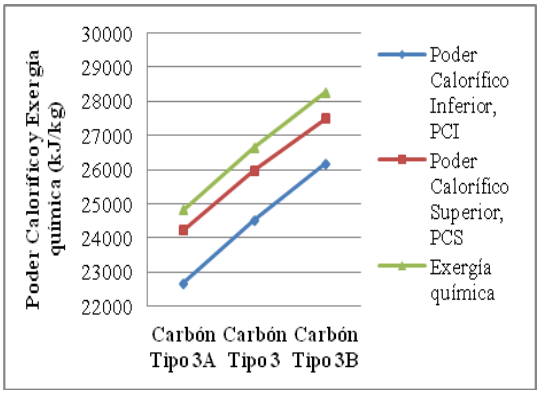

Fig. 3 Parámetros termodinámicos de los tipos de carbón 3, 3A y 3B

A continuación se graficó el PCI, PCS y Exergía química de los tipos de carbón 1B, 2B y 3B (Fig. 4) que fueron los que tuvieron los valores más altos.

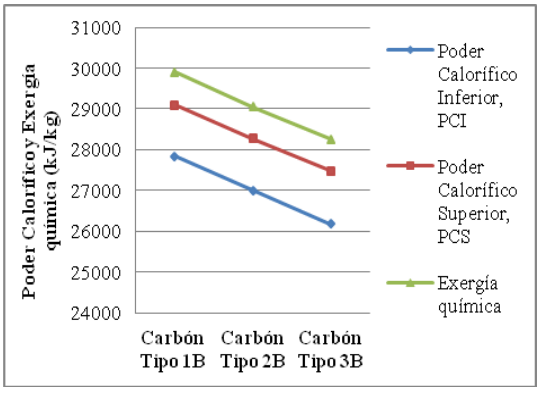

Fig. 4 Parámetros termodinámicos de los tipos de carbón 1B, 2B y 3B

IV. CONCLUSIONES

El factor que presentó mayor influencia tanto en los Poderes Caloríficos como en la Exergía química de los combustibles sólidos analizados fue el contenido de carbono.

De los factores estudiados que fueron: contenido de carbono, cenizas, humedad y materia volátil, se obtuvo que el contenido alto de carbono es benéfico para conseguir mayor energía disponible.

Por otro lado, el contenido alto de cenizas, humedad y materia volátil disminuyen la calidad del combustible, lo cual se refleja en su Poder Calorífico y Exergía química.

Los resultados del Poder Calorífico Inferior (PCI) de los carbones bituminosos estudiados se encuentran dentro del rango 22,000 kJ/kg a 28,000 kJ/kg lo cual concuerda con los valores publicados en [4].

La combinación de cantidades mínimas de humedad, cenizas y materia volátil incrementó el contenido de carbono en el combustible así como sus Poderes Caloríficos y Exergía química, por el contrario, a máximas cantidades de materia volátil, humedad y cenizas, el porcentaje de carbono fue el mínimo y del mismo modo lo fueron sus Poderes Caloríficos y Exergía química.

Los carbones tipo 1B, 2B y 3B resultaron con mejores características termodinámicas. El Carbón Tipo 1B alcanzó valores más altos de PCI, PCS y Exergía química, seguido del Carbón Tipo 2B, mientras que el Carbón Tipo 3B registro los valores más bajos.

Estos resultados son la base para realizar los cálculos de combustión y balance térmico del generador de vapor.

REFERENCIAS

[1] Grupo Funcional Desarrollo Económico, "Mantenimiento a unidades generadoras termoeléctricas de carbón 2011-2013, en la Central Termoeléctrica Presidente Plutarco Elías Calles ubicada en Petacalco, estado de Guerrero", Disponible en: http://www.asf.gob.mx/Trans/Informes/IR2013i/Documentos/Auditorias/2013_0366_a.pdf

[2] Convocatoria de la licitación pública internacional abierta considerando las reglas de los tratados 18164067-050-09(LI-550/09). Disponible en: http://licitaciones.dgmarket.com/tenders/np-notice.do?noticeId=4574634

[3] A. Zapien, "Análisis térmico de los tubos del recalentador del generador de vapor de la unidad 2 de 350 MW de la C.T. Pdte. Plutarco Elías Calles", Tesis de maestría. Instituto Politécnico Nacional, pp. Anexo 3 Marzo 2011.

[4] P. Brasu, C. Kefa, L. Jestin, "Boilers and Burners, Design and Theory", Springer, E.U.A. pp. 24-25, 2000.

[5] W. H. Severns, H. Degler, J. Miles, "Energía mediante Vapor, Aire o Gas", Reverté, España, p. 92, 2007.

[6] A. Bennett, "Power Plant Performance", Ed. Btterworth-Heinemann, p.55, 1984.

[7] Schvetz, et al., "Heat Engineering", Mir, Moscú, pp. 168-169, 1987.

[8] J. Gómez, M. Monleón, A. Ribes, "Termodinámica Análisis Exergético", Reverté, España, pp. 141-150, 1990.

Simulación numérica en 2D de la evaporación del agua de una alberca pública

. López Callejas, M. Vaca Mier, J. Morales Gómez, A. Lizardi Ramos,*
H. Terres Peña, S. Chávez y M. Noriega Hernández
Universidad Autónoma Metropolitana-Azcapotzalco,
Av. San Pablo No. 180, Col. Reynosa-Tamaulipas,
México, D.F. 02200.
*e-mail: rlc@correo.azc.uam.mx

Abstract— ***This paper presents the numerical simulation of evaporation of water in a public pool, during the night, i.e. between 21:00 and 6:00 hours of the following day. The physical dimensions of the pool are: 50 m long, 25 m wide and an average depth of water of 1.30 m. The premises dimensions are 56 m long, 31 m width and a height of 10 m. Azcapotzalco Aquatic Center is used as experimental model located in Azcapotzalco, in Mexico City.***

CFD Numerical Modeling is a useful tool to predict the ratio of evaporation of the fluid and the air flow paths, it is used to optimize and obtain the most efficient use of energy. The water in the temperature at the pool is 29 °C and that of the air contained within the premises 28 °C; the speed of the air in the entrance window (31 m long and 1 m high), is 1 m/s. An exit window of identical physical dimensions is located exactly on the opposite wall. The results show the distribution of velocities of air along the pool in addition to the moisture contents, the evaporation mass flow remained constant at a value of 15 g/s in most of simulation time and the total amount of evaporated water was 430 L.

Keywords— Public pool, night evaporation, numeric simulation.

Resumen En este trabajo se presenta la simulación numérica de la evaporación del agua en una alberca pública, en el horario nocturno, es decir, entre las 21:00 y 6:00 horas del día siguiente. Las dimensiones físicas de la alberca son: 50 m de longitud, 25 m de ancho y una profundidad promedio del agua de 1.30 m. Las dimensiones del recinto considerado son de 56 m de longitud, 31 m de ancho y una altura de 10 m. Como modelo experimental se utiliza Centro Acuático Azcapotzalco ubicada en la delegación Azcapotzalco en el Distrito Federal.

El modelado numérico con CFD es una herramienta muy útil para predecir la relación de evaporación del fluido y las trayectorias del flujo del aire, se emplea para optimizar y obtener el uso más eficiente de la energía. La temperatura del agua en la alberca es de 29 °C y la del aire contenido dentro del local 28 °C, la velocidad del aire en la ventana de entrada, de 1 m de altura y 31 m de largo, es de 1 m/s, la ventana de salida de idénticas dimensiones físicas está exactamente en la pared contraria. Los resultados obtenidos muestran la distribución de velocidades del aire a lo largo de la alberca además del contenido de humedad, el flujo másico de evaporación se mantuvo constante es un valor de 15 g/s en la mayor parte del tiempo de simulación y la cantidad total de agua evaporado fue de 430 L.

Palabras Clave: ***Alberca pública, Evaporación nocturna, simulación numérica*.**

I. INTRODUCCIÓN

Los centros acuáticos deben proporcionar condiciones de alta calidad para que los atletas puedan desempeñar su actividad deportiva de la mejor manera. Para lograr esto el agua de las albercas debe mantenerse en condiciones óptimas de temperatura y libre de partículas suspendidas u otros contaminantes que afectan la salud de los nadadores. Además de mantener el agua en condiciones de alta calidad, también es importante controlar parámetros de la atmósfera circundante como la humedad relativa, la renovación de aire y la temperatura del mismo, especialmente en climas extremos donde el atleta pueda verse expuesto a cambios bruscos de temperatura.

Determinar la cantidad de agua que se evapora de los depósitos de agua externos e internos ha sido un tema de interés para algunos investigadores [1-5], además cuando se trata de albercas que están dentro de algún local o recinto se debe tener presente también de la cantidad de energía que se emplea en el calentamiento del agua y en los sistemas de aire acondicionado para cuantificar los costos de operación. La diferencia de temperaturas que existe entre el agua de la alberca y la del medio ambiente dentro del local determinaran la cantidad de agua que se evaporará de la alberca, una correlación empírica que aún se utiliza para determinar está cantidad fue propuesta en 1918 [3], la cual relaciona la velocidad de evaporación con la diferencia de presiones del vapor y la velocidad del aire y que es recomendada como un primer cálculo por la ASHRAE. Existen algunas otras correlaciones empíricas que se utilizan para albercas con y sin personas para determinar la evaporación para diferentes condiciones de la diferencia de temperaturas y la velocidad del aire [7 y 8], todas estás involucran la presión de vapor o la humedad absoluta entre el aire cerca de la superficie del agua y el aire del medio ambiente, solo algunas de estas ecuaciones consideran el tamaño de la alberca.

El desarrollo de los métodos computacionales ha ayudado a mejorar el cálculo de la evaporación pero éstos requieren de los valores de algunas variables que únicamente se cuantifican con la experimentación, apoyándose en las correlaciones empíricas anteriormente mencionadas. Sin embargo, estos métodos ayudan a obtener el modelado de la complicada hidrodinámica que se presenta entre la superficie del agua y el aire circundante, por ejemplo en el trabajo presentado en [9]

se utiliza la correlación descrita en [4] y en el artículo de [10] se emplea la presentada en [5].

Los métodos computacionales comerciales de CFD resuelven las ecuaciones de Navier-Stokes modelando la turbulencia que se presenta en el fluido, en éstos se calcula la distribución de velocidades, temperaturas y el campo de humedad y se comparan contra los valores experimentales obtenidos previamente. La velocidad de evaporación no se calcula directamente sino que se emplea una correlación para verificar los resultados obtenidos.

El objetivo de este trabajo es evaluar las pérdidas de masa por evaporación que ocurren durante la noche en una alberca olímpica techada, considerando que no se utiliza cubierta plástica, sobre el agua, para minimizar las pérdidas por evaporación, utilizando el software COMSOL. La simulación en el software COMSOL permite aproximar de una manera confiable el comportamiento térmico de la alberca y arroja resultados que corresponden a la distribución de flujo del aire circundante, además permite calcular la tasa de evaporación de agua.

II. DESCRIPCIÓN DEL PROBLEMA

La simulación de la evaporación se realizará con una geometría 2D, la cual se origina de un corte longitudinal del recinto. La geometría 2D ofrece varias ventajas frente a una geometría 3D, la principal de ellas radica en el considerablemente menor número de operaciones que debe computar el procesador para arrojar los resultados correspondientes a la simulación. En la Fig. 1, se presenta La geometría empleada en este trabajo con un corte longitudinal de la alberca de 50 m de longitud, 25 m de ancho y una profundidad del agua de 1.30 m; el local tiene 56 m de longitud, 31 m de ancho y 10 m de altura.

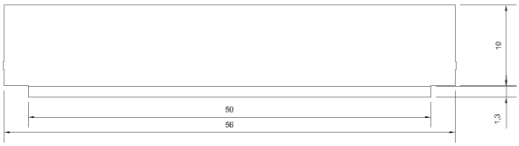

Fig. 1. Corte longitudinal de la alberca y el local que la contiene.

De acuerdo a las normas de funcionamiento de una alberca de este tipo conocida como "olímpica" la temperatura de confort a la que debe mantenerse el agua es de 29 °C [11]. Ésta a su vez está rodeada de aire contenido en un recinto techado de 10 metros de altura, sin embargo el aire del interior es constantemente renovado por aire proveniente de la atmósfera que entra a través de una ventila por uno de los extremos del recinto y sale por el extremo opuesto; las ventilas están situadas 2 m sobre la superficie del agua y tienen un metro de altura y el ancho es igual al de la pared. Las mediciones experimentales de la velocidad del aire que se realizaron en un recinto igual a este, fue en promedio de 1 m/s. Para modelar la evaporación de la superficie de la alberca hacia el aire se tomó como dominio solamente el aire circundante, la temperatura de toda la masa de aire es de 28 °C, un grado menor a la temperatura de la alberca, dado que la temperatura del agua de la alberca es de 29 °C entonces habrá transferencia de calor del agua hacia el aire. La concentración inicial del aire en el recinto y el aire de renovación que ingresa es de $0.38\ mol/m^3$ y corresponde a una humedad relativa del 40%, dicha humedad es típica en climas como el de la Ciudad de México y solo se ve alterada de manera significativa cuando existen precipitaciones pluviales.

En la superficie del dominio que se encuentra en contacto con el agua el aire se encuentra cercano al estado de saturación, por esto se dio un valor de concentración de $0.94\ mol/m^3$. La diferencia de concentraciones de humedad entre la frontera inferior y el volumen de aire ocasionará la transferencia de masa. Estas son las condiciones de frontera que se utilizaran en la solución del problema. El tiempo de interés en el estudio comprende nueve horas de la noche en las cuales la alberca permanece cerrada y sin ocupantes, de esta manera se determinará la cantidad de agua que se evapora en el periodo nocturno comprendido de las 21:00 horas hasta las 6:00 de la mañana del otro día.

Para la discretización de los cálculos se utilizó una malla gruesa con 2122 elementos pues una malla fina o extra fina requiere recursos de cómputo muy avanzados o un tiempo de solución de varios días. La Fig. 2, muestra la malla empleada en la solución del problema.

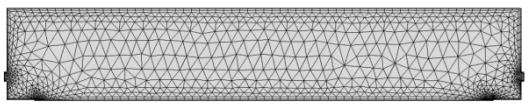

Fig. 2. Mallado utilizado en la solución del problema.

III. MODELO NUMÉRICO

El software COMSOL utiliza las ecuaciones de Navier-Stokes para describir el comportamiento de los fluidos bajo condiciones iniciales y de frontera, dichas ecuaciones son resueltas numéricamente por el software.

$$\rho\left(\frac{\partial \mathrm{u}}{\partial \mathrm{t}} + u \cdot \nabla u\right) = -\nabla p + \nabla \cdot \left(\mu(\nabla u + (\nabla u)^T) - \frac{2}{3}\mu(\nabla \cdot u)I\right) + F \quad (1)$$

Donde u representa la velocidad del fluido, p representa la presión del fluido, ρ representa la densidad y μ la viscosidad dinámica.

Además de la ecuación anterior, COMSOL utiliza también la ecuación de continuidad:

$$\nabla \cdot (\rho u) = \quad (2)$$

Para modelar la trasferencia de calor en fluidos COMSOL utiliza la solución numérica de la siguiente ecuación:

$$\rho C_p \frac{\partial \mathrm{T}}{\partial \mathrm{t}} + \rho C_p u \cdot \nabla T = \alpha_p \mathrm{T}\left(\frac{\partial p_A}{\partial \mathrm{t}} + \mathrm{u} \cdot \nabla p_A\right) + \tau : \mathrm{S} + \nabla \cdot (k \nabla T) + Q \quad (3)$$

Donde C_p representa al calor específico del fluido, T la temperatura, S el tensor de velocidad de deformación, k la conductividad térmica y Q la fuente de calor.

Para el transporte de especies diluidas COMSOL utiliza la siguiente ecuación:

$$\nabla \cdot (-D_i \nabla c_i) + u \cdot \nabla c_i = R_i \quad (4)$$

Donde D_i representa el coeficiente de difusión, c_i la concentración de especies y R_i la tasa de reacción para las especies. También utiliza la ecuación de discontinuidad de flujo:

$$N_i = -D_i \nabla c_i + u c_i \quad (5)$$

Donde N_i representa la discontinuidad de masa que atraviesa alguna frontera.

IV. Resultados obtenidos y discusión

En la Fig. 3 se presentan los resultados obtenidos por el software COMSOL, para el problema planteado y las condiciones de frontera anotadas, del lado izquierdo aparece la distribución de velocidades y del lado derecho la concentración de humedad obtenida.

A los diez minutos de iniciada la simulación se observa como el aire entra al local a la velocidad de 1 m/s, bajando el flujo inmediatamente a la superficie libre del agua hasta una longitud de 20 m de la alberca, en la parte superior se observa que el aire presenta un flujo en sentido inverso, es decir por abajo se desplaza hacia la derecha con una velocidad aproximada de 0.7 m/s, en la sección superior el flujo del aire es hacia la izquierda. Posteriormente el aire sube hasta el techo alrededor de los 35 m, aquí se presenta el fenómeno inverso al anterior, es decir el aire se desplaza por la parte superior hacia la derecha y por la inferior a la izquierda, finalmente el aire sale por la pared derecha. Con respecto a la humedad en este tiempo se observa que toda la sección de la superficie libre del agua se presenta el valor máximo de concentración de humedad, la línea roja lo muestra, entre los 20.00 y los 35.00 m hay un aumento de concentración en el aire y se desplaza hacia la salida con un valor de $0.47\ mol/m^3$.

A los 30 min, se ha incrementado la longitud de contacto del aire en movimiento hasta los 26.00 m pero la velocidad es de 0.65 m/s, en la parte superior el aire continua desplazándose hacia la izquierda. Posteriormente el aire sube hasta el techo del local y finalmente baja para salir por la ventana de la pared derecha. El contenido de humedad en el aire se ha desplazado hasta los 27.00 m y continua avanzando a la salida, el valor ha disminuido ligeramente a $0.45\ mol/m^3$.

Para primera hora la longitud del aire que se desplaza hacia la derecha aumenta 32.00 m con una velocidad de 0.60 m/s, el flujo en la parte superior no cambió, se mantiene a la izquierda. Más adelante el flujo continua con la misma tendencia, en la parte superior se dirige hacia la salida y por debajo hacia la izquierda, la velocidad del aire a la salida tiene un valor de 0.55 m/s. El contenido de humedad en este tiempo se mantiene constante que el caso anterior con una valor de $0.45\ mol/m^3$.

A las dos horas, el contacto del aire en movimiento con la superficie libre del agua se ha incrementado a una longitud de 35.00 m y la velocidad promedio es 0.6 m/s, El contenido de humedad en este tiempo se mantiene constante que el caso anterior con una valor de $0.45\ mol/m^3$.

Para la tercera hora y las siguientes las condiciones del flujo permanecen constantes hasta el fin de la simulación de 9 horas, la velocidad es constante con un valor de 0.6 m/s y el contenido de humedad es de $0.45\ mol/m^3$, al parecer el aire contenido en el local se satura y se llega a la permanencia.

En la Fig. 4, se muestra el flujo másico evaporado contra el tiempo de la simulación, al inicio se alcanza el máximo de 20.90 g/s, posteriormente baja un poco a un valor de 17.60 g/s que se mantiene hasta las 2.5 horas y finalmente se mantiene constante en 15.00 g/s. El área bajo la curva es la cantidad de agua evaporada total cuyo valor fue de 430 L en las nueve horas.

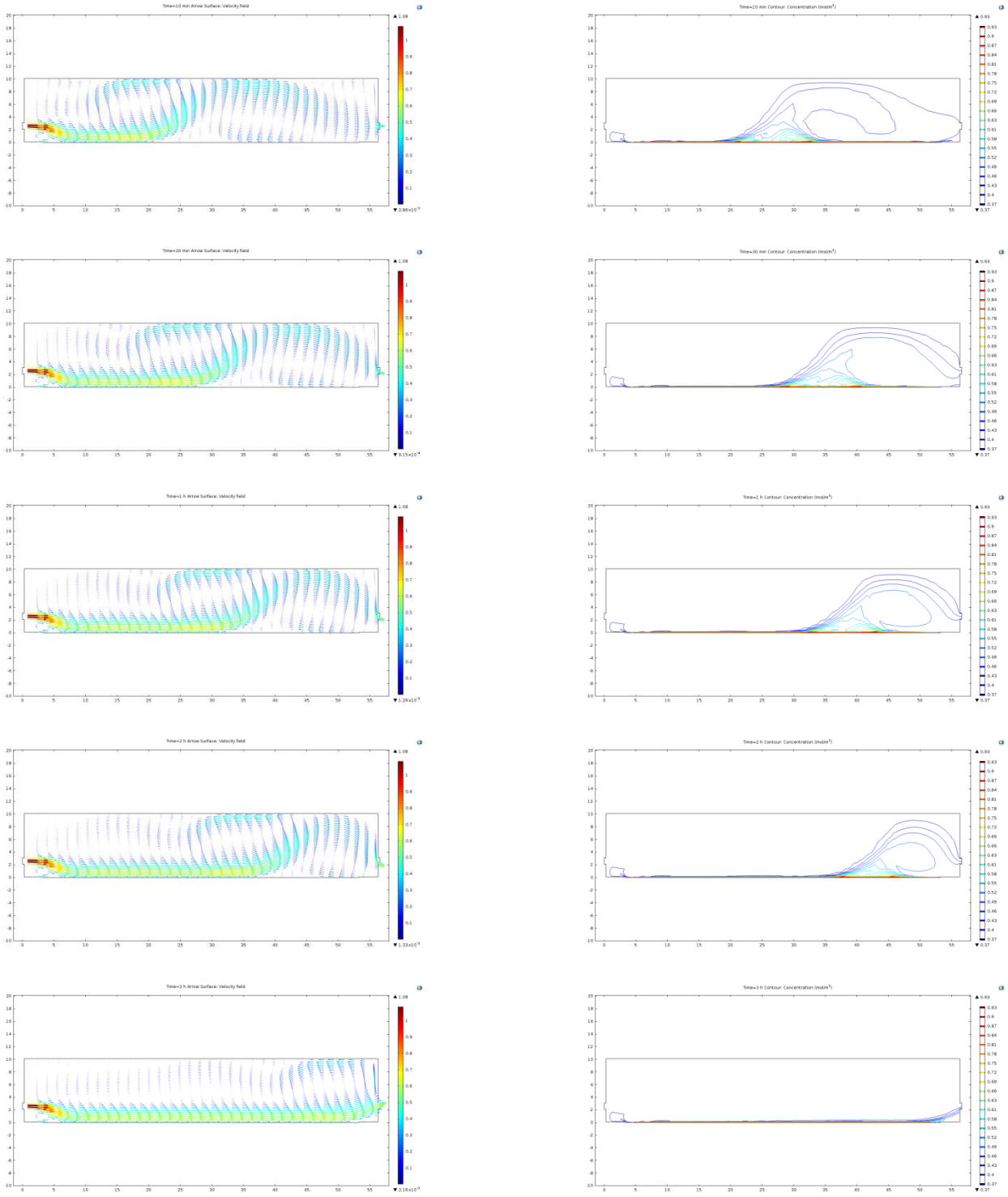

Fig. 3. Distribución de velocidades del aire es la columna del lado izquierdo y el contenido de humedad es el lado derecho.

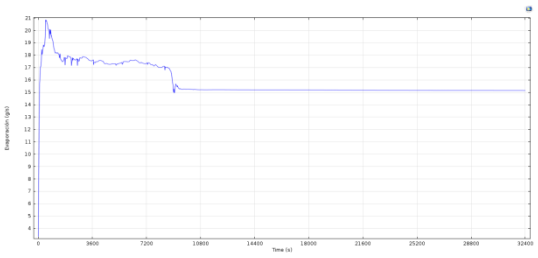

Fig. 4. Flujo másico evaporado en el periodo de simulación.

V. REFERENCIAS

[1] H. Hertz, 1882. Ueber die verdunstung der flüssigkeiten, insbesondere des quecksilbers, im luftleeren raume, (in German). Ann. Phys., vol. 17, pp. 177-197.

[2] M. Knudsen, 1915. Die maximale verdampfungsgeschwindigkeit des quecksilbers, (in German). Ann. NatPhys., vol. 47, pp. 697-708.

[3] W. H. Carrier, 1918. The temperature of evaporation. ASHVE Trans., vol. 24, pp. 25-50.

[4] G. W. Himus, J. W. Hinchly, 1924. The effect of a current of air on the rate of evaporation of water below the boiling point. Chemistry and Industry, vol. 22, pp. 840–845.

[5] M.M. Shah, 20063. Prediction of evaporation from occupied indoor swimming pools. Energy & Buildings, vol. 35, pp. 707-713.

[6] ASHRAE Handbook, 2003. HVAC Applications. Atlanta: American Society of Heating, Refrigerating and Air-Conditioning Engineers, Inc.

[7] M. Al-Shammiri, 2002. Evaporation rate as a function of water salinity, Desalination, vo1. 150, pp. 189-203.

[8] S.M. Bower and J.R. Saylor, 2009. A study of the Sherwood-Rayleigh relation for water undergoing natural convection-driven evaporation.nt. J. Heat Mass Transfer, vol. 52, pp. 3055-3063.

[9] S.J.K Bukhari and M.H.K. Siddiqui, 2007. Characteristics of air and water velocity fields during natural convection. Heat Mass Transfer, vol. 43, pp. 415-425.

[10] Z. Li and P. Heiselberg, 2005. CFD Simulations for water evaporation and airflow movement in swimming baths indoor environmental engineering. Aalborg University, Denmark, Report for the project “Optimization of ventilation system in swimming bath”.

[11] NOM-000-SSA1-2005. Requisitos sanitarios y calidad de agua que deben cumplir las albercas.

Visualización del flujo en válvulas

Gutiérrez Eudave, R. López Callejas, M. Vaca Mier, A. J. Osorio Vega, M. J. García Velázquez, S., A. Lizardi Ramos, H. Terres Peña.*
Universidad Autónoma Metropolitana-Azcapotzalco,
Av. San Pablo No. 180, Col. Reynosa-Tamaulipas,
México, D.F. 02200.
*e-mail: rlc@correo.azc.uam.mx

Abstract— **Visualization of the flow is a process that makes it possible that the physics of flow of a fluid (liquid or gas) be visible. In engineering three techniques or methods are mainly used: visualization of flow on a surface, tracking of a particle (gas or micro spheres) and the optical methods, which are very sophisticated and therefore very expensive. In this work, a Hele-Shaw visualizer has been used to observe what happens to water in laminar conditions flow as it passes through the inside of the gate and balloon valves with 50% and 25% openings. These were designed and manufactured according to the dimensions of similar but real valves of 0.05 m in nominal diameter. They were manufactured in 0.003 m thick neoprene rubber according to ASTM D-2240 standard. Methylene blue was used as a colorant. The number of Reynolds used in flow was laminar with a value of 1500. The experimental results for a flow with 1500 Reynolds number, were contrasted against those obtained by the simulation in the ANSYS software that was programmed with the same boundary conditions. Besides the numerical analysis was obtained between the difference of pressures and speeds and graphs were made to explain the flow behavior according to the equation of conservation of energy. The similarity between the experimental results and those obtained from the simulation is quite close, even observing the stagnation zones and eddies arising on the phenomenon.**
Keywords*— *Visualization flow, Hele-Shaw channel, gate valve, globe valve.

Resumen— **La visualización del flujo es un proceso que hace posible que la física del flujo de un fluido (líquido o gas) sea visible. En ingeniería se utilizan principalmente tres técnicas o métodos: la visualización del flujo sobre una superficie, el seguimiento de una partícula (gas o micro esferas) y los ópticos, que son muy sofisticados y por lo mismo muy costosos.**
En este trabajo se ha utilizado el visualizador de Hele-Shaw para observar lo que le sucede a un flujo de agua en condiciones de flujo laminar cuando pasa por el interior de las válvulas de compuerta y globo con una abertura del 50 y 25 %. Éstas se diseñaron y fabricaron de acuerdo a las dimensiones de válvulas semejantes pero reales de 0.05 m de diámetro nominal, fueron fabricadas en hule de neopreno de acuerdo a la norma ASTM D-2240, de 0.003 m de espesor. Como colorante se utilizó el azul de metileno. El número de Reynolds utilizado en el flujo fue laminar con un valor de 1500. Los resultados experimentales obtenidos, para un flujo con número de Reynolds de 1500, fueron contrastados contra los arrojados por la simulación realizada en el software ANSYS que se programa con iguales condiciones de frontera. Se obtuvo además el análisis numérico entre la diferencia de presiones y de velocidades y se graficó para entender lo que le pasó al flujo de acuerdo con la ecuación de conservación de energía. La similitud entre los resultados experimentales y los obtenidos de la simulación es bastante cercana, observándose hasta las zonas de estancamiento y los remolinos que se presentan en el fenómeno.
***Palabras Clave: Visualización de flujo, canal de Hele-Shaw, válvula de compuerta, válvula de globo*.**

I. INTRODUCCIÓN.

Las válvulas son dispositivos mecánicos que se utilizan en las tuberías para el control del flujo de un fluido: líquido, gaseoso o una combinación de ambos. En estás tuberías también habrá algunos otros dispositivos como codos, conexiones, ampliaciones y/o contracciones de diámetro, etc. todos ellos generarán una pérdida de energía al flujo, la cual se traduce en una disminución de la presión. Existen diferentes tipos de válvulas, aquí sólo de mencionarán dos, las de compuerta empleadas para la obstrucción total del flujo y las de globo utilizadas para su control. Para los fabricantes de estos dispositivos es muy importante conocer las características del flujo en su interior, por ejemplo la cavitación, debida a que la presión baja a valores cercanos a la presión de vaporización del fluido, este fenómeno causa ruido, vibración y el desgate de elemento obturador y por periodos prolongados también afectará a la tubería. La pérdida de energía se determina numéricamente aplicando las ecuaciones de conservación, o bien experimentalmente midiendo la diferencia de presión entre la entrada y la salida de la válvula.

En las válvulas es imposible observar lo que pasa con el flujo del fluido en el interior de ellas debido a los materiales que se emplean en su construcción, metales y PVC principalmente, la única manera sería construir una válvula de algún material 100 % transparente como el acrílico, por ejemplo, y utilizar algún método de visualización de flujo.

Alguna información del comportamiento hidráulico de las válvulas fue proporcionado por Hutchison [1], el cual determinó experimentalmente la relación que tenían el caudal y la pérdida de energía; Kirik y Driskell [2] También

proporcionaron información adicional de ellas. La información obtenida de esta manera fue utilizada para mejorar el diseño hidráulico de ellas, [3].

Debido al progreso en las áreas de visualización de flujo y de análisis computacional ahora es posible observar con mucho esmero el flujo en el interior de una válvula y obtener. El coeficiente de flujo, la caída de presión o pérdida d energía, el coeficiente de cavitación, y visualizar el flujo en el interior de la misma.

La visualización del flujo es un proceso que hace posible que la física del flujo de un fluido (líquido o gas) sea visible. En ingeniería se utilizan principalmente tres técnicas o métodos: la visualización del flujo sobre una superficie, el seguimiento de una partícula (gas o micro esferas) y los ópticos, que son muy sofisticados y por lo mismo muy costosos.

Por ejemplo, Chern, et al. 2007, [4], visualizaron el flujo de agua en una válvula de bola fabricada en acrílico, determinaron cuando se presentaba el fenómeno de cavitación a diferentes aberturas, el método de visualización de flujo usado fue el de seguimiento de partículas.

El primer artista que observó el flujo de un fluido fue Leonardo da Vinci, en su *"Treatise of painting"* compilado por su heredero Francesco Melzi y publicado por primera vez en 1651, pero en realidad sus notas fueron realmente leídas hasta el siglo XIX, [5]. El estudio el sistema cardiovascular en más de 50 páginas entre 1508 y 1509, [6, 7], en esté describió y analizó la importancia del corazón como motor de movimiento de la sangre [8].

La célula de Hele-Shaw es una herramienta de visualización de flujo muy poderosa que fue desarrollada por Henry Selby Hele-Shaw, en 1897 y desde entonces se ha utilizado ampliamente en el estudio de la dinámica de fluidos por su sencillez de construcción, funcionamiento y análisis de resultados. Una revisión histórica analizando la importancia y los alcances de su trabajo fue realizada por Vasil'ev 2009, [9].

En este trabajo se presentan los resultados obtenidos de la visualización de flujo de dos tipos de válvulas: de compuerta y de globo, en régimen de flujo laminar con dos aperturas diferentes utilizando el canal de Hele-Shaw. Los resultados experimentales obtenidos se comparan con la simulación realizada con el software ANSYS con iguales condiciones de flujo.

II. DESCRIPCIÓN DEL EQUIPO UTILIZADO.

El canal de Hele-Shaw utilizado tiene una sección de prueba de 0.30 m de ancho por 0.76 m de longitud, la altura del agua que sirve como energía para que fluya es de 0.03 m, la altura del depósito donde se coloca la sustancia que se utiliza como trazador es de 0.30 m. En este caso se utiliza el colorante azul de metileno, cuyo nombre científico es cloruro de metiltionina, es un compuesto químico heterocíclico aromático cuya fórmula molecular es $C_{16}H_{18}ClN_3S$. La sección de prueba o de visualización está formada por dos vidrios de borosilicato conocido con el nombre de vidrio Pyrex, la inferior es fija y la superior se puede desplazar, la separación entre ellas es de 0.002 m.

La energía del colorante se emplea para vencer las pérdidas que se presentan en el ducto que lo distribuye a lo largo de la sección transversal de prueba del canal, es una tubería de cobre tipo L de 0.019 m de diámetro nominal y los pequeños ductos por donde se distribuye dicho colorante tienen un diámetro de 0.001 m. La figura 1 presenta una fotografía de este dispositivo.

La sección transversal de las válvulas de compuerta y de globo fueron extraídas de dos válvulas reales de 0.0508 m de diámetro nominal, posteriormente se escalaron hasta que el diámetro interior fue de 0.10 m que es la sección de flujo, esto se realizó con la ayuda del software ANSYS. Con las dimensiones obtenidas, los modelos se fabricaron en placa de hule de neopreno, con una dureza de 65° SHORE "A" +/-5 ° de acuerdo con la norma ASTM D-2240, de 0.003 m de espesor. Se seleccionó este material por su facilidad de trabajo, el acabado espejo en las superficies que beneficia a las fotografías y porque permite el sellado entre las dos placas de vidrio del canal, evitando que el agua y el colorante pasen entre los vidrios y el modelo.

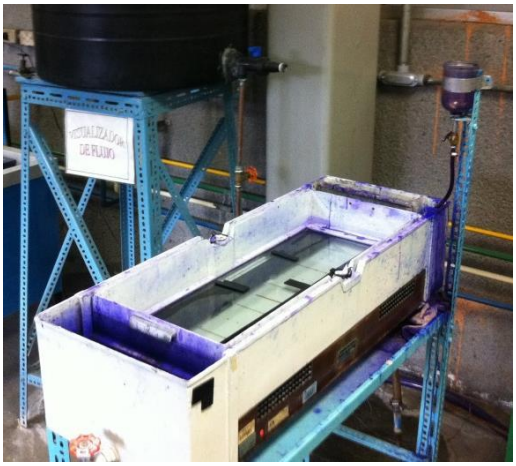

Fig. 1. Canal de Hele-Shaw, en la parte superior izquierda se aprecia el depósito del colorante.

III. PROCEDIMIENTO EXPERIMENTAL.

Se deben limpiar perfectamente bien las dos superficies de vidrio para que las fotografías que se registren sean lo mejor posible. Para obtener la solución del colorante que se utiliza en las pruebas se deben medir 5 mL del colorante y agregarle 1 L de agua, esta cantidad permite obtener líneas de flujo perfectamente bien definidas en el visualizador y se podrán realizar hasta ocho pruebas con una duración de 20 s cada una.

Colocar los hules que simulan la válvula en el vidrio inferior y colocar con mucho cuidado el vidrio superior

evitando que se mueva alguno de los componentes, para cada válvula se seleccionaron dos aberturas 25 y 50 %, está se simula con la acción del vástago del obturador.

Abrir la válvula que regula el paso del agua entre los dos vidrios, con una altura de 0.02 m por encima del vidrio inferior será suficiente para obtener el flujo necesario, en este caso se seleccionó un flujo de 7.54 x 10^{-5} m^3/s, con el cual se obtiene un número de Reynolds de aproximadamente 1500, lo que garantiza que es laminar. Posteriormente se abre ligeramente la válvula del depósito del colorante, un cuarto de vuelta bastará para permitir el paso del mismo y se realiza el registro de las fotografías.

La cámara fotográfica utilizada es de marca Nikon, modelo Coolpix P520, que permite obtener hasta 7 disparos por segundo, la calidad de las fotografías es de 18.1 megapixeles.

IV. Resultados obtenidos y discusión.

En la Fig. 2, se muestra la fotografía de la válvula de compuerta cuando la abertura es del 50 %, el número de Reynolds seleccionado es de 1500 y el flujo del fluido es de izquierda a derecha. En la sección agua arriba de la compuerta se observa que las líneas de corriente siguen un patrón de flujo uniforme hasta un poco antes de la compuerta, en la cual el flujo se deforma de tal manera que se forma una sección de estancamiento, parte izquierda superior, nótese que la última línea de corriente se deforma para pasar por debajo de la obstrucción. Al pasar por la obstrucción las líneas de corriente se comprimen incrementándose la velocidad del fluido, y de acuerdo con la ecuación de conservación de energía la presión debería de ser mínima. Aguas arriba de esta sección se forman dos secciones muy claras, la primera es el avance del fluido hacia la salida disminuyendo la velocidad del fluido ya que la sección transversal se incrementa y exactamente a un lado de la compuerta se forma un remolino debido a la depresión que se forma en esta sección. Este es la parte que daña a la compuerta cuando se le utiliza indebidamente como una válvula de control de flujo, ya que se provoca el fenómeno conocido como cavitación.

Con la finalidad de obtener una mayor comprensión del fenómeno se realizó la simulación del mismo con el software ANSYS, utilizando el mismo modelo con las condiciones de frontera semejantes. El resultado obtenido se muestra en la parte inferior de la Fig. 2, la semejanza entre lo fotografiado y lo obtenido en la simulación es enorme. El color azul indica que la velocidad del fluido es cero, es decir es la zona de estancamiento que corresponde a la esquina derecha superior de la compuerta. La velocidad máxima se presenta al centro de la obstrucción. En la figura también se muestran las gráficas del cambio de la presión y de la velocidad (entre la salida y la entrada) para la línea de corriente que pasa exactamente al centro de la figura, se observa como la diferencia de presión va de su valor máximo al cero y lo contrario para la velocidad. La diferencia de presión es pequeña (0.05 Pa) porque la sección de flujo no presenta una obstrucción considerable y la diferencia de velocidad también (0.20 m/s), esta diferencia es nula al inicio de la gráfica ya que de acuerdo a la ecuación de conservación de la masa al ser la sección transversal de flujo igual a la entrada y salida, entonces la velocidad del flujo también será la misma.

En la Fig. 3, se muestra la fotografía para la válvula de compuerta para una abertura del 25 % y el mismo número de Reynolds de 1500. Para la sección aguas arriba de la compuerta se aprecia un efecto similar al caso anterior en la parte superior izquierda es una zona de estancamiento, como se ha reducido la sección de flujo las líneas de flujo se han juntado más que en el caso anterior, pasando la sección de obstrucción el flujo muestra una cierta apariencia de inestabilidad formando una zona de estancamiento en la parte superior derecha de la compuerta y un remolino que deforma al flujo, finalmente el flujo adquiere cierta estabilidad.

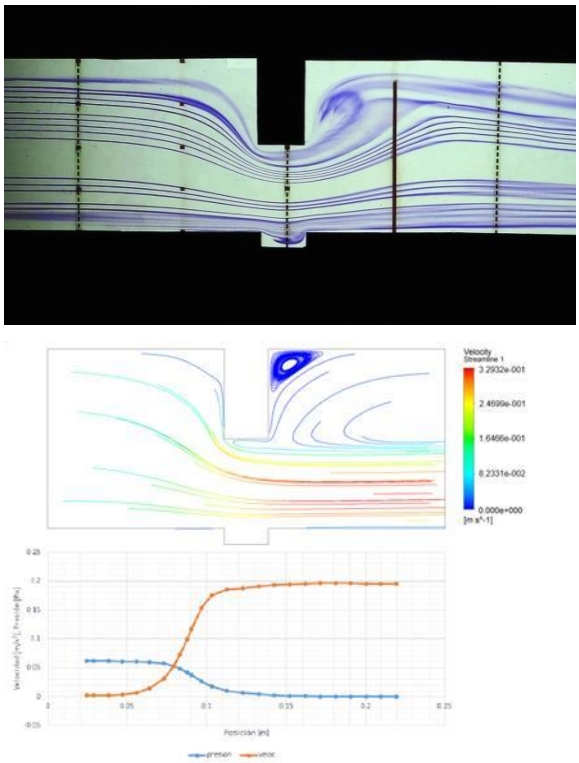

Fig. 2. Visualización de la válvula de compuerta con un 50 % de abertura.

En la parte inferior de la fotografía se muestra el resultado obtenido de la simulación, es de notarse las zonas de estancamiento a ambos lados de la compuerta en la parte superior pero la del lado derecho es más grande que la izquierda, en la sección de la obstrucción se aprecia como las líneas de corriente se juntan mostrando un aumento en la velocidad del fluido. Posteriormente en la sección aguas debajo de la compuerta justo debajo de la zona de estancamiento se aprecia que el fluido forma un remolino.

En la parte inferior de la figura se muestra la gráfica de la diferencia de presión y de velocidad entre la salida y la entrada, la diferencia de presión y de velocidad muestran valores numéricos mayores que en el caso anterior. Puesto que la sección de flujo se reduce la diferencia de velocidad es de 0.58 m/s y la diferencia de presión tiene un valor de 0.40 Pa, estos valores son mayores que en el caso anterior, para la misma condición de flujo.

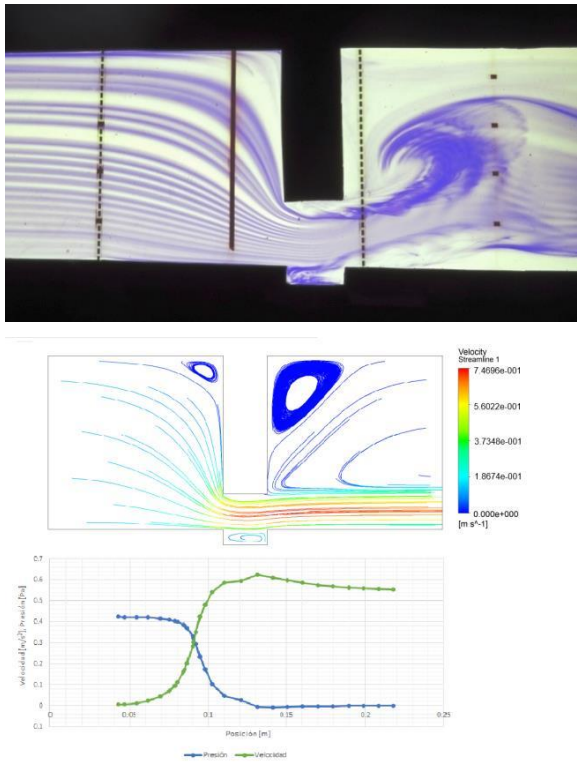

Fig. 3. Visualización de la válvula de compuerta con un 25 % de abertura.

La válvula de globo tiene un uso muy diferente a la de compuerta se emplea para el control del flujo por lo tanto su comportamiento hidrodinámico es diferente. Cuando la abertura de la válvula es del 50 % el disco obturador permite el paso del fluido que choca directamente en su base, posteriormente el fluido pasa aguas arriba de esta zona de control, para salir hacia la descarga. En la fotografía de la Fig. 4, se muestra el resultado experimental, para un número de Reynolds de 1500, en la sección de entrada las líneas de corriente son uniformes, pero al cambiar de dirección hacia el plato del obturador las líneas se deforman rápidamente hacia la salida pero en la parte contraria se forma una pequeña zona de estancamiento al igual que en la base y al salir de la válvula se diluyen debido al aumento de la velocidad por la obstrucción.

La simulación del fenómeno muestra resultados semejantes, se aprecian tres zonas de estancamiento dos antes del obturador y una tercera en la parte superior del mismo a la salida. Las líneas de corriente muestran se juntan apreciablemente aumentando su velocidad al reducir la sección transversal de flujo y en la parte inferior existe una zona donde hay un remolino con una zona de estancamiento. El cambio de la presión y de la velocidad entre la salida y la entrada se muestra en la parte inferior para la línea de flujo central. Los valores de la diferencia de presión y de velocidad para está válvula son mayores que en el caso de la válvula de compuerta, esto es debido a esta válvula se utiliza para el control del flujo. La diferencia de presión es de 0.28 Pa mientras que la diferencia de velocidad es 0.60 m/s.

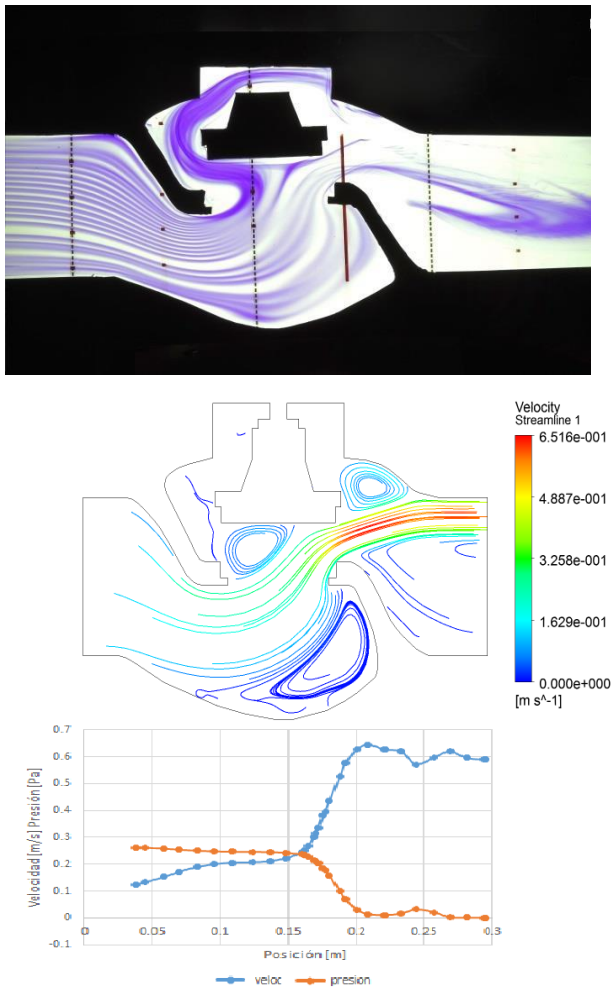

Fig. 4. Visualización de la válvula de globo con un 50 % de abertura.

Para el caso de apertura de la válvula de globo del 25 % y el mismo número de Reynolds de 1500, los resultados se muestran en la Fig. 5, las líneas de corriente a la entrada de la válvula son de un flujo uniforme hasta la sección de cambio de dirección del flujo, cuando se dirige hacia la base del obturador se deforman de tal manera que se forman dos zonas de estancamiento, una en la parte inferior del cuerpo de la

válvula y la otra en la base del obturador en la parte izquierda. Aguas arriba del obturador el flujo se acelera hacia la parte superior y forma una zona de estancamiento al igual que un remolino que se aprecia notablemente.

La simulación del fenómeno se presenta en la parte inferior de la Fig. 5, presentan las dos zonas de estancamiento anteriormente mencionadas, al pasar el fluido por la sección de flujo esté aumenta de velocidad considerablemente hacia la parte superior de la misma, entre el obturador y el flujo muestra una zona de un remolino. Las líneas de flujo tienen una velocidad mayor hacia la parte superior de la válvula y hacia la parte inferior muestra una zona de estancamiento.

La gran diferencia entre las gráficas de velocidad y presión en este caso son más notables que en los casos anteriores, la diferencia de presión al inicio es muy alta y por supuesto llega a cero a la salida de la válvula. En este caso como la válvula está más cerrada la diferencia de presión es de 1.30 Pa y la diferencia de velocidad es 0.60 m/s.

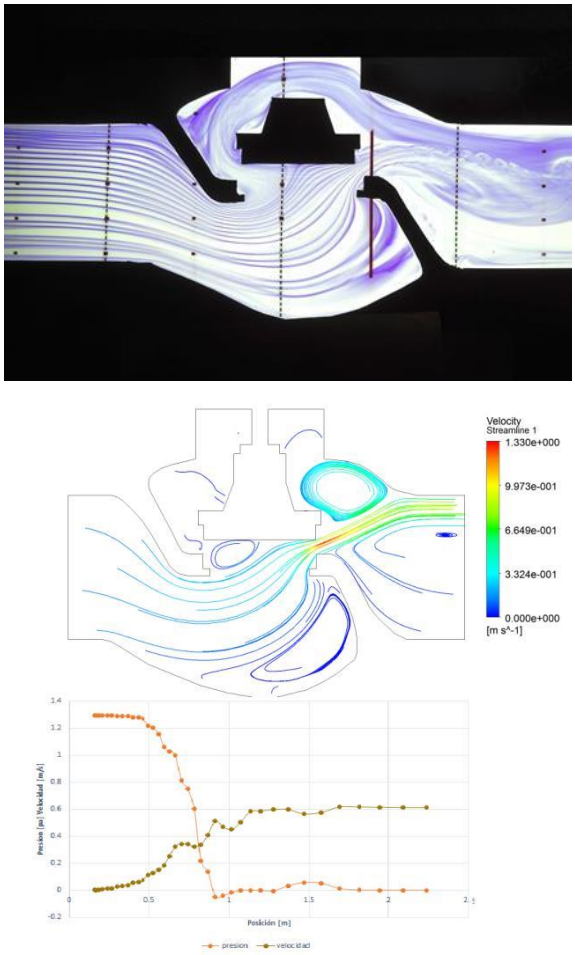

Fig. 5. Visualización de la válvula de globo con un 25 % de abertura.

V. CONCLUSIONES.

Se ha utilizado el visualizador de Hele-Shaw para observar lo que le pasa a un flujo de agua en condiciones de flujo laminar cuando pasa por el interior de las válvulas de compuerta y globo con una abertura del 50 y 25 %. Éstas se diseñaron y fabricaron de acuerdo a las dimensiones de válvulas semejantes pero reales de 0.05 m de diámetro nominal, fueron fabricadas en hule de neopreno de acuerdo a la norma ASTM D-2240, de 0.003 m de espesor. Como colorante se utilizó en azul de metileno. Los resultados experimentales obtenidos, para un flujo con número de Reynolds de 1500, fueron contrastados contra los arrojados por la simulación realizada en el software ANSYS que se programa con iguales condiciones de frontera. Se obtuvo además el análisis numérico entre la diferencia de presiones y de velocidades y se graficó para entender lo que le paso al flujo de acuerdo a la ecuación de conservación de energía. La similitud entre los resultados experimentales y los obtenidos de la simulación es bastante cercana, observándose hasta las zonas de estancamiento y los remolinos que se presentan en el fenómeno. La diferencia entre la pérdida de energía que se presenta entre ambas válvulas para iguales condiciones de flujo muestra el porqué de su uso, es decir, de acuerdo con los resultados obtenidos la válvula de globo proporciona una mayor pérdida de energía y por esto se utiliza para el control del flujo, en cambio para la válvula de compuerta no ya que su utilización es principalmente para aislar una parte del sistema sin controlar parcialmente el flujo.

VI. REFERENCIAS.

[1] J.W. Hutchison, (1976). ISA Handbook of Control Valves, second ed., Instrument Society of America, Pittsburgh.

[2] M.J. Kirik, L.R. Driskell, (1986). Flow Manual for Quarter-Turn Valves, Rockwell International Co.

[3] G.H. Pearson, (1978). Valve Design, Mechanical Engineering Publication, London.

[4] Ming-Jyh Chern, Chin-Cheng Wang and Chen-Hsuan Ma, 2007. Performance test and flow visualization of ball valve. Experimental Thermal and Fluid Science 31, 505–512.

[5] Richter JP (1970). The notebooks of Leonardo da Vinci, Vols I & II (Modern Edition). Dover Publications, Mineola, N.Y.

[6] O'Malley CD, Saunder JB (1983) Leonardo on the human body. Dover Publications, Mineola, N.Y.

[7] Keele K, Pedretti C (1979) Leonardo da Vinci. Corpus of anatomical studies in the collection of her majesty the queen at Windsor Castle. Harcourt Brace Jovanovich, New York

[8] Gharib M., Kremers D., Koochesfahani M.M., Kemp M., 2002. Leonardo's vision of flow visualization. Experiments in Fluids 33, 219–223. DOI 10.1007/s00348-002-0478-8

[9] Alexander Vasilév, 2009, From the Hele-Shaw Experiment to Integrable Systems: A Historical Overview. Complex Analysis and Operator Theory, 3, 551-585.

Determination of the operating windows of an sweetening sour gas plant employing rigorous process simulators

Hernández Martínez, I.,
Facultad de Ciencias Químicas
Universidad Veracruzana
Orizaba, Veracruz, 94340, México
Isai.hm.23@gmail.com

A. Osorio Mirón
Facultad de Ciencias Químicas
Universidad Veracruzana
Orizaba, Veracruz, 94340, México
anosorio@uv.mx

L. Guin Morales
Facultad de Ciencias Químicas
Universidad Veracruzana
Orizaba, Veracruz, 94340, México
lilimaestraguin@gmail.com

E. Hernández Aguilar
Facultad de Ciencias Químicas
Universidad Veracruzana
Orizaba, Veracruz, 94340, México
eduhernández@uv.mx

R. Melo-González
Facultad de Ciencias Químicas
Universidad Veracruzana
Orizaba, Veracruz, 94340, México
lmelog@uv.mx

***Abstract*—Marlin (2010) proposed a methodology to teach the subject process Operability students of chemical engineering. This paper applies the concept to an operating windows Sweetening sour gas plant, as a means of absorption using amines DEA (diethanolamine) and MDEA (methyldiethanolamine), emphasizing the quality of the response variable, the concentration of hydrogen sulfide in the gas at the outlet sweet absorption tower, which according to the NOM-001-SECRE-2010 should be reduced to 6 ppm of hydrogen sulfide (H_2S) concentration. A focus on what the "operating windows and mechanical integrity" API RP 584 (2014), which are associated with the mechanical integrity for relations H_2S / CO_2 greater than or equal to 1/19 is also made, to avoid corrosion process lines and may be lost or containment leak conducive to guarantee operation regions associated with process reliability and durability or life of the plant. In this paper the development and results of a series of simulations in steady state for this process with two absorbing medium is described.**

The simulations were performed with the process simulation package UniSim Design R390.1 to different possible operating conditions of the plant.

They were obtained from the simulation values of the input conditions sour gas (temperature, flow and pressure) that can meet sweet gas quality according to the Norma Oficial Mexicana. Likewise, surface response graphics were generated to analyze the behavior of the interaction of two factors, keeping one constant (temperature, flow, pressure) and observe their response in the concentration of H_2S and CO_2.

Keywords*—Operating Windows; process simulators; quality; mechanical integrity; sweetening of sour gas; amines; reliability; safety.

***Resumen*—Marlin (2010) propuso una metodología para enseñar el tema de Operabilidad de procesos a los estudiantes de ingeniería química. Este trabajo aplica el concepto Ventanas Operativas a una planta endulzadora de gas amargo, usando como medio de absorción las aminas DEA (dietanolamina) y MDEA (metildietanolamina) , enfatizando en el nivel de calidad de la variable de respuesta, la concentración de ácido sulfhídrico en el gas dulce a la salida de la torre de absorción, la cual según la NOM-001-SECRE-2010 debe tener una concentración menor a las 6 ppm de ácido sulfhídrico (H2S). Asimismo se hace un enfoque de lo que son las "Ventanas Operativas e integridad mecánica" API RP 584 (2014), que están asociadas a la integridad mecánica para relaciones de H2S/CO2 mayores o iguales a 1/19, esto para evitar corrosión en las líneas de proceso y posible pérdida de contención que propicien fugas, para garantizar regiones de operación asociadas a la confiabilidad del proceso y durabilidad o vida útil de la planta. En este trabajo se describe el desarrollo y resultados de una serie de simulaciones en estado estacionario para este proceso con los dos medios de absorción.**

Las simulaciones se realizaron con el paquete de simulación de procesos UniSim Design R390.1, ante diferentes posibles condiciones de operación de la planta.

Se obtuvieron de las simulaciones valores de las condiciones de entrada del gas amargo (temperatura, flujo y presión) que puedan cumplir con la calidad del gas dulce de acuerdo con la Norma Oficial Mexicana. Así mismo se generaron gráficos de superficie de respuesta para analizar el comportamiento de la interacción de dos factores, manteniendo uno constante (temperatura, flujo, presión) y observar su respuesta en la concentración de H2S y CO2.

I. Introduction

Marlin (2010) proposed a methodology to teach the subject process Operability students of chemical engineering.

This paper focuses on the first topic proposed by Marlin called "Operating Windows", which it is also found in document DCO operating windows of PEMEX (2008), which defines it as "the set of conditions and variables involved in the operation of a facility, adjusted to allow ranges operate reliably."

This first topic mentioned by Marlin, is applied to a sweetening sour gas plant with Girbortol process, using as absorption medium MDEA and DEA. The quality of natural gas according to the NOM-001-SECRE-2010, which specifies that the H_2S concentration should not exceed 6 ppm is taken as reference. Mention is also made to API RP 584 (2014) that is associated with the operating windows mechanical integrity for relations H_2S / CO_2 greater than or equal to 1/19, to avoid corrosion in the process lines and possible loss of containment propitiate leakage, the above operation ensures regions associated with process reliability and durability or life of the plant.

Melo et al. (2014) determined the Operating Windows of a sweetening sour gas plant using rigorous process simulators.

In this work the safe operating range, minimum and maximum variable flow, temperature and pressure process is determined, through multiple simulations using the rigorous steady state process simulator UniSim Design R390.1 using diethanolamine (DEA) and Methyldiethanolamine (MDEA) as a medium of absorption, obtaining plots of surface using statistical design of experiments for the above mentioned regions.

II. Operability

Marlin proposed a methodology to teach the subject process Operability students of chemical engineering. Chemical engineering professors and engineers who are in practice know that a process should be operable. However, the term operability is not used commonly. Give a concise definition of operability is difficult, so Marlin operability proposed eight topics to define the subject, these are:

- Operating Window.
- Flexibility and Controllability
- Reliability
- Safety and equipment protection
- Efficiency and product quality
- Operations during transitions
- Dynamic performance
- Monitoring and diagnosis

These topics are not new and have been recognizes for their industrial importance.

He also mentions that must be designed for real scenarios taking into account that not only operates at a point within a range, including the uncertainty associated with factors that can occur, such as changes in feed properties, production rates and specifications product and changes during startup, shutdown and removal of equipment maintenance, the equipment should be designed to operate as specified during these transitions using a good estimate of known variations in operating conditions and performance requirements.

Despite our best efforts, substantial uncertainty also exists, for example, correlations to process, physical properties and performance of equipment efficiencies. The design must meet the variability and uncertainty.

The rigorous process simulation is very useful as it is very difficult for management of a company allows engineers to arbitrarily make changes to a facility that operates successfully simply by seeing what also happens mathematical models processes can be manipulated, which is more difficult to do in real plants. They can be simulated operations outside conditions or normal operating ranges, including simulated unsafe operating conditions that may jeopardize the integrity of the plant.

III. Operating Windows

The operating windows establish operating controlled range in an industrial process where inputs are transformed into products through a safe and responsible operation economically optimized without interruptions or unplanned shutdowns and allowing maximize the lifecycle of assets. A key element of process safety is to maintain the mechanical integrity of the assets, meaning that this is achieved when an asset is carried out, operated and maintained as specified in the design, so that the risk to people, the environment and other assets minimized and the company image is enhanced.

The document DCO Operating Windows of PEMEX (2008) defines the operating windows as "the set of conditions and variables involved in the operation of a facility, adjusted to allow ranges operate reliably."

The variables to consider are:

• Process temperature, pressure, gravity, viscosity, contaminants, etc.

• Service: Water cooling, flushing, steam, lubrication, etc.

• Physical aspects vibration, speed, amperage, temperature, etc.

The operational context (2012) is important in establishing the operating variables of critical equipment, we provide a safe and reliable operation factor. Marlin (2010) mentions that one of the objectives of the process design is to ensure that the range of conditions defined in the specifications of operations is reached. They should consider the variability and uncertainty, which are based on the design specifications and a knowledge of process design models. They should also use first principles to determine the boundary conditions or "worst case", over a range of parameter values. When a range is specified for the parameters, engineers must use their knowledge and experience to understand the impact of the

values used. If a combination of extreme values for each parameter and the worst case for the selected variables are used, it is possible to have a plant on designed to unlikely scenarios.

IV. SOUR GAS SWEETENING

A. *Natural gas*

Natural gas is a nonrenewable resource comprising a mixture of hydrocarbons: methane (about 80%), ethane (6%) propane (4%), butane (2%), along with some impurities such as water vapor , sulfur compounds, carbon dioxide (CO_2), nitrogen (N_2) and trace amounts of heavier hydrocarbons. Its composition varies according to the site from which it was removed (Martinez, 2000)

The process of sweetening natural gas is one of the most important processes, which must undergo natural gas, since it involves removal of acid gases from the gas stream (H_2S and CO_2), because these compounds are gases that can cause problems in the handling and processing of gas as well as corrosion problems, harmful odors, emissions of acid rain-causing compounds, among others. This removal can be accomplished through various processes, such as absorption of the acid gases, with chemical solvents, physical and mixed.

B. *Sweetening sour gas plant*

The flowchart of a sweetening sour gas plant using amines shown in Figure 1. The acid gas is introduced to the absorber at the bottom where it is contacted countercurrently with the solution lean amine, thewhich it is fed by the dome and flows downwardly. The acid gas components, CO_2 and H_2S are absorbed by the amine solution, while the sweet gas leaving the absorber tower at the top , with a maximum of 6 ppm H_2S.

The rich amine solution, obtained by the bottons, is sent to a flash tank, where the absorbed hydrocarbons are released into the gas phase. Subsequently, the rich amine solution passes through a heat exchanger amine rich / lean to increase their temperature to 90-110 ° C. The heated rich amine enters the regenerating tower, wherein acid gases, dissolved hydrocarbons and water vapor may contain are released.

Exhausting pressure column must be maintained to increase the temperature of the reboiler and achieve optimized operation. However, care must be taken not to exceed the degradation temperature of the amine. A bomb is placed in the line of tower bottoms in order to send the lean amine to the absorber tower. An air cooler reduce the temperature of lean amine to the contactor tower for the absortion (Behroozsarand, 2011).

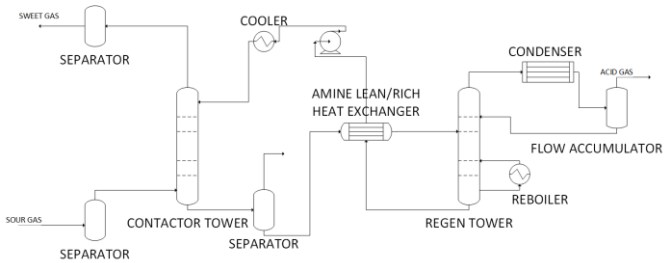

Fig. 1 A flowchart Sweetening sour gas plant

V. STEADY STATE SIMULATION USING DESIGN UNISIM R390.1

The simulation model of the process sweetening sour gas plant using DEA, MDEA as absorbing means shown in Figure 2.

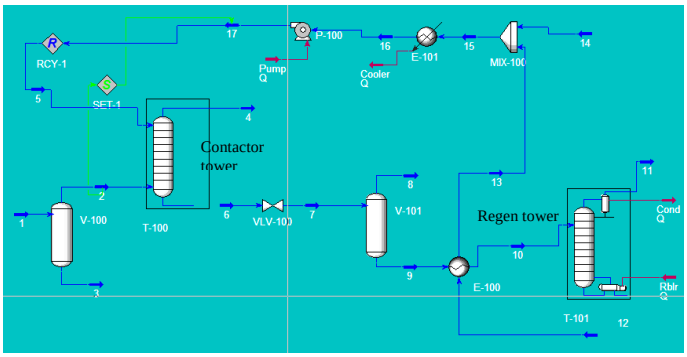

Fig. 2 Sweetening model sour gas plant

The name of the process streams are shown in Table 1 and the equipment in Table 2.

Name of the process streams	
Number of the stream	***Name of the stream***
1	Sour Gas
2	Gas to contactor
3	Sour water
4	Sweet gas
5	MDEA/DEA to contactor
6	Rich MDEA/DEA
7	MDEA/DEA to flash
8	Flash steam
9	MDEA/DEA to heat exchanger
10	Regen feed
11	Acid gas
12	Regen bottoms
13	Lean MDEA/DEA to mixer
14	Make up water
15	Lean MDEA/DEA to cooler
16	Lean MDEA/DEA pump
17	Lean MDEA/DEA to recycle

Table 1. Names of streams of the model

List of equipment of sweetening sour gas plant.	
V-100	Sour gas separator
T-100	Contactor tower
VLV-100	Valve
V-101	Hydrocarbons separator
E-100	Amine lean/rich heat exchanger
T-101	Regen tower
MIX-100	Mixer
E-101	Cooler
P-100	Pump

Table 2. List of equipment of sweetening sour gas plant.

The thermodynamic model used for the simulation Sweetening sour gas plant is the Kent-Eisenberg (Invensys, 2007) that is included in the package simulator amines Unism Design.

A. *Input data*

The specifications of the conditions of entry and composition of sour gas and absorption through the sweetening sour gas plant using DEA are shown in Tables 3, 4, 5, and 6 (Goméz, 2014)

Terms of sour gas. using DEA as absorption medium	
Temperature [=] °C	25
Pressure [=] Kg/cm^2	70
Flow [=] Kg mol/h	1250

Table 3. Conditions of entry of sour gas. Using DEA as absorption medium.

Sour gas composition [=] mole fraction	
Nitrogen	0.00160
H_2S	0.01720
CO_2	0.04130
Methane	0.86920
Ethane	0.03930
Propano	0.00930
i-Butane	0.00260
n-Butane	0.00290
i-Pentane	0.00140
n-Pentane	0.00120
n-Hexane	0.00180
Water	0.01220
DEA	0.00000

Table 4. Composition of sour gas [=] Mole fraction. Using DEA as a absorption medium.

DEA's entry conditions	
Temperature [=] °C	35
Pressure [=] kg/cm^2	70
Volumetric flow [=] USPGM	190

Table 5. Conditions of entry DEA amine solution.

Feed stream composition [=] mass fraction	
CO_2	0.0018
Water	0.7187
DEA	0.2795

Table 6. Feed stream composition [=] mass fraction.

The specifications of the conditions of entry and composition of sour gas and absorption through the sweetening sour gas plant using MDEA as absorbing medium are shown in Tables 7.8, 9 and 10. (Heredia, 2011).

Conditions of entry of sour gas. Using MDEA as absorption medium	
Temperature [=] °C	35
Pressure [=] Kg/cm^2	84.1
Flow [=] Kg mol/h	4483

Table 7. Conditions of entry of sour gas. Using MDEA as absorption medium

Sour gas composition [=]Mole fraction	
Nitrogen	0.02610
H_2S	0.02070
CO_2	0.01100
Methane	0.64510
Ethane	0.15240
Propane	0.06930
i-Butane	0.00830
n-Butane	0.02500
i-Pentane	0.00750
n-Pentane	0.01270
n-Hexane	0.02190
Water	0.00000
MDEA	0.00000

Table 8. Composition of sour gas [=] Mole fraction. Using MDEA as absorption medium.

MDEA's entry conditions	
TemperaturE [=] °C	40
Pressure [=] Kg/cm^2	83
Flow [=] Kg mol/h	9520

Table 9. Conditions of entry of sour gas. Using DEA as absorption medium

Feed stream composition [=] mole frac.	
Water	0.51000
MDEA	0.49000

Table 10. Feed stream composition [=] mole fraction

VI. Results

A. *Results of simulations using DEA as absortion medium*

First the focus of a factor applied both by varying each factor in a range, keeping the other two constant factors, to determine which of the three factors have a major influence on the ppm of H_2S and CO_2. The simulation results shown in Figures 3, 4, 5 and 6.

Secondly the factorial approach, where two factors were varied was applied together while keeping one. The results of the simulations are shown in Table 11 and Figures 7, 8, 9, 10 and 11.

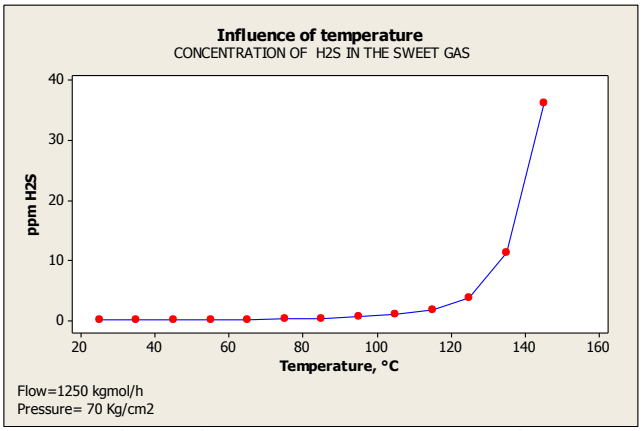

Fig. 3 Influence of temperature on the concentration of H_2S in the sweet gas stream. DEA using as absorption medium

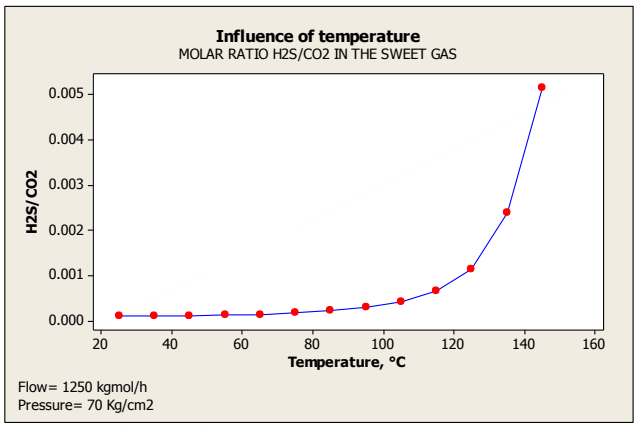

Fig . 4 Influence of temperature in the H_2S / CO_2 ratio in the stream of sweet gas. DEA using as absorption medium.

Temperature range from 25 °C to 145 °C was taken with a flow of 1250 kgmol / h and a pressure of 70 kg / cm2. It was observed that the concentration of H_2S and CO_2 as the temperature increased sour gas flow was increased. You can see that from 135 °C the concentration of H_2S out of specification, exceeding 6 ppm. It was also noted that these values of temperature approaches recommended ratio H_2S / CO_2 value, but this does not meet the required quality specifications.

The influence of pressure is also considered in the response variables of a range of 70 to 180 kg / cm^2 with a flow of 1250 kgmol / h at 25 ° C

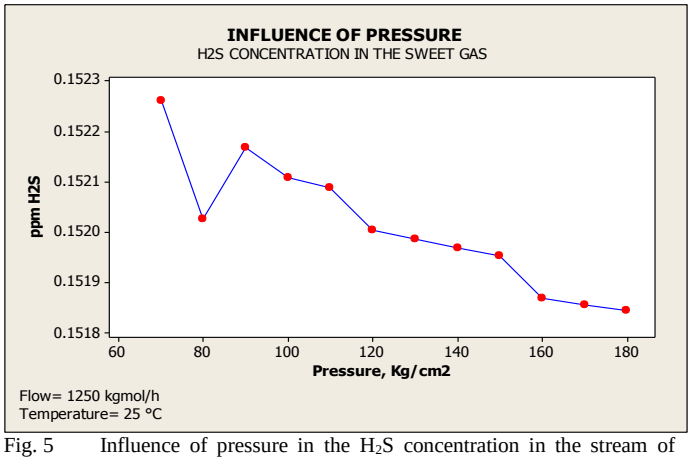

Fig. 5 Influence of pressure in the H_2S concentration in the stream of sweet gas. using DEA as absorption medium.

It can be seen in Figure 5 that the pressure itself has no significant influence on the response variables. However we noticed a slight decrease in concentration as the pressure drops to 80 kg / cm^2, as the pressure rises to 100 kg / cm^2 again ascener concentration then declined again.

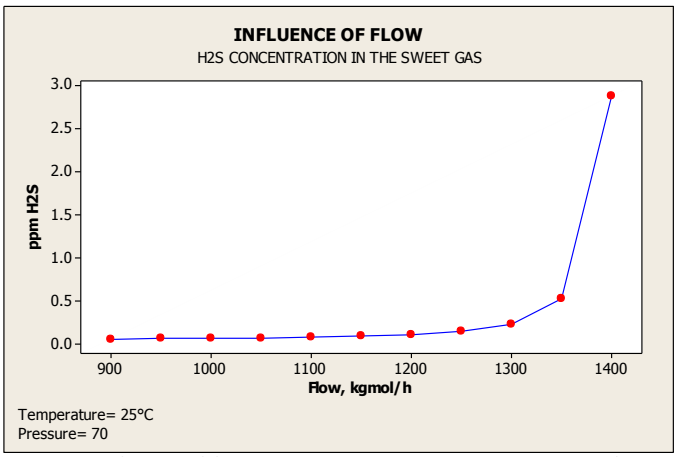

Fig. 6 Influence of flow in the H_2S concentration in the stream of sweet gas. DEA using as absorption medium.

The influence was also felt sour gas flow in response variables of a range of 900-1400 kgmol / h, with a temperature of 25 ° C and a pressure of 70 kg / cm2. It is noted that the influence of the flow in the H_2S concentration is greater than the influence of pressure, but lower than the temperature, as the flow increases the concentration of H_2S starts ascending where, from 1300 kgmol / h H_2S concentration starts to increase up out of specification.

To analyze the behavior of two factors simultaneously surface graphics were performed using the following combinations:

Flow [=]kgmol/h	Pressure [=]kg/cm^2	Temperature [=]°C	Ppm H_2S	H_2S/CO_2
1250	60→80	25→45	0.15→0.18	0.00010 →0.00012
1300	60→80	25→45	0.23→0.33	0.00014 →0.00019
1350	60→80	25→45	0.53→1.2	0.0002 →0.0005
1250→1350	60	25→45	0.15→1.24	0.00010 →0.00012
1250→1350	70	25→45	0.15→1.22	0.00014 →0.00019
1250→1350	80	25→45	0.15→1.22	0.0002 →0.0005
1250→1350	60→80	25	0.15→0.53	0.00010 →0.00027
1250→1350	60→80	35	0.16→0.76	0.00011 →0.00035
1250→1350	60→80	45	0.18→1.22	0.00012 →0.0005

Table 11. simulation results. Using DEA as absorption Medium. Simulator Unisim Design r390.1

Shown in Table 11 for all combinations of operating conditions, the ratio of H2S / CO2 are below 1/19.

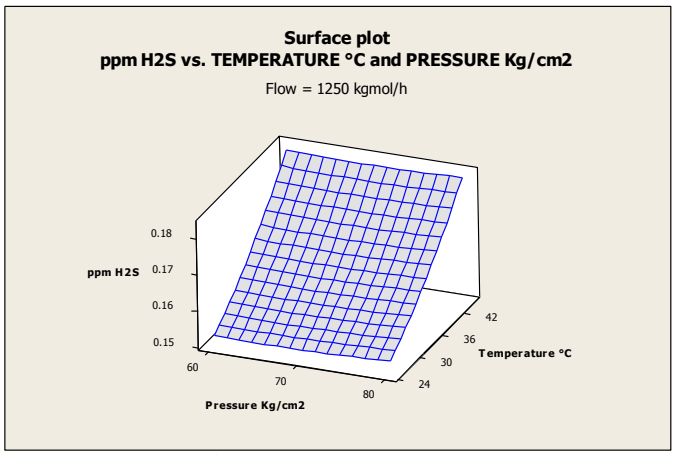

Fig. 7 Behavior of H_2S concentration with respect to the pressure and temperature. Sweetening sour gas plant using DEA as absorbing medium .

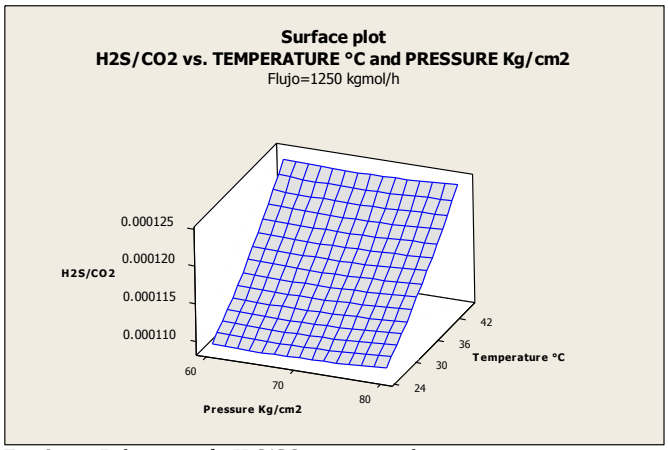

Fig. 8 Behavior of H_2S/CO_2 ratio with respect to pressure and temperature. Sweetening sour gas plant using DEA as absorbing medium .

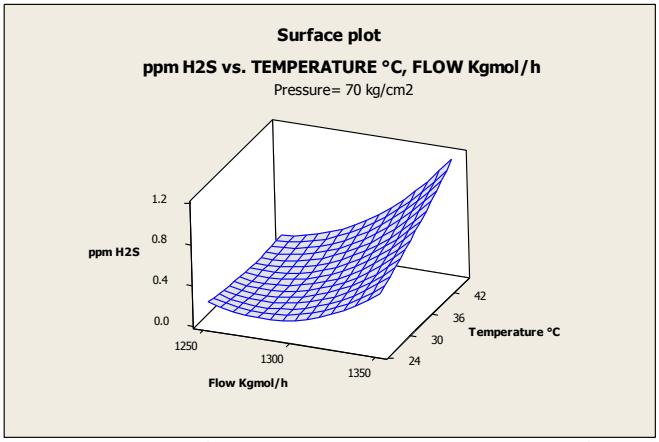

Fig. 9 Behavior of H_2S concentration with respect to the flow and temperature. Sweetening sour gas plant using DEA as absorbing medium

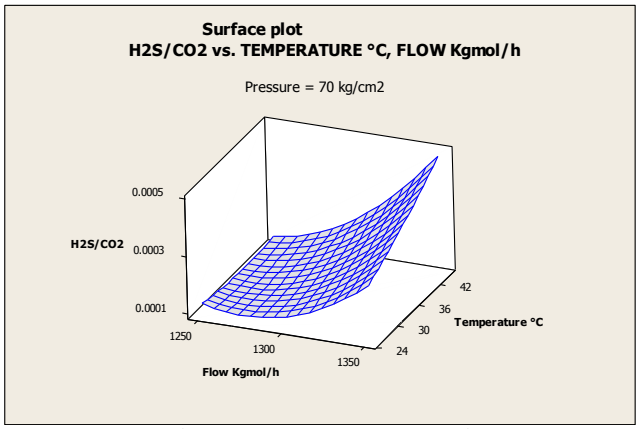

FIg. 10 Behavior of H_2S/CO_2 ratio with respect to flow and temperature. Sweetening sour gas plant using DEA as absorbing medium .

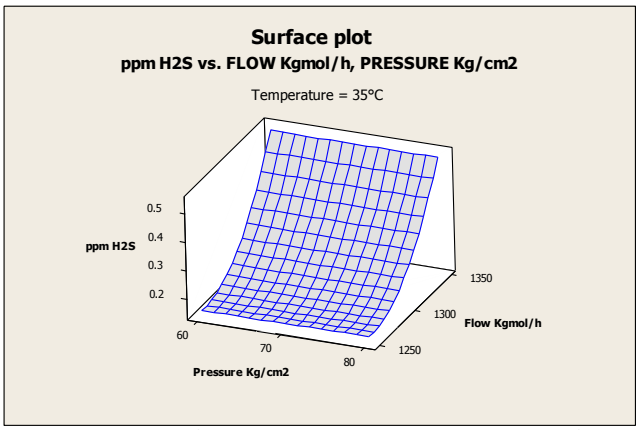

Fig. 11 Behavior of H_2S concentration with respect to the flow and pressure. Sweetening sour gas plant using DEA as absorbing medium

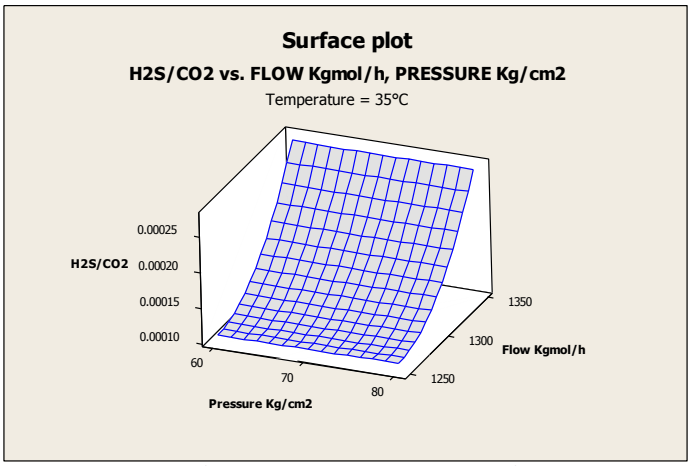

Fig. 12 Behavior of H_2S/CO_2 ratio with respect to flow and pressure Sweetening sour gas plant using DEA as absorbing.

B. Results of simulations using MDEA as absortion medium

Similarly, in the plant using the approach MDEA while a factor was first applied to determine the individual effect of temperature, flow and pressure in the response variables. The

results of the simulations using the rigorous process simulator Unisim Design R390.1 shown in Figures 13, 14, 15, 16 and 17.

Secondly the factorial approach, where two factors together will vary while keeping one applies. The results of the simulations are shown in Table 12 and Figures 21, 22 and 23.

First it took the temperature range 35 °C to 135 °C with a flow of 4483 kgmol / h and a pressure of 84.1 kg / cm^2.

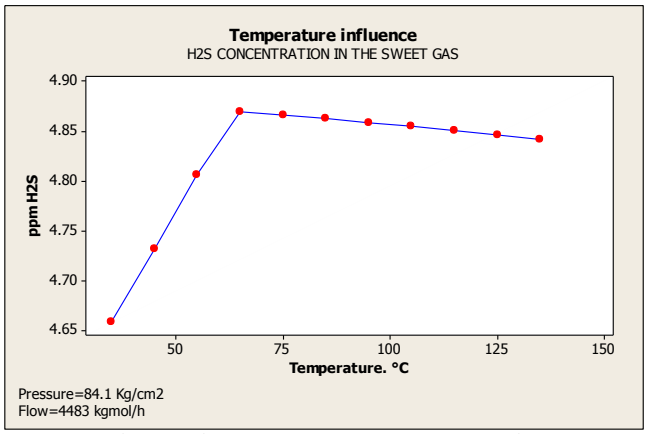

Fig. 13 Influence of temperature in the concentration of H_2S in the sweet gas stream.M DEA using as absorption medium

In Figure 13 it can be seen that the concentration of H_2S increases with respect to temperature up to a point about 60 °C wherein the temperature increases as the concentration starts to decrease.

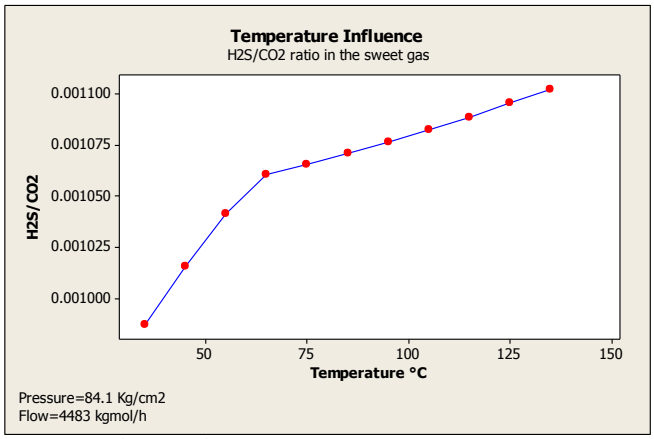

Fig. 14 Influence of temperature in the H_2S/CO_2 ratio in the sweet gas stream. MDEA using as absorption medium

It can be seen in Figure 14 the temperature causes the ratio H_2S / CO_2 will always constantly increasing.

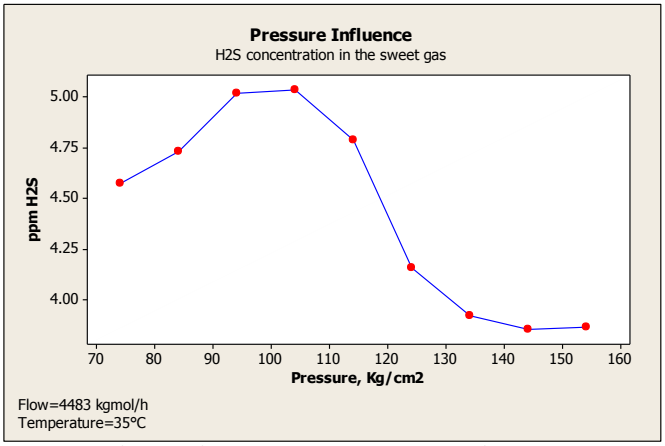

Fig. 15 Influence of pressure in the concentration of H_2S in the sweet gas stream.M DEA using as absorption medium

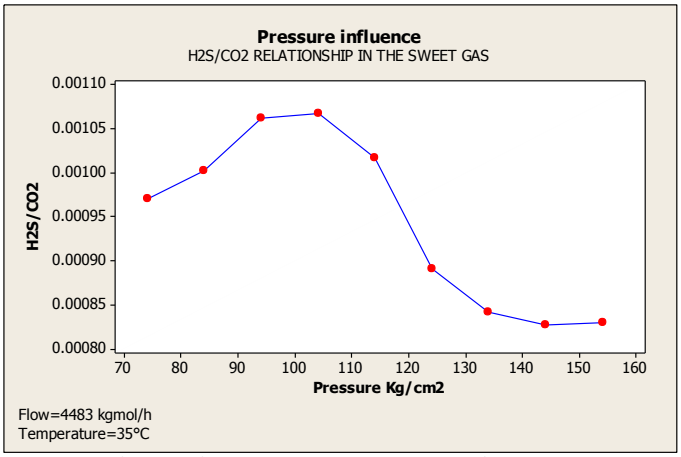

FIg. 16 Influence of pressure in the concentration of H_2S in the sweet gas stream.M DEA using as absorption medium

Figure 16 shows the behavior of the ratio of H_2S / CO_2 due to the increased pressure. We can also observe that the behavior is very similar to having the H_2S with pressure, this increase causes decrease the concentration of H_2S and CO_2 concentration increases as a result the ratio rises.

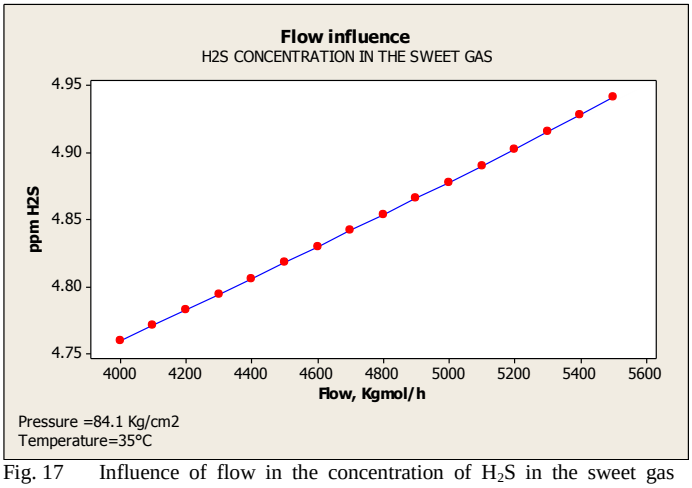

Fig. 17 Influence of flow in the concentration of H_2S in the sweet gas stream.M DEA using as absorption medium

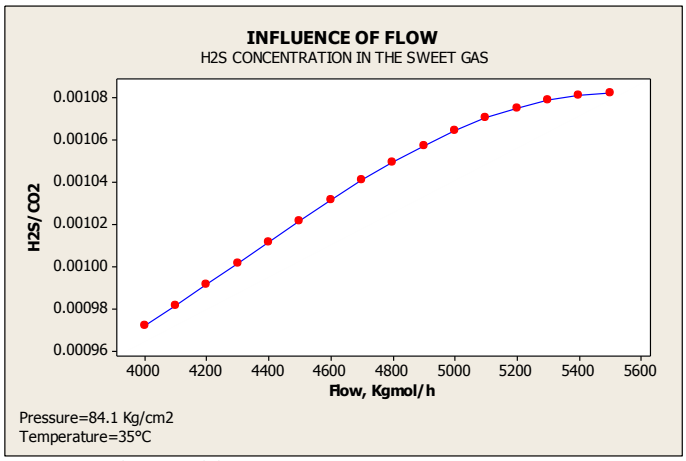

Fig. 18 Influence of flow in the H_2S/CO_2 ratio in the sweet gas stream.M DEA using as absorption medium

In Figure 18 we can see the behavior that the H_2S / CO_2 ratio to flow, the latter has a great influence on the relationship, because of the increased concentration of H_2S with respect to increased flow.

Flow [=] kgmol/h	Pressure [=] kg/cm^2	Temperature [=] °C	Ppm H_2S	H_2S/CO_2
4383	74.1→84.1	35→55	4.88→5.02	0.00085 →0.00108
4483	74.1→84.1	35→55	3.76→4.91	0.00082 →0.00107
4583	74.1→84.1	35→55	3.61→4.59	0.00078 →0.0010
4383 →4583	74.1	35→55	4.45→5.02	0.00077 →0.00108
4383 →4583	79.1	35→55	3.61→4.14	0.00095 →0.000108
4383 →4583	84.1	35→55	3.66→4.26	0.00077 →0.00087
4383 →4583	74.1→84.1	35	3.61→4.88	0.00077 →0.00103
4383 →4583	74.1→84.1	45	3.67→4.95	0.00080 →0.00106
4383 →4583	74.1→84.1	55	3.73→5.02	0.00088 →0.00108

Table 12. simulation results. Using MDEA absorption Medium. Simulator Unisim Design r390.1

Shown in Table 12 that combinations of operating conditions, the ratio H_2S / CO_2 are below 1/19, however the concentration of H_2S is below 6 ppm.

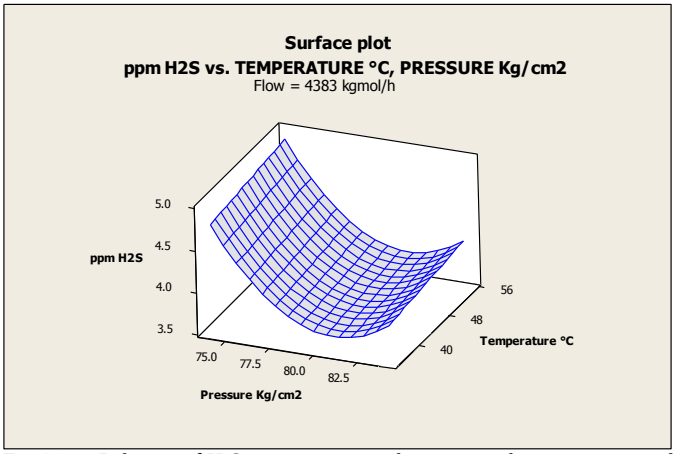

Fig. 21 Behavior of H_2S concentration with respect to the temperature and pressure. Sweetening sour gas plant using MDEA as absorbing medium

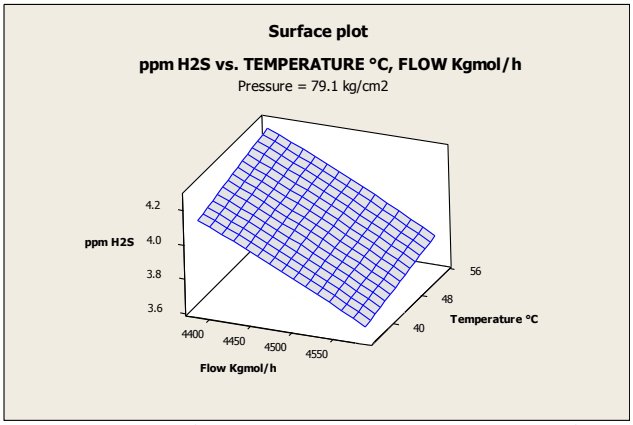

Fig. 22 Behavior of H_2S concentration with respect to the flow and temperature. Sweetening sour gas plant using MDEA as absorbing medium

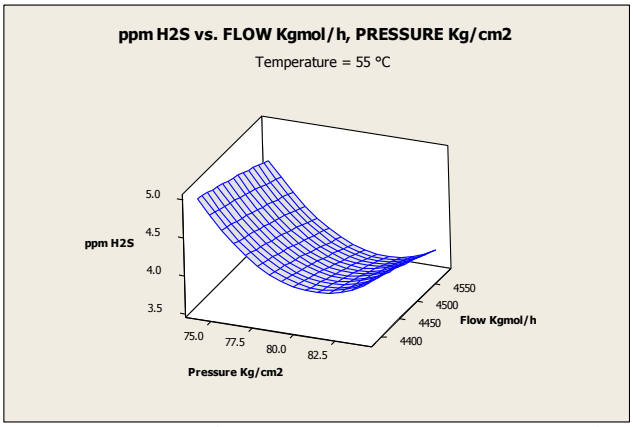

Fig. 23 Behavior of H_2S concentration with respect to the flow and pressure. Sweetening sour gas plant using MDEA as absorbing medium

VII. Conclusions

The operating window topic is of great current interest in chemical, petrochemical, refining, oil and gas because it can determine the maximum and minimum values of the process variables for this to operate reliably, making aim the H_2S content such compliance established by the standard and closer relationship H_2S / CO_2 from the recommended level.

Using a rigorous process simulator evaluates unsafe operating conditions that endanger the integrity of the floor, pushing the ratio H_2S / CO_2 at levels that promote corrosion of equipment.
In quality in the case of the DEA, the results show that temperatures below 120 ° C and lower flows to 1400 kgmol /h meet H_2S content.
However for MDEA must operate in temperature settings between 25 and 135 ° C and a pressure range between 70 and 160 kg / cm^2, and to the flow window is operational between 4000 and 5600 kgmol / h of sour gas . Operating outside these ranges the model does not converge or the product has concentrations above specification.

VIII. RECOMMENDATIONS

Performing a parametric sensitivity analysis to determine which other variables affect the response variables mentioned above.
Add the equation modified Kent-Eisenberg (2014) Simulator processes by developing the appropriate subroutine.
H2S operate with values greater than 1/19, recommended by the API RP 584 to prevent corrosion in the process equipment and care for their mechanical integrity and reliability to meet the life cycle of the plant.
Dynamic process simulators used to observe the behavior over time and analyzing both teams are affected.
Perform the analysis from the metallurgical point of view to determine the damage mechanism of damage being caused to operate below the 1/19 ratio of H_2S / CO_2.

IX. REFERENCES

[1] American Petroleum Institute (2014). API Recommended Practice 584. Integrity Operating Window. USA

[2] Behroozsarand A. & A. Zamaniyan (2011): "Multiobjetive optimizations scheme for industrial synthesis gas sweetening plant in GTL process". Journal of Gas Natural Chemistry 20, 99-109.

[3] Gómez-Ixmatlahua, A (2014). Simulación dinámica rigurosa de una planta endulzadora de gas para evaluar su desempeño ante descontroles de variables de proceso. Tesis. Facultad de Ciencias Químicas. Universidad Veracruzana. México.

[4] Gutiérrez, J. P. y colaboradores (2012). Simulación del proceso de endulzamiento de gas natural con Aminas. Análisis del uso de diferentes simuladores. XXVI Congreso Interamericano de Ingeniería Química. Montevideo. Uruguay.

[5] Hamzah, A.N. (2013). Evaluation of modified Kent-Eisenberg Model to predict Carbon Dioxide solubility in Methyldietanolamine (MDEA) Under Extended Operating Conditions. Tronoh, Perak. Malasia.

[6] Heredia-Moctezuma, M. (2011). Simulación del proceso de endulzamiento de gas natural. Tesis. Facultad de Ciencias Químicas. Universidad Veracruzana. México.

[7] Himmelblau, D,. & Riggs, J. (2012). Basic principles and calculations in chemical engineering (Octava ed..). Prentice Hall.

[8] Jana, A. (2001). Modelling and computer simulation (Second ed.). India: Eastern Economy Edition.

[9] Kasiri, N., & Ghayyem, M. (2008). Rate based moldeing in H2S and CO2 absortion column using alkanolamine solutions.

[10] Lazic, Z. (2004). Design of Experiments in Checmical Enginieering. Estados Unidos: Wiliey-VCH.

[11] Marlin, T.E. (2010). Teaching Operability in undergraduate chemical engineering education. Computers and Chemical Engenieering 34 (2010) 1421-1431. USA.

[12] Martínez Sifuentes, V. H. y colaboradores (2000). Simulación de procesos en Ingeniería Química. Ciudad de México: Plaza y Valdés Editores. México

[13] Martínez, M. (2000). Ingeniería de gas, principios y aplicaciones. Ingeniero consultores, S.R.L. Maracaibo, Venezuela

[14] Melo González, R. (2006). Análisis de la operabilidad de plantas de proceso y su control total a traves de la simulación dinámica de diagramas de flujo de proceso en tiempo real. Instituto Mexicano del Petroleo. México.

[15] Melo González, R., Reyes Grajales, L., Gómez Rodriguez, R., & Gómez Ixmatlahua, A. (2014). Ventanas operativas y su determinación empleando simuladores rigurosos de proceso. Estudio de caso: Una planta endulzadora de gas amargo. XVI Congreso de Confiabilidad. San Sebastián. España.

[16] Montgomery, D. C. (2012). Design and analisys of experiments (Séptima ed.). México: Limusa Wiley.

[17] PEMEX Dirección Corporativa de Operaciones. SMC (2008). Guía técnica de confiabilidad operacional para la mejor práctiva: Ventanas operativas. México.

[18] PEMEX Exploración Producción (2012). Sistema de Confiabilidad Operacional. Versión 3. México.

[19] Rivera Soto, M., Viera Bertrán, R., & Matos Durán, R. (2005). Análisis de sensibilidad Paramétrica en Reactores de Reformación Catalítica de LPG. Obtenido de http://ojs.uo.edu.cu/index.php/tq/article/viewFile/2207/1749

[20] Simsci-Esscor Invensys (2007). PRO II Reference manual. Components and Thermophysical properties (Vol. I).

[21] Torres Robles, R., & Catro Arellano, J. (2002). Análisis y simulación de procesos de refinación del petróleo. México: Alfaomega.

[22] Walpole, R., Myers, R., Myers , S., & Ye, K. (2012). Probability and Statistics for Engineers and Scientist (Novena ed.). USA: Prentice Hall .

Economic assessment of Velfor 100 Zeolite influence on alcoholic fermentation yields and productivity, performed by three strains of *Saccharomyces cerevisiae*.

Gabriela Hernández-Villa; Hugo Velasco-Bedrán
.lDepartamento de Ingeniería Bioquímica-
Escuela Nacional de Ciencias Biológicas, IPN
Ciudad de México, México.
hugalvebe@yahoo.com.mx

Margarita González Brambila, Eneida Campos Guzmán
Departamento de Energía
Universidad Autónoma Metropolitana.Azacapotzalco.
Ciudad de México, México

***Abstract*— Ethanol, as a product of fermentation of sugars by microorganisms such as yeast, including *Saccharomyces cerevisiae* is nowadays considered as an alternative for obtaining energy. It has been very important in the foo,d pharmaceutical and chemical industries. It has been found in prior studies that the addition of certain amount of zeolite produces an increase in the ethanol /glucose yield. In this work the effect of zeolite on the carbon flux of *S. cerevisiae* in different culture conditions is reported, for possible application in the improvement of industrial processes to obtain ethanol by fermentation resulting in a 20% increase in yield, thus lowering production costs and bettering the use of raw materials, which would increase the possibilities of using this alcohol as biofuel.**

***Keywords*— bio-fuel, ethanol, substrate yield, zeolite, process economics Introduction (Heading 1)**

I. INTRODUCTION

In recent years, ethanol has become an important source of energy as biofuel. Petrochemicals used traditionally are dependent of fossil fuels, which are a limited source. Besides ethanol is cleaner and more attractive from an environmental point of view. [10].

The increased use of ethanol as fuel is illustrated in Figure 1 Note that, since the 70s, the use of ethanol has been increasing as a biofuel, though its industrial use and as a beverage has not changed. Yeasts and other microorganisms can use a variety of raw materials as substrates for the production of ethanol, as molasses, corn and cassava. The use of lignocellulosic substrates proves to be a more economical solution for the raw material, however, it requires the use of genetically modified organisms. Hence the need to improve product-substrate yield, in order to decrease the high cost of raw materials.

It has been observed that the use of zeolites as catalyst in alcoholic fermentation substrate increases the product yield.

Figure 1. World ethanol output by industry [3]

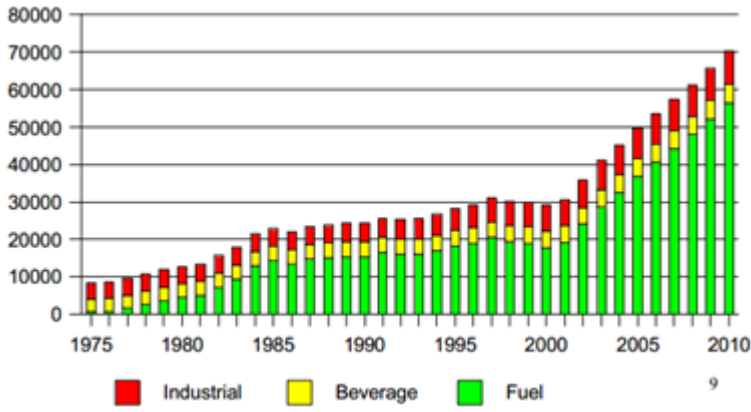

Zeolites are crystalline hydrophilic aluminosilicates, with a rigid skeleton and well defined channels and pores. They are widely used for ion exchange, adsorbents, acid catalysts and as molecular sieves. [7, 1] .

[8, 5, 2, 4] report up to 50 % increase in yield using up to 17 g/L zeolites (which are not described) The latter note that the zeolite effect is apparent after 20 h of cultivation. [9] report a 20 % increase in product yield using 0.5 g/L “Velfor 100” zeolite. In all of these reports a beneficial effect (ion removal, ethanol adsorption, pH buffering) is hypothezised to explain a greater yield.

[6] studied the kinetics and yield of seven strains isolated from agave fermentations for distilled beverages comparing them with a comercial strain. The found Y8 strain to perform with a higher yield.

We aim to define the effect of the presence of aluminum sodium silicate (“Velfor 100”) on the fermentation performance of three strains of *Saccharomyces cerevisiae* Y4, Y8 and Fermichamp [6].

II. Materials and Methods

A. Yeast strains. Three different strains of *Saccharomyces cerevisiae*: ScY4, ScY8 and Fermichamp, obtained from the collection of the Center of Genomics and Biotechnology (IPN) were tested. The lyophilizates were preserved in YPD médium and propagated in YPD liquid modified medium (6% glucose), at pH 5 for 72 hours, centrifuged and suspended in 20 mL of distilled water as inoculum

B. Experimental set up. Twelve fermentation batch experiments were performed at two different initial substrate conditions (70 and 170 g/L.

C. Reactor set up. 100 mg/L of zeolite Valfor-100 were immobilized on rubber mounts. (145ºC, 30 minutes) and were added to a 3 L fermenter jar with 1.5 L operating volume, prior to sterilization. A control fermenter jar (without zeolite) was also set up. Temperature was kept constant at 28 ° C (+- 2 °C) by thermostats and the jars were agitated by magnetic stirrers at 60 rpm. Initial pH was adjusted to 5 with analytical reagent sulphuric acid

D. .Analytical procedures. The concentrations of glucose, glycerol, ethanol and acetic acid were determined by HPLC chromatography (Hitachi Elite LaChrom). Determinations as in [6]. The biomass was determined by optical density at 600 nm.

III. RESULTS

III.1.- Zeolite pH kinetics.

A run was carried out with adhered zeolite in the fermentation medium in the absence of yeast cells. The results are shown in Figure 2.

Figure 2. pH kinetics in the presence (squares and dots) and absence (triangles) of zeolite.

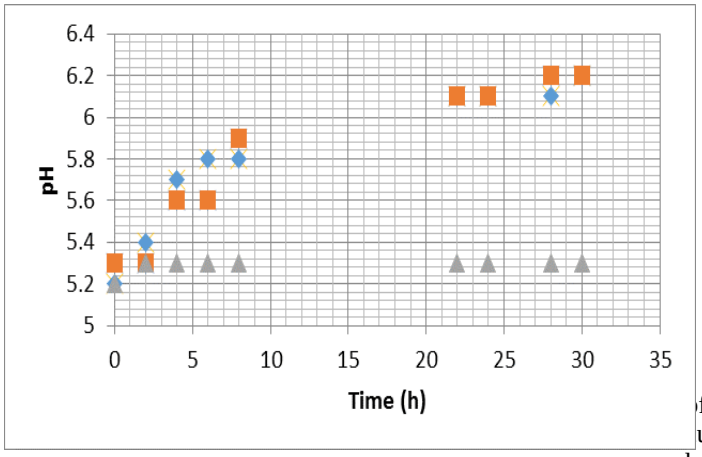

The presence of the zeolite in the culture medium increases the pH value by a pH unit. It can be said that the pH increase in culture media is a dynamic phenomenon in which the value of 6.14 corresponds to equilibrium.

Its effect on yeast culture medium pH is appreciated in the Figures 3, 4, and 5.

Figure 3.- Culture medium pH for Y8 strain (blue line: zeolite presence; red line: control).

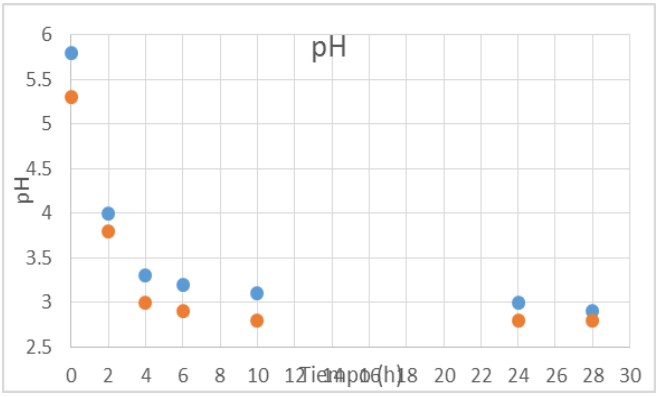

Figure 4.- Culture médium pH for Fermichamp strain (blue dots: zeolite presence, orange dots: control).

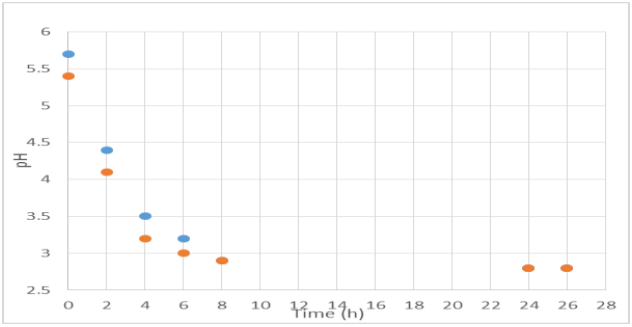

Figure 5.- Culture médium pH for Y4 strain (blue dots: zeolite presence; red dots: control).

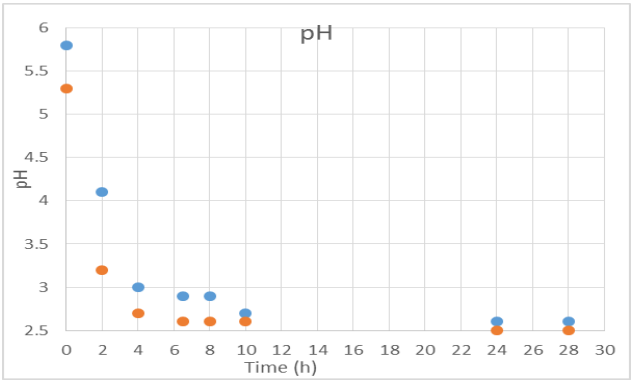

The kinetic effect of pH increase over 20 h in the presence of zeolite is shown altering the otherwise fast decrease of culture pH. A srtessing effect on the yeast environment is hypothezised.

III.2. Process yields and productivity results and analysis.

The average of duplicate product yield results (g ethanol/g glucose) are shown in Figures .6 and 7. In confirmation of the

findings of [6] Y8 strain performed better at the higher initial substrate concentration and showed the greatest yied increase in both initial substrate concentrations. It shows a high osmotolerance.

Figure 6 displays the average yield for fermentations run with 75 g/L initial glucose concentration. Figure 7 shows the average yield for fermentation runs with 170 g/L initial glucose concentration.

The effect of 170 g/L initial glucose concentration is to decrease the product yield as compared with the lower initial substrate concentration. An osmotic stress effect can explain these results. In all the experimental runs the presence of "Velfor 100" zeolite inreases the ethanol yield on glucose.

Figure 6.-. Average ethanol-glucose yields of experimental batch process at 70 g/L of initial glucose for the three strains tested in the presence (Z) and absence (S) of "Velfor 100" zeolite.

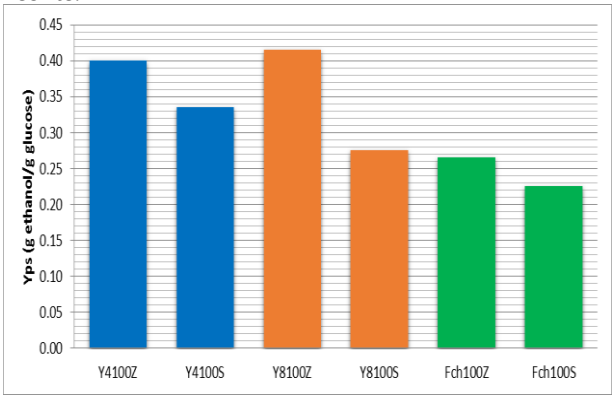

Figure 7.-. Average ethanol-glucose yields of experimental batch at 170 g/L of initial glucose for the three strains tested in the presence (Z) and absence (S) of "Velfor 100" zeolite.

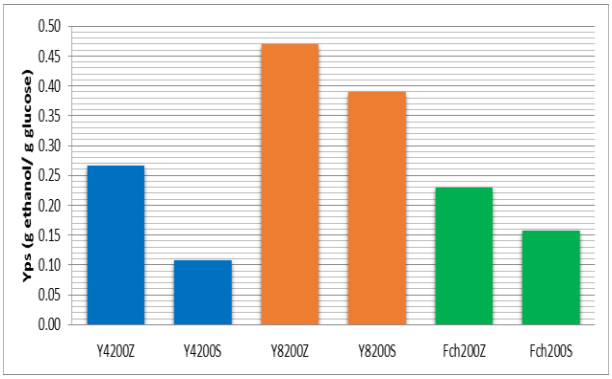

The productivity of each experimental run was also calculated and is shown in Figures 8 and 9 for the three strains at different initial glucose concentrations and in the presence and absence of "Velfor 100" zeolite.

Figure 8.-.Average experimental Productivity at 70 g/L of initial glucose in the presence (Z) and absence (S) of zeolite.

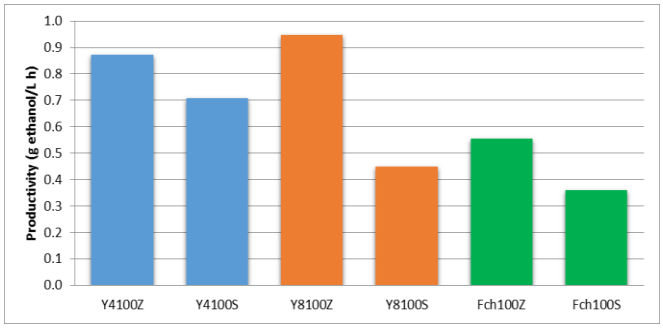

Figure 9. Average experimental Productivity (g ethanol/L h) at 170 g/L of initial glucose in the presence (Z) and absence (S) of zeolite.

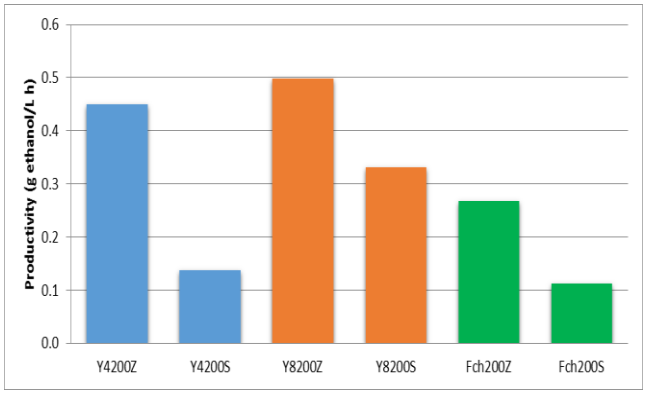

IV.- RESULTS.

An ethanol process plant using cane molasses as raw material and producing industrial 96 ° GL ethanol wais designed, The investment was calculated and its economic performance was estimated as return on investment (roi) considering standard process and the impact of using "Velfor 100" zeolite in the fermentation process.Table I sums the design basis values.

Table I.- Design basis for economic assessment.

Plant out put (m^3/y)	11740
Initial glucose in feed (g/L)	160
Final glucose in must (g/L)	10
Final ethanol in must (g/L)	58
Process time (h)	24
TAT (h)	6
Productivity (g/L h)	2
Product quality (° GL)	96

A total investment of Mx$ 131 841 600.00 was estimated. Current prices for cane molasses run at Mx$ 2 500/metric ton and prices for ethanol at the plant premises were estimated

conservatively at Mx$ 12,5/L. Mx$ 3.00/Kg was found for bakers yeast price as by-product.

Table II displays the return on investment (roi) estimated considering standard process and zeolite enhanced fermentation process.

Table II.- Return on investment for a 1 000 Kg/h ethanol fermentation plant in standard and zeolite-enhanced processes.

Standard process roi	0.1
18 % increase in yield roi	0.45

V.- CONCLUSIONS.

• In the presence of 100 mg/L of inmobilized zeolite, for the two conditions of initial substrate tested (70 and 170 g / L) and for the 3 strains studied (ScY4, ScY8 and Sc. Fermichamp), the speed of lowering of pH in the cultuire media is greater in comparison to control cultures.

• In all cases, the high initial concentration of substrate (170 g/L) decreases ethanol yield on glucose (Yp/s) and productivity (excepted for ScY8 strain, in which case, yield seems to increase). However the effect is more pronounced in the presence of zeolite in the medium relative to control cultures

. ° In all cases process productivity is enhanced by tge zeolite effect on the yeast metabolism.

• The increase in pH of the medium by the action of the zeolite is a dynamic phenomenon that over a period of time equivalent to 20 hours, is comparable to the dynamic growth phenomenon.

• We hypothezise that yeast responds to this increase in pH by acidifying the medium by proton pumping out of the cell, at the expense of cell growth and ATP consumption, which drives ATP formation through ethanol out put.

° Process economics for a 1 metric Ton/h ethanol production plant on cane molasses show a four-fold profit increase if the process employs zeolite.

ACKNOWLEDGMENT

We acknowledge the Center for Genomics and Biotechnology (IPN) for providing the yeast strains tessted and the Process Control Laboratory (UAM.A) for Laboratory facilities to assay process samples.

REFERENCES

[1] *Alvarez, R. R. (2002). Zeolitas. Alternativa de Eficiencia y Ecología. GMTerra Itda. Ecoterra inc.*

[2] *Baliga, S. A., Prabhune, A. A., Chandwadkar, A., & SivaRaman, H. (s.f.). Acceleration of ethanolic fermentation by zeolites. Biotechnology Techniques, 10(8), 589-594.*

[3] *Berg, C., Licht, F.(2004). World Fuel Ethanol. Analysis and Outlook: http://www.meti.go.jp/report/downloadfiles/g30819b40j.pdf*

[4] *Castellar, M. R., Aires Barrros, M. R., Cabral, J. M., & Iborra, J. L. (1998). Effect of Zeolite Addition on Ethanol Production from Glucose by Saccharomyces bayanus. J. Chem. Technol. Biotechnol, 73, 377-384.*

[5] *Mübeccer, E., Mutlu, S., & Özlem, G. (1997). Improved Ethanol Production by Saccharomyces cerevisiae with EDTA, Ferrocyanide and Zeolite X Adittion to sugar Beet Molasses. J. Chem.Tech.Biotechnol.*

[6] *Oliva-Hernández, A., Taillandier, P., Reséndiz-Pérez, D., Narváez Zapata, J. A., & Larralde Corona, C. P. (2013). The effect of hexose ratios on metabolite production in Saccharomyces strains obtained from the spontaneous fermentation of mezcal. Antoine van Leeuwenh, 833-843.*

[7] *Ramón, B. E. (1998). Identificación y caracterización de la zeolita natural tipo clinoptilolita*

[8] *Roque-Malherbe, R., Delgado, R., Contreras, O., & Lago, A. (1987). Behavior of yeast Fermentation in the presence of zeolite. Biotechnology Letters, 9(9), 640-642.*

[9] *Shizukawa, G. I. (2009). Evaluación del efecto de la zeolita en el metabolismo anaerobio de diversas levaduras. Tesis de doctorado en Ciencias en Alimentos. ENCB-IPN.*

[10] *Voit, N. T. (2002). Pathway Analysis and Optimization in Metabolic Engineering. Cambridge: Cambridge University Press.*

Hydrogen production by a sustainable photocatalytic process using copper metallurgical slag as catalyst

C. V. Montoya-Bautista, M. Solís-López, A. A. Morales-Pérez, R. M. Ramírez-Zamora*
Instituto de Ingeniería, Coordinación de Ingeniería Ambiental
UNAM
Mexico, Mexico
*RRamirezZ@iingen.unam.mx

***Abstract*—This work evaluated the simultaneous hydrogen production and glycerol degradation reactions developed by using a sustainable heterogeneous photocatalytic process, which employs copper metallurgical slag as a low cost and efficient photocatalyst. The copper slag showed high quantities of iron [32 %] and also low amounts of copper [1.41%], and both semiconductors can be present as chemical species that could be activated by light sources with wavelengths up to 377 nm (UVA region). The former transition metal was present in crystalline phases such as maghemite, fayalite and magnesioferrite, which can be able to act as very active photocatalysts. The maximum hydrogen production was 0.9 µmol/g of catalyst and 400 mg/L of glycerol were degraded (measured in terms of the residual content of dissolved organic carbon), after 4 hours of irradiation time and by using a pH value of 6.5 and 1g/L of photocatalyst.**

Keywords—Glycerol, degradation, industrial wastes, sacrificial agent

I. INTRODUCTION

The current consumption of fossil fuels increases year by year with negative impacts on the environment. For this reason, research is currently focused on producing renewable fuels with high energy content, being hydrogen an interesting option due to its specific energy power: the energy in 2.2 pounds (1 kilogram) of hydrogen gas contains about the same energy than 1 gasoline gallon [1].

Hydrogen can be produced by water dissociation (water splitting) into H_2 and O_2; this reaction can be performed by heterogeneous photocatalysis in aqueous medium using a semiconductor material, a light source and sacrificial agents as electron donors [2].

Photocatalytic reactions on semiconductors are initiated by the absorption of photons with energy equal to, or greater than, the semiconductor band gap value, which promotes electrons from the valence band (VB) to the conduction band (CB). This produces holes in the VB and the formation of electron (e_{CB}^-) – hole and (h_{VB}^+) pairs. The excitation energy is usually significantly greater than the energy required to overcome the ground state activation energy barrier of photochemical reactions; consequently, photocatalytic processes are generally unaffected to temperature and thus can be carried out at room temperature. Charge carriers produced in this way can either recombine, with the consequent loss of energy in the form of heat or emitted photons, or they can initiate electron transfer reactions at the semiconductor surface [3].

The titanium dioxide is widely employed as photocatalyst, but it is necessary a deposition of noble metals, including Pt, Au, Pd, Rh, Ni, Cu and Ag, for avoiding the recombination of charges. For this reason, the use of titanium dioxide with deposited nanoparticles of noble metals has been reported to be very effective for enhancing the hydrogen production reaction [2]. However, the main disadvantage of this type of photocatalyst is its high cost. Iron oxides are another type of effective photocatalysts, which are also abundant and readily available [4, 5, 6].

In the search for new efficient and inexpensive materials, waste and industrial by-products are quite attractive because of its low cost, and within these materials, stands metallurgical copper slag for its abundance and high oxide iron content (> 50 % m / m); this industrial waste is generated in high quantities (2.2-3 ton per ton of copper) by the smelting process of copper ores. Table 1, shows data of the copper slag generation in various regions [7, 8, 9].

TABLE 1. COPPER SLAG GENERATION

Region	Copper slag generation (ton per year × 10^6)
Asia	7.26
North America	5.90
Europe	5.56
South America	4.18
Africa	1.23
Oceania	0.45

On the other hand, several organic compounds have been evaluated as hole scavengers in photocatalytic processes for its degradation with a simultaneous hydrogen production. However, glycerol was used in this work as sacrificial agent due to its high hydrogen production with several photocatalysts [10, 11]. Furthermore, this compound is present in wastes generated in the production process of biodiesel.

I. EXPERIMENTAL

A. *Pretreatment of the photocatalyst*

The copper metallurgical slag was obtained from a metallurgical company of the state of Sonora, Mexico.

This material was ground and sieved using a 400 mesh (particle diameter =37 µm). Afterwards, it was washed with distilled water and dried at 100°C during two hours before use.

B. *Characterization of the photocatalyst*

The major and minor constituents of the metallurgical slag were determined by the X-Ray Fluorescence (XRF) technique using a Siemens SRS 3000 spectrometer. The crystalline phases were identified by X-ray Diffraction (XRD) in a Bruker D8 advance apparatus, equipped with a Cu Kα radiation source. Intensities were obtained in 2θ ranges between 20-70 with a step of 0.017º and a measuring time of 10 s per point.

Specific surface area BET, pore volume and average pore diameter were determined employing the nitrogen physisorption method at the liquid nitrogen temperature with a Belsorp-Mini II. The morphology of the copper slag was observed by Scanning Electron Microscopy on a JEOL JSM-6700F apparatus and the surface composition was analyzed by Energy Dispersive Spectroscopy (EDS). The UV-Vis absorption spectra were obtained with a Varian Cary 500 UV-Vis spectrophotometer coupled with an integration sphere for diffuse reflectance studies. Band gap value was determined using the Tauc plot method.

C. *Photocatalytic experiments: hydrogen production*

The apparatus used for these experiments consists of a borosilicate photoreactor of 600 mL (Parr Instrument 5103) assembled on-line to a hydrogen analysis system. The sacrificial agent was a [0.2 M] glycerol solution and the photocatalyst was copper slag (1 g/L).

The quantification of hydrogen was made using a Shimadzu GC-2014 gas chromatograph equipped with a thermal conductivity detector (TCD) and a MS-5Å packed column. The reactant mixture was stirred in the dark for 30 min for the homogenization of the system and the adsorption of glycerol. At the end of this time, the system was degassed by bubbling nitrogen prior to the photochemical reaction. Finally, the system was irradiated using three UV lamps (Hg low pressure) of 15 W and three halogen lamps (daylight) of 8 W each. The reaction was monitored at different time intervals by collecting liquid or gaseous samples during 4 h.

The Dissolved Organic Carbon content was quantified in a Shimadzu 5000A.

II. RESULTS AND DISCUSSION

A. *Chemical analysis(XRF) of slag*

Table 2 shows the chemical composition of the copper slag sample determined by X-ray fluorescence (XRF) analysis. This material showed high quantities of iron and silicon. Minor elements were reported in parts per million, being copper and zinc the ones of these elements present in higher proportion. These results are similar to data reported in several works [12, 13, 14]. Iron, copper, zinc, nickel, chromium and molybdenum can improve the photocatalytic material properties since these elements can act as antenna agents and prevent the fast recombination of charges (e^-/h^+) in the photocatalysts [15, 16, 17, 18].

TABLE 2. CHEMICAL ANALYSIS OF COPPER SLAG BY X-RAY FLOURESCENCE

Major Constituent	% mass	Minor Constituent	ppm
Fe_2O_3	60.895	Zn	16148
SiO_2	25.7754	Cu	15158
K_2O	1.136	Mo	4909
Al_2O_3	4.1854	Co	328
CaO	0.459	Cr	279
TiO_2	0.312	Zr	110
MgO	0.2662	Rb	64
Na_2O	0.2509	Sr	46
BaO	0.1172	Ni	42.3
MnO	0.047	V	25.2

A. *Crystalline phases of slag: X-Ray Difraction (XRD)*

Fig. 1 shows the crystalline phases identified in the copper slag sample: fayalite (Fe_2SiO_4) [JCPDS 76-0512], magnesioferrite ($MgFe_2O_4$) [JCPDS 36-0398] and maghemite (γ-Fe_2O_3) [JCPDS 80-2186]. These phases have been detected in similar slags [12, 19, 20]. Also, amorphous compounds are present in this waste.

To the best of our knowledge, fayalite and maghemite have not yet been reported as photocatalysts used in the hydrogen production process.

As a contrast, magnesioferrite has already been used for producing this renewable fuel. This mineral has a band gap value of 2.4 eV, and shows a crystalline structure of spinel-type and the unit cell is cubic; for this reason, the main advantage of this material is that the iron and magnesium are oriented in the edges of the crystal allowing for redox reactions, specifically the hydrogen reduction [21].

Minor compounds were not detected in the XRD difractograms due to the detection limit of this technique (2%).

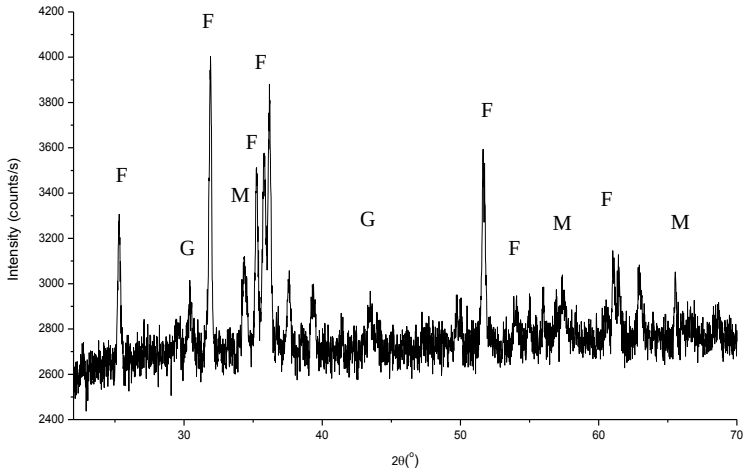

Fig. 1. XRD patterns of copper slag. Fayalite=F, Magnesioferrite=M and Maghemite=G

B. *Morphologie and textural propierties of slag*

Fig. 2 shows the nitrogen physisorption isotherm, which according to the IUPAC classification corresponds to a type II

isotherme without histeresis [22]. This isotherm showed multicaps of nitrogen adsorbed to high relative pressures, in mesoporous formed by interparticle contact.

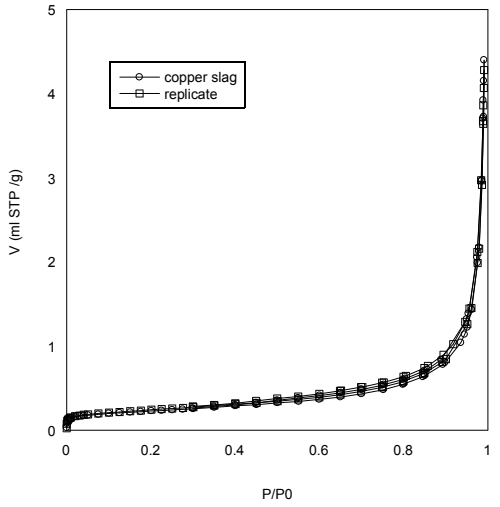

Fig. 2. Isotherm of N_2 by physical adsorption on copper slag.

Table 3 shows the textural properties of copper slag. The specific surface area was calculated using the BET equation; this value was lower than data reported for conventional catalysts (Table 4). This can be due to the low contribution of the slag microporosity. Only mesoporosity contributed to the area of this material, as observe on the plateau (in $0.1<P/P^0<0.8$) of Fig. 2; this was confirmed by the calculated values (Table 4) of pore volume and the average pore diameter (30.713 nm), which corresponds to the IUPAC classification for mesoporous materials.

TABLE 3 .TEXTURAL PROPERTIES OF COPPER SLAG

Parameter	Copper slag
Specific Surface area (m^2/g) (n=2)	0.805 ± 0.046
Volume of pore (cm^3/g) (n=2)	0.006 ± 0.000
Diameter of pore (nm) (n=2)	30.713 ± 1.248

TABLE 4.SPECIFIC SURFACE AREA OF OTHER PHOTOCATALYSTS

Photocatalysts	Specific surface area (m^2/g)	Reference
TiO_2-P25	50	[23]
CdS	46	[24]
$NiCo_2O_4$	25	[25]
GaN/ZnO	56.9	[26]

Fig. 3 Shows the morphology of slag particles was observed by means of the micrographies obtained by Scanning Electron Microscopy (SEM).

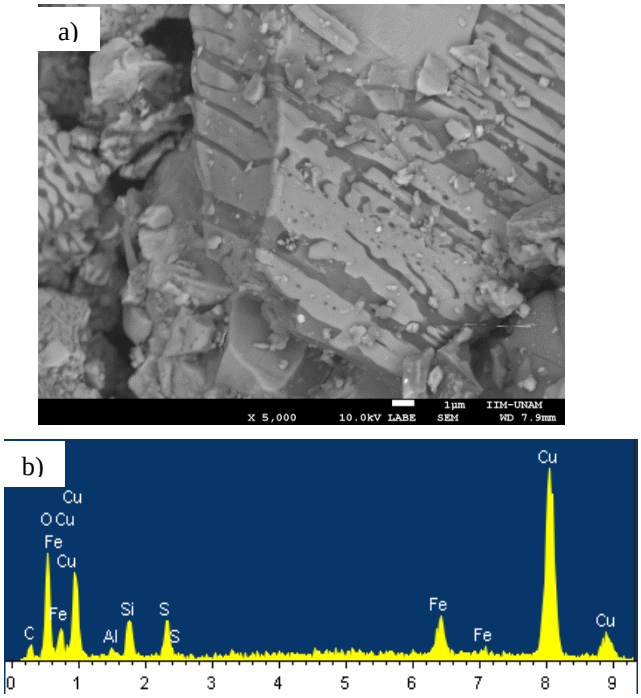

Fig. 3. 3.a) Morphology of a copper slag particle (x 5000) and 3. b) EDS of a copper slag particle.

The micrography 3a) shows copper slag particles having a rough external surface with channels, which were possibly created as a result of the grinding pretreatment.

The EDS analysis (Fig. 3b) shows the presence of copper, iron, silicon and aluminum on the external surface of the copper slag particle. The copper and iron could work as an antenna agent to prevent the recombination of charges during longer periods than those obtained using only titania.

C. Optical propierties (UV-Vis) of slag

Fig. 4 shows the UV-Vis absorption spectrum of the copper slag from 200 to 2500 nm. This material absorbs more energy in the UV region (<400nm) with respect the measured value in the visible region.

The band gap value determined using the Tauc plot method was 2.60 eV; the material could be activated by light with wavelengths up to 377 nm (UVA region).

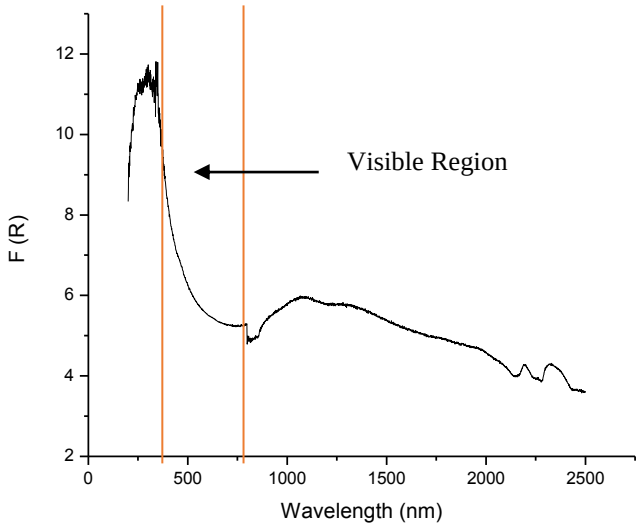

Fig. 4. Absorption spectrum of copper slag in function of Kubelka-Munk

D. *Hydrogen production*

The photocatalytic process using copper slag as catalyst was able to produce hydrogen through the degradation process of glycerol, which was used as sacrificial agent. This reaction was followed for 4 hours as shown in Fig. 5 and 6.

The hydrogen production continued increasing after 4 hours, with a yield of 0.9 µmol H_2/g (photocatalyst) at this reaction time; thus if the reaction undergoes during a longer period, a higher hydrogen production level can be achieved. This could indicate that a more effective irradiation system is necessary for having a faster hydrogen production rate, since the calculated value of this parameter was very low, as described below.

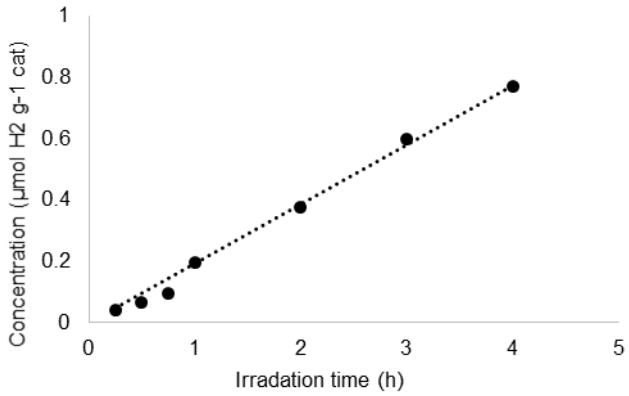

Fig. 5. Hydrogen yield obtained by the photocatalytic degradation of glycerol and employing copper slag as catalyst

During irradiation, the amount of hydrogen increased linearly in the gas phase (Fig. 5) according with a pseudo-zero order rate law, due to the high excess of reactants [27]. Thus, the rate of H_2 production was taken as the slope of the straight line of the produced amount (normalized per unit of catalyst weight) *vs.* irradiation time plot. The rate of the H_2 production reaction was 0.20 µmol H_2/h*g of catalyst.

E. *Degradation of glycerol*

Fig. 6 shows the glycerol degradation behavior during the hydrogen production process, in terms of the residual content of Dissolved Organic Carbon (DOC). The DOC content decreased 5.5% (400 mg/L) in the first 2 hours of the reaction time. At the same time, the pH decreased indicating a probable formation of glycolic acid during this reaction [28]. After this time, the DOC content kept almost constant. However, the pH value began to increase, probably due to the formation of glyceraldehyde, formic acid and formaldehyde, in accordance with Li and Roquet [28, 29].

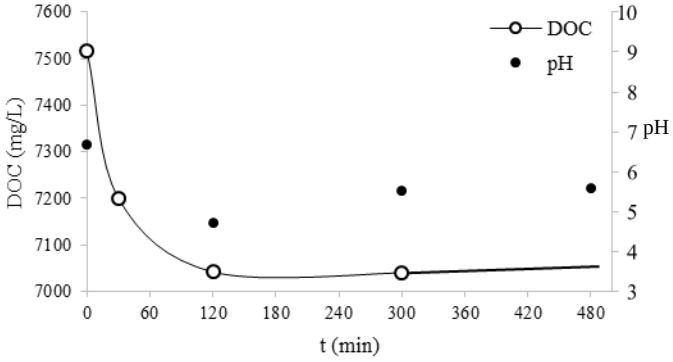

Fig. 6. Residual content of Dissolved Organic Carbon (DOC) and pH value during the degradation process of glycerol for hydrogen production.

III. CONCLUSIONS

The simultaneous hydrogen production and glycerol degradation by a sustainable photocatalytic process using copper metallurgical slag was demonstrated in this work. This waste showed high concentrations of iron and low contents of other elements such as copper, zinc, molybdenum, nickel and chromium, which can favor its use as a suitable semiconductor material in heterogeneous photocatalytic processes. Specifically, magnesioferrite, fayalite and maghemite can be one of the main crystalline phases acting as photocatalysts in the simultaneous reactions of the hydrogen production process and organic compounds degradation.

The hydrogen production data followed a pseudo-zero order rate law due to the high excess of reactants. The constant reaction rate of this reaction was very low (0.2 µmol H_2/h*g), indicating that several operating and design parameters of this process, such as the irradiation source, pH and photoreactor configuration, must be optimized for increasing its feasibility.

On the other hand, besides a hydrogen production, a depletion as a function of time of dissolved organic carbon and pH was observed as a result of the photocatalytic degradation reaction of glycerol, used as sacrificial agent for the hydrogen production, due to the formation of some by-products such as glycolic acid, glyceraldehyde, formic acid and formaldehyde.

ACKNOWLEDGMENTS

Authors are grateful to DGAPA (IT101314) and to Instituto de Ingeniería (*Proyecto de Colaboración Internacional 2013*), *Universidad Nacional Autonóma de México* for the financial support given to this project. C.V.M.B. wishes to thank CONACYT for the doctoral fellowship. Authors also would like to thank Dra. Aída Gutiérrez Alejandre (UNICAT, Facultad de Química) and Dr. Omar Novelo Peralta (*Instituto de Investigaciones en Materiales*) from the *Universidad Nacional Autónoma de México* for the UV-VIS and SEM-EDS analysis respectively.

REFERENCES

[1] Deparment of energy of United States of America. (2014). Hydrogen: hydrogen basics, USA Deparment of energy. Recovered of http://www.afdc.energy.gov/fuels/hydrogen_basics.html.

[2] Ni, M., Leung, M., Leung, D., Sumathy, K. (2007). Renew. Sust. Energ. Rev., 11, 401-425.

[3] Cheng, X-L., Jiang, J-S., Jin, C-Y., Lin, C-C., Zeng, Y., Zhang, Q-H. (2014). Chem. Eng. J., 236, 139-148.

[4] Nezamzadeh-Ejhieh, A. y Ghanbari-Mobarakeh, Z. (2015). J. Ind. Eng. Chem., 21, 668-676.

[5] Feng, X., Guo, H., Patel, K., Zhou, H. y Lou, X. (2014). Chem. Eng. J., 244, 327–334.

[6] Rozendaal, A. y Horn R. (2013). Minerals Engineering, 52, 184–190.

[7] Zazoua, H., Boudjemaa, A., Chebout, R y Bachari, K. (2014). Int. J. Energ. Res., 38, 2010–2018.

[8] Biswas, S., Satapathy, A. (2010) Use of copper slag in glass−epoxy composites for improved wear resistance. Wast. Man. Res. 28: 615−625.

[9] Zhang, J., Qi, Y-H., Yan, D-L., Xu, H-C. (2015). J. Ir. Steel Reser.Int. 22, 5, 396-401

[10] Daskalaski, V. M. and Kondarides, D. I. (2009).Catal. Today, 144, 75-80.

[11] Tasnadi-Asztalos, Z., Paul-Serban, A. and Calin-Cristian, C. (2015) Int. J. Hydrogen Energ., 40, 22, 7017-7027

[12] Chen, X., Shen, S., Guo, L. y Mao, S. S. (2010). Chemical reviews, 101, 11, 6503-6570.

[13] Abe, R. (2010). J. Photoch. Photobio. C, 11, 179–209.

[14] Sugrañez, R., Cruz-Yusta, M., Mármol, I., Morales, J. y Sánchez, L.(2013). Chem. Sus. Chem., 6, 2340-2347.

[15] Gao, B., Liu, L., Liu, J., Yang, F. (2014). *Appl. Catal. B* 147, 929-939.

[16] Gorai, B., Jana, R. K., Premchand, G. (2013). Resour. Conserv. Recy.g, 39, 4, 299-313.

[17] Al-Jabri, K. S., Abdullah, H. A., Taha, R. (2011). Constr. Build. Mater., 25, 2, 933-938.

[18] Zhang, F-S. y Itoh, H. (2006). Chemosphere, 65, 1, 125-131.

[19] Dom, R., Subasri, R., Radha, K. y Borse, P. H (2011). Solid State Commun., 151, 470-473.

[20] Alter, H. (2005). Resour. Conserv. Recy.g, 43, 353–360

[21] Gondal, M. A., Hameed, A., Yamani, Z. H. y Suwaiyan, A. (2004). Appl. Catal. A, 268, 159–167.

[22] Gregg, S.J. and Sing, K. S. W. (1982). Adsorption, surface area and porosity, 2nd Edn, Academic press, London.

[23] Mazloomi, T., H. S., Kazemeini, M., Fattahi, M. (2012). Scientia Iranica, 19, 6, 1626-1631

[24] Sathish, M., Viswanathan, B. and Viswanath, R.P. (2006). Int. J. Hydrogen Energ., 31, 891-898.

[25] Baydi, M.E., Tiwari, S.K., Singht, R. V. et al. (1995). J. Solid State chem., 116, 157-169.

[26] Adeli, B. and Taghipour, F. (2013). ECS J. Solid State Sci. Techn., 2, 7, Q-118 – Q-126

[27] Chiarello, G.L. Aguirre M.H. (2010) E. Selli J. Catal. 273, 182-190

[28] Li, M., Li, Y., Peng, S., Lu, G. y Li, S. (2009). Front. Chem. China, 4, 32-38.

[29] Roquet, L., Belgsir, E. M., Leger, J. M., Lamy, C. (1994). Electrochim. Acta, 39, 2387-2394.

Residential consumption of energy electric in Mazatlan: structure, alternatives and impact

Nildia Y. Mejias-Brizuela, José D. Velazquez-Lira y Pedro Armenta
Energy Engineering Department
Polytechnic University of Sinaloa, UPSIN
Mazatlan, Sinaloa, Mexico
nmejias@upsin.edu.mx.

***Abstract*— The residential sector is a substantial consumer of electric energy a global, national and community level, due the energetic needs and comforts required by people, therefore, exists a growing interest in reducing electric energy consumption and the associated greenhouse gas emissions a this sector of the economy. Comprehensive methodologies are needed to assess the sector structure, impact of adopting energy efficiency and renewable energy technologies suitable for residential applications. The aim of this paper is to provide an approach of the electric energy consumption of Mazatlan town, analyzing the estimated energy consumption of a representative set of individual households through applying the statistical method (survey). Next stage is to implement alternatives relating to the efficient use of electric energy through an education program applied in two communities of different socio-economic levels that combine different methods and sources of information, divulgation of energy renewable sources and its uses, consumption measurements in situ of equipment of high energetic demand (air conditioners, refrigerators), among others, and achieve an instrument that can be replicated in other Mazatlán communities.**

Keywords*— residential consumption, electric energy, energy efficiency, community, household, education.*

I. INTRODUCTION

Growth in population, increasing demand for housing building services and comfort, together with the in time inside households, assure that the upward trend in energy demand will continue in the future [1].

The electric energy consumption in residential sector has steadily increased reaching values of 27% to global level and 26% to national level, according to data reported in 2013 by the *Energy Secretariat Mexico* [2,3] therefore, this sector represents a key in the energy context global, national and municipality, given the importance their needs. The high energy consumption is due in many cases to the use of inefficient equipment or energetic mismanagement thereof.

Mazatlan is a municipality located in Sinaloa state, is the eighth largest city in the Mexico northwestern region, with more than 100,000 inhabitants [4]. The climate regime of Mazatlan city is warm sub wet, the temperature fluctuates between 10 to 35º C (60-90º F) during year and in summer months the wind chill is amply marked, for to factor relative humidity [5].

Due to climate, the households has a high electrical energy consumption, associated the use of air conditioning systems, refrigeration and other factors such as continuous use of electrical and electronic equipment of high energy demand and lighting that permit the family comfort.

For this reasons, residential energy efficiency is today a prime objective for energy policy at international levels [6], but not national and regional levels, due to that exist very few laws regarding the topic, no exist information programs and diffusion, programs educational, basic information on the electrics tariffs and therefore the population of low economic resources does not know the topic of efficiency and energy saving.

The aim of this paper is the analysis estimated of the electric energy consumption of a representative set of households Mazatlan city to implement a community energy efficiency program.

II. METHODOLOGY

The consumption of electric energy is determined through a survey realized in the Mazatlan residential area, therefore, was determinated the sample size with a confidence level of 95% [7]. The survey was realized in two residential communities and was focused in to several parameters related to the electric energy consumption and pattern of electricity saving in housing. We also question to the people about knowledge of renewable energy sources and the willingness to invest in these.

Second stage is to design alternatives for an education program based on divulgation of issues regarding: basic information about the rates of final consumption established by the Electricity Regulatory Commission, basic information on renewable energy sources feasible for the residential sector, specifically, systems solar photovoltaic and thermal systems for heating water (because Mazatlan has a high daily solar irradiance), information on economic benefit obtained to use these technologies, benefits to the environment and finally, development and implementation of a guide to saving electricity in the home.

Subsequently, a new survey will be applied to households to assess the impact of the implemented alternatives. We are currently at the stage of divulgation of information.

III. RESULTS

The housing main electricity consumption is the refrigeration and ventilation; therefore, we determinated uses and consumption of ventilation systems, assuming that the refrigeration for food preservation is in constant use. Fig. 1 shows the results: 60% has air conditioning (AC), as main ventilation system, 22% utilize fan, 3% do not use electricity in your ventilation system since it uses natural ventilation (NV) throughout the year and the remaining percentage is distributed in combinations (air conditioning-fan, air conditioning-fan-natural ventilation, fan-natural ventilation). The air conditioning use is in various year stations (spring, summer, autumn) approximately for 6 to 12 hours per day.

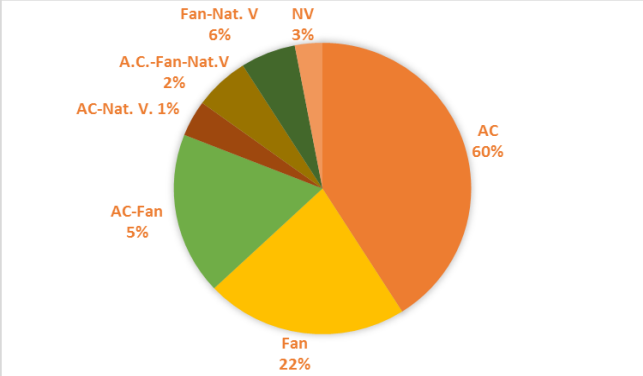

Fig. 1. Ventilation systems used in households surveyed

Other measured parameter is the type of lighting used in households, the responses were varied, because 69% of the sample use compact fluorescent luminaire, 17% incandescent lamps and 14% combines the previous two sources of lighting.

A relevant fact was that 94% of the sample unknown the energy consumption rates adjusted by the Electricity Regulatory Commission in Mazatlan, therefore also unknown the cost per watt/h consumed, this shows energetic culture low that exists in the population.

Similarly, 60% consider that their electric consumption, will increase the next two to three years due to the growth of the family or new electronic equipment acquired.

The knowledge that the population have of renewable energy sources, results shows that 60% surveyed people know at least one, through the television. Wind is the main source known.

The 60% surveyed people would like to implement renewable energy with government support, 20 % would do so with own investment and 10% do not would like. Fig. 2 shows graphic results obtained.

We recently started the educational program based on divulgation of energy efficiency issues, basic information on renewable energy sources feasible for the residential sector, and consumption measurements in situ of equipment of high energetic demand. The pilots communities have accepted voluntarily participate in the program. Subsequently, a new survey will be applied to households to assess the impact of the implemented alternatives.

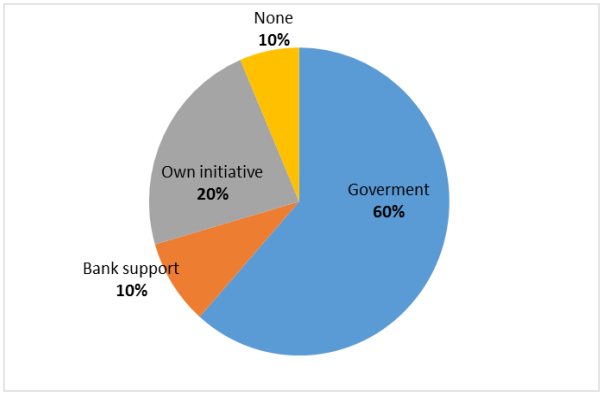

Fig. 2. Support energy transition.

IV. CONCLUSION

Results show that in residential sector of Mazatlan city there is low social consciousness respect to the efficient use and saving electricity. The cause can be by to ignore the real cost energy produced and consumed, because the information we have about this topic becomes scarce, and in some cases erroneous; therefore providing information to population, can to mitigate the effects of overconsumption.

We designed a strategy based information on efficient use of energy residential sector and we work in two pilots communities. A good form of disseminating information has been talks and workshops in communities, printed information and social networks.

REFERENCES

[1] L. G. Swan, V. I. Ugursal, “Modeling of end-use nenergy consumption in the residential sector: a review of modeling techniques”, Renewable and Sustainable Energy Reviews, vol. 13(8), pp. 1819-1835, January 2009.

[2] L. Beltrán, R. Rionda, J. Herrera, O. Ojeda, “Balance Nacional de Energia 2013”, 1st ed., Secretaria de Energía Mexico, 2014, pp. 34,35,37.

[3] R. Rionda, L. Guerrero, F. Rodriguez, A. Ubaldo, A. Ramos y F. Rueda, “Prospectiva del sector electrico 2014-2028”, Secretaria de Energía Mexico, 2014, pp. 36,37,50.

[4] Instituto Nacional de Estadistica y Geografia, INEGI, “Censo de población yvivienda 2010, Principales resultados por localidad (ITER), 2010. [online]. Available from: www.inei.org.mx. (Accessed: 01 june 2015)

[5] Ayuntamiento de Mazatlan, “Clima”, 2008. [online]. Available from: www.maztlan.gob.mx. (Accessed: 01 june 2015)

[6] L. Perez-Lombard, J. Ortiz, C. Pout, “A review on building energy consumption information”, Energy and Buildings, vol. 40 (3), pp. 394-398, March 2008.

[7] R. Walpole, R. Myers, S. Myers, K. Ye, “Probabilidad y estadistica para ingenieria y ciencias”, 8 ed., McGrawHill, 2007, pp 205-207.

Síntesis y optimización de un sistema de tratamiento selectivo de corrientes efluentes usando tres reactores electroquímicos continuos

Adrián López-Yáñez [a,*], Jorge Ramírez-Muñoz [a]
[a] Departamento de Energía, Universidad Autónoma Metropolitana – Azcapotzalco,
Av. San Pablo No. 180, Col. Reynosa Tamaulipas,
C.P. 02200, Delegación Azcapotzalco México, D. F.
[*]mixtili_5050@hotmail.com.

Juan Manuel Zamora-Mata [b],
[b] Departamento de Ingeniería de Procesos e Hidráulica, Universidad Autónoma Metropolitana – Iztapalapa,
Av. San Rafael Atlixco No. 186, Col. Vicentina,
C.P. 09340, México, D.F.

Resumen—En este trabajo se investigó el problema de síntesis y optimización de sistemas de tratamiento selectivo de corrientes efluentes de aguas residuales contaminadas con cromo hexavalente. Se propone un modelo de programación no lineal para la remoción electroquímica de cromo hexavalente (RECrVI). Con este propósito se planteó una configuración de superestructura básica de tratamiento de efluentes, la cual está compuesta por tres unidades de tratamiento sin recirculación UT_k, $k \in K = \{1, 2, 3\}$, la cual representa tres reactores electroquímicos continuos y pueden producir arreglos serie-paralelo. La función objetivo del modelo de RECrVI incluye las variables de flujo, consumo eléctrico y el volumen de la unidad de tratamiento. El desarrollo del modelo de programación no lineal (PNL) integra la función objetivo lo cual permite la síntesis de la estructura y el cálculo de sus propiedades al menor costo total anualizado (CTA). El modelo no lineal desarrollado puede ser utilizado para obtener un diseño de red de remoción óptima. La versatilidad y uso del modelo propuesto se muestran con la solución de dos ejemplos ilustrativos.

I. INTRODUCCIÓN

El agua por sus propiedades fisicoquímicas es uno de los insumos más usados por las industrias en sus procesos productivos, por lo cual la contaminación descontrolada de grandes volúmenes de agua ha provocado escases del vital líquido y por ende, los diferentes sectores, el social, el económico y el ambiental han sido seriamente afectados. Debido a esto, la optimización de redes de tratamiento de agua residual se ha convertido en un tema de extrema importancia en la actualidad. En la Figura 1 se presenta la configuración de un proceso productivo dentro de una industria, donde el agua que ingresa a la planta (in), es distribuida en cada uno de los procesos de producción (P_1, P_2, P_3), posteriormente las corrientes de agua que derivan de cada proceso son enviadas a la zona de tratamiento (UT_1, UT_2, UT_3), y una vez que los contaminantes han sido parcialmente removidos, el agua tratada pasa al punto de descarga (e) para finalmente ser enviada a un sumidero (S).

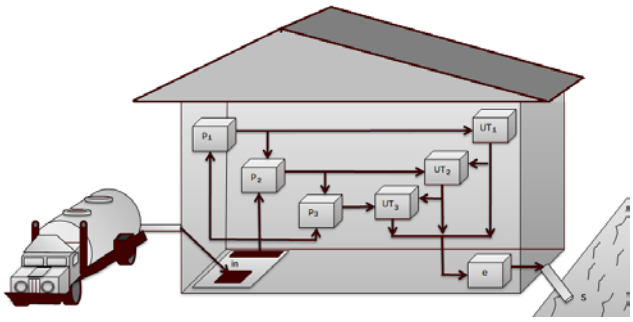

Figura 1. Representación de una industria usuaria de agua.

Las industrias dedicadas al recubrimiento de superficies metálicas, mineras y curtidoras de pieles, entre otras, disponen comúnmente en el agua de proceso una concentración de cromo hexavalente (Cr(VI)) altamente reactivo, lo cual se deriva de los diferentes procesos productivos, algunos de los cuales se presentan en la Tabla 1. Este contaminante tiene propiedades cancerígenas y debe ser removido de acuerdo a las especificaciones contenidas en la norma vigente para la descarga de residuos tóxicos en los cuerpos receptores. Esta situación crea la necesidad de retirar dicho contaminante del agua residual antes de ser descargado a la red pública de drenaje.

Tabla 1. Contenido de (CrVI) en aguas residuales [1].

Industria	Concentración de Cr(VI) (mg/L)
Fábrica de ferretería	60.0
Planta de curtido al cromo	3.7
Planta de galvanoplastia	1.0
Planta de electropulido	42.8
Planta de curtido	3,950.0
Planta de curtido	100.0
Planta de curtido	1,770.0
Planta de galvanoplastia	20.7
Planta de galvanoplastia	75.4
Planta de curtido	8.3

El cromo hexavalente puede ser reducido a cromo trivalente (Cr(III)) por medio de un tratamiento electroquímico, el cual es un ión mucho menos tóxico, y éste último puede ser removido posteriormente del agua por medio de un proceso de precipitación. La reacción general para la reducción del Cr(VI) que tiene lugar en el seno de la disolución [2], se puede representar por medio de la Ecuación (1):

$$7H^{+} + 3Fe^{2+}_{(ac)} + HCrO^{-}_{4(ac)} \longrightarrow 3Fe^{3+}_{(ac)} + Cr^{3+}_{(ac)} + 4H_2O_{(l)} \quad (1)$$

También existe una reacción de oxidación en el ánodo del sistema electrolítico como se muestra en la Ecuación (2). Esto sugiere que también es posible que el Cr(VI) se esté reduciendo en la interface electrodo-electrolito a partir de la liberación de iones hierro $\left(Fe^{2+}_{(aq)}\right)$:

$$Fe_{(S)} \longrightarrow Fe^{2+}_{(aq)} + 2e^{-} \quad (2)$$

Rodríguez y col. [3] estudiaron un sistema electroquímico de reactores continuos conectados en serie para la remoción de cromo y propusieron el siguiente modelo para el proceso de reducción de Cr(VI):

$$\frac{d}{dt}Cr(VI)_k = \frac{t_k}{V}Cr(VI)_{k-1} - \frac{t_k}{V}Cr(VI)_k - \frac{K_1 Cr(VI)_k}{1+K_2 Cr(VI)_k} \qquad k \in K \quad (3)$$

Por otro lado, en la literatura existen un gran número de estudios enfocados al diseño de redes de aguas residuales algunos de los cuales se mencionan a continuación. Wang y Smith [4], Galán y Grossmann [5], Grossmann y col. [6], Zamora y col. [7], Alva y col. [8], Cheng y Jui [9], Faria y Bagajewicz [10] y Jiménez y col. [11] plantearon estrategias de optimización para dar un tratamiento selectivo a corrientes de procesos con un enfoque basado en superestructuras.

Hernández [12] desarrolló un modelo de PNL a partir de una superestructura básica la cual representa el espacio de solución para el problema de diseño que abordó (Figura 2). En el presente trabajo se plantea una alternativa para el tratamiento de los flujos efluentes mediante un modelo PNL, el cual se compone de parámetros (P), función objetivo (FO) y un conjunto de restricciones (D).

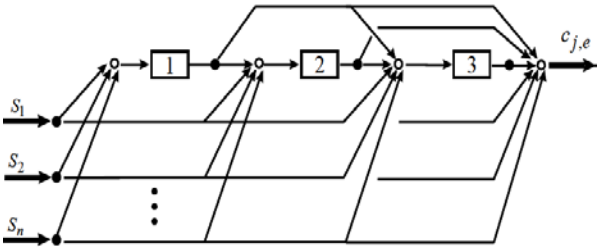

Figura 2. Superestructura básica que involucra tres unidades de tratamiento.

El diseño del sistema de tratamiento se obtuvo a partir del análisis de las soluciones óptimas locales del modelo de PNL, minimizando el CTA y obteniendo valores para las variables de diseño, que incluyen, entre otras, los flujos de efluentes a tratamiento t_k, los volúmenes de los reactores V_k, y las densidades de corriente eléctrica utilizadas I_k. Las restricciones del modelo incluyen ecuaciones que describen el tratamiento electroquímico con una tasa de remoción variable R_j^k y una cota superior a la concentración de Cr(VI) en la descarga de efluentes.

II. METODOLOGÍA

A continuación se explica el modelo de programación matemática desarrollado a partir de una superestructura básica para la optimización de sistemas selectivos de corrientes efluentes, la cual está constituida de corrientes a la entrada del sistema, divisores, mezcladores, unidades de tratamiento e interconexiones. Por otro lado, no se incluyen recirculaciones, como se muestra en la Figura 3. La superestructura básica presentada permite incluir todos los diseños posibles de tratamiento y eliminar características indeseables para la solución del modelo de PNL, además de suministrar la nomenclatura necesaria.

Los parámetros del modelo de PNL se definen en la superestructura básica de la Figura 3, donde S_i representa las corrientes efluentes *i* a la llegada de la red y $C_{i,j}$ es la concentración de contaminante *j* en la corriente *i*. La norma ambiental establece una cota superior $c^U_{j,e}$=0.5 mg/L para el cromo hexavalente [13].

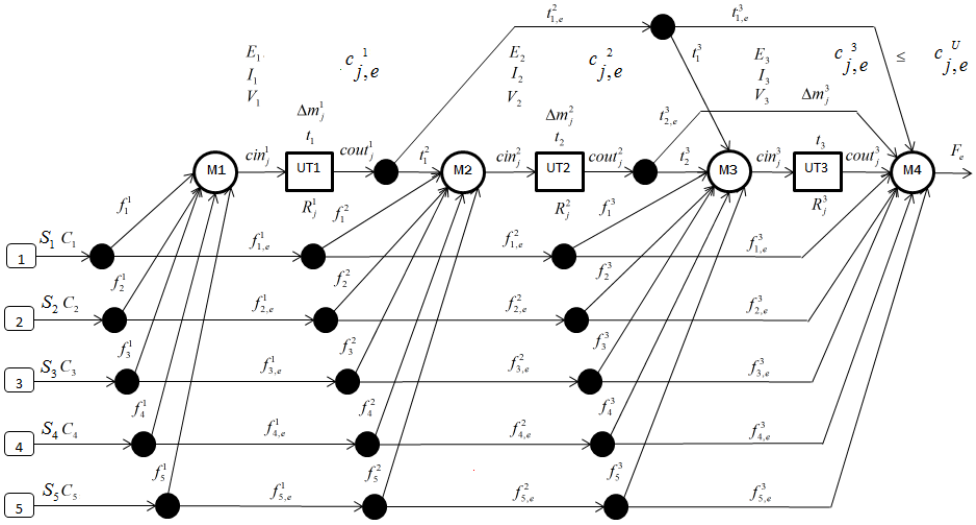

Figura 3. Superestructura básica para la remoción de CrVI.

La determinación de la mejor estructura de remoción se basa en un criterio de tipo económico mediante una función objetivo que minimiza el CTA en donde las variables t_k, I_k y V_k se relacionan directamente con los costos de capital y de operación del sistema de tratamiento. En las restricciones del modelo de RECrVI se incorpora una tecnología de tratamiento electroquímico reportada en la literatura con una cinética de remoción de contaminante de orden variable [3]. También se incluyen balances de materia para cada divisor de la superestructura, balances de materia en los mezcladores, balances de contaminante en cada UT$_k$, y el cálculo de la carga másica de contaminante Δm_j^k a remover en cada unidad de tratamiento. El modelo de RECrVI se implementó y resolvió en el sistema GAMS [14].

La función objetivo para el modelo de PNL considera los flujos que pasan a través de las unidades de tratamiento, la energía eléctrica consumida en el proceso electroquímico y el costo de capital de cada reactor. Para realizar dicha tarea se han obtenido de la literatura las expresiones matemáticas necesarias para calcular el costo de un reactor en función de su volumen, y el costo de la energía eléctrica consumida durante el proceso electroquímico en función de la densidad de corriente eléctrica, de tal manera que dichas variables puedan ser integradas en la función objetivo para su posterior optimización.

A. Costos de capital asociados al volumen del reactor electroquímico.

Los costos de los reactores utilizados en cada una de las unidades de tratamiento pueden ser calculados usando la Ecuación (4) [15].

$$C_e^k = \mathrm{a} + bV_k^n \qquad (4)$$

Dónde:

C_e^k = Costo del equipo en acero al carbón en dólares (US $).
$a,\ b$ = Coeficientes de costo.
V_k = Volumen del equipo (m^3).
n = Exponente del costo del equipo.

En la Tabla 2 se reportan las constantes que se usan en la Ecuación (4) para la estimación del costo del reactor.

Tabla 2. Constantes para estimar el costo de un reactor, [15].

Equipo: Reactor Enchaquetado con agitación					
Unidades	Tamaño		a	b	n
	Mínimo	Máximo			
Volumen (m3)	0.5	100	14000	15400	0.7

El factor de material (fm) es la relación entre el costo del equipo en la aleación de construcción y el costo del equipo construido en acero al carbón de acuerdo a la Ecuación (5):

$$fm = \frac{C_a^k}{C_e^k} \qquad (5)$$

Reacomodando la Ecuación (5) y dividiendo entre los periodos de amortización T, se obtiene la Ecuación (6):

$$C_a^k = \frac{fmC_e^k}{T} \qquad (6)$$

Dónde:

C_a^k = Costo del equipo en acero inoxidable 304, en dólares estadounidenses por año (US $/año).
fm = 1.30 (para el equipo en acero inoxidable 304).
T = 20 años (amortización del equipo).

Al sustituir la Ecuación (4) en la Ecuación (6) se obtiene una nueva expresión para el costo de capital anualizado de un reactor electroquímico en función del volumen V_k. El volumen V_k de la Ecuación (7) debe estar en unidades de metros cúbicos (m^3) de acuerdo a la Tabla 2. Considerando que en el sistema de tratamiento presentado por Rodríguez y col. [3], las unidades para el volumen de los reactores electroquímicos se utiliza en litros (L), por lo que se realizó una conversión de unidades de (L) a (m^3). i.e.

$$C_a^k = \left(\frac{fm}{T}\right)\left[a + b\left(\frac{V_k}{1000}\right)^n\right] \qquad (7)$$

B. Costos de operación asociados a la densidad de corriente eléctrica.

En la Figura 4 se muestran datos experimentales reportados por Barrera y col. [2], Rodríguez y col. [3] y Zongo y col. [17]. Como puede verse, la corriente eléctrica (i) tiene un comportamiento lineal con respecto al potencial aplicado (E), y con estos datos se obtuvo una relación para la densidad de corriente eléctrica I en función de E.

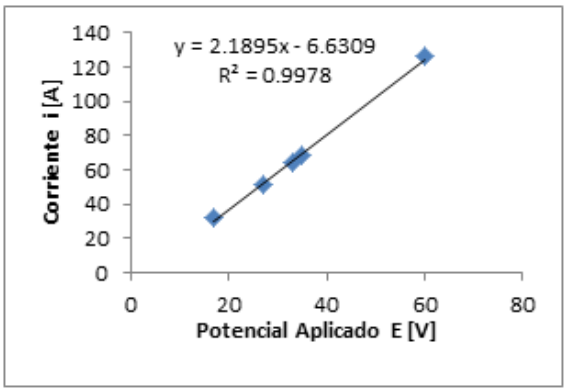

Figura 4. Corriente eléctrica i (A) en función del potencial E (V) aplicado al proceso electroquímico.

Con la función lineal ajustada a los datos de la Figura 4, se obtuvo una relación para el potencial aplicado al proceso electroquímico como se muestra en la Ecuación (8) para cada uno de los reactores:

$$ArI_k = 2.1895E_k - 6.6309 \quad k \in K = \{1,2,3\} \qquad (8)$$

El coeficiente Ar es el área anódica y al ser multiplicada por la densidad de corriente eléctrica (I_k) se obtiene la corriente eléctrica i_k. El consumo de energía fue calculado con la Ecuación (9) obtenida por Chen y col. [17], la cual determina el costo en dólares por año (US $/año) del consumo de energía eléctrica para cada uno de los reactores electroquímicos considerados:

$$CU_k = 0.31536E_kI_k \qquad k \in K = \{1,2,3\} \qquad (9)$$

Las unidades de CU_k están en US $/año. El costo de 1 kWh que se considera es 0.1 US $ [2].

C. Costos de operación asociados al flujo de efluentes en la unidad de tratamiento

Los flujos volumétricos que pasan a través de cada uno de los reactores electroquímicos tienen unidades de litros por minuto (L/min), por lo que en la Tabla 3 se presenta un coeficiente de costo por unidad de volumen tratado (US $/$m^3$). Lo anterior sugiere que los flujos sean transformados a metros cúbicos por año (m^3/año) y de esa manera se tendrán unidades de dólares por año (US $/año), [2].

Tabla 3. Costo del tratamiento electroquímico de 1 m^3 de agua residual contaminada con una concentración inicial de Cr (VI) $_{t=0}$=500 mg/L, [2].

Concepto	Costo (US $/$m^3$)
	Electroquimico (modo continuo)
pH inicial (pH 2)	0.15
Energía requerida para el bombeo de la solución a través del reactor	0.05
Energía de agitación	0.02
Base administrada para el pH	0.3
Polimero adicionado	0.04
Descarga de lodos	0.05
Transporte de lodos	0.44
Vertedero de lodos	0.70
Total	1.75

El coeficiente de costo unitario de tratamiento utilizado, es de 1.75 US $/$m^3$ y es incorporado en la Ecuación (10), la cual estima el costo de tratamiento en términos del flujo volumétrico.

$$Ct_k = \frac{919.8}{cref}t_k cin_k \qquad k \in K = \{1,2,3\} \qquad (10)$$

Las ecuaciones (7), (9) y (10) calculan el costo de capital del volumen del reactor V_k, el costo del consumo

eléctrico I_k y el costo del tratamiento del flujo en los reactores t_k, respectivamente. La función objetivo está en el sentido de minimización dado que es una función de costos y se organiza colocando primero los costos de capital y después los costos de operación como se muestra de manera sintética en la Ecuación (11):

$$\text{Minimizar } f(X) = \textit{Costos de Capital} + \textit{Costos de Operación} \quad (11)$$

$$\text{Minimizar } f(X) = \sum_{k \in K} \left(C_a^k + CU_k + Ct_k \right) \quad (12)$$

Siendo $X = V_k,\ t_k,\ I_k, E_k, cin_k, E_k \qquad k \in K = \{1,2,3\}$.

D-H. Modelo de Optimización RECrVI

Notación

UT_k =Unidad de tratamiento. $k \in K = \{1,2,3\}$.
M_1= Mezclador 1.
M_2= Mezclador 2.
M_3= Mezclador 3.
M_4= Mezclador 4.

Índices

i=Corriente efluente.
j=Contaminante en una corriente.
k=Unidad de tratamiento.
e=Punto de descarga.
l=Corrientes que pasan de una unidad de tratamiento a otra.

Conjuntos

$I = \{i : i \text{ es una corriente efluente}\}$
$J = \{j : j \text{ es un contaminante}\}$
$K = \{k : k \text{ es una unidad de tratamiento}\}$

E. Parámetros:

S_i = flujo de corriente efluente (L/min).
$C_{i,j}$ = concentración de contaminante en una corriente efluente (mg/L).
$c^U_{j,e}$ = concentración máxima de contaminante permitida en el punto de descarga (mg/L).
cin^L_j = cota inferior de contaminante a la entrada en cada UT_k (mg/L).
I^L = densidad de corriente mínima 0 A/m^2.
I^U = densidad de corriente máxima 500 A/m^2.
V^L = volumen de reacción mínimo 500 L.
V^U = volumen de reacción máximo 800 L.
Especificaciones para la obtención del costo de la UT_k:
$a = 1400,\ b = 15400,\ n = 0.7,\ fm = 1.3$
$T = 20$ años: Periodo de amortización para cada UT_k.

Especificaciones para la relación densidad de corriente eléctrica y potencial eléctrico de la UT_k:

$$Ar = 0.36,\ p = 2.1895,\ q = 6.6309 \quad (P1)$$

Δm^U_j = cota superior para la masa a removeren la UT_k :

$$\Delta m^U_j = \sum_{i \in I} S_i C_{i,j} \quad j \in J \quad (P2)$$

$use = 0.7$: Factor de uso anual del consumo eléctrico de la UT_k.

$cref$ = concentración de referencia para el factor de costo volumétrico 500 mg/L.

F_e = flujo total de efluentes en el punto de descarga (L/min):

$$F_e = \sum_{i \in I} S_i \quad (P3)$$

F. Variables continuas positivas:

f^k_i = flujo al mezclador que precede una unidad de tratamiento (L/min).
$f^k_{i,e}$ = flujo desviado al punto de descarga (L/min).
t_k = flujo a través de cada UT_k (L/min).
t^k_l = flujo entre unidades de tratamiento (L/min).
$t^k_{l,e}$ = flujo de la unidad de tratamiento al punto de descarga (L/min).
cin^k_j = concentración de contaminante a la entrada de una unidad de tratamiento (mg/L).
Δm^k_j = carga másica de contaminante a remover en una unidad d
$c^k_{j,e}$ = concentración alcanzada en cada sección de tratamiento
R^k_j = tasa de remoción de contaminante.
I_k = densidad de corriente eléctrica en una unidad de tratamiento (A/m^2).
E_k = Potencial eléctrico en una unidad de tratamiento (A/m^2).
V_k = Volumen de reacción de una unidad de tratamiento (L).

$cout_j^k$ = concentración de contaminante a la salida de una unidad de tratamiento (mg/L).	

G. Función objetivo:

$$\text{Minimizar} \quad f(X) = \frac{919.8}{cref}\sum_{k\in K} t_k cin_k + \left(\frac{fm}{T}\right)\sum_{k\in K}\left[a + b\left(\frac{V_k}{1000}\right)^n\right] + 0.31536 use \sum_{k\in K} E_k I_k \qquad \text{(M1)}$$

H. Restricciones del diseño:

Balances de agua en los divisores iniciales de la red:

$$S_i = f_i^1 + f_{i,e}^1 \qquad i \in I \qquad \text{(M2)}$$

Balance de agua en los divisores posteriores a la UT_k:

$$t_{l,e}^k = t_l^{k+1} + t_{l,e}^{k+1} \qquad k \in K; l \in K; l < k \qquad \text{(M3)}$$

$$t_l = t_l^k + t_{l,e}^k \qquad k \in K; l < k \qquad \text{(M4)}$$

$$f_{i,e}^k = f_i^{k+1} + f_{i,e}^{k+1} \qquad i \in I; k \in K \qquad \text{(M5)}$$

Balance de agua en los mezcladores M_k que preceden a cada UT_k:

$$\sum_{i\in I} f_i^k + \sum_{\substack{l\in K \\ l<k}} t_l^k = t_k \qquad k \in K \qquad \text{(M6)}$$

Balance de agua en un punto hipotético posterior a cada UT_k:

$$\sum_{i\in I} f_{i,e}^k + \sum_{\substack{l\in K \\ l<k}} t_{l,e}^k + t_k = F_k \qquad k \in K \qquad \text{(M7)}$$

Balance de contaminante en cada UT_k:

$$F_k c_{j,e}^{kU} = \sum_{i\in I} f_{i,e}^k C_{i,j} + \sum_{\substack{l\in K \\ l<k}} t_{l,e}^k cout_j^l + \left(1 - R_j^k\right)\left(\sum_{i\in I} f_i^k C_{i,j} + \sum_{\substack{l\in K \\ l<k}} t_l^k cout_j^l\right)$$

$$j \in J; k \in K \qquad \text{(M8)}$$

Carga másica de contaminante a remover en las UT_k:

$$\Delta m_j^k = R_j^k t_k cin_j^k (0.001) \qquad j \in J; k \in K \qquad \text{(M9)}$$

Concentración de contaminante en un punto hipotético posterior a la UT_k:

$$F_k c_{j,e}^k = t_k cout_j^k + \sum_{i\in I} f_{i,e}^k C_{i,j} + \sum_{\substack{l\in K \\ l<k}} t_{l,e}^k cout_j^l$$

$$j \in J; k \in K \qquad \text{(M10)}$$

Concentración de contaminante j en la entrada de cada UT_k:

$$t_k cin_j^k = \sum_{i\in I} f_i^k C_{i,j} + \sum_{\substack{l\in K \\ l<k}} + t_l^k cout_j^l$$

$$j \in J; k \in K \qquad \text{(M11)}$$

Concentración de contaminante j en la salida de cada UT_k:

$$t_k cout_j^k = \left(1 - R_j^k\right)\left(\sum_{i\in I} f_i^k C_{i,j} + \sum_{\substack{l\in K \\ l<k}} t_l^k cout_j^l\right)$$

$$j \in J;\ k \in K \qquad \text{(M12)}$$

Relación variable de remoción de contaminante en cada UT_k.

$$R_j^k = \frac{cin_j^k - cout_j^k}{cin_j^k} \qquad j \in J; k \in K \qquad \text{(M13)}$$

Balance de masa en estado estacionario en cada UT_k.

$$0 = \frac{t_k}{V_k}\left(cin_j^k - cout_j^k\right) - \frac{0.7486 e^{0.001 I_k} cout_j^k}{1 + 0.1772 e^{-0.003 I_k} cout_j^k}$$

$$j \in J; k \in K \qquad \text{(M14)}$$

Relación del potencial eléctrico con la densidad de corriente eléctrica.

$$ArI_k = pE_k - q \qquad k \in K \qquad \text{(M15)}$$

Algunas cotas razonables para las variables del modelo RECrVI.

$$f_i^k,\ f_{i,e}^k,\ t_k,\ t_l^k,\ t_{l,e}^k \ \le\ F_e$$

$$l < k,\ j \in J,\ k \in K \qquad \text{(M16)}$$

$$cin_j^k \le c_{j,e}^U \qquad j \in J,\ k \in K \qquad \text{(M17)}$$

$$\Delta m_j^k \le \Delta m_j^U \qquad j \in J,\ k \in K \qquad \text{(M18)}$$

$$I^L \le I_k \le I^U \qquad k \in K \qquad \text{(M19)}$$

$$V^L \le V_k \le V^U \qquad k \in K \qquad \text{(M20)}$$

$$0 \le R_j^k \le 1 \qquad j \in J,\ k \in K \qquad \text{(M21)}$$

III. RESULTADOS

A continuación se presentan los resultados obtenidos para los dos casos de estudio abordados en este trabajo. Los datos de entrada para el proceso de tratamiento de aguas residuales del Ejemplo 1 se resumen en la Tabla 4 y los datos de entrada para el proceso de tratamiento de aguas residuales del Ejemplo 2 se resumen en la Tabla 5, con una cota superior de: $c^{U}_{j,e} = 0.5$ mg/L para el cromo hexavalente en ambos casos [14].

Tabla 4. Datos de las corrientes efluentes del Ejemplo 1.

I	S_i (L/min)	$C_{i,j}$ (mg/L)	$m_{i,j}=S_{i,j}C_{i,j}x10^{-3}$ *(g/min)*
1	10	500	5
2	8	350	2.8
3	6	200	1.2
4	4.5	170	0.765
5	3	100	0.3
		$m_j = \Sigma m_{i,j}$	10.065

Tabla 5. Datos de las corrientes efluentes del Ejemplo 2.

I	S_i (L/min)	$C_{i,j}$ (mg/L)	$m_{i,j}=S_{i,j}C_{i,j}x10^{-3}$ *(g/min)*
1	3	500	1.5
2	8	350	2.8
3	6	200	1.2
4	4.5	170	0.765
5	10	0.45	4.5
		$m_j = \Sigma m_{i,j}$	10.765

A. Ejemplo 1:

El diseño óptimo de red de tratamiento particular presentado en la Figura 5 se obtuvo a partir del modelo RECrVI para el Ejemplo 1 (Tabla 4). En la Tabla 6 se resumen los valores de cada una de las variables de diseño presentado en la Figura 5. Se puede observar un tratamiento centralizado en UT_1, pero la mitad de la corriente t_1 es tratada en UT_2 y el restante es tratado en UT_3. Finalmente la corriente t_2 cumple con la norma ambiental por lo que no requiere ser tratada en UT_3 y es enviada al punto de descarga. La configuración presentada satisface las especificaciones para la descarga de efluentes, como se puede ver, la concentración obtenida en M_2 es 0.5 mg/L y la norma indica una cota superior de 0.5 mg/L. Una remoción precisa de Cr(VI) indica un menor costo de tratamiento, por lo que el CTA para este sistema de tratamiento es tan solo de 32697.4 US $/año.

Tabla 6. Resultados del modelo de programación RECrVI.

k	1	2	3
t_k	31.5	15.8	15.8
cin_i^k	319.5	19.03	19.03
$cout_j^k$	19.03	0.5	0.5
$_i^k$	9.47	0.29	0.29
c_{je}^k	19.03	9.767	0.5
R_i^k	0.94	0.974	0.974
I_k	446.8	48.373	48.373
V_k	800	800	800
E_k	76.5	10.982	10.98
CTA (US $/año) =	32697.4		

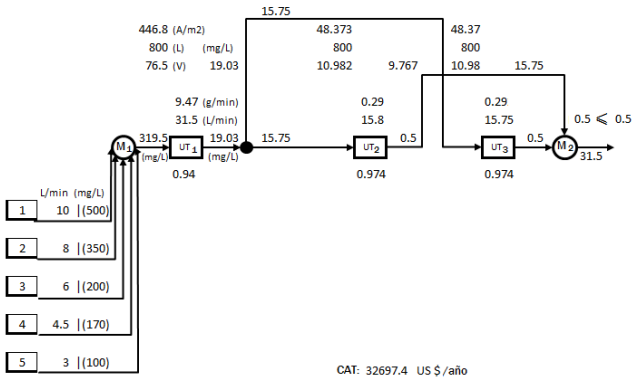

Figura 5. Diseño estructural óptimo local ejemplo 1 obtenido con la solución del modelo de RECrVI.

El diseño de red en la Figura 5 es muy probable que sea una solución óptima local debido a los términos bilineales presentes en los balances de efluente del modelo de RECrVI, donde la naturaleza no convexa del modelo sugiere la necesidad de investigar el conjunto solución. Para dicho propósito se proponen diferentes puntos de arranque para las variables del modelo de programación, en donde se realizó una corrida de 5000 iteraciones para los puntos de arranque de las variables del modelo RECrVI. En la Tabla 7 se presentan los resultados obtenidos de la experimentación y se observan seis soluciones óptimas locales.

Tabla 7. Soluciones óptimas locales del modelo RECrVI donde se muestra el CTA mínimo.

Óptimo Local	CTA US $/año
1	28464.97
2	31535.9
3	32697.4
4	40540.5
5	41771.4
6	41425.5

De esta manera, fue posible mejorar la solución óptima local de la Figura 5 a partir de la exploración del conjunto solución del modelo RECrVI. En la Tabla 8 se presentan los resultados de las propiedades de flujo, concentración y variables económicas t_k, I_k, V_k de la red de tratamiento particular. En la Figura 6 se presenta el diseño de red óptimo para la remoción de Cr(VI), donde se puede apreciar un tratamiento selectivo de las corrientes efluentes en UT_1 y un tratamiento centralizado en UT_2 y UT_3, sin embargo, los costos se ven afectados por una clara disminución en el consumo de la energía eléctrica para la reducción del Cr(VI). También se cumple con la norma ambiental que especifica una concentración máxima de 0.5 mg/L de Cr(VI) para su descarga. De ésta manera se logra disminuir los costos de tratamiento con un CTA de 28464.97 US $/año.

Tabla 8. Resultados del mejor diseño de red para el modelo de programación RECrVI.

k	1	2	3
t_k	17.72	31.50	31.50
cin_j^k	434.68	96.43	9.32
$cout_i^k$	37.97	9.32	0.50
$_i^k$	7.03	2.74	0.28
c_{je}^k	96.43	9.32	0.50
R_i^k	0.91	0.90	0.95
I_k	251.71	95.93	7.74
V_k	800	800	800
E_k	44.42	18.80	4.30
CTA (US $/año) =	28464.97		

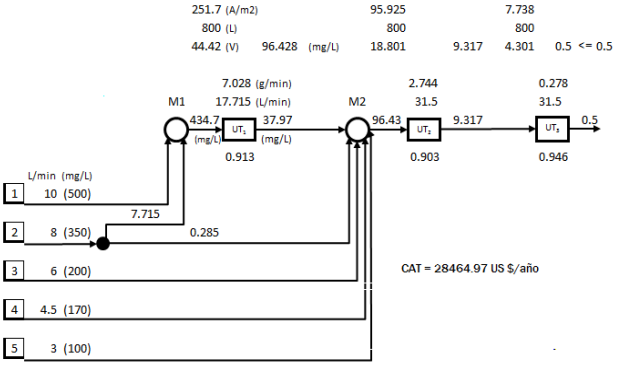

Figura 6. Diseño estructural del mejor óptimo local para el Ejemplo 1 determinado con la solución del modelo de RECrVI.

B. Ejemplo 2:

El diseño óptimo de red de tratamiento particular presentado en la Figura 7 se resolvió con el modelo RECrVI para el Ejemplo 2 (Tabla 5). En la Tabla 9 se resumen los valores de cada una de las variables del diseño presentado en la Figura 7. Se puede observar que las corrientes 2, 3, 4 y una fracción de la corriente 1 son tratadas en UT_1 y la fracción restante del flujo 1 es tratado en UT_3. Por otra parte, la corriente 5 es mezclada con el flujo t_1 para disminuir su concentración y posteriormente ser tratada en UT_2. Finalmente, debido a que la corriente t_2 cumple con la norma ambiental es enviada al punto de descarga en donde se mezcla con el flujo t_3 para satisfacer las especificaciones de la norma ambiental para la descarga de efluentes. Como se puede ver, la concentración obtenida en M_3 es 0.5 mg/L y la norma indica una cota superior de 0.5 mg/L. El costo óptimo de tratamiento para este sistema es de 20432.5 US $/año.

Tabla 9. Resultados del modelo de programación RECrVI para el Ejemplo 2.

k	1	2	3
t_k	19.9	29.9	1.59
cin_j^k	274.7	9.09	500
$cout_i^k$	13.44	0.44	1.68
$_i^k$	5.2	0.26	0.79
c_{je}^k	33.94	25.72	0.50
R_j^k	0.95	0.95	0.99
I_k	276.2	53.19	13.6
V_k	800	800	800
E_k	48.45	11.77	5.26
CTA (US $/año) =	20432.52		

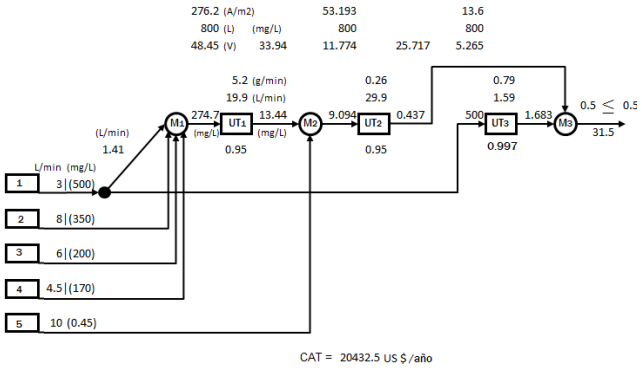

Figura 7. Diseño estructural óptimo local del Ejemplo 2 obtenido con la solución del modelo de RECrVI.

El diseño de red en la Figura 7 es una solución óptima local debido a los términos bilineales presentes en los balances de efluente del modelo de RECrVI, donde la naturaleza no convexa del modelo sugiere la necesidad de investigar el conjunto solución. Para dicho propósito se proponen diferentes puntos de arranque para las variables del modelo de programación. Se realizó una corrida de 5000 iteraciones para los puntos de arranque de las variables del modelo RECrVI. En la Tabla 10 se presentan los resultados obtenidos de la experimentación y se observan ocho soluciones óptimas locales.

Tabla 10. Soluciones óptimas locales del modelo RECrVI donde se muestra el CTA mínimo del Ejemplo 2.

Óptimo Local	CTA US $/año
1	17799.12
2	17849.56
3	19668.44
4	19678.73
5	20037.86
6	20417.96
7	20432.52
8	21021.12

En la Tabla 11 se resumen los resultados del diseño presentado en la Figura 8, el cual corresponde a la solución óptima local 1 de la Tabla 10. Las corrientes 3, 4 y una fracción de la corriente 2 son tratadas en UT_1 y la fracción restante de la corriente 2 es tratada en UT_2 junto con el flujo 1. Las corriente t_1 y t_2 son tratadas en UT_3. Finalmente, la corriente 5 que cumple con la norma ambiental es enviada al punto de descarga en donde se mezcla con el flujo t_3 para satisfacer la cota máxima de 0.5 mg/L para la descarga de efluentes. El costo óptimo de tratamiento para este sistema es de 17799.1 US $/año.

Tabla 11. Resultados del diseño de red óptima de tratamiento.

k	1	2	3
t_k	13.3	8.17	21.5
cin_j^k	221.7	405.09	13.94
$cout_j^k$	12.21	16.76	0.523
$_j^k$	2.79	3.17	0.29
c_{je}^k	110.4	9.657	0.5
R_j^k	0.95	0.96	0.96
I_k	63.37	71.27	4.59
V_k	800	800	800
E_k	13.45	14.75	3.78
CTA (US $/año)	=	17799.1	

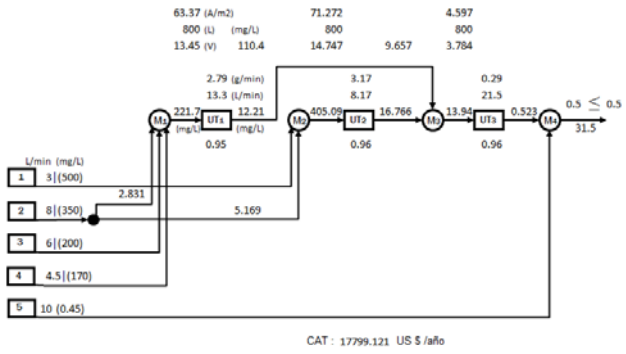

Figura 8. Diseño estructural del mejor óptimo local ejemplo 2 encontrado con la solución del modelo de RECrVI.

IV. CONCLUSIONES

En este trabajo se presentó un modelo de programación no lineal para el diseño óptimo de una red de tratamiento de efluentes contaminados con cromo hexavalente. El modelo propuesto permitió minimizar de manera sistemática el CTA de la red de tratamiento para los Ejemplos 1 y 2, de tal manera que al resolver el modelo RECrVI se obtuvo la topología y la determinación de los valores óptimos para el flujo efluente a tratar, densidad de corriente eléctrica y el volumen de los reactores. Los resultados obtenidos muestran que es factible desarrollar un modelo de programación matemática que incorpora una tecnología de tratamiento electroquímico para el caso presentado en la metodología, con tasas variables para la remoción de Cr(VI). Cabe señalar que como el modelo de programación matemática es de naturaleza no convexa, es necesario realizar un estudio de su conjunto solución, en este trabajo se encontraron diferentes soluciones óptimas locales para ambos casos de estudio abordados.

REFERENCIAS

[1]. Owlad M., Kheireddine M., Wan Daud W., Baroutian S. (2009) Removal of hexavalent chromium-contaminated water and wastewater: A review, Water Air Soil Pollut, 200, 59-77.
[2]. Barrera C., Palomar M., Romero M., S. Martínez. (2003) Chemical and electrochemical considerations on the removal process of hexavalent chromium from aqueous media, Journal of Applied Electrochemistry, 33, 61-71.
[3]. Rodríguez M., Mendoza V., Puebla H., Martínez S. (2008) Removal of Cr (VI) from wastewaters at semi-industrial electrochemical reactors with rotating ring electrodes, Journal of Hazardous Materials, Vol. 30, No. X, p. 1-9.
[4]. Wang Y. P., Smith R. (1994) Design of distributed effluent treatment systems. Chemical Engineering Science, 49 (18), 3127.
[5]. Galán B., Grossmann I. E. (1999) Optimization strategies for the design and synthesis of distributed wastewater treatment networks. Computers & Chemical Engineering, S161–S164.
[6]. Grossmann I. E., Caballero J. A., Yeomans, H. (1999) Mathematical Programming Approaches to the synthesis of Chemical Process Systems. Korean Journal of Chemical Engineering, 4, 407–426.
[7]. Zamora-Mata J.M., Hernández-Suárez R., Castellanos-Fernández J. (2004) Modelo de programación lineal para asistir en el diseño de sistemas distribuidos de tratamiento de efluentes, Revista Mexicana de Ingeniería Química, vol. 3, 121–134.
[8]. Alva A., Kokossis A., Smith R. (2007) The design of water-using systems in petroleum refining using a water-pinch decomposition, Chemical Engineering Journal, 128, 33-46.
[9]. Cheng C., Jui L. (2008) A graphical technique for the design of water-using networks in batch processes, Chemical Engineering Science, 63, 3740-3754.
[10]. Faria D., Bagajewicz M. (2009) Profit-based grassroots design and retrofit of water networks in process plants, Computers and Chemical Engineering, 33, 436–453.
[11]. Jiménez A., Lona J., Ponce J., Halwagi M. (2014) An MINLP model for the simultaneous integration of energy, mass and properties in water networks, Computers and Chemical Engineering, 71, 52-66.
[12]. Hernández-Suárez R., Optimización y síntesis de redes de agua asociadas a plantas de proceso, Tesis de Doctorado, Dpto. de Ing. de Procesos e Hidráulica, Universidad Autónoma Metropolitana-México (2004).
[13]. SEMARNAT, N0M-001-SEMARNAT-1996. México, 1997.

[14]. Brooke, A., Kendrick, D., Meeraus, A. y Raman, R. (2012). GAMS: a user's guide. GAMS Development Corporation, Estados Unidos de América.
[15]. González M. M., Introducción a la ingeniería de procesos. Limusa. México. 2013.
[16]. Zongo I., Leclerc J., Maïga H., Wéthé J., Lapicque F. (2009) Removal of hexavalent chromium from industrial wastewater by electrocoagulation: A comprehensive comparison of aluminium and iron electrodes, Separation and Purification Technology, 66, 159-166.
[17]. Chen X., Chen G., Yue L. (2002) Novel electrode system for electroflotation of wastewater, Environ Sci. Technol, 36, 778-783.

Optimización económica y ambiental del proceso para la purificación de biobutanol

Minimización del impacto económico y ambiental del proceso para la purificación de biobutanol utilizando Evolución Diferencial con Lista Tabú

J.J. Quiroz-Ramírez[a], E. Sánchez-Ramírez [a], J.G. Segovia-Hernández[a]*
[a] Universidad de Guanajuato, Campus Guanajuato, Guanajuato; Guanajuato , México.
*e-mail: gsegovia@ugto.mx

***Resumen*— La creciente demanda energética mundial ha motivado la búsqueda de fuentes de energía alternativas como un substituto a mediano y largo plazo para los combustibles de fuentes fósiles, recientemente se ha centrado la atención en alternativas renovables que puedan partir de materia prima lignocelulósica. Debido a las propiedades fisicoquímicas que presenta el butanol, se ha incrementado el interés para su desarrollo y posible implementación industrial. En este estudio se compararon cuatro diferentes rutas de proceso para la purificación de biobutanol procedente de un caldo de fermentación, mezclado con acetona, etanol y agua. Las rutas de proceso A, B y C, están formadas por columnas de destilación convencionales y un decantador, mientras que la ruta de proceso D remplaza la columna de destilación concentradora por una columna de extracción líquido-líquido. La evaluación de dichos procesos se realizó a través de un proceso de optimización multiobjetivo, siendo el costo total anual total el objetivo económico, y el eco-indicador 99 el objetivo para medir el impacto ambiental. El modelado de los procesos se realizó en Aspen Plus y la optimización multiobjetivo se realizó utilizando Evolución Diferencial con lista Tabú como un método de optimización híbrido estocástico. Los resultados indicaron que el proceso hibrido destilación-extracción liquido-liquido mostró mejores resultados evaluando el objetivo económico, sin embargo, la ruta de proceso C, donde únicamente es purificado el biobutanol y formada únicamente por columnas convencionales, mostró el menor impacto ambiental. Como un criterio alternativo para la evaluación de estas mismas rutas de proceso, se evaluó la tasa de retorno (ROI) en las condiciones actuales, reduciendo los complejos procesos en el flujo de efectivo a un simple número. Adicionalmente se comparó el uso de un colector solar contra el uso de vapor utilizado para producir la carga térmica necesaria al efectuar la separación y purificación.**

Palabras clave— Butanol, Optimización estocástica, Optimización Multiobjetivo, Biocombustible, Ahorro de Energía.

I. INTRODUCCIÓN

Debido al calentamiento global, el cambio climático y la volatilidad de precio del petróleo, durante años ha habido un creciente interés por las fuentes de energía renovables [1]. Otras preocupaciones ambientales han dado lugar a la acción gubernamental con el fin de establecer la independencia energética y para promover la investigación amigable con el ambiente [2]. Hoy en día, hay varias fuentes de energía que pueden ser producidas a través de la fermentación de biomasa lignocelulósica como el etanol y el biobutanol [3]. Aunque el etanol es actualmente el biocombustible más utilizado, varias propiedades de butanol como una mayor densidad de energía, una presión de vapor más baja, menor inflamabilidad y hidrofobicidad están dando lugar a un creciente interés en el biobutanol sobre etanol [3]. Particularmente en la industria, ha habido un interés en la producción biobutanol. En 2007 la empresa Green Biologist Ltd publico una tecnología patentada de hidrólisis que se integra en el proceso de fermentación de biocombustibles para reducir el costo de materias primas y su fabricación. El butanol se utiliza como disolvente, en fluidos hidráulicos, formulaciones de detergentes, antibióticos y en muchos otros aplicaciones [1], sin embargo, puede también ser utilizado como un combustible. Actualmente el butanol es producido principalmente por síntesis química a través del proceso oxo, sin embargo también el butanol puede ser producido a través de la fermentación.

El primer informe sobre el biobutanol producido a través de fermentación microbiana se reportó por Louis Pasteur en 1861 [1]. Varias especies de bacterias Clostridium son capaces de metabolizar diferentes azúcares, aminoácidos y ácidos orgánicos, polialcoholes y otros compuestos orgánicos a butanol y otros disolventes. El butanol de alta pureza tiene un valor relativamente alto. Sin embargo, la principal desventaja de biobutanol es la baja producción, este hecho se reflejó al elegir el etanol como fuente alternativa de combustible sobre el butanol durante la crisis del petróleo en los años 70 y 80. Sin embargo a pesar de los efectos de inhibición en la fermentación, mejoras importantes han sido reportadas para aumentar el nivel de tolerancia de butanol, esto se ve reflejado en las crecientes estudios sobre el biobutanol en los últimos años. Sin embargo una limitada atención se ha prestado al proceso de destilación en la producción de acetona / biobutanol y su optimización. En el proceso de destilación, el consumo de energía y la eficiencia de separación pueden ser muy

influenciados por el contenido de agua y biobutanol en el destilado de la columna de biobutanol (véase la Figura 1). Por lo tanto, la reducción del contenido biobutanol y de agua en el destilado de la columna de biobutanol puede reducir considerablemente el costo de la fermentación acetona-biobutanol.

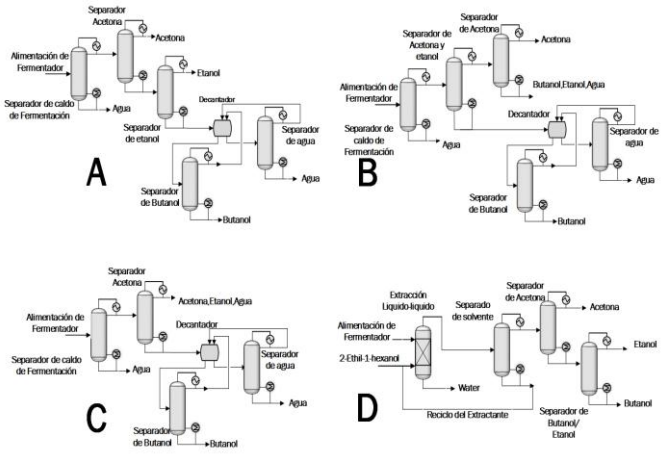

Figura 1. Procesos estudiados en la recuperación de biobutanol.

Hoy en día la optimización global es una herramienta muy adecuada para hacer frente a una amplia gama de procesos, ya que permiten el ahorro de la energía y un análisis económico de las condiciones de funcionamiento de una manera sistemática y rigurosa. Si se requiere tener en cuenta una visión más amplia, se puede encontrar que este tipo de soluciones pueden tener cargas ambientales adicionales en una parte del análisis de ciclo de vida. Por ejemplo, las unidades de tratamiento requeridas para las corrientes de proceso pueden aumentar la contaminación para el medio ambiente, o el uso de un tipo de fuente fresca de recurso pueden reducir la contaminación en la planta, pero la contaminación para el tratamiento de esa fuente fresca puede ser más alta que la evitada en la planta. En este contexto, un enfoque global que combina los impactos económicos y ambientales es particularmente útil. La evaluación del ciclo de vida (ACV) proporciona una herramienta útil para evaluar las cargas ambientales globales asociados a un proceso, producto o actividad que identifica y cuantifica los materiales y energía utilizada, así como los desechos liberados al medio ambiente. Los artículos por Alexander et al., [2] Guillen-Gosalbez et al. [14] y Gebreslassie et al. [12] presentar algunas aplicaciones de la metodología del ACV para algunos problemas de diseño de procesos químicos para mejorar su desempeño ambiental.

El objetivo de este trabajo es llevar a cabo el diseño de proceso, optimización multiobjetivo y comparación de cuatro diferentes rutas posibles procesos para la producción de biobutanol a escala industrial. Las rutas de pproceso A, B y C consiste en una columna destilación convencionales, mientras que en el Proceso D, una de las columnas de destilación se reemplaza con una columna de extracción líquido-líquido (véase la Figura 1). El modelado de procesos se realizó en Aspen Plus y la optimización se realizó utilizando el método de optimización estocástica, Evolución diferencial con la lista tabú, teniendo dos funciones objetivo, el costo total anual como un objetivo económico, mientras que la función objetivo ambiental se mide a través del eco-indicador 99 , que se basa en la metodología ACV [2].

II. PLANTEAMIENTO DEL PROBLEMA

Hay dos problemas básicos con la fermentación de butanol: i) el uso de una solución de azúcar diluida que se traduce en la obtención de un producto diluido; y ii) la alta demanda de energía debido a la recuperación intensiva de butanol del caldo de fermentación debido a que se encuentra muy diluida. Una solución a estos problemas puede abordarse de dos maneras: i) el uso de técnicas de ingeniería genética para desarrollar cepas que podían tolerar mayor concentración de butanol y azúcar y que podrían producir concentraciones más altas de butanol; ii) el uso de técnicas de ingeniería para fermentar y eliminar el producto al mismo tiempo de manera que una concentración butanol tóxica dentro del reactor no se alcanza nunca. La segunda solución consiste en la aplicación de técnicas de ingeniería para reducir la inhibición del producto y permitir el uso de soluciones concentradas de azúcar [7]. La técnica de recuperación debe exhibir una estabilidad a largo plazo, alta selectividad y tasas de eliminación y de bajo costo [8].

Recientemente, Van der Merwe et al. [25] reporto cuatro alternativas para purificar de todos los disolventes desde la fermentación ABE (Figura 1). Estas rutas de proceso emplean tecnologías similares a los procesos industriales para la producción de biobutanol, todos estos procesos se alimentan de un caldo de una fermentación por lotes seguido de varias columnas de destilación para purificar los disolventes. Para este trabajo, la ruta de proceso A (Figura 1) se definió mediante el caso base de diseño de procesos simulada en el estudio de Roffler et al. [20] en la que todos los disolventes provenientes de la fermentación ABE se purifican. Este diseño del proceso también incluye un decantador para realizar la separación azeotrópica heterogénea. La ruta de proceso B (Figura 1) se basa también en el diseño del proceso reportado por Roffler et al. [20]. Este diseño del proceso se alimenta por igual de un caldo de fermentación; sin embargo, el etanol de la tercera columna de destilación no se purifica tal como ruta de proceso A lo hace. En lugar de eso, el flujo de etanol es totalmente mezclado con restos de aguas residuales y de biobutanol. La ruta de proceso C (Figura 1) se definió mediante el diseño de los procesos estudiados por Marlatt y Datta [19]. En este diseño, sólo el flujo biobutanol se purifica, dejando que tanto el etanol y la acetona en el proceso de purificación se mezclen con los rastros de agua y biobutanol. Finalmente, ruta de proceso D (Figura 1) es ligeramente diferente que las rutas de proceso A, B y C, ya primera columna de destilación se reemplaza por una columna de extracción líquido-líquido, utilizando acetato de hexilo como agente extractante, a fin de separar los azeótropos homogéneo y heterogéneo que presenta la mezcla con el agua. Después de que las tres columnas de destilación realizar la separación de acetona, biobutanol y etanol.

En un trabajo previo Sánchez-Ramírez et al [22] se reportó que la ruta de proceso D tiene un impacto económico mucho

menor, donde se evaluó de TAC en un proceso de optimización rigurosa, sin embargo en la búsqueda e inclusión del impacto ambiental, el eco-indicador 99 se utiliza como una función objetivo medioambiental que podría llevar a un punto de vista más amplio sobre estas secuencias evaluadas.

En este estudio, todos estos casos de diseño se simularon inicialmente utilizando modelos de procesos de Aspen Plus. Teniendo en cuenta que estos modelos de procesos son robustos y termodinámicamente riguroso. Según Van der Merwe et al. [25] y Chapeaux et al. [5], el modelo termodinámico NRTL-HOC fue el más preciso para el cálculo de la propiedad física disponible para los componentes utilizados en las condiciones especificadas. Teniendo en cuenta la suposición de que todos los diseños de procesos tienen la misma corriente alimentación excepto el diseño LLE donde se añadió acetato de hexilo como extractante. Las Purezas de los producto se lograron en todas las simulaciones de proceso en al menos 99.5% para el biobutanol (% en peso), acetona 98% (% en peso), etanol 94% (% en peso), y 99.9% (% en peso) de recuperación de disolvente.

III. Problema de optimización

La optimización de los procesos de fermentación de biobutanol es esencial para impulsar la industria del biobutanol para que puede competir eficazmente con el butanol derivado de la ruta petroquímica, ya que la fermentación de acetona, biobutanol, y etanol (ABE), como normalmente se llama la fermentación para producir biobutanol, se caracteriza por su baja productividad. Además, el impacto medioambiental se debe tomar en el recuento con el fin de satisfacer todas las restricciones gubernamentales, así como la implementación de procesos ambientalmente competitivos. El impacto ambiental se cuantifica utilizando los principios del análisis de ciclo de vida (ACV), dando un enfoque que conduce a soluciones en las que el daño ambiental en general se minimiza.

3.1 Función objetivo Económico

En la ruta de proceso A y B, la función objetivo es la minimización del costo anual total (TAC), que es directamente proporcional al tamaño de las columna, la demanda de vapor y servicios . La minimización de este objetivo está sujeto a las recuperaciones y purezas requeridas en cada corriente de producto, es decir:

$$\text{Min (TAC)} = f\left(N_{tn}, N_{fn}, R_{rn}, F_{rn}, D_{cn}\right) \qquad (1)$$

$$\text{Sujeto a } \vec{y}_m \geq \vec{x}_m$$

donde Ntn son etapas totales de columna, Nfn es la etapa de alimentación de la columna, Rrn es la relación de reflujo, Frn es los flujos de destilado, Dcn es el diámetro de la columna, y x_m y_m son vectores de purezas obtenidos y requeridos para los componentes m, respectivamente. Esta minimización implica la manipulación de 25 variables continuas y discretas para cada proceso de ruta, donde se utilizan 5 variables para el diseño de cada columna. Tenga en cuenta que, las recuperaciones de los componentes clave de cada corriente de producto deben ser incluidos como una restricción para el problema de optimización. En proceso de la ruta A, la acetona, el biobutanol y etanol deben ser recuperados con su respectiva pureza; mientras que en la ruta de proceso B, sola la acetona y el biobutanol deben ser recuperados.

- Ruta de Proceso C

Esta ruta de proceso tiene también una función objetivo. La minimización de este objetivo está sujeto a las recuperaciones y purezas requeridas en cada corriente de producto y el problema de optimización se define como:

$$\text{Min (TAC)} = f\left(N_{tn}, N_{fn}, R_{rn}, F_{rn}, D_{cn}\right) \qquad (2)$$

$$\text{Sujeto a } \vec{y}_m \geq \vec{x}_m$$

Este problema de optimización implica la manipulación de las 20 variables de decisión para cada proceso de ruta. Tenga en cuenta que la diferencia entre esta ruta y rutas A y B, es las purezas en acetona y etanol de productos corrientes, y la recuperación de los mismos componentes.

- Ruta de Proceso D

Esta ruta tiene también la misma función objetivo. Sin embargo, la primera columna de destilación se reemplaza por una columna de extracción líquido-líquido, el número de variables de decisión se reduce en esa columna, donde las etapas de la columna y la etapa de alimentación sólo están optimizados. El problema de optimización se define como:

$$\text{Min (TAC)} = f\left(N_{tn}, N_{fn}, R_{rn}, F_{rn}, D_{cn}\right) \qquad (3)$$

$$\text{Sujeto a } \vec{y}_m \geq \vec{x}_m$$

III.II Función objetivo Ambiental

Esta función se mide a través del eco-indicador 99, que se basa en la metodología del análisis del ciclo de vida [14] y se define de la siguiente manera:

$$Min\ (Eco\ indicador) = \sum_b \sum_d \sum_{k \in K} \delta_d \omega_d \beta_b \alpha_{b,k} \qquad (4)$$

Dónde δ_b representa la cantidad total de producto químico b lanzado por unidad de flujo de referencia, debido a las emisiones directas , $\alpha_{b,k}$ es el daño causado en la categoría k por unidad de producto químico b liberada al medio ambiente, ω_d es un factor de ponderación de los daños en categoría d, y δ_d es el factor de normalización de los daños de categoría d.

De la misma manera que en el objetivo económico, todas las variables manipuladas se consideran en el diseño de todas las rutas de procesos.

Además, se hizo un escenario comparativo donde todo el vapor necesario en concepto de demanda de calor en cada columna de destilación fue reemplazado por los colectores solares, se realizó este escenario basado en que casi todas las emisiones de gases invernadero asociados con el uso de combustibles fósiles fueran anuladas. Por otra parte, teniendo en cuenta que cada colector solar tiene su propio impacto económico, se desarrolla un nuevo Pareto, donde se considera un TAC que incluye tanto TAC del proceso de purificación y colector solar, también se considera un colector solar con casi cero emisión de gases de invernadero. Una descripción completa de esta metodología es proporcionada por Lira-Barragán et al [18].

IV. Estrategia Global de optimización estocástica

En particular, la optimización y diseño de las rutas de procesos son altamente problemas multivariable no lineal y, con la presencia de variables de diseño continuas y discontinuas; Asimismo, las funciones objetivo utilizadas como criterio de optimización son potencialmente no convexo con la posible presencia de óptimos locales y sujeto a restricciones.

Por lo que, con el fin de optimizar las rutas de procesos para la producción de biobutanol, se utilizó un método de optimización estocástica, Evolucióńn diferencial con lista tabú (DETL) [23]. La Evolución Diferencial (DE) tiene su base en la teoría de la selección natural de Darwin, y es similar a los algoritmos genéticos (GA) a excepción de un factor importante: varios GA, en particular las versiones anteriores, las variables de decisión se codificar como cadenas de bits mientras que DE los codifica como puntos flotantes numéricos. Srinivas y Rangaiah [23] demostraron que el uso de algunos conceptos de metaheurístico como lista tabú puede mejorar el rendimiento del algoritmo DE. En particular, la lista tabú (TL) se puede utilizar para evitar la nueva visita del espacio de búsqueda al mantener registro de los puntos visitados recientemente, que puede evitar evaluaciones de función innecesarias. Con base en este hecho, Srinivas y Rangaiah [23] propusieron la DETL como método híbrido, que incluye los pasos de la DE clásica, TL y verificación tabú para realizar un seguimiento de los puntos evaluados para evitar nuevas visitas a los mismos puntos durante la búsqueda de optimización, aunado a un criterio de convergencia sobre la base de número máximo de generaciones. Una descripción completa de este algoritmo DETL es proporcionada por Srinivas y Rangaiah [23].

La implementación de este enfoque de optimización se realizó utilizando una plataforma híbrida utilizando Microsoft Excel y Aspen Plus. El vector de variables de decisión (es decir, las variables de diseño) se envían a Microsoft Excel para Aspen Plus usando DDE (Dynamic Data Exchange) a través de la tecnología COM. En Microsoft Excel, estos valores se atribuyen a las variables de proceso que Aspen Plus necesidad. Después de la que la simulación se lleva a cabo, Aspen Plus regreso a Microsoft Excel el vector resultante. Finalmente, Microsoft Excel analiza los valores de la función objetivo y propone nuevos valores de variables de decisión de acuerdo con el método de optimización estocástica utilizada. Para la optimización de las rutas de proceso que se ha analizado en este estudio, se han utilizado los siguientes parámetros para el método DETL: 200 individuos, 500 generaciones, una lista tabú del 50% del total de individuos, un radio tabú de 0.0000025, 0.80 y 0.6 de cruce y fracciones de mutación, respectivamente. Estos parámetros se obtuvieron a través de un proceso de ajuste a través de los cálculos preliminares. El proceso de ajuste consiste en realizar varias corridas con diferente número de individuos y generaciones, a fin de detectar los mejores parámetros que permiten obtener el mejor rendimiento de convergencia de DETL.

Con el fin de calcular el costo anual total (TAC) que se utiliza como función objetivo, se utilizó el método publicado por Guthrie [17], que fue modificado por Ulrich [18]. Se lleva a cabo la estimación de costos de una planta industrial separándola en unidades, y haciendo uso de ecuaciones publicadas por Turton et al. [19], se llevó a cabo una aproximación costo del proceso utilizando la ecuación (4), es decir:

$$TAC = \frac{\sum_{i=1}^{n} C_{TM,i}}{n} + \sum_{j=1}^{n} C_{ut,j} \quad (5)$$

Dónde TAC es el costo anual total, CTM es el costo de capital de la planta, n es el número total de unidades individuales y C_{ut} es el costo de los servicios, respectivamente.

Por otra parte, teniendo en cuenta que en la ingeniería, también se realiza la evaluación de los proyectos de uso de algunas otras medidas diferentes de TAC. Entre ellos, el retorno de la inversión (ROI) [20]. Esta medida tiene como objetivo reducir el complejo proceso de flujo de caja que tiene lugar en diferentes períodos de tiempo en el futuro a un solo número. El retorno de la inversión (ROI) se define en su forma más simplificada de la siguiente manera:

$$ROI = \frac{(\sum_{i=1}^{N} CF_i)/N}{I} \quad (6)$$

Donde N es el número de años del proyecto y un valor medio se utiliza después de los ingresos fiscales. Al dividir por la inversión, se puede obtener la velocidad a la que se recupera la inversión.

En la metodología de eco-indicador 99, 11 categorías de impacto se consideran [14]

1. Los efectos cancerígenos en los seres humanos

2. Los efectos respiratorios en los seres humanos que son causadas por sustancias orgánicas

3. Los efectos respiratorios en los seres humanos causados por sustancias inorgánicas

4. El daño a la salud humana que es causada por el cambio climático

5. Efectos sobre la salud humana que son causadas por las radiaciones ionizantes

6. Efectos sobre la salud humana causados por agotamiento de la capa de ozono

7. El daño a la calidad del ecosistema que es causada por las emisiones tóxicas de los ecosistemas

8. Los daños a la calidad del ecosistema que es causada por el efecto combinado de la acidificación y la eutrofización

9. El daño a la calidad del ecosistema que es causada por la ocupación de tierras y la conversión de tierras

10. El daño a los recursos causada por la extracción de minerales

11. El daño a los recursos causados por la extracción de combustibles fósiles.

Estas 11 categorías se agrupan en tres categorías principales daños: (1) la salud humana, (2) la calidad de los ecosistemas, y (3) el agotamiento de los recursos.

V. Resultados

Antes de realizar el proceso de optimización, todas las secuencias se modelaron y simularon rigurosamente en Aspen Plus mediante el módulo RadFrac. Esto significa que se obtuvieron todos los diseños presentados teniendo en cuenta el conjunto completo de ecuaciones MESH (balances de masa, relaciones de equilibrio, el balance energético, etc). La Figura 2 muestra el comportamiento de convergencia de las funciones objetivo utilizadas para la optimización de procesos. Los resultados se presentan hasta 100000 evaluaciones porque el vector de variables de decisión no produjo después de eso una mejora significativa. Bajo este escenario, se asumió que DETL logra la convergencia en las condiciones numéricas probadas y los resultados informados corresponden a la mejor solución obtenida por el método de DETL

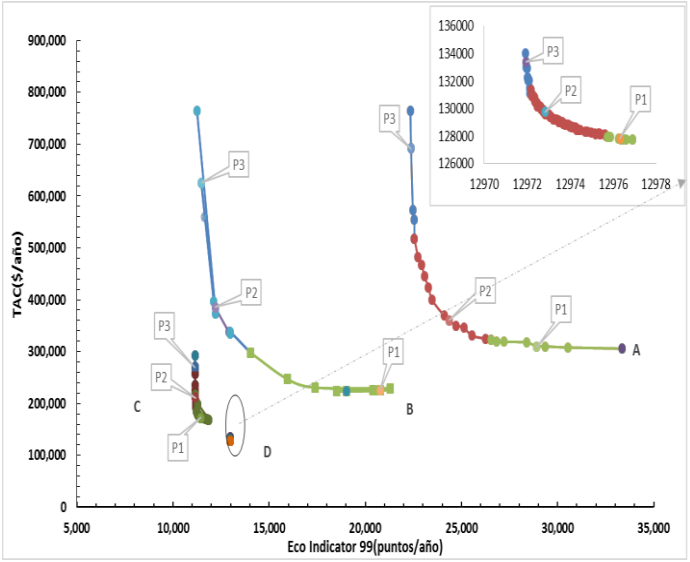

Fig. 2 Frente de Pareto de las rutas de proceso A-D

La Figura 2 representa los frentes de Pareto después del proceso de optimización, en la Figura 2, se puede identificar tres zonas en cada frente de Pareto, una parte donde se localiza los diseños más caros, pero estos mismos diseños presentan el menor impacto ambiental, al contrario se puede observar zonas en las que todos los diseños tienen el TAC más barato, sin embargo, eco-indicador es el más grande. En medio de ambas zonas se encuentra la zona de diseño más viable de todos los procesos, todos esos diseños logran purezas y recuperaciones necesarias y su TAC y eco-indicador 99 están en medio de los valores de las zonas extremas. Este comportamiento en la Figura 2 representa los objetivos en conflicto a lo largo de proceso de optimización, en una explicación breve, la zona roja consiste en diseños que incluyen preferiblemente un número alto de etapas, un diámetro relativamente grande de columna, pero requerimientos energéticos relativamente pequeños , este combinaciones producen la mayor TAC pero el eco-indicador más pequeño. La zona azul se compone de diseños que incluyen preferiblemente un número menor de etapas, el diámetro de columna relativamente pequeño, sin embargo una mayor demanda de calor, que produjo el TAC menor, pero el eco-indicador más grande. En medio de ambas zonas, las zonas verdes incluyen el diseño con las variables medias entre ambas zonas, que se refleja en la TAC y valores del eco indicador 99.

Comparando las cuatro rutas procesos, es claro que la ruta de proceso D tiene el TAC más pequeño debido a la incorporación de la columna de extracción líquido-líquido donde el agua se separa, lo que genera un ahorro energético por esa columna. También la ruta de proceso A, donde se purifican todos los disolventes tiene la mayor TAC, seguido de ruta de proceso B y C, respectivamente; en esta reducción en el TAC entre estas rutas de procesos es debido a la purificación de acetona y etanol, más allá, la purificación de etanol representa un enorme impacto económico que se puede ver comparando ruta de proceso B y C. Por otro lado, en la evaluación de impacto ambiental, a pesar de que la ruta proceso D exhibió la menor TAC, el resultado del eco-indicador no es el más pequeño. La

ruta de proceso C, donde sólo el biobutanol es purificado presentó el menor impacto ambiental, la distancia entre ambos procesos es pequeña, sin embargo esta diferencia se debe al tamaño de la columna (número de etapas), ya que la optimización de la ruta de proceso D convergente de preferencia a columnas más grandes si se comparan con ruta de proceso C, por lo que la contribución para el acero utilizado en cada columna del proceso C hacen la diferencia entre ellas.

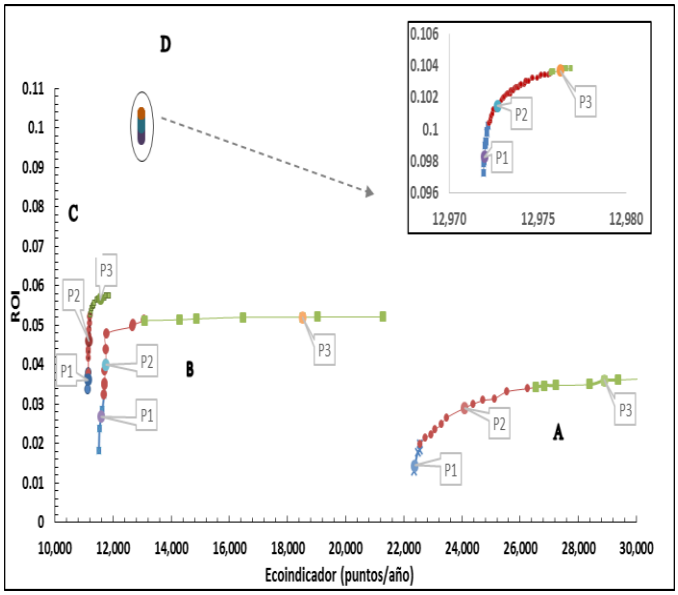

Figura 3. Frentes de Pareto que evalúan el rendimiento de la inversión.

Otro punto de vista económico, es la evaluación del ROI (Retorno de Inversión) en cada ruta de proceso, la Figura 3 representa el ROI de los cuatro procesos y es totalmente consistente con la Figura 2, en este caso el la ruta de proceso D tiene los mejores resultados económicos, las otras tres rutas de procesos muestran malas condiciones económicas bajo este escenario y en las condiciones actuales.

En la Figuras 4, únicamente por ejemplificar, se representa el impacto ambiental de un punto en el Pareto de la ruta de proceso A. Se puede observar el gran impacto ambiental generado relacionado con el uso de vapor en todo este proceso, las otras diez categorías contribuyen cada una con pocos menos orden de magnitud en comparación con vapor.

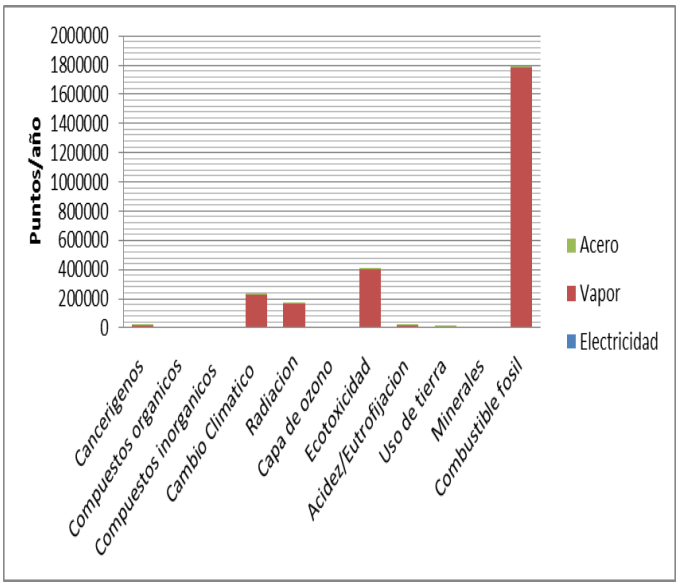

Figura 4. impacto ambiental anualizado del punto 3 de la ruta de proceso A.

Evidentemente el vapor tiene un papel muy importante cuando se mide el impacto ambiental, para ello se planteó un escenario alternativo donde todo el vapor requerido podría ser proporcionado utilizando colector solar, teniendo como hipótesis que toda las emisiones el gas invernadero podrían ser reducidas drásticamente, sin embargo, el impacto económico tendrá un efecto muy importante en un nuevo frente de Pareto.

Siguiendo la metodología de proporcionar por Lira-Barragán [18], y teniendo en cuenta una ubicación hipotéticamente de este proyecto en León, México, latitud de 21º 07 'y una longitud de 101º 41', se calculó el área de un colector solar tubular para cada una de las ruta de proceso, también el TAC se recalcula añadiendo el propio TAC del colector solar, y del mismo modo el eco-indicador 99 se vuelve a calcular considerando cero emisiones de gases debido al no uso de combustibles fósiles.

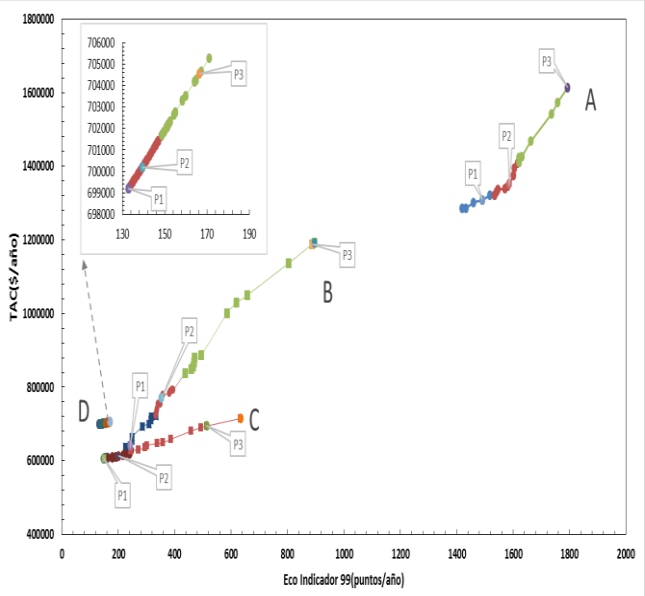

Figura 5 frentes de Pareto de cada ruta de proceso considerando los colectores solares.

De este modo, la Figura 5 muestra un frente de Pareto modificada para este caso, es evidente que el impacto principal en el eco-indicador 99 es el uso de vapor a partir de combustibles fósiles, por lo que, en este caso en el que se incluye un colector solar, este enorme impacto es eliminado, sin embargo hay un gran aumento en el TAC en comparación con el primer escenario (Figura 2). Además, la ruta de proceso A mostró una vez más el peor comportamiento debido a tener el mayor TAC y mayor demanda de energía térmica.

VI. Conclusiones

En este estudio, se ha aplicado un método de optimización global estocástico para el diseño de varias rutas para la producción de biobutanol para mejorar su costo e impacto ambiental. De acuerdo con los resultados, la ruta de proceso D mostró el TAC más pequeño, con una pequeña diferencia con respecto a la ruta procesar C. La ruta de proceso A, donde se purifican todos los disolventes, mostró el mayor TAC debido al costo de capital de los equipos y a la demanda de calor al realizar la purificación ABE. Teniendo en cuenta el impacto ambiental medido por el eco-indicador 99, la ruta de proceso C mostró el menor impacto, seguido muy de cerca por la ruta de proceso D, diferenciando ligeramente entre sí debido al tamaño de columna, el diámetro y la demanda de calor.

Evaluando el Retorno de la Inversión, la ruta de proceso D mostró los mejores escenarios de cerca de un retorno de la inversión con un valor cercano a 0.1, además se alejó completamente de las otras tres rutas de proceso. Bajo este escenario, el diseño del proceso C mostró el impacto menor medida a través del eco-indicador 99, seguido de cerca de nuevo por la vía de proceso de D.

Teniendo en cuenta la inclusión de un colector solar, para evitar el uso de vapor a partir de combustibles fósiles, los valores para el eco-indicador 99 mostraron una enorme disminución, sin embargo, al mismo tiempo hay un aumento importante en el TAC, mostrando de esta manera un nuevo y totalmente diferente escenario donde el impacto ambiental es pequeño y los costos de un impacto económico son más grande en cada proceso.

[1] Al-Shorgani NKN, Kalil MS, Ali E, Hamid AA Yusoff WMW (2012) The use of pretreated palm oil mill eluent or acetone-butanol-ethanol fermentation by Clostridium sccharoperbutylacetionicum N1-4. Clean Technologies and Environmental Policy 14(5):879-887.

[2] Alexander B, Barton G, Petrie J, Romagnoli J (2000) Process synthesis and optimization tools for environmental design: methodology and structure. Computers and Chemical Engineering 24:1195–1200.

[3] Bagajewicz M (2008) On the use of net present value in investment capacity planning models. Industrial and Engineering Chemistry Research 47(23):9413–9416.

[4] Brekke K (2007) Butanol: an energy alternative? Ethanol Today. 36–92.

[5] Chapeaux A, Simoni LD, Ronan TS, Stadtherr MA, Brennecke JF (2008) Extraction of alcohols from water with 1-hexyl-3-methylimidazolium bis(trifluoromethylsulfonyl)imide Green Chemistry 10(12):1301-1306.

[6] Chouinard-Dussault P, Bradt Laura, Ponce-Ortega JM, El-Halwagi MM (2011) Incorporation o process integration into lie cycle analysis for the production of biofuels. Clean Technologies and Environmental Policy 13(5):673-685.

[7] Delgado-Delgado R, Hernáncez S, Barroso-Muños FO, Segovia-Hernández JG, Rico-Ramirez V (2015) Some operational aspects and applications of dividing wall columns: energy requirements and carbon dioxide emissions. Clean Technologies and Environmental Policy. DOI: 10.1007/s10098-014-0822-8.

[8] Emtir M, Etoumi A (2008). Enhancement of conventional distillation configurations or ternary mixtures separation. Clean Technologies and Environmental Policy 11(1):123-131.

[9] Ezeji T, Qureshi N, Blaschek H (2004) Butanol fermentation research: upstream and downstream manipulations. The Chemical Record 4(5):305–314.

[10] Ezeji T, Qureshi N, Blaschek H. Bioproduction of butanol from biomass: from genes to bioreactors. Biotechnology 2007:220–7.

[11] García V, Päkkilä j, Ojamo H, Muurinen E, Keiski RL (2011) Challenges in Biobutanol production: How to improve the efficiency? Renewable and Sustainable Energy Reviews 15:964–980.

[12] Gebreslassie BH, Guillen-Gosalbez G, Jiménez L, Boer D (2009) Design of environmentally conscious absorption cooling systems via multiobjective optimization and life cycle assessment. Applied Energy 86:1712–1722.

[13] Geodkoop M, Spriensma R (2001) The eco-indicator 99. A damage oriented for life cycle impact assessment. Methodology report and manual for designers; Technical report, PRe´ Consultants, Amersfoort, The Netherlands.

[14] Guillén-Gosálbez G, Caballero JA, Jiménez L. (2008) Application of life cycle assessment to the structural optimization of process flowsheets. Industrial and Engineering Chemistry Research 47:777–789.

[15] Gupta S, Sarkar P, Singla E (2015) Understanding different stakeholders of sustainable product and service-based systems using genetic algorithm. Clean Technologies and Environmental Policy. DOI:10.1007/s10098-014-0880-y.

[16] Guthrie KM (1969) Capital cost estimating. Chemical Engineering 76(6):14-142.

[17] Gutierrez-Arriaga CG, Serna-González M, Ponce-Ortega JM, El-Halwagi MM (2013) Multi-objective optimization of steam power plants for sustainable generation of electricity. Clean Technologies and Environmental Policy 15(4):551-566.

[18] Lira-Barragan L, Ponce-Ortega JM, Serna-González M, El-Halwagi MM (2013) Synthesis of integrated adsorption refrigeration systems involving economic and environmental objectives and quantifying social benefits. Applied Thermal Engineering 52:402-419.

[19] Marlatt J, Datta R (1986) Acetone-biobutanol fermentation process development and economic evaluation. Biotechnology Progress 2:23–8.

[20] Roffler S, Blanch H, Wilke C (1987) Extractive fermentation of acetone and biobutanol: process design and economic evaluation. Biotechnology Progress 3:131–40.

[21] Sánchez-Bautista AF, Santibañez-Aguilar, JE, Ponce-Ortega JM, Nápoles-Rivera F, Serna-González M, El-Halwagi MM (2015) Optimal design of domestic water-heating solar systems. Clean Technologies and Environmental Policy. DOI: 10.1007/s10098-014-0818-4.

[22] Sánchez-Ramírez E, Quiroz-Ramírez JJ, Segovia-Hernández JG, Hernández S, Bonilla-Petriciolet A (2015) Process alternatives for biobutanol purification: Design and optimization. Industrial and Engineering Chemistry Research. DOI:10.1021/ie503975g.

[23] Srinivas M, Rangaiah GP (2007) Differential evolution with taboo list for solving nonlinear and mixed-integer nonlinear programming problems. Industrial and Engineering Chemistry Research 46:7126-7135.

[24] Turton R, Bailie RC, Whiting WB, Shaeiwitz JA (2009) Analysis, synthesis and design of chemical process, Third edition, Prentice Hall, USA.

Ulrich GD (1984) A guide to chemical engineering process design and economics, Wiley, New York, USA.

[25] Van der Merwe AB, Cheng H, Görgens JF, Knoetze JH (2013) Comparison of energy efficiency and economics of process designs for biobutanol production from sugarcane molasses. Fuel 105:451-458.

Tendencias actuales y futuras en catálisis para la Refinación

E. Mar_Juárez*
Gerencia de Transformación de la Biomasa
Instituto Mexicano del Petróleo
México, D.F. CP 07730. MÉXICO.
emar@imp.mx

Felipe de Jesus Ortega_García
Gerencia de Servicios Químicos
Instituto Mexicano del Petróleo
México, D.F. CP 07730. MÉXICO
fjortega@imp.mx

Abstract— **La innovación juega un papel clave en el desarrollo de cualquier industria al generar un impacto profundo y positivo en los procesos de producción. En el caso de los procesos catalíticos, fundamentales para la producción de combustibles, alimentos, productos químicos y farmacéuticos, entre muchos otros ha sido una herramienta utilizada constantemente para lograr los niveles de eficiencia observados en la industria hoy en día. Los procesos catalíticos tienen un gran impacto en la economía al generar una facturación anual de aproximadamente $ 15 mil millones a nivel mundial, y de acuerdo con estadísticas del 2009 de la Sociedad Norteamericana de Catálisis entre el 30 y el 40% del PIB mundial depende de procesos catalíticos.**

Así el conocimiento y evolución de la catálisis no sólo reviste gran importancia para la economía, sino también la generación de procesos eficientes, económicos y respetuosos del medio ambiente. La innovación se presenta como el punto de partida para propiciar una industria eficiente y sustentable que pueda satisfacer los estándares de vida deseados de los 9 mil millones de habitantes proyectados para habitar este planeta en el año 2050. Por lo tanto, un mapa tecnológico sobre Catálisis, vista está como un factor detonante del desarrollo dentro de la industria petrolera y en especial en los procesos de refinación, coloca la ruta de la innovación y de diagnóstico como una herramienta valiosa y estratégica.

En este trabajo se presenta una visión sobre la factibilidad de innovar e impactar de forma positiva en la industria de la refinación nacional explorando cuatro dimensiones: calidad de los combustibles, medio ambiente, aumento de la producción y economía.

Einstein dijo: *"Para generar nuevas preguntas, nuevas posibilidades, se tiene que considerar los viejos problemas desde un nuevo ángulo, se requiere imaginación creativa para marcar el avance real en la ciencia".*

Keywords— catálisis, refinación, innovación.

I. INTRODUCCIÓN

Desde mediados del siglo XX, la catálisis ha experimentado un desarrollo notable tanto desde el punto de vista del conocimiento fundamental como de sus aplicaciones. Al inicio de este nuevo siglo, entre el 80 y el 90% de los productos que se utilizan en la vida diaria han estado en "contacto" con un catalizador en algún momento de su producción. De acuerdo con la Sociedad Norteamericana de Catálisis [1] el volumen de mercado de catalizadores para el 2010 ascendió a $ 14.04 miles de millones de dólares al año (MMUSD/año) y se espera que en 2015 se registren $ 20.41 MMUSD/año. La demanda de catalizadores se centra en tres industrias: control de emisiones, refinación, industria química y de principalmente catalizadores para vehículos automotores. La participación de cada una de estas industrias se muestra en la Tabla I con sus respectivas proyecciones de ventas. Es importante mencionar que la industria que registrará el mayor crecimiento será el de control de emisiones (78%), mientras que la industria de la refinación registrará un descenso en su participación del 19%. Sin embargo, teniendo presente que la industria de la refinación basa sus procesos intrínsecos en el uso de catalizadores se proyecta que sus ventas ascenderán a $ 6.7 millones en 2019 [2].

La contribución económica de la catálisis es tan notable como el proceso mismo. Este análisis se centra en la industria de la refinación, la cual presentó un cambio notable cuando las regulaciones ambientales se tornaron más estrictas que obligaron a la industria a elegir esquemas de procesamiento que satisficieran las especificaciones de contenido de azufre en gasolina y diésel más estrictas. Así, la tecnología de procesos y catalizadores evolucionaron para cumplir con estas nuevas normas.

TABLE I. VOLUMEN DEL MERCADO DE CATALIZADORES (MMUSD/AÑO)

Industria	*2010*	*2015*
Refinación	4.03	4.81
Industria química	5.20	7.02
Control de emisiones	4.81	8.58
TOTAL	14.04	20.41

FUENTE: ELABORACIÓN PROPIA CON DATOS DE MARKETS&MARKETS [3]

Los catalizadores empleados en la industria de la refinación se pueden clasificar de acuerdo con el tamaño de sus mercados, en la Tabla II se muestran los catalizadores por las tasas de uso. De acuerdo a los reportes de mercado las tendencias globales definen que por tipo de catalizadores estos se ubican en catalizadores para FCC, para HDS, de hidrocraqueo y de alquilación. Por materiales son zeolitas, metales y compuestos químicos. Estas tendencias se basan en la demanda de consumo de energía prevista para las próximas décadas (2030-2050), siendo el factor clave las regulaciones ambientales. De los catalizadores los de hidroprocesamiento (HDS) se ubican en el segmento superior al registrar un aumento de su participación del 23% en tan sólo cinco años [2].

TABLE II. EMPLEO DE CATALIZADORES EN DIVERSOS PROCESOS

Alto uso	*Bajo uso*
Craqueo Catalítico (FCC)	Producción de hidrógeno
Hidroprocesamiento (HDS)	Azufre
Hidrocraqueo	Dimerización
Reformación	Metil Ter-Butil Éter
Isomerización	Alquilación (Fluoruro de hidrógeno)
Alquilación (Ácido Sulfúrico)	

FUENTE: ELABORACIÓN PROPIA CON DATOS DE FUEL [3]

Estas cifras muestran que el negocio de la refinación centra sus procesos en catalizadores heterogéneos, registrando en 2014 ventas por 4.7 mil millones de dólares. Las perspectivas de crecimiento en FCC y HDS es que aumentarán las ventas a más de $5 mil millones en los próximos cinco años. El catalizador que presentará el dominio del mercado será el HDS debido a las regulaciones de azufre en los combustibles líquidos.

Uno de los impulsores del mercado de catalizadores es China, economía emergente cuyo rápido crecimiento ha sido y será un factor que marcara la demanda de combustibles en el sector transporte, por ejemplo, se prevé que la venta de automóviles llegará a los 10 millones de unidades por año a finales de esta década (2020).

La figura 1 muestra la distribución y evolución del mercado de catalizadores en la industria de la refinación en los últimos 5 años [1].

Fig. 1. Evoluación del Uso de catalizadores por tipo de proceso dentro de la industria de la refinación

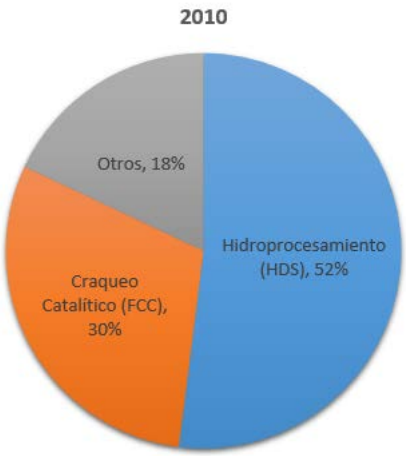

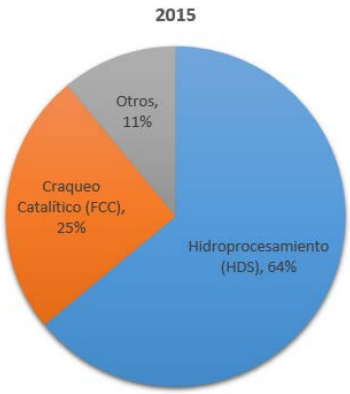

FUENTE: ELABORACIÓN PROPIA CON DATOS DE SOCIEDAD NORTEAMERICANA DE CATÁLISIS [1]

Durante los últimos 20 años, el negocio de la catálisis en la refinación ha pasado de ser una empresa regional a una empresa global. Al punto que la pregunta que da inicio a este análisis para la innovación es: ¿Qué papel jugará la catálisis en el siglo 21 ahora que las nuevas tecnologías están naciendo y desarrollándose a ritmos vertiginosos? Sería presuntuoso hacer una predicción a largo plazo, pero, sin embargo, es importante tratar de delinear el futuro de esta disciplina al tiempo que se delimita el ámbito de aplicación al campo de la industria petrolera.

Aunque el entorno es un factor importante los procesos de refinación son bastante genéricos, si bien nos enfocamos en México eso no delimita el campo de acción de los desarrollos tecnológicos para aplicar. Por último, se presentará un panorama general sobre como la revolución del shale gas puede afectar esta industria.

II. REFINACIÓN Y CATÁLISIS

La catálisis juega un papel clave en la industria de la refinación como la mayoría de los procesos catalíticos (ver Figura 2, donde se identifican los procesos que emplean catalizadores). Existen factores sobresalientes en el desarrollo de la catálisis específica para la industrial de la refinación y petroquímica los cuales se ubican en la segunda mitad del siglo 20.

El marco histórico bajo el cual evoluciona la catálisis en las tres últimas décadas se puede ubicar en un inicio en la crisis mundial del petróleo de la década de los 70's y el cambio de paradigma en el cual se creía que los recursos eran infinitos. En este momento histórico se establece que los recursos fósiles son limitados y se ubican en zonas geopolíticamente inestables lo que tuvo las siguientes consecuencias:

- Con respecto a la energía en general, hubo una búsqueda de sustitutos de los combustibles fósiles [1] y, en zonas carentes de estos recursos como es Europa, se inicia un interés por el desarrollo de combustibles alternativos. Pero el petróleo sigue siendo una materia prima estratégica y todavía predominante para el sector transporte.

- En refinación, se busca aprovechar todas las fracciones pesadas, es decir, eficientar los procesos para obtener la mayor cantidad de productos ligeros mediante la transformación de las fracciones pesadas. Esto impulso el desarrollo del cracking de residuos, mientras que la hidroconversión fue mucho más lenta debido a su alto costo.
- Los movimientos ambientalistas de esta década, promocionan acciones tendientes a proteger el medio ambiente contra las emisiones nocivas producidas por la actividad del ser humano, teniendo un fuerte impacto en la refinación y de forma particular en la calidad de los combustibles automotores. Las principales medidas adoptadas en Europa y Norteamérica se orientan a reducir el contenido de azufre de la gasolina y diesel. Actualmente se estima que las emisiones de gases nocivos procedentes de los vehículos de transporte se han reducido en un factor de alrededor de 100 en comparación con los niveles de 1970.

En la década de los 90's, la preocupación por el cambio climático debido a la emisión de gases de efecto invernadero y la preocupación generalizada de la sociedad por el medio ambiente hacen que se tomen nuevas acciones que mitiguen aquellos sectores que se consideran altamente contaminantes. Sí 21% de las emisiones mundiales de CO_2 proceden del transporte y el 8% de la industria del petróleo y gas [4,5], la orientación natural de las acciones para reducir las emisiones de CO_2 se ubican en estos dos sectores. Entonces las refinerías requerirán producir combustibles limpios y a la vez cambiar a procesos menos contaminantes.

Fig. 2. Esquema típico de una refinería moderna

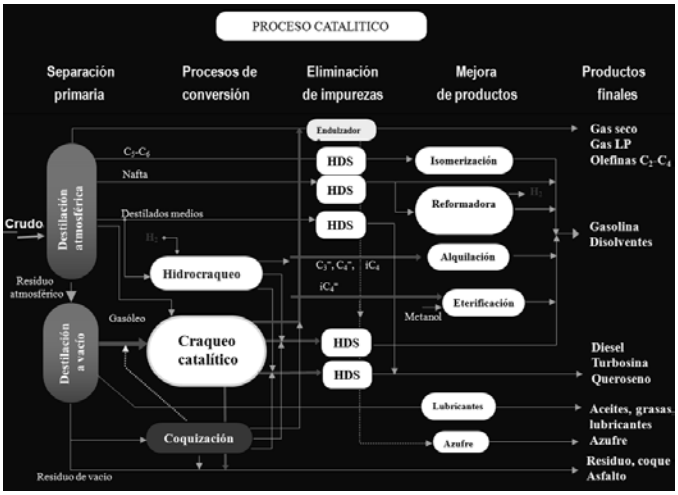

FUENTE: ELABORACIÓN PROPIA.

México demandó un total de petrolíferos de 1,463.7 miles de barriles diarios de petróleo crudo equivalente (mbdpce) a finales del 2012, registrando un aumento del 11.7% con respecto al 2002. Sin embargo la oferta nacional de derivados de petróleo se ubica por debajo de esa cantidad, por lo que las importaciones de petrolíferos presentaron una tasa de crecimiento anual del 9.4% en el periodo comprendido de 2002 a 2012. En 2012, las importaciones de petrolíferos registraron una cifra de 557.5 mbdpce, de esta cifra el principal combustible importado es la gasolina. De acuerdo a información estadística publicada por la Secretaria de Energía con estimaciones de demanda durante el periodo 2012-2027 se señala que las importaciones de gasolinas mostrarán un crecimiento promedio anual de 4.1%. La balanza comercial pasará de 394.5 mbd en 2012 a 534.5 mbd en 2018 y 717.3 mbd en 2027. Es decir, el déficit existente, de manera específica en gasolina, en 2012 continuará en los próximos años debido a la falta de capacidad de refinación: Si en 2012, las importaciones de gasolina representaron 49% de la demanda interna total, para 2018 la expectativa es que esta cifra aumente a un 50.4% y al final del periodo de situé en un 49.7% (véase Figura 3) [6].

Fig. 3. Importaciones de gasolina (2012-2027)

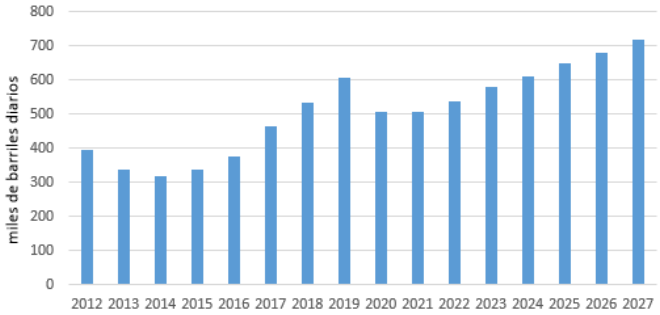

FUENTE: ELABORACIÓN PROPIA, DATOS SECRETARIA DE ENERGÍA 2012 [4]

Cabe señalar que el diagnóstico sobre la situación de PEMEX indica lo siguiente: Pemex-refinación no puede cubrir la demanda de combustibles; los márgenes de refinación, es decir, el ingreso por venta, descontando los costos por materia prima, ha descendido dramáticamente al pasar de 4.24 dólares por barril a 0.01. Según estimaciones de Pemex, la construcción de una refinería le reportaría un negocio con una rentabilidad a precios actuales de por lo menos 13 dólares por barril procesado. Ello permitiría a Pemex-Refinación reducir el gasto de 2 mdd diarios por la importación de combustibles automotrices. Con todo, las importaciones se mantendrían altas [7]. El problema de Pemex es complejo, la solución aún más.

A. Cambiando la visión: Identificando áreas de oportunidad

La industria de la refinación ha estado sujeta a una variedad de factores que han determinado su evolución o que marcan su operación día con día, la introducción de nuevos factores como el ambiental, la productividad y ahora la reforma energética introduce nuevos desafíos que marcarán una nueva tendencia.

A nivel internacional, las refinerías aprovechan los insumos disponibles al máximo y ponen especial énfasis en abatir el costo de la energía que consumen (eficiencia). También aprovechan las oportunidades que ofrece el mercado, procurando producir la mezcla de petrolíferos que más conviene en un momento dado.

En suma, la refinación es un negocio dinámico que premia la excelencia operativa y la eficiencia de los procesos. Cinco

factores sintetizan lo mencionado anteriormente, que son propensos a tener un mayor impacto en la industria de la refinación en un futuro próximo:

1. Costos y rentabilidad
2. Calidad de los combustibles
3. Medio ambiente y cambio climático
4. Crecimiento de la demanda e importación de combustibles
5. Seguridad Operacional

III. Dando los primeros pasos hacia la innovación

Si bien la catálisis ha jugado un papel fundamental durante la segunda mitad del siglo 20 en el desarrollo de las industrias de refinación y petroquímica, su evolución se ha dado en pequeños cambios sobre la misma variante. Por ejemplo, los catalizadores para hidroprocesamiento continúan basándose en las mismas especies activas (Co, Mo, Ni, W) y los avances se han dado en torno a la concentración y dispersión de estas especies, así como en los soportes empleados (ver Tabla III). De igual forma, desde 1964 los catalizadores para FCC se formulan con zeolita faujasita "Y" y aunque ha habido algunos intentos por sustituirla por otros materiales más activos, su facilidad de preparación y bajo costo le confieren una competitividad hasta hoy en día insuperable. De modo tal que las modificaciones han sido básicamente variando su relación Si/Al y tipo de matriz conforme a una aplicación particular, esto es, el concepto de catalizadores formulados a la medida [8].

TABLE III. Composición de los catalizadores empleados en el proceso de refinación.

Reacción	*Catalizadores industriales*
Refinación de petróleo	
Hidroprocesamiento	CoO(2-5%)MoO3(10-20%)P(0-2%)/Al2O3;
(HDS, HDN, HDO, HDM)	NiO(2-6%)MoO3(6-20%)P(0-2%)/Al2O3
Craqueo Catalítico	Zeolita (30-40%) (por ejemplo:REY,REHY,USY,REUSY) + Matriz (por ejemplo: SiO2, Al2O3 y SiO2-Al2O3,) + Aglutinante (por ejemplo: clorhidrol, alúmina peptizada, polisilıcico)+ Aditivos (por ejemplo: P-ZSM-5,Pt, Pd, Sb, Bi, Sn)
Alquilación	H2SO4, HF
Reformadora	Pt(0.30-0.35%)/Yγ-Al2O3; balance PT (0.22-0.35%-Re(0.22-0.35%)/γ- Al2O3; sesgada Pt(0.22-0.28%)-Re(0.42-0.75%)/γ- Al2O3; Pt(0.35%)-Sn(0.30%)/γ- Al2O3,Pt(0.3%)-Ir(0.3%)/γ-Al2O3

Fuente: Elaboración propia con datos IMP

A menos que ocurra un descubrimiento espectacular que revolucione la industria de catalizadores para refinación, es de esperar que el proceso de evolución continuará en base a pequeños cambios o innovaciones que no obstante ello, pueden resultar en importantes beneficios. Por ejemplo, el manejo adecuado y creativo de los catalizadores puede representar incrementos significativos en la producción o ahorros su consumo o en energía en los procesos donde se aplican. En este sentido la innovación juega un papel muy importante en el que pueden intervenir conjuntamente todos los involucrados en los procesos de producción: operadores, analistas, proveedores, mantenimiento, etc. Pues la innovación es un proceso que incluye:

- Mejoras en un proceso mediante el cual las empresas generan productos y procesos nuevos, ahorros de capital, reducción de costos o mejora de la calidad
- La habilidad de manejar el conocimiento creativamente en respuesta a situaciones particulares (o en este caso aspectos relevantes).
- La forma más eficiente en la que una empresa construye ventajas competitivas
- Ideas claras de donde se está y el saber a dónde ir.
- Mejoras en procesos y sistemas, modelos de negocio, productos y cadena de valor.

A. *Matriz de impactos cruzados*

Realizando una matriz de impacto cruzado entre proceso/uso de catalizadores/aspectos relevantes se obtiene el "impacto del uso de catalizadores en el proceso de refinación" (ver Tabla IV) [9].

TABLE IV. Matriz de impacto cruzado para la industria de la refinación vs catalizadores

Aspectos relevantes en la operación del sistema de refinación*	**Proceso**		
	FCC	***HDS***	***Claus***
Rentabilidad	+++	-	-
Calidad de combustibles	+	+++	=
Medio ambiente	+	++	+++
Demanda e importaciones	++	=	=

*Nota: No se adiciono el de seguridad operacional debido a que es más un aspecto de funcionalidad del mismo proceso en conjunto que por la función de los catalizadores

Fuente: Realización propia con datos de expertos del IMP

La Tabla IV, se leería de la siguiente forma:

- Aquellas innovaciones que realicemos en el Proceso FCC impactarán de forma positiva en la calidad de los combustibles y medio ambiente, pero será más que relevante en la rentabilidad del proceso, si se considera que es el proceso donde se produce y cualquier mejora que aumente su rendimiento permitirá incrementar la producción afectando el mercado de combustibles.
- Las mejoras que se realicen en la unidad de HDS permitirán producir mejores combustibles que tienen

un impacto directo con el medio ambiente, sin embargo, estas mejoras no aumenten la rentabilidad del proceso. Por consiguiente la mayoría de los esfuerzos deben direccionarse hacia cambios en la calidad de los combustibles pero sin tener como objetivo primario aumentar la productividad del proceso.

- El proceso Claus de forma genérica impacta en cuestiones ambientales y de seguridad. Durante el procesamiento de crudos se producen altas cantidades de azufre y nitrógeno que incrementan la formación de sulfuro de hidrógeno (H_2S) y amoniaco (NH_3). El proceso Claus, convierte el H_2S presente en el gas ácido y en el NH_3, en azufre elemental (puro) y además el NH_3 se descompone en nitrógeno no-contaminante (N_2) y vapor de agua (H_2O).

Una de las rutas más efectivas para la innovación es hacer la pregunta: ¿por qué no…? y dar una respuesta positiva que pueda implementarse sin mayores dificultades y en el menor tiempo posible. En la dinámica de los procesos de producción siempre hay una gran cantidad de áreas en las que nuevas ideas o enfoques pueden hacerlos más eficientes, para muestra a continuación se dan tres ejemplos.

*B. **Innovando en pequeñas etapas***

Rompiendo paradigmas. Suele ocurrir que los procedimientos y sistemas de trabajo son tan rígidos que prácticamente no permiten aprovechar oportunidades para obtener mejores resultados. Si existe una manera más eficiente o segura de hacer las cosas no hay razón para no ponerla en práctica y modificar o desechar los procedimientos establecidos en términos de conversión y rendimiento de productos. Los procesos son dinámicos y constantemente cambian, sin embargo, los procedimientos no, esto puede conducir a ineficiencias en los procesos. Por ejemplo, si la carga a una unidad FCC incrementa su contenido de metales, digamos en 5 ppm y no se ajusta la tasa de reposición de catalizador, en pocos días se notará una caída de 2 % en la conversión, lo que significa pérdida de productividad. Del mismo modo, es posible que incrementando la tasa de reposición en 1 ton/día, el rendimiento de productos aumente de modo que su valor económico sea mayor al del costo adicional del catalizador.

FUENTE: REALIZACIÓN PROPIA CON DATOS DE EXPERTOS DEL IMP.

Mejorando el manejo de catalizador y la carga a unidades de desintegración catalítica FCC. Cuando en una refinería se tienen dos unidades FCC se puede incrementar la eficiencia de ambas si se segrega y balancea la carga de modo tal que en una unidad se procesen gasóleos ligeros, libres de metales y con menor contenido de contaminantes y en la otra gasóleos ligeros y pesados conforme al balance donde se concentrarías los metales y demás contaminantes. La conversión global aumentaría alrededor de 3 % y los rendimientos de gas LP en 1 % y de gasolina en 2.5 %. El catalizador de equilibrio de la unidad procesando gasóleos ligeros prácticamente no se contaminaría por metales y podría usarse para la unidad que procesa la mezcla de gasóleos ligeros y pesados, ello significaría un ahorro de catalizador alrededor de 35 %. (Figura 5).

Fig. 4. Evaluación de la economía del proceso propuesto

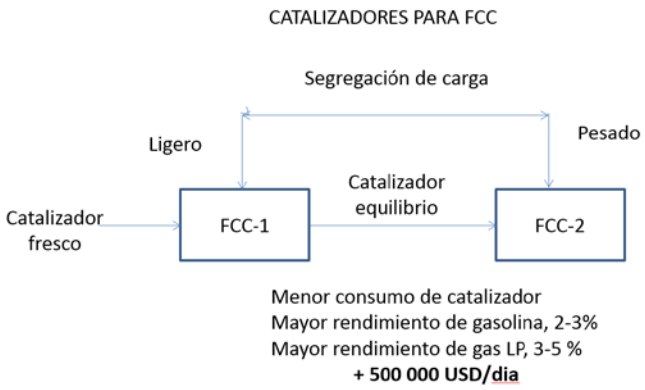

FUENTE: REALIZACIÓN PROPIA CON DATOS DE EXPERTOS DEL IMP.

Reciclando los catalizadores gastados de hidroprocesamiento.

La producción de diesel de ultra bajo azufre (10 ppm) ha acortado significativamente la vida útil de los catalizadores, tienen que ser descargados aun cuando no se han agotado completamente. Generalmente conservan actividad suficiente para ser empleados en otros procesos como el hidroprocesamiento de gasóleos o en las plantas de hidrodesintegración catalítica, donde no se requieren niveles tan altos de hidrodesulfuración. Por ejemplo, si se utilizan en una planta hidrodesintegradora como complemento del catalizador fresco en una proporción 50/50 se podría generar un ahorro de 3,2 MMUSD/año. Con objeto de reducir los gastos que implica el uso de catalizadores, la idea es re-emplear los catalizadores de hidrodesulfuración de naftas y diesel gastados en otra unidad de hidrodesulfuración para la producción de gasóleo. Esto permitirá generar ahorros importantes de aproximadamente 20,000 dólares/día (ver Figura 6).

Fig. 5. Diseño propuesto en el ahorro de catalizador

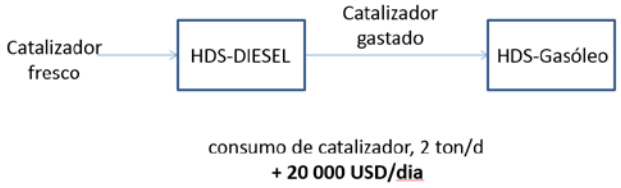

FUENTE: REALIZACIÓN PROPIA CON DATOS DE EXPERTOS DEL IMP

C. Nuevos actores y más innovación

La biomasa y el shale gas/oil se están erigiendo como fuentes alternativas y atractivas de energía, en ambos casos la producción de combustibles a partir de estos dos energéticos requiere el empleo de catalizadores [12].

- Biocombustibles/biomasa

En los últimos años los biocombustibles se han posicionado como una opción para el mercado energético debido principalmente a temas como las preocupaciones de seguridad nacional, y las posibles consecuencias del cambio climático. Además de la producción comercial de biodiesel y etanol base_maíz, la investigación se está centrando cada vez más en el desarrollo de procesos para la producción de combustibles líquidos a partir de biomasa lignocelulósica. Una de las tecnologías emergentes es la pirolisis rápida que produce altos rendimientos de un producto líquido, llamado bio-aceite, que contiene hasta 70% de la energía de la alimentación de biomasa [11]. Sin embargo, ciertas propiedades del bio-aceite, tales como su bajo poder calorífico, volatilidad limitada, alta acidez y la incompatibilidad con los combustibles derivados del petróleo restringen significativamente su aplicación [12]. Las propiedades indeseables del bio-aceite producido vía pirólisis derivan su composición química particularmente su alto contenido de diferentes clases de compuestos orgánicos oxigenados. La eliminación del oxígeno es necesario para transformar el bio-aceite en un combustible líquido que sería ampliamente empleado y económicamente atractivo. Dos tipos de procesos que se han utilizado para eliminar el oxígeno de las moléculas orgánicas son el hidrotratamiento y el craqueo catalítico. El primero utiliza hidrógeno para eliminar el oxígeno en forma de agua mientras que el segundo lleva a cabo la eliminación de oxígeno en la forma de agua y óxidos de carbono utilizando catalizadores zeolíticos. Si bien, los catalizadores actuales de hidroprocesamiento y desintegración catalítica pueden ser aplicados al procesamiento de la biomasa, estos no son precisamente los óptimos y por ello actualmente varias líneas de investigación se centran en innovaciones tendientes al empleo de catalizadores que permitan una producción masiva de bioenergéticos con mayor eficiencia y menor costo.

Así, la transformación catalítica de azúcares a combustibles de hidrocarburos líquidos es un proceso complicado, lo ideal sería combinar la eliminación de oxígeno y el ajuste del peso molecular con una utilización mínima de hidrógeno externa basada en combustibles fósiles. Este objetivo se puede lograr por (i) el uso de catalizadores multifuncionales capaces de llevar a cabo diferentes reacciones en el mismo reactor y (ii) la utilización de una fracción de la materia prima de azúcar como fuente de hidrógeno in situ a través de reacciones de gasificación.

Fig. 6. Proceso de producción de bioenergéticos empleando catalizadores o rutas biologicas

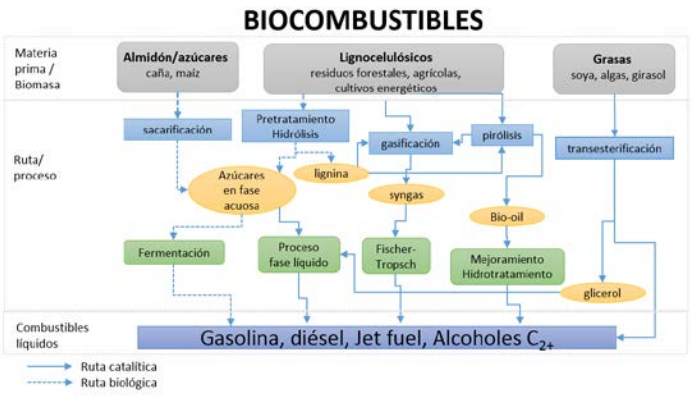

Fuente: Realización propia con datos de expertos del IMP.

Shale gas/oil

Estos nuevos energéticos han cambiado el panorama de la producción del gas natural, líquidos de gas natural y petróleo en Estados Unidos y en breve lo harán a nivel global. Es previsible que los procesos de producción de combustibles y petroquímicos a partir de gas de lutitas (shale gas) crecerá sustancialmente y será necesario el desarrollo de nuevos catalizadores para lograrlo, particularmente para los procesos de producción de combustibles mediante el proceso Fisher-Tropsch y los de síntesis y procesamiento de metanol para producir gasolina y diesel.

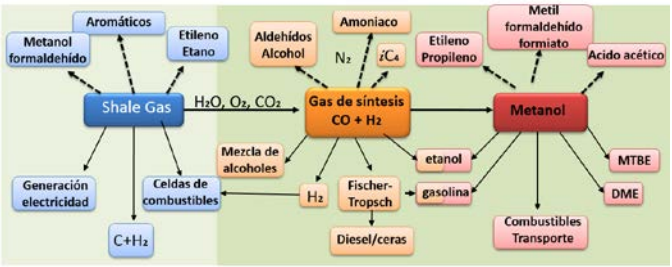

Fuente: Realización propia con datos de expertos del IMP.

Reflexiones

¿Qué papel jugará la catálisis en el siglo 21 ahora que la competitividad de las empresas es fundamental para su permanencia y crecimiento, y que las nuevas tecnologías están naciendo y desarrollándose a ritmos vertiginosos? Sería presuntuoso hacer una predicción a largo plazo, sin embargo, al menos en el corto plazo, se puede decir que la innovación jugará un papel fundamental tanto para mejorar los procesos de producción actuales como para buscar nuevas rutas para aprovechar las nuevas vetas de energía: shale gas y biomasa.

REFERENCIAS

[1] Sociedad Norte Americana de Catálisis.GlobalCatalysis.com, February 2008. Consulta http://nacatsoc.org/above/who-are-we/

[2] Markets&Markets. refinery-catalyst-advanced-technologies-and-global-market-84Consulta Agosto 2014. http://www.marketsandmarkets.com/

[3] Fuel . Global Demand for Catalytic Technology Increases, 2010. Consulta Agosto 2014. http://www.hartfuel.com/f.catalyst.html

[4] EIA International Energy Outlook, 2015, consulta abril 2015. www.eia.doe.gov/oiaf/ieo

[5] BP Statistical Review of World Energy, 2010, consulta noviembre 2014. http://bp.com/statisticalreview,.

[6] Secretaria de Energía. Prospectiva de petróleo y petrólíferos 2013-2027. SENER México 2013.

[7] Pétroleos Mexicanos. Informe de labores 2013. PEMEX, México 2013.

[8] A. Corma. "State of the art and future challenges of zeolites as catalysts". Journal of Catalysis, Vol 216. No. 1-2, pag 298-312, Estados Unidos, 2003.

[9] Universidad Nacional Autonoma de México, Tesis. "*Matriz de Impactos Cruzados*". UNAM. México 2011.

[10] W. Berger. "*A More Beautiful Question: The Power of Inquiry to Spark Breakthrough Ideas*" Editorial Bloomsbury. Estados Unidos, 2014.

[11] T. Werpy y G. Petersen, "*Value Added Chemicals from Biomass, Results of Screening for Potential Candidates from Sugars and Synthesis Gas"*. Departamento de Energía, estados Unidos; consulta nov 2014. http://www.nrel.gov/docs/fy04osti/35523.pdf, accessed September 2010.

[12] D. A. Simonetti y J. A. Dumesic, *Catal. Rev.*, 2009,Vol 51, pag 441. Estados Unidos 2009.

[13] J. C. Serrano-Ruiz, R. M. West y J. A. Dumesic. Revista Chemical Biomoleculas Eng., Vol 1pag 79-83. Estados Unidos 2010.

[14] J. Clerk Maxwell, A Treatise on Electricity and Magnetism, 3rd ed., vol. 2. Oxford: Clarendon, 1892, pp.68–73.

[15] I. S. Jacobs and C. P. Bean, "Fine particles, thin films and exchange anisotropy," in Magnetism, vol. III, G. T. Rado and H. Suhl, Eds. New York: Academic, 1963, pp. 271–350.

[16] K. Elissa, "Title of paper if known," unpublished.

[17] R. Nicole, "Title of paper with only first word capitalized," J. Name Stand. Abbrev., in press.

[18] Y. Yorozu, M. Hirano, K. Oka, and Y. Tagawa, "Electron spectroscopy studies on magneto-optical media and plastic substrate interface," IEEE Transl. J. Magn. Japan, vol. 2, pp. 740–741, August 1987 [Digests 9th Annual Conf. Magnetics Japan, p. 301, 1982].

[19] M. Young, The Technical Writer's Handbook. Mill Valley, CA: University Science, 1989.

Expansor rotatorio de desplazamiento positivo para aprovechamiento de energía presente en el peróxido de hidrógeno

Alejandro González
Centro de Manufactura Avanzada y Logística
Centro de Ingeniería y Desarrollo Industrial
Estado de México, México
alejandro.gonzalez@cidesi.mx

Ricardo Chicurel
Instituto de Ingeniería
Universidad Nacional Autónoma de México
Distrito Federal, México
rchicurelu@iingen.unam.mx

Abstract— El expansor rotatorio (motor) que es objeto del presente trabajo se desarrolló a partir de una máquina de geometría similar, la cual aprovechaba la energía de expansión de vapor para generar movimiento. En el caso del motor actual se han propuesto algunas modificaciones del diseño original con el propósito de mejorar el desempeño de la máquina. Dichas modificaciones se hicieron principalmente a los sistemas de admisión y de expulsión. Así mismo se propuso el aprovechamiento del vapor que se obtiene de la disociación de peróxido de hidrógeno, para lo cual se consideró la implantación de un sistema de dosificación del mismo, que comprende un depósito,una válvula dosificadora de peróxido, una cámara catalizadora, una válvula de admisión para los gases catalizados, así como los mecanismos necesarios para la sincronización de todos los anteriores.

La geometría básica del motor comprende cuatro rotores idénticos cuyos ejes son paralelos y giran sincronizados a la misma velocidad y en el mismo sentido, impulsados por la expansión del gas empleado como fluido de trabajo. Dado el arreglo geométrico de tales rotores, es posible obtener dos impulsos por revolución.

Keywords—Expansor, motor, peróxido, hidrógeno.

I. INTRODUCCIÓN

El encarecimiento y paulatina escasez de combustibles fósiles, así como la necesidad de reducir las emisiones contaminantes que se producen por el uso de los mismos, nos obligue como sociedad a desarrollar mecanismos sociales y técnicos que nos permitan usar de mejor manera los recursos naturales con que contamos. En ese sentido, uno de los objetivos primordiales del desarrollo tecnológico de una nueva máquina, particularmente un motor, debe ser producir una unidad de potencia altamente eficiente y al mismo tiempo buscar opciones viables de fuentes de energía.

El motor que se describe en el presente trabajo busca cumplir con ambas premisas, por una parte la simplicidad de su funcionamiento y el reducido número de partes móviles con que cuenta pueden asegurar una eficiencia mecánica alta y por otra parte, se ha previsto usar peróxido de hidrógeno (H_2O_2) como fuente de energía, para lo cual esta sustancia se hará pasar a través de un catalizador que la disocie en oxígeno (O_2) y vapor (H_2O) en una reacción altamente exotérmica.

El trabajo desarrollado hasta ahora comprende el diseño, fabricación y puesta en marcha de un prototipo que usa aire como fluido de trabajo y que es capaz de emplear los productos de la disociación de peróxido y de manera paralela la investigación de los métodos de producción de esta sustancia y de los dispositivos necesarios para su aprovechamiento.

Este artículo únicamente describe algunas de las partes más importantes y representativas de esta máquina.

II. PRINCIPIO DE OPERACIÓN

El expansor rotatorio (motor) que es objeto del presente trabajo se desarrolló a partir de una máquina similar desarrollada previamente en el Instituto de ingeniería de la UNAM, la cual empleaba vapor como fluido de trabajo.

El prototipo actual incorpora algunas modificaciones sustanciales de diseño con el propósito de mejorar su desempeño. Estas comprenden entre otras: la incorporación de sellos que se alojan en las caras y en las puntas de los rotores para garantizar la estanqueidad de la cámara de trabajo, el uso de una válvula que dosifica el fluido de trabajo, la existencia de puertos de salida para el escape de los gases de la cámara de trabajo, así como todos los dispositivos y mecanismos necesarios para el funcionamiento de todos ellos. Además, al contemplarse el uso de peróxido de hidrógeno como fuente de energía, se han debido diseñar los dispositivos necesarios para su manejo, disociación y dosificación.

La Fig. 1 muestra al motor con una de sus tapas removidas para poder observar sus componentes básicos. En ella se puede apreciar la existencia de cuatro rotores idénticos, cada uno de los cuales cuenta con sellos en sus puntas y en sus caras. Los cuatro rotores giran alrededor de ejes paralelos a la misma

velocidad y en el mismo sentido impulsados por la expansión del gas empleado como fluido de trabajo. Dado el arreglo geométrico de tales rotores, es posible obtener dos impulsos por cada revolución de la flecha de salida.

La Fig. 2 muestra de manera simplificada la secuencia de operación. El instante señalado como (1) corresponde al punto muerto superior y en él el volumen de la cámara es prácticamente cero. En (2) se inicia la admisión del fluido de trabajo a alta presión y alta temperatura. Los momentos resultantes de la aplicación de la presión sobre una parte de las caras de los rotores induce su movimiento y el crecimiento de la cámara de trabajo. La expansión de dicho fluido se extiende entonces hasta el punto (4), cuando al quedar expuestos los ductos de escape (señalados con líneas punteadas) a la cámara de trabajo, empieza la expulsión. Los rotores giran impulsados por su inercia haciendo decrecer la cámara de trabajo y expulsando los gases expandidos hasta el punto 6, donde se inicia un nuevo ciclo de trabajo. Es importante señalar que por cada revolución del motor suceden dos ciclos de trabajo.

III. Sellos.

Como se mencionó previamente, cada rotor está provisto con sellos en las puntas y en las caras que aseguran la estanqueidad de la cámara de trabajo. La geometría de tales sellos y de las superficies sobre las que se asientan permite garantizar el contacto continuo de las partes mencionadas.

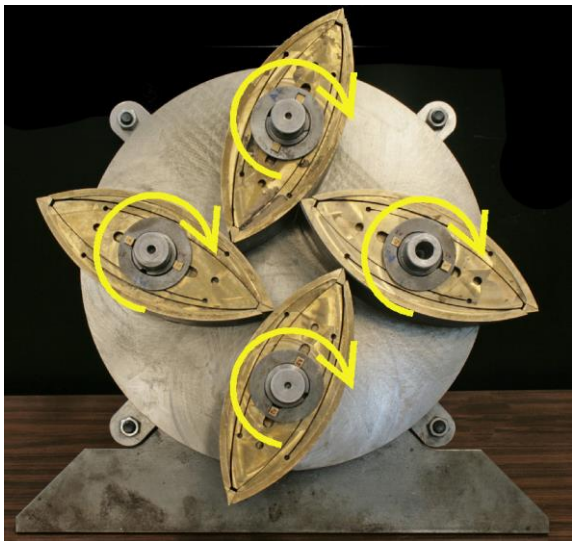

Fig. 1. Interior del prototipo donde se observan los rotores y los sellos.

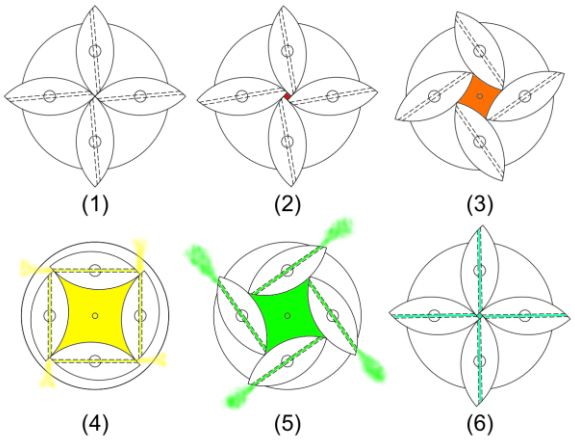

Fig. 2. Secuencia de operación

IV. Válvula balanceada.

Este motor producirá potencia a partir de la expansión de los gases que resultan de la disociación de peróxido de hidrógeno y para dosificarlos dentro de la cámara de trabajo de manera intermitente y en sincronía con el ciclo de la máquina se han incorporado una válvula y un mecanismo de biela-manivela (Fig. 3) que sincroniza la acción del conjunto al mantenerse acoplado permanentemente con el eje de uno de los rotores.
El diseño de la válvula, así como las dimensiones del mecanismo de biela-manivela, controlan la cantidad de fluido que se admite dentro de la cámara de trabajo.

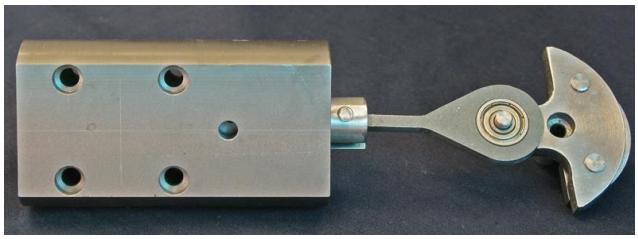

Fig. 3. Válvula balanceada.

V. Sistema desincronización.

Los rotores se sincronizan gracias a la acción de un conjunto de cinco engranes, como lo muestra la Fig. 4. Todos los engranes, son iguales, por lo cual la velocidad angular de la flecha del motor es idéntica, aunque de sentido opuesto a la de cada uno de sus rotores.

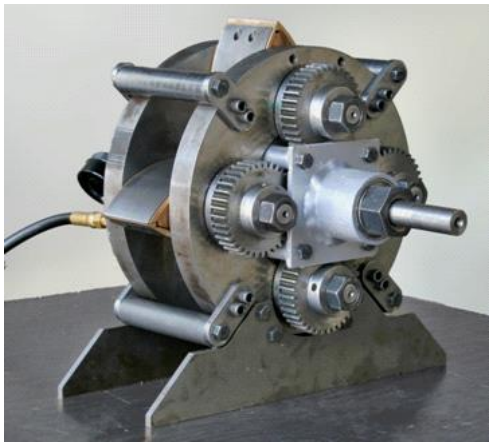

Fig. 4. Sistema de sincronización.

VI. Descripción de las pruebas y ajustes necesarios para la puesta en marcha del motor.

El proceso de puesta en marcha del motor comprendió la revisión del ensamble de los componentes y la interacción existente entre las piezas que componen los mecanismos. Los ajustes y corrección de fallos también se dio en esta etapa.

Las pruebas condujeron a modificaciones posteriores en los sellos de punta y de cara que estuvieron encaminadas a reducir la fricción. Tales modificaciones incluyen el rediseño de la geometría de los mismos y la selección de materiales nuevos. En ambos casos se remplazó el material original por una mezcla de politetrafluoroetileno y grafito con resultados preliminares satisfactorios.

Durante la ejecución de estas pruebas se instaló el prototipo de la válvula de admisión (incluida la cámara catalítica) y se hicieron las pruebas que permitieron poner en marcha por primera vez al motor.

VII. Determinación de las pérdidas por fricción debidas a los sellos de punta y de cara.

Las pérdidas de potencia más importantes son aquéllas generadas por la fricción que existe entre los sellos (de punta y de cara) y las superficies sobre las que actúan. Tales pérdidas pueden calcularse de manera teórica, sin embargo, dada su importancia se realizaron experimentos que permitieran caracterizarla con mayor precisión. Ref [2].

El experimento consistió en montar el motor en una máquina fresadora con control de velocidad empleando como acoplamiento un dispositivo mediante el cual es posible medir la magnitud de los momentos que se generan por la fricción existente entre los sellos y las superficies sobre las que se deslizan (figura 6.3).

Con el propósito de evitar el efecto de bombeo del motor mientras se realizaron las pruebas, se removió uno de los rotores y también los sellos correspondientes a dos de los rotores remanentes, de manera que sólo mantuvo su integridad aquel rotor que se localizaba en la posición opuesta a la del removido. Después, se desinstaló el resto de los sellos y se midió nuevamente la magnitud de las pérdidas, las cuales corresponden a aquéllas debidas a los engranes y los rodamientos del motor. Una vez realizadas ambas pruebas, se puede restar el resultado de la segunda a la primera para entonces obtener el valor correspondiente a las pérdidas del conjunto de sellos de un rotor. Tal valor se multiplica por cuatro y se tiene entonces el valor de las pérdidas debidas a todos los sellos instalados en los rotores.

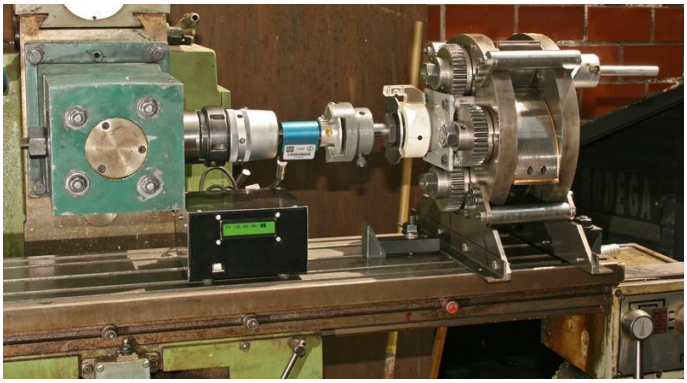

Fig. 5. Montaje del motor para medir las pérdidas por fricción.

Los valores de los momentos obtenidos en las mediciones se multiplican por la velocidad y se obtiene entonces el valor de las pérdidas de potencia para cada caso.

Las pérdidas totales debidas a la fricción de los sellos se muestran en la tabla 1 comparadas con aquellas obtenidas teóricamente para un valor del coeficiente de fricción de 0.2.

Tabla 1. Comparación de las pérdidas de potencia teóricas y experimentales.

Velocidad angular [rpm]	**Pérdida de potencia teórica (μ=0.2)**	**Pérdida de potencia obtenida experimentalmente [W]**
61.5	12.39	9.78
85	17.16	14.24
114	23.10	19.10
159	32.48	27.97
219	45.39	43.11
295	62.67	66.72
394	87.25	95.72
542	129.93	133.94

La gráfica de la figura 6.4 muestra los resultados de la tabla anterior.

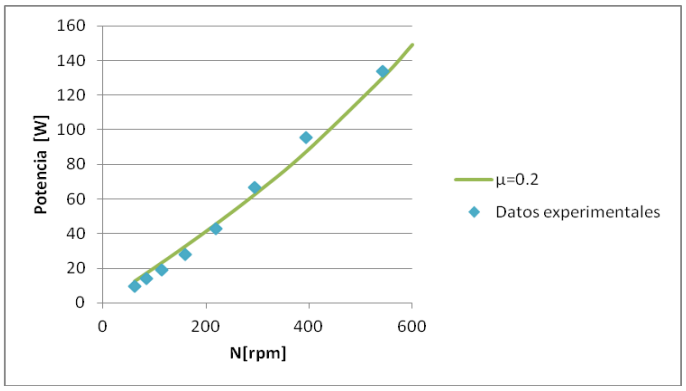

Fig. 6. Comparación de los datos de pérdidas teóricas y experimentales

Como puede notarse en la gráfica y tabla anteriores, los datos experimentales concuerdan con una buena aproximación con aquéllos obtenidos de manera teórica para un valor del coeficiente de fricción de 0.2.

VIII. 6.3. Pruebas realizadas para evaluar las fugas en la válvula de admisión.

La válvula de admisión debe mantener cierta hermeticidad que elimine, en la medida de lo posible, el escape del fluido de trabajo hacia la atmósfera sin haber pasado por la cámara de expansión. Además, el hecho de garantizar tal hermeticidad, permite también asegurar el máximo aprovechamiento posible de la energía asociada con las condiciones del fluido de trabajo.

Se realizaron pruebas a la válvula con el fin de evaluar la magnitud de las fugas presente en ella, lo cual condujo al rediseño de la misma para incluir la instalación de los sellos que se alojan adjuntos al puerto de salida de la válvula. Es importante señalar que estas pruebas se hicieron usando aire como fluido de trabajo.

El gasto de aire del motor se midió a distintos regímenes de velocidad en el dispositivo mostrado en la Fig. 7. De este modo se identificaron fugas que más tarde han sido atacadas mediante rediseño de distintas partes de la válvula de admisión y de los sellos.

IX. Conclusiones.

El trabajo experimental realizado para evaluar el desempeño general del motor y de sus partes ha permitido proponer modificaciones de diseño que lo han hecho evolucionar de manera constante, sin embargo es posible asegurar que se encuentra aún en una etapa muy temprana de su desarrollo.

El trabajo que actualmente se realiza para hacerlo trabajar con peróxido de hidrógeno parece marchar en una dirección prometedora y se contempla proponer mecanismos y procedimientos para producir peróxido en alta concentración y de manera segura, sin embargo este trabajo también merece más trabajo.

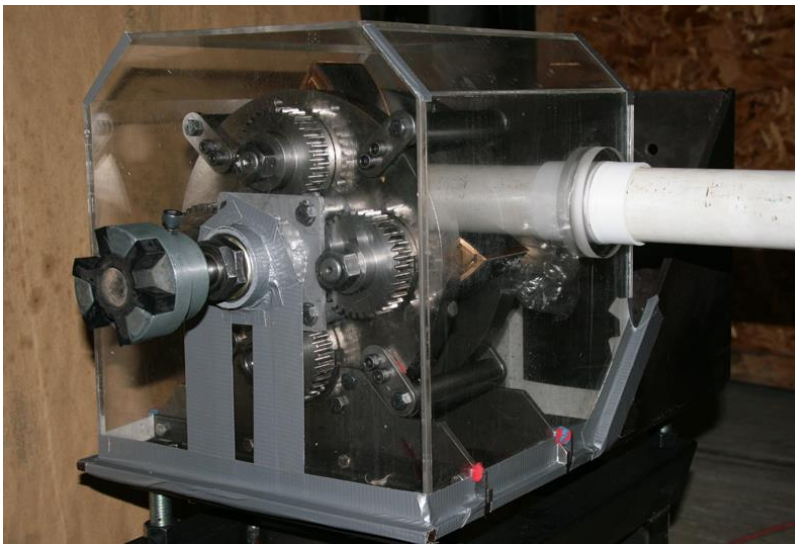

Fig. 7. Medición del gasto del motor.

Reconocimientos

Se reconoce la importante participación labor y patrocinio del Ing. Ernesto Terrazas de la empresa Electro Industrias Delta para la realización de este trabajo. Así mismo se reconoce la importante colaboración de la M. I. Isabel Rodríguez y del Dr. Enrique Naranjo quienes aportaron importantes ideas y observaciones.

Referencias

[1] Robinson, F. J. , “Performance Test on the RL-1 Trochoidal Expander”, Proceedings Fourteenth Intersociety Energy Conversion Engineering Conference”, Boston, Mass., Aug., 1979, pp. 1991- 1997.

[2] Chicurel, R., "Development of a Novel Rotary Engine", Proceedings Eleventh Intersociety Energy Conversion Engineering Conference, , Stateline, Nevada, pp. 73-79, sept. 1976.

[3] Chicurel, R., "Rotary Expander for a Solar Thermo Mechanical Conversion System", Proc. Silver Jubilee Congress International Solar Energy Soc., Atlanta, May-June, 1979, pp 1507-1510.

[4] Homan, W. A., “Rotary Engine”, U.S. patent no. 1,349,882, Aug., 1920.

[5] Hopkins, M. S., “Rotary Engine”, U.S. patent no. 2,097,881, Nov., 1937.

[6] Wise, R. H., and Walters, J. D., “Rotary Pump”, U.S. patent no. 3,234,888, Feb., 1966.

[7] Campbell, Jr., D. K., “Positive Displacement Internal Combustion Engine”, U.S. patent no. 3, 439,654, April, 1969.

[8] Zniszczynski, A., “Displacement Machines with Four Parallel Synchronous Rotors”, Mechanism and Machine Theory v.44, n. 9, 2009, pp. 1677-1688.

[9] Chicurel, R., González, A., Terrazas, E., Naranjo, J., “Sealing System for a Rotary Expander”, Mechanism and Machine Theory, v. 45, n. 9, September 2010, Pages 1357-1366

[10] González, A, Chicurel, R., Terrazas, E., Rodríguez, M. I., “Rotary Expander for Operation with Waste or Solar Derived Heat”, 13th World Congress in Mechanism and Machine Science, Guanajuato, México, 19-25 June, 2011.

Efecto de la temperatura y concentración en el coeficiente de partición de un trazador orgánico.

J. S. Martínez-Muñoz, B. E. Herrera-Gallardo, M. M. González-Brambila, C.R. Tapia-Medina, H. Puebla-Nuñez, J. A. Colín-Luna*.

Departamento de Energía
Universidad Autónoma Metropolitana-Azcapotzalco
D.F., México
*jacl@correo.azc.uam.mx

***Abstract*— En el presente trabajo se determinó el coeficiente de partición del acetato de etilo en una mezcla de agua y petróleo crudo en el rango de temperatura de 283–323 K utilizando el método shake flask. Los resultados mostraron que el reparto del acetato de etilo en el hidrocarburo aumenta de manera directa con la temperatura y disminuye inversamente con la concentración inicial de acetato de etilo en la solución. En base a estos datos, se propone un modelo matemático para la estimación del coeficiente de partición del acetato de etilo en estos disolventes. La representación matemática para la estimación de ésta propiedad serviría para la determinación de crudo remanente a través de la inyección del acetato como trazador en yacimientos naturalmente fracturados.**

Keywords—Coeficiente de partición, Trazador Químico, Yacimiento Naturalmente Fracturado, Pruebas de trazador de pozo simple.

I. INTRODUCCIÓN

En la industria petrolera, el coeficiente de partición es esencial para la estimación de la saturación de crudo remanente en yacimientos agotados utilizando pruebas de trazador de pozo simple. En estas pruebas, la diferencia en los coeficientes de partición de dos trazadores inyectados en el yacimiento causa un retraso en el tiempo de salida de los trazadores después de un periodo de residencia adecuado para la separación de ambos [1]. Esto dependerá de las propiedades de la sustancia inyectada como trazador.

El coeficiente de partición K o coeficiente de reparto, es la razón de distribución de una sustancia en una mezcla de dos disolventes inmiscibles entre ellos e indica el carácter de afinidad de la sustancia hacia un disolvente en particular debido a sus propiedades de polaridad [2].

La ley de Nernst explica la distribución de un soluto entre dos disolventes inmiscibles entre ellos y afirma que una determinada cantidad de soluto se reparte entre dos disolventes hasta alcanzar un estado de equilibrio en el que el potencial químico como la fugacidad del soluto sea el mismo en ambas fases de la mezcla. El coeficiente de partición está dado por

$$K_{OA} = C_{Orgánica} / C_{Acuosa} \quad (1)$$

Donde $C_{organica}$ y C_{acuosa} representan la concentración del soluto en cada fase. El coeficiente es adimensional y para valores altos usualmente se reporta en forma logarítmica base diez.

En el presente documento se reporta el coeficiente de partición del acetato de etilo en petróleo crudo y agua, evaluado de manera experimental empleando el método *shake flask* [3] a diferentes temperaturas y concentraciones iniciales, a condiciones de presión atmosférica. Estos resultados experimentales fueron ajustados a un modelo matemático en función de la temperatura y de la concentración inicial de acetato de etilo en la solución.

II. METODOLOGIA

A. Materiales.

Se utilizó acetato de etilo (99.9% pureza, Baker, Avantor Performance Materials, México) y agua desionizada (Ultrapura Tipo 1, Direct-Q 3UV) para preparar las soluciones. El hidrocarburo fue proporcionado por el Instituto Mexicano del Petróleo (Sitio Grande, Pozo 81, 24.2°API, pH 6.62). La Fig. 1 muestra el espectro IR del hidrocarburo empleado en este estudio. Los reactivos se mantuvieron cerrados y almacenados en frascos ámbar a temperatura ambiente.

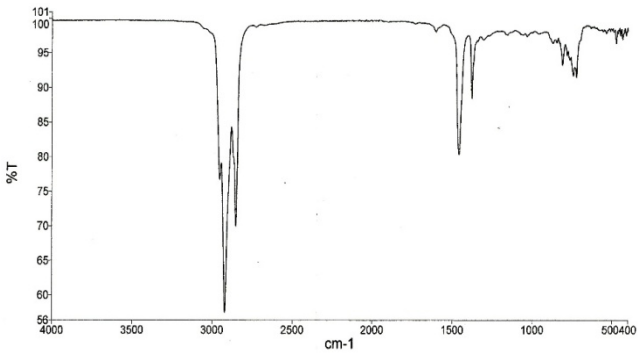

Fig. 1. Espectro IR del hidrocarburo crudo proveniente de Sitio Grande, México. 24.2°API.

B. *Análisis cuantitativo por IR.*

La cuantificación se realizó en un espectrofotómetro de infrarrojo marca PerkinElmer modelo Frontier FT-IR, módulo ATR universal (Diamante/KRS-5, ventanas de KBr). Los espectros se leyeron con cuatro barridos a 0.2 cm/s, en un rango de 1500 a 1000 cm^{-1}.

C. *Procedimiento.*

Se preparó una solución de acetato de etilo y agua, en concentración de 30 g/L. A partir de esta solución se prepararon estándares en el rango de 2.0 a 30 g/L, utilizando los espectros IR de cada estándar se construyó una curva de calibración considerando la altura del pico, correspondiente al acetato de etilo, en la longitud de onda 1380 cm^{-1}.

En matraces Erlenmeyer de 25mL se agregaron 3mL de petróleo y se colocaron en un baño de calentamiento hasta alcanzar la temperatura correspondiente. Se prepararon seis soluciones de acetato de etilo y se midieron las concentraciones correspondientes. Se agregaron 3mL de cada solución a los sistemas precalentados. Durante 5 min se agitó vigorosamente cada sistema procurando una mezcla homogénea. Los sistemas se mantuvieron en reposo durante 5 min para la separación de las fases. De la fase acuosa se extrajo una muestra de 1 mL de la cual se obtuvo el espectro correspondiente. Se estimó la cantidad de acetato de etilo en las muestras utilizando la curva de calibración realizada previamente.

El valor de la concentración de acetato de etilo en el crudo corresponde a la diferencia de la concentración inicial C_0, menos la concentración de la muestra. El valor de K_{OA} se obtuvo a partir de (1)

III. Resultados y Discusión

A. *Resultados experimentales*

Los coeficientes de partición para el acetato de etilo en la mezcla agua y crudo, y el comportamiento a diversas temperaturas se muestran en la Fig. 2.

Se observa que, en el rango de temperatura de las mediciones, el coeficiente de partición disminuye con el aumento en la concentración inicial de la solución a temperatura constante. Por otro lado, los coeficientes de partición aumentan con el incremento de la temperatura. Este fenómeno puede ser explicado por las interacciones dependientes de la temperatura que actúan entre el acetato de etilo en agua y crudo. La temperatura modifica el comportamiento de reparto, elevando la cantidad de soluto disuelto en el crudo. Este patrón se repite conforme aumenta la temperatura y es ocasionado por el incremento en la solubilidad del acetato de etilo en el crudo. Los datos experimentales se ajustaron a una tendencia lineal cuya tendencia es del orden de 0.83 a 0.95.

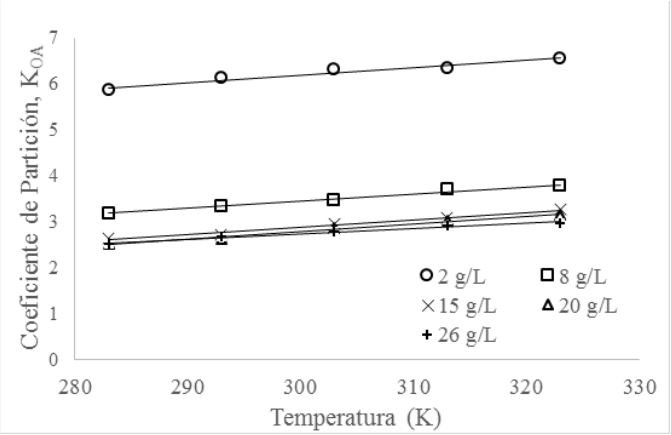

Fig. 2. Coeficiente de partición del acetato de etilo en agua y crudo, en función de la temperatura y concentración inicial.

B. *Resultados teoricos*

De acuerdo al comportamiento del coeficiente de partición descrito en la Fig. 2, se propone la ecuación (2) para la estimación de la partición del acetato de etilo en el crudo de estudio. Esta ecuación depende directamente de la temperatura (K) e inversamente a la concentración inicial (g/L) de acetato de etilo. Los valores para *a* y *b* se obtienen de la estimación lineal de K_{OA}/T con respecto a $1/C_0$.

$$K_{OA}/T = aT + b/C_0 \quad (2)$$

Los valores para las constantes a y b se obtuvieron a partir de los datos experimentales mostrados en Tabla 1. Para *a* se obtuvo un valor de 0.008178 K^{-1} y *b* corresponde a 0.024982 L/gK. La Tabla 1 muestra la comparación entre los valores experimentales y los estimados con (2). El error relativo absoluto es de 2.20%.

TABLA I. Comparación entre valores de coeficientes de partición experimentales y estimados con (2). C_0, concentración inicial de trazador en la solución.

C_0 (g/L)		283 K	293 K	303 K	313 K	323 K
2.0	Exp.	5.865	6.139	6.326	6.354	6.563
	Est.	5.849	6.056	6.263	6.469	6.676
	Err.	0.27	1.36	1.00	1.81	1.73
8.0	Exp.	3.182	3.350	3.467	3.719	3.781
	Est.	3.198	3.311	3.424	3.537	3.650
	Err.	0.49	1.16	1.24	4.90	3.46
15.0	Exp.	15.0	2.720	2.961	3.089	3.265
	Est.	2.786	2.884	2.983	3.081	3.179
	Err.	4.80	6.03	0.73	0.25	2.63
20.0	Exp.	20.0	2.634	2.874	3.018	3.150
	Est.	2.668	2.762	2.856	2.951	3.045
	Err.	5.69	4.88	0.61	2.23	3.33
26.0	Exp.	26.0	2.674	2.784	2.930	2.976
	Est.	2.586	2.678	2.769	2.860	2.952
	Err.	2.59	0.15	0.53	2.39	0.80

Err. = Desviación (%)

C. *Aplicación a condiciones de yacimiento*

Las condiciones de temperatura en el yacimiento son cercanas a los 423 K [4], mientras que la cantidad de trazador óptimo para pruebas de pozo simple se encuentra en el rango de 0.01 a 10 g/L [5]. Empleando estas condiciones en el modelo desarrollado se encontró que el valor de K_{OA} es de 4.50, cercano al valor experimental de 4.65 [1]. Por otro lado, se ha reportado un valor de K_{OA} para el acetato de etilo de 3.65 medido a 310K y 7g/L de concentración de trazador [6], a estas condiciones el valor calculado con el modelo propuesto es de 3.64. Las diferencias entre estos valores pueden atribuirse a la naturaleza del crudo en estudio.

IV. Conclusiones

En este trabajo se determinó de manera experimental el coeficiente de partición del acetato de etilo en una mezcla de agua y petróleo crudo, proveniente de un yacimiento mexicano. De acuerdo a los resultados se concluye que el coeficiente de partición del acetato de etilo entre agua y crudo es función de la temperatura y de la cantidad inicial de acetato de etilo presente en la solución.

Adicionalmente, se determinó que el comportamiento de reparto del acetato de etilo indica una capacidad aceptable para actuar como trazador líquido en la cuantificación de crudo, suponiendo que las condiciones de temperatura sean mayores a la ambiental y por debajo del punto de ebullición del trazador.

La ecuación de estimación propuesta muestra una habilidad de predicción satisfactoria, en el rango de temperaturas de estudio. El valor estimado a condiciones de temperatura de yacimiento muestra un acercamiento aceptable al reportado, por lo tanto, el modelo propuesto se puede utilizar para calcular los valores de partición conforme a las condiciones de las pruebas in situ.

Agradecimientos

Al apoyo otorgado por los colegas del Laboratorio de Análisis de Procesos de la Universidad Autónoma Metropolitana Azcapotzalco.

Referencias

[1] Serres-Piole C., Preud'homme H., Moradi-Tehrani N., Allanic C., Jullia H., Lobinski R., "Water tracers in oilfield applications: Guidelines" Journal of Petroleum Science and Engineering, 98-99, 22-39, 2012.

[2] Leo A., Hansch C., Elkins D., "Partition coefficients and their uses", Chem. Rev., 71, 525-616, 1971.

[3] OECD guideline for the testing of chemicals, Partition coefficient (n-octanol-water): Shake Flask Method. Guideline 117, 1995.

[4] Tomish J.F., Dalton R.L., Deans H.A., Shallenberg L.K., "Single-well tracer method to measure residual oil saturation", J. Pet. Technol., 25, 211-218, 1973.

[5] Keller T.E., Linda Y., Method for Determining Fluid Saturations in Petroleum Reservoirs, Publication no 312 814, 1972.

[6] Deans H.A., Carlisle C. T., "The Single-Well Chemical Tracer Test - A Method For Measuring Reservoir Fluid Saturations In Situ", Petroleum Engineering Handbook, Larry W. Lake, Editor, SPE, Volume V, Reservoir Engineering and Petrophysics, pp 615-649, 2007.

Evaluation of the content of hydrolysable sugars in silage supplement processes

Villa-Ramírez M.S.*, Ruíz-Font Angélica, Trejo-Estrada S.R.

Centro de Investigación en Biotecnología Aplicada – Instituto Politécnico Nacional.
San Juan Molino s/n, Km 1.5 carretera Tepetitla - Tecuexcomac, Tepetitla de Lardizábal, Tlaxcala C.P. 90600. Phones: +52-5557296000 ext 87812, Fax 012484870766.
convenios22@hotmail.com , sugeyrol@hotmail.com.

***Abstract*— Silage is forage conservation process that it have how objective, it to be used for animal food, in this process of fermentation of grasses, is produced lactic acid and different components that generate top features in the grasses, making them more palatable in the palate of the animals, exist many changes during this process, for example, it generate different types of microorganisms lactics and exist a decrease in pH below 5, due to the metabolism, that is generated for present microorganisms. This Process, allows maintain the nutritional qualities of the original grass much better than other processes of conservation of grasses. The main objective of the research was to improve, the forages used in animal feed, by organic additives and microorganisms with probiotic activity, the microorganisms were selected and isolated from the fermented sap of Agave atrovirens sp.**

The present study set out to design silages corn and sorghum, supplemented with molasses, and fermented Agave sap (pulque) this was pasteurized and additioned with and lactic microorganisms with probiotic activity for this research, was made 10 different types of micro-silage and was took sample at 0, 1, 2, 3, 7, 15, 25, 30 days was evaluated fiber raw, pH, sugars reducing and physical characteristics (organoleptic properties) of smell, color, texture, fragmenting of the silages and its content of sugars reducing. The best silage was with sorghum additioned with molasses, pulque and anaerobic probiotic microorganisms, this silage, showed better characteristics of smell, color, texture and fragmentation. And the results of biochemical studies showed higher amount of crude fiber, Reducing sugars, pH similar to that reported in studies carried out in other researchs.

Keywords—silage, probiotic microorganisms, lactic fermentation

I. INTRODUCTION

The main objective of this research was to improve, the forages used in animal feed, by addition with organic additives and microorganisms with probiotic activity, the microorganisms were selected and isolated from the fermented sap of Agave atrovirens.

The present study set out to design silage supplemented with molasses and fermented Agave sap (pulque) pasteurized and microorganisms probiotic activity. The purpose was not only conservation but generate fodder with features that allow more efficient digestion of animals that consume them (De la Roza et al., 2005; Vieira da Cunha, 2009)

For this analysis, there were 10 different types of micro-silage were sampled at 0, 1, 2, 3, 7, 15, 25, 30 days, studies were conducted during the evaluation period were: fiber raw, pH, ARD and organoleptic characteristics. The best silage was held with molasses-pulque-and probiotic microorganisms.

II. ANTECEDENTS

The main problem currently faced by farmers, is due to the use of antibiotics or chemotherapeutics in ruminant feed. Bacteria with probiotic activity exist, which have been used and act through more efficient digestion, and stimulate the immune response, reducing the use of antibiotics and hormones (Cañete y Sancha, 1998).

Proper conservation and management of fodder for livestock feed is a tool that allows you to store plant materials for prolonged periods, this process requires an adequate management of anaerobic conditions for successful conservation and use (Garcés et al., 2006).

A good material must meet the following requirements: be finely chopped into pieces of 2-4 cm, have a high proportion of grain, show not present fungi o mustiness, this must have sour smell (nice), olive brown coloration, present between 60 and 70% moisture and have a good taste (sweet and sour) for cattle to consume (Dairy Cattle, 1972).

The ultimate silage quality depends heavily on the types of materials that are used for silage and the silage proper technique. Among the factors that can produce variations in raw material in relation to the content of sugars, it can include cutting height , the humidity , the particle size, the porosity of the forage mass, the rate of photosynthesis (Paziani , 2004) , resistance to compaction (Jobim, 2007) and the fermentative quality , determined by the concentration of organic acids , pH and ammonia nitrogen. In general, in the environment the grass have a 6-8% concentration of soluble carbohydrates and dry matter content of about 32-35 % that constitute a suitable raw material for silage (Santana, 2004; Vieira da Cunha, 2009).

At the discretion of some authors , some studies that have been done indicate that using lactic bacterial inoculants, as Lactobacillus, Pediococcus, Streptococcus,in fermentacion of silage processes, it will can increase production in the animals that the consume such as: amount and / or milk composition , better body condition gain liveweight and reproductive parameters. Phipps et al. en 2000 observed that the corn silage treated with microbial additives improves production milk cows. Similarly, O'Doherty et al., in 1997, He demonstrated that the corn silage inoculated with microorganisms respond similarly to grass silage quality in pregnant ewes . In tropical grasses These additives improve quality and reduce losses fermentation for silage (Mulbach , 2001).

II. METHODOLOGY

For the silages processes, they were made 10 different treatments, taking 500 g of sterile straw, and added a percentage of 30% surcharge on the weight of the sample, the supplements were molasses (esterile), pulque (pasteurized) and aerobic and anaerobic microorganisms. Silages were added as follows:
for silage with 1 supplement, the process of silage was supplemented with molasses and /or applied pulque in relation of 30% (supplement: material), molasses was sterilized at 15 psi in autoclave and the pulque was pasteurized.

For silage with 2 supplements, in the silage process, is additioned pulque and molasses in proportion of15% molasses and 15% of pasteurized pulque (Relation, supplement: material).

For silage with 3 supplements to process was additioned with molasses, pulque and aerobic and / or anaerobic microorganisms, in where was added 14% molasses, 14% of pulque pasteurized and 2% of microorganisms (were using, 2 different types of lactic microorganisms, aerobic and anaerobic the microorganisms was additioned, in different treatments).

The microorganisms used, it was isolated of Agave sap fermented, this microorganism were identified and preserved in REVCO to -80ºC and plated in LB medium for its use in silage

III. RESULTS

The results shown for pH, in silage 30 days, indicate that there is greater variation in pH at the end of the process of silage of for samples corn silage, than sorghum samples (see Table 2).

Table 2.- pH comparative results of 0-30 days of silage used several treatments ensilage in samples of sorghum and corn forages.

Treatment	Ensilage types	pH time 0 days sorghum	pH time 0 days corn	pH time 30 days sorghum	pH time 30 days corn
1	molasses	4.94	4.21	4.71	4.25
2	Molasses + pulque	4.4	4.21	4.4	4.05
3	Molasses + pulque + microorganisms aerobic	5.29	4.3	5.29	3.95
4	Molasses + pulque + microorganisms anaerobic	5.5	4.19	5.5	3.78
5	Molasses + microorganisms aerobic	5.26	4.13	5.26	4.01
6	Molasses + microorganisms anaerobic	5.65	4.2	5.65	4.1
7	pulque	5.37	4.5	5.37	4.35
8	Pulque + microorganisms aerobic	6.39	4.23	6.39	4.15
9	Pulque + microorganisms anaerobic	5.06	4.13	5.06	4.035
10	*control*	7.92	3.5	7.92	4.95

The Addition of anaerobes of pulque, and allows a reduction of pH, to finished process of silage. The treatment was considered adequate was pulque + molasses + anaerobes. (see Table 1 and Graphic 1).

Table 1.- pH results of several treatments ensilage in samples of forage sorghum

treatment	Ensilage types	pH time 0 days	pH time 30 days
1	molasses	4.94	4.71
2	Molasses+pulque	4.4	4.53
3	Molasses+pulque+microorganisms aerobic	5.29	5.7
4	Molasses+pulque+microorganisms anaerobic	5.5	5.95
5	Molasses+ microorganisms aerobic	5.26	4.82
6	Molasses+ microorganisms anaaerobic	5.65	4.51
7	Pulque	5.37	6.81
8	Pulque+ microorganisms aerobic	6.39	6.72
9	Pulque+ microorganisms aerobic	5.06	5.87
10	control	7.92	6.13
Total 10 treatments		Inicial ensilage	Final silage

Results: comparative Data 0- 30 days.

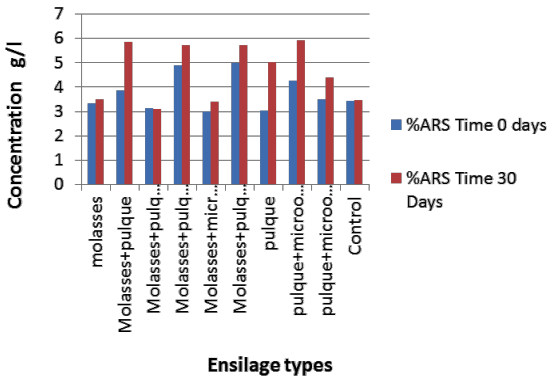

Table 4.- Direct Reducing Sugars (ARS) results of several treatments ensilage in samples of forage sorghum

Ensilage types	%ARS 0 days	%ARS 30 days
Molasses	3.32	3.51
Molasses+ pulque	3.86	5.87
Molasses+ pulque+ microorganisms aerobic	3.13	3.10
Molasses+ pulque+ microorganisms anaerobic	4.89	5.71
Molasses+ microorganisms aerobic	3.01	3.41
Molasses+ microorganisms anaaerobic	5.01	5.71
Pulque	3.05	5.02
Pulque+ microorganisms aerobic	4.26	4.38
Pulque+ microorganisms aerobic	3.51	5.91
control	3.42	3.47

technique used: Miller, 1958 porcentages calculated gram/liter

In all treatments as an additive where pulque, crude fiber content increased 30% compared with the other treatments, and 35% compared to the control treatment at the beginning and end of the silage. (see Table 3).

Table 3.- crude fiber percentage in different treatments of ensilage sorghum valued at 0,15 and 30 days

Ensilage types	% Crude fiber Time 0 days	% Crude fiber Time 15 days	% Crude fiber Time 30 days
Molasses	60	60	70
Molasses+pulque	60	70	70
Molasses+pulque+ microorganisms aerobic	60	60	60
Molasses+pulque+ microorganisms anaerobic	**70**	**70**	**70**
Molasses+ microorganisms aerobic	60	60	70
Molasses+ microorganisms anaerobic	**70**	**70**	**70**
Pulque	60	60	70
Pulque+ microorganisms aerobic	**70**	**70**	**70**
Pulque+ microorganisms anarobic	**70**	**70**	**70**
Control	50	50	50

method of Kjeldahl crude fiber determination

For Sugars Reducing,The treatments which are added as a supplement pulque and anaerobes sugar reducing content increased by 58.26% compared to treatments with molasses. (See Table 4 and Graphic 2).

Graphic 2.- % ARS results of several treatments in forage sorghum

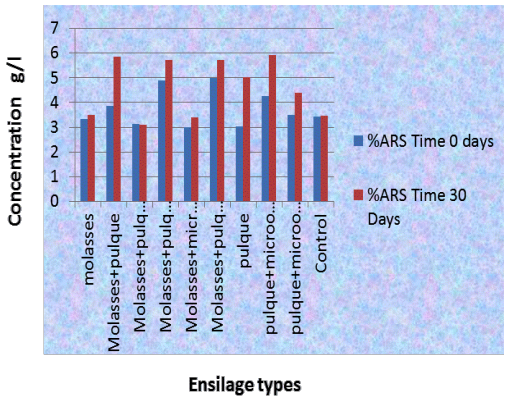

IV. CONCLUSIONS

The molasses are commonly used as a dietary supplement in forage, however, this study allows us to diversify the use of agave sap, as a supplement, because of the high content of lactic acid bacteria with probiotic activity.

The fermented sap analysis showed higher yields of ARS, and higher crude fiber content, compared with molasses.

Microorganisms allowed to conduct a proper process of silage are mostly anaerobic type.

The appropriate use of supplements during ensiling and control of microorganisms are key to the development of food fodder, enabling efficient digestion and to reduce the use of antibiotics and hormones in livestock that produce problems associated diseases.

V. REFERENCES

Clarke.M.A.,Roberts .J.E..(1999) composition the soluble indigennous polysacharydes from sugar cane. Int. Sugar Journal. Review.

Cornack, K.M. 1995. Increasing milk constituent yield through fibre supplementation of winter pastures in the subtropics. M. Agric. Sci. Thesis, University of Queensland

Cowan, R.T., Kerr, D.V., & Davison, T.M. 1991. Maize silage for dairy systems in northern Australia. p. 228-235, *in:* J. Moran (ed) *Maize in Australia - Food, Forage and Grain*. Incitec.

Fulkerson, W.J., & Michell, P. 1985. Effect of level of utilisation of pasture in spring on pasture composition in summer and on milk production in spring and summer. p. 66-67, *in: The challenge: Efficient Dairy Production.* Proc. Austr. New Zeal. Dairy Prod. Conf., Albury-Wodonga, ASAP/NZSAP.

Fulkerson, W.J., & Michell, P. 1985. Effect of level of utilisation of pasture in spring on pasture composition in summer and on milk production in spring and summer. p. 66-67, *in: The challenge: Efficient Dairy Production.* Proc. Austr. New Zeal. Dairy Prod. Conf., Albury-Wodonga, ASAP/NZSAP.

O'Kiely, P., & Muck, R.E. 1998. Grass silage. p. 223-251, *in:* J.H. Cherney& D.J.R. Cherney (eds) *Grass for dairy cattle.* CAB International.

Implementación y Control de un Ruteador de DC

Erick Mauricio Pérez Hernández
Instituto Politécnico Nacional, SEPI-ESIME Culhuacán
erick.perezhdez@gmail.com
Octavio Aguado Sánchez
Instituto Politécnico Nacional, SEPI-ESIME Culhuacán
octavio.oas@gmail.com

Domingo de Jesus Cortes Rodríguez
Instituto Politécnico Nacional, SEPI-ESIME Culhuacán
domingo.cortes@gmail.com

Resumen— **En este artículo se presenta el desarrollo experimental de un ruteador de energía de dc para dos fuentes. Un ruteador de energía es un dispositivo que suministra un voltaje constante a una carga a partir de dos fuentes de energía distintas. El origen del ruteador de energía surge del hecho de aprovechar las energías renovables de manera cooperativa bajo variaciones de carga y suministro ya que el ruteador es capaz de obtener energía de dos fuentes en proporciones distintas. En este artículo se presenta un prototipo de ruteador de 50 watts. El ruteador se compone de una etapa de potencia la cual consiste en un par de puentes 'H' conectados en paralelo, una etapa de filtrado que es un filtro de tipo LC pasa bajas, una etapa de medición la cual se encarga de tomar los valores de corriente que suministra cada fuente de energía así como el voltaje en la carga y una etapa de acoplamiento y control la cual recibe y acondiciona las lecturas de corriente y voltaje que utiliza el algoritmo de control.**

El objetivo consiste en mantener un voltaje constante a la salida del ruteador bajo variaciones de carga y suministro, en el primer caso (variaciones de carga) se propone un control por corriente, en el caso de variaciones de suministro el ruteador es capaz de tomar energía de dos fuentes en distintas proporciones.

Palabras clave—Ruteador; energía; Corriente directa; Fuentes renovables

I. INTRODUCCION

Los sistemas de ruteo de energía son requeridos en aquellos lugares en donde es posible obtener energía de diferentes maneras, estas suelen ser energías renovables; de la misma manera estos sistemas son pensados como alternativa para reducir el consumo de energía proveniente del tendido eléctrico, en general la versatilidad de un ruteador de energía nos permite darle una aplicación en diversas circunstancias ya sea en sistemas tipo isla o en lugares alimentados por una red eléctrica.

La idea general de un ruteador de energía es a partir de diferentes fuentes ejemplo: baterías, paneles solares, generadores eólicos, celdas de hidrogeno, suministro de compañía eléctrica, etc. Proveer una cantidad de energía constante a una carga esta puede tratarse de un alumbrado, un motor, cualquier electrodoméstico, una resistencia, etc.
Las aplicaciones de un ruteador de energía pueden ser variadas algunos ejemplos de estas son [1], [2]:

- Alumbrado publico
- Electrificación en viviendas.
- Vehículos.
- Aplicaciones agrarias.
- Entre otros.

Debido al auge de las energías limpias se han diseñado alternativas para a diversificación de la alimentación de los sistemas electrónicos por lo surge la idea de convertidor multipuerto el cual consiste en una etapa entre la carga y varios suministros de energía algunas topologías de convertidores multipuerto son [7], [8], [9]:

- Convertidor cd-cd de doble entrada una salida:
- Convertidor multientrada bidireccional
- Convertidor buck de dos entradas
- Convertidor buck-boost multipuerto

Para la implementación del ruteador de energía primero obtendremos un modelo del sistema a partir de una topología, una vez que se obtengan las ecuaciones del sistema se procederá a diseñar un sistema de control apropiado que permita el rechazo de perturbaciones, se generara una simulación para poder ajustar los parámetros de diseño y finalmente se presentaran los resultados obtenidos en el laboratorio.

II. MODELADO DE TOPOLOGIA DE RUTEADOR

A continuación se presenta el diagrama esquemático del ruteador de energía propuesto [3]:

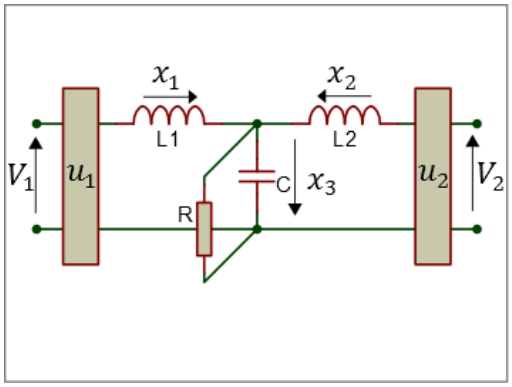

Fig. 1

Donde u_1 y $u_2 \ni \{0,1\}$ (para el caso de un ruteador de dc); considerando las dos posibilidades de los interruptores u se tiene el siguiente sistema de ecuaciones:

$$\dot{x}_1 = \frac{u_1 v_1 - x_3}{L1} \quad (1)$$

$$\dot{x}_2 = \frac{u_2 v_2 - x_3}{L2} \quad (2)$$

$$\dot{x}_3 = \frac{x_1 + x_2}{C} - \frac{x_3}{RC} \quad (3)$$

Como se puede observar se trata de un sistema no lineal con tres estados: x_1 (corriente en el inductor 1), x_2 (corriente en el inductor 2) y x_3 (voltaje en el capacitor).
Donde el voltaje en el capacitor c es el voltaje aplicado a la carga, dicho esto es necesario precisar que la idea es mantener una tensión constante sobre el capacitor (x_3) y que además x_3 solo es posible modificarlo por medio de x_1 y x_2 que son las corrientes de entrada que a su vez son reguladas por medio de u_1 y u_2.

III. CONTROL DE RUTEADOR DE ENERGIA

Para comenzar con el diseño de control de ruteador de energía planteamos el objetivo de control el cual consiste en llevar el estado x_3 a un valor deseado.

$$x_3 \rightarrow x_{3d} \quad (4)$$

El sistema de control es la clave para poder lograr el objetivo de control y en general este tipo de controladores utilizan una técnica de modulación por ancho de pulsos (PWM) para conmutar a los interruptores. Existen dos métodos principales para generar la señal PWM: el control en modo de voltaje y el control en modo de corriente.

El control en modo de voltaje fue el primero en implementarse, la señal que permite la conmutación de los interruptores se produce cuando se hace pasar un voltaje de control a la entrada de un generador PWM. El ciclo de trabajo de la señal PWM es proporcional al voltaje de control V_c y determina el porcentaje de tiempo durante el cual el elemento de conmutación conduce, el voltaje de control en este caso es la diferencia entre el voltaje medido y el voltaje deseado ($x_3 - x_{3d}$) mejor conocido como error de voltaje. Las desventajas de este control por voltaje tales como una respuesta lenta a variaciones de carga y que la ganancia del bucle varia con el voltaje de entrada, lo cual motivan al uso del control por corriente.

El control por corriente añade un segundo lazo de control capaz de realimentar la corriente del inductor con lo cual se puede corregir la respuesta lenta del control por voltaje debido a que la corriente del inductor se eleva con una pendiente determinada por la diferencia de los voltajes de entrada y salida y por lo tanto responde inmediatamente a los cambios de voltaje de línea o carga. Adicionalmente este control exhibe un mayor ancho de banda en ganancia si se compara con un dispositivo de control en modo de voltaje.

Una vez que se ha establecido el objetivo de control ($x_3 \rightarrow x_{3d}$) donde x_{3d} es una constante, se diseñara un control por corriente para cada fuente (V_1 y V_2).

La corriente que suministra cada fuente está dada por:

$$I_{V_1} = u_1 x_1$$
$$I_{V_2} = u_2 x_2$$

Por lo tanto la potencia en cada fuente es:

$$P_{V_1} = V_1 (u_1 x_1)$$
$$P_{V_2} = V_2 (u_2 x_2)$$

Así mismo la potencia en la carga es:

$$P_R = V_R I_R = x_3\left(\frac{x_3}{R}\right) = \frac{x_3^2}{R} \quad (5)$$

La potencia en la carga deberá ser suministrada por V_1 y V_2 , de esta manera se define a α_1 y α_2 como el porcentaje de energía que aportara cada fuente por lo que: $\alpha_1 + \alpha_2 = 1$ con lo cual se puede reescribir la potencia de cada fuente como:

$$P_{V_1} = V_1(u_1 x_1) \rightarrow \alpha_1 P_R \quad (6)$$
$$P_{V_2} = V_2(u_2 x_2) \rightarrow \alpha_2 P_R \quad (7)$$

En [6] se demostró que la topología de la figura 5 puede funcionar como ruteador de energía por lo tanto:

$$x_1 = \alpha_1 \frac{x_3}{R} \quad (8)$$
$$x_2 = \alpha_2 \frac{x_3}{R} \quad (9)$$

A continuación asimilamos la ecuación (3) a un sistema lineal de primer orden de la forma: $\dot{z} = az + bv$ quedando:

$$\dot{x_3} = -\frac{1}{RC}(x_3) + \frac{1}{c}(x_1 + x_2) \quad (10)$$

Con: $a = -\frac{1}{RC}$ $b = \frac{1}{c}$ $v = x_1 + x_2$

Asimilando a (10) como un sistema lineal de primer orden se puede implementar un controlador de tipo PI quedando el control v como:

$$v = K_p(x_{3d} - x_3) + K_i \int_0^t (x_{3d} - x_3)\, dt \quad (11)$$

Donde $x_{3d} - x_3$ es el error de voltaje e_v y $v = x_{1d} + x_{2d}$ es la corriente necesaria para que $x_3 \rightarrow x_{3d}$, entonces a partir de (8) y (9):

$$v = (\alpha_1 + \alpha_2)\left(K_p e_v + K_i \int_0^t e_v\, dt\right) \quad (12)$$

Ya que $\alpha_1 + \alpha_2 = 1$

Una vez calculado el valor de corriente deseado obtenemos la corriente que debe aportar cada fuente σ_i de la siguiente manera:

$$\sigma_i = x_i - x_{id} \quad (13)$$

O bien:

$$\sigma_i = x_i - \alpha_i\left(K_p e_v + K_i \int_0^t e_v\, dt\right) \quad (14)$$

Por lo que la ley de control para los interruptores [4], [5] u_1, u_2 (figura 5) se expresa como:

$$u_i = \begin{cases} 1, & \sigma_i < 0 \\ 0, & \sigma_i > 0 \end{cases} \quad (15)$$

Para $i = \{1,2\}$

IV. SIMULACION DE CONTROLDE RUTEADOR DE ENERGIA

Apoyados en Matlab Simulink Se realizó una simulación del sistema con los siguientes parámetros:

V_o	12 V_{cd}
$L1$	316μH
$L2$	316μH
C	20μF
$R1$	33Ω
$R2$	66Ω
V_1	24 V_{cd}
V_2	24 V_{cd}
α_1	0.4
α_2	0.6

El diagrama de control se muestra a continuación el cual incluye un variador de alfa y un variador de carga.

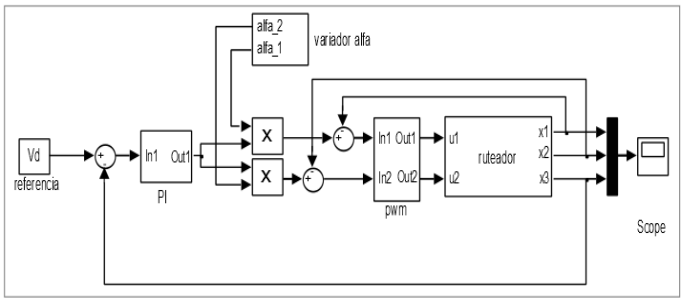

Fig. 2

Se calculan las ganancias K_p y K_i para el controlador PI con las técnicas clásicas de control, quedando: $K_p = 0.3730$ y $K_i = 3730$.

La simulación se realizó durante un tiempo de 0.003 segundos, se modifica el valor de $\propto$ de 0.4 a 0.6 a los 0.013 segundos y se varia el valor de R de 30 a 15 ohms cada 5 milisegundos. El resultado se observa en la figura 3 con voltaje de salida (x_3) y las corrientes que aporta cada una de las fuentes (x_1 y x_2)

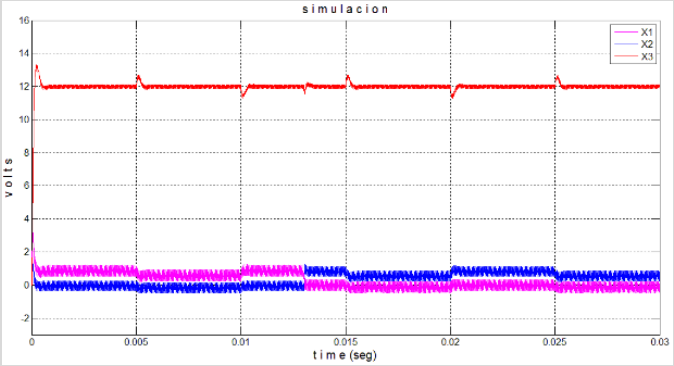

Fig. 3

V. RESULTADOS EXPERIMENTALES

La implementación del control del ruteador de energía se realiza en un microcontrolador de la serie k64 de la marca freescale (120 MHz) se diseña un PWM a una frecuencia de 20khz y se utilizan tres convertidores analógico digital para medir las corrientes x_2 y x_2 así como el voltaje en la carga x_3.

En la construcción del prototipo se deben mencionar algunas observaciones técnicas principalmente para evitar problemas causados por el ruido electromagnético, las más importantes a considerar son:

- Aislar las señales de control de las señales de potencia.
- Para obtener mejores resultados utilizamos un capacitor de polipropileno (conocidos como capacitores de película) a la salida del ruteador.
- La frecuencia de conmutación de los interruptores se hace por encima de los 20Khz para evitar el rango audible.
- Las fuentes que alimenta a los interruptores deberá llevar un capacitor de un valor sugerido de 100uF, este capacitor deberá estar lo más cercano a los transistores del puente.
- El arreglo LC de salida se diseña a una frecuencia de corte 1 década por debajo de la frecuencia de conmutación.

En el primer experimento se establece un voltaje de referencia de 14 V, seguido de un cambio de $\propto$ de 0.4 a 0.6 cada 2 segundos. Se observa la gráfica de voltaje de salida (cursor 1), y las corrientes subministradas por V_1 y V_2 (cursor 2 y 3 respectivamente).

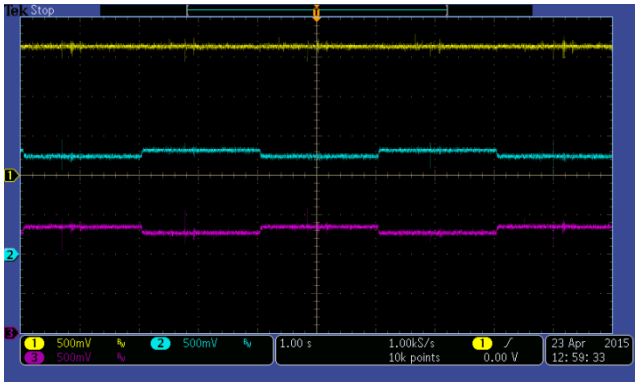

Fig. 4

En el segundo experimento (figura 5) se fijaron los valores de $\alpha_1 = 0.4$ y $\propto_2 = 0.6$ y se modificaron los valores de R de 33 a 16.5 cada 0.2 segundos, se observan las gráficas de corriente (cursor 2 y 3) y voltaje (cursor 1).

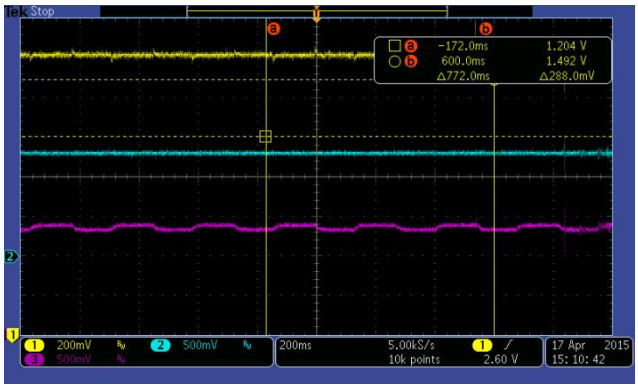

Fig. 5

En la figura 6 se observan las perturbaciones del voltaje de salida generadas por la variación de R sin embargo el controlador inmediatamente lleva el voltaje de salida a su valor deseado.

Finalmente se modifican α y R simultáneamente (figura 7), observamos que el sistema logra el rechazo de perturbaciones en α y R.

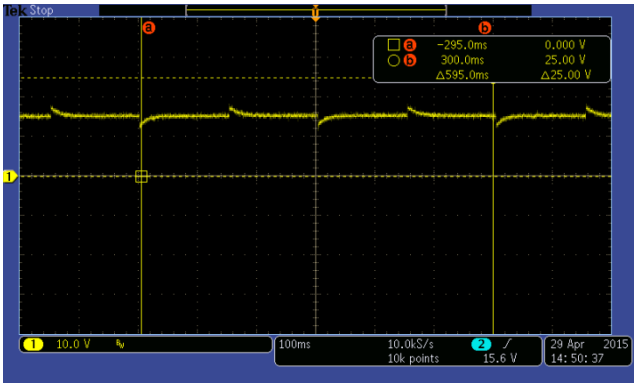

Fig. 6

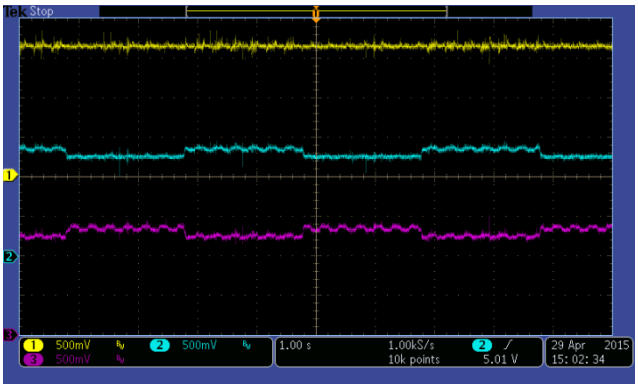

Fig. 7

VI. CONCLUSIONES

De este trabajo se puede concluir lo siguiente:

- es posible utilizar la topología presentada en este trabajo con 'n' cantidad de fuentes de energía de tal manera que: $\alpha_1 + \alpha_2 + \cdots + \alpha_n = 1$.
- Si los interruptores u_1 y u_2 cambian el rango de operación de {-1, 1} y de acuerdo al modelo del sistema es posible obtener referencias de voltajes negativos.
- Una extensión del ruteador de corriente directa seria el diseño de un ruteador en corriente alterna aplicando la idea de modificar el rango de los interruptores {-1,1} y hacer que $V_d \rightarrow Asen(\omega t)$.
- Si se aumenta la velocidad de conmutación de los transistores el comportamiento del sistema y principalmente del controlador se asemejara al diseño propuesto.

AGRADECIMIENTOS

Este artículo fue apoyado parcialmente por la secretaría de Ciencia, Tecnología e Innovación del Distrito Federal bajo el proyecto ICYTDF-198-2012.

REFERENCIAS

[1] R. Dufo Lopez, J.L. Bernal Agustín, F. Mendoza. "Diseño yanálisis económico de los sistemas PV-viento híbridos conectados a la red parala producción intermitente de hidrógeno." Energy policy, Vol. 37, No.8, Pag. 3082 (Agosto 2009).

[2] O. Beltrán, R. Barbosa, B. Escobar, J. Pacheco, Y. Verde. "Análisis y propuesta de un protocolo para la gestión de la energía de un sistema híbrido Eólico-Solar-Hidrógeno". Conr. int. ing. electrón. mem. Eléctro 2011, vol. 33, pp. 222-227 Chihuahua, Chih. México.

[3] Sánchez-Squella, A.; Ortega, R.; Griño, R.; Malo, S., "Dynamic Energy Router," Control Systems, IEEE , vol.30, no.6, pp.72,80, Dec. 2010 doi:10.1109/MCS.2010.938096

[4] Middlebrook R. D. (1989) "Modeling current-programmed buck and boost regulators". IEEE Trans. on Power Electronics, 4MI. Rolando Carrera (1):36–52

[5] Liu Yan-Fei, Sen, P.C. (1994) "A general unified large signal model for current programmed DC-to-DC converters" IEEE Transactions on Power Electronics, Volume:9 , Issue: 4

[6] D. Navarro, I. Macias, D. Cortes "Multi-input converters implemented as electric energy router".

[7] Ding, Guanyu Kwasinski, Alexis "Digital constant on-time controlled Multiple-input buck and buck-boost converters" Applied Power Electronics Conference and Exposition (APEC), 2013 Twenty-Eighth Annual IEEE , vol., no., pp.1376,1382, 17-21 March 2013 doi: 10.1109/APEC.2013.6520479

[8] Farjah, E.; Rezaee, S. ; Ghanbari, T."Sliding mode control of a novel multi-input split-inductor Buck-Boost converter" Electrical & Computer Engineering (CCECE), 2012 25th IEEE Canadian Conference on, vol., no., pp.1,4, April 29 2012-May 2 2012 doi:

10.1109/CCECE.2012.6334820

[9] Seung H. Choung and Alexis Kwasinski "Multiple-input DC-D converter topologies comparison" Industrial Electronics, 2008. IECON 2008. 34th Annual Conference of IEEE

Estudio de parámetros de transporte de masa y cinéticos de un trazador químico utilizado en la recuperación de aceites remanentes en yacimientos de petróleo

Martha Otero-López, Margarita M. González Brambila
Universidad Autónoma Metropolitana-Azcapotzalco,
Departamento de Energía,
Avenida San Pablo No. 180. Colonia Reynosa
Tamaulipas, México D.F. CP 02200.

Carlos O. Castillo Araiza
Universidad Autónoma Metropolitana-Iztapalapa,
Departamento de Ingeniería de Procesos e Hidráulica, San Rafael Atlixco No. 186, Col. Vicentina, Iztapalapa, México, D.F. CP 09340.

Jetzabeth Ramírez Sabag
Instituto Mexicano del Petróleo, Eje Central Lázaro Cárdenas 152, San Bartolo Atepehuacan, Gustavo A. Madero, México, D.F. CP 07730.

marthaot@gmail.com

***Resumen*- El acetato de etilo es utilizado en la industria petrolera como trazador químico. Los parámetros de transporte de masa, tales como: adsorción y partición así como la cinética química del trazador son importantes para entender y modelar el sistema roca-fluido de un yacimiento petrolero. El fluido que conduce el trazador químico dentro del pozo petrolero se denomina agua de formación, esta agua tiene un alto contenido en sales. En este trabajo se realizó el estudio del acetato de etilo en agua de formación para determinar los coeficientes de partición, adsorción y parámetros cinéticos. Los productos de reacción (ácido acético y etanol), así como el acetato de etilo se identificaron y cuantificaron por Cromatografía de Líquidos de Alta Resolución (HPLC) con detector de índice de refracción**

Palabras clave: trazador químico, cinética química, cromatografía de líquidos de alta resolución.

***Abstract*- The ethyl acetate has been used in the oil industry as chemical tracer. The mass transport parameters, such as adsorption and partition and chemical kinetics are important for understanding and modeling the rock-fluid system of an oil field. Driving fluid into the tracer chemical is denominated connate water; this water has a high salt content. In this work, we present the study of ethyl acetate in formation water was performed to determine the partition coefficients, adsorption and kinetic parameters. The reaction products and the ethyl acetate has been identified and quantified by high performance liquid chromatography (HPLC) with index refraction detection.**

Keywords: chemical tracer, chemical kinetics, cromatography liquid high resolution.

I. INTRODUCCIÓN

En la actualidad, el petróleo es la principal fuente de energía en el mundo. Se encuentra en trampas geológicas naturales denominadas yacimientos. Estas trampas son formaciones porosas y permeables constituidas principalmente por arenas, areniscas, calizas o dolomitas [1]. Un porcentaje alto de yacimientos (petrolíferos y geotérmicos) se encuentran en sistemas naturalmente fracturados [2, 3 y 4].

Los yacimientos de petróleo poseen características diferentes que varían de uno a otro; lo que significa que no existen dos yacimientos que se comporten exactamente de la misma manera y los fluidos que contienen están sujetos a la acción de fuerzas naturales que afectan su movimiento a través del medio poroso.

La vida de un yacimiento comienza con la exploración que conduce a su descubrimiento, el cual es seguido por la delimitación del yacimiento, desarrollo del campo, producción (primaria, secundaria y terciaria) y finalmente su abandono [5].

Existen una gran cantidad de yacimientos en etapa de abandono en el mundo. Debido al elevado número a nivel mundial de estos yacimientos, la industria petrolera se enfrenta al reto de estimar la saturación de aceite residual en yacimientos y evaluar la conveniencia de implementar proyectos de recuperación mejorada [5, 6]. Por lo que existe

un interés importante en caracterizar yacimientos naturalmente fracturados y desarrollar conocimiento acerca del flujo y saturación del aceite en el yacimiento

Existen herramientas denominadas pruebas de trazadores que ayudan al estudio de los mecanismos de transporte de masa que se llevan a cabo en un yacimiento naturalmente fracturado para su mejor entendimiento.
Dentro de una prueba de trazadores de un solo pozo, se realiza la inyección de un trazador (que es un compuesto que debe ser soluble, conservativo, no experimentar adsorción importante en el sólido y debe ser fácilmente cuantificable [5,6]) y se monitorea a la salida del yacimiento en función del tiempo. Las variaciones espaciales y temporales del trazador proporcionan información acerca del medio a través del cual fluye. Por lo tanto, uno de los propósitos de una prueba de trazadores consiste en determinar la dinámica de flujo y permeabilidad de una sustancia en un medio poroso [7].

A la fecha se han reportado muchos estudios utilizando pruebas de trazadores para poder describir los mecanismos de trasporte de masa dentro de un yacimiento naturalmente fracturado, sin embargo estos estudios consideran la adsorción y/o la partición pero no se tiene conocimiento de un estudio que considere la adsorción, la partición y la cinética química del trazador [8, 9, 10, 11 y 12].

En este trabajo se determinaron de forma independiente la adsorción, la partición y la cinética química del sistema roca-aceite-fluido, con el objetivo de desarrollar un modelo matemático que describa el comportamiento de un trazador químico en un prototipo de un YNF.

El trazador químico estudiado es el acetato de etilo y sus productos de reacción (ácido acético y etanol).

II. MARCO TEÓRICO

1) Cinética química

La velocidad de reacción se define como la variación de la concentración de reactivos o productos que toman parte en la rección, con el tiempo. En una reacción del tipo:

$$a\,A + b\,B \rightarrow c\,C + d\,D \qquad (1)$$

La velocidad de reacción se puede expresar de la siguiente forma:

$$-\frac{d[A]}{dt}; -\frac{d[B]}{dt}; \frac{d[C]}{dt}; \frac{d[D]}{dt} \qquad (2)$$

El signo negativo indica que la concentración de los reactivos disminuye con el tiempo. Para que la velocidad de reacción sea independiente del componente usado para definirla, se debe tener e cuenta su coeficiente estequimétrico. De esta manera, es posible definir una única velocidad de reacción, teniendo en cuenta la estequiometria de la reacción, por:

$$v = -\frac{1}{a}\frac{d[A]}{dt} = -\frac{1}{b}\frac{d[B]}{dt} = \frac{1}{c}\frac{d[C]}{dt} = \frac{1}{d}\frac{d[D]}{dt} \qquad (3)$$

A partir de observaciones experimentales, Arrhenius estableció la dependencia que la constante de velocidad específica de una reacción tiene con la temperatura:

$$k = Ae^{-\frac{E_a}{RT}} \qquad (4)$$

En esta expresión **k** es la constante de velocidad específica, **A** el denominado factor de frecuencia, $\mathbf{E_a}$ la energía de activación, **R** la constante de los gases y **T** la temperatura expresada en grados Kelvin [13]. De conformidad con la ecuación de Arrhenius, la velocidad de reacción aumenta exponencialmente con la temperatura.

2) Partición

La Ley de Nernst explica la distribución de un soluto entre dos disolventes inmiscibles entre ellos y afirma que una determinada cantidad de soluto se reparte entre dos disolventes hasta alcanzar un estado de equilibrio en el que le potencial químico como la fugacidad del soluto sea el mismo en ambas fases de la mezcla. Comúnmente se ha utilizado octanol como fase orgánica en la determinación del coeficiente de partición para compuestos de interés farmacéutico [14], puesto que modela las regiones hidrófobas de sistemas biológicos. Por lo tanto, el coeficiente de partición está dado por:

$$P_{OW} = \frac{C_{octanol}}{C_{agua}} \qquad (5)$$

Donde $\mathbf{C_{octanol}}$ y $\mathbf{C_{agua}}$ representan la concentración del soluto en cada fase. El coeficiente es adimensional y usualmente es reportado en su forma logarítmica en base diez.

3) Adsorción

La adsorción de una sustancia de una fase líquida sobre la superficie de un sólido implica la distribución de esa sustancia entre las dos fases en equilibrio. Esta distribución generalmente se describe expresando la cantidad de sustancia adsorbida por unidad de masa de adsorbente, q, como una función de la concentración del adsorbato en el fluido, C. Esta relación depende considerablemente de la temperatura del sistema, por ello se obtiene a temperatura constante y se denomina “Isoterma de Adsorción” [13 y 15]. La isoterma de adsorción es una característica intrínseca de un sistema de adsorción adsorbente-adsorbato concreto.

La cantidad adsorbida se puede obtener experimentalmente poniendo en contacto el sólido y el líquido en la relación deseada y se deja que se alcance el equilibrio. La cantidad de adsorbato que pasa a la fase sólida se obtendrá mediante un sencillo balance, conociendo las cantidades de adsorbato iniciales y finales para cada relación, como indica la ecuación

$$q = \frac{(C_0 - C).V.\rho}{m} \quad (6)$$

Donde:
C es la concentración final de adsorbato en el líquido, en mg/kg;
C_0 es la concentración inicial, en mg/kg;
V es el volumen de trazador, en L
ρ es la densidad del trazador, en kg/L;
m es la masa de roca, en g; y
q es la cantidad adsorbida, en mg de soluto / mg de adsorbente.

III. Parte Experimental

A. *Equipo*

La cuantificación del acetato de etilo se realizó mediante la técnica de cromatografía de líquidos de alta resolución (HPLC) con detector de índice de refracción. Utilizando una columna Hiplex-H 100 mm x 8 micras, flujo de 0.8 mL/min, fase móvil 0.005 M H2SO4, volumen de inyección 10 µL.

Se utilizó un reactor con volumen de 1 L, para controlar la temperatura se utilizó un baño con serpentín de circulación marca Cole-Palmer modelo 12108-00, así como también se monitoreo el pH con un potenciómetro marca OAKTON modelo PC-700.

Los disolventes utilizados fueron metanol (CH_3OH grado HPLC, J.T. Baker, 99.9%), ácido sulfúrico (H_2SO_4, J.T. Baker, 99.8%), agua (H_2O, desionizada, resistividad 18,2MΩ·cm). El acetato de etilo utilizado fue grado reactivo analítico (J.T. Baker, 99.9%).

Las soluciones estándar para las curvas de calibración y las soluciones de acetato de etilo utilizadas se prepararon con agua de formación sintética que tiene la siguiente composición que se muestra en la tabla 1:

TABLA 1. Composición del agua de formación sintética.

	Agua sintética propuesta
	moles/L
Cationes	
Na^+	1.729
Ca^+	0.027
Fe^{2+}	0.0003
Mg^+	0.004
Aniones	
SO_4^{2-}	0.004
Cl^-	1.738
HCO_3^-	0.018

Las soluciones estándar y las muestras fueron filtradas a través de acrodiscos GHP (0.45 µm). Los reactivos se pesaron en una balanza analítica marca OHAUS modelo Adventurer.

B. *Metodología*

1) *Cinética química*

Los estudios cinéticos se llevaron a cabo en un reactor de 1L a volumen constante y agitación magnética vigorosa. Estos estudios se realizaron a tres diferentes pH.

A pH = 1.1 se prepararon soluciones de 25 g/L de acetato de etilo y se aforaron con agua de formación sintética, se adicionó HCl a 0.28 M. Se controló la temperatura a 25°C. La reacción se monitoreó cada 10 minutos hasta los 190 minutos y después se dejó hasta las 24 horas para observar si existía algún cambio significativo.

A pH de 12.3 se prepararon soluciones de 25 g/L de acetato de etilo y se aforaron con agua de formación sintética, se le agregó NaOH (0.28 M). Se controló la temperatura a 25°C. La reacción se monitoreó cada 10 minutos hasta los 90 minutos, se dejó hasta las 24 horas para observa r si existía algún cambio significativo.

A pH de 7.1 se prepararon soluciones de 25 g/L de acetato de etilo y se aforaron con agua de formación sintética. Se controló la temperatura a 25°C. La reacción se monitoreo durante 90 minutos.

2) *Partición*

Se prepararon disoluciones de acetato de etilo con agua de formación sintética en el intervalo de 2.5 a 30 g/L, para construir la curva de calibración.

Se prepararon soluciones de concentración 8, 10, 15, 20 y 25 g/L. Posteriormente, en viales de fondo cónico y tapón de 15 mL se agregaron 5 mL de aceite (proporcionado por el Instituto Mexicano del Petróleo, IMP) se le agregan 5 mL de solución. Se cierra el vial y se agita a 300 rpm durante 90 minutos en un agitador Thermo Scientific modelo MAXQ 4450 a temperatura controlada de 25ºC. Los viales se dejan en reposo 24 horas más para favorecer la separación de fases; se muestreo la fase acuosa y se realiza

el análisis en el cromatógrafo de líquidos. El valor de P se obtuvo con el cociente de la resta de concentración inicial menos la concentración de la fase acuosa después del procedimiento, dividida entra la concentración inicial.

3) Adsorción

Para obtener las isotermas de adsorción se calculó la concentración del acetato de etilo al inicio y al equilibrio mediante cromatografía de líquidos de alta resolución (HPLC) con detector de índice de refracción.

Se prepararon 250 mL de soluciones de acetato de etilo y se aforaron con agua de formación sintética, las concentraciones de estas soluciones fueron: 1, 2.5, 5, 10, 15, 20 y 25 g/L. Para estos estudios se utilizó roca de un yacimiento del campo Cantarell que proporcionó el IMP.
Las soluciones se colocaron en matraces Erlenmeyer y se les agregó un gramo de roca pulverizado (tamaño de grano mesh 200). Estas soluciones se colocaron en un baño a temperatura controlada y agitación continua.

Se monitorearon aproximadamente cada 20 horas. Las muestras obtenidas se filtraban con un microfiltro de nylon y tamaño de poro de 0.45 μm para inyectarlo en el HPLC. Se realizaron isotermas a 22, 40 y 50°C.

IV. Resultados y Discusión

A. *Cinética química*

En la Fig. 1 se muestran los resultados del seguimiento de la reacción química de hidrólisis de acetato de etilo a diferentes pH. En pH neutro la tendencia de la velocidad de reacción es lineal lo que indica un orden de reacción cero. A pH ácido y básico la tendencia es logarítmica lo que indica orden de reacción uno.

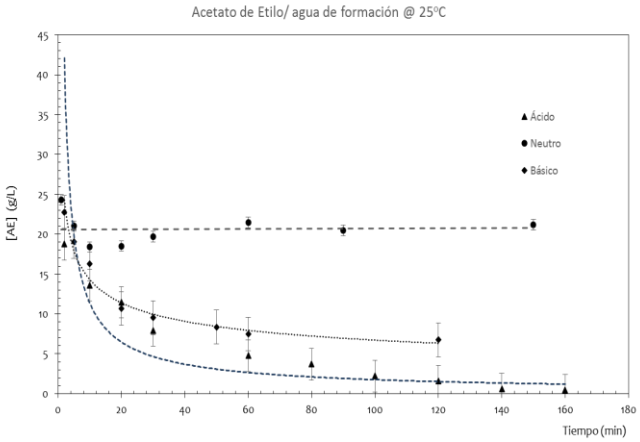

Fig. 1 Comportamiento de la velocidad de reacción del acetato de etilo en medio ácido a 25°C.

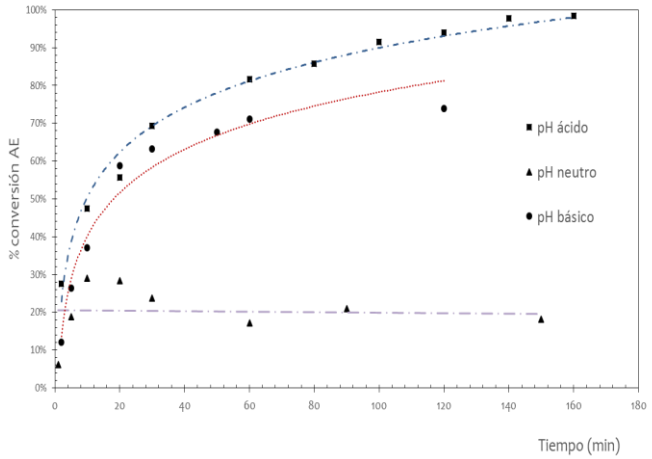

Fig. 2. Comparativo de la conversión de reacción a diferente pH.

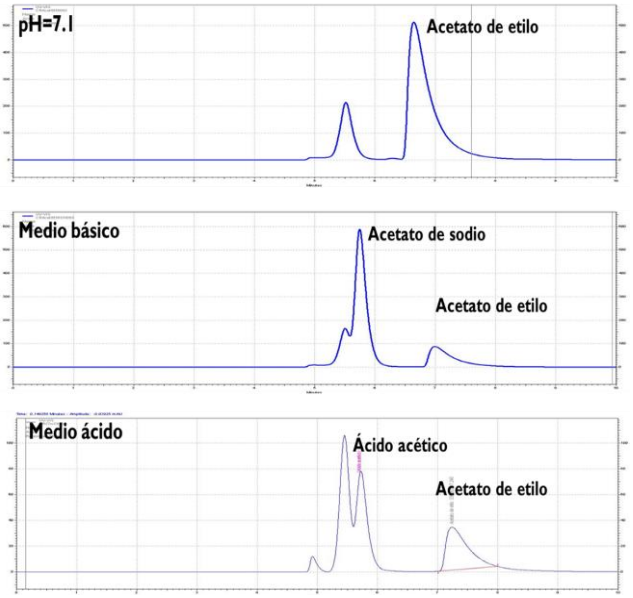

Fig. 3. Comparativo de cromatogramas de la cinética química del acetato de etilo y sus productos de reacción a diferentes pH.

B. *Partición*

En la tabla 2 se muestran los resultados de los experimentos de partición a diferentes concentraciones de acetato de etilo en agua de formación sintética a 25ºC y presión atmosférica. La tendencia del coeficiente de partición es que aumenta a concentraciones bajas de acetato de etilo y va disminuyendo conforme aumenta la concentración de acetato.

TABLA 2. Coeficientes de partición experimentales de acetato de etilo en agua de formación sintética y crudo a 25°C

Concentración inicial Acetato de etilo (g/L)	log P
8.09	0.90
10. 15	0.82
14.78	0.69
20.56	0.64
25.31	0.66

C. Adsorción

En la tabla 3 se muestran los resultados de los experimentos de adsorción del acetato de etilo en agua de formación sintética con roca de campo Cantarell a diferentes temperaturas.

TABLA 3. Resultados de cantidad adsorbida de acetato de etilo sobre roca Cantarell a diferentes temperaturas.

Tabla 3. Resultados de adsorción de Acetato de etilo (AE) con la roca Cantarell a diferentes temperaturas.

Ci AE (g/L)	Vol. Muestra (L)	Masa roca (g)	Temperatura (°C)	Ceq AE (g/L)	q (g trazador/g roca)
0.98	0.25	1.0014	20	0.873	0.0183
5.6	0.25	1.0075	20	5.193	0.101
7.5	0.25	1.0054	20	6.651	0.2111
9.86	0.25	1.0032	20	7.112	0.6806
15.72	0.25	1.0022	20	12.684	0.7561
19.87	0.25	1.0021	20	13.691	1.5418
1.3	0.25	1.0001	40	1.09	0.0525
2.5	0.25	1.0014	40	1.627	0.2183
5	0.25	1	40	2.082	0.7295
10	0.25	1.0005	40	4.633	1.3418
15	0.25	1.0003	40	6.435	2.1413
20	0.25	1.0012	40	10.425	2.3937
25	0.25	1.0008	40	10.365	3.6588
6.33	0.25	0.999	50	4.77	0.3904
20.3	0.25	0.9745	50	12.11	2.1011
12.17	0.25	1.0073	50	8.907	0.8103
15.4	0.25	1.0027	50	9.907	1.3686

V. CONCLUSIONES

Los mecanismos de la reacción de hidrólisis del acetato de etilo en agua de formación sintética son diferentes a diferentes pH, así como los porcentajes de conversión y la velocidad de reacción, por lo que es importante el control y monitoreo del pH en todo momento.
A pH neutro el orden de reacción de la hidrólisis del acetato de etilo es cero, mientras que a pH ácido y básico el orden de reacción es de uno, aunque la velocidad de reacción a pH ácido es mayor que a pH básico.

En cuanto al coeficiente de partición del acetato de etilo con el crudo proporcionado a 25ºC y presión atmosférica indican una alta solubilidad del acetato en el crudo, es decir que se tiene una mayor afinidad hacia la fase orgánica.

Las isotermas de adsorción obtenidas en el experimento se ajustan a la isoterma tipo Langmuir. La adsorción de trazador en la roca disminuye al aumentar la temperatura debido a que éste es un proceso exotérmico.

NOMENCLATURA

HPLC-IR High Performance Liquid Chromatography with Index Refraction
Ci Concentración inicial
Ceq Concentración al equilibrio
pH Potencial de hidrógeno
Kc Constante de equilibrio de adsorción
AE Acetato de etilo, trazador químico

Griegas

Ω Ohmio, unidad derivada de la resistencia eléctrica.

AGRADECIMIENTOS

Al apoyo otorgado por los colegas de los laboratorios de análisis de procesos y catálisis, así como al departamento de energía de la Universidad Autónoma Metropolitana Azcapotzalco, así como al equipo de trabajo del Instituto Mexicano del Petróleo encabezado por la Dra. Jetzabeth Ramírez Sabag.

REFERENCIAS

[1] Rodríguez José Ramón. Ingeniería básica de yacimientos. Venezuela. 2007. pág. 201.
[2] Paris Magdalena de Ferrer. Fundamentos de Ingeniería de Yacimientos. Maracaibo, Venezuela. Ediciones Astro Data, S.A., 2009. pág. 588.
[3] Ramírez, J.S.; Samaniego, F. Tracer flow in Naturally Fractured Reservoirs. SPE 25900. 1993 pp. 1-12.
[4] Isótopos ambientales en el ciclo hidrológico. IGME. Temas: Guías y manuales. ISBN: 84-7840-465-1, pp. 325-330.
[5] Ramírez Jetzabeth Sabag Pruebas de Trazadores en la Recuperación de Hidrocarburos. México, D.F. 2008. pág. 81.
[6] Coronado M. and Ramirez, J. Analytical model for tracer transport in reservoirs having a conductive geological fault. Journal of Petroleum Science and Engineering. Elsevier, 2008. Vol. 62. pp. 73-79.
[7] García, S., Pruebas de trazadores químicos en la estimación de la saturación de aceite residual. Tesis, UNAM. pp. 175.
[8] Serres-Piole C. Preud'homme H., Moradi-Tehrani N., Allanic C., Julia H. Lobinski R. Water Tracers in oilfield applications: Guidelines. J. of Pet. Sci. and Eng. 2012. pp. 22-39, 98-99.
[9] Warren J.E. y Root, P.J. The Behavior of naturally fractured reservoirs. SPEJ. 1963. pp. 245-255.
[10] Kazemi H. Merrill L. Porterfield K. Zeman P. Numerical Simulation of Water-Oil Flow in Naturally Fractured Reservoirs. 1976. Publicado en SPEJ Dec.
[11] Saniford, B. K. Method for Tracing the Flow of Water in Subterranean Formations. 1973. Publication no. 3 851 171.
[12] Sarma P. New transfer functions for simulation of naturally fractured reservoirs with dual porosity models. Tesis de grado en Ingeniería Petrolera. University of Stanford, U.S.A. 2003.
[13] Atkins, P. Fisicoquímica, Barcelona, 2007.Ed. Omega.
[14] Leo A., Hansch C., Elkins D., 1971, Partition coefficients and their uses, Chem. Rev., 71. 525-616.
[15] Geankoplis, C.J. Procesos de Transporte y Operaciones Unitarias. México, 1998. Compañía Editorial Continental, S.A. de C.V.
[16] McCabe, et. al. Operaciones Unitarias en Ingeniería Química, España, 1998. Ed. Mc GrawHill.

Desarrollo de un seguidor solar para un aprovechamiento eficiente de celdas fotovoltaicas para Ecatepec

Abdiel Olmedo Wooder[1], Miguel Guzmán Castillo[1], José Carlos Aguilar Anastacio[1], Wenceslao Bonilla-Blancas[1,*]
[1]Tecnologico de Estudios Superiores de Ecatepec, Departamento de ingeniería Mecatrónica e Industrial
Av. Tecnológico S/N, Col. Valle de Anáhuac, CP. 55210
Ecatepec de Morelos, México.
*E-mail: wbonillab@live.com.mx

***Resumen*— En las últimas décadas la comunidad científica ha hecho esfuerzos para analizar la problemática que implica el uso de combustibles fósiles como fuente principal de energía así como sus repercusiones al medio ambiente, además el crecimiento de la población implica una mayor demanda de recursos energéticos que sean sustentables y sin efectos secundarios contaminantes. Por lo anterior se ha incrementado el interés por crear nuevas alternativas en el uso de energías renovables, entre ellas la energía solar y su transformación en energía eléctrica mediante celdas fotovoltaicas. Uno de los problemas que se han encontrado en el uso de dichas celdas, se presenta al ser instaladas fijamente en una sola dirección que implica no obtener un aprovechamiento máximo de la energía solar. Las investigaciones han demostrado que para obtener una mayor eficiencia en las celdas fotovoltaicas es necesario colocar ortogonalmente las celdas fotovoltaicas al Sol para el aprovechamiento máximo de la incidencia solar. En el presente trabajo se presenta el diseño de un algoritmo para un seguidor solar cronológico a dos ejes haciendo uso del software y hardware de Arduino, logrando que se capte hasta un 70 % más de la radiación total que existe en una jornada diaria de 12 horas, satisfaciendo un elemento primordial que es aprovechar y explotar al máximo los recursos otorgados por el Sol. Este trabajo se desarrolla en el Estado de México, específicamente en el Municipio de Ecatepec, pero puede aplicarse el algoritmo en cualquier otro lugar.**

Palabras Clave: Celda Fotovoltaica; Arduino; Ángulo Altitudinal y Azimutal; Seguidor Cronológico.

I. INTRODUCCIÓN.

Diferentes tipos de energías renovables como la hidráulica, la eólica, la biomasa y la solar son utilizadas actualmente alrededor del mundo debido a la problemática asociada al uso de combustible fósiles como el carbón, gas natural, el petróleo y sus derivados para disminuir las emisiones de gases de efecto invernadero (CO_2, NOx, N_2O). De entre estas fuentes renovables la energía solar es la que cuenta con mayor presencia debido a su abundancia, sustentabilidad y tiene el beneficio de menor impacto ambiental. El desarrollo de sistemas de conversión basados en dichas fuentes se debe al nivel y a la demanda creciente de energía eléctrica a nivel mundial.

La energía solar se refiere a la conversión de los rayos solares en una forma útil de energía, como la eléctrica y a pesar de su intermitencia se puede disponer ampliamente de ella libre de costo. Una celda fotovoltaica, o comúnmente llamada celda solar, es un dispositivo que se usa para convertir la energía solar en energía eléctrica directamente. Se ha manifestado un interés creciente por el desarrollo e implementación de sistemas fotovoltaicos en áreas donde no se cuenta con un acceso a la red eléctrica, es limitada o costosa. El incremento en el uso de paneles fotovoltaicos ha permitido la reducción gradual de los costos de esta tecnología, permitiendo así una mayor aceptación de la misma. Del 2009 al 2010 la generación por medio de este proceso, se incrementó 59.9% a nivel mundial, pasando de 20,068 GWh a 32,093 GWh [1].

En México la generación de energía eléctrica mediante celdas fotovoltaicas no es significativa. La Comisión Federal de Electricidad (CFE) cuenta con sólo dos proyectos piloto fotovoltaicos en Santa Rosalía, BCS y Cerro Prieto en Mexicali, BC de 1 y 5 MW respectivamente para la generación de energía eléctrica para el sector público. Otros proyectos de este tipo se encuentran en estudio en otras regiones del país. Por otra parte, CFE ha atendido diversas solicitudes de inversionistas privados interesados en instalar proyectos de generación con tecnología solar. Se ha previsto que por parte de la iniciativa privada se realice una interconexión de tales proyectos a la red de servicio público, con una demanda aproximado de 642 Megawatts de potencia, dato registrado a finales del 2011 [2]. A pesar de esto se nota un creciente uso de éstas para alimentar señales de tránsito en autopistas, teléfonos públicos, lámparas LED para alumbrado público, entre otros. La gran mayoría de las celdas fotovoltaicas se encuentran fijas, colocadas en un ángulo de inclinación, el cual depende de la latitud de la zona donde se encuentra la celda solar y la altitud del Sol al medio día para así captar directamente los rayos del Sol a esta hora. Sin embargo al estar fijas desaprovechan un alto porcentaje de radiación solar debido a que el Sol se traslada de ESTE a OESTE (ángulo de Azimut) y la altitud de éste varía en las estaciones climáticas.

En las últimas décadas se ha incrementado vertiginosamente el desarrollado de los seguidores solares para mejorar los porcentajes óptimos de la eficiencia energética de las celdas fotovoltaicas. En este contexto se crean y se clasifican nuevos grupos de seguidores como son: activos pasivos y cronológicos [3]:

Los seguidores pasivos son aquellos en los que no interviene ningún tipo de control eléctrico o motor. La mayoría de los seguidores solares pasivos se basan en el ajuste manual del panel, la expansión térmica de aleaciones con memoria o dos tiras bimetálicas de aluminio y acero. Por lo general este tipo de seguidor se compone de dos actuadores que trabajan uno contra el otro, que al haber una iluminación equitativa, estos se equilibran. Otra tecnología de seguimiento pasivo se basa en el desequilibrio de la masa entre los dos extremos del panel, en los cuales hay un tubo con un líquido dentro. El Sol calienta el líquido dentro de los tubos cilíndricos lo que provoca la evaporación y su transferencia de un cilindro a otro, lo que crea el desequilibrio de la masa [4].

Los seguidores activos se pueden clasificar en tres formas: en base a microprocesadores; basados en el tiempo (temporizados) y en una celda solar bifacial auxiliar. En los sistemas de seguimiento solar basados en microprocesador se tiene un controlador conectado a los motores de corriente continua (DC). En este diseño de seguidor solar se emplean comúnmente sensores como los LDR (Light Dependent Resistor), resistencias variables que dependen de la cantidad de luz. En los seguidores temporizados, una vez que la ubicación es seleccionada, el rango de rotación de azimut es determinado y las medidas angulares son calculadas. Mientras que en los sistemas de celdas solares bifaciales auxiliares, la celda solar bifacial percibe y dirige el sistema seguidor a la posición deseada. En este diseño, los componentes como las baterías y la electrónica de conducción son eliminados [4]. Los seguidores cronológicos son aquellos que se basan en modelos matemáticos que se obtienen en función de la rotación de la Tierra y la posición del Sol, proporcionan información para la construcción de algoritmos de control [5].

Como los seguidores solares pasivos no son exactos y los seguidores solares activos en un eje también desaprovechan parte de la radiación solar al no seguir el movimiento del Sol a través de los meses, en este trabajo se presenta el diseño de un seguidor solar activo en dos ejes, de tipo cronológico debido a su mayor exactitud y por lo tanto un aumento en la eficiencia de la celda fotovoltaica. Se propone diseñar el control de un seguidor solar activo cronológico basado en el software de programación basada en C para Arduino y utilizando una tarjeta Arduino Uno. Al utilizar este software la programación será menos complicada y el control de los motores será más preciso gracias a sus librerías ya diseñadas para trabajar con ciertos dispositivos, como sensores, servomotores, reloj de tiempo real, entre otros.

II. ANTECEDENTES

En lo que respecta a seguidores solares activos Chin et al. (2011) propusieron un seguidor solar en un solo eje integrando la tecnología de seguimiento basado en el tiempo y la tecnología de seguimiento utilizando sensores de luz. Se optó por un seguidor a un solo eje ya que tomó en cuenta la ubicación en la que se desarrolló el proyecto, Singapur, el cual se encuentra casi en el Ecuador (su latitud es 1.290270°) y el Sol se levanta directamente en el ESTE y se pone directamente en el OESTE independientemente de la latitud. Su sistema de seguimiento solar es capaz de desempeñar los modos de operación automático y predeterminado, lo cual resulta ser una característica importante. La posición y la intensidad de la radiación solar son detectados por dos sensores LDR que están colocados a ambos lados de la superficie del panel fotovoltaico. En el modo automático, las señales resultantes de los sensores son alimentados a un sistema de control electrónico que opera un servomotor, un motor DC de baja velocidad, para girar el panel. En este modo el Sol no es seguido constantemente para prevenir el consumo de energía por parte del motor, y el sistema entra en modo de "reposo" cuando cae la noche. En el modo predeterminado, el seguidor solar gira en un ángulo predeterminado desde el amanecer hasta la puesta del Sol. Mientras que en el modo manual, el seguidor solar se establece en un ángulo deseado aumentando o disminuyendo el ángulo a través de la entrada del microcontrolador, manualmente. En todos los modos, un algoritmo de retorno nocturno resetea el panel a su estado inicial hacia el este para que esté listo al amanecer. En la Fig. 1 se muestra el prototipo creado.

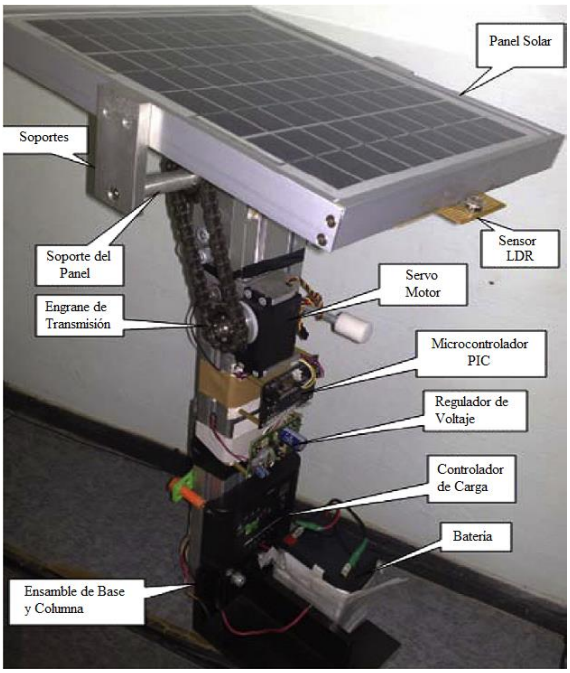

Fig. 1. Prototipo fabricado para el experimento por Chin et al. 2011.

El desempeño del seguidor solar fue modelado y simulado a través del software MATLAB™ y Simulink™. Después fue comparado con los resultados obtenidos experimentalmente y se demostró que la eficiencia de este seguidor solar es mayor a la de un panel fijo, e incluso fue mayor a los datos obtenidos en la simulación en aproximadamente un 20%. De la Cruz et al. [5] en 2012, diseñaron un seguidor solar adaptativo en un solo eje basado en un controlador lógico programable (PLC). El proyecto se llevó a cabo en la ciudad de Lima, Perú. Utilizó un sistema de seguimiento cronológico que se adapta a los cambios de números de horas útiles del Sol utilizando un sensor fotoeléctrico y a la vez corrige el error de forma reactiva. El resultado fue un seguidor cronológico adaptativo que puede corregir el error de seguimiento. De esta manera se evitan cálculos complejos en el microcontrolador del sistema cronológico. La ventaja de este sistema es que continúa el seguimiento del Sol aún en días nublados y no le toma tanto esfuerzo reorientarse de nuevo cuando el Sol se despeje.

El sistema cuenta con un PLC LOGO-SIEMENS con reloj para controlar el motorreductor que mueve el panel de ESTE a OESTE. El sistema cuenta con un sensor fotoeléctrico conformado por dos fotorresistencias colocadas como se muestra en la Fig. 2.

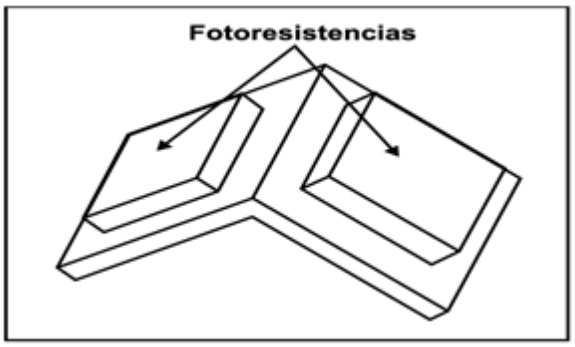

Fig. 2. Posición de las fotorresistencias en el sistema fotoeléctrico de sensado, Cruz et al. 2012.

Para seguir la posición del Sol. El PLC calcula la diferencia de voltajes de las fotorresistencias y las compara, calculando así el error de desviación del Sol y lleva el sistema a una posición en que ambas generen el mismo voltaje. Para la parte cronológica del sistema se propuso una ley de control adaptativo basado en un modelo matemático simplificado de la trayectoria de la carrera del Sol en la bóveda celeste, Fig. 3, el cual fue programado en el PLC. De esta forma el sistema continúa siguiendo al Sol a pesar de que el día esté nublado y las fotorresistencias no puedan ubicarlo. Después de simular el sistema en Simulink™ y hacer las pruebas experimentales, los resultados fueron favorables, y el sistema mostró en el peor de los casos un error de aproximadamente 15° en 10 horas en un día nublado. Ferdaus et al. (2014) en la ciudad de Dhaka, en Bangladesh, diseñó un seguidor solar en dos ejes híbrido.

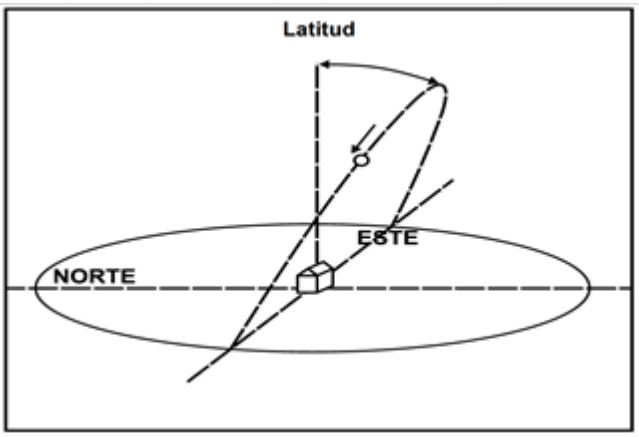

Fig. 3. Modelo simplificado de la trayectoria de la carrera del Sol en la bóveda celeste.

El objetivo de este seguidor es reducir el consumo de energía producida por el panel fotovoltaico por parte del sistema de control y los motores que suele haber en los seguidores activos en dos ejes, y mantener la exactitud del seguimiento del Sol. Así, un circuito de excitación se utilizó para aumentar la tensión y el nivel de corriente para el funcionamiento de los motores. Dos motores paso a paso se utilizaron para hacer girar el módulo solar en dos ejes diferentes (azimut y altitud). El movimiento anual del Sol, es decir, de Norte a Sur, fue seguido por un reloj de tiempo real (RTC) del dispositivo y un sensor de posición. El sensor de posición es una resistencia variable, así que cuando la resistividad de la resistencia variable cambia, la salida del circuito del sensor de posición también cambia. La salida de este circuito va al controlador y diferentes tensiones en la salida del circuito del sensor de posición representan diferentes ángulos de latitud del Sol por su movimiento anual. Un sistema mecánico versátil se introduce como un actuador lineal para crear el ángulo de inclinación adecuado, Fig. 4. Además, este actuador lineal tiene una capacidad de elevación de un gran peso que se observa experimentalmente. Se encontró que el seguidor de dos ejes híbrido produce casi la misma energía que el sistema de seguimiento solar de dos ejes. También se observa que en el sistema de seguimiento híbrido un motor puede permanecer inactivo durante un mes y por lo tanto reducir más de 44% el consumo de energía en comparación con el sistema de seguimiento solar de dos ejes.

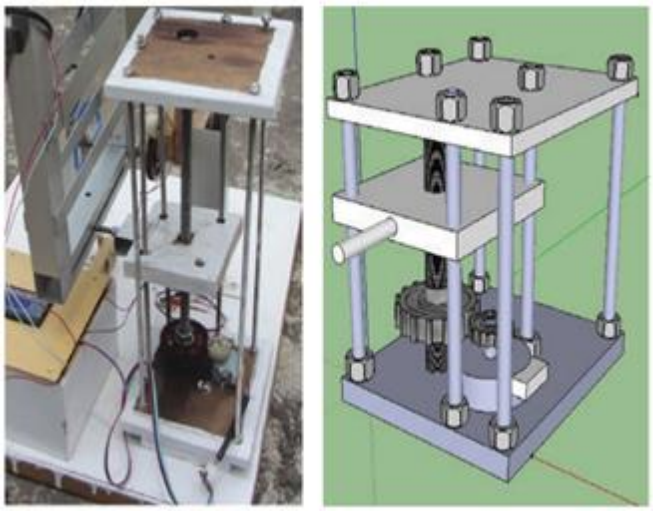

Fig. 4. Diseño e implementación del actuador lineal. a) aplicación y colocación del actuador lineal con el cuerpo de aluminio del porta paneles. b) diseño del hardware del actuador lineal en una herramienta de dibujo asistido por computadora (CAD).

III. MATERIALES Y MÉTODOS

Este trabajo se inició con el cálculo de cada uno de los ángulos de altitud y azimut para cada hora de trabajo durante el día y para todos los días del año para la zona de Ecatepec. Para ello se utilizaron las fórmulas de la literatura [8]. La ecuación 1, determina la declinación solar, el cual es el ángulo entre el plano del Ecuador y una línea imaginaria dibujada entre el centro del Sol y el centro de la Tierra, δ (*ver Fig.5*).

$$\delta = 23.45 sen\left[\frac{360}{365}(n-81)\right] \ldots\ldots (1)$$

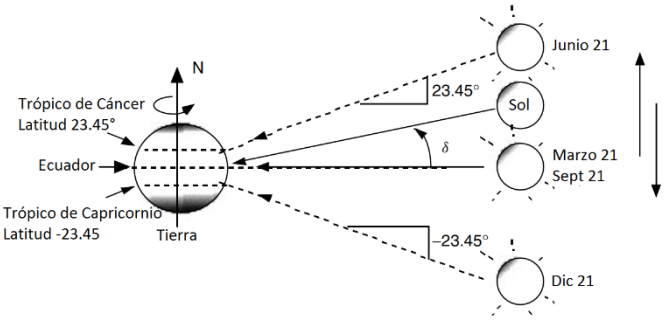

Fig. 5. El ángulo entre el Ecuador y el Sol es llamado declinación solar δ.

Dónde: n es el número del día del año correspondiente, ecuación 2, M número del mes, D día del mes, K toma valores de 1 cuando el año es bisiesto y 2 para un año común. [9]

$$n = INT\left(\frac{275M}{9}\right) - K(INT)\left[\frac{M+9}{12}\right] + D - 30 \ldots..(2)$$

El ángulo de declinación solar es necesario para realizar el cálculo de los ángulos de altitud y de azimut. El ángulo de altitud (β) es el ángulo entre el Sol y el horizonte local directamente bajo el Sol, ecuación 3. El ángulo de azimut (φ) es el que describe la ubicación del Sol en cualquier momento del día, ecuación (4). Fig. 6.

$$sen\beta = cosLcos\delta cosH + senLsen\delta \ldots..(3)$$

$$sen\varphi = \frac{cos\delta senH}{cos\beta} \ldots..(4)$$

H es el ángulo horario, que es el número de grados que la tierra debe girar antes de que el sol esté directamente sobre el meridiano local (línea de longitud). Considerando que la Tierra gira 360° en 24 h, o 15°/ h, el ángulo de horas se obtiene con la ecuación (5).

$$H=\left(\frac{15}{h}\right)(\text{horas antes del medio día solar}).....(5)$$

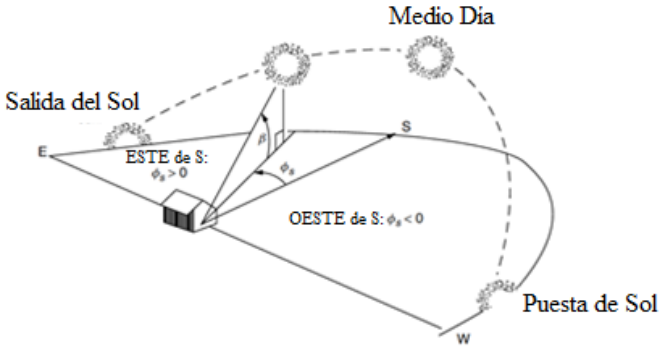

Fig. 6. La posición del Sol puede ser descrito por su ángulo de altitud β y su ángulo de azimut φs. Por convención, el ángulo de azimut se considera positivo antes del mediodía solar.

Con estas ecuaciones y considerando que la latitud de la zona de Ecatepec es 19.6° se realizaron los cálculos de los ángulos de altitud y azimut para cada hora de trabajo durante el día, las cuales se consideraron de las 7:00 a las 19:00, y para cada día del año mediante hojas de cálculo de Microsoft.

Con la información obtenida se construyó el programa de control. El cual se realizó en el software libre de Arduino por la facilidad con que permite hacer uso de dispositivos electrónicos. La placa electrónica de Arduino (Arduino, Italia) que se utilizó para almacenar el programa fue el modelo UNO R3. Su procesador es un ATmega328, tiene 14 pines de entrada/salida digitales de los cuales 6 pueden ser utilizados como salidas de modulador de ancho de pulso (PWM). Tiene además 6 entradas analógicas y un resonador cerámico de 16 MHz.

El programa controla, dos servomotores, uno para el eje del ángulo altitudinal y el segundo para el ángulo azimutal. Haciendo uso del reloj de tiempo real interno del microprocesador se programa la fecha y hora del día en que se pone en marcha. El programa toma los valores del mes, día y hora para realizar los cálculos de las ecuaciones antes mostradas. Para el ángulo de azimut el programa cambia al ángulo correspondiente cada hora, de las 7:00 hasta las 19:00 horas, para seguir el Sol durante su traslado de ESTE a OESTE. Al dar las 20 horas el programa reinicia los servomotores de altitud y acimut a su estado inicial para que el seguidor solar esté listo para el día siguiente. La base fundamental del programa se describe en el diagrama de flujo donde las únicas variables que se introducen por el usuario son la fecha y hora, como se observa en la Fig.7.

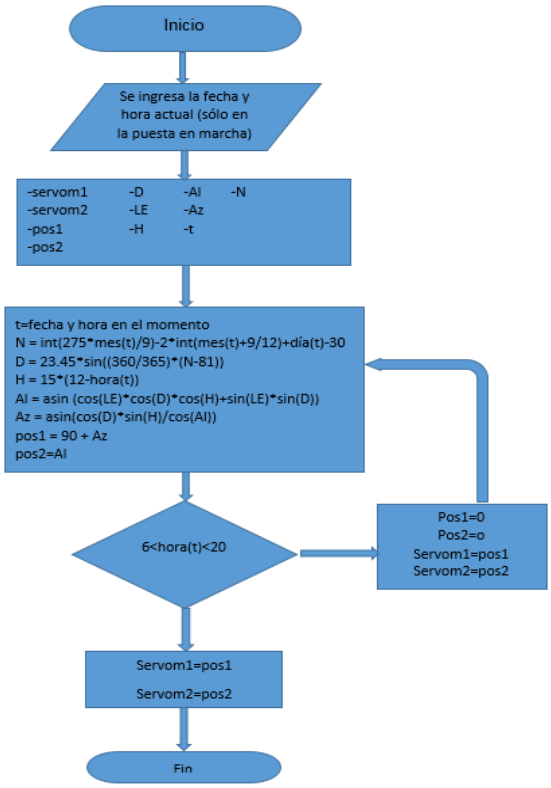

Fig. 7. Diagrama de flujo del programa del seguidor solar.

El código generado se introduce al microcontrolador de la tarjeta Arduino, los servomotores se conectan a la misma tarjeta con su respectiva etapa de potencia. Las características de los servomotores empleados son: TowerPro SG92R, con un desplazamiento angular de 180°, alimentación máxima de 5 volts y un torque máximo de 2.2 Kg/cm. La alimentación de los servomotores se realiza a partir de una fuente externa de 5volts a 1.5Amp. El ángulo de desplazamiento de cada motor se ejecuta dentro del programa donde, se realiza una comparación del ángulo dado por los servomotores, con respecto a los que se tienen en la base de datos de los ángulos calculados, para cada hora y día del año. De esta forma se lleva a cabo el funcionamiento del sistema de actuación.

IV. RESULTADOS Y DISCUSIÓN

Los datos calculados para el ángulo de azimut se muestran en la Fig. 8, en el eje X se observan los días del año, mientras que en el eje Y el ángulo de azimut. Cada línea mostrada representa el comportamiento del ángulo del azimut durante un año en cada hora del día. En la Fig. 9, se observan del mismo modo las líneas de comportamiento de los ángulos de altitud a horas específicas a lo largo del año. Al ejecutar el programa del seguimiento cronológico, se tomaron lecturas de los ángulos que varían a cada hora, la respuesta obtenida se observa que coinciden los datos de las gráficas con los movimientos efectuados por los servomotores

El comparativo de un sistema de lazo cerrado, tal como el sistema adaptativo tienden a utilizar más recursos y mayor complejidad en su diseño, ya que involucra la medición de múltiples variables, como la velocidad del viento, la incidencia solar, días nublados e incluso la humedad o lluvia, incrementando los costos de diseño y la complejidad del controlador, en comparación con el control cronológico, tiene como base fundamental ecuaciones que predicen la trayectoria del Sol, sin necesidad de utilizar sensores, ni sistemas de retroalimentación para la medición de las variables involucradas en el sistema de seguimiento. Esto lo hace más económico y confiable, pero no garantiza que el sistema se mantenga en condiciones normales de funcionamiento cuando exista un fenómeno natural en mayor dimensión, como por ejemplo el incremento de la velocidad del viento, este es un factor que podría perturbar su funcionamiento. [10][11].

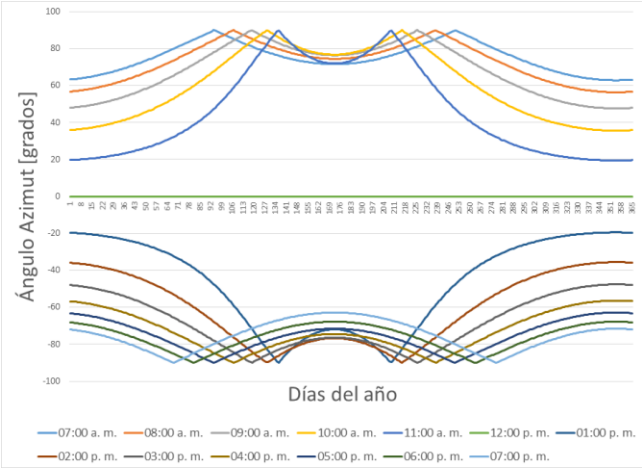

Fig. 8. Gráfica de ángulos de azimut.

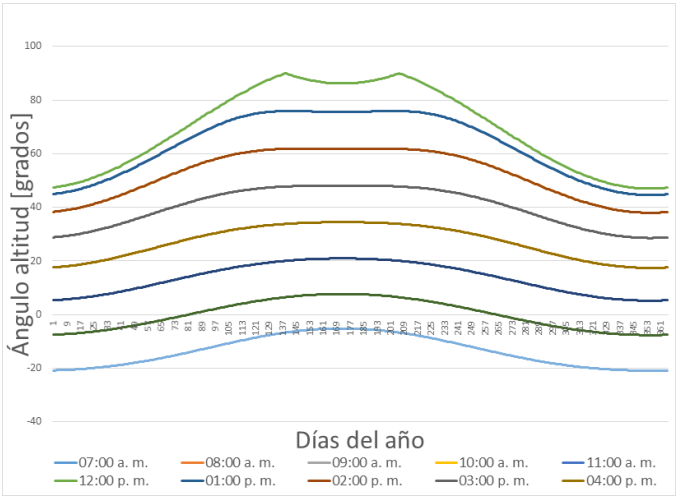

Fig. 9. Gráfica de ángulos de altitud.

La Fig. 10, muestra el prototipo de la estructura del seguidor solar, asistido por computadora, en el cual se implementaría el programa propuesto.

La discusión que se presentan en esté artículo son las irregularidades que se observan en las gráficas de la figuras 8 y 9, dado que las ecuaciones cronológicas tienen ciertas inconsistencias al calcular las trayectorias tanto del ángulo de azimut y altitud, los resultados en ciertos días del año, tienden a a perder la homogeneidad en el comportamiento de las trayectorias, por ejemplo en las gráficas del ángulo de altitud el comportamiento homogéneo se pierde a partir de las 12h entre los días del mes de abril, y en el desplazamiento del ángulo de azimut tomando como ejemplo el ángulo de 60°,en el intervalo de marzo a mayo se pierde la homogeneidad.

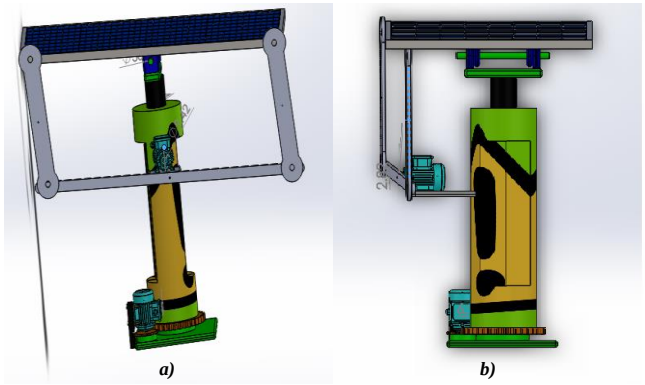

Fig. 10. Diseño de prototipo de seguidor solar a dos ejes: azimut y altitud, a) vista lateral, b) vista frontal.

V. CONCLUSIONES

La ventaja de la aplicación de este algoritmo es que el seguidor solar seguirá la trayectoria del Sol aun cuando no esté despejado evitando así corregir el error de seguimiento solar

cuando el Sol vuelva a despejarse. En un segundo trabajo se pretende aplicar este algoritmo de seguimiento cronológico a un sistema de mayores dimensiones con un arreglo de celdas solares con una capacidad de 100 Watts de potencia nominal, donde se tendrán como objetivos primordiales la lectura de múltiples variables como son: porcentaje de eficiencia solar, voltaje y corriente en función de la incidencia solar, entre otras. Marcando como nuevos objetivos el comparativo del porcentaje de la eficiencia de las celdas fotovoltaicas estáticas y las de seguimiento cronológico.

Uno de los problemas pendientes por corregir en el seguidor cronológico es el error obtenido en la gráfica de los ángulos de azimut debido a la función arco seno utilizada para el cálculo del ángulo ya que este error se debe a que la función solo tiene un comportamiento correcto en el intervalo de $-\pi/2$ a $\pi/2$, saliendo de ese intervalo surge un error en el desplazamiento en la trayectoria del ángulo de azimut.

Se tiene la visión de mejorar dicho proyecto en cuestión del problema que surge cuando se tengan las condiciones críticas de velocidad del viento ya que éste es una variable a la que está expuesto dicho proyecto.

VI. REFERENCIAS

[1] R. Banerjee, "Comparison of Options for Distributed Generation in India". Energy Policy, 2006, vol. 34, no 1, pp 105-110.

[2] SENER."Prospectiva del Sector Eléctrico 2013-2027", 2013, México.

[3] CFE."Programa de Obras e Inversiones del Sector Eléctrico 2012-2026". Edición 2013.

[4] A. Goetzberger, C. Hebling, , H. Schock,. "Photovoltaic materials, history, status and outlook". Materials Science and Engineering: R: Reports, 2002, vol. 40, no1, pp 1-46.

[5] C. De la Cruz, Seguidor Solar Cronológico Adaptativo para Paneles Fotovoltaicos. XIX Congreso Brasileño de Automática (CBA) 2012, pp. 4489-94.

[6] C.S. Chin, A. Babu, W. McBride, "Design, modeling and testing of a standalone single axis active solar tracker using MATLAB/Simulink". Renewable Energy, 2011, vol. 36, pp. 3075-3090.

[7] J. D. Manríquez-Chávez, M. Pineda-Arciniega, C. Hernández Flores y M.A. Arjona, Características de los Seguidores Solares en Aplicaciones Fotovoltaicas. 3er Congreso Nacional de Electromecánica y Electrónica (CONAEE) 2014.

[8] G. M. Masters, Renewable and Efficient Electric Power Systems, Ed. Wiley-Interscience, 2004, pp. 391-398.

[9] C. C. Julian, Physics of solar energy. Ed. Wiley, 2011, pp.84-86.

[10] R. C. Dorf. Sistemas de Control Moderno. Ed. Prentice Hall, 2005, pp 191-197.

[11] K. Ogata. Modern Control Engineering. Ed. Prentice Hall, 2010, pp 7-10.

Determinación de los parámetros de adsorción de un trazador químico en roca de formación.

B. E. Herrera-Gallardo, J. S. Martinez-Muñoz, M. M. González-Brambila, J. A. Colín-Luna
Departamento de Energía, Universidad Autónoma Metropolitana-Azcapotzalco, Distrito Federal, México.
*jacl@correo.azc.uam.mx

***Resumen*— En este trabajo se presentan las isotermas experimentales de la adsorción, el valor de la constante de equilibrio K_C y la energía de adsorción ΔH_a del acetato de etilo en roca proveniente de un yacimiento mexicano perteneciente al complejo Cantarel, así como los valores de un modelo tipo Arrhenius que describe el comportamiento del sistema estudiado. Los resultados mostraron una baja adsorción del trazador en la roca, la cual disminuye con el aumento de la temperatura, por lo que se espera que, a condiciones de yacimiento, la adsorción sea mínima. Los datos de K_C y ΔH_a son esenciales para la cuantificación de crudo remanente en yacimientos naturalmente fracturados.**

Palabras clave*— *Adsorción, Trazador Químico, Energía de Adsorción, Constante de Equilibrio de adsorción.

I. Introduccion

Debido a la demanda de hidrocarburos requerida en nuestro país, se vuelve cada vez más importante la cuantificación del crudo remanente en yacimientos agotados con el objetivo de planear proyectos de extracción secundarios debido al alto costo que esos procesos representan. Una manera de determinar la cantidad de crudo es a través de la inyección de trazadores orgánicos no contaminantes en el depósito petrolero, tales como el acetato de etilo, por lo tanto es necesario el conocimiento de las propiedades de transporte del trazador a condiciones de yacimiento [1]. El estudio de los fenómenos de adsorción de trazadores en roca proveniente de yacimientos naturalmente fracturados resulta necesario para predecir el comportamiento del trazador cuando se utiliza en técnicas de estimación de crudo remanente en el yacimiento.

El complejo Cantarel se ubica a 90km al norte de Ciudad del Carmen, Campeche, México, es una zona de 132km^2 en el Golfo de México que comprende varios campos adyacentes. La estructura rocosa de la zona está formada por Calizas del Terciario, Brecias, Calizas del Cretácico, Calcarenitas, Dolomitas, Turbiditas y Anhidritas. Esta característica litológica se atribuye a la formación del cráter post-impacto en Chicxulub [2].

La adsorción es el fenómeno en el cual un soluto, liquido o gaseoso, se adhiere a la superficie de un sólido, es un proceso exotérmico y depende de las características de la roca (v. e. superficie del sólido, composición química, tamaño del poro). La fisisorción es la forma más simple de adsorción y ocurre debido a fuerzas de atracción entre las especies involucradas (i. e. fuerzas de Van Der Waals o fuerzas de dispersión de London), son procesos reversibles, se forman capas simples (monocapa) del soluto sobre la superficie y se requiere poca energía de activación.

La isoterma de Langmuir es uno de los modelos usados con más frecuencia para describir los procesos de adsorción en los cuales un adsorbato se puede adsorber y desorber desde un sitio libre en la superficie de un sólido. Este modelo asume que la superficie del sólido contiene un número fijo de sitios disponibles energéticamente equivalentes en los cuales las moléculas de adsorbato se unirán a ellos de manera reversible, formando una cobertura de monocapa [3]. La Ec. 1 corresponde a la isoterma linealizada de Langmuir

$$q_e = K_c q_{máx} C_e + q_{máx} \quad (1)$$

donde q_e es la cantidad de soluto adsorbida en el equilibrio (g de trazador/g de roca), C_e es la concentración de soluto en el equilibrio (g/L), $q_{máx}$ es la capacidad máxima de adsorción del sólido (g de trazador / g de roca) y K_C es la constante de equilibrio relacionada con la energía de adsorción (L/g).

Los valores de K_C y $q_{máx}$ se obtienen del gráfico q_e contra C_e, en donde la pendiente m representa a $K_C q_{máx}$ y la ordenada b equivale a $q_{máx}$, por lo tanto el valor de K_C se obtiene a partir de la Ec. 2.

$$K_c = \frac{m}{b} \quad (2)$$

La energía de adsorción ΔH_a es la magnitud termodinámica de la fuerza de interacción entre un adsorbato y la superficie de un adsorbente [4], y se puede obtener a partir de la Ec. 3

$$K_c = A\, e^{-\frac{\Delta Ha}{RT}} \quad (3)$$

$$\ln K_c = \ln A - \frac{\Delta Ha}{R}\frac{1}{T} \quad (4)$$

Donde R es la constante de los gases (8.314 J/mol·K), T es la temperatura del experimento, A es una constante que contiene información sobre entropía y K_C es la constante de equilibrio obtenida mediante la Ec. 2. La Ec. 4 muestra la forma linealizada de la Ec. 3 de donde, al graficar $ln\ K_C$ contra $1/T$, se obtienen los valores de A y ΔH_a.

En el presente documento se reportan los resultados experimentales de la adsorción, el valor de la constante de equilibrio K_C y la energía de adsorción ΔH_a del acetato de etilo en roca proveniente de un yacimiento mexicano perteneciente al complejo Cantarel, así como los valores de un modelo tipo Arrhenius que describe el comportamiento del sistema estudiado.

II. METODOLOGIA EXPERIMENTAL

A. *Materiales*

Se utilizó acetato de etilo (99.9% pureza, Baker, Avantor Performance Materials, México), agua sintética de formación [5], y roca de yacimiento proveniente del complejo Cantarel, Campeche, México. La matriz porosa está compuesta en un 99% por dolomita, con un diámetro de poro promedio de 164Å [6].

B. *Análisis cuantitativo por IR.*

La cuantificación se realizó en un espectrofotómetro de infrarrojo marca PerkinElmer modelo Frontier FT-IR, módulo ATR universal (Diamante/KRS-5, ventanas de KBr). Los espectros se leyeron con cuatro barridos a 0.2 cm/s, en un rango de 1,500 a 1,000 cm^{-1}.

C. *Procedimiento.*

Se preparó una solución de acetato de etilo y agua de formación sintética en concentración de 30 g/L (30,000 ppm). A partir de esta solución se prepararon estándares en el rango de 2.0 a 30 g/L, utilizando los espectros IR de cada estándar se construyó una curva de calibración tomando como base el pico en la longitud 1,380 cm^{-1}.

Se prepararon seis soluciones de acetato de etilo y agua de formación sintética en el rango de 3 a 26 g/L para cada temperatura y se midió la concentración correspondiente a la C_0 de cada sistema. En matraces de 125mL se agregaron 100mL de cada solución y aproximadamente 1gr de polvo de roca de yacimiento tamizado a 200 mesh (75µm). Los sistemas sellados se colocaron en un baño de calentamiento y agitación constante durante 72 horas, tiempo en el que se alcanza el equilibrio de adsorción. Al término el experimento los sistemas se enfriaron bruscamente para evitar pérdidas por evaporación, después, se colectaron 3mL de muestra la cual se filtró para retener el polvo de roca disperso en la muestra. Se leyeron los espectros IR de cada muestra para la lectura de la concentración de equilibrio de cada sistema. La cantidad de acetato de etilo adsorbido en el equilibrio por unidad de masa de adsorbente se determinó de acuerdo a la siguiente ecuación

$$q_e = \frac{C_0 - C_e}{w} \qquad (5)$$

Donde w es la masa del adsorbente (g), V es el volumen de la solución (L), C_0 es la concentración inicial de trazador (g/L), C_e es la concentración de trazador en el equilibrio (g/L) y q_e es la cantidad de trazador adsorbido en el equilibrio (g de trazador /g de roca).

III. RESULTADOS Y DISCUSIÓN

A. *Resultados experimentales*

Los resultados experimentales de adsorción del trazador en roca de yacimiento a diferentes temperaturas se muestran en la Tabla 1, donde C_0 es la concentración inicial de acetato de etilo en la solución, C_e es la concentración en la que se alcanza el equilibrio, w es la masa de roca y q_e es la cantidad de trazador adsorbido por masa de roca. Se observa la dependencia entre la cantidad adsorbida en el equilibrio y la cantidad inicial del trazador en la solución. Esto es, con el aumento de trazador disponible, la adsorción aumentará hasta llegar a la saturación de la superficie.

En las isotermas de adsorción mostradas en la Fig. 1. se observa la influencia del aumento de la temperatura que ocasiona una disminución en la cantidad adsorbida del trazador en la roca. Este proceso se afirma como exotérmico, por lo que se espera que la adsorción a temperaturas de yacimiento sea menor a lo presentado (294K a 394K, [7]).

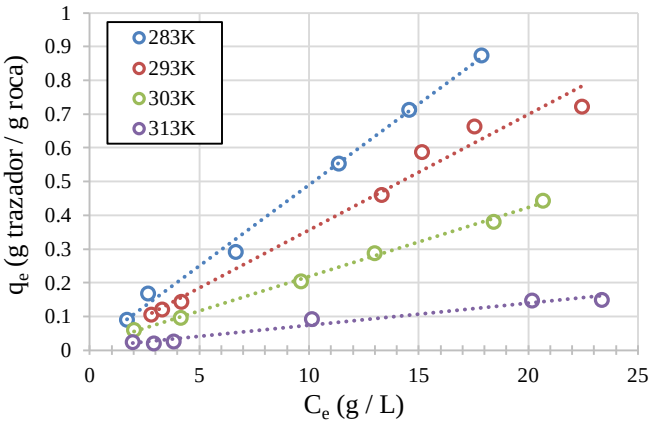

Fig. 1. Isotermas de adsorción de acetato de etilo en roca de yacimiento del complejo Cantarel, México.

En pruebas de trazadores en yacimientos petroleros, donde la concentración de trazador se encuentra alrededor de 10 g/L, se puede esperar que la cantidad de trazador adsorbido por el sistema rocoso se encuentre por debajo de 0.1 gr de trazador por gramo de roca, lo cual no representa una pérdida significante en la interpretación de los resultados de dichas pruebas debido al volumen de trazador inyectado.

TABLA I. Resultados experimentales de adsorción de acetato de etilo en roca del complejo Cantarel, México, a temperaturas T y presión atmosférica.

T (K)	C_0 (gL^{-1})	w (g)	C_e (gL^{-1})	q_e (gg^{-1})
283	2.61	1.0030	1.70	0.0907
	4.37	1.0128	2.66	0.1683
	9.61	1.0037	6.68	0.2924
	16.96	1.0102	11.36	0.5539
	21.80	1.0108	14.59	0.7132
	26.71	1.0103	17.88	0.8747
293	3.89	1.0016	2.83	0.1051
	4.54	1.0054	3.32	0.1212
	5.63	1.0035	4.20	0.1430
	17.95	1.0009	13.33	0.4610
	21.04	1.0032	15.15	0.5870
	24.24	1.0050	17.56	0.6644
	29.69	1.0013	22.46	0.7219
303	2.63	1.0004	2.03	0.0604
	5.14	1.0060	4.16	0.0968
	11.71	1.0006	9.66	0.2053
	15.90	1.0058	13.01	0.2877
	22.27	1.0059	18.44	0.3809
	25.12	1.0011	20.68	0.4439
313	2.22	1.0061	1.96	0.0251
	3.16	1.0039	2.95	0.0205

4.10	1.0045	3.84	0.0258
11.06	1.0072	10.14	0.0921
21.68	1.0086	20.19	0.1478
24.86	1.0002	23.36	0.1498

B. *Resultados teóricos*

A partir de la Ec. 2 utilizando los resultados experimentales mostrados en la Tabla 1 se obtienen los valores para K_C en cada temperatura.

TABLA II. Valores de pendiente *m* y ordenada al origen *b* para el ajuste lineal de las isotermas experimentales mostradas en la Fig. 1.

T (K)	m	b	K_C (L/g)
283	0.0479	0.0111	4.3325
293	0.0343	0.0143	2.4046
303	0.0204	0.0147	1.3913
313	0.0065	0.0090	0.7230

Utilizando de la Ec. 4 y los datos de K_C mostrados en la Tabla 2, se obtienen los valores para ΔH_a y A requeridos en la Ec. 3. Por lo tanto, la energía de adsorción ΔH_a para el sistema estudiado es de -43,526 J/mol y el valor de A es de 4.1172×10^{-8} L/g. La Tabla 3 muestra la desviación absoluta entre los resultados experimentales y la estimación calculada para cada condición de temperatura.

TABLA III. Porcentaje de desviación para K_C entre la estimación (K_C est.) y el valor experimental (K_C exp.) a diferentes T.

T (K)	K_C exp.	K_C est.	Desv. (%)
283	4.3325	4.4537	2.7987
293	2.4046	2.3688	1.4910
303	1.3913	1.3135	5.5963
313	0.7230	0.7563	4.6038

C. *Aplicación a condiciones de yacimiento*

Para condiciones de temperatura de yacimiento cercanas a los 423K [8], el valor de K_C obtenido a partir de la Ec. 3, es de 0.0097 L/g. La magnitud de este valor sugiere poca adsorción del trazador a la matriz porosa estudiada, por lo tanto, el fenómeno de adsorción en una prueba de trazadores para la estimación de crudo remanente en este yacimiento es bajo en comparación con fenómenos adicionales que se presentan en el flujo de fluidos subterráneos (v. e. partición [9]).

IV. Conclusiones

En este estudio se ha determinado la adsorción del acetato de etilo en roca proveniente de un yacimiento mexicano perteneciente al complejo Cantarel. Las siguientes conclusiones están basadas en el resultado de esta investigación.

De acuerdo a los resultados observados se concluye que las isotermas de adsorción obtenidas experimentalmente se pueden ajustar al modelo de Langmuir, las cuales afirman que la adsorción en la roca de estudio es de carácter exotérmico puesto que la cantidad adsorbida y los valores de la constante de equilibrio K_C disminuyen al aumentar la temperatura. Esto se debe a la naturaleza exotérmica del fenómeno, es decir, la fisisorción se favorece a bajas temperaturas.

Con esto, el modelo de Arrenius propuesto se ajusta satisfactoriamente a los valores obtenidos experimentalmente, por lo tanto la estimación de K_C a condiciones de yacimiento representa un acercamiento adecuado al valor real.

El fenómeno de adsorción del trazador en la roca estudiada se puede despreciar al realizar pruebas de trazadores en los posos del complejo Cantarel donde se encuentre roca dolomita, con esto, se reducen los parámetros matemáticos involucrados en los modelos que representan el flujo de fluidos subterráneos en las fracturas saturadas.

Referencias

[1] Coronado M., Ramirez-Sabag J., Valdiviezo-Mijangos O., Somaruga C., A test of the effect of boundary conditions on the use of tracers in reservoir characterization, Geofisica Internacional, 48: 185-194, 2009.

[2] Mayr S. I., Burkhardt H., Popov Y., Wittmann A., Estimation of hydraulic permeability considering the micro morphology of rocks of the borehole YAXCOPOIL-1 (impact crater Chicxulub, Mexico)., Int. J Earth Sci (Geol Rundsch), 97, 385-399, 2008.

[3] Epstein J., Michael J., Mandona C., Marques F., Dias-Cabral A.C., Thrash M., Modeling Langmuir isotherms with teh Gillespie stochastic algorithm, Journal of Chromatography, 1380, 81-87, 2015.

[4] Widegren J.A., Bruno T. J., Enthalpy of adsorption for hidrocarbons on concrete by inverse gas chromatography, Journal of Chromatography, 1218: 4474-4477, 2011.

[5] Méndez-Ortíz B. A., Geoquímica e isotropía de aguas de formación (salmueras petroleras) de campos mesozoicos de la cuenca del sureste de México: Implicación en su origen, evolución e interacción agua-roca en yacimientos petroleros., Tesis Dr. Ciencias. México, Universidad Nacional Autónoma de México, Centro de Geociencias, 2007, 223 p.

[6] Castro M., Mendoza de la Cruz J. L., Buenrostro-Gonzalez E., López-Ramírez S., Gil-Villegas A., Predicting adsorption isotherms of asphaltenes in porous materials, Fluid Phase Equilibria, 286, 113-119. 2009.

[7] Deans H.A., Carlisle C. T., "The Single-Well Chemical Tracer Test - A Method For Measuring Reservoir Fluid Saturations In Situ", Petroleum Engineering Handbook, Larry W. Lake, Editor, SPE, Volume V, Reservoir Engineering and Petrophysics, pp 615-649, 2007.

[8] Tomish J.F., Dalton R.L., Deans H.A., Shallenberg L.K., "Single-well tracer method to measure residual oil saturation", J. Pet. Technol., 25, 211-218, 1973.

[9] Serres-Piole C., Preud'homme H., Moradi-Tehrani N., Allanic C., Jullia H., Lobinski R., "Water tracers in oilfield applications: Guidelines" Journal of Petroleum Science and Engineering, 98-99, 22-39, 2012.

Microorganisms Isolated from Cattle Manure, Involved in the Production of Methane

F. A. Naranjo Castañeda, N. E. Altamirano Segovia, B.E. E. J. Galindo Pérez, F. García Franco.*
Department of Basic Sciences, UAM-Azcapotzalco
México D.F., México
*flexingambient@hotmail.com

M.M. González Brambila, B. E. Chávez Sandoval
Department of Energy, UAM-Azcapotzalco
México D.F., México
becs@azc.uam.mx

Abstract— The generation of biogas from manure cattle, represents a sustainable alternative to the use of fossil fuels. Hydrolysis, fermentation, acetogenesis and methanogenesis they are microbial processes that act sequentially to degrade biomass and produce biogas, in anaerobic conditions. The biogas is an energy resource, mainly composed of methane (CH_4) and carbon dioxide (CO_2). Methane is a gas, which can be used as fuel to produce heat and electricity.

The objective was to characterize the various microbial consortia present throughout the process in the generation of methane, such as aerobic bacteria, anaerobic bacteria, fungi and protozoa, which are involved in the degradation of organic matter to biogas generation. The methanogenic organisms can be considered the most important in the anaerobic consortium, as they are responsible for the formation of methane.

Three samples were taken during a retention time in the anaerobic bio-digestion system. 71,100 CFU/mL, fungus; 57,200 CFU/mL, anaerobic bacteria; 42,900 CFU/mL and protozoa; and 8,185 cells/mL aerobic bacteria, they were counted respectively. In the microbiological characterization, were found: 6 types of aerobic bacteria, 7 types of anaerobic bacteria, 8 types of fungi and 6 types of protozoa.

The results of monitoring of physicochemical parameters are shown as the average obtained from the conditions maintained throughout the whole process: pH 7, 100% humidity and temperature 22 ° C.

This system of anaerobic bio-digestion of organic waste, allows the production of biogas in a sustainable way. Furthermore isolate and identify the different types of microbial consortia present in each stage of biogas production, involves an opportunity to optimize these processes.

Keywords—Alternative energy, Biogas, Methane, Cattle manure, Methanogenic microorganisms.

I. INTRODUCTION

Methane production is a complex process and occurs naturally in any environment where organic compounds accumulate in anaerobic conditions. This process also known as methanogenesis can be considered as the final step of the decomposition of biomass, which is generated by the presence of consortia of microorganisms (bacteria, fungi and protozoa) closely associated throughout the process [1].

Methanogenic microorganisms are the most important within the consortium of anaerobic microorganisms, as they are responsible for the formation of methane [2].

Most of this consortium have replication times from several hours to several days, so its isolation and incubation are complicated process. It has identified about 70 species of methanogenic microorganisms belonging to 21 genera in different anaerobic habitats, only seven species have been isolated from the rumen. Of these the most studied are methanogenic bacteria that are part of the domain Archaea [3].

Blanquet, *et al.*, in 2013, building a bioreactor for anaerobic fermentation of cattle manure and obtaining methane, they isolate and identify 7 methanogenic strains, which showed that there is microbial variability predominating Gram positive, Gram negative bacillus and Gram positive cocci, important for the generation of methane [4].

This paper presents the results of the methane production in a bioreactor anaerobic of the static batch, also shows the microbial consortia associated to the throughout the process.

The system was monitored by measuring physicochemical parameters (pH, temperature and humidity). The identified microbial consortia present in methane production will be used to optimize the microbial anaerobic biodigestion by bioaugmentation in later stages of this project.

II. METHODOLOGY

A. *Preparation of the sample*

The sample was obtained from cattle manure on a dairy farm, located in Teoloyucan, State of Mexico, Mexico. About 400 liters of fresh manure excreted were collected into two plastic drums of 220 liters.

Methane-producing anaerobic system

An anaerobic methane-producing system, bioreactor anaerobic of the static batch, was installed and monitored it daily, three samples of manure was taken from effluent of the bioreactors, one sample by month.

B. *Count microorganisms*

In aseptic conditions serial dilutions of the samples were performed, poured into Petri dishes in triplicate with the corresponding culture medium (nutrient agar anaerobic to bacteria, Sabouraud dextrose agar, for fungi) and were incubated at 37°C for 24 hours to bacteria; 28°C during 48 hours to fungi, watching the growth of microorganisms. After the incubation period, counting the Colony Forming Units (CFU) and characterization was performed (Figure 1). Furthermore, protozoa counting was performed using a chamber Neubaguer [5].

Fig. 1. A) Aseptic conditions; B) Macroscopic characterization; C) Microscopic characterization

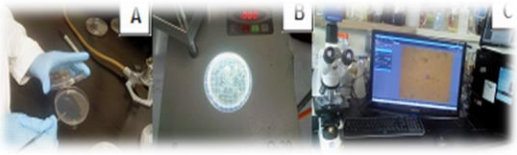

C. *Macroscopic and microscopic characterization*

Colonies of bacteria obtained were characterized macroscopically by size, color, shape, elevation, edge, etc., and microscopic characterization was made by Gram staining. Fungal microculture technique was made, capturing images, using an optical microscope.

D. *Degradation of cattle waste by physicochemical parameters monitored*

Throughout the process of degradation, it was monitored system methane production, composed mainly of two anaerobic bioreactors, through physicochemical parameters (pH, temperature and humidity) by different devices, Figure 2.

Fig. 2. A) pH meter and wet; B) Thermometer TATOR and C) HTC-1 digital hydrometer

E. *Determination of the amount of methane (CH_4)*

The amount of methane produced was quantified using water levels in plastic containers (Figure 3), the pressure of the methane gas flow was deposited on the first contender in which the volume proportion of water passing descended to the second container.

Fig. 3. Methane captator

III. RESULTS

A. General count of microorganisms consortia

The overall count in Colony Forming Units per milliliter (CFU/mL) was obtained from each of the consortia, by averaging the serial dilutions for each of the three samples; protozoa count for the concentration of cells per milliliter (cells/mL) was calculated, as shown in Table I.

TABLE I. GENERAL COUNTING MICROORGANISMS

Day	Bacteria	Fungi	Anaerobic	Protozoa
20	52000	52000	17400	6930
40	9700	4200	12200	910
60	9400	1000	13300	345

Also depicted graphically the overall count (Figure 4), which shows that there was a decreasing microbial consortia kinetics for both fungi, protozoa and bacteria, however showed consistent growth throughout the process anaerobic bacteria degradation, being the consortium with lower concentrations of colonies.

Fig. 4. Total count of microbial consortia

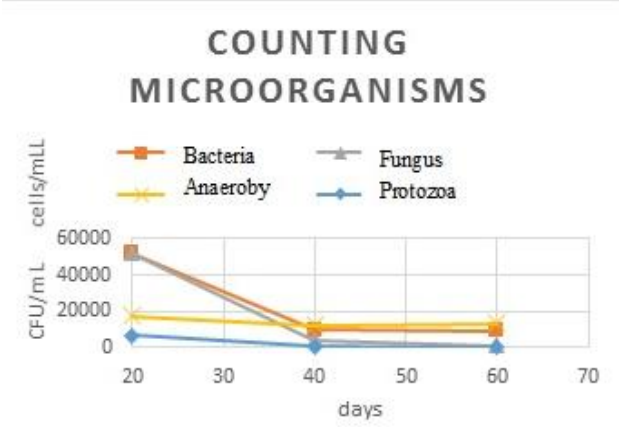

According to these results we can establish that the presence of consortia both fungi but primarily of bacteria can be grouped between fermentation and hydrolytic microorganisms in the process of biogas production, which are responsible for the breakdown of polysaccharides such as cellulose monomers glucose, in addition pyruvate convert glucose and H_2S, favoring the use of these free radicals by other microorganisms and bacterial groups, which transform to produce acetate, butyrate, propionate, H_2, CH_4 and other compounds [6].

B. *Characterization of microbial consortia*

Macroscopic and microscopic characterization of microorganisms in the three samples were observed, were compared and the best consortia to identify the types of consortia were chosen.

In table II, six types of aerobic bacteria which were present throughout the process of degradation of organic matter, is displayed.

TABLE II. *AEROBIC BACTERIA*

Type	Characterization	Macroscopic	Microscopic
1	7 mm, cream, Circular, umbone, festooned Long bacilli, Gram +	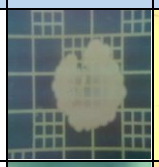	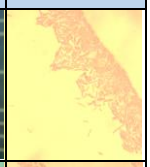
2	3 mm, White, Circle, Full, Wavy Long bacilli, Gram +	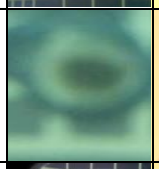	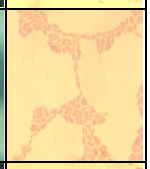
3	10.3 mm, White, Irregular, umbone, Lobed Short rods, Gram +	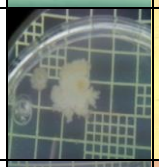	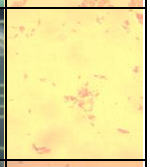
4	5mm, Cream, Circular, Convex, Whole Short rods, Gram +	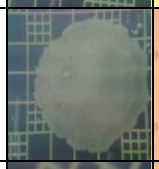	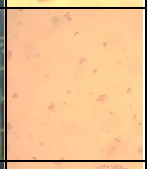
5	1.7 mm, White, Irregular, Flattened, Lobed Short rods, Gram +		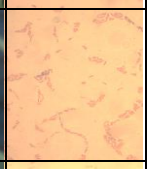
6	0.3 mm, Yellow, Circle, Pulvinada, Whole Short rods, Gram +	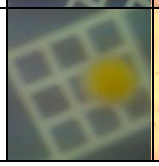	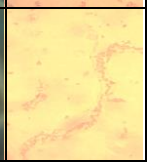

The identified aerobic bacteria grown in Petri dishes with nutrient agar was the growth medium for the consortium, its characterization was crucial, being long and short rods mostly Gram positive.

For the consortium of anaerobic bacterium, seen in table III, the seven types identified during biogas generation.

TABLE III. *ANAEROBIC BACTERIA*

Type	Characterization	Macroscopic	Microscopic
1	7 mm, White, Irregular, umbone, Wavy Long bacilli, Gram.		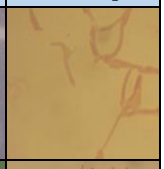
2	4 mm, White, Circular, umbone, Whole Long bacilli, Gram +		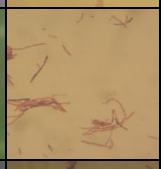
3	1 mm, White, Circular, Convex, Whole Long bacilli, Gram +		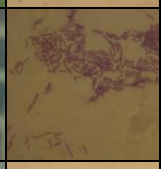
4	15 mm, White, Irregular, umbone, Wavy Long bacilli, Gram -		
5	10 mm, White, Irregular, High, Whole Long bacilli, Gram -		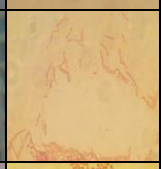
6	2 mm, White, stringy, Convex, Filamentosa Cocci, Gram -		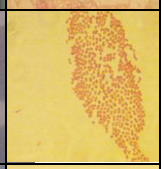
7	3 mm, cream, Circular, High, Lobed Cocci, Gram -		

For this work it was observed that there was increased presence of long rods and Gram negative cocci. But cells were also presented in the form of plates and filaments. In this respect we can say that the presence of this amount of anaerobic bacteria are part of the methanogenic microorganisms because methanogenic bacteria are strictly anaerobic.

So also presented in Table IV, the eight identified fungal types present along the degradative process.

TABLE IV. *FUNGI.*

Type	Characterization	Macroscopic	Microscopic
1	27 mm Green / coffee, Irregular, High, Filamentary, Granulated Septate hyphae and no sporangia	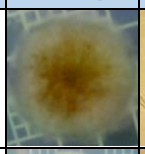	
2	35 mm, white / yellow, circular, umbone, Starry, Granular, radial roughness Septate hyphae and no sporangia	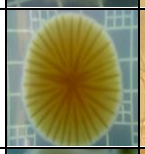	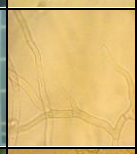
3	40 mm, white / brown, Circular, High, Starry, Granular radiated; Septate hyphae, nucleate and no sporangia		
4	45 mm, Coffee / white, Irregular, umbone lobulated Granular Without filamentous hyphae and sporangia	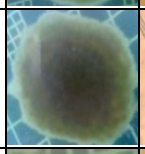	
5	3 mm, White / Yellow, Irregular, Convex, Filamtary Septate hyphae with sporangia		
6	6 mm, white, stringy, Pulvinada, Filamentary Filamentous hyphae, and no sporangia nucleate		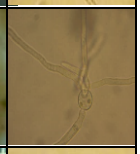
7	35 mm, cream / Filamentary, High, fluffy mycelium; Septate, nucleate hyphae and sporangia	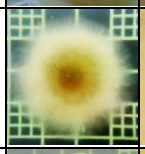	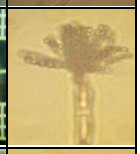
8	22 mm, cream, Circular, flattened Full, Granular Hyphae without sporangia		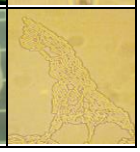

According to the characterization of fungal types mostly he found most fungi with septate hyphae and spores without exception type 5 and type 7. Circular flattened and bonded form.

Six types of representative protozoa common in cattle rumen (Table V) were found.

TABLE V. *PROTOZOAN*

Tipo	Caracterización	PROTOZOAN
1	*Rumen fluke type protozoan*	
2	Microalgae type Spirogyra, multicellular, polinucleous.	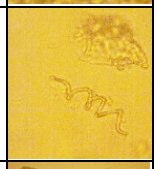
3	Helminth eggs	
4	*Microalgae type Spirogyra, multicellular, polinucleada*	
5	*Trematode Nemato type, flat parasitic worms*	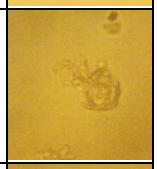
6	*Tubular protozoan, with cytostome, cytopharynx and apparent citopígeo.*	

According to these results the protozoa were identified and faciolas *Spirogyra*, likewise Nematodes are parasites which are found in the rumen.

C. Degradation of bovine waste physicochemical parameters

Throughout the process for the degradation it was monitored system methane production, composed mainly of two anaerobic bioreactors, through physicochemical parameters (pH, temperature and humidity).

Measuring the bioreactors maintained a pH range (7 to 8) as shown in Figure 5, which represent a neutral pH; pH1 is where the measurement in bioreactor 1 and measurement pH2 in bioreactor 2.

pH stability is essential for controlling the composition and feed rate [7].

Fig. 5. The pH of the bioreactors

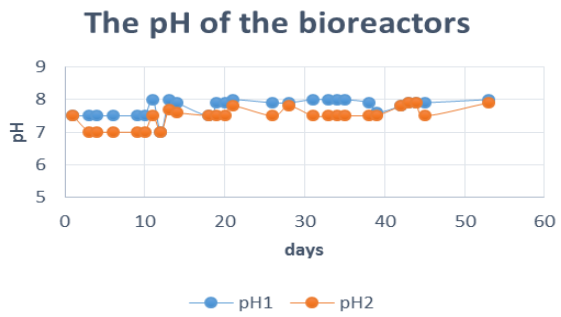

The humidity of the two bioreactors shown in Figure 6, a decrease during the first days after moisture day 35 bioreactor 1 began to rise due to agitation while moisture bioreactor 2 stable.

Fig. 6. Humidity in Bioreactors

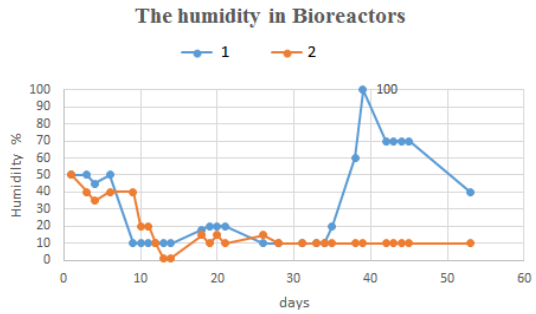

For variable temperature recorded throughout the process, it had a similar behavior is observed in figure 7 the environment temperature (T env.) was higher in relation to the two bioreactors (T1 and T2). The temperature of the bioreactor did not vary much. In the final stages of testing a drop in temperature due to environmental conditions present at the site, which generated a decrease in the concentration of microorganisms, because the temperature is a factor in the development of this process, they have studied the digester process at ambient temperatures of between 25 and 35°C, concluding that this temperature is close to the optimum for this process [8].

Fig. 7. Temperature in bioreactors. T1 Temperature in bioreactor one; T2 Temperature in bioreactor two, amd T env is the environmen Temperature

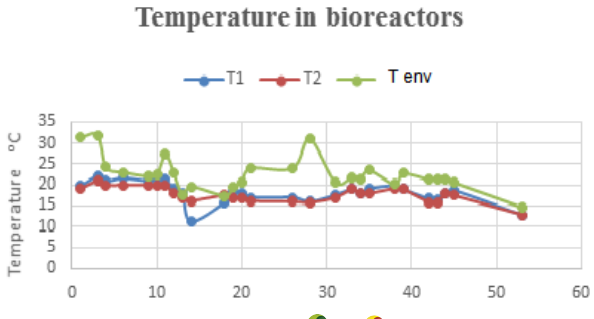

D. *Amount of methane (CH_4)*

This methane formation is caused by the conversion of different organic compounds from manure of cattle, generating CH_4 produced by microbial consortia. These microorganisms are found during methanogenesis, which are found in the natural environment and manage to serve many roles during anaerobic degradation of waste [9].

In Figure 8, the total amount of methane produced was 10.55 liters during a retention time for two months.

Fig. 8. Amount of methane generated in liters

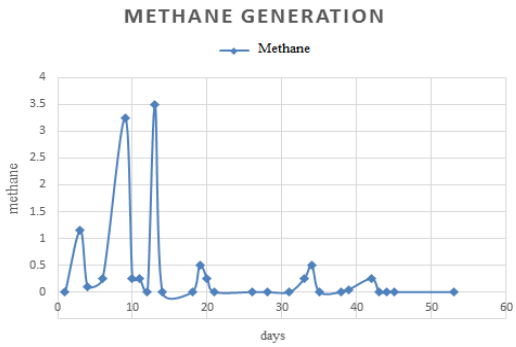

Increased production of this gas was obtained during the early stages of project development, 10 days 3.4 liters was found evaluating this content biogas can be determined that the yield was low, due to the environmental conditions of the place and the season winter, causing a decrease at the end of the 50 days, however, the methane generation process did not stop, even if these conditions were not favorable, that is why the care of this factor is essential for the production of methane.

The main advantages of methane production is to use a low amount of material and energy for the production of complex compounds unlike aerobic conditions. This allows used as an alternative source of energy, and in this anaerobic process does not require energy for aeration allowing minimize costs.

IV. CONCLUSIONS

Based on the evidence, methodology and analysis of results, the perspectives presented during the course of the research project, we reach the following conclusions:

The biogas obtained (0.17 liters per day) from 400 liters of cattle which manure was very low. 24 m3 obtained from 500 kg of cattle manure reported in literature [10].

The presence of four types of microorganisms (eubacteria, arquibacterias, protozoa and fungi) identified throughout the process, is a strong indicator that the four stages of the biogas production (hydrolysis, fermentation

and methanogenesis acetogenesis) are active and constant throughout the process of biogas production.

Temperature, pH, moisture are decisive for biogas production factors, which must be controlled to improve the process.

The identified microorganisms require to be identified with molecular methods to meet that species belong and know that enzymes are responsible for producing biogas processes.

Isolates can be used to biostimulate and make the process more efficient.

Several parasitic protozoa was identified as: faciolas nematodes and that are present in the bovine manure.

Building an anaerobic bio-digestion system can be very important to develop in rural areas, as the gas produced can be an alternative source of choice for these areas.

V. PERSPECTIVES

Using microbial consortia identified to bioaugmentation an anaerobic system, which will allow further degradation of organic waste. Taking into account mixing or recirculation of organic matter in the bioreactors in better retention time.

DNA extraction performed to have a molecular identification of microorganisms present in the process and degradation and thus determine the different microbial species occurring along this process.

VI. ACKNOWLEDGEMENTS

The authors thank J. A. Mendez Flores, S. Alvarado Vanegas, and UAM-A for the facilities to make this work.

VII. REFERENCES

[1] J. P. Jouany, «Methods of manipulating the microbial metabolism in the rumen,» *Ann Zootech*, vol. 43, pp. 49–62, 1994

[2] Y. Ferrer y H. Pérez, «Los microorganismos en la digestión anaerobia y la producción de biogás. Consideraciones en la elección del,» *ICIDCA*, vol. 43, nº 1, p. 920, 2010.

[3] A. Sosa, J. Galindo y R. Bocount, «Metanogénesis ruminal: aspectos generales y manipulación para su control,» *Revista Cubana de Ciencia Agrícola*, vol. 41, nº 2, 2007.

[4] C. N. Blanquet, «Aislamiento e identificación molecular de bacterias metanogénicas a partir de estiércol bovino,» de *Memorias del IV Congreso de Docencia e Investigación en Química*, México, D. F., Universidad Autónoma Metropolitana-Azcapotzalco, pp. 531–541, 2013.

[5] J. P. Jouany, «Methods of manipulating the microbial metabolism in the rumen,» *Ann Zootech*, vol. 43, pp. 49–62, 1994

[6] L. Rodriguez «Methane potential of sewage sludge to increase biogas production» TRITA LWR Degree Project 11:22, 2011

[7] E.Taiganides, Biogás: recuperación de energía de los excrementos animales. revista mundial de Zootecnia, 35:2–12, 1980.

[8] J. A. Pérez, "Estudio y diseño de un biodigestor para aplicación en pequeños ganaderos y lecheros", 2011

[9] R. Conrad, Contribution of hydrogen to methane production and control of hydrogen concentrations in methanogenic soils and sediments [review]. FEMS Microbiol. Ecol. 28:193–202, 1999.

[10] MINENERGIA / PNUD / FAO / GEF. Manual de biogás. 2011

Renewable energy and social development

C.O. Rivera-Blanco
Mechanical and Electrical Engineering Coordination
Universidad Iberoamericana Mexico City campus
Mexico
corb1120@yahoo.com.mx

Keywords— poverty, renewable energy, solar energy, wind energy, biomass

I. Introduction

Several states of Mexico, for historical reasons, have a large number of municipalities and in turn these have a significant number of locations, many of which have small population. Such is the case of the state of Veracruz has 212 municipalities where a lot of them have in turn a considerable number of communities, many with less than 100 inhabitants. The problems generated by this political divide, and that is accentuated in the states of the south-southeast of Mexico, is that governments, at any level, it is more challenging to provide services such as roads, schools, hospitals, sports facilities, recreational parks, water, sewage, electricity, etc., to those small communities which generates the level of the quality of life for residents of these communities is very low which causes most of these people are categorized as extreme poverty. So in the last census, Mexico has 11.7 million inhabitants population in extreme poverty and 40.3 classified as moderately poor [2].

Families who are in these conditions, and they make great efforts to try to get their children to acquire education, have a number of problems to overcome to achieve such problems such as the remoteness of schools, difficulty moving, time shuttle, the time children spend without feeding as they go, remain and return from school, or the need to give them money for transport and food, coupled with the kids come tired from long hours of daily journey and the bad power they have, means that many families give up and so the average schooling of those populations is extremely low. This problem creates a vicious circle and the gap between the quality of life of these communities and large cities widens, many of them choose to move to cities in the hope of finding a better life, but reality we encounter that for them there is no work that can reward them with dignity and do create problems for the city sleeping in parks and gardens, defecating on the street, begging for money on street corners or washing windshields, which also causes problems of road character since paralyzed the movement of vehicles when they are working and in many corners "mafias" of these people are formed and even traffic lights are controlled; clarify that are not always people coming from outside that cause these problems, and also in large cities there is considerable poverty niches.

In the state of Veracruz 25% of households do not have sewer service, 26.5% do not have piped water, 31% do not have refrigerators, 5.3% without electricity, 47% have no washing machine, the rate of illiteracy is 11.4%. Added to this situation, much of the state average temperatures to 39.5 ° C were recorded with an average relative humidity of 79%. Faced with these prospects, how can we ordinary citizens work together to solve this terrible problem of poverty, which in turn generates other major problems such as crime, drugs, migration, among others.

II. Potential of Renewable Energy

The International Energy Agency (IEA), Renewable Energy (RE) ranks as follows: solar, wind, geothermal, tidal, hydro and biomass. However it should be made clear that tidal is only considering the power generated by ocean waves that movement transform the kinetic energy into electrical energy (this is the wave power), regardless of temperature gradients generated due to depth, salinity and currents; ranking hydropower considers both large hydro as micro and mini hydro. It is important to note that large hydro often cause a significant environmental impact because sometimes divert riverbeds or retain large volumes of water when they are vented in the rainy season cause major flooding. Table 1 shows different applications of RE based on this classification but including the concept of tidal energy from temperature differences of the different layers of water.

RE involving a reduced environmental impact compared with the limited fossil resources, and they have certain autonomy as sources in some cases, inexhaustible energy that sooner or later will have an important role in energy reserves and in reducing environmental problems.

TABLE I. RENEWABLE ENERGY APPLICATIONS

SOLAR	FOTOVOLTAIC
	FOTOTHERMIC
WIND	HIGH POWER
	LOW POWER
GEOTERMIC	HIGH POWER
	THERMAL USES
TIDAL	OCEANIC THERMAL GRADIENT
	SALINITY
	MARINE CURRENTS
HYDRAULIC	BIG HYDROELECTRIC PLANTS
	MINI-HYDRAULIC GENERATION (>100KW)
BIOMASS	NATURAL: TREE BRANCHES AND LEAVES
	RESIDUAL: PRUNING, STUBBLE, ETC.
	ARISING FROM THE TRANSFORMATION OF WOOD
	ENERGY CROPS: GRAINS AND OTHERS

.

II. RENEWABLE ENERGY DEVELOPMENT

A. Solar energy

Regarding solar power, Mexico is one of the countries with the best solar radiation incidence, the northwestern part of the country receives a daily average radiation considered the best in the world, coupled with receiving the rest of the Republic It is also high.

Thechnologies for harnessing solar energy are usually classified into two main branches: photothermal processes and photovoltaic processes. The first start of the fact to heat a working fluid can have a number of applications such as producing steam, electricity, cold, among others. The latter produce electricity from the direct conversion of solar energy into electrical energy. Fig. 1 shows some technological applications from solar energy.

Thermal systems can be classified according to the type of hub used or according to the operating temperature. In the final application of thermal energy obtained depending on the type of concentrator used influences the temperature range that can be achieved and therefore the type of application.

In concentrating solar technologies for generating electrical power are thermal solar power plants consisting essentially of two parts: one that collects solar energy and converts it to heat, and another that converts heat into electricity [3]. In addition can have thermal storage devices and / or support based on conventional fuel.

Parabolic trough systems use parabolic mirrors shaped channel focus sunlight on tubular receptors high efficiency, through which a thermal fluid circulates. Hub technology linear fresnel type, with one axis tracking, differs from parabolic trough, that the absorber is fixed in space at the focal zone. The reflector is comprised of many long thin mirror segments, which rotate on parallel axes simultaneously to focus solar radiation onto the receiver. Table 2 shows the different types of concentrators and temperature range.

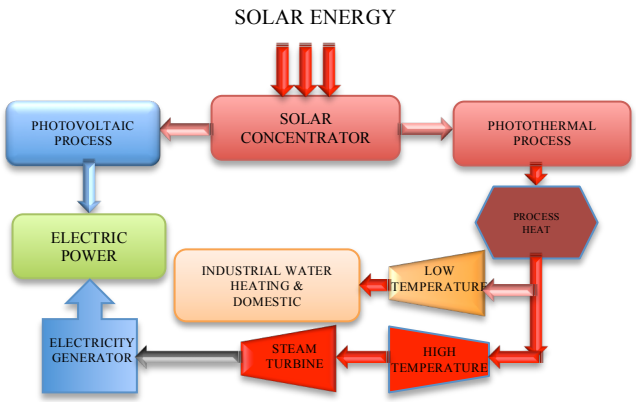

Fig. 1 Solar thecnologies

The drive systems consist of a paraboloidal concentrator parabolic dish-shaped, with a receiver in the focal zone. These hubs are mounted on a structure with a system of two-axis tracking. The collected heat is used directly by an internal combustion engine mounted receiver moving with plate structure. Stirling cycle engines and Brayton cycle currently used for converting thermal energy to electric power [4].

TABLE II. MAIN TYPES OF SOLAR COLLECTORS AND TYPICAL TEMPERATURE RANGES

TYPE OF CONCENTRATOR	TEMPERATURE (˚C)
Plane	30-80
Evacuated tube	50-190
Compound (CPC)	70-290
Parabolic through	70-290
Parabolic dish	70-930
Central tower	130-2700
Solar oven	600-3000

Central tower systems use a large field of flat mirrors with two-axis tracking, called heliostats, which track the sun to focus solar radiation onto a central receiver (heat exchanger) mounted atop a tower, they produce temperatures of approximately 500 to 1500 ° C. These plants are ideal to scale in the range of 30 to 400 MW. Solar-electric efficiency achieved by these plants is in the range of 8 to 13% [1].

Due to its thermal nature, each concentrating solar technologies can be developed in hybrid form (annealing) or operated in combination with fossil fuels. The designs of integrated solar systems and combined cycle (ISCCS) offer a number of potential advantages to both technologies. For systems of Central Tower Power, hybridization is possible with a combined cycle natural gas or coal and fuel oil Rankine cycle. The most advanced thermal storage techniques have been applied to the technology of Central Tower Power.

Investment costs and electricity generation depend on many factors related to technology, logistics and local market conditions and circumstances. Only for parabolic trough technology they have been proven investment costs through marketing. Costs for systems Central Power Tower and Dish / Stirling are still based pilot or demonstration plants need confirmation. Differences in investment costs and generation for concentrated solar power systems (CSP) can be explained by the difference in the maturity of the technology and the different technological solutions for each use.

Investment costs are one of the most important factors that determine the cost of a plant CSP. Typically, depreciation represents 25 to 40% of the cost of generation and operation and maintenance costs by 10 to 15%. The useful life of a CSP plant is 20-30 years. The remaining generation costs depend mainly on the level of solar irradiation. The most competitive prices are reached in areas where radiation levels are particularly high, higher than 1,700 kWh/m2-year [6].

Industry concentrating solar technologies increases day by day, especially developing countries, including China, have understood the importance of the RE and companies devote part of its development to this type of energy and other new open offering different technological alternatives to RE. Current research and pilot projects are combining solar concentrator technology with new designs for gas turbine and combined cycle plants. Increases in capital costs and operation and maintenance (O & M) of the core are compensated with higher efficiencies, reduced losses at startup and the dual use of critical system elements. Future cost reductions are possible with the direct steam generation (DSG), which eliminates the need for heat transfer fluid (HTF) and reduces the loss of efficiency that involves using a heat exchanger to generate steam.

Solar Concentrators: The solar concentrator is the most expensive component of a solar concentration. Best reflective material aspect of mirrors, structural design and guidelines promise future cost reductions. New reflective materials and optimizing hub designs reduce the structural costs.

Two non-technical aspects could have a greater impact on future costs and market for concentrated solar technology:
a) The development of multiple plants in the same location, in a park of solar energy, reduces technology costs because it provides O & M costs, reduced engineering and development.
b) The financial structure of the projects is also an important aspect. Concentrated solar plants require a high initial capital, and the capital cost and type of project financing can have a significant impact on the final cost of energy.

The National Solar Energy Association of Mexico (ANES), has identified some 50 manufacturers of solar heaters levels throughout Mexico, mainly concentrated in the cities of Guadalajara, Cuernavaca, Mexico City, Puebla and Morelia.

B. Wind Power

The wind resource utilization depends on the sites where the infrastructure is in place. The topography of the place has a great influence on the wind characteristics. On the other hand, the extremely strong dependence of the power generated in a

wind turbine with the wind speed (varies with the cube of the speed) makes the in situ measurements are absolutely necessary. It is true that in general, you can see that areas of certain regions have good wind conditions, but it is necessary to evaluate the resource. Wind power is varies with the height, the center of rotation of large wind turbines of 1MW power is about 70 m high, so to evaluate the resource for those conditions, it shall be measured for at least two years to a statistical analysis of the electric potential can be obtained at the site. In Mexico, they have identified sites where the wind speed exceeds 6 m / s, the design team should be according to the maximum air currents detected in order to ensure the reliability of the equipment.

Small-scale wind power generation has developed in recent years and is very useful when it is required to provide energy at a low level, but enough room for up to 6 people home, we are talking about low-rise wind turbines can provide all electrical services to a room home, where they could operate all appliances including air conditioning.

C. Geothermal energy

Geothermal resources are more likely to exist in geological zones of volcanic character, so Mexico is a country with good prospects in the magnitude of this natural resource. In general, these natural resources are categorized as follows: hydrothermal resources, resources based on dry rock systems geopressured resources, marine resources and magmatic resources.

Worldwide, only the first commercially exploited; Mexico is the third largest producer of electricity based on this type of geothermal resources, with 960 MWe and some (not electric) thermal applications running. This type of action involves the combination of a shallow aquifer thermal anomaly and a geological system sealant, which forms a reservoir [5].

Applications using heat pumps have boomed and conditioned by centralized district heating surface has increased markedly in recent years.

D. Biomass

This category includes the following resources: energy crops for the production of wood fuels, waste to energy plantations and production of liquid fuels, and agricultural waste.

The first category relates to forest resources that generate direct wood fuels from either natural forests or energy plantations and indirect wood fuels, such as sawdust.

The first type, direct fuel woods are divided into those generated in nature and expressly plantation. Of those generated in nature, there are woods, forests, thickets and hydrophilic vegetation; Mexico estimated for these four types varies between 748-1287 Petajoules Total per year (PJ / year). The estimated resource from forest plantations is expressly equivalent to 716 PJ / year [5].

Regarding indirect wood fuels, corresponding to timber wastes generated during harvesting practices of commercial timber and waste are generated mainly in sawmills as an energy resource estimate corresponds to 53 PJ / year.

The estimated energy resource of the first category corresponding to forest resources directly and indirectly generating wood fuel, total is from 1.517 to 2.056 PJ / year. The second category relates to energy crops and waste for the production of liquid fuels, specifically biodiesel and ethanol.

As for biomass resource to produce biodiesel, the most important sources are palm oil, rapeseed, soybean, castor oil, sorghum and sunflower, other sources are animal and used cooking oil fats. As for ethanol production, the resource is considered corn and sugarcane as the main input. In this category you have to be careful, but through appropriate programs could provide sources of employment for the inhabitants of marginalized communities to produce biofuels.
The third category relates to the use of agricultural waste such as bagasse, rice husks, coconut shell, and the corn stover corn. The main processes are energy for use as combustion and gasification. An estimated worldwide total of these agricultural waste is 59 million tons, which corresponds to 886 PJ / year.

E. Tidal energy

In Mexico there have been studies of oceanic potential, and have carried out projects in the field of research, however much to be done on the subject, inter alia, resource assessment.

CONCLUSIONS

The subject is vast and there is a chance that with proper implementation of RE program in communities that suffer from serious shortcomings as those described above, it would be possible to improve the quality of life of people.

It can implement systems to provide electricity through photovoltaic systems, the cost per kWh of a photovoltaic system is only $0.23, would be worth implementing these systems in underserved communities [7].

Photovoltaic pumping systems of water may help solve the problems of irrigation and improve agricultural production in our country.

Photothermal solar energy is useful in poor communities, to heat water, which can be used to process food in a traditional way, in addition to covering the basic needs of personal cleanliness.

Solar cooling systems require no power source other than the sun to operate and can produce ice for the needs of food storage.

Low wind power systems are feasible for use in places where the wind blows at speeds greater than 3 m / s (10.8 km / h). In the Mexican coast there are plenty of places where these conditions, the wind turbines are installed from 2-5 m in diameter and are not installed to greater heights to 10 m are given.

The use of biomass can be varied and it can generate biogas for household use with small digesters that can be built at low cost.

Small hydroelectric plants have the advantage that can be installed in rivers of low flow and not divert the course of these or store water in large quantities as large dams.

In conclusion, the use and installation of the RE in those communities which lack many services and that most of its inhabitants live in poverty, can significantly improve their quality of life with the implementation and use of these.

REFERENCES

[1] K. Ahmed. Renewable Energ Technologies. A review of the status and cost of selected technologies. Washington, D.C.: The world bank., 1994.

[2] CONEVAL. Consejo Nacional de Evaluacion de la Politica de Desarrollo Social, Medición de Pobreza en México, 2010: http://www.coneval.gob.mx/Informes/Med_Pobreza/Como_se_mide_la_pobreza_en%20Mexico.pdf

[3] D. R. Mills. Solar Thermal Electricity. Solar Energy , 577-651, 2001.

[4] D. R.Mills & G.L. Morrison. Compact Linear Fresnel Reflector Solar Thermal Power plants. Solar Energy , 263-283, 2000.

[5] SENER. Una visión al 2030 de la utilización de las energias renovables en México. Obtenido de Capitulo 2. Estimaciones del Recurso Energético Renovable, 2005: www.sener.gob.mx/webSener/res/168/Cap2_EstimaRE.pdf

[6] A. Tejeda, C. Gay, G. Cuevas, & C.O. Rivera. Escenarios de Energias Renovables en México bajo cambio climático, 2007: http://www.inecc.gob.mx/descargas/cclimatico/e2007q.pdf

[7] Twenergy. July 13, 2012: http://twenergy.com/energia-solar/la-energia-solar-sera-mas-barata-que-las-energias-fosiles-en-2018-580

Paquete computacional para el cálculo de flujos de potencia por coordenadas de fase

F. Toledo T., P. A. Chávez M., J.D. Juárez C., V. Ayala A.
Universidad Autónoma Metropolitana–Azcapotzalco, Av. San Pablo 180
Azcapotzalco CP 02200, D. F, México
ava@correo.azc.uam.mx

***Resumen*—Se presenta un algoritmo computacional en Visual Fortran como herramienta para realizar un estudio de flujos de potencia para un sistema trifásico en condiciones desbalanceadas, el algoritmo computacional simula condiciones desequilibradas tanto de carga como de componentes del sistema; utiliza los cálculos tradicionales para un estudio de flujos de potencia, mediante el método iterativo de Gauss-Seidel, incorporando la modelación en coordenadas de fase.**

***Palabras clave*—Flujos de potencia, coordenadas de fase, sistemas eléctricos de potencia, Gauss-Seidel, voltajes nodales, matriz de impedancia primitiva.**

I. Introducción

En el análisis tradicional de un sistema eléctrico en baja y mediana tensión, por razones económicas y técnicas, se considera balanceado. En la práctica, elementos como: Cargas monofásicas y bifásicas; líneas sin transposiciones; transformadores trifásicos, entre otros, implican la presencia de desbalances [1].

La solución que se obtiene al suponer el sistema eléctrico balanceado es aproximada; por lo tanto, si se requiere obtener la solución real es necesario modelar el sistema incluyendo los desequilibrios, tanto en la red como en las cargas. Cuando un sistema está operando en régimen desequilibrado, consecuentemente no se podrá analizar mediante el modelo tradicional monofásico, por lo que se utilizan técnicas alternativas, como la de componentes simétricas y coordenadas de fase [1], [2].

El modelo matemático en coordenadas de fase implica que cada elemento debe ser modelado mediante una matriz de 3x3. Esto representa una desventaja con respecto a la tradicional formulación por fase, ya que se requieren mayores recursos computacionales (memoria y tiempo de cálculo) en la solución.

Sin embargo, actualmente estos problemas no son tan significativos, debido a los desarrollos en el campo de la computación y al uso de técnicas computacionales más eficientes.

Desde los años 60's se han desarrollado diferentes metodologías para realizar estudios de flujos de potencia. Algunas de las técnicas más conocidas son: Método de Gauss-Seidel, Método de Newton-Raphson y Método desacoplado, entre otras. Estas técnicas se han desarrollado para Sistemas Eléctricos de Potencia (SEP) en condiciones balanceadas; en condiciones desbalanceadas se utiliza la metodología en coordenadas de fase la cual es aplicable a cualquiera de las metodologías para la obtención de flujos de potencia [3], [5].

II. Modelado en coordenadas de fase

El modelado en coordenadas de fase, parte de la matriz de impedancia primitiva de fase para cada elemento [4], dicha matriz contiene los diferentes valores de impedancias propias y mutuas por fase de cada elemento; la ecuación (1) presenta este planteamiento.

$$\mathfrak{Z}_{elem}^{ABC} = \begin{bmatrix} \mathfrak{Z}_{AA} & \mathfrak{Z}_{AB} & \mathfrak{Z}_{AC} \\ \mathfrak{Z}_{BA} & \mathfrak{Z}_{BB} & \mathfrak{Z}_{BC} \\ \mathfrak{Z}_{CA} & \mathfrak{Z}_{CB} & \mathfrak{Z}_{CC} \end{bmatrix} \quad (1)$$

La figura 1 presenta el modelo clásico de un enlace, en la cual se observa la impedancia primitiva entre los nodos p-q representada como: $\mathfrak{Z}_{pq}$, dónde:

$$\mathfrak{Z}_{pq} = \mathfrak{Z}_a = \mathfrak{Z}_b = \mathfrak{Z}_c$$

Este modelo asume que la impedancia primitiva de un enlace $\mathfrak{Z}_{pq}$ para un sistema trifásico balanceado, es igual a las impedancias primitivas y mutuas de cada fase.

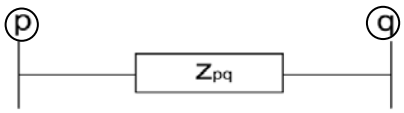

Fig. 1. Representación de una línea de transmisión balanceada.

Esta consideración tiene sus limitaciones tanto en mediana como en baja tensión, en donde se presentan desequilibrios naturales tanto en impedancias como en potencias. Por

consiguiente la representación de las impedancias primitivas propias y mutuas del enlace ya no se puede representar como una sola impedancia, si no que estos parámetros (propios y mutuos de fase) tienen que ser tomados en cuenta para efectos de análisis en la red, figura 2.

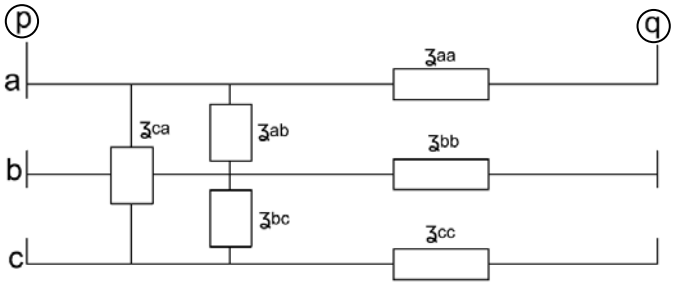

Fig. 2. Representación de una línea de transmisión desbalanceada.

Para obtener la matriz de impedancias primitivas por coordenadas de fase se utiliza la *transformación de componentes simétricas* [3], [5], el cual establece que un sistema trifásico desbalanceado se puede analizar mediante tres sistemas monofásicos. Con el teorema antes descrito se puede obtener una relación de transformación de componentes simétricas a componentes de fase, ecuación (2), la cual permite obtener la matriz de impedancia primitiva por coordenadas de fase (1), a través de una matriz conocida en componentes simétricas [4].

$$Z_{ABC} = A\ Z_{012}\ A^{-1} \tag{2}$$

Dónde:

$$A=\begin{bmatrix}1 & 1 & 1\\ a^2 & a & 1\\ a & a^2 & 1\end{bmatrix} \qquad \text{con} \qquad a=1\angle 120°$$

III. Método de Gauss-Seidel en coordenadas de fase

El estudio de flujos de potencia puede resolverse por el método tradicional de Gauss-Seidel, en razón del conjunto de ecuaciones de voltajes no lineales que se tienen para cada nodo del SEP. El método ya mencionado parte de la asignación de voltajes a todos los nodos excepto el nodo compensador (slack), en este nodo se fija un voltaje de referencia y se calcula la corriente para los demás nodos, utilizando el concepto básico del conjugado de la potencia compleja neta para el nodo *p* [3]:

$$I_p^{ABC}=\left(\left[P_p^{ABC}\right]-\left[jQ_p^{ABC}\right]\right)*\left[E_p^{*ABC}\right]^{-1} \tag{3}$$

$$p = 1,\ n$$

Donde *n* es el número de nodos. El comportamiento de la red puede ser obtenido de la ecuación:

$$I_{BUS}^{ABC}= Y_{BUS}^{ABC} E_{BUS}^{ABC} \tag{4}$$

Seleccionando la tierra como nodo de referencia, un conjunto de *n-1* ecuaciones puede ser escrito como:

$$E_p^{ABC}= \left[Y_{pp}^{ABC}\right]^{-1}\left(I_p^{ABC}- \sum_{\substack{q=1\\ q\neq p}}^{n} Y_{pq}^{ABC}*E_q^{ABC}\right) \tag{5}$$

La corriente calculada en la ecuación (3), y el voltaje obtenido para el nodo compensador (slack) se sustituyen en la ecuación (5), para obtener un nuevo conjunto de ecuaciones de voltajes para los nodos. Estos nuevos voltajes son utilizados en la ecuación (3) para recalcular las corrientes de los nodos para una subsecuente solución de la ecuación. El proceso continúa hasta que el cambio en los voltajes nodales es despreciable. La ecuación de red (5) y la ecuación del nodo de carga (3) pueden ser combinadas para obtener [4]:

$$E_p^{ABC}= \left[Y_{pp}^{ABC}\right]^{-1}\left(\left(\left[P_p^{ABC}\right]-\left[jQ_p^{ABC}\right]\right)*\left[E_p^{*ABC}\right]^{-1}- \sum_{\substack{q=1\\ q\neq p}}^{n} Y_{pq}^{ABC}*E_q^{ABC}\right) \tag{6}$$

Formulando el problema de flujos de potencia de esta manera, resulta en un conjunto de ecuaciones *no lineales* las cuales deben de resolverse mediante algún método iterativo.

Para obtener una reducción significativa en los cálculos para la obtención de la solución, es realizar previamente algunos cálculos como lo son:

$$YL_{pq}^{ABC}= \left[Y_{pq}^{ABC}\right]\left[Y_{pp}^{ABC}\right]^{-1}$$

y

$$KL_p^{ABC} = \left[P_P^{ABC} - jQ_P^{ABC}\right]\left[Y_{pp}^{ABC}\right]^{-1}$$

La ecuación (6) se simplifica a:

$$E_p^{ABC}=\left[KL_p^{ABC}\right]*\left[E_p^{ABC^*}\right]^{-1} - \sum_{\substack{q=1\\ q\neq p}}^{p} YL_{pq}^{ABC}*E_q^{ABC} \tag{7}$$

Una vez obtenida la ecuación para la obtención de los voltajes nodales de la red, se procede a aplicar la solución iterativa de Gauss-Seidel que previamente se mencionó su utilización debido a la no linealidad de la ecuación (7). El procedimiento normal para este estudio de flujos de potencia es asumir que no hay acoplamientos mutuos entre elementos, por lo que la matriz Y_{BUS}^{ABC} puede ser obtenida por inspección de la red. El diagrama de flujos para la solución por el método de Gauss-Seidel, se presenta en la figura 3.

Posteriormente de la obtención de los voltajes nodales, los flujos a través de las líneas se calculan [4]. Para esto se cuenta con el voltaje y la admitancia con lo cual se puede obtener la corriente en el nodo *p* al nodo *q*:

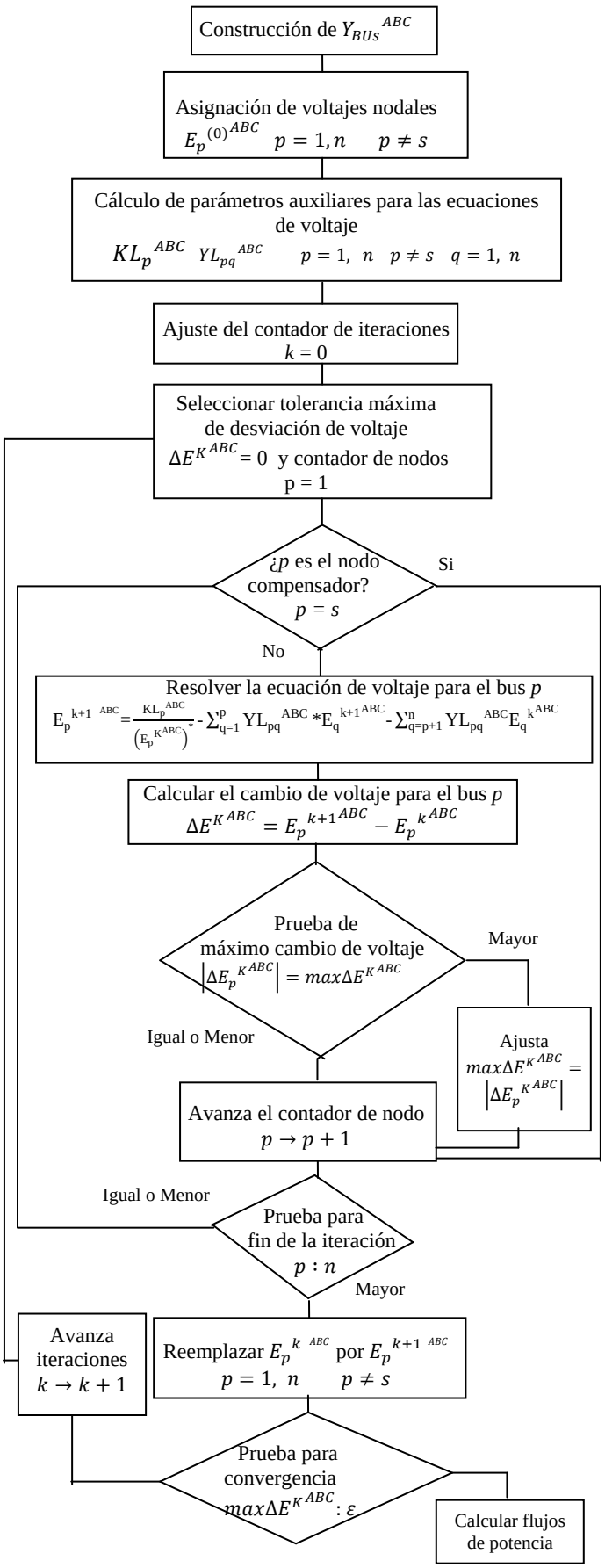

Fig. 3. Diagrama de flujos para la solución por el método de Gauss-Seidel

$$i_{pq}{}^{ABC} = ([E_p{}^{ABC}] - [E_q{}^{ABC}]) * [Y_{pq}{}^{ABC}] + [E_p{}^{ABC}] * [Y_{pq}{}^{'ABC}] * \frac{1}{2} \quad (8)$$

Se define el conjugado del flujo de potencia compleja del nodo *p* al nodo *q* como:

$$P_{pq}{}^{ABC} - j\, Q_{pq}{}^{ABC} = E_p{}^{*ABC} i_{pq}{}^{ABC} \quad (9)$$

Sustituyendo (8) en (9), tenemos el flujo de potencia del nodo *p* al nodo *q*:

$$[S_{pq}{}^{*ABC}] = [E_p{}^{*ABC}] * ([E_p{}^{ABC}] - [E_q{}^{ABC}]) * [Y_{pq}{}^{ABC}] + [E_p{}^{ABC}] * [E_p{}^{*ABC}] * [Y_{pq}{}^{'ABC}] * \frac{1}{2} \quad (10)$$

Y simultáneamente para el flujo del nodo *q* al nodo *p*:

$$[S_{qp}{}^{*ABC}] = [E_q{}^{*ABC}] * ([E_q{}^{ABC}] - [E_p{}^{ABC}]) * [Y_{pq}{}^{ABC}] + [E_q{}^{ABC}] * [E_q{}^{*ABC}] * [Y_{pq}{}^{'ABC}] * \frac{1}{2} \quad (11)$$

IV. Proyecto Computacional

Se desarrolló en lenguaje *Visual Fortran*, con el compilador *PGI VisualFortran ver.11.6*, el paquete computacional *FlujosABC*, de conformidad al diagrama de la figura3. La figura 4 muestra las unidades de trabajo (rutinas y funciones) que integran el paquete computacional para el cálculo de flujos por coordenadas de fase:

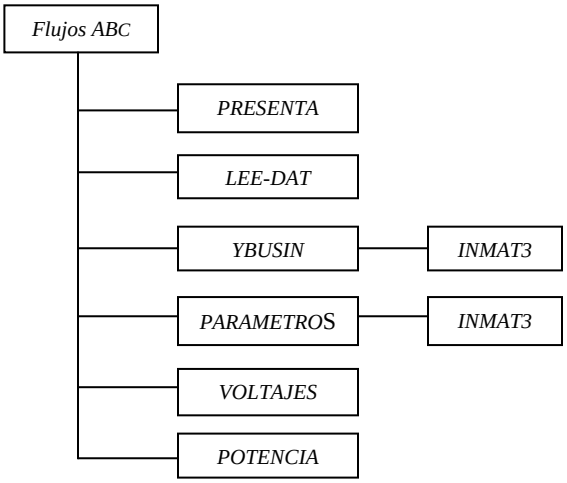

Fig. 4. Diagrama a bloques, funciones y subrutinas del programa.

El seguimiento dado al desarrollo de la metodología para la solución de flujos en coordenadas de fase, parte del programa principal *FlujosABC*, rutina que controla la ejecucion en secuencia de las subrutinas .

PRESENTA pide y abre los archivos de entrada y salida del programa ademas de imprimir en el ejecutable datos personales.

LEE-DAT lee los datos correspondientes al sistema, los transfiere y los imprime en el archivo de resultados.

YBUSIN obtiene la matriz $Ybus^{ABC}$ del sistema por inspección de la red, y la imprime en el archivo de resultados.

PARAMETROS calcula los parámetros auxiliares $KL_p{}^{ABC}$ y $YL_{pq}{}^{ABC}$ y los imprime en la hoja de resultados, los parámetros auxiliares posteriormente son utilizados en la ecuación de voltaje nodales.

VOLTAJES obtiene los voltajes nodales de la red bajo análisis mediante la ecuación (18), aplicando la solución iterativa de Gauss-Seidel.

POTENCIAS obtiene los flujos de potencia así como la potencia neta en el nodo compensador, pérdidas de nodo a nodo, balance de potencia reactiva y activa en el sistema y el factor de potencia en el nodo compensador.

INMAT3 obtiene la inversa de matrices complejas de orden 3x3.

Para las subrutinas se utilizaron los módulos de transferencia de datos siguientes: *mARCHIVO*, *mDATA01*, *mDATA02*, *mDATA03*, *mDATA04*, *mDATA05* y *mUNOCERO*, en los cuales se tienen las variables utilizadas a lo largo de cada rutina en los cálculos de la solución de flujos de potencia.

V. Resultados de la Simulación

Los resultados obtenidos con el paquete computacional desarrollado en lenguaje *Visual Fortran* [7], [8] en coordenadas de fase son validados con un sistema de prueba IEEE, figura 5.

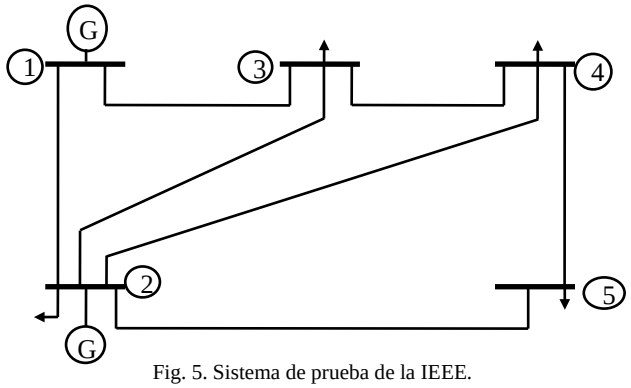

Fig. 5. Sistema de prueba de la IEEE.

Se utiliza un factor de aceleración de 1.4 y una tolerancia de 0.0001. Los datos de líneas y nodos se especifican en las tablas I y II.

TABLA I
Valores de impedancias del sistema de prueba (pu)

Código de bus **p-q**	Impedancia **Zpq**	Admitancia **y´pq/2**
1-2	0.02 + j0.06	0.0 + j0.030
1-3	0.08 + j0.24	0.0 + j0.025
2-3	0.06 + j0.18	0.0 + j0.020
2-4	0.06 + j0.18	0.0 + j0.020
2-5	0.04 + j0.12	0.0 + j0.015
3-4	0.01 + j0.03	0.0 + j0.010

TABLA I I
VALORES DE GENERACIÓN Y CARGA DEL SISTEMA DE PRUEBA (PU)

Código de bus p	Voltaje asumido del bus	Generación		Carga	
		Megawatts	Megavars	Megawatts	Megavars
1	1.0 + j0.0	0	0	0	0
2	1.0 + j0.0	40	30	20	10
3	1.0 + j0.0	0	0	45	15
4	1.0 + j0.0	0	0	40	5
5	1.0 + j0.0	0	0	60	10
4-5		0.08 + j0.24		0.0 + j0.010	

Se presenta para la figura 5 un listado de resultados realizados en con paquete computacional elaborado en *Visual Fortran*, con el procedimiento antes descrito.

Para poder realizar la simulación en coordenadas de fase con un sistema balanceado, se realiza la suposición de que las impedancias primitivas mutuas no existen por lo que solo se tendrán impedancias primitivas propias, es decir, la matriz de impedancia primitiva solo tendrá valores en la diagonal principal todo lo demás será cero. Se muestran a continuación, resultados resumidos:

```
   NUMERO DE NODOS           5
   NUMERO DE ELEMENTOS       7


  <<<<Condiciones para la simulación>>>>

   Potencia base =     100.000
   Iteraciones Max =  15
   Tolerancia Max =  0.000100000
   Factor de Acel = 1.40

<<<<<<<<<<<<<PARAMETROS KLp (abc)>>>>>>>>>>>>>>>>>>

               KLp (2, a) = .7405E-02  + j  .3695E-02
               KLp (2, b) = .7405E-02  + j  .3695E-02
               KLp (2, c) = .7405E-02  + j  .3695E-02

               KLp (3, a) =-.6981E-02  + j -.9299E-02
               KLp (3, b) =-.6981E-02  + j -.9299E-02
               KLp (3, c) =-.6981E-02  + j -.9299E-02

               KLp (4, a) =-.4267E-02  + j -.8913E-02
               KLp (4, b) =-.4267E-02  + j -.8913E-02
               KLp (4, c) =-.4267E-02  + j -.8913E-02

               KLp (5, a) =-.2413E-01  + j -.4545E-01
               KLp (5, b) =-.2413E-01  + j -.4545E-01
               KLp (5, c) =-.2413E-01  + j -.4545E-01

<<<<<<<<<<<<<PARAMETROS YLpq (abc)>>>>>>>>>>>>>>>>>>

   YLpq (2, 1, a, a) =-.4626E+00  + j  .3638E-03
   YLpq (2, 1, a, b) = .0000E+00  + j  .0000E+00
   YLpq (2, 1, a, c) = .0000E+00  + j  .0000E+00
   YLpq (2, 1, b, a) = .0000E+00  + j  .0000E+00
   YLpq (2, 1, b, b) =-.4626E+00  + j  .3638E-03
   YLpq (2, 1, b, c) = .0000E+00  + j  .0000E+00
   YLpq (2, 1, c, a) = .0000E+00  + j  .0000E+00
   YLpq (2, 1, c, b) = .0000E+00  + j  .0000E+00
   YLpq (2, 1, c, c) =-.4626E+00  + j  .3638E-03

   YLpq (2, 3, a, a) =-.1542E+00  + j  .1213E-03
   YLpq (2, 3, a, b) = .0000E+00  + j  .0000E+00
   YLpq (2, 3, a, c) = .0000E+00  + j  .0000E+00
   YLpq (2, 3, b, a) = .0000E+00  + j  .0000E+00
   YLpq (2, 3, b, b) =-.1542E+00  + j  .1213E-03
   YLpq (2, 3, b, c) = .0000E+00  + j  .0000E+00
   YLpq (2, 3, c, a) = .0000E+00  + j  .0000E+00
   YLpq (2, 3, c, b) = .0000E+00  + j  .0000E+00
   YLpq (2, 3, c, c) =-.1542E+00  + j  .1213E-03

   YLpq (2, 4, a, a) =-.1542E+00  + j  .1213E-03
   YLpq (2, 4, a, b) = .0000E+00  + j  .0000E+00
   YLpq (2, 4, a, c) = .0000E+00  + j  .0000E+00
   YLpq (2, 4, b, a) = .0000E+00  + j  .0000E+00
   YLpq (2, 4, b, b) =-.1542E+00  + j  .1213E-03
   YLpq (2, 4, b, c) = .0000E+00  + j  .0000E+00
   YLpq (2, 4, c, a) = .0000E+00  + j  .0000E+00
```

```
     YLpq (2, 4, c, b) = .0000E+00  + j  .0000E+00
     YLpq (2, 4, c, c) =-.1542E+00  + j  .1213E-03

     YLpq (2, 5, a, a) =-.2313E+00  + j  .1819E-03
     YLpq (2, 5, a, b) = .0000E+00  + j  .0000E+00
     YLpq (2, 5, a, c) = .0000E+00  + j  .0000E+00
     YLpq (2, 5, b, a) = .0000E+00  + j  .0000E+00
     YLpq (2, 5, b, b) =-.2313E+00  + j  .1819E-03
     YLpq (2, 5, b, c) = .0000E+00  + j  .0000E+00
     YLpq (2, 5, c, a) = .0000E+00  + j  .0000E+00
     YLpq (2, 5, c, b) = .0000E+00  + j  .0000E+00
     YLpq (2, 5, c, c) =-.2313E+00  + j  .1819E-03

<<<<<<<<<<<<EL  SISTEMA  CONVERGE  EN   11ITERACIONES>>>>>>>>>>>>>

 << VOLTAJES CALCULADOS (PU)         magnitud           ángulo >>

Voltaje en el NODO 1 Fase a     =     1.000000       .000000 grados
Voltaje en el NODO 1 Fase b     =     1.000000       .000000 grados
Voltaje en el NODO 1 Fase c     =     1.000000       .000000 grados

Voltaje en el NODO 2 Fase a     =     .984651      -3.137205 grados
Voltaje en el NODO 2 Fase b     =     .984651      -3.137205 grados
Voltaje en el NODO 2 Fase c     =     .984651      -3.137205 grados

Voltaje en el NODO 3 Fase a     =     .959208      -5.614429 grados
Voltaje en el NODO 3 Fase b     =     .959208      -5.614429 grados
Voltaje en el NODO 3 Fase c     =     .959208      -5.614429 grados

Voltaje en el NODO 4 Fase a     =     .958396      -5.991539 grados
Voltaje en el NODO 4 Fase b     =     .958396      -5.991539 grados
Voltaje en el NODO 4 Fase c     =     .958396      -5.991539 grados

Voltaje en el NODO 5 Fase a     =     .952248      -6.928322 grados
Voltaje en el NODO 5 Fase b     =     .952248      -6.928322 grados
Voltaje en el NODO 5 Fase c     =     .952248      -6.928322 grados


<<<<<<<<<FLUJOS DE POTENCIA EN ELEMENTOS VALORES EN MW Y MVAR>>>>>>>

FLUJOS DE POTENCIA EN ELEMENTO: p (1), q (2)
                     FASE  a =   89.24319 (MW) + j  -4.70633 (MVAR)
                     FASE  b =   89.24319 (MW) + j  -4.70633 (MVAR)
                     FASE  c =   89.24319 (MW) + j  -4.70633 (MVAR)

FLUJOS DE POTENCIA EN ELEMENTO: p (1), q (3)
                     FASE  a =   40.86517 (MW) + j   2.79205 (MVAR)
                     FASE  b =   40.86517 (MW) + j   2.79205 (MVAR)
                     FASE  c =   40.86517 (MW) + j   2.79205 (MVAR)

FLUJOS DE POTENCIA EN ELEMENTO: p (2), q (3)
                     FASE  a =   24.73381 (MW) + j   4.22436 (MVAR)
                     FASE  b =   24.73381 (MW) + j   4.22436 (MVAR)
                     FASE  c =   24.73381 (MW) + j   4.22436 (MVAR)

FLUJOS DE POTENCIA EN ELEMENTO: p (2), q (4)
                     FASE  a =   28.00009 (MW) + j   3.74012 (MVAR)
                     FASE  b =   28.00009 (MW) + j   3.74012 (MVAR)
                     FASE  c =   28.00009 (MW) + j   3.74012 (MVAR)

FLUJOS DE POTENCIA EN ELEMENTO: p (2), q (5)
                     FASE  a =   54.98588 (MW) + j   8.51465 (MVAR)
                     FASE  b =   54.98588 (MW) + j   8.51465 (MVAR)
                     FASE  c =   54.98588 (MW) + j   8.51465 (MVAR)

FLUJOS DE POTENCIA EN ELEMENTO: p (3), q (4)
                     FASE  a =   18.95112 (MW) + j  -4.57296 (MVAR)
                     FASE  b =   18.95112 (MW) + j  -4.57296 (MVAR)
                     FASE  c =   18.95112 (MW) + j  -4.57296 (MVAR)

FLUJOS DE POTENCIA EN ELEMENTO: p (4), q (5)
                     FASE  a =    6.34705 (MW) + j  -1.90614 (MVAR)
                     FASE  b =    6.34705 (MW) + j  -1.90614 (MVAR)
                     FASE  c =    6.34705 (MW) + j  -1.90614 (MVAR)

FLUJOS DE POTENCIA DE ELEMENTO: q (2), p (1)
                     FASE  a =  -87.64974 (MW) + j   3.57807 (MVAR)
                     FASE  b =  -87.64974 (MW) + j   3.57807 (MVAR)
                     FASE  c =  -87.64974 (MW) + j   3.57807 (MVAR)

FUJOS DE POTENCIA DE ELEMENTO: q (3), p (1)
                     FASE  a =  -39.50679 (MW) + j  -3.51713 (MVAR)
                     FASE  b =  -39.50679 (MW) + j  -3.51713 (MVAR)
                     FASE  c =  -39.50679 (MW) + j  -3.51713 (MVAR)

FLUJOS DE POTENCIA DE ELEMENTO: q (3), p (2)
                     FASE  a =  -24.33171 (MW) + j  -6.79730 (MVAR)
                     FASE  b =  -24.33171 (MW) + j  -6.79730 (MVAR)
                     FASE  c =  -24.33171 (MW) + j  -6.79730 (MVAR)

FLUJOS DE POTENCIA DE ELEMENTO: q (4), p (2)
                     FASE  a =  -27.49494 (MW) + j  -6.00081 (MVAR)
                     FASE  b =  -27.49494 (MW) + j  -6.00081 (MVAR)
                     FASE  c =  -27.49494 (MW) + j  -6.00081 (MVAR)

FLUJOS DE POTENCIA DE ELEMENTO: q (5), p (2)
                     FASE  a =  -53.69750 (MW) + j  -7.46398 (MVAR)
                     FASE  b =  -53.69750 (MW) + j  -7.46398 (MVAR)
                     FASE  c =  -53.69750 (MW) + j  -7.46398 (MVAR)

FLUJOS DE POTENCIA DE ELEMENTO: q (4), p (3)
                     FASE  a =  -18.91064 (MW) + j   2.85581 (MVAR)
                     FASE  b =  -18.91064 (MW) + j   2.85581 (MVAR)
                     FASE  c =  -18.91064 (MW) + j   2.85581 (MVAR)

FLUJOS DE POTENCIA DE ELEMENTO: q (5), p (4)
                     FASE  a =   -6.31183 (MW) + j  -2.55145 (MVAR)
                     FASE  b =   -6.31183 (MW) + j  -2.55145 (MVAR)
                     FASE  c =   -6.31183 (MW) + j  -2.55145 (MVAR)

 <<<<<<<POTENCIA NETA DEL NODO COMPENSADOR Y FACTOR DE POTENCIA>>>>>
  FASE  a = 130.10840 (MW) + j  -1.91428 (MVAR)     fp =   .9999
  FASE  b = 130.10840 (MW) + j  -1.91428 (MVAR)     fp =   .9999
  FASE  c = 130.10840 (MW) + j  -1.91428 (MVAR)     fp =   .9999

<<<<<<<<PERDIDAS DEL NODO q =  2 AL NODO p =  1>>>>>>>>>>
    PERDIDAS DE LA FASE a =    1.59345 (MW) + j  -1.12826 (MVAR)
    PERDIDAS DE LA FASE b =    1.59345 (MW) + j  -1.12826 (MVAR)
    PERDIDAS DE LA FASE c =    1.59345 (MW) + j  -1.12826 (MVAR)

<<<<<<<<PERDIDAS DEL NODO q =  3 AL NODO p =  1>>>>>>>>>>
    PERDIDAS DE LA FASE a =    1.35837 (MW) + j   -.72508 (MVAR)
    PERDIDAS DE LA FASE b =    1.35837 (MW) + j   -.72508 (MVAR)
    PERDIDAS DE LA FASE c =    1.35837 (MW) + j   -.72508 (MVAR)

<<<<<<<<PERDIDAS DEL NODO q =  3 AL NODO p =  2>>>>>>>>>>
    PERDIDAS DE LA FASE a =     .40210 (MW) + j  -2.57294 (MVAR)
    PERDIDAS DE LA FASE b =     .40210 (MW) + j  -2.57294 (MVAR)
    PERDIDAS DE LA FASE c =     .40210 (MW) + j  -2.57294 (MVAR)

<<<<<<<<PERDIDAS DEL NODO q =  4 AL NODO p =  2>>>>>>>>>>
    PERDIDAS DE LA FASE a =     .50514 (MW) + j  -2.26069 (MVAR)
    PERDIDAS DE LA FASE b =     .50514 (MW) + j  -2.26069 (MVAR)
    PERDIDAS DE LA FASE c =     .50514 (MW) + j  -2.26069 (MVAR)

<<<<<<<<PERDIDAS DEL NODO q =  5 AL NODO p =  2>>>>>>>>>>
    PERDIDAS DE LA FASE a =    1.28838 (MW) + j   1.05067 (MVAR)
    PERDIDAS DE LA FASE b =    1.28838 (MW) + j   1.05067 (MVAR)
    PERDIDAS DE LA FASE c =    1.28838 (MW) + j   1.05067 (MVAR)

<<<<<<<<PERDIDAS DEL NODO q =  4 AL NODO p =  3>>>>>>>>>>
    PERDIDAS DE LA FASE a =     .04048 (MW) + j  -1.71715 (MVAR)
    PERDIDAS DE LA FASE b =     .04048 (MW) + j  -1.71715 (MVAR)
    PERDIDAS DE LA FASE c =     .04048 (MW) + j  -1.71715 (MVAR)

<<<<<<<<PERDIDAS DEL NODO q =  5 AL NODO p =  4>>>>>>>>>>
    PERDIDAS DE LA FASE a =     .03522 (MW) + j  -4.45759 (MVAR)
    PERDIDAS DE LA FASE b =     .03522 (MW) + j  -4.45759 (MVAR)
    PERDIDAS DE LA FASE c =     .03522 (MW) + j  -4.45759 (MVAR)


  <<<<<<<<<<<<<<BALANCE DE POTENCIAS DEL SISTEMA>>>>>>>>>>>>>>>>>>>>

                PERDIDAS TOTALES EN LA FASE a =     5.2232 (MW)
                BALANCE REACTIVO EN LA FASE a =   -11.8110 (MVAR)

  <<<<<<<<<<<<<<BALANCE DE POTENCIAS DEL SISTEMA>>>>>>>>>>>>>>>>>>>>

                PERDIDAS TOTALES EN LA FASE b =     5.2232 (MW)
                BALANCE REACTIVO EN LA FASE b =   -11.8110 (MVAR)

  <<<<<<<<<<<<<<BALANCE DE POTENCIAS DEL SISTEMA>>>>>>>>>>>>>>>>>>>>

                PERDIDAS TOTALES EN LA FASE c =     5.2232 (MW)
                BALANCE REACTIVO EN LA FASE c =  -11.8110 (MVAR)
```

VI. CONCLUSIONES

- En la actualidad los estudios de flujos de potencia se realizan bajo la suposición de que el sistema esta balanceado con lo cual se reducen considerablemente las operaciones matemáticas. En la realidad los SEP presentan un desbalance, con lo cual las operaciones matemáticas se hacen más complejas pero se obtiene un estudio más preciso de las condiciones reales de operación del sistema.
- En el trabajo realizado se desarrolló un paquete computacional para el cálculo de los flujos de potencia el cual puede ser aplicado a condiciones de operación tanto balanceadas como desbalanceadas.
- Se utilizó un modelo computacional de *memoria dinámica* por lo que no se tiene limitación en cuanto al número de nodos y elementos. Esto representa un

apoyo didáctico significativo para el apoyo de actividades docentes en el área de ingeniería eléctrica.

- Mediante el paquete *FlujosABC* se tiene una herramienta de análisis de SEP con la cual se pueden obtener parámetros por fase del sistema como: voltajes nodales, potencias activa y reactiva, entre otros.
- Cabe mencionar que la parte de los circuitos asociados a redes de distribución en baja y mediana tensión, *operan naturalmente desbalanceados*, por lo que la herramienta desarrollada tiene aplicaciones significativas en ésta área.
- El paquete desarrollado puede obtenerse gratuitamente, para fines didácticos, a las direcciones electrónicas de los autores.

REFERENCIAS

[1] Juan Marcos García Martínez, "Análisis de sistemas desbalanceados para el diseño y operación de redes", Tesis de Maestría. Universidad Autónoma de Nuevo León, Monterrey. N. L. Diciembre de 1989.
[2] J. M. García, F. Aboytes. "*Análisis de Sistemas de Potencia Desbalanceados*", Parte 4, Estudio de flujos de potencia en sistemas desbalanceados. U.A.N.L., F.I.M.E. , DIE-87-02, Agosto de 1987.
[3] Fernando Toledo Toledo (2001). Departamento de Energía. Área Eléctrica. UAM Azcapotzalco. *Análisis de Sistemas de Potencia: Algoritmos y Programas Computacionales.*
[4] William D. Stevenson Jr. (1996). *Power System Analysis.* McGraw-Hill.
[5] J. C. Das. *Power System Analysis "short-Circuit Load Flow and Harmonics"*. Marcel Dekker, Inc. New York. Basel.
[6] PGI® Visual FORTRAN User's Guide. Parallel FORTRAN for Scientists and Engineers Release 2011. The Portland Group.
[7] Compaq Visual FORTRAN Programmer´s Guide. Compaq Computer Corporation. Houston, Texas. August 2001

Fernando Toledo Toledo Ingeniero Industrial en Electricidad (ITRO), realizó estudios de Maestría y Doctorado en Ciencias (Ing. Eléctrica) por la Sección de Estudios de Posgrado e Investigación de la ESIME-IPN. Profesor investigador y consultor de la UAM-A donde produce software didáctico y comercial para el análisis de sistemas eléctricos, siendo también responsable de programas de vinculación con el sector industrial.
ftoledo2@azc.uam.mx

Chávez Mendoza Pablo Arturo. Técnico en Mantenimiento Industrial (CECYTEM 2008), Egresado de la carrera de Ingeniería Eléctrica en la UAM Azcapotzalco (2014). El presente trabajo es parte de su tesis de licenciatura.
pabloarturo11@gmail.com

José Dolores Juárez Cervantes. Maestro en Ciencias (Ing. Eléctrica) por el Instituto Politécnico de Kíev. Profesor investigador de la UAM desde 1987, donde imparte cursos relacionados con los sistemas eléctricos de potencia. Ha publicado tres libros.
jjc@correo.azc.uam.mx.

Vicente Ayala Ahumada. Ingeniero Electricista, M. en C. y Dr. en Ciencias (Administración) por la ESIME y la ESCA del IPN. Profesor investigador de la UAM desde 1984; imparte cursos relacionados con sistemas eléctricos industriales y desarrolla prototipos y equipos tridimensionales para apoyo a la docencia, investigación y cursos de educación continua.
ava@correo.azc.uam.mx

Life cycle greenhouse gas emissions of electricity generated from a cogeneration project in Morelos Petrochemical Complex and CO_2 capture options

M.C. Avalos-Islas
Subgerencia de Protección Ambiental. PEMEX, Jacarandas No. 100, Col. Rancho Alegre
Coatzacoalcos, Ver. CP. 96558, México

S.A. Martínez-Delgadillo
Depto. Ciencias Básicas, Universidad Autónoma Metropolitana–Azcapotzalco, Av. San Pablo 180
Azcapotzalco CP 02200, D. F, México

C. Pretelín Vergara
Facultad de Ingeniería Química· Benemérita Universidad Autónoma de Puebla. Edificio 105 H, Prol 14 Sur s/n, Cd Universitaria, 72570 Heróica Puebla de Zaragoza, Pue

M.A. Morales-Mora*
Subgerencia de Protección Ambiental. PEMEX, Jacarandas No. 100, Col. Rancho Alegre
Coatzacoalcos, Ver. CP. 96558, México
e-mail: *miguel.angel.moralesmo@pemex.com

Abstract: **The CO_2 emissions from Morelos petrochemical complex (MPC) reach the 1.7 million of ton per year, which are generated through the combined production of heat and power (CHP) which has an efficiency of 58%. This study performs a life cycle assessment (LCA) of the greenhouse gas emissions (GHG) of fossil fuel fired power plant in the cogeneration project. The functional unit is 1 MWh. The project considers changing the current steam-turbine generators (Scenario A) to gas turbine (Scenario B).**

The environmental impacts of the greenhouse gas emission were analyzed through life cycle impact assessment in both scenarios. The cogeneration project will record a reduction in all categories of impact evaluated in comparison to the current operation of the plant.

The climatic change and fossil depletion impact categories registered the greatest reductions, 23.4 % and 31.9 %, respectively. The emission factor of GHG for each MWh will change from 626 $kgCO_{2e}$/MWh in the scenario A to 460 $kgCO_{2e}$/MWh in the scenario B (Figure 1). This value is similar to the GHG emission of natural gas combined cycle (NGCC) power plant. Also, the cogeneration project will allow a reduction of GHG emissions per unit of production, from 2.23 tCO_{2e}/t to 1.88 tCO_{2e}/t. With this project, the neutralization of the GHG emission could reach 1 million tCO2e/year.

In addition, the possibilities of incorporating a plant of CO_2 capture for enhance oil recovery (EOR) or sequestration in the project was analyzed. Preliminary result showed that the emission factor of GHG with CO_2 capture could reach a value of 80 $kgCO_{2e}$/MWh.

Keywords: Environmental impact, life cycle assessment, gas turbine, steam-turbine generators

I. INTRODUCION

El incremento de la concentración de gases de efecto invernadero (GEI) en la atmósfera al alcanzar 49 (±4.5) $GtCO_{2e}$/año en 2010, con una contribución del 35% del total por el sector de energía. Esta circunstancia ha obligado al sector a identificar oportunidades efectivas para mitigar sus emisiones, contribuyendo a la estabilización de las concentraciones de CO_2 por debajo de los 450 ppm y mantener como límite entre 2 y 2.4°C como valor promedio de temperatura a nivel mundial [1].

México se situó en el décimo lugar entre los países con mayor producción de energía primaria con 1.8% de la energía total producida en el mundo durante 2012. Los hidrocarburos (petróleo crudo, gas natural y condensados) continúan siendo la principal fuente de energía primaria con un 90.5%; la energía producida a partir de fuentes renovables, 6.2%; el carbón mineral, 2.2% y la energía nuclear, 1.1% [2]. El consumo per cápita anual de energía fue de 75.2 GJ, equivalente a 9.86 barriles de petróleo por habitante.

En un análisis efectuado a 16 ramas del sector industrial Mexicano en 2003 [3], registró un consumo final de energía de 1143.07 PJ, en la cual la industria petroquímica representó 24.22 PJ, equivalente a una emisión de 1.34 Mton CO_2 o el 2.06 % del total del sector Industrial Mexicano. De acuerdo a [4], en 2012 el sector petroquímico paraestatal emitió 6,1 Mton de GEI (CO_2 y metano) de sus emisiones directas. En este contexto, el Programa Especial de Cambio Climático (2014-2018) del Gobierno Mexicano [5], establece, dentro de sus acción de mitigación, promover y fomentar el desarrollo de mecanismos para proveer información confiable y oportuna al consumidor sobre eficiencia energética y emisiones de GEI.

PEMEX tiene un conjunto de acciones en su Plan de Acción Climática en el rubro de mitigación para reducir sus emisiones de GEI por sus operaciones actuales y futuras, continuando con la producción y uso de combustibles fósiles y participando en el proceso de des-carbonización del sector energético para contrarrestar los efectos del cambio climático. Sin embargo, se ha observado que las estimaciones de reducción de GEI se llevan a cabo mediante el uso de factores de caracterización (FC) solo del CO_2, NOx y CH_4, sin incorporar todas las

sustancias en la cadena de valor de un proceso, producto o servicio tiene las sustancias diferentes FC con potencial de GEI. Por lo tanto, en muchos casos se tienen subestimaciones de la emisión o de reducción de un determinado proyecto. En el caso específico del área de petroquímica, la energía eléctrica y el vapor generado en el Complejo Petroquímico Morelos (CPQM) se lleva a cabo mediante la producción combinada de calor y electricidad (CHP) para sus operaciones, con baja eficiencia: 58 % CHP. Así por ejemplo, las plantas de generación de electricidad con carbón en USA registran una emisión promedio de 712 kg CO_2/MWh [6] y las de Ciclo Combinado que usan gas natural (NGCC), un rango de 344 a 378 kg de CO_2/MWh y de 40-66 CO_2/MWh para plantas con captura de CO_2 [7].

Actualmente en el CPQM se lleva a cabo la ingeniera básica para realizar el proyecto de cogeneración, en el cual se pretende cambiar los turbogeneradores a vapor por dos turbogeneradores a gas de 72 MW con recuperación de calor, a fin de incrementar su eficiencia, reducir costos, disminuir el consumo de gas combustible y por ende las emisiones de gases de efecto invernadero (Fig.1).

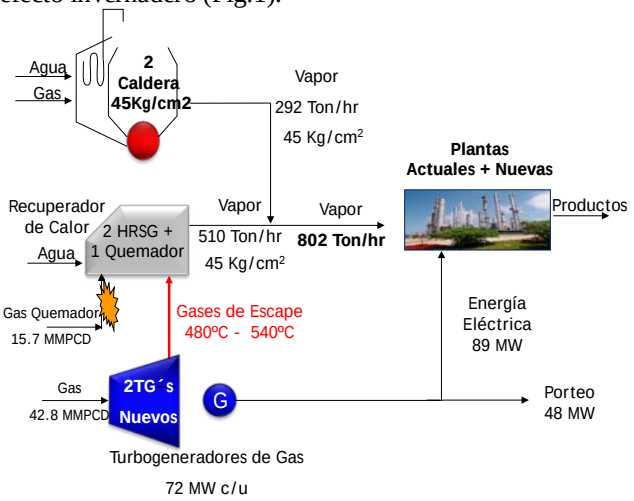

Fig.1. Proyecto de Cogeneración en el CPQM

El objetivo general de este trabajo fue evaluar el impacto ambiental usando el análisis de ciclo de vida (ACV) para el proyecto de cogeneración del CPQM, de acuerdo a la Norma ISO 14040-14044 [8;9], en el cual se discute la opción de captura post-combustión, separando el CO_2 de los gases de combustión como opción de utilización para los proyectos de recuperación mejorada (EOR) en el área del Activo Integral Cinco Presidentes (AICP), en el marco de la futura regulación en USA de plantas de generación de electricidad y su conexión con la tecnología de captura, uso y almacenamiento de CO_2 [10, 11].

En el presente trabajo, los objetivos específicos fueron:

a) Estimar los impactos ambientales y las emisiones de gases de efecto invernadero (GEI) presentes de la operación (Escenario A) de los servicios auxiliares y la reducción de estos por los proyectos de cogeneración (Escenario B).

b) Estimar la emisión de GEI por cada MWh producido para ambos escenarios.

II. METODOLOGÍA

II.1 Alcance estudio, unidad funcional y límites del sistema

El estudio considera las plantas de generación de vapor y energía eléctrica actuales del CPQM, así como la planta de cogeneración futura.

La función principal del proceso es generar vapor y electricidad para las operaciones de los Complejos Petroquímicos. Para evaluar sus potenciales impactos ambientales del proyecto, se consideran dos escenarios de evaluación para propósitos de comparación (Tabla 1).

Tabla 1. ESCENARIOS EVALUADOS PARA EL PROCESO DE PRODUCCIÓN DE VAPOR Y ELECTRICIDAD

Instalación	*Escenario A*	*Escenario B*
CPQM	- - Producción de vapor y electricidad - Capacidad: 3 turbogeneradores a vapor de 48 MW c/u - Eficiencia CHP: 58 %	- Producción de vapor y electricidad - Capacidad: 2 turbogeneradores a gas de 72 MW c/u - Eficiencia CHP: > 80 %

Unidad funcional: Se considera la producción de 1 MWh equivalente a: 0.1487 MWh (17.46 %) para la electricidad + 0.851 MWh (82.53 %) de vapor.

Se consideran los límites del sistema para los dos escenarios de producción de vapor y electricidad en la planta de servicios auxiliares ubicada en el CPQM. Se utilizó un modelo basado en el sistema de expansión [12], como procedimiento de asignación. No se incluyen la etapa de obtención de la materia prima, distribución y consumo de productos finales (uso).

Para el caso del escenario A, no se consideran cargas evitadas. En ambos escenarios, el vapor y la electricidad es el producto principal. Para el escenario B, la reducción de agua de enfriamiento y la electricidad de las correspondientes torres de enfriamiento que dejaran de usarse, se consideran productos evitados. La carga ambiental de estos insumos evitados tiene signo negativo, es decir, se resta del impacto global del sistema. Esto significa, cuantificar los recursos y emisiones evitadas por dejar de operar 9 celdas de 14 en la torre de enfriamiento y 6 calderas (3 de 45 kg/cm^2 y 3 de 60 kg/cm^2) en el CPQM. Para la evaluación de impactos se utilizó el método de ReCiPe [13] (Goedkoop, et al., 2009) mediante el uso del software SimaPro 7.3.3, por lo que se evalúan 18 categorías de puntos intermedios y tres categorías de punto final o áreas de protección. Asimismo, se estiman las emisiones de GEI como CO_2 equivalente (CO_{2e}) mediante el modelo del IPCC (Panel Intergubernamental de Cambio Climático) para 20 años.

Los datos del inventario de las plantas generación de vapor y generación eléctrica y del proyecto de cogeneración se presentan en las Figuras 2 y 3, los cuales sirvieron de base para el ACV.

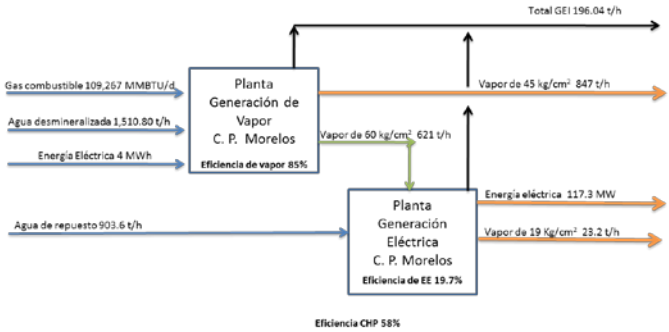

Fig. 2. Entradas y salidas de la planta de generación vapor y eléctrica del CPQM (Escenario A)

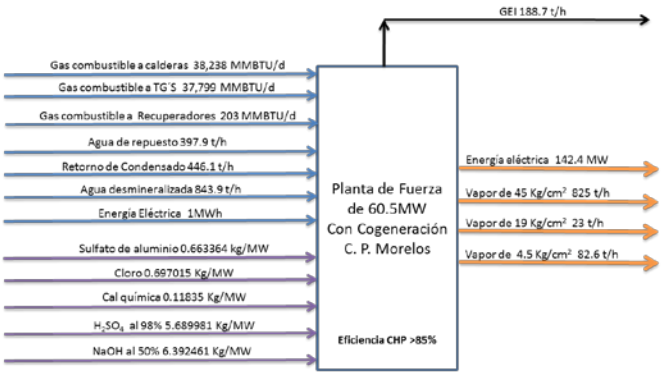

Fig.3. Entradas y salidas de la planta de generación vapor y eléctrica del CPQM (Escenario B)

Fueron tomados datos de entrada y salida típicos de una planta de NGCC con captura de CO_2 para modelar las emisiones del proyecto de cogeneración del CPQM con captura [14;15] .

III. RESULTADOS Y DISCUSION

III. Evaluación de impactos ambientales

En la figura 4 podemos observar el resultado de reducción de 11 de 18 categorías de impactos ambientales normalizadas para el escenario B (Cogeneración).
En la tabla 2 se muestran los resultados comparativos de los impactos ambientales del diseño original de la planta de vapor y energía eléctrica (Escenario A) y el proyecto de cogeneración (Escenario B) del CPQM. Las categorías de impacto que mayor relevancia tienen desde el punto de vista de masa; cambio climático y agotamiento de combustibles registraron una disminución del 25.9 y 35.4 %, con respecto al Escenario B.

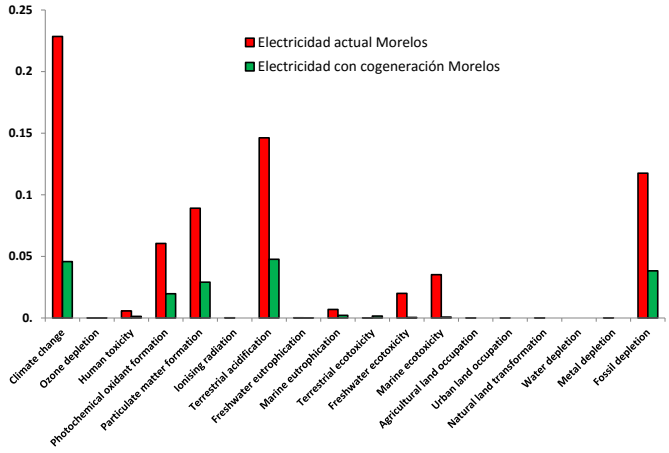

Fig. 4. Evaluación de categorías de impacto entre el diseño original (Escenario A) y el rediseño (Escenario B)

Solo la categoría de impacto toxicidad terrestre tuvo un incremento en el escenario B.

Tabla 2. RESULTADOS COMPARATIVOS Y PORCENTAJE DE REDUCCIÓN DE CATEGORÍAS DE IMPACTOS AMBIENTALES INTERMEDIOS

Categoría de impacto	Unidad	Escenario (A)	Escenario (B)	% reducción IA: A vs B
Climate change	kg CO2 eq	581.74	431.01	25.91
Ozone depletion	kg CFC-11 eq	0.00	0.00	67.41
Human toxicity	kg 1,4-DB eq	0.67	0.30	54.60
Photochemical oxidant formation	kg NMVOC	2.96	1.92	35.30
Particulate matter formation	kg PM10 eq	1.25	0.81	35.36
Ionising radiation	kg U235 eq	0.26	0.00	100.00
Terrestrial acidification	kg SO2 eq	5.58	3.61	35.33
Freshwater eutrophication	kg P eq	0.00	0.00	90.11
Marine eutrophication	kg N eq	0.05	0.03	37.19
Terrestrial ecotoxicity	kg 1,4-DB eq	0.00	0.01	-1783.15
Freshwater ecotoxicity	kg 1,4-DB eq	0.09	0.00	95.92
Marine ecotoxicity	kg 1,4-DB eq	0.08	0.00	96.05
Agricultural land occupation	m2a	0.00	0.00	100.00
Urban land occupation	m2a	0.00	0.00	100.00
Natural land transformation	m2	0.00	0.00	100.00
Water depletion	m3	1.08	0.41	61.65
Metal depletion	kg Fe eq	0.05	0.00	100.00
Fossil depletion	kg oil eq	161.45	104.36	35.36

Si analizamos la categoría de calentamiento global para ambos escenarios con FC del IPCC, el factor de emisión de CO_{2e} por cada MWh paso de 626 $kgCO_{2e}$/MWh a 460 $kgCO_{2e}$/MWh (Figura 5).

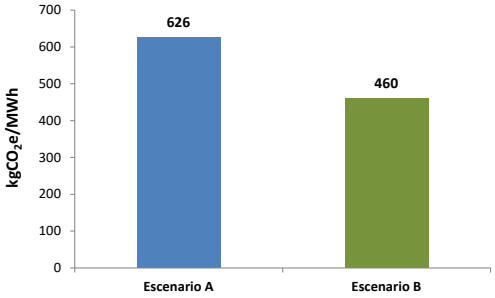

Fig. 5. Factor de emisión por cada MWh entre la operación actual (Escenario A) y el proyecto de cogeneración (Escenario B).

Es decir, el equivalente a una reducción del 26.5 % para el proyecto de cogeneración Este resultado aún está por encima del promedio del factor de emisión por cada MWh para planta de NGCC en USA, el cual es de 367 $kgCO_2$/MWh [7].

En la figura 6 podemos observar los principales procesos aportadores de emisiones de CO_{2e}, mediante un diagrama jerárquico del modelo empleado para la generación de 1 MWh. Asimismo, la figura muestran (en color rojo) la huella de carbono de la electricidad y la de la energía total producida por el proyecto de cogeneración propuesto.

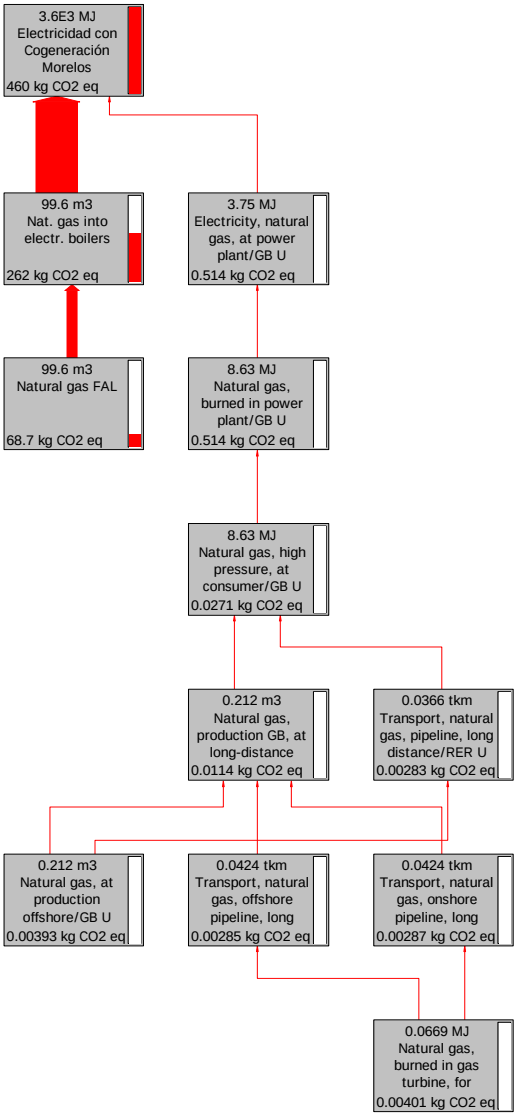

Fig. 6. Diagrama jerárquico de asignación de impactos en la categoria calentamiento global del proyecto de cogeneración Escenario B para 1 MWh.

En el caso de la producción de petroquímicos y electricidad en el CPQM; el cual registró una producción en el 2013 de 2,014,680 toneladas y de 7,792,720 MWh; se tiene un factor de emisión equivalente de 2.23 tCO_{2e}/t petroquímico para el escenario A y para el escenario B con la misma producción, pero con un valor de 8,392,518 MWh, se tendría una emisión de 1.88 tCO_{2e}/t petroquímico, es decir, una reducción del 15.6% en términos netos. Con base a este factor de emisión CO_{2e} obtenido, el proyecto de cogeneración dejaría de emitir 1,017,684.9 tCO_{2e}/año.

En la figura 7 se muestra la estimación preliminar del impacto ambiental que tendría el proyecto de cogeneración con captura post-combustión de CO_2, al registrar un valor de 310 $kgCO_2$/MWh, estando este resultado por arriba del rango de factor de emisión de planta de NGCC con captura para USA [7].

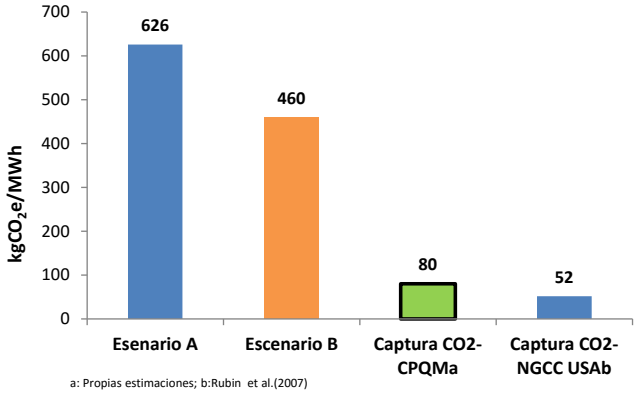

Fig. 7. Estimación preliminar del valor factor de emisión por cada MWh considerando la opción de captura post-combustión de CO_2

CONCLUSIONES

El proyecto de cogeneración registrará una reducción en todas las categorías de impacto ambiental evaluadas con respecto a la operación actual de la planta de generación de vapor y energía eléctrica. Las categorías de cambio climático y consumo de gas combustible en términos de masa son las que registran las mayores reducciones de impacto (23.4 % y 31.9 %, respectivamente). El factor de emisión de GEI con captura de CO_2 registraría un valor de 80 $kgCO_{2e}$/MWh. Asimismo, el proyecto de cogeneración permitirá que por unidad de producción las emisiones pasen de 2.23 tCO_{2e}/t en el escenario A, a 1.88 tCO_{2e}/t petroquímico para el escenario B.

REFERENCIAS

[1] IPCC, 2014. Climate Change 2014: Mitigation of Climate Change. Working Group III Contribution to the IPCC 5th Assessment Report Changes to the underlying Scientific/Technical Assessment. 101 p.

[2] SEMARNAT-INECC, 2012. Quinta Comunicación Nacional ante la Convención Marco de las Naciones Unidas sobre el Cambio Climático. México, D.F. 399 p

[3] González D. and M. Martínez, 2012. Decomposition analysis of CO_2 emissions in the Mexican industrial sector. Energy for Sustainable Development 16, 204–215.

[4] PEMEX, 2013. PEMEX, 2013. Informe de Responsabilidad Social.http://www.pemex.mx/responsabilidad/desarrollo_sustentable/Paginas/informes.aspx. *Accessed* Julio 16th 2014.

[5] INECC, 2014. Programa especial de Cambio Climático. Disponible: http://www.inecc.gob.mx/descargas/difusion/2015_pecc_vdifusion.pdf

[6] Jaramillo, P., Griffin, W.M., McCoy, S.T., 2009. Life cycle inventory of CO2 in an EOR system. Environmental Science and Technology 43 (21), 8027–8032

[7] Rubin, E.S., Rao, A.B., Chen, C., 2007. Cost and performance of fossil fuel power plants with CO2 capture and storage. Energy Policy 35 (9), 4444–4454

[8] ISO (2006) ISO 14040: Environmentalmanagement, life cycle assessment, principles and framework. International Standard Organization,Geneva

[9] International Standards Organization (ISO), 2006b. ISO 14044 – EnvironmentalManagement – Life Cycle Assessment – Requirements and Guidelines. International Standards Organization, Geneva, Switzerland.

[10] EPA, 2014. Regulatory Impact Analysis for the Proposed Standards of Performance for Greenhouse Gas Emissions for New Stationary Sources: Electric Utility Generating Units. EPA-452/R-13-003

[11] SENER, 2014. Mapa de Ruta Tecnológica de CCUS en Mexico. Mexico, DF. 31 p

[12] JRC (2010) ILCD handbook: general guide for life cycle assessment—detailed guidance. European Commission, Joint Research Centre, Brussels

[13] Goedkoop M, Heijungs R, Huijbregts M, De Schryver A, Struijs J, VanZelm R (2009) ReCiPe 2008: A life cycle impact assessment methodwhich comprises harmonised category indicators at the midpointand the endpoint level. VROM Ruimte en Milieu, Ministerie vanVolkshuisvesting, Ruimtelijke Ordening en Milieubeheer, http://www.lcia-recipe.net

[14] Modahl IS, Nyland CA, Raadahl HL (2009) Life Cycle Assessment of Electricity, including Carbon Capture and Storage – A Study of a Gas Power Plant Case with Post-combustion CO2 Capture at Tjeldbergodden, Ostfold Research AS, OR 15.09 (Confidential), Fredrikstad, Norway

[15] Brekke A., Askham C., Modahl I. S., Vold B. I. y Johnsen F.M., 2012. Environmental Assessment of Amine-Based Carbon Capture. Scenario modeling with Life Cycle Assessment (LCA).

Understanding biodiesel spray by study of primary atomization phenomena implementing hybrid numerical schemes.

Rogelio D. Conde Orrante
Sección de Estudios de Posgrado e Investigación,
Escuela Superior de Ingeniería Mecánica y Eléctrica
Unidad Culhuacán, Instituto Politécnico Nacional.
México, D.F.
rcondeo1300@alumno.ipn.mx

Rubén Vázquez Medina
Sección de Estudios de Posgrado e Investigación,
Escuela Superior de Ingeniería Mecánica y Eléctrica
Unidad Culhuacán, Instituto Politécnico Nacional.
México, D.F.

Felipe A. Perdomo Hurtado
Facultad de Ingeniería, Departamento de Ingeniería
Química, Universidad de Bogotá Jorge Tadelo Lozano.
Bogotá, Colombia

Miguel Cruz Irisson
Sección de Estudios de Posgrado e Investigación,
Escuela Superior de Ingeniería Mecánica y Eléctrica
Unidad Culhuacán, Instituto Politécnico Nacional.
México, D.F.

***Abstract*— The breakup of liquid masses by high speed air streams is an amazingly complex phenomena that occurs in many natural and made-man circumstances. In the industrial domain, liquid fuel combustion in many types of engines requires the atomization of the fluid before evaporation and combustion can occur. The quality of the combustion and rather pollutant generation depend on the characteristics of fuel atomization. Biodiesel has large amount of oxygen in itself, which make it very efficient in reducing exhaust emission by improving combustion inside an engine. But biodiesel has a low temperature flow problem because it has a high viscosity. The accurate modeling of spray process is vital to well understand the combustion process of biodiesel fuels in diesel engines. In this study we present a simulation of primary biodiesel breakup using an Eulerian-lagrangian coupled method for resolving both the continuous and disperse phases implementing hybrid numerical schemes based in Finite Differences in complex geometries.**

Keywords*— Atomization phenomena, Biodiesel-fuel, Eulerian – Lagrangian approach Introduction.

I. INTRODUCCION

Los combustibles químicos [1] son sustancias altamente reactivas que generan energía al reaccionar con substancias de su entorno; generalmente se pueden clasificar en dos grupos, a saber:

- ***Combustibles fósiles o minerales:*** Principalmente este grupo está constituido en su mayoría por hidrocarburos, los cuales pueden o no ser derivados de fuentes biológicas como el alquitrán, el carbón, el gas natural, el petróleo etc. Son fuentes de energía no renovables y se pueden encontrar en cualquier estado de agregación de la materia.
- ***Biocombustibles:*** Principalmente este grupo está constituido en su mayoría por hidrocarburos, los cuales son producidos por una fuente renovable de carbón (biomasa) y se pueden encontrar en cualquier estado de agregación de la materia.

De estas dos categorías se ha destacado, por su uso indiscriminado, los denominados combustibles fósiles, los cuales a lo largo de la historia, han traído consigo un importante crecimiento industrial y tecnológico.

Sin embargo ante la inminente realidad de que estos combustibles se están agotando y a los estragos económicos, políticos, sociales y ecológicos que trajeron consigo, es necesario encontrar fuentes de energías alternativas, eficientes y limpias.

En los últimos años algunos biocombustibles han gozado de cierto auge dentro de la comunidad académica e industrial, teniendo como principal exponente al biodiesel.

El Biodiesel, es un biocombustible, producido a partir del proceso de transesterificación, el cual consiste en promover el intercambio de grupos orgánicos R1, R2, R3 (pertenecientes a un glicérido) con el grupo orgánico de un alcohol R', como se muestra en (1), para formar un ácido graso metil (o etil) ester (FAME), el cual posee una composición similar al diésel fósil,

$$\begin{matrix} CH_2-OOC-R_1 \\ CH-OOC-R_2 \\ CH_2-OOC-R_1 \end{matrix} + 3R'OH \xleftrightarrow{Catalizador} \begin{matrix} R_1-COO-R' \\ R_2-COO-R' \\ R_3-COO-R' \end{matrix} + \begin{matrix} CH_2-OH \\ CH-OH \\ CH_2-OH \end{matrix} \quad (1)$$

Glicéridos Alcohol Glicerina Ésteres

tal como se muestra en la TABLA 1, por desgracia este combustible aun no puede ser utilizado en un motor diésel a una concentración del 100% [] debido a que:

- Degrada de forma natural de las juntas de caucho y mangueras en presencia del biodiesel
- Tapa los filtros y en si el biodiesel se descompone en los depósitos.
- Se presenta un incremento en los índices de NOx.
- El decrecimiento material particulado es inversamente proporcional a la formación de óxidos de nitrógeno con lo que se contribuye al a formación de humo (smog).

Se reduce la potencia en un 10%.

- La alta viscosidad del biodiesel dificulta el bombeo en frio y por consiguiente la inyección.
- Los aceites insaturados son químicamente menos estables, lo cual afecta el almacenamiento y promueve depósitos en los componentes del inyector y pisto.
- Existe una incompatibilidad con lubricantes de motores.

Sin embargo se ha demostrado que las propiedades físicas de un biocombustible suelen variar, dependiendo de la materia prima (biomasa) empleado para su caracterización [2].

TABLA 1 COMPARACIÓN ENTRE NORMAS PARA EL BIODIESEL.

Parámetro	Unidad	EN14214	Método de ensayo	ASTM D6751	Método de ensayo	Brasil	Método de ensayo
Apariencia							
Conetnido de Ester	% m/m	≥96.5	EN 14103			Solo registro	EN 14103
Densidad a °15C	kg/m^3	860-900	EN ISO 3675/12185				
Densidad a °20C	kg/m^3					Solo registro	ASTM D 4052 ,ASTMD 1298
Densidad a °40C	kg/m^3						
Viscosidad a 40°C	mm^2/s	3.5-5	EN ISO 3104	1.9 - 6	ASTM D 445	Solo registro	ASTM D 445, ISO 3104
Punto de inflamacion	°C	≥101	EN ISO 3679	≥93	ASTM D 93	≥ 100	ASTM D 93, ISO 3679
Contenido de Azufre	mg/kg	≤10	EN ISO 20846	≤15≰500	ASTM D 5453	Solo registro	ASTM D 5453, ASTM 4294, 1459
	mg/kg	≤10	EN ISO 20884				
Residuo de Carbon	% m/m			≤ 0.05	ASTM D 4530	≤ 0.1	STM D 189, ASTM D 4530, ISO 10
(residuo de la destilacion 10%)	% m/m	≤ 0.3	EN ISO 10370				
Indice de cetano							
No. decetano		≥ 51	EN ISO 5165	≥ 47	ASTM D 613	Solo registro	ISO 5165, ASTM D 613
Sulfato contenido en cenizas	% m/m	≤ 0.02	ISO 3987	≤ 0.02	ASTM D 874	≤ 0.02	ISO 3967, ASTM D 874
Contenido de agua	mg/kg	≤ 500	EN ISO 12937				
Contaminacion total	mg/kg	≤ 24	EN 12662				
Agua y sedimentos	% vol/vol			≤ 0.05	ASTM D 2709	≤ 0.05	ASTM D 2709
Corrosion en cobre		≤ 1	EN ISO 2160	≤ 3	ASTM D 130	≤ 1	ASTM D 130, ISO 2160
Estabilidad de oxidacion, 110°C	h	≥ 6	EN ISO 14112/prEN15751	≥ 3	EN 14112	≥ 6	EN 14112
Valor acido	mg KOH/g	≤ 0.5	EN 14104	≤ 0.5	ASTM D 664	≤ 0.8	ASTM D 664, EN 14104
Valor yodo		≤ 120	EN 14111			≤ 120	EN 14111
ester metil linolénico	% m/m	≤ 12	EN 14103				
Ester metil polisaturado	% m/m	≤ 1	EN5779				
Contenido de mono alcohol	% m/m					≤ 0.5	EN 14110
Contenido de Metanol	% m/m	≤ 0.2	EN 14110		EN 14110		
Glicerol libre	% m/m	≤ 0.02	EN 14105	≤ 0.02	ASM D 6584	≤ 0.02	EN 14105, EN 14106, ASTM D 65
	% m/m	≤ 0.02	EN 14106				
Monogliceridos	% m/m	≤ 0.8	EN 14105	≤ 0.02		Solo registro	EN 14105
Digliceridos	% m/m	≤ 0.2	EN 14105			Solo registro	EN 14105
Trigliceridos	% m/m	≤ 0.2	EN 14105			Solo registro	EN 14105
Total glicerol	% m/m	≤ 0.25	EN 14105	≤ 0.24	ASTM D 6584	≤ 0.38	EN 14105, ASTM D 6584
Grupo I Metales (Na + K)	mg/kg	≤ 5	EN 14538	≤ 5	EN 14538	≤ 10	EN 14108/ EN 14109
Grupo II de metales (Ca + Mg)	mg/kg	≤ 5	EN 14538	≤ 5	EN 14538	Solo registro	EN 14538
Contenido de Fosforo	mg/kg	≤ 4	EN 14107	≤ 10	ASTM D 4951	Solo registro	EN 14107
CFPP	°C	(nat. req)	EN 116				
Filtrabilidad	s			≤ 360	ASTM D 6217		
Punto de nube	°C			reportado	ASTM D 2500		
Temperatura de destilacion 90	°C			360	ASTM D 1160	360	ASTM D 1160

Tabla. 1 Se presentan los parámetros y métodos de ensayo que consideran las normas Europeas (EN14214), americanas (ASTM D6751) y brasileñas (Brasil).

I. ECUACIONES QUE DESCRIBEN EL COMPORTAMIENTO DE UN FLUIDO.

Básicamente las ecuaciones que describen el comportamiento de un fluido son [3]:

- La Ecuación de Continuidad (Conservación de masa):

$$\frac{\partial \rho}{\partial x}\upsilon_x + + \frac{\partial \rho}{\partial y}\upsilon_y + \frac{\partial \rho}{\partial z}\upsilon_z + \frac{\partial \rho}{\partial t} = -\left(\rho\frac{\partial \upsilon_x}{\partial x} + \rho\frac{\partial \upsilon_y}{\partial y} + \rho\frac{\partial \upsilon_z}{\partial z}\right) \quad (2)$$

La cual al emplear el concepto de derivada sustancial y divergencia se tiene:

$$\frac{D\rho}{Dt} = -\rho(\nabla\bullet\upsilon) \quad (3)$$

- La Ecuación de Conservación de cantidad del Momentum.

$$\frac{\partial(\rho\upsilon_x)}{\partial t} = -[\nabla\bullet(\rho\upsilon\upsilon)] - [\nabla\bullet\tau] - \nabla P + \rho g$$

Ganancia o perdida de cantidad de momento con respecto al tiempo	Perdida o gananacia de cantidad de momento debido al flujo convectico	Perdida o gananacia de cantidad de momento debido a las fuerzas vis cos as	Perdida o gananacia de cantidad de momento debido a la Presion	Perdida o gananacia de cantidad de momento debido a la Gravedad

(4)

- La Ecuación de Conservación de la Energía.

$$\rho\frac{D}{Dt}\left[\hat{u}\right] + \rho\frac{D}{Dt}\left[\frac{1}{2}\upsilon^2\right] = -\left[\nabla\bullet\left(\dot{q}\right)\right] - \left[P\nabla\bullet(\vec{\upsilon})\right] - \left[\tau : \nabla\bullet(\vec{\upsilon})\right] \quad (5)$$

A partir de (2) y (3) y de los esfuerzos cortantes newtonianos que se muestran en la TABLA 2.

TABLA 2 ESFUERZOS CORTANTES NEWTONEANOS

$\tau_{xx} = -2\mu\left(\frac{\partial \upsilon_x}{\partial x}\right) + \frac{2}{3}\mu\nabla\bullet\upsilon$	$\tau_{yx} = \tau_{xy} = -\mu\left(\frac{\partial \upsilon_x}{\partial y} + \frac{\partial \upsilon_y}{\partial x}\right)$
$\tau_{yy} = -2\mu\left(\frac{\partial \upsilon_y}{\partial y}\right) + \frac{2}{3}\mu\nabla\bullet\upsilon$	$\tau_{zy} = \tau_{yz} = -\mu\left(\frac{\partial \upsilon_z}{\partial y} + \frac{\partial \upsilon_y}{\partial z}\right)$
$\tau_{zz} = -2\mu\left(\frac{\partial \upsilon_z}{\partial z}\right) + \frac{2}{3}\mu\nabla\bullet\upsilon$	$\tau_{zx} = \tau_{xz} = -\mu\left(\frac{\partial \upsilon_z}{\partial x} + \frac{\partial \upsilon_x}{\partial z}\right)$

Se deriva la ecuación de Navier-Stokes:

$$\frac{D(\rho\upsilon)}{Dt} = -\nabla P + \mu\nabla^2\upsilon + \rho g \quad (6)$$

II. ECUACIONES QUE DESCRIBEN EL COMPORTAMIENTO DE UN FLUIDO BIFASICO.

Para un fluido bifásico cuya densidad es variable, la ecuación (6) toma la forma:

$$\rho\frac{\partial\upsilon}{\partial t} + \rho\nabla\bullet\upsilon\upsilon = -\nabla P + \rho g + \nabla\bullet\mu\left(\nabla\upsilon + \nabla^T\upsilon\right) + f \quad (7)$$

Dicha ecuación se resolverá empleando la discretización propuesta por Francis. Harlow y Eddie Welch (1965) denominado: método Marker and Cell [], la cual establece la siguiente serie de ecuaciones para:

- Calculo de las componentes del vector velocidad.

$$u^*_{i+\frac{1}{2},j} = u^n_{i+\frac{1}{2},j} + \Delta t\left\{\left(-A_x\right)^n_{i+\frac{1}{2},j} + \left(g_x\right)^n_{i+\frac{1}{2},j} + \frac{2}{\left(\rho^n_{i+1,j} + \rho^n_{i,j}\right)}\left(D_x\right)^n_{i+\frac{1}{2},j}\right\}$$

(8)

$$v^*_{i,j+\frac{1}{2}} = v^n_{i,j+\frac{1}{2}} + \Delta t\left\{\left(-A_y\right)^n_{i,j+\frac{1}{2}} + \left(g_y\right)^n_{i,j+\frac{1}{2}} + \frac{2}{\left(\rho^n_{i,j+1} + \rho^n_{i,j}\right)}\left(D_y\right)^n_{i,j+\frac{1}{2}}\right\}$$

(9)

- Calculo de la Advección.

$$\left(A_x\right)^n_{i+\frac{1}{2},j} = \frac{1}{\Delta x}\left[\left(\frac{u^n_{i+\frac{3}{2},j} + u^n_{i+\frac{1}{2},j}}{2}\right)^2 - \left(\frac{u^n_{i+\frac{1}{2},j} + u^n_{i-\frac{1}{2},j}}{2}\right)^2\right] + \bullet\bullet\bullet$$
$$+ \bullet\bullet\bullet\frac{1}{\Delta y}\left[\left(\frac{u^n_{i+\frac{1}{2},j+1} + u^n_{i+\frac{1}{2},j}}{2}\right)\left(\frac{v^n_{i+1,j+\frac{1}{2}} + v^n_{i,j+\frac{1}{2}}}{2}\right) - \bullet\bullet\bullet\right.$$
$$\left. - \bullet\bullet\bullet\left(\frac{u^n_{i+\frac{1}{2},j} + u^n_{i+\frac{1}{2},j-1}}{2}\right)\left(\frac{v^n_{i+1,j-\frac{1}{2}} + v^n_{i,j-\frac{1}{2}}}{2}\right)\right]$$

(10)

$$\left(A_y\right)^n_{i,j+\frac{1}{2}} = \frac{1}{\Delta x}\left[\left(\frac{u^n_{i+\frac{1}{2},j} + u^n_{i+\frac{1}{2},j+1}}{2}\right)\left(\frac{v^n_{i,j+\frac{1}{2}} + v^n_{i+1,j+\frac{1}{2}}}{2}\right) - \bullet\bullet\bullet\right.$$
$$\left. - \bullet\bullet\bullet\left(\frac{u^n_{i-\frac{1}{2},j+1} + u^n_{i-\frac{1}{2},j}}{2}\right)\left(\frac{v^n_{i,j+\frac{1}{2}} + v^n_{i-1,j+\frac{1}{2}}}{2}\right)\right] + \bullet\bullet\bullet$$
$$+ \bullet\bullet\bullet\frac{1}{\Delta y}\left[\left(\frac{v^n_{i,j+\frac{3}{2}} + v^n_{i,j+\frac{1}{2}}}{2}\right)^2 - \left(\frac{v^n_{i,j+\frac{1}{2}} + v^n_{i,j-\frac{1}{2}}}{2}\right)^2\right]$$

(11)

- Flujo Viscoso en las fronteras.

$$\left(D_x\right)^n_{i+\frac{1}{2},j} = \mu_0\left\{\left(\frac{u^n_{i+\frac{3}{2},j} - 2u^n_{i+\frac{1}{2},j} + u^n_{i-\frac{1}{2},j}}{\Delta x^2}\right) + \left(\frac{u^n_{i+\frac{1}{2},j+1} - 2u^n_{i+\frac{1}{2},j} + u^n_{i+\frac{1}{2},j-1}}{\Delta y^2}\right)\right\}$$

(12)

$$\left(D_y\right)^n_{i,j+\frac{1}{2}} = \mu_0\left\{\left(\frac{v^n_{i+1,j+\frac{1}{2}} - 2v^n_{i,j+\frac{1}{2}} + v^n_{i-1,j+\frac{1}{2}}}{\Delta x^2}\right) + \left(\frac{v^n_{i,j+\frac{3}{2}} - 2v^n_{i,j+\frac{1}{2}} + v^n_{i,j-\frac{1}{2}}}{\Delta y^2}\right)\right\}$$

(13)

- Calculo de la presión en la malla central.

$$\frac{1}{\Delta x^2}\left(\frac{P_{i+1,j} - P_{i,j}}{\rho^n_{i+1,j} + \rho^n_{i,j}} - \frac{P_{i,j} - P_{i-1,j}}{\rho^n_{i,j} + \rho^n_{i-1,j}}\right) + \frac{1}{\Delta y^2}\left(\frac{P_{i,j+1} - P_{i,j}}{\rho^n_{i,j+1} + \rho^n_{i,j}} - \frac{P_{i,j} - P_{i,j-1}}{\rho^n_{i,j} + \rho^n_{i,j-1}}\right) = \frac{1}{2\Delta t}\left(\frac{u^*_{i+\frac{1}{2},j} - u^*_{i-\frac{1}{2},j}}{\Delta x} + \frac{v^*_{i,j+\frac{1}{2}} - v^*_{i,j-\frac{1}{2}}}{\Delta y}\right)$$

(14)

- Calculo de la presión en las fronteras.

$$\frac{1}{\Delta x^2}\left(\frac{P_{i+1,j}-P_{i,j}}{\rho^n_{i+1,j}+\rho^n_{i,j}}-\right)+\frac{1}{\Delta y^2}\left(\frac{P_{i,j+1}-P_{i,j}}{\rho^n_{i,j+1}+\rho^n_{i,j}}-\frac{P_{i,j}-P_{i,j-1}}{\rho^n_{i,j}+\rho^n_{i,j-1}}\right)=\frac{1}{2\Delta t}\left(\frac{u^*_{i+1/2,j}-U_{b,j}}{\Delta x}+\frac{v^*_{i,j+1/2}-v^*_{i,j-1/2}}{\Delta y}\right)$$

(15)

- Corrección de las componentes de la velocidad.

$$u^{n+1}_{i+1/2,j}=u^*_{i+1/2,j}-\frac{2\Delta t\left(P_{i+1,j}-P_{i,j}\right)}{\Delta x\left(\rho^n_{i+1,j}+\rho^n_{i,j}\right)} \quad (16)$$

$$v^{n+1}_{i,j+1/2}=v^*_{i,j+1/2}-\frac{2\Delta t\left(P_{i,j+1}-P_{i,j}\right)}{\Delta y\left(\rho^n_{i,j+1}+\rho^n_{i,j}\right)} \quad (17)$$

III. Método Númerico

Algoritmo [4]:

Empleando el siguiente mallado Fig. 1:

Fig. 1 Ejemplo del Mallado

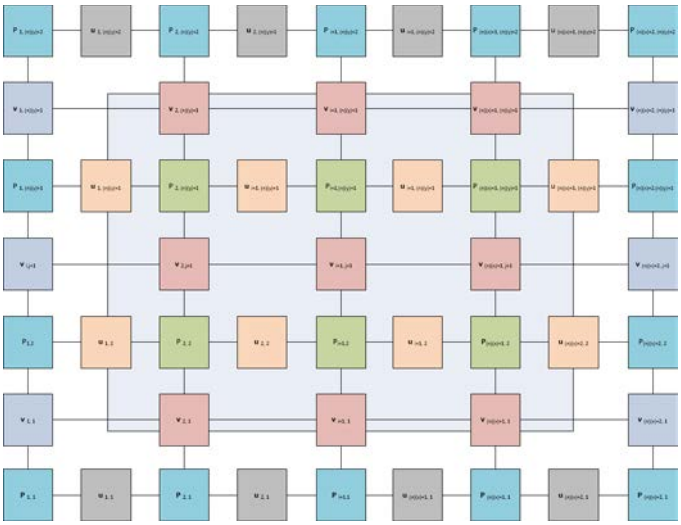

Fig. 1 Representa de forma esquemática la disposición del mallado, propuesto por el método Marker and Cell.

Se procede a:

1. Se calcula el campo de velocidad usando las ecuaciones (8) y (9) con los términos de la advección usando las ecuación (10) y (11), flujo viscoso en las fronteras (12) y (13).
2. Se calcula la presión usando la ecuación (14) con las condiciones de equilibrio (15).
3. Se corrigen las componentes de la velocidad del campo de velocidades usando (16) y (17).

IV. Resultados

Al implementar el algoritmo se obtienen gráficas, del campo de velocidades mostrados en la Fig. 2:

Fig. 2 Capturas del campo de velocidades

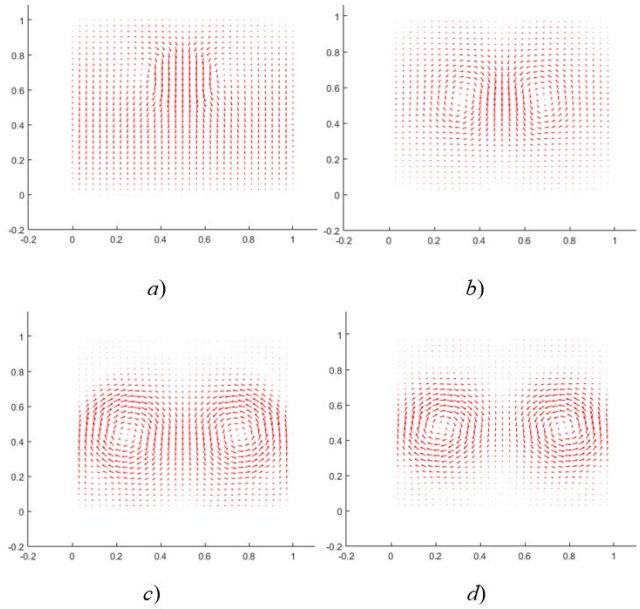

Fig. 2 Se presentan: a) El campo de velocidades en un tiempo cero. b) El campo de velocidades cuando la gota ha sido soltada y comienza la deformación de la gota. c) Campo de velocidades cuando comienza de la división de la gota. d) Campo de velocidades cuando finaliza la división de la gota.

V. Conclusiones

La mayoría de los métodos numéricos usados recientemente para detallar y simular flujos multifasicos son formulados con la finalidad de resolver las ecuaciones de Navier Stokes (ecuaciones que describen el flujo de los fluidos involucrados). Algunos métodos son más eficientes que otros sin embargo el método Marker and Cell (MAC) mostrado ha sido ampliamente empleado debido a su gran practicidad cuando el sistema tiene las siguientes condiciones:

$$\frac{\mu\Delta t}{\rho h^2}\le\frac{1}{4} \qquad (u\bullet u)\frac{\rho\Delta t}{\mu}\le 2$$

Sin embargo cuando se requiere un análisis más riguroso es recomendable emplear otro tipo de método como el: Volume of Fluid (VOF) o Large-Eddy (LES) [5].

VI. Referencias.

[1] Abhijeet, R. Sujeet & Derrick, *Evaluation of Bio Diesel as a Fuel for Diesel Engine.*Mumbai: LAMBERT Academic Publishing, 2012

[2] SENER., Prospectiva de Eenergías Renovables 2012-2026, 2012. D F, Cd. México.

[3] G. P. Galdi, An Introduction to the Mathematical Theory of the Navier-Stokes Equatons, Ed. Springer, 2011

[4] Francis H.Harlow and J. Eddie Welch, Numerical Calculation of Time-Dependent Viscous Incompressible Flow of Fluid with Free Surface, The physics of fluids, 1965, pp. 2182–2189.

[5] R. D. Conde Orrante, M. Cruz Irisson, F. A. Perdmo Hurtado y R. Vázquez Medina, Fenomeno de atomización: una revision de las aportaciones más recientes., CCIM 2014, Cuba.

VII. AGRADECIMIENTOS

R. D. Conde-Orrante agradece la beca otorgada por el Consejo Nacional de Ciencia y Tecnología (CONACYT) para la realización de sus estudios de posgrado en la Maestría en Ciencias de Ingeniería en Sistemas Energéticos que se imparte en la Sección de Estudios de Posgrado e Investigación de la ESIME Unidad Culhuacán del IPN. Este trabajo fue parcialmente apoyado por el Instituto Politécnico Nacional a través del Proyecto Institucional SIP-IPN número: 20140299.

VIII. SOBRE LOS AUTORES

Ing. Rogelio David Conde Orrante. Alumno del segundo semestre de la Maestría en Ciencias de Ingeniería en Sistemas Energéticos en la Sección de Estudios de Posgrado e Investigación de la Escuela Superior de Ingeniería Mecánica y Eléctrica Unidad Culhuacán del Instituto Politécnico Nacional.

Dr. Rubén Vázquez Medina: Instituto Politécnico Nacional, Centro Mexicano para la Producción más Limpia, Profesor Investigador, Categoría Titular e Investigador Nacional Nivel 1.

Dr. Miguel Cruz Irisson: Instituto Politécnico Nacional, Escuela Superior de Ingeniería Mecánica y Eléctrica Unidad Culhuacán, Sección de Estudios de Posgrado e Investigación, Profesor Investigador, Categoría Titular e Investigador Nacional Nivel 2.

Dr. Felipe. A. Perdomo Hurtado: Facultad de Ingeniería, Departamento de Ingeniería Química, Universidad de Bogotá Jorge Tadelo Lozano. Bogotá, Colombia.

Olefins and ethanol from polyolefins; chemical recycling simulation of poly(ethylene) and poly(propylene)

A. Vargas Santillána, A. J. Castro Montoya, J. C. Farias Sanchez, M. G. Pineda Pimentel
Facultad de Ingeniería Química, División de Estudios de Posgrado de Ciencias en Ingeniería Química
Universidad Michoacana de San Nicolás de Hidalgo
Morelia Michoacán México
alphonsev88@gmail.com

***Abstract*— The following work studies the possibilities of poly(ethylene) and poly(propylene) recycling. Plastic solid waste (PSW) presents challenges and opportunities to society regardless of their sustainability awareness and technological advances. A special emphasis is paid on waste generated from polyolefinic sources, which makes up a great percentage of our daily single-life cycle plastic products. In Mexico 7.6 millions of tons of plastics in 2013 were wasted which PE, PP and PET were the most abundant.**

Increasing cost, and decreasing space of landfills are forcing considerations of alternative options for PSW disposal. Years of research, study and testing have resulted in a number of treatment, recycling and recovery methods for PSW that can be economically, and environmentally viable.

Advanced thermo-chemical treatment methods cover a wide range of technologies, and produce either fuels or petrochemical feedstock. Nowadays, non-catalytic thermal cracking (thermolysis) is receiving renewed attention, due to the fact of added value on a crude oil barrel and its very valuable yielded products, but a fact remains that advanced thermo-chemical recycling of PSW (namely polyolefins) still lacks the proper design, and kinetic background to target certain desired products and/or chemicals.

ASPEN Plus is used to simulate de pyrolysis (non-catalytic thermal cracking) process. Ethylene, propylene and ethanol is obtained from such process. ASPEN Economics is used to find the feasibility of the pyrolysis and ethanol production.

***Keywords*— ASPEN, pyrolysis, polyethylene, polypropylene, ethanol.**

I. INTRODUCTION

Low density polyethylene (LDPE) and polypropylene (PP) have excelled among many other materials due to its properties, such polymers are used as containers for different products, mainly in the food, agricultural, construction, textile, automotive among others. Plastics have accelerated their output by continuously adding new products to be emerging in the market. China leads world production with 15% of all world plastic followed by Germany with 7%; Mexico produces only 2% of the 241 million tons produced globally.

The plastic products industry is important in Mexico since nationwide equal to 3.6% of gross domestic product manufacturing (GDP). Figure 1 shows the consumption of plastics worldwide, reaching nearly 250 million tons in 2012 [1].

In Mexico about 5.2 million tonnes were consumed in 2012, of which PP, polyethylene (PE) and polyethylene terephthalate (PET) were the most popular with its chemical, thermal and mechanical properties [2].

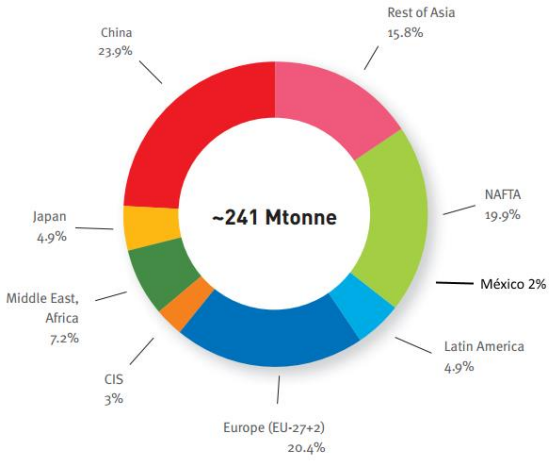

Fig. 1. World plastics materials production 2012.

In Mexico it is only recycled 11% of the 4.2 million tons of garbage produced per year and only 2% is used for energy recovery, discarding more than 3.6 million tons of plastic waste per year, it has to be analyzed what is the best alternative in the reuse of waste sources, that can replace fossil and agricultural sources.

In this sense it is necessary to propose methods for recycling or reuse of plastic solid waste (PSW) generated by the different products. The challenge of this work is to simulate a thermochemical process in order to find the best technical and economical choice.

PSW from commercial grade resins have been successfully recycled from a number of end-products, including: automobile parts, appliances, textiles, mulches, greenhouses and films [3]. PSW treatment and recycling processes could be allocated to four major categories [4], re-extrusion (primary), mechanical (secondary), chemical (tertiary) and energy recovery (quaternary) as shown in Figure 2. Each method provides a unique set of advantages that make it particularly beneficial for specific locations, applications or requirements. Mechanical recycling (i.e. secondary or material recycling) involves physical treatment, whilst chemical recycling and treatment (i.e. tertiary encompassing feedstock recycling) produces feedstock chemicals for the chemical industry. Energy recovery involves complete or partial oxidation of the material [5], producing heat, power and/or gaseous fuels, oils and chars besides by-products that must be disposed of, such as ash.

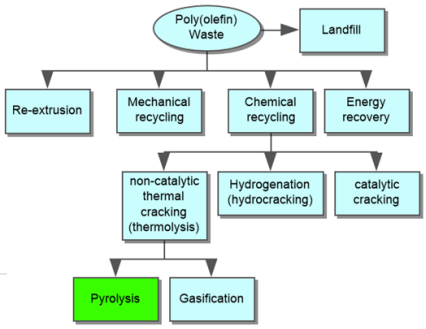

Fig. 2. Recycling options of plastics solids wastes.

II. Material and Methods

Ethanol, ethylene and propylene has several applications, but considering the established biofuel worldwide and the potential increase of plastics market, these uses are the most promising [6]. In this sense the objective of this study was to evaluate process that produce raw material for the market needs (Figure 3).

Pyrolysis

The Pyrolysis process models available in literature can be generally classified under steady state or quasi-steady state or transient state models [7]. The steady state models do not consider the time derivatives and are further classified as kinetics free equilibrium models or kinetic rate models [8].

The following assumptions are made in the current study for developing the process model.

- All the chemical reactions were assumed to have reached equilibrium within the pyrolysis.
- The olefin that enters into the reactor is pure (LDPE or PP).
- Only ethylene, propylene, α-butylene, cis-β-butylene, trans-β-butylene, isobutylene, methane, ethane, propane, butane and polymer were considered to be present in the product stream in the pyrolysis reactor; and only ethanol, ethylene and water in the production of ethanol reactor [9].
- Preliminary research prove that LDPE and PP have the same behavior in pyrolysis reactor, then the difference will be just the simulation and economic study.
- The primary products are ethylene, propylene and ethanol for the simulation.

The entire process was modeled using Aspen's built-in unit operation library in three stages; pyrolysis, ethanol production and energy recovery. The three stages are discussed separately in the following sections.

Pyrolysis Modeling

Aspen Plus is basically a program simulation of chemical processes, which in addition to flowcharts simulations, it can perform: (1) estimation of properties of compounds, (2) sensitivity analysis of process variables, (3) obtain process design specifications, and (4) synthesis and analysis of chemical processes, among other tasks of process design and equipment [10]. Many authors have worked in gasification and pyrolysis of PE and PP, in such research demonstrates the efficiency of experimental chemical processes [11]. In this work PP and LDPE are studied by thermochemical pyrolysis method in ASPEN 8.4 simulation, experimental test has proved that pyrolysis process produce mainly ethylene and propylene from polyolefin [12].

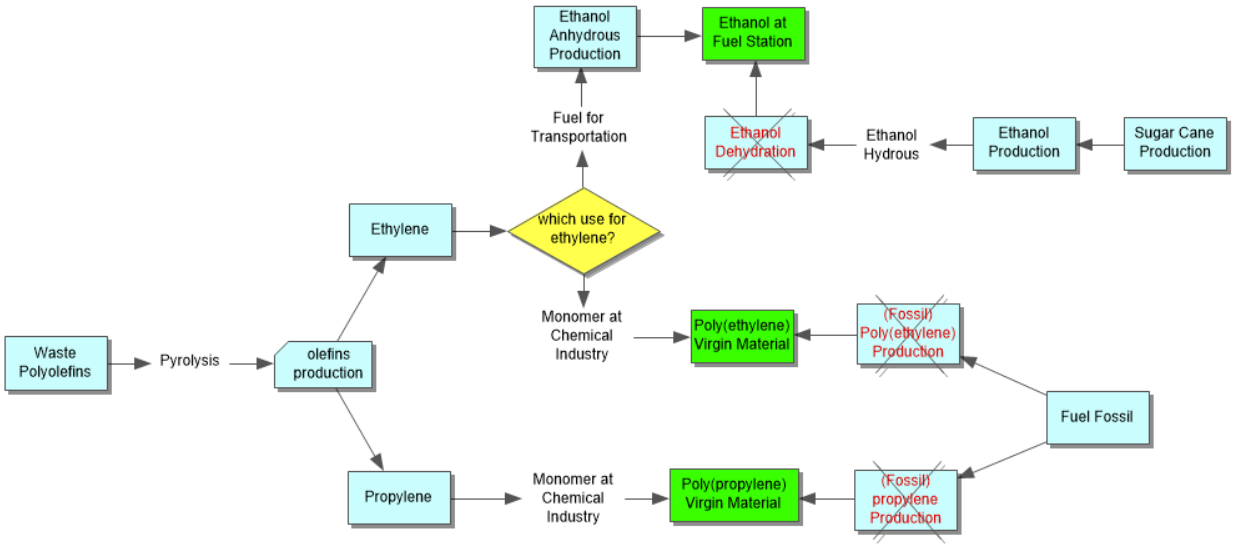

Fig. 3. Simplified flowchart of the three possible uses for polyolefin considered in this study.

Figure 4 illustrates the process flow sheet of the simplified model. The first stage corresponds to the pyrolysis where the polyethylene and polypropylene sample was processed to crack into monomers and obtaining ethylene and propylene. The polymer stream labeled as "POLYMER" was defined as an oligomer stream and the monomer ethylene-r and propylene-r were used to obtain the polymer properties. Polymer NRTL equation of state with Henry's law "POLYNRTL" was chosen as parameter models to calculate the thermo physical properties of the components.

At first, the polymer stream was first introduced into a pyrolysis unit "PYROLYS", which was modeled in Aspen Plus using an RGibbs module. A temperature from 340 to 950 °C and a pressure from 1 to 10 atm were selected as pyrolysis operating conditions. The stream leaving the pyrolysis, labeled "PYROGAS" contains ethylene, propylene, α-butylene, cis-β-butylene, trans-β-butylene, isobutylene mainly in gas phase.

This stream was fed to a heat exchanger unit "HEAT" that recover the energy stream of "PYROGAS" and heats up "HOTW" stream that is taking the energy to produce electricity in a turbine. The cold stream labeled "CPYROGAS" is into a RadFrac that separates ethylene in "ETHYLEN" stream and the rest of the components in "PROPYLENE".

Ethanol Production Modeling

In ethanol step, the ethylene is separated from the other components by using a column. The stream "ETHYLEN" is feed into RGibbs reactor with water to produce ethanol. The product labeled "PROD-NOL" contains water, ethylene and ethanol. The stream reach in ethanol is separated in a flash equipment. The stream called "ETHANOL" must contains

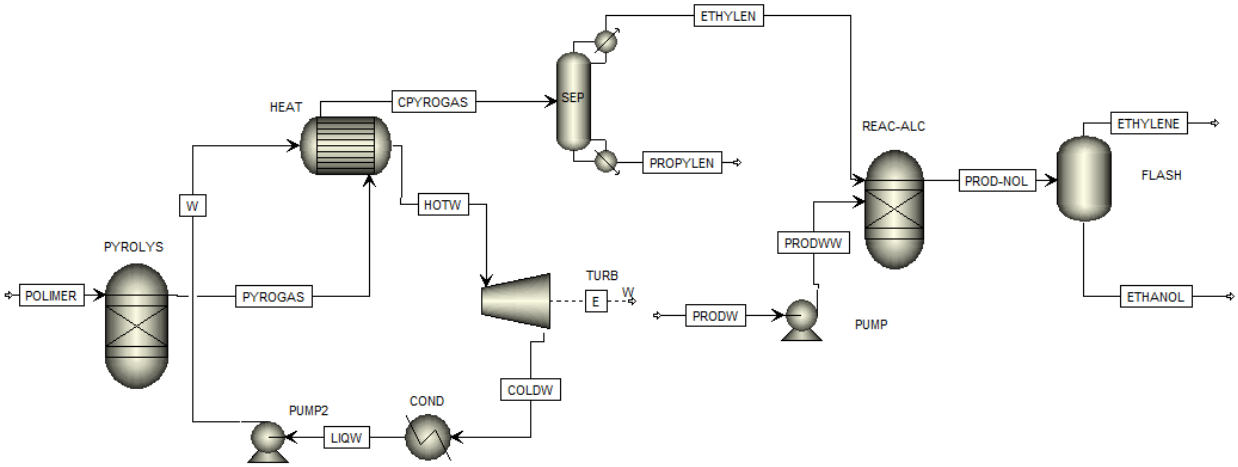

Fig. 4. Process flow diagram of polymer pyrolysis and ethanol production in ASPEN Plus.

99.7% ethanol.

Energy Recovery

The stream "W" contains liquid water that is heated with the energy from the pyrolysis. A turbine is used to generate electricity and the cold water is sent to a condenser then the water is pumped and refeed to the exchanger in a Rankine cycle.

Process performance

In this work, a response surface was proposed to investigate the performance characteristics of the polymer pyrolysis process, separation of olefins in a column and the ethanol production. In each case the pressure is changed, and different variables are used to generate the response surface in order to find the best response in each case.

Process Economics

The simulator Aspen Plus has a useful tool for assessing the cost of the process to be simulated, taking place the specifications introduced in the simulator and the concern that might be needed in a real plant.

Some of the features that has ASPEN Economic Evaluation are: (i) Generate conceptual and detailed estimates of costs, (ii) Estimate the cost of the product from the process, (ii) optimizes the process design finding better routes.

The total capital investment (TCI) is first computed from the total equipment cost and cash flow in ASPEN Economics. With these costs, cash flow analysis is used to determine the minimum ethanol selling price (MESP) required to obtain a zero net present value (NPV) with a finite internal rate of return (IRR).

III. Results and Discussion

Pirolysys

For pyrolysis simulation an important issue is the mass fraction of olefin (LDPE or PP) produced in the reactor, it is the reason that it is used as a response variable. With sensitivity analysis an operating pressure range of 1-10 atm is set and the temperature is set from 340 to 950 °C. Figure 5 shows the response surface of mass fraction of ethylene at that process conditions. As mass basis is used 100 kg/h in pyrolysis reactor. The output from the pyrolysis seems to be the top level of ethylene at 950 °C and 1atm.

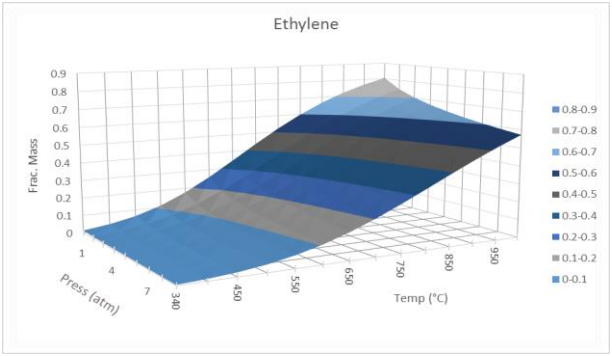

Fig. 5. Output mass fraction of ethylene from pyrolysis reactor

The next Figures show the different products that are obtained from the pyrolysis reactor. Figure 6 shows that the output from 600 °C to 750 °C is the richest in polyethylene. Figure 7 show that as long the temperature is more elevated it gets low products of α-butylene, cis-β-butylene, trans-β-butylene and isobutylene.

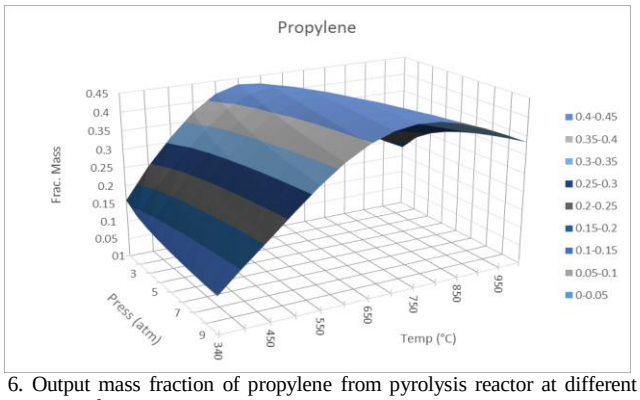

Fig. 6. Output mass fraction of propylene from pyrolysis reactor at different temperature and pressure.

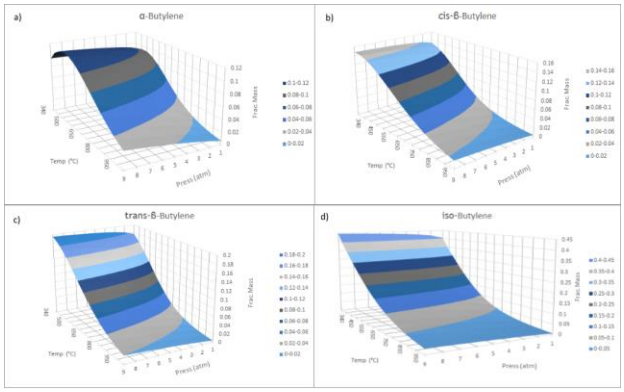

Fig. 7. Output mass fraction a) α-butylene b) cis-β-butylene c) trans-β-butylene d) iso-butylene from pyrolysis reactor at different temperature and pressure.

For this reason it can be concluded that as long the temperature grows up the polymer chain get cracked and the product is a smaller molecule that is ethylene, and the α-butylene, cis-β-butylene, trans-β-butylene and isobutylene contributes to the formation of ethylene at this conditions.

The response surfaces show the importance of the temperature effects to produce ethylene and propylene. The pressure effect seems to be not as important as the temperature, however pressure is an important variable in real pyrolysis reactors, for this reason it should be considered.

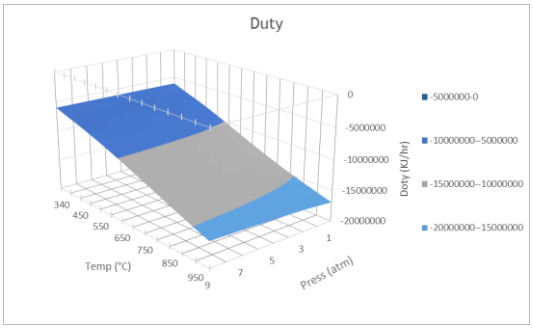

Fig. 8. Input of energy (kJ/hr) to pyrolysis reactor at different pressure and temperature.

As it is to be expected as long the temperature is up the energy demand in the process is greater (Figure 8), however pressure do not affect as much as temperature. Figure 5 is used in order to obtain the greatest ethylene production, the process conditions are 1atm and 950°C. After the pyrolysis, the ethylene must be separated from the others products. Ethylene must be pure to produce anhydrous ethanol.

Olefins separation.

Ethylene refinement is an important issue in order to produce anhydrous ethanol, for that reason a separation column is used to get pure ethylene from the pyrolysis gas [13]. With sensitivity analysis a RadFrac is used to simulate the column and Reflux Ratio. (0.4-10), Number of Stages (2-13) and Pressure as variables to find the best way to separate ethylene.

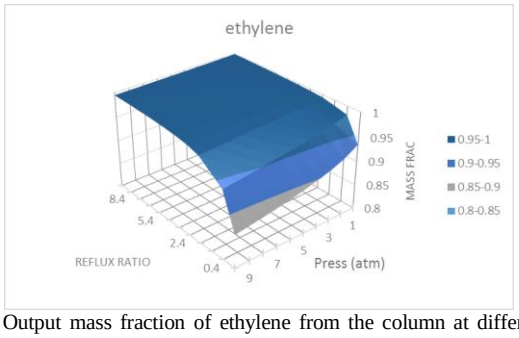

Fig. 9. Output mass fraction of ethylene from the column at different reflux ratio and temperature.

As it is known reflux ratio required energy in condenser and reboiler. In Figure 9 shows that the best reflux ratio is 1.4 and in Figure 11 shows the required duty for reboiler and condenser.

The investment is another important issue to be considered. The bigger the column is the more expensive is the cost of the equipment then the investment could increase. For this reason the number of stages must be specified. Figure 10 shows the mass fraction of ethylene in distillate flow and Figure 11 shows the energy demand for condenser and the reboiler column.

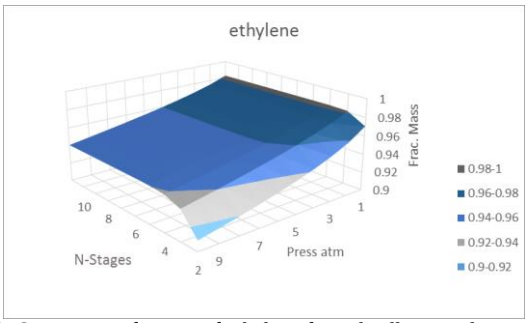

Fig. 10. Output mass fraction of ethylene from distillation column at different pressure and number stages.

In order to decrease the utility of process an energy analysis was developed. Figure 11 a) shows that the bigger reflux ratio is the more energy the process require, pressure response do not have the same behavior. The second analysis shows that after the stage 6 there is no more energy demand, however the pressure do have influence in energy demand.

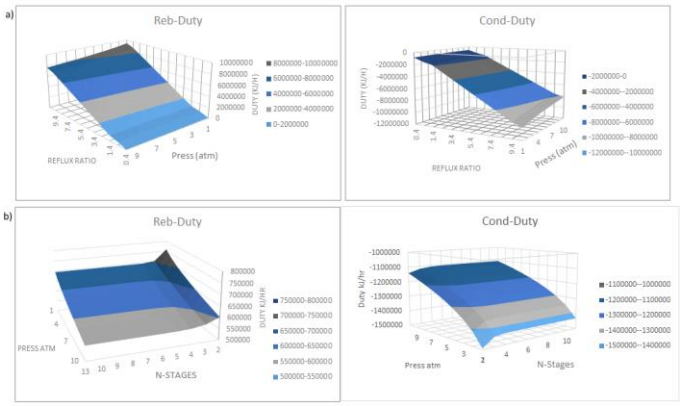

Fig. 11. Energy demand in rebolier and condenser distillation column a) different pressure and number of stages b) pressure and reflux ratio.

The final results of the column optimization are 1.4 for reflux ratio, 6 stages and 10 atm pressure. This information important for the process development.

Ethanol production

The alcohol production and the energy demand for this reaction is another study case, Figure 12a shows that the yield of ethanol at 20°C and 81atm is almost 1. At this conditions water and ethylene consumed in the reaction. The energy analysis (Figure 12b) shows that at same conditions the energy demand is nearly to 0.

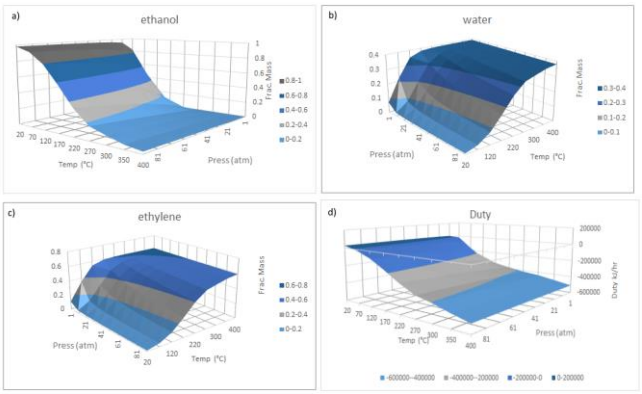

Fig. 12. Ethanol production responses a) ethanol yield b) water consumption c) ethylene consumption d) energy demand.

Process Economics

The ultimate purpose for developing such a process design, simulation model, is to determine the economics of ethanol production. This time the deferens between LDPE and PP

First the total capital investment (TCI) is shown in table 2. It should be emphasized that the investment is the same for a plant of LDPE or PP.

Table 2

Total Capital investment plant	
Purchased Equipment	$7,928,100.00
Equipment Setting	$250,007.00
Piping	$3,830,850.00
Civil	$445,583.00
Steel	$72,242.1.00
Instrumentation	$898,867.00
Electrical	$748,900.00
Insulation	$103,124.00
Paint	$89,994.50
Other	$5,654,000.00
Subcontracts	0
G and A Overheads	$542,852.00
Contract Fee	$760,596.00
Escalation	0
Contingencies	$3,838,520.00
Total Project Cost	$25,163,600.00

Total operating costs, which include raw materials, utility, operating labor, and Maintenance, are incurred only when the process is operating. Building on design reports published in 2007 NREL (Renewable Energy Laboratory), performed a complete review of the process design and economic model for the biomass-to-ethanol process from corn for 61MMgal/year, this reference will be used to escalate and compared the plant. Quantities of process were determined and compared whit total products sales, Figure 13 shows cash flow per year for LDPE.

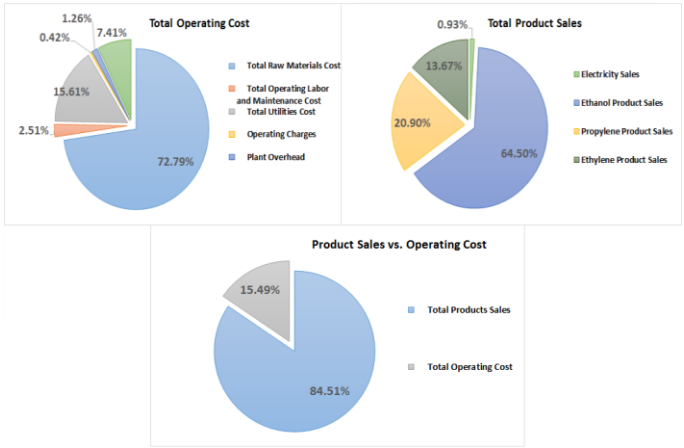

Fig. 13. Cash flow percentage for LDPE plant a) operating cost b) product sales c) sales and operating cost comparison.

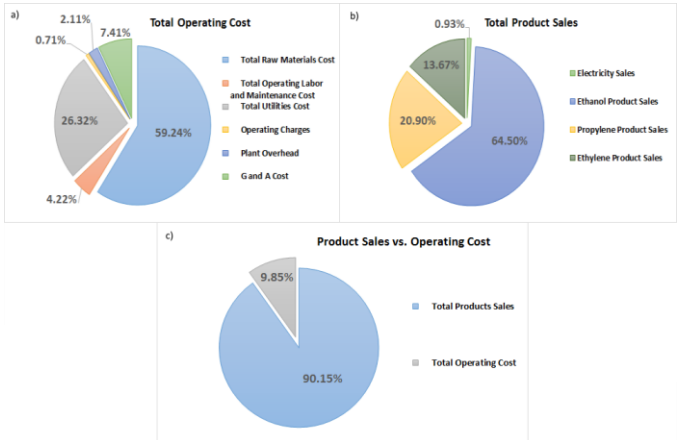

Fig. 14. Cash flow percentage for PP plant a) operating cost b) product sales c) sales and operating cost comparison.

There is a difference between LDPE and PP process economics, and it is the row material cost. Then the difference of total operating cost is caused because of LDPE and PP price. In table 3 row material and product prices until May are shown [14].

Table 3

Row Material and Product Prices	
LDPE	0.24 USD/kg
PP	0.12 USD/kg
Water	0.0028 USD/kg
Ethanol Anhydrous	1.14 USD/kg
Ethylene	1.7 USD/kg
Propylene	1.57 USD/kg

Once the total capital investment and variable operating costs, a discounted cash flow rate of return (DCFROR) analysis can be used to determine the minimum selling price per gallon of ethanol produced. The discounted cash flow analysis is calculated by iterating the selling cost of ethanol until the net present value of the project is zero [15]. This analysis requires that the discount rate, depreciation method, income tax rates, plant life, and construction start-up duration be specified [16]. Because this plant is equity-financed, some assumptions about the loan terms are also required. Table 4 shows the terms for this analysis.

Table 4

Discounted Cash Flow Analysis Parameters	
IRR	10%
Plant Lifetime	30 years
Loan terms	10-year loan at 8% APR
Construction Period	3 years
IRS	35%
General plant recovery period	7 years

Analysis does not take into account any policy factors such as subsidies, mandates, or carbon credits because these would be purely speculative. The purpose of analysis is to demonstrate whether or not ethanol from polymers can be cost-competitive. Table 5 shows the Minimum Ethanol Selling Price for this process analysis and the project summary.

Table 5

Ethanol Production Process Engineering Analysis LDPE	
Minimum Ethanol Selling Price (MESP)	$0.10 (USD/gal)
Gasoline-Equivalent MESP	$3.27 (USD/gal gasoline eq.)
Total Project Capital Cost	$28,269,817.00 (USD)
Total Raw Materials Cost	$43,499,700.00 (USD/year)
Total Products Sales	$325,994,000.00 (USD/year)
Total Operating Labor and Maintenance Cost	$1,502,270.00 (USD/year)
Total Utilities Cost	$9,328,340.00 (USD/year)
Total Operating Cost	$59,760,200.00 (USD/year)

Ethanol Production Process Engineering Analysis PP	
Minimum Ethanol Selling Price (MESP)	$0.05 (USD/gal)
Gasoline-Equivalent MESP	$3.27 (USD/gal gasoline eq.)
Total Project Capital Cost	$28,304,034.00 (USD)
Total Raw Materials Cost	$21,113,200.00 (USD/year)
Total Products Sales	$325,994,000.00 (USD/year)
Total Operating Labor and Maintenance Cost	$1,502,270.00 (USD/year)
Total Utilities Cost	$9,380,340.00 (USD/year)
Total Operating Cost	$35,638,900.00 (USD/year)

IV. Conclusions

The Pyrolysis waste polyethylene and polypropylene was successfully modeled using a combination of various unit operation modules available in Aspen Plus simulation package. The equilibrium model developed in this study enables one to predict the behavior of LDPE and PP pyrolysis process under various operating conditions. Moreover, the results obtained are easy to interpret.

Process conditions were optimized in order to attain the appropriate mass fraction suitable for different applications that ideally lies between high temperature low pressure value for pyrolysis and low temperature low pressure value to ethanol production. The following results summarize the findings from this study:

- Optimum temperature in pyrolysis process was determined to be 950°C and 1 atm pressure. Under this condition, the yield of ethylene efficiency reaches a maximum.
- The RadFrac pressure at 10 atm, 6 stages and 1.4 of reflux ratio could obtain ethylene 0.997 mass fraction in distillate flow.
- Sensitivity analysis of ethanol production shows optimum value of 20°C and 1 atm. Under this condition it can gets 99.3% ethanol anhydrous.
- The end result of the economic analysis was a predicted minimum ethanol selling price (MESP) of $0.10 USD/gal and $0.05 USD/gal. The reason is that ethylene and propylene as secondary products are profitable.

References

[1] Plasticseurope “An analysis of European latest plastics production, demand and waste data” Plastics – the Facts 2013, Association of plastics manufacturing. http://www.plasticseurope.org Last wiew December 2014.

[2] M. Paloma Conde Ortiz "Presente Futuro de la Industria del Plástico en México" Pemex Petroquímica, Ambiente Plástico Revista con Visión Global (2013).

[3] S.M. Al-Salem, P. Lettieri, J. Baeyens "Recycling and recovery routes of plastic solid waste (PSW): A review" Waste Management 29 (2009) 2625–2643.

[4] M.L. Mastellone, "Thermal treatments of plastic wastes by means of fluidized bed reactors." Ph.D. Thesis, Department of Chemical Engineering, Second University of Naples, Italy (1999).

[5] J. Troitsch, 1990. International Plastics Flammability Handbook. Hanser Publishers, Munich.

[6] Rodrigo A .F. Alvarenga, Jo Dewulf "Plastic vs. fuel: Which use of the Brazilian ethanol can bring more environmental gains?" Renewable Energy 59 (2013) 49-52.

[7] S.M. Al-Salem, P. Lettieri, J. Baeyens, "Thermal pyrolysis of high density polyethylene (HDPE)." In: Proceedings of the Ninth European Gasification Conference: Clean Energy and Chemicals, Düsseldorf, Germany, 23–25 March 2009.

[8] F. Paviet, F. Chazarenc, M. Tazerout, "Thermo Chemical Equilibrium Modelling of a Biomass Gasifying Process Using ASPEN PLUS." Int. J. Chem. Reactor Eng. 7: 18-(2009).

[9] W. Kaminsky, B. Schlesselmann, C. Simon, "Olefins from polyolefins and mixed plastics by pyrolysis" Journal of Analytical and Applied Pyrolysis (1995) 32 19-27.

[10] N. R. Mitta, S. Ferrer-Nadal, A. M. Lazovic, J. F. Parales, E. Velo, L. Puigjaner (2006) Modelling and simulation of a tyre gasification plant for synthesis gas production. Comput. Aided Chem. Eng. 21: 1771-1776.

[11] Pravin Kannan, Ahmed Al Shoaibi and C. Srinivasakannan "Optimization of Waste Plastics Gasification Process Using Aspen-Plus" Chapter 11 INTECH (2011).

[12] A. Tukker, H. de Groot, L. Simons, S. Wiegersma, "Chemical recycling of plastic waste: PVC and other resins." European Commission, DG III, Final Report 1999, STB-99-55 Final. Delft, the Netherlands.

[13] Ascensión Sanz Tejedor "Alcoholes de interés industrial" Química Orgánica Industrial, Escuela de Ingenierías Industriales (2008) – Uva.

[14] USDA Livestock, Poultry & Grain Market News (May 2015) National Weekly Ag Energy Round-Up.

[15] W. Short, D.J. Packey, T. Holt, "A Manual for the Economic Evaluation and Energy Efficiency and Renewable Energy Technologies." Report No. TP-462-5173. Golden, CO: National Renewable Energy Laboratory, March 1995.

[16] D. Humbird, R. Davis, L. Tao, C. Kinchin, D. Hsu, A. Aden "Process Design and Economics for Biochemical Conversion of Lignocellulosic Biomass to Ethanol" (2011) NREL/TP-5100-47764.

Conversion and use of biomass of *agave atrovirens* for the production of fuel bioethanol

Villa- Ramírez M.S., Plascencia- Espinosa M.A., Trejo-Estrada S.R.**
Centro de Investigación en Biotecnología Aplicada, Instituto Politécnico Nacional, Tepetitla, Tlaxcala, C.P. 90700, México.
sugeyrol@hotmail.com, sertre@hotmail.com

***Abstract*— Recently the exhaustion of fossil fuels and its high cost, has supported research into alternative energy source, currently in our country, there is an urgent need to generate a mega plant of biocombustibles production and better exploit, the vegetable residues from industry. These residues are transformed by fragmentation, thermal treatments, and different bioconversion processes, how enzymatic treatment, and some times with treatments chemical, physical . Plant biomass representing cellulosic residues is composed of 3 major components: cellulose, hemicellulose, and lignin, and may vary according to the type of material. Ethanol production from vegetable residues from industrial where is used Agave atrovirens sp requires lengthy procedures for obtaining.**
In semi-arid areas of the central highlands of Mexico, a small part of the increasingly eroded soils, is being restored using pulquero maguey (Agave atrovirens sp).

In our work, agave biomass can be converted to ethanol by chemical processes by autoclaving at 121 ° C and 15 PSI and subsequent hydrolysis using commercial enzyme preparations glucanases and hemicellulases estimated. The resulting hydrolyzates were analyzed with respect to its concentration of total soluble carbohydrate and reducing sugars content of cellulose, hemicellulose and lignin present in the lignocellulosic materials, may vary according to the type of material and are indicated by measuring, ° Brix for refractometry ARD and ART by Miller Method, and specifically by HPLC.

***Keywords*— hydrolysis / biofuel / lignocellulosic materials / vegetal residues**

I. INTRODUCTION

Agave atrovirens is a plant suculent that grown in semi-arid soil, Mexico, is the most important center of biodiversity of these species that find it in the meseta central of México.
This plant it belong from the *Agaveceae* family with about 166 species; the Principal Uses of agave plants are food, fiber, fodder, medicine, textile, construction, and the most important in our country is production of alcoholic beverages. During the manufacturing processes of agave beverages, the leaves are discarded and only it considered the "pinapple of Agave" or portion central of agave, this portion of agave is the most important, for the process of beverages how tequila and mezcal and recently pulcatta from *A. atrovirens* (company Desarrollos agropecuarios, 2015), because with She, is possible to obtain fermentable sugars, transformables, to ethanol. From this process, Agave residues could be used to produce fiber for the production of paper, cellulose, lignin, bioethanol, and other chemicals. In most cases, this not get happen, the leaves and residues of agave, are abandoned in the field, wasting much of the residue materials of Agave (Narvaéz-Zapata & Sánchez-Teyer, 2009, Salinas-Bedolla, 2009).

Recently, there have been studies for the use and convertion of lignocellulosic residues for the production of combustibles alternative of second generation, this it will be, alternative to fossil fuels. the use of different types of natural fibers to produce paper and textiles from Agave plants has been studied

Agave atrovirens is a good source of cellulose and lignin; nevertheless, the microstructural changes that happen during delignification have scarcely been studied, by processes of hydrolysis, using different chemical solutions how hydrochloric acid, sulfuric acid, alcalis and, enzymatics complex of the lignocelluloses (Azwa Z.N., Yousif B.F., Manalo A.C., & Karunasena W., 2013).

A. atrovirens is a excellent source of cellulose and lignin, recently, the microstructural changes during delignification have been studied (Kitano, M.,Yakabe Y. 1994).

The aim of this work was to study the sugars content, that present in the biomass of agave, by means of tecniques of sugars medicion by Miller method with acid dinitrosalicylic, ºBrix, and specifically for measurement of sugars glucose, xilose, cellobiose by HPLC.

II. METODOLOGY

The fibers of A. atrovirens were obtained from leaves and other residues of agave from industrial process of pulque, In the In the agave plants morphometric measurements were made, were later collected and the materials were drying to 60ºC por 72 hours to constant weight, its grinding was conducted with cutter mill, and sieving with sieve 40/60 and particle size 0.5 to 1.2 cm. Fibers were processed using method with addition of different concentrations of acid hydrochloric 2%, , and alkaline treatment with NaOH 3.5% , this concentrations were selected by means of pre-testing, where we got the best yields of sugars, the analysis all samples was made for triplicate.

Afterwards, all samples of Agave, was placed in the autoclave for 4 hours, to 121º C for processes humidification of fibers agave, followed of this process of hydrolysis thermic for autoclaved, Samples were taken, and its was chilled to room temperature, and adjusted pH 7.

Aftherthat, was added different commercial enzymes, the enzymes used were, viscozyme L, novozyme, cellubrist, celluclast, this enzymatic complexes were tested according to the recommendations of its technical use at 55ºC for 3 hours, to pH 7 in Water bath, then the samples was tempered to room temperature, followed, it was added distilled water up to proportion 1:30 (sample:water-chemical solutions). To calculate the percent hydrolysis and saccharification according to the calibration curve of glucose with DNS, and where used solution glucose 0.2% , the line equation:

$$(y = mx + b),$$

given by the straight calibration curve was used , The percent hydrolysis is calculated from the following formula :

$$\% \text{ de hydrolysis} = \frac{\text{g/L x total volume}}{\text{dry weight}} \times 100$$

Furthermore in the samples was measured with refractometer its ºbrix, this represent the soluble solid content in the samples of Agave, its components *Agave atrovirens*, and for analysis more specialized was measured for HPLC in the samples, its sugars contents, glucose, xilose and celullose in HPLC, and the lignin content, was measured with Klason method.

II. RESULTS

To obtain the results in the analysis of *Agave atrovirens*, the materials were milled in cutter mill, and was wetted autoclave, and then they were hydrolyzed with 2% HCl and NaOH 3.5%. The Enzymes used in the materials were Novozymes and vicozyme Celluclast and Pulzyme from Novozymes, Those which they showed good performance in preliminary tests of hydrolysis, and were selected to be evaluated partially, in this analysis not show results for acid hydrolysis because the yield in this treatment was low

The results showed in the morphometric of analysis the integral parts of the Agave, classified as pineapple and pencas (leaves), that content of Agave sugars, was increased relative to other parts of the plant, and exist differences in relation to age, being the content of reducing sugars, very high at 4 years and with yields similar to 10 years (this results not show). This analysis may represent an advantage at industrial. The samples was analyzed by the method Miller 1959 (Armstrong & Bennet,1982), for the obtain reducing sugars of hydrolysis process, and it is determined with DNS method that is a colorimetric reaction where Acid Dinitrosalicylic 3,5 acid is used, it took how reference, a calibration curve of 0.2% reagent grade glucose (SIGMA). Measurements were performed in a spectrophotometer brand Hewlett Packard model 8453 to 400 nm (Armstrong & Bennet, 1982).

For this analysis were used 45 samples of Agave. The analysis was accomplished with penca and pinapple of Agave. The results shown here, are of integral form for all the plant.

We can obtain in plants of 4 year old, levels of sugar high, in relation to the waiting time of plant growth, very similar to yields of sugars from plant 10 years but yet the plants they have not acquired sufficient biomass, despite very its high yields of sugar (see figure 1).

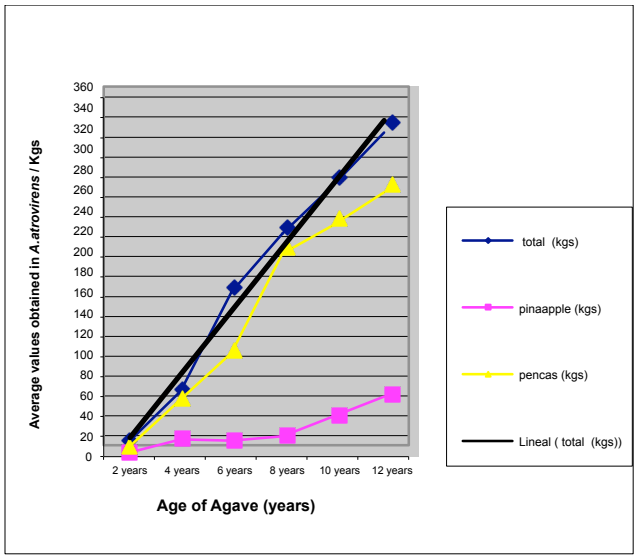

Figure 1. Effect of age of *A. atrovirens* in relation to the production of biomass (stalk weight ratio, pineapple and total weight).

Reducing sugars obtained of materials lignocellulosic residuals of *A. atrovirens*, were fragmented with milling cutter, and we obtained size particles between 0.7-13 mm, Aftherthat, the lignocellulosic materials was drying to 60ºC for 72 hrs and after was additioned with chemical solutions alkaline of NaOH 2%, for processes humitification. For processes enzymatics, the wetted samples with NaOH 2%, was additioned by enzymatically with commercial enzymes, additioned 1 ml for each 30 g of sample, in this processes, are put it at 55 ° C for 4 hours and they were quantified the sugars by the method of Miller 1958.

The Results here shown, only are for method alkaline-enzymatic because this method, showed the better yields of hydrolysis, and this was obtained with Celluclast 18% and cellubrix 16% at pH 5.5 and comparatively Viscozyme , Novozymes and pulzyme enzymes only it can give lower yields to 50% that Celluclast and Cellubrix (see figure 2).

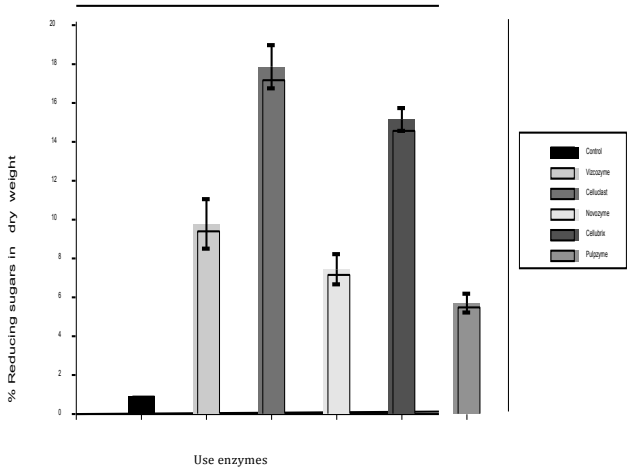

Figure 2. Percentage of reducing sugar by method Miller with different enzymes in residues of *A. Atrovirens* of 10 years old.

The results obtained in relation to the estimation of biomass quantified in 45 samples agaves, were on average 15 kg biomass estimable, for agave 2 years of age, and 272kg for mature agaves.

The results obtained from the quantification of glucose, cellulose, xilose was made for HPLC method. The yields obtained cellulose, are very similar among agaves of 2 and 10 years old and there is an average difference of only 2% between they.

In relation to of lignin, comparatively showed differences in agaves of 2 and 10 years old, the difference in content is 60% and is higher for mature agaves, we mention also that there are differences regarding the content of lignin between leaves and pineapples of Agave, for pineapples of Agave, the results obtained was 4.28% and 7.05% leaves, showing that, the leaves, to be support of plant It tend to have better content of lignin than the pinapple of Agave.

The glucose content represents the amount of convertible sugars by fermentation processes and in mature agaves we can transform up to 29.45% of sugars by fermentation processes, this results can only be obtained by optimized method of alkaline- enzymatic hydrolysis and the better results was that was obtained with enzyme Celluclast and Cellubrix (see figure 2).

for the xylose component that was obtained by alkaline-enzymatic hydrolysis method and quantified with HPLC, the highest performance was Celluclast and better results was with mature agave of 10 year old, in where the yield obtained were 7.51%, the table 1 shows only results for Agaves of 2 and10 years old, the better yield was with pineapple of Agave. (see Table 1).

Table 1. Cuantification of glucose, cellose, xilose and lignin in *Agave atrovirens* in dry base

Age Agave	Biomasss total	*%Celullose g/L	**Lignin g/L	standard desviation	*%Glucose g/L	*%Xilose g/L
2	15	63.5	5.66	0.426	17.3	3.24
4	65			0.426		
6	165			0.288		
8	223			0		
10	272	64.85	14.34	0.193	29.45	7.51

*glucose, celullose and xilose by method HPLC
**lignin by method Klason

IV. CONCLUSIONS

Polysaccharides of *A. Atrovirens* were quantified by methods with refractometry, method of Miller and HPLC, these compounds are essential for many food processes, however, this analysis was done for production of second generation biofuels, analysis was performed from residues industrial of Agave, since many of the agricultural-industrial residues process are underutilized.

The results show us, that that biomass, that it can estimate in the field, for analysis morphometric and we can quantify polymers that are present in the residue materials, and to estimate the approximate returns that we can get for later conversion to bioethanol.

The methods with acid, alkaline and alkaline-enzymatic, allows that the disaccharides and polysaccharides of plant materials can be decomposed to monosaccharides. Cellulose fibers of residues Agave, are basically composed of crystalline regions, and amorphous regions, and this polysaccharides, are modified structurally in the hydrolysis process.

The study allowed quantifying sugars by 3 different methods, acid, alkaline and alkaline-enzimatic, being the alkaline-enzymatic method, the method that allow us to obtain higher yields efficiency and reproducibility of results.
For treatments with enzyme addition in the residue materials of *A. Atrovirens,* the effectiveness of enzymes, depends largely control of its variables pH, temperature of exposure, of temperature of storage and shelf life of the enzymes, for to obtain better results.

The reports on the cellulose content in plants, show it that the content, varies in relation to the taxonomic group, and this varies ranges it is located between 35-50%, however, the method that we used, allowed, liberate, high contents of cellulose of around of 65% Comparatively with results reported by other authors who conducted similar studies of alkaline-enzymatic hydrolysis with others commercial enzymes.

The results which they have been reported by other authors, for compounds of lignin and hemicellulose are of 20 -35%, for this work we obtained 14.3% where we conclude that *A. Atrovirens* is a plant that have contains low porcentage for lignin, comparatively to tree materials, with low porcentage lignin (Martínez-Anaya et al., 2008, Saha, 2003).
Hemicelluloses quantified for this study were pentoses (xylose) and hexoses (glucose) these have varying degrees of polymerization and therefore are polydisperse, we can conclude that the results obtained, show it data similar those obtained by Puls et al., 2008, with softwoods, but in our studies it is needed, to determine, the content of glucomannan which is a principal component found, in woods of this type.

The main challenge of these processes, was to obtain the highest yield of polysaccharides transformable and to find, the efficient hydrolysis method, and later its conversion to ethanol by fermentation with microorganisms, currently they performed, studies necessary, for obtain Suitable processes for obtaining fuel ethanol. Currently they produced biofuels that representing only 1% cover needs of fuel total required worldwide, is necessary to find sustainable alternatives that do not compromise plant food, and these may be, of alternative use, for this reason, recent agricultural practices it will should change, our method developed, allowed to obtain higher yields of celluloses and very similar to those reported by other authors in relation to porcentage of glucose, xylose and lignin. For this work were considered studies of sugars obtained by optimized hydrolysis. The parameters considered were, fragmentation by physical methods, exposure time and wetting by autoclaving, and 3 hydrolysis methods acid, alkaline, and alkaline-enzymatic hydrolysis, the results obtained about proper optimization of the various parameters of hydrolysis, It allows to improve yield in the fermentation process**.**

V. ACKOWLEGEMENTS

CONACyT for to give we the needed recurse for to release this proyect, and Desarrollos Agropecuarios Company, for give we the different lignocelullosic material for its analysis, to SAGARPA-HIDALGO, MÉXICO, for giving facilities to carry out the study inthe field of materials agave.

VII. BIBLIOGRAFY

Azwa Z.N., Yousif B.F., Manalo A.C., & Karunasena W., 2013 A review on the degradability of polymeric composites base don natural fibres. Materials & Designs, 47,424-442.

Bhat, M.K., 2000. Cellulases and related enzymes in Biotechology.

Biotechnology Advances, 18,355-383.

B.S. Montenecourt, D.E. Eveleigh, TAPPI 28, 101 (1979).

Bhat, M.K., Bhat, S. (1997) Cellulose degrading enzymes and their potential industrial applications.

Biotechnology Advences, 15: 583-620.

Bhat, M.K. (2000)Cellulases and related enzymes in biotechnology, Biotechnology Advences, 18: 355-387.

C.A, Cardona, O.J, Sánchez, M.I, Montoya, J.A, Quintero. 2005. Producción de etanol carburante:
material lignocelulósicos una nueva alternativa, (Universidad del Valle),". Vol. II, núm. 1, pp. 47-55.

Dashtban, M., Heidi S., Wensheng Q,. 2009. Fugal Bioconversion of Lignocellulosic Residues: Oportunities & Perspectives. *International Journal of Biological Sciences 6*, 578–595

E, Escudero Escudero Alvarez Alvarez y P Gonzalez Gonzalez Sanchez Sanchez. 2005. La fibra dietética dietética. Nutrición Nutrición Hosp.vol 21, supl 2.

Gerpen J.V., Jürgen K., 2005 The Biodiesel Handbook , Ed. .AOCS Press, Champaign, Illinois.

Gao J. M., Weng H. B., Zhu D. H., Yuan M. X., Guan F. X, Xi Y. (2008). Production and characterization of cellulolytic enzymes from the thermoacidophilic fungal Aspergillus terreus M11 under solid-state cultivation of corn stover. Bioresour. Technol. 99: 7623-7629.

González, A. F. (2008). Biocombustibles de segunda generación y Biodiesel: Una mirada a la contribución de la Universidad de los Andes [Revista en línea]. Disponible:https://revistaing.uniandes.edu.co/pdf/a%2028%20corr.pdf [Consulta: 2013, Marzo 02]

J. Sánchez. Producción de etanol a partir de basura orgánica. El programa PERSEO aplicado a México, (Universidad Juárez del Estado de Durango),. México, 2010.

Kitano M, Yakabe Y., 1994. Strategy for biodegradability testing in OECD. Estudies in polymer science, vol 12, No. 1 p. 25-33.

Kirk O., Borchert T.V., Fuglsang C.C. 2002. Industrial enzyme applications. Current Opinion in Biotechnology 13, 345-351.Macromol Symp. 232, 85-92.

Lehninger Principles of Biochemistry. 5ª. Ed. Freeman, 2009. Cap 7.

Martinez Anaya C., Balcázar-López., Dántan-González E., Folch-Mallol J., 2008. Celulasas fúngicas: Aspectos biológicos y aplicaciones en la industria energética.

Nelson N. A Photometric adaptation of the Somogyi method for determination of glucose. J Biol Chem. 1944;153:378-380.

Ponce, T. ; Pérez, O. (2002). Celulasas y xilanasas en la industria. En Avance y Perspectiva [En línea] vol. 21 septiembre-octubre.

Puls, J.Schroder, N.,Stein, A. Janson, R& Saake, B. 2005. Xylans from Oat Spelts and Birch Kraft pul.

Saha B.C, 2003. Hemicelullose convertion. J Ind Microbiol Biotechnol. 30, 279-91.

Sánchez-Contreras Ángeles. 2008. Perspectivas en la producción de bioetanol a partir de diversos residuos agroindustriales. En: 1er Foro sobre Bioenergia, Valencia J., Fundación Produce Yucatan A.C., .México, p: 28-37

Tejeda L., Quintana J., Pérez J.,Young H. 2011 Obtención de etanol a partir de residuos de poda, mediante hidrólisis ácida e hidrólisis enzimática, (Fundación Universitaria Tecnológico Comfenalco),. Rev. U.D.C.A. Cartagena, pp. 111-116.

Venkatesh P.S., Volker S.U., Heller W.T., McGaughey J., Miller S., Hester R., 2010. Concentrated Acid Conversion of Pine Softwood to Sugars. Part I: Use of a Twin–Screw Reactor for Hydrolysis Pretreatment. *Chemical Engineering Communications 194*, 85–102.

Velkovsca S., Marten M., Ollis D. "Kinetic model for batch cellulase production by *Trichoderma reesei* RUT C30". J. Biotechnol., 54 (1997) 83-94

Reducción de la contaminación atmosférica en Lima Metropolitana por el uso de combustibles gaseosos en el parque automotor

Freddy Jesús Rojas Chávez
Pontificia Universidad Católica del Perú
Lima, Perú
Av. Universitaria 1801, San Miguel

Milka Marina Perales Llanos
Pontificia Universidad Católica del Perú
Lima, Perú
Av. Universitaria 1801, San Miguel

***Resumen*—Según, el Ministerio del Ambiente, el 70 por ciento del parque automotor es el causante de la contaminación del aire en Lima Metropolitana. En el 2011, en la zona Lima Este se sobrepasó los límites máximos permisibles en PM10. Según, la Organización Mundial de la Salud (2009) Lima lideraba con peores indicadores de calidad de aire revelando más de la mitad de la población limeña que reside en urbes con índices de polución 2.5 veces mayores de los recomendados. La Dirección de Salud V "DISA V", manifiesta estadísticamente que la morbilidad en Lima Metropolitana en el año 2006 y 2007 se debe por afecciones respiratorias en un 25 %. El objetivo principal es determinar matemáticamente la reducción de emisiones gaseosas (CO, NOx y SO2) y material particulado (PM10 y PM2.5) por el uso de gas natural con una proyección al 2030. Se concluyó que los porcentajes de reducción por emisiones gaseosas es 5 % en CO, de 1 % en NOx y 4 % en SO2; y en 1 % en material particulado PM2.5, y 63 % en material particulado PM10 aproximadamente.**

Palabras clave*— *contaminación atmosférica, emisiones gaseosas, gas natural vehicular, material particulado.

I. INTRODUCCIÓN

A. *Contaminación del aire*

La contaminación ambiental es toda materia o energía que al incorporarse o al actuar en el ambiente degrada su calidad original a un nivel perjudicial para la salud, el bienestar humano o los ecosistemas [1].

La Organización Mundial de la Salud define al aire puro como "mezcla de gases, vapor de agua y partículas sólidas y liquidas cuyo tamaño varía desde unos cuantos nanómetros hasta 0.5 milímetros" los cuales en su conjunto envuelven al globo terrestre.

Los principales gases que conforman el aire son el Nitrógeno, el Oxígeno y el porcentaje restante (como el Argón) pertenece a otras sustancias. Otros gases que pertenecen a este grupo son el ozono (O3), óxidos de azufre (SOX), óxidos de nitrógeno (NOX), monóxido de carbono (CO) y material particulado(PM) [2].

TABLA I. COMPOSICIÓN DEL AIRE ATMOSFÉRICO (EN PORCENTAJE) [3]

CONSTITUYENTE	SÍMBOLO	PORCENTAJE (%)
Nitrógeno	N_2	78.08
Oxígeno	O_2	20.95
Dióxido de carbono	CO_2	0.03
Gases raros y otros		0.94

Las fuentes de contaminación del aire se pueden considerar de orígenes de transporte, calefacción doméstica, producción de energía eléctrica, incineración de desechos y combustión de las industrias y emisiones debidas a los procesos de las mismas. De todas estas fuentes de contaminación la que genera mayor porcentaje es el transporte (R.D.ROSS, 1974).

B. *Situación actual*

El parque automotor es el responsable del 70% de la contaminación del aire existente en Lima Metropolitana- Perú y el porcentaje restante se le atribuye a la industria estacionaria [4]. Entre los principales contaminantes que genera el parque automotor son el Dióxido de Azufre, Dióxido de Nitrógeno, Monóxido de Carbono, el Material Particulado PM2.5 y el Material Particulado PM10, según el MINAM.

La variación del dióxido de azufre entre los año 2007 hasta el 2010 se muestra en el Figura 1.

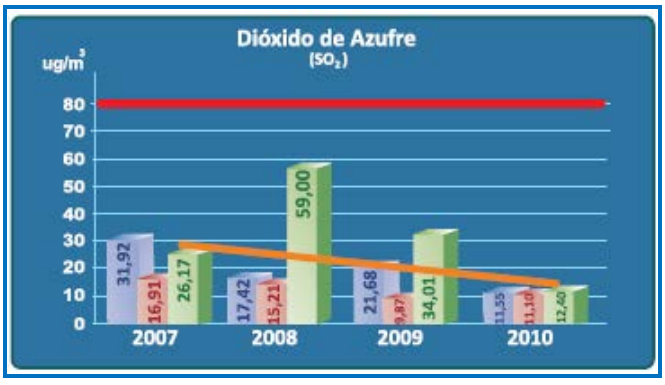

Fig. 1. Calidad del aire según estaciones de monitoreo en Lima-SO2 [5]

Según, la Figura 1 se puede observar una tendencia decreciente del SO2 y se encuentra por debajo de la ECA, y una de las razones por la cual mantiene esta tendencia es por la aplicación de la norma que regula el contenido de azufre en el diésel según la Ley N° 28694.

En la Figura 2 se muestra la variación del dióxido de nitrógeno entre los años 2007 hasta el 2010.

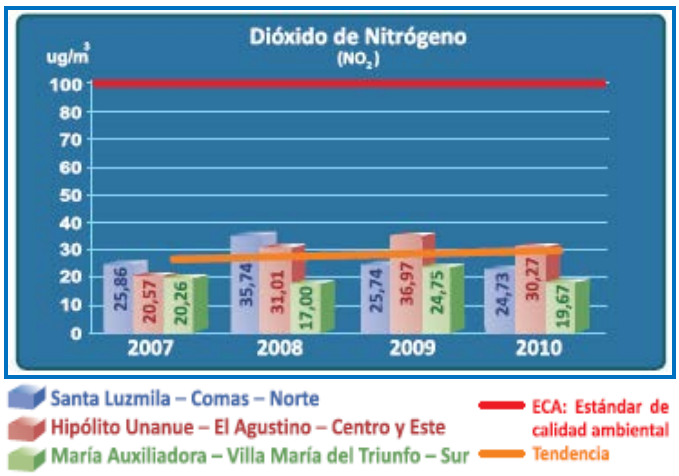

Fig. 2. Calidad del aire según estaciones de monitoreo en Lima-NO2 [5]

Según, la Figura 2 para el caso del NO2, se encuentra por debajo del ECA; sin embargo, se presenta una tendencia ligeramente creciente. Principalmente proviene de la combustión interna de los motores de automóviles.

La variación del PM10 entre los año 2007 hasta el 2010 se muestra en la Figura 3.

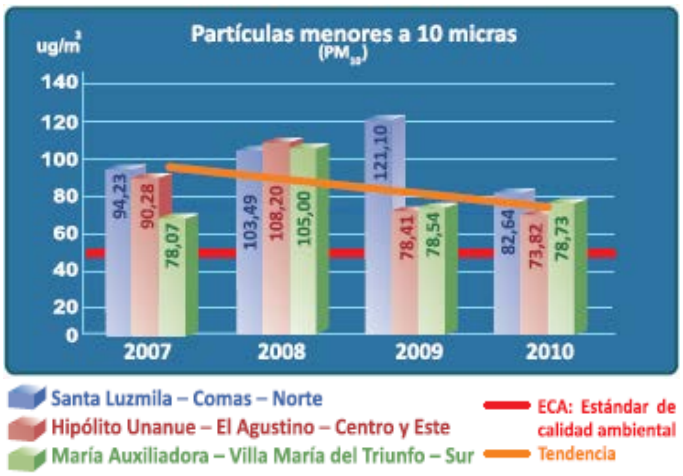

Fig. 3. Calidad del aire según estaciones de monitoreo en Lima-PM10 [5]

La Figura 3 muestra una tendencia decreciente del Material Particulado PM10, debido a las revisiones técnicas e introducción de vehículos de gas natural/gas licuado de petróleo. Para la zona Sur, la contaminación proveniente de fuentes naturales (erosión eólica) hace variable la tendencia del PM10.

La variación del PM2.5 entre los año 2007 hasta el 2010 se muestra en la Figura 4.

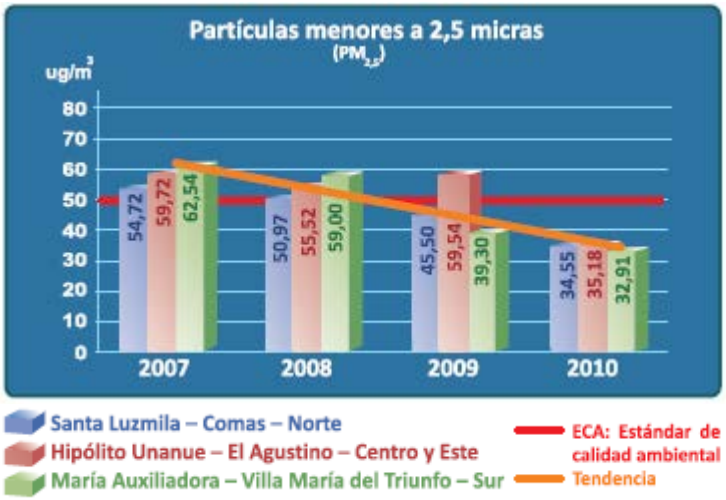

Fig. 4. Calidad del aire según estaciones de monitoreo en Lima-PM2.5 [5]

La Figura 4 muestra una tendencia decreciente, a partir de los 4 últimos años. Las partículas provenientes de las fuentes móviles (vehículos) se reducen debido a la aplicación de las revisiones técnicas y mejoras en la eficiencia de la combustión de los motores.

La principal consecuencia de la contaminación son las enfermedades respiratorias. La Tabla II muestra la cantidad de enfermos en Lima Metropolitana.

TABLA II. CANTIDAD DE PACIENTES CON AFECCIONES RESPIRATORIAS AL AÑO [6]

AÑO	AFECCIONES RESPIRATORIAS
2006	3,330,185
2007	3,876,350
2008	3,902,028
2009	3,927,705
2010	4,176,790
2011	4,208,090

II. MATERIALES Y MÉTODOS

A. *Parque automotor*

La tabla III muestra la data histórica de cantidad en vehículos en Lima Metropolitana.

TABLA III. CANTIDAD DE VEHÍCULOS EN LIMA METROPOLITANA (EN UNIDADES) [7]

N°	AÑO	VEHÍCULOS
1	2001	802,748
2	2002	829,214

3	2003	851,360
4	2004	866,881
5	2005	885,636
6	2006	912,763
7	2007	957,368
8	2008	1,036,850
9	2009	1,106,444
10	2010	1,195,353
11	2011	1,287,454
12	2012	1,395,576
13	2013	1,450,804

La Tabla IV Muestra la clasificación del parque automotor por tipo de vehículo en Lima Metropolitana.

TABLA IV. CLASIFICACIÓN DEL PARQUE AUTOMOTOR POR TIPO DE VEHÍCULO (UNIDADES) [8]

AÑO	AUTOMÓVIL	STATION WAGON	ÓMNIBUS	CAMIONETA RURAL	CAMIONETA PANEL	CAMIONETA PICK UP	CAMIÓN	REMOLCADOR	REMOLQUE Y SEMIREMOLQUE
2001	445,200	107,300	29,700	69,900	13,400	75,100	45,700	8,100	8,400
2002	445,200	120,600	29,400	72,000	14,200	75,900	45,400	8,600	8,900
2003	461,500	131,100	29,100	73,400	14,900	77,500	45,100	8,800	9,900
2004	464,300	139,600	28,900	75,000	15,800	79,100	44,800	9,100	10,300
2005	468,800	146,400	28,900	78,100	16,700	81,800	45,000	8,600	11,200
2006	476,800	154,000	29,100	83,500	17,600	85,000	45,700	9,100	11,900
2007	490,800	164,000	29,700	91,700	18,500	90,700	47,900	10,600	13,400
2008	523,800	173,400	31,000	107,300	20,500	99,700	52,400	12,900	16,000
2009	551,300	184,200	32,500	121,800	21,700	106,900	56,600	13,900	17,600
2010	589,600	195,000	34,800	138,200	22,900	119,300	61,000	15,100	19,500
2011	629,200	198,800	36,700	163,300	24,300	129,400	67,500	16,700	21,600
2012	681,100	202,600	38,600	191,100	25,400	141,100	73,200	18,400	23,900
2013	708,300	200,500	39,300	208,400	25,900	148,100	75,800	19,200	25,300

A partir de la tabla IV podemos clasificar al parque automotor por el uso de combustible, los cuales, actualmente, en Lima Metropolitana son principalmente la gasolina, diésel. El gas licuado de petróleo y el gas natural vehicular son consecuencia de la conversión mayoritaria de los vehículos que usan gasolina.

$$Gasolina = automóvil + station\ wagon \quad (1)$$

Los vehículos que usan gasolina, el 19% son de uso privado y el restante de uso para taxi.

$$Diesel = omnibus + camioneta\ rural camioneta\ panel + camioneta\ pick\ up + camión + remolcador + remolque\ y\ semiremolque \quad (2)$$

La Tabla V muestra como está conformado el parque automotor por tipo de combustible.

TABLA V. PARQUE VEHICULAR POR EL TIPO DE COMBUSTIBLE (EN UNIDADES)

AÑO	GASOLINA		DIESEL	GLP	GNV
	AUTO PRIVADO	TAXI			
2006	106,401	453,605	281,900	65,305	5,489
2007	101,024	430,679	302,500	99,139	23,958
2008	97,004	413,545	339,800	129,232	57,419
2009	100,346	427,793	371,000	126,332	81,029
2010	101,715	433,626	410,800	145,547	103,712
2011	101,878	434,324	459,500	166,279	125,519

Fuente: (*): Elaboración Propia

B. Factores de emisión

Para el análisis de inventario de emisiones del parque automotor, se utilizara el método de la evaluación rápida, según la Tabla 6.

TABLA VI. FACTORES DE EMISIONES (KG/KM)

SUSTANCIA	GASOLINA	DIÉSEL	GLP	GNV
Monóxido de Carbono	0.000984	0.0006104	0.0004465	0.0004465
Óxidos de Nitrógeno	0.0000513	0.000518	0.00002064	0.00002064
Material Particulado PM2.5)	0.00000848	0.0000371	0.000007367	0.000007367
Material Particulado (PTS)	0.000078	0.0000793	0.000078	0.000078
Material Particulado PM10)	0.00001355	0.00001594	0.0000134	0.0000134
Dióxido de Azufre	0.000006034	0.00000554	9.412E-07	9.412E-07

Fuente: ECOIVENT 2008

DISTANCIA PROMEDIO= 93 600 Km/año por vehículo para gasolina (taxis).

DISTANCIA PROMEDIO= 20 000 Km/año por vehículo para gasolina (privado).

Para determinar la cantidad de emisiones por cada contaminante del parque automotor se empleará la Ec. (3)

$$EMISIONES = NÚMERO\ VEHÍCULOS\ SEGÚN\ TIPO\ DE\ COMBUSTIBLE \times FACTOR\ DE\ EMISIÓN \times DISTANCIA\ PROMEDIO. \quad (3)$$

III. RESULTADOS

La Tabla VII muestra la cantidad total de emisiones por contaminante hasta el año 2040 en el comportamiento actual del parque automotor en Lima Metropolitana.

TABLA VII. TOTAL DE EMISIONES POR CONTAMINANTE (KG/AÑO)

	CO	NO_x	MP2.5	MP10	SO_2
2006	40,817,872	10,631,269	909,898	1,826,628	281,120
2007	40,594,146	11,238,029	952,701	1,996,509	279,986
2008	41,801,131	12,420,717	1,044,101	2,326,395	287,816
2009	44,578,921	13,502,890	1,134,836	2,607,158	305,696
2010	47,100,471	14,831,295	1,240,150	2,918,090	323,067
2011	49,595,277	16,426,938	1,362,626	3,263,900	341,364
2012	79,540,983	28,914,899	2,342,465	5,390,504	562,391
2013	85,033,606	31,763,639	2,563,259	5,950,311	602,809
2014	91,104,256	34,908,198	2,806,433	6,556,820	647,753
2015	97,792,740	38,378,132	3,074,131	7,214,586	697,570
2016	105,144,618	42,206,136	3,368,732	7,928,658	752,650
2017	113,211,272	46,428,435	3,391,184	8,585,293	768,626
2018	122,049,949	51,084,906	4,049,467	9,548,685	880,406
2019	131,724,195	56,219,711	4,441,734	10,467,640	954,110
2020	142,303,847	61,881,408	4,873,218	11,469,011	1,035,139
2035	485,630,586	264,104,518	19,988,040	24,454,172	3,780,724
2036	528,591,786	291,070,296	21,983,226	26,274,444	4,132,822
2037	575,511,986	320,802,350	24,180,176	28,237,706	4,518,659
2038	626,766,211	353,585,281	26,599,479	30,355,994	4,941,515
2039	682,766,422	389,732,948	29,263,835	32,642,453	5,404,994
2040	743,965,004	429,591,635	32,198,275	35,111,407	5,913,066

La Tabla VIII (Fuente: elaboración propia), muestra la cantidad de emisiones en un supuesto incremento del 3% adicional al comportamiento actual de conversión de vehículos a gasolina a gas natural vehicular.

TABLA VIII. TOTAL DE EMISIONES POR CONTAMINANTE - PROPUESTO (1000KG/AÑO)

AÑO	CO	NO_x	MP2.5	MP10	SO_2
2015	92,641,886	38,105,041	3,035,820	10,134,397	662,881
2016	99,603,155	41,912,466	3,327,340	10,974,155	715,420
2017	107,234,685	46,111,841	3,648,051	11,890,141	773,372
2018	115,591,897	50,742,947	4,000,848	12,889,109	837,212
2019	124,736,290	55,849,837	4,388,937	13,978,551	907,469
2020	134,735,456	61,480,953	4,815,844	15,166,701	984,721
2021	145,664,169	67,689,906	5,285,471	16,462,669	1,069,611
2022	157,604,504	74,535,759	5,802,116	17,876,467	1,162,842
2023	170,646,630	82,083,696	6,370,519	19,419,116	1,265,190
2024	184,889,717	90,405,615	6,995,906	21,102,746	1,377,509
2025	200,442,507	99,580,792	7,684,038	22,940,688	1,500,736
2033	389,119,358	216,349,412	16,365,718	45,307,164	3,027,434
2034	423,509,982	238,445,453	17,998,653	49,404,370	3,310,017
2035	461,095,789	262,810,219	19,796,878	53,889,514	3,619,921
2036	502,181,467	289,677,189	21,777,274	58,800,641	3,959,818
2037	547,101,703	319,303,878	23,958,453	64,179,606	4,332,643
2038	596,224,465	351,974,517	26,360,949	70,072,493	4,741,630
2039	649,954,221	388,002,569	29,007,401	76,530,021	5,190,338
2040	708,735,466	427,733,903	31,922,779	83,608,016	5,682,683

Por lo tanto, la Tabla IX muestra la reducción de emisiones que se conseguiría al incrementar el 3% adicional al comportamiento actual del parque automotor. Esta reducción de emisiones contribuiría a reducir las enfermedades respiratorias en un 17% y reducir los costos originados

TABLA IX. CANTIDAD TOTAL REDUCIDA DE CONTAMINACIÓN POR COMBUSTIBLE Y MATERIAL PARTICULADO

AÑO	CANTIDAD DE VEHÍCULOS CONVERTIDOS	REDUCCIÓN DE CO	REDUCCIÓN DE NOx	REDUCCIÓN DE MP2.5	REDUCCIÓN DE MP10	REDUCCIÓN DE SO
2015	27,836	5,150,853	273,092	38,311	5,308,120	34,689
2016	29,147	5,541,463	293,670	41,391	5,861,201	37,230
2017	30,606	5,976,587	316,594	43,520	6,342,014	40,746
2018	32,221	6,458,052	341,959	48,619	7,113,418	43,194
2019	33,998	6,987,905	369,873	52,797	7,822,733	46,641
2020	35,946	7,568,391	400,455	57,374	8,595,184	50,418
2021	38,071	8,201,988	433,835	62,371	6,047,687	54,540
2022	40,383	8,891,362	470,154	67,807	6,425,324	59,025
2023	42,892	9,639,365	509,561	73,705	6,826,672	63,892
2024	45,608	10,449,083	552,219	80,090	7,252,978	69,160
2025	48,542	11,323,790	598,302	86,987	7,705,566	74,851
2034	86,958	22,777,043	1,201,695	177,302	13,227,000	149,366
2035	92,854	24,534,796	1,294,299	191,162	14,036,700	160,803
2036	99,145	26,410,319	1,393,108	205,952	14,894,027	173,005
2037	105,853	28,410,283	1,498,472	221,722	15,801,679	186,017
2038	113,002	30,541,745	1,610,764	238,530	16,762,510	199,884
2039	120,618	32,812,201	1,730,379	256,434	17,779,552	214,656
2040	128,726	35,229,538	1,857,732	275,495	18,855,993	230,383

CONCLUSIONES

1. Se logra una reducción de las emisiones de contaminación por CO en un 5% con el aumento generado de la conversión del parque vehicular.
2. Se logra una reducción de las emisiones de contaminación por NOx en un 1% con el aumento generado de la conversión del parque vehicular.
3. Se logra una reducción de las emisiones de contaminación por MP2.5 en un 1% con el aumento generado de la conversión del parque vehicular.
4. Se logra una reducción de las emisiones de contaminación por MP10 en un 63% con el aumento generado de la conversión del parque vehicular.
5. Se logra una reducción de las emisiones de contaminación por SO2 en un 4% con el aumento generado de la conversión del parque vehicular.
6. Se logra una reducción de las enfermedades por vías respiratorias en un 4% con el aumento generado de la conversión del parque vehicular.
7. Se logra una reducción en los costos de salud en un 4% con el aumento generado de la conversión del parque vehicular.
8. Se logra una reducción en los costos de inasistencia en un 4% con el aumento generado de la conversión del parque vehicular

REFERENCIAS

[1] N. de Nevers, Introducción al Control de la Contaminación del Aire, México: McgGraw-Hill Interamericana Editores S.A. de C.V., pp. 9.

[2] M. Romero, F. Olite, M. Álvarez, La Contaminación del Aire: su repercusión como problema de salud, Revista Cubana de Higiene y Epidemiología. Ciudad de La Habana. Consulta: 19 de setiembre de 2012. http://scielo.sld.cu/scielo.php?pid=S156130032006000200008&script=sci_arttext

[3] Agencia de Protección Ambiental de Estados Unidos, Programa Ambiental de los EE.UU.-México, Frontera 2012. Red de Transferencia de Tecnología Centro de Información sobre Contaminación de Aire (CICA) para la frontera entre EE. UU. - México. Estados Unidos. Consulta: 21 de setiembre de 2012. http://www.epa.gov/ttncatc1/cica/indexs.html

[4] Ministerio del Ambiente, Parque Automotor ocasiona el 70% de la Contaminación del Perú, Diario El Comercio. Fecha de Publicación: 27 de Marzo. Ciudad Lima. Consulta: 19 de setiembre de 2012. http://elcomercio.pe/planeta/1388897/noticia-parque-automotor-ocasiona-70-contaminacion-peru

[5] Ministerio del Ambiente, Vehículos por cada mil habitantes. Sistema Nacional de Información Ambiental. Ciudad Lima. Consulta: 05 de Octubre del 2012.

[6] Instituto Nacional de Estadística e Informática, Perú Compendio Estadístico 2011, Perú: Sistema Estadístico Nacional. Tomo N° 1.

[7] Instituto Nacional de Estadística e Informática, Perú Compendio Estadístico 2011, Perú: Sistema Estadístico Nacional. Tomo N° 2.

[8] R. Webb, G. Fernández, Anuario Estadístico. Instituto Cuánto. Perú en Cifras 2012. Lima: Octubre del 2012.

Autoabastecimiento energético en una comunidad rural tipo a partir de la biomasa

Esparza Isunza R.S. , Esparza Isunza T.
Departamento de Ingeniería de Procesos e Hidráulica, Universidad Autónoma Metropolitana.
P.A. 55-535, 09340 Iztapalapa, México D.F., México,
e-mail: tris@xanum.uam.mx

Resumen— Este trabajo considera una propuesta teórico-metodológica para el autoabastecimiento energético en una comunidad rural tipo. Se describe la comunidad seleccionada, exponiendo consideraciones que comprenden tanto su morfología física y ubicación Geográfica, como su estructura sociocultural, revisando así mismo los recursos energéticos más utilizados y el potencial biomásico existente en la comunidad. Por último, se contrasta el costo económico del proyecto de autoabastecimiento energético contra la alternativa de conectarse a la red eléctrica local.

Palabras clave: teórico-metodológica,* autoabastecimiento energético*, potencial biomásico.

I. Introducción

El consumo de energía se ha convertido en uno de los problemas más graves de la actualidad. Es evidente la necesidad de incorporar a miles de comunidades rurales en América Latina y, en particular en nuestro país, al desarrollo y bienestar social. La Ingeniería puede participar así en la solución de uno de los problemas más acuciantes de nuestro tiempo: la creciente migración campesina a las ciudades en busca de alternativas económicas y sociales. En este contexto, este trabajo considera una propuesta teórico-metodológica para el autoabastecimiento energético en una comunidad rural tipo. Se describe la comunidad seleccionada, exponiendo consideraciones que comprenden tanto su morfología física y ubicación Geográfica, como su estructura sociocultural, revisando así mismo los recursos energéticos más utilizados y el potencial biomásico existente en la región. También se caracteriza económicamente, presentando los objetivos específicos del proyecto para la zona rural, la estructura de la demanda energética y el modelo energético de la producción de biomasa. Se analiza, además, la cuantificación de las necesidades de potencia según el uso Terminal dentro de la comunidad rural. Posteriormente, se define la disponibilidad de biogas abordando cuestiones técnicas sobre el diseño y operación del biodigestor.

II. Metodología

La metodología de un proyecto de este tipo implica, en primer lugar, ir de lo general alo particular, por lo que se debe:

1) determinar la geografía del sitio (ubicación y clima)
2) las actividades económicas
3) las condiciones socioeconómicas de la comunidad

En segundo lugar, se debe caracterizar la unidad económica particular.

A. Caracterización de la unidad económica

El sitio del proyecto es un predio agrícola ejidal ubicado en el estado de Puebla, en el Municipio de Xiutetelco; localizado en los 19º 47’ N y los 97º 19’ W, a una altitud de 1920m. Con una extensión aproximada de 715 Ha, en las que, según su destino, se dividen en: a) forestal, 200 Ha; b) agrícola, 250 Ha; c) pastos, 250 Ha y d) frutales, 15 Ha. El resto del terreno esta ocupado por lecho rocoso, caminos y viviendas, cuya estructura económica corresponde a la de una zona rural con bajo nivel de desarrollo. El predio no cuenta con energía eléctrica, drenaje, ni servicio de agua potable. Las actividades productivas típicas son: la agricultura, la avicultura en mediana escala (se cuenta con un criadero de 880 aves), la crianza de 210 cerdos estabulados y la de 30 vacas y 25 novillos para explotación de carne y leche. Dentro del predio viven 8 familias con un total de 46 personas que habitan 8 viviendas independientes.

B. Clima

La tendencia climática es característica de una zona de clima templado (Temperatura media = 16.4 ºC), con una pluviosidad constante a lo largo del año (2301.7 mm), pero

más abundante de junio a octubre. Es importante señalar que la humedad presente en el medio ambiente favorece la opción de un tratamiento anaeróbico de los desechos orgánicos.

C. *Actividades económicas*

Se dedican al cultivo cíclico de temporal de: maíz, frijol, trigo, cebada, haba y papa; así como de frutales: manzano, ciruelo, aguacate, pera y durazno. Se cuenta con existencia de ganado bovino, ovino y porcícola, además de una población avícola importante [1]. El nivel educativo puede considerarse de bajo a medio, y se tiene una escasa tecnificación de las actividades productivas y de la vida doméstica [op. cit]. Los recursos energéticos más usados son la leña, carbón de leña y residuos agroforestales destinados a calefacción y cocción de alimentos. Se puede concluir que existe un importante potencial biomásico relativamente concentrado en algunas áreas de la región, el cual puede ser empleado con fines energéticos.

III. OBJETIVOS DEL PROYECTO ESPECÍFICO DE LA ZONA RURAL.

A. *General*

Autoabastecimiento energético de una comunidad rural

B. *Particulares*

- Utilizar de manera eficiente el recurso bimásico de una comunidad rural
- Resolver la demanda energética doméstica y las derivadas de crianza animal avícola.
- Instalar un equipo motobomba acondicionado con biogas para satisfacer la demanda de agua

TABLA 1. ESTRUCTURA DE LA DEMANDA ENERGÉTICA

Demanda	Frecuencia mensual	Frecuencia Horaria (h/día)
a) Doméstica		
Iluminación	Todo el año	6
Electrodomésticos	Todo el año	6
Cocina	Todo el año	6
Agua (bombeo)	Todo el año	1
Calefacción	N,D,E,F	6
Calentamiento H_2O	Todo el año	2
b) Ganadería y Avícola		
Iluminación	Todo el año	40
Calefacción	N,D,E,F	12
Agua (bombeo)	Todo el año	1
Calentamiento H_2O	Todo el año	6
c) Agrícola		
regadio	D,E,F,M,A	8

IV. MODELO ENERGÉTICO DE LA PRODUCCIÓN DE BIOMASA

La fuente primaria de energía es la radiación solar, de la que solo una mínima fracción es empleada y transformada en crecimiento neto de las plantas. El esquema de la fig. 2 representa al predio agrícola como un sistema abierto que intercambia energía y masa con su medio ambiente.

Fig. 1 Esquema del modelo energético de la producción de biomasa

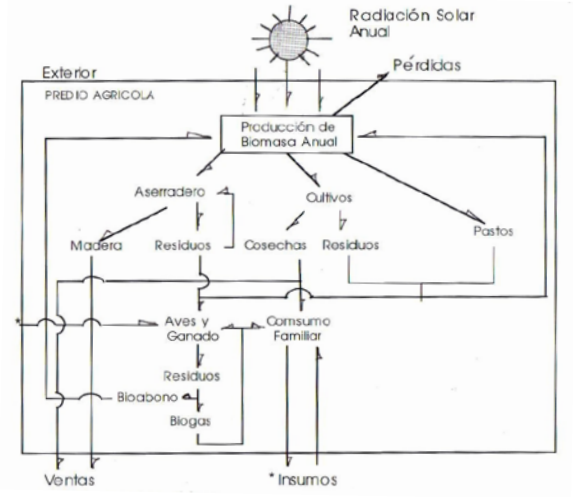

El rendimiento energético global del predio (η_G), sería:

Rendimiento energético global de la producción de biomasa forestal (η_1)
Energía solar total anual (A) = $1.718X10^6$ Kcal/m^2-año
Energía producida como biomasa forestal (B) = $5.25X10^9$ Kcal/año
Rendimiento energético global de la producción de biomasa agrícola (η_2)
Equivalente energético para la producción anual de biomasa agrícola (C) = $6.1X10^9$ Kcal/año
Energía solar global anual incidente durante los meses de cultivo (D) = $1.42X10^6$ Kcal/m^2-año

$$\eta_1 = A/B = 0.15\ \%$$

$$\eta_2 = C/D = 0.17\ \%$$

$$\eta_G = \eta_{1+}\ \eta_2 = 0.15 + 0.17 = 0.22\ \%$$

V. CUANTIFICACIÓN DE LOS REQUERIMIENTOS DE POTENCIA

El cálculo de las necesidades de potencia se realizara en base a las necesidades energéticas horarias dadas en el Cuadro 1 que sigue:

TABLA 2 ESTIMACIÓN DE LAS NECESIDADES ENERGÉTICAS HORARIAS

Hora	Iluminación					cocina	Calefacción		Electro domésticos		Bombeo agua		Calentamiento agua	
	domicilio	vacuno	aves	cerdos	pasillo gallinas		domicilio	cerdos	radio y televisión	plancha	domicilio	regadio	domicilio	otros
1														
2														
3														
4														
5														
6														
7														
8														
9														
10														
11														
12														
13														
14														
15														
16														
17														
18														
19														
20														
21														
22														
23														
24														
	Todo el Año	Todo el Año	Todo el Año	Todo el Año	Todo el Año	Todo el Año	Nov. Dic. Ene. Feb.	Nov. Dic. Ene. Feb.	Todo el Año	Todo el Año	Todo el Año	Nov. Dic. Ene. Feb.	Todo el Año	Todo el Año

VI. OFERTA DE BIOGAS

TABLA 3 OFERTA DE BIOGAS DEL PREDIO RURAL

Animal	PE (kg/día)	S V (kg/día)	PB_1 (m^3/KgSV)	Cantidad	Peso (kg)	PB_2 (m^3/día)	VDB (m^3)	CDE (Kg)	CAL (L)	CSV (KgSV/KgE)	FIDR (L/día)
Porcino	8.6	0.86	0.38	210	50	28.35	18.47	525	628.5	0.052	1209.2
Acuno	5.2	0.70	0.50	30	300	29.41	22.69	774	1161	0.040	1935
Novillo	5.0	0.60	0.45	25	100	8.75	5.13	145.5	213.75	0.049	356.4
Aves	9.0	1.25	0.55	880	1	5.98	3.22	79.2	356.4	0.025	436.5
Total	--	3.41	--	1145	50	72.5	49.51	1520.7	2413.6	--	3957.5 [≡] 4m^3

PE: Producción de Excremento; SV: Sólidos Volátiles; PB_1: Producción de Biogas (SV); PB_2: Producción de Biogas (día); VDB: Volumen de Diseño de Biodigestor por tipo de residuo; CDE: Cantidad Diaria de Excremento; CAL: Cantidad de Agua de Lavado; CSV: Concentración de Sólidos Volátiles; FIDR: Flujo Individual Diario de Residuos

.

Para el diseño del equipo se debe considerar:

- Volumen Total de Diseño (VTD = ∑VDB)
- Producción de Biogas Total (PBT = ∑ PB_2)
- Tiempo de Residencia (TR)
- Flujo Volumétrico Total de Residuos (FVTR)

Cálculo del volumen del digestor

Carga Volumétrica (CV)	CV = SV/m^3	3.41 KgSV/día m^3
Biogas Total (BG)	BG = PB_2/VDP	1.46 m^3 Biogas/m^3 Biodigestor
Tiempo de Retención (TR)	TR = VDP/FIDR	12.37 días

Para determinar el FVTR debe conocerse la cantidad total diaria de excremento por tipo de animal, así como el porcentaje de Sólidos Totales (ST) de la mezcla con que se carga el digestor. Este es un elemento relevante pues uno de los factores que aseguran un proceso fermentativo satisfactorio. Experimentalmente se ha demostrado que una carga que contenga 8 % de ST [2] es óptima para la digestión. Para lograr dicha concentración es necesario mezclar los residuos con agua (llamada agua de lavado), según las proporciones señaladas en el Cuadro 3.

TABLA 4 AGUA DE LAVADO SEGÚN TIPO DE MATERIA ORGÁNICA [OP. CIT].

Estiércol	Sólidos Totales (%)	Volumen de agua de lavado (L/Kg)[1]
Vaca	20	1.5
Cerdo	18	1.3
Novillo	14	0.95
Gallinas	44	4.4

[1] Litros de agua/Kg de excremento para lograr una concentración de 8 % de Sólidos Totales

VII. CÁLCULO DEL EQUIPO

Se debe considerar: 1) el equipo seleccionado; 2) modo de operación (en este caso, semicontinuo y estado estacionario, ya que todas las variables de operación son constantes durante todo el año); 3) la energía total demandada (ver Cuadro 1, que en este caso exige una Potencia Real Demandada ,PRD = 397.8 KW); 4) la Producción Total de Biogas, PTB, que en el caso que nos ocupa produce una Potencia Diaria, PD = 448.8 KW (en nuestro caso la PD es mayor que la PRD en un 11 %, lo cual nos asegura el suministro energético) y 5) selección del tipo de biodigestor (en este caso se selecciono la tecnología guatemalteca). Respecto a este último inciso, la selección obedeció a:

- Este tipo de digestores se recomienda cuando se requiere trabajar con volúmenes mayores a los 15 m^3, para los cuales la excavación de un pozo vertical resulta muy problemática. Estos aparatos están diseñados para producir biogas para necesidades comunales, tales como accionar motores para bombeo, molienda o generación de electricidad.
- Se construye con técnicas convencionales de albañilería y su forma permite un mínimo de problemas en la construcción.
- Es más barato por m^3 de digestor.
- Necesita escaso mantenimiento y tiene larga vida útil.

VIII. ANÁLISIS ECONÓMICO DEL PROYECTO RURAL Y ALTERNATIVA ENERGÉTICA

El Cuadro 4 muestra el contraste económico entre el proyecto de autoabastecimiento energético o la conección a la red eléctrica local. Se presenta la comparación de la inversión, los costos de operación y el valor actualizado neto, entre las opciones de construcción del biodigestor y la alternativa de conectarse a la red de energía eléctrica (sin considerar el costo de los postes). El biodigestor resulta ser 12000 USD más barato.

TABLA 5 INVERSIÓN COMPARATIVA

Opción	Inversión USD	Costo de operación USD	Valor actualizado neto USD
Biodigestor	2213.50	1915.80	4129.30
Red eléctrica	3112.50	13290.8	16403.30

IX. CONCLUSIONES

Las tecnologías de producción de combustibles a partir de la biomasa son simples en su mayoría y de un costo relativamente bajo. En particular, la producción de biogas resulta muy conveniente, pues los equipos digestores son de fácil construcción, costo moderado, escaso mantenimiento y larga vida útil. Es factible combinar la explotación de un conjunto de diferentes recursos biomásicos con el propósito de satisfacer las necesidades energéticas de una zona rural determinada sin inversiones honerosas. En la mayoría de los casos, esto se logra racionalizando la explotación de los recursos naturales.

X. REFERENCIAS

1. INEGI. XI Censo de Población y Vivienda 1990. México, 1992.
2. Mandujano, M. I, F. A. Alfonso y Martinez, A. M., Biogas: Energía y Fertilizantes a partir de desechos orgánicos, Manual para el promotor de la tecnología. Cuernavaca. México. OLADE, IIE, 1981.S.P.E.Nº6.

XI. BIBLIOGRAFÍA

Esparza, I. R. S., Autoabastecimiento Energético por medio de Fuentes Alternativas y Renovables en una Comunidad Rural Tipo, Tésis. Universidad Autónoma de México. México. D.F., 2000.

Eliminación de compuestos orgánicos volátiles: Simulación de un reactor catalítico de lecho empacado para la eliminación total de tolueno

Esparza Isunza T., López Isunza F.
Departamento de Ingeniería de Procesos e Hidráulica, Universidad Autónoma Metropolitana.
CP, 09340 Iztapalapa, México D.F., México.
felipe@xanum.uam.mx

Resumen— Se propone un modelo dinámico que describe a un reactor catalítico de lecho fijo, usado para la oxidación total de Tolueno con una corriente de aire. El problema a resolver es la determinación de los valores de la concentración ($C_{A}o$), y temperatura (To), de alimentación de Tolueno, así como la temperatura de la pared del reactor (Tw); esto, durante una operación no adiabática, de tal forma que el reactor se encienda. Debido a los enormes gradientes de temperatura en el reactor, la solución numérica del modelo se ve complicada por la naturaleza transitoria de la operación al variar C_{AO} y To, ya que el sistema opera en un estado de alta sensibilidad paramétrica, como sucede con las reacciones altamente exotérmicas de oxidación total. Además, durante la operación transitoria, existen perfiles apreciables de temperatura en direcciones axial y radial en el reactor, así como su desplazamiento a lo largo del mismo [1,2]. Por estas razones, es necesario emplear un esquema numérico robusto para la solución del modelo.

Palabras clave— reactor catalítico de lecho fijo, oxidación total de Tolueno

I. INTRODUCCIÓN

Debido a que son un subproducto de diversos procesos industriales, los Compuestos Orgánicos Volátiles (VOC) son los principales contaminantes aéreos. Dado que ellos son muy abundantes en la atmósfera, existe una imperiosa necesidad de reducir su producción y su presencia, eliminándolos de las diversas corrientes gaseosas que los producen. Esto ha llevado al desarrollo de varios tipos de procesos, entre los que se encuentra el que se describe en este trabajo. El proceso consiste en una secuencia de adsorción-reacción para eliminar los VOC, llevándolos hasta su oxidación total (Fig. A). El VOC en estas corrientes se encuentra muy diluido (<500 ppmv), y es necesario concentrarlo para su eliminación por oxidación total. Así, en la primera etapa, la corriente original pasa por una columna de adsorción, hasta saturar la capacidad del adsorbente. En la segunda etapa, el VOC se desorbe utilizando un flujo menor de aire que el de la corriente original, a mayor temperatura, y que se alimenta después al reactor catalítico. Sin embargo, en este proceso, el reactor opera con una alta sensibilidad paramétrica, y dado que las altas temperaturas dentro del reactor podrían dañar de manera irreversible, tanto a este, como al catalizador, es necesario conocer su comportamiento dinámico para implementar sistemas de control seguros y eficientes.

II. METODOLOGÍA

Se desarrolló un modelo pseudo-heterogéneo para el reactor catalítico de lecho empacado, y se utilizó un modelo cinético Redox propuesto por Mars - van Krevelen y publicado por Ordoñez et al [3]. Posteriormente, se resolvió numéricamente el modelo, utilizando el método de Colocación Ortogonal en elemento finito.

El modelo redox de Mars y van Krevelen , describe la oxidación total del Tolueno utilizando un catalizador de Pt soportado en γ-alúmina, el cual funciona en realidad como un catalizador externamente depositado; prácticamente, el interior de este no sería utilizado, debido en primer lugar a la gran exotermicidad de la reacción y, en segundo término, a la enorme resistencia al transporte de calor en la interfase gas-sólido**.** En esencia, se postula lo siguiente para la reacción de oxidación total de Tolueno:

$$R_n = \frac{k_o k_n p_n p_{O2}}{k_o p_{O2} + \nu k_n p_n} \qquad (1)$$

Dónde: ν es el coeficiente estequiométrico para el Oxígeno en la reacción de oxidación total del Tolueno (mol O_2/mol de hidrocarburo).

III. El modelo dinámico del reactor catalítico de lecho empacado

El modelo pseudo-heterogéneo del reactor que se usa en este trabajo se describe a continuación:

A. *Los Balances de Masa y Calor para la Superficie del Catalizador*

Las ecuaciones (2) a (8), que se enumeran en seguida, describen a los balances de calor y masa y las condiciones inicial y de frontera para la oxidación total de Tolueno; estas están en términos de los transportes interfaciales y la reacción superficial en ambos casos; el balance de la fase sólida también considera a las dispersiones axial y radial de calor por el sólido. Estos balances están acoplados a los balances de masa y calor de la fase gas inter-partícula, a través de los transportes interfaciales gas-sólido.

$$\frac{\partial C_{nS}}{\partial t} = k_g a_v (C_{nG} - C_{nS}) - \rho_b S_g R_n \qquad (2)$$

$$\rho_b Cp_S \frac{\partial T_S}{\partial t} = ha_v (T_G - T_S) - k_{efAS}\left(\frac{\partial^2 T_S}{\partial z^2}\right) - k_{efRS}\left(\frac{\partial^2 T_S}{\partial r^2} + \frac{1}{r}\frac{\partial T_S}{\partial r}\right) + \rho_b S_g \sum_i^{NR} (-\Delta H_i) R_i \qquad (3)$$

Las condición inicial y las condiciones de frontera son las siguientes:

A t=0: $C_{ns}(0)=0$ y $T_s=T_{so}$ (4)

en $r = 0$: $$\frac{\partial T_S}{\partial r} = 0 \qquad (5)$$

en $r = R$: $$T_S = Tw \qquad (6)$$

en $z=0$: $$h_O(T_G|_{0-} - T_S|_{0-}) = -k_{efAS}\frac{\partial T_S}{\partial z}\bigg|_{0+} \qquad (7)$$

en $z=L$: $$\frac{\partial T_S}{\partial z}\bigg|_{L+} = 0 \qquad (8)$$

B. *Los Balances de Masa y Calor inter-partícula en el Reactor*

Los balances de masa para la especie *n* y de calor, son:

$$\varepsilon\left[\frac{\partial C_{nG}}{\partial t} + u\frac{\partial C_{nG}}{\partial z} - D_A\left(\frac{\partial^2 C_{nG}}{\partial z^2}\right) - D_R\left(\frac{\partial^2 C_{nG}}{\partial r^2} + \frac{1}{r}\frac{\partial C_{nG}}{\partial r}\right)\right] = \varepsilon k_g a_v (C_{ns} - C_{nG}) \qquad (9)$$

$$\varepsilon\rho C_p\left[\frac{\partial T_G}{\partial t} + u\frac{\partial T_G}{\partial z} - k_{efA}\left(\frac{\partial^2 T_G}{\partial z^2}\right) - k_{eR}\left(\frac{\partial^2 T_G}{\partial r^2} + \frac{1}{r}\frac{\partial T_G}{\partial r}\right)\right] = \varepsilon ha_v (T_S - T_G) \qquad (10)$$

Las Condiciones Inicial y de Frontera de la Fase Fluida Inter-partícula

Inicialmente, en el tiempo t=0, existen perfiles iniciales de concentración y temperatura en el lecho fijo, los cuales pueden considerarse como la condición de arranque del reactor, y que en su forma más general están representados como sigue:

a t=0: $C_{nG}(0,r,z)=C_{nGo}(r,z)$

$T_G(0,r,z)= T_G(r,z)$ (11)

Las condiciones de frontera que se usan aquí, son las de Danckwerts [4] :

en $z=0$: $$uC_{nG}|_{0-} = uC_{nG}|_{0+} - D_A\frac{\partial C_{nG}}{\partial z}\bigg|_{0+} \qquad (12)$$

$$u\rho C_p T_G|_{0-} = u\rho C_p T_G|_{0+} - k_{efA}\frac{\partial T_G}{\partial z}\bigg|_{0+} \qquad (13)$$

en $z=L$ $$\frac{\partial C_{nG}}{\partial z}\bigg|_{L-} = 0 \qquad (14)$$

$$\frac{\partial T_G}{\partial z}\bigg|_{L-} = 0 \qquad (15)$$

Las condiciones de frontera en dirección radial, establecen una situación de simetría (un máximo o un mínimo en el valor de la concentración y temperatura) en el centro del reactor, $r = 0$, y la presencia de paredes impermeables al transporte de masa en la pared del mismo, es decir que el flux es cero cuando $r = R$. Esto se expresa como sigue:

en $r = 0$, y $r = R$: $$\frac{\partial C_n}{\partial r} = 0 \qquad (16)$$

Si el reactor opera de forma no adiabática y no isotérmica, entonces las condiciones de frontera son:

en r = 0: $$\frac{\partial T_G}{\partial r} = 0 \qquad (17)$$

en r= R: $$-k_{efR}\frac{\partial T_G}{\partial r} = h_w\left(T_G - T_w\right) \qquad (18)$$

La ecuación (18) indica que en la pared del reactor, el fluido intercambia calor con la pared del baño de enfriamiento.

El modelo dinámico del reactor de oxidación total descrito por los balances de masa y calor en el gas y en la superficie del catalizador (ec. 2-18), se resuelve numéricamente utilizado colocación ortogonal en elementos finitos [5] en la dirección axial (hasta 50 elementos con cuatro puntos interiores de colocación en cada uno) para describir adecuadamente el movimiento axial de los perfiles de temperatura y concentración; sin embargo, en la dirección radial ha sido adecuado el uso de un solo punto interior. La cinética de oxidación total del tolueno ha sido tomada de la literatura [3]; los coeficientes de transporte de calor y masa han sido calculados usando correlaciones de la literatura, y se ha considerado que las propiedades físicas de las dos fases son constantes.

IV. Resultados y discusión

Las dimensiones del reactor son: longitud=10 cm; diámetro=1.5 cm; diámetro de partícula=0.5 cm; C_{AO}=0.1 a 0.5 % en mol; To=200 a 230 ^oC; Tw=185 a 225 ^oC; flujo=0.5 a 1 Lt/seg; P=1.85 atm (abs).

El primer caso considera la simulación de cambios (arbitrarios) en la alimentación de tolueno proveniente de dos ciclos de desorción, (C_{AO}=0.5 %) como se muestra en la figura 1. La respuesta dinámica a la salida del reactor se muestra en la misma figura 1, donde las respuestas inversas típicas de estos sistemas no lineales se aprecian bien en el intervalo de t=90 a 100 s, justo cuando se suprime, y posteriormente se restablece, la alimentación de tolueno al reactor. La fig.2 muestra la evolución dinámica de los perfiles de temperatura correspondientes a la perturvación de la concentración de la alimentación de la fig. 1.

Fig. 1 Respuestas transitorias de la concentración y temperatura en la fase gas

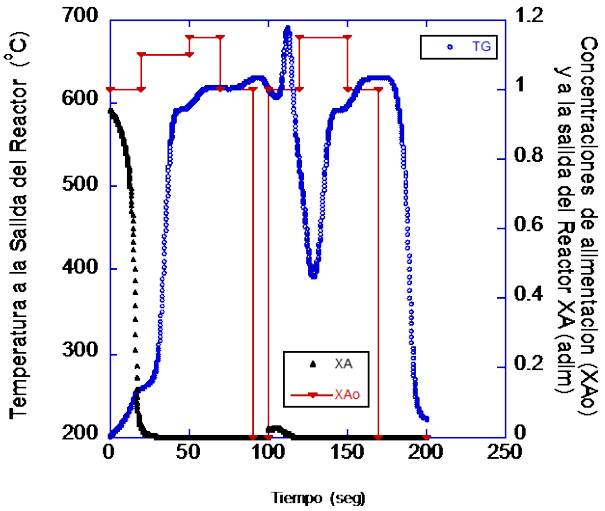

Fig. 2 Evolución de los perfiles de temperatura a la dinámica de la concentración de alimentación

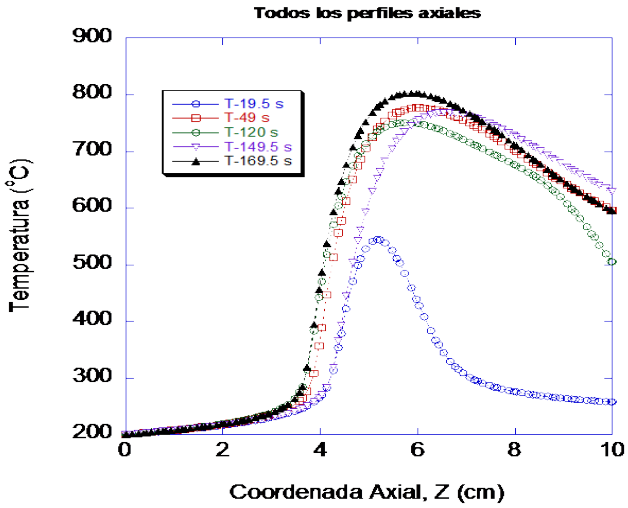

A. La sensibilidad paramétrica del reactor a perturbaciones en las condiciones de alimentación y la multiplicidad de estados estacionarios

En los dos siguientes casos se comparan las respuestas dinámicas del reactor a cambios escalonados en la concentración (C_{AO}) y temperatura (To) de alimentación, para las mismas dimensiones del reactor y temperatura del medio de enfriamiento, solo que C_{A0}=.25, es la mitad del caso anterior. La fig.3 muestra la evolución de los perfiles axiales de temperatura durante el arranque del reactor hasta alcanzar el estado estacionario (la curva T7), lo cual ocurre a los 48 s. Estos perfiles indican lo adecuado del método numérico empleado en su descripción, utilizando 20 elementos finitos, cada uno con 4 puntos interiores de colocación, que corresponde a una longitud efectiva del reactor de 0.5 cm. Por otro lado, las Figs. 4 y 5 muestran las perturbaciones en C_{A0} y T_0 respectivamente, iniciadas 130 s después del arranque del reactor, correspondiente a un tiempo de 70 s después de alcanzado el estado estacionario.

Fig. 3 Evolución de los perfiles de temperatura durante el arranque de alimentación de la fase gas.

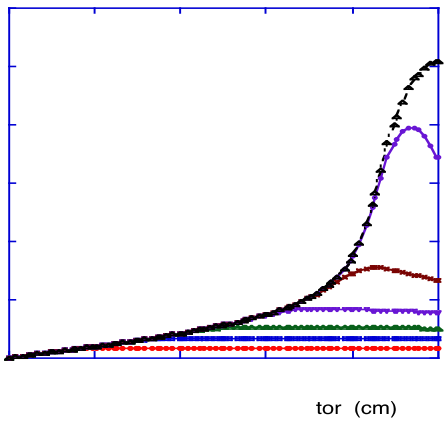

Fig. 4 Perturbaciones en la temperatura del reactor adimensional

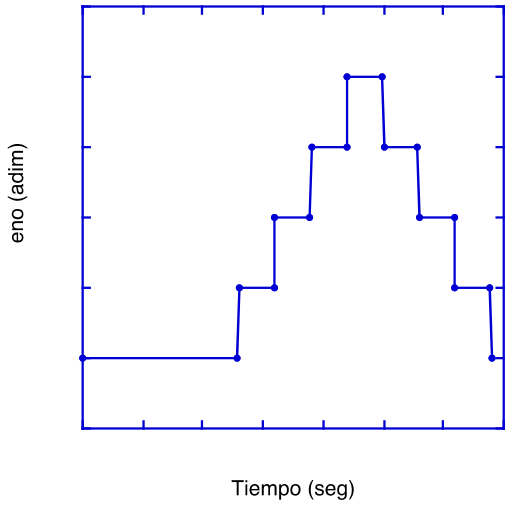

Fig. 5 Perturbaciones en la concentración adimensional de alimentación de la fase gas.

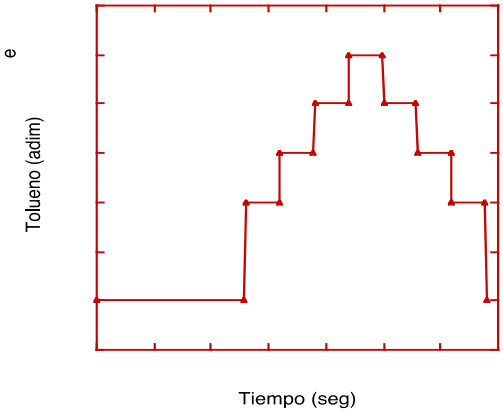

Fig. 6 Respuesta transitoria de la concentración y temperatura en la fase gas a la salida del reactor para perturbaciones en la temperatura de alimentación al reactor (ver figura 4)

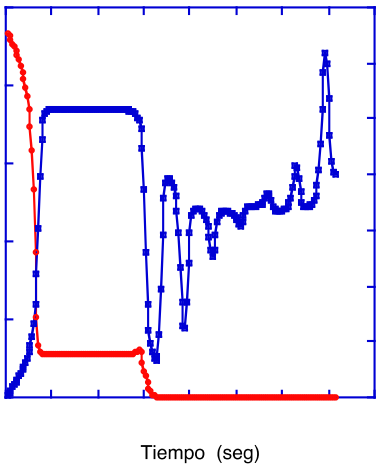

Fig. 7 Evolución de los perfiles axiales de temperatura en el reactor perturbaciones en la concentración de alimentación (ver figura 5).

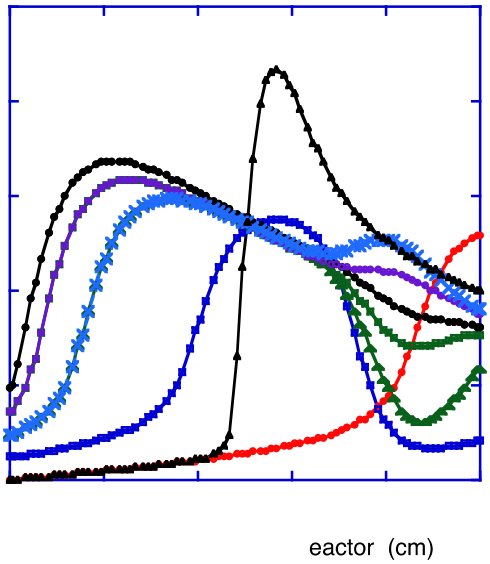

Fig. 8 Evolución de los perfiles de temperatura para perturbaciones en la temperatura de alimentación (ver figura 4).

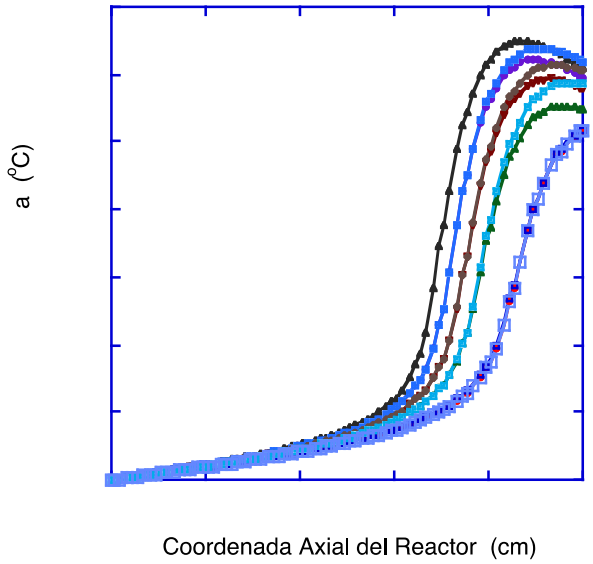

Como se observa en la figura 7, la perturbación en T_0, que regresa a su valor inicial después de 230 seg, ocasiona cambios en el modelo redox y produce dos estados estacionarios (para las mismas condiciones de T_0, C_{A0} y T_W. El perfil T1 corresponde a un estado estacionario, mientras que el perfil T8(cuando el sistema vuelve a su estado original, correspondiente al tiempo final de perturbación de T_0, de la figura 10) corresponde a un estado estacionario diferente. Por otro lado, los cambios en C_{A0} no producen multiplicidad y se llega al mismo estado estacionario inicial, como lo muestra la figura 8 con los perfiles T8 y T17.Todo esto muestra una mayor sensibilidad del reactor a los cambios en la temperatura de alimentación, T_0, que a los cambios en la concentración de alimentación C_{A0}.

Finalmente, se realizó una simulación para encontrar nuevamente la posibilidad de obtener múltiples estados estacionarios cuando la temperatura de alimentación varía de forma reversible.

Las Figuras 9 y 10 muestran los diferentes estados estacionarios (EE) para cada uno de tres valores de las temperaturas de alimentación: 200, 211.8 y 223.7 °C, sin embargo, estos tres EE realmente corresponden a 3 diferentes condiciones de operación, y en estas Figuras realmente se observa que cuando To va de 200 °C a 211.8 °C, y luego hasta 223,7 °C para finalmente regresar de nuevo (después de 600 seg) a 200 °C, se obtiene el mismo EE, por lo que no se presenta ninguna multiplicidad, ya que los perfiles axiales de concentración y temperatura en el reactor (el estado del sistema) son los mismos. De lo anterior, podemos ver que cuando el reactor está sujeto a una perturbación a estas condiciones de operación, no predice ninguna multiplicidad de estados estacionarios. Por último, la Figura 11 muestra la evolución de los perfiles axiales de temperatura durante los cambios en la temperatura de alimentación To, de 200 °C a 211.8 °C, luego hasta 223.7 °C, para finalmente regresar de nuevo (después de 600 seg) a 200 °C. Una ves más, la Figura 18 muestra la eficiencia del método numérico utilizado, el cual describe adecuadamente los cambios dinámicos del perfil axial de temperatura (o movimiento de frentes de reacción) en el reactor.

Fig. 9 Los tres estados estacionarios de perfiles axiales de temperatura para los tres valores de temperatura de alimentación

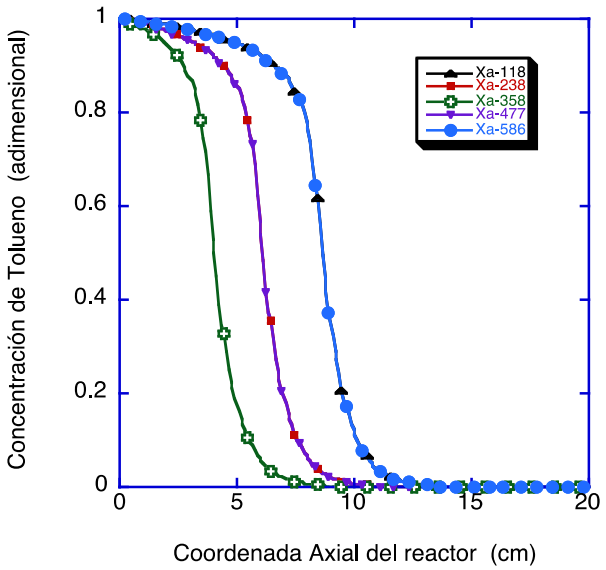

Fig. 10 Los tres estados estacionarios de perfiles axiales de concentración para los tres valores de temperatura de alimentación

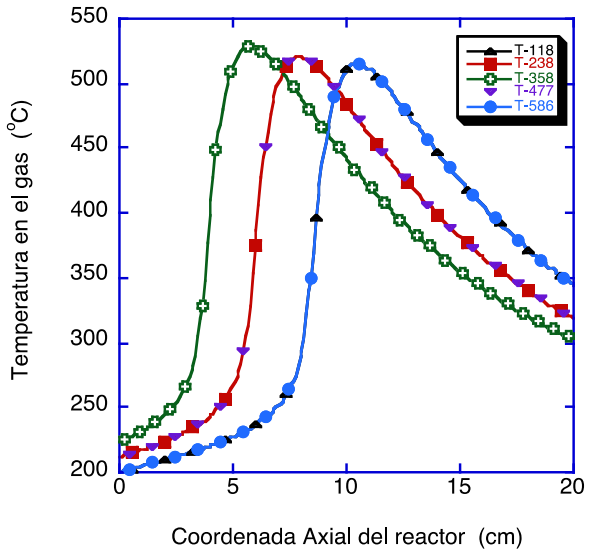

Fig. 11 Evolución de los perfiles axiales de temperatura correspondientes a la simulación del comportamiento dinámico del reactor

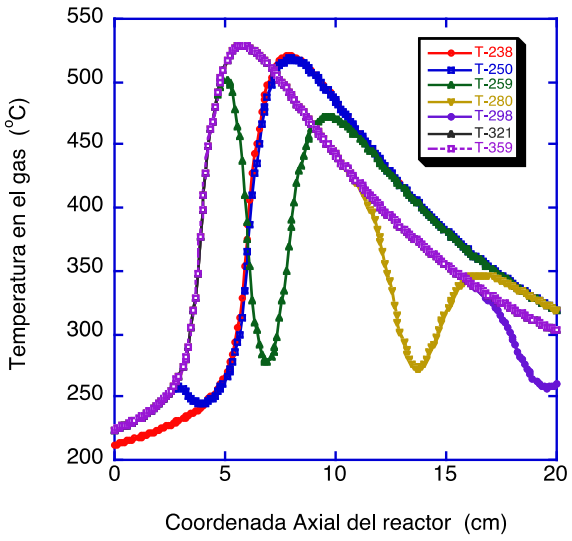

Fig. 12 Sistema de adsorción-desorción-reacción

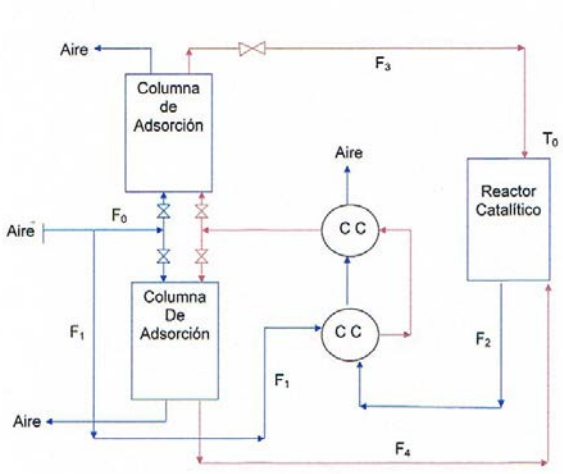

V. Conclusiones

Este trabajo representa una buena aproximación teórico-metodológica para la eliminación de Compuestos Orgánicos Volátiles por la técnica de oxidación total catalítica. Se muestra el comportamiento dinámico de un reactor de oxidación total de Tolueno. Las simulaciones realizadas con el modelo prueban el éxito de un sistema computacional robusto, el cual es capaz de describir la operación del reactor sin que se presenten problemas de estabilidad numérica, como suele suceder en reactores altamente exotérmicos de este tipo. Este modelo puede ser modificado fácilmente en el futuro, para considerar una mezcla de VOC, como las que reportan Barresi y Baldi [6] (Benceno, Tolueno, Etil-benceno, O-xileno y Estireno, y sus mezclas), donde ahora existirían otros problemas asociados con: la "reactividad" de cada compuesto en la mezcla, la determinación de una temperatura de ignición, así como los valores de

los parámetros cinéticos para un esquema redox multicomponente, que son indispensables para la simulación dinámica de este proceso.

REFERENCIAS

1. Young L. C., Finlayson B. A., 1974, Mathematical modeling of the monolith converter, Adv. Chem. Ser. **133** (Chemical Reaction Engineering II), pp. 629-643.
2. Oh S. H., Cavendish J. C., 1982, Transients of monolithic catalytic converters: Response to step changes in feedstream temperature as related to controlling automobile emissions, Ind. Eng. Chem. Prod. Res. Dev. **21**, pp. 43-50.
3. Ordoñez S. at al., 2002, Kinetics of the deep oxidation of benzene, toluene, n-hexane and their binary mixtures over platinum on g-alumina catalyst, **38**, pp 139-149.
4. Dankcwerts, P.V. 1953. Continuous flow systems. Chem. Engn. Sci. **2**, 1-13.
5. Carey G. F. y Finlayson, B.A. Orthogonal Collocation on finite elements. Chem. Engn. Sci. **2**, 1-13, 1977.
6. Barresi A. A., Baldi G., 1994. Deep catalytic oxidation of aromatic hydrocarbon mixtures: reciprocal inhibition effects and kinetics. Ind. Eng. Chem. Res. **33**, 2964-2974.

Technology, urban society and nutritional sustainability for everyone

Loukas Kalarchakis, Oscar Alvarado Nava, Margarita M. González Brambila
Ciencias Básicas e Ingeniería
Universidad Autónoma Metropolitana - Azcapotzalco
México DF, México
mmgb@correo.azc.uam.mx

***Abstract*—this document provides a brief explanation of a way to grow and provide high quality vegetables and at the same time minimize the environmental impact of doing it, by using an embedded system application and organization in cooperatives.**

Keywords—hydroponics; automation; urban garden; social education; sustainability; alternative economies; networking;

I. INTRODUCTION

Hydroponics is a safe and efficient alternative to grow high quality products however, they require specific expertise and great care from the farmers. Benefiting by the current technological developments people can get closer to this type of crops, minimizing the need for the specific knowledge and intensive care required.

This project was conceived by observing the global tendencies for sustainable food production, the vegetable quality, the climate conditions in Mexico City and with the intention to prepare the ground for alimentary autonomy in densely urbanized cities while reducing pollution, through alternative economies and exchange that may spring forth through the organization of producer and consumer cooperative networks.

II. HOW TO ACHIEVE IT

A. *Freeing the user*

Growing in hydroponics as the greek root of the word suggests -"ύδωρ" means water and "πόνος" means labor- is a very demanding way to cultive something, because by artificial means, man tries to emulate an environment where the plans will find the best possible conditions in order to bloom in their most splendid way. The main objective of this project is to take out the laborious part which include the user training and major part of the work on the field. This can be achieved by implementing an application, that can give total independence to the end user from the constant re-adjustment to the optimum conditions that this system needs. This represents more than the 85% of the total workload a crop requires. The user will just have to install the system, maintain it and be alert for a possible disease development.

B. *How it works*

This application is built as an embedded system with a user-friendly interface, that incorporates sensors and actuators by using computational algorithms that create and maintain a specified environment for the plants. This makes growing fully automated. The water is measured through pH and EC (electric conductivity) sensors and is modified to the optimal values by injecting acids, fertilizers and/or water to the tank. Proper liquid level is calculated for the irrigation mix, clean water, fertilizer and acids. Multi-parameter irrigation schedules and root cleansing cycles can be applied easily. Humidity and temperature are measured and adjusted in case of an indoor facility. Data logging function is implemented to facilitate the crop event history and thus availability of the records for any possible use. These records are represented by statistical graphics. The system can be accessed over the Internet using a secure communication protocol and provide the user with configuration options, alerts, calendar and graphic reports. The application can be used with any type of hydroponic system.

C. *From the producer to the consumer*

The organization of the production and making available the products can be made by creating consumer and producer cooperatives. Neighbors from a building or various buildings can form an independent cooperative. Each cooperative shall produce of just one or two products with similar growing specifications. This way the farmers will just have to learn some very few details about plague prevention and how to combat them on the plant they grow. By that expertise to the only part that is not yet automatic, can be achieved easily and since there will be various cooperatives growing diverse vegetables in the area, between them they can exchange products so that everybody can have access to different varieties without any extra cost or know-how. These cooperatives can provide their products directly their

members, sell them or exchange them with consumer cooperatives.

D. Social Benefit

The social benefits from such organization are very important since people shall have better quality vegetables, create and maintain a capital which can be used to finance similar projects and improve the local area income by taxation. People involved to cooperatives, shall learn how to work in a group, try to achieve common goals within it, intensify their interest about their nutrition and their environment. This cooperative model can be applied to every building has space to host it a garden and/or a shop to sell the products and can create working positions even for people with poor education or physical capabilities.

Environmental Benefit

Environmentally, the benefits of such application are very important due to the fact that there are no gas emissions involved for the transportation of the product to the final consumer. Apart from that, since no chemical fertilizer is used on the earth, no toxic accumulations are made so there is no leaking to natural deposits, aquifers, lakes, rivers and the sea.

III. WHY TO USE IT

By using this application, the prospect of a healthier way of life combining less environmental pollution, job creation and local economic benefits, do not depend on specific knowledge nor extensive physical labor in order to achieve it.

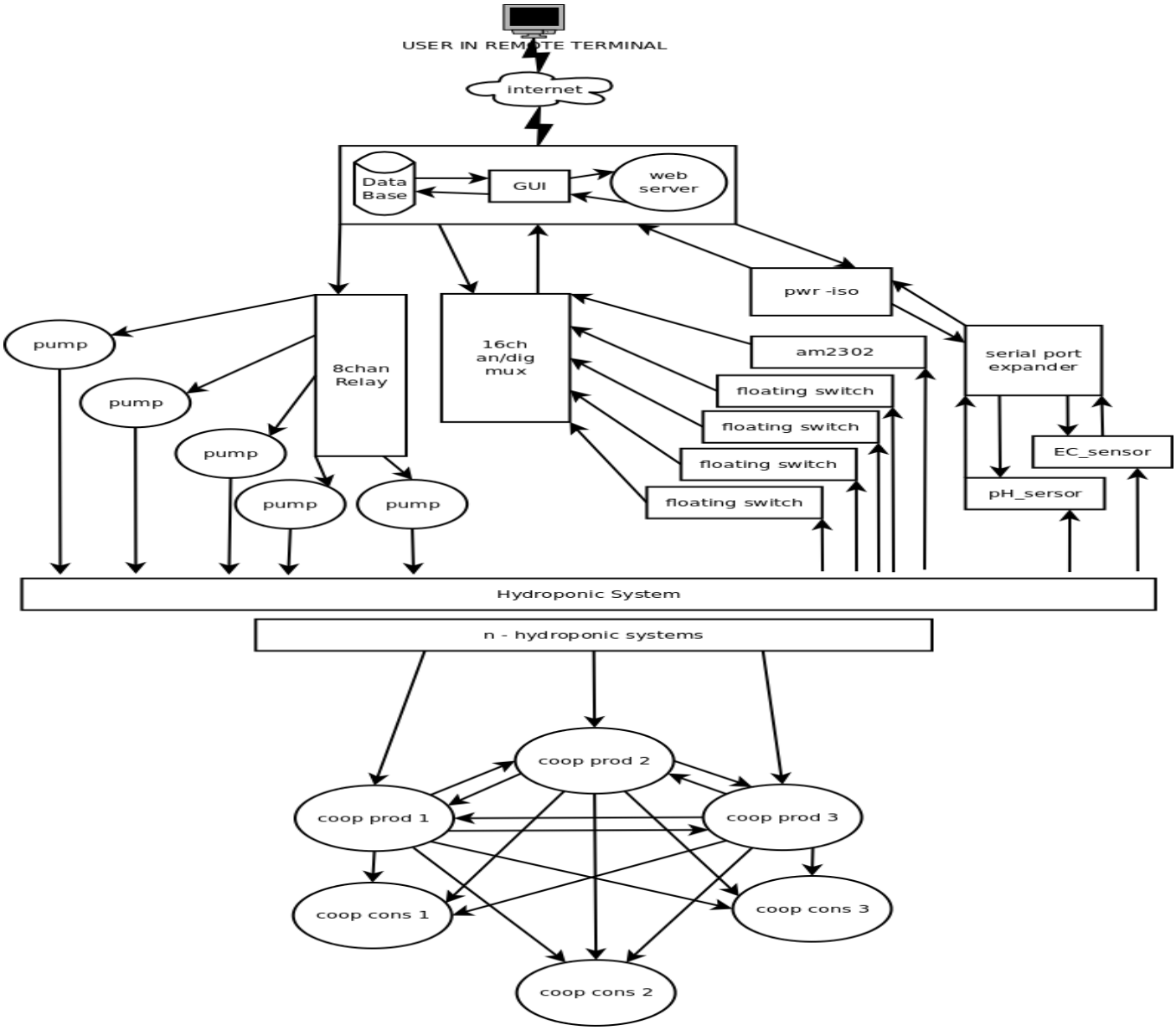

REFERENCES

[1] Infocir, “Hidroponia: Altos Rednimientos en el cultivo de hortalizas”, No.2 Vol 1 , México, 2005

[2] Esteban Favela Chávez, Pablo Preciado Rangel, Adalberto Benavides Mendoza, “Manual para la preparación de soluciones nutritivas”, Universidad Autonoma Agraria Antonio Narro, Coahuila, 2006

[3] Carlos Baixauli Soria,José M. Aguilar Olivert , “Cultivo sin Suelo de Hortalizas ”, Generalitat Valenciana, Valencia, 2002

[4] Mark Mitchell, Jeffrey Oldham, Alex Samuel , “Advanced Linux Programming ”, New Riders Publishing , 2001

[5] Eric Freeman Elisabeth Freeman,Kathy Sierra, Bert Batesl , “Head First Design Patterns ”, O'Reilly, 2004

[6] SAGARPA,”¿De donde viene mi comida?”, SIAP, 2012

[7] Cámara de Diputados del H. Congréso de la Unión, “Ley General de las Sociedades Cooperativas”, Secretaria General, 2009

Índice de autores/Author Index

A

Aguado Sánchez, Octavio, 393
Aguilar Anastacio, José Carlos, 406
Aguilar Osorio, Rita, 236
Aguilar López, Ricardo, 12, 308
Alcántara Alza, Víctor, 280
Alonso, Alejandro, Gómez, 185, 221
Alonso Piña, Ernesto, 49
Altamirano Segovia, Norma E., 413
Alvarado Morales, Merlín, 227
Alvarado Nava, Oscar, 469
Álvarez, Gilberto, 115
Álvarez Macías, Carlos, 266
Álvarez Castañeda, William Fernando, 160
Anzelmetti Zaragoza, Juan C., 90
Aquino Ch., E., 254
Arancibia Bulnes, Camilo Alberto, 164
Araujo Vargas, Ismael, 66
Ariza Ortega, José Alberto, 84
Armenta, Pedro, 355
Avalos Farfán, Sandra, 227
Avalos Islas, M. C., 430
Ayala Ahumada, Vicente, 224, 424

B

Barbosa Saldaña, Juan Gabriel, 1
Barrera Calva, Enrique, 49, 266
Barthram, Thomas, 96
Bautista Rodríguez, Celso Moisés, 200
Bonilla Blancas, Wenceslao, 404

C

Calvino, Marbella, 60

Campos Guzmán, Eneida, 346
Cardona Alzate, Carlos Ariel, 121
Carmona Cuevas, Edgar, 200
Carvajal, Eliel, 60, 139, 243, 292
Carvajal Mariscal, Ignacio, 154
Castillo Araiza, Carlos Omar, 44, 180, 398
Castillo Jimenez, V., 191
Castillo Rodríguez, Julio Cesar, 180
Castro Montoya, Agustín Jaime, 121, 440
Cervantes Jáuregui, Jorge, 143
Chávez Mendoza, Pablo Arturo, 424
Chávez, Sandra, 326
Chávez Sandoval, Blanca Estela, 413
Che Galicia, Gamaliel, 44
Chicurel, Ricardo, 382
Colín Luna, José Antonio, 49, 185, 319, 386, 410
Colorado Garrido, Darío, 254
Conde Rogelio, David, 435
Contreras, Ernesto Enciso, 1
Contreras, J. L., 271
Contreras Rascón, Jorge I., 84
Cortés, Domingo, 248, 393
Crisóstomo, Margarita C., 60, 139, 292
Cruz González, Daniel, 200
Cruz-Irisson, Miguel, 60, 139, 243, 292, 435

D

De Cruz, Mauricio, 7
De la Concha, Aarón D., 221
De la Cruz Ávila, Mauricio, 148
Del Ángel Ramos, Jorge Arturo, 134
Del Muro Cuéllar, Basilio, 54, 169
Díaz Reyes, Joel, 84
Dutta, Abhishek, 44

E

Enríquez Poy, ManuelA, 227
Esparza Isunza, R. S., 457
Esparza Isunza, T., 457, 462

Espinoza Tapia, Julio César, 49

F

Farías Sánchez, Juan Carlos, 440
Flores Altamirano, V. M., 224
Flores Rodríguez, Julio, 31
Fuentes, G. A., 271

G

Galindo Pérez, Ezel Jacome, 413
Gamiño Arroyo, Zeferino, 227
García Cortés, Daniel, 185
García Franco, F., 413
García García, Blanca A., 121
García Sánchez, Ignacio, 80
García Velázquez, Mijaíl, 331
Gerling Garza, Luciano Augusto, 109, 214
Gómez Castro, Fernando I., 227
González, Alejandro, 382
González Avilés, Mauricio, 39, 297
González Brambila, Margarita M., 185, 275, 346, 386, 398, 410, 413, 469
González G., Federico, 266
González Reyes, I., 319
Gordon, Manuel, 129, 196, 208
Güin Morales, Lili Beth, 336
Gutiérrez, Víctor Javier, 174
Gutiérrez Eudave, Alex, 331
Gutiérrez Torres, Claudia Del Carmen, 1
Guzmán Gil, Raymundo, 275
Guzmán Castillo, Miguel, 404

H

Haro, Catalina, 221
Hernández, Germán, 169
Hernández, Máximo, 174
Hernández, Sergio A., 160
Hernández Aguilar, Eduardo, 336
Hernández Martínez, Isaí, 336

Hernández P., Carlos., 266
Hernández Pérez, Isaías, 49, 319
Hernández Pérez, Miguel Ángel, 54
Hernández Villa, Norma Gabriela, 346
Herrera Gallardo, Brenda E., 386, 410
Herrera Romero, José Vidal, 254

I

Iturrios, María Isabel, 60, 139, 292

J

Jarquín López, Guillermo, 7, 16, 322
Jiménez, Homero, 115
Jiménez Bernal, José Alfredo, 1
Juárez Cervantes, José Dolores, 224, 424
Juárez Morán, Luis Alberto, 84

K

Kalarchakis, Loukas, 469

L

Lara Guzmán, Laura Carolina, 322
Lara Valdivia, Araceli, 31, 129, 196, 208
Lizardi Ramos, Arturo, 31, 129, 326, 331
López Arroyo, Mónica, 191
López Callejas, Raymundo, 31, 129, 326, 331
López Isunza, Felipe, 44, 462
López Meraz, Raúl Alberto, 134
López Pérez, Pablo A., 308
López Sosa, Luis Bernardo, 39
López Yáñez, Adrián, 357
Luna, R. 271

M

Madrigal, Manuel, 174
Maldonado, Susana, 129, 196, 208
Mar Juárez, Elizabeth, 285, 375

Marquina Chávez, Alejandro, 90
Martínez de Jesús, G., 185
Martínez Delgadillo, S. A., 430
Martínez-Rendón, Laura, 22
Martínez de Jesus, Gastón, 185
Martínez Huitle, Uriel Alejandro, 236
Martínez Tejada, Laura Alejandra, 160
Martínez Muñoz, J. Salvador, 386, 410
Medina, Yadir Fernando, 160
Mejías, Nildia, 355
Melo González, Rafael, 302, 336
Molina Gómez, Jimena, 214
Montejo Ehuán, M. A., 148
Montesinos Castellanos, Alejandro, 109, 214
Montoya Bautista, Claudia-Victoria, 350
Morales Máximo, Mario, 297
Morales Gómez, Juan, 326
Morales Mora, M. A., 430
Morales Pérez, Ariadna, 350
Morales Rodríguez, Ricardo, 227
Muhl, Stephen, 236

N

Naranjo Castañeda, Félix Antonio, 413
Navarro, David, 248
Navarro Soto, R., 148
Novella, D. F., 169
Núñez Correa, Sara, 254
Nuño L., 271

O

Ocampo Gaspar M., 315, 319
Olmedo Wooder, Abdiel, 404
Ortega García, Felipe De Jesús, 285, 375
Ortiz, M. A., 271
Osorio Mirón, Anselmo, 302, 336
Osorio Vega, Andrea, 331
Otero López, Martha, 398

P

Páez García, C. T., 74
Payan Martínez L. F., 315, 319
Perales Llanos, Milka Marina, 453
Perdomo Hurtado, Felipe Antonio, 435
Pérez Cisneros, Eduardo S., 227
Pérez Díaz, Oscar, 27
Pérez Hernández, Erick Mauricio, 393
Pérez López, Luis Antonio, 243
Pérez Pastenes, Hugo, 254, 302
Pilo, Jorge, 139
Pineda Pimentel, M. G., 440
Plascencia Espinosa, Miguel Ángel, 448
Polupan, Georgiy, 7, 16, 148, 322
Ponciano, José Nicolás, 174
Pretelín Vergara, C., 430
Puebla Núñez, Héctor, 308, 386
Puerta Huerta, P., 224

Q

Quintana B., 271
Quiroga González, Enrique, 27
Quiroz Ramírez, Juan José, 367

R

Ramírez Muñoz, Jorge, 185, 221, 357
Ramírez Márquez, Cesar, 143
Ramírez Sabag, Jetzabeth, 398
Ramírez Zamora, Rosa-María, 350
Reyes, Roberto Carlos, 174
Reyes Grajales, Luis Miguel, 302
Reyes Santiago, Guillermo, 16
Rivera Blanco, Carlos O., 419
Rivera Solorio, Carlos Iván, 96, 103
Rodarte Gutiérrez, Francisco Emilio, 66
Rodríguez Gómez, Divanery, 227
Rodríguez Guerrero, J. M., 224
Rodríguez Hernández, Ingrid Nayeli, 302

Rojas Chávez, Freddy Jesús, 453
Romero Paredes Rubio, Hernando, 164, 191
Romo Rico, Daniel, 22
Rosas, J. L., 292
Rosas C., Ricardo, 266
Ruiz Font, Angélica, 389
Ruiz Martinez, Richard Steve, 44, 180

S

Salazar, Araceli, 129, 196, 208
Salazar Posadas, Fernando, 243
Salmones, J., 271
Samarti Ríos, Lissette, 227
Sánchez C., Elisa, 266
Sánchez Rosas, Teresa De Jesús, 49
Sánchez Morales, Maribel, 227
Sánchez Ramírez, Eduardo, 367
Sánchez S. 129
Sánchez Silva, Florencio, 154
Saucedo Luna, Jaime, 121
Segovia Hernández, Juan Gabriel, 143, 367
Serrano Rodríguez, Moisés, 7, 148
Servín Campuzano, Hermelinda, 297
Silva González, Nicolás Rutilo, 27
Solís López, Myriam, 350
Solís Correa, Hugo, 275
Suárez Parra R., 315, 319

T

Tagle Salazar, Pablo, 103
Tapia Medina, Carlos R., 386
Tapia, C., 271
Teodoro Cristóbal, Rigoberto, 154
Tepale Ochoa, Nancy, 200
Terres Peña, Hilario, 31, 129, 196, 208, 326, 331
Toledo Toledo, Fernando, 224, 424
Torres Domingo, 174
Trejo, Alejandro, 60
Trejo Estrada, Sergio Rubén, 389, 448

Tzompantzi Flores, Clara, 180

V

Vaca Mier, Mabel, 31, 326, 331
Valadez Pelayo, Patricio Javier, 164
Valdés Parada, Francisco J., 74
Valle Hernández, Julio, 191
Vargas Santillán, Alfonso, 440
Vázquez Vázquez, Carlos, 80
Vázquez, Nimrod, 248
Vázquez Medina, Rubén, 139, 435
Velasco Bedrán, Hugo, 346
Velázquez Lira José D., 355
Velázquez Sánchez, Hugo Iván, 308
Villafan Vidales, Heidi Isabel, 164
Villagrán Villegas, Luz Y., 90
Villa Ramírez, María Del Sugeyrol, 389, 448

Z

Zamora Mata, Juan Manuel, 357
Zeifert, B., 271